Civil Engineering Research Association of Ireland

www.cerai.net

Proceedings

28-29 August 2014



Civil Engineering Research Association of Ireland

Proudly presents

Civil Engineering Research in Ireland

CERI 2014

Hosted by

The Queen's University of Belfast



Editors:

Sreejith Nanukuttan

Jamie Goggins

Assistant Editors:

Ken Gavin

Vikram Pakrashi

Alan O'Connor

Paul Archbold

Bryan Magee

Published in 2014
ISBN 978-0-9573957-0-2

Published by
Civil Engineering Research Association of Ireland

© Copyright Declaration
All rights of papers in this publication rest with the authors.

This publication is part of the proceedings
of the Civil Engineering Research in
Ireland conference held at Queen's University Belfast,
Northern Ireland, on 28-29 August 2014.

Copies of these proceedings are available from:

Dr. Mark Russell
School of Planning, Architecture and Civil Engineering
David Keir Building
Stranmillis Road,
Queen's University Belfast
Belfast, BT9 5AG,
Northern Ireland

Papers are also available via the conference portal; for access visit www.cerai.net

Website and conference engine by
Ex Ordo www.exordo.com

Organising Committee Members 2014

President:	Alan O'Connor		Trinity College Dublin
Chair:	Sree Nanukuttan		Queen's University Belfast
Vice Chair:	Jamie Goggins		National University of Ireland Galway
Secretary:	Bryan Magee		Ulster University Jordanstown
Treasurers:	Roger West		Trinity College Dublin
	Mark Russell		Queen's University Belfast
Ex Officio:	Des Walsh		Cork Institute of Technology
	Roger West		Trinity College Dublin
	David Cadogan		Cork Institute of Technology
Theme leaders	**Geotechnics**	Ken Gavin	University College Dublin
	Structures	Vikram Pakrashi	University College Cork
	Bridges	Alan O'Connor	Trinity College Dublin
	Concrete	Paul Archbold	Athlone Institute of Technology
Members with independent responsibilities	Muhammed Basheer		Queen's University Belfast
	Giuseppina Amato		Queen's University Belfast
	Niall Holmes		Dublin Institute of Technology

Scientific Committee Members 2014

Aidan Duffy	Dublin Institute of Technology
Albert Daly	National Roads Authority
Annette Harte	NUI Galway
Bernard Enright	Dublin Institute of Technology
Brian Broderick	Trinity College Dublin
Brian O'Rourke	Cork Institute of Technology
Brian Solan	University of Ulster
Bryan Magee	University of Ulster
Ciaran McNally	University College Dublin
Daniel Cantero	ROD-IS Consulting Engineering

Daniel McCrum	Queen's University Belfast
David Cadogan	Cork Institute of Technology
David Cleland	Queen's University Belfast
David Gill	AGL Consulting
David Hester	Queen's University Belfast
David Holleran	Oran Precast
David Igoe	University College Dublin
David Porter	Rivers Agency
David Woodward	University of Ulster
Dermot O'Dwyer	Trinity College Dublin
Des Robinson	Queen's University Belfast
Des Walsh	Cork Institute of Technology
Donal Ryan	University of Ulster
Eammon Cannon	Independent Consultant
Eanna Nolan	Irish Cement
Eric Farrell	Trinity College Dublin
Gary Raftery	University of Auckland
Giuseppina Amato	Queen's University Belfast
Jacek Kwasny	Queen's University Belfast
Jack English	AECOM, New Zealand
Jamie Goggins	NUI Galway
John Justin Murphy	Cork Institute of Technology
Ken Gavin	University College Dublin
John McRobert	Roads Service Northern Ireland
Kieran Owens	Price waterhouse Coopers
Marios Soutsos	Queen's University Belfast
Martin Mannion	Cork Institute of Technology
Michael Creed	University College Cork

Michael Minehane	RPS Consulting Engineers
Mike Long	University College Dublin
Mohammed Sonebi	Queen's University Belfast
Niall Holmes	Dublin Institute of Technology
Niamh Power	Cork Institute of Technology
Padraic O'Donoghue	NUI Galway
Patrick McGetrick	Queen's University Belfast
Paul Archbold	Athlone Institute of Technology
Paul Quigley	Arup Consulting Engineers
Peter Deegan	Banagher concrete
Peter Flynn	Arup Consulting Engineers
Peter Seymour	Ecocem
Roger West	Trinity College Dublin
Sara Pavia	Trinity College Dublin
Sarah Prichard	Burohappold
Shane Newell	Galway-Mayo Institute of Technology
Siva Vinayagamoothy	Queen's University Belfast
Sree Nanukuttan	Queen's University Belfast
Suhaib Salawdeh	NUI Galway
Tom Casey	National Roads Authority
Tom Cosgrove	University of Limerick
Vikram Pakrashi	University College Cork
William Finnegan	NUI Galway

This conference is kindly supported by the following organisations:

Gold Sponsors

Roughan & O'Donovan Consulting Engineers
www.rod.ie

Cement Manufacturers Ireland
www.cement.ie

CPD & Members discount provided by

Engineers Ireland

www.engineersireland.ie

Silver sponsors

Netzsch

www.netzsch.com

Polytec

www.polytec-ltd.co.uk

Zwick

www.zwick.co.uk

Controls

www.controlstesting.co.uk

Irish Concrete Society

www.concrete.ie

Student Prizes Sponsored by

Institution of Civil Engineers

www.ice.org.uk

Northern Ireland Concrete Society

www.concrete.org.uk

Conference reception supported by

Preface

We are delighted to welcome you all to the first Civil Engineering Research in Ireland conference and to the lovely city of Belfast. This is the first major event organised by the Civil Engineering Research Association of Ireland (CERAI) since its inception in 2012. CERAI was formed for the purpose of promoting and communicating civil engineering research and practice in Ireland to academics and practitioners alike. The breadth of topics covered at this conference reflects positively on the strength of civil engineering research in Ireland and we are confident going forward that the Association and this conference series will be able to further strengthen the link between research and practice and that many research projects can be identified for technology transfer to end users.

We received over 80 papers on a wide range of topics including asphalt, bridges, cement, concrete, computational methods, durability, geotechnics, hydraulics, structures and timber. Additionally, there are keynote papers from eminent scholars on Bridge maintenance, offshore Structures, offshore Geotechnics and making an impact with Concrete. We hope the conference will become an opportunity to kindle and strengthen relationships, encourage and invigorate minds, promote and nurture budding researchers, establish good practice in research as well as strengthen research ethos in all participants.

A special feature of this conference series is the emphasis placed on student participation. All student papers have been entered into 'Best Student Paper' competitions from our 4 main themes. The prizes will be allocated based on quality of the original paper and an assessment of the presentation given at the conference.

We offer our appreciation to Mr. Barry Colford, Prof. Alistair Borthwick, Prof. Bob Gilbert and Dr. Roger West, our four keynote speakers, for taking time off their busy schedule to share their expertise and opinions with us.

On your behalf, we also extend our thanks and appreciation to the members of the Scientific Committee. Over the past 6 months, they generously gave of their valuable time and expertise to review the papers in order to ensure quality and rigour.

We are extremely grateful to Queen's University Belfast for facilitating this event. In particular, the committee wish to thank Prof. Trevor Whittaker, Head of School of Planning, Architecture and Civil Engineering, and administrative staff Ms. Fionnuala Lavery, Ms. Andrea Fordham and Ms. Carole Maslowski. Several of our post graduate students played a major part in coordinating this conference, our sincere thanks to their effort.

Special thanks are also due to the Paul Killoran, James Field Corbett and Dermot Lally of Ex Ordo for developing the CERAI website and making the conference organisation less painful with their conference engine.

We are most grateful to our sponsors: Belfast City Council, Cement Manufacturers Ireland, Controls Testing Ltd, Engineers Ireland, Institution of Civil Engineers, Irish Concrete Society, Netzsch, Northern Ireland Concrete Society, Polytec,Ltd, Roughan & O'Donovan and Zwick Testing Machines Ltd. Without their kind and generous support it simply would not be possible to deliver the conference to the same quality and value. The sponsorship ensures that the association can deliver its promise to encourage and support young researchers.

A core group of people, the Organising Committee, worked tirelessly over the last two years to bring this conference to you. We acknowledge their dedication and commitment to our new venture and thank them sincerely for their efforts.

Finally, we would like to thank all authors for their valued contributions and for responding so well to the various deadlines imposed by the organisers. We simply dedicate the proceedings to all of the authors. We hope the Proceedings will be of interest and use to all and will be a good reference to both researchers and practising engineers.

Dr. Sree Nanukuttan,
Dr. Jamie Goggins,
Chairs, CERI 2014

4th Joe O’Donovan Memorial Keynote Lecture

Maintenance of the Forth Road Bridge 1
B. Colford

Keynote Lecture

Large Events in Waves on the Continental Shelf 7
M. R. M. Haniffah, P. H. Taylor, C. Swan, V. Katsardi, A. Borthwick

Bridge I

Managing Ireland's National Road Bridges 15
L. Duffy
Administration of Abnormal Vehicles in Ireland 21
R. Corbally, A. O'Connor, F. Cahill, A. Daly
Seismic Testing and Analysis of the FlexiArch™ 27
C. McCracken, S. Taylor, P. McNulty, M. Lydon, D. McCrum, D. Robinson
Probabilistic Analysis of Potential Impact of Extreme Weather Events on Infrastructures 33
A. O'Connor, E. O’Brien, D. Hajializadeh
The Full Potential of Energy Harvesting from Train Induced Responses in Bridges 39
P. Cahill, N. Jackson, A. Mathewson, V. Pakrashi
Design of scaled bridge prototype for energy harvesting testing 45
P. Cahill, G. Amato, N. Jackson, A. Mathewson, V. Pakrashi
Parameter Importance Measure Studies on Prestressed Concrete Bridges in Ireland 51
C. Hanley, V. Pakrashi
A study of transverse load distribution in masonry arch bridges 57
H. Dunne, J. J. Murphy, K. Ruane

Timber

Irish Timber – Characterisation, Potential and Innovation 63
A. Harte, D. McPolin, K. Sikora, C. O'Neill, C. O'Ceallaigh
Life Cycle Assessment of Sawn Timber Produced from Irish forests 69
D. Dolan, A. Harte
Multi-storey construction in Timber 75
A. Harte, C. Glennon
Structural Performance of Timber Connections 81
D. Coleman, J. J. Murphy
Bond quality of cross-laminated timber from Irish Sitka spruce 87
K. Sikora, A. Harte, D. McPolin
Post-Tensioning of Timber Beams with Steel Rods 93
E. McConnell, D. McPolin, S. Taylor

Mechano-sorptive Creep of FRP Reinforced Laminated Timber Beams 99
C. O'Ceallaigh, A. Harte, K. Sikora, D. McPolin
Influence of embedded length of BFRP rods bonded parallel to the grain of low grade timber by pullout-bending tests 105
C. O'Neill, D. McPolin, S. Taylor, A. Harte

Bridge II

A Bayesian Approach For Estimating Characteristic Bridge Traffic Load Effects 111
B. Enright, C. Leahy, E. O'Brien
Allowing for a Rocking Datum in the Analysis of Drive-By Bridge Inspections 117
J. Keenahan, E. O'Brien
Dynamic amplification factor of continuous versus simply supported bridges due to the action of a moving load 125
O. Mohammed, D. Cantero, A. González, S. A. Al-Sabah
Monitoring of Structural Performance 131
D. Hester, J. Brownjohn
Probabilistic-Based Modelling and Assessment of a Steel Truss Railway Bridge 137
A. O'Connor, L. Connolly, M. Ní Choine

Materials I

Development of a Geopolymer Binder from the Interbasaltic Laterites of Northern Ireland 143
J. McIntosh, M. Soutsos
Chloride ingress through alkali activated slag concretes 149
M. Basheer, Q. Ma, S. Nanukuttan, Y. Bai, C. Yang
Characterisation of Irish sandstones used for building 155
P. Kissane, S. Pavia, O. Kinnane
The influence of heat transfer and storage in structural precast building components on indoor environments 161
M. Hajdukiewicz, J. Goggins
Thermo-mechanical fatigue in power plant steels: Enhanced numerical modelling with experimental validation 167
P. O'Donoghue, R. Barrett, S. Scully, S. Reape, C. Hyde, S. Leen

Bridge III

Statistical Analysis of HGV Bridge loading for a DBFO scheme Using Northern Ireland (NI) Weigh-In-Motion (WIM) Data 173
C. Doherty, A. Heanen, S. Taylor, D. Cleland, M. Lydon
BridgeMon: Improved Monitoring Techniques for Bridges 179
P. Favai, E. O'Brien, A. Žnidarič, H. van Loo, P. Kolakowski, R. Corbally
Development of a new generation Bridge Weigh in Motion System 185
M. Lydon, S. Taylor, D. Robinson, C. Doherty
Next generation Structural Health Monitoring using Wireless Sensor Network Technology 193
B. O'Flynn, H. Woershing, D. Boyle

Application of output-only modal method to the monitoring of bridges using an instrumented vehicle 199
A. Malekjafarian, E. O'Brien

Materials II

Ceramic Waste Sludge as a Partial Cement Replacement 205
F. Kenna, P. Archbold
Impact of hydration in the properties of lime hemp concretes made with commercial binder 211
R. Walker, S. Pavia
A study on cement grout rheology: Optimum dosage of SP related to their composition and interaction with mineral additions 217
E. García-Taengua, M. Sonebi, S. Taylor, L. Ferrara, P. Deegan, A. Pattarini
An assessment of some properties of Roman cement 223
S. Pavia

Testing, Monitoring & Modelling

Real time monitoring and performance of retaining structures 229
E. Baily, B. McCabe, J. Goggins, P. Kieran
The Use of 3D Laser Scanning Technology for Bridge Inspection and Assessment 235
M. Minehane, R. O'Donovan, K. Ruane, B. O'Keeffe
Underwater Imaging Research and Implementation on Bridges and Marine Infrastructure 241
T. Browne, T. Collins
The hydraulics and resulting bed scour within the vicinity of Submerged Single Span Arch Bridges 247
D. Ryan, G. Hamill, J. McRobert, W. Smyth
Numerical simulation of fluid flow around an array of cylinders at low Reynolds number 253
W. Finnegan, J. Goggins
Contact Mechanics for Fretting in Flexible Marine Risers 259
S. O'Halloran, A. Connaire, S. Leen, A. Harte

Materials III/Durability

A Comparison of Techniques to Determine Surface Texture Data 265
G. McQuaid, P. Millar, D. Woodward
Bond Coats and Asphalt Durability under Cyclic Freeze Thaw Conditions 273
P. McManus, D. Woodward, A. Strong
Development of a Method to Predict the Durability of Warm Mix Asphalt 277
K. Kennedy, D. Woodward, R. Mitchell, P. Millar
Non-contact evaluation of geometric properties of highway surfacing materials 283
P. Millar, D. Woodward, G. McQuaid
The Performance of a Cathodic Protection System in Reinforced Concrete Structure: Monitoring and Service Life Modelling 289
C. Ward, S. Nanukuttan, J. McRobert

A New Performance Based Method for Design and Maintenance of Reinforced Concrete Structures 295
C. Green, S. Nanukuttan, M. Basheer

Keynote Lectures

Opportunities for Innovation in Offshore Geotechnical Engineering 301
R. B. Gilbert, D. Bruton
Concrete – Making an Impact 303
R. West

Structural Concrete I

Ultimate Structural Capacity of Very High Dosage Steel Fibre Concrete Beams and Slabs 311
A. Donnelly, R. West, A. K. Mohammed, M. Grimes
Effect of fibre type and dosage on early tensile strength of high performance mortar 317
J. Backus, M. Sonebi, T. Moore, D. Hughes
Real-time monitoring of a hybrid precast and insitu concrete flat slab system 321
J. Goggins, S. Newell, D. King, M. Hajdukiewicz
Impact Resistance of High-Dosage Steel Fibre Reinforced Concrete Slabs 327
R. West, M. R. Dousti
Strength and Deformation Characteristics of Concrete Containing Recycled Aggregates Fines 333
D. Collery, P. McKenna, D. Dunne, K. Paine

Geotechnics I

Assessing the reliability of pile driveability predictions from wave equations 339
E. Farrell, D. Gill, N. Farrell
Finite element analyses of the installation of offshore foundations 345
S. Fallah, K. Gavin
Reassessing Foundation Reuse Assessment Tools 351
D. Laefer, K. Farrell
Soil nailing optimisation: lost opportunities in current practice 357
D. Laefer, C. McGroarty, O. O'Murchu
The Effect of Scour on the Dynamic Response of an Offshore Wind Turbine 363
L. Prendergast, K. Gavin, P. Doherty

Structural Concrete II

Mechanical Resistance Characteristics of GGBS Concrete in Fire 367
T. McKenna, M. Richardson, B. O'Rourke
Shear Behaviour of Precast Prestressed Hollowcore Slabs 373
C. Twomey, B. O'Rourke, D. Hodge

The Behaviour of Connections in Segmental Precast Concrete Pile Systems 379
E. Causer, K. Ruane
Shear Capacity of Insulated Precast Concrete Façade Panels 385
O. Kinnane, R. West, M. Grimes, J. Grimes
An Investigation into the Capabilities of Design Codes to Determine the Load Capacities of RC Deep Beams 391
D. Shinnick, D. Walsh, K. Ruane

Geotechnics II

The Overconsolidation Ratio of the Dublin Port Clay 397
D. Gill, E. Farrell
A novel triaxial testing procedure to model the action of lubricants in pipe jacking 403
C. Reilly, T. Orr
A systematic review of common correlations between unconfined compressive strength and point load index for Dublin calp Limestone 409
P. Casey, M. Fleming
Some geotechnical characteristics of a soft soil deposit along the Foyle Valley 415
P. Quigley, M. Long, S. Solera, D. Raynor, C. Ruta
Implications of geometrical variations on the pull-out capacity of plate anchors 421
S. Jalilvand, K. Gavin, P. Doherty

Structures

Effect of prestress force and eccentricity on natural frequencies of prestressed concrete structures 427
D. Noble, M. Nogal, A. O'Connor, V. Pakrashi
Stressing Geometry Control of Cable-Stayed Bridges 433
J. Barry, K. Ruane, J. J. Murphy
The Design of Moment Connections between Rectangular Hollow Sections 439
B. Allen, J. J. Murphy
Detailing & Curtailment of Steel Reinforcement to Eurocode 2 445
B. O'Riordan, T. McKenna, D. Coleman
Performance of vinyl on concrete floors subject to pull off testing 451
N. Holmes, R. West

Performance of Concrete

Combined chloride and carbon dioxide ingression in concrete exposed to cyclic wetting and drying 457
J. Backus, D. McPolin, N. Holmes, A. Long
A Study of Chlorides in a Reinforced Concrete Bridge 463
R. O'Donovan, B. O'Rourke, K. Ruane, J. J. Murphy
Performance of GGBS Concretes in Acidic Wastewater Environments 469
D. Coleman, C. McNally, B. O'Rourke, M. Richardson

Influence of compressive loading on chloride ingress through concrete 475
J. Wang, M. Basheer, S. Nanukuttan, Y. Bai
Effects of Turbidity and Lighting on an Image Processing based Crack Detection Technique 481
M. O'Byrne, B. Ghosh, V. Pakrashi, F. Schoefs

Research in Civil Engineering

A research-based approach to exploring the adoption of novel UK-based concrete test methods in Chinese construction sector 487
B. Magee, M. Basheer, S. Nanukuttan, T. Y. Hao, Z. G. Wu
PD6694 and the Design of Gravity Retaining Walls 493
B. Solan, S. Orr, J. Withworth, P. McMenamin
Vibration based seismic damage identification procedure for a steel concentrically braced frame structure 499
D. McCrum, A. Staino
Resistance of Plated Concrete to Impact Loading 505
D. Dunne, D. Collery, P. McKenna
Preservation of Titanic's Dry Dock 511
M. Watley, G. Hennity, B. Devlin
Evaluation and Maintenance of Inland Waterway Weirs 517
J. Harvey, K. Gillen

Maintenance of the Forth Road Bridge

Barry Colford
Chief Engineer & Bridge Master
Forth Road Bridge, Administration Office, South Queensferry, West Lothian, Scotland
Email: Barry.Colford@forthroadbridge.org

1. BACKGROUND AND LOCATION

The Forth Road Bridge (FRB) is a long span suspension bridge and was opened in September 1964. At the time of opening, the bridge had the fourth longest main span in the world of 1006 metres. The bridges having longer spans were Golden Gate, Mackinac Straits and George Washington were all built in the USA, and so, Forth Road Bridge was the first long span bridge to be built outwith the US.

The bridge crosses the Firth of Forth at South Queensferry, some 15km west of Edinburgh and is a vital link in Scotland's strategic road network. The bridge deck supports a dual two lane carriageway without hard shoulders or strips. There is a separate footway/cycletrack on either side. Over 25 million vehicles now cross the bridge each year. The historic importance of the structure to Scotland was recognised in 2001 when the bridge was classed as a Category A listed structure.

The bridge had been a tolled crossing since opening. However, in February 2008 tolls were removed on FRB following an Act of the Scottish Parliament which removed tolls from all of Scotland's tolled bridges.

Funding for maintenance and operation of the bridge now comes via a Scottish Government annual grant.

2. DETAILS OF THE CONSTRUCTION

The Forth Road Bridge has a main span of 1006 metres and the side spans are each 408 metres long. The orthotropic deck on the main span is made up of a 12.7 mm stiffened steel plate overlain with a 38 mm thick mastic asphalt, on a waterproofing layer. The deck to the side spans is a 203 mm thick reinforced concrete slab with a similar surfacing detail to the main span. The decks on both the main and side spans are supported on steel stringer beams that span between large steel cross girders spaced at 9.14 metre centres. These cross girders are supported by two longitudinal stiffening trusses which in turn are supported by the main cables. The main cables are 600 mm nominal diameter and are made up of 11618, 4.98 mm diameter galvanized wires that transfer the loads from the bridge to the main and side towers and also down to the north and south anchorages. The anchorages are tapered rock tunnels, filled with concrete and post tensioned. Linking the stiffening trusses to the main cables are 192 sets of steel wire rope hangers at 18.29 metre centres that vary in length from 2.5 metres at mid span to 90 metres adjacent to the main towers.

The cables at the main towers, side towers and in the anchorage chambers are seated directly on cast saddles. These saddles on the main tower are fixed directly onto each tower leg whilst those at the side towers and anchorages are fixed to steel rocker boxes that are free to rotate in the direction of the bridge axis.



Figure 1. FRB from the north side looking southeast.

The main towers are of steel box construction rising some 156 metres above river level and are formed from three fabricated steel boxes that are joined by cover plates to provide a five cell structure in plan. The legs of each tower are connected by cross members at the top, and just below deck level, and by diagonal stiffened box bracing above and below the deck.

The approach viaducts to the bridge are themselves significant structures, made up of large steel and twin box girders with a reinforced concrete deck slab. The eleven span south viaduct is 438 metres long and the six span north viaduct is 253 metres long.

The design and construction of the bridge is described in the Proceedings of the Institution of Civil Engineers [(1)].

The maintenance and operation of the bridge and some of the major improvement works carried out are described fully in a paper given to the 5th International Cable-Supported Bridge Operator's Conference, New York, August 2006 (2).

3. SUMMARY OF MAJOR IMPROVEMENT WORKS

In the first 35 years from opening several major capital projects have been carried out to replace, strengthen or improve elements of the structure. These projects were necessary due to changes in traffic loading; design code changes; deterioration of components and a risk assessment of shipping impact.

These projects are listed below:

Strengthening of Viaduct Box Girders	£1,145,485
Main Tower Wind Bracing Strengthening	£2,916,312
Main Tower Strengthening	£12,742,999
Construction of Pier Defences	£9,914,357
Hangar Replacement	£9,706,998

Between year 2000/01 and 2013/14 a total of over £104 million pounds has been spent on a further program of strengthening and improvement works. The schemes carried out which had a value more than £1 million include:

Main Span Resurfacing overlay	£1,068,893
Reconstruct Toll Plaza	£1,323,532
Main Span Surfacing South	£3,614,494
New Gantry & Runway	£3,134,495
Main Tower Painting	£7,497,980
A8000 Approach Road Upgrade	£16,633,843
Main Cable Acoustic Monitoring	£1,182,215
Main Cable First internal Inspection	£5,472,439
Toll Equipment Replacement	£8,331,885
Viaduct Bearing Replacement	£18,650,176
Main Expansion Joints Replacement	£3,060,480
Anchorages Investigation	£5,198,514
Main Cable Dehumidification	£11,532,067
Main Cable Replacement/Augmentation Study	£1,023,873
Cable Band Bolt Replacement	£4,374,281

In addition to the improvement or strengthening projects already carried out, painting of the bridge is a high cost recurring items of work. There are almost 270,000 sqm of steelwork surface area, excluding the main cables and parapets, on the bridge and maintenance painting is almost a continual process. Re-painting of the suspended span truss which has over 202,000 sqm of surface area is estimated to cost £65 million as the existing chlorinated based paint cannot be overcoated with modern epoxy based systems. Therefore, all the existing coatings is likely to have to be removed before application of a 20/30 year epoxy system can be applied. This work will involve extensive access and full containment systems.

Main Cable First Internal Inspection

The main cables of a suspension bridge are the primary load carrying members and on FRB were formed by aerially spinning 11,618 high tensile galvanised steel wires of approximately 4.98 mm diameter into strands then compacting together to form a cable of around 600mm diameter. To protect the cable red lead paste was applied and a softer 9 gauge galvanized wire wound round the circumference of the cables then a paint system was applied. The main cables on Forth have been regularly inspected externally and re painted. No leaching of water or moisture staining had ever been recorded. However, it was acknowledged that the condition of the individual wires within the cables could not be determined with any certainty.

The U.S.A. has many more suspension bridges of a greater age than Forth and concerns over deterioration within the cables of these bridges due to corrosion led to the U.S. Transport Research Board of the National Academies commissioning a guide for main cable inspection and strength evaluation under the direction of consultant Weidlinger Associates Inc of New York. This guide was to become known as NCHRP Report 534 (3).

In 2003/4, a decision was taken to open up the cables of FRB and carry out an internal inspection. Access and containment are the biggest challenges when carrying out any maintenance on suspension bridge cables as work is being carried out above the thousands of vehicles using the bridge each day. On FRB, bespoke access platforms were designed and built to carry out the inspection work. Once access was in place the wrapping wire was removed on a panel (a panel is the length of main cable between vertical hangers) Wedge lines were then opened around the cable, as shown in Figure 2, using brass chisels and then driving in hardwood and plastic wedges. This allowed inspection to take place down to the middle of the cable



Figure 2. Wrapping removed and wedges driven.

This first internal inspection work on FRB was completed in 2004/5 and a total of ten 18 metre long panels at various points on both cables were opened and inspected. Sample lengths of wire were removed to enable tensile and other tests

to be carried out. After each panel had been inspected and sampled, it was re-compacted and re-wrapped.

Much to the surprise of the inspection team fairly extensive corrosion and wire breaks, although these were relatively small in number, were found in some panels. Given the relatively young age of the bridge these results gave cause for concern.



Figure 3. Main Cable Broken Wires

Based upon the results of this limited intrusive inspection of the main cables, the Authority's consultants concluded that the loss of strength of the cables, based on the worst section uncovered, was estimated to be 8%. This value of the current cable strength was determined from statistics obtained from the wire testing using the Brittle Wire Model Method of analysis as defined in the NCHRP Report. The consultants were asked to project those figures to try to determine what the likely cable strength would be over the next 5, 10 and 15 years, if no steps were taken to halt the deterioration. It was recognised that the figures from such a projection would have to be treated with caution. However, it was predicted that, if deterioration could not be halted, the cable could lose 13% of original strength by 2014 and 17% by 2019.

Main cables of suspension bridges have traditionally been designed on the simple working stress approach. In the original design the direct stress in the main cables on Forth was limited to 40 tons/sq.in (618 N/sq.mm) and a minimum wire tensile strength of 100 tons/sq.in (1544 N/ sq.mm) was specified . This would result in a factor of safety (FOS) of 100/40 = 2.50 and it should be noted that this factor is against ultimate failure.

Assuming a strength loss of 8%, the 2004 FOS was calculated to have dropped to 2.27 and was projected to fall below 2 between 2014 and 2019. It should be noted that in order to determine the FOS, the panel found to have suffered the highest loss of strength was used but the load adopted was that found in the highest loaded panel. This was a conservative approach but one that was felt to be justified given that only ten out of 198 cable panels were inspected.

There is no absolute number that determines the minimum acceptable FOS of the main cables of a suspension bridge. The NCHRP 534 Report refers to a figure of 2.15 and, from discussion with some US bridge authorities, the feeling was that a number of owners would be uncomfortable running uncontrolled traffic with a value less than 2 as a permanent condition.

The results of the first internal inspection of the main cables at Forth were not only significant for the Bridge Authority but also to the wider bridge community. The results suggested that there were serious doubts over the use of paint systems to try to protect the cables of suspension bridges. As a consequence of the work at Forth, the owners of Severn and Humber Bridges in England, and Storebaelt in Denmark instigated a programme of cable inspections.

At Forth, it was concluded that if the rate of deterioration due to corrosion could not be halted consideration would have to be given to the possibility of introducing loading restrictions on the bridge around 2014. Given the significance of the crossing both strategically and locally, this news caused quite a political and media stir within Scotland.

It was clear that action was required to try to halt or limit the corrosion and to try to monitor the cables and the following works and studies were commissioned:

- Installation of Acoustic Monitoring on both cables.
- Installation of a Dehumidification System on both cables.

Acoustic Monitoring

An Acoustic Monitoring System was fitted to the main cables and commissioned in August 2006. Since commissioning, to April 2014, a total of 85 events have been determined as wire breaks and seven events as possible wire breaks. However, given that there are 11618 individual wires in each cable it is not considered that this activity is significant enough to warrant action except to continue to monitor the situation and review it over time. Information on wire breaks is useful intelligence when selecting panels to open up for the next internal inspection of the cables.



Figure 4. Acoustic Monitoring

Dehumidification

Following discussions with other bridge operators in Europe, Japan and the USA a decision was taken to install a system of dehumidification on Forth Road Bridge. This work involves pumping dried air into the cables at various points having first wrapped it in an airtight neoprene membrane.

Dehumidification is a well-tried system of preventing corrosion of steelwork. Although it was already being used in box girders of some bridges and indeed in the anchor chambers at Forth, its application to main cables of suspension bridges was relatively new.. It has been shown that a piece of galvanised wire in a chamber with a relative humidity of under 40% will not corrode. Therefore, if air with a relative humidity of under 40% can be introduced into the cable and surround all the wires, then the capacity for further corrosion is likely to be negated

As already described above, the main cables are made up of 11618 parallel wires that have been compacted. However, within the cross section of the cable between the contact points of the wires there are voids and at Forth these voids make up 20.5% of the cross sectional area. The key objective in dehumidification is to fill the voids with air with a low relative humidity.

The works to complete the dehumidification of both cables was successfully completed in October 2009.



Figure 5. An exhaust outlet on a main cable.

It should be stressed whilst it is considered that there is good reason to have confidence that dehumidification will slow down or halt corrosion it remains to be seen what will happen to already cracked and damaged wires under load.

A full description of this work is described in a paper given to the 5th International Cable-Supported Bridge Operator's Conference, New York, August 2006[4].

Prior to the dehumidification system being commissioned on the east cable a full internal inspection of three panels at mid span was carried out in 2008 to benchmark the condition of the cable prior to starting dehumidification and to determine the strength loss in the cable since 2004/5. This limited inspection showed that the strength of the cables had dropped further and the loss of strength was around 10% just before dehumidification was installed.

A third internal inspection of the main cables was carried out in 2012 to verify that the dehumidification system was protecting the cables and determine the estimated current and future strength of the cables. The results of this inspection found that the factor of safety on the cables has not materially diminished and that gave strong comfort that the newly installed dehumidification system was retarding the corrosion of the bridge wires. However, it was recognised that although wire corrosion appeared to have been slowed down there are still existing cracks in some of the wires that might propagate from corrosion pits that existed prior to installation of the dehumidification system. These cracks may eventually lead to the wire fractures but the rate of breakages is expected to slow significantly. Given this, it is expected that the factor of safety of the main cables will not diminish significantly in the future as long as the dehumidification system continues to function effectively.

There is little doubt that a degree of uncertainty concerning the magnitude of future strength loss of the main cables will always remain and the cables will require to be continually monitored, and be subject to a regime of internal inspections and strength evaluations, for the remainder of the service life of the bridge. However, the results of this latest inspection, albeit reduced in scope, were encouraging. The dehumidification system applied to both cables appeared to be slowing down the rate of deterioration.

4. ANCHORAGES INVESTIGATION

The anchorages of the main cables of a suspension bridge are critical elements of the structure. At Forth Road Bridge, tunnels were formed within the rock at each of the four anchor points and filled with concrete. See Figure 6.

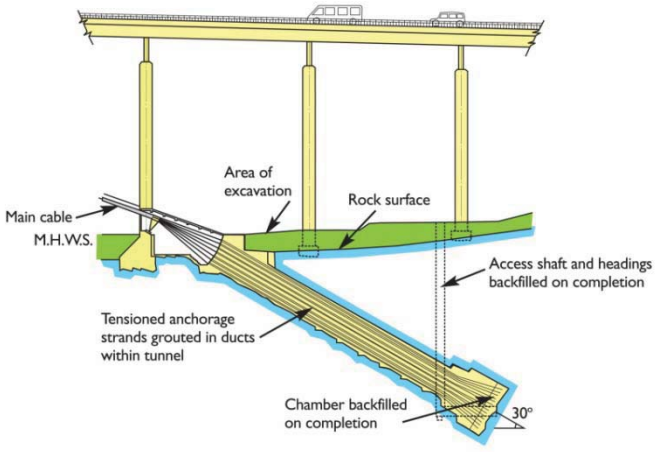


Figure 6. Section showing Anchorage

The main cable wires splay out in the anchorage chambers and loop round strand shoes which are in turn bolted to the face of the concrete tunnels. See Figure 7. Friction between the concrete tunnel and the rock, and the weight of the

overburden above, prevents the cables pulling the concrete tunnel out of the ground. The concrete in the tunnel itself is not strong enough to withstand the forces from the cables and was strengthened using post tensioned galvanised, high tensile steel wire tendons. The tendons consisted of four 32mm diameter strands in a 100 mm diameter steel duct which was then filled with grout. The strands are made up mainly of 6mm diameter galvanised wires. There were 114 tendons per anchorage and each tendon was pre-tensioned with a 152 tonnes load. This use of pre-tensioning in the buried concrete anchorage tunnels at Forth was considered innovative at the time. Unfortunately, this form of construction can be vulnerable to corrosion and deterioration especially in a saline environment such as is found at Forth.



Figure 7. Anchorage Strand Shoes

Records and papers acquired around 2005, relating to the construction of the existing anchorages highlighted various problems during construction particularly in relation to early depletion of the galvanising protecting the post tensioning strands which are housed in grouted ducts set in the concrete tunnel.

The reports on the issues and conditions encountered during construction determined the need to carry out a special inspection or investigation to try to establish the condition of the post tensioning strands.

Frequent inspections are carried out to monitor for movement within the anchorage chambers at the tunnel/strand shoe interface and no signs of distress or movement had ever been recorded.
Nevertheless, it was considered that the investigation was necessary to ensure the long term structural integrity of the anchorages and was also considered to be a pro-active measure to ensure that all accessible parts of the structure were inspected.

There is guidance from the UK Department of Transport for inspecting post tensioning in bridges as it is acknowledged that there can be problems with this type of construction. The guidelines refer mainly to the difficulties in establishing the condition of post tensioning strand in bridge decks. These difficulties are exacerbated in a tunnel. Following much discussion, research and consultation with various specialists, it was concluded that the most suitable method was to excavate behind the anchorage chambers down to the top of the tunnel to expose and inspect the post tensioning strands.

A decision was made to excavate at the south anchorage as it was expected that if corrosion of the strands had occurred it will be worse at this location.

The excavation was expected to be difficult as the ground conditions vary and there is methane present within the shale. The work was further complicated by the close proximity of the foundations to the viaduct piers. Safety of the workforce, the bridge and users governed all aspects of this complex project.

Work on the anchorages was not anticipated to involve major disruption to bridge traffic. However, given the nature of the works there was expected to be significant environmental issues to be dealt with especially with regard to noise, dust and discharge from the excavation and hydrodemolition.

If the investigation revealed significant deterioration in the steel strands within the anchorage tunnels then, depending on the level of that deterioration, the Authority were aware that measures would have to be considered to limit loading on the bridge.

When exposed, the strands were found to be in remarkably good condition with no visible signs of corrosion of the wires. Where access permitted, the diameter of the strands was checked and no evidence of a change in diameter was found suggesting no internal corrosion had occurred. Careful wedging using hand tools and hardwood wedges was used to separate the strands to enable a visual inspection to be made around the circumference of the strands. See Figure 8. The dull grey colour of the galvanising on the surface of the strands indicated oxidation of the zinc coating had occurred and localised darker areas on the strands were noted suggesting that these areas had oxidised to a greater degree. However, overall the strands that were inspected were in good condition with no evidence to suggest that they had deteriorated from the time they had been grouted.



Figure 8. Exposed Pretensioned Anchorages Strand

The investigation had been limited in nature, and it was not possible to access the wedging area at the bottom of the anchorage tunnels. In addition, it has not been possible to reconcile the apparent concerns with hydrogen emissions noted during the original construction (and the possible consequences for loss of galvanising on the strands) and the general good condition of the galvanising and strands themselves that was found during the inspection.
Based on the information available from the investigation, it was considered that the risk of the structural integrity of the southern anchorages being compromised has been reduced significantly as a result of these findings.

In addition, given the history of the construction of the anchorages both north and south, and the better conditions on the north side, it was recommended that no investigation work was carried out at the north anchorages.

From the information obtained from the investigation it was also concluded that the risk of having to replace the anchorages during the remaining service life of the bridge was relatively low and the investigation concluded and the protective system to the ducts reinstated and the site backfilled with mass concrete.

The Authority's own staff continue to inspect and monitor the anchorage sockets and plates within the existing anchorage chambers, on the north and south sides, as part of the on going inspection of the bridge. The frequency of those inspections reflects the criticality and vulnerability of the anchorages and takes account of the investigation results.

5. NEW BRIDGE ACROSS THE FORTH AT QUEENSFERRY

In 2008 there were a number of issues relating to Forth Road Bridge that were causing concerns not only to the Authority but also to the Scottish Government and the wider public. These were the condition of the main cables and the likely disruption to users during any possible replacement or augmentation of the cables; the unknown condition of the anchorages and the major deck resurfacing and joint replacement work being scheduled.



Figure 9. Proposed 3 tower cable stayed bridge – The Queensferry Crossing

As a consequence of these issues, the Scottish Government decided to commence the process to build a new crossing across the Forth at Queensferry to ensure resilience in the transport system on the East side of Scotland.

Work is currently underway on building the new bridge, named the Queensferry Crossing, a three tower cable stayed bridge with two main spans of 650 metres. Construction is expected to be completed in 2016.

Following a review in 2011, the Scottish Government announced their intention to dissolve FETA and contract out the maintenance and operation of the Forth Road Bridge and the new Queensferry Crossing to a private operator. The contract to maintain and operate both bridges will also include some 20km of approach roads on both sides of the Forth and is due to commence on 1 June 2015.

6. CONCLUSIONS

The cost of the operation and maintenance of large cable supported bridges is often underestimated by governments and other bodies providing the capital funding for the construction of such bridges. Ensuring there is an adequate funding stream to enable maintenance to be carried out over the whole life of the bridge is vital. Experience has shown that the only way that to achieve this is to ensure that mechanisms are in place to ring fence funding in order to protect the asset.

Further research is required in a number of vital areas such as the behaviour of high tensile steel wire used in hostile environments; the use of dehumidification in main cables and validation of acoustic monitoring of main cables. Much is also still needed to be done to determine how these long span bridges actually behave under transient loads. Structural health monitoring may be the way forward but more work is required to ensure monitoring systems are both robust and fit for purpose.

Unfortunately, it still seems that the design of these large structures is being undertaken without much reference to those who have the experience of maintaining and operating these bridges. Until that issue is addressed it is difficult to see how mistakes made in the past are going to be avoided in the future.

REFERENCES

[1] The Forth Road Bridge Proceedings of the Institution of Civil Engineers, 1965. Republished in 1967

[2] Forth Road Bridge - Maintenance Challenges, Andrew A.S. Andrew, General Manager & Bridgemaster and B.R. Colford Depute General Manager, Forth Estuary Transport Authority

[3] NCHRP Report 534, 'Guidelines for Inspection and Strength Evaluation of Suspension Bridge Parallel Wire Cables'.

[4] 'Forth Road Bridge – First Internal Inspection, Strength Evaluation, Acoustic Monitoring and Dehumidification of the Main Cables', Barry Colford and Charles Cocksedge.

Large Events in Waves on the Continental Shelf

Mohd. R.M. Haniffah[1], Paul H. Taylor[2], Chris Swan[3], Vanessa Katsardi[3,4], Alistair G.L. Borthwick[5]
[1]Faculty of Civil Engineering, Universiti Teknologi Malaysia, Malaysia
[2]Department of Engineering Science, University of Oxford, Parks Road, Oxford OX1 3PJ, U.K.
[3]Department of Civil and Environmental Engineering, Imperial College, London, SW7 2AZ, U.K.
[4]Department of Civil Engineering, University of Thessaly, Greece
[5]School of Engineering, The University of Edinburgh, Edinburgh, EH9 3JL, Scotland
…
email: mridza@utm.my, paul.taylor@eng.ox.ac.uk, c.swan@imperial.ac.uk, vkatsardi@civ.uth.gr, alistair.borthwick@ed.ac.uk

ABSTRACT: Offshore structures located on the continental shelf experience loading from locally extreme events in storm-induced wave groups as they shoal. This paper examines modern developments in assessing the transformations that take place to ocean wave spectra as the bathymetry shallows, and examines laboratory data obtained from tests undertaken at Imperial College London on random waves as they travel over gently sloping beds. The data show that NewWave provides a satisfactory fit to the largest crest- and trough- focused events in all depths of water, until wave breaking occurs. The paper also considers how well NewWave models the linear behavior of extreme waves in shallowing water, and presents results from a Stokes-like expansion accounting for the asymmetry of large waves. It is shown that the largest crest elevations, lowest trough elevations, and breaking wave heights are all limited by a modified Miche criterion. The findings should be useful to offshore engineers required to assess the air gap elevation of structures located on the continental shelf.

KEY WORDS: Offshore structures; Extreme waves; NewWave; Limiting height.

1 INTRODUCTION

The continental shelf comprises a gently sloping landmass that extends outwards from the coastal shoreline to a depth of about 140 m beyond which the ocean depth rapidly increases. Many offshore oil and gas platforms, maritime jetties, and other structures are located on the continental shelf, and are subject to loading from storm-driven waves that shoal as they travel inshore from the deep ocean waters. Engineers are required to design structures whose decks are above the level of the highest wave crest elevation and whose support structures can withstand the most extreme wave loadings. This paper addresses the former problem by considering the use of a focused wave methodology to represent non-breaking extreme wave events, and limiting elevation/height criteria to design for breaking and broken waves.

For more than 20 years, NewWave has been used in the design of deep water offshore structures. The NewWave concept originated from statistical theory aimed at determining the shape of the extreme event in a time history related to a given spectrum [1], [2], was applied to ocean waves by Tromans and colleagues [3]. The idea of a wave group proved useful for numerical simulation, [4], and for the analysis of wave data from the open sea, [5], [6]. It was validated through meticulous laboratory experiments by Rapp and Melville [7], Baldock *et al*. [8], Johannessen and Swan [9], [10], amongst others. The free surface elevation of a focused wave group is given by NewWave as

$$\eta_{\mathrm{NW}}(t) = A\frac{\int S(\omega)\cos\omega t\,\mathrm{d}\omega}{\int S(\omega)\,\mathrm{d}\omega} \qquad (1)$$

in which A is the wave amplitude of the focused wave group, $S(\omega)$ is the wave energy spectral density at wave angular frequency ω, and t is time.

As storm-driven waves pass over the continental shelf, they shoal, their crests narrow and troughs broaden, and as the water depth reduces they break. Miche [11] obtained a limiting height criterion for waves passing over a horizontal bed, which Katsardi [12] modified for very mild slopes, giving

$$H_{\max} = 0.12\,\lambda\tanh kd \qquad (2)$$

in which $H_{\max}$ is the wave height at breaking, λ is the wave length, k is the wave number, and d is the local water depth.

In the mid-2000s, a series of laboratory tests were undertaken at Imperial College, London, as part of a Joint Industry Project to assess extreme wave behaviour over mild slopes in shallow water. This paper presents some of the measurements, and describes how the data were interpreted in terms of large events. A Stokes-like expansion approach is used to study the harmonic structure of the wave free surface elevation time history. The paper briefly outlines the laboratory test facility and the wave gauge instrumentation before separately considering non-breaking and broken wave behaviour. The possible use of NewWave and the modified Miche criterion to represent such events is considered.

2 IMPERIAL COLLEGE WAVE FLUME

Irregular waves were generated in a 60 m long flume of width 0.3 m, where the still water depth was 0.7 m at the paddles. Tests were undertaken for three beach configurations, one a raised horizontal bed with constant still water depth of 0.3 m along its length, the second a 1:100 plane beach with toe still water depth of 0.5 m, and the third a 1:250 plane beach with toe still water depth of 0.3 m. A transitional bed ramp of slope 1:15 joined the bed at the paddles to the beaches. A series of resistance-type wave gauges were located along the flume centreline, providing measurements of the water surface level, accurate to within 0.5 mm.

Irregular wave trains were generated, corresponding to a JONSWAP spectrum with a peak enhancement factor of $\gamma = 2.5$; with all other properties being listed in Table 1). In each case, measurements were collected at 128 Hz for an ensemble of eight free surface elevation time histories, each lasting 256 s. The resulting time series included 1200 to 1700 waves covering a total duration of 2048 s. Further details are given by Katsardi [12] and Katsardi et al. [13]

Table 1. Input parameters.

Case	Bed Slope	T_p (s)	H_{so} (m)
Case A1a	1/100	1.2	96.0
Case A1b	1/100	1.2	120.2
Case A3a	1/100	1.5	11.2
Case A3b	1/100	1.5	29.2
Case A3c	1/100	1.5	83.3
Case A3d	1/100	1.5	102.9
Case A3e	1/100	1.5	121.3
Case B1b	1/250	1.2	119.1
Case B3e	1/250	1.5	122.2
Case C1b	Horizontal	1.2	120.1
Case C3e	Horizontal	1.5	128.9

3 RESULTS

3.1 Largest Free Surface Events in Time

We first consider the free surface elevation behaviour at three gauges, G2 where d = 0.35 m, G6 where d = 0.15 m, and G8 where d = 0.05 m. Figure 1 shows portions of the time histories of free surface elevation obtained at each of these gauges. In the deeper water at G2, the waves are more sinusoidal in form. In the shallower depth at G6, the non-broken waves have steepened (with narrower, more pointed crests), and the the largest waves have broken.

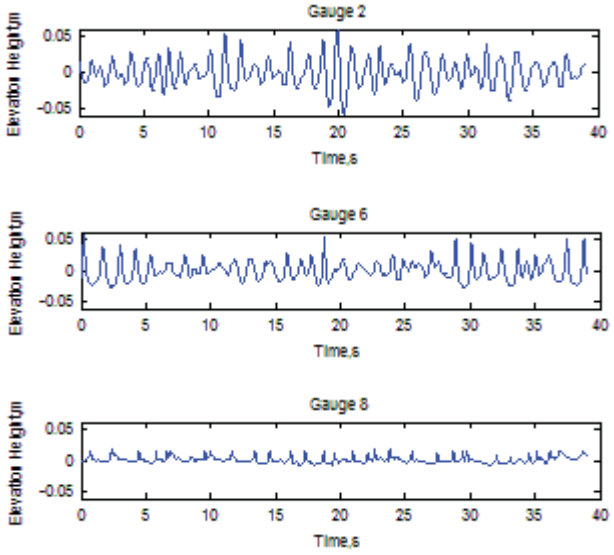


Figure 1. Surface elevation time histories in progressively shallow water depths at Gauges G2, G6 and G8 for Case A1a.

At the gauge in the shallowest depth, G8, almost all the waves have broken, and these progress up the beach as hydraulic bores. By this stage the maximum free surface elevation appears to have saturated at a limiting value.

Figure 2 presents the superimposed free surface elevation time histories containing the largest 10% crests. It can be seen that the profiles at G2 collapse onto a nearly constant wave shape for almost a typical wave period (i.e. ~ 1 s) either side of the maxima. At more distant times, the wave surface elevation behaviour loses its universality and appears to be almost random.

By G8, almost all the waves have broken, are effectively asymmetric, and have a fairly constant maximum elevation with time.

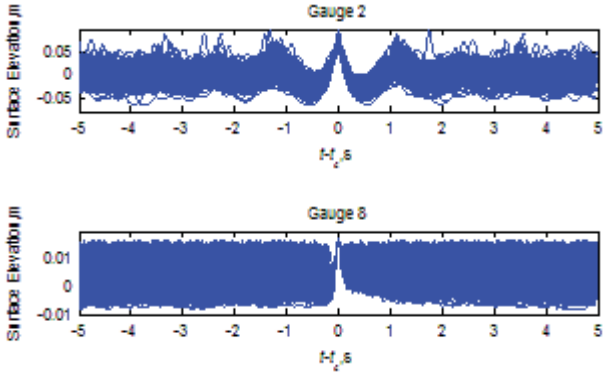


Figure 2. Case A1a: largest 10 % crest surface elevation time histories plotted relative to time the maximum surface elevation occurs (t - t_c). Upper plot: G2; lower plot: G8.

Figure 3 presents the averaged free surface with time for the 10% largest waves, with the time-reversed mirror image superimposed (in order to highlight symmetry). The largest crest events are quite symmetric at G2, but become increasingly asymmetric as the water shallows, due to the growth of wave nonlinearity until breaking occurs, after which the shape is saw-toothed.

Using Stokes theory, the free surface elevations averaged over the top 10 % of crest and troughs may be expressed as

$$\eta_c = S_0 A^2 + A\cos(\omega t) + S_2 A^2 \cos(2\omega t) + S_3 A^3 \cos(3\omega t) + \ldots + S_n A^n \cos(n\omega t) \quad (2)$$

and

$$\eta_t = S_0 A^2 - A\cos(\omega t) + S_2 A^2 \cos(2\omega t) - S_3 A^3 \cos(3\omega t) + \ldots + S_n A^n \cos(n\omega t) \quad (3)$$

in which η_c is the 10% largest crest averaged time series, η_t is the 10% largest trough averaged time series, S_i is a coefficient that defines the size of the i-th wave component, n is the number of components, A is the overall wave amplitude, ω is the wave angular frequency, and t is time. Of course, for an irregular wave train, the amplitude A and frequency ω are slowly varying functions of time, and the first term on the RHS of equations (2) and (3) is the slowly varying long wave

set-down term. Following Baldock et al. [8], Johannessen and Swan [10], Hunt et al. [14] and Borthwick et al. [15], the odd harmonics are given by

$$\frac{\eta_c - \eta_t}{2} = A\cos(\omega t) + S_3 A^3 \cos(3\omega t) + \ldots + S_{n-1} A^{n-1} \cos((n-1)\omega t) \quad (4)$$

and even harmonics by

$$\frac{\eta_c + \eta_t}{2} = S_0 A^2 \cos(0) + S_2 A^2 \cos(2\omega t) + \ldots + S_n A^n \cos(n\omega t) \quad (5)$$

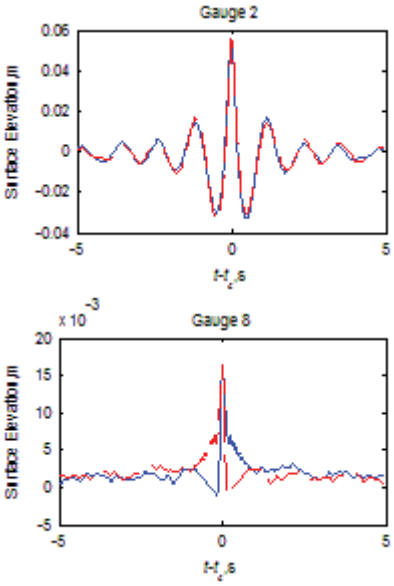


Figure 3. Case A1a: averaged 10 % largest-crest surface elevation time histories relative to time the maximum surface elevation occurs (t - t_c), and overlapped with reversed time.

By plotting the subtraction time series given by Equation (4) with the mirror image reversed time series (as shown in Figure 4), the odd harmonics exhibit symmetry in deep water (e.g. for Gauge G2) for depths reducing to 0.15 m, after which the methodology breaks down once the waves have broken.

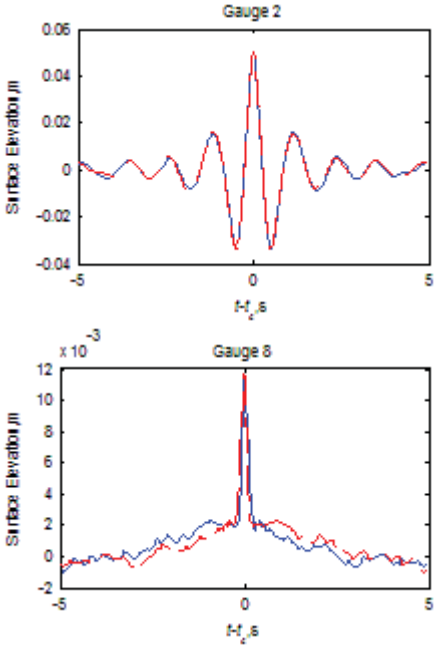


Figure 4. Case A1a: subtracted averaged 10 % crest-trough elevation [η_c - η_t]/2 time series relative to time maximum surface elevation occurs, overlapped with reversed time series.

Averaged crest- and trough-focused time series, which show the even wave harmonics are presented in Figure 5 for gauges G2 and G8. Before wave breaking occurs, the even harmonics contain a dominant component at half the first-order period (determined from the subtraction series). Post-breaking, the even harmonics are essentially anti-asymmetric.

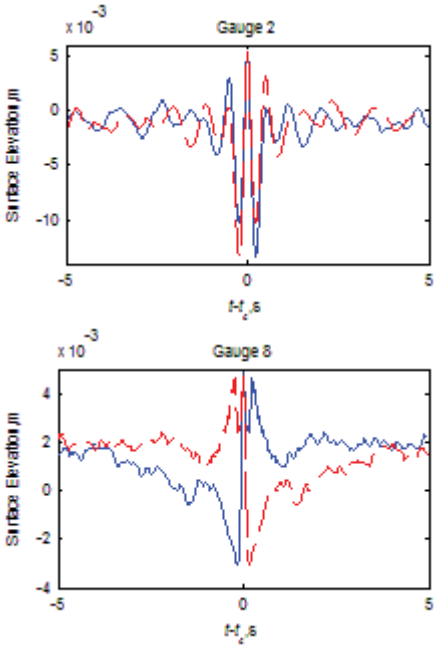


Figure 5. Case A1a: Added averaged 10 % crest-trough elevation [η_c + η_t]/2 time series relative to time maximum surface elevation occurs, overlapped with reversed time series.

Analysis of the extreme events in the free surface elevation time series obtained for the irregular waves in the Imperial College flume is useful in validating how well NewWave models the first-, second- and third-order wave components.

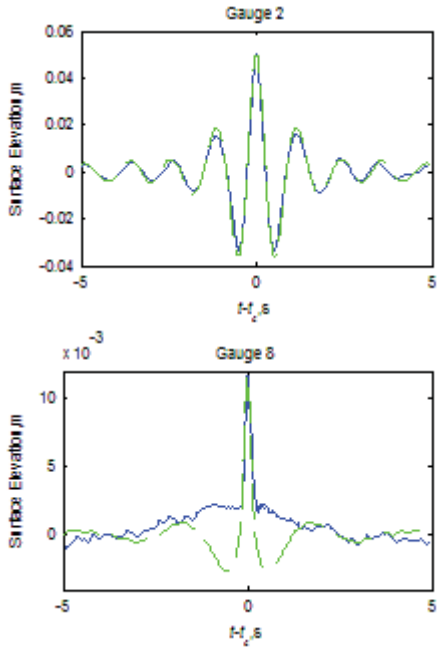


Figure 6. NewWave (with normalized height) compared with the average top 10 % average [η_c - η_t]/2 time series (blue line) for Case A1a, at G2 and G8.

Figure 6 illustrates the excellent fit obtained between NewWave (the height is normalized with the odd harmonics free surface elevation to compare the shapes) and the odd harmonic free surface elevation at G2, located offshore of the breaker line. There is a much poorer fit at G8, where all the primary waves have broken. For comparison in terms of magnitudes, the magnitudes of the linear and third-order harmonics are estimated from

$$\frac{\eta_c - \eta_t}{2} = A_1 \mathrm{NW} + A_3 \mathrm{NW}_3 \qquad (6)$$

in which

$$A_1 = \frac{\int \left(\frac{\eta_c - \eta_t}{2} \right) \mathrm{NW}\, \mathrm{d}t}{\int \mathrm{NW}^2\, \mathrm{d}t} \qquad (7a)$$

and

$$A_3 = \frac{\int \left(\frac{\eta_c - \eta_t}{2} \right) \mathrm{NW}_3\, \mathrm{d}t}{\int \mathrm{NW}_3{}^2\, \mathrm{d}t} \qquad (7b)$$

where

$$\mathrm{NW}_3 = \mathrm{NW}^3 - 3\mathrm{NW}_\mathrm{H}^2.\mathrm{NW} \ . \qquad (8)$$

In the foregoing, NW is the linear term, NW_3 is a representation of the third-order triple frequency term, and NW_H is the Hilbert transform of the NewWave time series. Figure 7 illustrates how well Equation (6) matches the [η_c - η_t]/2 time series [averaged with its time-reversed counterpart] for gauges up to up to G6 for Case A3e, being the most extreme case of all.

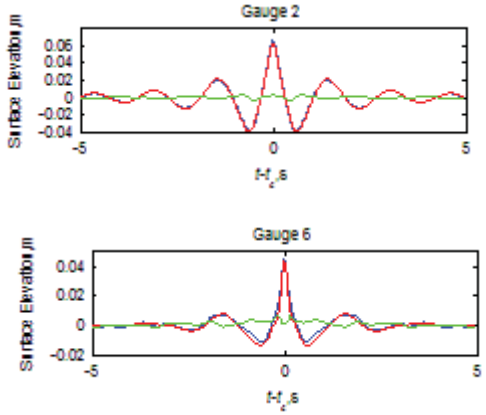


Figure 7. Time histories of averaged odd harmonics from the top 10 % crest- and trough focused wave groups (blue line), and linear (red line) and third (green line)-order NewWave terms for Case A3e, at G2 and G6.

A similar analysis is next performed for the even harmonics obtained from the addition of the crest- and trough-focused time series. This added series is first filtered to separate out the second-order sum and difference terms, and the magnitude of the filtered second-order term determined from

$$A_2 = \frac{\int \left(\frac{\eta_c - \eta_t}{2} \right) \mathrm{NW}_2\, \mathrm{d}t}{\int \mathrm{NW}_2{}^2\, \mathrm{d}t} \qquad (9)$$

in which

$$\mathrm{NW}_2 = \mathrm{NW}^2 - \mathrm{NW}_\mathrm{H}^2 \qquad (10)$$

where NW_2 is the second-order term. Figure 8 displays the close agreement obtained by the NewWave second-order component NW_2 to the filtered second-order sum components of the free surface time series at gauges G1 at d = 0.4 m and G7 at d = 0.1 m. Note that NW_2 has been normalised in terms of its height so that clear comparison can be made of the shape. From Equation (9), the percentage difference of magnitude between the two ranges from 5 % to 16 % for all gauges.

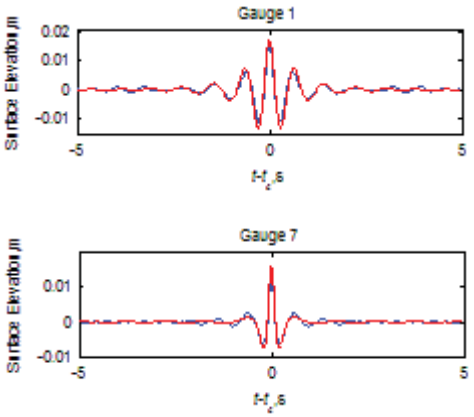


Figure 8. Time histories of averaged even harmonics from the top 10 % crest- and trough-focused wave groups (with normalized height), and Hilbert-transform approximation of NewWave terms (red line) for Case A3e at G1 and G7.

Returning to the Stokes expansion, by analogy with a regular wave train, we define modified Stokes coefficients, following Walker et al. [16] as) as $S_2 = S_{22}/d$ and $S_3 = S_{33}/d^2$, such that the free surface time series can be expressed in truncated form as

$$\eta = A\cos\theta + \frac{S_{22}}{d}A^2\cos 2\theta + \frac{S_{33}}{d^2}A^3\cos 3\theta\,. \quad (11)$$

From equations (6) and (11), it may deduced that

$$S_{22\,\mathrm{NW}} = \frac{A_2 d}{A^2} \quad \text{and} \quad S_{33\,\mathrm{NW}} = \frac{A_3 d^2}{A^3}\,. \quad (12)$$

A comparison between the experimental (Equation 12) and theoretical Stokes coefficients is shown in Figure 9, where it can be seen that the NewWave approximations and exact Stokes coefficients agree well over much of the range of *kd* values considered. There is no simple regular wave correction for the 2nd order difference component, but we do observe that each 2nd order double frquency term is associated with a difference term: each wave group propagates on a set-down (hole) of its own making.

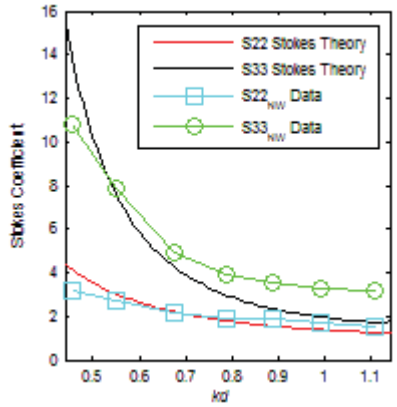
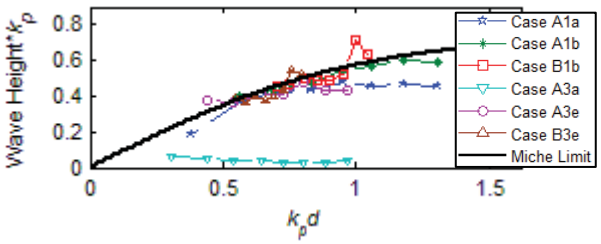


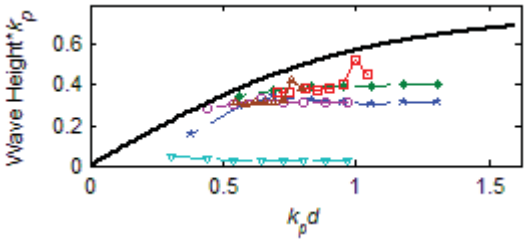
Figure 9. Stokes second- and third-order sum coefficients, S_{22} and S_{33}, plotted against *kd*.

3.2 *Breaking Waves*

For each case, the largest crest elevations, deepest troughs, and extreme wave heights were computed from the free surface time series. Figure 10 shows the non-dimensional maximum wave height ($H_{\max}k_{\mathrm{p}}$) and non-dimensional average height of the 10% largest waves ($H_{\max}k_{\mathrm{p}}$) as functions of the non-dimensional water depth ($k_{\mathrm{p}}d$). Here, k_{p} is the wave number corresponding to the deep water spectral peak period, T_{p}. The modified Miche limiting criterion given by Equation (2) is superimposed on Figure 10.



(a) Non-dimensional maximum wave height against non-dimensional depth



(b) Non-dimensional average value of 10% largest wave heights against non-dimensional water depth

Figure 10. Non-dimensional largest wave heights against non-dimensional water depth for Cases A1a, A1b, B1b, A3a, A3e and B3e, using the wave number, k_{p}, corresponding to the deep water spectral peak to non-dimensionalise the height and still water depth values.

It is obvious that the modified Miche criterion provides a limit to the maximum heights of broken waves.

3.3 *Broken Waves*

Once waves have broken, they cease to be dispersive, and behave more like solitary waves or hydraulic bores. This short section includes a simple analysis of both types of wave behaviour, and how well the analogies fit the measured data from the Imperial College laboratory flume.

The free surface motion of a solitary wave propagating over a steady, uniform current may be expressed using the Korteweg-de-Vries equation by

$$\eta = H + \mathrm{sech}^2\left[\frac{\sqrt{3}}{2}\left(\frac{H}{d^3}\right)^{1/2}(x - c't)\right] \quad (13)$$

where H is the height of the solitary wave, d is the still water depth, x is distance in the direction of propagation, c' is the modified solitary wave speed observed by a stationary observer, and t is time. In a current of speed u_{c},

$$c' = c_{sol} + u_c \quad , \tag{14}$$

in which c_{sol} is the solitary wave speed in the absence of the current, given by

$$c_{sol} = \sqrt{gd\left(1+\frac{H}{d}\right)}. \tag{15}$$

Figure 11 shows a fit of solitary wave theory (given by equations (13) to (15)) to the time history of the mean surface elevation of the top 20 crests at gauge G7 for $kd = 0.56$. The model appears reasonable for the single peak crest. This was not the case for $kd < 0.4$.

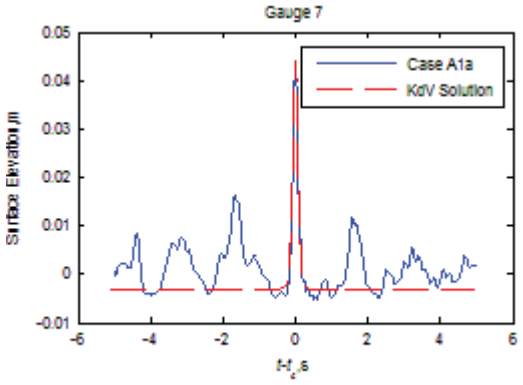


Figure 11. Solitary wave fitted to the mean of the surface elevation time histories corresponding to the top 20 crests for Case A1a at gauge G7. u_c is 0.6 ms^{-1}.

The alternative approach is to model the broken wave as a hydraulic bore. Following [17], a hydraulic bore travelling on a current of speed u_c, has a front speed given by

$$c' = c_{hj} + u_c \tag{16}$$

where c_{hj} is the speed the bore front would have in otherwise still water, and is given by

$$c_{hj} = \sqrt{g(d+H)\left(1+\frac{H}{2d}\right)}. \tag{17}$$

Figure 12 presents a plot of the ratio of the modified front speed of broken waves modelled as bores to their corresponding front speeds in otherwise still water. The behaviour is reasonable, given that the front speed of a bore travelling on a current can be increased by up to 20%.

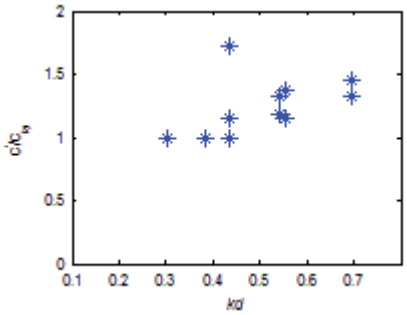


Figure 12. Non-dimensional effective wave speed for top 10 % of waves with each modelled as a hydraulic jump

4 CONCLUSIONS

This paper has presented an analysis of laboratory measurements of irregular waves propagating over mild bed slopes, characteristic of the continental shelf. Wave gauge data were interpreted in terms of the largest crest and trough events, and comparisons made with NewWave theory in deep water, a modified Miche criterion at breaking, and solitary wave theory and hydraulic bores for broken waves. From the raw data, it was observed that the wave crests sharpened and troughs widened during shoaling. In deep water, the wave time histories exhibited short term symmetry either side of a major event; this symmetry was lost once the waves broke.

NewWave was found to provide a reasonably accurate representation of the behaviour of the largest dispersive non-breaking waves in water of deep to intermediate depths, provided $kd > 0.5$. It was found that a truncated Stokes-like expansion gave a close approximation to the behaviour of extreme wave events in shoaling waters. By utilising a Hilbert-transformation approach, it was shown that NewWave gives an accurate representation of the magnitude and shape of second- and third-order components in irregular waves in the vicinity of maximum crests and troughs. These higher order contributions increased in magnitude as the depth reduced, until wave breaking occurred (for $kd < 0.5$), and NewWave theory no longer applied. Indeed, Katsardi et al. [13], have noted that the dispersive characteristics of the wave group is dominated by the effective water depth, kd. This factor becomes more important once the local significant wave height increases. The consequent increased nonlinearity of the wave group limits the applicability of the NewWave theory to larger effective water depths. For example, for the most nonlinear case examined in this paper (Case A3e, Table 1) NewWave theory can be applied with relative success up to $kd > 0.75$. The physical explanation for this lies in the effect of wave breaking and its dependence on both the wave steepness and the effective local water depth.

A modified Miche criterion was found to give an accurate upper bound estimate of maximum wave height, crest elevation and deepest trough elevation. At the point of breaking, the largest waves lost temporal symmetry as they changed abruptly into bore-like, non-dispersive waves. For the broken waves, either hydraulic bore or solitary wave theory should be appropriate, in which case the limiting wave height should be $H_{max}/d = 0.754$.

In short, designers of offshore structures located on the continental shelf should: (1) model non-broken extreme waves using NewWave, or similar, based on a specified offshore wave energy spectrum, provided $kd > 0.75$; (2) utilise the modified Miche criterion to estimate whether wave breaking has occurred; and (3) utilise the hydraulic bore analogy to model broken waves, though with caution as the fits to the data are less good than for the NewWave models for waves on deeper water.

ACKNOWLEDGMENTS

The LoWiSh Joint Industry Project (JIP) was sponsored by Shell International, Total, BP, ChevronTexaco, ConocoPhillips, ExxonMobil, Statoil, and Woodside Energy.

REFERENCES

[1] Lindgren, G. (1970), 'Some properties of a normal process near a local maximum', *The Annals of Mathematical Statistics*, 41, 1870-1883.

[2] Boccotti, P. (1983), 'Some new results on statistical properties of wind waves', *Applied Ocean Research*, 5(3), 134-140.

[3] Tromans, P.S., Anaturk, A., and Hagemeijer, P. (1991), 'A new model for the kinematics of large ocean waves – application as a design wave', *Proc. 1st Int. Offshore and Polar Engng Conf.*, Edin., U.K., 3, 64-71.

[4] Taylor, P.H., and Haagsma, I.J. (1994), 'Focussing of steep waves on deep water', *Proc. Int. Symp: Waves – Physical and Numerical Modelling*, Vancouver, Canada, Vol. 2, 862-870.

[5] Jonathan, P., and Taylor, P.H. (1997), 'Irregular, nonlinear waves in a spread sea', ASME, *J. Offshore Mech. Arct. Eng*., 119, 134–139.

[6] Taylor, P.H., Williams, B.A. (2004), 'Wave statistics for intermediate depth water - New waves and symmetry'. *Journal of Offshore Mechanics and Arctic Engineering*, 126 (1), 54-59.

[7] Rapp, R. J., and Melville, W. K., (1990), 'Laboratory measurements of deep water breaking waves', *Phil. Trans. R. Soc. A*, 331, 735–800.

[8] Baldock, T.E., Swan, C. and Taylor, P.H. (1996), 'A laboratory study of nonlinear surface waves on water', *Philos. Trans. R. Soc. Lond., A* 354: 649–676.

[9] Johannessen, T., and Swan, C. (2001), 'A laboratory study of the focusing of transient and directionally spread surface water waves', *Proc. R. Soc. London A*, 457, 971–1006.

[10] Johannessen, T. B., and Swan, C. (2003), 'On the nonlinear dynamics of wave groups produced by the focusing of surface-water waves', *Proc. R. Soc. A*, 459, 1021–1052.

[11] Miche, R. (1944), ' Undulatory movements of the sea in constant and decreasing depth', *Ann. De Ponts et Chaussees* (May-June, July-August): 25-78, 131-164, 270-292, 369-406.

[12] Katsardi, V. (2009) *Surface water waves in intermediate and shallow water depths*. PhD dissertation, Imperial College, London.

[13] Katsardi, V, de Lutio, L., and Swan C. (2013), 'An experimental study of large waves in intermediate and shallow water depths. Part I: Wave height and crest height statistics', *Coastal Engineering*, 73: 43-57.

[14] Hunt, A.C., Taylor, P.H., Borthwick, A.G.L. and Stansby, P.K. (2005), 'Phase inversion and the identification of harmonic structure in coastal engineering experiments', *Proceedings of ASCE 29th International Conference on Coastal Engineering*, Lisbon, 1047–1059.

[15] Borthwick, A.G.L., Hunt, A.C., Feng, T., Taylor, P.H. and Stansby, P.K. (2006), 'Flow kinematics of focused wave groups on a plane beach in the U.K. Coastal Research Facility', *Coastal Engineering*, 53(12), 1033-1044.

[16] Walker, D.A.G., Taylor, P.H., and Eatock Taylor R. (2004), 'The shape of large surface waves on the open sea and the Draupner New Year wave', *Applied Ocean Research*, 26, 73-83

[17] Chow, V.T. (1985) *Open-channel Hydraulics*, 21st Printing, McGraw-Hill, Singapore, 1985.

Managing Ireland's National Road Bridges

Liam Duffy
National Roads Authority, St Martin's House, Waterloo Road, Dublin 4, Ireland
email: lduffy@nra.ie

ABSTRACT: In 2001 the National Roads Authority in the Republic of Ireland implemented the Eirspan Bridge Management System to introduce central co-ordination of bridge management activities relating to National Roads and Motorways. The Bridge Management System helped to standardise inspection types and introduced a consistency to the quality of inspections with the aim of optimising the decision-making process for prioritising repairs and rehabilitation of the concrete, masonry and steel structures across the country. This paper describes the core activities required to effectively manage a range of structure types and ages from 14th Century stone masonry arches to modern post-tensioned concrete structures. It will explain how the NRA utilises a range of cyclical and non-cyclical inspection and structural assessment programmes to make well-considered structural intervention decisions, and will address how bridge managers deal with bridge deterioration which poses a high risk to road users. A range of typical work types will be presented to outline how modern structures are managed in order to reach and exceed their 120 year design life, and how ancient structures are managed to ensure they continue to remain serviceable despite carrying significantly heavier loads than the horse and cart for which they were designed.

KEY WORDS: Bridge Management, Bridge Inspections, Bridge Repairs

1 INTRODUCTION

There are 2,996 structures in Ireland carrying and crossing the Motorway, National Primary and National Secondary Road network[1] which are managed by the National Roads Authority and a number of Public Private Partnership Concessionaires. The National Roads Authority commenced the implementation of the Eirspan Bridge Management System in 2001whereby all structures with a span greater than or equal to 2.0metres was subjected to inventory gathering and a Principal Inspection, in accordance with Eirspan principles. The Eirspan Bridge Management System is based on the DANBRO Bridge Management System[2], which was customised for use in Ireland. Routine inspection and maintenance, structure repairs, replacement of essential components, structural assessments, and strengthening of structures which are assessed as weak are also integral components of the bridge management system.

2 BRIDGE STOCK COMPOSITION

2.1 Bridge Numbers

Table 1. Bridge Numbers (2013)

	Northwest	Leinster	Munster	Total
NRA	676	976	923	2575
PPP	54	276	91	421
Total	730	1252	1014	2996

There are 2996 structures on the Motorway, National Primary and National Secondary Road network (2013 data) which are managed by the NRA or by Public Private Partnership Concessionaires as shown in Table 1.

2.2 Changing Structure Types

The significant expansion of the major inter-urban road network in recent years led to the construction of many new bridges and the de-classification of a significant number of older structures. Table 2 shows a breakdown of structure types as they existed on the network in 2004, and Table 3 shows a breakdown of structure types as they existed on the network in 2013. The very significant increase in the number of concrete structures (including reinforced concrete, structures constructed with prestressed pre-tensioned beams and in situ prestressed post-tensioned concrete) is not surprising, nor is the significant reduction in the number of masonry (including both stone masonry arch and stone 'clapper' slab) structures on the network in 2013 compared to 2004.

Table 2. Bridge Type Summary 2004 Excluding PPP Bridges

	Northwest	Leinster	Munster	Total
Masonry	328	214	335	877
Concrete	195	408	284	887
Steel	17	26	29	72
Corrugated Steel	48	45	30	123
Pipe Culvert	24	30	35	89
Not Registered	30	62	44	136
Total	642	785	757	2184

Some masonry structures were necessarily replaced under the bridge strengthening programme, however the Authority does have a policy of 'retain and repair' rather than replace, where

possible, in relation to masonry structures. The heritage value of the masonry bridge stock is held in high regard by the Authority and considerable expertise has been used in managing these structures to ensure they are repaired in sympathy with their character.

Table 3. Bridge Type Summary 2013 Excluding PPP Bridges

	Northwest	Leinster	Munster	Total
Masonry	297	116	275	688
Concrete	285	724	524	1533
Steel	20	45	34	99
Corrugated Steel	47	33	33	113
Pipe Culvert	25	54	40	119
Not Registered	2	4	17	23
Total	676	976	923	2575

The number of steel structures in the tables includes for composite steel/concrete structures and the structures which are 'not registered' include railway structures and structures for which the inventory is incomplete.

3 MANAGEMENT TEAM

The Author is responsible for bridge management within the National Roads Authority, reporting to Head of Structures. A team of regional engineers based in Donegal, Naas and Cork help to implement bridge management in the regions of Northwest, Leinster and Munster respectively and undertake the bridge management activities in accordance with NRA protocol.

Consultants have been used to undertake bridge inspections as well as designs for bridge repair, strengthening, widening and rehabilitation schemes and the supervision of construction work. Framework Agreements for Engineering Services have been used since 2001 to compile a list of Framework Participants who then bid for mini-competitions for the Services required within particular task orders. The Framework Agreement for Engineering Services is due for re-advertising in 2015.

4 CORE BRIDGE MANAGEMENT ACTIVITIES

4.1 Inventory Gathering

When the implementation of the Eirspan Bridge Management System commenced in 2001 the first activities which were carried out were inventory gathering and a first Principal Inspection. Inventory gathering includes for collecting basic data which a bridge manager needs such as bridge co-ordinates, form of structure, material types for various components, expansion joint and bearing types. Geometrical data including span length, carriageway arrangement, and vertical clearances are also recorded.

4.2 Principal Inspection

An Eirspan Principal Inspection is a visual inspection of all accessible components on a structure with the aim of recording the condition of each component, the need for repair, and cost data for repairs. Testing is not undertaken during a Principal Inspection. If the inspector considers that a particular defect warrants closer investigation including testing he can recommend a Special Inspection in order to fully investigate the source of the defect and better gauge an appropriate repair strategy. Principal Inspection records are stored on the Eirspan database and allow bridge managers to monitor changes in the condition of structures with the passing of time.

The list of components is as follows:

1. Bridge Surface
2. Expansion Joints
3. Footways/Median
4. Parapets/Safety Barriers
5. Embankments/Slopes
6. Wingwalls/Retaining Walls
7. Abutments
8. Piers
9. Bearings
10. Deck
11. Beams/Girders
12. Riverbed
13. Other Elements
14. Structure in General

Each of the standard components 1 to 13 is given a Condition Rating ranging from 0 (no or insignificant damage) to 5 (the component has failed or is in danger of total failure with possible implications for traffic safety). Component 14 is given a condition rating which depends on the rating of the most important components.



Figure 1 Inspection of Substructure of Spectacle Bridge County Clare

Description of the damage along with a cost estimate and an estimated year of repair are given and digital photographs are included with the report, which is stored on the Eirspan database.

Consistency of inspection is extremely important and the NRA have set minimum qualification and experience requirements for potential Principal Inspection Team Leaders, whose CVs are vetted prior to being accepted. Every Team Leader attends a four-day hands-on bridge inspection workshop during which the Eirspan manuals are reviewed and inventory gathering and inspections are carried out in the field and analysed in detail to identify potential trends in inconsistent reporting. Only trained Principal Inspection Team Leaders may lead an inspection team, and the Team Leader must undertake the inventory gathering and Principal Inspection with assistance as required.

The inspection interval varies between one and six years. The inspector uses his engineering judgement to consider the expected rate of deterioration of any defect, and its significance, when deciding the year of next inspection, and uses this in conjunction with the age and traffic intensity carried by the bridge to decide on an appropriate interval.

The condition ratings given during Principal Inspections are used to rank structures for repair and assist in the compilation of future structure repair lists.

In relation to consistency of inspection the UK and Ireland Bridge Owners Forum commenced a project with the UK Department for Transport to set up a Bridge Inspection Competence Certification Scheme with the aim of certifying bridge inspectors and putting in place a register of trained inspectors to service the needs of bridge owners and maintaining agents across the countries. At the time of publishing this paper the UK Department for Transport were about to advertise for a Scheme Administrator to operate the certification scheme.

4.3 Special Inspection

A Special Inspection can be called by NRA bridge management as part of a nationwide tranche of targeted inspections, for example underwater inspections or inspection of potentially vulnerable post-tensioned bridges, and can also be requested by an inspector during a Principal Inspection in order to determine in detail the nature, extent and cause of damage to a structure.

Testing in the form of destructive or non-destructive testing could be undertaken, for example to determine the extent of corrosion of steel reinforcement in a reinforced concrete slab and to confirm the extent of chloride ingress or carbonation of the concrete. A life cycle cost analysis of repair strategies may be undertaken to evaluate the direct and indirect cost of proposals such that best value is offered when choosing an appropriate repair strategy.

Special Inspection programmes such as underwater inspections have been extremely useful to bridge managers in helping to identify the need for scour repair works. The Special Inspection of post-tensioned structures has not identified any significant areas of deterioration to date which would necessitate structural intervention.



Figure 2 Special Inspection of Post-Tensioning System on Youghal Bridge County Waterford

4.4 Routine Inspection

In the past Local Authorities have undertaken routine inspection and maintenance activities under specific maintenance grants issued by the NRA but in recent years the Authority has moved towards using consultants to undertake routine inspections and term maintenance contractors to undertake routine maintenance on a regional basis.

The routine inspection is an annual inspection to record the routine maintenance needs of a structure with reference to items such as vegetation clearance, cleaning the drainage systems and repointing of masonry stonework. It forms an integral part of the bridge management process.

4.5 Structural Assessment

Most masonry arch structures on National routes were constructed in the late 18th and early 19th Centuries and were designed to carry the transport of the day which was horse and cart. Modern bridges designed after 1980 and prior to the introduction of Eurocodes in 2010 have been designed to BS5400 and the loading Standards of the UK and Ireland Design Manuals for Roads and Bridges, and are therefore capable of carrying HA loading including cars, buses, and rigid and articulated Heavy Goods Vehicles with a Gross Vehicle Weight up to 40/44 tonnes. Recent work by the NRA verified that allowing for a 6-axle 46 tonne vehicle would be less onerous than the current design load models which led to acceptance of 46 tonne vehicles on Irish roads in 2013. Most structures will also have been designed to carry abnormal loading appropriate to a particular HB vehicle as set out in the UK Design Manual for Roads and Bridges (DMRB), or SV vehicles in the case of bridges designed to Eurocodes.

However bridges designed before 1980 are likely to have been designed for lower loads and therefore need to be assessed to in accordance with DMRB BD21[3]. Also, bridges which were designed to BS5400, or indeed Eurocodes, which have suffered significant deterioration may also require a structural assessment. The NRA has managed a programme of structural assessments for the older structures using a combination of the Modified MEXE analysis, as outlined in DMRB BA16[4], and a three hinge mechanism analysis to screen the masonry

arch bridge stock and identify bridges which do not meet the loading requirement. Bridges which fail the initial assessment are subject to closer scrutiny in the form of structural investigations to evaluate whether haunching is present above the arch springings, and to confirm arch ring thickness at critical locations along the barrel. The structures are re-assessed using the gathered data and those that fail this Stage 2 assessment will be subjected to further refined analysis, if it is believed that such analysis may conceivably lead to an assessment pass for 40T assessment live loading, otherwise the structure will be strengthened.



Figure 3 Coring of masonry arch barrel to gather assessment data

Modern slab structures designed prior to 1980 are assessed using basic analysis in the first instance under a Stage 1 assessment which may include a metre strip analysis or a grillage analysis if transverse distribution properties are appropriate. More refined assessment techniques are used in the Stage 2 assessment of structures which fail the basic assessment. The NRA expect that further refined analysis including probabilistic analysis will be used to target specific structures for which strengthening would be prohibitively expensive, or particularly inconvenient in relation to traffic diversions for very large volumes of traffic. The use of such 'virtual strengthening' techniques has the potential to bring huge savings to the Government when compared to the cost of on-site strengthening Works.

5 BRIDGEWORKS

There are a multitude of reasons which lead to the need for bridgeworks. Some of the more common reasons include; failed structural assessments necessitating bridge strengthening; durability issues; failed components which require replacing; narrow bridges which require widening, defects highlighted in Principal Inspections reports which require repair; urgent scour repairs. Bridge managers should give careful consideration to the timing and nature of structural interventions to ensure the many parameters which influence the decision-making process are well considered.

For example, if rehabilitation works are required on any bridge and yet that bridge was designed prior to 1980 and has not been assessed for load-carrying capacity, rehabilitation works ought to be delayed until the load-carrying capacity assessment is undertaken. If the rehabilitation works are carried out before the assessment is completed, and if a subsequent structural assessment shows that strengthening is required, a revisit to the bridge may be required to strengthen it. Two visits within a short timeframe to undertake Works will not be viewed as positive by road users, politicians or the holders of the purse-strings.

5.1 Structure Work Types

Bridges are designed today for a 120 year design life however they will not reach that lifespan unless they are inspected regularly and well-maintained. Expansion joints will typically have a lifespan of 5 to 15 years depending on joint type, traffic usage and exposure to braking loads. Sprayed waterproofing membranes are applied to modern structures to prevent the ingress of chlorides and other water-borne agents of deterioration but how long will the membranes last? The NRA has undertaken bridge bearing replacement on some structures which are approximately 60 years old. The phenomenon of scour damage has given rise to the need for emergency works on several bridges.



Figure 4: Assessment of scour damage to masonry arch

Masonry arch bridges with their shallow foundations are particularly susceptible to scour damage; bridge owners and managers need to be aware of the risk posed by significant vegetation gathering on the upstream side of structures which may lead to unusual erosion patterns on the riverbed, to which the bridge may not have been subjected before, as the water powers between branches and through the masonry spans.

Some of the more common types of bridgeworks are listed in Table 4. The second column of Table 4 gives the percentage of that particular type of bridgeworks which has been undertaken in the context of all of the structures which have received significant work since Eirspan commenced in 2001 (2013 figures).

Table 4 shows that masonry arch bridge strengthening and rehabilitation was a focal point of bridge management activity. Many of these structures had suffered significant mortar loss and were repointed with lime mortar either to strengthen them (if they failed assessment) or as good bridge management practice.

Table 4 Structure Work Types and Percentages

Road bridge replacement	14%
New or replacement footbridge	1%
Bridge widening	6%
Masonry Arch bridge strengthening or rehabilitation	28%
Concrete bridge strengthening or rehabilitation	13%
Steel bridge strengthening or rehabilitation	3%
Expansion joint replacement only	18%
Parapet & safety barrier works only	14%
Scour repair only	2%
Retaining wall works only	1%

Bridges which were visited only to replace expansion joints also featured highly in the table at 18%. Expansion joint replacement would also have featured within the concrete and steel bridge rehabilitation works categories. The NRA have undertaken many bridge joint replacement contracts as this component requires replacing on a cyclical basis in order to prevent leakage of water, perhaps laden with de-icing salts, onto the bearing shelves, and in order to ensure a smooth ride quality for road users, particularly motorcyclists. Many bridges are now designed with integral construction in accordance with DMRB BD57[5] which removes the need for bearings and the need for expansion joints on the bridge deck.

5.2 Masonry Arch Bridge Repairs

The Authority has largely treated the stock of masonry arch bridges with great care given the significant heritage and cultural value these bridges represent in Ireland. Many of them needed to be repaired quickly following the first tranche of inspections in 2001 and a range of defect types was found. Many structures, particularly on Secondary routes, are not paved for the full width between the parapets and therefore water can percolate through the soft verges and adjacent to the parapets and remove the fines from the backfill and wash out the mortar from between the voussoir stones which form the arch barrel. Such structures were constructed with lime mortar and it is the mortar which is designed to act as the sacrificial layer in the stone/mortar matrix which leads to a need to repoint masonry stonework periodically.

Given the scale of repointing repairs required to masonry arches the Authority undertook trials of various lime mortar mixes and application methods to establish a working specification for undertaking horizontal, vertical and overhead repointing in areas where the mortar loss is as deep as 250mm and as wide as 80mm between stones in the arch intrados.

There are two significant reasons for repointing with lime mortar rather than cementitious mortar. Firstly the use of lime is in keeping with the character of the bridge given it was constructed with lime mortar and such repairs make a significant contribution to the built heritage of the nation. Secondly there are technical reasons for using lime mortar as it has a higher flexural strength than cementitious mortar and is therefore more likely to accommodate the thermal and load-induced movements of the arch barrel without giving rise to cracking of the mortar or the stones.
The NRA worked with a contractor to develop his sprayed concrete apparatus to facilitate its use for adopting a mechanical method of applying lime mortar in order to improve the rate of application of the mortar which proved very successful.

The work which was developed during the trials has formed the basis of a new section in the NRA's revised Specification Series 2400[6] to address repointing of historic structures.

It is important that masonry arch defects are diagnosed correctly and that appropriate repairs are chosen. Sometimes a 'do nothing' approach is the best option. For example consider the not uncommon defect of a crack manifesting between the spandrel wall and the arch barrel of a masonry arch bridge.

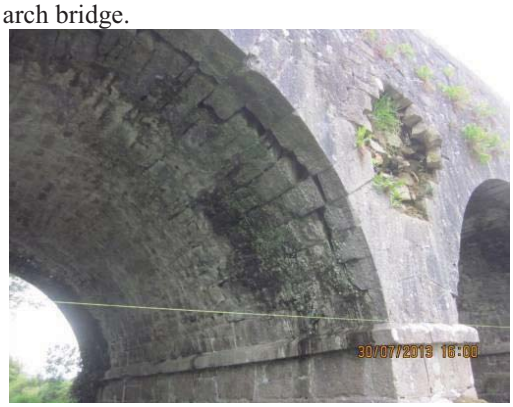


Figure 5 Spandrel Wall/Arch barrel crack

In many cases this defect arises due to the difference in stiffness between the rigid spandrel wall and the less rigid arch barrel which may flex under live loading. If the crack has opened significantly as shown in Figure 5, perhaps as a result of centrifugal live loading due to the location of the bridge on a bend in the road, or significant surcharge loading from the backfill perhaps with wheel loads close to the parapet, then an appropriate and aesthetically pleasing solution would include for core drilling through the spandrel walls and using stainless steel tie-bars and pattress plates to restrain the wall from further outward movement. However if the crack is as narrow as the existing joints and is indicative of vertical shear only, and no horizontal movement is expected then provided the structure has passed its load-carrying capacity assessment the bridge manager may consider a 'do nothing' option. Such defects have on occasions been repaired by stitching across the crack with stainless steel dowels and this may lead to further circumferential cracking developing as the plane of weakness is moved towards the centre of the bridge.

It is worth highlighting the importance of previous inspection reports, or old photographs, which play an important part in helping a bridge manager decide whether a defect such as a crack, a bulge or a rotated retaining wall is active or historic. A 'do nothing' approach could be considered for some historic defects, whilst if a bridge manager has documents

which show a defect is active he is more likely to monitor the defect or act to repair it.

6 CONCLUSIONS

Successful bridge management requires a multi-pronged approach to implementing a range of cyclical and non-cyclical inspection processes to inform the bridge manager regarding the condition and ongoing rate of deterioration of his structure stock. However whilst such inspections can highlight defects in structures it is also important to consider durability and strength issues before recommending repair options if optimal value for money is to be obtained for the limited budgets available.

Deciding where to target funding when the full range of masonry, concrete and steel bridges need repairing, strengthening, rehabilitating, and widening is not an easy process but the bridge manager must balance the needs of ancient structures such as Adare Bridge, constructed in 1410 with the needs of more recently completed concrete structures which may require expansion joint replacement, both of which carry modern traffic loading. Whilst a Bridge Management System serves as a useful tool, good engineering judgement is still very much an essential quality of today's bridge manager.

ACKNOWLEDGMENTS

The Author would like to thank John Iliff, Head of Structures at NRA and Fred Barry, CEO of NRA for giving permission to write this paper.

REFERENCES

6.1 References

[1] Eirspan Bridge Management System, National Roads Authority, Dublin, Ireland, 2001.
[2] DANBRO Bridge Management System, Danish Roads Directorate, Copenhagen, Denmark.
[3] Highways Agency, 'Design Manual for Roads and Bridges, BD21/01 The Assessment of Highway Bridges and Structures', Highways Agency, London, England, 2001.
[4] Highways Agency, 'Design Manual for Roads and Bridges, BA16/97 The Assessment of Highway Bridges and Structures', Highways Agency, London, England, 1997.
[5] National Roads Authority, 'Design Manual for Roads and Bridges, BD57/10, Design for Durability', National Roads Authority, Dublin, Ireland, 2010.
[6] National Roads Authority, 'Manual of Contract Documents for Roadworks, Specification Series 2400 Brickwork, Blockwork and Stonework', National Roads Authority, Dublin, Ireland, 2013.

Administration of Abnormal Vehicles in Ireland

Robert Corbally[1], Alan O'Connor[1], Fergal Cahill[2], Albert Daly[2]

[1]Roughan & O'Donovan Innovative Solutions, Arena House, Arena Road, Sandyford, Dublin 18, Ireland.
[2]National Roads Authority, St. Martin's House, Waterloo Road, Dublin 4, Ireland.

email: robert.corbally@rod.ie, alan.oconnor@rod.ie, fcahill@nra.ie, adaly@nra.ie.

ABSTRACT: With increasing demand to transport heavy loads by road, the effects of abnormally loaded vehicles on bridge safety must be considered. Currently no loading analysis is undertaken by local authorities or law-enforcement agencies when deciding whether or not to issue a permit for an abnormal vehicle. This paper presents the results from a detailed study which aimed to improve current procedures for granting permits by considering the effects of these vehicles on bridges. The primary objectives were (i) to develop a table of 'Abnormal Vehicle Silhouettes' representative of abnormal vehicles that can feasibly be anticipated on the Irish Major Inter-Urban (MIU) network and (ii) to develop a software tool which could be used to assist in the decision making process for issuing of permits for abnormal vehicles wishing to travel on the Irish MIU network. Initially, abnormal vehicle records were obtained from the local authorities but these were found to be insufficiently detailed to be of use, so an extensive Weigh-in-Motion (WIM) database from the U.K. was used to study the types of vehicles being used to transport abnormal loads. Using this WIM database, a set of representative abnormal vehicle silhouettes was developed for weight classes ranging from 50t-150t. A software tool was then created which estimates the proportion of the design load effect, of bridges on the MIU network, which is utilised during the passage of a particular abnormal vehicle. Finally, a *'Green Motorway Network'* map was developed, indicating that typical abnormal vehicles weighing up to 100t are likely to be granted permits to travel on the Irish MIU network. The development of this software tool along with the *'Green Motorway Network'* map will allow informed decisions to be made and should improve and unify current procedures for issuing abnormal vehicle permits.

KEY WORDS: Abnormal Vehicle Loading; Major Inter-Urban Network; Bridge; Green Motorway Network; Ireland.

1 INTRODUCTION

In Ireland, legislation governing normal vehicles specifies limits on the maximum allowable weights and dimensions for vehicles which are legally allowed to travel on the roads [1]. Current weight limits for standard 5-axle and 6-axle trucks are 40t and 46 t respectively. Any vehicles which do not comply with the regulations are required to obtain a permit in accordance with [2]. These 'Abnormal Vehicles' include vehicles which transport extremely heavy indivisible loads, far in excess of the everyday normal traffic loading experienced by bridges on Irish roads. The effects of this abnormal loading must be considered when making a decision as to whether or not a permit should be granted for a particular abnormal vehicle. At present it appears that no loading analysis is undertaken by local authorities or law-enforcement agencies as part of the decision making process.

This study aimed to develop tools which would improve current procedures for issuing abnormal vehicle permits by considering the effects that these vehicles are likely to have on bridges. Only bridges on the Irish Major Inter-Urban (MIU) network were considered. Figure 1 outlines the MIU network (indicated by the thick red lines).

The two primary objectives of the study were (i) to develop a table of 'Abnormal Vehicle Silhouettes' which are representative of the abnormal vehicles which can feasibly be anticipated on the Irish-MIU network and (ii) to develop a software tool to assist in deciding whether or not it is appropriate to issue a permit for an abnormal vehicle travelling on the MIU network.

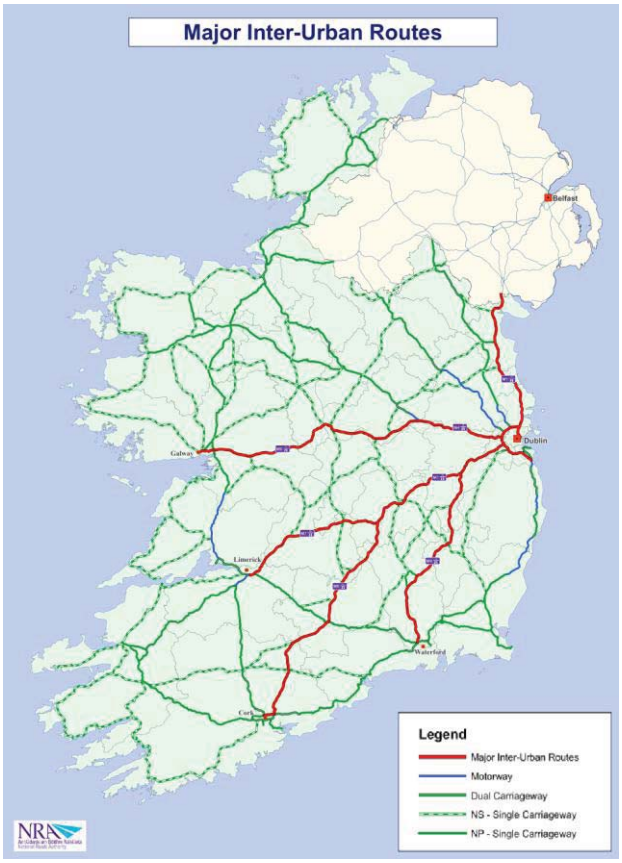


Figure 1. Major inter-urban network.

2 PRELIMINARY ANALYSIS

At the outset of the project it was necessary to identify the information that was available regarding the types of bridges on the MIU network in addition to the types of abnormal vehicles which are currently travelling on Irish roads. The use of this information allowed the definition of a number of analysis assumptions which were used throughout.

2.1 Definition of Considered Structures and Load Effects

In order to assess the effects of abnormal vehicle loading on bridges on the MIU network it was necessary to identify the types of bridges present on these roads, and hence define the critical load effects for these structures. It is noted that this task aimed to identify the most common bridge types on the network rather than study the structural configuration of every single bridge individually.

The EIRSPAN database of Irish bridges was consulted and the under-bridges on the MIU network were examined. Based on the results it was agreed that the influence lines illustrated in Figure 2 were deemed to be representative of the critical load effects for the majority of structures on the MIU network.

Influence Line Number	Representation	Description of the Influence Line
I0		Total load.
I1, I2		Maximum bending moment of a simply supported and double fixed[1] span, respectively.
I3		Maximum bending moment at the support of the former double fixed beam[1].
I4, I5		Shear force at the ends of simply supported bridge (assuming traffic flowing left to right).
I6		Moment at centre of central span in 3-span bridge with span ratios 0.7L:1.0L:0.7L (I6a) and 0.4L:1.0L:0.4L (I6b).
I7, I8		Minimum and maximum bending moment at mid-span of the first of two spans of a two span continuous beam.
I9		Continuous support moment of the former two span beam.
I10		Continuous support reaction of the former two span beam.

[1]with an inertia strongly varying between the mid-span and the ends

Figure 2. Representative bridge structures and influence lines.

These influence lines were evaluated for bridge lengths ranging from 2m to 75m and represent the main structural effects for bridge deck configurations which are (i) simply supported, (ii) continuous (2-span and 3-span) and (iii) fully fixed. It is noted that a similar set of influence lines formed the basis for the recalibration of the Eurocode LM1 [3].

2.2 Review of Available Information on Abnormal Vehicles

In order to identify the types of vehicles being used to transport abnormal loads on Irish roads all of the local authorities in Ireland were contacted and information on records for permits issued over the last four years was requested. The information received varied in format and content between the different local authorities with a great deal of it being unreliable or lacking sufficient detail for use in this study. Only a limited number of records contained information on axle-weights or axle-spacings, making it very difficult to identify the common types of vehicles being used to carry abnormal loads.

It was found that there were not enough useful details in this data set to meet the requirements of this study, thus a database of Weigh-in-Motion (WIM) records from the U.K. was employed instead. This database contained weights for approximately 2.9 million trucks (where a truck was regarded as any vehicle with a gross weight in excess of 3.5t). The recorded data came from 12 different sites, with every site having records from January 2010 and one site also having February 2010 recorded. The database only contained records for up to 10 axles per vehicle. Figure 3 shows the distribution of gross vehicle weights (GVW) for all of these trucks. It can be seen that the majority of the vehicles (97%) weighed less than 50t, with the inset histogram showing the distribution of weights for vehicles over 50t. These vehicles were of interest for the study of vehicles transporting abnormal loads.

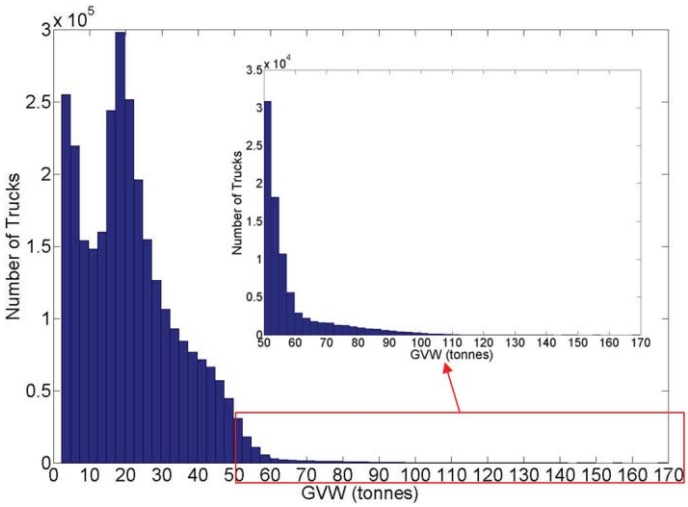


Figure 3. Gross vehicle weight distribution of UK WIM data.

The information on the axle spacings and weights of these trucks was used to identify the most common types/configurations of abnormal vehicles on the roads. This allowed the derivation of a set of abnormal vehicle silhouettes which were representative of the standard abnormal vehicle configurations (see Section 3).

2.3 Definition of Analysis Procedures

The derivation of abnormal vehicle silhouettes along with the development of a software tool to assist in issuing abnormal vehicle permits required a set of analysis assumptions to be made. The majority of the analysis that served as the basis for this work involved comparing the load effects induced by an abnormal vehicle to those induced by the codified design load models for abnormal loading. Bridges on the Irish MIU network are required to be designed using the SV196 load model [4] since the introduction of the Eurocodes in 2010. Prior to this, Irish MIU bridges were designed using the HB45 load model [5]. As such, both of these load models were considered in the analysis. The results of the calculations were expressed as load effect ratios (LER) as per Eq. 1.

$$LER = \frac{LE\ induced\ by\ abnormal\ vehicle}{LE\ induced\ by\ codified\ design\ load\ model} \quad (1)$$

Figure 4 outlines the HB load model, which consists of four axles with a variable central spacing as shown. The spacing which induces the most severe load effect for a particular analysis should be used. It is noted that HB45 refers to 45 units of HB, i.e. 45t on each of the four axles of the HB load

model (one 'unit' of HB loading is defined as 10kN per axle) . This is the level of abnormal loading, along with HA normal loading, for which bridges on the Irish MIU network should have been designed prior to 2010.

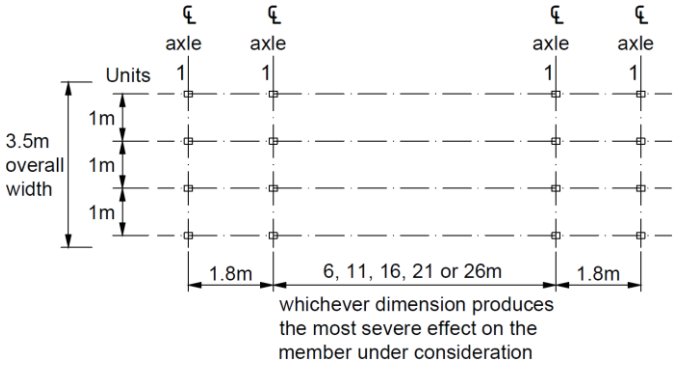


Figure 4. HB load model.

Figure 5 outlines the SV196 load model which is now used in the design of motorway bridges in Ireland.

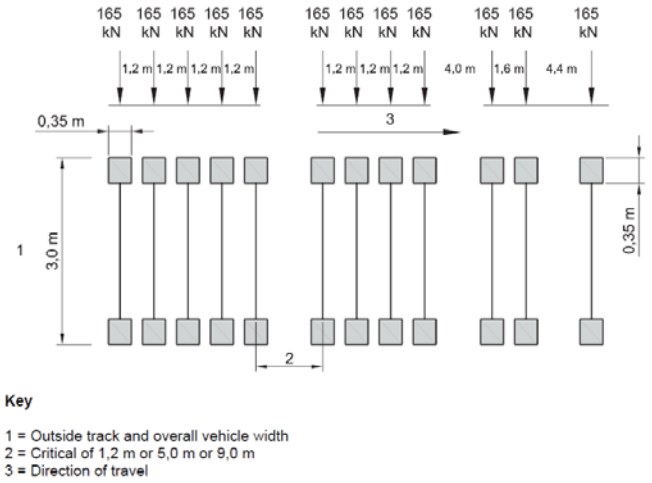


Figure 5. SV196 load model.

All of the assumptions made were defined in such a way as to be conservative in the evaluation of Eq. 1, where a conservative assumption was defined as one which maximised the load effect ratio given by Eq. 1. A detailed analysis showed that it was most conservative to assume a single 3m wide lane of traffic in the analysis. In order to carry out the analysis, a set of passage conditions were defined. It was necessary to define passage conditions for three different situations as listed below:

- Passage of an actual abnormal vehicle.
- Passage of the HB45 load model.
- Passage of the SV196 load model.

Each of these was defined in accordance with the relevant codes, with the passage condition for the actual abnormal vehicle being defined in accordance with [6]. It is noted that [4], [5] and [6] all specify that additional loading be included in the same lane as the vehicle or load model being considered. This additional loading is included in order to account for traffic that may be on the bridge at the same time as the abnormal vehicle. HA loading, as specified by [5] and [6] consists of a UDL and a knife-edge load (KEL). When HA loading is being included within the same lane as the abnormal vehicle, or HB45 load model the KEL is omitted. When applying the SV196 load model, LM1 loading must also be included, as specified by [4]. LM1 loading consists of a UDL and a tandem axle.

Figure 6 shows the passage conditions which were used in the analysis. It is noted that when analysing the passage of an abnormal vehicle, 'low speed' and 'normal speed' checks should be carried out in order to determine which is most severe. The 'low speed' check allows for a greater amount of additional traffic loading on the bridge, but does not apply a dynamic amplification factor (DAF) to the axles of the vehicle.

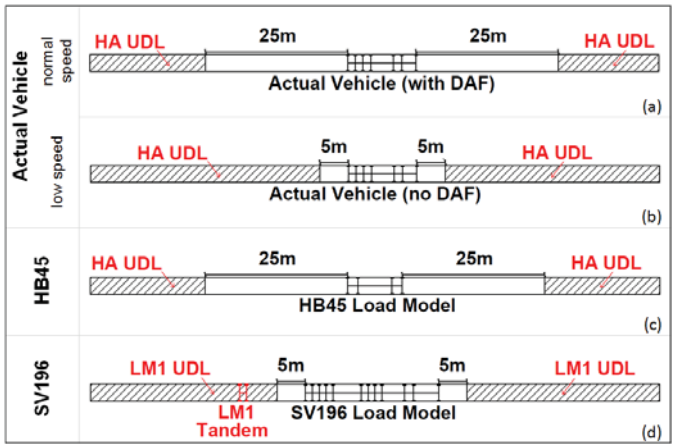


Figure 6. Passage conditions for: (a, b) abnormal vehicle, (c) HB45 load model and (d) SV196 load model.

When applying the passage conditions shown in Figure 6, all of the loads were factored in accordance with the relevant standards [4, 5, 6].

3 DERIVATION OF ABNORMAL VEHICLE SILHOUETTES

One of the primary objectives of this study was to develop a set of abnormal vehicle 'silhouettes' which could be used to represent typical abnormal vehicle configurations. Using the WIM data described in Section 2.2 the typical configurations of vehicles in a number of weight classes were considered. Eight different weight classes, ranging from 50t-150t were defined as shown in Table 1:

Table 1. Weight classes.

Weight Class	GVW Limits
50t	45t ≤ GVW < 55t
60t	55t ≤ GVW < 65t
70t	65t ≤ GVW < 75t
80t	75t ≤ GVW < 85t
90t	85t ≤ GVW < 95t
100t	95t ≤ GVW < 112.5t
125t	112.5t ≤ GVW < 137.5t
150t	137.5t ≤ GVW < 175t

The most common vehicle configuration in each of these weight classes was identified from the WIM data. These eight vehicle types were chosen as the representative vehicle configuration for each weight class. In order to develop a set of abnormal vehicle silhouettes the axle weights on each of

these representative vehicles had to be decided. This was done by optimising the axle weight distribution so as to induce the maximum load effect ratios (as per Eq. 1) when considering all of the influence lines shown in Figure 2 for bridge lengths ranging from 2m to 75m. The optimisation was carried out using the passage classes illustrated in Figure 6.

Figure 7 outlines the procedure used to develop the set of abnormal vehicle silhouettes with Figure 8 illustrating the final set of representative abnormal vehicle silhouettes which were derived.

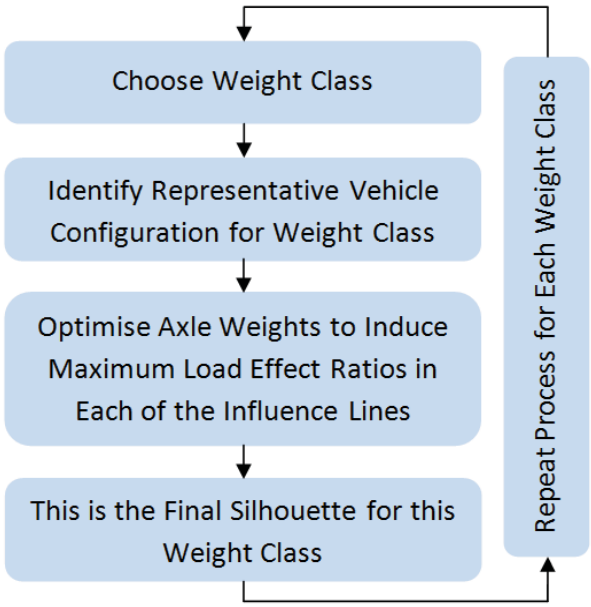


Figure 7. Procedure for deriving abnormal vehicle silhouettes.

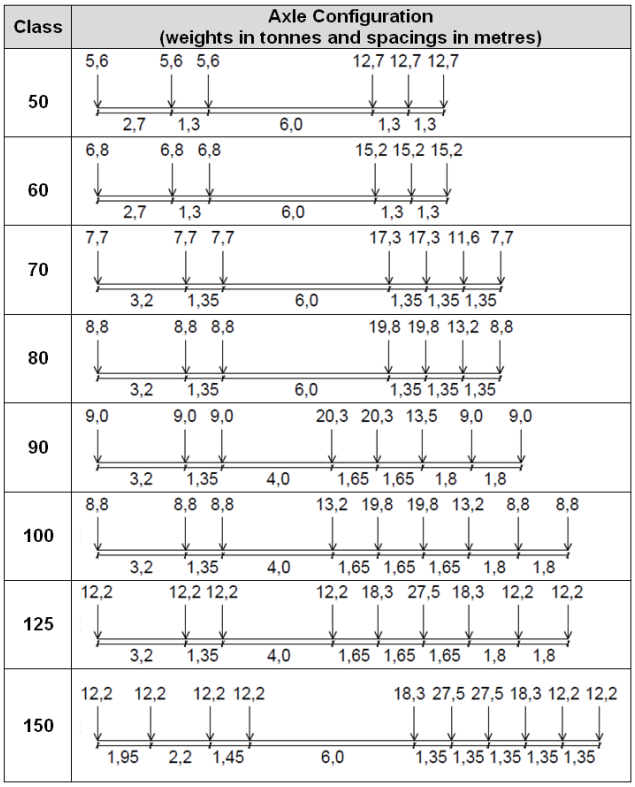


Figure 8. Representative abnormal vehicle silhouettes.

The silhouettes shown in Figure 8 were deemed to represent the typical configurations of abnormal vehicles of different weights. These silhouettes were used in the classification of a *'Green Motorway Network'* as described in Section 5.

4 DEVELOPMENT OF TOOL TO ASSIST IN ISSUING OF PERMITS FOR ABNORMAL VEHICLES

The main objective of this work was to improve current procedures for the issuing of abnormal vehicle permits. Based on an examination of records on recently issued permits it was clear that there is no unified approach in place at present. In addition, it appears that in the majority of cases, no specific analysis is carried out to quantify the effects of these vehicles on the bridges which they will encounter. The development of a simple tool which can provide an indication of the effect that a particular abnormal vehicle is likely to have on typical bridges on the MIU network would be of great benefit, and a major improvement on current practices.

In this regard, a software tool, in the form of an excel spreadsheet interface, with VBA code written to carry out the analysis, was developed. This tool requires the user to input the axle-weights and axle-spacings of an abnormal vehicle applying for a permit. When the analysis is run, the maximum load effect that the abnormal vehicle induces on each of the influence lines shown in Figure 2 is evaluated. These load effects are evaluated using the passage conditions shown in Figure 6 (a) & (b). The load effects induced by the HB45 and SV196 load models are similarly calculated using their relevant passage classes from Figure 6. The load effect ratios for all influence lines are then calculated as per Eq. 1 and if any of these are greater than 1.0 the user is informed that a permit should not be issued. Figure 9 describes the principle of operation for the tool.

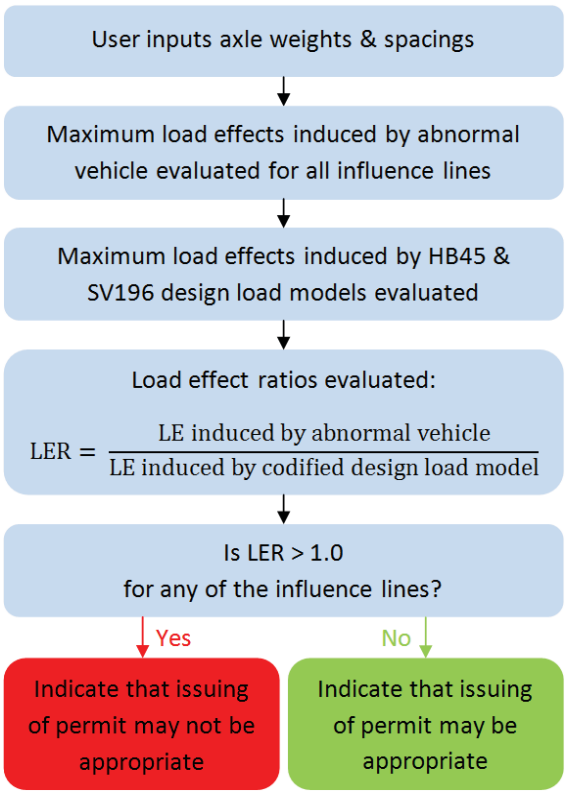


Figure 9. Principle of operation for software tool.

The software tool considers 391 different influence lines in the analysis. The influence lines described in Figure 2 are all analysed for bridge lengths ranging from 2m to 75m with some additional influence lines included to account for structures which were not covered by those presented in Figure 2.

Upon completion of the analysis the user is informed as to whether or not a permit should be issued. The maximum load effect ratio for each of the influence lines is displayed on screen to allow the user to identify which type of structure may be critical. The tool is designed to be as user friendly as possible, with the user only required to input the number of axles, axle-weights and axle-spacings for the vehicle which has applied for a permit. The user clicks the 'Check Vehicle' button and the analysis is carried out. The load effect ratios with respect to both the HB45 and the SV196 load models are calculated. All of the analysis and assumptions made are contained within the VBA coding and cannot be altered by the user.

It is envisaged that this tool will be used by local authorities and law enforcement agencies to aid in the decision making process for issuing of abnormal vehicle permits that wish to travel on the Irish MIU network. It is noted that the tool uses a conservative set of assumptions in the analysis. For particular permit applications where these assumptions are not deemed to be suitable, it may be appropriate to carry out a more detailed bridge-specific analysis.

Figure 10 shows the user-interface of the software tool, outlining the section which needs to be filled in by the user along with the section that displays the load effect ratios calculated in the analysis.

Despite the assumptions being made in a conservative manner, such a simplified analysis cannot take any bridge specific information into account. The influence lines analysed by the tool have been chosen to represent load effects which are expected to be critical for the most common structural configurations of bridges on the MIU network, however load effects outside those represented by these influence lines have not been included.

The basis of the analysis is a comparison of the load effects induced by an abnormal vehicle and those induced by the design load models. Thus, an implicit assumption is made that the bridges have retained their design capacity, as no deterioration or reduction in capacity is allowed for in the analysis. In addition, only bridges on the MIU network (Figure 1) have been considered in this study. All of these bridges are modern bridges which can, for the most part, be represented by the influence lines shown in Figure 2. It was considered infeasible to include bridges beyond those on the MIU network, due to the large variability in type and condition of these bridges. As a result, the software tool cannot be used where an abnormal vehicle wishes to make a journey on another route.

This tool should improve current practices for issuing permits for abnormal vehicles travelling on the MIU network by giving an indication of the load effects that a particular abnormal vehicle is inducing in the bridges, compared to the load effects which the bridges have been designed to withstand. This will allow informed decisions to be made when deciding whether or not it may be appropriate to issue a permit for a particular abnormal vehicle.

5 GREEN MOTORWAY NETWORK

5.1 Administration of abnormal vehicles in Denmark

The Danish Roads Directorate has developed a specific classification system devoted to the administration of heavy vehicles [7]. This system uses a set of abnormal vehicle silhouettes, similar to those developed in this study, to 'rate' the load carrying capacity of bridges, under normal or restricted passage conditions. Using these bridge ratings a so called '*Blue Road Network'* has been identified for Denmark, on which all bridges are rated at a minimum of 100t. This allows informed decisions to be made when managing the administration of abnormal vehicle permits in Denmark.

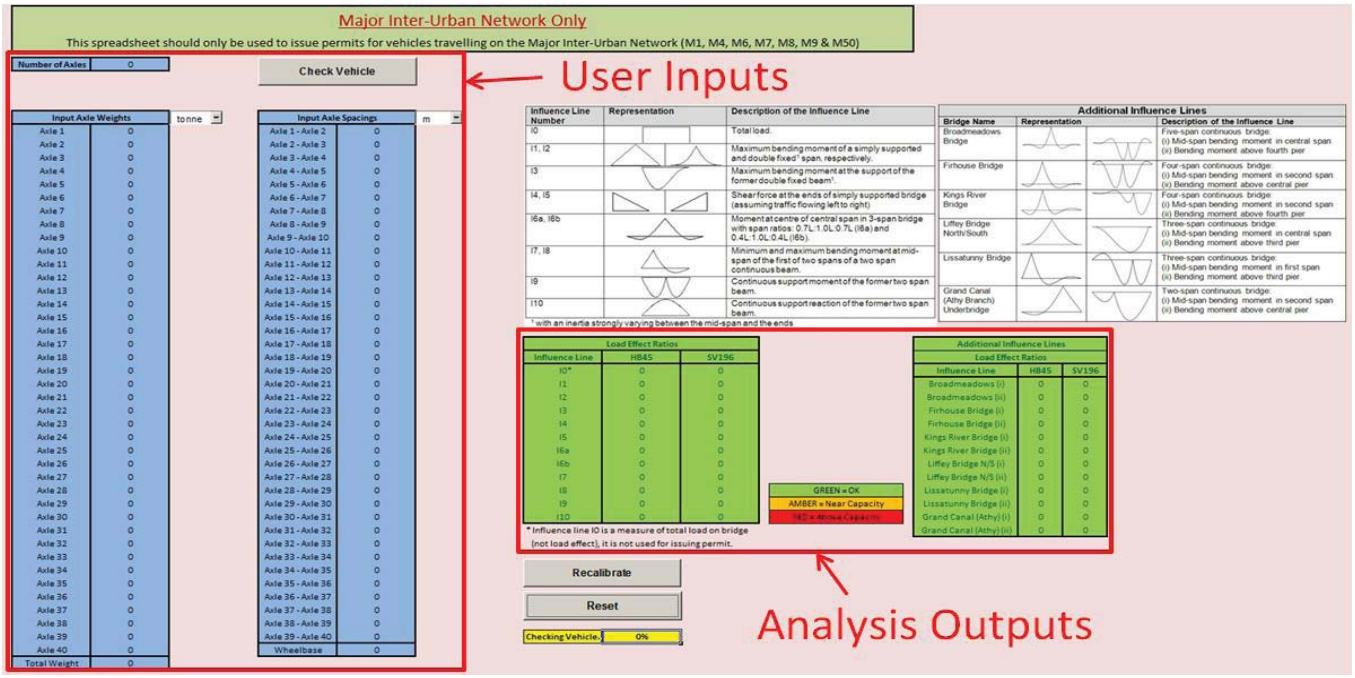


Figure 10. Software tool for to assist in decision making process for issuing abnormal vehicle permits.

5.2 Development of a 'Green Motorway Network'

The final stage of this study involved developing a '*Green Motorway Network'* for Ireland. This was done using the abnormal vehicle silhouettes illustrated in Figure 8 along with the software tool. Each of the silhouettes, starting with the 50t class, were analysed using the software tool and the resulting load effect ratios were recorded. At the time that the work was carried out (November 2013), no bridge structures on the MIU network had been designed using the Eurocode SV196 load model. Hence only the load effect ratios with respect to HB45 were examined. It was found that none of the silhouettes from 50t to 100t induced a load effect ratio greater than 1.0 with respect to HB45, while both the 125t and the 150t silhouette induced load effect ratios greater than 1.0.

Based on these results, a generalised classification of 100t may be assigned to the Irish MIU network, thus identifying the MIU network as a '*Green Motorway Network'* for Ireland. This network provides an indication that it is likely that typical abnormal vehicles, similar to those represented by the silhouettes, weighing up to 100t, are likely to be granted a permit

Due to the simplicity of the analysis involved in the derivation of the *'Green Motorway Network'* it can only be used as a general indication of the types of vehicles that are likely to be granted permits. The effect that an abnormal vehicle applying for a permit will have on the bridges on its route should still be assessed for each individual permit application.

6 CONCLUSION

Currently it appears that no loading analysis is undertaken by local authorities or law-enforcement agencies to examine the effects of abnormal vehicles on bridges as part of the decision making process for granting permits. This paper presents the results from a detailed study which aimed to examine current procedures for administering abnormal vehicle permits in Ireland with a view to improving the system by considering the effects that these vehicles have on bridges.

Preliminary work involved a study of the types of bridge structures present on the MIU network, the examination of records on abnormal permits granted by the local authorities and the definition of a number of passage conditions to consider in the analysis.

Using a set of influence lines which were deemed appropriate to represent the critical load effects for the majority of bridges on the MIU network, along with information from an extensive WIM database from the U.K., a table of representative abnormal vehicle silhouettes, ranging from 50t to 150t, was developed.

In addition, a software tool, which uses the representative influence lines to compare the load effects induced by an abnormal vehicle to those induced by two codified abnormal loading design load models (HB45 and SV196), was developed. It is envisaged that this tool could be used by local authorities and law-enforcement agencies to assist in the decision making process for issuing permits for abnormal vehicles.

Finally, it was determined that when using the representative abnormal vehicle silhouettes, the Irish MIU network may be classified as a *'Green Motorway Network'*, on which permits are likely to be granted for typical abnormal vehicle configurations weighing up to 100t.

The development of the software tool and the *'Green Motorway Network'* map will allow informed decisions to be made when issuing permits for abnormal vehicles travelling on the MIU network. This should improve and unify current procedures for issuing abnormal vehicle permits.

ACKNOWLEDGMENTS

The authors would like to gratefully acknowledge the U.K. Department for Transport for the provision of the Weigh-in-Motion data which was used in this study.

REFERENCES

[1] Statutory Instrument No. 5 of 2003, 'Road traffic (construction and use of vehicles) regulations 2003', as amended.

[2] Statutory Instrument No. 283 of 2007, 'Road traffic (special permits for particular vehicles) regulations 2007'

[3] A. O'Connor, B. Jacob, E. O'Brien and M.Prat (2001), 'Report of current studies performed on normal load model of EC1-traffic loads on bridges', *Revue Française de Génie Civil (RFGC), Hermes Science Publications,* 5 (4), 411-434.

[4] IS EN 1991-2 NA (2003), 'Eurocode 1: Actions on structures – part 2: traffic loads on bridges', NSAI.

[5] BD 37/01, 'Loads for highway bridges', *Design Manual for Roads and Bridges*, volume 1, section 3 part 14. Highways Agency, UK.

[6] BD 86/11, 'The assessment of highway bridges and structures for the effects of special types general order (STGO) and special order (SO) vehicles', *Design Manual for Roads and Bridges*, volume 3, section 4, part 19. Highways Agency, UK.

[7] Vejdirektoratet (1996), *Beregningsregler for eksisterende broers baereevne,* (In Danish: Guideline for assessment of the load carrying capacity of bridges).

Seismic Testing and Analysis of the FlexiArch

Christopher McCracken[1], Su Taylor[2], Paul McNulty[3], Myra Lydon[4], Daniel McCrum[5], Desmond Robinson[6]
[1-6] SPACE, Queen's University Belfast, David Keir Building, Belfast, BT9 5AG, Northern Ireland

email: cmccracken07@qub.ac.uk, s.e.taylor@qub.ac.uk, pmcnulty06@qub.ac.uk, mlydon01@qub.ac.uk, d.mccrum@qub.ac.uk, des.robinson@qub.ac.uk

ABSTRACT: The FlexiArch is a novel bridge system developed through a Knowledge Transfer Partnership between Queen's University Belfast and Macrete Ltd. The design incorporates unreinforced concrete voussoirs connected by a polymeric membrane resulting in an arch ring that can be transported flat to site and lifted quickly and easily into position. Previous collaborative research has resulted in numerous arches being constructed throughout the UK and Ireland with a range of dimensions. With the intention to expand the FlexiArch into seismically active regions there is a need to investigate its dynamic behaviour and address the knowledge gap in order to evaluate seismic resistance. This paper presents work which forms part of a PhD research project on the seismic behaviour of the Flexiarch bridge system. Experimental shake table tests were carried out at the University of California San Diego (UCSD) under a UK Royal Academy of Engineering Global Research Award. A three ring specimen was subjected to white noise excitations and earthquake simulations of varying intensities, yielding an array of accelerometer data. The accelerations were post processed in the frequency domain and singular value decomposition (SVD) was used to estimate the natural vibrating frequencies. Dynamic characteristics determined from the experimental results will be used to validate future numerical models, in order to conduct a parametric study without continued testing. This paper summarises the experimental procedure and details the post processing carried out in obtaining the natural frequencies; which indicated a change in natural vibrating frequency before and after earthquake exposure.

KEY WORDS: FlexiArch™; Seismic Loading; Modal Analysis.

NOMENCLATURE

n	Sensor outputs	-
$[M]$	Mass matrix	$n \times n$
$[C]$	Damping Matrix	$n \times n$
$[K]$	Stiffness matrix	$n \times n$
$\{u(t)\}$	Displacement (time varying)	$n \times 1$
$\{p(t)\}$	Applied Force	$n \times 1$
$\{\ddot{u}_H(t)\}$	Horizontal Sensor Accelerations	$n/2 \times 1$
$\{\ddot{u}_V(t)\}$	Vertical Sensor Accelerations	$n/2 \times 1$
$\{\ddot{u}_T(t)\}$	Table Acceleration	$n/2 \times 1$
$\{U(\omega)\}$	Displacement Fourier Coefficients	$n \times 1$
$\{P(\omega)\}$	Applied Force Fourier Coefficient	$n \times 1$
i	$\sqrt{-1}$	-
e	Exponential Function	-
t	time	-
ω	Angular frequency	-
g	Acceleration due to gravity	-
$A(\omega)$	Accelerance Response Function	$n \times n$
$\alpha(\omega)$	Receptance Response Function	$n \times n$
$H(\omega)$	General Freq. Response Function	$n \times n$
$G_{yy}(\omega)$	Power Spectral Density of Output	$n \times n$
$G_{xx}\omega)$	Power Spectral Density of Input	$n \times n$
$[U]$	Unitary Matrix of Singular Vectors	$n \times n$
$[S]$	Diagonal Matrix of Singular Values	$n \times n$

1 INTRODUCTION

The FlexiArch bridge system has been developed under a Knowledge Transfer Partnership between Queen's University Belfast and Macrete Ltd. The system embraces the desirable qualities from traditional masonry arch bridges, but meets the modern day demands, by incorporating further sustainability considerations into the design and construction process. The FlexiArch deisgn includes a prefabricated flexible arch which is transported flat to site and lifted quickly and easily into position (defined by seating units) without the need for the labour intensive centring process. Precast spandrel walls are added and the ring is stabilised by granular backfill. The flexible arch ring consists of unreinforced concrete voussoirs cast horizontally and connected along the top face via a polymeric membrane. The membrane layer is designed to resist tensile forces formed by the self weight under lifting and the arch contains no corrodible steel reinforcement, in accordance with advice given by the Highways Agency [1]. Previous collaborative research has resulted in numerous arches with varying dimension being constructed throughout the UK and Ireland [2,3]. With the intention to expand the FlexiArch into seismically active regions such as New Zealand and Japan, there is a need to investigate the dynamic behaviour of the arch and establish seismic resistance.

2 RESEARCH OBJECTIVES

The work presented in this paper forms part of a PhD research project on the seismic behaviour of the FlexiArch. The objective of the PhD is to investigate the seismic behaviour of

the FlexiArch through the analysis of experimental results and numerical modelling.

The aim of the work presented in this paper was to determine the natural vibrating frequencies and mode shapes of the tested specimen, before and after earthquake exposure.

3 EXPERIMENTAL PROGRAM

The experimental program was carried out at the facilities of the University of California San Diego under a UK Royal Academy of Engineering Global Research Award.



Figure 1. Experimental assembly

3.1 Arch Details

A three ring 2.5m x 1.0m (span x rise) specimen with 23 voussoirs was tested. The assembly included a Perspex spandrel wall and the granular backfill was restrained laterally and horizontally by a steel frame and shuttering. The assembly and arch details can be seen in Figure 1 and Table 1.

Table 1. Arch Specimen Details

Arch Details	
Span	2500 mm
Rise	1000 mm
Total Width	1500 mm
Fill Level Above Crown	300 mm
Voussoir Details	
Voussoir Length Top	162 mm
Voussoir Length Bottom	150 mm
Voussoir Depth	100 mm
Screed Depth	20 mm
Number of Voussoirs	23
Number of Rings	3
Polymer Layer Details	
Cross-sectional Area per Strip	23.04 mm^2
Number of Strips per Ring	5

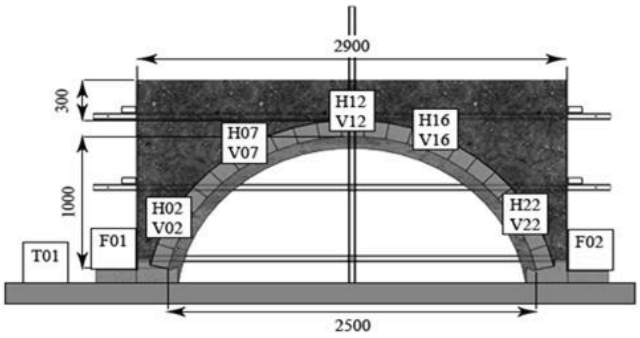


Figure 2. Accelerometer sensor locations

3.2 Instrumentation

2G and 4G accelerometers were positioned at expected critical hinge locations in both horizontal (H02-H22) and vertical (V02-V22) directions. Previous static tests provided knowledge of expected hinge locations. Additional accelerometers were placed in the horizontal directions on the seating units (F01-F02) and shake table surface (T01). The positions can be seen in Figure 2. Horizontal displacements and accelerations of the input excitations were also recorded from the actuator.

Table 2. Experimental Program

Test	Excitation	Scaling (%)	Peak Input Accel. (g)	Peak Meas. Table Disp. (mm)
001	White Noise	100	0.40	20.6
002	White Noise	100	0.40	16.9
003	Northridge	20	0.35	22.7
004	Chi Chi	50	0.48	14.1
005	Loma Prieta	20	0.41	17.4
006	Northridge	50	0.51	56.7
007	Chi Chi	100	0.62	28.3
008	Loma Prieta	50	0.62	43.5
009	Northridge	100	0.75	113.1
010	Loma Prieta	100	0.84	87.2
011	Loma Prieta	120	0.94	104.6
012	Loma Prieta	150	0.90	122.1
013	Loma Prieta	150	1.06	130.8
014	White Noise	100	0.52	16.7

3.3 Earthquake Excitations

The FlexiArch was initially subjected to white noise excitations containing frequency content up to 50Hz and peak acceleration of 0.4g. The structure was undamaged at this stage. The arch was then consecutively exposed to earthquake excitations (Loma Prieta, Chi Chi and Northridge) of varying intensities up to a peak acceleration of 1.1g to initiate damage. A final white noise excitation was again applied with varying

frequency up to 50Hz. The details of the experimental program and excitations can be seen in Table 2 and Figures 3-6 respectively. White noise was applied to the undamaged structure in Tests 1-2, then increasing levels of earthquake ground accelerations time histories were applied to the structure in Tests 3-13 to damage the structure. The damaged structure was tested using the same white noise signal in Test 14.

Figures 3 to 6 show the 100% scaled white noise and Chi-Chi, Northridge and Loma Pieta displacement and acceleration time histories measured by the table accelerometer.

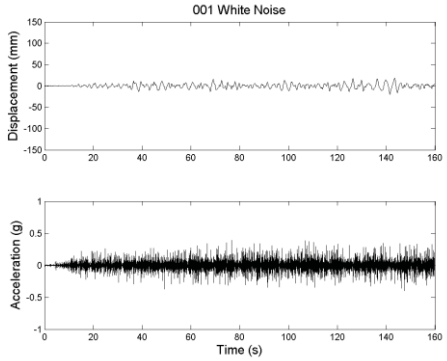


Figure 3. Input White Noise Excitation 100% Intensity for Test 2; (a) Displacement and; (b) Acceleration

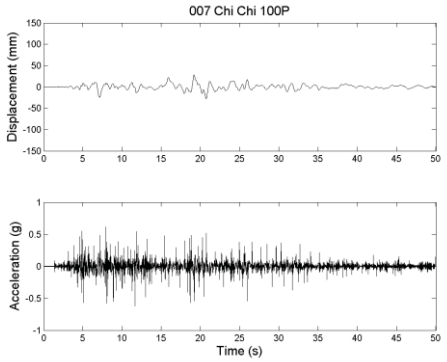


Figure 4. Input Chi Chi Earthquake 100% Intensity for Test 7; (a) Displacement and; (b) Acceleration

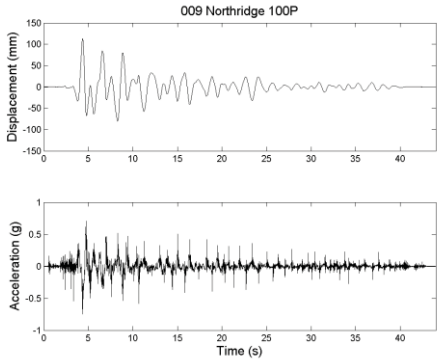


Figure 5. Input Northridge Earthquake 100% Intensity For Test 9; (a) Displacement and; (b) Acceleration

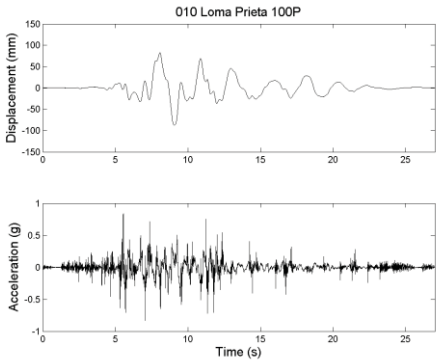


Figure 6. Input Loma Prieta Earthquake 100% Intensity For Test 10; (a) Displacement and; (b) Acceleration

4 POST PROCESSING

4.1 Frequency Response Function

The acceleration data was analysed in the frequency domain in order to determine the natural vibrating frequencies and mode shapes.

The relationship between the table input accelerations (T01), output sensor accelerations (H02-V22) and structural properties can be expressed through a generalised frequency response function, developed from the equations of motion.

Dynamic equilibrium for a MDOF system with viscous damping and subjected to a time varying force can be expressed as [4]:

$$[M]\{\ddot{u}(t)\} + [C]\{\dot{u}(t)\} + [K]\{u(t)\} = \{p(t)\} \quad (1)$$

Where for the FlexiArch experiment, the displacements can be expressed in terms of the n sensor locations (H02-V22):

$$\{u(t)\} = \begin{Bmatrix} u_H(t) \\ u_V(t) \end{Bmatrix} \quad (2)$$

And the forcing term can be expressed in terms of the FlexiArch mass and table acceleration (T01):

$$\{p(t)\} = -[M]\begin{Bmatrix} \ddot{u}_T(t) \\ 0 \end{Bmatrix} \quad (3)$$

Where $\ddot{u}_T(t)$ is an input acceleration signal such as that in Figure 3(b).

Taking the Fourier transform of Equation 1 and cancelling $e^{i\omega t}$ terms yields:

$$[M]\{\ddot{U}(\omega)\} + [C]\{\dot{U}(\omega)\} + [K]\{U(\omega)\} = \{P(\omega)\} \quad (4)$$

Where $\{\ddot{U}(\omega)\}$ denotes a column of complex Fourier coefficients representing the time varying signal in the frequency domain.

Expressing the acceleration and velocity in terms of displacement yields:

$$-\omega^2[M]\{U(\omega)\} + i\omega[C]\{U(\omega)\} + [K]\{U(\omega)\} = \{P(\omega)\} \quad (5)$$

and grouping terms:

$$(-\omega^2[M] + i\omega[C] + [K])\{U(\omega)\} = \{P(\omega)\} \quad (6)$$

taking the inverse the terms in brackets gives:

$$\{U(\omega)\} = (-\omega^2[M] + i\omega[C] + [K])^{-1}\{P(\omega)\} \quad (7)$$

or

$$\{U(\omega)\} = [\alpha(\omega)]\{P(\omega)\} \quad (8)$$

where $[\alpha(\omega)]$ is commonly known as the receptance frequency response function (FRF) matrix.

Expanding the terms in Equation 7 specific to the FlexiArch experiment gives:

$$\begin{Bmatrix} U_H(\omega) \\ U_V(\omega) \end{Bmatrix} = (-\omega^2[M] + i\omega[C] + [K])^{-1}[M]\begin{Bmatrix} \ddot{U}_T(\omega) \\ 0 \end{Bmatrix} \quad (9)$$

and expressing the sensor displacements in terms of accelerations gives:

$$\begin{Bmatrix} \ddot{U}_H(\omega) \\ \ddot{U}_V(\omega) \end{Bmatrix} = -\omega^2(-\omega^2[M] + i\omega[C] + [K])^{-1}[M]\begin{Bmatrix} \ddot{U}_T(\omega) \\ 0 \end{Bmatrix} \quad (10)$$

or

$$\begin{Bmatrix} \ddot{U}_H(\omega) \\ \ddot{U}_V(\omega) \end{Bmatrix} = [A(\omega)][M]\begin{Bmatrix} \ddot{U}_T(\omega) \\ 0 \end{Bmatrix} \quad (11)$$

Where $[A(\omega)]$ is commonly known as the accelerance FRF matrix [5].

Incorporating the accelerance FRF matrix and mass matrix into one term gives the relationship between the excitation input signals (T01), the recorded output acceleration signals (H02-V22) and FlexiArch structural properties:

$$\begin{Bmatrix} \ddot{U}_H(\omega) \\ \ddot{U}_V(\omega) \end{Bmatrix} = [H(\omega)]\begin{Bmatrix} \ddot{U}_T(\omega) \\ 0 \end{Bmatrix} \quad (12)$$

The $[H(\omega)]$ matrix represents the relationship of the table acceleration input to the sensor accelerations in the frequency domain. Where each individual sensor output is created by the corresponding row in the FRF matrix $h(\omega)$. Depending on the frequency content of the excitation signal the FRF matrix will scale the input signals and produce the corresponding output accelerations. At resonance, when the excitation signal contains frequencies close to the natural vibrating frequency higher outputs will be experienced. Correspondingly the graph of $[|h(\omega)|]$ or $[|H(\omega)|]$ vs. frequency will display peaks at the natural vibrating frequency of the structure, as the inputs are increasingly scaled by the dynamic system due to resonance. Graphs of $h(\omega)$ vs. frequency can be seen in Figures 7-8. The first natural frequency is quite apparent from Figures 7 & 8, however, the second natural frequency and higher natural frequencies are not conclusively shown. Figure 7 represents the undamaged structure and Figure 8 represents the damaged structure. It can be seen that the approximate second natural frequency appears to have shifted in Figure 8 as compared to Figure 7.

4.2 Singular Value Decomposition

The input-output relationship of a general dynamic system can be expressed in the frequency domain as [6]:

$$\{G_{yy}(\omega)\} = \overline{[H(\omega)]}\{G_{xx}(\omega)\}[H(\omega)]^T \quad (13)$$

where $\{G_{yy}\}$ is the power spectral density (PSD) matrix of the output and $\{G_{xx}\}$ is the PSD matrix of the input.

Singular value decomposition (SVD) can be used at each frequency to decompose the output PSD matrix $\{G_{yy}\}$ into the form [7]:

$$\{G_{yy}(\omega)\} = [U][S][U]^T \quad (14)$$

Where $[S]$ is a diagonal matrix which holds the singular values of the matrix $\{G_{yy}\}$ and $[U] = [u_1, u_2 \ldots u_n]$ is a unitary matrix holding the singular vectors. At a resonance peak only one mode will be dominating in the response and the first singular vector in matrix $[U]$ is an estimate of the mode shape. The first singular value is equal to the input component at that frequency squared multiplied by the peaks in the FRF squared. If the input signal contains equal components of frequency along the range of interest, a plot of singular values of the output PSD matrix vs. frequency will yield peaks at the natural frequency of the system.

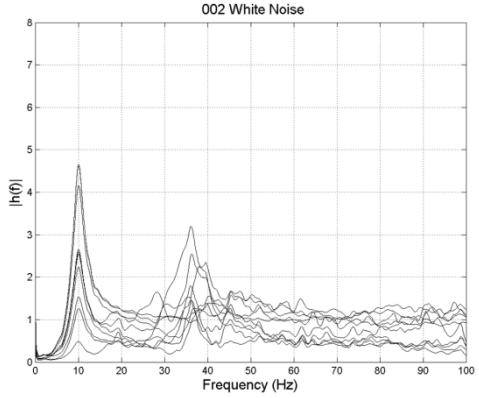


Figure 7. Frequency response functions h(f) for all sensor locations during Test 2 White Noise excitation

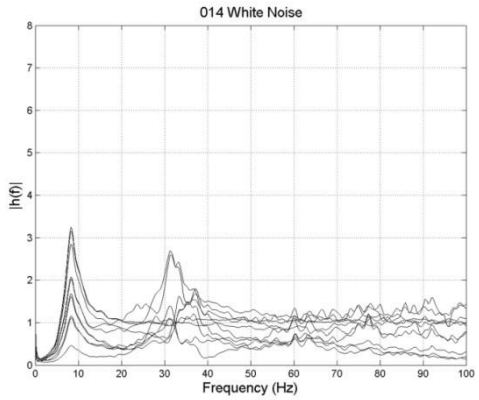


Figure 8. Frequency response functions h(f) for all sensors locations during Test 14 White Noise excitation

4.3 Estimation of Natural Frequency and Mode Shape

The singular value decomposition technique has been used previously to decompose output signals in order to determine natural frequencies and mode shapes [8,9]. This approach assumed that the input white noise excitations contained equal components of frequency across the range of interest; and so the output signal was a direct representation of the systems FRF matrix. The excitations used in the FlexiArch white noise experiments, and indeed the earthquake simulations, contained varying components of frequency across the range of interest. In performing SVD these varying components can result in peaks that appear due to the input frequency components and not due to the system properties. To avoid this issue, the SVD technique was performed on the estimated FRF matrix components$h(\omega)$. This can be seen as the same as normalising the input to a constant across the frequency range. The peaks from the SVD and $h(\omega)$ graphs were used to estimate the natural frequencies and the singular vectors were used to estimate the corresponding mode shapes (Figures 11-14).

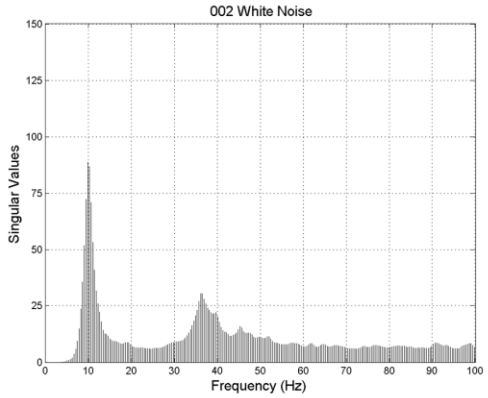


Figure 9. Singular values vs. frequency (Test 2 WhiteNoise)

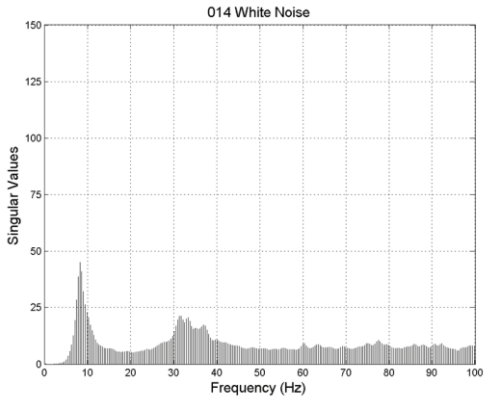


Figure 10. Singular values vs. frequency (Test 14 WhiteNoise)

The steps employed in determining the natural frequency and mode shapes were as follows:

1. Remove the table accelerations from the horizontal sensors in the time domain (to ensure the accelerations are relative to the base)
2. Perform the Fast Fourier Transform (FFT) on all the acceleration data
3. Smooth the data using a moving average to reduce the noise in the frequency domain plots
4. Divide each frequency component of the sensor output FFTs (H02-V22) with the corresponding component of the input FFT (T01) to normalise the input (and produce $h(\omega)$ graphs)
5. Create a power spectral density (PSD) matrix from the estimated FRF graphs $h(\omega)$ for each frequency component
6. Perform the singular value decomposition technique on the PSD matrix for each component of frequency
7. Plot the singular values against frequency and identify peaks
8. Perform the SVD technique on the PSD matrix formed from the original FFT data to obtain an estimate of the mode shapes at desired frequencies

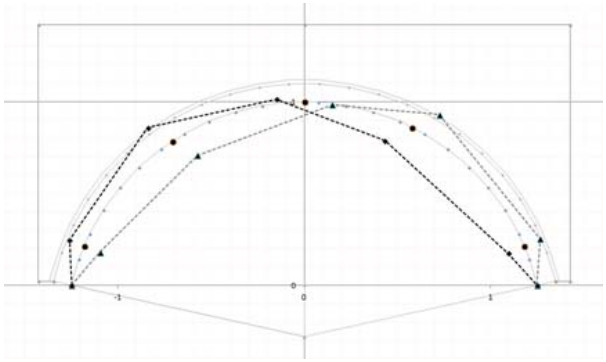


Figure 11. Mode shape at 10.5Hz (Test 2 WhiteNoise)

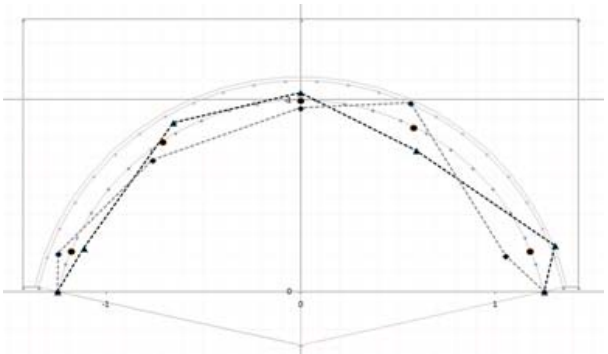


Figure 12. Mode shape at 35.9Hz (Test 2 WhiteNoise)

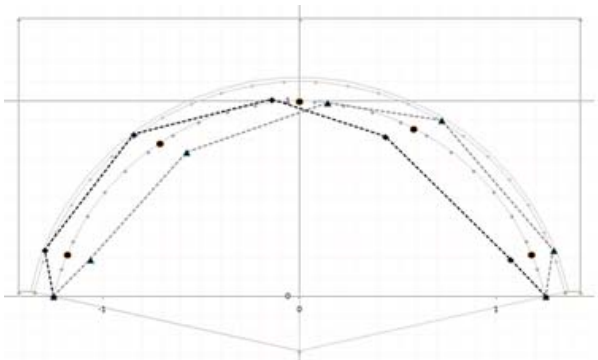


Figure 13. Mode shape at 8.4Hz (Test 14 WhiteNoise)

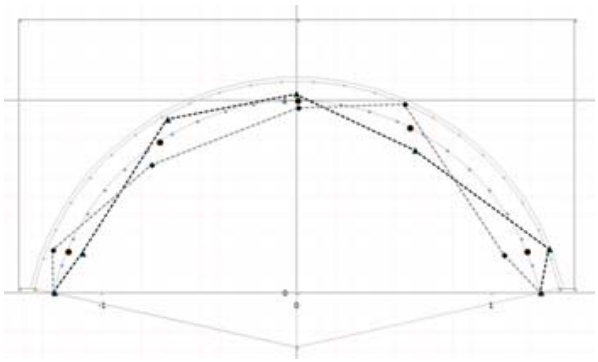


Figure 14. Mode shape at 31.9Hz (Test 14 WhiteNoise)

The mode shapes of the white noise test before damage for the first two natural frequencies are shown in Figures 9 and 10, respectively. The first natural frequency in Figure 11 is seen to be translational rocking. A hinge is seen to form at Voussoir 2 and 7 (refer to Figure 1). The second natural frequency in Figure 12 is seen to be horizontal and vertical rocking with hinge formation at Voussoir 22. Comparison of the undamaged mode shapes (Figures 11 & 12) and the damaged mode shapes (Figures 13 & 14) indicate no change in the form of the mode first two mode shapes before and after damage.

5. DISCUSSION OF RESULTS

The plots of $h(\omega)$ vs. frequency before and after damage resulting from a number of scaled earthquake excitations were applied can be seen in Figures 7-8, respectively. Prominent peaks can be seen around 10Hz and 30-35Hz in Figure 7 & 8. To investigate this in greater detail and help identify exact natural frequencies, singular value decomposition on the FRF components was performed.

Using singular value decomposition on the FRF components provided a clearer depiction of the fundamental natural vibrating frequencies at 10.5Hz and 8.4Hz, but also identified secondary vibration modes at 35.9Hz and 31.9Hz respectively; which originally was not clear from the FRF plots. The secondary peak also reduced in height and in frequency to 31.9Hz after earthquake exposure. This suggests that irreversible damage occurred during the earthquake simulations and there has been a reduction in stiffness in order to reduce the natural frequency. The height of the peaks in Figure 10 can be seen to be less than the peaks in Figure 9. This suggests that more energy is being dissipated per vibration and the level of damping has increased. Energy dissipation in the system potentially results from the backfill soil-structure interaction and elongation of the polymer layers connection the voussoirs. One of the future aims in this project is to verify and quantify the mechanisms of energy dissipation in this system.

Figures 11-14 show the mode shapes for the corresponding frequencies. Both the fundamental and higher mode shapes did not change after corresponding reductions in natural frequencies.

CONCLUSIONS

The paper presented an overview of the experimental programme conducted on a FlexiArch specimen at the University of California, Sandiego. The specimen was subjected to white noise excitations and earthquake simulations of varying intensities. The acceleration data from the experimental programme was analysed in the frequency domain and natural vibrating frequencies were determined through the use of a generalised frequency response function. The frequencies were estimated before and after earthquake exposure as an indicator of whether irreversible damage had taken place. The estimation of natural vibrating frequencies were emphasised through the use of singular value decomposition on elements of the FRF matrix. The results showed a reduction in natural vibrating frequencies of 10.5Hz and 35.9Hz to 8.4Hz and 31.9Hz respectively. The heights of the corresponding peaks also reduced after earthquake exposure. This change in properties indicated that a reduction in stiffness occurred and also the level of damping increased. The singular value decomposition technique was used to estimate modes shapes for the corresponding identified frequencies.

The natural frequencies and mode shapes obtained from this experimental program will be used to validate future numerical models to be used in a parametric study as part of the ongoing PhD project.

REFERENCES

[1] UK Highways Agency, (1995). BD57/95, Design for Durability, Design Manual for Roads and Bridges, Volume 1, Section 3, Department of Transport, Highway and Traffic, UK.

[2] Taylor, S.E., Long, A. and Robinson, D. (2007), 'Development of a Flexible Concrete Arch', *Concrete,* August 2007, 33-57

[3] Taylor, S.E., Gupta, A. and Kirkpatrick, J. (2007) 'Testing of a novel flexible concrete arch', *Proceedings of ACIC 07 Advanced Composites in Construction*, University of Bath, Bath, UK

[4] Clough, R.W and Penzien, J., *Dynamics of Structures*, McGraw Hill, New York, second edition, 1993.

[5] He, J. and Fu, Z., *Modal Analysis,* Butterworth-Heinemann, Oxford, 2001

[6] Bendat, J.S. and Piersol, A.G., *Engineering Applications of Correlation and Spectral Analysis,* John Wiley & Sons, 1993.

[7] Brinker, R., Zhang, L. and Anderson, P. (2000) 'Modal Identification from Ambient Responses using Frequency Domain Decomposition', *Proceedings of the 18th International Modal Analysis Conference,* San Antonio, Texas 7-10

Probabilistic Analysis of Potential Impact of Extreme Weather Events on Infrastructures

Alan O'Connor[1], Eugene J. OBrien[2], Donya Hajializadeh[3]
[1] Roughan and O'Donovan Innovative Solutions, Ireland
[2]Department of Civil Engineering, University College Dublin, Ireland
[3]Roughan and O'Donovan Innovative Solutions, Ireland
email: Alan.O'connor@rod.ie, eugene.obrien@ucd.ie, donya.hajializadeh@rod.ie

ABSTRACT: In recent years, a variety of extreme weather events, including droughts, rain induced landslides, river floods, winter storms, wildfire, and hurricanes, have threatened and damaged many different regions across Europe and worldwide. These events can have devastating impact on critical infrastructure systems. The 7th Framework RAIN project will address these issues, involving partners from Ireland, Belgium, Germany, Finland, Italy, Netherlands, Slovenia and Spain. In this project, the impact of critical infrastructure failure on society, on security issues and on the economy will be examined. Based on the impacts of the failures, quantifiable benefits (from a societal, security and economic standpoint) of providing resilient infrastructure will be identified. In this project, a means of quantifying the level of risk will be established, first due to single land transport mode failures, and second due to selected multi-mode-interdependent failure scenarios (e.g. failure of power stations result in failure of electrical train lines). This paper introduces the RAIN project and its goal of developing a methodology to create an advanced risk assessment procedure, including a probabilistic based approach, to derive a measurable indicator of risk.

KEY WORDS: Operational Analysis Framework, Infrastructure, Resilience, Risk Analysis, Mitigation Strategies, Societal Vulnerability/Security, Economic & Social Markers

1 INTRODUCTION

The recent extreme weather events in Europe and around the world have thrown the organisation and management of critical infrastructures into chaos. This chaos is a product of uncertainty and a lack of information on how the infrastructures we take for granted in our daily lives, will manage with these extreme events. The existence of chaos and uncertainty in these situations can result in disruptions to transport, power outages and in the most extreme instances loss of life. For example, in Germany and the Czech Republic, the worst affected areas in Europe flood in August 2002, the effects on infrastructure consisted of electricity failures, disconnected telecommunication links, damage to approximately 250 roads and 256 bridge structures (Figure1), disruption to the Gas service due to damaged pipelines and contamination of clean water with flood water (Figure 2).



Figure 2-damaged bridges during European Flood in 2002 [1,2]

Removing uncertainty and gaining a better understanding of how our critical infrastructures will cope and adapt to weather events will help ensure the security of vital utilities. Within the context of an extreme event one would typically see interaction between several entities such as; emergency planners, utility operators, first responders, engineers and most importantly the citizens living in the area of the extreme event. Given the diversity of those involved in such an event – the answers to improving the outcomes of such events cannot be considered in isolation by any one discipline.



Figure 1: Prague Zoo flooded by the swollen river Vltava [3]

The objective of the Risk Analysis of Infrastructure Networks in response to extreme weather (RAIN) project is to provide an operational analysis framework to minimize the impact of major weather events on the EU land. A holistic risk mitigation approach will be used to establish the key components of existing infrastructure network and assess the

sensitivity of these components to extreme weather and consequent socio-political effects. This project aims to predict the sensitivity of European infrastructure to widespread disruption due to extreme weather events to reduce the impact of possible future events.

RAIN aims to quantify the complex interaction of existing infrastructure systems and their interrelated damage potential in the event of specific extreme weather events. One of the main objectives of this project is to improve the robustness of European Networks in order to avoid disproportionate damage or disruption due to extreme events. This involves increasing the level of redundancy in the infrastructure networks at critical nodes, improving the performance of key infrastructure and developing detailed plans for a range of potential emergency scenarios.

The project is the collaboration between fifteen organizations in eight countries (Figure 3): Roughan & O'Donovan Ltd (ROD), Trinity College Dublin (TCD) and Gavin and Dehorty Geosolutions Ltd (GDG) in Ireland, European Sever Storms Laboratory (ESSL) and Freie Universitaet Berlin (FU-Berlin) in Germany, Zilinska Universiteit Delft (UNIZA) in Slovakia, Technische Universiteit Delft (TU-Delft) and Prak Security and Judgment (PSJ) in Netherlands, Dragados SA (DSA), Union Fenosa Distribution SA (UFD) and Applicaciones En Informatica Avanzada SL (AIA) in Spain, Hellenberg International OY (HI) and Finnish Meteorological Institute (Ilmatieteen Laitos, FMI) in Finland, Instituto di Sociologia Internazionale di Gorizia (ISIG) in Italy, Youris.com (Youris) in Belgium.



Figure 3: Consortium

The RAIN consortium is carefully chosen group of organizations involved in research in the areas of critical land based infrastructure systems. These organizations contribute toward developing the frameworks and policy that reinforce the safety of the European infrastructure networks. The consortium is multidisciplinary including meteorologists (FMI), climate researchers (ESSL), economists (TCD), energy specialists (UFD), infrastructure risk analysts (TU-Delft), specialist engineering designers and planners (ROD and GDG). Furthermore, the advisory group has been developed to ensure the more widespread applicability of the results to industry by establishing a direct liaison with infrastructure owners and managers. For example within the advisory board, the utilities EDF and RWE will contribute toward power grid operability, while FEHRL, PRORAIL, and DeutscheBahn will contribute toward transport system management.

The consortium therefore has an appropriate distribution of different level partners to make up a credible partnership for R&D in Cost-effective improvement of the resilience of EU infrastructure in response to extreme weather events.

The members of the consortium gather high level expertise on all aspects of critical infrastructure protection and/or weather assessment to study three main research threads in the project:

- Weather and climate modelling with respect to critical infrastructure
- Critical infrastructure

Risk analysis tools for critical infrastructure

2 WEATHER AND CLIMATE MODELLING WITH RESPECT TO CRITICAL INFRASTRUCTURE

Previous projects that addressed the sensitivity of transport systems to extreme weather, in particular the FP7 projects EWENT (East-West European Network) and WEATHER (Weather Extremes: Impacts on Transport Systems and Hazards for European), form the starting points for the Hazard Identification work. Questions on time-perspectives of weather information are partly answered in EWENT project, providing the frequencies of extreme weather in different parts of Europe and probabilities of adverse weather affecting transport in Europe [4-6].

Physical impacts and the economic costs of extreme weather event on transport systems and identify the costs and benefits of suitable adaption an emergency management strategies.

Estimating the present occurrence frequency of the small but intense thunderstorm-related events, such as damaging lightning, local extreme winds, large hail, lightning and tornadoes, is challenging because they are too small and short-lived to be resolved by measurement networks of the National Meteorological Services [7]. Nevertheless, improved data is becoming available, especially within the European Severe Weather Database, which is being developed and maintained by ESSL. An additional difficulty is that the small size and short duration of the events also prevents them from being explicitly simulated even by state-of-the-art climate models. As of now no study has produced a regionalized projection of the future trend of such events across Europe.

The critical weather events are usually considered as sudden but for the protection of infrastructure and the security of citizens there are also events that develop over a longer time scale. Obtaining these "critical weather chains" will be a new approach but one which is already familiar to FMI. However, the trends in such "chains" have not yet been analysed. When completed in RAIN, there will be new means of providing warnings of singular catastrophes, multiple severe catastrophes and a variety of cascading events both in the early warning and climate watch scale. The critical winter weather episodes that FMI will focus on are related to synoptical situations causing abundant snowfall, heavy snow loads, icing and freezing rain. The increase in the fire risk is identified by warm spells, drought and wind. All of these aspects are critical in assessing, for example, the impact on hydrology and drinking water - if snow melts suddenly then the question arises as to how much contamination will be generated from the agricultural fields and the roads? Similarly, how early will the fire risk start? - this depends on

the lack of snow in winter and drought in the winter and spring. New methodologies for drinking water alerts can be developed in RAIN when the snow and drought aspects are both included in the methodology.

In climate change projections these "critical weather event chains" related to critical weather episodes, or the timing of these event chains, have also not yet been considered. Determining these chains, on both temporally and spatially, will result in a significant scientific break-through and obtain the urgently needed climate change impact projections for both the protection of infrastructure and the security of citizens.

In terms of the predictability of severe weather, RAIN will, for the first time, address several different types of severe weather, and through a combination of research and literature reviews, will establish an overview of the typical levels of confidence available at various lead times before severe weather strikes and address implications for the design of early warning systems.

3 CRITICAL INFRASTRUCTURE

The understanding and definition of the term 'resilience' has different interpretations and a universal conception and measuring of it is therefore a very unlikely result of any research project. However, for the purpose of this work, the UN/ISDR definition is used as a starting point, as it highlights the crucial factors to be taken into account when resilience is at stake. It is defined as the "capacity of a system, community or society potentially exposed to hazards to adapt, by resisting or changing in order to reach and maintain an acceptable level of functioning and structure. This is determined by the degree to which the social system is capable of organising itself to increase this capacity for learning from past disasters for better future protection and to improve risk reduction measures" [8].

To determine vulnerability it is necessary to adopt a more complex perspective to address resilience. In this perspective, the understanding of the effects of actual policies (i.e. by means of institutional analysis) is put in place to enhance resilience of infrastructural (and related social) systems offer a practical and effective way to start addressing this complex mechanism.

It is therefore crucial to explore financial, institutional and social aspects behind the enhancement of resilience of transport and energy/telecommunication infrastructures exposed to the impact of extreme weather hazards.

Critical Infrastructures Protection is something that sometimes overlaps national territories and goes beyond territorial delimitation. For their connecting roles, critical infrastructures are better framed in regional or trans-regional perspectives than purely national ones. Thus, the EU promoted a specific program to help member states to implement common strategies for critical infrastructure protection, without aiming at substituting or duplicating the prerogatives of each member state.

From an early stage in the project, critical infrastructure will be identified based on performance level, impact of disruption and exposure to significant hazards to provide an inventory of target typologies, which will form the basis of the key input required for later stages of the project. The project will assess and utilise the newly developed concept of European Critical Infrastructure [9], an area that has not received significant attention. Several different performances will be explored, in relation to the regulations in Europe and their unification, as currently, different laws and standards are applicable across the European Union. Problem specific methods and standards will be defined and developed, which will represent a main advance towards harmonization in hazard and risk assessment on a European basis.

Network usage gives information about the impact that an element will have in the system. Moreover, network usage forecast provides information about how close to the operational limits the network is working. When the network is working in a safe condition, the system is robust and can cater for some anomalies or fluctuations. However, when the system is working close to the operational limit, small anomalies or disturbances may produce a collapse in the whole network. Consequently it is essential to be able to provide information about the network usage as it presently exists and as it will exist in the future.

It is also critical to know the probability of failure of each element in the network under different weather conditions. This will provide information about the likelihood of element and system failure.

Combining network usage and equipment failure probability, RAIN will provide information about the likelihood of element failure and the resulting impact. Together, these two forecasting capabilities provides working tools to study the resilience (or vulnerability) of critical infrastructure under extreme conditions. Performing what- if simulations will enable the conditions which affect the network to be examined.

RAIN forecasting capabilities are based on the assumption of modulating the problem, not just the result. RAIN will study 'symbols' - these symbols are elements that modify the forecasted variable. In an electric demand forecast, for example, symbols may be the laborality calendar, temperature, domestic profile, industrial category, nubosity, etc.

Modelling the problem in a symbolic approach, RAIN is not only able to provide future estimations, but also provide other high-valued capabilities, such as;

Trusting margins - the trusting margin is based on the expected error in the forecasting module. This error is based on the possible variations in each symbol. The error on each symbol is modelled, providing a maximum and minimum value for each estimation.

What-if simulations - Apart from typical forecasting, a symbolic forecast may provide simulations for different scenarios. For example, a system is able to provide network usage estimations for cold, warm and hot temperature years, for rainy months, combinations of weather effects, etc.

Aggregations - A symbolic forecasting can provide estimations for each element or any aggregation which is the cumulative estimation per area, region, country, climatic zone, etc. This will provide a very useful tool in assessing pan-European security.

The forecasting module will provide a powerful tool to help operators to study their critical infrastructure under several extreme situations. The forecasting module will help operators

examine under which situations the different networks may collapse, the probability that some element fails under normal or exceptional situations, the weakest points in the network and the more critical elements, from a social or financial point of view, between other elements. The RAIN forecasting module will be of high-value for operators, helping them to understand the potential risks on the network and how the system will behave under both an external situation (weather) or an internal situation (element state or network usage).

The project outputs will contribute to the process of knowledge management development used in the protection of Critical Infrastructure and will provide the basis for the development of decision support systems - from the view of maximum effectiveness of the first response on the violation of critical infrastructure functionality caused by extreme weather events.

4 RISK ANALYSIS TOOLS FOR CRITICAL INFRASTRUCTURE

A number of methodologies, applications and software tools have been developed, worldwide, for critical infrastructure protection and a detailed summary can be found in [8]. Modelling techniques include decision making procedures, multi-agent systems, system dynamics, rating matrices, relational databases and network theory. These are supplemented by computational methods such as time step simulation, Monte Carlo simulation, decision trees, GIS, risk management techniques and event monitoring or real time recording.

In these methods, road, highway and rail infrastructure are given the least attention, approximately in only 10% of cases, with IT and Telecoms covered in about 21% of cases with 11% related to human activities queries and response checking [9]. Approximately one quarter of the methodologies and applications have limited availability or are restricted and so there is limited exchange of information occurring between the Governments/policy makers and researchers and of the commercial packages available, most are used in the energy sector. Only approximately 12% of the modelling techniques employed have been focused on implementation of policies and regulations.

The majority of the critical infrastructure protection plans have been based on a risk management framework, with rating matrices being the most widely used modelling technique. Network theory and system dynamics, which consider internal feedback loops and time delays that affect the behaviour of the entire system, and network modelling are the least utilised techniques.

In identifying risks, there are a number of techniques used, however a variety of strategies are used to quantify the risk, with no singular method being dominant. For example, vulnerability assessment of infrastructural nodes in relation to seismic and flood hazard is carried out mainly through empirical evidence and historical records of failure. While this is acceptable in areas of relatively high risk with frequent damaging events, is not directly transferable to high density/ low probability events, which might have devastating consequences to regions and assets with low risk perception.

Previously, the Morlet continuous wavelet transform has been used to analyse the temporal and spatial fluctuation of environmetric (hydro meteorological) cycles and can be applied to response variables (such as the annual water discharges time series). In recent years, many authors have presented results of hydrological variability using such wavelets [11-13], therefore wavelets can be considered as a current state of art. However, the application of wavelet results to stress testing has not been investigated before and represents a novel approach to stress testing infrastructure.

Updated existing and new modelling concepts (wavelets, morphological analysis, network analysis, & Objective Ranking Tool (ORT) methods as described below) will be applied to critical infrastructure risk and resilience assessment procedures. Success in assessing the effect of such events in a timely and realistic manner requires the development of new vulnerability models which look at effect propagation of highly destructive localised events to interconnected networks. The project will deliver simple analytical vulnerability models for transport infrastructure, with a particular focus on linear infrastructure systems such as road and rail networks. The specific infrastructure components will be evaluated and used to rank the susceptibility of the network to damage (using a ranking index). This index will categorise the infrastructure into various subsets which can then be combined with potential failure modes (i.e. caused by extreme weather events). The output will identify hot-spot vulnerability in the form of critical parameters affecting performance under extreme events and quantifying their predicted range of operability during these events.

A logic tree approach will be used to define damage modes and extents and derive fragility functions. Such modelling is associated with several levels of uncertainties, both epistemic and aleatoric, which will be quantified and propagated throughout all stages of the explicit risk analysis. Wavelets can be considered as one of the most suitable and powerful approaches to model the temporal and spatial variability fully and can be applied directly to the source or response variables (hazard or effect). Integrating wavelet results within a risk based network infrastructure model will pose a big challenge but will lead to a methodology in which the output of wavelets, or the interdependence between the variables can be used as input for critical weather events which may not have been experienced in the past.

Non-quantified inference models representing those aspects of the results of the project, which cannot be (meaningfully) rendered as quantitative models will be developed and employed to simulate the 'what if' wildcard scenarios. These morphological models, which simulate genuine uncertainty, are computer-based, and the recipients of the project's results receive software in order to run them. The development of these interactive morphological inference models of the total problem space and the bounded solution space, including structured, interactive scenario and strategy models, will be a new departure from critical infrastructure assessment, which has previously been utilised in defence and military applications. Both single hazard and multi hazard risk GIS models will be generated, with the aim of producing a harmonised GIS model of individual risk methodologies, contributing to greater economy, efficiency and decision making across the infrastructure network. Probabilistic approaches will be used to develop realistic event scenarios through full simulation of the event, thus maximising the

efficiency of the inputs into the harmonised risk methodologies. An ORT will be adopted to rank and prioritise the outcomes of the results.

Furthermore, the impact of extreme weather is assessed not only based upon physical vulnerability of the infrastructure, but also the interaction of humans relying on these infrastructures connected as networks. A hierarchy framework will be developed to accommodate the spatio-temporal variability to undergo multi-risk stress test scenarios, including people dynamics. With the introduction of complex network analysis we can investigate the topologies and hierarchical structures of infrastructure interdependencies. In this sense we can envisage infrastructure networks as a multilayer system. In network analysis standard approaches have focused on the study of a single non-interacting network, while a comprehensive synthetic paradigm, which takes infrastructure multilayer networks into account, is still missing, thus building on existing approaches currently adopted.

RAIN will leverage recent results in the development of platforms for sharing environmental information between relevant stakeholders in the risk assessment domain using cloud processes. The project will enable better interoperability and sharing of environmental data, results of simulation models, real-time data, as well as services by deploying platforms to relevant stakeholders. This will enhance information sharing which is limited at present.

Based on the principles of similarity judgment, RAIN will develop a web based tool to facilitate the computation process, i.e., of prioritizing the need to act when judging hazards and their impact to infrastructures. This web based tool will be used during several stages of the project to provide the different working packages with the ability to classify and rank different outcomes. To ensure a proper usage of the outcomes of RAIN a dedicated training program and further education course will be implemented.

The web based tool will be made available for companies and governments working in the area of the transport and telecommunications infrastructure. This will help the respective companies and governments to identify the consequences of extreme weather events for their own situations.

5 METHODOLOGY AND ASSOCIATED WORK PLAN

The research activities are organised around six technical work packages (WP), each organised around a core topic necessary for the complete description of the problem dynamic. One of these, WP2, focuses on hazard identification, while the second and third work packages, WP3 and WP4 respectively, focus on the elements of critical infrastructure addressed in RAIN. Development of the Risk Analysis framework, identifying measurable risks and benefits, and developing mitigation strategies are covered in WP5, WP6 and WP7 respectively. Management and dissemination activities complete the work plan, as indicated in Figure 4. The diagram also serves to show the interaction and interdependencies between WP's.

Authors' main contribution to this project is to develop methods to create an advanced risk assessment procedure, including a probabilistic based approach, to derive a measurable indicator of risk for single and multi mode failure risks, in the 6th work package. The economic benefit of multifaceted approach to improve security of infrastructure then will be produced.

In this work package, a means of quantifying the level of risk will be established, based on the mapping protocol of risk analysis framework developed in WP 5, first due to single land transport mode failures, and second due to selected multi-mode-interdependent failure scenarios (e.g failure of power stations result in failure of electrical train lines). The impacts will be assessed in each case.

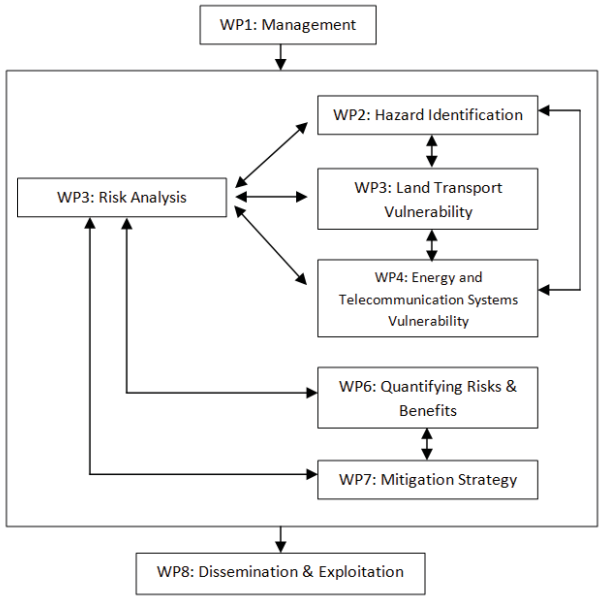


Figure 4: Work Plan Strategy & Methodological Diagram

The WP 6 will result in three deliverablese and two milstones which will be provided in the form of technicl papers detailing the probabilistic approaches, and the variables proposed to quantify single and multi mode risks and their societal, security and economic impacts and also a report on benefit of critical infrastructure protection, providing the building of the methodologies an findings of the workpackage to asse the multifacted economic benefts of critical infrastructure resilience.

6 ACKNOWLEDGMENT

RAIN project is a 7th Framework Project funded under the Industry and Academia Partnerships and Pathways call. The Project will commence in April 2014 and is continuing for 3 years until April 2017.

7 REFRENCES

[1] www.bussinessweek.com
[2] http://www.prague.net/
[3] www.dailymail.co.uk/
[4] Leviäkangas, P. (2011). ITS in a Changing Climate-a Savior Tool or Another Vulnerable System. 18th World Congress on Intelligent Transport Systems, Orlando, USA
[5] Leviäkangas, P., Hietajärvi, A.M. (2010) Value of Weather Information for Road Management. 15th SIRWEC conference, Quebec City, Canada.
[6] Leviäkangas, P., Öörni, R., Hautala, R., Rossa, A. and Domenichini, F. (2010). Fog Warning System in Venice Region. 17th ITS World Congress, Busan, Korea.

[7] Dotzek, N., Groenemeijer, P., Feuerstein, B., & Holzer, A. M. (2009). Overview of ESSL's Severe Convective Storms Research Using the European Severe Weather Database ESWD. *Atmospheric Research,* **93**(1), 575-586.

[8] UN/ISDR (2006) World Conference on Disaster Reduction Kobe, 18–22 January 2005. http://www.unisdr.org/.

[9] EC. (2008). Council Directive 2008/114/EC of 8 December 2008 on the Identification and Designation of European Critical Infrastructures and the Assessment of the Need to Improve Their Protection, Brussels.

[10] Yusta, J. M., Correa, G. J., & Lacal-Arántegui, R. (2011). Methodologies and applications for critical infrastructure protection: State-of-the-art. *Energy policy,* **39**(10), 6100-6119.

[11] Lucero, O. A., & Rodriguez, N. C. (2001). Spatial organization of decadal and bidecadal rainfall fluctuations in southern North America and southern South America. *Atmospheric Research,* **57**(4), 219-246.

[12] Anctil, F., & Coulibaly, P. (2004). Wavelet analysis of the interannual variability in southern Quebec streamflow. *Journal of climate,* **17**(1).

[13] Labat, D., Ronchail, J., Callede, J., Guyot, J. L., De Oliveira, E., & Guimarães, W. (2004). Wavelet analysis of Amazon hydrological regime variability. *Geophysical Research Letters,* **31**(2).

The Full Potential of Energy Harvesting from Train Induced Responses in Bridges

Paul Cahill[1], Nathan Jackson[2], Alan Mathewson[2], Vikram Pakrashi[1]

[1] Dynamical Systems & Risk Laboratory, School of Engineering, University College Cork, Cork, Ireland

[2] Heterogeneous Systems Integration Group, Microsystems Group, Tyndall National Institute, University College Cork, Cork, Ireland.

email: p.a.cahill@umail.ucc.ie, nathan.jackson@tyndall.ie, alan.mathewson@tyndall.ie, v.pakrashi@ucc.ie.

ABSTRACT:
The potential for energy harvesting from civil infrastructure elements to power small scale electrical systems offers many new applications in both civil engineering and micro-electronics. But how much energy can be generated from infrastructure? This paper establishes the theoretical maximum amount of energy the can be harvested from a bridge using train induced responses including material and device limiting parameters. A finite element model is constructed in this regard. An assessment of an international train fleet is conducted, with the optimum train and speed configuration for energy harvesting identified. The maximum amount of energy which can be harvested if the entire bridge structure was to be equipped with piezoelectric energy harvesting materials is determined. Two different piezoelectric materials, PVDF and PZT, are investigated to form the basis of the energy harvesting system. The effects of adhesion on the strain conditions on the surface of the energy harvester are investigated, as are the effects of a storage circuit attached to the energy harvesters, with the efficiency factor and reduction in power through the circuit established. It is determined that the maximum theoretical power outputs with no limiting factors are 3.482 mW for the PVDF based harvester and 6.667 mW for the PZT harvester. The maximum potential energy outputs, taking into account of limiting factors, are 2.672 mW and 5.121 mW for PVDF and PZT harvesters, respectively. A discussion on the cost benefit and practical nature of the system is also completed. Through this investigation, the maximum amount of energy which can be harvested from train induced responses in bridges is determined. Furthermore, influencing factors are taken into account and the maximum feasible energy which can be harvested is found.

KEY WORDS: Energy Harvesting; Piezoelectric, Bridge-Vehicle, Finite Element Analysis

1 INTRODUCTION

The potential for utilizing energy harvesting technology for the purposes of powering small scale devices is a rapidly developing field. Many advances have been made in the design and optimisation of energy harvesting devices which, when coupled with advances in Micro-Electro-Mechanical Systems (MEMS), has resulted in the potential for the development of a self-powering wireless sensor network a definite possibility. While some research has taken place into the applications of energy harvesting for large scale civil infrastructure, it has been confined to single devices located on the structure. This leads to two fundamental questions, how much energy can be generated from an entire infrastructure element and what are the practical limitations of the system?

Of all energy harvesting technologies, the harvesting of ambient kinetic energy has proven to have the greatest potential for the power of MEMS [1]. Through the use of electromagnetic, electrostatic and piezoelectric based devices, ambient vibration energy may be used as the excitation source and of these piezoelectric devices have proven especially adapt [2]. The most preferred piezoelectric energy harvesting device chosen for investigations is by far the cantilever based harvester. One such device consisted of a piezoelectric material bonded to a silicon cantilever and a tip mass at the end, which, when excited at its natural frequency at 1g acceleration, a peak to peak voltage of 898 mV was obtained [3]. Bimorph cantilever energy harvesters have also been investigated, with one such device consisting of two piezoelectric materials attached on opposite sides of a brass substructure and a variable tip mass [4]. Research has also taken place into the optimisation of the shape of the cantilever harvester, with triangular shaped in nature being preferable to rectangular in both the uni-morph and bimorph configuration [5] [6]. A configuration of two cantilever energy harvesters coming into contact has also been devised, with one acting as a driving beam having a low natural frequency and the other being the generating beam with a high natural frequency, however no fatigue analysis from the constant contacts was performed [7]. The application of these energy harvesting devices into a variety of real world applications has recently begun to receive attention. An energy harvester utilising the motion of a person has been proposed, both in the form of a shoe based energy harvester [8] and also through an energy harvester integrated into a backpack [9]. A vehicle tyre with an integrated energy harvester was investigated and the power

output determined [10], as has the use of unsteady fluid flow acting over the surface of a piezoelectric harvester [11].

There have been a number of studies in recent times into energy harvesting from bridge infrastructure, but the field is still very much in its initial stages. Recently formulated is energy harvesting from a bridge-vehicle model, with the bridge model being traversed by a singular point load and the potential energy harvesting output found [12]. The use of both a cantilever device and a surface patch device for energy harvesting for train-bridge interaction has also received some investigation [13]. Utilising a singular piezoelectric cantilever based energy harvester, the power output of a prestressed highway bridge from bridge-vehicle interaction was determined [14]. These studies have established the feasibility of using a singular device.

This paper determines the amount of energy which can be harvested from bridge-vehicle interaction if the entire bridge were to be utilised. A finite element model bridge is constructed in this regard. The model is analysed during a train passage and the amount of energy which can be harvested from energy harvesters based on two types of piezoelectric materials evaluated. The effect of a bonding agent on the energy harvesting potential is determined. The cumulative energy for the entire structure is established. This paper provides a benchmark for energy harvesting from civil infrastructure.

2 BRIDGE-VEHICLE AND ENERGY HARVESTING MODELS

The following section outlines the modelling of a bridge to determine the response induced through train passages, the modelling of energy harvesting devices and the determining of the full energy harvesting potential of a bridge.

2.1 Finite Element Model

For the purposes of investigating the energy harvesting potential from bridge-vehicle interaction, it was decided upon to create a finite element model of a reinforced concrete bridge. The single span bridge, of span of 10.6m, width of 10m and depth of 0.9m, was modelled as a three dimensional solid using Strand7 Finite Element Analysis software and consisted of Hexa20 Brick elements [Figure 1]. The bridge consisted of a deck and five support beams and had a natural frequency of the bridge is 13.2 Hz and damping ratio of .0216. It was decided upon using train induced vibrations as the source for energy harvesting and thus the model was constructed including ballasts and tracks, with two tracks spanning the length of the model.

An investigation into an international train fleet, which consisted of two diesel locomotive trains used in the Irish fleet, the 071Loco and 201Loco sets, and three electric trains, namely the French TGV, the Japanese Shinkansen and the German ICE, was performed to determine the train which was most favourable to energy harvesting. The trains were modelled traversing the bridge model along loading paths with the loadings from the wheels acting as point loads at spacing as determined by the axle spacing. The models were analysed and the power output determined, as outlined in the subsequent section.

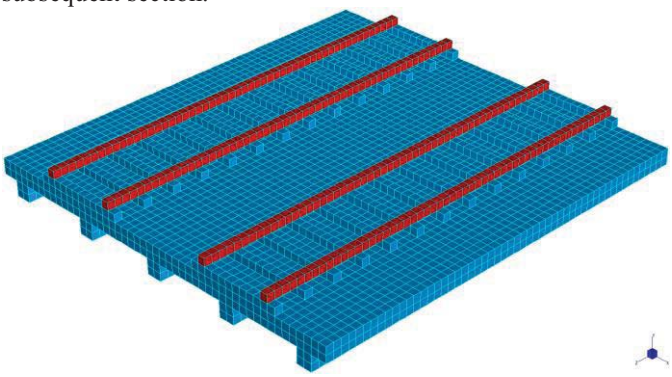


Figure 1. Finite Element Model Bridge.

2.2 Energy Harvesting Devices

To determine the full potential of a bridge element for the purposes of energy harvesting it was decided to investigate two piezoelectric materials as the basis of the energy harvesters. The first is PolyVinyliDene Fluoride (PVDF), a polymer which has a high mechanical strength yet retains excellent flexibility. It is straightforward to handle and can be formed easy into various shapes. The physical and piezoelectric properties of PVDF are outlined in Table 1. The second piezoelectric material chosen is Lead Zirconate Titanate (PZT), the most popular piezoelectric material used in energy harvesting. This is a result of PZT having excellent piezoelectric properties, giving higher outputs than PVDF under similar conditions. However, a drawback of PZT lies in its physical properties, in that it is a ceramic material and is thus is brittle. The physical and piezoelectric properties of PZT are outlined in Table 2.

The energy harvesting devices are modelled as a patch based harvester to be bonded directly to the host structure. The potential voltage output of the energy harvesters was determined by

$$V_p = \frac{d_{31} E b}{C_p} \int_l \varepsilon \tag{1}$$

Where V_p is the potential voltage output, $d_{31,}$ E and C_p are the piezoelectric constant, Young's modulus and capacitance of the material, respectively, and ε, b, l are the evaluated strain over the harvester, the width and length of the harvester, respectively. From this, the potential power output can be calculated through

$$P = \frac{(V_{RMS})^2}{R} = \frac{\left(\sqrt{\frac{1}{T}\int_0^T {V_p}^2(t)\partial t}\right)^2}{R} \tag{2}$$

Where V_{RMS} is the root mean square of the voltage, R is the resistance of the piezoelectric material and load resistance and t and T are the time and total length of time, respectively.

Table 1. Physical and Piezoelectric Properties of PVDF

Property	Value	Unit
Piezoelectric Constant, d_{31}	$24x10^{-12}$	C/N
Dielectric Permittivity, e_{33}	$0.106x10^{-9}$	F/m
Young's Modulus	6	GPa
Thickness	110	μm

Table 2. Physical and Piezoelectric Properties of PZT

Property	Value	Unit
Piezoelectric Constant, d_{31}	$-274x10^{-12}$	C/N
Dielectric Permittivity, e_{33}	$30.1x10^{-9}$	F/m
Young's Modulus	71	GPa
Thickness	320	μm

2.3 Train with Maximum Potential Power Output

The energy harvesting potential for the international train fleet was determined for a single PVDF based device and an equivalent PZT based device, at location of maximum energy harvesting on the underside of the bridge model. It was found that over the range of speed considered, from 40 km/hr to 160 km/hr, the train with the highest potential power output was determined to be the Irish 201Loco train [15]. The train set consisted of a single diesel locomotive, with wheel loadings of 91.25 kN, and seven passenger carriages, with wheel loadings of 58.85 kN, so as to match the typical operational configuration of the train [Figure 2]. This leads to a total loading of 4,390 kN and an overall train length of 182m. The power output of the 201Loco train ranged from 0.38 mW and 0.20 mW for a PZT based and PVDF based device respectively at a speed of 40 km/hr, to 0.40 mW and 0.21 mW for a speed of 160 km/hr [Figure 3]. These were for devices with a piezoelectric surface area of 0.005 m^2, at a circuit resistance of 100 kΩ.

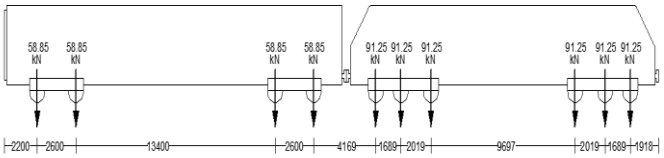


Figure 2. Axle Spacing and Loading for 201Loco Train

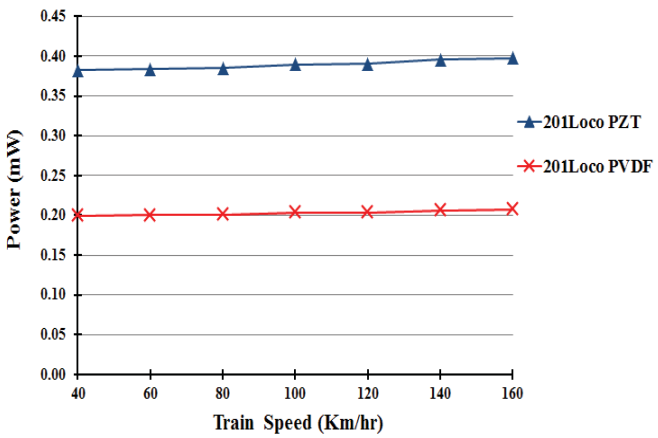


Figure 3. Power Output of 201Loco at Varying Speeds.

2.4 Applying a Discrete Surface to Bridge Model

A discrete surface was then applied to the underside of the bridge model for determining its full energy harvesting potential from train induced vibrations. The surface is required so as to account for all areas when considering the maximum energy harvesting potential of the train-bridge interaction. A two dimensional surface consisting of the elements location on the x-z plane was determined [Figure 4]. A total of 297 discrete point sets were formed and the energy harvesting potential at these locations determined. This results in the energy harvesting devices having surface areas ranging from 0.16 to 0.32 m^2.

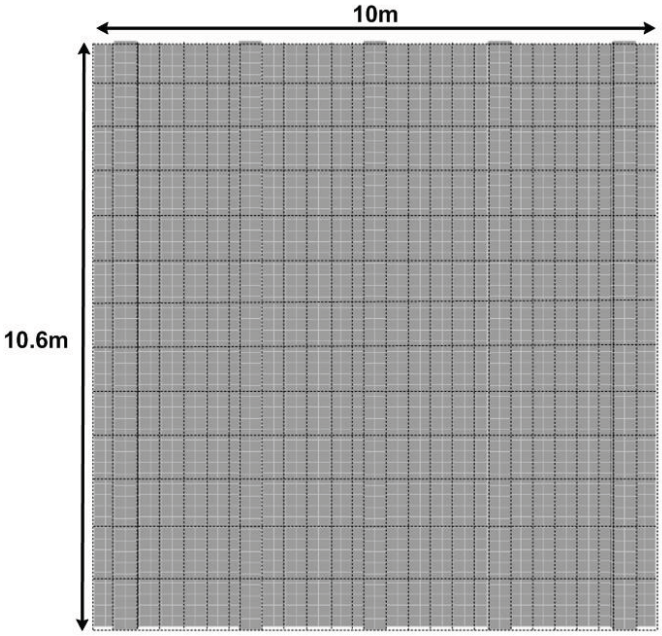


Figure 4. Discrete Grid of Bridge Model.

3 RESULTS

The entire bridge model was analysed for the 201Loco train passage at a speed of 160km/hr based on the discrete grid. The amount of energy which could potential harvested was calculated for the PVDF and the PZT based device. The effects of limiting factors was then taken into account and the amount of energy which could feasible be harvested from the bridge under operation conditions determined. The total amount of energy from the entire bridge structure for each case is determined.

3.1 Maximum Potential Energy Harvesting

Firstly, the total potential energy which can be harvested with no losses was determined. It was found that for both the PVDF energy harvester and the PZT energy harvester, the area directly under the train run proved to have the most harvestable energy, as was expected. The supporting beams were more favorable to energy harvesting compared to the deck, as was expected due to their being farther from the neutral axis, thus displaying higher strain conditions. It was found that along the length of the bridge, the support at a distance 0.6m, which is directly under the train passage, the

amount of energy which could be harvested ranged from 0.03 to 0.13 mW of power, with a combined power output of 1mW [Figure 5]. In comparison, the deck at a distance of 1.4m produced a combined power output of 0.13mW. It was found that the entire bridge structure gives a potential power output of 3.482mW for the train passage which took a total of 7 seconds. It was found that for the equivalent PZT energy harvesting device, along the support at a distance of 0.6m, the amount of energy harvested ranged from 0.8 to 0.24 mW, with a combined power output of 1.91 mW [Figure 6]. The entire bridge structure produced a combined power output of 6.667 mW, again over the same 7 second period.

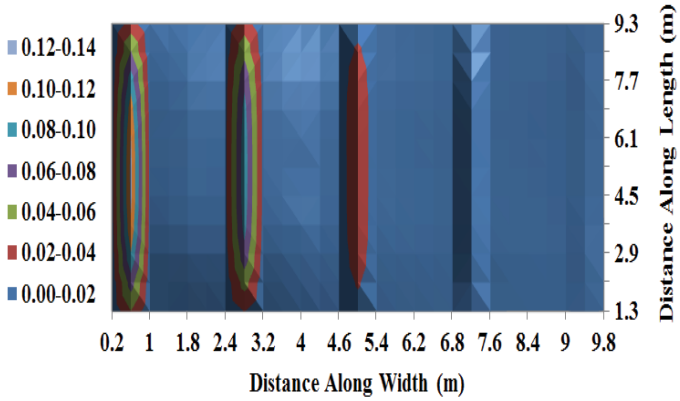


Figure 5. Maximum Power Output (mW) of PVDF based Energy Harvester for a 201Loco Train Passage at 160km.hr.

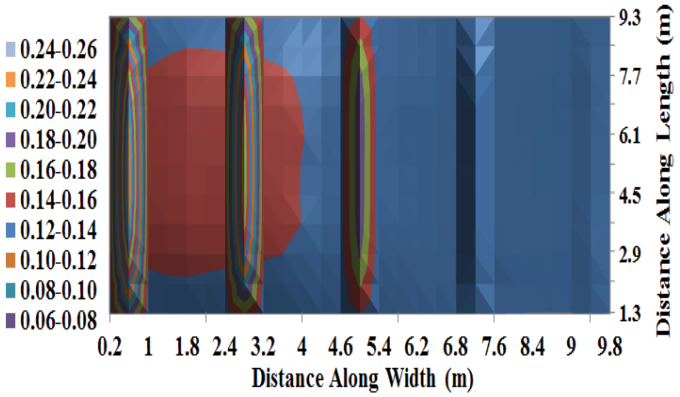


Figure 6. Maximum Power Output (mW) of PZT based Energy Harvester for a 201Loco Train Passage at 160km.hr

3.2 Energy Harvesting Including Limiting Factors.

There are two major limiting factors of the amount of energy which can be harvested when comparing the theoretical maximum and the potential under operational conditions.

First, for the maximum power output it is assumed that there is a perfect connection between the energy harvesting devices and the host surface to which it has been bonded to. This would mean that the adhesive used, such as an epoxy, transfers the all of the strain conditions from the host structure to the surface of the piezoelectric material, and thus identical conditions act on both. This, however, is not the case under operational conditions. Some losses due to the adhesive is to be expected. There have been studies into these losses, and figures ranged from 80% efficiency to 20% efficiency of the adhesive to transfer the strain conditions [16]. For the purposes of this investigation, it is taken that the adhesive is 80% efficient, thus a reduction of 20% of the strain between the surfaces is taken into account.

The second limiting factor is the efficiency of the circuit which is used to store the harvested energy and the applications of MEMS devices with such. There is a loss due to the voltage having to be rectified through a full diode bridge to allow for DC current to be stored. Again, as for the adhesive, for the maximum theoretical these losses are assumed to be zero, while under operational conditions there will be losses. These losses, however, are ever being reduced due to the advances in electronics and circuits. Indeed, the efficiency of some prototype circuits are up to 96% for the storage of harvested energy [17]. For this investigation, this 94% efficiency is incorporated into the amount of energy which can be harvested from the operational conditions.

The effects of these limiting conditions were then taken into account for both the PVDF and PZT energy harvesting devices. It was found that the energy harvested utilizing the PVDF energy harvester with the limiting factors along the supporting beam at a distance of 0.6m ranged from 0.03mW to 0.10mW, with a combined power output of 0.76 mW, a reduction of 0.24 mW when compared to the maximum theoretical output [Figure 7]. It was found that the overall power output of the entire structure was 2.674 mW for the 7 second train passage, a reduction of 0.808 mW. For the same supporting beam, it was found for the PZT energy harvesting device, power output ranged from 0.04 mW to 0.19 mW, with a combined power output of 1.46 mW [Figure 8]. This is a reduction of 0.44 mW of power from the maximum theoretical output with no limiting factors. The overall surface produced a combined 5.121 mW of power, a reduction of 1.547 mW of power.

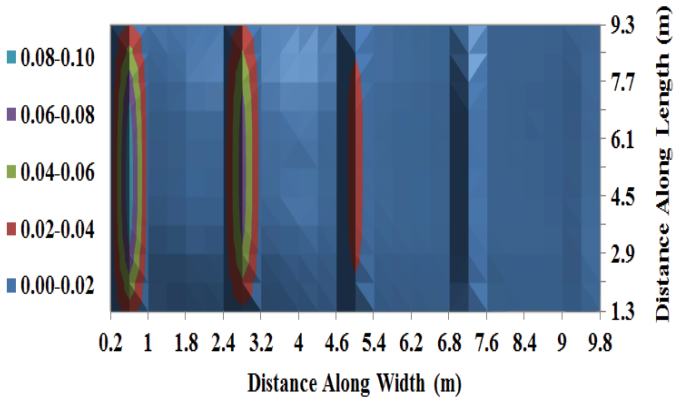


Figure 7. Power Output (mW) of PVDF based Energy Harvester under Operational Conditions for a 201Loco Train Passage at 160km.hr.

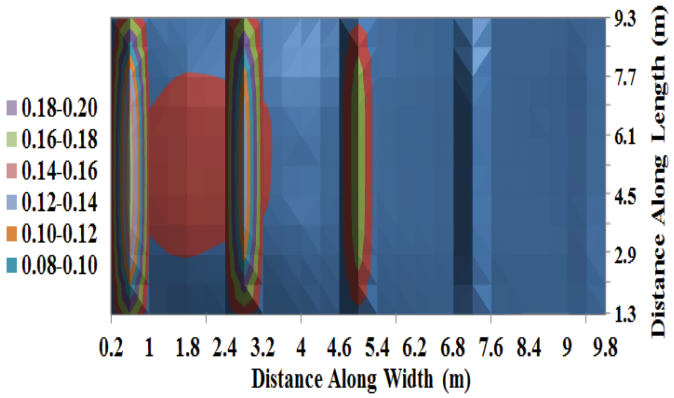


Figure 8. Power Output (mW) of PZT based Energy Harvester under Operational Conditions for a 201Loco Train Passage at 160km.hr.

3.3 Discussion of Results.

The entire underside surface of the bridge was analyzed and the maximum potential power, inclusive of limiting factors associated with adhesion and circuit losses, was established for a single train passage. The midspan of the bridge, the position of maximum deflection, generates the highest levels of power, particularly the supporting beams when compared to the deck. The beam located directly under the train track accounts for 4% of the total surface area considered. It accounts, however, for 28.6% of the total accumulative energy harvested during a train passage. Thus, areas which experience higher dynamics lend themselves more favorably to energy harvesting than areas which are more inactive. Therefore, a cost analysis should be performed and only areas which will offer financially acceptable returns be chosen.

Small scale wireless sensors have a typical power requirement in the low milliwatt range, dependent on the sampling rate and time between transmissions. For example, a commercially available wireless accelerometer, which has a communication range of up to 2 km (line of sight), has a power consumption ranging from 0.63, 1.04, 2.50 and 10.57 mW for 1 burst every 24hrs, 4hrs, 1hrs and 10 minutes, respectively. Thus using energy harvesting devices with electrical power storage, the power requirements of such devices may be achieved using train-bridge interaction as a source and the creation of a wireless sensor network is achievable.

4 CONCLUSION

This paper establishes the full potential of a bridge for the purposes of energy harvesting. A finite element model of a bridge element is constructed in this regard and the effects of train-bridge interaction investigated. The 201Loco train is chosen and the effects of speed investigated, with a speed of 160 km/hr chosen due to its higher voltage output, when compared against other speeds. Two piezoelectric materials are chosen as the basis of energy harvesting devices, PVDF and PZT. The maximum theoretical power output of the devices for a single train passage is determined as 3.482 mW and 6.667 mW for PVDF and PZT devices respectively. Limiting factors on the amount of energy which can be harvesting are investigated including the losses associated with an adhesive and circuit losses. The maximum practical power outputs proved to be 2.672 mW and 5.121 mW for PVDF and PZT respectively. The use of train-bridge interaction for the powering of wireless sensor nodes is discussed and the levels of generated power were found to be adequate for powering of such nodes.

ACKNOWLEDGMENTS

This work has been supported through the Irish Research Council Government of Ireland Postgraduate Scholarship Scheme.

REFERENCES

[1] Williams, C. B., and Yates, R. B. (1996) 'Analysis of a micro-electric generator for microsystems' *Sensor Actuat. A-Phys.,* Vol. 53(1-3), pp. 8 – 11.

[2] Priya, S. (2007) 'Advances in Energy Harvesting using low profile piezoelectric transducers' *Electroceram*., Vol. 19(1), pp. 165 – 182.

[3] Fang, H-B., Liu, J-Q., Xu Z-Y., Dong, L., Wang, L., Chen, D., Cai, B-C., and Liu, Y. (2006) 'Fabrication and performance of MEMS-based piezoelectric power generator for vibration energy harvesting' *Microelectr. J.* Vol. 37(11), pp. 1280 – 1284.

[4] Erturk, A., and Inman, D. J. (2009) 'An experimentally validated bimorph cantilever model for piezoelectric energy harvesting from base excitations', *Smart Mater. Struct.*, Vol. 18(2), 025009, 18pp.

[5] Goldschmidtboeing, F., and Woias, P. (2008) 'Characterisation of different beam shapes for piezoelectric energy harvesting' *J. Micromech. Microeng.,* Vol. 18(10), 104013, 7pp.

[6] Dietl, J. M., and Garcia, E. (2010) 'Beam shape optimisation for power harvesting', *J. Intell. Mater. Syst. and Struct.* Vol. 21(6), pp. 633 – 646.

[7] Gu, L., abd Livermore, C. (2011) 'Impact-driven, frequency up-converting coupled vibration energy harvesting device for low frequency operation' *Smart Mater. Struct.* Vol. 20(4), 045004, 10pp.

[8] Mateu, L., and Moll, F. (2005) 'Optimum piezoelectric bending beam structures for energy harvesting using shoe inserts', *J. Intell. Mater. Syst. and Struct.* Vol. 16(10), pp. 835 – 845.

[9] Feenstra, J., Granstrom, J., and Sodano, H. (2008) 'Energy Harvesting through a backpack employing a mechanically amplified piezoelectric stack', *Mech. Syst. Signal Pro.* Vol. 22(3), pp. 721 – 734.

[10] Van den Ende, D. A., van de Wiel, H. J., Groen, W. A., and van der Zwagg, S. (2012) 'Direct strain energy harvesting in automobile tires using piezoelectric PZT-polymer composites' *Smart Mater. Struct.* Vol. 21(1), 015011, 11pp.

[11] Akaydin, H. D., Elvin, N., and Andreopoulos, Y. (2010) 'Energy harvesting from highly unsteady fluid flows using piezoelectric materials' *J. Intell. Mater. Syst. and Struct.* Vol. 21(13), pp. 1263 – 1278.

[12] Ali, S. F., Friswell, M. I., and Adhikari, S. (2011) 'Analysis of energy harvesters for highway bridges' *J Intel. Mat. Syst. Str.* Vol. 22(16), 1929 – 1938.

[13] Erturk, A. (2011) 'Piezoelectric Energy Harvesting for Civil Infrastructure System Applications: Moving Loads and Surface Strain Fluctuations', *J Intel. Mat. Syst. Str.* Vol. 22(17), 1959 – 1973.

[14] Peigney, M., and Siegert, D. (2013) 'Piezoelectric energy harvesting from traffic-induced bridge vibrations' *Smart Mater. Struct.* Vol. 22(9), 095019.

[15] Cahill, P. A., Nuallain, N. A., Jackson, N., Mathewson, A., Karoumi, R. and Pakrashi, V. (2014) 'Energy Harvesting from Train-Induced Response in Bridges.' *J Bridge Eng.*, 10.1061/(ASCE)BE.1943-5592.0000608.

[16] Sheu, W-J, Huang R-T., and Wang, C-C. (2008) 'Influence of bonding glues on the vibration of piezoelectric fans' *Sensor Actuat. A-Phys.,* Vol. 148(1), pp. 115 – 121.

[17] Mango, M., Jackson, N., Mathewson, A., and Popovici, E. (2013) 'Combination of hybrid energy harvesters with MEMS piezoelectric and nano-watt radio wake up to extend lifetime of system for wireless sensor nodes' *Proc. Int. Conference on Architecture of Computing Systems,* VDE Verlag, GMCH, Berlin.

Design of Scaled Bridge Prototype for Energy Harvesting Testing

Paul Cahill[1], Giuseppina Amato[2], Nathan Jackson[3], Alan Mathewson[3], Vikram Pakrashi[1]
[1] Dynamical Systems & Risk Laboratory, School of Engineering, University College Cork, Cork, Ireland
[2] School of Planning, Architecture and Civil Engineering, Queens University Belfast, University Road, Belfast, BT7 1NN, Northern Ireland.
[3] Heterogeneous Systems Integration Group, Microsystems Group, Tyndall National Institute, University College Cork, Cork, Ireland.
email: p.a.cahill@umail.ucc.ie, g.amato@qub.ac.uk, nathan.jackson@tyndall.ie, alan.mathewson@tyndall.ie, v.pakrashi@ucc.ie.

ABSTRACT: Energy harvesting from ambient vibration is a promising field, especially for applications in larger infrastructures such as bridges. These structures are more frequently monitored for damage detection because of their extended life, increased traffic load and environmental deterioration. In this regard, the possibility of sourcing the power necessary for the sensors from devices embedded in the structure, thus cutting the cost due to the management of battery replacing over the lifespan of the structure, is particularly attracting. Among others, piezoelectric devices have proven to be especially effective and easy to apply since they can be bonded to existing host structure. For these devices the energy harvesting capacity is achieved directly from the variation in the strain conditions from the surface of the structure. However these systems need to undergo significant research for optimisation of their harvesting capacity and for assessing the feasibility of application to various ranges of bridge span and load. In this regard scaled bridge prototypes can be effectively used not only to assess numerical models and studies in an inexpensive and repeatable way but also to test the electronic devices under realistic field conditions. In this paper the theory of physical similitude is applied to the design of bridge beams with embedded energy harvesting systems and health monitoring sensors. It will show both how bridge beams can be scaled in such a way to apply and test energy harvesting systems and 2) how experimental data from existing bridges can be applied to prototypes in a laboratory environment. The study will be used for assessing the reliability of the system over a train bridge case study undergoing a set load cycles and induced localised damage.

KEY WORDS: Energy Harvesting; Structural Health Monitoring; Experimental Analysis.

1 INTRODUCTION

The ambient vibration of infrastructure elements is considered problematic, with many attempts for its elimination having been formulated. Such vibrations may, however, be harnessed to provide the basis of smart technology for a wide range of applications, such as energy harvesting and structural health monitoring. Through the use of such energy harvesting technology, large scale civil infrastructure experiencing significant vibrations can be used to power small scale wireless devices, which can be used as a health monitoring system. While recent studies establish this principle in theory, experimental investigations into this area are lacking, with two key factors being primarily responsible. First is the expensive, and, often impractical, nature of conducting full scale testing of such novel technology for diverse infrastructure elements. The second key factor is the difficulty in providing scaled laboratory experiments of multiple systems operating concurrently. The provision of such scaled experiments would provide an inexpensive method to verify the feasibility and reliability of novel systems coupled with large scale civil infrastructure projects.

The field of energy harvesting has undergone immense change in recent times in a quest to find a sustainable energy source for small scale electronics. Kinetic energy harvesting as the basis of such an energy source has come to the fore, due particularity to its harnessing of ambient vibrations of host structures. Piezoelectric, electromagnetic and electrostatic are the most popular types of kinetic energy harvesting technologies, with piezoelectric energy harvesting proving especially promising [1]. There has been intense research into the design and optimisation of piezoelectric devices [2] [3], with the effects of parameters such as the amplitude of the applied vibration frequency and the external resistance, on the power output being investigated [4]. A bimorph cantilever harvester, which consisted of two layers of piezoelectric material, was created and the maximum power output under sinusoidal loading determined [5]. A multi-cantilever energy harvester, consisting of cantilevers of varying natural frequencies, was created so as to extend the bandwidth of the devices natural frequency [6]. The vast majority of these energy harvesting devices, however, have a high frequency, most often in the 10^2 Hz and above. This renders them unsuitable for applications pertaining to civil infrastructure elements, which typically have a natural frequency in the region of 10^1 Hz.

Research into the application of energy harvesting devices for use with civil infrastructure is very much in its early stages. Indeed, only recently has the application of cantilever based and patch based energy harvesters utilising civil infrastructure as the excitation source being investigated [7]. The use of bridge infrastructure, specifically utilising bridge-vehicle interaction, as the basis for powering such energy harvesters has also been established [8] [9]. The experimental verification of such applications can, however, be a complex problem.

Experimental analysis of cantilever based energy harvesters can be achieved in a straight forward manner. Acceleration data, from theoretical modelling or full scale testing, can be inputted directly as the base excitation. The power output of the energy harvester can therefore be determined for a wide range of applications using vibration testing apparatus. However, a patch based harvester, which directly converts any variations in strain on the host surface into electrical energy, is difficult to verify experimentally. A scaled model of bridge-vehicle interaction with an attached energy harvesting device is required to determine experimentally the energy harvesting potential. While there exists a huge amount of literature on bridge-vehicle interaction [10, 11, 12, 13], the experimental validation of combining bridge-vehicle interaction and energy harvesters has yet to receive attention it warrants.

This paper investigates the design of a scaled bridge prototype for the purpose of energy harvesting testing. Three different bridge-vehicle interaction models are investigated and compared in this regard. The creation of a bridge prototype and the validation of a patch based energy harvester are discussed. An investigation into the experimental setup for energy harvesting from bridge-vehicle interaction using a cantilever based harvester is conducted. An energy harvester with a low natural frequency is created, so as to maximise its energy harvesting potential from large scale structures. This paper established the potential for utilising scaled bridge prototypes and a laboratory setting to validate the energy harvesting potential of large scale civil infrastructure elements.

2 DESIGN OF SCALED BRIDGE PROTOTYPE

A patch based energy harvester, as previously stated, converts variations in strain energy from the surface of the host structure to which it is bonded into electrical energy. Thus to experimentally verify the harvester, the strain conditions it experiences in the laboratory setting must be identical to that of the real structure. The most practical method to achieve this is the creation of a scaled model of the host structure to which it is bonded. For energy harvesting from bridge-vehicle interaction, both the bridge and the loading to which it is subjected must be scaled so as to achieve accurate results. The scaling of the bridge model is outlined below, along with three loading models of varying complexity.

2.1 Bridge Model

For the purposes of this investigation, the model is that of a simply supported Euler Bernoulli beam, with a simply supported length L. The free vibration equation for the beam can be given as

$$EI\frac{\partial^4 y(x,t)}{\partial x^4} + \rho A\frac{\partial^2 y(x,t)}{\partial t^2} = 0 \quad (1)$$

Where E, I, ρ and A are the Young's Modulus, second moment of area about the neutral axis, density and the cross sectional area of the beam. With respect to the static equilibrium position, the displacement of the beam is given by $y(x,t)$, where x is the position from the left hand support of the beam at time t after the vehicle enters the beams. The equation for the forced vibration of the beam including damping is written as:

$$EI\frac{\partial^4 y(x,t)}{\partial x^4} + \rho A\frac{\partial^2 y(x,t)}{\partial t^2} + c\frac{\partial y(x,t)}{\partial t} = F_p(x,t) \quad (2)$$

Where c is the equivalent viscous structural damping of the beam and $F_p(x,t)$ is the forced vibration on the beam due to the passage of the vehicle. Using the separation of variables technique and considering n number of normal displacement mode shapes, the response, $y(x,t)$, can be written reasonably accurately with the choice of an adequately high value of n, as

$$y(x,t) = \sum_{j=1}^{n} q_j(t)\Phi_j(x) \quad (3)$$

Where $q_j(t)$ is the time domain response associated with $\Phi_j(x)$, the j^{th} mode shape of the beam. For a simply supported beam,

$$\Phi_j(x) = sin\frac{j\pi x}{L} \quad (4)$$

Substituting Equation 3 into Equation 2, multiplying both sides by $\Phi_j(x)$ and integrating over the length L, the following is obtained:

$$\ddot{q}_j(t) + 2\xi_j\omega_j\dot{q}_j(t) + \omega^2{}_j q_j(t) = R_j(t) \quad (5)$$

Where ξ_j is the equivalent viscous damping ratio of the beam, ω_j is the natural frequency for the j^{th} mode and $R_j(t)$ the forcing function for the j^{th} mode. The natural frequency can be expressed as:

$$\omega_j = \frac{j^2\pi^2}{L^2}\sqrt{\frac{EI}{\rho A}} \quad (6)$$

The loading $Rj(t)$ can be considered at different degrees of complexity and in this paper three different loading models are investigated. The first is a constant force model, the second is a spring mass model and the third is a quarter car model. The vibration force of each is outlined and the scaling of the three models is established. For each of the cases it is assumed that the load is moving from left to right at a constant speed.

2.1.1 Constant Force Model

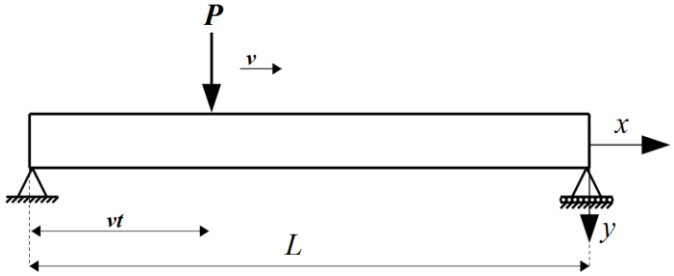


Figure 1. Constant Force Model.

The first model examined considers a constant force, P, traversing the beam at a constant velocity, v [Figure 1]. The forced vibration is now

$$F_p(x,t) = P\delta(x - vt) \quad (7)$$

With δ being the Dirac Delta function. Following Equation 5 and using the sampling property of Dirac Delta function integration, the forced vibration function becomes

$$R_j(t) = \frac{P}{\rho A \bar{K}_j}\Phi_j(vt) \quad (8)$$

$$\bar{K}_j = \int_0^L \Phi_j(x)^2 dx \quad (9)$$

$$\ddot{q}_j(t) + 2\xi_j\omega_j\dot{q}_j(t) + \omega^2{}_j q_j(t) = \frac{P}{\rho A \bar{K}_j} sin\left(\frac{j\pi vt}{L}\right) \quad (10)$$

With a displacement term y_m is defined as

$$y_m = \frac{P}{\rho A L \omega_1{}^2} \quad (11)$$

And time is non-dimensionalised as

$$\tau = \omega_1 t \quad (12)$$

Where ω_1 is the first natural frequency (j =1) of the beam. A non-dimensional equation describing the forced vibrations for the beam traversed by a constant force can be written as

$$\ddot{u}_j(\tau) + 2\xi_j\Omega\dot{u}_j(\tau) + \Omega^2 u_j(\tau) = \frac{L}{\bar{K}_j} sin(j\pi\xi_v) \quad (13)$$

where

$$u_j = \frac{q_j}{y_m} \quad (14)$$

$$\Omega = \frac{\omega_j}{\omega_1} \quad (15)$$

$$\xi_v = \frac{vt}{L} \quad (16)$$

2.1.2 Spring Mass Model

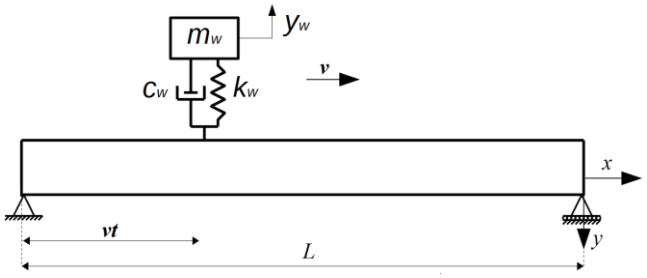


Figure 2. Spring Mass Model.

The next model considered is the spring mass model, consisting of a mass, spring and damper traversing the beam at constant speed v [Figure 2]. Taking the dynamic equilibrium conditions for the degree of freedom in the y_w direction (the degree of freedom for the vehicle) as

$$m_w\ddot{y}_w + c_w(\dot{y}_w + \dot{y}) + k_w(y_w + y) = 0 \quad (17)$$

Where m_w is the mass and c_w and k_w are the structural damping coefficient and the spring stiffness of the vehicle respectively. This results in forced vibration function, with the inertial effects of the vehicle taken into account, given as

$$F_p(t) = (m_w\ddot{y}_w + m_w g)\delta(x - vt) \quad (18)$$

Taking Equation 18, and applying similar steps as those previously taken to obtain Equation 5, the forcing function becomes

$$R_j(t) = \frac{1}{\rho A \bar{K}_j}(m_w\ddot{y}_w + m_w g)\Phi_j(vt) \quad (19)$$

Which when combined with Equation 5, results in

$$\ddot{q}_j(t) + 2\xi_j\omega_j\dot{q}_j(t) + \omega^2{}_j q_j(t) = \frac{P}{\rho A \bar{K}_j}[m_w\ddot{y}_w + m_w g]\, sin\left(\frac{j\pi vt}{L}\right) \quad (20)$$

From Equation 20, the non-dimensional equation for the forced vibrations of a spring mass model traversing the beam is given as

$$\ddot{u}_j(\tau) + 2\xi_j\Omega\dot{u}_j(\tau) + \Omega^2 u_j(\tau) = \frac{L}{\bar{K}_j}(\varepsilon_w\ddot{Y}_w + \varepsilon_w\theta)\, sin(j\pi\xi_v) \quad (21)$$

Where

$$Y_w = \frac{y_w}{y_m} \quad (22)$$

$$\varepsilon_w = \frac{m_w}{\rho A L} \quad (23)$$

$$\theta = \frac{g}{\omega_1 y_m} \quad (24)$$

2.1.3 Quarter Car Model

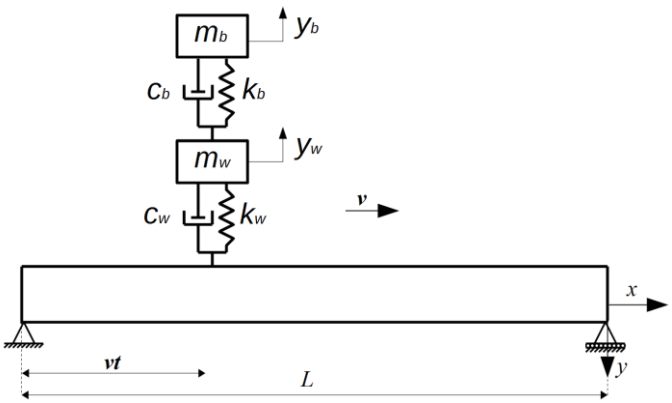


Figure 3. Quarter Car Model.

The third and final model chosen for the purposes of this investigation is that of a quarter car model. The loading traversing the beam has two degrees of freedom, an upper mass m_b, with a damping coefficient c_b and spring stiffness k_b and a lower mass m_w, with a damping coefficient c_w and spring stiffness k_w. The vehicle travels at constant velocity v and the equations of motion, in the y_b and y_w direction corresponding to the two degrees of freedom of the vehicle can be written as:

$$m_b\ddot{y}_b + c_b(\dot{y}_b + \dot{y}_w) + k_b(y_b + y_w) = 0 \quad (25)$$

$$m_w\ddot{y}_w + m_b\ddot{y}_b + c_w(\dot{y}_w + \dot{y}) + k_w(y_w + y) = 0 \quad (26)$$

Which represent the body and the wheel of the vehicle respectively. The forced vibration function can thus be written as:

$$F_p(t) = (m_w\ddot{y}_w + m_b\ddot{y}_b + (m_w + m_b)g)\delta(x - vt) \quad (27)$$

Again following the steps taken to solve Equation 5, the forced vibration function following from Equation 27 can be written as

$$R_j(t) = \frac{1}{\rho A\bar{K}_j}(m_w\ddot{y}_w + m_b\ddot{y}_b + (m_w + m_b)g)\Phi_j(vt) \quad (28)$$

Which, when combined with Equation 5, results in

$$\ddot{q}_j(t) + 2\xi_j\omega_j\dot{q}_j(t) + \omega^2{}_jq_j(t) = \frac{1}{\rho A\bar{K}_j}[m_w\ddot{y}_w + m_b\ddot{y}_b + (m_w + m_b)g]\sin\left(\frac{j\pi vt}{L}\right) \quad (29)$$

A non-dimensional equation can now be obtained for the quarter car model traversing the beam, given by

$$\ddot{u}_j(\tau) + 2\xi_j\Omega\dot{u}_j(\tau) + \Omega^2u_j(\tau) = \frac{L}{\bar{K}_j}(\varepsilon_b\ddot{Y}_b + \varepsilon_w\ddot{Y}_w + \varepsilon\theta)\sin(j\pi\xi_v) \quad (30)$$

Where

$$Y_b = \frac{y_b}{y_m} \quad (31)$$

$$\varepsilon_b = \frac{m_b}{\rho AL} \quad (32)$$

$$\varepsilon = \frac{m_w + m_b}{\rho AL} \quad (33)$$

2.2 Use of Scaled Forcing Functions for Design of Bridge Prototype and Impact on Energy Harvesting Potential

Energy harvesting devices are driven through the excitation caused by the host structure, as previously outlined. The models, as formulated in this paper, provide non-dimensional equations for the excitation caused by the host structure, of varying degrees of complexity. The design of the scaled bridge prototype will thus be dependent primarily on appropriate scaling of the bridge model to that of the corresponding, full scale structure of interest. The effects of loading on the beam will be dependent on the vehicle of interest, with the constant force model being the most conservative of those investigated. With the bonding of a patch based energy harvester to the scaled prototype, the voltage output due to train-bridge interaction can be experimentally validated in a laboratory setting. Through an appropriately designed experimental prototype, whereby the strain conditions of the prototype and the structure of interest correspond to a reasonable level, the energy harvesting potential of the device can be determined.

Following from this, the introduction of damage to the bridge-vehicle interaction model will allow for the effect of damage to be detected through the output of the energy harvester. With the introduction of damage, the strain conditions will vary and thus the voltage output of the device will change. Through an appropriately design damage prototype, scaled laboratory experiments for the structural health monitoring of bridge infrastructure through energy harvesting from bridge-vehicle interaction can be validated.

3 EXPERIMENTAL ANALYSIS OF CANTILEVER BASED ENERGY HARVESTER

A cantilever based energy harvester can be experimentally validated provided bridge-vehicle interaction acceleration data is available. The acceleration is provided as a base excitation to the cantilever and this can be validated using laboratory vibration testing equipment. The design of the cantilever is also of note. As previously stated, most energy harvesting devices are designed for very high frequency applications, which render them unsuitable for civil infrastructure applications. Thus, the design of the harvester to have a low natural frequency is paramount. The following section investigates the potential for determining the potential power and voltage output from an energy harvesting device through experimental means. The energy harvester is designed and manufactured and the effects of low frequency loading investigated.

3.1 Design, Fabrication and Properties of Energy Harvester

For the purposes of this investigation, it was decided to use the piezoelectric material PolyVinyliDene Fluoride (PVDF) with the chemical equation $(C_2H_2F_2)_n$, as opposed to the more popular Lead Zirconate Titanate (PZT), $Pb(Zr_xTi_{1-x})O_3$. The reason for this is due to the difference in physical properties. PVDF is a polymer and has a high mechanical strength while maintaining flexibility [14]. It is thus easy to handle and can be used for complex design applications. PZT has better piezoelectric properties then PVDF, which results in a greater energy output when compared to PVDF under similar operating conditions. The drawback of PZT is its physical properties, it is a ceramic and is thus brittle [15].

A 52μm thick PVDF sheet with silver electrodes was obtained and cut into dimensions of 150mm and 40mm, length and width respectively [Figure 4]. This was bonded to an aluminum beam, of dimensions 220 x 50 x 2 mm and tip

mass of 0.1kg, using a nonelectrical conductive epoxy. The resultant capacitance of the energy harvester is calculated at 10.1 nF and the first mode of the natural frequency was calculated to be 12.01Hz.

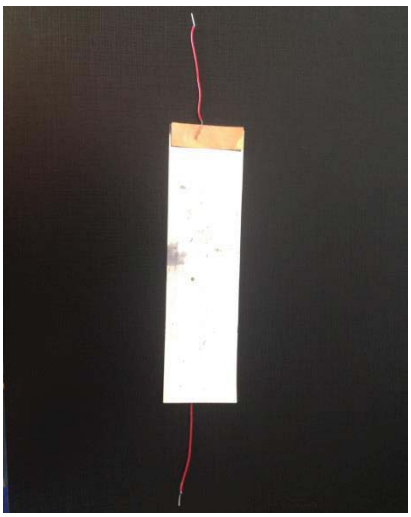


Figure 4. PVDF film with Silver Electrodes.

Two base plates were attached so as to make the energy harvester a fixed end cantilever and the energy harvester was than tested using an LDS Permanent Magnet Shaker [Figure 5]. Continuous sinusoidal loading of varying amplitude and frequency was applied as base excitation for the energy harvester and the voltage output measured.

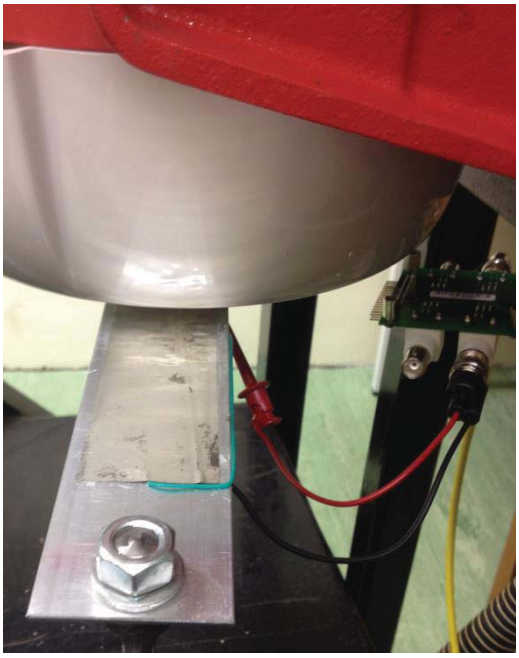


Figure 5. Energy Harvester Connected to Shaker unit and Oscilloscope.

3.2 *Experimental Results*

The voltage output from the energy harvester for different loading conditions was obtained. With a view at large scale civil infrastructure applications, it was designed so as to have a low natural frequency. As the natural frequency is the frequency with the largest deflection, it will result in the highest voltage output. Under a continuous sinusoidal load of 1g, a sweep of the frequency of the loading was performed between 5 and 20 Hz [Figure 6]. It was found that the natural frequency of the energy harvester was 12.35Hz, which is within 97% of the calculated natural frequency. As can be seen, there is a dramatic increase in the voltage output about the natural frequency, as was expected. At 12.35 Hz, the voltage output was 22.817 V AC, with a peak to peak voltage of 45.63V. As the frequency shifts away from the natural frequency, the voltage drops off with a voltage output of 2.82, 1.71 and 1.12 at 11, 10 and 9 Hz respectively.

The varying of the amplitude of the loading was also investigated, with excitations of 0.75g and 0.5g being applied to the energy harvester [Figure 7]. At the natural frequency, a voltage output of 14.31V and 11.454V was obtained loading of amplitude 0.75g and 0.5g respectively. When compared against loading of 1g at varying frequency, the amplitude of loading against the voltage is found to be a linear.

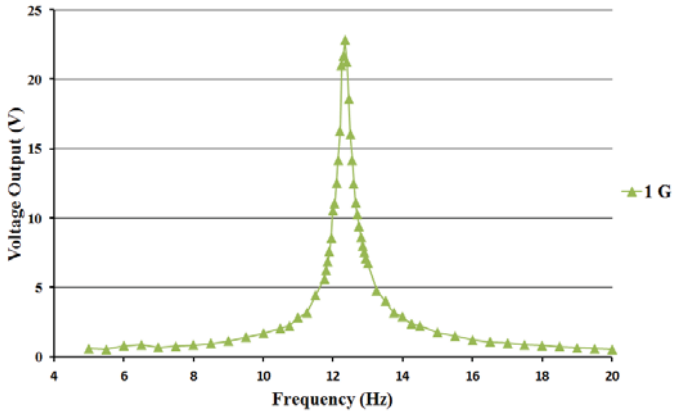


Figure 6. Voltage Output of Energy Harvester under 1g Excitation at Varying Frequencies.

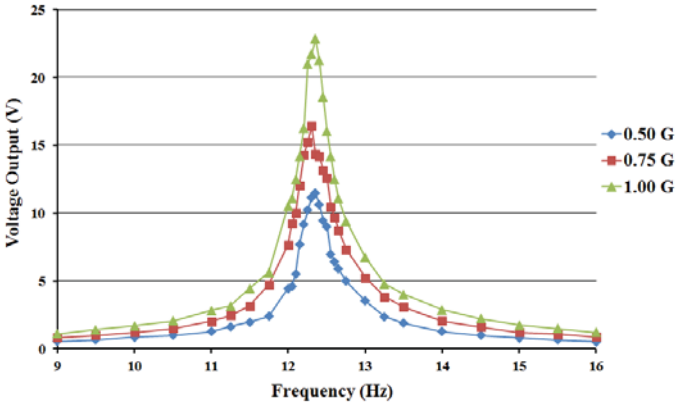


Figure 7. Voltage Output of Energy Harvester under 1g, 0.75g and 0.5g Excitation at Varying Frequencies.

4 CONCLUSION

This paper investigated the design of scaled bridge prototypes for energy harvesting testing. Three different loading models of bridge-vehicle interaction were investigated in this regard, a constant force model, spring mass model and quarter car model. A model bridge under the different loading models was investigated and subsequently scaled. The design of a scaled bridge prototype utilizing the different scaled loading models was discussed, as were the implications of the scaled models on the validation of patch based energy harvesters. A potential application of Structural Health Monitoring using the patch based harvesters and its subsequent validation is observed. The design, fabrication and testing of a cantilever based energy harvester in a laboratory setting was outlined. Experimental analysis of the harvester was conducted and, subjected to 1g excitation at the natural frequency; a voltage output of 22.817 V was obtained. The effects of varying the amplitude and frequency of the loading were investigated. This paper establishes the potential for the use of scaled bridge prototypes and laboratory based vibration testing for validation of energy harvesting from civil infrastructure.

ACKNOWLEDGMENTS

This work was made possible through the Irish Research Council Government of Ireland Postgraduate Scholarship Scheme.

REFERENCES

[1] Beeby, S.P., Tudor, M.J., and White, N.M (2007) 'Energy Harvesting Vibration Sources for Microsystems Applications', *Measurement Science and Technology*, Vol. 17(12), R175 – 195.

[2] Anton, S.R., and Sodano, H. A. (2007) 'A Review of Power Harvesting using Piezoelectric Materials (2003 – 2006)', *Smart Mater. Struct.,* Vol. 16(3), R1 – 21.

[3] Priya, S. (2007) 'Advances in Energy Harvesting using low Profile Piezoelectric Transducers', *J Electroceram.,* Vol. 19(1), 165 - 182.

[4] Lu, F., Lee, H. P., and Lim, S. P. (2004) 'Modeling and analysis of micro piezoelectric power generators for micro-electromechanical-systems applications', *Smart Mater. Struct.,* Vol. 13(1), 57 – 63.

[5] Ajitsaria, J., Choe, S. Y., Shen, D., and Kim, D. J. (2007) 'Modeling and analysis of a bimorph piezoelectric cantilever beam for voltage generation', *Smart Mater. Struct,* Vol. 16(2), 447 – 454.

[6] Liu, J-Q., Fang, H-B., Xu, Z-Y., Mao, X-H., Shen, X-C., Chen, D., Liao, H., and Cai, B-C. (2008) 'A MEMS-based piezoelectric power generator array for vibration energy harvesting', *Microelectr. J,* Vol. 39(5), 802 -806.

[7] Erturk, A. (2011) 'Piezoelectric Energy Harvesting for Civil Infrastructure System Applications: Moving Loads and Surface Strain Fluctuations', *J Intel. Mat. Syst. Str.* Vol. 22(17), 1959 – 1973.

[8] Ali, S. F., Friswell, M. I., and Adhikari, S. (2011) 'Analysis of energy harvesters for highway bridges' *J Intel. Mat. Syst. Str.* Vol. 22(16), 1929 – 1938.

[9] Cahill, P. A., Nuallain, N. A., Jackson, N., Mathewson, A., Karoumi, R. and Pakrashi, V. (2014) 'Energy Harvesting from Train-Induced Response in Bridges.' *J Bridge Eng.*, 10.1061/(ASCE)BE.1943-5592.0000608.

[10] Delgado, R. M., and dos Santos, R. M., (1997) 'Modelling of railway bridge-vehicle interaction on high speed tracks', *Comput. Struct.* Vol. 63(3), 511 - 523.

[11] Fryba, L. (1999) 'Vibrations of solids and structures under moving loads'. Thomas Telford.

[12] Law, S. S., and Zhu, X. Q, (2004) 'Dynamic behaviour of damaged concrete bridge structures under moving vehicular loads' *Eng. Struct.,* Vol. 26(9), 1279 – 1293.

[13] Pakrashi, V., O'Connor, A., and Basu, B. (2010) 'Effect of tuned mass damper on the interaction of a quarter car model with a damaged bridge', *Struct. Infrastruct. E.*, Vol. 6(4), 409 – 421.

[14] Vinogradov, A., and Hollowar, F. (1999) 'Electric-mechanical properties of the piezoelectric polymer PVDF' *Ferroelectrics*, Vol. 226(1), 169 - 181.

[15] Woo, S.C., and Goo, N. S. (2007) 'Identification of failure mechanisms in a smart composite actuator with a thin sandwiched PZT plate based on waveform and primary frequency analysis' *Smart Mater. Struct.* Vol. 16(4), 1460 – 1470.

Parameter Importance Measure Studies on Prestressed Concrete Bridges in Ireland

Ciarán Hanley[1] & Vikram Pakrashi[1]
[1]Dynamical Systems & Risk Laboratory, School of Engineering, University College Cork, Ireland
email: c.m.hanley@umail.ucc.ie, v.pakrashi@ucc.ie

ABSTRACT: This paper presents a reliability based study to prioritise monitoring and intervention strategies for bridge asset management. Three prestressed concrete bridges of similar form have been analysed through reliability methods. Sensitivity studies and parameter importance measures were established. These measures highlight which parameters contribute most to the safety classification of each bridge, and how they are affected by a change in material property or geometry. The analysis has been conducted for various levels of uncertainty, and shows how this uncertainty, with regard to assessing the system, can affect the safety classification, even when no variation in parameters has occurred. The critical parameters for each bridge are evaluated and a correlation between them is established. This calibration can then be used to prioritise assessment of these bridge types, and a basic safety level can be established based on this framework, in the absence of a site-specific probabilistic analysis. A case is made to expand this analysis to a wider array of networks, and encourages the stakeholders of bridges to share network-level information in order to create a repository for the calibration of different bridge forms.

KEY WORDS: Reliability analysis; Parameter importance; Parametric Sensitivity, Bridges, Concrete.

1 INTRODUCTION

In order to ensure an adequate level of safety for the aging bridge stock in Ireland, it is necessary to implement an effective asset management strategy [1]. Such an asset management strategy can allow stakeholders prioritise intervention options for degrading infrastructure, such as; maintain, repair, or replace. A reliability analysis approach offers an effective and sophisticated method to establish the safety level of a bridge [2], in isolation or as part of a greater network of bridges [3, 4]. The benefits to infrastructure asset stakeholders from using this method are that it can it can be modelled to account for asset degradation over time and uncertainty regarding loading and capacity, as well as highlight the relative importance and sensitivity of the parameters involved in the model.

The question of how to effectively allocate capital resources, and the sophisticated methods used to answer this question, are prevalent in a modern economy that seeks to minimise the inherent risks associated with investments [5]. For a bridge manager, these parameter studies can prove vital in the question of where to allocate resources as these rankings will indicate which parameters contribute most to the structural safety of the bridge, and thus which are at most risk to cause structural failure in the event of damage or deterioration.

The objective of this paper is to investigate a number of prestressed concrete composite bridges, and determine the parameters that are most critical to structural safety, through a probabilistic reliability analysis. This is conducted with a view to establishing an inspection framework that prioritises the most critical parameters, in a way to best eliminate uncertainty and subjectivity for the bridge manager.

A background to probabilistic analysis is presented, as well as the assessment methodology and description of the asset base. The results of the reliability analysis are presented, with special attention being paid to the parametric importance and sensitivity studies. A discussion on the implications of the findings is presented in the conclusions.

2 RELIABILITY ANALYSIS

Probabilistic structural analysis allows the determination of the probability of failure, P_f, of a structure for a given limit state, and is defined as the probability of the exceedance of the limit state. Generically, the limit state, g, is exceeded when the applied load, Q, is greater than the capacity of the structure, R, to resist the load.

$$g = R - Q \tag{1}$$

And thus, the failure probability for this generic limit state is expressed as:

$$P_f = P(g < 0) = P[(R - Q) < 0] \tag{2}$$

Using the standard normal distribution function, Φ, the failure probability is related to the reliability index, β, after converting all involved parameters into a multidimensional space, typically through a Rosenblatt transformation [6].

$$\beta = -\Phi^{-1}(P_f) \tag{3}$$

The reliability index β is a probabilistic measure of safety, and can be interpreted as the least distance to a limit state failure surface in a probability preserving standard normal space [7]. The location of this point is considered to be the design point, the point in this space with the highest probability density.

Common methods in probabilistic analysis are the first-order reliability method (FORM) and the second-order reliability method (SORM) [8]. In FORM, the failure probability is obtained by linearizing the limit state functions in a standard normal space at an optimal point, under the assumption that, at this point, the functions are continuous and differentiable.

SORM extends from FORM by approximating the limit state surface to a hyper-paraboloid, as opposed to a hyper-plane in FORM [9]. Both methods were employed for this paper, in order to verify the model accuracy.

Analysing a structure probabilistically provides a framework by which to conduct a sensitivity analysis for parameters involved in the limit state equation. For a sensitivity study, the parameters are nominally perturbed and the effect of this perturbance on the measure of safety is recorded. This enables the identification and quantification of design, model, and construction error [10]. The parametric sensitivity factor for β is defined as the derivative $\delta\beta/\delta\theta$ [11].

The relative importance of each parameter, θ, to the limit state equation can be determined from this sensitivity analysis. These importance measures, expressed as a percentage of the total set of involved parameters, show the extent to which each parameter influences the failure probability of the system [12], and provide a basis for which to prioritise a monitoring hierarchy for each bridge type.

3 DESCRIPTION OF ASSET BASE AND ASSESSMENT METHODOLOGY

Three bridges were selected for a detailed probabilistic analysis, of varying age and exposure (Table 1). All assets had composite decks, comprising prestressed concrete beams with in-situ concrete infill, and were simply supported spans (Figure 1).

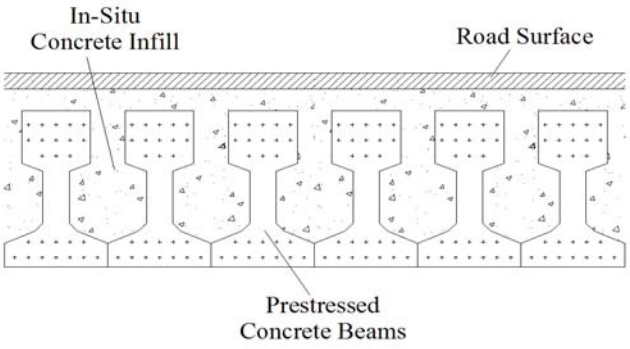


Figure 1 Bridge cross-section

The assessed limit states were for bending and shear, assessed at critical locations, which were established through deterministic analysis, using hand calculations and computational methods. Three load cases of permanent (dead load and superimposed dead load) and the combination of permanent and live loads were assessed; normal (HA) and abnormal (HB), in accordance with BD37/01 [13]. Thus, this paper will refer to three load cases, LC; LC 1 (dead load only), LC2 (dead load and HA), and LC3 (dead load and HB). It is noted that axle loads from HB loading have been converted to a uniformly distributed load, based on the number of axles of loading, for model simplification.

Table 1 Description of assets

Bridge No.	No. of Spans	Length (m)	Width (m)	Age (years)
1	5	60.9	11.6	53
2	4	45.8	12.93	38
3	3	27.5	12.9	38

In reference to the generic limit state function, the applied loads Q and characteristic resistance R were established, and a stress index was defined as the ration Q/R. A stress index less than or equal to unity indicates compliance with safety standards and stress index exceeding this unity indicates noncompliance with the standards. This method in the assessment of structures can only give generalised indication of the level of safety present, and does not correspond to the true safety level of a structure [14].

$$Q = M_d, V_d\,(b_x, h, L_{EFF}, P_{HA}, w_{DL}, w_{SDL}, w_{HA}, w_{Hb}) \quad (4)$$

$$R = M_R, V_R\,(b, d_c, f_{cu}, f_{pt}, h, h_c, I_{xx}, M_T, y) \quad (5)$$

For a probabilistic analysis, as opposed to a deterministic analysis, each parameter (Table 2) can be modelled as stochastic, with an associated probability density function. As the effect of uncertainty within the parameters is being investigated, each mean value has been modelled with an increasing value of Coefficient of Variance (CoV), rather than an inherent standard deviation, σ. Thus, the effect of various levels of uncertainty for different parameters can be established.

Table 2 Limit state parameters

Description	Symbol
Section width	b
Dispersed wheel perimeter	b_x
Depth from compression fibre to centroid of tendons	d_c
Concrete strength	f_{cu}
Stress due to prestress	f_{pt}
Overall section height	h
Depth of compressive section above NA	h_c
Second moment of area	I_{xx}
Effective span	L_{EFF}
Point load for HA	P_{HA}
Tensile resistance moment	M_T
Centroid of composite section	y
Dead load	w_{DL}
Normal transient load (HA)	w_{HA}
Abnormal transient load (HB)	w_{HB}
Superimposed dead load	w_{SDL}

As the level of information regarding the bridge geometry is typically high, by way of as-built drawings or field measurements, the associated parameters have been classed as fixed values (Table 3). Conversely, as information pertaining to material properties can be difficult to obtain, these parameters have been assigned probability distributions. The parameters relating to dead load have been assigned a probability distribution to account for any unknowns in the construction materials. As the live loading prescribed in design standards correspond to worst-case events, a Weibull distribution has been determined to provide a reasonable representation of the extreme value effects of vehicular live loads [15].

4 RESULTS

4.1 Reliability Indices

A target reliability index of $\beta_{min} = 3.75$ was taken as to be the minimum acceptable level of safety, based on that prescribed in the Eurocodes [16]. For the bending limit state

(Figure 2), it is observed that for a CoV=0.1 (i.e., 10% uncertainty), each bridge satisfies the minimum level of safety for each load case. As the model uncertainty is increased, β begins to decrease, at a seemingly parallel rate, across each bridge and load case. Thus, it can be seen that a high dispersion of β for CoV=0.1 begins to converge for increasing CoV. Such a convergence of safety measure for increasing uncertainty levels highlights how safety classification can be skewed conditional on the inspector's confidence in the model parameters. Thus, the requirement to remove subjectivity from this method is apparent.

Table 3 Mean values for reliability analysis

Var	Distribut.	Units	Bridge No.		
			1	2	3
b	Fixed	mm	300	495	300
b_x	Fixed	mm	1157.6	1269.80	1369.8
d	Fixed	mm	503	500	624.6
d_c	Fixed	mm	414.958	454.286	567.35
f_{cu}	Lognorm.	N/mm^2	54.765	54.6	53.9
f_{pt}	Lognorm.	N/mm^2	6.087	0.364	2.259
h	Fixed	mm	533	550	650
h_c	Fixed	mm	167.678	69.205	141.88
I_{xx}	Fixed	mm^4	3.79E+9	6.86E+9	6.87E+9
L_{EFF}	Fixed	m	12.5	7.6	11.3
P_{HA}	Weibull	kN	13.09	24.68	14.05
M_T	Normal	kNm	296.166	293.761	397.48
y	Fixed	mm	266.5	275	325
w_{DL}	Normal	kN/m	4.85	8.27	5.92
w_{HA}	Weibull	kN/m	6.75	17.76	7.75
w_{HB}	Weibull	kN/m	72.09	98.78	51.44
w_{SDL}	Normal	kN/m	0.97	2.1	1.27

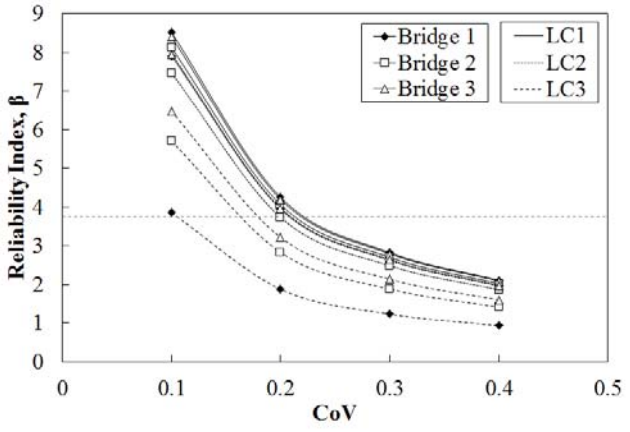


Figure 2 β for bending limit state with increasing CoV

It is interesting to note that at no point of increasing uncertainty does β for a bridge under a specific load case surpass that of a bridge and load case that initially had a greater level of safety for CoV=0.1. This is important as it establishes a uniform probabilistic behaviour for a specific bridge type. It is also notable that, across each bridge and limit state, the reliability indices for CoV=0.2 were approximately 49.5% of the corresponding values for CoV=0.1. For CoV=0.3, this relationship became 32.6%, and for CoV=0.4, 24.1%. A similar spectrum of relationships was observed during the sensitivity analysis. The results obtained for the shear limit-state (Figure 3) were observed to be much higher than for bending and thus was deemed to be non-critical.

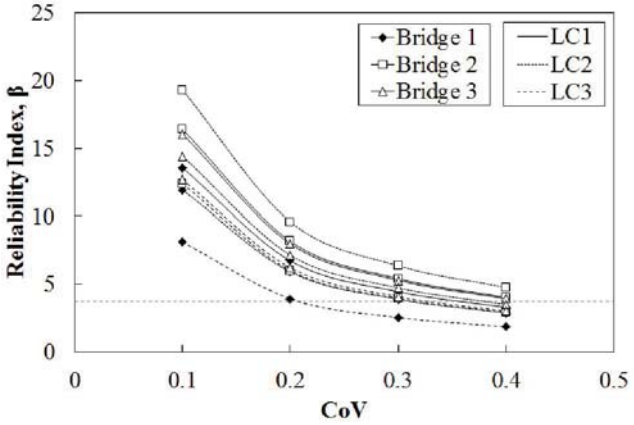


Figure 3 β for shear limit state with increasing CoV

4.2 Sensitivity Studies

A sensitivity analysis was conducted by applying a 10% perturbation to the limit state parameters. The results have been presented for CoV=0.1. As the previously established relationship holds, the results can be extrapolated to determine the sensitivities for the remaining CoV. For this bridge type, it can be seen that the most negatively sensitive parameter for the bending limit state (Figure 4) is the effective length of the span, L_{EFF}. This is at its most apparent for Bridge 1, where a 10% increase in the effective length results in a reduction of β by 1.61. For CoV=0.2, this reduction is by 0.8, 0.53 for CoV=0.3, and 0.39 for CoV=0.4. While it may seem that a greater uncertainty results in smaller reduction in safety level, these values must be interpreted in relation to the lower safety classifications for these uncertainties.

While the effective length of an existing structure is rarely subject to uncertainty or change, these results have implications for the design stage of these bridge types. The other parameters that produce the most unfavourable changes to the reliability index are the in the increase in dead load, w_{DL}, and the uncertainty in the tensile resistance moment of the prestressing, M_T. This means that while and increase in M_T is favourable, the uncertainty related to this increase is unfavourable. It is notable that the parameters that respond positively to this increase are the ones that contribute to the section capacity.

The instances where this perturbance would result in a negative change in the safety classification for this failure mode are for M_T and L_{EFF} for Bridge 2, for CoV=0.2 under LC1, Bridge 1, for CoV=0.1 under LC3, and for CoV=0.2 for LC2. A 10% increase in the parameters b, f_{cu}, h_c, and M_T would enact a positive change to the safety classification of Bridge 2, for CoV=0.2 under LC2.

For the shear limit state (Figure 5), it can be seen that a 10% perturbance in L_{EFF} causes a significant decrease in beta. However, it is to be noted that reliability indices for this limit state were much higher than that for bending, and so this change is proportional to initial values.

This is also evident with the parameters that positively contribute to the safety level. It is evident that there is a consistent behaviour in the parameters for this bridge type, with the exception of some slight deviations.

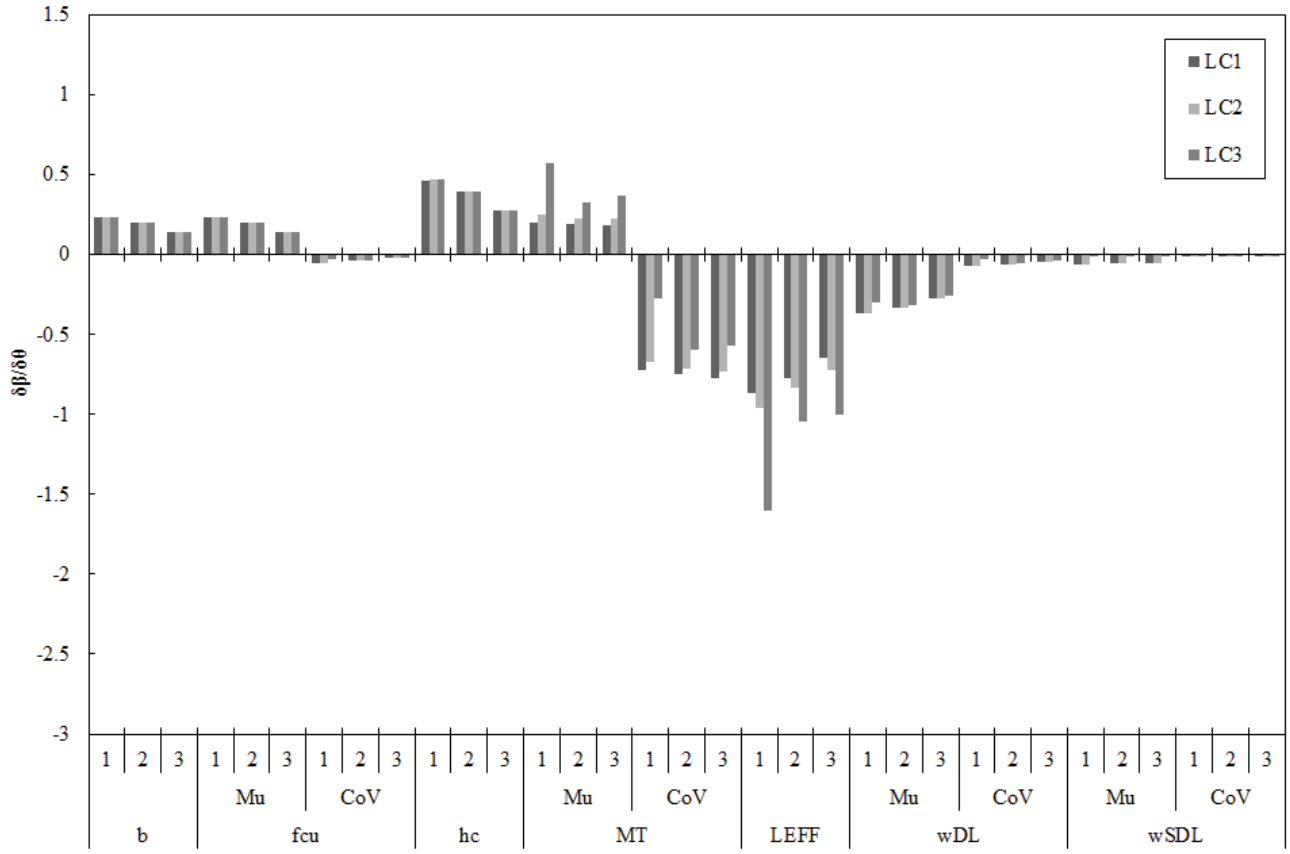


Figure 4 Parametric sensitivity for 10% perturbance for bending limit state (CoV=0.1)

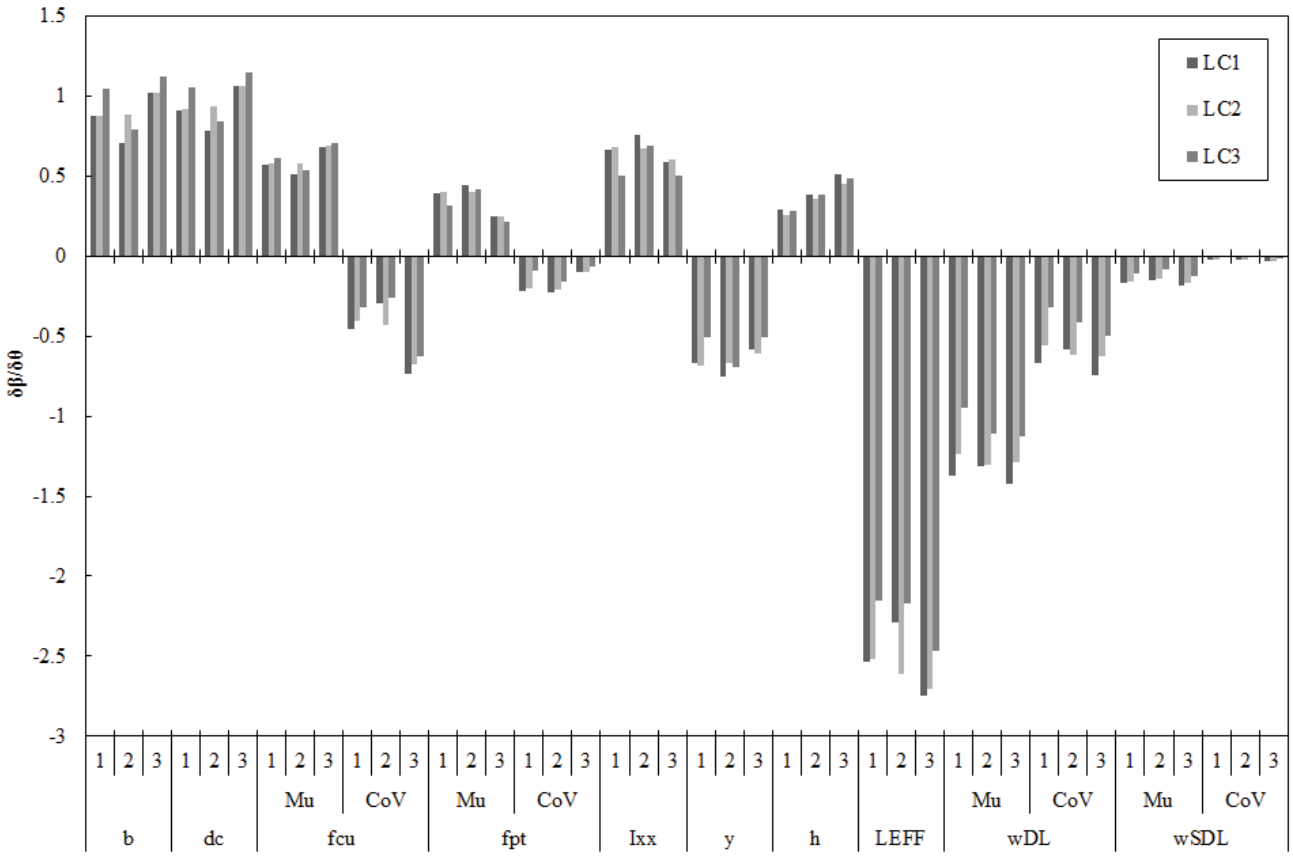


Figure 5 Parametric sensitivity for 10% perturbance for shear limit state (CoV=0.1)

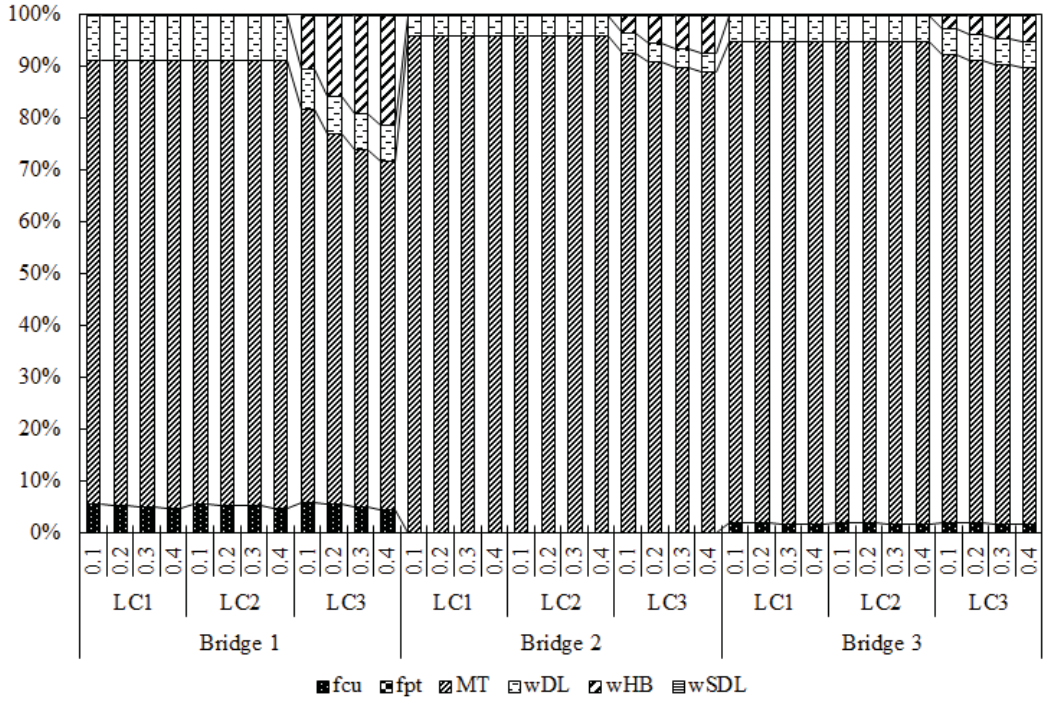


Figure 6 Relative importance of the parameters for the bending limit state

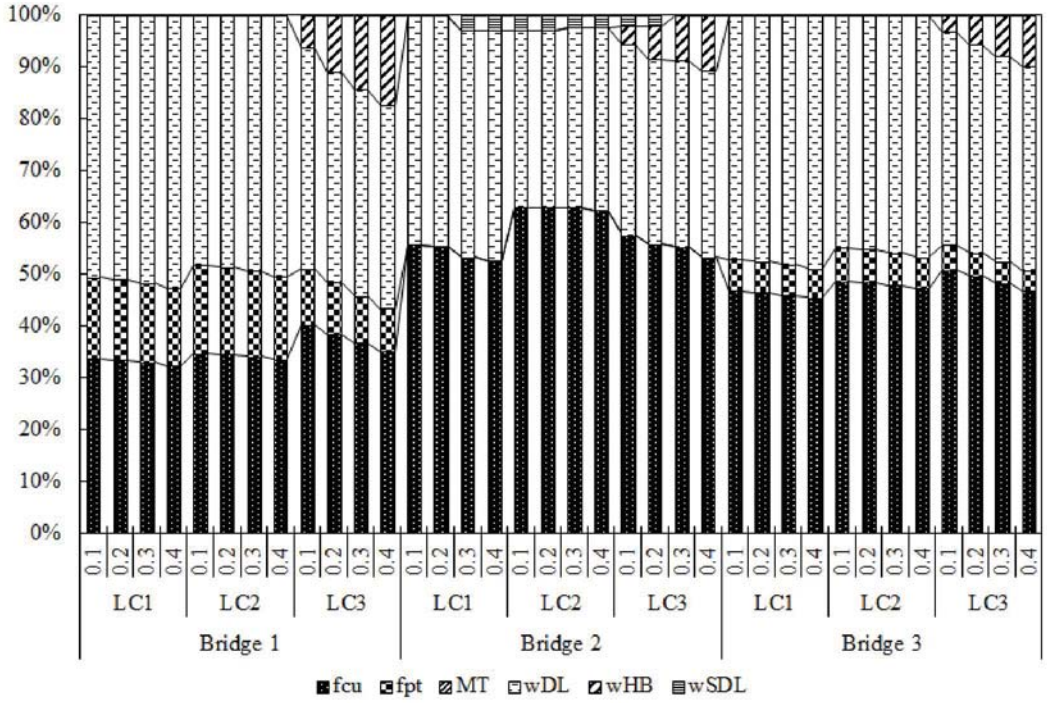


Figure 7 Relative importance of the parameters for the shear limit state

4.3 Parameter Importance

Parameter importance measures were determined to allow the relative ranking of parameters to aid the assessment process. While the sensitivity studies were dominated by the fixed parameters, the parameter importance measures concerns the parameters that were assigned distributions. For prestressed bridges, considering the bending limit state (Figure 6), it is observed that the most significant parameter that contributes to the safety is the tensile resistance moment, M_T. For Bridge 1 under LC 1, M_T accounts for 85.4% importance for CoV=0.1, and increases gradually to 86.1% for CoV=0.4. Under LC2, it begins at 85.1% and increases slightly to 85.8%, but for LC3, it begins at 75.8% and decreased to 67.4%. This can be seen to be due to the influence of abnormal live loading, w_{HB}, which begins at 10.4% and increases to 21.2%. For LC1, w_{DL} remains at a constant level of 8.8%, 8.7% for LC2, and decreases from 7.8% to 6.9% for

LC3. For all load cases, f_{cu} ranges from 4.5% to 6%. For Bridge 2, f_{cu} is not seen to be an important factor, with M_T having a relative importance of approximately 95% across LC1 and LC2 for each CoV, with a reduction for LC3 of 92% to 88.3%, due to the introduction of w_{HB}, which ranged from 3.5% to 7.2%, increasing with CoV. The dead load parameter importance measures for w_{DL}, ranged from 3.7% to 3.9% throughout. Bridge 3 is seen to have similar importance levels as Bridge 2, except with the reintroduction of f_{cu}, ranging from 1.6% to 2% importance. It is seen that w_{DL} maintains a constant level of 5.2% throughout all load cases, and once again w_{HB} impacts LC3, however at lower levels than Bridges 1 and 2, ranging from 2.6% to 5.2%. M_T ranges from 88.2% to 92.8% throughout.

For the shear limit state (Figure 7), f_{cu} and w_{DL} are the two most important factors. However, it is seen that the most important parameter of the two varies across each bridge, load case, and CoV. It is seen for Bridge 1 that w_{DL} is most important across all load cases, ranging from 38.9% importance to 51.6%, whereas f_{cu} ranges from 31.7% to 39.7%. However, for Bridge 2, f_{cu} is observed to be most important throughout, with relative importance ranging from 52.1% to 62.2% against the importance of w_{DL} of 33.7% to 44.2%. The relative importance of the two parameters converge for Bridge 3, with w_{DL} being most important for LC1, but f_{cu} the being most important for LC2 and LC3. It is also noted that for LC2, w_{DL} increases to 44.9% from 43.7%, while f_{cu} decreases from 47.1% to 45.4%. The trend would infer that for a CoV higher than 0.4, w_{DL} would become the most important parameter in this load case. It is also noted that f_{pt} has an importance rating for Bridge 1 and 3, ranging from 8.2% to 16.6% and 3.8% to 6.3%, respectively. Again, w_{HB} features for each bridge in LC3, the superimposed dead load, w_{SDL}, has a relative importance ranging from 2.2% to 2.8% for Bridge 2. It is also observed that for increasing CoV, w_{HB} changes from being less important than f_{pt}, to more important.

5 CONCLUSION

A probabilistic analysis was conducted for three prestressed concrete composite bridges in Ireland, under the limit states of bending and shear, for three separate load cases. The parametric sensitivity and importance measures were established, and showed a high degree of correlation across the three bridges, with nominal deviation. This is significant as it establishes definite relationship for parameter importance for a specific bridge type, as well as the variations of β for various degrees of uncertainty. This infers, subject to further research on a larger asset sample, that for a specific bridge types, probabilistic levels of safety can be determined using existing known information on an individual asset. The degree of confidence in the classification can be enhanced due to removal of uncertainty, by way of field measurements or special inspections. These inspections can then be prioritised by focusing on the parameters that contribute most to the level of structural safety and, consequently, lead to a greater understanding of the most beneficial allocation of resources for an infrastructure management framework.

ACKNOWLEDGMENTS

The authors would like to thank Mr Liam Duffy, National Roads Authority, Ireland, for supporting this research and to gratefully acknowledge the financial support from the John Sisk Postgraduate Research Scholarship.

REFERENCES

[1] Pakrashi, V. et al., (2011). A review of road structure data in six European countries. *Proceedings of the ICE - Urban Design and Planning*, 164(4), pp.225–232.

[2] Akgül, F. & Frangopol, D.M., (2004). Bridge Rating and Reliability Correlation: Comprehensive Study for Different Bridge Types. *Journal of Structural Engineering*, 130(7), pp.1063–1074.

[3] O'Connor, A. & Enevoldsen, I., (2008). Probability based modelling and assessment of an existing post-tensioned concrete slab bridge. *Engineering Structures*, 30(5), pp.1408–1416.

[4] Estes, A.C. & Frangopol, D.M., (2003). Updating Bridge Reliability Based on Bridge Management Systems Visual Inspection Results. *Journal of Bridge Engineering*, 8(6), pp.374–382.

[5] Mueller, J. & Stewart, M.G., (2011). The Price is Not Right: The U.S. spends too much money to fight terrorism. *Playboy*, Oct, pp.149-50.

[6] Ditlevsen, O. & Madsen, H.O., (2005). Structural Reliability Methods *2nd ed*.

[7] Shinozuka, M., (1983). Basic Analysis of Structural Safety. *Journal of Structural Engineering*, 109(3), pp.721–740.

[8] Sarveswaran, V. & Roberts, M.B., (1999). Reliability analysis of deteriorating structures — the experience and needs of practising engineers. *Structural Safety*, 21(4), pp.357–372.

[9] Der Kieureghian, A., (2005). First- and Second-Order Reliability Methods. *Engineering Design Reliability Handbook*, CRC Press.

[10] Nowak, A.S. & Carr, R.I., (1985). Sensitivity Analysis for Structural Errors. *Journal of Structural Engineering,* 111(8), pp.1734–1746.

[11] Bjerager, P. & Krenk, S., (1989). Parametric Sensitivity in First Order Reliability Theory. *Journal of Engineering Mechanics*, 115(7), pp.1577–1582.

[12] O'Connor, A. & Enevoldsen, I., (2007). Probability-based bridge assessment. *Proceedings of the ICE - Bridge Engineering*, 160(3), pp.129–137.

[13] Highways Agency (2001). Loads for Highways Bridges. Design Manual for Roads and Bridges: Volume 1. Highway Structures: Approval Procedures and General Design, Section 3, Part 14, BD 37/01. *Her Majesty's Stationary Office, London*.

[14] O'Connor, A. & Pakrashi, V., (2011). Recent Advances in Reliability based Assessment of Highway Bridges. *In Applications of Statistics and Probability in Civil Engineering*. Zurich, Switzerland, pp. 101–110.

[15] O'Connor, A. & Eichinger, E.M., (2007). Site-specific traffic load modelling for bridge assessment. *Proceedings of the ICE - Bridge Engineering*, 160(4), pp.185–194.

[16] European Committee for Standardisation (2002). EN 1990:2002. Eurocode – Basis for structural design.

A study of transverse load distribution in masonry arch bridges

Helen Dunne[1], John J. Murphy[1], Kieran Ruane[1,2]
[1] Department of Civil, Structural and Environmental Engineering, Cork Institute of Technology, Bishopstown, Cork, Ireland
[2] RPS Consulting Engineers, Innishmore, Ballincollig, Co. Cork
email: helen.dunne@mycit.ie, john.justinmurphy@cit.ie, kieran.ruane@rpsgroup.com

ABSTRACT: Masonry arch bridges comprise a significant proportion of the bridge stock both nationally and internationally. They have proven to be enduring structures, far surpassing their design lives and with relatively low life-cycle costs. New masonry arch bridges are not generally constructed. However, their ageing materials paired with ever increasing traffic loads have led to the necessity for their periodic re-assessment. Masonry arch bridge design was predominantly by rule of thumb and their re-assessment has been subject to a number of simplified assumptions. One such simplification, the bridge "effective width" is studied in this paper with the use of LUSAS finite element analysis software. A preliminary study was carried out on a masonry arch, assessing six point load locations. Arch displacements, axial stresses and axial force envelopes were determined. This informed a more complex study, where parameters such as: arch stiffness, fill stiffness, fill depth, arch shape, arch span/rise, abutment stiffness, ring thickness and bridge skew were studied. This model was verified using displacement test data obtained from the literature. The effective widths of a series of bridges with varying parameters were studied. Statistical analysis was used to determine the most influential factors on the effective widths of masonry arch bridges. Once these were determined, a formula for the calculation of effective width was derived and compared with the effective width prescribed in the current design code.

KEY WORDS: Masonry arch, Transverse load distribution, Finite element analysis, Effective width.

1 INTRODUCTION

Although new masonry arch bridges are not generally constructed, they have been used extensively for the last 2000 years. Many masonry arch bridges were constructed by 'rule of thumb', and with ever increasing traffic loading there is a need for their reassessment in order to determine their true load capacity. Masonry arch bridges account for a significant proportion of global bridge stock. In Ireland, 36% of the bridge stock on national roads comprises masonry arches [1]. By international standards for strategic transport routes, this is high.

Currently, the modified MEXE method of analysis [2] is the most popular method of assessment of masonry arch bridges. This method has, however, proven to be inaccurate in many instances [3]. Analysis through computer modelling programs such as LimitState Ring and Archie M is becoming increasingly popular and these packages offer essentially two dimensional analysis with simplified transverse distribution rules.

Masonry arch bridges comprise many components that complicate their analysis. The principal element is the arch barrel, which reacts against large abutments and piers. The arch barrel supports spandrel walls, which retain backfill over the arch. The fill material comprises soils and gravels that are placed and compacted over the barrel and between the spandrel walls to provide a formation layer for the road pavement. The masonry bridge is completed with parapet walls to retain errant vehicles and the like. There is a number of specific terms used in the description of masonry arch bridges, which are illustrated in Figure 1.

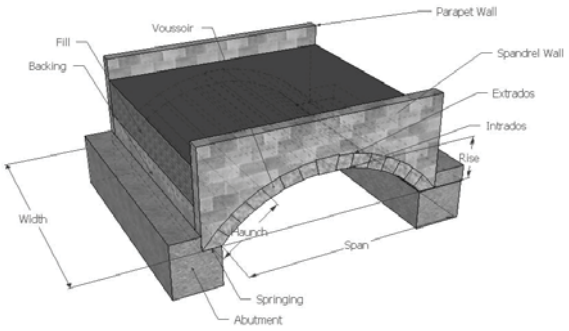


Figure 1. Masonry arch bridge features

Although numerous studies have been undertaken to analyse arch behaviour along the span, few explore how the arch distributes applied forces transversely. In practice, loads are not applied uniformly across the arch width and thus the distribution of loads needs consideration.

Skewed bridges have significant three dimensional characteristics. The current prescribed analysis for masonry arch bridges maintains that a skew arch transfers loads across the shortest span available. This induces large shear stresses on the obtuse corners, with the abutments providing rotational resistance to torsional moments.

The aim of this paper is to assess transverse load distribution in masonry arch bridges subject to point loads at different locations and to compare the findings with the current prescribed analysis method set out in BD21/01 [4]. In addition the load distribution within skewed arch bridges is assessed.

2 CURRENT ANALYSIS METHODS

Analytical methods for masonry arches can be split into three categories: maximum stress analysis, thrust line analysis and mechanism methods. Semi-empirical analysis methods have also been developed, utilising laboratory tests and field tests as a basis to derive assessment techniques [5].

2.1 Modified MEXE method

The MEXE method was first set out by the British military as a means to carry out rapid field assessments of arch bridges due to military loads during World War II. The method was developed from theoretical research supported by field and laboratory tests carried out by Pippard in 1936 [6]. The modified MEXE method is a semi-empirical analysis method that has evolved from this. The load carrying capacity of the bridge is calculated using empirical formulas before applying a series of modification factors to this capacity [7].

The arch is surveyed, and parameters such as span, rise at centre, rise at quarterpoints, ring thickness and fill depth are recorded. Parameters relating to the bridge profile, materials, and condition are also established. A nomogram of span and crown thickness is used to determine a provisional axle loading. This axle loading is then adjusted by a series of modification factors. These factors relate mainly to the bridge condition and material types. There is no factor dependent on the bridge width, and thus transverse distribution is not considered.

2.2 Computer applications

Analytical methods have given rise to the development of specialized computer programmes for the assessment of masonry arch bridges.

Heyman's equilibrium theory has been developed by Harvey and Smith in the form of the masonry arch computer analysis program Archie-M [8]. This software calculates the thrust zone for a given applied load. The passive pressure distribution, the load dispersal angle and the height of any backing can be input into the program. Archie-M allows for the application of the prescribed rules set out in BD21/01 [4] when considering the effect of transverse load distribution.

Limitstate Ring is a rigid block analysis computer package developed in conjunction with the International Union of Railways [9]. The software idealises a masonry bridge as a series of rigid blocks in order to carry out a computational upper bound limit analysis. Limitstate Ring requires a user specified fixed bridge width and does not account for the effects of spandrel walls. There is an option for the input of user defined simple transverse distribution rules.

The finite element method has been applied in varying complexities to the analysis of masonry arch bridges. The complexity of the model developed is related to the precision and nature of output needed. Complex modelling approaches are often beneficial. However, decreasing the dimensions of elements may not provide additional information to the designer.

Finite element analyses were carried out to investigate transverse loading effects by Fanning et al. [10]. Three dimensional nonlinear models were created of the Oberlin Bridge and the Jones Bridge in Ohio, USA, as well as the Chester Bridge, Pennsylvania, USA. These bridges had previously been tested to collapse [11] [12] [13]. The models divided the masonry arch bridge into three main components: the masonry, the fill and the pavement. The masonry was modelled using a homogeneous isotropic material with a failure criterion similar to that of concrete. The fill was modelled using a Drucker-Prager yield criterion, which uses parameters such as cohesion, angle of internal friction and dilatancy angle. One-dimensional friction elements were used between the fill and the masonry. Truck loads were placed on the model, and displacements as well as crack patterns were established.

2.3 Transverse behaviour analysis of masonry arches

BD21/01 of the Department of Transport Design Manual for Roads and Bridges [4] specifies an effective width of bridge to be used when analysing a masonry arch or a series of masonry arches under a point load or a wheel load (see Table 1 and Figure 2). This approach is based on dispersal under the load of two vertical to one horizontal through the fill and a further dispersal by transverse structural action of the arch. This method generates a uniform effective strip width for the full bridge span for the load under consideration.

Table 1. Effective width given in BD21/01 [4].

	BD21/01
Effective width	(Clause 6.22 & Figure 6.3) Effective width w $w = h + 1.5$ h **(varies)** - is the fill depth at the point under consideration

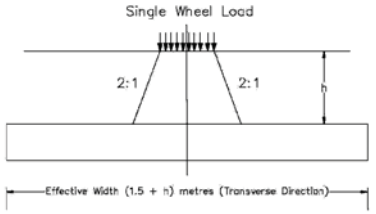


Figure 2. Effective width BD 21/01[4].

The formulas were derived based on testing carried out by Davy [14] and Chettoe and Henderson [15]. The formula for a single wheel load was determined by Davy, based on experimental test work on Alcester Bridge, Warwickshire. It is acknowledged in BD21/01 that the formula is conservative, as it is unclear whether the effective width may become smaller approaching failure loads. It is also noted, that "the true effective width would depend on a number of factors", and "the formula should be used as a conservative approximation until further work is carried out to investigate the transverse distribution of load effects" [4]. This effective width does not take bridge span or width into consideration. It also does not account for any increased distribution of the load away from the load application point.

Testing was carried out by Royles and Hendry [16] on 24 scale masonry arches. The arches varied in shape from near flat to semi-circular, and in span, with spans 1.0 m, 2.08 m and 2.48 m. The data gathered showed that the presence of spandrel walls increased the capacity of an arch by factors ranging from two to twelve times the capacity of the arch alone. It was concluded that an arch is a three dimensional

structure, and analysis of a 2-D strip of the vault is unreliable. Service load testing was carried out by Page [17] [18] on the Kimbolton Butts Bridge, the Shortwood Bridge and the Egremont Bridge in the UK. Page noted how displacements varied across the arch barrel transversely and that they were much lower at the spandrels than at the centreline. This shows that transverse bending occurred in all the test bridges. Page also emphasised the importance of measuring the horizontal displacements at the abutments.

3 FINITE ELEMENT MODEL

3.1 Preliminary model

A preliminary investigation of a masonry arch bridge was initially undertaken. The bridge was simplified to its principal member, the arch. A LUSAS thick shell model was created to estimate arch behaviour under various point loads. The arch barrel was divided into 31 voussoirs. Each voussoir was assigned typical isotropic material properties for a stone arch, with parameters input for Young's Modulus of Elasticity (E), Poisson's Ratio (υ) and Mass Density (ρ).

Results were obtained for six point load locations, which can be seen in Table 2 and Figure 3. Each point load was a square patch 300 mm x 300 mm, as specified in Annex D of BD21/01, and was of magnitude 100 kN. For this analysis fill was not accounted for; the point load was applied directly to the arch barrel, and load distribution through the arch was solely considered. Varying distributed loading was applied to the arch to simulate the weight of backfill to 0.5 m above the crown of the arch and the loading due to the self-weight of the bridge was also applied. This enabled the resultant thrust line due to the combination of the backfill, arch self-weight and the applied point load to be determined.

Table 2. Loadcases for 2D arch study

Loadcase	X (m)	Z (m)	Span	Width
1	1.25	-5.0	Eighth	Mid
2	2.5	-5.0	Quarter	Mid
3	5.0	-5.0	Mid	Mid
4	2.5	-2.5	Quarter	Quarter
5	5.0	-2.5	Mid	Quarter
6	2.5	-1.25	Quarter	Eighth

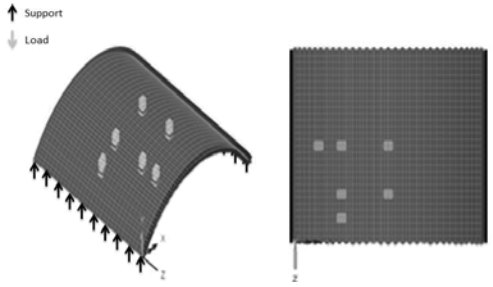


Figure 3. 2D arch model showing point load locations.

The arch skew was varied in order to determine skew effects on arch behaviour. Results were obtained for a straight arch (no skew) and for skews of 20°, 30° and 45°.

Axial stress, moment, and displacement results were obtained from the LUSAS model. The six loadcases were analysed when developing the three dimensional (3D) model in order to compare the results with the shell model. However, it was noted that Loadcase 1 and Loadcase 2 showed similar results, as did Loadcase 4 and Loadcase 6. It was decided to reduce to four loadcases for the majority of the 3D assessment. It was noted that the 20°, 30°, and 45° skew bridges displayed similar results for displacement, stress and thrust eccentricity, and for further analysis a 30° skew was solely considered.

3.2 Three dimensional model

A three dimensional (3D) finite element masonry arch bridge model was developed in stages (see Figure 4). The bridge was divided into four groups: arch, fill, abutments and spandrel walls. Results were recorded after each group was added to the model.

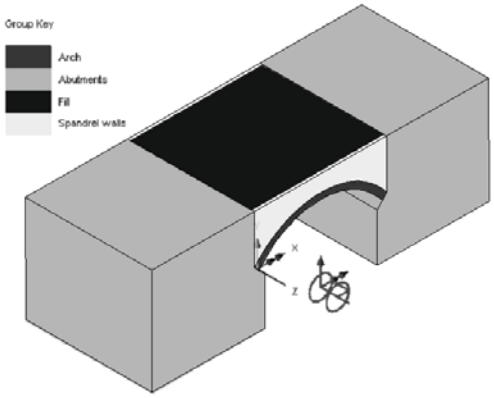


Figure 4. 3D masonry arch bridge model stages.

At Stage 1, the load was applied directly to the arch. From Stage 2 onwards, the load was applied to the top surface of the fill. The fill was supported by applying a horizontal restraint boundary condition for Stages 2 and 3, until the spandrel walls were added to the model in Stage 4.

3D isoparametric solid continuum elements of a linear interpolation order were used to create a solid volume model of the masonry arch bridge. A mesh refinement study was carried out after each stage of the model development. The arch comprised 8000 mesh elements, with 40 element divisions in the transverse direction, 50 in the longitudinal direction and four through the arch thickness. Tied slidelines were used between the volume interfaces to tie together dissimilar meshes. This allowed for a higher level of mesh refinement in the arch than the fill, and in the fill than the abutments. A "Sliding" slideline was assigned between the fill and the spandrel walls. Contact was maintained between the fill and the spandrels but sliding was allowed between the elements.

The stone and mortar joints were macro-modelled in the three dimensional volumetric model. This treated the masonry as a homogenous material, with material properties in between the values for the stone voussoirs and the lime mortar. The masonry and fill were assigned Young's Moduli of 7000 MPa and 3200 MPa and Poisson's Ratios of 0.3 amd 0.2 respectively. Material properties for the fill and the abutments were taken as consistent. The value of Young's Modulus of Elasticity used in computer analysis for the fill material in masonry arch bridges varies significantly in the literature. Fill material property values were selected in accordance with modelling carried out by Milani and Lorenco [19].

Fixed boundary conditions were assigned to the underside of the abutments and an iterative approach was taken to determine an appropriate abutment length of 8m.

4 MODEL VALIDATION

The maximum tensile stresses were checked to fall below an adopted maximum tensile stress σ_t = 0.5 N/mm2, indicating that the masonry stresses were within the linear range, and a nonlinear analysis was not needed [20]. The FE modelling was also validated against previous test data available in the literature for Griffith Bridge in Dublin.

Griffith Bridge is a single 9.46 m span three-centred masonry arch bridge, 7.84 m in width with a rise of 2.7 m. It comprises a 0.446 m thick ashlar limestone arch ring with granite fascia stones. Non-destructive testing was carried out on this bridge by Fanning and Boothby [21].

The bridge was loaded with an empty truck and a full truck in separate loadcases. Displacements were recorded at the centreline, haunch (the lower section of the arch barrel towards the springing), crown and the edge of the bridge. A three dimensional nonlinear finite element model was developed and the displacement results were compared to the test results. Boundary conditions were applied to the model which restrained the fill in the span direction at both ends of the bridge. The underside of the fill was restrained vertically and the base of the arch barrel was restrained vertically and in the span direction. The bases of the spandrel walls were restrained in the vertical and transverse directions. An axis of symmetry boundary condition was applied to the model, as the bridge geometry and the loading are both symmetrical about the longitudinal axis. A contact surface, which was modelled between the masonry and the fill, was assigned a coefficient of friction value of 0.4 [21].

A LUSAS model of Griffith Bridge was created, and compared to the Boothby and Fanning model. The boundary conditions, excluding the axis of symmetry boundary condition, were modelled as set out by Boothby and Fanning. The linear set of material properties from the Boothby and Fanning model was also applied to the LUSAS model. Friction slidelines require a nonlinear analysis in LUSAS, and were not incorporated into the model.

The results presented for displacements (see Table 3) and deformed mesh (see Figure 5) indicated that there was good agreement between the Fanning and Boothby model and the LUSAS model developed in this study.

Table 3. Displacement results for Fanning and Boothby model and LUSAS FE model.

	Haunch Peak Displacements		
	Test (μm)	F&B (μm)	DUNNE (μm)
Truck Empty	172	237	237
Truck Full	331	387	366

The study carried out by Fanning and Boothby incorporated collapse loads on the bridge, and as such, nonlinear parameters were needed. Increasing the complexity of the LUSAS FE model for this study is not justified, as it would take an excessive length of time to run each FE model with little increase of accuracy, as the stresses remain in the linear range.

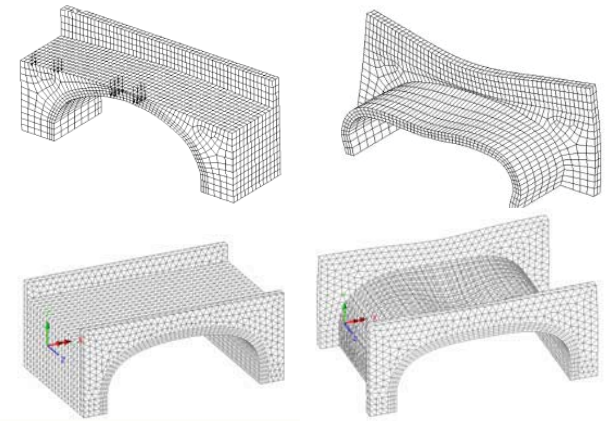


Figure 5. Above left, Boothby and Fanning Griffith Bridge FE model. Above right, deflected arch shape with axle at crown [21]. Below left, LUSAS Griffith Bridge FE model. Below right, deflected arch shape with axle at crown.

5 PARAMETRIC STUDY

The verified LUSAS 3D masonry arch bridge volume model was adapted to generate a variety of masonry arch bridges. Loads were applied to the surface of the bridge fill and the importance of each parameter to the transverse distribution was established through statistical comparison. Parameters that were studied include:

- Arch shape. Segmental, three-centred and semi-circular arch bridges were studied.
- Span/rise. Span/rise ratios ranging from 2 to 5 were studied.
- Arch ring thickness. The thickness of the arch was varied, ranging from 400 mm to 600 mm.
- Masonry stiffness. The stiffness of the arch and spandrel walls was varied from 10000 N/mm^2 to 15000 N/ mm^2.
- Fill stiffness. The stiffness of the fill material was varied, ranging from 350 N/ mm^2 to 5000 N/ mm^2.
- Fill depth to crown. The fill depth between the arch extrados and the road surface at the crown was varied, ranging from 15 mm to 1000 mm.
- Bridge skew. Nine bridges with a skew angle of 30° were studied as well as 63 straight bridges.
- Abutment stiffness. The stiffness of the material assigned to the abutments was altered ranging from 350 N/ mm^2 to 5000 N/ mm^2.
- Stone backing. Masonry backing was added to some bridge models, up as far as the arch quarterpoint and was assigned the same material stiffness as the arch. The fill material extends from the top of the backing to the road surface.
- Spandrel walls. For most of the bridges, the spandrel walls (SW) included 750 mm parapet walls above the fill. For some bridges the spandrel and parapet walls were removed in order to determine their effect on transverse load distribution.

Four loadcases were considered for the three dimensional bridge models (see Figure 6). Each loadcase comprised a 300

mm x 300 mm square patch of magnitude 100 kN applied to the surface of the fill.

The full bridge set contains bridges with a variety of different parameters. Statistical analysis was carried out on the effective widths of the bridges, in order to determine which parameters had the most influence over the effective width. Parameters with the largest influence over the effective widths were then used in the development of a formula to calculate the effective width of any bridge subject to a point load.

The results are statistically verified using IBM SPSS statistics software version 20 [22]. G*Power software version 3.1.6 [23] was used in conjunction with SPSS to determine the power of significant results obtained.

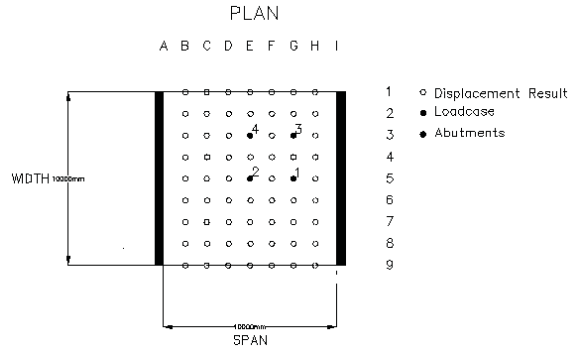


Figure 6. Arch loading and displacement result arrangement.

Displacement results were obtained at the intrados of the arch at the locations shown in Figure 6. The displacement results were used to obtain effective bridge widths for each bridge. This was set as the width of the bridge that gave an area under the displacement curve of 90% of the total area under the curve. The effective widths were calculated at seven transverse sections along the bridge span (see Figure 7).

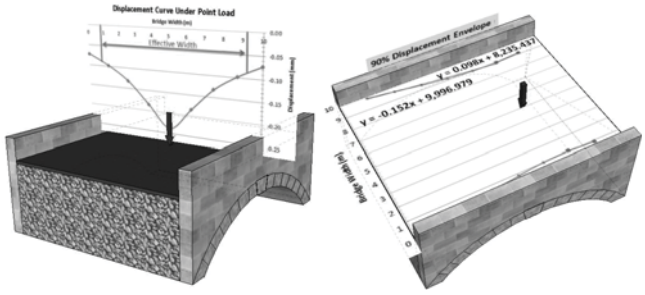


Figure 7. Bridge effective width envelope.

5.1 Skew bridge data

The literature review suggested a possible link between abutment material stiffness and bridge response for skew bridges. This concept was examined by comparing three bridge shapes, segmental, three-centred and semi-circular, which only differed in abutment material stiffness [24] [25].

6 RESULTS

The most significant factors influencing the effective widths for the four loadcases were determined in the statistical analysis (see Table 4).

Table 4. Factors influencing effective widths.

Loadcase 1	Loadcase 2	Loadcase 3	Loadcase 4
Spandrel Wall Presence	Spandrel Wall Presence	Fill and Abutment Stiffness	Fill Depth
Fill and Abutment Stiffness	Fill and Abutment Stiffness	Fill Depth	Fill and Abutment Stiffness
Fill Depth	Ring Thickness	Arch Shape	Ring Thickness
Ring Thickness	Fill Depth	Ring Thickness	

The effective width currently used in BD21/01 [4] is given in Equation 1.

$$EW = 1.5 + h \tag{1}$$

where:
h = depth of the fill in metres at the location of the point load.

On the basis of the results obtained, a formula to calculate the effective width of a bridge subject to a point load along the bridge longitudinal centreline is proposed here. It was found during the statistical analysis that the stiffness of the fill, the thickness of the arch ring, and the spandrel walls contribute to the effective width for these loadcases. When spandrel walls were excluded from the model, the effective widths increased. A conservative approach was taken, and the effect of spandrel walls was omitted from the proposed formula. A formula for the calculation of effective width was iteratively deduced using Excel. This proposed formula to calculate the effective width of a masonry arch bridge is shown in Equation 2.

$$EW = 0.8s + 0.3d + r \tag{2}$$

where:
s = fill stiffness factor, determined from Equation 3,
d = fill depth factor, determined from Equation 4,
r = thickness of the arch ring in metres.

$$s = 9.4a^{-0.068} \tag{3}$$

where:
a = fill stiffness in MPa.

$$d = 6.34b^{0.368} \tag{4}$$

where:
b = fill depth in m.

It is proposed that the effective widths for point loads away from the longitudinal centreline, the smaller effective width obtained from Equation 2 and Equation 5 should be used.

$$EW = \frac{0.8s+0.3d+r}{2} + 0.8c \tag{5}$$

where:
c = the closest offset of the load from the edge of the bridge.

The effective widths obtained from a number of the LUSAS bridge models, the effective widths from the BD21/01 formula and the effective widths determined using the proposed effective width formula are compared in Figure 8. It is noted

that the formula in BD21/01 was intended to produce conservative results [4].

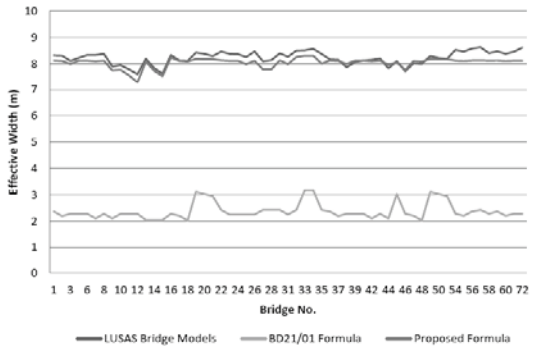


Figure 8: Bridge effective width comparison, Loadcase 1

6.1 Skew bridge results

The abutment stiffnesses used in the study were varied from 50 MPa to 2000 MPa. The displacement envelope results for segmental bridges for Loadcase 2 can be seen in Figure 9.

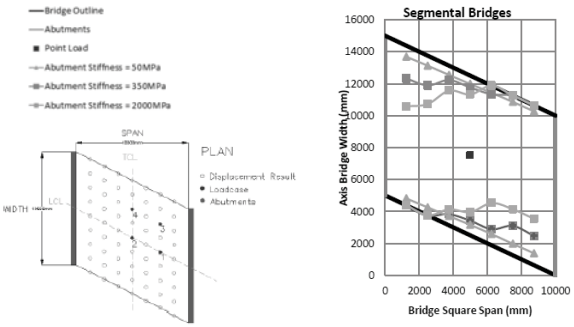


Figure 9. Plan view of skew bridges showing 90% displacement envelopes for Loadcase 2

7 DISCUSSION AND CONCLUSION

It was found that the width of bridge affected by a point load was substantially larger than that set out in BD21/01 [4]. The depth of fill, stiffness of fill, and ring thickness influenced the effective widths determined. Increasing fill depth and increasing ring thickness increased the effective width, while increasing fill stiffness reduced the effective width. In BD21/01, the fill depth is the only parameter taken into consideration when determining the effective width.

It was found that a point load away from the bridge longitudinal centreline produced a smaller effective width than a point load along the longitudinal centreline. In BD21/01, no allowance is made for the location of the point load on the bridge effective width.

7.1 Skew bridge

The current prescribed analysis for masonry arch bridges maintains that a skew arch transfers loads across the shortest span available [24]. For the skew bridges studied, the results show a link between the stiffness of the bridge abutments and the response of a skew bridge subject to a point load. The displacement envelopes for Loadcase 2 were found to follow the line of the skew arch when the abutment stiffness was reduced, and follow the line of the straight span when the stiffness was increased.

REFERENCES

[1] Duffy, L., 2004. 'Development of Eirspan: Ireland's bridge management system'. *Proceedings of the ICE: Bridge Engineering*, 157(3), pp. 139-146.

[2] Department of Transport, 1997. BA16/97 *The Assessment of Highway Bridges and Structures*, Design Manual for Roads and Bridges, Volume 3, Section 4, Part 4, London: HMSO.

[3] Melbourne, C., Wang, J. and Gilbert, M.S.C., 2009. *Review of Assessment Methods for Masonry Arch Bridges*. CSS Masonry Arch Research Project, Final Draft Report.

[4] Department of Transport, 2001. BD21/01 *The Assessment of Highway Bridges and Structures*, Design Manual for Roads and Bridges, Volume 3, Section 4, Part 3,London: HMSO.

[5] Sustainable Bridges D4.7, 2007. *Methods of Analysis of Damaged Masonry Arch Bridges* - Background Document D4.7.3: Sustainable Bridges – Assessment for Future Traffic Demands and Longer Lives.

[6] Wang, J. and Melbourne, C., 2010. 'Mechanics of MEXE method for masonry arch bridge assessment'. *ICE Engineering and Computational Mechanics*, III (162), pp. 187-202.

[7] Orban, Z., 2007. 'Assessment, reliability and maintenance of masonry arch railway bridges in Europe'. *Arch '07: Fifth International Conference on Arch Bridges*, Madeira, pp. 3-12.

[8] Obvis Ltd, 2012. *Archie-M: Obvis*. [Online] Available at: http://www.obvis.com/archiem/ [Accessed 7 March 2013].

[9] Limitstate Ltd, 2011. *Limitstate Ring Theory and Modelling Guide*.

[10] Fanning, P., Boothby, T. and Roberts, B., 2000. 'Longitudinal and transverse effects in masonry arch assessment'. *Construction and Building Materials*, 15(1), pp. 51-60.

[11] Boothby, T., Domalik, D. and Dalal, V., 1998a. 'Service load response of masonry arch bridges'. *Journal of Structural Engineering*, I (124), pp. 17-23.

[12] Boothby, T. and Domalik, D., 1994. *Field testing of random stone masonry arch bridges*, report no. 270 in Chester County, Pennsylvania, Pennsylvania: Research Report No. PTI 9513.

[13] Boothby, T., Domalik, D. and Elgin, C., 1998b. *Load-rating of masonry arch bridges and culverts*, Ohio: Ohio Department of Transportation.

[14] Davy, N., 1953. *Tests on Road Bridges*. National Building Studies Research Paper No. 16. HMSO.

[15] Chettoe, C. and Henderson, W., 1957. 'Masonry Arch Bridges. A Study'. *Proceedings of the ICE*, 7, pp. 723-744.

[16] Royles, R. and Hendry, A., 1991. 'Model Tests on Masonry Arch Bridges'. *Proceedings of the ICE*, 91(2) pp. 299-321.

[17] Page, J., 1995a. 'Load tests for assessment of in-service arch bridges'. *Proceedings of the First International Conference on Arch Bridges*, Bolton, 3-6 September, Bolton: Thomas Telford, pp. 299-308.

[18] Page, J., 1995b. 'Load Tests to Collapse on Masonry Arch Bridges'. *Proceedings of the First International Conference on Arch Bridges*, Bolton, 3-6 September, Bolton: Thomas Telford, pp. 289-298.

[19] Milani, G. and Lourenco, P., 2012. '3D non-linear behaviour of masonry arch bridges'. *Computers & Structures*, Volume 110-111, pp. 133-150.

[20] Lourenco, P.B., 2001. 'Analysis of historical constructions: From thrust-lines to advanced simulations'. Proceedings of the Third International Seminar on Historical Constructions, Guimaraes, University of Minho, pp. 91-116.

[21] Fanning, P.J. and Boothby, T.E., 2001. 'Three-dimensional modelling and full-scale testing of stone arch bridges'. *Computers and Structures*, 79(29), pp. 2645-2662.

[22] IBM, 2013. *Analytics: Software*: IBM. [Online] Available at: http://www.01.ibm.com/software/analytics/spss/ [Accessed 16 April 2013].

[23] Erdfelder, E., Faul, F. and Buchner, A., 1996. 'GPOWER: A general power analysis program.'. *Instruments & Computers*, I (28), pp. 1-11.

[24] McKibbins, L., Melbourne, C., Sawar, N. and Gallard, C.S., 'CIRIA C656', 2006. *Masonry arch bridges: Condition appraisal and remedial treatment*, London: CIRIA.

[25] Martin-Caro, J. and Morales, G., 2007. 'Numerical analysis of a load test on a skewed masonry arch'. Arch '07: Fifth International Conference on Arch Bridges, Madeira, pp. 569-576.

Irish Timber – Characterisation, Potential and Innovation

Annette Harte[1], Daniel McPolin[2] , Karol Sikora[1], Caoimhe O'Neill[2], Conan O'Ceallaigh[1]
[1]College of Engineering & Informatics, National University of Ireland, Galway, University Road, Galway, Ireland
[2]School of Planning, Architecture and Civil Engineering, Queen's University Belfast, University Road, Belfast BT7 1NN, UK
email: annette.harte@nuigalway.ie, d.mcpolin@qub.ac.uk, karol.sikora@nuigalway.ie, coneill86@qub.ac.uk, c.oceallaigh1@nuigalway.ie

ABSTRACT:
In order to increase the utilisation of Irish timber in construction and novel engineered wood products, the mechanical and physical properties of the material must be established. For timber products used for structural applications, the fundamental properties are the modulus of elasticity, bending strength, density and dimensional stability as these define the structural grade of the material. In order to develop engineering design models for applications such as reinforced timber, knowledge of the nonlinear stress-strain behaviour in compression is also required.
The paper presents the programme and results of an ongoing research project 'Innovation in Irish Timber Usage' which focuses on the characterisation of Sitka spruce as it is the most widely grown species in Ireland. In the past, a number of studies have been conducted to determine the properties of Irish-grown Sitka spruce. Nevertheless, due to the changes that have taken place in silvicultural practices since the publication of these studies, there is a need to determine how these properties have changed. This paper presents the data gathered from historical studies together with the results of an extensive test programme undertaken to characterise the properties of the present resource.
Moreover, the paper examines the potential use of Irish grown Sitka spruce in novel timber products. Construction applications, such as fibre-reinforced polymer reinforced timber elements and connections, and cross-laminated timber are investigated.

KEY WORDS: Sitka spruce, timber properties, reinforced timber, Cross-laminated timber

1 INTRODUCTION

Due to the increasing focus on the use of sustainable construction materials to meet environmental targets related to efficient energy use and emissions, a significant opportunity exists for the Irish wood products sector. In 2012, the Irish forestry and forest products sector generated €2.2 billion in annual output, representing 1.3% GDP, and employed approximately 12,000 people [1]. Moreover, there exists a substantial potential to expand production. According to COFORD [2] half of the forest estate is less than 25 years old and further expansion of forest cover is planned by policymakers. Forest products to a value of €303 million were exported: including €73 million worth of sawn softwood and €179 million worth of wood-based panels. In general, 89% of the wood-based panels were exported [1]. The supply of roundwood from Irish forests is projected to increase from 3903 million m^3 in 2011 to 7110 million m^3 in 2028. These figures show the potential of Irish forests to provide increased and sustainable supplies of wood products [3]. Increased sales of existing products and the development of new markets at home and abroad for new added-value wood products will lead to job creation across the sector.

In order to increase the utilisation of Irish timber in construction, the mechanical and physical properties of the material must be established. For timber products used for structural applications, the fundamental properties are the bending modulus of elasticity (MOE), the modulus of rupture (MOR), the density and the dimensional stability as these define the structural grade of the material. In order to develop engineering design models for reinforced timber, knowledge of the nonlinear stress-strain behaviour in compression is also required.

As part of the project 'Innovation in Irish Timber Usage', funded by the Department of Agriculture, Food and Marine of the Republic of Ireland under FIRM/RSF/COFORD scheme, all of the available historical data on the properties of Irish Sitka spruce, from published and unpublished sources, is being collated. Moreover, testing of a large number of samples is being carried out to establish the mechanical and physical properties of the current resource. Furthermore, in order to investigate the potential for new add-value timber construction products, the two key research areas are addressed, namely, Fibre-Reinforced Polymer (FRP) reinforced timber and Cross-Laminated Timber (CLT).

2 CHARACTERISATION OF IRISH TIMBER

2.1 Introduction

The focus of this paper will be on timber from Sitka spruce as it is the most widely grown species in Ireland. Irish-grown Sitka spruce is characterised as a fast growing, low density species due to the rapid growth condition in Ireland and short rotation length. As a result of these growth conditions, the most common structural grade achieved by Irish-grown Sitka spruce is C16 grade.

In the past, a number of studies have been conducted on the properties of Irish-grown Sitka spruce [4-16]. This species is native to a narrow belt of the Pacific North West coast of

North America, along Alaska in the north, down through British Columbia, Washington and Oregon to California. Due to similarities in climate between this region and Ireland, it was first introduced to Ireland in 1831. The wide ranging site types suited to growing Sitka spruce vary from very fertile mineral to impoverished peaty soils [17].

A large study (the SIRT project) on Scottish Sitka spruce was undertaken in Scotland in recent years [18]. This has resulted in the publication of a report by the Forestry Commission entitled 'Wood properties and uses of Sitka spruce in Britain' [19]. This report is important for Ireland as the growing conditions in Scotland are similar to those in Ireland and the likelihood is that the physical and mechanical properties of the timber produced in both countries will be comparable.

In the following sections, properties of Irish Sitka spruce from selected studies are presented.

2.2 Mechanical properties

Investigations and grading results carried out by sawmills confirm that Irish Sitka spruce meets predominantly the requirements of strength class of C16. Table 1 presents the main strength requirements for C16 according to EN 338 [20]

Table 1. EN 338 [20] main characteristic values for C16.

Bending strength ($f_{m,k}$)	Compressive strength parallel to grain ($f_{c,0,k}$)	Mean modulus of elasticity parallel ($E_{0,mean}$)	Mean density (ρ_{mean})
16 N/mm^2	17 N/mm^2	8 kN/mm^2	370 kg/m^3

Picardo [4] undertook a large-scale testing programme to evaluate the influence of a number of classifying variables such as yield class (mean of cubic metres of solid stem wood added to an area of woodland per hectare per year [m^3/ha/yr]) , section size and forest on the strength and stiffness of Irish Sitka spruce. From tests on 1487 planks, he found that only section size had a practical influence on the MOR.

Ní Dhubháin et al. [5] examined the influence of compression wood on the bending MOE and MOR properties. This study had a relatively small sample size of 100 specimens of single cross-sectional size. They found that increased percentages of compression wood resulted in a decrease in MOE but appeared to have no effect on MOR.

Picardo [6] conducted another large study involving the machine grading of about 5000 pieces of timber into different strength classes. This study found that the yields for C14 and C16 were very high and the thickness has a significant impact on the yield. He did not undertake destructive mechanical tests.

Lucey et al. [7] investigated the utilisation of Irish grown Sitka Spruce timber (from forests in County Galway) in I-joists. It was reported that the stiffness of the I-joist has a high correlation to the stiffness of both tension and compression flanges. There was only a low level correlation between the strength of the web material and the strength of I-joist. Therefore, extensive testing programme was carried out on specimens used for the flanges. The MOR of the flange materials, presented in Table 2, was measured as described in EN 408 [21]. The average MOR results ranged from 22.2 N/mm^2 to 25.4 N/mm^2 for all cross-sectional sizes. However, the dimensions had an influence on the standard deviation of and 5-percentile of the MOR, which was lower for the smaller cross-sections.

Table 2. MOR parallel to grain results for square beams [7].

Specimen type & size	No. of specimens	Mean MOR [N/mm^2]	S. D. [N/mm^2]	5-percen. [N/mm^2]
compression flanges: 44 x 44 mm^2	31	22.2	4.6	13.5
tension flanges: 44 x 44 mm^2	31	22.3	3.9	15.5
compression flanges: 65 x 65 mm^2	11	24.8	2.0	21.9
tension flanges: 65 x 65 mm^2	11	24.4	4.0	18.1
compression flanges: 65 x 65 mm^2	10	25.5	2.1	22.9
tension flanges: 65 x 65 mm^2	10	25.4	2.8	20.9

The MOE parallel to grain was also measured in specimens stressed in both tension and compression. The results differed depending on cross-section size, and reached almost 8 MPa for the bigger sizes and 7 MPa for the smaller ones. These results for MOE testing are shown in Table 3.

Table 3. MOE parallel to grain results for square beams [7].

Specimen type & size	No. of specimens	Mean MOE [N/mm^2]	S. D. [N/mm^2]	5-percen. [N/mm^2]
compression flanges: 44 x 44 mm^2	29	7027	1026	5148
tension flanges: 44 x 44 mm^2	29	7106	945	5610
compression flanges: 65 x 65 mm^2	11	7533	627	6770
tension flanges: 65 x 65 mm^2	11	7531	1319	5573
compression flanges: 65 x 65 mm^2	10	7997	606	7180
tension flanges: 65 x 65 mm^2	10	7999	885	6696

In addition to bending properties, Lucey et al. [7] examined compression parallel to grain and tension strengths for various

sizes of samples using Irish Sitka spruce. The results of these mechanical properties are summarised in: Table 4 – compression strength parallel to grain and Table 5 – Tension strength.

Table 4. Compressive strength parallel to grain results [7].

Specimen size [mm x mm x mm]	No. of specimens	Compressive Strength [N/mm^2]	S. D. [N/mm^2]	5-percen. [N/mm^2]
44 x 19 x 19	31	24.9	4.8	17.2
65 x 40 x 39	11	24.4	1.8	22.4

Table 5. Tensile strength parallel to grain results [7].

Specimen size [mm x mm x mm]	No. of specimens	Mean tensile strength [N/mm^2]	S. D. [N/mm^2]	5-percen. [N/mm^2]
44 x 19 x 10	31	23.9	4.3	16.3
65 x 40 x 20	11	24.6	2.9	20.2
65 x 40 x 20	10	25.1	2.1	22.2

Raftery and Harte [8] undertook a comprehensive study in order to assess the relationship between mechanical properties and physical characteristics in the longitudinal direction on clear and in-grade samples. Parameters, which were studied, included density, knot area ratio, MOE and ultimate strength. The results of this investigation might be essential in terms on the future development, design and optimisation of engineered wood products from Irish Sitka Spruce. It was concluded that MOE was the most highly correlated parameter to the tensile strength for both clear and in-grade specimens. Furthermore, the knot area ratio had a considerable influence on the strength of the timber both in compression and tension. Density was more highly correlated to ultimate compressive strength than ultimate tensile strength in clear wood specimens. In addition, the authors reported that MOE in tension had a poor correlation to the density of clear wood and was also poorly correlated to the knot area ratio and the density of in-grade specimens.

Moreover, testing of Irish timber has been undertaken in Irish third level institutions as part of the research for MSc and PhD theses. Not all of this data has been published in the available literature. Nevertheless, some of these results are shown in the following paragraphs.

The quality of Irish Sitka spruce was extensively investigated by Evertsen [9] using destructive and non-destructive methods. In order to determine the MOE and MOR, static four point bending tests were carried out on over 200 planed planks of different sizes taken from woodlands of yield classes 16 and 20. The moisture content of the samples during test was generally at 15 ± 2%. The mean, maximum, and minimum MOE and MOE results, including standard deviation, for different yield classes are presented in Tables 6 and 7.

Table 6. MOE parallel to grain from destructive tests [9].

Yield class	No. of specimens	Mean MOE [N/mm^2]	S. D. [N/mm^2]	Min. [N/mm^2]	Max. [N/mm^2]
16	64	8623	2757	1044	18424
20	116	9291	2511	3707	15772
16&20	180	9053	2601	1044	15772

Table 7. MOR parallel to grain from destructive tests [9].

Yield class	No. of specimens	Mean MOR [N/mm^2]	S. D. [N/mm^2]	Min. [N/mm^2]	Max. [N/mm^2]
16	64	24.4	9.4	0.4	44.5
20	116	26.3	7.5	7.2	47.8
16&20	180	25.6	8.2	0.4	47.8

For the non-destructive determination of the mechanical strength properties, an ultrasonic testing method was used by Evertsen [9]. This technique was developed by Bucur [10, 11], who had found that the MOE for small clear specimens had a high correlation with the ultrasound propagation speed in increment core sized samples. 300 small clear specimens were tested including 240 of yield class 16 and 60 of yield class 20. The obtained average MOE values were 8639 N/mm^2 and 7677 N/mm^2 for the first and second batch, respectively, and the average MOR values were 73.8 N/mm^2 and 67.2 N/mm^2, respectively.

Subsequently, tests results published by Patrick [12] confirmed that Sitka spruce has a brittle mode of failure in axial tension influenced by larger knot occurrence. The characteristic in-grade strength of 14.4 N/mm^2 was obtained in comparison to mean in-grade strength of 27.1 N/mm^2. These values were approximately half of the characteristic and mean strengths for clear timber, respectively. On the other hand, the mean and characteristic compressive strengths showed less variability reaching 30.6 N/mm^2 and 21.0 N/mm^2, respectively, for in-grade samples. The value of MOE in compression of 9125 N/mm^2 was found.

For the purpose of the studies carried out by Bourke [13, 14] a substantial number of pieces were selected in order to represent a typical forestry region and divided into three batches. Bending MOE tests were carried out in accordance to EN 408 [21] and the results are shown in Table 8.

Table 8. Mean MOE results [13,14].

Batch ID	No. of specimens	Mean MOE [N/mm^2]	S. D. [N/mm^2]
A	85	9367	1492
B	85	7475	1335
C	64	9036	-

In addition to these studies, Treacy et al. [15, 16] examined the influence of density and microfibril angle on the bending MOE and MOR of clear wood specimens from Sitka spruce of four different provenances. This study was confined to small clear samples and only 96 samples were subjected to bending tests. A linear relationship, the same for all examined

provenances, was found between microfibril angle and strength.

2.3 Physical properities

Evertsen [9] undertook an extensive testing programme to determine the physical properties of Irish Sitka spruce. Densities were examined by different testing procedures, including oven drying, infra-density and microdensitometry (optical density). The mean density (oven dry) of 273 specimens was 370 kg/m^3 with standard deviation of 46.2 kg/m^3. The average of basic density (wood dry mass over wood fresh volume) of 480 samples was 366 kg/m^3. X-ray microdensitometry was used to determine the density of specimens cut at different radial distances from the core. Specimens were conditioned to a moisture content of 15 %, prior to testing. These results for microdensitometry are summarised in Table 9.

Table 9. Microdensitometry results [9].

Wood type	Mean [kg/m^3]	Max. [kg/m^3]	Min. [kg/m^3]
Juvenile wood	472	864	306
Adult wood	451	812	259
Yield class 16	462	838	283
Yield class 20	424	781	242

Other timber properties determined by Evertsen [9] include values of twists and shrinkage. Mean values of twist and shrinkage for samples of yield classes 16 and 20, are shown in Tables 10 and 11, respectively.

Table 10. Twist results [9].

Yield classes	Samples no.	Mean twist [mm/3m]	S. D. [mm/3m]
16	80	6.38	4.81
20	159	7.17	4.49
16&20	239	6.90	4.60

Table 11. Dimensional shrinkage values [9].

Yield class	No. of specimens	Length [%]		Width [%]		Depth [%]	
		Mean	S.D.	Mean	S.D.	Mean	S.D.
16	78	0.055	0.037	2.17	0.76	1.88	0.62
20	157	0.041	0.030	1.52	0.75	1.37	0.52
16&20	235	0.045	0.033	1.73	0.81	1.54	0.60

Mean values of shrinkage for 960 specimens of yield class 20 were 4.21% with standard deviation of 0.94% for the tangential direction and 2.15% with standard deviation of 0.69% for the radial direction.

Bourke [13, 14] investigated distortion in timber from fast-grown Irish Sitka spruce, dried to 12% moisture content. The results demonstrated that the dominant mode of distortion was twist, which results in significant reduction of load bearing capacity. It was found that almost all the planks were within specification for both bow and crook, even for stricter limits for special structural (SS) material. An analysis of the location in the logs from which each board was sawn shows significant variation with respect to radial position. A strong negative correlation was demonstrated between distance from the pith and the degree of twist that developed during drying.

Currently, as a part of the project 'Innovation in Irish Timber Usage', the MOE and MOR are being determined from flexural testing. Physical properties including moisture content and density of each specimen are also being verified. These tests are being carried out in order to establish the variability in the mechanical properties including an assessment of the in-board and between board variability in the MOE, and to investigate the relationship between board MOE, density and the timber origin.

3 POTENTIAL & INNOVATION

3.1 Introduction

The capacity of lower grade timber can be enhanced by its utilisation in novel engineered wood products. The properties of timber elements can be greatly improved through the reinforcement by various materials. This strategy has been successfully implemented within the construction industry and has grown in recent years. The methodologies, with large potential for Irish timber, are presented in the following paragraphs.

3.2 FRP Reinforced Timber

Fibre reinforced polymer (FRP) is a composite consisting of reinforcing fibres bound together in a polymer matrix. The most common reinforcing fibre materials are glass, carbon and aramid. These FRP materials are commonly used in the aerospace, automotive and marine sectors due to their high strength to weight ratio [22]. Timber has been reinforced using FRP material in various configurations such as plates or near surface mounted rods. Although FRP has been largely used for retrofitting and repairing old timber structures there is potential for the development of design codes to incorporate the use of FRP material into new composite timber engineering design.

Along with more commonly used FRP materials, increasing focus on environmental issues has promoted the use of natural fibres within FRP materials. Basalt fibre reinforced polymer (BFRP) is a lesser known fibre which has the potential to rival and surpass more commonly used fibres. BFRP is formed similarly to many other reinforcing fibres. The basalt rock is pre-treated and melted and the filaments are created as the molten rock passes through hundreds of small orifices. Lopresto et al. [23] compared basalt and glass fibre reinforcement. The results showed a high tensile modulus, compressive strength and bending strength for BFRP material. The BFRP reinforcement also showed a 35 - 42 % higher elastic modulus when compared to that of glass fibre reinforced polymer (GFRP) reinforcement. This material shows promising results both structurally when comparing material properties and economically when looking at a cost comparison with more expensive fibres such as carbon and aramid fibres.

Many researchers have shown that the addition of FRP reinforcement to solid timber beams results in an increase in strength and stiffness [24, 25]. These enhancements are also experienced in glued laminated beams. Glulam beams reinforced with modest percentage reinforcement ratios (0.4

% - 2.9 %) of FRP material have been shown to demonstrate superior strength, stiffness and ultimate moment capacity when compared to glulam beams in their unreinforced state [26, 27]. Hansson and Kristoffer [27], observed an increase in bending stiffness of 85 % with a percentage reinforced area of 2 % using carbon fibre reinforced polymer (CFRP) reinforcement plates. Raftery et al. [29], examined the effect of GFRP rods on the structural properties of Irish-grown Sitka spruce glued laminated beams. With a modest percentage reinforcement of 1.4 %, a mean stiffness enhancement of 13.9 % and a mean improvement in the ultimate moment capacity of 68 % was achieved when compared to beams in their unreinforced state. Kelly [30] examined the effect of BFRP rod reinforcement on low grade timber beams. The results indicated an increase in bending stiffness of 12 %, with a percentage reinforcement of 1.2 %, when compared to the timber beams in their unreinforced state. These results show great potential for such a low percentage reinforcement.

Much of the studies undertaken to date in the field of reinforced timber have highlighted the positive effect of the reinforcement on the short-term behaviour in bending. I. The research being carried out as part of the project 'Innovation in Irish Timber Usage' aims to determine the long-term performance of such reinforced timber beams with respect to load duration and variable climate and to develop appropriate modification factors for design purposes.

3.3 Reinforced Timber joints

In timber engineering the critical elements in the design of a structure are generally the joints. The most prevalent type of joints found in timber structures are pinned joints. Moment connections, however, are more versatile but these are less common as they are perceived to be more expensive. Moment connections can be achieved by using bolted plates, dowels positioned in a circular arrangement or glued-in rods [31, 32].

Glued-in rod connections, as shown in Figure 1, can be extremely efficient and possess many desirable attributes in terms of manufacture, performance, aesthetics and cost compared to the cumbersome conventional steel moment connections that are often encountered in timber construction. Not only do connections with glued-in rods look better than conventional connections, they also have enhanced fire protection as the rods which transfer moment are embedded inside, and are therefore protected by, the timber.

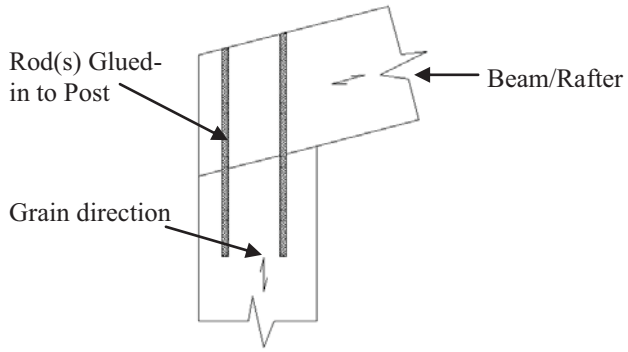


Figure 1. Sketch of Glued-in Rod Connection

With regards to new-build construction, Gehri [33] identified five areas where glued-in rods may be used for connections: frame corner, beam-post connection, beam-beam joint, supports and hinged joints.

Over the past two decades there have been many national and international research projects commissioned on the use of glued-in rods in timber joints e.g. GIROD, LICONS [34] and Bainbridge and Mettem [35]. In spite of this, no universal standard exists for their design. There had been an informative annex in prBS ENV 1995-2 [36] which provided limited coverage of the design of glued-in rods using steel bars however this document was replaced by BS EN 1995-2:2004 [37] and no guidance is included in the current document. The three main elements to be considered when designing glued-in rod connections are: the timber, rod and adhesive. The most significant challenge in the development of a standard design method is the many varying approaches to defining these joint properties as each of these elements can be expanded further, thus making the definition of design rules more complicated.

The majority of research done in this area to date comprises steel rods glued-in to glued laminated (glulam) elements with lamellae of a high strength class timber. The investigation on the use of locally sourced Irish Sitka Spruce is a part of the project 'Innovation in Irish Timber Usage'.

3.4 Cross-laminated timber (CLT)

Cross-laminated timber (CLT) is a prefabricated multi-layer engineered wood product made of at least three orthogonally bonded layers of timber. In order to increase rigidity and stability, successive layers of boards are placed cross-wise to form a solid timber panel, as show in Figure 2.

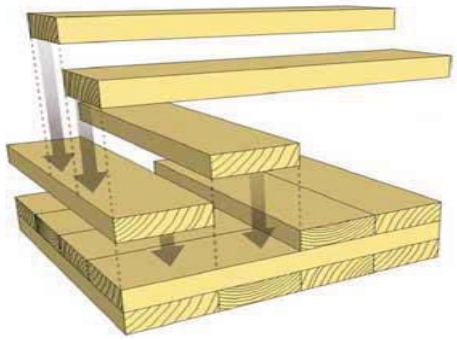


Figure 2. CLT panel schema [38].

Load-bearing CLT wall and floor panels are easily assembled on site to form multi-storey buildings. This improves construction and project delivery time, reduces costs, and maximises efficiency on all levels [39-41]. In this project, the feasibility of using Irish Sitka spruce to produce commercial CLT panels is being investigated.

4 CONCLUSIONS

In the past, a number of studies has been conducted to determine the properties of Irish-grown Sitka spruce. Nevertheless, due to the changes in that have taken place in silvicultural practices since the publication of these studies, there is a need to determine how these properties have changed.

As a part of 'Innovation in Irish Timber Usage' ongoing project testing of a large number of samples will be undertaken to establish the properties of the current resource. Comparative analysis will be undertaken with the data produced for Scottish Sitka spruce in the SIRT project and with historical data.

Other objectives of the project include determination of the durability of reinforced timber beams with respect to load duration and variable climate and to develop appropriate strength modification factors.

The next aim of the research programme is to investigate and develop a sustainable means of creating moment resistant connections within timber frames using bonded-in FRP rods, with a specific emphasis on the portal frame.

Moreover, the suitability of Irish-grown Sitka Spruce for the manufacture of cross-laminated timber panels (CLT) is investigated. This is vital in order to develop the necessary engineering data to support the commercialisation of Irish-made CLT.

ACKNOWLEDGMENTS

This work has been carried out as part of the project entitled 'Innovation in Irish timber Usage' (project ref. 11/C/207) funded by the Department of Agriculture, Food and the Marine of the Republic of Ireland under the FIRM/RSF/COFORD scheme. The authors would also like to thank ECC Ltd. (Earrai Coillte Chonnacht Teoranta) for supplying the timber used in this project.

REFERENCES

[1] Irish Forestry and Forest Products Association (IFFPA), *An overview of the Irish forestry and forest products sector 2013,* www.iffpa.ie, 2014.

[2] COFORD, *Forecast report 2011,* www.coford.ie, 2011.

[3] Phillips, H. (2011), *All Ireland Roundwood Production Forecast 2011-2028,* Dublin.

[4] Picardo, V. (1987). *Effects of yield class, tree section, forest and size on strength of home grown Sitka spruce*, Paper no CIB-W18A/20-6-2, CIB W18 meeting, Dublin.

[5] Ni Dhubhain, A., Evertsen, J.A., and Gardiner, J. J. (1988), *The influence of compression wood on the strength properties of Sitka spruce*, Forest Products Journal 38(9)67-69.

[6] Picardo, V. (2000), Quantification of the yields of Irish grown Sitka spruce in the new CEN stgrength classes, COFORD.

[7] Lucey, D. J., Mahony, R., and Kirk, D. (2001). *The Design and Performances of Thin Web Timber I-joists (Using Irish Timber and Oriented Strand Board)*, Report, Dublin Institute of Technology.

[8] Raftery, G.M. and Harte, A.M, (2014). *Material characterisation of fast-grown plantation spruce*, Structures and Buildings, DOI: 10.1680/stbu.12.00052.

[9] Evertsen, J. A. (1988), *Determintion of wood quality in Sitka spruce (Picea sitchensis (Bong.) Carr) by destructive and non-destructive methods*, PhD thesis, University College Dublin.

[10] Bucur, V. (1980), *Resonance Wood Acoustical Properties Modified by Long-Term Loading*, Annales Des Sciences Forestieres*,* 37 (3), 249-64.

[11] Bucur, V. (1981), 'Wood Dynamical Young Modulus Determination on Increment Core', Annales Des Sciences Forestieres, 38 (2), 283-98.

[12] Patrick, G. (2004), *The structral performance of FRP reinforced glue laminated beams made from homegrown Sitka Spruce*, PhD thesis, Queen's University Belfast.

[13] Bourke, M. (2007), *Distortion Reduction Strategies for Irish Softwoods*, MSc thesis, University of Limerick.

[14] Bourke, M. (2008), *Improving the stability of structural timber*, COFORD connects.

[15] Treacy M. (1999), The relationship between wood microstructure and wood quality in four Irish grown sitka spruce (Picea sitchensis (Bong.) Carr.) provenances. MSc thesis, University College Dublin.

[16] Treacy M., Evertsen, J., and Ní Dhubháin, A., (2000), *A comparison of mechanical and physical wood properties of a range of Sitka spruce provenances*, COFORD.

[17] Department of Agriculture, Food and the Marine, *Sitka spruce (Picea sitchensis (Bong.) Carr.)*, www.agriculture.gov.ie/media/migration/forestry/publications/SitkaSpruce_low.pdf.

[18] Moore, J., Lyon, A., Ridley-Ellis, D., and Gardiner, B. (2008). *Properties of UK-grown Sitka spruce: Extent and sources of variation*, Proceedings of the 10th World Conference on Timber Engineering, Miyazaki.

[19] Moore, J. (2011). *Wood properties and uses of Sitka spruce in Britain*, Forestry Commission Research Report, Forestry Commission, Edinburgh.

[20] EN 338:2009 Structural timber – Strength classes, CEN.

[21] EN 408:2010+A1:2012 Timber structures – Structural timber and glued laminated timber – Determination of some physical and mechanical properties, CEN.

[22] Zaman, A., Gutub, S. A., and Wafa, M. A. (2013), *A review on FRP composites applications and durability concerns in the construction sector*, Journal of Reinforced Plastics and Composites*,* 32 (24), 1966-88.

[23] Lopresto, V., Leone, C., and De Iorio, I. (2011), *Mechanical characterisation of basalt fibre reinforced plastic*, Composites Part B: Engineering*,* 42 (4), 717-23.

[24] Kliger, R. I. and André, A. (2013), *Enhanced timber properties with FRP composites*, Cost Action FP1004 - Innovative Timber Composites-Improving wood with other materials, pp. 11.

[25] Plevris, N. and Triantafillou, T. (1992*), FRP-Reinforced Wood as Structural Material*, Journal of Materials in Civil Engineering*,* 4 (3), 300-17.

[26] Raftery, G. M. and Harte, A. M. (2011), *Low-grade glued laminated timber reinforced with FRP plate*, Composites Part B: Engineering, 42 (4), 724-35.

[27] Gilfillan, J. R., Gilbert, S.G., and Russell, D.P. (2001b), *Enhancement of the structural performance of glue laminated, homegrown Sitka spruce, using carbonfibre-reinforced polymer*, Structural Engineer, 79 (8), 23-28.

[28] Hansson, S. and Kristoffer, K. (2007), *Moisture-related creep of reinforced timber*, Chalmers University of Technology, Goteborg, Sweden.

[29] Raftery, G., Whelan, C., and Harte, A. (2012), *Bonded in GFRP rods For the repair of Glud Laminated Timber*, World Conference of Timber Engineering, Auckland 2012, 16-19 July, Auckland, New Zealand.

[30] Kelly, F. (2012), *Basalt FRP rods for strengthening and repair of glued laminated timber*, MSc thesis National University of Ireland, Glaway.

[31] Ozelton, E.C and Baird, J.A. (2006). *Timber Designers' Manual*, Third Edition, Blackwell Publishing, Oxford UK.

[32] *Porteous, J.;Kermani,A.; 2007,* Structural Timber Design to Eurocode 5, Blackwell Publishing, Oxford UK.

[33] Gehri, E. (2010), *High Performing Jointing Technique Using Glued-in Rods* [online] Available at http://www.ewpa.com/Archive/2010/june/Paper_095.pdf

[34] Broughton, J.G. and Hutchinson, A.R. (2004). LICONS Task 2-Sub tast 2.2, Oxford Brookes University

[35] Bainbridge, R.J. and Mettem, C.J. (1998*). A Review of Moment-Resistant Structural Timber Connection*. Proceedings of the ICE - Structures and Buildings 128(4), 323–331.

[36] prEN 1995-2: Design of timber structures, Part 2: Bridges. Final Project Team draft. Stage 34, CEN.

[37] EN 1995-2:2004 Eurocode 5. Design of timber structures. Bridges, CEN.

[38] Rimetz, B. (2011). Future of Wood Update / X Marks the Opportunity, ProSales, http://www.prosalesmagazine.com/products/lumber/x-marks-the-opportunity_o.

[39] Handbook 1. Timber structures (2008). Leonardo da Vinci Pilot Project.

[40] Crespell, P., and Gagnon, S., (2010). *Cross Laminated Timber: a Premier*, FPInnovations

[41] Yeh, B., Gagnon, S., Williamson, T., Pirvu, C., Lum, C., and Kretschmann, D. (2012). Wood Design Focus, 22(2)13-21.

Life Cycle Assessment of Sawn Timber Produced from Irish forests

Desmond Dolan[1], Dr. Annette Harte[2]
[1,2]Civil Engineering, College of Engineering and Informatics & Ryan Institute,
NUI Galway, University Road, Galway, Ireland
Email: desmond.dolan@nuigalway.ie, annette.harte@nuigalway.ie

ABSTRACT: Climate change is widely accepted as the greatest environmental challenge facing the world today, predominantly due to the increase of greenhouse gas emissions, especially CO_2. As buildings account for 36% of EU CO_2 emissions, the environmental impacts associated with building materials are becoming increasingly important. The use of sustainable construction materials, such as sawn timber, has a major role to play in the reducing CO_2 emissions.

The aim of this paper is to outline the methodology associated with, and demonstrate the importance of, developing primary country specific data when analysing the carbon impacts associated with sawn timber production in Ireland using Life Cycle Assessment (LCA). LCA is an internationally accepted method of analysing and quantifying the total environmental impacts generated by a product at each stage of its life cycle from raw material extraction through to disposal or recycling. This involves quantifying the inputs and outputs, such as the energy and material usage, generated at each stage and assessing the total environmental impact associated with each. There is a huge variability associated with LCA data from timber construction products due to local climates, forestry conditions and manufacturing processes from country to country. Therefore, it is critical that Irish specific data be quantified from actual production figures to measure the true environmental impact of sawn timber beams and in turn, timber buildings, in Ireland.

KEY WORDS: Life Cycle Assessment; Sawn Timber; Embodied Carbon; Embodied Energy.

1 INTRODUCTION

As buildings account for 36% of the EU's CO_2 emissions [1], the move towards wood-based materials is becoming increasingly important. During tree growth, CO_2 is sequestered in the wood and this is then stored in wood-based products for the duration of their life making them unique among major construction products. This, combined with the other environmentally beneficial aspects of wood-based products, makes it possible to produce carbon negative construction products and ultimately carbon negative buildings.

In line with EU policy, it is becoming accepted that a life-cycle approach to product development and construction must be adopted. This allows the total environmental impacts associated with these products to be quantified.

The aim of the current project is to quantify the total carbon impact factors along with the various other environmental burdens associated with the production of sawn timber from Irish forests using an environmental assessment technique known as Life Cycle Assessment (LCA). This involves quantifying the inputs and outputs, such as the energy and material usage, generated at each stage of its life cycle and assessing the total environmental emissions associated with each. Unlike many other construction products these values for timber products can vary significantly from country to country due to differences in local climate and in forestry, manufacture and construction practices. Therefore, in order to accurately quantify the total environmental impacts associated with the production of such products, country specific data from actual production must be quantified.

2 RESEARCH MOTIVATION

The manufacturing of sawn timber, like all products, has certain environmental consequences, such as the release of Green House Gases (GHGs), fossil fuel depletion and eutrophication (excessive richness of nutrients in a body of water) for example, that must be taken into account and analysed should it be considered as a sustainable building product. It is the purpose of this study to describe how LCA can be used to fully quantify these impacts in relation to the production process of sawn timber in Ireland and to highlight the main issues associated with using secondary data while dealing with timber construction products.

Climate change is widely accepted as the greatest environmental challenge facing the world today. Increases in the emission of GHGs*, especially CO_2, to the atmosphere as a result of human activity contribute to climate change. In order to stabilise CO_2 concentrations in the atmosphere, GHG emissions must be reduced or climate change must be adapted to. The Tyndall Centre for Climate Change Research, a UK based organisation dedicated to developing various options to mitigate climate change, has suggested that a 70% reduction in CO_2 emissions will be required by 2030 compared to 1990 levels to prevent temperatures rising by more than 1 degree Celsius by the end of the century [2].

In Europe alone the European Union Climate and Energy Directives [3] provide for a 20% reduction in CO_2 emissions by 2020 relative to 1990 and a 20% increase in energy efficiency over projected levels.

(*The defining unit in quantifying GHGs is CO_2 equivalents (CO_2eq) which account for not only CO_2 but also include other GHGs as set out in the Kyoto protocol such as methane (CH_4), nitrous oxide (N_2O), and PFCs.)

As buildings accounted for 36% of EU CO_2 emissions in 1990 [1] and remain a major contributor to Europe's CO_2 emissions, the use of sustainable construction materials, such as sawn timber, has a major role to play in the achievement of this objective. Understanding and accurately quantifying these emissions is vital in order to develop effective measures to reduce these increasing emissions and to comply with regulations.

Undertaking such an LCA will be also be important for the wood products industry in providing benchmarks of environmental performance for sawn timber manufacturers and buildings products manufacturers alike. It will allow manufacturers to identify 'hot-spots' within their production chain and analyse the total effect of process alternatives. Quantifying Irish specific LCA data will also allow other LCA practitioners to accurately assess the true environmental impact of timber buildings produced in Ireland which could then be compared with their steel or concrete equivalent. In addition it provides wood product manufacturers with the necessary data for the development of environmental product declarations (EPDs). An EPD is a type III eco-label that gives a summary of the environmental impacts associated with producing and using a product or service. Several countries are today considering requiring EPD documentation in international trade [4]. For example, France is piloting an ambitious plan to require environmental labels on all consumer goods on sale in France. This is a national initiative that will inform consumers of the environmental impacts of products through environmental labelling. It will involve displaying the carbon footprint and two other appropriate environmental indicators for products on sale across all sectors. The calculation standards were drafted in 2010 and in early 2011 a pilot phase began. Hence, developing EPDs and the supporting LCA data will become essential for maintaining access to global markets in the future.

3 LIFE CYCLE ASSESSMENT

LCA is an internationally accepted analytical method that analyses and quantifies the total environmental impacts generated by a product at each stage of its life cycle. The environmental impacts assessed, include energy and material usage, emissions to air and water as well as solid waste generated at each stage. LCA typically considers materials over the course of their entire lives, from extraction through manufacturing, transportation, installation, use, maintenance, and disposal or recycling. However, depending on the scope of the project, various system boundaries can be set.

To ensure clarity, consistency and accuracy LCA studies are governed by the ISO standards which were published in 2006, most notably:

- ISO 14040 Environmental management – Life Cycle Assessment – Principles and framework [5] and
- ISO 14044 Environmental management – Life Cycle Assessment – Requirements and guidelines. [6]

The use of LCA as an environmental management tool began in the late 1960s, however, in these early years it was known under different names and was used in a variety of different ways. Some forms of LCA originally assessed operational and maintenance costs over the life cycle of a product, however, this has since become known as 'life cycle accounting' or 'life cycle costing'. LCA has since been adapted to reflect environmental life-cycle studies. One of the first appearances of LCA as it is commonly known today was seen in a study conducted by the Coca Cola Company in 1969. They compared the environmental effects of their product packaging from cradle to grave using LCA or as it was commonly know up to the 1990s, 'Resource and Environmental Profile Analysis'. As part of this study they examined the possibility of using a disposable plastic bottle and compared its environmental impacts with those associated with refillable bottles [7]. The concept and methodology slowly developed with significant inputs from such groups as the Society of Environmental Toxicology and Chemistry (SETAC) until it became the basis for the ISO standards that are in use today.

A LCA study is divided into four key phases.

- The first phase, the goal and scope definition phase, outlines the context and purpose of the study.
- The second phase, the inventory analysis phase, quantifies the total input and outputs associated with the product system.
- The third phase, the impact assessment phase, quantifies the potential impacts associated with these inputs and outputs.
- The fourth and final phase, the interpretation phase, interprets the inventory data and impact assessment data in relation to the goal and scope.

The Life Cycle Assessment framework according to ISO 14040:2006 is shown in Figure 1 indicating how each part of the assessment is closely linked to the others and the iterative nature of undertaking an LCA.

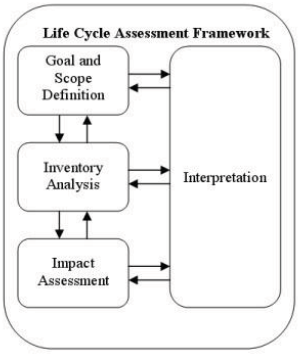


Figure 1. Life Cycle Assessment Framework (ISO: 14044)

4 UNDERTAKING AN LCA OF SAWN TIMBER

4.1 Goal and Scope

The first phase in undertaking an LCA is defining the goal and scope of the project. This includes describing the product, the level of detail required, allocation methods, any assumptions made, data quality and the intended use of the study. Three vital aspects that must be considered during this phase of the LCA when considering sawn timber products are defining the

System Boundaries, Functional Unit and Allocation Procedures.

The system boundary defines the unit processes to be included in the system. In establishing the systems boundary, an imaginary line is drawn around the life cycle. Boundaries for a system in LCA should be set as broadly as possible. Processes involved in the extraction of raw materials and production of ancillary (intermediate) materials must be included in addition to accounting for the energy and material flows of the primary product. Ancillary materials are used indirectly in the manufacture of the final product, for example fertilisers used in the production of biomass. Disposal, by-products, and wastes are also included within the life cycle boundary. System boundaries can be used to indicate whether the LCA is part of a so-called "cradle-to-grave" or "cradle-to gate" LCA study [8] as shown in Figure 2. This paper concentrates on demonstrating how a cradle-to-gate LCA which focuses primarily on the impacts associated from the raw material extraction phase through to the manufacturing phase is conducted. Secondary (existing) data will be used for all other ancillary materials entering the system boundary such as fuels, electricity, preservatives and packaging. A typical system boundary (dashed line) for a cradle to gate LCA of planed, kiln dried timber is shown in Figure 3. All inputs and outputs that cross that line including energy, products, emissions and waste must be recorded to complete the LCA.

The functional unit is the important basis that enables alternative goods, or services, to be compared and analysed. The primary purpose of a functional unit is to provide a reference to which the inputs and outputs are related [5]. The typical functional unit used when undertaking an LCA for sawn timber is $1m^3$ with a declared density and moisture content. However, in some cases the functional unit is taken as one thousand board feet or 1MFBM (1000 square feet of 1" lumber).

Allocation is another issue that has led to much debate when considering the LCA of timber products. Allocation refers to the distribution of the environmental burdens associated with a process where two or more products are produced from that process. For example, when dealing with sawn timber such co-products as bark and wood chips are produced while sawing the logs and these are then sold to board mills and farmers as well as being used as a fuel on site. Various solutions have been presented over the years describing how to overcome the issue such as allocating by mass or by economic value. Particular care must be taken when considering allocation with timber products as the CO_2 sequestered or released must be allocated by mass as the CO_2 stored is directly proportional to the mass of the material. However, the remainder of the emissions, and in turn, impacts, can be allocated by a number of other methodologies, such as by volume or economic value which can then cause confusion.

Although there are set guidelines for undertaking an LCA as defined by the ISO standards the methodology is still evolving and there is still a lot of debate on best practice techniques, particularly in the wood product industry. Therefore, it is worth noting that unless the assumptions, system boundaries, functional unit and allocation methodologies for two or more studies are identical, the results of the studies cannot be compared.

Work is underway to develop Product Category Rules (PCRs) which are currently required to be used in line with with the ISO standards in order to create EPDs. These PCRs will further define LCA rules and requirements for analysing a particular group of products, such as construction wood products which would then allow future studies to be compared more easily [9].

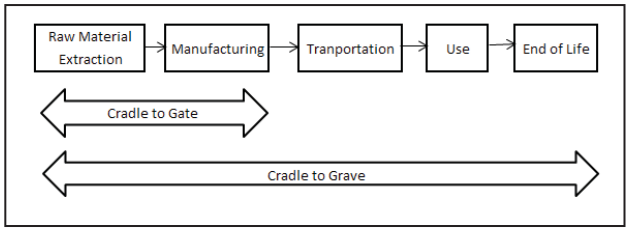


Figure 2. Typical Life Cycle System Boundaries

4.2 Product Description

At the goal and scope stage it is beneficial to describe in detail the industry, product and the process flow and to highlight the potentially important environmental issues associated with each phase.

4.2.1 Sawn Timber Industry in Ireland

As of December 2011 approximately 10.6% of Ireland's land area is under forest [10]. Ireland has the fastest growing rate of forest in Europe (Figure 4) resulting in a sequestration rate of approximately 4 to 8 metric tonnes of carbon per hectare per year (tC ha^{-1} yr^{-1}) [11].

Sitka Spruce (Picea Sitchensis) is the most common species found in Irish forests and accounts for over 90% of the softwood processed within the Irish sawmills. The three main sectors that sawn timber is primarily used for in Ireland are construction and structural purposes, pallet and packing purposes and also for fencing purposes [10].

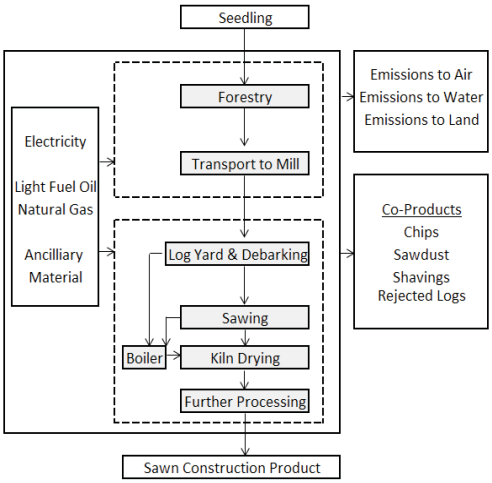


Figure 3.Typical System Boundary of LCA of Sawn Timber

The method for producing sawn timber is relatively consistent across Ireland and ultimately the final product is

shipped to various wholesalers or building sites both in Ireland and the UK. In recent years, Irish sawmills have also developed markets in France, the Netherlands and Turkey. The annual production of sawn softwood timber for 2012 was 900,000m^3 and over 2.84 million m^3 of roundwood was harvested from Irish forests. [10]

4.2.2 Process Description

Raw Material Extraction and Transport to Mill.
During the forestry process seedlings are transported from the nursery before they are planted in the forest and managed until they are ready to be harvested. This process incorporates all inputs associated from the forest management including road construction, the use of fertilizers, thinning, final harvest and transport to the gate of the sawmill. This also includes shipping for the logs that have been imported from abroad. The primary inputs are diesel fuel, fertilisers and pesticides for this process.

Log Yard Activities.
This process includes the unloading of the logs from the truck, all sorting, scaling, storing and all forklift operations throughout the process. It also includes the debarking of the logs. The primary inputs throughout this process include electricity, fuel, logs with bark and lubricants. The outputs include debarked logs, reject logs, butt chips and bark.

Sawing.
The sawing process includes sawing the debarked logs into various sizes suitable for further processing and sorting and stacking the sawn timber. The inputs for this process include debarked logs, electricity, lubricants, fuel and the outputs include green sawn timber, wood chips and sawdust.

Heat Generation and Drying.
This process involves drying the rough green timber in kilns and sorting and stacking all sawn timber once dried. Sawdust, bark, chips and other co-products are used in boilers as a fuel to produce heat for the kilns and plant or, if a CHP is used, it may also provide electricity. The inputs for this process include green sawn timber, wood fuel, electricity and other fuels. Outputs include dry sawn timber, steam, boiler/CHP emissions, ash and electricity.

Further Processing.
Further processing includes logs that require any further work prior to leaving the plant, such as planing, grading and preserving timber products. It may not be possible to distinguish the environmental burdens associated with each process individually due to the manner in which data is recorded. Primary inputs include green and dry sawn timber, electricity, lubricant and preservatives. Outputs include processed sawn timber, shavings and sawdust.

4.3 Life Cycle Inventory

The Life Cycle Inventory (LCI) Phase involves collecting of all the primary data required to meet the goals defined in phase one of the LCA. An inventory of all the input/output data with regard the system being studied must be compiled. A life cycle diagram is often used in this phase to outline the life cycle phases (Figure 3). Each phase within the system boundary is then considered in turn and described in greater detail; the level of detail required will depend on the complexity of each phase, some of which require their own life cycle diagrams. Once these phases have been described in significant detail all the required input and output data are collected and generally stored on LCA software or spreadsheets. Data for each unit process within the system boundary can be classified under major headings, including:

- Energy inputs, raw material inputs, ancillary inputs, and other physical inputs;
- Products, co-products and waste;
- Emissions to air, discharges to water and soil; and
- Other environmental aspects.



Figure 4, the best growing climate in Europe ($m^3ha^{-1}yr^{-1}$)

Numerous databases have been developed which provide secondary inventory data on various materials such as Ecoinvent [12] and the U.S Life Cycle Inventory Database [13]. However, one must ensure that the assumptions made in these data sets match the data assumptions required outlined in the goal and scope phase.

4.4 Life Cycle Impact Assessment

The third phase of LCA is known as the Life Cycle Impact Assessment (LCIA) Phase. A LCIA interprets the material and energy flows determined throughout the inventory phase and assigns them to various environmental themes such as acidification or climate change. LCIA therefore presents information on impacts on the environment, as opposed to just information on emissions and resource use as seen in the inventory phase. Accordingly, every LCA must at least include classification (aggregating the inventory data according to the type of environmental impact to which it contributes) and characterisation (calculation of the contribution of emissions and resource consumptions to each impact). If such procedures are not applied, then the study can only be referred to as a 'Life Cycle Inventory' as opposed to a Life Cycle Assessment. LCIA results are often calculated using either midpoint or endpoint modelling methodologies. Characterisation at the midpoint level is an indicator located somewhere along the environmental mechanism i.e. ozone depletion. Characterisation at the endpoint level aggregates these impacts further and models emission's relative importance on specific issues of concern such as skin cancer, crop damage and marine life damage. Figure 5 illustrates how

the LCI results are converted to midpoint results and then to endpoint results in the LCAI. There are pros and cons associated with each methodology. Endpoint results have the benefit of being concise and easy to understand, and, for communicating with a non-LCA audience, they tend to make more sense. However, endpoint assessments also lower the level of certainty of the results compared to midpoint assessments as the sources of the environmental impacts are further aggregated with each other in order provide concise results.

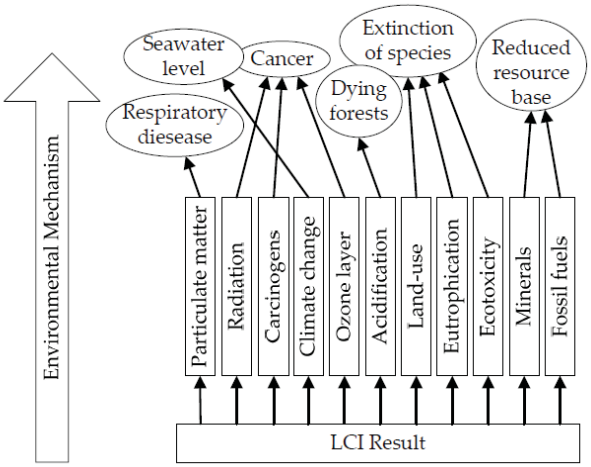


Figure 5 Structure of Impact Assessment Method [14]

A number of life cycle impact assessment methodologies (LCIAMs) are commercially available such as CML 2001, Ecological footprint, EPS 2000 and IMPACT 2000+. Each methodology, whether it is a midpoint or endpoint methodology, has its own advantages and disadvantages such as the inclusion of certain environmental issues or the level of detail. Two of the most commonly used impact assessment methodologies are the ECO-Indicator 99 and CML. However, as CML does not include land use or particulate formation, both of which are crucial when considering the manufacturing of timber construction products, therefore, these methodologies would be ruled out for such a study. A relatively new impact assessment methodology, ReCiPe, incorporating the Eco-Indictor 99 methodology, has been developed to present results at both midpoint and endpoint in up to 18 categories and provides more up-to-date characterisation factors [15]. Therefore, for the purpose of quantifying the total environmental impacts associated with the production of sawn timber in Ireland both the Eco-Indicator 99 and the ReCiPe methodologies are recommended.

There is still much debate over the life cycle impact assessment phase in relation to different products and associated impact categories. Bodies such as SETAC, ISO and BRE are continuing their efforts to standardise the LCIA phase through the introduction of PCRs for example which would require studies conducted within the same field to use the same LCIA methodology and hence be comparable with one another.

4.5 Interpretation

During this final phase, which was previously known as the improvement phase, the results of the preceding phases are summarised and discussed as a basis for conclusions, recommendations and decision making in accordance with the goal and scope definition. The interpretation of LCIA results should also demonstrate that the results indicate potential environmental effects, and that they do not predict actual impacts on category endpoints. Curran [9] identifies three key steps to interpreting the results of the LCA: (i) identification of the significant issues, (ii) evaluation which considers completeness, sensitivity, and consistency checks and (iii) conclusions, recommendations, and reporting. These steps help provide a systematic approach to interpreting the life cycle. Significant issues may include inventory parameters (e.g. energy use, emissions, waste); impact category indicators (e.g. health impacts, resource depletion); and essential contributions for life cycle stages (e.g. raw material extraction, processing, transportation). The evaluation step establishes the confidence in and reliability of the results of the LCA.

5 EXISTING STUDIES

Relatively little primary LCI data has been collected to date in relation to construction products in Ireland, in particular with timber products. Over the past decade there has been an increased application of Life Cycle Assessment to construction products across much of the world. A lot of the European construction LCI data can be applicable to Irish products and buildings. However, due to the unique nature of construction wood products, Irish specific data is required to accurately quantify the environmental burdens associated with sawn timber and existing data is not necessarily representative of the Irish production process.

This issue has been noted by various LCI database providers such as the USLCI or the Inventory of Carbon & Energy (ICE) database, which focuses primarily on embodied carbon and energy of construction products [16]. It states that timber products presented the most difficulty of all buildings products due its natural variations such as the change in moisture content and density of wood and also transport distances and variations in fuel mix.

An example of this can be seen in two separate studies conducted by CORRIM (Consortium for Research and Renewable Materials) in which the total energy consumptions required to produce $1m^3$ of sawn timber in the 2 different regions of the US, the Pacific Northwest and Southeast. It was found that the energy required varied from $216kMJ/m^3$ to $324kMJ/m^3$ to produce the same product [17][18]. It was suggested that the higher energy requirements for sawing and drying the timber produced in the southwest region is due primarily to its higher density and moisture content.

The ICE database compiled 33 studies from various locations around the world and aggregated the results. It was found that the average calculated carbon released and energy used for the production of 1kg of sawn timber was approximately 0.2 CO_2e/kg and 7.4 MJ/kg, respectively which includes 4.2MJ of bio-energy (bio-energy is a form of renewable energy sourced from various forms of biomass, such as wood) [14]. However, the results for the embodied

energy ranged from 0.72 to 13MJ/kJ highlighting the variation from study to study. The author noted that timber presented the most difficulties to the ICE database due to the lack of existing detailed studies and also the large variation in results due to the high element of natural variation and also variations associated with fuel mix and manufacturing processes.

These figures do not include the beneficial aspect of carbon sequestration which takes into account CO_2 absorbed by the trees while growing which is then stored in the wood product for the duration of its life. This demonstrates the potential to produce carbon negative construction products. Although the biomass combustion throughout the production of timber construction products is considered carbon neutral, there is still major debate over how to treat sequestered carbon. It is considered best practice to present both the original CO_2 figure and the CO_2 less the sequestered carbon together, as a consensus has yet to be reached on whether or not the data should be included. However, in order to present both figures a full cradle to grave LCA would have to be completed and that is outside the scope of either a cradle-to-gate or gate-to-gate analysis.

6 CURRENT PROGRESS

To date, the primary softwood timber production data has been collected both on site and by written surveys in order to compile sufficient LCI data for the manufacture of sawn timber products produced in Ireland. The data received covered operations in the mills for one full calendar year, including both winter and summer operations between 2011 and 2012 in accordance with ISO standards.

Throughout Ireland 8 companies form the core of the sawmill industry in Ireland and together they produced 867,000 and 900,000m^3 in 2011 and 2012 respectively [10]. Data is currently being collected from three representative softwood manufacturers. From the data received the combined annual production was approximately 40% of the total sawn product production of 2012. However, due to the mix of mill sizes and technologies covered by this study the representativeness of these results is likely to be closer to 70% for sawn construction products produced in Ireland.

Once the remainder of the data has been collected, an aggregated composite sawmill will be analysed using weighted data from each of the participating sawmills in the study. The LCA of this sawmill will then provide accurate data on the total environmental impacts associated with sawn timber produced in Ireland which can then be used to analyse higher level products such as timber windows, walls or even buildings.

7 CONCLUSIONS

Due to climate change and current legislation there is a growing need for need for 'greener' construction produces such as timber construction products. LCA is an effective environmental assessment technique that can be used to assess the total environmental impacts associated with the manufacturing of sawn timber in a holistic manner. LCA can be used to assess the total environmental impacts associated with a product over its whole life cycle, cradle to grave, or could focus primarily on the manufacturing phase gate-to-gate. LCA is split up into 4 main phases including goal and scope phase, the inventory analysis phase, the life cycle impact assessment phase and the interpretation phase.

When using LCA to assess sawn timber production special care has to be given to identifying the main environmental aspects throughout the process such as the release of particulates and GHGs. Data can then be collected on the production process which can then be assessed using a LCIAM. When using secondary data it is essential that the dataset used is relevant as there can be a huge variation in data from different regions, particularly within the wood product industry. Care must also be taken in choosing which Impact assessment methodology to use to ensure all relevant impact categories are included such as land use and particulate formation. There is a significant knowledge gap when it comes to the LCA data of timber construction products produced form Irish forests which will need to be examined. It is the aim of the author's project to fill this knowledge gap.

ACKNOWLEDGMENTS

The author would like to acknowledge the financial support of both Coillte and the Irish Research Council to this project.

REFERENCES

[1] European-Commission (2010): www.europa.eu.: Retrieved 15/ 5/ 2012, from ec.europa.eu/energy/efficiency/buildings_en.htm.

[2] Bows, A. and Mander, S. et al. (2006): Living within a carbon budget. Report for Friends of the Earth and The Co-operative Bank: The University of Manchester.

[3] European-Commission (2007): 2020 Vision: Saving our Energy:

[4] Bergman, R. and Taylor, A. (2011),'EPD-Environmental product declarations for wood products - An application of life cycle information about forest products', *Forest Products Journal* 61(3): 192-201.

[5] ISO-14040 (2006a): Environmental Management - Life Cycle Assessment - Principles and framework: ISO.

[6] ISO-14044 (2006b): Environmental Management - Life Cycle Assessment - Requirements and Guidelines: ISO.

[7] Hunt, R., and Franklin, W. (1996) 'LCA - How it came about', *The International Journal of Life Cycle Assessment*.

[8] Curran, M. (2006),'Life Cycle Assessment: Principles and Practice: U.S. Environmental Protection Agency Cincinnati, USA.

[9] BS EN 15804 (2012): Sustainability of construction works Environmental product declarations - Core rules for the product category of construction products: CEN

[10] Irish Forestry and Forest Product Sector Association and IBEC,'*An Overview of the Irish Forestry and Forest Product Sector 2013*.

[11] Black, K.G. and Farrell, E.P. (eds). (2006). '*Carbon sequestration and Irish forest ecosystems'*. COFORD, Dublin.

[12] Ecoinvent Centre (2013), Ecoinvent data v.3.0. Swiss Centre for Life Cycle Inventories, St. Gallen, retrieved from: www.ecoinvent.org

[13] "U.S. Life Cycle Inventory Database." (2012). National Renewable Energy Laboratory, 2012. Accessed November 19, 2012: https://www.lcacommons.gov/nrel/search

[14] Pre Consultants (2008): http://www.pre-sustainability.com/learning-center: Retrieved 19/5/2013

[15] Goedkoop, M., Heijungs, R., Huijbregts, M.m Schryver, AD., Struijs, J., Van Zelm, R. (2009),'ReCiPe 2008 - A life cycle impact assessment method which compares harmonised category indicators at the midpoint and the endpoint level. First edition, report I: Characterisation. Ministry of Housing, Spatial Planning and the Environment (VROM), Den Haag.

[16] Hammond, G.P., and Jones, C. I., (2011),'Inventory of carbon and energy (ICE) Version 2.0': Retrieved on 20th of August 2012, from http://www.bath.ac.uk/mech-eng/sert/embodied.

[17] Puettmann, M., Wagner, F. and Johnson L. (2009), 'Life Cycle Inventory of Softwood Lumber from the Inland Northwest US', Wood and Fiber Science, 42, 52-66.

[18] Milota, MR., West, CD. and Hartley ID. (2005), 'Gate-to-Gate Life Cycle Inventory of Softwood Lumber Production', Wood and Fiber Science, 37, 47-57.

Multi-storey Construction in Timber

Dr. Annette Harte[1], Cian Glennon[2]
[1,2]Civil Engineering, College of Engineering and Informatics & Ryan Institute,
NUI Galway, University Road, Galway, Ireland
email: annette.harte@nuigalway.ie; c.glennon2@nuigalway.ie

ABSTRACT: Building with timber has been gaining in popularity around the world in the last decade. Timber construction is set to play an important role in the move to sustainable construction. Innovations in engineered timber technology and environmental impacts have led to timber being considered a viable material for multi storey construction. The most important advancement is the development of Cross Laminated Timber (CLT). CLT panels are made by gluing together wooden boards to form solid wood slabs and are typically used as wall or floor panels.
This paper examines the issues associated with construction using CLT. The design of a ten-storey hotel building located in Ireland is described. This structure will comply with Irish building regulations. As Eurocode 5 does not currently have design procedures for CLT, the design used are based on the draft regulations emerging from the CEN TC/250 Committee.

KEY WORDS: Multi-storey buildings; structural design; cross-laminated timber.

1 INTRODUCTION

Timber construction is set to play an important part in the aim for sustainable construction. Advancements in engineered timber technology and environmental impacts have led to timber being considered a viable material for multi-storey construction. Recent examples include the Stadthaus in London, The Forté Building in Melbourne and the Limnologen in Växjö, Sweden. These buildings all incorporate cross-laminate timber panels as wall and floor elements.

Cross Laminated Timber panels are made by gluing together wooden boards to form solid wood slabs. These slabs are then bonded together in an odd number of layers, typically 3 to 9 layers, with the grains in adjacent layers running perpendicular to each other, as shown in Figure 1. These solid wood panels can then be used as structural or non-structural elements in construction. CLT panels are prefabricated off-site and all service ducts, window and floor openings are cut using high-precision CNC equipment.

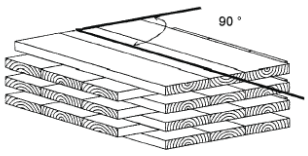


Figure 1 General Arrangement of CLT Slab

CLT is strongest when loaded in-plane, parallel to the direction of the grain. Wall slabs act as deep beams, supporting the floors above. Its use as floor and wall elements will be investigated for its ability to bear the required loads applied.

In the current project, examples of multi-storey construction in timber are examined and international best practise in the design of these buildings is applied to the design of a 10-storey hotel building for a site in the docklands area of Galway city.

2 CASE STUDIES

The number of multi-storey timber buildings across the world is growing rapidly as design codes and building regulations are changed to allow for construction in CLT. Two example buildings are described.

2.1 Stadthaus, Murray Grove, Hackney, London

The nine-storey Stadthaus in London was completed in 2009 and at the time was the tallest residential timber building in the world. The Stadthaus is 9 storeys tall and has a footprint of 17m x 17m and is 29.75 m tall, as seen in Figure 2.

The Stadthaus was designed in a honeycomb pattern around a central core (lift shafts and stair wells). Walls, floors and cores were all designed to be load bearing. The external walls were designed with sufficient capacity to allow for rotating floor plans, avoiding repetitive elevations.

From floor 1 to 9 the structure is constructed completely from CLT panels. These panels have a maximum size of 16.5m X 2.95m [1], the largest size that is easily transportable. The floor panels are typically 146mm thickness and the wall panels are 128mm thickness [1].

Stadthaus was designed to avoid large bearing forces on the floor panels where possible. However, this was unavoidable in certain locations. The compressive strength of the CLT panel perpendicular to the panel is 2.7 N/mm^2. The bearing

capacity was increased with screw or nail arrays at highly loaded points.



Figure 2 The Stadhaus, London [1]

2.2 *Limnologen, Växjö, Sweden*

The Limnologen was constructed as part of the Välle Broar project in Växjö, Sweden (Figure 3). Limnologen is constructed mainly of CLT panels as load bearing walls and floors. The ground floor is constructed in concrete with floors 1 to 7 constructed in timber. The timber structure is constructed with CLT panels but is also supplemented with Glulam elements where required. The wall panels are 85mm thick, consisting of 3 layers, with the middle layer being thicker than the outer layers. The floor panels are only 73mm thick; however additional Glulam beams act as load bearing elements [2]. A glulam beam is attached perpendicular to the underside of the floor panel, interacting fully as a web. A glulam beam is attached to the web, interacting fully as a flange.



Figure 3Limnologen, Vaxjo [3]

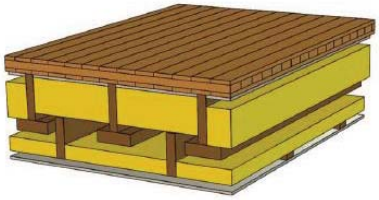


Figure 4 Floor element used in Limnologen[3]

The stabilisation of the structure consists of the external walls, internal walls and floors. The horizontal loads are transferred by the floor panels – acting as stiff plates – to the top of the walls. The timber structure is anchored to the concrete structure using 48 tension rods [3]. These rods run from the concrete structure to the top of the timber structure to prevent overturning from wind loads.

Limnologen was subject to a long term deformation study by Linnaeus University. Overall, a vertical displacement was calculated at 21.1mm after 2 years. This was over a height of 17.95m, an overall displacement of 0.12%, as seen in Figure 5.

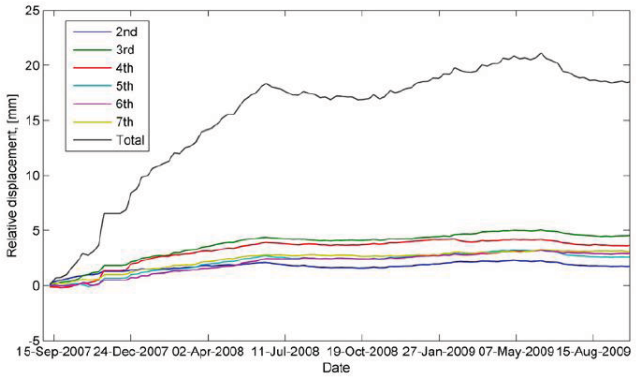


Figure 5 Relative displacement as a function of time for each of the six storeys and cumulative total [2]

3 TIMBER HOTEL CONCEPT

The aim of this project is to design a 10-storey Hotel Building. This hotel is to be constructed on a site in the docklands area of Galway City. The site is adjacent to the Docks and the Harbour Hotel Galway. This hotel will meet 4 star requirements. A total 216 guest rooms will be provided, each incorporating a private bathroom en suite. An isometric of the propose structure is shown in Figure 6

This structure will comply with Irish building regulations. The loadings are determined using I.S. EN 1991-1-1:2002 and I.S. EN 1991-1-4:2005. As Eurocode 5 does not currently have design guidelines for CLT elements, the design is based on the published literature.

The basement and ground floor are to be constructed from reinforced concrete. This is due to a number of factors. The concrete sub-structure and floors provides a weight to anchor the timber structure above. It also keeps the timber structure away from the ground, protecting it from moisture ingress. The open plan and spans required for these floors are not possible using CLT.

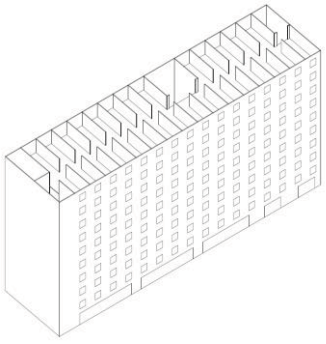


Figure 6 Galway Docklands Hotel layout

4 STRUCTURAL DESIGN

The structure will comprise 9 floors of CLT panels with the floors made up of CLT panels, supported CLT panels acting as walls. This will be constructed above a concrete substructure. For the purpose of this study only the CLT structure will be considered.

4.1 Wall Panels

4.1.1 Loadings

Two loading actions are considered for this structure, namely General Actions: dead and imposed loads, and wind actions.

4.1.2 General Actions

For the calculation of the general actions acting on this structure the actions taken into account will be the imposed loads according to the category of use of an area and the dead loads from the construction materials.

The imposed loads used in this design are taken from I.S. EN 1991-1-1 Table NA.2.
Hallways in Hotels

- Category C1 $q_k = 3.0 kN/m^2$

The dead loads used in this design are based on the size and density of the construction material used.

Table 1: Characteristic Loading of Bedroom Floor, including 125mm CLT Panel

Dead Loads (UDL)	Thickness (mm)	Density (kg/m^3)	Loading (kN/m^2)	Partial Factor for Actions	Factored Loading (kN/m^2)
Self Weight of Panel	125	530	0.650		
Ceiling					
Mech and Elec Services			0.5		
Insulation	50	20	0.010		
FermaCell Ceiling Panels	37.5	1150	0.423		
Floor					
Insulation	20	20	0.004		
Screed	50	2000	0.981		
Total Dead Load		g_k=	2.57	1.35	3.47
Imposed Loads					
Bedroom Areas		q_k=	3	1.5	4.5
				q_d =	7.97

4.1.3 Design Methods

Cross Laminated Timber is not mentioned in the design codes for timber, Eurocode 5. However, it may be designed using two different approaches: The Composite Theory, described by Blass and Fellmoser [5], and the Theory of Mechanically Jointed Beams, from I.S. EN1995-1-1 [6].

4.1.3.a Composite Theory Method

This method accounts for the strength and stiffness of each layer in the CLT panel, regardless of orientation. The shear deformation of members is not regarded. Due to this only panels with a high span to depth ratio may be considered for this approach.

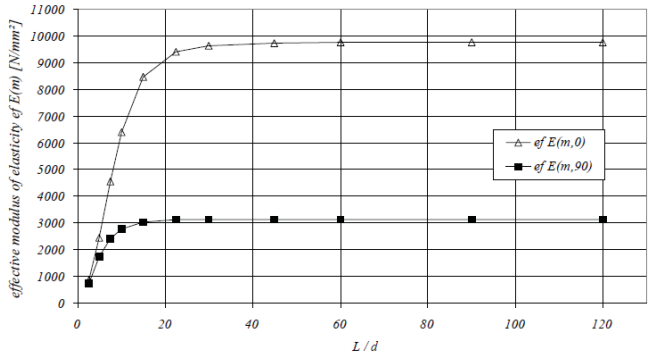


Figure 7 Effective Modulus of Elasticity vs. L/d ratio for bending perpendicular to the grain

The influence of shear is demonstrated in Fig. 7. For panels loaded perpendicular to the plane, $E_{eff,m,0}$ is shown to decrease significantly when L/d <30. For panels loaded in plane, $E_{eff,m,90}$ is shown to decrease significantly when L/d <20. This illustrates the limits of the applicability of the Composite Theory.

Calculations using this method are based on composition factors. The composition factor is the ratio between the strength or stiffness, respectively, of the considered cross section and the strength or stiffness, respectively, of a fictitious homogeneous cross section with the grain direction of all layers parallel to the direction of the stress [4].

4.1.3.b Mechanically Jointed Beams

This method of design is based on the Theory of Mechanically Jointed Beams, which is described in Annex B of Eurocode 5. This method is also known as the "Gamma Method". It is based on the theory of linear elasticity. Due to this method accounting for shear deformation in the cross layers, it can be used for small span-to-depth ratios.

The connection efficiency factor, γ (gamma), describes the degree of interaction between the parallel layers.

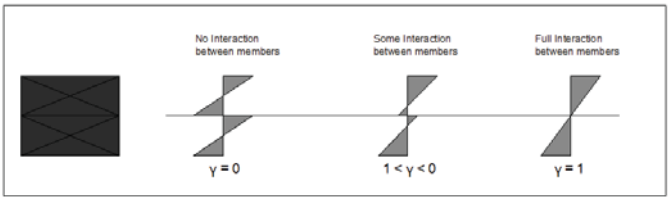


Figure 8 Stress Distribution in Mechanically Jointed Beams [6]

This theory has been adapted for use with Cross Laminated Timber panels. Only layers with grain direction parallel to the line of action are considered for the calculation of the effective stiffness of the panel. Rolling shear in the layers perpendicular to the line of action is considered in the Mechanically Jointed Beams Method. Cross layers are considered as "imaginary" fasteners, whose stiffness is taken as the rolling shear of the cross layers.

4.1.4 Floor Panel Design Examples

Two calculations are provided to display the design methods and where they are applicable. One is a floor in the bedroom area and the second is in the more highly loaded corridor area.

4.1.4.a Composite Theory Method

This design is based on the loadings for a bedroom panel.

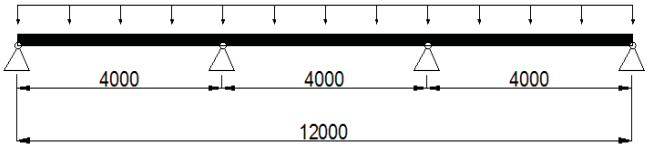


Figure 9 Span of 12m CLT Floor Panel

The thickness is estimated using span tables provided by the manufacturer. A panel of 125mm is chosen. This gives a span-to-depth ratio of 32. Composite Theory is applicable. Design stresses are calculated based on the loadings:

M_d= 14.88 kNm/m width V_d= 38.16 kN/m width

Table 2: Mechanical Properties of CLT Floor Panel

CLT Properties			
CLT		C24	
Bending Strength			
Parallel to grain of top board	$f_{m,k}$	24	N/mm^2
Shear Strength			
Parallel to grain of top board	$f_{v,k}$	2.7	N/mm^2
Perpendicular to grain of top board	$f_{R,v,k}$	1.5	N/mm^2
Modulus of Elasticity			
Perpendicular to grain of top board	$E_{90,mean}$	370	N/mm^2
Parallel to grain of top board	$E_{0,mean}$	12000	N/mm^2
Shear Modulus			
Perpendicular to grain of top board	$G_{R,mean}$	50	N/mm^2

The structure is assigned service class 2. The service class allows a number of parameters to be chosen.

γ_m= 1.25 k_{mod}= 0.8 k_{def}= 0.8

The CLT panel chosen has a thickness of 125mm, with 5 layers, as seen in Figure 10.

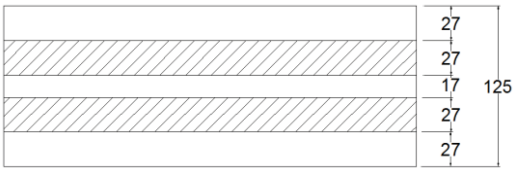


Figure 10 Cross-Section Dimensions of 125mm CLT Panel

For this lay-up:

$a_m = 125mm \quad a_{m-2} = 71mm \quad a_{m-4} = 17mm$

The composition factor from Blass [4]:

$$k_1 = 1 - \left(1 - \frac{E_{90}}{E_0}\right).\frac{a_{m-2}{}^3 - a_{m-4}{}^3}{a_m{}^3} \qquad (1)$$

$$k_1 = 1 - \left(1 - \frac{370}{12000}\right).\frac{71^3 - 17^3}{125^3} = 0.73$$

The effective bending stiffness [4]:

$$(EI)_{eff} = E_0 \cdot \frac{b.a_m{}^3}{12} \cdot k_1 \qquad (2)$$

Using Eqn (2) the effective bending stiffness is found to be 1.61 x 10^{12} Nmm^2/m.

Flexure Check:

The governing stresses are the bending stresses at the outermost fibre of the outer panel, with the line of action parallel to the line of action. The outer fibre bending stress, bending perpendicular to the plane and parallel to the grain direction of the outer layer is given by[4]:

$$\sigma_{m,d} = \frac{M}{(EI)_{eff}} . E_0 . \frac{a_m}{2} \qquad (3)$$

The design bending stress from Eqn, (3) is 6.93 N/mm2.

The bending strength is given by:

$$f_{m,d} = \frac{k_{mod} \cdot f_{m,k} \cdot k_1}{\gamma_m} \qquad (4)$$

The bending strength calculated using Eqn (4) is 12.67 N/mm^2 so the panel is okay in flexure.

Shear Check:

The verification of shear forces is based on the simplified method [5]. In this method the maximum shear stress is verified with the maximum allowable rolling shear stress.

The maximum shear stress is given by:

$$\tau_{v,d} = \frac{1.5\ x\ V_d}{A_{net}} \qquad (5)$$

The design shear stress calculated using Eqn (5) is 0.81 N/mm^2.

The design rolling shear strength is given by:

$$f_{r,d} = \frac{k_{mod}\ x f_{r,k}}{\gamma_m} \qquad (6)$$

The design shear strength calculated using Eqn (6) is 0.96 N/mm^2 so the panel is okay in shear

Deflection Check:

The deflection is limited to L/250 based on Table NA.3 of Eurocode 5:1-1. The calculated deflection is determined from Eqn (7.2) of Eurocode 5: 1-1.

$$Allowable\ Deflection: u_{allow} = \frac{4000}{250} = 16mm$$

Total deformation is calculated based on deformation caused by permanent actions, G, and variable actions, Q.

$U_{fin} = u_{fin,G} + u_{fin,Q}$ (7)

$u_{fin} = 7.44 + 4.16 =$ 8.98 mm

The deflection limit is not exceeded for this panel.

4.1.4.b Mechanically Jointed Beams Method

The same loadings as used for the Composite Method calculations will be applied for the Mechanically Jointed Beams method.

$$M_d = 14.88\ kNm/m\ width \qquad \tau_d = 38.16\ kN/m\ width$$

The CLT panel chosen has a thickness of 125mm, with 5 layers, as seen in Figure 11.

The connection efficiency factors are given by [6]:

$$\gamma_1 = \left(1 + \frac{\pi^2 . E . A_1 . d_2}{l^2 . G_r . b}\right)^{-1} \quad (8)$$

$$\gamma_3 = 1$$

$$\gamma_5 = \left(1 + \frac{\pi^2 . E A_5 . d_4}{l^2 . G_r . b}\right)^{-1} \quad (9)$$

$$\gamma_1 = \gamma_5 = \left(1 + \frac{\pi^2 x 12000 x 27000 x 27}{3200 x 50 x 1000}\right)^{-1} = 0.86$$

For the selected panel configuration, γ_1 and γ_5 are both equal to 0.86.

The effective second moment of area, I_{eff}, is then found from Eqn (10) to be 1.15 x 10^8 mm^4/m.

$$I_{eff} = I_1 + I_3 + I_5 + \gamma_1 a_1{}^2 A_1 + \gamma_3 a_3{}^2 A_3 + \gamma_5 a_5{}^2 A_5 \quad (10)$$

Flexure Check:

The panel is to be checked for flexure. The governing stresses are the bending stresses at the outermost fibre of the outer panel:

$$\sigma_{m,d} = \frac{M}{I_{eff}} . \left(\gamma_1 a_1 + \frac{d_1}{2}\right) \quad (11)$$

For the design bending moment, the bending stress is 7.19 N/mm^2.

The bending strength is given by:

$$f_{m,d} = \frac{k_{mod} \cdot f_{m,k}}{\gamma_m} \quad (12)$$

Using Eqn (12), the design bending strength is 15.36 N/mm2 so the flexural stresses are safe.

Shear Check:

The maximum shear stress is as above in the Composite Theory Method

Deflection Check:

The calculated final deflection, of 8.39 mm, is less than the allowable deflection of 16 mm so this serviceability condition is satisfied.

4.2 Wall Panel Design

The wall panel design is based on the Composite theory method. The critically loaded wall panel is on floor 2.

Table 3: Loadings on CLT Wall Panel

	Thickness (mm)	Characteristic Density (kg/m^3)	Loading (kN/m^2)
Wall Panel			
CLT Panel	153	530	0.795
Fermacell Wall panel (2 x 30)	60	1150	0.677
		g_k (kN/m^2)=	1.472
		Wall Height (m)=	3
		g_k (kN/m)	4.42

Of particular interest with the wall panel design is the racking loads due to wind.

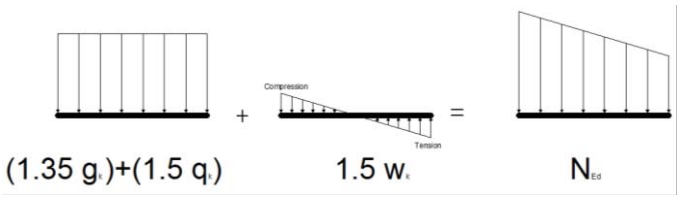


Figure 11 Load acting on Internal Wall

A wall panel of 153mm thickness was chosen. This satisfied the design for end bearing capacity and Compression Strength considering buckling.

4.3 Bearing Resistance

With the use of the platform method of construction, the bearing resistance of the floor panels becomes a critical issue. At floor 2 and floor 3 the bearing resistance of the 125mm thick floor panel was insufficient. Additional measures were required to reinforce the floor panel.

At floor 3 the floor panel was reinforced using self-tapping screws. Screws of Ø 5mm and a length of 120mm were provided.

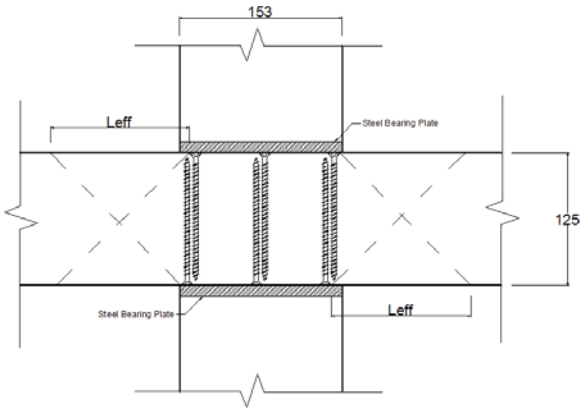


Figure 12 Arrangement of Bearing Reinforcement with Self-Tapping Screws

At floor 2, no arrangement of self-tapping screws was found to adequately reinforce the area. The use of steel dowels was found to provide the required reinforcement. Steel dowels of grade S275 and Ø 14mm were used. 19 dowels were required per metre.

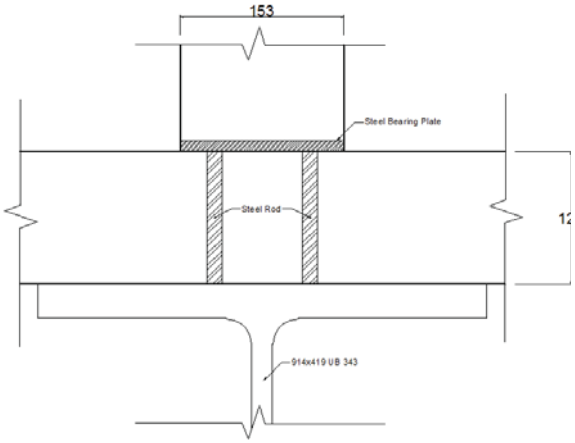


Figure 13 Arrangement of Bearing Reinforcement with Steel Dowels

4.4 Connection Design

Due to the wind loads, steel brackets were provided as hold-down and sliding fixings.

Hold-down fixings were required where tension forces at the extreme ends of the wall panels occur. Tension forces are due to wind loading. The tension forces at the extreme end of the wall panels on floor 2 are the critical loading. The tension force per wall is 50.88kN. This creates a tension force in the vertical screws in the fixings and a shear force in the horizontal screws. A bracket is placed on both sides of the wall panel at each end. 9 vertical screws are required per bracket and13 horizontal screws are required per bracket.

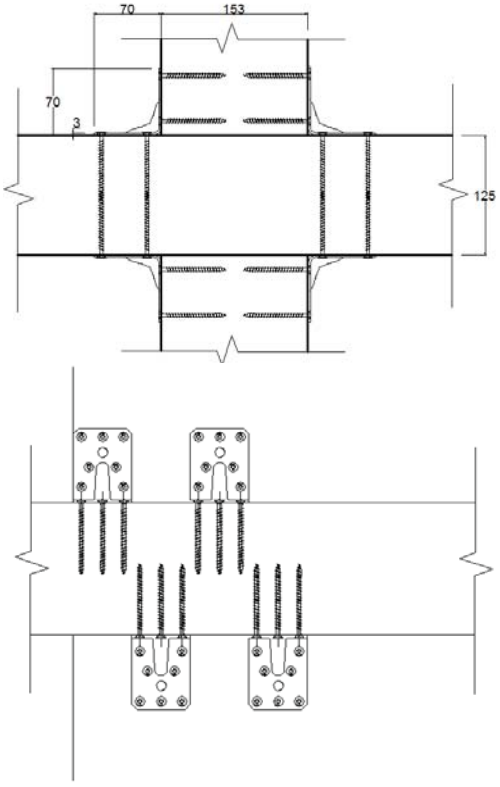


Figure 14 Arrangement of Hold-Down Fixings

Fixings were required to prevent sliding between wall and floor panels. The dead load and friction forces are discounted for this design. The sliding forces at floor 2 are the critical loading. The sliding force, per wall, is 91.37kN. A total of 45 screws were required per wall. These were divided between 6 brackets per wall

5 CONCLUSION

The advent of new engineered wood products, such has cross laminated timber, has paved the way for more demanding applications for timber in construction. In recent years, several multi-storey buildings in timber have been completed using this technology.

Some examples of this are described and the technology has been used in the design of a10 storey hotel building. The design approach for those solid wood panels has been demonstrated for sample floor and wall panels. With timber construction, the design of connections is an important consideration, with the consideration of wind loading being paramount. The bearing resistance of CLT floor panels is a critical issue, with reinforcement being required in some instances.

REFERENCES

[1] Thomson, H (2011). *A Process Revealed Auf Dem Holzweg*. London: Murray and Sorrell FUEL. 80.
[2] Enquist, B., Serrano, E., Vessby, J. (2010). Vertical relative displacements in a medium-rise CLT-building. Structures and Architecture: Proceedings of the First International Conference on Structures and Architecture, ICSA 2010, Guimarães, Portugal, 388-395
[3] Serrano, E. (2009). Documentation of the Limnologen Project: Overview and Summaries of Sub Projects Results.
[4] Blass, H. J., Fellmoser, P., "Design of solid wood panels with cross layers", proceedings of the 8th World Conference on Timber Engineering, WCTE 2004, June 14-17, Lahti, Finland, 2004, pp. 543-548.
[5] TRADA (2009). Worked Example: 12-storey building of Cross Laminated Timber.
[6] NSAI (2005). I.S. EN 1995-1-1:2005+NA:2010
[7] Metsä Wood (2012) Leno Cross laminated Timber- CLT

Structural Performance of Timber Connections

Daniel Coleman[1], John Justin Murphy[1]
[1]Department of Civil, Structural and Environmental Engineering, Cork Institute of Technology, Rossa Ave, Co. Cork, Ireland
email: daniel.coleman@mycit.ie, John.JustinMurphy@cit.ie

ABSTRACT: This paper sets out to assess the stiffness of nailed corbel timber-to-timber connections, and presents the results of physical testing undertaken using moment-rotation curves. The Eurocode design moment resistances for the nail configurations tested are also presented. Three-dimensional models were developed accounting for fastener-timber and timber-timber interaction. The finite element software package LUSAS V14.7 was used to model the connections and the results obtained were compared with the experimental tests. It was found that for some of the tests undertaken, the Eurocode design moment resistances were slightly higher than the test elastic moments. Initial studies suggest that the intricate behaviour at the nail-to-timber interface is best modelled using joint elements to simulate the nail-holding force.

KEY WORDS: Timber; Nail; Connection; FE-model.

1.0 INTRODUCTION

Timber is a non-homogeneous and orthotropic material, and thus strength is affected by the direction of load relative to the direction of the grain [1]. Structural properties of timber vary within and between species, and because timber is biological in nature it is very susceptible to variations in environmental conditions.

The strength and stability of any structure depends on the connections holding components together, whether fastened using nails, bolts or glue.

In a nailed connection, timber under a nail shank shows very intricate behaviour. In contrast to other dowel-type connections, the complexity associated with nailed connections arises from the existence of a nail-holding force and the different failure criteria applicable [2]. On driving a nail into timber, the timber fibres are displaced by the nail. The movement of these fibres is restricted by the surrounding timber causing compressive normal stresses to develop at the nail-timber interface. Such stresses produce the high initial stiffness of nailed connections counteracting pointside withdrawal of a nail. When an external load is applied, withdrawal resistance induces tension in the nail resulting in a pre-tensioning effect on the timber. Friction generated between members is caused by nail tensioning, further adding to the initial stiffness of nailed connections.

The knowledge of the mechanical behaviour of joints is particularly important for timber engineers. Two possible approaches in the field of joint mechanics are:

- Experimental;
- Numerical.

The aim of the paper is to assess the behaviour of nailed timber connections by means of testing and finite element modelling and to compare the results with those obtained using the Eurocode I.S. EN 1995-1 (EC5) [8].

2.0 EXPERIMENTAL TESTING

2.1 Test Setup

This part of the study presents results of a typical experimental programme that comprised 18 tests, performed in accordance with BS EN 26891:1991 [9]. Figure 1 shows the joint geometry and test configuration. Three different nail configurations were tested for two nail types. Three tests were carried out for each nail type and configuration. The joint geometries have been summarised in Table 1.

The connection consisted of two timber members (225 x 40 mm) of equal length cantilevering from a vertical member measuring 225 x 75 mm (see Figure 1 (a)). All timber sections were structural grade C24, Sitka Spruce. The moisture content of the timber used for testing varied from 14% to 20%.

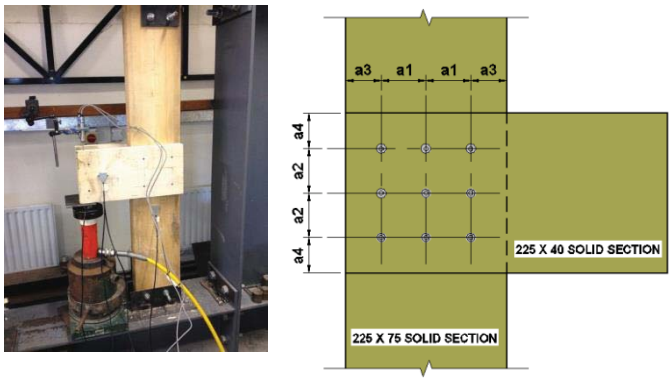


Figure 1. Joint geometry and nail configuration.

As outlined in Table 1, the corbel tests were completed using 100 mm and 75 mm nail shaft lengths. The nail diameters also differed. For the purposes of identification, the 100 mm nails were denoted *"nail type A"* and the 75 mm nails denoted *"nail type B"*.

A load cell, inclinometers and displacement transducers were mounted to record digital values of load, rotations and displacements. Figure 2 shows the sensor layout, which is similar for each test undertaken.

Table 1. Geometries of the timber-to-timber joints

Nail Configuration		Nail Size (mm)			Nail Spacing – cantilever member (mm)			
Ref. No.	Layout	$Ø_h$	$Ø_s$	L_s	a_1	a_2	a_3	a_4
1	2 x 2	8.83	4.52	100	125	125	50	50
2	2 x 3	8.83	4.52	100	62.5	125	50	50
3	3 x 3	8.83	4.52	100	62.5	62.5	50	50
4	2 x 2	8.23	4.02	75	125	125	50	50
5	2 x 3	8.23	4.02	75	62.5	125	50	50
6	3 x 3	8.23	4.02	75	62.5	62.5	50	50

Note: $Ø_s$ is the head diameter
$Ø_s$ is the shaft diameter
L_s is the shaft length

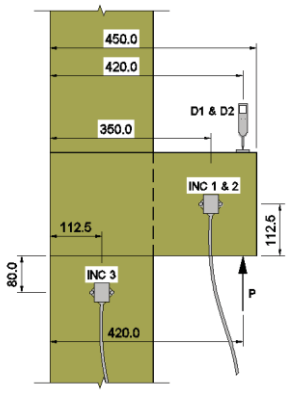


Figure 2. Sensor layout – corbel connection.

2.2 *Experimental Results – Moment Rotation Curves*

For each of the nail layouts tested, the applied moment was plotted against the rotations measured on inclinometers 1 and 2. Rotations calculated from deflections measured on deflection gauges 1 and 2 enabled the identification of variations between test results.

The results recorded for both inclinometers and deflection gauges were broadly similar; thus, only inclinometer 1 results are presented here. Figure 3, Figure 4 and Figure 5 show the combined moment-rotation curves for nail type A; Figure 6, Figure 7 and Figure 8 show the combined moment-rotation curves for nail type B.

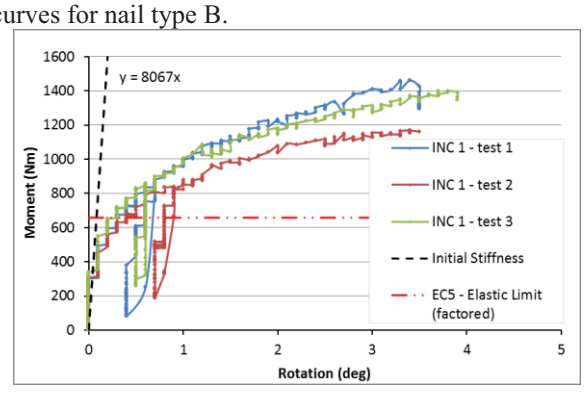


Figure 3. Moment-rotation curve (2 x 2, nail type A).

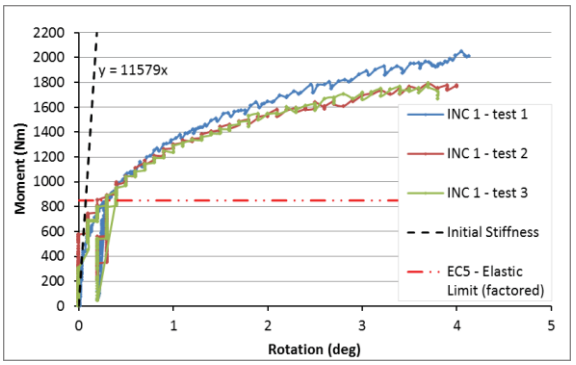


Figure 4. Moment-rotation curve (3 x 2, nail type A).

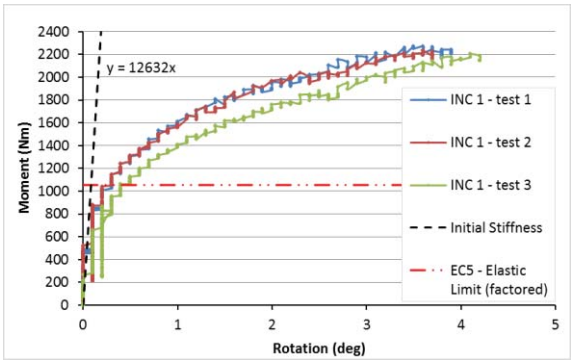


Figure 5. Moment-rotation curve (3 x 3, nail type A).

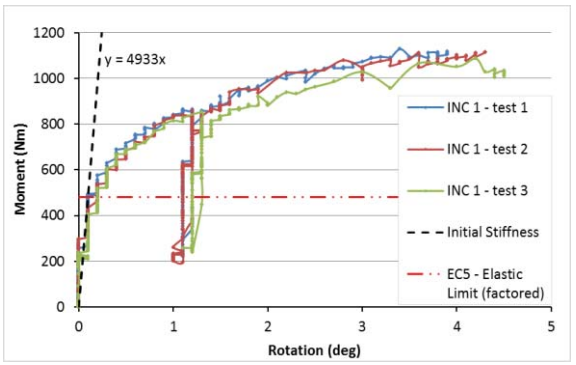


Figure 6. Moment-rotation curve (2 x 2, nail type B).

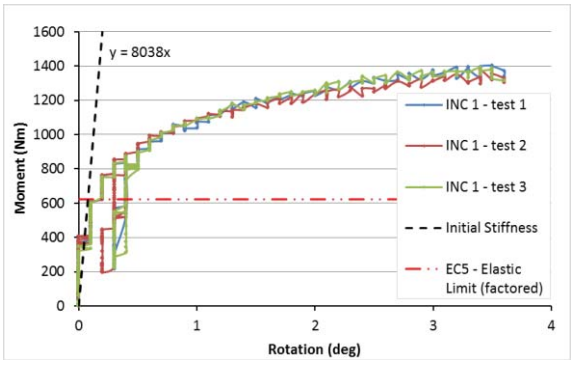


Figure 7. Moment-rotation curve (3 x 2, nail type B).

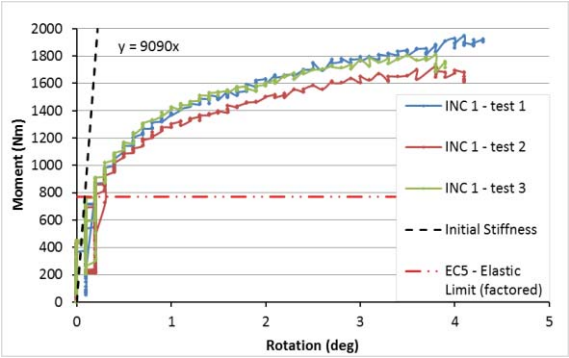


Figure 8. Moment-rotation curve (3 x 3, nail type B).

Considering the inherent variability of timber, the results for each nail configuration show good agreement.

The initial stiffness of each connection was plotted based on the line of best fit and the slope calculated. The equivalent EC5 factored elastic moment capacities for the specified nail configuration, represented by the dashed red lines.

An important part of this analysis was the determination of the initial stiffness of each connection. The difference in moment-rotation curves was also assessed. Table 2 shows the initial stiffnesses based on test data for each connection. As expected, the initial stiffnesses and resultant moment capacities were lower for nail type B (75 mm nails) than for nail type A (100 mm nails).

Table 2. Initial stiffnesses and EC5 moment capacities.

Ref. No.	Initial Stiffness	EC5 Design Moment	Test Elastic Moment	Maximum Test Moment
	(kNm/ °)	(Nm)	(Nm)	(Nm)
1 (2x2, nail A)	8.0	658	550	1315
2 (3x2, nail A)	11.6	850	750	1918
3 (3x3, nail A)	12.6	1054	825	2238
4 (2x2, nail B)	4.9	481	475	1108
5 (3x2, nail B)	8.0	622	625	1388
6 (3x3, nail B)	9.1	771	775	1835

Table 2 also shows the test elastic moments and the maximum test moments recorded. For each nail configuration, the test elastic moment was between 37% and 45% of the maximum test moment. The EC5 design moment resistances are also presented. For nail type A, the EC5 design moments are greater than the test elastic moments, while for nail type B the values are almost identical.

The elastic moment capacity of each connection occurred at a net rotation approximately equal to 0.6° regardless of the number of nails, nail configuration and nail geometric properties.

2.3 Additional Testing

2.3.1 Nail Strength

Destructive tests were carried out on three 100 mm common wire nails, to determine their characteristic strength. At failure a tensile capacity of 861 MPa was recorded for a nail diameter of 4.52 mm.

2.3.2 Friction Coefficient

A test was carried out to determine the friction coefficient (μ) for the contacting timber members; an average value of μ = 0.55 was obtained.

2.4 Prediction of the Elastic Moment Capacity

When a shear force is applied at an eccentricity to the centroid of a nail group, the effects on the nail group must be considered. The force distribution was determined on the basis of an elastic analysis.

The translation force, F_s was calculated by dividing the applied load, P by the number of nails (N). Figure 9 shows the nail reaction forces due to the rotational forces. The rotational force, F_T requires the use of an elastic torsion equation, based on the assumptions that:

- The stress in each nail is proportional to its distance from the centroid of the nail group.
- The nail reaction forces are perpendicular to their radial line from the centroid of the nail group.

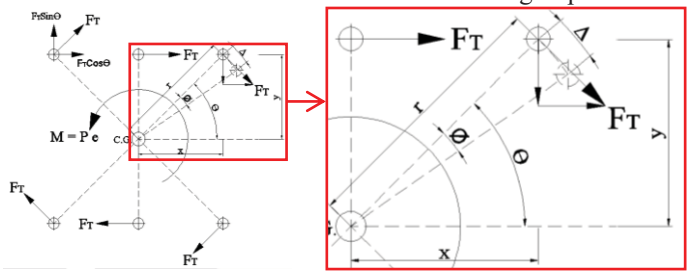


Figure 9. Rotational reactions.

Based on these assumptions, the nail reaction forces were resolved into horizontal and vertical components. The component forces were vectorially added to the results of the translational computations. The resultant vector forces were used to determine the force in a single nail, F_{NAIL} (see Equations 1 and 2).

$$F_{NAIL} = \sqrt{F_S^2 + F_T^2 + 2F_S F_T \text{Cos}\emptyset} \quad (1)$$

where, F_S translational nail force,
F_T rotational nail force.

$$F_{NAIL} = \left\{ \left(\frac{P}{N}\right)^2 + \left(\frac{\text{Per}_i}{\sum x^2 + y^2}\right)^2 + 2\left(\frac{P}{N}\right)\left(\frac{\text{Per}_i}{\sum x^2 + y^2}\right)\text{Cos}\emptyset \right\}^{1/2} \quad (2)$$

where, P applied load,
N number of nails,
e eccentricity to centroid of nail group,
r distance from centroid of nail group to nail considered,
x distance from centroid of nail group to nail considered in the x-direction,
y distance from centroid of nail group to nail considered in the y-direction,
Ø angular rotation of a single nail.

The allowable load, P was calculated by letting F_{NAIL} equal to the allowable load carrying capacity of a nail in single shear calculated using Expression 8.6 in EC5.

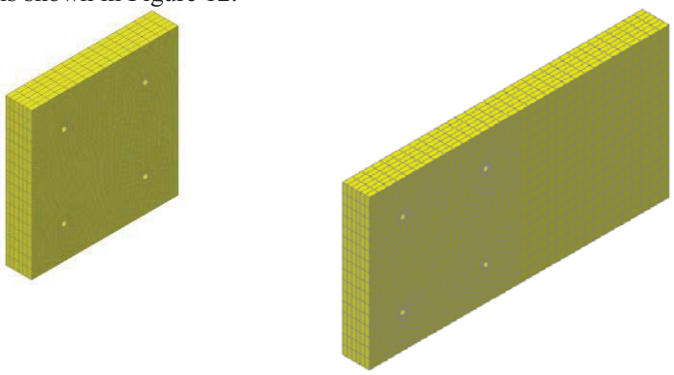
3.0 FINITE ELEMENT MODELLING

Preliminary work on finite element modelling was undertaken. The modelling process is graphical and divided into a number of sub-sections. In the following, the structure of the model is described.

3.1 Model Build Up

The connection modelled for this analysis consisted of five different parts. Parts 1 to 5 comprise solid elements that create the corbel connection. Each component was first modelled in the x-y plane using a coordinate system. Attributes were assigned, and then the planes were extruded in the z-direction to the required thickness.

In Parts 1 and 2, which are the column and beam components shown in Figure 10 (a) and (b), holes have been made for the wooden rings twice the diameter of the nails. The wooden rings (Parts 3 and 4) are constructed from a cylinder fitting the holes generated in Parts 1 and 2. A hole through the cylinder was defined to facilitate the nail. Attributes assigned to the wooden rings for the column and beam section differ. The wooden rings are shown in Figure 11. The nail was modelled as a solid element similar to a dowel. To reduce mesh density and slideline assignments, the nail head was not modelled. The nail is denoted as Part 5 and is shown in Figure 12.



(a) **(b)**

Figure 10. (a) Part 1 – Half of the column, (b) Part 2 – 225 x 40mm cantilever beam.

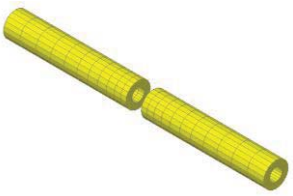


Figure 11. Parts 3 and 4 – Beam and column wooden rings.



Figure 12. Part 5 – One of the common wire nails.

3.2 Meshing and Boundary Conditions

Typically, dowel type connections are three-dimensional problems. Thus, in this study, a 3D-FEM model was developed using the LUSAS software package. 8-noded hexahedral elements were used. Two types of external boundary conditions were considered: those due to symmetry considerations and those due to the loads. By considering symmetry only half the cantilever member and column were modelled.

3.3 Material Modelling

3.3.1 Steel

The steel used for the nails in the analysis has a Modulus of Elasticity of E_s = 210,000 MPa, a Poisson's ratio of v_s = 0.3, and a characteristic yield strength of f_{uk} = 861 MPa. A bi-linear stress-strain curve was used to define the steel fasteners.

3.3.2 Timber

Timber is an orthotropic material with different material properties in three perpendicular directions - longitudinal, *l*, radial, *r*, and tangential, *t* as shown in Figure 13. When calculating the load carrying capacities of the nails, the strength parameters were based on structural strength class C24, with a density of ρ_k = 420 kg/ m^3.

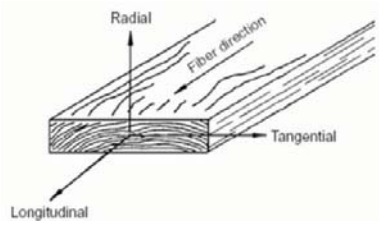


Figure 13. Three orthotropic material directions [4].

Table 3 indicates the values of Young's Modulus, *E,* Poisson's ratio, *v*, and Shear Modulus, *G*, as inputted into the LUSAS software package. Due to the orthotropic behaviour of timber, the stiffness parameters shown in Table 3 vary for each of the three directions. Radial and tangential directions are interchangeable. Given that the beam orientation was perpendicular to the column, LUSAS input values differed.

Table 3. Stiffness properties of timber (beam).

LUSAS Input	**Units**	***Beam***		***Column***	
E_x	MPa	E_l	10890	E_t	468.3
E_y	MPa	E_t	468.3	E_l	10890
E_z	MPa	E_r	849.4	E_r	849.4
G_{xy}	MPa	G_{lt}	664.3	G_{tl}	664.3
G_{yz}	MPa	G_{tr}	32.7	G_{lr}	697
G_{xz}	MPa	G_{lr}	6967	G_{tr}	32.7
v_{xy}	-	v_{lt}	0.467	v_{tl}	0.025
v_{yz}	-	v_{tr}	0.245	v_{lr}	0.372
v_{xz}	-	v_{lr}	0.372	v_{tr}	0.245

The values of Young's Modulus, Shear Modulus and Poissons's ratio in Table 3 are obtained from Table 1 of IS EN 338: 2003 [3] and research by *Green et al.* [5].

The timber was modelled as an orthotropic material with linear elastic-plastic behaviour with the yield surface defined using the Hill failure criterion, which is a generalised version of the von Mises yield criterion that accounts for the anisotropy of the material [6].

Dias et al. [6] present a relationship between yield stresses used to define the Hill failure criterion and suggest that the equivalent yield strength of spruce is 33 MPa. The ratios between the yield strengths and the equivalent yield strength for Hill failure criterion are defined according to Equation 3[(6)].

$$\frac{\sigma_0}{\bar{\sigma}} = 1; \quad \frac{\sigma_{90}}{\bar{\sigma}} = 0.19; \quad \frac{\sqrt{3}\sigma_v}{\bar{\sigma}} = 0.38 \tag{3}$$

where, σ equivalent yield stress for isotropic behaviour,
σ yield strength in the direction parallel to the grain,
σ_{90} yielding strength in the direction perpendicular to the grain,
σ_v yield shear strength.

The values used to describe the timber failure are shown in Table 4 and are based on an equivalent yield strength equal to 33 MPa.

Table 4. Hill failure criterion specified.

LUSAS Input		Units
TEN/ COMP. Yield Stress (tangential, t direction)	6.27	MPa
TEN./ COMP. Yield Stress (longitudinal, l direction)	33	MPa
TEN./ COMP. Yield Stress (radial, r direction)	6.27	MPa
Shear Yield Stress (tl)	7.24	MPa
Shear Yield Stress (lr)	7.24	MPa
Shear Yield Stress (tr)	7.24	MPa
Initial Uniaxial Yield Stress	33	MPa

3.4 Contact Description

Three different models were generated to determine the optimum method of modelling the timber-timber and nail-timber interaction.

3.4.1 Approach 1

In the interaction segment of the modelling process, the contact behaviour between the surfaces was defined. For Approach 1 the interaction between different members was modelled using frictional slidelines. Slideline properties are defined in a slideline attribute, which is assigned to each of the contacting bodies using a master and slave assignment [7].

The friction coefficient between the fasteners and the timber was set equal to 0.65; the timber-to-timber friction coefficient was set equal to 0.55.

3.4.2 Approach 2 – Model 1

The interaction between the nail and timber was defined using joint elements with three translational degrees of freedom. Joint elements are used to connect two or more nodes by springs, with translational and rotational stiffnesses.

Firstly, independent joint elements were assigned to the column and beam members. Within each member, two types of joint material properties were designated, depending on the expected deformed shape of the nail and nail hole.

As the load, *P,* is applied the beam rotates, causing the nails to deform. The deformation of the nails causes crushing of the timber over a given surface area, while the nail separates from the timber at other contact surfaces. The red arc in Figure 15 highlights the expected crush zone of the beam component for the given nail configuration. Therefore the springs defining the interaction between the nail and timber were assigned an infinite stiffness in the x and y directions along the red arc. This ensured that the specified nail surface remained in contact with the opposing wooden rings throughout the analysis. The three remaining quadrants were assigned a low stiffness of 0.2 N/ mm/ mm^2, allowing the nail to pull away from the timber enabling bending of the nail to occur.

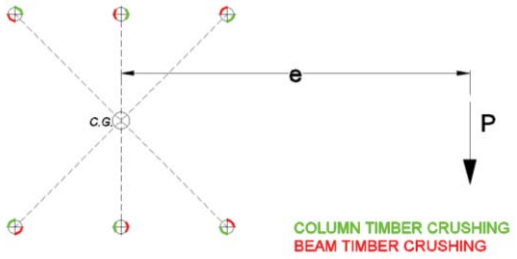


Figure 14. Infinite stiffness assignments in the xy plane.

The green arc in Figure 15 shows the expected crush zone in the column where infinitely stiff springs were assigned. Aside from enabling nail bending to occur, this also ensured that the nail did not penetrate the timber. The remaining quadrants were assigned a similar stiffness to the equivalent interface surfaces of the beam.

Stiffness in the z-direction i.e. out of plane was relatively low, allowing withdrawal to occur once the withdrawal resistance of a nail defined by the spring stiffness was exceeded.

The timber-to-timber interface was defined using friction slidelines as for the preceding model with $\mu = 0.55$.

3.4.3 Approach 2 – Model 2

Joint elements were used to define both nail-to-timber and timber-to-timber interaction. The joint elements used to define the contact behaviour between the nail and timber were the same as for Approach 2 – model 1.

A 3 mm gap was defined between adjacent timber members. The purpose of the gap was to enable the nail to bend and capture the failure of the connection. The model used spring elements with three translational degrees of freedom, similar to the nail-timber interaction defined. Stiffness parameters assigned in the x and y directions were 0.01 N/ mm/ mm^2. The joint elements assigned were used to model the effect of friction at the timber interface.

3.5 Numerical Results and Analysis

To calibrate the FE model generated, load-displacement curves were plotted (see Figure 15). The data set for connection Ref. No. 4 was plotted and the results of the numerical analysis superimposed.

3.5.1 Approach 1

The curve for the numerical analysis shows signs of non-linearity; this is primarily due to the timber crushing. The numerical simulation underestimates the initial stiffness of the connection.

Slidelines did not account for the compressive stresses on the nail shaft. A limited nail-holding force and resultant nail-tensioning effect at the timber interface have caused the poor representation of initial stiffness.

3.5.2 Approach 2 – Model 1

The Approach 2 load-displacement curve gives a better representation of initial stiffness than Approach 1. The elastic limit of the connection was overestimated.

3.5.3 Approach 2 – Model 2

The numerical model underestimated the initial stiffness of the connection similar to Approach 1; however, the load-displacement curve was a better representation of the connection failure than previous models generated. The elastic limit of the connection was overestimated.

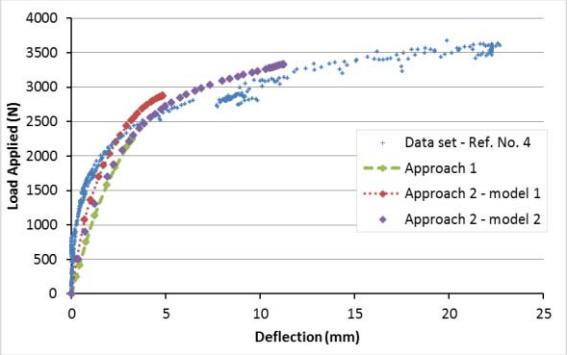


Figure 15. Load-displacement curve – FE models.

3.6 Summary of Numerical Study

It is evident that Approach 2 best represents the tests undertaken. Model 1 provides a good representation of initial stiffness and while model 2 overestimates the capacity of the connection, it produces a good representation of ultimate failure of the test connection. The 3 mm gap between adjacent members for Approach 2 - model 2 was the cause of the reduced initial stiffness.

Springs stiffnesses were assigned based on the deformed shape of FE model Approach 1 and the theoretical distribution of nail forces i.e. user defined specification of restraint conditions at the nail-timber interface.

The main factor affecting FE model Approach 1 was the failure of the slideline attribute to simulate the nail-to-timber interaction. The nail-holding forces, exerted by the compressive normal stresses by the displaced timber fibres were not taken into account.

An automatic approach using elasto-plastic (tension and compression unequal) joint elements is therefore proposed. This would enable the specification of initial spring stiffnesses and tension and compression yield stresses beyond which the spring stiffnesses change to a user-defined value. The model would automatically identify between areas of compression and tension.

4.0 CONCLUSIONS

The physical testing undertaken has shown the influence of nail configuration on a connection's initial stiffness, and elastic and ultimate moment capacities. Increasing shaft length and nail diameter increases a connection's initial stiffness and subsequent moment capacity. The test results indicate an initial yield point, which is approximately 40% of the ultimate moment capacity.

Based on EC5 and an elastic analysis of nail forces, the elastic moment capacities of the nail configurations tested were determined. For nail type A, the EC5 design moment resistances are greater than the test elastic moments, while for nail type B the values are almost identical.

The proposed FE models show the capacity to describe the behaviour of timber-to-timber joints made with nail fasteners using LUSAS. The load-deflection curves obtained from the testing undertaken were used to validate the finite element models generated. Three models were generated using different techniques to define the nail-to-timber and timber-to-timber interaction. The ability of the models to simulate the actual behaviour was investigated by comparing the models with experimental results. Approach 2 - model 1 best represents the desired load-displacement curve for connection Ref. No. 4. The intricate behaviour at the nail-to-timber interface was best modelled using joint elements to simulate the nail-holding force. Observations suggest that the most appropriate method of modelling initial stiffness is through the use of frictional slidelines at the timber-to-timber interface.

5.0 RECOMMENDATIONS

Future research should expand on present research, considering:

- Accurate definition of the nail-to-timber contact behaviour;
- Timber failure definition using the Hill failure criterion in which it is proposed that failure parameters be determined by testing;
- Effect of a nail-holding force and nail-tensioning on a connection's initial stiffness;
- Further development of the LUSAS model incorporating additional joint arrangements;
- Elasto-plastic joint element's ability to replicate the the nail-to-timber interaction;
- Assessment of the influence of fracture mechanics and damage evolution on the ability of a model to simulate the mechanical behaviour of a given connection.

REFERENCES

[1] Aghayere, A. and Vigil, J. *Structural Wood Design: A Practice-Oriented Approach Using the ASD Method.* Hoboken, New Jersey: John Wiley & Sons, 2007.

[2] Hong, J.P. and Barrett, D.J. *Three-dimensional finite element analysis of nailed connections.* Vancouver, Canada: University of British Columbia, 2010.

[3] IS EN 338:2003. *Structural Timber. Strength Classes.* NSAI, 2003.

[4] Redzuan, A. *Mechanical Properties and Bending Strength Theory for Malaysian Structural Timber.* Malaysia: University Technology Malaysia, 2008.

[5] Green, D.W., Winady, J.E. and Kretschmann, D.E. *Mechanical Properties of Wood Chpt. 4.* 2002.

[6] Dias, A.M.P.G., Van de Kuilen, J.W., Lopes, S. and Cruz, H. *A non-linear 3D FEM model to simulate timber-concrete joints.* pp. 552-530. Vol. 38, Advances in Engineering Software: Elsevier Ltd., 2005.

[7] LUSAS_14.5. *LUSAS Modeller On-line Help.* LUSAS Version 14.5, 2011.

[8] IS EN 1995-1-1:2005. *Eurocode 5: Design of timber structures - Part 1-1: General - Common rules and rules for buildings.* NSAI, 2008.

[9] BS EN 26891:1991. *Timber structures - Joints made with mechanical fasteners - General principles for the determination of strength and deformation characteristics.* BSI, 1991.

Bond quality of cross-laminated timber from Irish Sitka spruce

Karol Sikora[1], Annette Harte[1], Daniel McPolin[2]
[1]College of Engineering & Informatics, National University of Ireland, Galway, University Road, Galway, Ireland
[2]School of Planning, Architecture and Civil Engineering, Queen's University Belfast, University Road, Belfast BT7 1NN, UK
email: karol.sikora@nuigalway.ie, annette.harte@nuigalway.ie, d.mcpolin@qub.ac.uk

ABSTRACT:
The potential use of Irish-grown Sitka spruce for cross-laminated timber (CLT) manufacture is investigated as this would present new opportunities and novel products for Irish timber in the home and export markets. CLT is a prefabricated multi-layer engineered wood product made of at least three orthogonally bonded layers of timber. In order to increase rigidity and stability, successive layers of boards are placed cross-wise to form a solid timber panel. Load-bearing CLT wall and floor panels are easily assembled on site to form multi-storey buildings. This improves construction and project delivery time, reduces costs, and maximises efficiency on all levels.
The paper addresses the quality of the interface bond between the laminations making up the panels, which is of fundamental importance to the load bearing capacity. Therefore, shear tests were carried out on nine test bars of three glue lines each. Moreover, delamination tests were performed on samples subjected to accelerated aging, in order to assess the durability of bonds subjected to severe environmental conditions. In addition, this paper gives an indication on thickness tolerances of planed Irish Sitka spruce lamellas, which is likely to be a critical factor for bonding quality and adhesive selection. The test results of bond quality presented in this study were within requirements of prEN 16351:2013.

KEY WORDS: Sitka spruce, timber bonding, Cross-laminated timber

1 INTRODUCTION

More and more often construction materials are expected to comply with requirements reaching far beyond a general utility market. New high-performance materials are required not only to be more durable and exhibit a longer life time, even under severe environmental conditions but having consumed less energy during their life cycle. When compared with ordinary materials, they have to be more ecologically friendly and follow sustainability trends. One promising product satisfying such criteria is Cross-Laminated Timber (CLT).

CLT is a prefabricated multi-layer engineered panel wood product manufactured by gluing at least three layers of parallel boards. The wood grains of each layer are orientated perpendicular to wood grains of layers with which it is in contact. The number of laminates in CLT is odd, therefore face layers are parallel to each other. The advantages of this specific orientation between the laminates in regard to the load displacement and failure behaviour of such composite include increase in bearing capacity against in-plane and out-of-plane stresses, rigidity and stability [1-5]. The natural variations in timber strength, such as knots, are reduced in CLT in comparison with construction timber. Furthermore it is reported that cross-lamination of the boards reduces the degree of anisotropy in properties in the plane of the panel [6-9]. Moreover, load-bearing CLT wall and floor panels are easily assembled on site to form multi-storey buildings. This improves construction and project delivery time, reduces costs, and maximises efficiency on all levels [5, 10-13].

In order to investigate the suitability and to support the commercialisation of Irish-grown Sitka spruce for the manufacture of CLT panels, the development of necessary engineering data is required. The quality of the interface bond between the laminations making up the panels is of fundamental importance to the load bearing capacity. As a part of the testing programme of the project 'Innovation in Irish Timber Usage', shear tests were carried out on Sitka spruce bars with edge bonds in order to investigate their shear performance. Shear tests of glue lines are required in the course of factory production control in CLT plants. In most of the standards, the method of applying shear stress to the glue line is only given by a schematic diagram [14, 15]. The shear test tool used in the present study was manufactured in accordance with Annex D of prEN 16351:2013 Timber structures – Cross laminated timber – Requirements [16] that is based on EN 392 [17] and dimensions proposed by Steiger et al. [14, 15]. Moreover, delamination tests were performed on samples subjected to pressure soak-drying cycles, in order to assess the durability of bonds subjected to severe environmental conditions.

2 MATERIALS AND METHODS

The investigation of the quality of the bonded interface involved thickness tolerance testing of the boards, shear tests of the edge bonds and delamination testing.

2.1 Materials

In order to ensure a uniform moisture content in the specimens during the testing, boards of Irish Sitka spruce were stored in conditioning chamber (65±5% R.H., 20±2°C) for 3 months before specimen preparation. Subsequently, all sides of the boards were planed by a specialised company to cross-sectional dimensions of 96 mm by 30 mm.

A tight tolerance on the lamination thickness is required for the production of CLT due to the thin bond lines used. Because of this, thickness measurements were taken on the boards immediately after planing to determine whether the required tolerance of 0.1 mm is achieved. Thickness measurements were taken at 0.3 m, 0.6 m and 0.9 m from one end of the board. Two measurements were taken at each location, giving a total of 6 measurements per board. The maximum and minimum thickness values for each board are reported in Table 1, together with the deviation from the nominal value of 30 mm (green shadings for deviation ≤ 0.10 mm and light green for 0.11 mm & 0.12 mm). Only one sample failed to meet the required tolerance (board 5; red shading) and this board was excluded when the test specimens were manufactured.

Table 1. Thickness deviation results.

Board ID	Min value [mm]	Max value [mm]	30 – Min [mm]	Max – 30 [mm]
1	30.03	30.12	-0.03	0.12
2	29.93	30.12	0.07	0.12
3	29.88	30.02	0.12	0.02
4	29.99	30.11	0.01	0.11
5	29.75	30.02	0.25	0.02
6	29.97	30.10	0.03	0.10
7	29.97	30.08	0.03	0.08
8	29.99	30.09	0.01	0.09
9	29.98	30.11	0.02	0.11
10	29.88	30.07	0.12	0.07

For the purpose of specimens manufacture for shear tests, boards were cut to lengths of 300 mm. Two blocks comprising of 4 edge bonded 300 mm long boards were prepared. A single-component polyurethane adhesive, formulated for the manufacture of engineered wood products (PURBOND HB S309), was used to bond the edges of the shear test specimens. The 0.1 mm adhesive layer was applied on one surface of each glue line and 1 MPa pressure was applied by compressive testing machine for 120 minutes. Figure 1 shows the pressing process of shear tests samples.



Figure 1. Pressing of the shear test specimens

After reconditioning (65±5% R.H., 20±2°C), 9 test bars were cut from the blocks. Each of the test bars comprised three glue lines. The dimensions of these tests specimens were in accordance with prEN 16351:2013 [16] and were: 30 mm thick, 384 mm (4 glued pieces of 96 mm) long and 50 mm wide, see Figure 2.

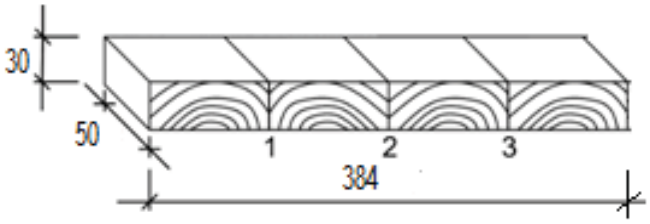


Figure 2. Shear test specimen dimensions

In order to prepare specimens for the delamination tests, a sample CLT panel of 90 mm (3 layers of 30 mm) thickness, 600 mm length and 192 mm width was manufactured. The same adhesive, thickness of adhesive layer was applied as for the shear tests samples. The pressure of 0.8 MPa was applied by compressive testing machine for 120 minutes. After reconditioning, specimens for the delamination tests of glue lines between layers were cut from this panel. Tests were carried out on 10 specimens of 105 mm by 96 mm by 90 mm, as shown in Figure 3.

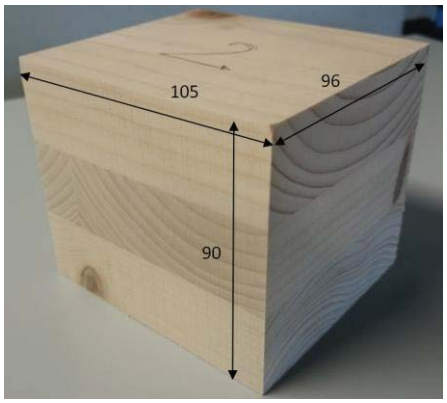


Figure 3. CLT delamination test specimen

2.2 Experimental techniques

The shear tests were carried out by applying a compression force using the shearing tool, which is illustrated in Figure 4. The cylindrical bearing was able to self-align so that the test piece could load at the end-grain with a stress field uniform in the width direction. A compressive testing machine was used to apply a compressive force to the shearing tool, as seen in Figure 5.

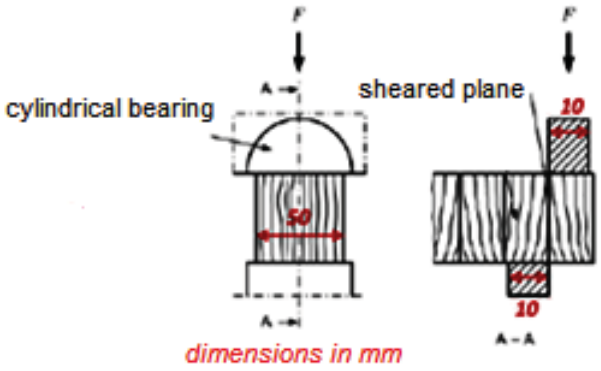


Figure 4. Shearing tool with a test bar inserted (adapted from [16, 17])

The test programme and procedure were in accordance with Annex D of prEN 16351:2013 Timber structures – Cross laminated timber – Requirements [16] that is based on EN 392 [17]. Loading was applied under displacement control at a rate of 3 mm/min, ensuring failure after no less than 20 s, which is in accordance with prEN 16351:2013 [16] and studies by Steiger et al. [14, 15]. The laboratory temperature and relative humidity were recorded as 17.9 ˚C and 63%, respectively. Just after the shearing tests, four samples 50 mm long from each test bar (central parts between glue lines or glue line and end) were cut and weighted in order to determine the density.



Figure 5. Test bar during testing in shearing tool

Test pieces for the glue line delamination tests were placed in the pressure vessel, as shown in Figure 6, and submerged in water at a temperature of about 15 °C. Then a vacuum of about 80 kPa was drawn and held for 30 min. Subsequently, the vacuum was released and pressure of about 550 kPa was applied for 2 h. Later, the test pieces were dried for a period of approximately 15 h in a circulating oven at a temperature of 70±5 °C. After removal from the oven, the delaminated length for each of the two glue lines was measured around the perimeter of the specimen. The maximum delamination length, $l_{max,delam}$ is the greater of these two values and the total delamination length, $l_{tot,glueline}$ is the sum of these two values. The two glue lines were then split using a wedge and hammer, and the wood failure percentage was estimated visually. The lower of the wood failure percentages from the two glue lines, FF_{min} was recorded.
The test programme and procedure were in accordance with Annex C of prEN 16351:2013 [16].

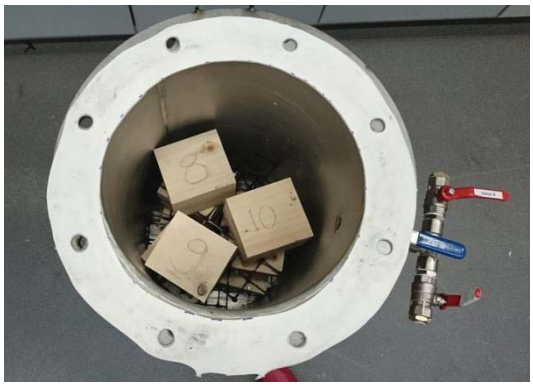


Figure 6. Delamination test samples in pressure vessel

3 RESULTS AND DISCUSSION

3.1 Shear strength

The shear strength was determined for every of 3 glue lines (a, b, c) from nine test bars and the results are given in Table 2. The shear strength was calculated in accordance with prEN 16351:2013 [16] as

$$f_v = k\frac{F_u}{A}$$

where:
F_u is the ultimate load (in N),
A is the sheared area (in mm^2),
k is a modification factor: k = 078 + 0.0044t,
t is thickness (in mm).

Table 2 presents the wood failure percentage of a split glue area that is the ratio of the area with wood failures and the glued area before splitting. Ultimate loads of each test and the determined average densities of two specimens from both sides of glue line for each glue line are also given in the Table 2.

The wood percentage failures were above 80% with exception of 75% for 7a. Wood failure percentages results for PUR type adhesives were generally very high and exhibited a small variation, which corresponds to results obtained by Steiger et al. [14, 15]. It is likely that low percentage in glueline 7a resulted from the presence of a knot on one of the sheared faces that increased the wood strength in this area. Figure 7 shows the glue line 7a after testing in comparison to glue line 8c with 100% wood failure.

The characteristic shear strength, $f_{v,k}$ for all tested glue lines was 7.24 N/mm^2, and mean shear strength was 8.11 N/mm^2 with standard deviation of 0.47 N/mm^2. These results were within the minimum requirement of 3.5 N/mm^2 for characteristic shear strength in accordance with prEN 16351 [16]. These results are also consistent with the findings of Raftery et al. [18] for the shear strength of Sitka spruce specimens bonded using a single component PU adhesive and tested in accordance with ISO 6238. Since the shear strength for each single glue line was above the threshold value of 2 N/mm^2 there is no condition to be satisfied in relation to the wood failure percentage [16]. for glue line a in sample 9, the requirement of wood failure percentage of 100% for each tested glue line with shear strength below 2 N/mm^2, in accordance with prEN16351 [16], was satisfied. However, considering the fact that the mechanical performance of CLT

is largely determined by rolling shear and there is lack of available research on this property for Sitka spruce, the rolling shear strength of Sitka spruce should be comprehensively researched and established.

Table 2. Shear strength and wood percentage failure

Specimen ID		Ultimate load [kN]	Wood percentage failure [%]	Shear strength [N//mm^2]	Density [kg/m^3]
	a	13.64	100	8.29	412.87
	b	13.63	100	8.29	402.13
1	c	12.9	100	7.84	391.29
	a	14.01	100	8.52	401.16
	b	14.12	80	8.58	420.19
2	c	13.21	95	8.03	420.73
	a	13.57	100	8.25	450.91
	b	12.84	90	7.81	408.90
3	c	13.9	100	8.45	412.35
	a	13.52	100	8.22	402.16
	b	13.63	100	8.29	399.43
4	c	13.31	100	8.09	407.93
	a	13.91	100	8.46	407.82
	b	12.91	90	7.85	396.83
5	c	13.38	95	8.14	404.47
	a	13.83	100	8.41	407.89
	b	14.37	100	8.74	406.25
6	c	12.45	90	7.57	416.52
	a	11.75	75	7.14	442.03
	b	14.19	100	8.63	436.33
7	c	13.92	100	8.46	452.14
	a	13.85	90	8.42	458.23
	b	14.06	95	8.55	440.33
8	c	12.39	100	7.53	452.93
	a	11.31	100	6.88	424.25
	b	13.48	100	8.20	438.13
9	c	12.28	100	7.47	459.05
5-percentile Shear strength, $f_{v,k}$:				7.24	
Mean Shear strength:				8.11	
Standard deviation:				0.47	



Figure 7. Glue line 7a (left, 75% wood failure) and 8c (right, 100% wood failure) after test

The maximum delamination $Delam_{max}$ of a single glue line in each test piece was calculated from following formula:

$$\mathrm{Delam_{max}} = 100\,\frac{l_{max,delam}}{l_{glueline}}\ [\%]$$

where:
$l_{max,delam}$ is the maximum delamination length (in mm),
$l_{glueline}$ is the perimeter of one glue line in a delamination specimen (in mm).

The values of total delamination of each test piece and maximum delamination of a single line in each test piece are shown in Table 4. The delamination requirement in prEN16351 [16] can be satisfied in one of two ways:

(1) $\mathrm{Delam_{tot}} \leq 10\%$ and $\mathrm{Delam_{max}} \leq 40\%$ for all samples
or
(2) If condition (1) is not satisfied, the wood failure percentage for each split glued area, FF, must be $\geq 50\%$ and for the sum of the two split areas must be $\geq 70\%$.

None of the specimens passed Condition (1) but all tested specimens fulfilled Condition (2). The delamination occurred only in one of two glue lines for every tested specimen and the wood failure percentage for this glueline is reported in Table 3. As the FF value for the second glueline is 100% the requirement of the minimum wood failure percentage of the sum of all split glued areas ≥ 70% was also satisfied.

Table 3. Total and maximum delamination, and wood percentage failure

Specimen ID	$\mathrm{Delam_{tot}}$ [%]	$\mathrm{Delam_{max}}$ [%]	$\mathrm{FF_{min}}$ [%]
1	16.8	33.7	80%
2	17.6	35.2	75%
3	27.3	54.2	60%
4	16.0	32.0	85%
5	19.5	38.9	70%
6	21.7	43.7	65%
7	17.0	34.0	80%
8	23.1	46.2	65%
9	19.8	39.6	70%
10	28.2	56.3	60%

Although delamination results vary significantly between the test pieces, it is very likely that the mechanism resulted in the delamination of glue lines was the same for all specimens. In all cases delamination occurred in one glue line along one side as presented in Figure 8. Since the vacuum-pressure soak

cycle resulted in swelling, which was much higher in the tangential and radial directions than the longitudinal direction for the timber, it induced significant internal shear stresses between the bonded surfaces.
Furthermore, since there was no edge bonding of the boards in each CLT layer, the lowest bonding area was in the narrowest timber elements, which were part of middle layers in every specimen. Since these elements were placed in one side of test piece, delamination occurred at their surfaces, which may be observed in Figure 9.
Moreover, widths of the narrowest timber elements in each test piece determined the depth of delamination.



Figure 8. Delamination of specimen 6. after vacuum-pressure cycle

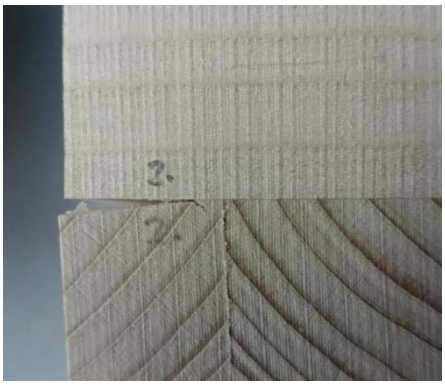


Figure 9. Delamination of specimen 2. after vacuum-pressure cycle

4 CONCLUSIONS

Preliminary investigations presented in this paper can lead to the following conclusions:

- it was confirmed that wood percentage failure results for PUR type adhesives are very high with small variations,
- the results presented for the shear strength and delamination were within requirements of prEN 16351:2013,
- the widths of the narrowest timber elements in CLT test piece determine the depth of delamination.

ACKNOWLEDGMENTS

This work has been carried out as part of the project entitled 'Innovation in Irish timber Usage' (project ref. 11/C/207) funded by the Department of Agriculture, Food and the Marine of the Republic of Ireland under the FIRM/RSF/COFORD scheme. The authors would also like to thank ECC Ltd. (Earrai Coillte Chonnacht Teoranta) for supplying the timber and Purbond AG for supplying the adhesive used in this project.

REFERENCES

[1] Schickhofer G. (1994). *Starrer und nachgiebiger Verbund bei geschichteten, flächenhaften Holzstrukturen*, PhD Thesis, Institute of Steel, Timber and Shell Structures, Graz University of Technology.
[2] Salmén L. (2004). *Micromechanical understanding of the cell-wall structure*, C. R. Biologies, 327:873-880.
[3] Wathén R. (2006). *Studies on fiber strength and its effect on paper properties*, PhD Thesis, KLC communications, No. 11, University of Technology, Helsinki, Finland, ISSN 1457-6252, p. 97.
[4] Brandner R. (2012). *Stochastic System Actions and Effects in Engineered Timber Products and Structures*, PhD Thesis, Institute of Timber Engineering and Wood Technology, Graz University of Technology, p. 467.
[5] Brandner R. (2013). *Production and Technology of Cross Laminated Timber (CLT): A state-of-the-art Report,* ECOST-MEETING-FP1004-210513-028873, ISBN 1 85790 181 9, p. 3-36.
[6] Jobstl, R.A., Bogensperger, T., and Schickhofer, G. (2008*) In-plane shear strength of Cross Laminated Timber*, CIB-W18/41-21-3, St. Andrews.
[7] Mestek, P., Kreuzinger, H., and Winter, S. (2008). *Design of Cross Laminated Timber (CLT)*, WCTE 2008 - 10th World Conference on Timber Engineering, Miyazaki, Japan.
[8] Vessby, J., Enquist, B., Petersson, H., and Alsmarker, T. (2009). *Experimental study of cross-laminated timber wall panels*, European Journal of Wood Products, 67: 211-218.
[9] Fortune, A.L., Quenneville, P. (2010). *Feasibility study of New Zealan radiata pine crosslam*, in S. Setunge (ed.) Incorporating sustainable practise in mechanics and structures of materials, CRC Press.
[10] Leonardo da Vinci Pilot Project. (2008). Handbook 1. Timber structures, Educational Materials for Designing and Testing Timber Structures – TEMTIS.
[11] Crespell, P., and Gagnon, S., (2010) Cross Laminated Timber: a Premier, FPInnovations.
[12] Rimetz, B. (2011). Future of Wood Update / X Marks the Opportunity, ProSales, http://www.prosalesmagazine.com/products/lumber/x-marks-the-opportunity_o.
[13] Yeh, B., Gagnon, S., Williamson, T., Pirvu, C., Lum, C., and Kretschmann, D. (2012). *The North American product standard for cross-laminated timber*, Wood Design Focus, 22(2):13-21.
[14] Steiger, R. and Gehri, E. (2010*). Quality control of glulam: Improved method for shear testing of glue lines* 'The Future of Quality Control for Wood & Wood Products' The Final Conference of COST Action E53, Edinburgh.
[15] Steiger, R., Gehri, E., and Richter K. (2010). *Quality control of glulam: shear testing of bondlines*, Eur. J. Wood Prod. 68: 243–256.
[16] prEN 16351:2013 Timber structures – Cross laminated timber – Requirements, CEN.
[17] EN 392:1995 Glued Laminated Timber – Shear Test of glue lines, CEN.
[18] Raftery, G., Harte, A., Rodd, P. (2008). *Qualification of wood adhesives for structural softwood glulam with large juvenile wood contentJ*. J. of Institute of Wood Science, 18(1): 24-34.

Post-tensioning of Timber Beams with Steel Rods

E McConnell[1], D McPolin[1], S Taylor[1]
[1]Department of Civil Engineering, Queens University Belfast, University Road, Belfast, Northern Ireland

email: emcconnell10@qub.ac.uk, d.mcpolin@qub.ac.uk, s.e.taylor@qub.ac.uk

ABSTRACT: Improvements in the structural performance of glulam timber beams by the inclusion of reinforcing materials can increase both the service performance and ultimate capacity. In recent years research focusing on the addition of fibre reinforced polymers (FRP) to strengthen members has yielded positive results. However, the FRP material is still relatively expensive and its full potential in combination with structural timber has not been realised. This paper describes a series of four-point bending tests that were conducted, under service and ultimate loads, on reinforced and post-tensioned glulam timber beams where the reinforcing tendon used was 12 mm diameter toughened steel bar. Steel has been chosen as it is a typical reinforcing material and will provide a suitable benchmark for comparison with planned, future investigations. The research was designed to evaluate the additional benefits of including an active type of reinforcement, by post-tensioning the steel tendon, as opposed to the passive approach of simply reinforcing the timber beam.

From the laboratory investigations, it was established that there was a 9% increase in load carrying capacity when the post-tensioned members were compared to those with the passive reinforcement and an overall 40% increase when compared to a solid timber beam. Furthermore, when the post-tensioned timber composite members were compared with control timber specimens the increase in stiffness gave a 28% reduction of deflection under service loads. Additionally a more favourable ductile failure mode was witnessed compared to the brittle failure of an unreinforced timber beam. The results support the assumption that by initially stressing the embedded reinforcing tendon the behaviour of the glulam timber is enhanced both in stiffness and strength, indicating that there is significant scope for this approach in practical applications.

KEY WORDS: Post-tension; Timber; Steel; Glulam.

1 INTRODUCTION

Timber sourced from sustainable forests is considerably less damaging to the environment than other construction materials. The act of forestry is regarded as a beneficial process as it has the potential to reduce the concentration of atmospheric carbon dioxide by sequestrating carbon. Timber has an excellent strength to weight ratio, as well as being renewable with a potentially low embodied energy. Despite the many benefits offered by timber use compared with other construction materials it remains underused in the industry. 'timber is not widely used for primary structural elements, even though a substantial volume of renewable native material is available'[1]. The underuse of timber as a structural material may be attributed to the naturally occurring defects within its structure. Undesirable characteristics include the presence of knots and grain defects, susceptibility to the effects of moisture and other time dependent vulnerabilities, such as the occurrence of creep, which will affect the material's structural performance.

The limitations experienced when using timber in construction have been continually addressed in the past with the development of LVL and glulam to reduce the presence of natural defects. More recently, research has been completed regarding the reinforcement of timber using various metals and fibre reinforced polymers as an attempt to enhance the timber's strength and stiffness[2-5]. Steel is a typical material used in various situations as a reinforcing member and, as such, was regarded as an appropriate initial material to use within this research. A 12mm diameter steel bar has sufficient tensile strength to comfortably permit a 20.0kN tensile force to be applied directly, while additional loading is applied to the beam.

Some research in reinforcing timber has been previously undertaken where researchers have concluded that the addition of FRP reinforcement can be equated to the addition of a single timber lamina[4&6]. It is arguable that the reinforcement utilised in these investigations is not being fully exploited as only a fraction of it's structural potential is used. By initially tensioning the material and therefore using active reinforcement a number of advantages can be further realised as, 'prestressing effectively increases flexural strength by introducing an initial compressive stress into the timber fibres that in service are under tension'[7].

2 RESEARCH OBJECTIVES

This research evaluated the feasibility of strengthening timber beams by the addition of a post-tensioned steel rod. Throughout the full investigation, a combination of unreinforced, reinforced and post-tensioned GL28 timber beams, with both unbonded and bonded steel rods, were tested experimentally to determine the structural advantages. This paper discusses the investigation of unreinforced and steel reinforced timber sections. Extensive material testing and theoretical investigations examining the various stresses

occurring throughout the materials, during the testing process, were undertaken and analysed to allow the creation of a theoretical stress model capable of accurately predicting the behaviour of the system.

3 EXPERIMENTAL TESTING

Twenty glulam timber beams (grade GL28), 3m length, were machined to a cross-section of 45mm x 155mm. Members that were to be reinforced were further machined to create a 16mm diameter circular void throughout the length, its centre located 22.5mm from the soffit. The void was created by removing half a lamina, 22.5mm, from the soffit of the timber and subsequently routering two semi-circular groves, diameter of 16mm, into each surface. The two sections were then bonded under pressure using a two-part epoxy resin to create the glulam beams with a 16mm void. The beams were then divided into four groups of five members, with moisture content and a visual inspection being recorded for each

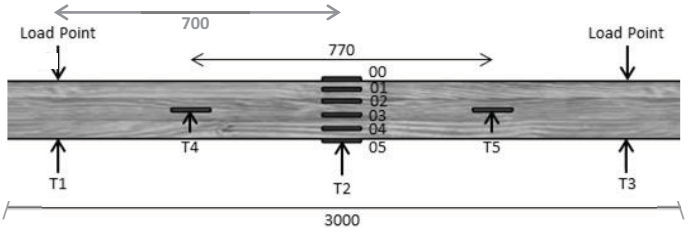
3.1 Test Variables

The instrumentation and test set-up shown in Figure 1 illustrates the flexural tests conducted on each beam within the series. As timber is a particularly variable material it was crucial to conduct numerous service load tests at each stage of the post-tensioning process to allow direct comparisons to be drawn between the results. To facilitate this each beam within the relevant series was tested as follows;

- timber with 16mm void
- timber with 12mm steel rod slotted, untensioned (slack), through the void
- timber with 12mm steel post-tensioned to 20kN, unbonded
- timber with 12mm steel post-tensioned to 20kN, bonded

The sets of tests discussed within this paper are;

- 5 No. 45x155x3000mm timber beams, tested both elastically and to failure, (C1-C5)
- 5 No. 45x155x3000mm timber beams reinforced with a bonded 12mm diameter steel bar, tested elastically and to failure, (R1-R5)
- 5 No. 45x155x3000mm timber beams reinforced with an unbonded post-tensioned 12mm diameter steel bar, tested elastically
- 5 No. 45x155x3000mm timber beams reinforced with a bonded post-tensioned 12mm diameter steel bar, tested both elastically and to failure (B1-B5).



ERS Gauge: 00-05 at midpoint
LVDT : T1-T5

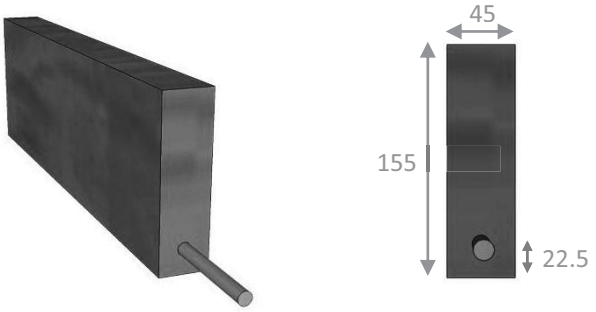


Figure 1. Test Instrumentation and Set-up

3.2 Flexural Test Procedure

Beams were tested using the four point bending method in accordance to *BS EN 408*[8] as shown in Figure 1. The beams were supported on roller supports, as was the spreader bar underneath the loading point. Lateral supports were provided to prevent any lateral torsional effects. For the elastic tests, an initial load of 10kN was applied twice in increments of 1kN with data recorded at each interval on all instrumentation. The 10kN load was held for five minutes, unloaded incrementally and all load removed for a further five minutes prior to the second elastic loading test which proceeded in the same manner. Following the elastic tests, the beams were tested to failure. The response was monitored both through instrumentation, but additionally documented using digital imagery.

The post-tensioned beams where initially tested as above, prior to the application of the tension force. Once complete the steel tendon was tensioned using a 13 ton hollow plunger cylindrical ram, located at one end of the beam. The ram was secured using open grip barrel and wedge clamps, with a load cell and bearing plates located against the timber. The tensile force was applied in increments, with deflection, strain and force data gathered at each interval. Once the tensile force was recorded at 20kN, elastic loading followed by loading to failure occurred as detailed previously.

3.3 Material Testing

Samples were taken for material tests to test the feasibility and accuracy of the test procedures rather than gain a comprehensive representation of the timber properties, at this stage. Tensile and compressive tests were carried out in accordance with BS EN 408[8]. Compressive blocks, 45x155x270mm, were crushed parallel to the grain using an accurately calibrated hydraulic actuator. For tension tests 9mm x12mm dog bone samples were tested in an accurately calibrated direct tension testing machine.

4 RESULTS

4.1 Material Testing Results

Table 1 & 2 below show a sample of the material testing results gathered from the compressive and tensile tests. As is true for clear timber, timber with no natural defects such as knots, the tensile and compressive stress values are similar indicating that these results may be representative of the

material. However, as timber frequently fails because of the presence of natural defects further material testing is planned to allow both the mean and characteristic values of the structural properties to be calculated. Preliminary theoretical calculations have been completed using the average value from the test results in Table 1. These were significantly higher than the values specified for GL28 timber..

Table 1 – Preliminary compressive test results

Sample No.	Failure Load (kN)	Compressive Stress (N/mm^2)
1	264.94	37.4
2	281.78	39.8
3	247.63	34.9
4	273.41	38.6
5	260.26	36.7
Average	265.60	37.5

Table 2 – Preliminary tensile test results

Sample No.	Failure Load (kN)	Tensile Stress (N/mm^2)
1	3.65	33.8
2	3.68	34.1
3	3.33	30.8
4	5.02	46.48
5	5.77	53.4
Average	4.29	39.7

4.2 Flexural Testing Results

4.2.1 Unreinforced Beams

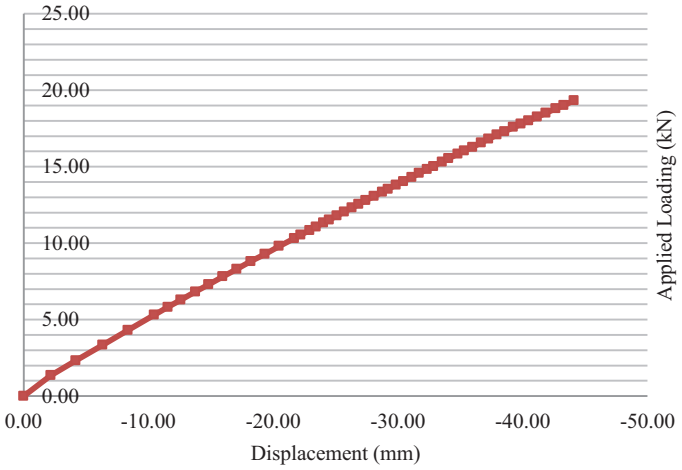


Figure 2. Typical Load/Deflection Graph of Unreinforced Beam

Figure 2 represents the typical deflection response of an unreinforced timber beam used throughout the experimental programme. As is evident from the figure the typically proportional trend line continues until the failure of the beam indicating that the failure mode was sudden and brittle. Using the deflection formula, Equation 1, with any shear deformation ignored, the modulus of elasticity can be calculated for the average unreinforced timber beam tested.

$$\Delta = \frac{Pl^3}{6EI}\left(\frac{3a}{4l} - \left(\frac{a}{l}\right)^3\right) \quad (1)$$

where P (kN): applied load; E (N/mm^2): modulus of elasticity; I (mm^4): second moment of area; a (mm) distance from load point to nearest support; l (mm): length of beam.

By using the average results yielded from this series of tests a value of $9200N/mm^2$ is obtained. This value is considerably lower than that expected from a GL28 sample, however it may be used to quickly calculate and compare the relative increase in stiffness, EI, that the post-tensioning process causes.

4.2.2 Reinforced Beams

Timbers with a bonded 12mm diameter steel reinforcing tendon were tested, as detailed previously, to provide a comparison between active and passive reinforcement.

As shown in Table 3 there was approximately a 30% increase in the flexural strength on average when compared with the results from the solid timber members. This considerable increase may be attributed to the addition of the steel member, which increases the tensile strength of the glulam timber, therefore increasing its ultimate capacity by preventing a premature failure caused by a natural defect.

The results shown provide a good basis for comparison with the post-tensioned members, allowing the additional advantages of post-tensioning to be clearly identified.

4.2.3 Post-tensioned Beams

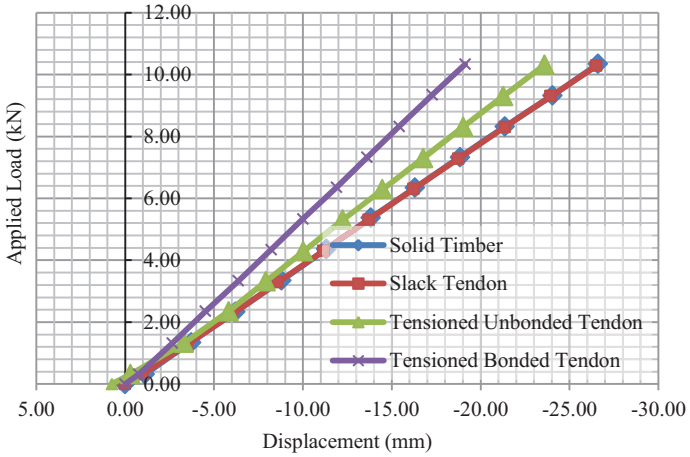


Figure 3. Load/Deflection Response under Service Loading

Figure 3 shows a typical load/deflection response of a beam at various stages of construction, under service loading. It is

initially evident that with the application of post-tensioning, both with the tendon bonded and unbonded, there is an increase in stiffness, particularly evident under the 10kN applied load. From the figure it can be seen that there is approximately a 7.5mm reduction, 28%, in service deflection between the solid timber beam and the post-tensioned beam with the steel tendon bonded in place at a 10kN applied load.

As is evident from Figure 3 the simple act of inserting the steel tendon through the 3m long beam has little to no effect on the overall stiffness of the member. Although the steel has a considerably higher elastic modulus the tendon alone is not sufficiently stiff over this length to result in a noticeable difference during this testing phase. This then indicates that the increase of stiffness and the resulting advantages, seen throughout these tests, can be attributed to the post-tensioning process. The graph represents the typical deflection response of the beams under service loading with the precamber induced by the post-tensioning ignored, meaning that there are further benefits offered by the post-tensioning process that are not initially evident from the figure.

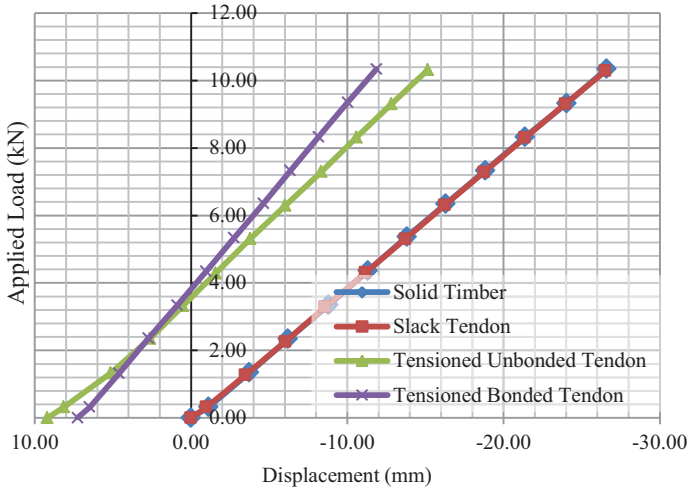


Figure 4. Load/Deflection Response under Service Loading with Precamber Effects Considered

Figure 4, above, represents the typical deflection response under elastic loading of the same beam represented in Figure 3, but with the induced precamber considered. It is immediately evident that the 8mm precamber combined with the increased stiffness of the composite member greatly reduced the net deflection, with a reduction of 55% being realised in this average case.

Table 3 further highlights the difference between the various test series conducted, at the point of failure. From the failure loads, it is evident that there is an increase in capacity when timber is post-tensioned. In this particular series of tests there was a 40% increase in strength when comparing the solid timber to the post-tensioned timber composite. There is an additional 9% increase when the post-tensioned average is compared to the reinforced average, indicating the process of post-tensioned does further enhance timber's flexural strength.

Table 3 – Collapse Load & Predicted Capacity of Unreinforced and Post-tensioned Beams

Beam No.	Failure Load (kN)	Failure Mode
C1	16.25	tensile split on soffit
C2	19.25	tensile split on soffit
C3	23.75	tensile split on soffit
C4	22.50	tensile split on soffit
C5	17.50	tensile split on soffit
Av.	**19.9**	
R1	26.25	tensile failure on soffit with indication of compression cracking
R2	24.40	compression failure causing outward buckling
R3	26.75	lateral torsional buckling
R4	24.50	compression cracking on top face with finger soffit split on soffit
R5	26.50	compression cracking under load points
Av.	**25.7**	
B1	27.25	compression failure of finger joint on top surface
B2	29.75	considerable buckling with compression/shear failure on surface
B3	26.80	knot on soffit split but held in place by steel tendon
B4	26.90	compression failure occurring in top third
B5	29.15	compression fractures under loading with split of knot occurring on soffit
Av.	**28.0**	

Although timber is not strictly comparable in this manner, due to the inherent variability of its nature, these results indicate a positive shift in the material's capabilities when post-tensioned, in comparison to simply being reinforced.

The theoretical work, which will form a significant part of this research, is primarily based upon the predicted strain/stress profiles that are formed as the timber is loaded. As such ERS gauges distributed over the timber's face were used to gather strain data as the beams were loaded. Figure 5 displays a series of typical profiles that were obtained during the testing.

As is evident from the figure the process of post-tensioning actively reduces the tensile stresses experienced during loading. Timber primarily fails in flexure due to the tensile stresses exceeding the tensile strength of the material, which is weakened through the presence of knots and other defects. A 55% reduction in the stress value on the soffit of the timber is evident when the solid timber specimen is compared to the

post-tensioned composite under the service loading. This figure provides a basic explanation of how the addition of post-tensioning strengthens the timber. Furthermore, it illustrates the stresses occurring within the timber at the point of failure. As expected there is a tensile peak that corresponds to the position of the tensioned steel tendon during the failure loading. In addition the compressive stress maximum can be seen to occur below the surface of the beam. This plastic failure stress block corresponds well with previous work conducted in Queen's University Belfast by Patrick[3] indicating that this experimental work is valid and may be used within the theoretical investigation.

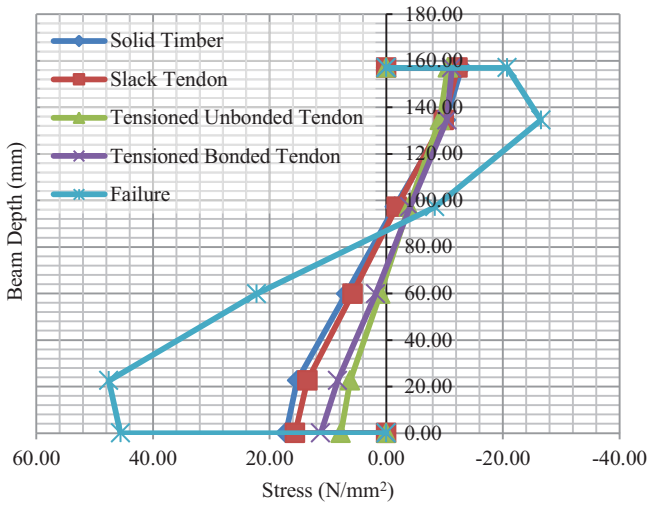


Figure 5. Stress Profiles of a Typical Post-tensioned Timber under 10.0kN Elastic Load

5 THEORETICAL METHODOLOGY

The principle and behaviour of linear elastic stress development is a well-understood theory commonly used within the concrete industry, where the process of post-tensioning is frequently undertaken. As a preliminary investigation the theory has been applied to this process and has yielded positive initial results with the theoretical predictions being within a couple of kiloNewtons of the failure loads experimentally obtained.

The stresses induced by the application of both a post-tensioning force and a load were considered separately, as shown in Figure 6. By using the compressive and tensile strength of the timber it was possible to calculate the applied load required to remove the induced stresses caused by the post-tensioning, returning the beam to a neutral position. This value being the additional loading that the timber would be able to support following post-tensioning.

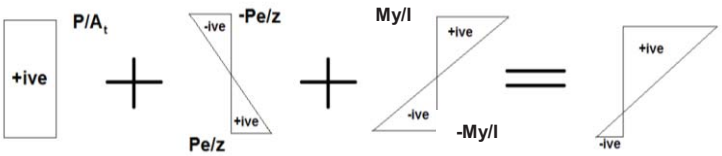


Figure 6. Induced Stresses from Post-tensioning and Load Application

6 CONCLUSIONS

Although the small number of samples must be considered when evaluating the following conclusions the process of post-tensioning offers a number of advantages when applied to timber. Examining the data set indicated that there was an overall flexural strength gain of 40%. This value corresponds reasonably with the theoretical investigations that have been carried out to date. Additionally a significant shift in the failure mode of the timber beams was seen, with compression cracking becoming the primary cause of failure, which is a more ductile and desirable failure mode than the typical failure of a solid timber member.

The stiffness results of the various beams tested are also encouraging; the steel, having a considerably higher modulus of elasticity than the timber, increased the stiffness of the beams under a 10kN applied load by 28% when the precamber was not considered. When considering the precamber the advantages significantly increase making post-tensioning a viable and worthwhile process in the efforts to strengthen timber and increase its usability within construction.

A number of additional investigations are currently underway with regards to this research topic, including an examination of the long-term behaviour of post-tensioned glulam beams.

ACKNOWLEDGMENTS

The author gratefully acknowledges the continued work and support from her supervisors and the laboratory technicians within the university.

REFERENCES

[1] Gilfillan, J.R., Gilbert, S.G. & Patrick, G.R.H., *The use of FRP composites in enhancing the structural behaviour of timber beams*, Journal of Reinforced Plastics and Composites, 22(15):1373-1388. 2003

[2] Yeboah, D., Taylor, S.E. and McPolin, D. *Pull-out behaviour of axially loaded Basalt Fibre Reinforced Polymer (BFRP) rods bonded perpendicular to the grain of glulam elements* Construction and Building Materials, Vol. 38, Jan. 2013, pp. 962–969, 2013.

[3] Patrick, G., *The structural performance of FRP reinforced glued laminated beams made from homegrown Sitka spruce*, Thesis. Ph.D. (Faculty of Engineering), Queen's University of Belfast. 2004

[4] Martin, Z.A. Stith, J.K. & Tingley, D.A. *Commercialisation of FRP reinforced glulam beam technology*. Proceedings of the 6th World Conference on Timber Engineering (WTCE). Canada, UBC Press. 2000.

[5] Plevris, N. and Triantafillou, T. *FRP-Reinforced Wood as Structural Material*. Journal of Material Civ. Eng., 4(3): 300–317. 1992

[6] Negrao, J. Brunner, M. & Lehmann, M. *Pre-stressing of Timber. Bonding of Timber*: Core document of the COST Action E34. Vienna: University of Natural Resources and Applied Life Sciences. 2008.

[7] Brady, F. & Harte, A. *Prestressed FRP Flexural Strengthening of Softwood Glue-Laminated Timber Beams,* 10th World Conference on Timber Engineering (WCTE), 2 - 5 June 2008.

[8] British Standards Institution, 2010. BS EN 408:2010 *Timber structures. Structural timber and glued laminated timber. Determination of some physical and mechanical properties*: BSI

Mechano-sorptive Creep of FRP Reinforced Laminated Timber Beams

Conan O'Ceallaigh[1], Annette Harte[1], Karol Sikora[1], Daniel McPolin[2]
[1] College of Engineering & Informatics, National University of Ireland, Galway, University Rd., Galway, Ireland
[2]School of Planning, Architecture and Civil Engineering, Queen's University Belfast, University Road, Belfast BT7 1NN, UK
Email: conan.oceallaigh@nuigalway.ie, Annette.harte@nuigalway.ie, Karol.sikora@nuigalway.ie, d.mcpolin@qub.ac.uk

ABSTRACT: The reinforcement of timber using fibre reinforced polymer (FRP) rods or plates is widely accepted as an effective method of increasing the strength and stiffness of members, while at the same time reducing the variability in properties. The short-term behaviour of these reinforced members is well understood. The long-term or creep behaviour has received less attention. Due to the hygroscopic nature of timber, creep is accelerated by moisture variations, resulting in the so-called mechano-sorptive effect. In reinforced timber beams, the influence of the reinforcement and adhesive on the long-term response must be taken into account.

The objectives of the present work are to determine the durability of reinforced timber beams with respect to load duration (viscoelastic creep) and variable climate (mechano-sorptive creep), and to develop appropriate modification factors for design purposes. Sitka spruce is the most widely grown specie in Ireland and is the focus of this study. Glued Laminated (Glulam) beams were manufactured from Sitka spruce and a selected portion of them was reinforced with basalt-fibre reinforced polymer (BFRP) rods. The test programme has been designed to determine the flexural behaviour of the beams with respect to load duration and variable climate. One sub-sample of the beams is to be tested at constant temperature and relative humidity and a second sub-sample in a climate with varying temperature and relative humidity. This paper contains a description of the test set-up and presents the short-term modulus of elasticity (MOE) results for reinforced and unreinforced beams and details the experimental procedure for creep measurements.

KEY WORDS: BFRP, Glued Laminated Timber, Irish Grown Sitka Spruce, Mechano-sorptive Creep

1 INTRODUCTION

The mechanical and physical properties of softwood timber can vary considerably as a result of the age and rate of growth of the tree and other environmental factors which affect the wood cell density and strength [1]. Sitka spruce is characterised as a fast growing, low density timber which when subjected to flexural loading generally fails in tension due to the presence of knots [2]. In Ireland, this species has an average rotation length of 30 – 40 years [3]. This low density timber demonstrates limited capacity to carry substantial loads. However, when combined to create a composite element such as a glued laminated beam, the capacity of this softwood timber may be greatly increased.

The performance of glued laminated beams may also be enhanced with the addition of fibre reinforced polymer (FRP) composite reinforcement. It has been seen that the addition of modest reinforcement ratios can delay tension failure in glued laminated elements. The additional reinforcement utilises the additional capacity of the timber in the compression zone resulting in much more consistent behaviour as well as a significant increase in flexural stiffness [4].

Long term effects in these timber beams are of crucial importance to structural engineers when designing timber structures. Duration of load and creep effects must be understood as excessive deflection will result in failure. These effects result when the beam is stressed under load for a long period of time. The duration of load effect is a loss of strength with time under a sustained load. Similarly with creep, there is a reduction in stiffness in time. This effect manifests itself as an increase in deflection with time under constant stress. Mechano-sorptive creep occurs due to an interaction between stress and moisture content change. Depending on environmental conditions, this effect can greatly increase the creep deflection of a beam and ultimately lead to failure. To the authors knowledge, only one study addresses these effects on unreinforced and reinforced glulam beams made from Irish grown Sitka spruce [2].

2 LITERATURE REVIEW

Mechanical degradation is commonly seen in timber when stressed under load for long periods of time. The most common effects of mechanical degradation are known as duration of load effect and creep effect. For solid timber the strength reduction under a sustained load for ten years can be as high as 40% [5, 6]. The creep effect is the increase in deflection with time for a given constant load. Creep can be divided into two categories, namely viscoelastic creep and mechano-sorptive creep. Timber is a viscoelastic material so its deformation response is a combination of both elastic and viscous components. Since viscoelastic creep is time dependent, at any instant in time under load its performance will be a function of its past history. Viscoelastic creep is defined as a deformation with time at constant stress and at constant environmental conditions. Mechano-sorptive behaviour is a deformation due to an interaction between stress and moisture content change [7, 8]. It is independent of

time and it does not occur in constant temperature and relative humidity conditions [9]. It is directly related to the change in moisture content and mechanical stress.

These phenomena have been the subject of particular interest for the timber engineering research community.

Viscoelastic and mechano-sorptive creep within timber is difficult to separate and monitor as each effect operates simultaneously. Apart from these two effects a third, pseudo-creep and recovery that has been ascribed to differential swelling and shrinkage must also be monitored. Creep is quantified by a number of time dependent parameters. The most common are creep compliance and relative creep. Creep compliance may be described by the following formula:

$$C_C(t) = \frac{\Delta\varepsilon(t)}{\sigma_0} \tag{1}$$

where:

C_C = Creep compliance,

$\Delta\varepsilon = \varepsilon_t - \varepsilon_0$ = Change in strain with time,

σ_0 = Applied constant stress.

Relative creep (C_R) is defined as the increase in deflection at time t, expressed in terms of the initial elastic deflection, as follows:

$$C_R(t) = \frac{\Delta\varepsilon(t)}{\varepsilon_0} = \frac{\varepsilon_t - \varepsilon_0}{\varepsilon_0} \tag{2}$$

where:

C_R = Relative creep,

ε_0 = Initial strain.

Relative creep has also been expressed as the change in creep compliance ($Cc(t)$) at time t divided by the initial creep compliance (Cc_0). As was mentioned above, viscoelastic creep is described as deflection with time at constant moisture content and environmental conditions, however, the magnitude of viscoelastic creep is dependent on the stress level and moisture content. A higher stress level will result in greater creep. Similarly, a higher initial equilibrium moisture content will result in higher viscoelastic creep. When moisture content and environmental conditions change, mechano-sorptive creep is induced.

Changes in the moisture content of timber result not only in mechano-sorptive creep effects but also in dimensional changes of timber. These dimensional changes (shrinkage and swelling (ε_s)) result in increased deflection and must be monitored.

The total measured strain ε_m, may be written as

$$\varepsilon_m = \varepsilon_{vc} + \varepsilon_{ms} + \varepsilon_s \tag{3}$$

where:

ε_{vc} = Viscoelastic strain,

ε_{ms} = Mechano-sorptive strain,

ε_s = Swelling/shrinkage strain of a matched zero-load control specimen.

The mechano-sorptive component may then be calculated as

$$\varepsilon_{ms} = \varepsilon_m - \left(\varepsilon_{vc} + \varepsilon_s\right) \tag{4}$$

Mechano-sorptive behaviour has been the focus of many studies, due to its ability to increase deflection and cause premature failure of timber beams. There is no defined method for examining the creep factors of timber beam elements. As a result, many methods and test rigs have been designed and used to examine creep deflection. The majority of authors implement a four-point bending test setup in accordance with EN 408, however, in some cases a three-point bending test set up [10] or an evenly distributed load across the whole length of the member have been used [11].

Due to the complex nature of timber, and the numerous variables involved, quantifying creep, both viscoelastic and mechano-sorptive, can be difficult. Many researchers have attempted to examine the many variables and their effect on creep behaviour. Bengtsson [12] monitored the influence of many material parameters on mechano-sorptive creep in Norway spruce. These parameters included annual ring width, slope of grain, knots, compression wood, density and modulus of elasticity. It was seen that the relationship between relative creep and elastic modulus was strongly correlated, however, other comparisons demonstrated weaker correlations.

Changes in moisture content of timber arise due to variations in relative humidity. The greater the moisture differential in each relative humidity cycle, the higher the amount of creep [7]. The differential in each moisture cycle is important for design purposes. EN 1156 [13] describes procedures for determining the creep factors of wood based panels. It recommends the moisture cycle implemented must be designed to coincide with a Service Class as defined in Eurocode 5 [14]. There are 3 service classes. Service Class 1 would be described as dry conditions which is characterised by a material moisture content corresponding to a temperature of 20°C and a relative humidity only exceeding 65% for a few weeks per year. Service class 2 would be described as humid conditions which is characterised by a material moisture content corresponding to a temperature of 20°C and a relative humidity only exceeding 85% for a few weeks per year. Service Class 3 would be described as exterior conditions which is characterised by a material moisture content corresponding to climatic conditions leading to higher moisture contents than in Service Class 2.

Hunt [15] questioned the importance of humidity changes and suggested the speed of moisture change might be important in mechano-sorptive creep. The speed of moisture change indicates a size effect that has previously been predicted by van der Put [16]. It is easy to see that the full extent of the mechano-sorptive effect will require the timber to adjust to the equilibrium moisture content of its new environmental conditions. For this reason short moisture cycles on full scale tests on in-grade timber specimens will provide inaccurate results. Duration of creep tests and moisture cycles vary considerably in the literature.

Abdul-Wahab et al. [17] performed long-term creep tests on 65 unreinforced glued laminated and solid timber beam specimens under different environmental conditions over an eight year period. The beams were subject to four-point bending as shown in Figure 1. These beams were subjected to

three sets of environmental conditions. Although not deliberate, these conditions happened to coincide with Service Classes 1, 2 and 3 as defined in Eurocode 5 [11]. Environmental condition 1 was set at a constant temperature of 20°C and a constant relative humidity of 60 ± 10%. Environmental condition 2 was a variable climate condition with a constant temperature of 20°C and a variable relative humidity ranging between 30% and 70%. Environmental condition 3 was an external climate in a covered enclosure with a variable relative humidity ranging between 30% and 100%. Moisture measurements were taken regularly as well as temperature and relative humidity. It was noted that for a six week wetting/drying period that equilibrium moisture content was not achieved. In order to fully understand the mechano-sorptive effect longer relative humidity cycles are required. The size and shape of the beam is also of great importance. The shape and size of section, expressed in terms of volume/surface area, has a significant effect on creep. The smaller the ratio, the greater is the creep tendency.

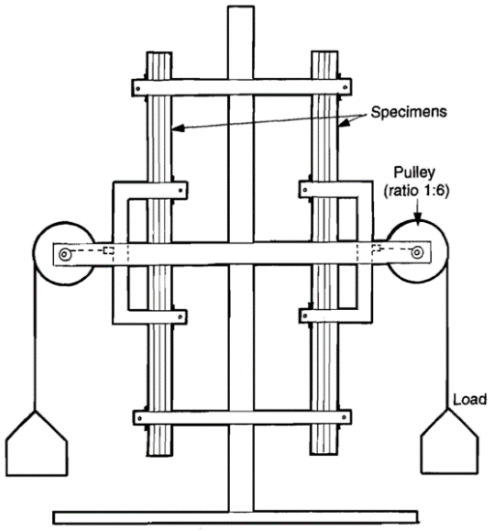


Figure 1. Vertical creep experimental rig [14].

Abdul-Wahab et al. [17] found that Service Class 3 beams experienced the greatest creep averaging a 285% increase in creep when compared to Service Class 1 beams at constant temperature and relative humidity. Service Class 2 in the variable climate experienced an increase in creep of 165% when compared to the beams at Service Class 1 at constant temperature and relative humidity. These deformations are significant and motivate the need for greater understanding of these effects.

3 EXPERIMENTAL PROCEDURE

This project is designed to study the long-term effects on FRP reinforced glued laminated beams manufactured from Irish grown Sitka spruce. Long-term creep tests will be performed under varying environmental condition and appropriate modification factors will be determined for design purposes. This paper details the short-term experiments, which were carried out prior to long-term creep tests. In total, thirty six glulam beams were manufactured in the Timber Engineering Laboratory at the National University of Ireland, Galway. Thirty beams used in the experimental programme will be subject to creep tests and six supplementary beams will be used to monitor shrinkage/swelling and moisture content variations during creep testing. The beams consist of four laminations. Each beam measures 98 mm x 125 mm x 2300 mm. The beams are divided into two matched groups, one group will be tested in a controlled climate at 20 ± 2°C and at a relative humidity of 65 ± 5% and the other group will be placed in a variable climate chamber. Each beam will be subjected to four-point bending for a period of at least two years to examine the duration of load effects and the creep effects in different climate conditions.

3.1 Glulam Manufacture

Each laminate was strength graded using a mechanical grading machine. From these results, each laminate was ranked in descending order of modulus of elasticity (1 being the highest MOE and 150 being the lowest MOE). This ranked table was divided into 4 divisions with the 1st division representing the highest MOE laminates and the 4th division representing the lowest MOE laminates. In each division there is a maximum and minimum value and by balancing between each division, 36 beams of similar properties were created. Division 1 contains the strongest 36 laminates which make up the 36 bottom tensile laminates for each beam. Division 2 is the 2nd strongest group and contains laminates ranked 37-73. These laminates are situated in the top of each beam and applied in ascending order of strength (73-37) to balance each beam and create beams of similar properties. So if a beam has the strongest tensile laminate ranked laminate number 1 in division 1, it received the weakest laminate in division 2 (laminate number 73). Division 3 contains laminates ranked 74-110, and is situated on top of the tensile laminate. Division 4 contains the weakest laminates ranked 111-147 and is located below the top laminate. Similar to division 2, division 4 is applied in ascending order of strength (147-111) to create beams of similar properties. This is illustrated in Figure 2.

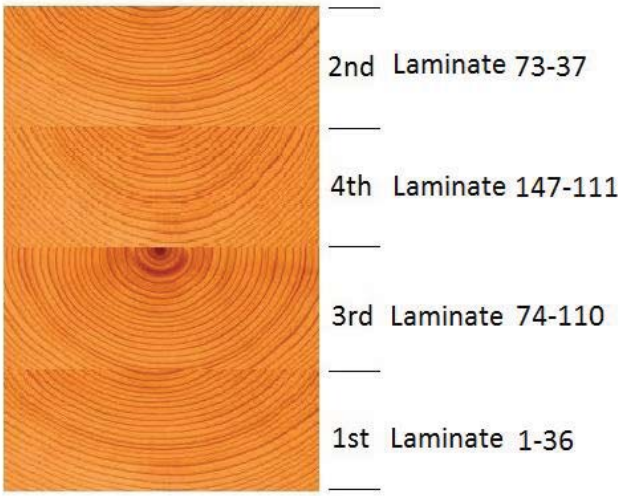


Figure 2. Glulam beam lay up.

To create a secure bond at the timber interface, each laminate was knife planed in order to create a smooth surface with

which to adhere, free from irregularities and torn grain in accordance with EN 14080 [18].

It should also be free from impurities such as oils, dirt and other debris as these will affect both the mechanical and chemical bonding process at the timber interface. After planing, the thickness of each laminate was 31.25 mm on average. In order to achieve the best bond, the adhesive was applied within 2 hours after planing so that the wood pores opened by the planing process could absorb the glue applied [19]. The glue applied is a 1:1 phenol resorcinol formaldehyde



Figure 3. Clamping Rig.

adhesive which is fully weatherproof as well as being suitable for structural applications such as wooden laminated beams. Adhesive was applied to all interfaces to be bonded ensuring an even spread of a minimum of 350 g/m². In order to ensure complete coverage and an even distribution, 200 g/m^2 was applied to each face using a rubber roller.

The beams were clamped in a rig applying a minimum pressure of 0.6 N/mm^2 in accordance with EN 14080 [18] as seen in Figure 3. The beams remained in the clamping rig for 24 hours after which they were placed into a conditioning chamber to cure for 5 weeks at 20 ± 2 °C and at a relative humidity of 65 ± 5% prior to short term testing.

3.2 Reinforcing glued laminated beams

From the 36 beams created, 20 of the beams were reinforced with basalt fibre reinforced polymer (BFRP). Two 12 mm BFRP rods were inserted into two circular grooves routed the full length of bottom tensile laminate and centered 30 mm from each edge as shown in Figure 4. The grooves were measured to account for the BFRP rod diameter plus a 2 mm glue line. These two BFRP rods accumulate to a percentage reinforcement ratio of 1.85%.

To guarantee a solid bond, each groove was cleaned using compressed air to ensure it is free from dust and other impurities. A two part thixotropic structural epoxy adhesive was chosen to bond the reinforcement to the timber as it is specially formulated for the bonding of FRP to timber [20]. The two parts were mixed together from their pre-packaged containers. The paste was mixed thoroughly and placed into a cartridge for application using an injection gun. The groove was initially filled to approximately two-thirds of the routed depth. The BFRP rod was then inserted into the groove forcing excess adhesive around the sides of the rout up to the top of the rod. Additional adhesive was then applied to complete the 2 mm glue line. The beams were then placed in the conditioning chamber with a temperature of 20 ± 2 ºC and with a relative humidity of 65 ± 5%, where they remained to cure for a period of 3 weeks.

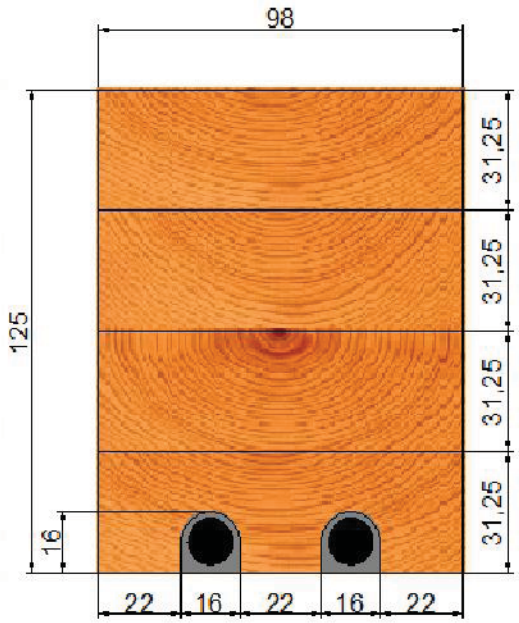


Figure 4. Reinforcement detail.

3.3 Short Term Testing

The bending test set up is in accordance with EN 408 [21]. The beams were loaded at a constant cross head rate of 0.15 mm/s (< 0.003 x h limit) to a maximum stroke of 15 mm to ensure that the deflection did not exceed the elastic limit of the beam and that the maximum load was less than 40% of the estimated ultimate failure load. The deflection of the midspan of the beam was measured using two LVDTs, one for determining the local stiffness and the other for the global stiffness. In order to determine the local bending stiffness, the deflection was measured over a gauge length of 625 mm = 5h, where h is the height of the beam, using a hanger suspended to the neutral axis, as seen in Figure 5. The LVDT for global stiffness measurement was fixed centrally on the top surface to the beam. Plates were used under at each support and load head to avoid indentation and inaccurate deflection measurement.

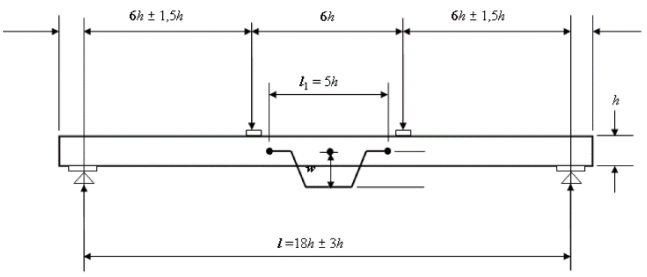


Figure 5. Beam bending set-up [18].

As a precaution each beam was supported laterally using polytetraflourethylene strips and packing to counteract lateral torsional bucking during bending. These strips are free to slide over one another so as not to fully restrain the beam at this location [22]. Subsequent to these 4-point bending tests, the recorded local and global deflection data was plotted against the applied load to obtain the stiffness values. The resulting increment in displacement (w_2 - w_1) corresponding to the load increment (F_2 - F_1) was substituted into Equations (5) and (6) to obtain the values for local and global stiffnesses, respectively:

$$(EI)_{m,l} = \frac{a l_1^{\,2}(F_2 - F_1)}{16(w_2 - w_1)} \tag{5}$$

$$(EI)_{m,g} = \frac{l^3(F_2 - F_1)}{12(w_2 - w_1)}\left[\left(\frac{3a}{4l}\right) - \left(\frac{a}{l}\right)^3\right] \tag{6}$$

In these equations ***a*** is the distance between the load head and the nearest support, l_1 is equal to the gauge length (5 x h) for local modulus measurement, ***l*** is equal to the span and F_1 and F_2 are the loads corresponding to 0.1 and 0.4 $F_{max,}$ respectively. Similarly w_1 and w_2 are the deflections corresponding to 0.1 and 0.4 $F_{max,}$ respectively. These tests were performed on the unreinforced beams and subsequently on twenty of the reinforced beams. The test set up remained constant throughout allowing the percentage increase in stiffness to be calculated.

3.4 Proposed Creep Testing

As discussed in the introduction one sub group consisting of 15 beams will be subject to creep testing for at least 2 years in a constant environment and one sub group also consisting of 15 beams will be subject to creep testing in a variable climate. The constant climate condition will be at 20 ± 2°C and at a relative humidity of 65 ± 5% (This will coincide with Service Class 1 as defined in Eurocode 5 [14]). The constant climate conditions will provide data for the analyses of viscoelastic creep. The variable climate condition will encompass viscoelastic creep together with mechano-sorptive creep and strains due to swelling and shrinkage.

The test set up will be similar to that in Figure 5. Each beam will be subjected to four-point bending for a period of at least 2 years. A series of strategically placed strain gauges will be used to monitor the deformation of each beam. Swelling and shrinkage strains will be monitored on zero load control beams. Moisture content will be monitored constantly. Moisture probes will be placed at various depths within the timber to monitor the varying moisture penetration due to the environmental conditions.

4 RESULTS

Once the beams had been tested in their unreinforced state, six matched groups were created. Four of these groups were subsequently reinforced as described in section 3.2. The average increase in bending stiffness of each reinforced group is calculated relative to the stiffness in its unreinforced state. These results can be seen in Table 1 and Figure 6.

The average increase in the local bending stiffness is 16.30% with a standard deviation of 1.65% and the average increase in global bending stiffness is 8.80% with a standard deviation of 3.65%. The elastic modulus (E) is measured both globally and locally. Once reinforced the local elastic modulus (E_L) had a mean value of 10727 N/mm^2 and the global elastic modulus (E_G) had a mean value of 9307 N/mm^2.

Table 1. Percentage increase in stiffness.

GROUP	Average Local EI Increase (%)	Average Global EI Increase (%)
1	15.30%	6.54%
2	17.86%	14.14%
3	14.51%	8.15%
4	17.54%	6.36%
Average	16.30%	8.80%
Standard Dev.	1.65%	3.65%
Median	16.42%	7.34%

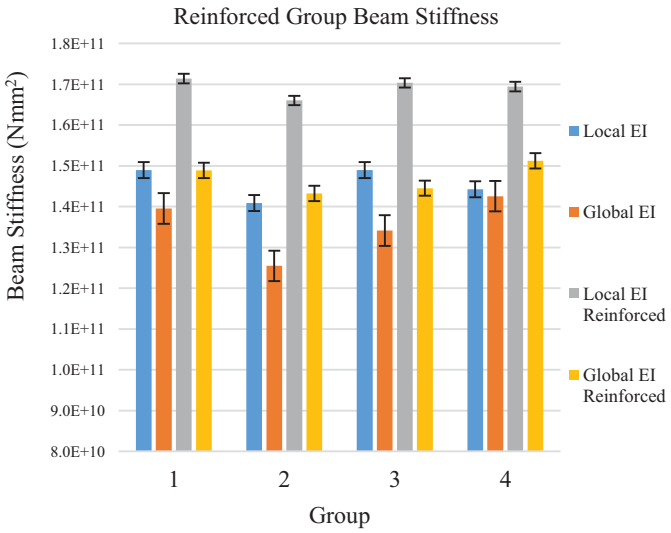


Figure 6. Reinforced group beam stiffness.

The increase in the global bending stiffness of group 2 in Table 1 is significantly higher than that realised in other

groups. This may be due to the lower initial global stiffness of group 2 in its unreinforced state. The lower the initial stiffness, the greater is the effect of FRP reinforcement.

The addition of reinforcement has resulted in reduced variability within each group as seen in Figure 6.

5 CONCLUSION

The long-term effects with regards to the duration of load and creep effects in timber and the experimental programme have been described. The short-term testing has been completed and provide a reliable basis for comparable studies in future work. The four-point bending tests demonstrated that the addition of BFRP rod reinforcement in modest quantities can greatly increase the short-term stiffness of glued laminated beams. An average increase in local bending stiffness of 16.3% was observed for a moderate percentage reinforcement of 1.85%.

The proposed creep study will examine the long-term effects of these Sitka spruce glued laminated beams in both constant and varying climate. The addition of reinforcement and its influence on the long-term effects will also be examined.

ACKNOWLEDGMENTS

This work has been carried out as part of the project entitled 'Innovation in Irish timber Usage' (project ref. 11/C/207) funded by the Department of Agriculture, Food and the Marine of the Republic of Ireland under the FIRM/RSF/COFORD scheme. The authors would also like to thank ECC Ltd. (Earrai Coillte Chonnacht Teoranta) for supplying all the timber used in this project.

REFERENCES

[1] Treacy, M., J. Evertsen, and N. Dhubháin, *A comparison of mechanical and physical wood properties of a range of Sitka spruce provences*. 2000, COFORD, National Council for Forest Research and Development.

[2] Gilfillan, J.R., S.G. Gilbert, and G.R.H. Patrick, *The use of FRP composites in enhancing the structural behavior of timber beams.* Journal of Reinforced Plastics and Composites, 2003. **22**(15): p. 1373-1388.

[3] Moloney, S. and M. Bourke. *Adding value to fast grown Irish Sitka spruce through drying and re-engineering,*. in *Proceedings of the COST E15 Conference*. 2004. Athens, Greece.

[4] Gilfillan, J.R., S.G. Gilbert, and G.R.H. Patrick, *The Improved Performance of Home Grown Timber Glulam Beams Using Fibre Reinforcement.* Journal of the Institute of Wood Science, 2001a. **15**(6): p. 307-317.

[5] Thelandersson, S. and H.J. Larsen, *Timber Engineering*. 2003, Wiley & Sons: London. p. 11.1 -11.25.

[6] Harte, A., *Introduction to timber as an engineering material.* ICE Manual of Construction Materials (Forde M (ed.)). Thomas Telford, London, UK, 2009. **2**: p. 707-715.

[7] Armstrong, L. and R. Kingston, *Effect of moisture changes on creep in wood.* Nature, London, 1960. **185**(4716): p. 862-3.

[8] Armstrong, L. and G. Christensen, *Influence of moisture changes on deformation of wood under stress.* Nature, 1961. **191**: p. 869-870.

[9] Armstrong, L., *Deformation of wood in compression during moisture movement.* Wood Sci, 1972. **5**(2): p. 81-86.

[10] Plevris, N. and T. Triantafillou, *Creep Behavior of FRP-Reinforced Wood Members.* Journal of Structural Engineering, 1995. **121**(2): p. 174-186.

[11] Runyen, R.W., et al., *Creep behavior of wood I-joists with web openings exposed to normal and low relative humidity conditions.*, in *11th World Conference on Timber Engineering 2010, WCTE 2010, June 20, 2010 - June 24, 2010*. 2010: Trento, Italy.

[12] Bengtsson, C., *Mechano-sorptive bending creep of timber - influence of material parameters.* Holz Als Roh-Und Werkstoff, 2001b. **59**(4): p. 229-236.

[13] NSAI, *I.S. EN 1156*, in *Wood-based panels - Determination of duration of load and creep factors*. 2013.

[14] NSAI, *I.S. EN 1995-1-1*, in *Eurocode 5: Design of timber structures - Part 1-1: General - Common rules and rules for buildings*. 2005+NA:2010+A1:2013.

[15] Hunt, D.G., *A unified approach to creep of wood.* Proceedings of the Royal Society of London Series a-Mathematical Physical and Engineering Sciences, 1999. **455**(1991): p. 4077-4095.

[16] van der Put, T., *Theoretical Explanation of The Mechano-sorptive Effect in Wood.* Wood and Fiber Science, 1989. **21**(3): p. 219-230.

[17] Abdul-Wahab, H., et al., *Measurement and modelling of long-term creep in glued laminated timber beams used in structural building frames.* Structural Engineer, 1998. **76**: p. 271-282.

[18] NSAI, *I.S. EN 14080* in *Timber Structures - Glued laminated timber and glued solid timber - Requirements*. 2013.

[19] Raftery, G.M., A.M. Harte, and P.D. Rodd, *Bond quality at the FRP-wood interface using wood-laminating adhesives.* International Journal of Adhesion and Adhesives, 2009. **29**(2): p. 101-110.

[20] Rotafix, *Material Data Sheet*, Rotafix House, Editor.: Abercraf, Swansea, SA9 1UR, U.K.

[21] NSAI, *I.S. EN 408* in *Timber Structures - Structural Timber and Glued laminated timber - Determination of some physical and mechanical properties*. 2010+A1-2012.

[22] Raftery, G.M. and A.M. Harte, *Low-grade glued laminated timber reinforced with FRP plate.* Composites Part B: Engineering, 2011. **42**(4): p. 724-735.

Influence of embedded length on strength of BFRP rods bonded parallel to the grain in low grade timber by pullout-bending tests

Caoimhe O'Neill[1], Daniel McPolin[1], Su Taylor[1], Annette Harte[2]
[1]School of Planning, Architecture and Civil Engineering, David Kier Building, Queen's University Belfast, Belfast, Co. Antrim, Northern Ireland, BT9 5AG
[2]College of Engineering and Informatics, Engineering Building, National University of Ireland, Galway, University Road, Galway, Co. Galway, Ireland.
email: coneill86@qub.ac.uk, d.mcpolin@qub.ac.uk, s.e.taylor@qub.ac.uk, annette.harte@nuigalway.ie

ABSTRACT: Bonded-in rod connections in timber possess many desirable attributes in terms of efficiency, manufacture, performance, aesthetics and cost. In recent years research has been conducted on such connections using fibre reinforced polymers (FRPs) as an alternative to steel. This research programme investigates the pull-out capacity of Basalt FRP rods bonded-in in low grade Irish Sitka Spruce. Embedded length is thought to be the most influential variable contributing to pull-out capacity of bonded-in rods after rod diameter. Previous work has established an optimum embedded length of 15 times the hole diameter. However, this work only considered the effects of axial stress on the bond using a pull-compression testing system which may have given an artificially high pull out capacity as bending effects were neglected. A hinge system was utilised that allows the effects of bending force to be taken in to consideration along with axial forces in a pull-out test. This paper describes an experimental programme where such pull-bending tests were carried out on samples constructed of 12mm diameter BFRP bars with a 2mm glueline thickness and embedded lengths between 80mm and 280mm bonded-in to low-grade timber with an epoxy resin. Nine repetitions of each were tested. A clear increase in pull-out strength was found with increasing embedded length.

KEY WORDS: Low-grade timber; Basalt FRP; Composites; Bonded-in rods; Pull-out capacity; Pullout-bending; Parallel-to-grain.

1 INTRODUCTION

Bonded-in rods present a sustainable, aesthetically pleasing alternative to the cumbersome conventional steel moment connections that are often encountered in timber construction. Not only do connections with bonded-in rods look better than conventional connections, they also have enhanced fire protection as the rods which transfer moment are embedded inside, and are therefore protected by, the timber.

Bonded-in rods have great potential in a wide range of both new build and restoration projects. Successful renovation has been carried out in roof and floor beams in buildings subject to decay [1], [2]. In new build, five areas were identified where bonded-in rods may be used for connections: frame corner, beam-post connection, beam-beam joint, supports and hinged joints [3].

Since the late 1980s there have been many research projects commissioned on the use of bonded-in rods in timber construction e.g. GIROD and LICONS [4], [5]. In spite of this, no universal standard exists for their design. There had been an informative annex in the pre-standard PrBS ENV 1995-2:1997 which provided limited coverage of the design of bonded-in rods using steel bars however this document was replaced by BS EN 1995-2:2004 and no guidance is included in this current document.

There are three key elements to be considered when designing bonded-in rod connections: the timber, the rod and the adhesive. The most significant challenge in the development of a standard design method is the many varying approaches to defining each of these joint properties.

2 THEORETICAL BACKGROUND

2.1 Materials

The majority of research done in this area to date comprises steel rods bonded-in to glued laminated (glulam) elements with lamellae of a high strength class timber. There has however been some degree of research on the behaviour of bonded-in rods in lower grade timber eg. glulam beams using laminations of low-grade Sitka Spruce [6] and Spruce of strength class C16 in its sawn form [7]. In tests of reinforcement of timber beams with carbon fibre reinforced polymer (CFRP) and basalt fibre reinforced polymer (BFRP) materials locally sourced Pine beams have been used [8], whilst the use of bonded-in rods in Beech laminated veneer lumber has been investigated also [9].

This research investigates the use of locally sourced Irish grown Sitka Spruce. Sitka Spruce grown in Ireland has a fast growth time of approximately 30 to 40 years [10], as a result of this high growth rate the cell structure of the wood is less dense and therefore the timber generally has relatively poor strength and is of a low classification, typically C16 [11]. However, low transportation costs relative to imported timber means that Irish Sitka Spruce can be a very cost-effective building material if its full potential is utilised.

As well as alternative timber types, rod materials other than steel are being investigated, namely Fibre Reinforced Polymers (FRPs). FRPs are composite materials made of a polymer matrix reinforced with different fibres. They are

more corrosion-resistant than steel and so they will have a longer service life, with less maintenance and monitoring required. Even the weakest FRP is stronger in tension than steel and they are all much lighter, meaning that an equally strong joint can be formed with less material being required.

Earlier studies investigated the use of glass fibre reinforced polymer (GFRP) as an alternative to steel [12]–[14] while carbon fibre reinforced polymer (CFRP) has been used more recently [15]. Despite its significant cost effectiveness compared to CFRP and its greater tensile strength compared to GFRP, basalt fibre reinforced polymer (BFRP) has only been touched upon in the literature with regards to its use in bonded-in technology [16]. BFRP has a Young's modulus closer to timber than the more commonly used material, steel. It is also a much lower cost material compared to the other FRPs. These advantages resulted in BFRP being selected for use in this research.

Many investigations have been undertaken to determine which adhesive type is best suited to glued-in rod applications. The adhesive must have good gap-filling properties to ensure a good bond along the entire length of rod, good adhesion to both the rod material and the timber and higher shear strength and stiffness than the timber being used. In a number of studies it was determined that epoxy adhesives had higher strength than phenol resorcinol and polyurethane alternatives and that epoxies are most suitable for glued-in rod applications [17], [18]. A two-part thixotropic gap filling epoxy was used. This adhesive only flows under shear so is ideal for applications such as overhead beam repair and jointing overhead.

In order to create a strong connection, a large surface area of the glue around each rod must be in contact with the timber. Variables that can be altered to increase this surface area include: thickness of the glue-line, length of rod glued (embedded length), number of rods used and rod diameter. Edge distance between the centre of the rod and the edge of the sample must also be considered to ensure the connection does not split prematurely.

2.2 Pull-out test methods

There are several test configurations seen in the literature that can be used to assess pull-out capacity of a rod bonded-in to timber. The five most common are pull-pull, pull-push, pull-pile foundation, pull-beam and pull-bending. Each test method has its own merits and demerits but pull-pull was identified as the more representative, producing relatively higher pull-out strengths [19]. However in a moment resisting timber connection, such as a knee joint in a portal frame structure, it is highly likely that some bending forces would be acting on the glued-in rod rather than axial-only as in the pull-pull set-up. In order to include these bending effects a hinge system, based on the concrete beam test proposed by RILEM 1982 [20] will be used. This type of pull-out test is known as a pull-bending test.

The pull-bending set-up allows the effects of bending forces to be taken in to consideration along with axial forces in what is essentially a pull-pull type test. The system allows bending strength of the bonded-in rod connection to be evaluated by removing the timber in the section being loaded so that the only resistance is from the BFRP bars bonded-in to the timber.

This type of pull-out test has been used successfully in investigating the bond behaviour between glulam elements and GFRP [21], [22]. It is this system that will be used in this research to establish pull-out capacity.

2.3 Embedded Length, l_b

Embedded length is thought to be the most influential variable contributing to pull-out capacity after diameter of the rods used [23], [12]. Following a series of pull-out testing of BFRP rods bonded in to glulam elements with an epoxy resin, it was found that the ultimate pull-out capacity would be reached at a rod embedment length of 15d i.e. 15 times the rod diameter [24]. However, the pull-out testing set-up used to determine this only considered the effects of axial stress using a push-pull testing system which may have given an artificially high pull out capacity as bending effects were neglected.

2.4 Edge Distance, a

A minimum edge distance, i.e. the cross-sectional distance between the centre of the bar and the edge of the timber, must be prescribed in order to prevent the timber from splitting prematurely. As well as this it has been stated that small edge distances can result in a lesser bond strength and a decrease in average pull-out capacity [25]. Most of the latest design approaches use an edge distance of $2.5d$ [26]; [27]. However, there has not been a significant amount of research in this area to date.

2.5 Glueline Thickness, t

In an experimental study on load capacity of bonded-in rods it was found that a larger glue-line thicknesses resulted in an increase in ultimate load [28]. Pull-out capacity of the joint was also found to increase with increasing glue-line thickness beyond a minimum thickness of 2mm [12]. This is a result of a larger shear area with the increased thickness of glueline and hence an increase in capacity. However this advantage must be weighed against the disadvantage of an increase in cost when more glue is required as well as the possibility of an increase in void formation and micro-cavities with increased glueline thickness.

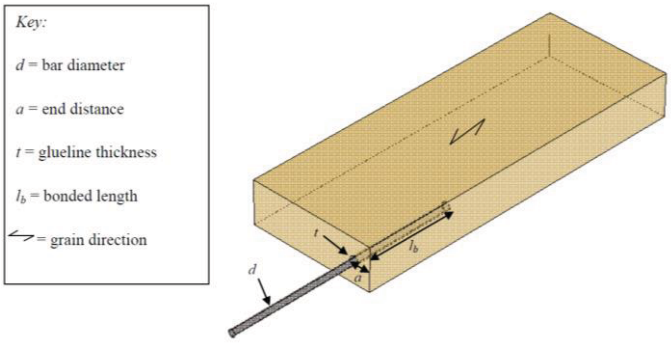


Figure 1: Specimen Geometric Variables

Table 1: Specimen Variables

Embedded length, l_b (mm)	Rod Diameter, d (mm)	Edge Distance, a (mm)	Glueline Thickness, t (mm)	Direction to grain	Moisture Content	No. Repetitions
80	12	30	2	Parallel	9-11%	9
130	12	30	2	Parallel	9-11%	9
180	12	30	2	Parallel	9-11%	9
230	12	30	2	Parallel	9-11%	9
280	12	30	2	Parallel	9-11%	9
330	12	30	2	Parallel	9-11%	9
380	12	30	2	Parallel	9-11%	9
600	12	30	2	Parallel	9-11%	9

3 TESTING

3.1 Timber

Class C16 Irish Sitka Spruce (Picea sitchensis), sourced from Balcas Sawmill, Co. Fermanagh, with a size of 75mm x 225mm sawn section was used. The C16 classification shows that the timber has a 5th percentile bending strength of 16N/mm^2 and a density of 370kg/m^3. Material testing will establish these strengths.

3.2 Rod

12mm diameter Basalt Fibre Reinforced Polymer (BFRP) rods were used in this experimental programme. These rods were found to have a tensile strength of 920 N/mm^2 under a low loading rate of 0.2kN/s [29]. Unlike steel or some other FRPs, no extensive cleaning of the rods was required prior to bonding as they are sand-coated which provides a good surface for adhesion.

3.3 Adhesive

A two-part thixotropic gap filling epoxy was used. This adhesive only flows under shear so is ideal for applications such as overhead beam repair, jointing overhead and such.

3.4 Sample fabrication

Samples were prepared as per the specification given in Table 1.

Moisture content of each sample was recorded during sample preparation and before testing using a handheld moisture meter. Moisture content was found to range from 9% to 11%, which corresponds to Service Class 1 (EC5, Part 1-1).

An auger drill bit was used to drill holes of 16mm diameter, thus producing a glueline thickness of 2mm all around the 12mm diameter rods. Guide blocks were used to ensure the holes were drilled accurately. Drilled lengths varied from a minimum of 80mm in steps to a maximum of 600mm, as shown in Table 1. The holes were drilled 30mm in from the specimen edge; this corresponds to an edge distance, $a = 2.5d$ where d is rod diameter.

The surface of the specimen around the drilled hole was sealed with candlewax to ensure that any glue overspill would not penetrate the sample and result in a false increase in strength around the hole.

The holes were 2/3rds filled with glue using a hose cut to the length of the drilled hole on the end of the nozzle of the glue cartridge to ensure that the glue filled all voids from the very bottom of the hole to the top.

Rods were twisted into place to allow any trapped air to be expelled and for the glue to fully coat the surface of the rods.

A device was used to hold the sample in place and ensure the 2mm bondline was maintained whilst drying. When the glue had hardened the steel hinges and strain gauges were fitted. The samples were then left until the glue had a minimum of 7 days to cure fully before testing.

3.5 Testing Set-up

The pull-bending test set-up was used as it more closely imitates the forces which a bonded-in rod connection would be under in a real application. This test requires a hinge system to be developed that can transfer load through the sample such that the bonded-in rod is under bending forces as well as axial forces. Figure 2 below shows this pull-bending test set-up.

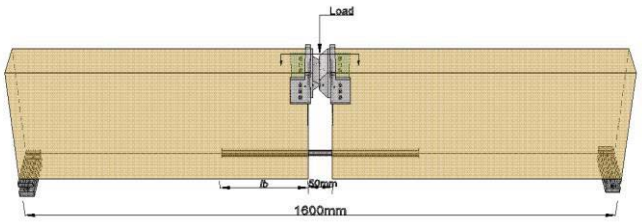


Figure 2: Pull-Bending Test Set-up

A strain gauge was placed on the BFRP rod at mid-span on each sample to monitor the stress-strain in the rod as the sample is loaded.

Samples were loaded in 0.5kN increments to failure using the accurately calibrated 600kN capacity hydraulic actuator.

Deflection at mid-span and net horizontal movement of the bar as the sample was loaded was recorded with data acquisition connected to the transducer, as shown in Figure 3.

Failure load was recorded when the sample could not take any additional load. The mode of failure was recorded also –

percentage failure mode was then calculated for each bonded length.

As per Table 1, each test was repeated multiple times due to the high variability of the timber used.



Figure 3: Transducer Set-up Used to Monitor Movement

4 RESULTS

4.1 General

Table 2 below details the failure modes observed within each sample set. The observed failure modes are illustrated in Figure 4. All specimens failed in a sudden, brittle manner.

Table 2: Failure Modes Experienced

	Percentage of Failure Mode Observed					
Embedded Length, l_b	Shear failure in Timber	Timber Splitting	Rod/Adhesive failure	Shear failure within adhesive	Tensile failure of Rod	Coating of bar failure
80	83	0	17	0	0	0
130	78	22	0	0	0	0
180	67	11	22	0	0	0
230	56	11	33	0	0	0
280	56	11	33	0	0	0
330	67	22	11	0	0	0
380	78	11	0	0	0	11
600*	22	22	0	0	0	0

*crushing of timber experienced in 67% of 600mm long samples

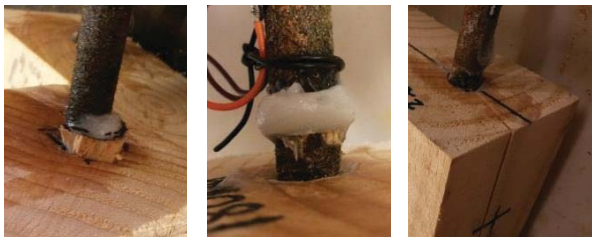


Figure 4: Failure modes observed: a) Shear in timber; b) Rod/Adhesive Failure; c) Timber Splitting

The most prevalent failure mode was a failure in shear of the timber with a total of 64% of all samples failing in this manner. This was as expected due to the timber being the weakest element in the bond. When splitting of the timber occurred the length of the split was often equal to the embedded length of rod. Tensile failure of the rod never occurred as the load required for the rupture of the rod was never reached.

4.2 Influence of increasing embedded length on pull-out capacity

A clear increase in pull-out strength was observed with an increase in embedded length. Figure 5 shows this relationship.

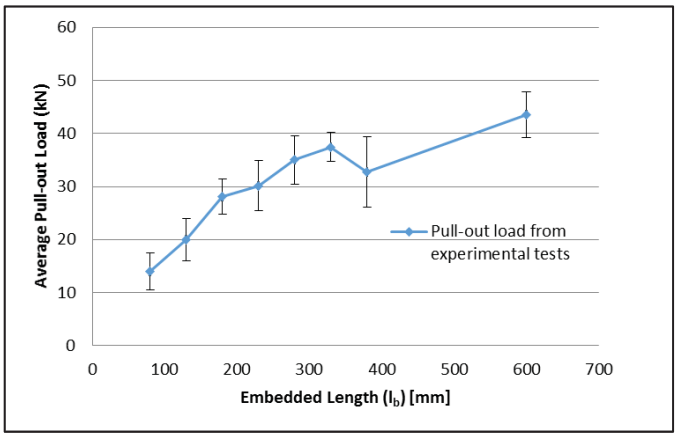


Figure 5: Average Failure Load vs Embedded Length

An increase in pull-out capacity of 168% was observed between the shortest embedded length of 80mm and the longest length of 330mm. The overall relationship between embedded length and pull-out capacity was almost linear.

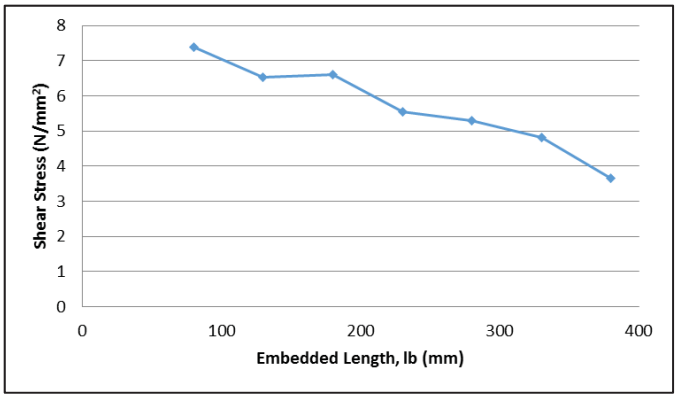


Figure 6: Peak Shear Stress at Timber/Adhesive Interface

Failure mode noticeably shifted from mainly failing in timber shear in the shortest embedded length to other failure modes in the longest embedded length. This is supported by the way in which shear stress at the timber/adhesive bond decreases with increasing embedded length, as detailed in Figure 6. Shear stress at the timber/adhesive bond decreased steadily with increasing embedded length with the exception of Sample B-Sample C where a slight increase was observed.

The applied load at which the samples failed at is presented in the figures below however the geometry of the test rig can

be used to evaluate the equivalent axial stress and thus the data obtained can be compared with established design models for axial-only loading.

5 CONCLUSIONS

A clear increase in pull-out capacity with increased embedded length of the bonded-in BFRP rods was seen, which is reaching a plateau as failure is occurring in the timber as opposed to in the bond.

Material testing will be carried out to determine the properties of the timber, adhesive and rod. This will allow comparisons to be made between the achieved results and predictions from models developed by other researchers. Thus, the significance of the induced bending forces can be determined.

It is planned that additional longer embedded lengths will be investigated to determine at what point the additional length becomes inactive. It is suggested also that an investigation is undertaken where edge distance is increased to determine if failure due to splitting of timber can be avoided.

ACKNOWLEDGMENTS

This research is funded by the Department of Agriculture, Food and the Marine of the Republic of Ireland under the FIRM/RSF/COFORD scheme as part of 'Innovation in Irish timber Usage' (project ref. 11/C/207). The authors would also like to thank the technical staff in QUB for their assistance in the lab.

REFERENCES

[1] D. Smedley, P. Alam, and M. Ansell, "George Street, St. Albans, UK–a case study in the repair of historic timber structures using bonded-in pultruded plates," *... 9th World Conf. Timber ...*, no. 2006, 2006.

[2] K. U. Schober and K. Rautenstrauch, "Experimental Investigations on Flexural Strengthening of Timber Structures with CFRP," in *Proceedings of the International Symposium on Bond Behaviour of FRP in Structures (BBFS 2005)*, 2005, pp. 457–464.

[3] E. Gehri, "High Performing Jointing Technique Using Glued-in Rods," 2010. [Online]. Available: http://www.ewpa.com/Archive/2010/june/Paper_095.pdf?PHPSESSID=kp6fvne92tisofdus2d0hjnv07. [Accessed: 06-Feb-2014].

[4] J. G. Broughton and A. R. Hutchinson, "LICONS Task 2-Sub tast 2.2," 2004.

[5] R. Bainbridge and C. Mettem, "Bonded-in rods for timber structures: a versatile method for achieving structural connections," *Struct. Eng.*, vol. Volume 77, no. Issue 5, pp. p24–27, 1999.

[6] G. M. Raftery and C. Whelan, "Low-grade glued laminated timber beams reinforced using improved arrangements of bonded-in GFRP rods," *Constr. Build. Mater.*, vol. 52, pp. 209–220, Feb. 2014.

[7] P. Alam, M. P. Ansell, and D. Smedley, "Mechanical repair of timber beams fractured in flexure using bonded-in reinforcements," *Compos. Part B Eng.*, vol. 40, no. 2, pp. 95–106, Mar. 2009.

[8] P. de la Rosa García, A. C. Escamilla, and M. Nieves González García, "Bending reinforcement of timber beams with composite carbon fiber and basalt fiber materials," *Compos. Part B Eng.*, vol. 55, pp. 528–536, Dec. 2013.

[9] M. Stepinac, "Joints in beech-LVL timber frames : STSM Report for COST Action FP1004," 2012.

[10] Irish Forestry and Forest Products Association, "An overview of the Irish forestry and forest products sector," Dublin, 2012.

[11] "UNECE Timber Committee Market Report for Ireland 2011," 2011.

[12] K. Harvey and M. P. Ansell, "Improved timber connections using bonded-in GFRP rods," in *Proceedings of 6th World Conference on Timber Engineering, Whitsler, British Columbia,*, 2000.

[13] M. Madhoushi and M. P. Ansell, "Experimental study of static and fatigue strengths of pultruded GFRP rods bonded into LVL and glulam," *Int. J. Adhes. Adhes.*, vol. 24, no. 4, pp. 319–325, Aug. 2004.

[14] M. Ansell and D. Smedley, "Briefing: Bonded-in technology for structural timber," *Proc. ICE-Construction ...*, vol. 160, no. 3, pp. 95–98, Jan. 2007.

[15] L. F. P. Juvandes and R. M. T. Barbosa, "Bond Analysis of Timber Structures Strengthened with FRP Systems," *Strain*, vol. 48, no. 2, pp. 124–135, 2012.

[16] D. Yeboah, "Rigid Connections in Structural Timber Assemblies," Queen's University Belfast, 2012.

[17] E. Serrano, "Glued-in rods for timber structures — a 3D model and finite element parameter studies," *Int. J. Adhes. Adhes.*, vol. Vol. 21, no. Issue 2, p. p 115–127, 2001.

[18] J. G. Broughton and A. R. Hutchinson, "Adhesive systems for structural connections in timber," *Int. J. Adhes. Adhes.*, vol. 21, no. 3, pp. 177–186, 2001.

[19] P. Gustafsson, E. Serrano, S. Aicher, and C. Johansson, "A strength design equation for glued-in rods," *Proc. Int. ...*, vol. 3, no. 1, 2001.

[20] RILEM TC, "RC 5 Bond test for reinforcement steel. 1. Beam test, 1982," in *RILEM Recommendations for the Testing and Use of Constructions Materials*, RILEM, Ed. E & FN SPON, 1994, pp. 213 – 217.

[21] J. Sena-Cruz, J. Branco, M. Jorge, J. A. O. Barros, C. Silva, and V. M. C. F. Cunha, "Bond behavior between glulam and GFRP's by pullout tests," *Compos. Part B Eng.*, vol. 43, no. 3, pp. 1045–1055, Apr. 2012.

[22] J. Barros, J. Sena-Cruz, and R. Faria, "Assessing the embedded length of epoxy-bonded carbon laminates by pull-out bending tests," 2001.

[23] R. Steiger, E. Gehri, and R. Widmann, "Pull-out strength of axially loaded steel rods bonded in glulam parallel to the grain," - *Mater. Struct.*, vol. Vol. 40, no. 8, p. p 69–78, Jan. 2006.

[24] D. Yeboah, S. Taylor, D. McPolin, and R. Gilfillan, "Pull-out behaviour of axially loaded basalt fibre reinforced polymer (BFRP) rods bonded parallel to the grain of glulam elements," *Struct. Eng.*, vol. May, pp. p42–51, 2012.

[25] G. Tlustochowicz, E. Serrano, and R. Steiger, "State-of-the-art review on timber connections with glued-in steel rods," - *Mater. Struct.*, vol. 44, no. 5, pp. 997–1020, 2011.

[26] R. Widmann, R. Steiger, and E. Gehri, "Pull-out strength of axially loaded steel rods bonded in glulam perpendicular to the grain," *Mater. Struct.*, vol. 40, no. 8, pp. 827–838, Jan. 2007.

[27] E. Serrano, R. Steiger, and P. Lavisci, "Core Document of the COST Action E34 'Bonding of Timber,'" in *Lignovisionen*, University of Natural Resources and Applied Life Sciences, Vienna, 2008.

[28] R. Steiger, E. Gehri, and R. Widmann, "Pull-out strength of axially loaded steel rods bonded in glulam parallel to the grain," *Mater. Struct.*, vol. Vol. 40, p. p 69–78, 2006.

[29] G. Tharmarajah, "Compressive Membrane Action in Fibre Reinforced Polymer (FRP) Reinforced Concrete Slabs," Queen's University Belfast, 2010.

A Bayesian Approach For Estimating Characteristic Bridge Traffic Load Effects

Enright, B.[1], Leahy, C.[2] and OBrien, E.J.[2&3]
[1]School of Civil Engineering, Dublin Institute of Technology, Bolton Street, Dublin 1, Ireland
[2]Roughan & O'Donovan Innovative Solutions, Arena Road, Sandyford, Dublin 18, Ireland
[3]School of Civil, Structural & Environmental Engineering, University College Dublin, Newstead, Dublin 4, Ireland
email: bernard.enright@dit.ie, cathal.leahy@rod.ie, eugene.obrien@ucd.ie

ABSTRACT: This paper investigates the use of Bayesian updating to improve estimates of characteristic bridge traffic loading. Over recent years the use Weigh-In-Motion technologies has increased hugely. Large Weigh-In-Motion databases are now available for multiple sites on many road networks. The objective of this work is to use data gathered throughout a road network to improve site-specific estimates of bridge loading at a specific Weigh-In-Motion site on the network. Bayesian updating is a mathematical framework for combining prior knowledge with new sample data. The approach is applied here to bridge loading using a database of 81.6 million truck records, gathered at 19 sites in the US. The database represents the prior knowledge of loading throughout the road network and a new site on the network is simulated. The Bayesian approach is compared with a non-Bayesian approach, which uses only the site-specific data, and the results compared. It is found that the Bayesian approach significantly improves the accuracy of estimates of 75-year loading and, in particular, considerably reduces the standard deviation of the error. With the proposed approach less site-specific WIM data is required to obtain an accurate estimate of loading. This is particularly useful where there is concern over an existing bridge and accurate estimates of loading are required as a matter of urgency.

KEY WORDS: Bayesian; Updating; Bridge; Characteristic; Traffic; Load; Modelling.

1 INTRODUCTION

Accurate modelling of bridge traffic loading is critically important in bridge engineering. At the design stage it allows the design of bridges which are fit for purpose, while reducing the waste associated with overdesign. In the assessment of existing structures, estimates of traffic loading are possibly more important. Where there is concern over an existing bridge, this information will determine whether a bridge needs to be repaired or replaced. If a bridge is saved as a result, significant cost savings can be made.

The most accurate method for modelling bridge traffic loading is to use Weigh-In-Motion (WIM) data. WIM systems measure truck weights and axle configurations as they pass along a road at normal highway speeds [1]. Statistical methods are generally used to extrapolate from the relatively short WIM measurement period to the return period used for bridge design/assessment. Return periods of 75 years [2] or 1000 years [3] are commonly used.

A common extrapolation approach is to fit a statistical distribution to the measured data and to extrapolate to the required return period. The generalized extreme value distribution is a popular choice in the literature. This distribution can be separated into a family of three extreme value distributions, comprising of the Gumbel (type I), Fréchet (type II) and Weibull (type III) distributions. The type I Gumbel distribution is used by some authors [4], [5] but the type III Weibull distribution is perhaps the most common [6–9]. These extreme value distributions must be fitted to block maxima, with maximum daily or weekly values often used.

As an alternative to direct extrapolation from WIM data, Monte Carlo simulations can also be used. With these simulations, statistical distributions are fitted to the properties of the measured traffic and a new stream of traffic is simulated [10–12]. Hundreds or thousands of years of traffic can be simulated in this way and the characteristic load effects can be obtained directly from the simulated traffic, without the need for extrapolation. These long run simulations are time consuming but they allow for loading scenarios, such as truck meeting or overtaking events, which did not occur during the WIM measuring period.

WIM data is becoming increasingly more common and this is reflected in recent bridge loading literature. Enright et al. [13] used 21 million trucks from 11 sites to examine long span bridge loading in Alabama. Nowak & Rakoczy [14] simulated bridge loading using 35 million truck records from 32 sites in the US and Fu & You [15] examine multi-truck loading events using 63 million truck records gathered in New York.

This paper develops a method for using the large amounts of data which are now available for many road networks to help estimate loading at a new site on the same network. Bayesian updating is used as it provides a mathematical framework for combining prior knowledge about a certain statistical property with new sample data [16]. This is useful in engineering where data from various sources must be combined in the decision-making process and has been used for many civil engineering applications. For example, Hong and Prozzi [17] use this approach to update the parameter distributions for a pavement performance model. Enright and Frangopol [18] use it to predict the deterioration of concrete bridges as it allows the results of bridge inspections to be combined with prior information to obtain improved predictions. Other studies [19], [20] also apply a Bayesian approach to improve the accuracy of structural engineering models.

In this work 81.6 million trucks from 19 sites in the US are used to test the approach. These truck records provide the prior knowledge about loading in the US. This prior data is then combined with new site-specific data, using the Bayesian approach, in order to obtain improved estimates of characteristic loading at the new site. The Bayesian approach is compared with a Weibull extrapolation approach, which uses only site-specific data, and the improvements in accuracy examined. The proposed approach reduces the amount of WIM data required to make accurate estimates of loading. This is very useful where there is concern over the safety of an existing bridge and an estimate of loading is required in order to make a prompt decision about the future of the bridge.

2 METHODOLOGY

2.1 Bayesian updating

A random variable (maximum weekly GVW) is described by a parameter vector θ (e.g. for a Weibull distribution with three parameters, $\theta = (\mu, \sigma, \xi)$). However, these parameters are themselves random variables due to the uncertainty associated with parameter estimation. These random variables have an assumed 'prior' distribution $f'(\theta)$. When a new set of sample data, x, is acquired this prior distribution can be updated to obtain the 'posterior' distribution $f''(\theta)$. The posterior distribution is calculated as:

$$f''(\theta) = \frac{P(x|\theta)f'(\theta)}{\int_{-\infty}^{\infty} P(x|\theta)f'(\theta)d\theta} \quad (1)$$

where $P(x|\theta)$ = conditional probability, or likelihood $L(\theta)$, of the new data x, given θ.

The denominator is a normalising constant which ensures that $f''(\theta)$ is a complete probability density function (PDF). As a result Eq. (1) can be rewritten as:

$$f''(\theta) = kL(\theta)f'(\theta) \quad (2)$$

This is the approach used here as it avoids the computationally intensive calculation of the denominator $\int_{-\infty}^{\infty} P(x|\theta)f'(\theta)d\theta$. The likelihood function is calculated for the new set of data as:

$$L(\theta) = \prod_{i=1}^{n} f(x_i; \theta) \quad (3)$$

The posterior $f''(\theta)$ is often used to obtain the expected value of θ, which gives a point estimator of the parameter vector. However the approach used in this work includes the uncertainty associated with estimating the value of θ. The posterior distribution of the parameter vector can be used to calculate the cumulative distribution function (cdf) for the underlying random variable X (in this case the maximum weekly GVW), and this cdf can be used to calculate characteristic values:

$$P(X \leq z) = \int P\big((X \leq z)\big|\theta\big) f''(\theta)d\theta \quad (4)$$

The prior distribution of the parameter vector is obtained by fitting a Weibull distribution to each site-year of prior data. The data from the Colorado site is used to simulate the new site-specific data and is not included in the prior data. This new site-specific data is modelled by randomly sampling 25 non-consecutive weeks of data from the Colorado site. Bayesian updating is then used obtain the posterior distribution of the parameter vector and hence the cdf for loading at that site. For the Bayesian approach, the Weibull distribution must be fitted to the entire distribution, rather than the tail of the maximum daily values, which is commonly used [8], [21], [22]. With the aim of examining the trend in this tail region, the Weibull distribution is fitted to maximum weekly GVWs, rather than maximum daily. GVW is used here to assess the proposed method but the same approach could easily be applied to bridge load effects required for assessment.

The Generalized Extreme Value (GEV) distribution is given by:

$$F(x;\ \mu, \sigma, \xi) = exp\left\{-\left[1 + \xi\left(\frac{x-\mu}{\sigma}\right)\right]^{-\frac{1}{\xi}}\right\} \quad (5)$$

defined on $\{x : 1 + \xi(x - \mu)/\sigma > 0\}$, where:

μ = location parameter, $-\infty < \mu < \infty$
σ = scale parameter, $\sigma > 0$
ξ = shape parameter

The Weibull distribution is a subset of the GEV distribution, where the shape parameter ξ is negative. The location and scale parameters are similar to mean and standard deviation and the shape parameter describes the behaviour in the tail of the distribution.

2.2 WIM Data

The prior data used here is WIM data from the United States Federal Highway Administration's Long-Term Pavement Performance (LTPP) Program. Initially the LTPP collected WIM data with inconsistent quality control measures [23]. In 1999 a plan was developed which, among other things, improved and centralised quality control. This led to a significant improvement in WIM data reliability and since 2003 'research quality' WIM data is being collected at 28 of the Specific Pavement Studies LTPP sites. The 81.6 million truck records were collected over the period 2005-2012 and are detailed in Table 1.

Table 1. WIM Data

Site	State	Years of Data	Trucks/ Weekday	MMW GVW[2]
1	Arizona	5.7	575	63
2	Arizona	5.7	4,988	93
3	Arkansas	6.0	5,526	100
4	California	5.0	5,939	68
5[1]	Colorado	6.5	1,473	73
6	Delaware	5.5	930	66
7	Illinois	7.4	3,139	98
8	Indiana	4.5	1,489	69
9	Kansas	6.6	1,851	81
10	Louisiana	4.9	506	77
11	Maine	4.4	835	67
12	Maryland	6.8	1,030	51
13	Minnesota	6.2	316	67
14	New Mexico	4.7	716	61
15	New Mexico	4.7	2,934	89
16	Pennsylvania	5.6	5,315	90
17	Tennessee	5.6	5,474	89
18	Virginia	6.0	1,082	63
19	Wisconsin	5.3	987	73

[1]Site used to test the Bayesian approach
[2] MMW GVW: mean maximum weekly gross vehicle weight (a good measure of intensity of loading at a site [24])

Bridges in the US are designed and assessed using the HL-93 load model [2], [25]. This model applies to "normal vehicular use" (all legal trucks, illegal overloads and un-analysed routine permits) and does not include special permit vehicles. In order to describe a methodology which can be used to examine "normal vehicular use", special permit vehicles are removed from the database. These vehicles are identified in the WIM data using filtering rules, as described by Leahy [26].

2.3 Estimating the prior distribution using kernel density estimators (KDE)

The Colorado site is used as the test data for the Bayesian approach. The other 18 sites are used as the prior data. Four years of data are used from each site as this amount is available for each site and gives each site an equal weighting. A Weibull distribution is fitted to the maximum weekly GVWs for each site-year of prior data – see Figure 1. This gives 72 sets of Weibull parameters (μ, σ, ξ). These parameter values are shown in Figure 2. In this figure, values of σ are plotted against μ for different ranges of the shape factor, ξ.

Figure 1 also shows the Colorado site used to test the Bayesian approach. It can be seen that the loading at the Colorado site agrees well with the general trend of the prior data. As a result it is expected that the proposed method will perform well with this test site.

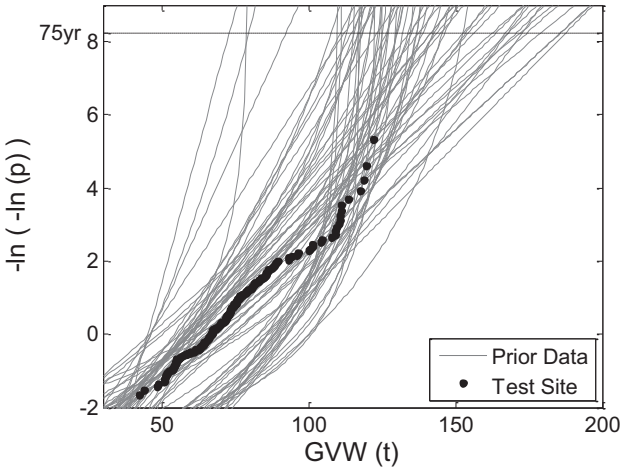


Figure 1. Weibull distributions of the prior data alongside the Illinois site used to test the proposed approach.

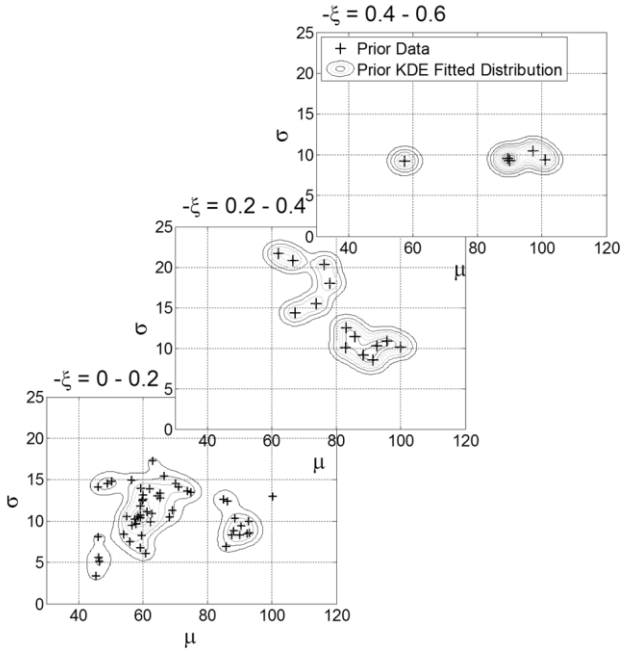
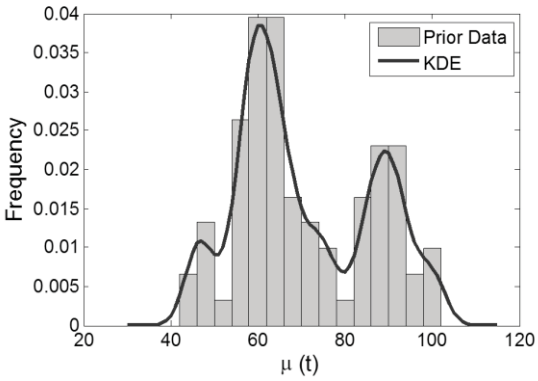


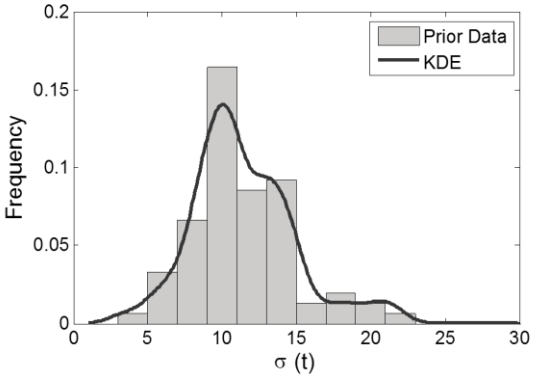
Figure 2. Prior data used with kernel density estimated distribution for different ranges of shape parameter ξ.

A continuous distribution, rather than discrete points, is needed for the prior distribution. In order to fit a distribution to the 72 data points, kerned density estimators (KDEs) are used. With the KDE method, each data point is replaced with a component density. These densities are known as kernel functions and are added to obtain an estimate of the overall distribution. Any distribution can be used for the kernel functions but the normal distribution is a popular choice and is used here. The product kernel method, as described by Scott [27], is used. The kernel function is essentially a trivariate normal distribution where all variables are independent. The estimated distribution is shown in Figure 2. For visualisation purposes, the distribution is plotted for different ranges of the shape parameter ξ.

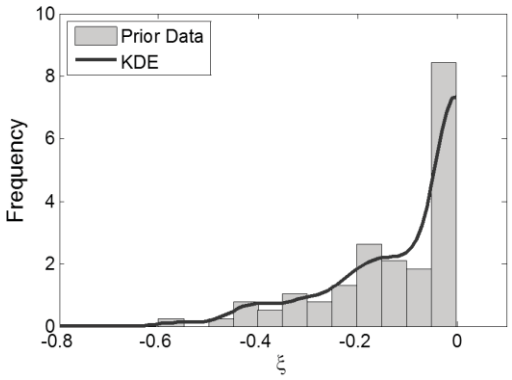
In the Bayesian calculations, the weighting of the prior data, with respect to the new data, is determined by the bandwidth of the kernel function. The bandwidth, in this case, refers to the variance of the trivariate normal distribution, where each of the three variables has its own independent standard deviation. If the bandwidth is too large, oversmoothing will occur and the trends in the prior data will be lost. On the other hand, if the bandwidth is too small the posterior distribution will be restricted to match very closely to the prior data. Optimal bandwidths exist for sample data which matches a certain theoretical distribution, but this is not the case here. In this work a trial and error approach, as recommended by Silverman [28], is used and an optimal value selected by visual inspection of the marginal distributions – see Figure 3. Bandwidth values of three tonnes, one tonne and 0.04 are used for μ, σ and ξ, respectively. The selection of these values is somewhat subjective but when applying this approach bandwidth selection should be carefully considered as it does influence the results.



(a) Location parameter



(b) Scale parameter



(c) Shape parameter

Figure 3. Histograms of marginal distributions of prior data with the kernel density estimated distribution.

2.4 Assessing accuracy of proposed Bayesian approach

The Bayesian approach is assessed to determine its accuracy in estimating the 75-year load. 75 years is the design life used in US bridge design [2]. The benchmark 75-year load is first calculated by fitting a Weibull distribution to all the data available at the Colorado site (6.5 years) and extrapolating to the 75-year load – see Figure 4. This approach assumes that this extrapolation from 6.5 year of data represents the true 75-year loading.

The accuracy of the method is assessed by randomly selecting 25 non-consecutive maximum weekly values from the Colorado data. The Bayesian approach, using the prior data, is then applied to this sample dataset and the 75-year load estimated. The accuracy of the estimate is then determined by comparison with the benchmark.

A non-Bayesian approach, where no prior data is used, is then applied to the same sample data. A Weibull distribution is fitted directly to the 25-week sample. The accuracy in estimating the 75-year value can then be compared with the Bayesian approach – see Figure 4. This process is then repeated for 100 different random datasets in order to assess the standard deviation of the error.

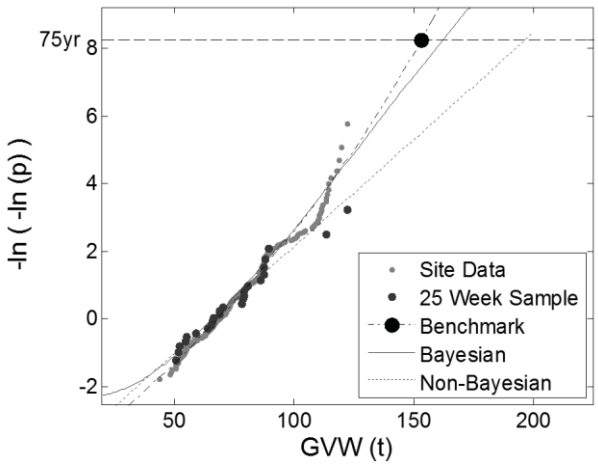


Figure 4. Example of the Bayesian and Weibull approach applied to a 25-week sample from the Colorado site ("Site data" includes the weekly maxima from 6.5 years of measurements at the site).

3 RESULTS

The errors for both the Bayesian and non-Bayesian approaches are shown in Figure 5 and Table 2. A mean error of zero with a small standard deviation is preferable. It can be seen for the non-Bayesian approach, where no prior data is used, that there is large variation in the errors. This variation is not desirable when estimating characteristic loading on bridges as it may result in an estimate of loading which is significantly greater or less than the true value. This variation is significantly reduced with the Bayesian approach, with the standard deviation reducing from 19.3% to 4.4%. The mean error is also improved from 7.8% to 2.3%.

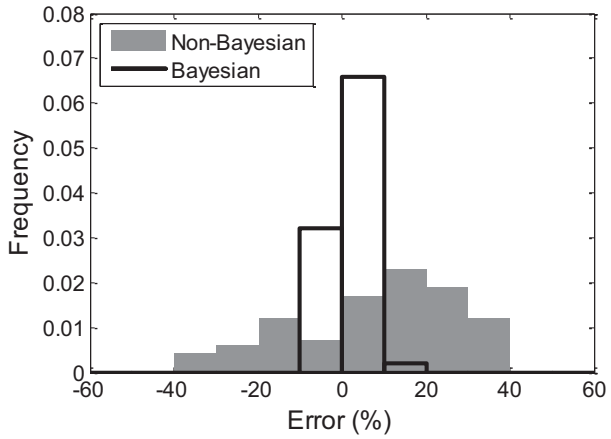


Figure 5. Errors in estimating 75-year load for the Bayesian and non-Bayesian approaches, for 100 sample datasets.

Table 2. Error with Bayesian and non-Bayesian approaches

	Mean	Standard Deviation
Bayesian	2.3%	4.4%
Non-Bayesian	7.8%	19.3%

4 CONCLUSION

A Bayesian methodology is proposed for obtaining additional value from the large amount of WIM data which are available for multiple sites on many road networks. The approach uses this existing, or 'prior', network data to help predict site-specific loading at a new site on the network. The prior data used here is from 18 WIM sites in the US. This WIM data is used to determine the prior distribution of the parameters of a Weibull distribution and this prior distribution is updated using the new site-specific data. The Bayesian approach is compared with the alternative of fitting a Weibull distribution directly to the site-specific data without using any prior data.

The errors in estimating characteristic loading are compared for the proposed Bayesian approach and the non-Bayesian approach. The Bayesian approach achieves significant reductions in the variation of the error while also improving the mean of the error. The proposed method allows accurate estimates of loading to be achieved with less site-specific WIM data. This is particularly useful where there is concern over the safety of an existing bridge and accurate estimates of loading are required to make a prompt decision about the future of the bridge.

The method performs well with the Colorado site used to test it. However, this site has similar loading to the general trend in the prior data. It is possible that the Bayesian approach may not perform as well at a site with unusually low or high levels of loading as the method may tend to push estimates of loading closer to that of an average site.

The proposed Bayesian approach examined here used a large WIM database as the prior data. The WIM measurements were gathered at 18 WIM sites which were subject to strict quality control measures. The results of the method depend on the extent of good quality prior data which is available. It is acknowledged such a large database of good quality prior data may often not be available when assessing bridge traffic loading and that the improvement in accuracy may not be as significant if less prior data is available.

ACKNOWLEDGMENTS

The authors gratefully acknowledge the Federal Highway Administration's Long-Term Pavement Performance Program for access to an extensive WIM database and the Irish National Roads Authority for their financial support.

REFERENCES

[1] COST323, *Weigh-in-Motion of Road Vehicles - Final Report*. PARIS: LCPC, 2002.

[2] AASHTO, *AASHTO LRFD Bridge Design Specifications*, 5th ed. Washington D.C.: American Association of State Highway and Transportation Officials, 2010.

[3] EC1, *Eurocode 1: Actions on structures, Part 2: Traffic loads on bridges. European Standard EN 1991-2:2003*. Brussels: European Committee for Standardization, 2003.

[4] D. I. Cooper, "Development of short span bridge-specific assessment live loading," in *Safety of Bridges*, P. C. Das, Ed. London: Thomas Telford, 1997, 64-89.

[5] A. O'Connor and E. Eichinger, "Site-specific traffic load modelling for bridge assessment," *Proceedings of The Institution of Civil Engineers. Bridge Engineering*, vol. 160, no. 4, 185-194, 2007.

[6] S. F. Bailey and R. Bez, "Site specific probability distribution of extreme traffic action effects," *Probabilistic engineering mechanics*, vol. 14, no. 1, 19-26, 1999.

[7] T. J. Miao and T. H. T. Chan, "Bridge live load models from WIM data," *Engineering Structures*, vol. 24, no. 8, 1071-1084, 2002.

[8] E. J. OBrien, B. Enright, and A. Getachew, "Importance of the tail in truck weight modelling for bridge assessment," *ASCE Journal of Bridge Engineering*, vol. 15, no. 2, 210-213, 2010.

[9] S. A. Graves, E. J. OBrien, and A. O'Connor, "The Determination of Site-Specific Imposed Traffic Loadings on Existing Bridges," in M. J. Ryal, G. A. R. Parke, & J. E. Harding. (Eds.), *The Fourth International Conference on Bridge Management*, London, 2000.

[10] B. Enright and E. J. OBrien, "Monte Carlo simulation of extreme traffic loading on short and medium span bridges," *Structure and Infrastructure Engineering*, vol. 9, no. 12, 1267-1282, 2013.

[11] A. O'Connor and E. J. OBrien, "Traffic load modelling and factors influencing the accuracy of predicted extremes," *Canadian Journal of Civil Engineering*, vol. 32, no. 1, 270-278, 2005.

[12] B. Sivakumar, M. Ghosn, and F. Moses, *Protocols for Collecting and Using Traffic Data in Bridge Design - NCHRP Report 683*. Washington D.C.: Transport Research Board, 2008.

[13] B. Enright, C. Carey, and C. C. Caprani, "Microsimulation Evaluation of Eurocode Load Model for American Long-Span Bridges," *Journal of Bridge Engineering*, vol. 18, no. 12, 1252-1260, 2013.

[14] A. Nowak and P. Rakoczy, "WIM Based Simulation Model Of Site Specific Live Load Effect On The Bridges," in B. Jacob, A. H. Mcdonnell, F. Schmidt, & W. Cunagin (Eds.), *6th International Conference on Weigh-In-Motion*, Dallas, 2012, 352-358.

[15] G. Fu and J. You, "Truck load modeling and bridge code calibration," in Faber, Kohler, & Nishijima (Eds.), *Applications of Statistics and Probability in Civil Engineering*, London, 2011, 406-413.
[16] A. H.-S. Ang and W. H. Tang, *Probability concepts in engineering : emphasis on applications in civil & environmental engineering*, 2nd ed. Wiley, New York, 2007.
[17] F. Hong and J. A. Prozzi, "Estimation of pavement performance deterioration using Bayesian approach," *Journal of infrastructure systems*, vol. 12, no. 2, 77-86, 2006.
[18] M. P. Enright and D. M. Frangopol, "Condition prediction of deteriorating concrete bridges using Bayesian updating," *Journal of Structural Engineering*, vol. 125, no. 10, 1118-1125, 1999.
[19] T. Igusa, S. G. Buonopane, and B. R. Ellingwood, "Bayesian analysis of uncertainty for structural engineering applications," *Structural Safety*, vol. 24, no. 2, 165-186, 2002.
[20] J. L. Beck and S.-K. Au, "Bayesian updating of structural models and reliability using Markov chain Monte Carlo simulation," *Journal of Engineering Mechanics*, vol. 128, no. 4, 380-391, 2002.
[21] B. Enright, "Simulation of traffic loading on highway bridges," PhD Thesis, University College Dublin, 2010.
[22] OBrien, E. J., Schmidt, F., Hajializadeh, D., Zhou, X.-Y., Enright, B., Caprani, C. C., … Sheils, E., "A Review of Probabilistic Methods of Assessment of Load Effects in Bridges," *Submitted for publication*, 2013.
[23] D. Walker and D. Cebon, "The Metamorphosis of LTPP Traffic Data," in B. Jacob, A. H. Mcdonnell, F. Schmidt, & W. Cunagin (Eds.), *6th International Conference on Weigh-In-Motion*, Dallas, 2012, 242 - 249.
[24] E. J. OBrien and B. Enright, "Using Weigh-In-Motion Data to Determine Aggressiveness of Traffic for Bridge Loading," *Journal of Bridge Engineering, ASCE*, vol. 18, no. 3, 232-239, 2012.
[25] AASHTO, *The Manual for Bridge Evaluation*, 2nd ed. Washington D.C.: American Association of State Highway and Transportation Officials, 2011.
[26] C. Leahy, "Predicting Extreme Traffic Loading on Bridges Using Weigh-In-Motion Data," PhD Thesis, University College Dublin, 2014.
[27] D. W. Scott, *Multivariate density estimation: theory, practice, and visualization*, vol. 383. John Wiley & Sons, 1992.
[28] B. W. Silverman, *Density estimation for statistics and data analysis*, vol. 26. London: Chapman & Hall, 1986.

Allowing for a Rocking Datum in the Analysis of Drive-by Bridge Inspections

J. KEENAHAN[1] & E.J. OBRIEN[1]
[1]Dept. of Civil, Structural and Environmental Engineering, University College Dublin, Ireland

Abstract
'Drive-By' damage detection is the concept of using sensors on a passing vehicle to detect damage in a bridge. At highway speeds, the vehicle spends a short amount of time on the bridge: it may not even go through a full cycle of vibration, resulting in only a partial signal of the bridge motion being detected. Given that the spectral resolution of standard signal processing techniques depends on the length of data in the signal, they cannot be used to identify the bridge frequency accurately. In addition, the nonlinear and non-stationary nature of the vehicle-bridge interaction system poses challenges. The aim of this study is to model a 'drive-by' bridge inspection approach using a beam in free vibration. An optimisation approach is proposed in numerical simulations as an alternative to standard signal processing techniques to overcome the challenges of short signals and the nonlinear nature of the drive-by system.

Keywords: bridge, damage, drive-by, inspection, SHM, short

1. Introduction

'Drive-by' bridge inspection (Kim and Kawatani, 2009) involves the instrumentation of a vehicle, rather than the bridge, in order to assess bridge condition. A significant limitation to date has been the need for the vehicle to traverse the bridge at low speeds (Lin and Yang, 2005; Toshinami et al., 2010). At highway speeds, the vehicle spends a short amount of time on the bridge which may not go through a full oscillation during the time that the vehicle is on it. As a result only a partial signal of the bridge motion is detected.

Many bridge damage detection methods use Fourier analysis as the principal signal-processing tool (Staszewski and Robertson, 2007). However, Fourier analysis has several shortcomings; it is unable to accurately represent non-periodic functions (Pines and Salvino, 2006), non-stationary functions (Qian and Chen, 1999) and it requires linearity. This is a challenge as available data in the 'drive-by' context is from a nonlinear system (Huang et al. 1998). Measured signals produced resulting from structural damage are of a non-stationary nature (Staszewski and Robertson, 2007) and the signals are short in duration (Kim and Melhem, 2004).

The Short Time Fourier Transform (STFT) was later developed for processing non-stationary signals. The width of the window remains constant throughout the analysis and therefore represents a compromise between time and frequency-based views of a signal. Cerda et al. (2012) examine the 'drive-by' concept. Vertical acceleration signals from the vehicle are processed using the STFT, and results show that low vehicle speeds are needed to accurately identify changes in bridge natural frequency.

The Wavelet Transform represents the next logical step in the development of signal processing methods: a windowing technique with variable size windows. Other basis functions, such as the Haar, Mexican hat, Coiflet, Daubechies and Morlet, can be

used (Kim and Melhem, 2004). However, the Wavelet Transform still suffers from the convolution of the signal with an *a priori* basis function (Ayenu-Prah and Attoh-Okine, 2009) as available wavelet dictionaries are often not appropriate for analysing the nonlinear behaviour of many structural systems (Salvino et al. 2005).

The Hilbert Transform has long been proposed as an advanced signal processing technique (Huang et al. 1998). It is the convolution of the signal with the function $\frac{1}{\pi t}$. However, a drawback in the 'drive-by' context is that it requires a signal where the instantaneous frequency does not change with time, and intra-wave frequency modulation is typical of nonlinear systems (Cantero and OBrien, 2013). A more recently developed method, the Hilbert-Huang Transform (HHT), has been proposed to overcome this challenge. The HHT uses Empirical Mode Decomposition (EMD) to decompose the signal into functions where the frequency does not change with time and then applies the Hilbert Transform. However, authors that have used the HHT with EMD in a moving load context have found that the speed of the vehicle negatively impacts the success of damage detection (Bradley et al. 2010).

This limitation of vehicle-bridge interaction in detecting the modal properties of a bridge cannot be overcome by increasing the scanning frequency of the sensors (Keenahan et al., 2014). The underlying problem is that often the bridge has not undergone a full period of its fundamental frequency in the time it takes the vehicle to cross the bridge. Therefore, the only practical solution, if standard signal processing is to be used, is to decrease the velocity of the vehicle to capture more oscillations. In this paper, an optimisation approach is proposed as an alternative to standard signal processing techniques to overcome the challenges of short signals, an example of which is the nonlinear system of 'drive-by' monitoring at highway speeds.

2. Optimisation as an Alternative to Standard Signal Processing Techniques

The concept of using an optimisation approach to determine the bridge frequency is based on minimising the sum of the squares of the differences between measured data and a theoretical expression, with frequency as the decision variable. Initially, the equation for a beam in free vibration is used to generate the measured data as this is comparable to the motion of a bridge exposed to the passing of a vehicle of much less mass:

$$u(x,t) = C\cos(\omega t - \alpha)\sin\left(\frac{n\pi x}{L}\right) \quad (1)$$

where $u(x,t)$ is the displacement at position, x, and time, t, C is a constant representing the amplitude, ω is the frequency of vibration, α is a phase angle, n is the mode number and L is the length of the beam. The frequency of vibration, in rad s-1, is determined from:

$$\omega = \left(\frac{n\pi}{L}\right)^2 k \quad (2)$$

where k is the square root of the ration of beam stiffness to beam mass. Taking values of C = 1, α = 0, k = 50, L = 10 and n = 1, the frequency is analytically determined from equation (2) to be 4.9348 rad s-1. Beam displacements are determined using equation (1) for x varying in 0.1 m increments, and t varying in 0.005 s increments,

corresponding to a speed of 20 m s-1. The value for $C = 1$ is chosen so that the displacements are normalised.

3. One mode of vibration

Initially, a single sensor is visualised on a vehicle model, that can measure absolute vertical translation of the bridge. For the purpose of determining the data that this sensor would read, it was envisaged that the vehicle model would traverse the beam, but with no vehicle-bridge interaction. Figure 1 illustrates the data that would be read by the sensor if it were present on the vehicle.

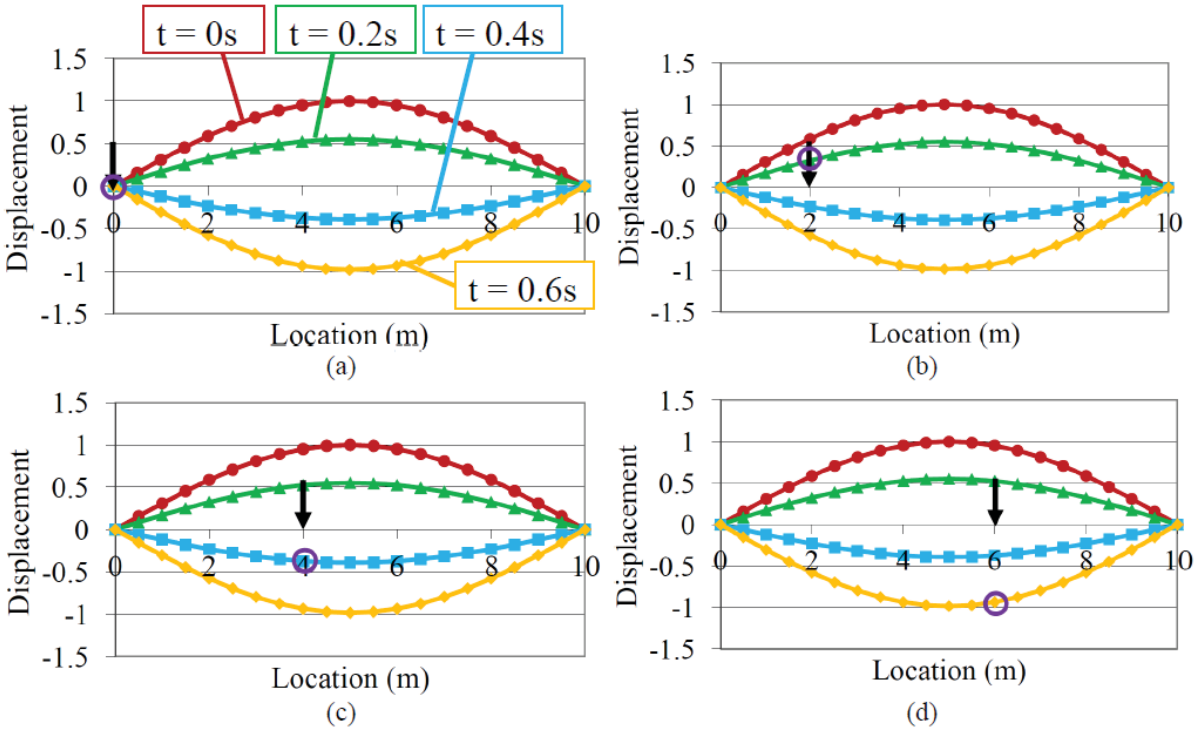


Figure 1: Bridge displacements read by the sensor on the vehicle model: (a) vehicle at start of bridge; (b) vehicle at 0.2L; (c) vehicle at 0.4L; (d) vehicle at 0.6L

In Figure 1(a), the sensor on the vehicle model reads the displacement at position x = 0 m at time t = 0. In Figure 1(b), the vehicle has moved 0.2L along the bridge. The displacement read by the sensor is from the second time curve (triangular data points) at t = 0.2, enclosed by the dark circle. In Figure 1(c), the vehicle has moved even further along the bridge and the displacement is read from the third time curve (square data points) at t = 0.4 and at position x = 0.4L. Scans of the bridge deflections are taken by the moving vehicle model at a spacing step of 0.1 m and a time step of 0.005 s, and are shown in Figure 2.

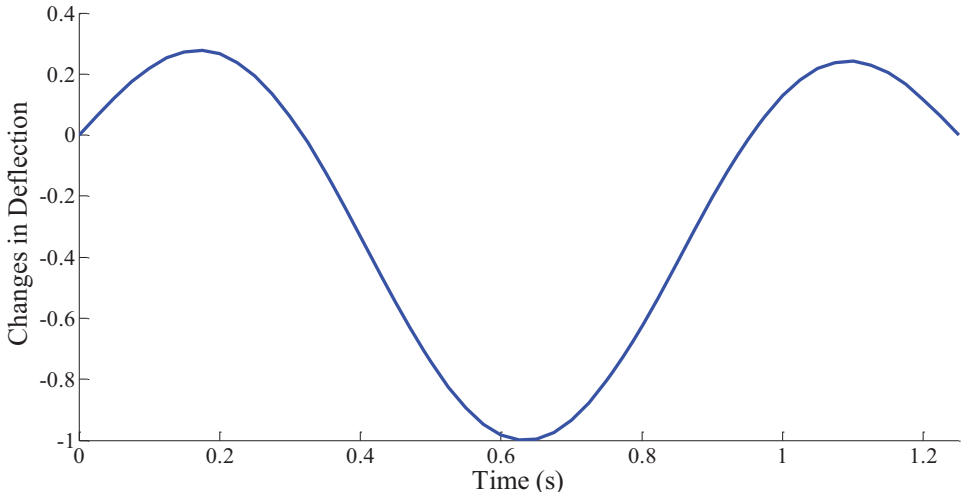


Figure 2: Scan of the bridge deflections from the moving vehicle model for a single mode of vibration

An optimisation approach, which seeks to minimise the difference between measured data and a theoretical expression, is used. The stream of displacements in Figure 2 is taken as the measured data and equation (1) as the theoretical expression. The optimisation approach correctly determines the unknown bridge frequency in equation (1) to be 4.9348 rad s-1.

Global damage is simulated as a change in the '*k*' parameter of equation (2). The actual frequencies for each damage level are determined analytically from equation (2). These frequencies, along with those determined by the optimisation approach, are presented in Table 1 and are identical at five places of decminal.

Table 1 - Actual and inferred frequencies for a range of damage levels

k	**Actual Frequency (rad s-1)**	**Frequency from optimisation (rad s-1)**
50	4.9348	4.9348
49	4.8361	4.8361
48	4.7374	4.7374
47	4.6387	4.6387
46	4.5400	4.5400

Figure 3 illustrates the scanned bridge deflections from the moving vehicle model for different damage levels. There is a clear distinction between the curves, even for small changes in damage.

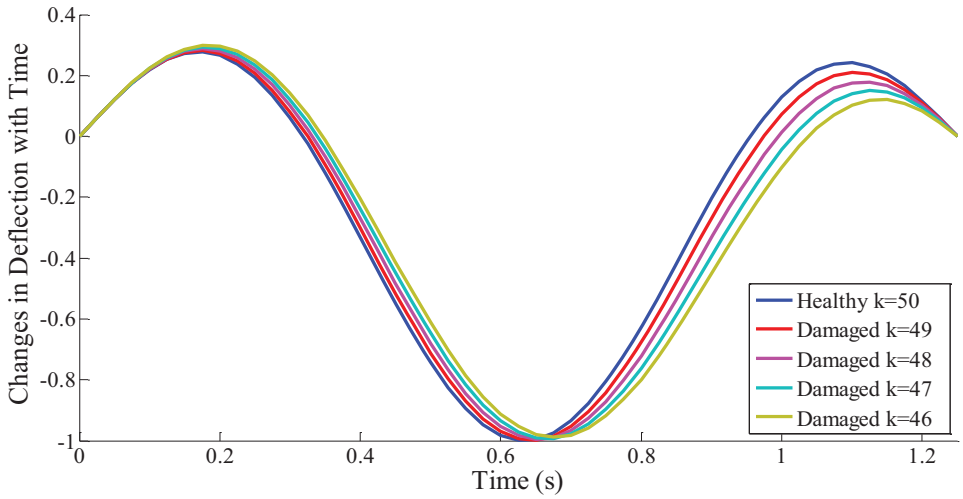


Figure 3: Bridge deflections from the vehicle model for different levels of damage for a single mode of vibration

4. Two modes of vibration

The inclusion of a second mode of vibration results in a more complex expression for the displacement of the beam in free vibration:

$$u(x,t) = C_1 \cos(\omega_1 t - \alpha_1) \sin\left(\frac{1\pi x}{L}\right) + C_2 \cos(\omega_2 t - \alpha_2) \sin\left(\frac{2\pi x}{L}\right) \quad (3)$$

where C_1 and C_2 represent the amplitudes of the first and second mode respectively, ω_1 and ω_2 are the frequencies and α_1 and α_2 are the phase angles. Using the parameter values of Table 2, Figure 4 gives the deformed shape of the bridge at a range of points in time. As before, the value of C_1 = 1 is chosen such that the mode one displacements are normalised, and the amplitude of mode two is taken to be one tenth of the amplitude of mode one.

Table 2 - Parameter values for two modes of vibration

Parameter	**Mode 1**	**Mode 2**
C	1	0.1
α	0	0.7854
n	1	2
k	50	50
L	10	10

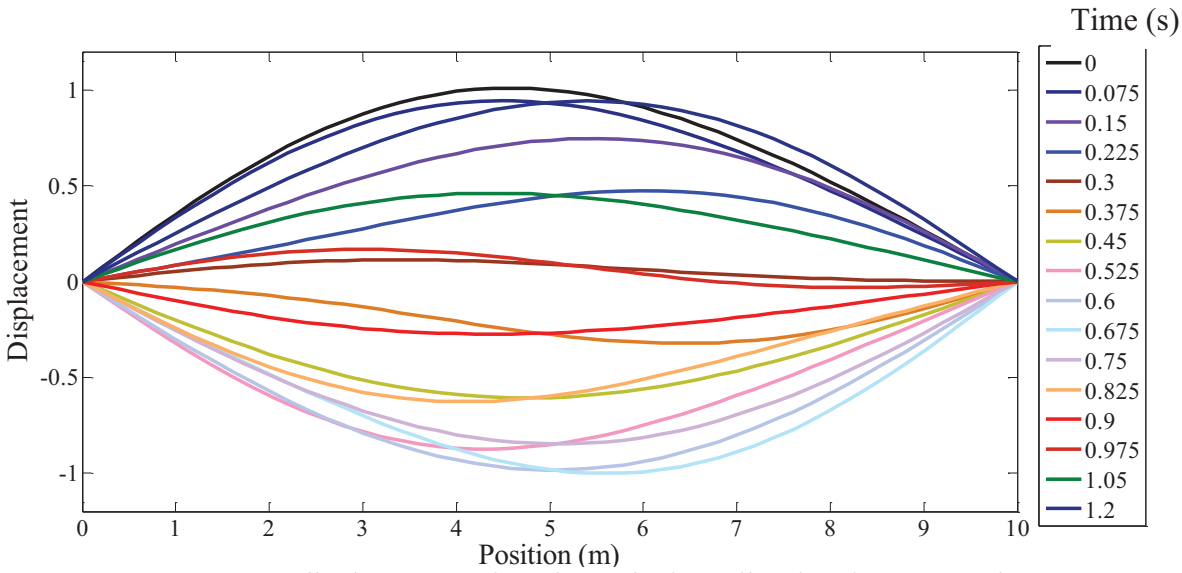


Figure 4: Beam displacements for a beam in free vibration for two modes

As before, a vehicle containing one sensor is considered to be traversing the beam at a speed of 20 m s-1 and scanning deflections every 0.005 s. Global damage is again simulated as a change in the '*k*' parameter of equation (2). Figure 5 illustrates a scan of the bridge deflections from the vehicle for different levels of damage.

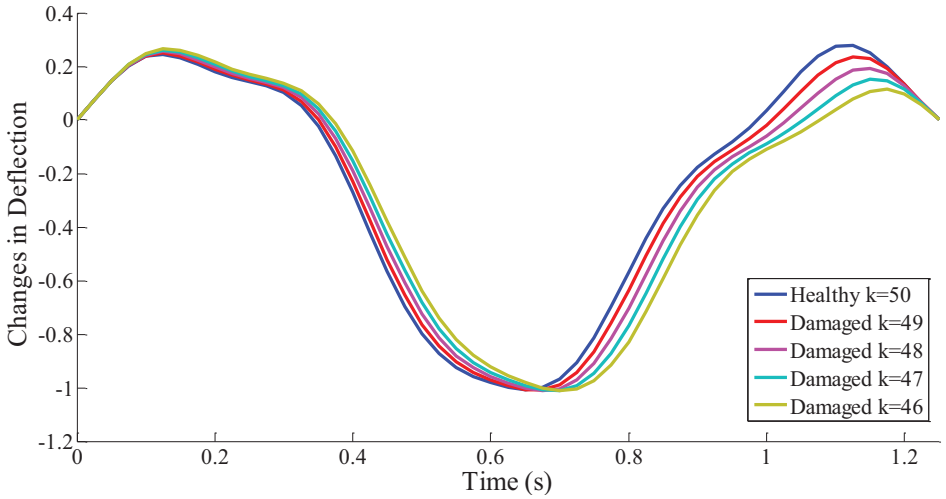


Figure 5: Bridge deflections from the moving vehicle for different levels of damage for two modes of vibration

It clearly illustrates that damage can be detected from a scan of bridge deflections read by a sensor on the vehicle model. A similar optimisation approach is used in this example where there are now five unknown variables; two frequencies, two amplitudes and the difference in phase angle between the modes. It is assumed here that the phase angle of the first mode is zero. The variables, correctly determined from the optimisation procedure, are given in the Table 3 and exactly match the actual values in the number of significant digits shown.

Table 3 - Inferred frequencies, amplitudes and phase difference for a range of damage levels

k	Frequency mode 1 (rad s-1)	Frequency mode 2 (rad s-1)	Amplitude mode 1	Amplitude mode 2	Difference in Phase angle (rad)
50	4.9348	19.73	1.00	0.10	0.7854
49	4.8361	19.34	1.00	0.10	0.7854
48	4.7374	18.94	1.00	0.10	0.7854
47	4.6387	18.55	1.00	0.10	0.7854
46	4.5400	18.16	1.00	0.10	0.7854

To gain an understanding of the conditioning of the system, a plot of the contours of the objective function (considering only the two frequencies as variables) is shown in Figure 6, where the objective function is the sum of the squares of the differences between measured and theoretical data.

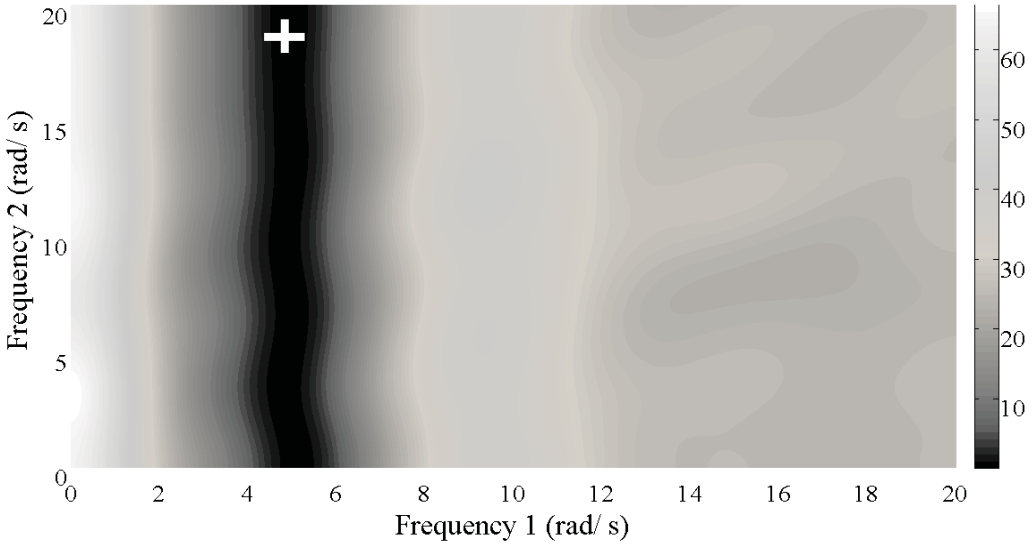


Figure 6: Contours of the objective function (undamaged, $k = 50$)

The figure shows that the optimisation approach can find the global minimum in the range of frequencies from 0 to 20 rad s-1. The minimum is indicated in the figure by the white cross. The objective function is highly sensitive to the first natural frequency but insensitive to the second. However, it should be noted that it is the frequency of the first mode that will be used for damage detection and so the accuracy of the inferred second natural frequency is unimportant.

5. Conclusions

This paper investigates the feasibility of using an instrumented vehicle model to detect damage in a bridge. An optimisation approach is proposed as an alternative to standard signal processing techniques because of the brevity of the signal. Simulations show that modest losses of stiffness in the bridge can be detected using the vehicle measurements. Overall the results presented in the paper indicate that the method has the potential to be developed as an effective tool for the monitoring of bridge damage.

References

Ayenu-Prah, A. and Attoh-Okine, N. (2009) 'Comparison study of hilbert-huang transform, fourier transform and wavelet transform in pavement profile analysis' *Vehicle System Dynamics* 47 437–456.
Bradley, M., González, A. and Hester, D. (2010), 'Analysis of the structural response of a moving load using empirical mode decomposition' *In: Proceedings of the 5th International Conference on Bridge Maintenance, Safety and Management*, Philadelphia, USA, 356–363.
Cantero, D. and OBrien, E.J. (2013) 'Tracing the evolution of bridge natural frequencies as a vehicle traverses the bridge' *In: Proceedings of the 11th International Conference on Vibration Problems*, Lisbon, Portugal.
Cerda, F., Garrett, J., Bielak, J., Barrera, J., Zhuang, Z., Chen, S., McCann, M., Kovacevic, J. and Rizzo, P. (2012), 'Indirect structural health monitoring in bridges: scale experiments' *In: Bridge Maintenance, Safety, Management, Resiliance and Sustainability*, Stresa, Italy, 346–353.
Huang, N.E., Shen, S., Long, S., Wu, M., Shih, H., Zheng, Q., Yen, N., Tung, C. and Liu, H. (1998), 'The empirical mode decomposition and the hilbert spectrum for nonliner and nonstationary time series analysis' *Proceedings of the Royal Society of London A* 454 903–995.
Keenahan, J., OBrien, E.J., McGetrick, P.J. and González, A. (2014), 'The use of a dynamic truck-trailer drive-by system to monitor bridge damping' *Journal of Structural Health Monitoring*, accepted for publication.
Kim, C.W. and Kawatani, M. (2009), 'Challenge for a drive-by bridge inspection' in *Proceedings of the 10th International Conference on Structural Safety and Reliability*, Osaka, Japan, 758–765.
Kim, H. and Melhem, H. (2004), 'Damage detection of structures by wavelet analysis' *Engineering Structures* 26 347–362.
Lin, C.W. and Yang, Y.B. (2005), 'Use of a passing vehicle to scan the fundamental bridge frequencies: An experimental verification', *Engineering Structures* 27: 1865-1878.
Pines, D. and Salvino, L. (2006) 'Structural health monitoring using empirical mode decomposition and the Hilbert phase' *Journal of Sound and Vibration* 294 97–124.
Qian, S. and Chen, D. (1999), 'Joint time-frequency analysis' *Signal Processing Magazine*, IEEE 16 52–67.
Salvino, L.W., Pines, D.J., Todd, M. and Nichols, J.M. (2005), 'EMD and Instantaneous Phase Detection of Structural Damage, in Hilbert-Huang transform and its applications', *World Scientific Publishing*, Singapore, 227–261.
Staszewski, W.J. and Robertson, A.N. (2007), 'Time-frequency and time-scale analyses for structura health monitoring' *Philosophical Transactions of the Royal Society A*, 365 449–477.
Toshinami, T., Kawatani, M. and Kim, C.W. (2010), 'Feasibility investigation for identifying bridge's fundamental frequencies from vehicle vibrations' in *Proceedings of the Fifth International Conference on Bridge Maintenance, Safety and Management*, USA, 317–322.

DYNAMIC AMPLIFICATION FACTOR OF CONTINUOUS VERSUS SIMPLY SUPPORTED BRIDGES DUE THE ACTION OF A MOVING LOAD

Omar Mohammed[1, 2], Daniel Cantero[3], Arturo Gonzalez[1], Salam Al-Sabah[1]
[1]Department of Civil Engineering, University College Dublin, Belfield, Dublin 4, Ireland
[2]Former Department of Civil Engineering, University of Anbar, Al-Anbar, Al-Ramadi, Iraq
[3] Roughan and O'Donovan Innovative Solutions, Ireland
email: omar.sattar@ucdconnect.ie, canterolauer@gmail.com, arturo.gonzalez@ucd.ie, salam.al-sabah@ucd.ie

ABSTRACT: This paper extends the research on dynamic amplification factors (DAFs) caused by traffic loading from simply supported to continuous (highway and railway) bridges. DAF is defined here as the ratio of maximum total load effect to maximum static load effect at a given section (mid-span). Another dynamic amplification factor FDAF can be defined as the ratio of the maximum total load effect throughout the entire bridge length to the maximum static load effect at a given section (mid-span). DAF/FDAF can be determined for both sagging and hogging bending moments in a continuous beam. Noticeable differences appear among DAF/FDAF of mid-span bending moment in a simply supported beam, DAF/FDAF of the mid-span bending moment in a continuous beam and the DAF/FDAF of the bending moment over the internal support in a continuous beam. Three span lengths are tested in the simply supported beam models as well as three continuous beams made of two equal spans. Each model is subjected to a moving constant point load that travels at different velocities. The location of the maximum total moment varies depending on the velocity. FDAF and DAF are plotted versus frequency ratio to allow for a generalisation of the results. The results show that FDAF is often greater than DAF in simply supported and continuous beams. Also, FDAF of sagging bending moment in continuous beam is about 12% greater than that the simply supported case Moreover, FDAF of hogging bending moments is about 16% greater than those of sagging bending moments in the continuous beam. Consequently, all FDAF values in the continuous beam are larger than those of the simply supported case.

KEY WORDS: Dynamics; Vibration; Continuous bridges; Moving load.

1 INTRODUCTION

The dynamic behaviour of beam structures subjected to moving loads, such as bridges on highways and railways, has been investigated over a century [1]. Most of this research has been focused on simply supported structures even though continuous structures represent a significant proportion of the bridge stock. Therefore, this paper will focus on investigating the dynamic amplification of continuous structures due to a moving load and compare them to the simply supported case. From the structural point of view, the use of continuous deck reduces the bridge deck thickness. Also, the reduction of joints number in bridge structures represents substantial cost savings arising from the construction and maintenance costs of movement joints [2]. The influence of factors such as rail irregularity, ballast stiffness, suspension stiffness and suspension damping appears to be small for continuous bridges in comparison with simply supported bridges. These factors can affect drastically the riding comfort of the train cars traveling over bridges [3].

The amplification of the static response due to the vibration of the structure is characterized in many ways in literature. Cantieni [4] uses the term 'dynamic increment'. Other terms are 'impact factor' or 'dynamic load allowance' [5], 'dynamic increment factor' [6], or 'dynamic load allowance' [7]. This paper uses the 'Dynamic Amplification Factor' (DAF) concept. However, there also exists different definitions for DAF. [7] defines DAF as the 'increase in the design traffic load resulting from the interaction of moving vehicles and the bridge structure and it is described in terms of the static equivalent of the dynamic and vibratory effects'. In [8], DAF is 'a ratio between the maximum dynamic deflection in the moving mass problem and that in the corresponding moving force problem', and in [9], is 'the ratio of the maximum dynamic load effect induced by the vehicle to the maximum static load effect induced in the bridge from a vehicle'.

The static load effect at a given section is going to vary as the load crosses the structure, and it is possible to select a maximum static load effect from this time history. Similarly, the total (= static + dynamic) load effect will also vary with time and a maximum total load will be reached at some point during the load crossing. In this paper, DAF (Equation (1)) is going to mean the ratio of maximum total load effect to maximum static load effect for a given section location 'A-A' due to the crossing of a load. For the simply supported cases, the 'A-A' location will be mid-span (Figure 1). For the continuous cases, three different sections will be chosen as location 'C-C' and 'B-B' where these locations of these two sections are shown in Figure 2 as will be explained in section 3.2.

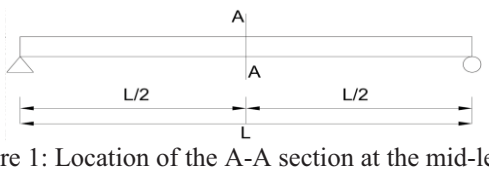


Figure 1: Location of the A-A section at the mid-length of simply supported beam

$$DAF = \frac{Max.total\ load\ effect\ at\ sec.A-A}{Max.static\ load\ effect\ at\ sec.A-A} \quad (1)$$

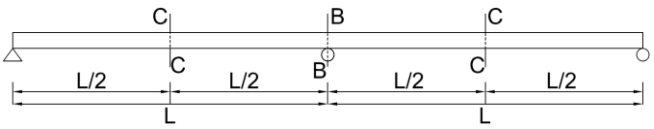


Figure 2: Location of the C-C sections at the mid-length of each of the two equal spans of continuous beam and the location of B-B section over the internal support.

Full Dynamic Amplification Factor (FDAF) is introduced first by Cantero et al. [10] and also used in this investigation for both simply supported and continuous bridges. In the latter, two FDAFs are suggested: one for sagging and another for hogging moments. FDAF gives an indication of the highest possible moment in any section of the bridge with respect to the maximum static moment at a selected section 'A-A' (Equation (2)). The numerator of Equation (2) is not necessarily the location 'A', but the section holding the highest moment during the load crossing. Therefore, FDAF must always be equal or greater than DAF.

$$FDAF = \frac{Max.total\ load\ effect\ accross\ the\ beam\ length}{Max.static\ load\ effect\ at\ sec.A-A} \quad (2)$$

2 SIMULATION MODELS

1-D element Euler-Bernoulli beam elements with two degrees of freedom (2-DOF) at each node are assembled using finite element theory to build the bridge models. The length of each discretized element is 0.1 m. The bridge models are assumed to be homogenous with a modulus of elasticity of 35 GPa. A constant point load of 98.1 kN moving at velocities within a range from 1 km/h to 300 km/h is applied to the beam. This simple model of a single point load is used to represent a single vehicle/axle crossing simply supported and continuous bridges at constant velocity. This model has several significant simplifications. The mass of the vehicle is assumed to be small compared to the mass of the bridge. The vibration of the vehicle is ignored; therefore the interaction between the vehicle and the bridge is also ignored. This model is obviously different from the reality in many respects. It is employed here only to obtain an understanding of some of the principal factors which result in high amplification factors such the vehicle velocity. The Wilson-θ method [12] is used here to integrate the equations of motion and to obtain the displacements, velocities and accelerations along the beam traversed by the load. The time interval is 0.0005 and the damping ratio is 0.03. Further details on this method can be found in [12].

A one-dimensional model of the simply supported beam with a first natural frequency of 11.52 Hz is validated by comparison to the results of the closed form solution by [1] as it can be seen in Figure 3 for a load travelling at 20 m/s.

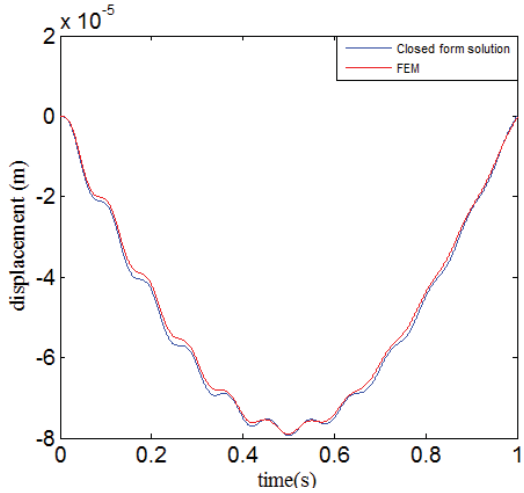
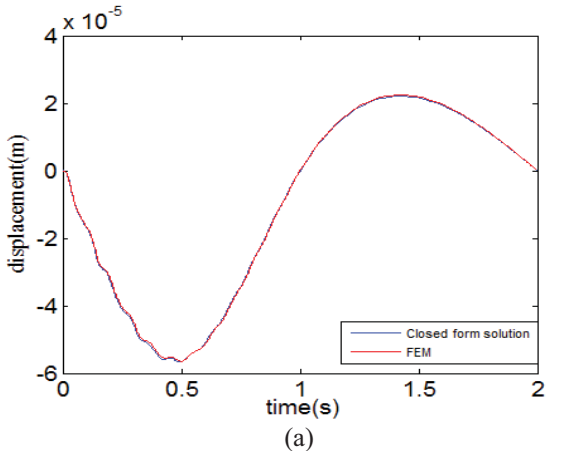
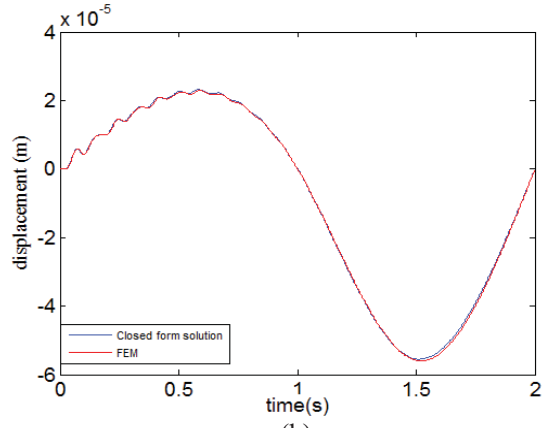


Figure 3: Displacement versus time of (20 m) simply supported beam subjected to a moving (constant) point load

A continuous beam model with first natural frequency of 11.52 Hz is also validated by comparison to approach by [13] as shown in Figure 4 for a load travelling at 20 m/s.



(a)



(b)

Figure 4: Displacement versus time of 40 m continuous beam with two equal spans subjected to a moving (constant) point load (a) Mid-length of first span (b) Mid-length of second span

Table 1 summarises the properties of the three simply supported beam models (10 m, 20 m and 30 m) as well as the three continuous beams made of two equal spans (10 m, 20 m

and 30 m each span) that will be analysed in the sections that follow. These properties are based on [11], where the bridge cross-sections are made of T-beam or Y-beams depending on the bridge span.

Table 1 General characteristics of the bridge models.

Type of the beam	Total length (m)	Mass per unit length (kg/m)	Second moment of inertia (m^4)	1st natural frequency (Hz)
S.S T-beam	10	18750	0.16783	8.79
S.S T-beam	20	37500	1.271233	4.27
S.S Y-beam	30	21080.5	2.2752	3.39
Con. T-beam	20	18750	0.16783	8.79
Con. T-beam	40	37500	1.271233	4.27
Con. Y-beam	60	21080.5	2.2752	3.39

3 DYNAMIC AMPLIFICATION FACTOR AND FULL DYNAMIC AMPLIFICATION FACTOR

3.1 *Simply supported beams*

Three beams with different span lengths are tested (10 m, 20 m and 30 m). As per Equation (1), DAF due to a constant moving point load is the ratio of maximum total load (static plus dynamic) effect to maximum static load effect at a given section (mid-span in this case). The static bending moment is calculated at the mid-span of the simply supported beam. The total bending moment (static plus dynamic) is also calculated at the mid-span [14]. As per Equation (2), FDAF is the ratio of the maximum total load effect across the entire bridge length to the maximum static load effect at a given section (mid-span in this case).

FDAF and DAF are plotted versus the non-dimensional Alpha parameter in Figure 5. Alpha is also known as speed parameter in [1] or frequency ratio in [9]. It is defined as the ratio of load circular frequency to the first circular frequency of the beam (Equation (3)).

$$Alpha = \frac{c}{2fL} \tag{3}$$

Where c is the velocity of the vehicle in m/s, f is the bridge natural frequency in Hz and L is the pan length in m.

As expected, DAF is less than FDAF [10]. The difference between DAF and FDAF generally increases as the location of the critical section (i.e., section holding the highest total moment across the beam length for the entire load crossing) moves away from mid-span due to changing of the load velocity. Maximum FDAFs and DAFs occur at a number of critical frequency ratios where the oscillatory nature of the dynamic component of the response reaches a maximum together with the maximum static.

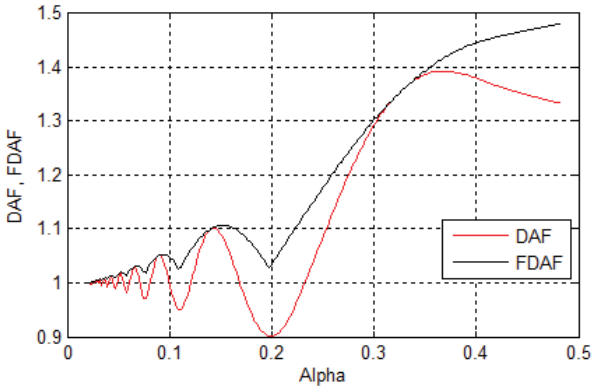
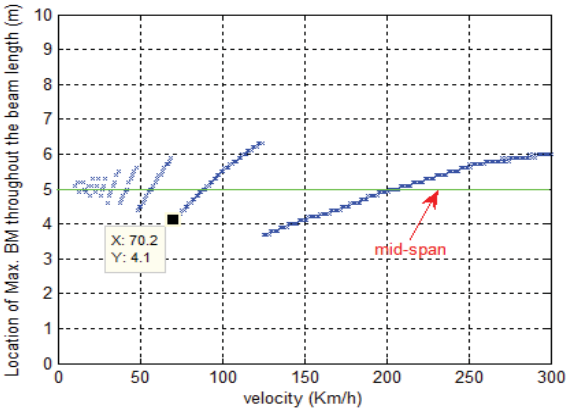


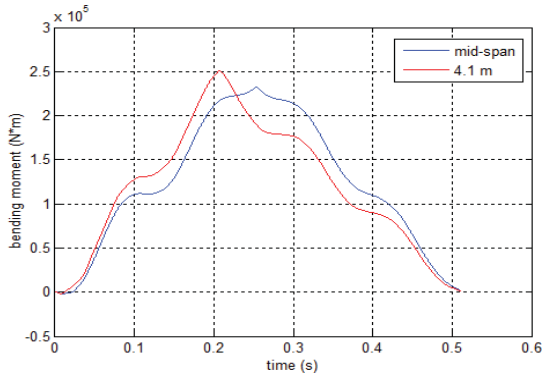
Figure 5: DAF and FDAF versus Alpha of 10 m simply supported beam

Figure 6 shows the variation of the location of maximum bending moment at the 10 m simply supported beam when subjected to a moving point load travelling at velocities from 1 km/h to 300 km/h (with a velocity increment 1 km/h). Figure 6(a) illustrates the location of the maximum total bending moment versus velocity of the moving point load acting on the beam. It is shown that, at the velocity of 70.2 km/h, the location of the maximum total bending moment is located at 4.1 m away from the left support of the beam. Figure 6(b) shows the total bending moment versus time (from the time the load enters the bridge) at the mid-span section and at a section 4.1 m away from the left support for a load velocity of 70.2 km/h. It can show the total bending moment at 4.1 m is greater than that at the mid-span of the beam.



(a)

Since different span lengths are used for simply supported bridges in this study; Figure 7 shows the FDAF versus Alpha. It can be seen that changes in the span lengths do not affect the FDAF value. Therefore, DAF and FDAF values due to a single point load can be generalized to any span length provided they are plotted versus the Alpha parameter. For a particular bridge length, Alpha parameter can be easily converted to speed or vice versa by simply applying Equation (3).



(b)

Figure 6: Critical locations in a 10 m simply supported beam: (a) location of max. total BM throughout the beam length, (b) Max. total BM in two locations

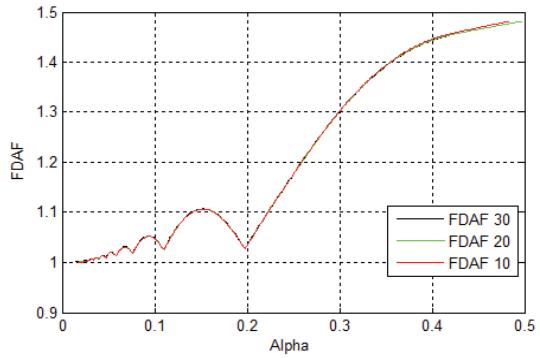


Figure 7: FDAF versus Alpha of 10 m, 20 m and 30 m simply supported beams.

3.2 *Continuous beams of two equal spans*

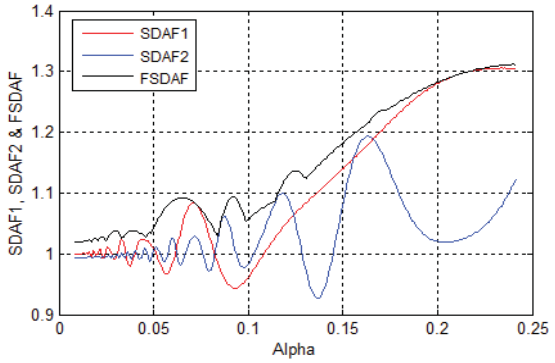
The main aim of this paper is to quantify the dynamic amplification factor of a continuous bridge compared to the simply supported. Here, continuous beams consist of two equal spans (10 m, 20 m and 30 m each span). Mid-length of the first and second spans are the two selected locations at which to refer the static sagging bending moments. Therefore, there are two DAFs of sagging moment: one for the first span (i.e., SDAF1 in Figure 8(a) which is DAF for a location 'C-C' in Equation (4) being mid-span of the 1st span) and another for the second span (i.e., SDAF2 in Figure 8(a) which is DAF for a location 'C-C' in Equation (4) being mid-span of the 2nd span).

$$SDAF = \frac{Max.total\ load\ effect\ at\ Sec.\ C-C}{Max.static\ load\ effect\ at\ sec.C-C} \qquad (4)$$

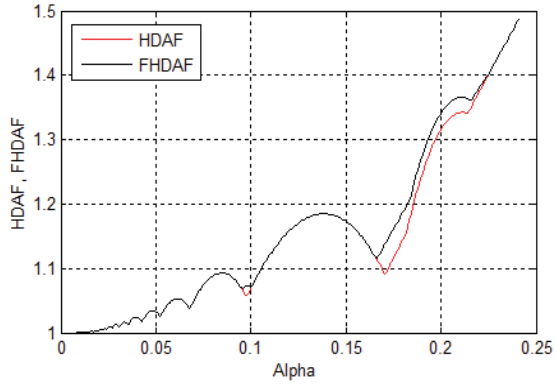
A third DAF is introduced to characterize the hogging bending moment over the internal support (i.e., HDAF in Figure 8(b) which is DAF for a location 'B-B' in Equation (5) being the section at the internal support).

$$HDAF = \frac{Max.total\ load\ effect\ at\ Sec.\ B-B}{Max.static\ load\ effect\ at\ sec.B-B} \qquad (5)$$

For clarity, FDAFs (Equation (4)) are redefined here for the three selected 'C-C' locations. FDAF for sagging bending moment (i.e., FSDAF in Figure 8(a)) is the ratio of the maximum total sagging bending moment across the beam length to the maximum static sagging bending moment at the mid-length of the first span (Note: Maximum static moment at the mid-length of the first span and the second span are equal because it is a continuous beam of two equal spans). FDAF for hogging bending moment (i.e., FHDAF in Figure 8(b)) is the ratio of the maximum total hogging bending moment across the beam length to the maximum static hogging bending moment over the internal support (section B-B in Figure 2). It can be seen that FDAF is equal or larger than DAF. As before, the difference between DAF and FDAF increases as the location of the critical section varies across the beam length due to changes in load velocity. Maximum FDAFs and DAFs occur at a number of critical frequency ratios (i.e., critical speeds causing a larger dynamic amplification can be predetermined if the bridge frequency and length are known). Also FDAF and DAF of hogging bending moment is greater that of sagging bending moment.



(a)



(b)

Figure 8: DAF and FDAF versus Alpha of 20 m continuous beam (a) DAF of 1st span and 2nd span, and FDAF of sagging bending moment versus Alpha (b) DAF and FDAF of hogging bending moment versus Alpha

Figure 9 shows the bending moment versus time at mid-length of the first span, mid-length of second span and over the internal support of a 20 m continuous beam with two equal spans subjected to a moving point load travelling at 1.08 km/h (0.3 m/s, i.e., practically the static component of any response to a moving point load at these locations). Figure 9(a) and (c) show the variation of the location of the maximum total hogging and sagging bending moment respectively with

velocity (with a velocity increment of 1 km/h) for a point load moving on a 20 m continuous beam.

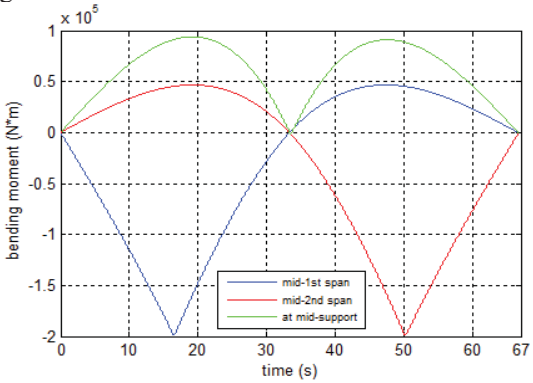
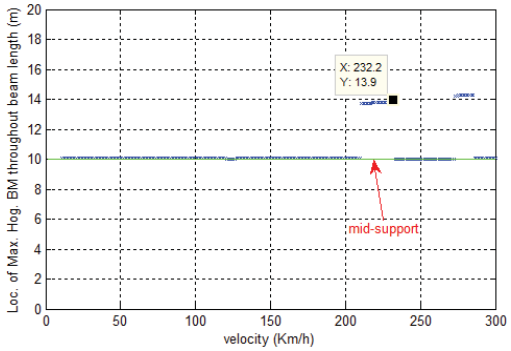
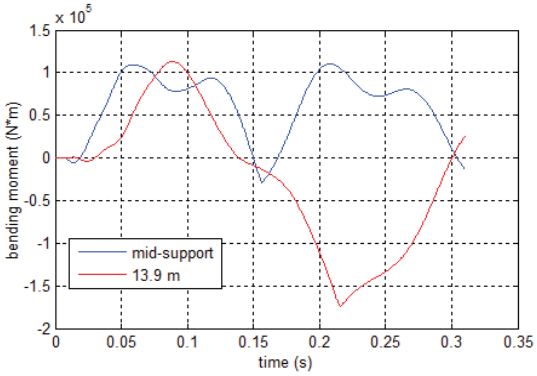


Figure 9: Bending moment versus time for a load velocity of 1.08 km/h on a 20 m continuous beam with two equal spans

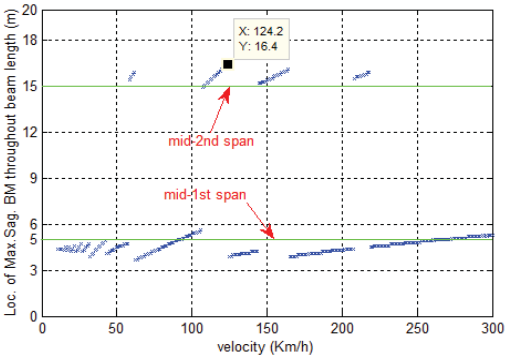
In Figure 10(a), maximum total hogging moment commonly develops over the internal support, however, for a velocity of 232.2 km/h the maximum total hogging bending moment appears at 13.9 m of the beam length. Figure 10(b) illustrates the total hogging bending moment at the mid-support and 13.9 m of the beam length for this scenario at 232.2 km/h. Figure 10(c) illustrates the location of the maximum sagging bending moment for a range of load velocities (with a velocity increment of 1 km/h). Maximum sagging moment typically takes place in the 1st span, although there are a few velocities that are an excpetion. For example, at 124.2 km/h, the maximum total sagging bending moment is located at 16.4 m from the first support. Figure 10(d) illustrates this particular scenario where the maximum total sagging bending moment at 16.4 m exceeds both sagging moments at the mid-length of the two spans.



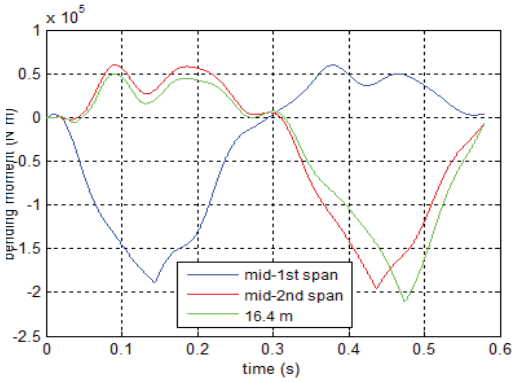
(a)



(b)



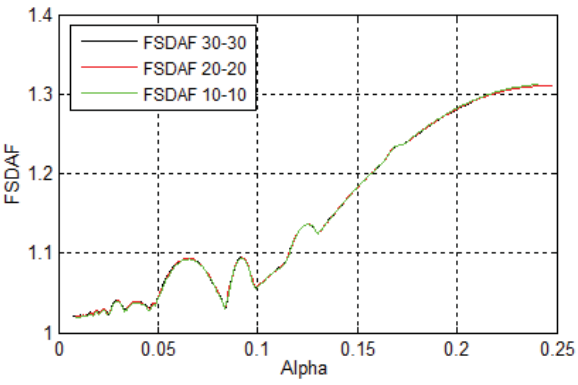
(c)



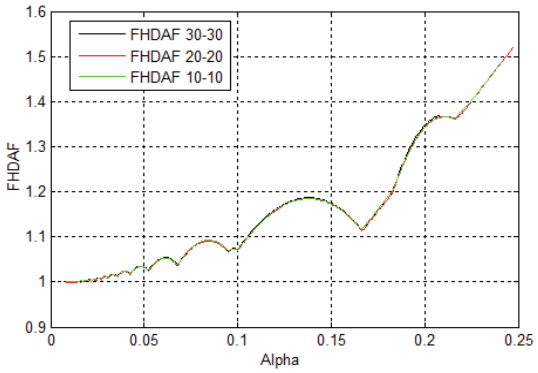
(d)

Figure 10: Critical locations in a 20 m continuous beam: (a) Location of max. total hog. BM throughout the beam length versus velocity of the moving load (b) Total BM versus time at two locations when velocity is 232.2 km/h (c) Location max. total sag. BM throughout the beam length versus velocity of the moving load (d) Total BM versus time at three locations when velocity is 124.2 km/h.

Figure 11(a) and (b) show the FDAF of sagging and hogging bending moment respectively versus Alpha for different lengths of the continuous beam. It can be seen that FDAF is not affected by changes in the span length for sagging or hogging bending moments. It can also be noticed that the FDAF of sagging bending moment in continuous beam is about 12 % greater than that the simply supported case Moreover, the results showed that FDAF of hogging bending moments is about 16 % greater than those of sagging bending moments in continuous beam.



(a)



(b)

Figure 11: FDAF versus Alpha for 20 m, 40 m and 60 m continuous beams: (a) FDAF of sagging bending moment versus Alpha (b) FDAF of hogging bending moment versus Alpha

4 CONCLUSIONS

In this paper, the authors present a comparison on DAF and FDAF of continuous beams of two equal spans to those of simply supported beams. In continuous beams, two DAFs have been used to characterize sagging bending moment at the two mid-sections of the first and second spans. A third DAF has been employed to quantify the dynamic amplification for hogging bending moment over the internal support. FDAF for sagging bending moment and FDAF for hogging bending moment have also been calculated to assess the highest maximum moment and the critical sections at which they occur for each velocity of the moving load.

As expected, FDAF has been found to be greater than DAF in continuous and simply supported beams. The differences between DAF and FDAF have generally increased for those velocities where the critical section holding the maximum total moment has moved apart from the reference sections at mid-span and over the internal support. Maximum FDAFs/DAFs occur at a number of critical normalized frequency ratios (i.e., Alpha) that can be generalized to a beam model of any length when analysing the response to a single point load. DAF of sagging bending moment of continuous beam has been found to be greater than that of the simply supported beam. FDAF of sagging bending moment in continuous beam has been about 12% greater than that the simply supported case. Finally, FDAF of the hogging bending moment has been about 16% greater than that of the sagging bending moment in a continuous beam 6.Therefore, this research has demonstrated that a location apparently with little dynamics as that over the internal support can lead to a more significant dynamic amplification of the hogging moment than other sagging locations.

5 ACKNOWLEDGEMENTS

The authors would like to express their gratitude to the Iraqi Ministry of Higher Education and Scientific Research (MoHESR) for the financial support towards this investigation.

6 REFERENCES

[1] Frýba, L., *Vibration of solids and structures under moving loads*, Groningen, The Netherlands: Noordhoff International Publishing, 1972.

[2] Vincent,T., H. CHU, Mastering *Different Fields of Civil Engineering Works* (VC-Q&A Method) 2010.

[3] Yang, Y. B., Yau, J. D. & Wu, Y. S. *Vehicle bridge interaction dynamics with application to high-speed railways,* World Scientific Publishing Co. Pte. Ltd, 2004.

[4] Cantieni, R. *Dynamic Load Testing of Highway Bridges*. IABSE proceedings, P-75/84, IABSE perodica, Vol. 3, pp. 57-72, 1984.

[5] Green, M. F., Cebon, D. & Cole, D. J. *Effects of Vehicle Suspension Design on Dynamics of Highway Bridges*. Journal of Structural Engineering, Vol. 121, No. 2, pp.272-282, 1995.

[6] Yang, Y. B., Liao, S. S. & Lin, B. H. *Impact Formulas for Vehicles Moving Over Simple and Continuous Beams*. Journal of Structural Engineering, Vol. 121, No. 11, pp.1644-1650, 1995.

[7] Chan, T. H. & O'Connor, C. *Vehicle Model for Highway Bridge Impact. Journal of Structural Engineering,* Vol. 116, No. 7, pp. 1772-1793, 1990.

[8] Ichikawa, M., Miyakawa Y. & Matsuda, A. (2000) *Vibration Analysis of the Continuous Beam Subjected to a Moving Mass*. Journal of Sound and Vibration, Vol. 230, No. 3, pp. 493-506.

[9] Brady, S.P., OBrien, E.J. and Žnidaric, A. (2006). *The effect of vehicle velocity on the dynamic amplification of a vehicle crossing a simply supported bridge*, *ASCE Journal of Bridge Engineering*, **11**(2): 241-249.

[10] Cantero, D. Gonzalez, A. and Obrien,E.J. (2009). Maximum dynamic stress on bridges traversed by moving loads, *ASCE Journal of Bridge Engineering*, **162**(2): 75-85

[11] Li, Y. (2006). *Factors affecting the dynamic interaction of bridges and vehicle loads*. PhD thesis, University College Dublin, Dublin, Ireland.

[12] Tedesco JW, McDougal WG and Ross CS. *Structural Dynamics: theory and applications*. California, USA: Addison-Wesley Longman, 1999

[13] Johansson, C., Pacoste, C. and Karoumi, R. (2013). *Closed-form solution for the mode superposition analysis of the vibration in multi-span beam bridges caused by concentrated moving loads*. Computers & Structures, 119:85-94.

[14] Asnachinda, P., Pinkaew and T., Laman, J.A. (2008). *Multiple vehicle axle load identification from continuous bridge bending moment response.* Engineering structures Vol. 30, No.10, PP. 2800-2817.

Monitoring of Structural Performance

David Hester[1], James Brownjohn[1]
[1]Vibration Engineering Section, College of Engineering Mathematics and Physical Sciences, University of Exeter, North Park Road Exeter, EX4 4QF
email: d.hester@exeter.ac.uk, j.brownjohn@exeter.ac.uk

ABSTRACT: Bridges are a critical element of the European transport network and therefore their effective management is important to the functioning of the European economy. Managing bridge assets is a very challenging task both logistically (i.e. there are thousands of bridges distributed across a vast network) and financially (budgets for monitoring and maintenance are limited, and in many cases decreasing). Management involves making decision about the structure and in any system, the quality of decision making is related to the quality of information available. For the vast majority of bridges the information available is visual in nature and therefore the quality of information is significantly dependant on the skill/knowledge of the inspector. Even when there is electronic monitoring data available for a bridge one of the great difficulties is that the data is not easily interpreted. This is because bridges are complex systems whose response signatures are significantly affected by external factors such as temperature or traffic load and as a result it can take years to learn the bridge's 'normal' response envelope. Bradly speaking it is this complexity that makes bridge SHM more challenging than SHM in mechanical systems. Mechanical systems tend to have a relatively narrow response signal under 'normal' monitoring conditions which makes the detection of anomalies easier than is the case for bridges. The research project (*Monitoring of Structural Performance*) presented in this paper aims to contribute to addressing the above challenge by developing a decision support system to assist bridge operators make decisions about their structures. The project aims to do this by making use of physics-driven and data-driven modelling methods to produce metrics that are useful for decision support.

KEY WORDS: Bridges; Monitoring; SHM; Decision support.

1 INTRODUCTION

Transportation infrastructure is crucial to the functioning of a developed economy. For a large trading block such as the European Union this infrastructure is especially important as it facilitates trade across the entire Euro zone. Continued growth in Europe needs a functioning low cost transport infrastructure. Bridges are a key element of the transport network as they are multi modal in nature i.e. they are relevant to road, rail and (even) waterway transport.

However, bridges deteriorate over time and there is no easy way to measure this. The cost of repairing faults in a bridge, once the fault starts to approach criticality, is enormous both in terms of cost and traffic delays. For example, the American Association of State Highway and Transport Officials (ASSHTO) produced a report in 2007 titled 'Bridging the Gap' [1] which estimated that it would cost $140 billion to repair every deficient bridge in the US. If flaws in a structure could be identified early using Structural Health Monitoring (SHM), the cost of repair could be vastly reduced and congestion could be minimised through optimised intervention.

Across Europe there are a substantial number of bridges that are vital to the economies they serve, and which, if taken out of commission would have a devastating impact on local, national, and international economies. For example Humber Bridge in the UK (Figure 1) carries 120,000 vehicles per week, if the bridge were closed the detour would add approximately 90km to the original journey and result in substantial congestion.



Figure 1. Humber Bridge, England.

A recent example of the transport chaos that can ensue as a result of the closure of a bridge was the 2011 closure of the Hammersmith flyover due to concerns about the condition of the post tensioning tendons. This closure highlighted the difficulties when there is a lack of prior structural performance track record and means to assess impact of the

discovered damage. In a similar situation the M4 Boston Manor viaduct was closed three weeks before the 2012 Olympics due to discovery of a new crack in a "sensitive location" during minor repairs.
These kinds of shock events highlight the very important and difficult task that bridge/road and rail authorities face. *Monitoring of Structural Performance (MOSP)* aims to contribute to this task by developing a decision support system for bridge management.

2 OVERVIEW OF CHALLENGE

The concept of Structural Health Monitoring (SHM) of physical assets started in the power generation industry in the 1970s. Dimagronas [2] gives a comprehensive review of the evolution of SHM since that time and broadly speaking it has proved to be quite effective for monitoring mechanical systems, particularly rotating machinery. The last quarter of a centenary has seen the same philosophy of instrumentation and monitoring applied to valuable civil engineering assets such as large bridges. For example many of Europe's large bridges (such as the Millau Viaduct) already have instrumentation installed to detect movements. However, for the most part the results for bridge SHM have not been as successful as SHM for mechanical systems. In the opinion of the authors this is primarily due to the fact that broadly speaking it is more difficult to interpret bridge data than mechanical data. For example, within a mechanical system the response signature of given parameter (e.g. strain in a component) is relatively narrow. However, the response signature for a bridge (e.g. strain in a particular component) can vary substantially even under normal operating conditions due to changes in temperature, traffic load and boundary conditions. Therefore typically it takes a long time to learn 'normal' patterns for the bridge and as a result this makes the identification of anomalies difficult.

The ultimate goal of this research is to try and develop a Decision Support System (DSS) for bridge managers, i.e. we want the DSS to output metrics of use for decision making.

For larger bridges (that typically have permanent instrumentation and therefore much data is available) the challenge is to develop a data fusion system capable of interpreting the data and outputting tangible metrics that can be used by bridge managers to make cost effective decisions.

For smaller bridges (no permanent sensor installation) the challenge is to utilise recent advances in sensor technology to collect (limited) data within the financial and logistical constraints that network operators function under but still provide some metrics useful for decision making. It is envisaged that the metrics produced by the DSS will complement the (primarily visual) information that is currently used to make decisions. Essentially we want to see if sensor data can add value to the existing decision making process. The graphic in Figure 2 illustrates the concept.

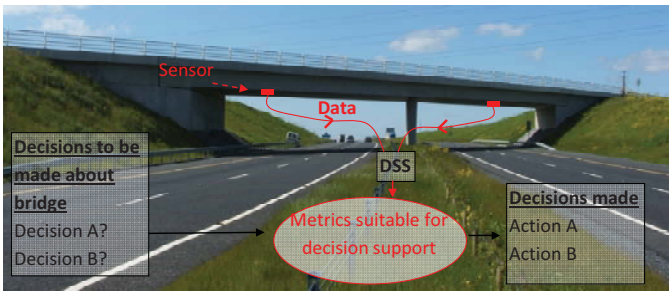


Figure 2. Flow chart showing concept behind DSS.

3 OUTLINE OF PROJECT

Monitoring of Structural Performance (MOSP) will carry out research to try and develop an advanced computerised Decision Support System (DSS) to assist bridge managers in making cost effective decisions. Many of Europe's larger bridges already have instrumentation that provides information on displacement, acceleration, temperature, wind speed, traffic load, etc.. This data can be used as an input to the new system. The objective is to 'fuse' the data in a logical manner i.e. the system will attempt to integrate the disparate pieces of information to form a picture of how the structure is performing. The flow chart in Figure 3 illustrates the concept of the procedure. In the figure a truck is shown crossing a bridge. At the same time the bridge is subject to wind loading and, depending on environmental conditions, it is also affected by temperature fluctuations. Sensors can be used to monitor variables such as temperature, wind speed and bridge acceleration and some sample plots are shown in the second part of the flow chart. The challenge is to fuse this disparate data into a coherent picture to provide information of use for making effective decisions regarding the structure.

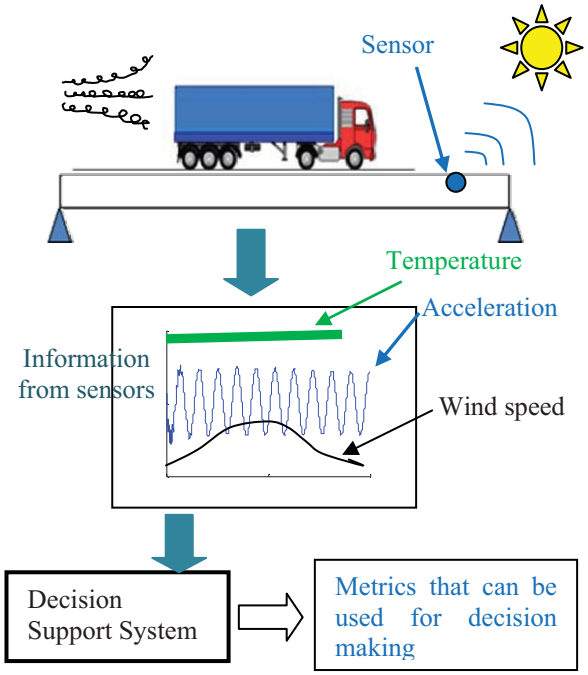


Figure 3. Sequence for using new Decision Support System.

The current state of the art for bridge monitoring techniques can be classified as either **Physics-driven**' or '**Data-driven'**. Table 1 gives a summary of the philosophy behind each of these two techniques and the text following the table gives a literature review.

Table 1. Physics-driven Vs Data-driven

Physics-driven	Data-driven
Physics-based techniques utilise our physical understanding of the system. Equations that define relationships between the different system variables are used to construct numerical models of the system. For example, prepare a finite element model of a bridge and calculate the displacement due to a given load. If the observed displacement due to the same load increases, this could be an indication that the bridge has experienced some damage.	Data-driven approaches are appropriate when the understanding of first principles of system operation is not comprehensive or when the system is sufficiently complex that developing an accurate model is prohibitively expensive. These algorithms are designed to 'learn' characteristics of a time series generated by sensor data during a period called the initialisation phase during which the structure is assumed to behave normally. This phase subsequently helps identify those behaviours which can be classified as anomalous. For example, the displacement of the bridge may be monitored for two years during the initialisation phase. If in subsequent years the displacement is observed to go outside the envelope established during the initialisation phase it indicates that the bridge has experienced some damage.

Physics-based Catbas et al. [3] provide a comprehensive report on applying physics based models to bridges. Numerous researchers have applied physics based models to actual constructed systems, [4,5]. These models are typically used to model the behaviour of the structure under critical loading. They are also used to diagnose the causes of changes in behaviour. For example Teughels and De Roeck [6] use the method to identify structural damage in a Swiss highway bridge. The principal drawback of the approach is that even when the model is tuned using experimental data the behaviours predicted by the updated model may not be correct due to uncertainty and parameter compensation [7]. In recent work Goulet et al. [8] allow for uncertainty in their model(s) and they show that using this approach they were able to falsify the hypothesis that the bridge under investigation was behaving as designed when subjected to ambient vibration inputs.

Data-based Several authors have investigated the use of data based approaches to model structures [9,10]. The primary advantage of these approaches is that they are solely dependant on the data provided, this makes them attractive for the modelling complex phenomena. Posenato et al. [11] describe a typical data based bridge monitoring system. The drawbacks of the data based approach are the length of time needed to train the model and also the difficulty in identifying the effect of individual inputs. For example the deflection of the bridge is larger during the day than at night. This is due to the higher traffic load and the increase in temperature, however it is very difficult to say what portion of the deflection is due to traffic alone.

Both methods (Physics-driven' and 'Data-driven') have strengths and weaknesses so the logical approach is to exploit the advantages of each method by implementing both when monitoring the structure. The objective of MOSP is to integrate the Physics-driven and Data-drive methods into one system that will provide performance prognosis and support decision making. Essentially, both methods will be applied to a given structure and the results from each method will be input into a decision support system (DSS). The DSS will support evidenced based reasoning under uncertainty. A schematic of the procedure is given in Figure 4.

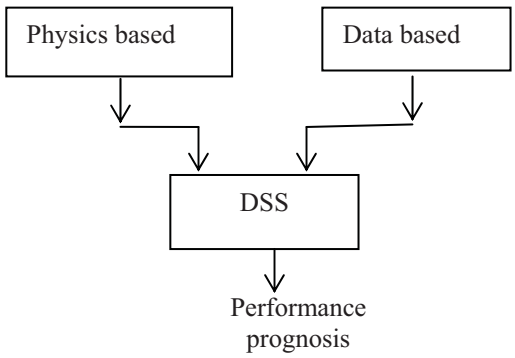


Figure 4. Concept for Decision Support system

Broadly The project is broken into six separate stages.

- Stage1 dialogue with stakeholders to identify desired outputs from DSS
- Stages 2&3 Physics-based modelling
- Stage 4 Instrumentation
- Stage 5 Data-based modelling
- Stage 6 Development of novel DSS

and these are dealt with in the following section.

4 PROJECT STAGES

Stage 1: Talk to stake holders and identify what performance metrics they have faith in. This is a crucial step because it identifies from the outset the outputs we want from the DSS. The stakeholders include bridge operators and road authorities.

Stage 2 conceptualisation of the physical model, in this case a Finite Element (FE) model will be used. Using dimensions measured in the field and any available drawings, the model geometry and element selection for a number of bridges will be prepared. Note at this stage no material properties will be assigned to the model. In relative terms, ascertaining accurate geometric properties for an existing structure is substantially easier than ascertaining accurate material properties. Therefore the material properties will be assigned using a separate process in stage 3. This approach, has previously been used by Exeter's Vibration engineering Section (VES) to prepare the geometric part of the FE model for Tamar Bridge (Figure 5). Tamar is a suspension bridge with a 335 m centre span and it carries approximately 40,000 vehicles per day between Devon in the UK.

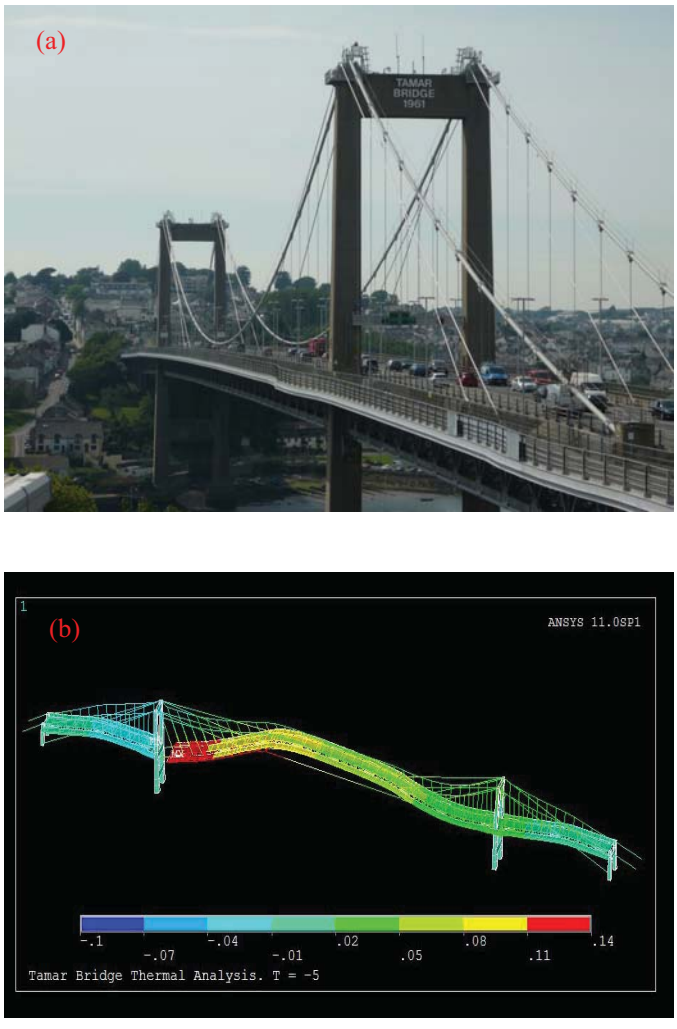


Figure 5. Tamar Bridge; (a) Photograph of structure, (b) Finite element model of structure.

Stage 3 'Model updating' leading to single/multiple physics-based models. Once the geometric part of the model has been established the next step is to assign material properties to the structure. Obviously selecting the correct material properties is crucial if the model is to accurately simulate the behaviour of the real structure. The performance of the model can be checked against measured results and the input properties can be 'updated' using an iterative process so that the outputs of the model match the measured behaviour. This is the traditional approach to tuning a model. However, in work by [8] it is shown that parameter compensation can occur resulting in errors in the models. They found that creating multiple models from a statistical distribution of material properties and then disregarding all the models except the handful that match the observed behaviour worked best.

Stage 4 Instrumentation layout. For long term monitoring the instrumentation design requires the use of methodologies for optimal sensor placement [4]. Variables to be measured include displacement, acceleration and temperature.

Stage 5 Development of new data based systems. Here we take existing data-based systems similar to those described in section 3. However, before applying them to the field data some modifications/improvements will be made to the methods. In particular it is hoped that the following two new features will be introduced to the models:

- Adaptive baselines- As described in section 3, when using data-based methods anomalies are detected when the metric being observed goes outside the boundary of what was measured in the initialisation phase. It would be extremely useful if the baseline/threshold values in the data models adapt automatically to new information.
- Single input – Single output load responses- It has already been highlighted that one of the limitations of data-based methods is that the metric being observed is often influenced by several factors, e.g. displacement is influenced by traffic load, wind load and temperature. For future scenario analysis it would be very useful to be able to say what portion of displacement is generated by traffic, what portion is caused by wind and what portion is due to temperature. We hope to be able to develop such a capacity by applying co-integration to the problem. Co-integration has been used in economics and finance since the 1980s since the approach was formalised by Nobel Laureates Engle and Granger. If two or more series are individually integrated (in the time series sense) but some linear combination of them has a lower order of integration, then the series are said to be co-integrated. This process of untangling the various strands is analogous to removing the haystack to find the needle.

Stage 6 Scenario simulation for decision support and prognosis. The aim of the DSS is to use state of the art technology to provide stakeholders with diagnostic and prognostic information shaped to give them optimal decision support. Performance prognosis is likely to prove possible in the coupled data-driven and physics-based approach proposed here via stages 3 and 5. A combination of the two approaches will be used to predict performance for events out of the observed range of experience. It is envisaged that an approach will be adopted similar to that used in the VES Structural Health Monitoring system 'VESHMS' which has been developed to manage existing structures such as Humber

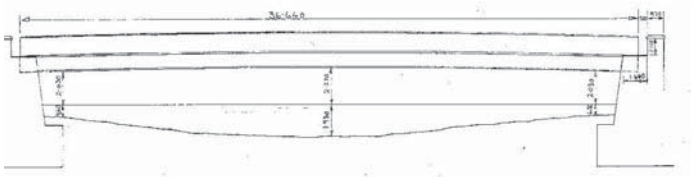
bridge in the UK, (span 2,200 m, see Figure 1). This is a data-based system and it operates as described in section 3, so essentially it currently monitors and records what is happening to the bridge. We aim to upgrade this system to include the features described in stages 1-5. It is hoped that the new system will have a new physical-modelling capability as well as improved data-modelling features.

5 EXAMPLE OF MONITORING PERFORMANCE

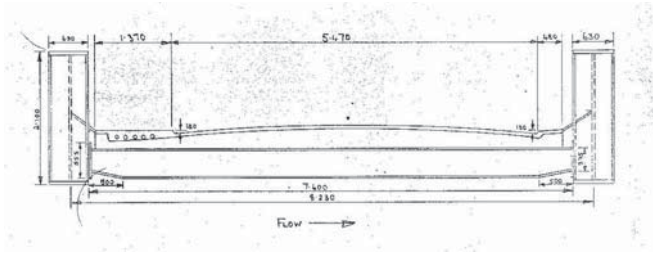
This section describes an example of quantitative monitoring that was carried on a steel bridge over the River Exe in Devon. The bridge is a single span half through steel bridge on concrete abutments. The clear span between the bearings is 36m, the main beams are 2.1m deep and the flanges are 630mm wide. The bridge runs approximately East-West and Figure 6 is a photo of the North elevation of the bridge. Figure 7shows drawings of the bridge.



Figure 6, North Elevation of bridge.



(a)



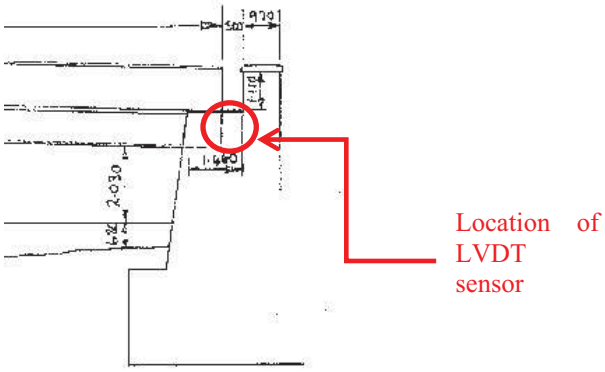
(b)

Figure 7, Steel bridge over the river Exe, (a) Elevation, (b) Section through the deck.

The goal of the study was to examine the regular movements that could be expected from the bridge. Although other measurements were recorded on the day (e.g. bridge accelerations) in this paper we will focus on the range of movement that could be expected from the bearings. Figure 8 shows the expansion joint at the east end of the bridge.



Figure 8, Deck expansion at the east end of the bridge, (this view is looking north).



(a)



Figure 9, Location and arrangement of LVDT sensor (a) Location, (b) Arrangement

The LVDT sensor shown in Figure 9(b) measures the relative displacement between the end of the steel beam and the curtain wall at the back of the abutment. The LVDT is mounted on a retort stand whose base is attached to the end of the steel beam using a magnet. The movement of the joint was observed from 10.00 hours to 16.50 hours. As well as measuring displacement a thermocouple was used to record the temperature at a point on the east end of the main beam on the north side of the bridge. Figure 10 shows the movement between the north beam and the east abutment, this movement is plotted with respect to the left hand y-axis. The figure also shows the temperature of the steel beam at the location described above. The temperature information is plotted with respect to the y-axis on the right hand side. It can be seen in the figure that the temperature of the steel increases from approx. 9.5^{o}C at 10.00 hours to a maximum of 15^{o}C at 14.45 hours and this results in the joint closing by approximately 2.5mm. From 14.45 hours onward the temperature of the steel starts to reduce and the joint starts to open slowly.

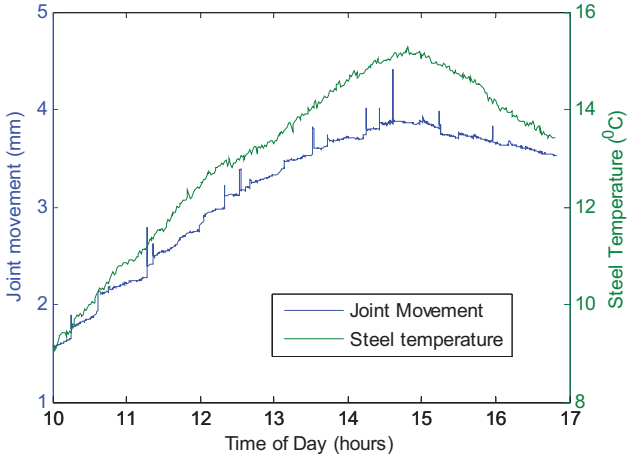


Figure 10, Steel temperature an associated joint movement.

6 CONCLUSIONS

This paper outlines the Marie Curie FP7 Monitoring of Structural Performance (MOSP) research project. The goal of the project is to provide a decision support system for bridge management to assist in providing for reliable and efficient operation of European bridges. The project aims to combine data based and physics based modelling techniques to develop a more holistic approach to bridge monitoring. The outputs from the project should result in enhanced reliability and productivity for bridges on Europe's transport networks.

ACKNOWLEDGMENTS

This research was supported by a Marie Curie Intra European Fellowship within the 7th European Community Framework Programme.

REFERENCES

[1] Bridging the Gap (2008), American Association of State Highway and Transportation Officials

[2] Dimagrogonas A.D. (1996) Vibration of cracked structures, *Engineering Fracture Mechanics,* **55** (5): 831-857.

[3] Catbas FN, Kijewski-correa T, Aktan EA (Eds) (2013), Structural Identification of Constructed Systems. Approaches, Methods, and Technologies for Effective Practice of St-Id. Amercian Scoiety of Civil Engineers

[4] Brownjohn, J. M. W. (2003). "Ambient vibration studies for system identification of tall buildings." *Earthquake Engineering and Structural Dynamics,* 32(1)

[5] Farrar, C. & Doebling, S. W. (1998). "Damage detection II: Field applications to large structures." *Proceedings of NATO Advanced Study Instituteon Modal Analysis and Testing,*

[6] Teughels, A.& De Roeck, G. (2004). Structural damage identification of the highway bridge Z24 by FE model updating. *Journal of Sound and Vibration,* 278(3), 589-610.

[7] Goulet JA.; Kripakaran P, Smith IFC (2010). Multimodel structural performance monitoring. Journal of Structural Engineering-ASCE 136(10) p1309-1318.

[8] Goulet JA, 2012, Probabilistic model falsification for infrastructure diagnosis. PhD Thesis. 5417, EPFL.

[9] Chang, C., Chang, T. & Zhang, Q.. (2001). "Ambient vibration of long-span cable-stayed bridge." *ASCE Journal of Bridge Engineering,* 6(1), 46-53.

[10] Zapico, J. L., Gonzalez, M. P., and Worden, K. (2003). "Damage assessment using neural networks." *Mechanical Systems and Signal Processing,* 17(1), 119-125

[11] Posenato, D. Lanata, F, & Inaudi, D. (2008) Model free data interpretation for continuous monitoring of complex structures Advanced Engineering Informatics, 22 p135-144.

Probabilistic-Based Modelling and Assessment of a Steel Truss Railway Bridge

Alan O' Connor[1], Lorcan Connolly[1], Mairéad Ní Choinne[1]
[1]Roughan O' Donovan Innovative Solutions, Arena House, Arena Road, Sandyford, Dublin 18, Co. Dublin.
email: Alan.O'Connor@rod.ie, Lorcan.Connolly@rod.ie, Mairead.nichoinne@rod.ie,

ABSTRACT: Maintenance associated with an ageing bridge stock has become a major problem for bridge owners and managers throughout Europe. In response to this problem, there has been increased interest in the use of probabilistic methods for the assessment of ageing bridges. This paper presents a probabilistic assessment of a 40 year old steel truss railway bridge in Nieporet, Poland. The purpose of using probabilistic methods to assess the performance of a bridge is to avoid unnecessary repair/rehabilitation and/or to optimise any repairs that are shown to be necessary. In this study, a 3D Finite Element (FE) model of the bridge was developed using MIDAS CIVIL software. The model was used to carry out a deterministic assessment of the bridge according to I.S. EN 1991-2:2003, using the rail traffic load model (Load Model 71). The results of the deterministic assessment showed that the stresses induced in the cross beams were sufficiently high to cause failure. Therefore, a probabilistic assessment of the most critical cross beam was carried out. The probabilistic analysis incorporated bridge specific loading (Weigh in Motion data) and stochastic modelling and showed sufficient reliability (i.e. sufficiently low failure probability) of the cross beam in accordance with ISO 2394:1998. The financial benefits to the bridge owners are apparent from the results, which suggest that costly bridge repair/rehabilitation can be avoided or optimised.

KEY WORDS: Probabilistic assessment; Bridge assessment; Bridge modelling;

1 INTRODUCTION

Bridge owners and managers commonly face the issue of optimizing the operation and maintenance of an ageing bridge stock. In the past, costly bridge repairs would commence after a deterministic assessment has shown a structure to be unsafe. The use of probabilistic bridge assessment allows more accurate modelling of the load/resistance parameters, through incorporation of bridge-specific information, and can often show sufficient reliability, even after a deterministic assessment has rendered the bridge unsafe. Potential is also offered to optimise any repairs that are shown to be necessary.

This paper demonstrates a probability based assessment which was carried out on a steel truss railway bridge as part of the SMARTRAIL 7th Framework Programme. The bridge is located in Nieporęt, near Warsaw and was constructed in the 1970s. It is one of over one thousand similar bridges in Poland [1] and has been the subject of much research in the past. Figure 1 shows an elevation of the Nieporęt Bridge.



Figure 1. Nieporet bridge elevation

2 FINITE ELEMENT MODEL

A Finite Element (FE) model was created using the Midas finite element software package [2]. The bridge was modelled using linear elastic beam elements with full fixity at the node points. The design drawings for the bridge were used to set up the geometry and to calculate the section properties of each of the members. The bridge in question spans 40 m and consists of five 8 m long bays. The vehicle load is transferred onto two 'stringer' beams. The stringer beams span longitudinally between six cross beams which connect to the node points of the truss. There is diagonal wind bracing at the top and bottom of the structure. A Young's Modulus of 2.1×10^8 kN/m^2 was assigned to all steel members. Figure 2 shows an outline view of the Midas model. The track and sleepers are omitted from the figure for clarity.

The bridge and model have four supports which allow sufficient movement to prohibit the occurrence of thermal stresses in the structure.

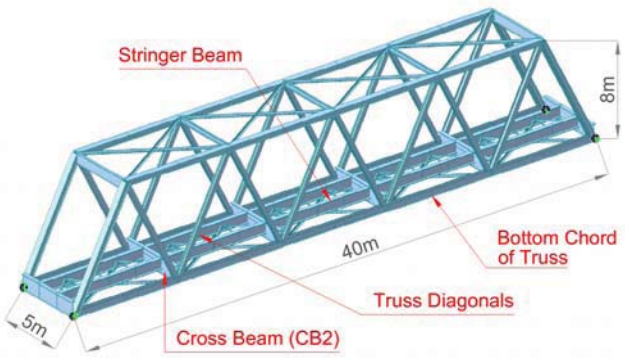


Figure 2. Nieporet bridge FE MIDAS model

2.1 Model Validation

Previous research on the Nieporet bridge focused on measuring the response of the bridge due to the passage of an ET22 locomotive [1]. The measured response (voltage) taken from the underside of the stringer beam in the first bay was examined. The signal for the slowest speed (37 km/h) was compared with the signal generated by the static model created for the current study as this signal contained the least dynamics. As the conversion factor between voltage and stress or strain for the sensor was unknown, the only comparison that could be made was the shape of the signal and not the magnitude of the response. The theoretical signal generated from the model at this location showed a good match in the shape of the measured and theoretical responses. The shape of the signal alone may not be sufficient to confirm the accuracy of the Midas model. Therefore, a stress signal provided by [1] for the top side of the stringer beam in the first bay was compared to that of the current study. The theoretical (static) signal generated by the Midas model for the current study showed close agreement in both the shape and magnitude of the stress signal.

Finally, the stress signal in one of the truss diagonals due to the passage of an ET22 locomotive, calculated from the Midas model for the current study, was compared to those derived from strain gauge measurements and numerical model calculation by [1]. The comparison is shown in Figure 3. It is clear that the shape and magnitude of the stress signal generated by the current model (right) is very close to those calculated by [1] (left and centre).

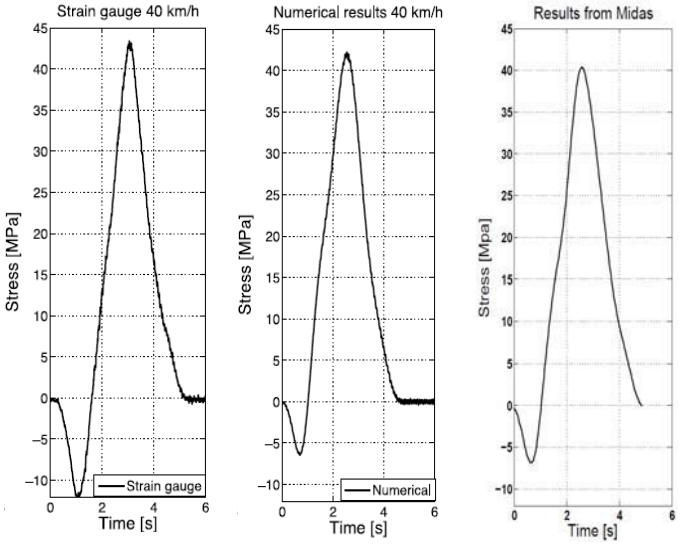


Figure 3. Stress signal in truss diagonal from strain gauge measurements (left), model by Kolakowski et al. (centre), and current model (right)

Bridge-specific data such as the data calculated in [1] can be used to tailor the response of numerical models for accuracy. However, the model created for the current study showed close enough agreement with the measurements that this was not deemed to be necessary.

3 DETERMINISTIC ASSESSMENT

3.1 Load Model

The railway load model from Eurocode 1 (I.S. EN 1991-2:2003) [3], Load Model 71, consists of 4 x 250 kN axles, spaced at 1.6m, with a UDL of 80 kN/m at a distance of 0.8m in front of and behind the axles. Figure 4 illustrates Load Model 71 (LM 71).

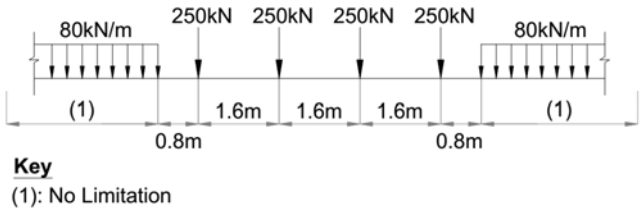


Figure 4. LM 71 from EN 1991-2:2003

These loads were multiplied by the following load factors in accordance with Eurocode 1:

- Adjustment factor α to account for rail traffic which is heavier or lighter than normal rail traffic. This factor was taken as 1.1 (recommended in IS EN 1991-2:2003 NA).
- Dynamic factor Φ to account for dynamic magnification of stresses and vibration effects in the structure.

The dynamic factor Φ for a carefully maintained deck is given as:

$$\Phi = \frac{1.44}{\sqrt{L_\Phi} - 0.2} + 0.82 \quad (1)$$

The determinant length, L_Φ, is given in EN 1991-2:2003, Table 6.2, for rail bearers (stringers) and cross beams as part of a steel grillage as:

- L_Φ (stringer) = 3 times cross girder spacing = 24m.
- L_Φ (cross beam) = Twice cross girder length = 10m.

Thus, the dynamic factors for the stringers and cross beams were calculated as $\Phi_{stringer}$ = 1.13; $\Phi_{cross\ beam}$ = 1.31. As no determinant length is specified in the code for members other than cross beams and stringers, the dynamic factor for all bridge members other than the stringers was conservatively assumed to be equal to the cross beam dynamic factor.

3.2 Analysis

The model created in Midas is a static model of the bridge, i.e. no vehicle or bridge dynamics are considered. It is not a simple task to generate signals due to moving loads traversing the bridge in Midas. Therefore, influence lines for total stress for different members in the model were exported to Matlab. The Navier stress influence line ordinates are calculated in Midas as shown in equation 2.

$$i_{\sigma t} = \frac{i_{mx} y}{I_x} + \frac{i_{my} x}{I_y} + \frac{i_{pz}}{A} \quad (2)$$

Where $i_{\sigma t}$ are the influence line ordinates for total stress, i_{mx} & i_{my} are the influence line ordinates for bending in each direction, i_{pz} are the influence line ordinates for axial force, y & x are the distances to the maximum point of stress in the member, I_x & I_y are the moments of inertia about each axis of bending and A is the cross sectional area. Figure 5 shows the

total stress influence line for the second cross beam from the left support.

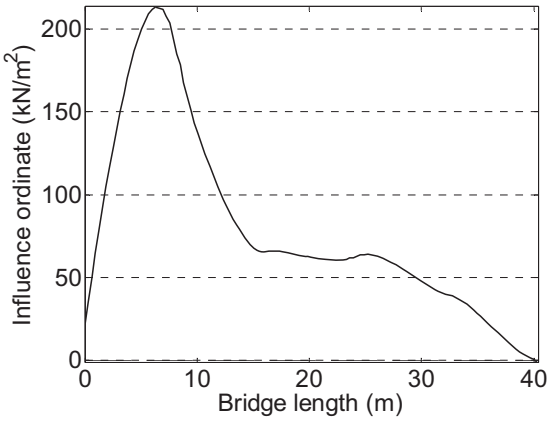


Figure 5. Stress influence line for cross beam 2

In Matlab, Load Model 71 was run across the length of the influence line to identify the maximum stress induced for each member. The front UDL was first run across the influence line, followed by the axles and the back UDL. The combined stresses due to live load (LM 71) and dead load (self-weight) were calculated for the critical member of each type and are summarised in Table 1. The load ratio is also calculated in Table 1, defined as the induced stress / yield stress (f_y). In the absence of strength test information from the bridge, a yield stress of 275 MPa was assumed. This was modelled more accurately as part of the probabilistic assessment.

Table 1. Stresses due to live-load and self-weight.

Member	Stress (MPa)	Load ratio
Bottom cross beam	321.7	1.17
Top cross beam	55.7	0.20
Stringer beam	168.9	0.61
Truss diagonal	201.8	0.73
Truss bottom chord	132.7	0.48
Truss top chord	127.0	0.46
Top diag. bracing	94.7	0.34
Bottom diag. bracing	29.1	0.11
Bottom cross bracing	22.5	0.08

It is shown in Table 1 that the critical cross beam of the structure has failed due to the application of the applied loading. The cross beam in question (hereafter referred to as 'CB2') is the cross beam between the first and second bay (on each side), as shown in Figure 2. Therefore, a probability based analysis was performed on this member to better assess if the member was structurally safe. Although combinations of wind, nosing and traction / braking forces were not considered in Table 1, these were later applied to each other member and it was found that the load ratios were all below 1 (i.e. no further assessment was required).

4 PROBABILISTIC ASSESSMENT

In the probabilistic assessment, all parameters which relate to the load and resistance equation of the ULS were modelled stochastically. This means that the static analysis was run a number of times, varying each parameter by randomly sampling from a distribution with a mean value (μ), and standard deviation (σ). A Matlab random number generator was used to perform the sampling.

The critical ULS for CB2 was based on a check of Navier stresses, as for the deterministic assessment, described as:

$$g \leq 0 \quad where \quad g = f_y - |\sigma| \tag{3}$$

Where f_y describes the yield strength of the structural steel and $|\sigma|$ is the induced Navier stress due to the applied loading, equal to $\sigma_{Fx} + \sigma_{My} + \sigma_{Mx}$. The variables to be modelled stochastically included traffic load, dynamic amplification, dead load, superimposed dead load and steel yield strength. Therefore, the secondary effects of wind, side impact and traction/braking were incorporated deterministically.

4.1 Traffic Load

In order to obtain a model for train wagon loads, data was gathered from a Weigh-in-Motion (WIM) system on the Nieporet bridge. WIM systems are comprised of a series of sensors which measure strain signals. These strain signals can be used to calculate the weights of vehicles as they traverse the bridge. The Nieporet bridge was instrumented at the cross beams, truss diagonals and stringer beams. At the time of inspection, 10-12 trains traversed the bridge per day. Based on this, the level of WIM data was enhanced to one month using statistical operations. Figure 6 shows a histogram of the derived train wagon weights for a period of one month. Statically weighed trains were also used to derive the data.

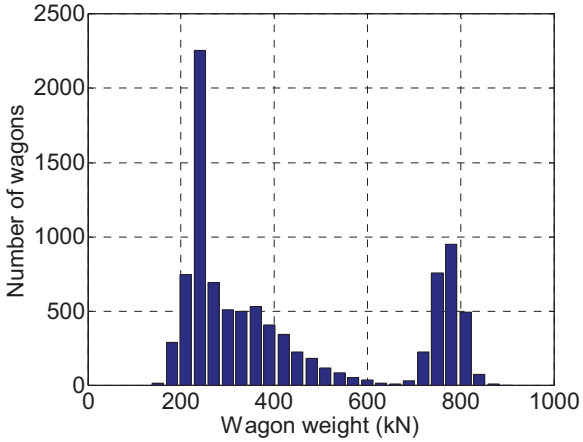


Figure 6. Wagon weight histogram

Normal distributions were fitted to axle spacing data in order to obtain a standard wagon configuration. Figure 7 shows the derived wagon configuration.

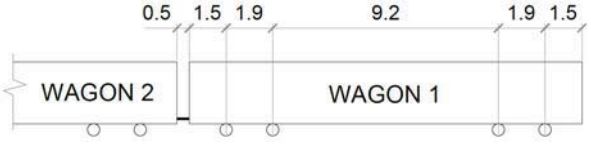


Figure 7. Wagon configuration

Extreme value modelling was used to derive train wagon weights. The parameters μ and σ of the Extreme Value

Distribution (EVD) were required. The parameters are based on a Gumbel fit [4] to the 30 maximum daily observations over a period of one month. The equation of the Cumulative Distribution Function (CDF) for the Gumbel EVD is:

$$F_x(x) = \exp\left(-\exp\left[\frac{-(x-\lambda)}{\delta}\right]\right) \quad (4)$$

The threshold, λ, and the scaling parameter, δ, of the Gumbel law, $F_x(x)$, are estimated by minimisation of the error between the empirical and modelled distribution. Figure 8 presents the CDF of the modelled Gumbel distribution fitted to the empirical data of maximum wagon weight for a 30 day period.

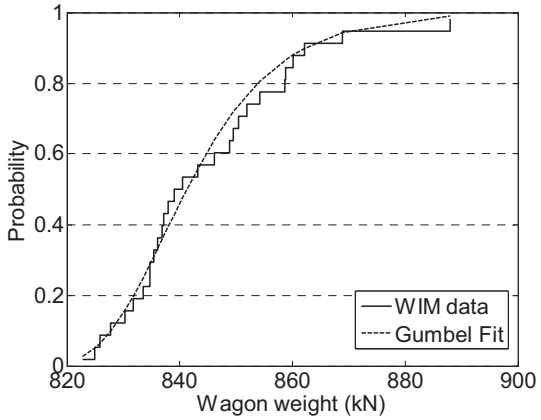


Figure 8. Gumbel fit to maximum monthly wagon weight data

Considering the stress influence line for CB2 (Figure 5) and the wagon configuration (Figure 7), it is clear that no more than 3 wagons would be positioned over the adverse portion of the influence line at any time. Therefore, it is appropriate that the Gumbel distribution is based on a fit to the maximum daily values of the total weight of 3 adjacent wagons. The distribution of 30 daily maximum observations, $F_x(x)$,was converted to the yearly distribution of maxima, $F_{max}(x)$, as:

$$F_{\max}(x) = \exp[-N(1-F_x(x))] \quad (5)$$

Where N is equal to 250, for 250 working days per year.

The Gumbel parameters μ and σ, for 3 wagons were calculated as 2,688 kN and 32 kN, respectively. Therefore, the normalised values for 1 wagon are 896 kN and 10.7 kN (CoV = 1.19%), respectively. Figure 9 illustrates the CDF of wagon weights for the daily and yearly data.

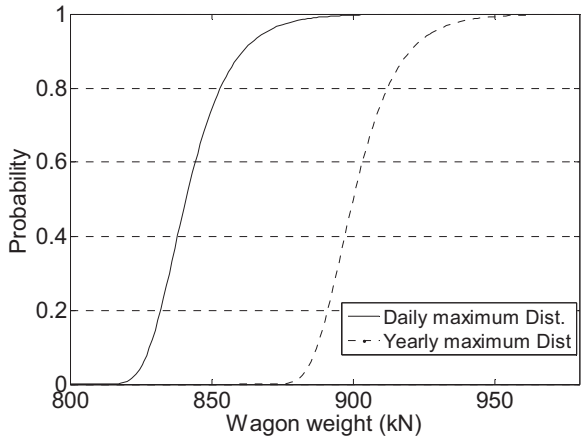


Figure 9. Daily & yearly Gumbel CDF of wagon weight

Model uncertainty should always be taken into account for loading and capacity [5]. The model uncertainty for wagon weight was considered as normally distributed with a mean of 1 and a Coefficient of Variation (CoV) of 10%, relating to a *small* level of uncertainty [5]. This is considered as conservative since the CoV in the data is quite low (1.19%) and considering the strict protocols used in the loading of train wagons.

4.2 Dynamic Amplification

The dynamic amplification factor in the probabilistic assessment is modelled as:

$$K_s = 1 + \varepsilon \quad (6)$$

Where ε is the dynamic increment, which is modelled as a normally distributed variable. The CoV of ε is given as 1 [6]. The dynamic increment represents the 98% fractile value of the deterministically calculated supplement [6], herein calculated as 0.31. Therefore, to ensure that a 98% fractile value of 0.31 is achieved, the mean and standard deviation are required to be 0.101 and 0.101, respectively.

4.3 Dead Load

The stress due to dead load is modelled as normally distributed with a mean value, calculated for CB2 from the FE model, equal to 16.3 MPa. Note that this stress is due to the total dead load without considering the superimposed dead load (track and sleepers), which is modelled separately. The CoV for dead load (V_M) is taken as 5% with an additional 5% to model uncertainty (V_{IM}) [5]. Since both CoVs are normally distributed, they can be combined as shown in equation 7 to calculate the total CoV in stresses due to dead load (V):

$$V^2 = V_M^2 + V_{IM}^2 \quad (7)$$

Therefore, V is calculated as 7.1%.

4.4 Superimposed Dead Load

The stress due to superimposed dead load (composed solely of the track and sleepers) is also modelled as normally distributed with a mean value, calculated for CB2 from the FE model, equal to 4.5 MPa. The CoV for superimposed dead load is taken as 10% with an additional 5% to model uncertainty [5]. Therefore, the overall CoV for superimposed dead load is calculated as 11.2%, using a formulation similar to equation 7.

4.5 Steel Yield Stress

The Yield stress (f_y) is modelled as logarithmic-normally distributed [5]. In the absence of specific testing, St.37 steel is conservatively assumed [5]. Therefore, with a minimum thickness (t) = 12mm the mean value of the yield stress is taken as 304 MPa with a standard deviation of 25 MPa [5]. The model uncertainty for the yield strength must take account of:

- The accuracy of the calculation model;
- Uncertainty in determining material parameters from control specimens;
- Material Identity.

The accuracy of the calculation model is taken as *good* due to the verification of the model, as described in section 2.1. The uncertainty in determining material parameters is classified as

medium as this is assumed in the determination of f_y [5]. The uncertainty associated with material identity is classified as *normal* due to the lack of test data. On the basis of these distinctions, the model uncertainty for the yield stress was modelled as logarithmic-normally distributed with a mean value of 1 and a standard deviation of 8.7%. Again, the contribution of the CoV of the yield stress and the associated model uncertainty can be combined in a formulation similar to equation 7 to give an overall CoV equal to 12%.

4.6 Incorporation of Additional Loads

In order to incorporate the effects of wind, nosing and braking/traction, the factored contribution of the stresses due to these loads were calculated deterministically. The worst case load combination from I.S EN 1991-2:2003 was calculated as: 1.0(DL) + 1.0(SDL) + 1.0(LL) + 0.5(nosing) + 1.0(traction/braking) + 0(wind). Therefore, wind is not incorporated, in conformance with the code. The total factored contribution of the nosing and traction/braking forces were calculated as 30.2 MPa. This value was subtracted from the mean value of the yield stress. This stochastic-deterministic combination is only possible as the contribution of the deterministically calculated stresses is small in relation to the total stresses (<10%) and is conservative [6]. A summary of all variables modelled is given in Table 2.

Table 2. Models and Parameters for variables of CB2

Variable	Distribution	μ	*CoV*
Yield Strength	LogNorm	304 MPa	0.08
Mod. Unc. yield strength	LogNorm	1	0.09
Dead Load Stress	Norm	16.3 MPa	0.05
Mod. Unc.- Dead Load Stress	Norm	1	0.05
Superimp. Dead Load Stress	Norm	4.5 MPa	0.10
Mod Unc.– SDL stress	Norm	1	0.05
Wagon Weight (3 wagons)	Gumb	2,688 kN	0.01
Mod Unc.- Wagon Weight	Norm	1	0.10
Dynamic Amp. ε increment	Norm	0.1	1.00
Wind, Nosing & Traction	-	-	-

5 RESULTS

5.1 Calculation of Reliability Index, β

A First Order Reliability Method (FORM) [7] was used to estimate the reliability index, β, of the performance function presented in Equation 3, which can also be written as:

$$g(R,S) = R - S = 0 \tag{8}$$

Where R is the steel yield strength (i.e. resistance) and S is the induced Navier stress due to applied loading (i.e. load effect). The distributions of the resistance and load effect were found through 10,000 runs of the static analysis, with parameters varying about mean values with CoVs as presented in Table 2. A lognormal distribution was found to be a good fit for both the yield strength and the induced Navier stress. The probability of failure is defined as:

$$P_f = P[g < 0] \tag{9}$$

Where the notation [$g < 0$] denotes the failure region. For this analysis, the Hasofer-Lind method was used to estimate β [7]. The Hasofer-Lind method involves transforming the random variables from their original space to standard normal space and finding the shortest distance from the origin to the limit state function. In standard normalized space, the shortest distance from the origin to the failure surface is equal to the reliability index as shown:

$$\beta = \frac{\mu_R - \mu_S}{\sqrt{\sigma_R^2 + \sigma_S^2}} \tag{10}$$

Where μ_R and μ_S are the mean values of the random variables R and S, respectively and σ_R and σ_S are the standard deviations of R and S, respectively. A requirement of FORM is that the variables in equation 10 are normal and independent. Given the non normal nature of the load effect and resistance variables in this case, the Rackwitz Fiessler method [7] is used, which involves the transformation of non-normal distributions into equivalent normal distributions.

A beta value of 4.26 was determined for CB2. From ISO 2394:1998 [8], a minimum beta value of 3.8 is deemed appropriate for ULS with a *"great"* consequence of failure and a *"Medium"* relative cost of repairs. That is, the beta value determined is sufficiently high for the bridge to be considered safe. This code is considered appropriate for comparison with the Nieporet bridge as it considers reliability of existing structures. It should be noted, however, that various levels of reliability are specified (Table 3).

Table 3. Minimum Reliability Indices from ISO 2394:1998

Failure Consequence	*Relative Cost of Repairs*		
	Low	Medium	High
Small	2.3	1.3	0.0
Some	3.1	2.3	1.5
Moderate	3.8	3.1	2.3
Great	4.3	3.8	3.1

For the example of the current analysis, if a higher level of reliability was required for CB2, a repair strategy could be optimised. This could include, for example, the application of a Carbon Fibre Reinforced Polymer (CFRP) to the underside of the steel beam, in order to resist bending about the primary axis. The probabilistic analysis would be re-run with the stress/strength parameters re-calculated until an appropriate level of reliability was achieved.

5.2 Sensitivity Analysis

A reliability based classification should always be accompanied by a sensitivity analysis to evaluate the robustness of the result and to determine if the reliability index is overly sensitive to any of the modelled parameters [6]. The sensitivity is measured by the ratio of the change in reliability index to the change in any particular parameter ($\delta\beta$ / $\delta parameter$). In the current analysis, the sensitivity of the analysis to each parameter is measured with respect to a 10% increase in the parameter value. The results are shown in Figure 8. For example, it can be seen that the analysis is most sensitive to the mean yield strength with a 17% increase in reliability index due to a 10% increase in the mean yield strength (i.e. δβ / δparameter = 1.7). As expected, the mean

wagon weight is also an important parameter, with a 16% decrease in reliability index due to a 10% increase in weight. When reading Figure 8, note that Fy is the yield stress of the steel, Unc_wag is the model uncertainty associated with the weight of a single wagon, DL is the dead load, SDL is the superimposed dead load, Wag is the wagon weight, DAF is the dynamic amplification factor. The postscripts mean and sig denote the mean and standard deviation respectively. Note that while the uncertainty associated with the wagon weight is the only uncertainty model analysed for sensitivity, the uncertainty models for each of the other parameters are accounted for in the standard deviation of that parameter.

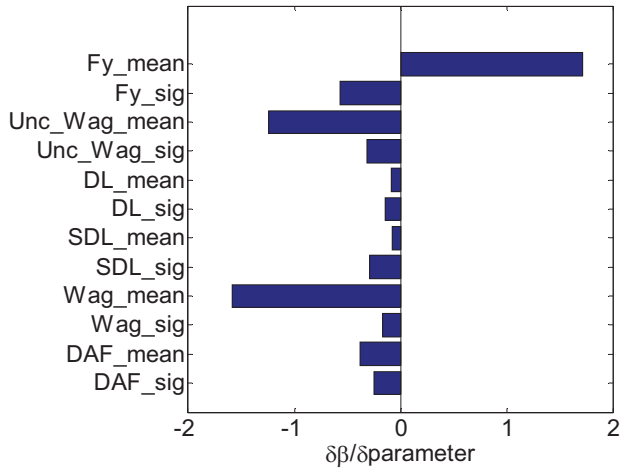


Figure 8. δβ for a 10% increase in the mean and variation coefficient of each parameter

It is clear from the sensitivity analysis that the incorporation of additional testing on the strength properties of the steel could result in higher levels of reliability. In the current analysis, the minimum yield strength was assumed from [5], therefore, further analysis would not only reduce the uncertainty associated with the strength modelling, but may also lead to the allowance of higher mean yield strengths, increasing the reliability index.

Since the WIM database had to be artificially enhanced in the current analysis, and considering the high sensitivity to the mean wagon weight parameter, a full month of WIM data would be preferable to accurately model the distribution of train wagon weights. While this may result in either increased or decreased wagon weights, it would be accompanied by a reduction in the uncertainty associated with the mean wagon weights. It is clear from figure 8 that this reduction in uncertainty would have a significant beneficial impact on the reliability index.

6 CONCLUSIONS

While the assessment of existing bridges by applications of guidelines from a general code is quick and efficient at a consultancy level, probabilistic based assessment may prove a bridge to be structurally safe, even if the specific requirements of the general code are not fulfilled. The justification of using these probabilistic measures for assessment is simple; essentially, they form the basis of the background documents to the design/assessment codes.

In the current assessment, a deterministic analysis of a steel truss railway bridge showed that the cross beams of the structure did not have sufficient capacity to resist the live loading from LM1 of EN 1991-2:2003. A probabilistic approach showed the reliability index of the bridge element to be sufficiently high to provide adequate safety in accordance with ISO 2394:1998. The potential cost savings to the owner are clear as unnecessary repair/replacement can be avoided.

It should be noted that while various codes have published target reliability indices, and not all are in agreement with one another, the target reliability levels referenced in Table 3 of this report are considered the most appropriate for the bridge in question.

In the event that a specific target reliability level is not met, a repair strategy can be optimised. For the example of the current analysis, if a higher level of reliability was required for CB2, a repair strategy might include the application of a Carbon Fibre Reinforced Polymer (CFRP) to the underside of the steel beam, in order to resist bending about the primary axis. The level of reinforcement required could be calculated in conjunction with providing a sufficient reliability index.

As outlined by the sensitivity analysis, the current assessment would benefit from additional bridge-specific information. Specifically, the provision of steel testing to obtain a more accurate model for the mean and standard deviation of the yield strength of the steel could prove to increase the reliability index. In addition, it is noted that a full month of WIM data for the bridge would be required to more accurately model the railway live load at the site.

ACKNOWLEDGMENTS

The research leading to these results was part of the SMARTRAIL project, a project funded by the EU 7th Framework Programme under call SST.2011.5.2-6 Cost-effective improvement of rail transport infrastructure. Grant agreement no: 285683

REFERENCES

[1] Kołakowski, P., Szelazek, J., Sekuła, K., Swiercz, A., Mizerski, K. and Gutkiewicz, P. (2011) 'Structural health monitoring of a railway truss bridge using vibration-based and ultrasonic methods', *Smart Materials and Structures, 20 (3)*.

[2] Midas Information Technology Co., Ltd. Midas User Support System Available at: http://en.midasuser.com/products/products.asp?nCat=352&idx=29133 [Accessed 10 January 2014]

[3] EN 1991-2, (2003), Eurocode 1: Actions on structures – Part 2: Traffic loads on bridges, European Standard, CEN, Brussels, 2003.

[4] Castillo, E., *Extreme Value Theory in Engineering*, Academic Press Inc., London, 1988

[5] Danish Roads Directorate (2004), Report 291, 'Reliability-Based Classification of the Load Carrying Capacity of Existing Bridges', *Roads Directorate, Ministry of Transport, Denmark, 2004.*

[6] O'Connor A., Pedersen C., Gustavsson L., Enevoldsen I. (2009), 'Probability based assessment and optimised maintenance planning for a large riveted truss railway bridge', *Structural Engineering International*. 19(4), 375 - 383.

[7] Choi, S-K., Grandhi, V., Canfield, R.A., *Reliability-Based Structural Design*. London: Springer. 2007

[8] ISO 2394, (1998), "General Principles on Reliability for Structures".

Development of a Geopolymer Binder from the Interbasaltic Laterites of Northern Ireland

McIntosh J. A.[1], Soutsos M. N.[2]
[1]banah UK Ltd, 1b Letterloan Road, Macosquin, Coleraine, Co. Londonderry BT51 4PP
[2]School of Planning, Architecture and Civil Engineering, Queen's University Belfast, Stranmillis Road, Belfast, BT1 5AG
email: [1]andrew@banahuk.co.uk, [2]m.soutsos@qub.ac.uk

ABSTRACT: Alkali activated binders have emerged as more eco-friendly and more durable alternatives to Portland cements. These binders have been shown to offer rapid strength gain, increased resistance to acid and sulfate attack, increased fire resistance and much reduced CO_2 emissions during manufacture. Most research to date has concentrated on either pulverised fuel ash (PFA) or a high purity dehydroxylated kaolin (metakaolin) as the main precursors. However, due to difficulty in obtaining a consistent source of PFA and the high cost of metakaolin, attention has turned to alternative, lower purity geological materials, in particular, calcined laterites, which are abundant throughout the globe. In County Antrim there exist large deposits of lateritic clays (known as the Interbasaltic Formation) which offer a mineralogy that may be suited to geopolymer binder production. This paper presents the initial results from experimental work carried out in order to develop a high-quality geopolymer binder using material taken from one location in North Antrim. The influence of mineralogy and activator composition has been examined and it was found that by using this high iron content precursor and formulating a geopolymer mixture with a typical Si:Al ratio of 2:1, a binder with compressive strengths of up to 130 MPa could be achieved. Physical properties of mortars and concretes manufactured using this binder, such as strength development, acid resistance and high temperature performance, are also reported and have been found to be much improved over Portland cement-based systems. A brief examination of the environmental impact of this binder in comparison to Portland cement is also considered and it was found to offer a reduction of up to 77% on Portland cement emissions.

KEY WORDS: geopolymer concrete; alkali activated binders, kaolinitic clay; strength development; acid resistance; durability.

1 INTRODUCTION

In recent times, interest has been growing in the subject of novel cements and binders, particularly in the area of construction [1]. One of the many drivers for this increase in interest has been the realisation of the impact of Portland cements on global warming and the high embodied CO_2 within these products [2]–[4]. The main players in this field of alternative binders are geopolymers (a sub-group of inorganic polymer cements or alkali-activated cements), magnesium phosphate cements and magnesium oxide cements. The focus of this particular research has been on geopolymer binders, or rather one area within geopolymer chemistry – those based on calcined clay, as these show the greatest potential for realistic development and commercialisation [3], [5]. In addition, there are added benefits as geopolymeric concretes and mortars offer improved physical properties when compared to Portland cement equivalents. If correctly formulated, they show higher resistance to acid and sulfate attack, lower shrinkage, increased stability at high temperatures and rapid strength gain [6–10].

While the waste-based precursor, pulverised fuel ash (PFA) – produced by coal-fired power stations, is readily available throughout the world, research has shown that the source of the coal, the type of furnace where the coal is burnt and the temperature of burning influence the chemical and the morphological properties of PFA, which consequently affects the potential to form a consistent geopolymer material [6], [11]. This leads to an exceedingly variable precursor that requires significant reformulation of the geopolymer binder between batches to achieve a consistent performance. In addition, it is well known that in the UK and Europe, the supply of PFA is limited and will become more so due to the move away from fossil fuels for electricity generation. At present, according to the Department of Energy and Climate change (DECC) figures, power generation using coal in the UK is as high as it is going to be [12] and continuing demand on PFA for use as a supplementary cementitious material (SCM) in cement-based systems will cause increased pressure on PFA supplies.

Metakaolin (MK), on the other hand, which is produced by the calcination of kaolinite causing dehydroxylation of the aluminosilicate mineral, can be easily defined by mineralogical testing of geological sources and will produce consistent results in a geopolymer binder subject to the MK content kept constant [8], [11], [13]. Much testing has been carried out by many geopolymer scientists on this pure material due to the high reactivity of metakaolin in an alkaline medium [14 - 15]. However, there are disadvantages in use of this material as a precursor due to the high costs involved in the production of high purity metakaolin which render it uneconomical for use in many concretes and mortars. While there are larger resources of kaolin than PFA within the UK [12], there are still limits on the quantities of this high quality clay available. Furthermore, work carried out by Lloyd [16] and de Silva *et al.* [17] has suggested that geopolymer matrices formed using a pure metakaolin are unstable and tend to transform from an amorphous structure to an increasingly crystalline one with reducing compressive strengths.

However, there are other potential sources of kaolin available for use as geopolymeric precursors. It has long been known that low purity kaolinitic clays, often contaminated with silica sand or feldspar minerals, may be used to successfully produce a geopolymer binder [18]. If these resources are taken into account, the quantity of material available – not only in the UK, but globally – for producing geopolymer binders is immense.

In Northern Ireland, there are multiple sources of a ferruginous kaolinitic clay known as Lithomarge found as part of the Interbasaltic Formation (IBF) in association with the Antrim Lava Group [19]. This material is plentiful – usually occurring in deposits of 10–15 metres in depth, but which may extend up to 30 metres [20] and has been exposed in numerous quarries throughout Northern Ireland, offering real potential for development as a low cost kaolinitic geopolymer precursor. It has been found that, contrary to previous work carried out using high-iron PFA where the iron oxides reduced the performance of the binder[6], this material with a high iron oxide content is still a good precursor for a geopolymeric binder.

This paper presents work carried out by banah UK Ltd to develop the functional geopolymer binder, banahCEM, using material available locally as the principle component and takes a brief look at a number of the physical properties of such a product.

The banahCEM geopolymer binder is a two component system comprising banahCEM (a), the powder component, and banahCEM (b), the liquid activator component.

2 MATERIALS AND METHODS

2.1 Geological precursor

In Northern Ireland, successive volcanic episodes have resulted in a number of layers of basalt having been laid down. Periods of warm humid climate that existed in the years between these eruptions caused extensive weathering of the exposed basalts producing horizons typical of that seen in Figure 1[20]. Further eruptions covered this soft material and protected it from subsequent erosion [19]. The lateritic material has been exploited previously by industry as a source of iron ore in the 19th and early 20th centuries, but these mines are now long gone.

The aluminosilicate precursor used in the manufacture of banahCEM originates from quarries that have removed the upper basalt layer and exposed the IBF. The mineralogy of the material is of the utmost importance in obtaining a reactive powder, therefore techniques such as X-Ray Diffraction (XRD) and X-Ray Fluoresence (XRF) need to be used to characterise the material.

In sourcing the geological component, it was also important to keep in mind the environmental credentials of the final product, so the material was obtained from existing quarries rather than examining green field sites.

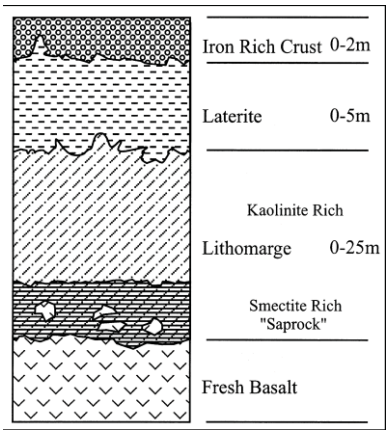


Figure 1 – Horizons within the Interbasaltic Formation (IBF) (*reproduced from* [20])

Finally, it was necessary to thermally pre-treat the raw material to dehydroxylate the main mineral component. The calcination was carried out using a Carbolite laboratory furnace at a temperature of 750 °C.

2.2 Alkali activator

The second component of the banahCEM system is the alkali activator solution. This is based on an alkali silicate and is formulated so as not only to provide the correct alkalinity to the binder system to cause the dissolution of Al and Si from the precursor, but also to supply additional soluble silica, so that a binder matrix with a defined Si:Al ratio is formed.

Currently there are two routes open to manufacturing this component, *i.e.* either by modifying commercially available solutions or by producing an alkali silicate using by-products or waste materials from other industries.

2.3 Geopolymer binder characterisation

Having developed an optimised binder formulation, the microstructure and chemical composition was then characterized using a Jeol 6500 FEG Scanning Electron Microscope (SEM) with Energy Dispersive X-Ray analysis (EDX). XRD was also used to confirm the amorphous nature of the binder using a PANalytical XRD (X'Pert PRO MPD) in conjunction with PANalytical's X'Pert Highscore software.

The heat of reaction (heat of hydration in cement chemistry) was measured using a Thermometrics 8 channel isothermal heat conduction calorimeter (TAM Air).

2.4 Physical properties and durability

It was essential that this new binder was assessed for fitness for purpose. This commenced by measuring the compressive strength development of mortars and concretes made using banahCEM as the principle binder.

Where possible, existing test methods in use for Portland cement based products were used. However, due to the fact that the basic chemistry of banahCEM and geopolymer binders in general is fundamentally different, there are some tests that are specified in concrete standards that, if applied to geopolymer binders, will give the appearance that the specimen has failed, but in reality it is the test method that is giving the wrong feedback. These fall outside the scope of this paper, but as an example, the accelerated carbonation test falls into this category [21]. In all tests where comparisons were

made to Portland cement products, the classification of Portland cement used was CEM II/A-L.

Unfortunately, current codes and standards for in-situ concretes, *e.g*. BS 8500 [22 - 23], have been developed around Portland cement technology, and specifications for concretes for the various exposure classes are prescribed in terms of minimum cement content and maximum water/cement ratios. Cements specified in these standards must conform to BS EN 197-1:2011[24], BS EN 14216:2004, or BS 8500-2:2006 [23].

For these reasons, a RILEM Technical Committee (TC 247-DTA) [25] has been set up to look at test methods for geopolymer binders with a view to gaining wider acceptance in the engineering community.

In the meantime, to try and assess the potential for changes in the geopolymer binder, an accelerated aging test used by Lloyd [16], which used the assumption that curing at elevated temperatures would simulate long term aging, was followed. banahCEM paste samples were cured for 28 days and then subjected to temperatures of 95 °C and 95% RH. XRD analysis was performed on the paste at intervals to assess whether there were phase changes from amorphous to crystalline structure – indicating the development of zeolites. If this were to occur, it would be an indication that the binder matrix is unstable over time and will result in the loss of compressive strength.

Resistance to harsh acidic environments was tested by measuring the mass loss of a 55 MPa banahCEM-based mortar immersed in 10% H_2SO_4 solution or 1.8% HCl solution over a period of 45 days. Acid solutions were replaced periodically to maintain the designed pH. A Portland cement-based mortar designed to the same compressive strength (3:1 sand : cement ratio and w/c ratio of 0.5) was tested for comparison. The specimens were cured for 28 days at 95% RH and 20 °C before being exposed to the acid solutions.

The manufacture of lightweight building units are also of interest as a potential use for geopolymer binders. Thermal conductivity tests were carried out on specimens of various densities and the results compared to existing products. The reduction in density was obtained by preparing a foamed geopolymer mortar which was cast in plastic moulds. The density of the specimens was varied by changing the foam content. Following curing for 28 days at 95% RH and 20 °C, the specimens were dried for 24 hours at 60 °C. Thermal conductivity values were obtained using a heat flow meter.

The material was tested for thermal conductivity in a Lasercomp Fox600 rotatable heat flow meter which meets ASTM C 518 [26] and ISO 8301 [27] standards. The heat flow meter tests were conducted with cold side upper plate temperature of 0 °C and a warm side lower plate temperature of 20 °C.

Finally, banahCEM-based products exhibit enhanced fire resistance over Portland cement. To demonstrate this, 50 mm 90 MPa mortar cubes were cured for 28 days and then placed in a furnace where the temperature was increased by 200 °C every 2 hours up to a maximum of 1000 °C. The dimensions were measured at each stage.

2.5 Environmental impact

Basic environmental data has been gathered on the banahCEM product which allows comparison with other binders such as Portland cements. Total CO_2 emissions for banahCEM have been calculated taking into account current alkali silicate manufacturing techniques and CO_2 emitted during manufacture of the powder component. For comparison, the figure used for Portland cement is the average CO_2 for total cement sales of CEM I, II, III and IV sold by British Cement Association (BCA) members in 2010 [28]. The hole-in-the-ground factor is calculated using data from the British Geological Survey for both KCl and Portland cement production [27 -28].

3 RESULTS AND DISCUSSION

3.1 Geological precursor

Numerous samples of lateritic materials were collected from across Co. Antrim. Using semi-quantitative XRD analysis in conjunction with chemical composition from XRF, suitable raw materials were identified and the total reactive powder content within these samples calculated.

Calcination was carried out over a range of temperatures to assess the optimum temperature for dehydroxylation of the hydrated aluminosilicates. Using DTA, this was found to be 750 °C. Following calcination, the product was ground to provide a powder with d_{99} = 100 µm and d_{50} = 20 µm.

3.2 Alkali activator

In the development of the activator solution, consideration of the end user‘s health and safety in addition to transport regulations was of high importance. Soluble silicate glasses are classified according to SiO_2:M_2O molar ratio (where M refers to alkali metal). According to guidance given by the Centre Européen d‘Etude des Silicates [31], a silicate solution with a molar ratio ≥1.6 is classified as an irritant and does not fall under EU transport regulations.

Having obtained the chemical composition of the precursor powder (component a), the alkalinity and dosage of activator (component b) could then be determined. This would allow the production of a binder matrix with a specific target Si:Al ratio.

Due to the fact that not all of the powder component will take part in the reaction, empirical testing had to be undertaken to optimise the ratio of banahCEM (a) to banahCEM (b).

In the formulation of a geopolymer binder, it is possible to use soluble silicates based on three main alkali metals, *viz.* Na, K and Li. Of these, Na and K are the most suitable due to the high cost of Li based silicates. K-silicates offer enhanced properties over Na-silicates such as reduced viscosity, lower potential for efflorescence in the finished product and higher compressive strength gain, but also increased raw material cost. Due to the enhanced physical properties, the banahCEM product is based mainly on the K-silicates.

3.3 banahCEM binder characterisation

Initial optimisation of the binder was completed using compressive strength of a mortar with a 1:1 w/w ratio of sand to powder component. This ratio of binder : sand produced

mortars that would consistently achieve compressive strengths of 100 MPa. Microstructural analysis of the paste was then carried out.

3.3.1 XRD

The XRD trace for a fully reacted banahCEM binder is shown in Figure 2. The trademark geopolymer amorphous mineral hump along with hematite peaks can be seen.

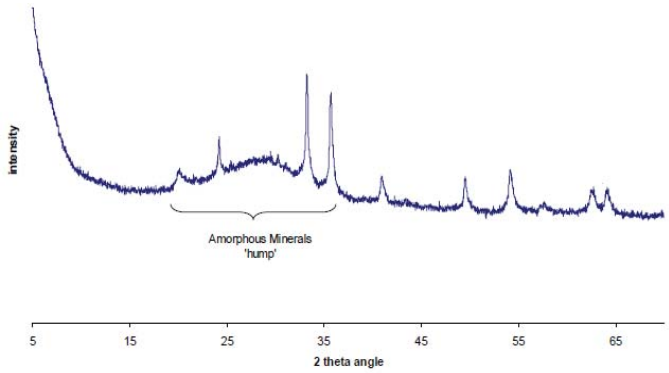


Figure 2 – XRD trace of reacted banahCEM

3.3.2 SEM

SEM micrographs of banahCEM paste are shown in Figure 3 and the surface chemical composition as analysed by EDX in Table 1. The micrographs show a gel-type formation rather than the crystalline growths that are generally associated with calcium silicate hydrate (C-S-H) type cements.

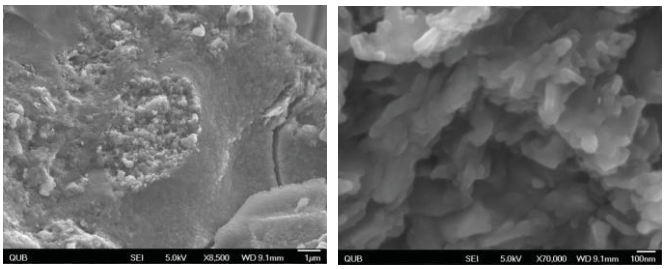


Figure 3 – SEM micrographs of banahCEM; ×8,500(L), ×70,000(R)

Table 1 – Typical chemical composition

Element	Weight %	Atomic %
O K	19.94	34.29
Al K	12.65	12.90
Si K	27.17	26.61
K K	22.17	15.60
Ca K	8.78	6.03
Fe K	9.29	4.58

3.3.3 Isothermal conduction calorimetry

An important consideration in the use of cements for mass concrete pours is the heat of hydration. As the reaction in geopolymers is not hydration, but rather the formation of a gel followed by polycondensation [32], it is preferred to use the term – heat of reaction. Work was carried out to calculate the heat evolution for comparison with Portland cement. As shown in Figure 4a and 4b, the maximum heat evolution was 20 minutes after the mixing of the powder and liquid components. Total heat evolution over 72 hours was 130 J/g where most of the evolution was in the early stages, before placement and setting had occurred. This is somewhat lower than CEM I which is typically 160–180 J/g at this point [33].

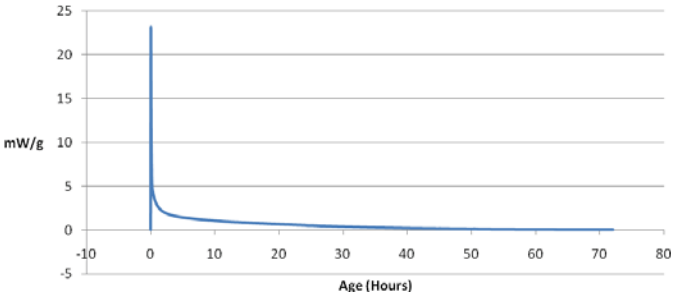


Figure 4a – Heat of reaction

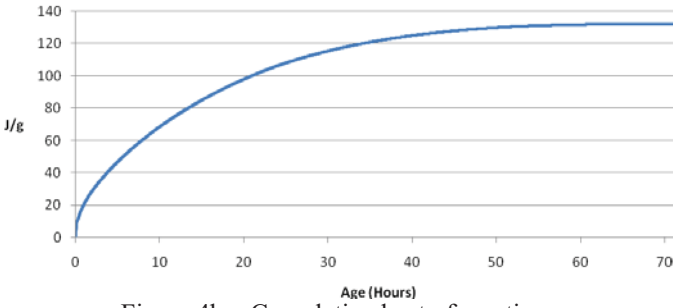


Figure 4b – Cumulative heat of reaction

3.4 Physical properties and durability

3.4.1 Binder content vs compressive strength

To enable assessment of the effect of binder content on the compressive strength of geopolymer concretes, trials have been carried out to plot the relationship of these two values using both 20 mm and 10 mm sized aggregate in concretes with a fixed workability of 85 mm slump. The relationship between these factors is shown in Figure 5.

Flexural strength testing found that the average flexural to compressive strength ratio was 1:7 for both banahCEM-based concrete and a CEM II/A-L based concrete.

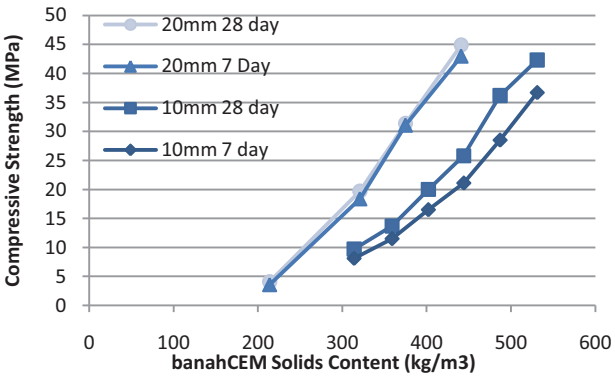


Figure 5 – Compressive strength vs binder content

3.4.2 Accelerated aging

Figure 7 shows the comparison of XRD traces for banahCEM pre- and post accelerated ageing. Each of the samples were

cured for 28 days at 95% RH and 20 °C before commencing the test. One set was maintained at 20 °C, while the other set was subjected to 95% RH and 95 °C for a further 28 days. No increase in crystalline structure was observed - indicating a stable geopolymer matrix. These results are contrary to what was found by Lloyd [16] and show the importance of selecting a suitable precursor and careful formulation of the activator composition.

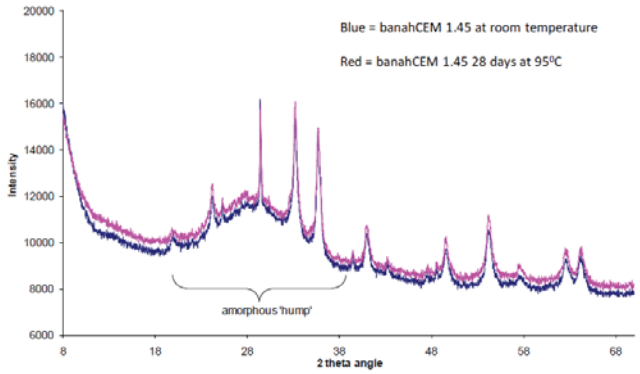


Figure 7 – Comparison of XRD traces before and after accelerated ageing treatment

3.4.3 *Acid resistance*

Figure 8 shows that for both acids the banahCEM-based mortar lost mass initially, but this did not continue over time, levelling off at approximately 12%. On the other hand, the Portland cement mortar continued to lose mass until the end of the test, although the loss was less severe on the specimens subjected to HCl attack, in part due to the lower concentration of the acid solution.

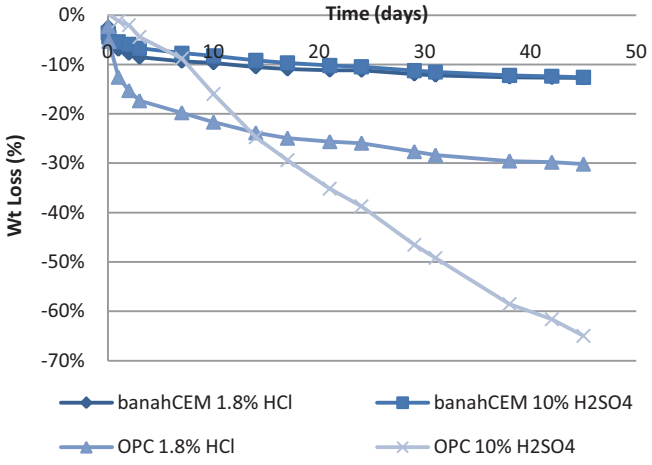


Figure 8 – Acid resistance

3.4.4 *Thermal conductivity*

A comparison of thermal conductivity values of lightweight banahCEM based building units and aircrete blocks is shown in Figure 9. In each case, values for the banahCEM product are *ca.* 0.06 $Wm^{-1}K^{-1}$ lower than the aircrete equivalent. The reason for this improved performance is currently being investigated.

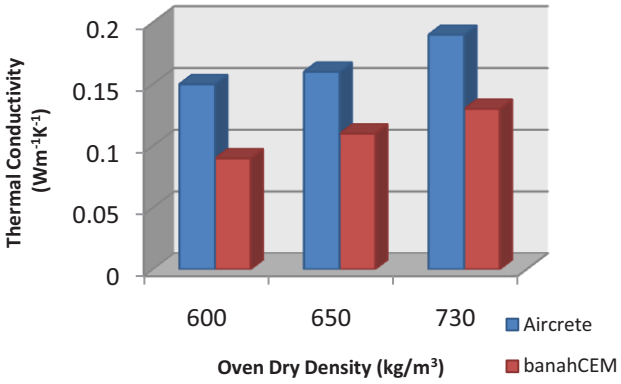


Figure 9 – Thermal conductivity values

3.4.5 *Fire Resistance*

Geopolymer mortar cubes remained dimensionally stable up to 800 °C and retained their integrity up to 1000 °C. Figure 10 shows a cube before and after heating to 1000 °C where deformation of the cube was limited to shrinkage of 1–2 mm.

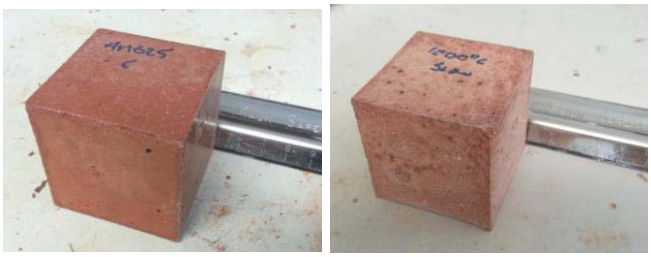


Figure 10 – Before (L) and after (R) heating to 1000 °C

3.5 *Environmental impact*

When compared to CO_2 emissions for all CEM I, II, III and IV sold by BCA members in 2010, banahCEM offers up to 77% reduction in CO_2 – from an average of 787 kg/tonne for the Portland cements mentioned above, to 184 kg per tonne of banahCEM solids.

In terms of quantity of material extracted from the ground to produce 1 tonne of product, banahCEM manufactured using a by-product based activator solution, offers a reduction of almost 50%. For a CEM I approximately 2 tonnes of material – made up of 1650 kg limestone and 400 of clay (based on figures from the British Geological Survey [34]) – needs to be excavated. banahCEM production requires approximately 1 tonne of raw material per tonne of finished product, where 770 kg of clay are required for the powder component and 360 kg of minerals for the activator component.

4 CONCLUSIONS AND FURTHER WORK

A new geopolymer binder based on locally available ‗nuisance' materials has been developed that can be used as an alternative to Portland cements in harsh acidic environments such as sewer pipes. It is also inherently more resistant to fire, offers a massive reduction in CO_2 emissions during manufacture and reduced thermal conductivity opening up a large range of potential applications.

As discussed, the potential for use of the banahCEM material for in-situ applications is somewhat restricted due to

the prescriptive nature of current concrete standards. However, there is great potential for use in precast applications with performance-based standards where the binder type is not restricted to cement described in EN 197-1:2001 [24]

Looking forward, the banahCEM production plant will be completed within the next year. In addition, a large collaborative R&D project, funded by Invest Northern Ireland, has commenced with the School of Planning, Architecture and Civil Engineering in Queen‘s University Belfast, which will enable further characterization of the performance of banahCEM-based concretes.

Initial discussions have been held between a number of parties in the UK who have an interest in the development of geopolymer binders, both commercial and regulatory bodies, with a view to commencing the process of gaining technical approval for such binders. Whether this takes the form of gaining a European Technical Approval (ETA) rather than seeking to change the current cement standards [35], remains to be seen. In the meantime each project must be considered in its own right, where the testing of the final products, for example precast concrete pipes, is required to ensure conformance to performance standards rather than specified ingredients.

REFERENCES

[1] J. Davidovits, “World-wide increase in geopolymer research,” 2010. [Online]. Available: http://www.geopolymer.org/science/world-wide-increase-in-geopolymer-research. [Accessed: 20-Mar-2013].

[2] K. L. Scrivener and R. J. Kirkpatrick, “Innovation in use and research on cementitious material,” *Cem. Concr. Res.*, vol. 38, no. 2, pp. 128–136, Feb. 2008.

[3] British Cement Association, “Novel Cements : Low energy , low carbon cements,” 2009.

[4] J. S. J. Deventer, J. L. Provis, P. Duxson, and D. G. Brice, “Chemical Research and Climate Change as Drivers in the Commercial Adoption of Alkali Activated Materials,” *Waste and Biomass Valorization*, vol. 1, no. 1, pp. 145–155, Feb. 2010.

[5] R. S. McLeod, “Ordinary Portland Cement with extraordinary high CO2 emissions,” *Newbuilder*, pp. 30–33, 2005.

[6] J. Davidovits, *Geopolymer Chemistry and Applications*, 3rd ed. Saint Quentin, France: Institute Geopolymere, 2011.

[7] J. Davidovits, “Geopolymers. Inorganic polymeric new materials,” *J. Therm. Anal.*, vol. 37, pp. 1–14, 1991.

[8] a. Palomo, M. T. Blanco-Varela, M. L. Granizo, F. Puertas, T. Vazquez, and M. W. Grutzeck, “Chemical stability of cementitious materials based on metakaolin,” *Cem. Concr. Res.*, vol. 29, no. 7, pp. 997–1004, Jul. 1999.

[9] S. E. Wallah, “Performance of fly ash-based geopolymer concrete under sulfate and acid exposure,” in *Geopolymer ’05*, 2005.

[10] S. E. Wallah, “Drying Shrinkage of Heat-Cured Fly Ash-Based Geopolymer Concrete,” *Mod. Appl. Sci.*, vol. 3, no. 12, pp. 14–21, 2009.

[11] P. Duxson, A. Fernández-Jiménez, J. L. Provis, G. C. Lukey, A. Palomo, and J. S. J. Deventer, “Geopolymer technology: the current state of the art,” *J. Mater. Sci.*, vol. 42, no. 9, pp. 2917–2933, Dec. 2006.

[12] A. Heath, K. Paine, and S. Goodhew, “The potential for using geopolymer concrete in the UK,” vol. 166, pp. 195–203, 2013.

[13] H. Xu and J. S. J. Van Deventer, “Geopolymerisation of multiple minerals,” *Miner. Eng.*, vol. 15, no. 12, pp. 1131–1139, Dec. 2002.

[14] H. Wang, H. Li, and F. Yan, “Synthesis and mechanical properties of metakaolinite-based geopolymer,” *Colloids Surfaces A Physicochem. Eng. Asp.*, vol. 268, no. 1–3, pp. 1–6, Oct. 2005.

[15] J. Davidovits, “Geopolymer Cement, a review,” 2013.

[16] R. R. Lloyd, “Accelerated ageing of geopolymers,” in in *Geopolymers - Structures, Processing, Properties and Industrial Applications*, J. L. Provis and J. S. J. van Deventer, Eds. Abingdon, UK: Woodhead Publishing, 2009, pp. 139–166.

[17] P. De Silva, K. Sagoe-Crenstil, and V. Sirivivatnanon, “Kinetics of geopolymerization: Role of Al2O3 and SiO2,” *Cem. Concr. Res.*, vol. 37, no. 4, pp. 512–518, Apr. 2007.

[18] R. Cioffi, L. Maffucci, and L. Santoro, “Optimization of geopolymer synthesis by calcination and polycondensation of a kaolinitic residue,” *Resour. Conserv. Recycl.*, vol. 40, no. 1, pp. 27–38, Dec. 2003.

[19] M. R. Cooper, “Paleogene Extrusive Igneous Rocks,” in in *The Geology of Northern Ireland*, W. I. Mitchell, Ed. Belfast, N. Ireland: Geological Survey of Northern Ireland, 2004, pp. 167–178.

[20] I. . Hill, R. . Worden, and I. . Meighan, “Geochemical evolution of a palaeolaterite: the Interbasaltic Formation, Northern Ireland,” *Chem. Geol.*, vol. 166, no. 1–2, pp. 65–84, May 2000.

[21] J. L. Provis, “Geopolymers in the 21st Century Construction Materials Landscape,” in *Applications of Geopolymers*, 2012.

[22] British Standards Institution, “BS 8500-1:2006+A1:2012 Concrete – Complementary British Standard to BS EN 206-1 – guidance for the specifier,” no. 1. 2012.

[23] British Standards Institution, “BS 8500-2:2006+A1:2012 Concrete – Complementary British Standard to BS EN 206-1 – constituent materials and concrete,” no. 1. 2012.

[24] British Standards Institution, “EN 197-1:2000 Cement — Part 1: Composition, specifications and conformity criteria for common cements,” vol. 3. 2000.

[25] J. L. Provis and F. Winnefeld, “Durability testing of alkali-activated materials - RILEM Technical Committee 247-DTA,” 2012.

[26] ASTM C518, “Standard Test Method for Steady-State Thermal Transmission Properties by Means of the Heat Flow Meter Apparatus.” West Conshohocken, PA, 2010.

[27] ISO 8301, “Thermal insulation -- Determination of steady-state thermal resistance and related properties -- Heat flow meter apparatus.” International Organization for Standardization, 1991.

[28] MPA, CSMA, and UKQAA, “Embodied CO2e of UK cement , additions and cementitious material,” 2010.

[29] British Geological Survey, “Mineral Planning Factsheet - Cement,” 2008.

[30] British Geological Survey, “Mineral Planning Factsheet,” 2011.

[31] European Chemical Industry Council, “Soluble Silicates: Chemical, toxicological, ecological and legal aspects of production, transport, handling and application,” Brussels, 2013.

[32] J. L. Provis, “Modelling the Formation of Geopolymers,” University of Melbourne, 2006.

[33] K. Owens, M. I. Russell, G. Donnely, and P. a. M. Basheer, “The use of a Nano-crystal seeding chemical admixture in improving Portland cement strength development: application for the precast concrete industry,” in *32nd Cement and Concrete Science Conference*, 2012, pp. 45–49.

[34] British Geological Survey, “MINERAL PROFILE CEMENT RAW November 2005,” 2005.

[35] A. M. Dunster and K. C. Quillin, “Low Carbon Cements - addressing the barriers to mainstreaming,” in *32nd Cement and Concrete Science Conference*, 2012, pp. 70–72.

Chloride ingress through alkali activated slag concretes

P. A. Muhammed Basheer[1], Qianmin Ma[1&2*], Sreejith V. Nanukuttan[1], Yun Bai[3] and Changhui Yang[4]
[1]School of Planning, Architecture and Civil Engineering, Queen's University Belfast, University Road, Belfast, UK
[2]Faculty of Civil Engineering and Mechanics, Kunming University of Science and Technology, Jingming South Road, Kunming, China
[3]Department of Civil, Environmental & Geomatic Engineering, University College London, Gower Street, London, UK
[4]School of Materials Science and Engineering, Chongqing University, Shapingba Main Street, Chongqing, China
email: m.basheer@qub.ac.uk, qma01@qub.ac.uk, s.nanukuttan@qub.ac.uk, yun.bai@ucl.ac.uk, ychh@cqu.edu.cn
*corresponding author

ABSTRACT: Alkali activated slag (AAS) is a credible alternative to Portland cement (PC) based binder systems. The superior strength gain and low embodied carbon make it a potential binder for next generation concretes. However there is little known about the long term durability of AAS systems, especially the chloride transport and subsequent corrosion of reinforcing steel. In this study, chloride transport through 12 AAS concretes with different alkali concentrations (Na_2O% of mass of slag) and different modulus (Ms) of sodium silicate solution activator was investigated. A non-steady state chloride diffusion test was used for this study due to its similarity to the real exposure environment in terms of chloride transport through concrete. The results showed that the chloride concentration at the surface (C_s) of AAS concretes was higher than that for PC concrete. However, lower non-steady state chloride diffusion coefficient (D_{nssd}) was obtained for the AAS concretes. The D_{nssd} of the AAS concretes decreased with the increase of Na_2O% and Ms of 1.50 gave the lowest D_{nssd}. The results are encouraging and it can be concluded that AAS concrete offers a superior performance in terms of chloride transport.

KEY WORDS: AAS; chloride diffusion; anionic exchange; pore structure; chloride binding.

1 INTRODUCTION

Slag, which is a by-product from steel industry, is activated by using alkali activator to produce AAS. Compared to PC, AAS is an environmentally friendly cementitious material. Besides, it has higher strength and superior durability [1]. As a result, there is a global increase in research in this area to determine if such materials have the potential to compete with PC based concretes.

Chloride induced corrosion of steel in reinforced concrete is a major cause of deterioration for structures in the U.K. and Ireland. [2]. Besides the surface chloride concentration, the pore structure and pore solution chemistry of concrete have significant influence on controlling the transport of chloride ions [3]. As a novel cementing material, the pore structure and pore solution chemistry of AAS are different from those of PC [4, 5]. They will vary largely based on the Na_2O% and Ms when sodium silicate solution is used as the activator. With a change in Na_2O% and Ms, the resultant concretes will not only have a different pore structure, but it will also have significantly different ionic structure. The influence of the above factors on chloride transport is not clearly known and therefore, an experimental programme was developed to address this shortcoming in knowledge.

2 EXPERIMENTAL PROGRAMME

Pore structure and pore solution of the AAS concretes was characterized and expressed with an attempt to identify their effect on chloride transport. Furthermore, the effect of Na_2O% of slag and Ms of activator on chloride transport in AAS concretes was also investigated. Details of which are explained in the following sections.

2.1 Materials

Sodium silicate solution (or commonly known as water glass), which is available as 'Crystal 0503' from Tennants Distribution Ltd., UK was used as the activator for Ground Granulated Blastfurnace Slag (GGBS). Industrial grade sodium hydroxide powder with a purity of 99% was used to modulate the modulus of the sodium silicate solution to the required values. The GGBS was provided by Civil and Marine Ltd., UK. A commercial retarder 'YP-1'® [6] was used to retard the setting of the AAS concretes. Portland cement (CEM I) used in PC control mix was supplied by QUINN Cement. Superplasticiser used in the PC mix was CHEMCRETE HP3 provided by Larsen. The chemical composition and physical properties of the GGBS, the sodium silicate solution and the Portland cement are reported in Table 1.

Crushed basalt with specific gravity of 2.75 and size fractions of 20mm and 10mm combined in a ratio of 1:1 was used as the coarse aggregate. Natural sand with specific gravity of 2.73 and fineness modulus of 3.68 was used as the fine aggregate. Mixing water was from the mains water supply.

2.2 Mix proportion

Twelve AAS mixes with different Na_2O% of 4, 6 and 8 and different Ms of 0.75, 1.00, 1.50 and 2.00 were studied. One PC mix was studied as well as reference. For the AAS concretes, the total binder content, which was considered as the sum of the GGBS and the solid component in the activator, and the water-binder ratio (w/b) were kept the same at 400kg/m^3 and 0.47, respectively. The water content in the sodium silicate solution was considered in the calculation of w/b. This w/b was determined in order to make the AAS

mixes to achieve the minimum requirement of slump class S2 specified in BS EN 206-1. The content of retarder was 0.3% of the mass of the GGBS for all AAS mixes. The binder content (400kg/m^3) was kept the same for the PC concrete. The w/b of 0.42 was used for the PC concrete, which was considered to allow the PC concrete to meet the requirement of maximum w/b and minimum compressive strength under the exposure class XS3 specified in BS EN 206-1. 0.5% (by the mass of cement) superplasticiser was added for the PC concrete to achieve a workability that meets the minimum requirement for S2 slump class. The water content (40%) in the superplasticiser was also considered in the calculation of w/b for the PC mix. A ratio of 36% between fine aggregate and total aggregates was used for both the AAS and the PC concretes. The mix design of PC mix was based on the DoE method. The mix proportions are given in Table 2.

Table 1. Chemical composition and physical properties of the raw materials.

	GGBS	PC (CEM I)	Sodium silicate solution 'Crystal 0503'	
CaO%	39.4	61.3	Ms	2.58
SiO_2%	34.3	23	Na_2O%	12.45
Al_2O_3%	15	6.15	SiO_2%	31.1
MgO%	8	1.8	Water content%	56.45
Sulfide%	0.8	2.5		
Na_2O%	0.45	0.22	Viscosity (20°C)	400 poises
Fe_2O_3%	0.4	2.95		
K_2O%	0.38	0.68	Specific gravity	1.5
LOI%	0.7	2.78		
Specific surface area	527 m^2/kg	386 m^2/kg		
Specific gravity	2.89	3.13		

2.3 Casting, curing test specimens

Three 250×250×110mm slabs and nine 100×100×100mm cubes per mix were cast for the tests to be detailed in the section 2.4.

After casting, the specimens were covered with thin polythene sheets to minimise the evaporation of water from the surface of concrete. Approximately 1 hour after the concrete surface became stiff, the moulds were covered with layers of previously wetted hessian and polythene sheets. The specimens were stored in this condition for three days. The moisture condition of the hessian was maintained every six hours. After demoulding, the concrete specimens were covered with wet hessian and wrapped in plastic bags, storing in constant temperature room at 20±1°C until testing. The moisture condition of the hessian was checked every two weeks.

2.4 Test methods

2.4.1 Tests for slump and compressive strength

Slump test specified in BS EN 12350-2 was carried out on the fresh concretes. The compressive strength test according to BS EN 12390-3 was carried out on the 100mm cubes at 3, 28 and 91 days of age. The strength to be reported is an average of three values.

Table 2. Concrete mix proportions (kg/m^3).

Mix	S	C	WG	NaOH	CA	FA	W	SP	R
4%-0.75	371		34.6	13.6	1163	654	199		1.1
4%-1.00	368		45.8	11.6	1164	655	192		1.1
4%-1.50	362		67.7	7.8	1167	656	180		1.1
4%-2.00	357		88.9	4.2	1170	658	168		1.1
6%-0.75	358		50.2	19.7	1163	654	190		1.1
6%-1.00	354		66.2	16.8	1165	655	181		1.1
6%-1.50	346		97.0	11.2	1169	658	170		1.0
6%-2.00	339		127	5.9	1173	660	153		1.0
8%-0.75	346		64.7	25.4	1163	654	188		1.0
8%-1.00	341		85.0	21.6	1166	656	176		1.0
8%-1.50	332		124	14.3	1171	658	154		1.0
8%-2.00	322		161	7.5	1175	661	134		1.0
PC		400			1220	686	168	1.6	

Note: S—slag, C—cement, WG—sodium silicate solution, CA—coarse aggregate, FA—fine aggregate, W—water, SP—superplasticiser, R—retarder

2.4.2 Test for chloride diffusion

The non-steady state chloride diffusion test for the concretes was carried out by following the procedure given in NT BUILD 443 [7] and the samples were tested at an age of 91 days. The testing specimens were three Ø100×60mm cores taken from the three 250×250×110mm slabs for each concrete mix. The vacuum saturation regime similar to that of NT BUILD 492 [8] was used to precondition the cores. In NT BUILD 492 after the application of the vacuum, saturated $Ca(OH)_2$ solution is introduced into the container. However this is likely to lead to leaching of ions from the samples. Therefore, in this research, after the application of the vacuum, the vacuum was released, samples were wrapped in deionised water saturated hessian and placed back in the container. The vacuum was again applied. The purpose of this change was to prevent calcium hydroxide solution used for saturation affecting the pore solution chemistry of the concrete samples and minimise the loss of ions from the concrete samples. The mould finish face of the specimens was exposed to the salt solution. The duration of immersion was 3 months. After the immersion, the cores were ground in layers to obtain sufficient concrete dust from different depths; at an increment of 3mm and up to a depth of 30mm. RILEM TC 178-TMC recommendations [9, 10] was

followed to dissolve the dust in acid and water, respectively, to obtain the chloride containing solutions. A pre-calibrated potentiometric titration was carried out on the acid dissolved samples to determine the total chloride content in the solution. A non-linear regression analysis based on Fick's second law was performed to determine the D_{nssd} and the C_s of the concrete cores once the chloride profile was obtained. The D_{nssd} and the C_s to be reported are an average of three values.

pH of the water dissolved solution was measured in order to monitor the change of alkalinity in the concretes due to the chloride transport.

2.4.3 Test for pore structure indication

Before the chloride diffusion test, bulk electrical resistivity of the concrete cores was measured according to the literature [11] in order to indicate the pore structure of the concretes. Under the consideration of the effect of pore solution on the bulk electrical resistivity measurement, pore solution conductivity of the concretes was also measured (details in the next section) and the pore solution resistivity to be reported with the bulk electrical resistivity is the reciprocal of the pore solution conductivity.

2.4.4 Test for pore solution expression

Concrete cores with size of Ø60×100mm were taken from the 250×250×110mm slabs to be used for extracting pore solution at an age of 91 days. The sample preparation regime was similar to that of the chloride diffusion test. Pore solution of the cores was extracted by using a specialist pore fluid extraction device which compressed the specimen under pressures up to 1000MPa. pH and conductivity of the pore solution collected were measured immediately after the extraction by using a pH meter and a conductivity meter, respectively. Concentration of Na^+ in the pore solution was measured subsequently by using Inductively Coupled Plasma-Optical Emission Spectrometer technique.

3 RESULTS AND DISCUSSION

3.1 Slump

The slump results of the concretes are presented in Figure 1. The mix design principle for the AAS concretes was to use a fixed w/b allowing all of them to meet the minimum slump requirement for its use in chloride environments, such as S2 in marine environments as specified in BS 8500-1. The mix design for the PC reference concrete also followed the same principle. Therefore, the slump results of all 13 mixes met the minimum requirement of S2 which is 50mm. It is also found that the slump of the AAS concretes increased with Na_2O%. The plasticizing effect provided by Na_2O component in the activator may be responsible for this [12].

3.2 Compressive strength

Figure 2 presents the compressive strength of the concretes at the ages of 3d, 28d and 91d.

Due to the presence of retarder in the AAS concretes, some of them showed an unfavourable compressive strength at the age of 3d. The mix design for the PC reference concrete was to meet the requirement for XS3 and XD3 exposure environments specified in BS 8500-1. From the compressive strength results at the age of 28d it can be seen that not all the AAS concretes achieved the required strength (58MPa) for the two exposure classes. However, most of the AAS concretes met the strength requirement of 50MPa for the exposure classes XS1, XD1 and XD2. It should be noted that the w/b used for the AAS concretes (0.47) was higher than that for the PC concrete (0.42). Therefore, an improved compressive strength could be expected if a lower w/b was used for the AAS concretes. An AAS superplasticiser may be required in those instances.

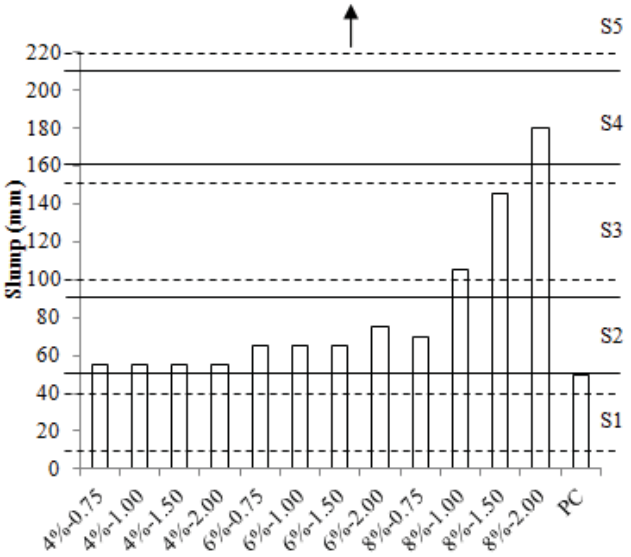


Figure 1. Slump results of the concretes.

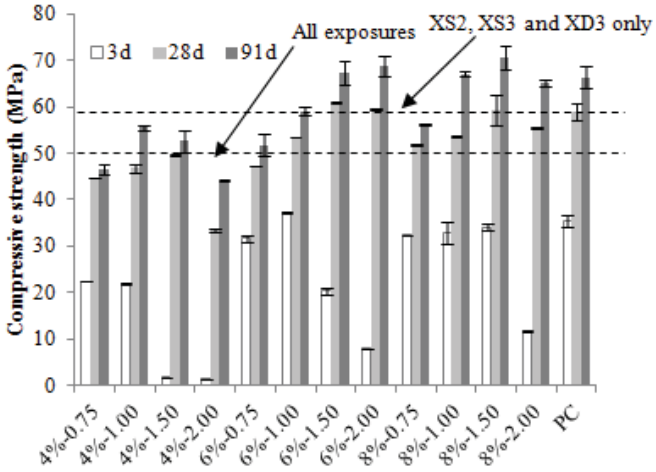


Figure 2. Compressive strength of the concretes at the ages of 3d, 28d and 91d.

3.3 Non-steady state chloride diffusion coefficient (D_{nssd})

Figure 3 presents the D_{nssd} of the concretes. It can be seen that the D_{nssd} of the AAS concretes was much smaller than the corresponding value obtained for the PC concrete despite the higher w/b of the AAS concretes.

Bulk electrical resistivity of the concretes was measured with an attempt to indicate pore structure of the concretes and the results are plotted in Figure 4. To study the effect of pore solution conductivity on the bulk electrical resistivity measurement [13], pore solution conductivity of the concretes

was also measured and its reciprocal (pore solution resistivity) was reported in Figure 4 as well for comparison.

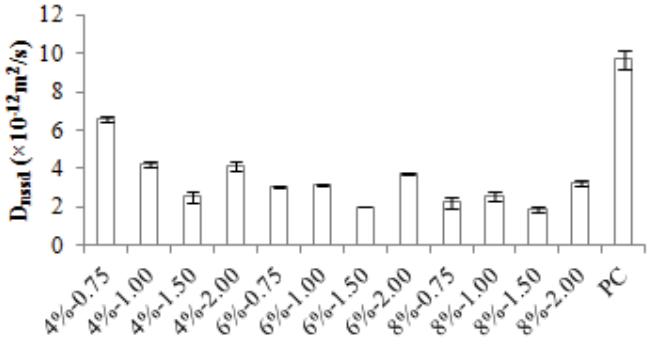


Figure 3. D_{nssd} of the concretes.

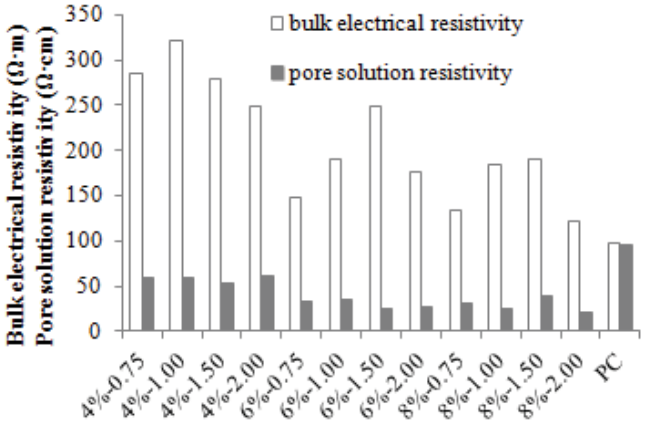


Figure 4. Bulk electrical resistivity of concrete plotted alongside its pore solution resistivity.

As shown in Figure 4, the AAS concretes had lower pore solution resistivity than the PC concrete owing to its highly ionic nature. Therefore, according to the model proposed by Whittington et al. [14], the reason for the higher bulk electrical resistivity of the AAS concretes could be attributed to they had denser pore structure and/or their binder matrix was less conductive. When the pore solution is highly ionic and conductive, the conductivity of binder matrix will be insignificant (under normal circumstances). Suggesting that more ionic flow will take place through the pore solution and the binder will play insignificant role in the overall electrical resistivity. This would also mean the higher bulk electrical resistivity shown in Figure 4 and the lower chloride diffusivity shown in Figure 3 is a result of the denser pore structure.

The hydration products of AAS, such as C-S-H(I), C-A-S-H and hydrotalcite [15] have much potential to bind alkali cations [16]. During the transport of chloride ions, the binding of the accompany cations could retard the further ingress of chloride anions [3]. At the beginning of the mixing, large amount of sodium cations was introduced in the AAS concretes (refer to AAS with Na_2O% of 4 was used by Puertas et al. [5], concentration of sodium ions of 60000ppm was observed in AAS at the age of 3 hours). However, after three months of curing, a dramatic reduction in the concentration of sodium ions was observed in the AAS concretes as reported in Table 3. This suggests that the matrix is capable of binding sodium ions in high proportion. It is assumed that this binding nature will also continue during the chloride ingress phase. This could further retard the movement of chloride ions and reduce their overall chloride diffusivity.

Table 3. Pore solution chemistry of the concretes.

Mix	pH	Na^+ (ppm)	Mix	pH	Na^+ (ppm)
4%-0.75	11.7	2154	6%-2.00	9.9	18.20
4%-1.00	11.9	4740	8%-0.75	12.4	202.0
4%-1.50	10.5	58.96	8%-1.00	12.2	244.0
4%-2.00	9.9	121.2	8%-1.50	10.8	185.3
6%-0.75	11.9	96.26	8%-2.00	11.9	64.34
6%-1.00	11.9	69.19	PC	12.5	1234
6%-1.50	11.4	42.81			

Chloride binding may be enhanced when the concrete is less alkaline [17]. As reported in Table 3, the AAS concretes had a lower alkalinity than the PC concrete. Therefore, it is anticipated that more chlorides might have been bound by the hydration products of the AAS concretes delaying their further ingress. This may also explain the lower D_{nssd} obtained for the AAS concretes.

3.4 Effect of Na_2O% and Ms on the D_{nssd} of the AAS concretes

Effects of Na_2O% and Ms on the D_{nssd} of the AAS concretes are presented in Figures 5 and 6, respectively.

From Figure 5 it can be seen that the D_{nssd} of the AAS concretes decreased with the increase of Na_2O% from 4 to 8. As reported by Karahan and Yakupoglu [18], porosity of AAS is reduced with the increase of Na_2O%. This could be one of the primary reasons for the reduction in D_{nssd} with the increase of Na_2O% for the AAS concretes in Figure 5.

Besides, hydration degree of AAS increases with the increase of Na_2O% [19]. As a result, more hydration products such as C-S-H gel and hydrotalcite would be formed in the AAS with a higher Na_2O%. Such hydration products show potential to bind chlorides during their transport in AAS. Therefore, chloride binding in the AAS concretes might have been enhanced with the increase of Na_2O% delaying further ingress of chlorides. This could be also responsible for the reduced D_{nssd} of the AAS concretes with the increase of Na_2O% in Figure 5.

Ms around 1.50 is optimum for the hydration of AAS [20, 21]. Therefore, as a result of the possibly reduced porosity and improved chloride binding, the AAS concretes with Ms of 1.50 gave the lowest D_{nssd} as shown in Figure 6.

3.5 Chloride concentration at the surface (C_s)

Figure 7 presents the estimated total C_s of the concretes by using Fick's second law based curve fitting. It can be seen that the C_s of the AAS concretes was higher than that obtained from the PC concrete.

As stated by Buenfield et al. [22], for sake of electron-neutrality, the transport of chloride anions in concrete should be balanced by an outward transport of other anions (such as hydroxyl anions) from the concrete.

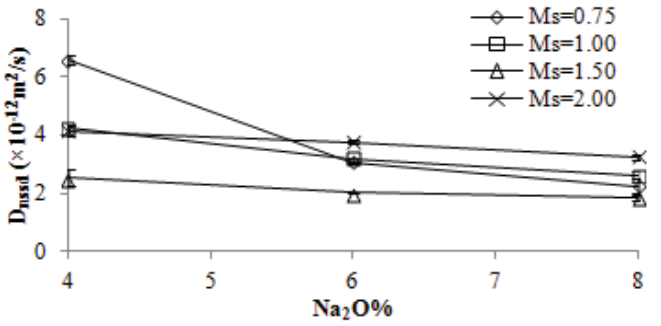


Figure 5. Effect of Na_2O% on the D_{nssd} of the AAS concretes at different Ms.

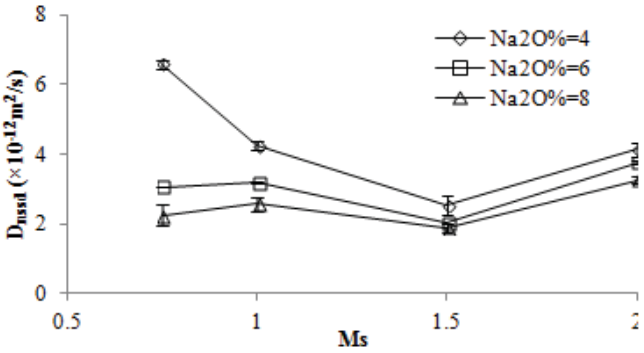


Figure 6. Effect of Ms on the D_{nssd} of the AAS concretes at different Na_2O%.

Figure 8 presents the pH profiles of concretes after chloride immersion test. It is clear to see that the pH values drop dramatically in the near surface zone of AAS concretes.

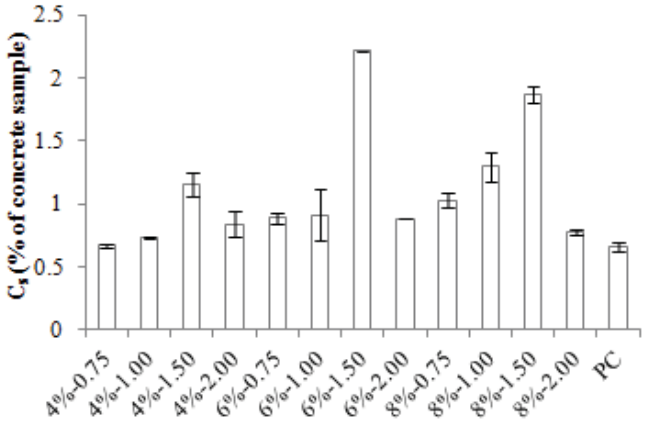


Figure 7. Total C_s of the concretes.

When the outward diffusion of hydroxyl ions occurs in PC concrete, $Ca(OH)_2$ would dissolve in the pore solution to buffer its alkalinity [23]. This may have explained the constant pH values in the PC concrete with depth as shown in Figure 8. However, $Ca(OH)_2$ is not one of the hydration products of AAS [15]. Without the buffering effect, the loss of alkalinity would be more severe in the case of the AAS concretes as shown in Figure 8. This is particularly significant in the near surface zone.

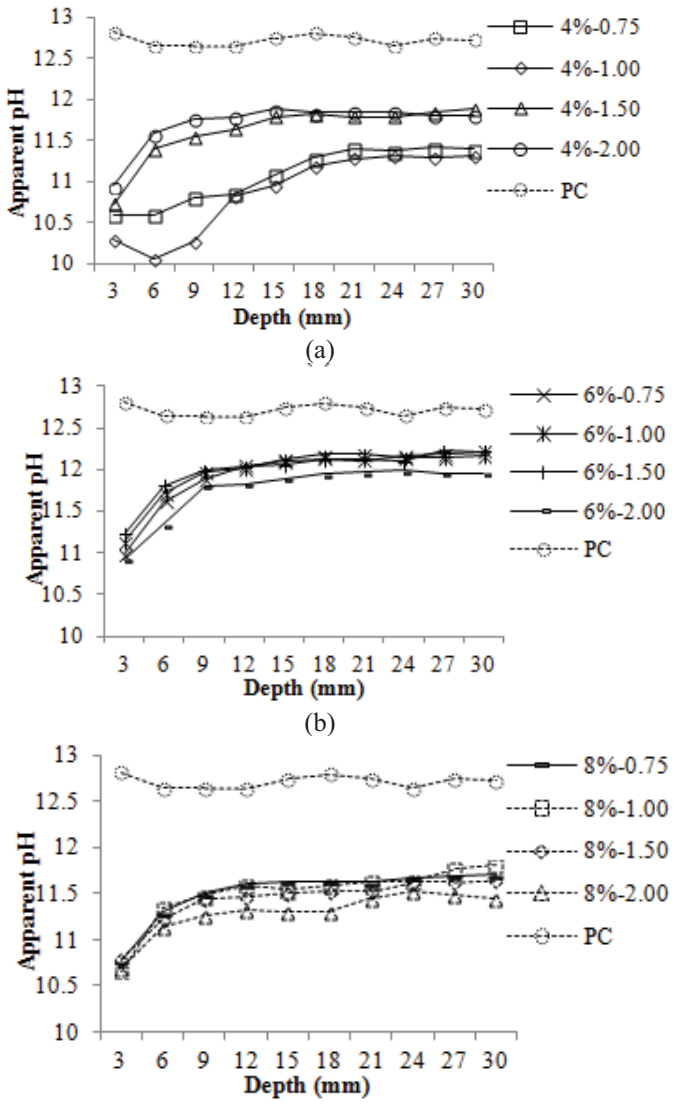


Figure 8. Apparent pH profiles of the concretes after the chloride immersion test.

As a result of the outward diffusion of hydroxyl ions, chloride ions of the same charge penetrated into the concretes to take the sites originally occupied by hydroxyl ions [22]. The AAS concretes lose hydroxyl ions from the near surface zone and there no further hydroxides generated by the binder, more chlorides from outside will migrate and occupy the sites. This may explain the higher chloride content observed at the surface of the AAS concretes as presented in Figure 7. The reduction of alkalinity in such concretes will enhance the binding capacity as discussed earlier. This could also be a contributing factor for the increase in C_s as shown in Figure 7.

4 CONCLUSION

- Surface chloride concentration (Cs) for the AAS concretes was found to be higher than that of the PC concrete. Severe loss of hydroxyl ions and subsequent improvement in chloride binding could explain the increased C_s values.

- Chloride diffusivity, D_{nssd} of the AAS concretes was lower than that of the PC concrete. Based on the analysis and interpretation, the AAS concretes were found to have (1) denser pore structure, (2) higher binding capacity of alkali cations and (3) possibly improved chloride binding capacity. All of the above factors individually or collectively help to explain the lower D_{nssd} observed for AAS concrete.
- The D_{nssd} of the AAS concretes decreased with the increase of Na_2O% from 4 to 8, and the AAS concretes with Ms of 1.50 had the lowest D_{nssd}. These are cohesive with the effect of Na_2O% and Ms on the hydration of AAS.

ACKNOWLEDGMENTS

This project was sponsored by UK-China Science Bridge project (EPSRC/G042594/1) and Dr. Ma was sponsored by China Scholarship Council studentship for her PhD at Queen's University Belfast. The slag used in this research was supplied by Civil and Marine. All these are grateful acknowledged.

REFERENCES

[1] Rodriguez, E., Bernal, S., Mejia de Gutierrez, R. and Puertas, F. (2008), 'Alternative concrete based on alkali-activated slag', *Materiales de Construccion,* 58, 53-67.

[2] J. P. Broomfield, *Corrosion of steel in concrete: understanding, investigation and repair,* Taylor and Francis, London, UK, second edition, 2007.

[3] L.-P. Tang, L.-O. Nilsson and P. A. M. Basheer, *Resistance of concrete to chloride ingress testing and modelling,* Spon Press, London, UK, 2012.

[4] Shi, C. and Day, R. L. (1996), Alkali-slag cements for the solidification of radioactive wastes in Gilliam and Wiles (eds) *Stabilisation and solidification of hazardous, radioactive, and mixed wastes,* ASTM STP 1240, American Society for Testing and Materials, Philadelphia, USA, 163-173.

[5] Puertas, F., Fermandez-Jimenez, A. and Blanco-Varela, M. T. (2004), 'Pore solution in alkali-activated slag cement pastes. Relation to the composition and structure of calcium silicate hydrate, *Cement and Concrete Research,* 34, 139-148.

[6] Yang, C. and Pu, X., Retarder of alkali activated slag, Chinese patent, 91108316.2, 1993.

[7] NT BUILD 443 Concrete, hardened: accelerated chloride penetration, (1995)

[8] NT BUILD 492 Concrete, mortar and cement-based repair materials: chloride migration coefficient from non-steady-state migration experiments, (1999)

[9] RILEM TC 178-TMC: 'Testing and modelling chloride penetration in concrete' Analysis of total chloride content in concrete recommendation, *Materials and Structures,* 35, 583-585, (2002)

[10] RILEM TC 178-TMC: 'Testing and modelling chloride penetration in concrete' Analysis of water soluble chloride content in concrete recommendation, *Materials and Structures,* 35, 586-588, (2002)

[11] Tang, L., 'Guideline for practical use of methods for testing the resistance of concrete to chloride ingress', Chlortest Report, (2005)

[12] Allahverdi, A., Shaverdi, B. and Najafi K. E., 'Influence of sodium oxide on properties of fresh and hardened paste of alkali-activated blast-furnace slag', *International Journal of Civil Engineering,* 8, No. 4, 304-314, (2010)

[13] Basheer, P. A. M., Gilleece, P. R. V., Long, A. E. and Mc Carter, W. J. (2002), 'Monitoring electrical resistance of concretes containing alternative cementitious materials to assess their resistance to chloride penetration', *Cement and Concrete Composites,* 24, No. 5, 437-449.

[14] Whittington, H. W., McCarter, J. and Forde, M. C. (1981), 'The conduction of electricity through concrete', *Magazine of Concrete Research,* 33, No. 114, 48-60.

[15] Wang, S. D. and Scrivener, K. L. (1995), 'Hydration products of alkali activated slag cement', *Cement and Concrete Research,* 25, No. 3, 561-571.

[16] Hong, S.-Y. and Glasser, F. P. (1999), 'Alkali binding in cement pastes part I. the C-S-H phase', *Cement and Concrete Research,* 29, 1893-1903.

[17] Tritthart, J. (1999), 'Chloride binding in cement II. The influence of the hydroxide concentration in the pore solution of hardened cement paste on chloride binding', *Cement and Concrete Research,* 19, 683-691.

[18] Karahan, O. and Yakupoglu, A. (2011), 'Resistance of alkali-activated slag mortar to abrasion and fire', *Advances in Cement Research,* 23, No. 6, 289-297.

[19] Hong, S. Y., Kim, J. C. and Kim, J. K. (1993), 'Studies on the hydration of alkali activated slag', *3rd Beijing International Symposium on Cement and Concrete,* Beijing, China, 1059-1063.

[20] Krizan, D. and Zivanovic, B. (2002), 'Effects of dosage and modulus of water glass on early hydration of alkali-slag cements', *Cement and Concrete Research,* 32, No. 8, 1181-1188.

[21] Bernal, S. A., Provis, J. L., Rose V. and Mejía de Gutierrez, R. (2011), 'Evolution of binder structure in sodium silicate-activated slag-metakaolin blends', *Cement and Concrete Composites,* 33, No. 1, 46-54.

[22] Buenfeld, N. R. and Okundi, E. (1998), 'Effect of cement content on transport in concrete', *Magazine of Concrete Research,*50, No. 4, 339-351.

[23] Page, C. L. (1975), 'Mechanism of corrosion protection in reinforced concrete marine structures', *Nature,* 258, 514-515.

Characterisation of Irish sandstones used for building.

Paul Kissane[1], Sara Pavia[2] Oliver Kinnane[3]

[1] Roughan & O'Donovan Limited, Arena Road, Sandyford, Dublin 18.
[2,3] Department of Civil Engineering, University of Dublin, Trinity College.

email: kissanet@tcd.ie, pavias@tcd.ie, Oliver.Kinnane@tcd.ie

ABSTRACT: This study examines several sandstones used in monumental and vernacular structures. They were sourced at Manorhamilton, Co. Leitrim; Clara, Co. Offaly; Drumbane, Co. Tipperary and Killaloe, Co. Clare. The Manorhamilton rock is used by the Office of Public Works for restoration while the Clara, Killaloe and Drumbane stones were used to build some of Ireland's most important monuments including Cormac's Chapel on the Rock of Cashel, St. Brendan's Cathedral, Clonfert, and Clonmacnoise Monastery. It is necessary to establish the properties of these sandstones to understand their current condition and facilitate decision making to conserve them. This paper determines composition, mass structure (density and porosity), moisture behaviour (capillarity and evaporation) and mechanical properties including compressive strength, modulus of elasticity and surface hardness. These properties largely determine compatibility between the sandstones and consolidant treatments as well as mortar repairs. All sandstones are siliceous, dense, strong, stiff materials of low porosity and permeability, brittle behaviour and typical shear failure. Their property values compare well with those of granite and other strong, durable igneous rocks. Therefore, in sound condition, they are compatible with mortars of medium to high hydraulicity. The Drumbane (siliceous variety), Manorhamilton and Killaloe sandstones are the strongest and stiffest; their strength and stiffness are well over those of Portland cement concrete and engineering grade brick. The Clara Hill is the weakest and less stiff sandstone however, its strength and stiffness are well over those of conventional building units, closer to engineering grade materials. In the most ferruginous sandstones (Drumbane and Clara Hill), there is an inverse relationship between compressive strength/density and iron cement (haematite): as the iron lowers, the rocks become denser and stronger as well as less porous and permeable.

KEY WORDS: Irish Sandstone; Density; Porosity; Capillary suction; Compressive strength; Elastic modulus; Surface hardness.

1 INTRODUCTION

This study is part of wider research carried out in the Department of Civil Engineering, Trinity College Dublin. The aim of this research was to preserve monumental Irish sandstone. Two conservation areas were considered: stone consolidation and the repointing of masonry with compatible mortars. Rocks lose material over time as a result of weathering. Consolidants are chemical substances aimed at replacing the cohesive strength between particles where cementitious materials have been lost. A variety of consolidants have been used on monumental stone. For this research, Tetraethoxysilane (TEOS) consolidants were chosen because they are silica based materials chemically compatible with most Irish sandstones; they have a significant history of use and are continuously available [1].

The mass structure, moisture behaviour and mechanical properties of the sandstones were investigated in order to ensure compatibility between the sandstone and conservation repairs including consolidants and mortars.

Penetration is essential for a consolidant to work and also to avoid damage to the substrate. Penetration relates to permeability which is determined by the mass structure and pore system characteristics therefore, the density, porosity, capillary suction and evaporation of the sandstones were investigated. Permeability and strength are critical properties in the context of consolidation: the treatment must not undermine the ability of the stone to follow the prevalent moisture regime and; in addition, the consolidant treatment must not increase the likelihood of differential stresses developing between the outer exposed treated surfaces and underlying substrates.

In relation to mortar repairs, most historic and traditional masonries are built with lime mortars which weather over time and often need to be repaired. The new mortar needs to be compatible with the building units. Compatibility refers to chemical composition but also to physical properties such as strength and permeability. A mortar stronger and more impermeable than its substrate can damage the masonry as it drives moisture into the building units enhancing all weathering processes related to the presence and movement of moisture such as expansion by evaporation, freeze-thaw, mineral dissolution, biological colonization and salt crystallization. Therefore, the sandstone properties related to moisture transfer including porosity, capillary suction and evaporation, were characterised in order to ensure compatibility with mortar repairs. In addition, a mortar too strong and stiff does not accommodate movement transferring stresses to the masonry units which may eventually fracture. Therefore, the strength and stiffness of the sandstones were measured in order to ensure mortar compatibility.

2 MATERIALS AND METHODS

2.1 Materials

The sandstones were sourced at Manorhamilton, Co. Leitrim; Killaloe, Co. Clare, Drumbane, Co. Tipperary and Clara, Co.Offaly. The Manorhamilton sandstone comes from the Mullaghmore Sandstone Formation in Co. Leitrim [2] and the

Killaloe sandstone from quarries near Killaloe town, on the River Shannon, in the mid-west of Ireland [3]. The Drumbane sandstone was sourced from a quarry north of Cashel, Co. Tipperary in the Cappagh White Old Red Sandstone Formation [4]; and the Clara sandstone from a quarry in Clara Hill, Co.Offaly . The Manorhamilton sandstone is currently used for restoration works while the Killaloe and Drumbane sandstones were used to build some of Ireland's most important national monuments. Drumbane sandstone can be seen in Cormac's Chapel on the Rock of Cashel. Killaloe sandstone can be seen in the doorway of St. Brendan's Cathedral, Clonfert and in the several structures at Clonmacnoise, which has been nominated for acceptance as a UNESCO World Heritage Site. The Clara sandstone was also used to build Clonmacnoise. The sandstones were tested according to EN standards and RILEM recommendations.

2.2 Petrographic Analysis, Density, Porosity, Evaporation and Capillary Absorption

Petrographic examination was carried out according to EN 12407 [5]. The mass structure properties were characterised by measuring the apparent density and open porosity in accordance with EN1936 [6]. Evaporation curves and water absorption by capillarity were measured in accordance with RILEM Recommendations [7].

The samples were dried in an oven at 105˚C for 24 hours and the dry mass, md, calculated. They were then placed in a tray containing approximately 2mm depth of water and the capillary absorption measured by taking readings of time and mass, ti & Mi.

The specimens were later immersed in water under vacuum pressure for 24hrs. The hydrostatic and surface saturated masses were measured, mh and ms. Finally, the samples were wrapped on 5 sides with cling film and left to dry, taking mass readings to measure evaporation with time, ti and Mi. Readings were typically taken at 15mins, 30mins, 1hr, 3hrs, 8hrs, 24hrs and 48hrs.

Apparent density (kg/m^3),

$$\rho b = md /(ms - mh)*\rho w \quad (1)$$

Open porosity (%),

$$po = (ms - md)/(ms - mh)*100 \quad (2)$$

Evaporation rate (g/m^2/hr),

$$q = m / t \; ; \; m = Mw /area; \; Mw = Mo - Mi \quad (3)$$

Capillary absorption rate (g/m^2/s^{½})

$$A = m / \sqrt{t}; \; m = Mw /area; \; Mw = Mo - Mi \quad (4)$$

2.3 Compressive Strength and Modulus of Elasticity

The compressive strength (maximum stress at failure - N/mm^2), was determined according to EN 1926 [8]. Data for stress, strain and displacement were also obtained, allowing calculation of the modulus of elasticity (E= Stress/Strain – equation 5- kN/mm^2). Strain gauges were attached to the faces of the specimens using an epoxy resin. The load vs strain was monitored using a System 5000 workstation connected to the strain gauges and a 100kN load cell.

$$E = \sigma/\varepsilon \quad (5)$$

2.4 Surface Hardness

It was measured with a Schmidt hammer rebound which uses a spring mechanism to determine the strength of the surface. The samples were placed flat on a covered concrete floor, making sure that the bottom surface was smooth and resting uniformly on the floor. The piston was gradually pressed down onto the surface and the rebound of the hammer noted. This value is translated into compressive strength (uniaxial, unconfined) when used in conjunction with calibration charts.

3 RESULTS AND DISCUSSION

3.1 Petrographic Analysis

The Drumbane sandstone is a quartzitic sandstone of varying composition (Fifuer 1). Grey (siliceous) and rust (ferruginous) varieties were sampled from the quarries. The grey stone is well sorted with fine quartz and infrequent mica. It contains fine pores, some refilled by secondary iron, and fissures of clay or iron liable to open. Increasing iron turns the rock into a rust colour. The rust stone is also fine-grained but less dense. It contains significant clay mineral matrix and iron oxide cement (mainly haematite); and has a more open, fine-medium, pore structure. Haematite can also accumulate in layers (Figure 2).



Figure 1. Drumbane sandstone: abundant clay matrix and significant iron cement and pores. X2 polarized light



Figure 2. Drumbane sandstone: low porosity with clay mineral matrix and layered iron cement. X2 polarized light.

The Manorhamilton sandstone is a fine to medium grained, quartzitic sandstone with occasional mica and feldspar, clay mineral matrix and iron cement (Figures 3 and 4). Colour varies from grey to brown and sand (finer pores), depending

on the iron content. Variations can be seen along strata. The quartz grains are coarser where the iron and feldspar contents are greater. Pores have a wide size distribution (medium to very fine).

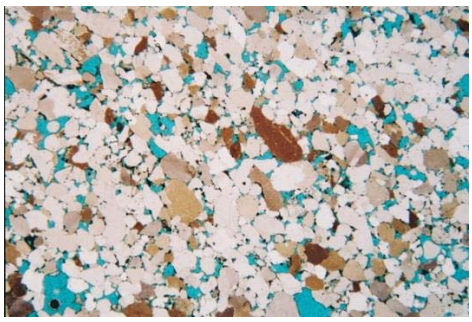


Figure 3. Manorhamilton sandstone with abundant quartz, little cement and matrix and substantial pores. 2X polarized light

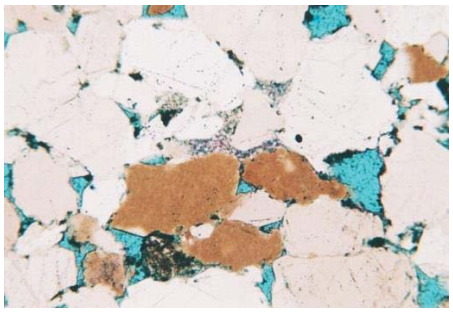


Figure 4. Manorhamilton sandstone detail of clay mineral matrix, quartz and pores.10X polarized light

The Killaloe sandstone is a mature quartzitic rock with varying ferruginous content and large differences in colour [2]. It periodically contains mica, feldspar, clay mineral matrix and iron, silica and carbonate (dolomite) cements (Figures 5 and 6). The majority of the stone is dense and compact with low pore volume. Darker varieties are more weakly cemented and contain medium-coarse pores. The grey/ green varieties include glauconite (Figure 6) and biotite.

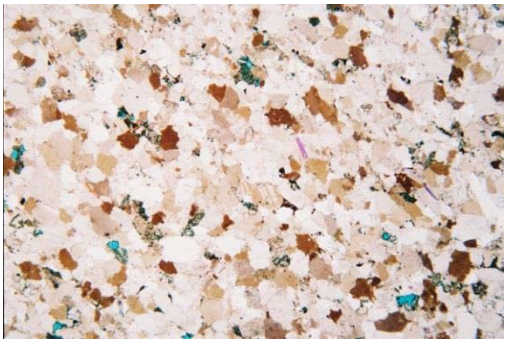


Figure 5. Killaloe sandstone including abundant quartz and scarce feldspar and mica. Low porosity. X2 polarized light.

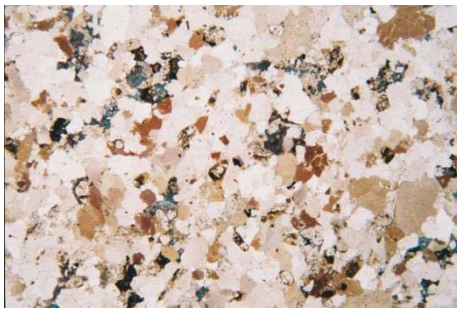


Figure 6. Killaloe sandstone: occasional carbonate cement (dolomite) and significant glauconite. X2 polarized light.

Table 1. Mineral composition and petrography.

	Drumbane	Manorhamilton	Killaloe	Clara Hill
Colour	grey, rust, brown	grey, white, brown, sand	buff, brown, grey, green	grey, white, yellow
Mineral comp-osition (%by volume)	quartz 60 clay 15-30 mica <2 iron 6-15	quartz 70+ clay 5 mica <2 iron <6	quartz 85 clay, silica cem 5 mica, dol <2 iron 5-10 feldspar 5	quartz60-80 clay 10-15 mica <2 iron 7-15 feldspar <2
Pores	Fine, occ. medium	Fine to medium, wide distribution	Fine to medium, Dark coarser.	Fine, coarser in yellow variety
fracture	occasional inter granular 0.1-1mm by >30mm	occasional large inter granular 0.1-0.5mm wide.	occasional curved open fractures with deposits	occasional inter granular

The Clara Hill sandstone is also quartzitic. It includes substantial clay mineral matrix and iron cement and a considerable pore volume with a wide size distribution (Figure 7). It periodically contains feldspar and mica. The yellow variety has more abundant clay and more abundant, coarser pores (Figure 8).



Figure 7. Clara Hill sandstone with abundant clay matrix and iron cement. X2 polarized light.

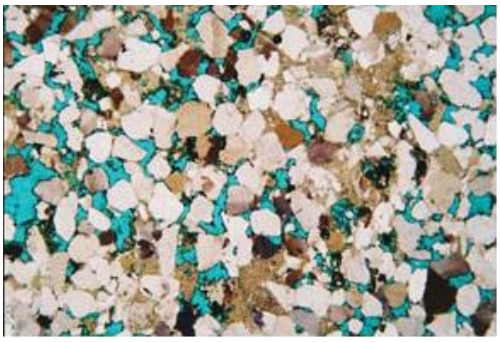


Figure 8. Clara Hill sandstone with significant clay matrix, iron cement and pores. X2 polarized light.

3.2 Density and Porosity

Most sandstones are dense materials of low porosity. The results agree with the petrography evidencing that the sandstones are dense and compact with a low pore volume. The Manorhamilton and Clara Hill yellow are slightly less dense and more porous.

The results (table 2) revealed that the Drumbane sandstone is a dense, low porosity rock; and agree with the petrographic analysis evidencing the rust (ferruginous) stone as less dense with a more open, coarser pore structure. Therefore, a clear relationship can be established between increasing porosity and decreasing density as the iron content rises: the grey rock is denser and less porous while the ferruginous (rust) quarry sandstone with abundant iron is more porous and less dense (table 2). A similar relationship is evident in the Clara Hill sandstone.

With the exception of the dark grey variety, the Killaloe sandstone is a dense, low porosity rock. This agrees with the petrographic results evidencing that the majority of the stone is dense and compact with low pore volume, but the darker varieties are more weakly cemented and contain larger pores.

Table 2. Mass properties of sandstones.

Sandstone	variety	Porosity %	Density-kg/m^3
Drumbane	grey-siliceous	3.6	2561
	ochre-ferruginous	8	2323
Manorhamilton		11.0	2329
Killaloe	buff	2.3	2550
	green/grey	1.5	2660
	ochre	2.7	2543
	dark grey	8.3	2436
Clara Hill	grey	4.7	2481
	yellow	15	2188

3.3 Capillary absorption and evaporation

As expected for materials with the range of porosity and pore characteristics above, capillary suction is rather low, and there is a significant reduction in the moisture transport in the 2nd 24 hours (Figure 9). The results evidenced that, in general, capillary absorption relates well to porosity therefore, the pore system of the sandstones is well interconnected and efficient in transporting fluids. The Manorhamilton stone has a slightly lower capillarity than expected from its porosity therefore, its pore system may not be as well connected as the other sandstones, a lower early evaporation rate (Figure 10) reinforces the inferior pore connection. The results agree with the porosity and density results as the sandstones with lower density and higher porosity show a greater capillary suction (Manorhamilton and Clara Hill yellow and Drumbane ferruginous variety).

The ferruginous Drumbane Sandstone (Dfer in Figure 9) is substantially more permeable than the siliceous rock: the pore structure of the less dense, ferruginous rock facilitated the movement of up to ⅔ more moisture by capillary absorption and almost twice as much by evaporation (Figure 10), compared to the siliceous type.

The Killaloe sandstone displays a low capillary absorption and evaporation, except for the dark grey porous material which shows greater values. The ochre variety has higher capillarity and evaporation and similar porosity than the other varieties; its pores are therefore narrower facilitating greater capillary movement.

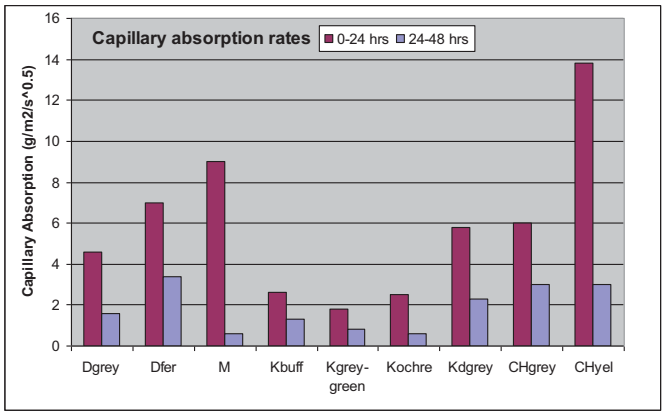


Figure 9. Capillary absorption of the sandstones.

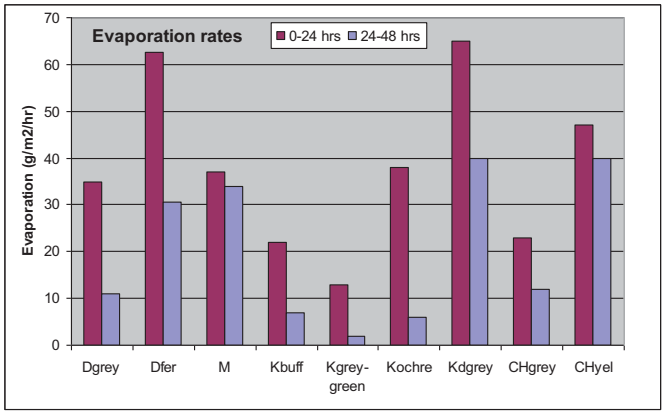


Figure 10. Evaporation rates of the sandstones.

3.4 Compressive strength and Elastic Modulus

The sandstones investigated are strong and stiff materials of brittle behaviour, typical shear failure and high surface hardness. Their mechanical properties compare well with those of granite and other strong, durable igneous rocks and agree with previous results evidencing the sandstones as dense, compact materials of low pore volume and permeability.

The Drumbane (siliceous variety), Manorhamilton and Killaloe sandstones are the strongest and stiffest rocks, their strength and stiffness is well over that of typical Portland cement concrete and engineering grade brick. The Clara Hill is the weakest and less stiff sandstone however its strength and stiffness are well over those of most conventional building units, closer to engineering grade materials.

Most of the crushed samples displayed near perfect shear cones. However, the stiffest specimens were more brittle and displayed failure along steeper planes The values showed acceptable coefficient of variation. In the Drumbane sandstone, strength was on average 17 % lower when the axial load was applied along the bedding. The results agree with Wilkinson [9] who reports the force required to crush a 1" cube of ferruginous Drumbane stone as 10290 lbs, which is equivalent to a strength of approximately 84 N/mm^2. The siliceous variety is significantly stronger, however as stiff, as the ferruginous one. This agrees with previous results evidencing the ferruginous variety as less dense, with greater porosity and permeability due to a more open and coarser pore structure. Therefore, there is an inverse relationship between compressive strength and iron content. This relationship is maintained in the Clara Hill sandstone. The surface hardness values correlate well with the strength measured. Extrapolation outside the range of the manufacturer's calibration chart was required to correlate the hardness readings to compressive strength, as a result, as indicated, it can be an approximate 10% error on the results (table 4).

The Manorhamilton sandstone is slightly less dense and more porous that the other sandstones and yet it is as strong and often stiffer. This may be related to the lower interconnections of its pore system previously evidenced resulting in a stronger microstructure.

The compressive strength of the Killaloe sandstone is very high ranging from 108 to 156N/mm^2. The rock is a stiff material with a modulus of elasticity ranging from 13-15 GPa. Similarly to the other sandstones, the crushed samples exhibited shear failure, some brittle specimens displaying high angle planes of failure. The ochre and dark grey varieties were not tested in compression however, the strength obtained with the hardness tests agrees with the crushing strength of the other specimens. The buff coloured variety is stronger however as stiff as other types (standard deviation of 1.8 GPa).

Table 4. Mechanical properties of sandstones. All shear failure. E-Modulus of elasticity.

Sandstone	variety	Compressive strength N/mm^2	E GPa	Hardness N/mm^2
Drumbane	grey-siliceous	121	32	130±13
	ochre-ferruginous	70	26	76±8
Manorhamilton		105	36	90±8
Killaloe	buff	156	47	170±17
	green/grey	108	32	130±13
	ochre	-	-	130±13
	dark grey	-	-	120±12
Clara Hill	grey	62	15	80±8
	yellow	50	13	-

4 CONCLUSION

All sandstones investigated are siliceous. They are dense, strong and stiff materials of low porosity and permeability, brittle behaviour and typical shear failure. Their property values compare well to those of granite and other strong, durable igneous rocks. Therefore, in sound condition, they are compatible with mortars of medium and high hydraulicity; and their siliceous composition is compatible with TEOS consolidants which would allow chemical bonding of the new silicates to the quartz forming the pore walls.

The Drumbane (siliceous variety), Manorhamilton and Killaloe sandstones are the strongest and stiffest rocks, their strength and stiffness is well over that of typical Portland cement concrete and engineering grade brick. The Clara Hill is the weakest and less stiff sandstone however, its strength and stiffness are well over those of most conventional building units, closer to engineering grade materials. The Manorhamilton sandstone is slightly less dense and more porous than the other sandstones and yet it is as strong and often stiffer, this may be related to the limited interconnection of its pore system resulting in a stronger microstructure

In the most ferruginous rocks (Drumbane and Clara Hill sandstones), there is an inverse relationship between compressive strength/density and iron content: as the iron cement (haematite) lowers, the rocks become denser and mechanically stronger as well as less porous and permeable.

Two clear varieties of the Drumbane sandstone can be evidenced with the naked eye in the quarry just by the colour (grey and rust). The grey variety is more siliceous, significantly denser and stronger, with lower permeability and porosity than the rust one. The rust (ferruginous) variety contains significant iron oxides (mainly haematite) which are responsible for the colour change. This rock is mechanically weaker and less dense, with greater porosity and permeability due to a more open and coarser pore structure.

ACKNOWLEDGMENTS

The authors thank the Office of Public Works for funding this research. Thanks to Paul McMahon (National Monuments) and the technical staff of the Civil Engineering Dept. for their assistance; and to Neil Kearney of the Dept of Geology for his help cutting the rocks.

REFERENCES

[1] Kissane, P. (2007), Consolidation of Irish Sandstone, PhD Thesis, University of Dublin Trinity College, Ireland.
[2] MacDermot, 1996, Geology of Sligo-Leitrim, Geological Survey Ireland
[3] Bolton J. & Pavía (2002) The sandstone at St. Brendan's Cathedral, Clonfert, Co. Galway, Conservation Plan, Unpublished.
[4] Archer, J.B. (1996) Geology of Tipperary, Geological Survey of Ireland
[5] EN 12407:2000 Natural stone test methods. Petrographic examination.
[6] EN 1936:1999 Natural stone test methods. Determination of real density and apparent density and of total and open porosity
[7] RILEM Commission 25-PEM Protection et Érosion des Monuments, 1980, Recommended tests to measure the deterioration of stone and to assess the effectiveness of treatment methods
[8] EN 1926:1999 stone test methods. Determination of compressive strength
[9] Wilkinson, G. (1845) Practical geology and ancient architecture of Ireland, Dublin

The influence of heat transfer and storage in structural precast building components on indoor environments

Magdalena Hajdukiewicz[1, 2, 3], Jamie Goggins[1, 2]
[1]Department of Civil Engineering, National University of Ireland Galway
[2]Ryan Institute, National University of Ireland Galway
[3]Informatics Research Unit for Sustainable Engineering, National University of Ireland Galway
email: jamie.goggins@nuigalway.ie

ABSTRACT: Knowledge about the heat transfer and storage in concrete components of the building envelope is vital in evaluating the environmental and energy performance of buildings. Providing sufficient thermal mass of the building envelope is crucial in delivering optimal indoor conditions while reducing the energy consumption in buildings.
This paper presents a project that focuses on evaluating the thermal performance of precast concrete building structural elements (i.e. twinwall, hollowcore and lattice slab), regarding their thermal properties on indoor environments. The motivation, objectives and method description of the project are described. The analysis proposed in this project will provide (i) better prediction of indoor environmental conditions; (ii) healthier, more comfortable and productive indoor environments; and (iii) reduced/optimised energy consumption in buildings.

KEY WORDS: Buildings, thermal properties, indoor environments, precast concrete

1 INTRODUCTION

Human-induced climate change is occurring globally and has already made a significant impact on the environment and society, due to increased levels of greenhouse gases. The building sector is responsible for 40% of the total final energy consumption and 36% of total CO_2 emissions in the European Union (EU) [1]. Figure 1 shows the energy consumed by residential and commercial buildings in Europe. In Ireland, primary energy use in the building sector is associated with heating/cooling and lighting of buildings. In 2011, primary energy use in Irish buildings accounted for 41% of primary energy supply [2].

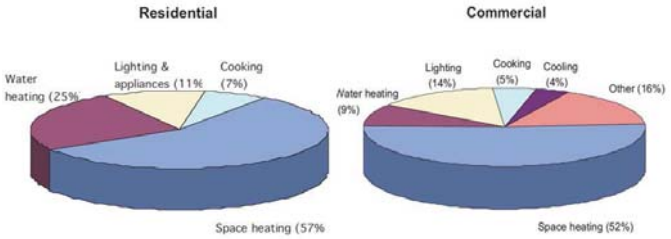


Figure 1. EU building energy consumption for residential and commercial buildings [3].

On May 19th, 2010, the EU adopted the Directive 2010/31/EU [4], which aimed to reduce energy consumed by buildings. Member States are requested to adopt a methodology for calculating the energy performance of buildings (energy performance certification). The objective of the Directive 2010/31/EU is to ensure all new buildings are almost zero-energy consumption buildings by the end of 2020.

At the same time, people spend approximately 90% of their lives indoors [5]. Thus, it is very important to have healthy and comfortable conditions in buildings, including thermal comfort, air quality, or visual and aural comfort. Knowledge about the heat transfer and storage in concrete components of the building envelope is vital in evaluating the occupants thermal comfort and energy performance of buildings. Providing sufficient thermal mass of the building envelope is crucial in delivering optimal indoor conditions while reducing the energy consumption in buildings.

Building regulations and standards incorporate rules for design, construction and operation of existing and new buildings. Those rules are specified in order to ensure safe and accessible buildings that cause limited waste and environmental damage. The compliance with those regulations and standards is crucial for all existing and new buildings. Since, the properties of the building materials are key in building performance, it is essential to accurately assess thermal properties of those materials [6].

2 AVAILABLE METHODS

There are three main evaluation methods that can be used to assess thermal performance of building materials:

- Theoretical design methods.
- Experimental methods.
- Numerical approaches (finite element, finite difference and finite volume methods).

In the theoretical design models thermal resistances of the materials are treated as electrical resistances. However, the design thermal conductivities do not always represent the in situ material properties. Moreover, the design calculations of heat transmission coefficients do not reflect multi-dimensional heat flow conditions [7]. Thus, those theoretical design methods cannot always be used.

The experimental methods such as a guarded hot box or hot plate tests are quite popular. For instance, Kim et al. [8] investigated experimentally thermal properties of lightweight aggregate concrete using a heat flow meter. It was found that the thermal conductivity linearly decreased as the concrete porosity increased, regardless of the location of pores.

Another study measured thermal conductivity of newspaper sandwiched aerated lightweight concrete panels using a guarded hot plate method [9]. It has been known that quartzite, sandstone and other quartzose rocks are the most thermally conductive aggregates. Granite, gneiss, limestone and dolomite have an intermediate thermal conductivity, while basalt and dolerite are the least thermally conductive. Thus, Khan [10] experimentally investigated thermal conductivity of mortar, concrete and its aggregates. The study found the type of aggregate, porosity and moisture content to have a strong influence on thermal conductivity of concrete. Moreover, the study showed that the aggregate type may increase the thermal conductivity of concrete almost twofold.

The numerical methods have been previously utilised in order to investigate thermal performance of building envelope materials. For instance, Lee and Pessiki [11] evaluated the thermal resistance of a three-wythe panel using the finite element method. While, Zhang and Wachenfeldt [12] also utilised this method in order to investigate the effect of air cavities on the heat transfer behaviour and diurnal heat storing capacity of the hollowcore concrete slabs. Furthermore, the study by Del Coz Diaz et al. [13]optimised the lightweight hollow block design for internal floors in respect to energy savings with the support of finite element analysis.

Often, the numerical analysis is supported by experimental data in order to validate the model predictions. Such as in a study that investigated the heat transfer through an in situ constructed, insulated and reinforced (with a truss wire) concrete sandwich wall [14]. This work developed numerical models supported by the laboratory test data (guarded hot box). The computational fluid dynamics (finite volume method), together with experimental tests (guarded hot box unit), facilitated the analysis of heat transfer through a variable aspect ratio cavity wall [15], or a hollow brick wall [16]. The finite difference method supported by experimental tests assisted in the investigation of thermal inertia [17], transient thermal behaviour and surface temperature [18] of aerated lightweight concrete wall panels.

3 PROJECT SCOPE

This paper presents a project that focuses on evaluating the thermal performance of precast concrete building structural elements (i.e. twinwall, hollowcore and lattice slab), regarding their thermal properties on indoor environments.

At the first stage of the project, the real time field measurements are being obtained from the Life Course Studies Institute (LCSI) building at the National University of Ireland Galway. The measurements include monitoring of the (i) weather data with a locally installed weather station, (ii) temperature with thermistors embedded in building's structural precast components (floor/roof slabs and walls), (iii) surface temperature with thermal camera, (iv) indoor air temperature, (v) relative humidity. Next, those measurements will be used to create calibrated CFD models of the precast components design. Those models will be utilised to investigate the heat transfer and storage in precast concrete components. The influence of those phenomena on indoor environmental conditions, including occupants comfort, will be evaluated.

This paper presents the motivation, objectives and method description of the project that investigates the influence of heat transfer and storage in precast building envelope elements on indoor environments. The proposed analysis will provide (i) better prediction of indoor environmental conditions; (ii) healthier, more comfortable and productive indoor environments; and (iii) reduced/optimised energy consumption in buildings.

4 DEMONSTRATION BUILDING

4.1 Building description

The LCSI building at NUI Galway is used in this research to analyse the performance of precast concrete building structural elements on indoor environments. The construction of the LCSI building commenced in July 2013 and is expected to be completed by May 2014. The building is partially 3 storey and partially 2 storey with a gross floor area of 3633 m^2 (Figure 2). It is predominately a precast concrete building with the precast elements designed, manufactured and installed by Oran Precast Ltd.

The building accommodates mainly office spaces, seminar rooms and lecture theatres. The building operates with mixed mode ventilation. The part of the building accommodating offices is naturally ventilated, while the seminar rooms and lecture theatres are air conditioned.



Figure 2. The Life Course Studies Institute (LCSI) building © Simon J Kelly Architects.

4.2 Precast concrete technology

The LCSI building is mainly built in precast concrete technology, including the building frame, twinwall system, lattice and hollowcore slabs. Precast concrete solutions increase the speed of building erection on site while maintaining the site safer and cleaner when compared to standard construction methods.

Concrete is a long lasting building material that does not require any maintenance, replacement or application of toxic paints or preservatives. Moreover, the thermal capacity of concrete leads to thermal stability and thus offers considerable energy savings and good quality of indoor environment. Hence, concrete is the primary construction material in most of the sustainable developments in Europe [19]. According to the Irish Concrete Society and Irish Concrete Federation '*Exposed concrete acts as a thermal moderator preventing rapid thermal swings, greatly reducing the need to cool office buildings, which is typically the biggest running cost. Only 10% is related to the construction of the building. Designing with energy in mind can reduce in-use energy costs by up to 75% and greatly reduce carbon dioxide emissions*' [20]. The benefits of concrete thermal mass in buildings include [3]:

- Reduction in heating fuel due to solar gains.
- Reduction in heating energy consumption by 2–15%.

- Reduction in the building energy cost.
- Stable indoor temperatures, without high fluctuations.
- Delay in peak indoor temperatures in commercial buildings until the occupants have left.
- Reduction in peak indoor temperatures.
- The possibility of night-time ventilation to eliminate the need for day-time cooling.
- In combination with air-conditioning, concrete thermal mass can reduce the energy used for cooling by up to 50%.

Precast reinforced and pre-stressed concrete is widely regarded as an economic, structurally-sound and architecturally versatile building medium. Controlled and cost-effective manufacturing processes guarantee high quality products at a reduced cost and a minimum design/ manufacturing/ construction time. Despite the popularity of concrete as a building material in Ireland and Europe and its well-known structural properties, there is a dearth of research available on the interaction between the building structure and indoor environments.

4.3 Building instrumentation

Precast concrete technology allows mechanical and electrical products, including sensors to be embedded in the building structure. In order to monitor the thermal performance of structural elements in the LCSI building, over 120 temperature sensors were embedded in the internal and external twinwalls; ground floor hollowcore and in situ slabs; internal and roof lattice slabs. IP68 rated (double insulated, fully encapsulated, protected against water submersion) thermistor sensors (Figure 3) were embedded in the precast and in situ part of the concrete structure. Those thermistors were capable of measuring concrete temperature in the range of between -60/+150^{o}C with a 1% tolerance [21].



Figure 3. Thermistors embedded in the (a) precast and (b) in situ concrete in the LCSI building.

This paper describes the details of installation and the initial results of the thermistors embedded in three representative building elements (X0 exposure class – concrete inside buildings with very low air humidity [22]): (i) first floor external twinwall (East facing wall in the West wing), (ii) flat lattice roof slab (East wing), and (iii) suspended ground floor hollowcore slab (0.5 m void, naturally ventilated with external air; East wing with windows facing East).

Figure 4 and Figure 5 show the locations of thermistors in the plan/elevation and across the depth of the precast slab and wall elements, respectively. Thermistors were regularly located at one or two locations and three different depths of each wall/slab in order to measure the temperature distribution profile in the wall/slab. For the external twinwall, at locations 1 and 2, there was one thermistor placed in each of the precast biscuits (T1,2b,t) and one in the middle (T1,2m) of the in situ concrete. For the lattice roof slab, at locations 3 and 4, there was one thermistor placed in the precast biscuit (T4b, *note: T3b & T4t were damaged during the precast manufacturing process*) and two thermistors in the in situ part (T3m,t, T4m). Because of the manufacturing process of the ground floor hollowcore slab, thermistors were embedded into the finished slab by drilling a hole and securing the sensors in locations 5 and 6.

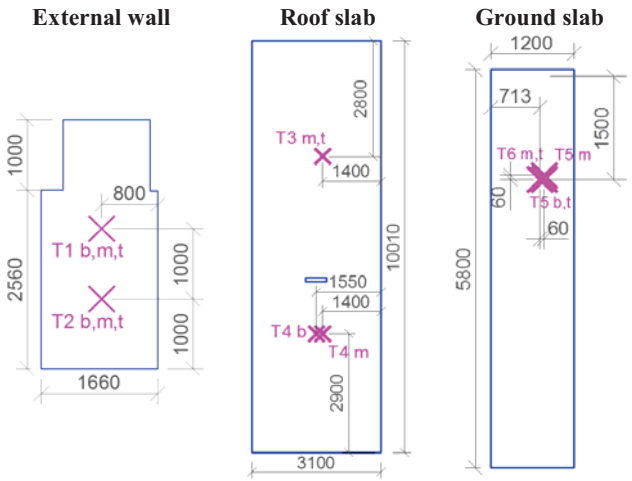


Figure 4. Location of thermistors across the plan of walls and slabs in the LCSI building (dimensions in mm).

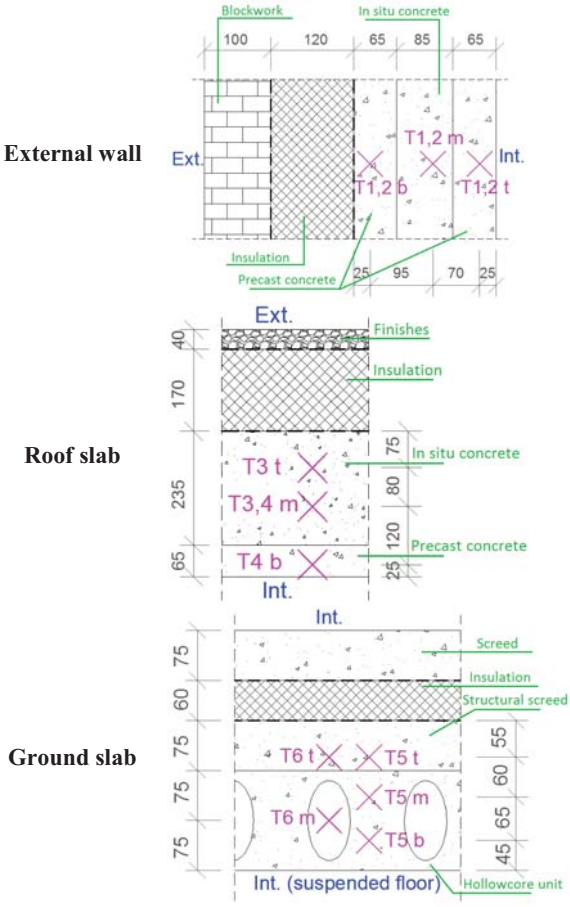


Figure 5. Location of thermistors across the depth of walls and slabs in the LCSI building (dimensions in mm).

4.4 Data acquisition system

The data acquisition system consisting of CR1000 data loggers and AM16/32B multiplexers obtained from Campbell Scientific was employed to collect and store live data measured by the temperature sensors. This system has been automatically logging data from the sensors embedded in the reinforced precast concrete slabs and wall systems since their initial installation. During the construction phase, data is being stored on a flash memory card, which is weekly manually downloaded onto a laptop and backed-up on a server. However, after the building commissioning, data communication will relay on the use of Campbell Scientific's NL115 Ethernet and Compact Flash Module and will allow for data collection over a local network.

4.5 Weather monitoring

The outdoor weather conditions are provided by an automatic weather station [23] at the NUI Galway campus [24]. The station has been continuously reporting weather conditions since July 2010, with a frequency of 1 min. It is located on the roof of one of the University buildings (in the centre of the campus), approximately 1.5 km from the LCSI building. The weather station measures dry-bulb air temperature (^{o}C) and relative humidity (%), barometric pressure (mBar), wind speed (m/s) and wind direction (^{o}), global and diffuse solar irradiance (W/m^2) and rainfall (mm).

4.6 Laboratory experiments

Complementary laboratory experiments will be carried out in order to specify thermal properties of concrete used in the LCSI building, particularly the coefficient of thermal expansion or thermal conductivity. Figure 6 presents the laboratory measurement setup with thermistors embedded in the concrete cylinder, which is placed in a controlled temperature water bath.



Figure 6. Water bath of the sample concrete cylinders.

5 PRELIMINARY RESULTS

5.1 U-values

The calculation of thermal properties of building materials according to the ISO 6946 standard [25] requires:

- Calculating the thermal resistance of each homogeneous layer of the building component;
- Combining these individual resistances in order to obtain the total thermal resistance of the building component, including the effect of surface resistances;

Calculating the thermal transmittance (U-value) of the building component.

Table 1 shows compliance of calculated *U*-values of the building envelope element in the LCSI building with the current Irish Building Regulations [26].

Table 1. *U*-values of building envelope elements in the LCSI building.

***U*-value [W/m^{2}K]**	**Building Regulations** [26]	**LCSI**
External wall	0.27	0.17 (215 mm cavity twinwall with 80 mm insulation and 100 mm blockwork)
Roof slab	0.22	0.12 (300 mm lattice slab with 170 mm insulation)
Ground slab	0.25	0.24 (150 mm suspended hollowcore slab, 75 mm screed, 60 mm insulation, 75 mm screed)

5.2 Physical measurements

This paper presents the measurements obtained from the thermistors embedded in the external twinwall, roof lattice slab and ground floor hollowcore slab between February 11th, 2014 and March 15th, 2014. The temperature was measured in the external wall every 1 min and in the ground/roof slabs every 6 mins.

During that period, the construction of each considered envelope elements was completed, accordingly to Figure 5. However, the building was not fully enclosed, with many windows and doors yet to be installed (particularly those located on the first and second floor). Thus, Figure 7 Figure 9 compare the temperature distribution in the monitored envelope elements to the outdoor air temperature [24]. It is clear that changes in the outdoor air temperature significantly influenced the temperature distribution in the external twinwall and the lattice roof slab (Figure 7 and Figure 8). There was a clear lag in the wall/slab temperature change in comparison to outdoor air temperature change, i.e. thermal lag. This lag was caused by the thermal mass of the wall/slab, which slowed the heat flow through the element. Figure 7 also shows the temperature of sample concrete cylinder located inside the building. The cylinder temperature profile matched the wall temperature distribution. However, the cylinder temperature was more influenced by outdoor air temperature than wall temperatures. This was due to lack of any insulation on the cylinder.

Temperatures recorded by the thermistors embedded in the suspended ground floor hollowcore slab did not change significantly over the period monitored and were not influenced by the outdoor air temperature (Figure 9). This might have been due to the fact that the hollowcore slab was well insulated from the outdoor temperatures by the underfloor void (with low air exchange) on one side, and 60 mm insulation and enclosed ground floor on the other side.

This suggests that it is not possible to directly utilise the thermal mass of this type of system to regulate the temperature of the space above the floor. However, if designed correctly, it may be possible to take advantage of the relatively constant temperature of underfloor void as part of a heating and/or cooling system for the indoor environment within the building.

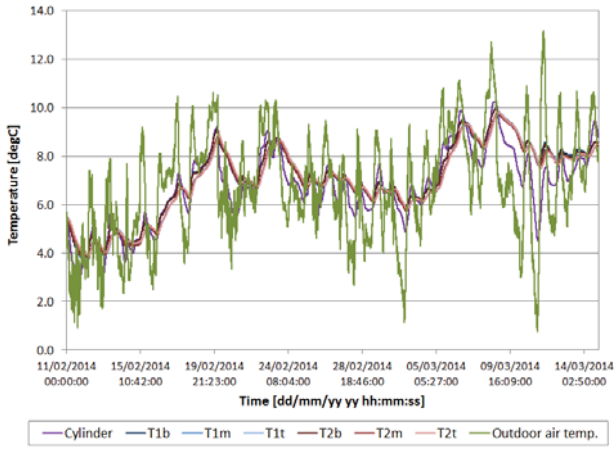


Figure 7. Temperature distribution in the external twinwall.

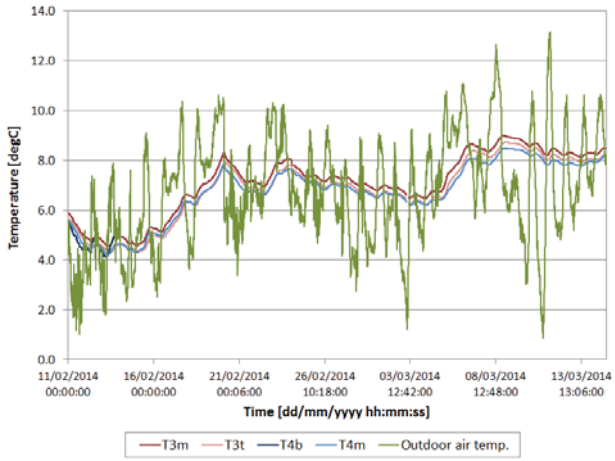


Figure 8. Temperature distribution in the lattice roof slab.

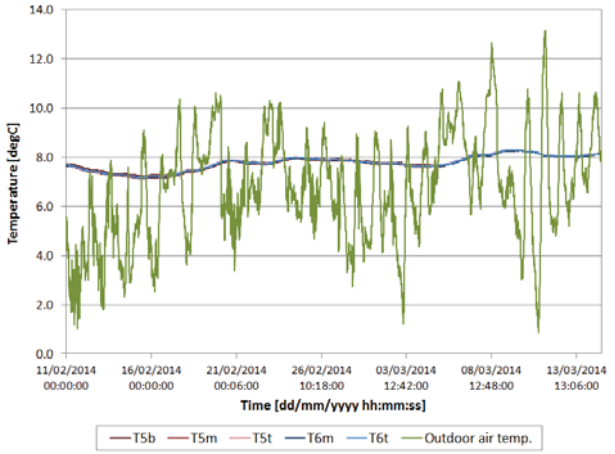


Figure 9. Temperature distribution in the ground floor hollowcore slab.

The correlation coefficients between the outdoor air temperature and the temperatures of the (i) external twinwall, (ii) lattice roof slab, and (iii) ground floor hollowcore slab varied between (i) 0.48 – 0.59, (ii) 0.43 – 0.47, and (iii) 0.20 - 0.28, respectively. Those results reassured previous statements that there was a clear thermal lag in the wall/roof slab temperature change in comparison to outdoor air temperature change and, thus, the correlation coefficient was only ~0.5. Moreover, a good insulation protected the hollowcore ground slab from the influence of outdoor air temperature, resulting in a low correlation coefficient between those two sets of measurements. The correlation coefficient between the outdoor and concrete elements temperature datasets was calculated based on the equation:

$$correl(X,Y) = \frac{\sum(x - x_{ave})(y - y_{ave})}{\sqrt{\sum(x - x_{ave})^2 \sum(y - y_{ave})^2}} \quad (1)$$

where x_{ave}, y_{ave} are the average values of each data set.

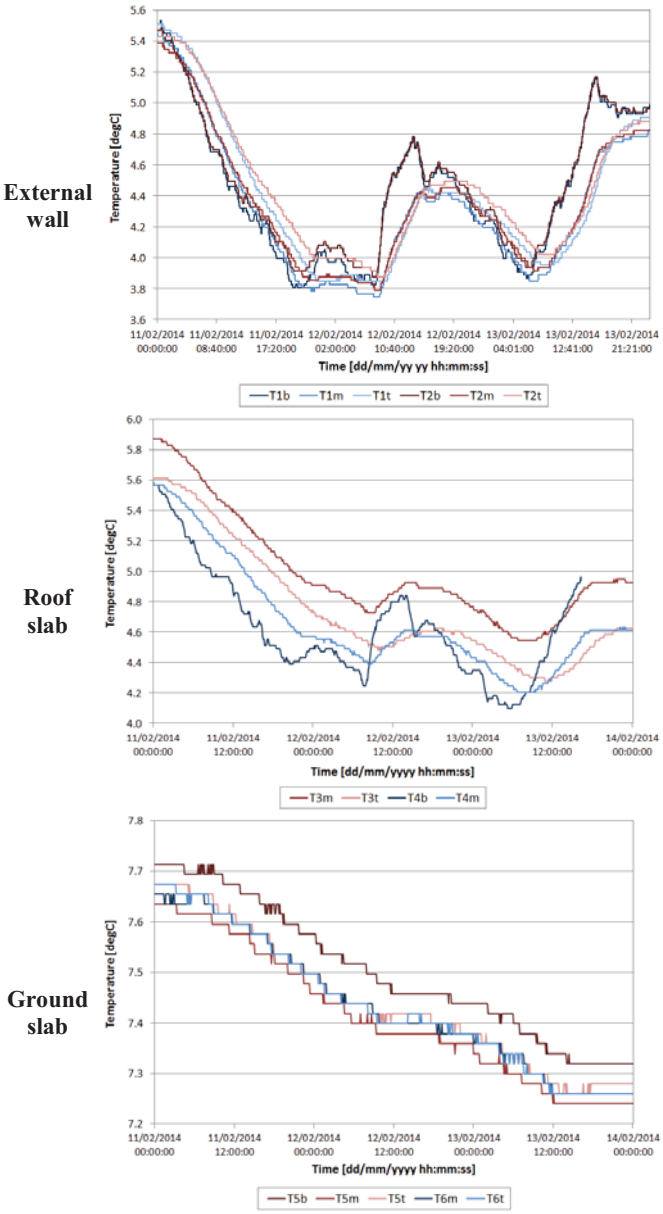


Figure 10. Detailed temperature distribution within the envelope elements (11-14 February 2014).

Figure 10 shows a detailed comparison of temperatures recorded by thermistors embedded at different locations/depths in the envelope elements over a 3 days period. Measured temperatures within the particular envelope element (regardless of location or depth) followed similar profile in time. Generally, there were no significant differences in temperatures at different locations/depths in considered wall and slabs. The reason for that was the fact that the building was not completed at the time of the measurements and there were no significant differences between the indoor/outdoor air temperatures. There were some irregular differences that occurred between different element depths/locations. Those differences might have been caused by localised thermal effects. The sources of those effects were difficult to establish due to ongoing site works. However, the initial results presented here showed a satisfactory performance of installed thermistors and provided an important basis for future thermal performance measurements in the operating building.

6 CONCLUSIONS AND FUTURE WORK

This paper presents the motivation, objectives and method description of the project that investigates the influence of heat transfer and storage in precast building envelope elements on indoor environments. The preliminary results include (i) the measurement setup, both in the operating building as well as the laboratory experiments; (ii) the theoretical analysis of the thermal properties of proposed precast components; and (iii) the early stage measurements from the sensors installed in the LCSI building.

Those results provide the first assessment of the performance of the measurement platform installed in the LCSI building. Moreover, those results together with the measurements taken during the operation phase of the building will support the future generation of CFD models to investigate the heat transfer and storage in precast concrete components and their influence on indoor environmental conditions, including occupants comfort, will be evaluated.

The proposed analysis will provide (i) better prediction of indoor environmental conditions; (ii) healthier, more comfortable and productive indoor environments; and (iii) reduced/optimised energy consumption in buildings.

ACKNOWLEDGMENTS

The authors would like to thank the Irish Research Council and Oran Pre-Cast Ltd. for funding this research. The authors would also like to thank the National University of Ireland Galway and particularly the Department of Civil Engineering for the help with the instrumentation in the demonstration building.

REFERENCES

[1] European Union, “Official website of the European Union” 2014. Available: http://www.europa.eu.

[2] SEAI, *Energy in Ireland 1990-2011*. Dublin, Ireland: Sustainable Energy Authority of Ireland, 2012.

[3] ICF, “Concrete for energy efficient buildings: The benefits of thermal mass” Dublin, Ireland: Irish Concrete Federation, 2008.

[4] European Commission, “Directive 2010/31/EU on the energy performance of buildings” *Off. J. Eur. Union*, 2010.

[5] US EPA, “United States Environmental Protection Agency” 2012. Available: http://www.epa.gov/.

[6] CIBSE, *Guide A: Environmental design*, 7th Ed. London, UK: Chartered Institution of Building Service Engineers, 2006.

[7] L. S. Shu, A. E. Fiorato, J. W. Howanski, “Heat transmission coefficients of concrete block walls with core insulation” in *ASHRAE/DOE-ORNL Conference, Thermal Performance of the Exterior Envelopes of Buildings*, 1979, pp. 421–435.

[8] H. K. Kim, J. H. Jeon, H. K. Lee, “Workability, and mechanical, acoustic and thermal properties of lightweight aggregate concrete with a high volume of entrained air” *Constr. Build. Mater.*, vol. 29, pp. 193–200, 2012.

[9] S.-C. Ng, K.-S. Low, “Thermal conductivity of newspaper sandwiched aerated lightweight concrete panel” *Energy Build.*, vol. 42(12), pp. 2452–2456, 2010.

[10] M. . Khan, “Factors affecting the thermal properties of concrete and applicability of its prediction models” *Build. Environ.*, vol. 37(6), pp. 607–614, 2002.

[11] B.-J. Lee, S. Pessiki, “Thermal performance evaluation of precast concrete three-wythe sandwich wall panels” *Energy Build.*, vol. 38(8), pp. 1006–1014, 2006.

[12] Z. L. Zhang, B. J. Wachenfeldt, “Numerical study on the heat storing capacity of concrete walls with air cavities” *Energy Build.*, vol. 41(7), pp. 769–773, 2009.

[13] J. J. del Coz Díaz, P. J. García Nieto, J. Domínguez Hernández, A. Suárez Sánchez, “Thermal design optimization of lightweight concrete blocks for internal one-way spanning slabs floors by FEM” *Energy Build.*, vol. 41(12), pp. 1276–1287, 2009.

[14] G. . Jones, R. . Jones, “Steady-state heat transfer in an insulated, reinforced concrete wall: theory, numerical simulations, and experiments” *Energy Build.*, vol. 29(3), pp. 293–305, 1999.

[15] D. P. Aviram, A. N. Fried, J. J. Roberts, “Thermal properties of a variable cavity wall” *Build. Environ.*, vol. 36(9), pp. 1057–1072, 2001.

[16] J. M. Sala, A. Urresti, K. Martín, I. Flores, A. Apaolaza, “Static and dynamic thermal characterisation of a hollow brick wall: Tests and numerical analysis” *Energy Build.*, vol. 40(8), pp. 1513–1520, 2008.

[17] S.-C. Ng, K.-S. Low, N.-H. Tioh, “Thermal inertia of newspaper sandwiched aerated lightweight concrete wall panels: Experimental study” *Energy Build.*, vol. 43, no. 10, pp. 2956–2960, Oct. 2011.

[18] S.-C. Ng, K.-S. Low, and N.-H. Tioh, “Newspaper sandwiched aerated lightweight concrete wall panels—Thermal inertia, transient thermal behavior and surface temperature prediction” *Energy Build.*, vol. 43(7), pp. 1636–1645, 2011.

[19] IPCA, “Precast concrete: Frames guide” Dublin, Ireland: Irish Precast Concrete Association, 2005.

[20] ICS and ICF, “The new concrete standards: An introduction to EN 206-1” Drogheda, Ireland: Irish Concrete Society and Dublin, Ireland: Irish Concrete Federation, 2004.

[21] ATC Semitec, “Thermal components” 2014. Available: www.atcsemitec.co.uk.

[22] CEN, “EN 206: Concrete - Part 1 : Specification, performance, production and conformity” Brussels, Belgium: European Committee for Standardization, 2002.

[23] Campbell Scientific, “Campbell Scientific, Inc.” 2014. Available: http://www.campbellsci.co.uk/.

[24] IRUSE, “IRUSE weather website” 2014. Available: http://weather.nuigalway.ie/.

[25] ISO, “6946: 2007. Building components and building elements - Thermal resistance and thermal transmittance - Calculation method” Geneva, Switzerland: International Organization for Standardization, 2007.

[26] Irish Government, “Building Regulations. Part L: Conservation of fuel and energy - Buildings other than dwellings” Environment, Heritage and Local Government, Ireland, Dublin, Ireland: Environment, Heritage and Local Government, 2008.

Thermo-mechanical fatigue in power plant steels: Enhanced numerical modelling with experimental validation

P.E. O'Donoghue[1,2], R.A. Barrett[2,3], S. Reape[3], S. Scully[4], C.J. Hyde[5], S.B. Leen[2,3]
[1] Civil Engineering, College of Engineering and Informatics, NUI Galway, Galway, Ireland
[2] Ryan Institute for Environmental, Marine and Energy Research, NUI Galway, Galway, Ireland
[3] Mechanical Engineering, College of Engineering and Informatics, NUI Galway, Galway, Ireland
[4] ESB Energy International, ESB Head Office, 27 Fitzwilliam Street, Dublin 2, Dublin, Ireland
[5] Dept. of Mechanical, Materials and Manufacturing Engineering University of Nottingham, Nottingham NG7 2RD, UK
e-mail: padraic.odonoghue@nuigalway.ie, r.barrett2@nuigalway.ie, sean.leen@nuigalway.ie

ABSTRACT: This research is motivated by the requirement for next generation power plants to operate with greater flexibility due to the need to accommodate renewables and to operate under more extreme loading to improve efficiency. Under these conditions, thermo-mechanical fatigue will be particularly important for power plant steels where a significant stress range is experienced, with the increased possibility of failure occurring in critical regions such as the weld zone. A hyperbolic sine unified cyclic viscoplasticity model was recently developed and has been implemented in a finite element package. The model incorporates the key high temperature cyclic deformation phenomena of cyclic softening and non-linear kinematic hardening and has been calibrated to accurately represent the cyclic high temperature constitutive behaviour. The applicability of the model is extended here to additional temperatures and loading configurations through an integrated programme of testing and computational analysis. The testing programme involves the use of ex-service material. Good validation of results is obtained with life predictions for these materials, being within 13% of experimental values. The work is augmented by a case study that looks at the failure in a welded T-piece header connection. The computed results, using a multi-material model, indicate that the failure location is consistent with the observations in the field and the failure times also show reasonable consistency.

KEY WORDS: Power plant steel, Cyclic viscoplasticity, Thermo-mechanical fatigue, High temperature creep, Life prediction.

1 INTRODUCTION

Modern power generation plants are in transition from base-load (constant load) to load-following operation (intermittent mode) due to (i) the need for flexible use resulting from renewable sources of energy and mixing of energy sources and (ii) the demand for more efficient plants with associated higher operating temperatures and pressures. Typically, the steels used in these components are 9-12Cr steels. These steels have been developed for power plant units as they have (i) a high creep strength at high temperatures [1], (ii) increased resistance to thermal fatigue compared to other materials [2] and (iii) a lower value of thermal expansion when contrasted with stainless steels [3], enabling smaller wall thickness and hence lower commercial cost.

The key strategic goal of next generation, ultra-supercritical (USC) plant operation (e.g. steam pressure increased from 16 MPa to 27 MPa [4] and steam temperature to increase beyond 600 °C) is to significantly increase overall plant efficiency and reduce emissions. This will require an improved family of materials with the capability to withstand high temperature fatigue, creep loading conditions and increased steam corrosion. As a result, plant components, such as header units, are subjected to thermo-mechanical fatigue (TMF) due to the thermal gradients observed during start-up attemperation cycles (e.g. see [5]) and more severe creep-fatigue (CF) loading due to increased temperatures and pressures.

As a result, the complex operational cycles [5, 6], which current and future plant must endure, leads to TMF and CF failures. These failures commonly occur within the heat affected zone (HAZ) of welded connections (Type IV cracking), sometimes as early as 5-10% of the plant design life. The operational capability of these steels under cyclic (flexible) loading conditions however has not received much consideration. During flexible high temperature loading, phenomena such as strain-rate sensitivity and cyclic softening, which result in a reduction of the materials creep strength, have been observed in isothermal fatigue (IF) and TMF tests [7-10]. However, these factors have not been fully accounted for in current materials design processes.

Thus, there is a particular need to develop and apply constitutive models to characterise and to simulate these materials under realistic loading conditions. This was the basis of earlier work by Barrett et al [11, 12] wherein an improved unified viscoplastic constitutive model for strain-rate sensitivity in high temperature fatigue was developed. The work was conducted as part of a broader initiative to establish a multi-scale Materials Design Tool (MDT), as illustrated in Figure 1. The multi-scale modelling was dictated by the complex nature of power plant steel microstructures, although the focus of the work reported herein is confined to the macro-scale aspects [11-13]. The MDT approach includes an integrated programme of model development and experimental validation. Firstly, this provides an accurate method of characterising the current generation of materials under intermittent mode loading conditions and secondly, provides the optimum key material parameters for next generation loading conditions.

Section 2 briefly reviews the development of the recently developed constitutive. Section 3 describes some additional tests that were recently conducted on ex-service power plant header material. This allows an extension of the validation range for the model and this is described in Section 4. This section also includes an industrial application of the analysis approach to a welded T-piece header connection.

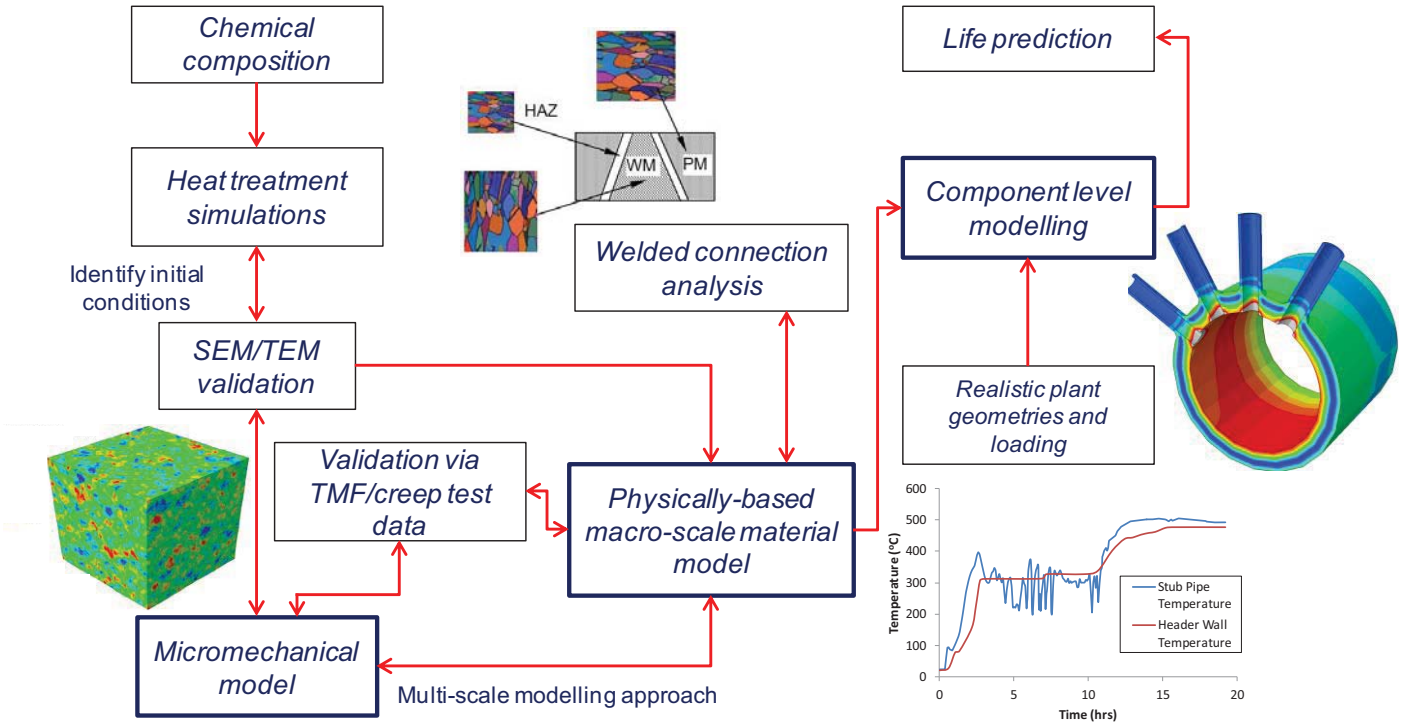


Figure 1: Proposed framework for a Materials Design Tool (MDT) for development of advanced materials for flexible operation of next generation power plant.

2 MODELLING FRAMEWORK

The material model is a recently developed multi-axial unified viscoplastic material model [11, 12] for TMF loading. The increment in stress, $\Delta\boldsymbol{\sigma}$, is obtained from Hooke's law:

$$\Delta\boldsymbol{\sigma} = 2\mu\left(\Delta\boldsymbol{\varepsilon} - \Delta\boldsymbol{\varepsilon}^{\text{th}}\right) + \lambda \text{Tr}\left(\Delta\boldsymbol{\varepsilon} - \Delta\boldsymbol{\varepsilon}^{\text{th}}\right)\mathbf{I} - 2\mu\Delta\boldsymbol{\varepsilon}^{\text{pl}} \qquad (1)$$

where μ and λ are Lamé's constants and $\Delta\boldsymbol{\varepsilon}$, $\Delta\boldsymbol{\varepsilon}^{\text{pl}}$ and $\Delta\boldsymbol{\varepsilon}^{\text{th}}$ are the increments in strain, viscoplastic strain and thermal strain respectively. The constitutive equation defining the accumulative effective plastic strain-rate, $\dot{p}$, is a variation of the Chaboche power law model [14, 15], which uses a hyperbolic sine function to enable variable strain-rate sensitivity. Thus, the flow rule that describes the viscoplastic strain-rate is [12]:

$$\dot{\boldsymbol{\varepsilon}}^{\text{pl}} = \dot{p}\mathbf{n} = \alpha \sinh\left\langle \beta\left(\text{J}_2\left(\boldsymbol{\sigma} - \boldsymbol{\chi}\right) - R - k\right)\right\rangle \mathbf{n} \qquad (2)$$

where α and β are the cyclic viscoplastic material parameters, $\boldsymbol{\sigma}$ is the stress tensor, $\boldsymbol{\chi}$ is the backstress tensor, R is isotropic hardening, k is cyclic yield stress and $\mathbf{n}$ is the normal tensor.

The backstress is composed of two parts; the first term corresponds to the initial region of strain hardening and the second term represents the later stages of strain hardening. The two backtstresses are superimposed such that the overall backstress is $\boldsymbol{\chi} = \boldsymbol{\chi}_1 + \boldsymbol{\chi}_2$. The Armstrong-Frederick non-linear kinematic hardening (NLKH) model [16] is used to obtain the evolution of the kinematic hardening backstress, with a temperature-rate term included [17] to account for the influence of the temperature variations on the resulting backstress:

$$\dot{\boldsymbol{\chi}}_{\text{i}} = \frac{2}{3} C_{\text{i}} \dot{\boldsymbol{\varepsilon}}^{\text{pl}} - \gamma_{\text{i}} \boldsymbol{\chi}_{\text{i}} \dot{p} + \frac{1}{C_{\text{i}}} \frac{\partial C_{\text{i}}}{\partial T} \boldsymbol{\chi}_{\text{i}} \dot{T} \qquad (3)$$

where C_{i} is temperature-dependent hardening modulus and γ_{i} is a temperature-dependent NLKH material parameter.

As 9-12Cr steels cyclically soften, the isotropic hardening term of equation (2), R, is replaced with a softening term, similar to that of the Chaboche equation. As outlined in [18], cyclic softening may also be divided into primary, secondary and failure cyclic softening regions. Thus, by neglecting the failure region, the cyclic softening term is $R = R_1 + R_2$, where the evolution of the cyclic softening terms is defined using the temperature-dependent model of [20]:

$$\dot{R}_{\text{i}} = b_{\text{i}}\left(Q_{\text{i}} - R_{\text{i}}\right)\dot{p} + \left(\frac{1}{b_{\text{i}}}\frac{\partial b_{\text{i}}}{\partial T} + \frac{1}{Q_{\text{i}}}\frac{\partial Q_{\text{i}}}{\partial T}\right) R_{\text{i}} \dot{T} \qquad (4)$$

where Q_{i} is a temperature-dependent saturation value and b_{i} is an exponent related to the rate of decay of the softening stress. From the work of Saad and co-workers [9], a negative value of the saturation stress, Q, enables the capturing of cyclic softening.

The above model is implemented in a UMAT user material subroutine using an implicit integration scheme for use in the commercial finite element (FE) code Abaqus. The identification procedure for the relevant material parameters is presented in [18].

3 EXPERIMENTAL TESTING

In the present study, an ex-service header unit of P91 steel is used to manufacture parent material (PM), weld material (WM) and cross weld (CW) specimens. These specimens

were tested at temperatures of 20 °C, 400 °C, 500 °C and 600 °C using the high temperature low-cycle fatigue (HTLCF) test rig at NUI Galway and the TMF test machine at the University of Nottingham. The broad range of experiments conducted in this program includes (i) dwell tests (stress relaxation), (ii) HTLCF tests and (iii) TMF tests at various strain-rates and strain-ranges.

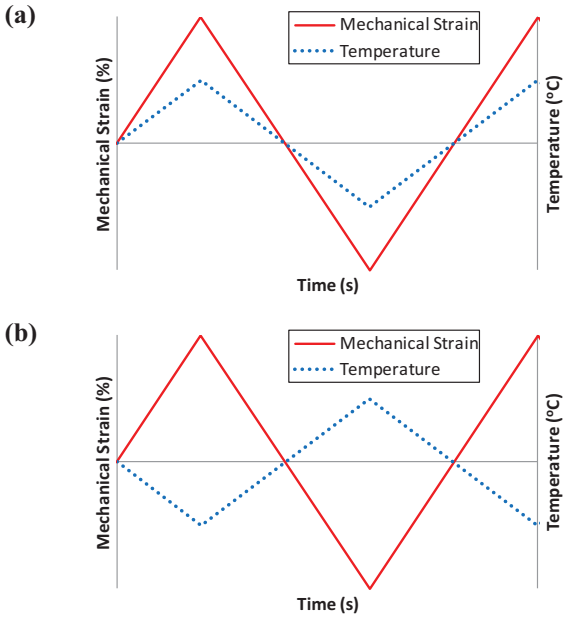


Figure 2: Schematic representation of (a) TMF-IP and (b) TMF-OP loading conditions.

HTLCF and dwell tests were carried out on the PM, WM and CW specimens [5, 8] at strain-rates of 0.1 %/s, 0.033 %/s and 0.025 %/s and strain-ranges of ±0.5 %, ±0.4 % and ±0.3 %. All tests exhibited considerable cyclic softening behaviour and a significant strain-rate effect is also observed during tests at 600 °C. The strain-rate effect diminishes with decreasing temperature. From earlier optical microscopy work [20], fatigue-dominated failure has been identified as the main failure mechanism in all specimens and failure of the CW specimens was observed in the intercritical (IC)-HAZ (Type IV) region, which is the material of lowest hardness.

TMF tests are conducted under in-phase (TMF-IP) and out-of-phase (TMF-OP) loading conditions, as illustrated by the schematics in Fig. 2. The TMF-OP case is important as it is more representative of field observations for power plant operation. Fig. 3 illustrates the typical 1st cycle stress-mechanical strain observed during a TMF test and Fig. 4 highlights the effect of thermo-mechanical loading when compared to the isothermal fatigue (IF) data for the parent material. The significantly lower life observed during TMF-OP loading is expected as the material is subjected to higher strains (alternating between a maximum mechanical and thermal strain contribution) for a much longer period of time. It can also be seen in Fig. 4 that the isothermal fatigue tests give the longest lives. The results of component level modelling of a superheater header unit illustrate that loading is typically asymmetric during plant operation [6]. Hence, a series of asymmetric TMF tests have also been conducted to produce more representative loading conditions.

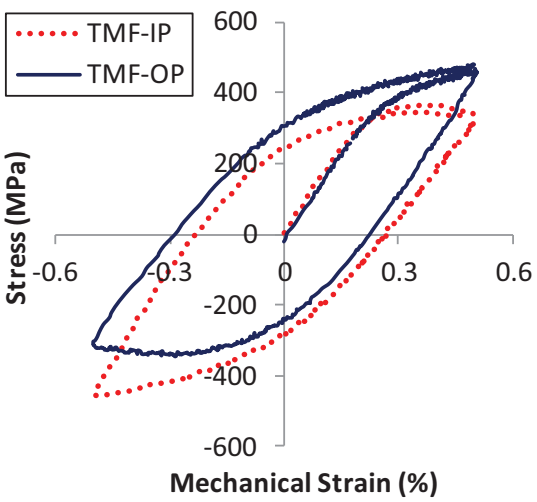


Figure 3: Comparison of TMF-IP and TMF-OP experimental results at a strain-rate of 0.025 %/s and a temperature range of 400 to 600 °C.

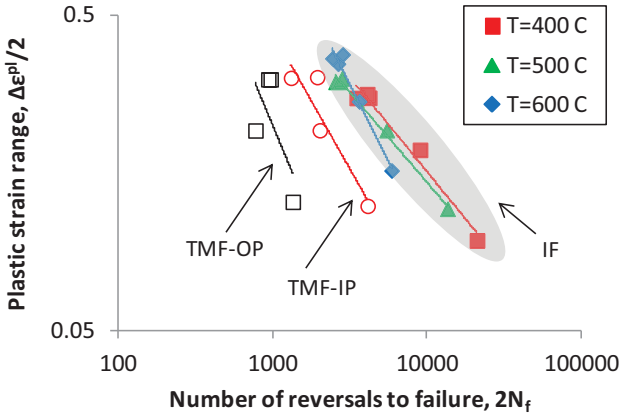


Figure 4: Experimentally observed cycles to failure and plastic strain-range in the 400 °C to 600 °C temperature range for IF and TMF tests.

4 ANALYSIS RESULTS

4.1 Material model calibration and validation

Calibration of the material model was conducted earlier [18], under the calibration conditions consisting of a strain-rate of 0.1 %/s and a strain-range of ±0.5 %. Fig. 5 provides a comparison of the model with experimental data for two different strain-rates illustrating (i) the strain-rate effect observed at a temperature of 600 °C and (ii) the ability of the model to capture this strain-rate effect. Isothermal validation of the material model at 600 °C is presented in Fig. 6, where good agreement with the experimental data is obtained for a different strain-rate of 0.033 %/s and strain-range of ±0.4 %. For HTLCF loading, the number of cycles to failure, N_f, can be estimated using the Coffin-Manson equation (C-M):

$$\frac{\Delta\varepsilon^{pl}}{2} = \varepsilon_f'\left(2N_f\right)^c \qquad (5)$$

where ε_f' and c are the fatigue ductility coefficient and exponent respectively (as identified in [18]) and $\Delta\varepsilon^{pl}$, here, is

the FE predicted plastic strain range at the half life. In Fig. 7, the model is shown to predict failure to within 13 % of the experimentally observed values.

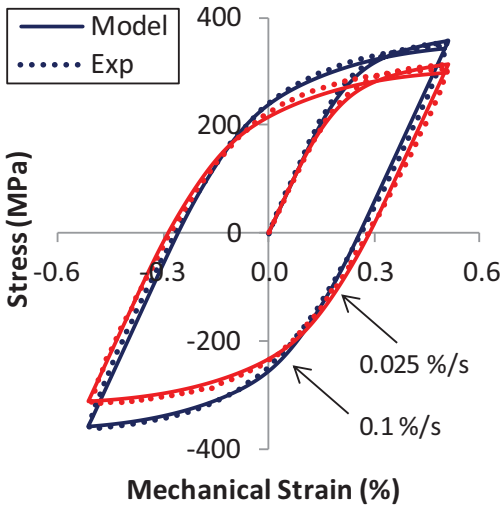


Figure 5: Comparison of the experimentally measured and FE predicted stress-strain response illustrating the strain-rate effect at 600 °C for the initial cycle.

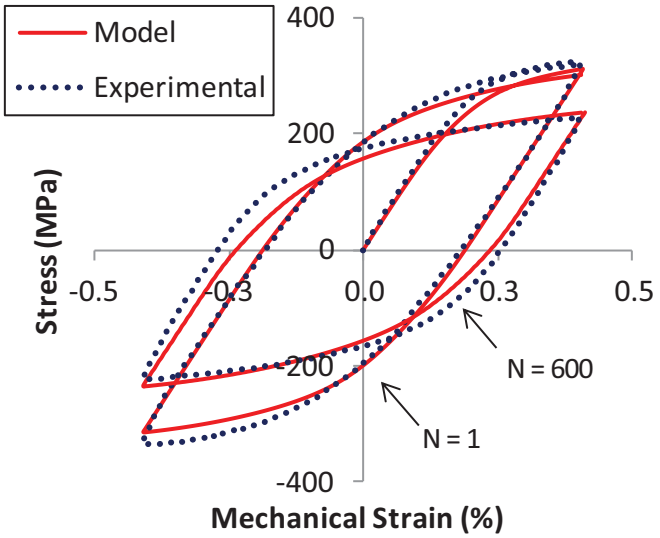


Figure 6: Comparison of the predicted stress-strain response with experimental data for the initial and 600th cycles for a strain-rate of 0.033 %/s and strain-range of ±0.4 % at 600 °C.

4.2 TMF modelling

Further validation of the material model is achieved via comparison with TMF data for both TMF-IP and TMF-OP loading conditions. Figs. 8 and 9 illustrate the typical correlation with experimental data for TMF-IP and TMF-OP loading respectively. Fig. 10 illustrates the evolution of the stress-strain response for TMF-IP loading and highlights the cyclic softening observed in P91 steel experimentally and the ability of the model to capture this behaviour.

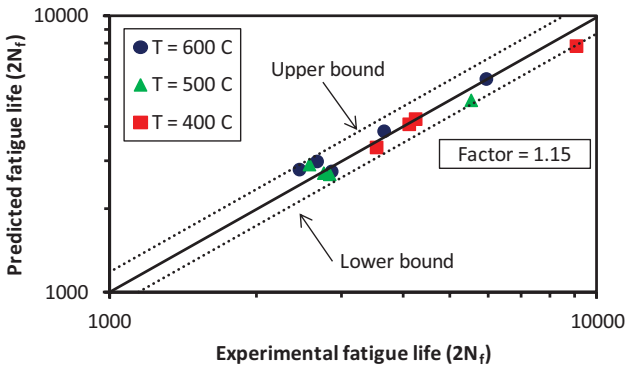


Figure 7: Comparison of the C-M predicted cycles to failure with the experimentally observed HTLCF cycles to failure.

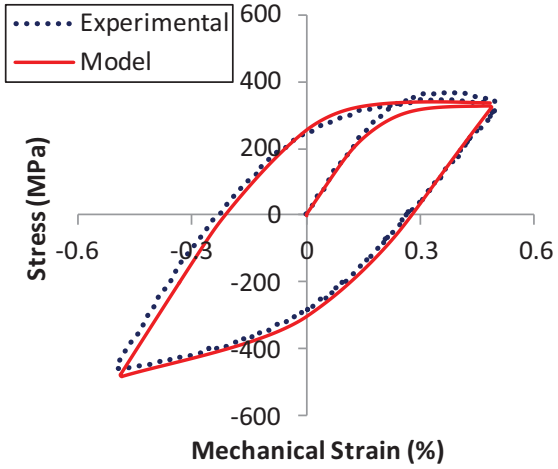


Figure 8: Comparison of the FE predicted stress-strain response with experimental data for TMF-IP loading at a strain-rate of 0.025 %/s and strain-range of ±0.5 %, for the 400 to 600 °C temperature range.

4.3 Industrial application

Of particular concern to power plant operators is the performance of welded connections. An example industrial case study of a welded T-piece header connection with significant geometric mismatch is analysed here. In this component, cracking was observed at the saddle position within the welded region after about 10,000 hours of operation, apparently due to excursion to a temperature of 621 °C. The objective of this study is to assess the performance of an FE-based model, using available P91 creep data, vis-à-vis the observed location and time to cracking. In this preliminary analysis, a simple Norton steady-state creep model, $\dot{\varepsilon}^{cr} = A\sigma^{n}$, is employed. A feature of this model is the use of multi-material (steady-state) properties with different properties used for the weld (WM), parent (PM) and heat-affected zones (HAZ) [21]. The secondary creep behaviour of all three zones is modelled here. A multiaxial steady-state rupture stress approach [22] is adopted for failure prediction, using the following equation to define rupture stress, σ_r:

$$\sigma_r = \alpha\sigma_1 + (1-\alpha)\sigma_e \qquad (6)$$

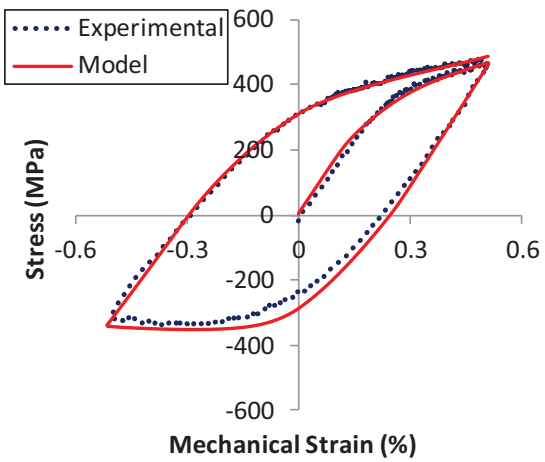


Figure 9: Comparison of the FE predicted stress-strain response with experimental data for TMF-OP loading at a strain-rate of 0.025 %/s and strain-range of ±0.5 %, for the 400 to 600 °C temperature range.

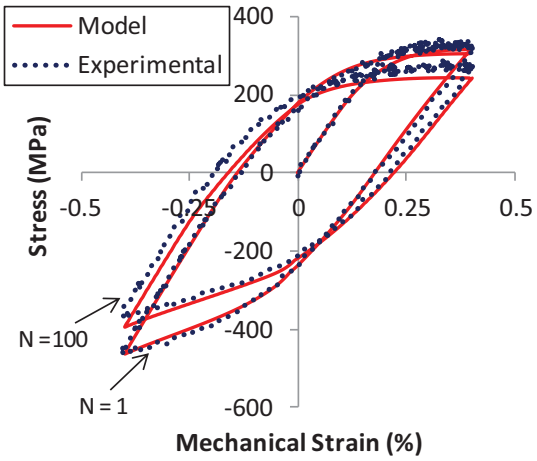


Figure 10: Comparison of the FE predicted initial and 100th cycle stress-strain response with experimental data for TMF-OP loading at a strain-rate of 0.033 %/s and strain-range of ±0.4 %, for the 400 to 600 °C temperature range.

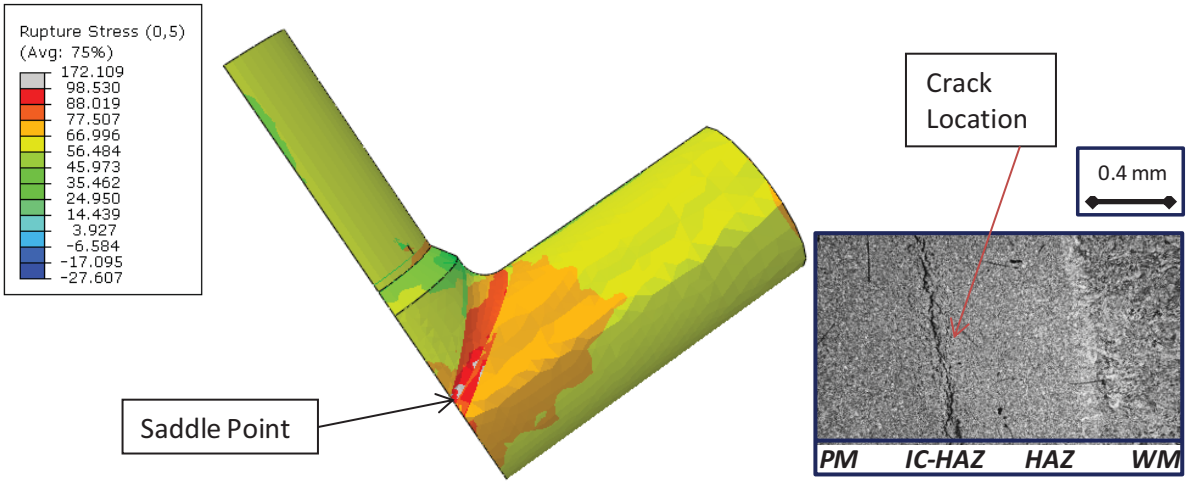


Figure 11: T-piece geometry (a) FE-predicted contour plot of multi-material, steady-state rupture stress in the T-piece geometry and (b) optical micrograph illustrating component failure in the IC-HAZ region.

where σ_1 and σ_e are maximum principal and von Mises equivalent stress, respectively, and α is a multi-axial rupture constant. The FE-predicted contour plot of the rupture stress is shown in Fig. 11a. The predicted location of maximum rupture stress and minimum life is the saddle position (shown). This is in agreement with the observed crack location in the plant component. Steady-state creep rupture life predictions are presented in Table 1, for different material zones of the T-piece geometry, using the following equation:

$$t_f = \sigma_r^{-X} / B(1-\varphi) \quad (7)$$

where X, B and φ are material parameters, dependant on the material zone. Clearly the results are in agreement with the observed time to failure, in predicting less than 10,000 hours to cracking.

5 DISCUSSION

To characterise the performance of P91 steel under flexible loading conditions, a comprehensive test program was conducted on PM, WM and CW specimens under HTLCF,

Table 1: FE predicted time to failure of the PM, WM and HAZ regions in the T-piece geometry using the rupture stress method for a temperature of 625 °C.

Temperature	PM	WM	HAZ
625 °C	33194 hrs	8064 hrs	3587 hrs

TMF and stress relaxation loading conditions. The P91 steel used in these experiments is an ex-service material which was subjected to temperatures below 500 °C during 36,000 hrs service. Fig. 4 compares HTLCF and TMF behaviour for experiments conducted in the 400 to 600 °C temperature range, highlighting the potentially detrimental effect thermal gradients (in particular TMF-OP) may have on the performance of P91 and hence, modern plant components.

As cyclic softening and strain-rate effects are also observed as life limiting factors in the experiments, any constitutive model applied to such materials must be able to account for both effects. Figs. 5 and 6 illustrate the capability of the hyperbolic sine material model presented here to capture the strain-rate effect observed at a temperature of 600 °C and Fig.

7 illustrates the ability of the model to predict the correct plastic strain range and hence fatigue life across a wide range of loading conditions. In Figs. 8 to 10 the FE predicted TMF-IP and TMF-OP comparisons with experimental data highlight the potential of the model to capture (i) varying temperature effects and (ii) cyclic softening, which are of vital importance to plant operating under flexible loading.

The initial multi-material steady-state creep analysis conducted on the T-piece component (see Fig. 11) and subsequent multi-material stress rupture life prediction are shown to predict a component life and location of failure consistent with that observed under service conditions. This result concludes that P91 steels should not be operated in plant at temperatures greater than 600 °C as the component life is significantly less than an estimated design life of up to 200,000 hrs. However, further experiments and analysis with more detailed creep damage models (e.g. [23]) are required to analyse (i) a wider temperature range and (ii) the role geometry has on component life.

Furthermore, as illustrated in Fig. 1, the complex loading which modern plant components are subjected to results in thermal gradients and ultimately TMF at the component level, which has not been included in the present study. From Fig. 4, it is evident that TMF has a significant effect on the life of P91 steel. Hence, there is a need to account for TMF when modelling realistic plant components (i.e. via the cyclic viscoplasticity model presented in Section 2) and this is the subject of ongoing analysis by the present group. In particular, failures in the IC-HAZ (Type IV) region (i.e. see Fig. 11) are being investigated via the MDT approach of Fig. 1 and inclusion of microstructure sensitive parameters within the modelling framework presented here [24].

6 CONCLUSIONS

The key achievements of this paper include:

- A TMF test program has been conducted on an ex-service P91 steel with a significant reduction in life compared to isothermal fatigue loading conditions.
- Determination of HTLCF parameters at 600 °C and subsequent life prediction using Coffin-Manson illustrates an accuracy of agreement with experiments within 13 %.
- Validation of material model for TMF-IP and TMF-OP loading conditions across a range of strain-rates and strain-ranges.
- Initial analysis of a T-piece welded connection predicted failure at the saddle location as illustrated in service with a predicted life of 3587 hours, similar to what has been observed in service.

ACKNOWLEDGMENTS

This publication has emanated from research conducted with the financial support of Science Foundation Ireland under Grant SFI/2010/IN.1/I3015. The Authors also acknowledge the contributions made by the collaborators in this project, including Dr. T.P. Farragher of NUI Galway, Prof. N.P. O'Dowd, Dr. P. Tiernan, Dr. D. Li and Mr. B.J. Golden of the University of Limerick and Professor T.H. Hyde and Dr. W. Sun of the University of Nottingham.

REFERENCES

[1] F. Abe, Precipitate design for creep strengthening of 9% Cr tempered martensitic steel for ultra-supercritical power plants, *Science and Technology of Advanced Materials*, 9 (2008) 013002.

[2] R.W. Swindeman, M.L. Santella, P.J. Maziasz, B.W. Roberts, K. Coleman, Issues in replacing Cr–Mo steels and stainless steels with 9Cr–1Mo–V steel, *International Journal of Pressure Vessels and Piping*, 81 (2004) 507-512.

[3] M. Kimura, K. Yamaguchi, M. Hayakawa, K. Kobayashi, K. Kanazawa, Microstructures of creep-fatigued 9–12% Cr ferritic heat-resisting steels, *International Journal of Fatigue*, 28 (2006) 300-308.

[4] J. Zachary, P. Kochis, R. Narula, Steam turbine design considerations for supercritical cycles, Milwaukee, WI: *Coal Gen*, 2007.

[5] T.P. Farragher, S. Scully, N.P. O'Dowd, S.B. Leen, Thermomechanical Analysis of a Pressurized Pipe Under Plant Conditions, *Journal of Pressure Vessel Technology*, 135 (2013) 011204-011209.

[6] T.P. Farragher, S. Scully, N.P. O'Dowd, S.B. Leen, Development of life assessment procedures for power plant headers operated under flexible loading scenarios, *International Journal of Fatigue*, 49 (2013) 50-61.

[7] T.P. Farragher, C.J. Hyde, W. Sun, T.H. Hyde, N.P. O'Dowd, S. Scully, S.B. Leen, High temperature low cycle fatigue behaviour of service-aged P91 material, in: *9th International Conference on Creep and Fatigue at Elevated Temperatures*, IOM3, London, UK, 2012.

[8] C.J. Hyde, W. Sun, T.H. Hyde, J.P. Rouse, T.P. Farragher, S.B. Leen, Cyclic visco-plasticity testing and modelling of a service-aged P91 steel, in: *Proceedings of the ASME 2012 Pressure Vessels and Piping Division Conference*, ASME, Toronto, Ontario, Canada, 2012.

[9] A.A. Saad, C.J. Hyde, W. Sun, T.H. Hyde, Thermal-mechanical fatigue simulation of a P91 steel in a temperature range of 400 - 600°C, *Materials at High Temperatures*, 28 (2011) 212-218.

[10] B. Fournier, F. Dalle, M. Sauzay, J. Longour, M. Salvi, C. Caës, I. Tournié, P.F. Giroux, S.H. Kim, Comparison of various 9–12%Cr steels under fatigue and creep-fatigue loadings at high temperature, *Materials Science and Engineering: A*, 528 (2011) 6934-6945.

[11] R.A. Barrett, P.E. O'Donoghue, S.B. Leen, An improved unified viscoplastic constitutive model for strain-rate sensitivity in high temperature fatigue, *International Journal of Fatigue*, 48 (2013) 192-204.

[12] R.A. Barrett, P.E. O'Donoghue, S.B. Leen, Finite element modelling of the thermo-mechanical behaviour of a 9Cr martensitic steel, in: H. Altenbach, S. Kruch (Eds.) *Advanced Materials Modelling for Structures*, Springer Berlin Heidelberg, Berlin, Germany, 2013, pp. 31-41.

[13] D.-F. Li, N.P. O'Dowd, On the evolution of lattice deformation in austenitic stainless steels—The role of work hardening at finite strains, *Journal of the Mechanics and Physics of Solids*, 59 (2011) 2421-2441.

[14] J.L. Chaboche, G. Rousselier, On the Plastic and Viscoplastic Constitutive Equations---Part I: Rules Developed With Internal Variable Concept, *Journal of Pressure Vessel Technology*, 105 (1983) 153-158.

[15] J.L. Chaboche, G. Rousselier, On the Plastic and Viscoplastic Constitutive Equations---Part II: Application of Internal Variable Concepts to the 316 Stainless Steel, *Journal of Pressure Vessel Technology*, 105 (1983) 159-164.

[16] C.O. Frederick, P.J. Armstrong, A mathematical representation of the multiaxial Bauschinger effect, *Materials High Temperatures*, 24 (2007) 1-26.

[17] J.L. Chaboche, A review of some plasticity and viscoplasticity constitutive theories, *International Journal of Plasticity*, 24 (2008) 1642..

[18] R.A. Barrett, T.P. Farragher, C.J. Hyde, N.P. O'Dowd, P.E. O'Donoghue, S.B. Leen, A Unified Viscoplastic Model for High Temperature Low Cycle Fatigue of Service-Aged P91 Steel, *Journal of Pressure Vessel Technology*, 136 (2014) 021402-021402.

[19] Z. Zhang, D. Delagnes, G. Bernhart, Anisothermal cyclic plasticity modelling of martensitic steels, *International Journal of Fatigue*, 24 (2002) 635-648.

[20] T.P. Farragher, *Thermomechanical Analysis of P91 Power Plant Components*, PhD Thesis, NUI Galway (2013).

[21] T.H. Hyde, A.A. Becker, W. Sun, J.A. Williams, Finite-element creep damage analyses of P91 pipes, *International Journal of Pressure Vessels and Piping*, 83 (2006) 853-863.

[22] D.R. Hayhurst, Creep rupture under multi-axial states of stress, *Journal of the Mechanics and Physics of Solids*, 20 (1972) 381-382.

[23] I.J. Perrin, D.R. Hayhurst. Creep constitutive equations for a 0.5Cr-0.5Mo-0.25V ferritic steel in the temperature range 600-675 °C. *Journal of Strain Analysis*, 31 (1996) 299-314.

[24] R.A. Barrett, P.E. O'Donoghue, S.B. Leen. A dislocation-based model for high temperature cyclic viscoplasticity of 9-12Cr steels. *Computational Materials Science*, 92 (2014) 286-297.

Statistical Analysis of HGV Bridge loading for a DBFO scheme Using Northern Ireland (NI) Weigh-In-Motion (WIM) Data

Ciarán DOHERTY[1&2], Alistair HEANEN[1], Su TAYLOR[2], David CLELAND[2] and Myra LYDON[2]
1. Amey Consulting, Rushmere House, Belfast, N. Ireland,
2. School of Planning, Architecture and Civil Engineering
Queens University Belfast, Northern Ireland

ABSTRACT Weigh-in-Motion (WIM) systems use a range of sensors in the road pavement and serve two major functions. Firstly, and the main purpose, is to identify and subsequently reduce illegally overloaded vehicles. If uncontrolled, these overloaded vehicles cause premature deterioration of our bridges. Secondly, the data collected can be used for future design and assessment of our existing bridge assets and help in extending the life of bridges. WIM systems can measure weights of vehicles travelling at highway speeds without interrupting traffic. This study involves statistical evaluation of traffic from a newly installed WIM station in Northern Ireland. Historically, there has been little detail information of truck movements within the region and this is the first modern WIM site in all of Ireland, installed in accordance with COST 323 Specification. The system is located adjacent to a newly constructed integral concrete bridge in Loughbrickland, Northern Ireland, along the A1 corridor connecting the two cities of Belfast and Dublin. For each measured vehicle passing, the recorded information includes the time stamp, gross vehicle weight (GVW), number of axles, load per axle, axle spacing, vehicle class, lane of travel and speed.
This study provided analysis of the WIM data collected and a better understanding of the traffic and loads on our networks.. In Northern Ireland, overload enforcement is currently performed by static weighing of trucks. Now with WIM data and a better understanding of truck loading from real time results there is the opportunity of using WIM data as a pre-selection and enforcement tool. Also, using this intelligent transportation system (ITS) data, there is the potential to expand our understanding and prepare more efficiently for the future needs of our regional transportation systems.

KEY WORDS: Weigh-In-Motion (WIM) Systems; Structural health management; Monitoring of bridges; Remote monitoring system.

1 INTRODUCTION

The ability to weigh vehicles as they travel at motorway speed is known as Weigh-in-Motion (WIM). Using WIM technology, a system can record 100% of traffic data for analysis or enforcement purposes. The United Kingdom has been involved in the field of weigh-in-motion for over 40 years when early research projects were carried out by the Transport Research Laboratory [1]. Historically Northern Ireland has not been involved in this research and field work until recently and there is not much historical traffic data for this region. Subsequently, the newly installed system, in 2012, on the A1 at Loughbrickland is the first modern WIM site in all of Ireland, installed in accordance with COST 323(1999) [1].

The system has been installed as part of a wider US/Ireland research project investigating B-WIM technologies, axle detection and sensors types. The site was chosen as it is along the A1 corridor connecting the two cities of Belfast and Dublin and one of the busiest sections of roads in Northern Ireland as it is the main North/South artery carrying a large range of loads and vehicle types. The information gathered from the system can be stored locally for retrieval, transmitted immediately in real time or uploaded to servers from the WIM site via conventional mobile data networks.

This paper focuses on the results of the sensors to inform on movement trends and load analysis of the vehicles crossing the site each day and in particular the common Heavy Goods Vehicle (HGV) truck loads. This road network is managed through a 30 year Design, Build, Finance & Operate (DBFO) Project which has seen quite a number of new bridge structures and junction upgrades in recent years. The bridge site, in Loughbrickland was chosen as it is a recently constructed 18m pre-stressed beam and reinforced concrete slab underbridge suitable for development and comparison of WIM / B-WIM sensor systems that is a key focus of the current research.

Another huge benefit of the chosen location was the close proximity of a nearby self operated weigh station for trucks and local enforcement. These factors, together with high traffic volumes and central route through the country have made this an optimum location to carry out the study. See Figure 1 below for location of Loughbrickland WIM site.

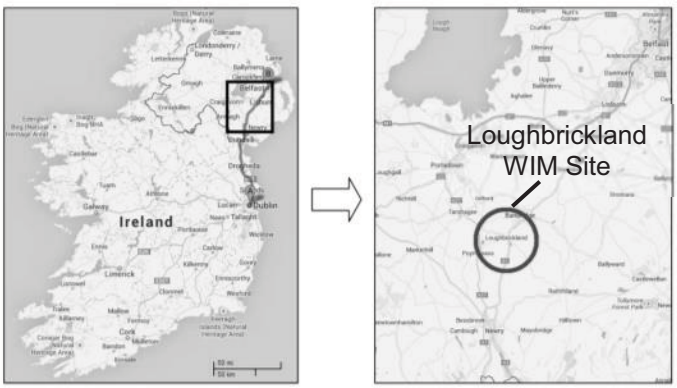


Figure 1 - Loughbrickland WIM System Location Maps

2 LOUGHBRICKLAND WIM SYSTEM

2.1 WIM Arrangement

The WIM system in Loughbrickland takes the form of a Piezo-Loop-Piezo sensor arrangement. The piezo sensors are used for weighing, as when pressure is applied to the piezo-electric material an electric charge is produced. The sensor is embedded in a narrow strip of resin in the pavement and the load is then transferred through the pavement to the sensor. The characteristics of the pavement therefore have an effect on the output signal. By measuring and analysing the charge produced, the sensor is used to measure the weight of the passing tyre or axle group [3]. Two piezo sensors were installed per lane and a resultant average used for in the post analysis. Within the two piezo sensors is an inductive loop measuring 2m x 2m. This is also embedded in the pavement and is used to classify and count the vehicle parameters. This arrangement was used in both lane 1 and 2 of the northbound carriageway as illustrated in Figure 2.

2.2 Installation & Learning

As with any system, the test results and system accuracy are dependent upon the integrity and standard of the system installation. Following the initial installation, some vital lessons were learned as it was soon discovered the piezo sensors were not performing accurately due to an installation error. Failure to finish the surrounding resin to the correct height meant that once the resin cured, the surface was not flush with the pavement and was outputting loads that were much lower than the actual loads, as measured independently on the weigh bridge. The sensors were replaced in a second phase of traffic management arrangements. This proved to be an important lesson particularly when the cost of traffic management was taken into account to permit replacement works. With the system control cabinet and civils works completed at the roadside, TDC Traffic systems supplied and installed the high speed WIM equipment to control the two lanes of WIM sensors. Extra precautions were taken to safeguard the newly installed system. Feedback from previous WIM installations in UK and USA advised of harm caused to systems from rodents damaging cables and also cases were members of the public had vandalised the system hardware. Therefore, all cables were installed in protective ducting with sealed ends and a secure weather-proof housing erected to safeguard and protect the system's hardware.

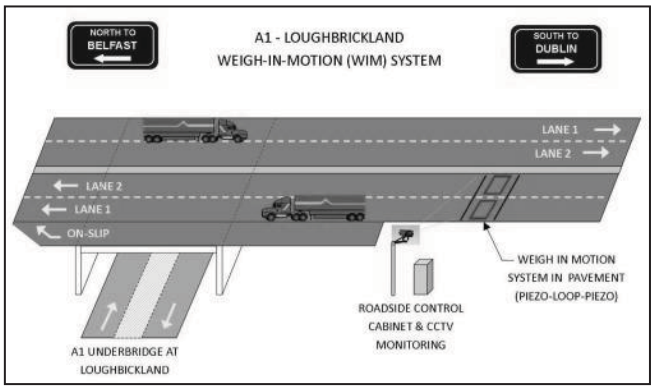


Figure 2 - Schematic of Loughbrickland WIM System

2.3 System Calibration & accuracy

During the site selection process for the WIM, visual surveys were of the upmost importance to ensure the physical aspects of the site met the recommendations of COST323 (1999). For operation of successful WIM sites we were able to satisfy these recommendations:

- Free flowing traffic movement; that is, no acceleration/deceleration zones
- Robust pavement construction
- High percentage of heavy goods vehicle traffic

Figure 3 below shows the completed WIM installation in Lane 1 and Lane 2 of the northbound carriageway.

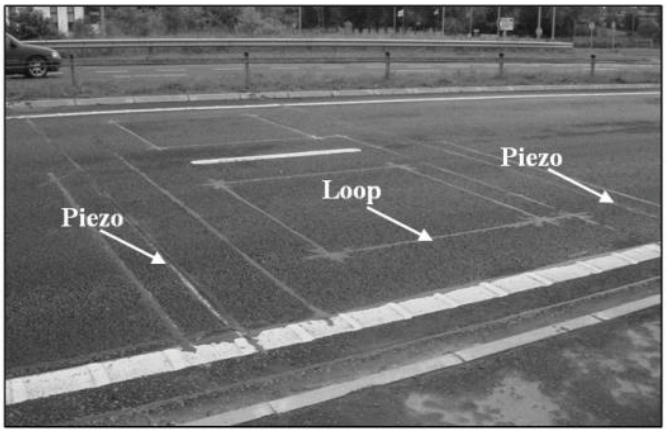


Figure 3 - Piezo-Loop-Piezo arrangement in A1 Pavement

Calibration of the system was carried out using a pre-weighed calibration truck which conformed to the full repeatability condition recommendations of COST 323. The close proximity of a static self weigh station proved valuable during this process as it enables repeat runs of the truck in a short space of time. Figures 4-7 shows the calibration process and WIM system on site.



Figures 4-7 Pre-weighing, Calibration & Control Cabinet

Installing CCTV vehicle monitoring on site was an additional asset to the WIM system and proved useful when addressing abnormalities in site results and in checking overloaded axles. The camera has a clear view of the carriageway and records continuously. The WIM system operates to a B(10) accuracy class, as detailed in COST 323. The system outputs the following vehicle parameters as listed in Figure 8 below. The WIM software can also be operated remotely with a tablet device or computer via controlled mobile data communication link. This facilitates quick access for monitoring.

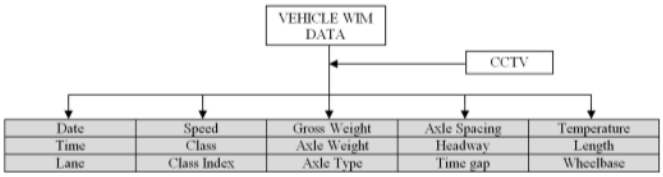


Figure 8 – WIM Data Collected

2.4 Vehicle Class Analysis

The WIM system has been operational for the past eight months in Loughbrickland and the presented analysis includes all of the data collected over this period. The statistics are based on over 2 million vehicle movements along the northbound lanes of the A1, that is towards Belfast.

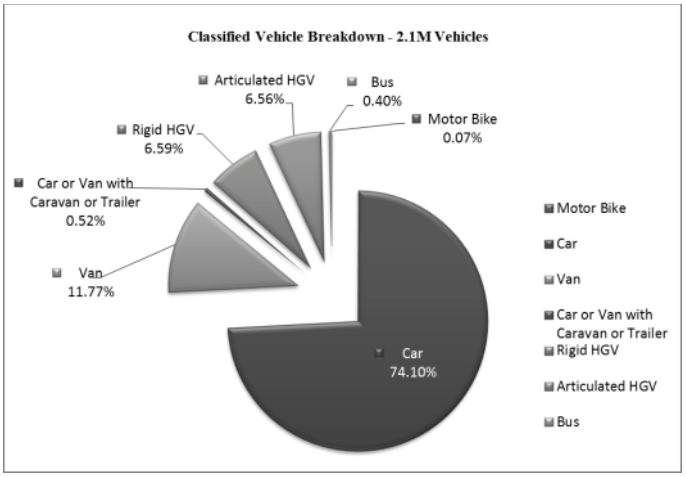


Figure 9 – Distribution of All WIM Vehicle Classes

The vehicle class analysis in Figure 9 provides a percentage breakdown of all vehicles classes that have been recorded since calibration of the WIM site last year. It is clear that the most common vehicle types using the A1 are cars followed by vans. However, one of the main vehicle classes of interest are the Articulated (artic) HGV's as they are most likely to cause both pavement wear and structural damage along the local network.

2.5 Articulated HGV Gross Vehicle Weight (GVW)

A closer investigation of the results for artic HGV's shows that the 5-axle artic (Class 55) and the 6-axle Artic (Class 56) are the most common Artic type at 59% and 25% respectively of all Artic HGV's. The percentage of all Artic HGV's for the site is shown in Figure 10

Vehicle Class	Description	Axle Arrangement	Graphic	Artic HGV Percentage %
51	Artic, 2 axle unit + 1 axle semi-trailer	1-1-1		1%
52	Artic, 2 axle unit + 2 axle semi-trailer	1-1-2		14%
53	Artic, 3 axle unit + 1 axle semi-trailer	1-2-1		0%
54	Artic, 3 axle unit + 2 axle semi-trailer	1-2-2		1%
55	Artic, 2 axle unit + 3 axle semi-trailer	1-1-3		59% ✓
56	Artic, 3 axle unit + 3 axle semi-trailer	1-2-3		25% ✓

Figure 10 – Distribution of Artic HGV's Class

From Figure 11 the GVW of artic HGV's shows an interesting spread and it is apparent that there is a higher frequency of lighter Artic HGV's than heavy ones passing the WIM site. The two peaks in the data at the 12-14 ton range and the 32-34 ton range highlight the two most common GVW's for Artic HGVs. The lighter trucks are those carrying no freight or low weight freight. It is likely that the majority of these lighter trucks are in fact loaded with light weight goods as hauliers are unlikely to be running unloaded trucks due to the high running costs, particularly in the current economic climate. With the data plotted individually for both lanes of traffic, it can be seen that lane 1 receives the majority of HGV traffic with 96% in lane 1 and only 4% in lane 2. This confirms that the majority of pavement damage occurs in the inside lane (usually slower), lane 1. The information in Figure 11 is for all 6 classes of Artic HGV's but the most common categories were investigated further.

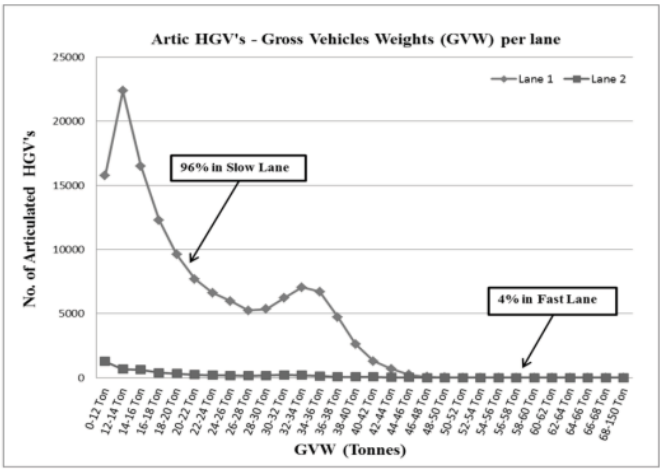


Figure 11 – Distribution of Artic HGV's Class

The legal maximum GVW limit for the Class 55 and for the Class 56 was increased, by the Department for Transport (DfT) in 2001, to 40 ton and 44 ton respectively. Individual analysis of GVW was carried out for both classes to assess their overweight statistics. The results are shown in Figure 12. Whilst the overweight percentages are small, they are having a significant impact on the damage to the road pavements and structures over a long-term period. This has been confirmed by the road operators who are undertaking the majority of their pavement repairs in lane 1.

Class 55 HGV's – Exceeding GVW of 40Ton	0.52%
Class 56 HGV's – Exceeding GVW of 44Ton	0.96%

Figure 12 – Exceeded GVW for Class 55 & 56 HGV's

Comparing the GVW distribution of Class 55 and Class 56 HGV's in Figures 13 and 14 shows one clear difference. Figure 13 has a left hand skew as opposed to Figure 14 which has a right hand skew, demonstrating that the majority of Class 55 trucks are lighter than the Class 56 trucks. Class 55 trucks are carrying lighter loads and have on average a GWV approximately 10 tonnes lower than that of the Class 56 truck. This observation is also evident in results shown in Figure 17. Another worthwhile observation is that a low percentage of Class 55 trucks actually run well under their legal gross weight limit, whereas the Class 56 trucks have a greater percentage running near their legal gross weight limit.

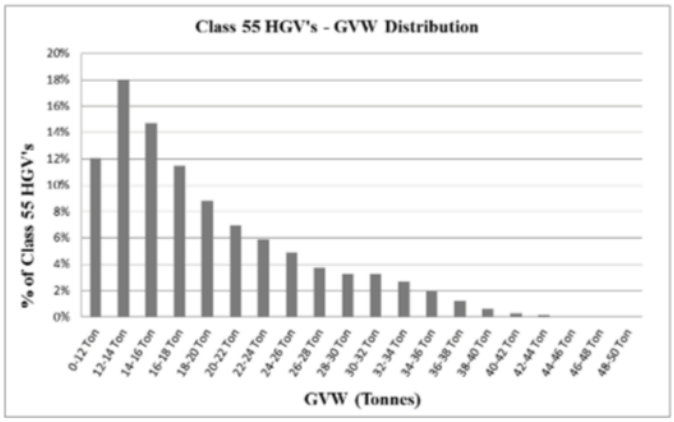


Figure 13 – Class 55 GVW Distribution

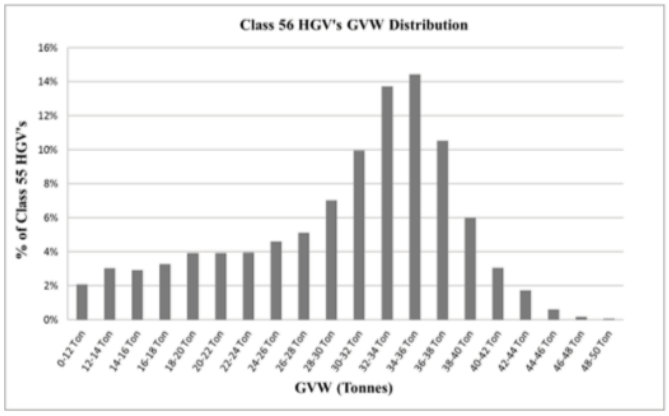


Figure 14 – Class 56 GVW Distribution

2.6 Articulated HGV Axle Weights (GVW)

An analysis of the individual axle weights for both classes was carried out and the axle weight distributions for Classes 55 & 56 are shown in Figures 15 & 16 respectively. Class 55 have a more severe left hand skew than the Class 56 results, thus illustrating that the majority of axle weight for the Class 55 are much lower. Figure 17 shows the estimate for average axle weight for Classes 55 and 56 is 3.79 ton and 5.01 ton respectively. The numbers of axles in each class type that are overweight are quite low and again less than 1%.

Interestingly the average axle weight of the Class 56 trucks is approximately 30% greater than that of the Class 55 trucks. This sharp increase would not be expected as the idea of a sixth axle on the Class 56 trucks should suitably accommodate the extra loading requirements of roughly 4 to 5 ton above that of a Class 55 truck, whilst keeping the average axle weight around the same.

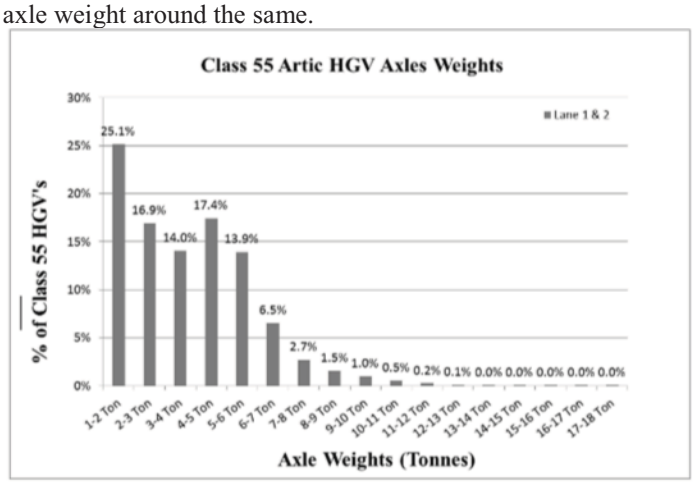


Figure 15 – Class 55 Axle Weight Distribution

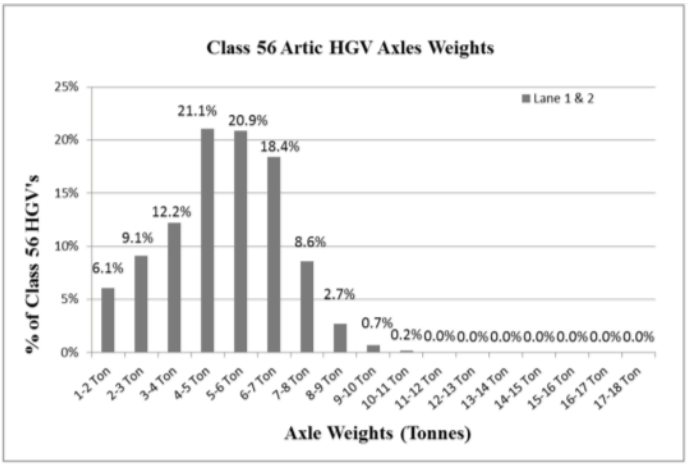


Figure 16 – Class 56 Axle Weight Distribution

The variance and standard deviation for the GVW of the Class 56 HGV is slightly higher than that of the Class 55 HGV. The reason for this is due to the fact that the Class 56 HGV can ultimately carry a larger range of loads as the upper limit if loaded to its maximum legal GVW can reach 44 ton. This maximum GVW is set at 40 ton for Class 55. When looking at the variance and standard deviation for the Axle Weights, the

trend is opposite with the Class 56 HGV's being slightly lower than Class 55 HGV's. As discussed above the average axle weights of these two classes would be expected to be approximately the same. A possible reason for this change in trend is discussed later in the results.

	Gross Vehicle Weight (GVW)		Axle Weight	
HGV Vehicle Class	*Class 55*	*Class 56*	*Class 55*	*Class 56*
Mean	18.37 t	29.87 t	3.79 t	5.01 t
Variance	62.34 t	70.15 t	4.09 t	3.22 t
Standard Deviation	7.9 t	8.38 t	2.02 t	1.8 t

Figure 17 – Class 55 & 56 Analysis Outputs for GVW and Axle Weights

3 RESULTS AND DISCUSSIONS

The WIM site in Loughbrickland has on average 11000 vehicles travelling northbound each day on lanes 1 and 2 of the A1. Of these vehicles, approximately 420 are of Class 55 and 180 are of Class 56. The majority of these truck movements are likely to be carrying freight to and from the city and port in Belfast. Statistical results from the WIM system and in particular Figure's 13 & 14 seem to contain abnormalities in that it appears as though most Class 56 HGV's running with a GVW of greater than 25ton. However, the Class 55 trucks appear to have the majority of trucks running with GVW's under 25 ton and relatively fewer near its legal limit of 40 ton. Initially this may seem to make sense as the heavier Class 56 trucks are generally only required by hauliers transporting heavier freight and needing a higher legal GVW allowance.

Another reason for this trend became apparent when taking a closer look at the WIM data. If a Class 56 truck is running at a lower GVW the driver almost always raises the secondary rear axle on the unit as there is no legal requirement to use it to spread the trailer load to the road. In these instances the WIM system weighs only 5 axles and incorrectly classifies the HGV as a 5-axle, class 55 HGV. Refer to Figure 18 below which shows an example of this. As a result a Class 56 HGV (1-2-3), if running light, with an axle raised is classified as a Class 55 HGV (1-1-3) or (1-2-2).

This explains why the GVW of Class 55 is skewed towards the left and as biased towards the lighter GVW's. The system is essentially counting all light Class 56 HGV's with a raised axle as a Class 55 HGV and the Class 55 count in this weight band is incorrectly increased. This same problem explains why there are few light Class 56 trucks in Figure 14, as only heavy loads with the 6th axle lowered is getting correctly classified. If correctly counted, the skews on Figures 13 & 14 would move back towards the centre. The axle weights particularly would be much closer as should be the case with these two HGV classes. The variance and standard deviation would both balance a little more, but should still be a little higher for the Class 56 GVW.



Figure 18 – Class 56 HGV with raised unit axl

4 CONCLUSIONS

This paper has presented initial findings of a newly installed WIM site in Loughbrickland, Northern Ireland and generated statistics of the HGV gross and axle loadings that are applied to the pavements and bridges along the A1. It is recognised that there are some minor flaws in the system but it provides a large database of vehicle information for this local region and many more analyses will be carried out on the continually growing log of WIM data and compared to the B-WiM system on the adjacent bridge. It is important for any WIM operator to understand how the results from these systems are generated and to study any abnormalities. The addition of a CCTV or Vehicle Imaging is a vital asset to a WIM system and is becoming more common in the UK. Understanding the loadings on the structures and pavements can assist the operator and design team with structural health management when assessing and design repairs on the network. This WIM system will continue to be developed and will be used as a reference tool to assist in further research with B-WIM and sensor technologies on the Loughbrickland Underpass Bridge at the site.

5 REFERENCES

[1] Trott, J.J. and Grainger, J.W. (1986). "Design of a dynamic weighbridge for recording vehicle wheel loads", Report LR 219 Road Research laboratory TRL Crowthorne

[2] COST323 (1999). "European Specification on Weigh-in-Motion of Road Vehicles", EUCO-COST323, LCPC,Paris

[3] Quilligan, M. (2003). "Bridge Weigh-in-Motion Development of 2D Multi Vehicle Algorithm", Licentiate Thesis Department of Civil and Architectural Engineering, Royal Instituite of Technology Sweden

BridgeMon: Improved Monitoring Techniques for Bridges

Peter Favai[1], Eugene OBrien[2], Aleš Žnidarič[3], Hans Van Loo[4], Przemyslaw Kolakowski[5], Robert Corbally[2]

[1]Cestel, Slovenia.
[2]Roughan & O'Donovan Innovative Solutions, Ireland.
[3]Slovenian National Building and Civil Engineering Institute, ZAG, Slovenia.
[4]Corner Stone International, Switzerland.
[5]Adaptronica, Poland.

email: peter.favai@cestel.si, eugene.obrien@rod.ie, ales.znidaric@zag.si, hans.vanloo.int@gmail.com, przemyslaw.kolakowski@adaptronica.pl, robert.corbally@rod.ie.

ABSTRACT: Many bridges in the world's transport infrastructure are old and have deteriorated over time. The solution to this problem is to either repair or replace a bridge or to establish its safety and maintain it in service. It is generally very costly to repair or replace a bridge. With reduced maintenance budgets there is an increasing interest in maintaining these old bridges in service by using probabilistic methods to prove that they are safe. Bridge safety is assessed based on (i) the loading which it will experience in service and (ii) the resistance of the structure. Improved knowledge of loading and resistance allows a more accurate assessment of whether a bridge is safe to remain in service without the requirement for expensive repair or replacement strategies. BridgeMon is an EU-FP7 funded project which aims to improve current monitoring techniques for road and rail bridges. This will be done by developing improved methods of evaluating traffic loading on bridges and carrying out Structural Health Monitoring (SHM) to identify damage and assess their remaining resistance. Bridge Weigh-in-Motion (B-WIM) refers to the technique of using the measured response of a bridge to calculate the vehicle loads crossing it and is a useful tool in monitoring traffic loading on bridges. BridgeMon will improve the accuracy of current B-WIM technologies and develop the first B-WIM system for railways. It is also developing the concept of virtual monitoring, whereby sensors are used to calculate vehicle weights which are then used to calculate stress histories throughout the bridge. Results from testing of a rail B-WIM system indicate that the it is capable of accurately calculating train weights, however changing velocity must be considered.

KEY WORDS: Bridge; Weigh-in-Motion; B-WIM; WIM; Structural Health Monitoring; SHM; Railway; Train; Loading.

1 INTRODUCTION

Major transport networks rely heavily on the safety and serviceability of bridges located on these routes. Failure of a bridge can have devastating effects from both an economic perspective and regarding loss of human life. It is therefore imperative that the safety of these bridges is ensured. A vast number of bridges which are critical to the efficiency of road and rail transport networks are old and have deteriorated since their construction. In many cases these bridges have reached their design lives and, as such, a decision must be made as to whether the bridge needs to be repaired or replaced, or whether it is safe to retain in service.

With limited maintenance budgets available, replacing old bridges which have exceeded their design lives is an expensive and time-consuming strategy. Many bridges have been designed for loading scenarios far in excess of any which have been experienced during the working life of the structure. As such, these bridges may exhibit the necessary capacity to remain in service without the requirement for expensive repairs or replacement.

In order for these bridges to remain in service it must be proven that it is safe to retain them, i.e. that their probability of failure is below an acceptable level. Bridge safety can be evaluated by comparing the maximum loading that is expected to the resistance of the structure to that loading. Therefore, an accurate safety assessment requires detailed knowledge of the loading on the bridge along with its resistance.

The BridgeMon project aims to improve current bridge monitoring techniques in order to allow accurate evaluation of both loading and resistance characteristics for road and rail bridges.

2 OBJECTIVES OF BRIDGEMON

BridgeMon (**Bridge** Safety **Mon**itoring) is an EU FP7 funded project which has been supported under the 'Research for the Benefit of SMEs' programme. The project focuses on developing new monitoring techniques for the evaluation of bridge loading and resistance. Applications for both road and rail bridges are considered within BridgeMon.

2.1 Bridge Weigh-in-Motion

Weigh-in-Motion (WIM) is a term used to collectively refer to the various technologies which have been developed to allow the weighing of vehicles which are travelling at full traffic speed. Conventional WIM systems are pavement based, mostly involving pressure sensors embedded in the road pavement. B-WIM refers to an alternative WIM approach whereby the structural response of a bridge is measured during the passage of a vehicle and is then used to calculate the weight of that vehicle and its axles. B-WIM has the advantage of being portable, as well as providing direct information on the structural behaviour of the bridge being used. The ability to weigh vehicles without having to stop them allows for large scale collection of traffic loading data for roads and bridges. Figure 1 illustrates the B-WIM concept.

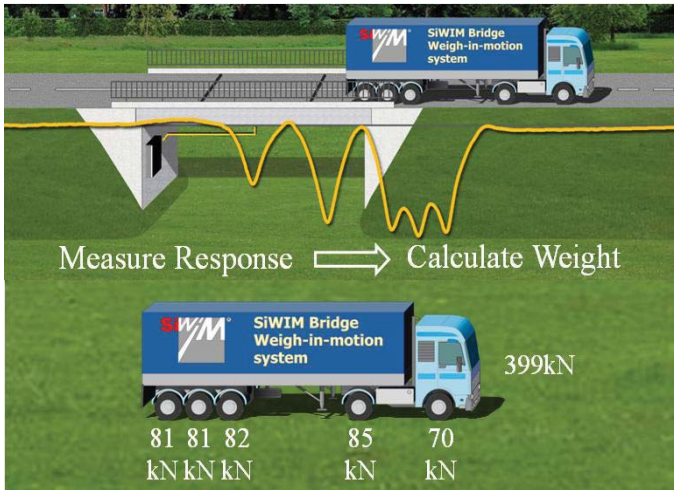


Figure 1. Bridge-WIM Concept.

B-WIM technology is quite well established for traffic load monitoring on road bridges [1, 2]. Cestel d.o.o. is a Slovenian company which markets a B-WIM system known as SiWIM. As part of BridgeMon, SiWIM is being enhanced to include novel developments in the field of B-WIM research.

While B-WIM has been applied successfully to road bridges, this is not the case for rail bridges. Accurate safety assessment of rail bridges requires a detailed knowledge of the actual train loading being experienced by the bridge, particularly on networks where the track manager does not own the railway stock. While certain technologies do exist for weighing trains, they are often very slow or cumbersome [3, 4] and are not feasible for large scale data collection on train weights. The development of a rail B-WIM system would make it possible to obtain a great deal of information on train loading which could be used in the safety assessment of rail bridges. As part of BridgeMon the B-WIM concept is being extended to rail bridges in this regard.

2.2 Virtual Monitoring

BridgeMon is also examining the concept of 'Virtual Monitoring' of bridges. The virtual monitoring concept uses a combination of a B-WIM system which is installed on the bridge along with a finite element model of the structure. Using the loading information obtained from the B-WIM sensors, the stresses at other locations, where sensors have not been installed, can be 'virtually' monitored. This allows stress levels at many critical locations to be measured without the requirement for a vast number of sensors. The remaining fatigue life of steel bridges can be estimated using the virtual monitoring system.

The Harmsen Bridge in the Netherlands has been instrumented for the application of the virtual monitoring concept, and work on the development of virtual monitoring software is ongoing. Figure 2 shows a photograph of the bridge along with a finite element model that has been developed for virtual monitoring.

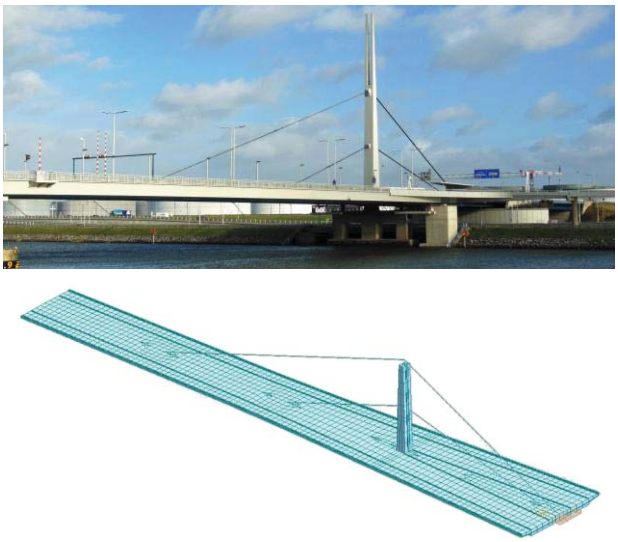


Figure 2. Photograph and FE model of the Harmsen Bridge.

2.3 Combined Bridge-WIM & Structural Health Monitoring

While B-WIM is primarily employed to gather information on traffic loading it can also be used in combination with a Structural Health Monitoring (SHM) system for a bridge. B-WIM relies on strain measurements from a bridge to calculate the weight of trucks or trains. Damage to a structure will very often result in a change in magnitude in the measured strains, and hence manifest itself in a change in the calculated weights. This has particular significance in railway applications where there are generally only a small number of different train locomotives whose weights remain relatively constant and changes in calculated weights would signify a change in the bridge response, possibly due to damage.

Damage to a structure can also manifest itself in changes to the dynamic characteristics, specifically the natural frequencies and mode shapes. Numerical modelling can be used to determine the optimum instrumentation setup for a particular bridge by identifying the locations most sensitive to damage.

Using the combination of B-WIM and SHM, real time monitoring of the health of a structure can be achieved. This allows the collection of loading information for a bridge, in addition to providing detailed information on its condition. Figure 3 shows a train-track-bridge interaction model which models the dynamic interaction between a train and a bridge, while accounting for the influence of the rail, sleepers and ballast. This model has been developed for use with the combined B-WIM and SHM concept. The model can be used to decide on the optimal locations for instrumentation as well as being used to simulate damage at different locations in order to aid the SHM system in detecting it.

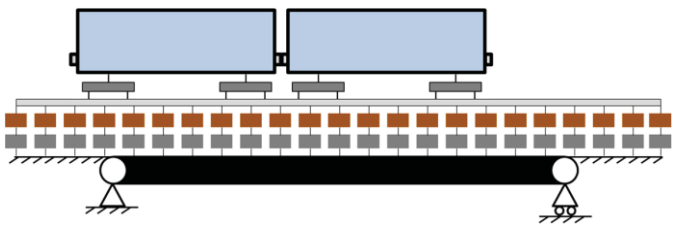


Figure 3. Train-track-bridge interaction model.

3 DEVELOPMENT OF A RAILWAY BRIDGE-WIM SYSTEM

One of the primary focuses of BridgeMon is the development of B-WIM technology as an efficient tool to gather information on traffic loading for bridges. Central to this is the development of a B-WIM system which can be used to calculate the weights of trains on railway bridges. At present, accurate weighing of trains is a slow and cumbersome procedure, which can cause disruption to railway schedules and is not convenient for large scale collection of information on train weights [3]. Procedures for weighing trains in motion do exist [5] and an attempt has been made to apply the B-WIM concept to railways [6], but with limited success.

The ability to accurately weigh trains in motion would be of great benefit to railway infrastructure managers, from the perspective of safety assessment of bridges, but also with respect to the enforcement of legal weight limits for trains.

While the B-WIM concept for road and rail bridges is very similar, there are some key differences between the two which have been identified. The accuracy of road B-WIM has been shown to be influenced by vehicle transverse position as well as the roughness of the road surface [7]. For railway applications, trains are constrained to run on tracks, which are much smoother than roads. In addition train configurations do not vary a great deal, making it less difficult to identify the axle configurations. In contrast, trains have far more axles than trucks and are heavier, which may cause inaccuracies in B-WIM predictions as a result of ill-conditioned equations in the algorithm and increased dynamics.

3.1 Bridge-WIM Theory

The vast majority of B-WIM approaches are based on the original idea proposed by Moses [8]. This conventional approach uses the assumption that the measured response (i.e. strain) from a bridge can be approximated by multiplying the axle weights of a vehicle by the corresponding influence line ordinates and summing the responses of all axles. Using this assumption, along with a known influence line for a bridge, the axle weights of the vehicle can be estimated by finding the values which provide the best fit to the measured response.

Sensors are located across the width of the bridge at a single longitudinal location (usually mid-span). The problem is generally reduced from that of two dimensions to one dimension by summing the signals measured in each of the sensors to give a single response for each train location. Figure 4 shows the assumption used within the B-WIM algorithm.

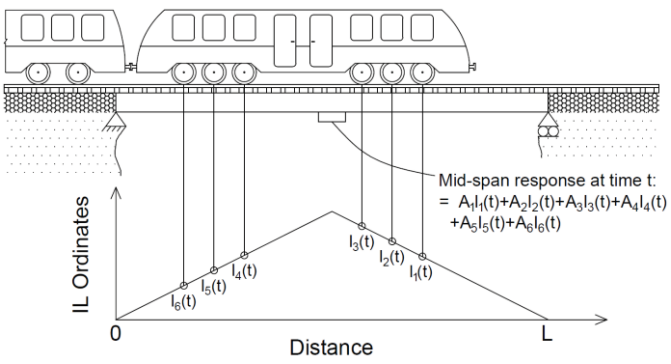


Figure 4. Basis of B-WIM calculations.

In order to solve for the axle weights, a least squares minimisation between the measured signal and the theoretical signal (based on the assumption in Figure 4) is carried out. The error function is defined as follows:

$$E = \sum_{t=1}^{T} (\varepsilon_t^{Me} - \varepsilon_t^{Th})^2 \quad (1)$$

where t is the scan number corresponding to a point in time during the crossing of the train, T is the total number of scans and ε_t^{Me} & ε_t^{Th} are the measured and theoretical strain signals at scan t respectively.

Using the assumption outlined in Figure 4 to substitute for the theoretical strain, the error function shown in Eq. 1 can be rewritten as:

$$E = \sum_{t=1}^{T} \left(\varepsilon_t^{Me} - \left[A_1 I_{1(t)} + A_2 I_{2(t)} + \cdots + A_N I_{N(t)} \right] \right)^2 \quad (2)$$

where A_n represents the n^{th} axle of the train, N is the total number of axles and $I_{n(t)}$ is the strain influence line ordinate for axle n at time t.

Differentiating Eq. 2 with respect to each of the axle weights and setting each of the partial derivatives to zero gives a set of N simultaneous equations in the form of Eq. 3:

$$[H]_{N\times N} \{A\}_{N\times 1} = \{B\}_{N\times 1} \quad (3)$$

where $[H]$ is a matrix of influence line ordinates, $\{A\}$ is the vector of unknown axle weights and $\{B\}$ is a vector which contains products of the influence line ordinates and the measured strains from the bridge. Eq. 3 can be solved to find the axle weights which provide the best fit to the measured response from the bridge.

3.2 Field Testing of Bridge-WIM System in Poland

In order to assess the suitability of the B-WIM concept for measuring the weights of trains in motion, a bridge in Poland was selected for testing. The bridge (Figure 5) is located in Nieporęt, near Warsaw. The steel truss bridge was constructed in the 1970s and is one of over one thousand similar railway bridges in Poland [9].



Figure 5. Nieporęt rail bridge - for testing of B-WIM.

The bridge which spans 40m is simply supported on two bearings at either end and carries a single un-ballasted railway track. The truss consists of five bays and is 8m in height. Figure 6 shows an outline of the main structural elements (the rail and sleepers are removed for clarity).

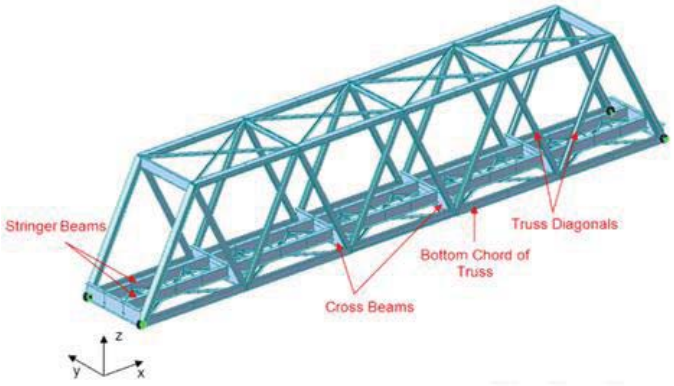


Figure 6. Structural configuration of Nieporęt bridge.

The track is supported by timber sleepers which rest on two main longitudinal stringer beams. These stringer beams span between six cross beams which are located at the node points of the bottom chord of the truss.

The bridge was instrumented with SiWIM sensors, which were attached at the locations shown in Figure 7. This figure shows a plan view of the bridge at track level. Sensors 1, 4, 5 and 8 are attached to the stringer beams, sensors 3 and 6 are attached to the bottom chord of the truss, sensor 2 is attached to the underside of the rail and sensor 7 is located on a cross beam.

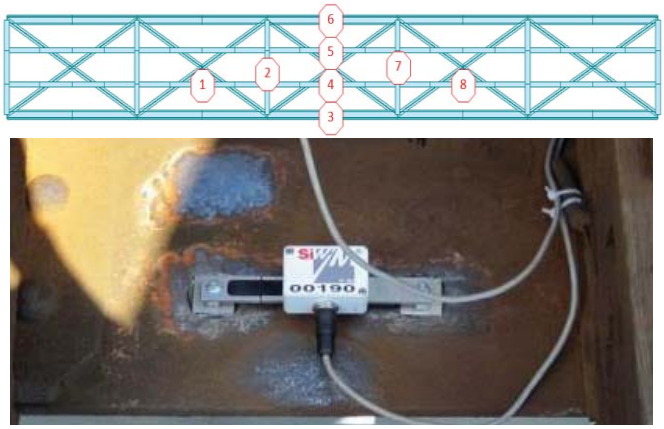


Figure 7. Sensor locations for B-WIM (above) and strain transducer (below).

When applying the B-WIM algorithm to calculate train weights, sensors 3-6 were used for applying weighing algorithm, while sensors 1 and 8 were used to calculate the speed of the train. Detection of axles was carried out using sensor 2 which recorded distinct peaks for each of the individual axles. Sensor 7 did not provide useful information for the application of B-WIM. The SiWIM software, which has been developed for use on road bridges, was re-configured to give suitable outputs for railway applications.

Over a period of three days, signals were recorded for the passage of around 40 passenger and freight trains. Figure 8 shows the signals recorded in sensors 3-6 due to the passage of one freight train with a locomotive pulling 34 wagons.

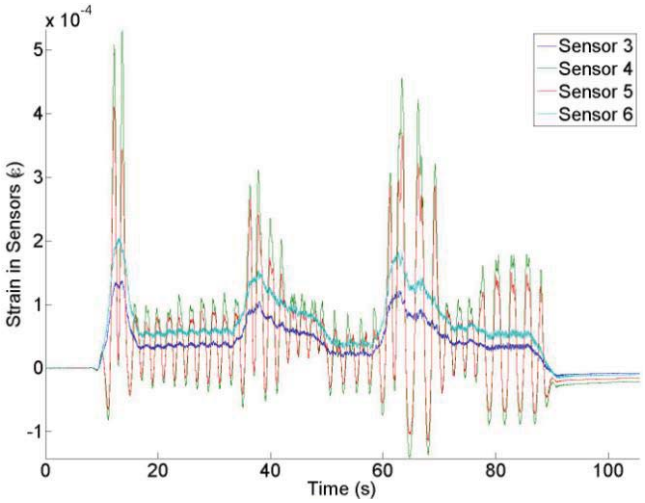


Figure 8. Measured strain during passage of freight train.

It is clear that the signals recorded from the stringers (sensors 4 and 5) show distinct localised peaks compared to the more global response that is obtained from the sensors measuring strain on the bottom chord of the truss.

Once the installation had been carried out it was necessary to calculate an influence line which could be used to represent the bridge response (i.e. the total combined response of sensors 3-6) and hence be used in the calculation of weights as outlined in Section 3.1. It has been shown [10] that the theoretical influence line for a structure rarely matches the actual influence line. In order to calculate the actual influence line for the bridge, an optimisation technique, which calculates the shape of the influence line that provides the best fit to the signal, was employed. This influence line was then used within the B-WIM algorithm to calculate the weights of trains - Figure 9.

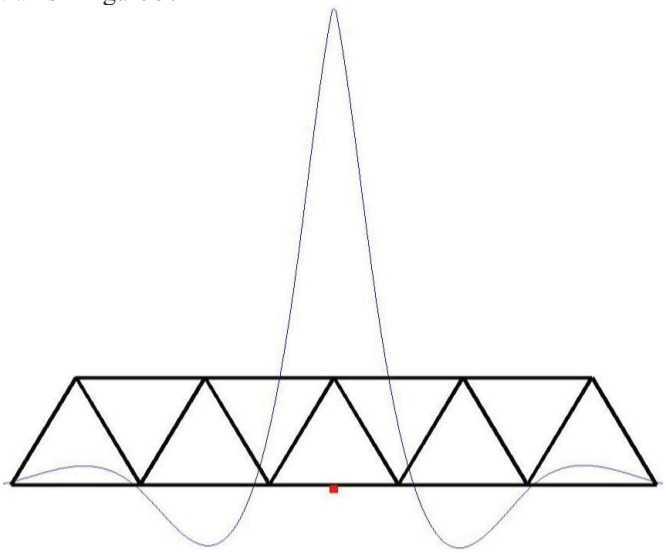


Figure 9. Influence line for mid-span bridge response.

3.3 Low-Speed Weighing of Trains

In order to assess the accuracy of the weights being calculated by the B-WIM system, four of the freight trains that passed over the bridge were diverted to a low-speed weighing site in

a rail yard in Warsaw. These weighing scales can accurately weigh trains as they move across at speeds below 5km/h. Figure 10 shows an image of this scales.

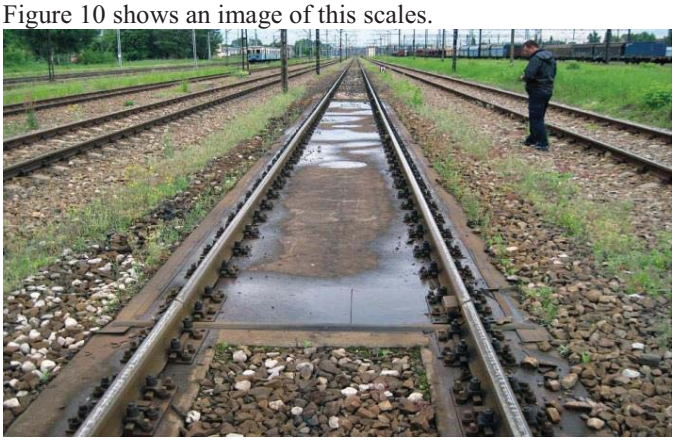


Figure 10. Low-speed weighing scales for trains.

The low-speed weighing provided accurate weights for each of the carriages on these four trains. Using these known weights, the accuracy of the B-WIM weight predictions was assessed.

3.4 Bridge-WIM Results

The calculated weights from the B-WIM system, for each of the carriages on the four freight trains, were compared to the weights obtained from the low-speed weighing. The accuracy of the prediction for each of the carriages was then calculated. Figure 11 shows the error in the predicted carriage weights for a train with a locomotive pulling 25 wagons.

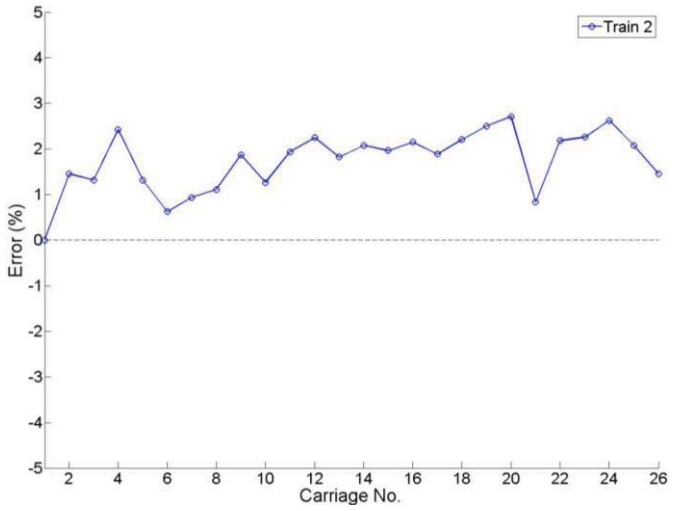


Figure 11. B-WIM prediction errors.

From Figure 11 it can be seen that the weights predicted by the B-WIM algorithm were very accurate for this train. All of the calculated carriage weights were within 3% of their actual weight.

The calculated weights for the four other trains were considerably less accurate. Examining these results more closely showed that the inaccuracies in the B-WIM weights for these trains resulted from the fact that the velocity of these trains did not remain constant during their passage over the bridge.

3.5 Influence of Train Velocity on Accuracy

In order to carry out the B-WIM calculations, it was necessary to calculate the velocity of the train. This was done by examining the signals in sensors 1 and 8 (see Figure 7), and calculating the offset between the two signals. Using the fact that the distance between these sensors is known, the velocity of the train can be calculated.

It is important to note that a common assumption in most B-WIM algorithms is made, whereby the velocity is assumed to remain constant during the crossing. Using this assumption for road bridge applications is generally reasonable as the vehicles are short and the bridges chosen are usually quite short also. Thus their speed tends to remain relatively constant during the short time which they are on the bridge. This was found not be to be the case for the trains crossing the Nieporęt Bridge.

The trains observed during testing were between 370-630m in length with some of the trains taking nearly 3 minutes to cross the bridge. Due to a speed restriction it is unreasonable to assume that the velocity of these trains actually remained constant for the whole time that they were on the bridge. The Nieporęt Bridge has a speed limit of 20km/h, which results in trains rapidly decelerating as they approach the bridge in order to meet the speed restriction and accelerating as they leave it, while some of the rear carriages may still be on the bridge.

Comparing the calculated axle spacings for the carriages, which were obtained using the constant velocity assumption, to the actual spacings for these types of carriage allowed their individual velocities to be calculated. Examining their relative velocities for each of the four trains showed that any major inaccuracies were due to the changing velocity of the train as it crossed the bridge. The velocity of the train whose carriage weights were predicted very accurately (Figure 11) was seen to remain almost constant as it traversed the bridge.

3.6 Suggestions for Improved Accuracy

It is expected that addressing the issue of train velocity will show an improvement in the accuracy of the railway B-WIM system. As work on BridgeMon continues, the algorithm will be adjusted to calculate the individual velocities for each of the carriages on the train rather than the average velocity of the whole train.

Some inaccuracy was also found to occur when fully loaded wagons were located adjacent to empty wagons. In these cases the individual contribution of the lighter axles could not be distinguished within the overall response in the measured signals and the predictions were less accurate. These errors result from ill-conditioning of the equations. Further work in BridgeMon will see the implementation of a numerical regularisation technique in order to reduce errors due to ill-conditioning.

4 CONCLUSION

Accurate safety assessment of bridges requires detailed information on the loading being experienced by the structure along with its health. The BridgeMon project aims to improve current bridge monitoring techniques for road and rail bridges.

This paper gives a brief overview of the work being carried out as part of the project, whereby B-WIM technologies are being advanced to develop convenient and accurate systems for monitoring traffic loading on bridges. In addition, the concept of virtual monitoring of bridges is being developed along with methods of incorporating B-WIM measurements into SHM systems in order to evaluate the health of the structure.

BridgeMon aims to apply the B-WIM concept to rail bridges for the first time, in an effort to develop the first B-WIM system for monitoring train loading. Results are presented from experimental testing of a railway B-WIM system on a truss bridge in Poland. The results for one train show that all of the carriage weights calculated by the B-WIM system are within 3% of their actual weight. Initial results for other trains show larger errors, when the effect of changing velocity is not corrected.

Work on the BridgeMon project is ongoing and the results from the experimental testing of a rail B-WIM system are promising. Further work will address the issue of inaccuracies caused by changing train velocity as well as the application of a numerical regularisation technique in an attempt to improve inaccuracies which occurred when heavily loaded carriages were located next to empty carriages.

ACKNOWLEDGMENTS

The research leading to these results has received funding from the European Community's Seventh Framework Programme (FP7/2007-2013) under grant agreement no. 315629.

REFERENCES

[1] E.J. O'Brien, A. Žnidarič and A.T. Dempsey (1999) 'Comparison of two independently developed Bridge Weigh-in-Motion systems', *International Journal of Heavy Vehicle Systems'* 6(1), 147-161.

[2] P. McNulty and E.J. O'Brien (2003) 'Testing of Bridge Weigh-in-Motion system in sub-Arctic climate', *Journal of Testing and Evaluation,* 31(6), 1-10.

[3] K. Sekula and P. Kolakowski (2010), 'Piezo-based weigh-in-motion system for railway transport', *Structural Control and Health Monitoring,* 19 (2), 199-215.

[4] D. Graaf, D. Jong and V.d. Hoek (2005) 'Gotcha: compact system for measuring train weight and wheel defects', *Fourth International Conference on Weigh-in-Motion – ICWIM. Eds. OBrien, E.J., Jacob, B., Gonzlaez, A. and Chou, C.-P.* Taipei: National Taiwan University, 153-163.

[5] G. James (2005) 'Analysis of traffic load effects on railway bridges using weigh-in-motion data' *Fourth International Conference on Weigh-in-Motion – ICWIM. Eds. OBrien, E.J., Jacob, B., Gonzlaez, A. and Chou, C.-P.* Taipei: National Taiwan University.

[6] A. Liljencrantz, R. Karoumi and P. Olofsson (2005) 'Implementation of bridge weigh-in-motion for railway traffic', *Fourth International Conference on Weigh-in-Motion – ICWIM. Eds. OBrien, E.J., Jacob, B., Gonzlaez, A. and Chou, C.-P.* Taipei: National Taiwan University, 142-152.

[7] T. Deesomsuk & T. Pinkaew (2009) 'Effectiveness of vehicle weight estimation from bridge weigh-in-motion', *Advances in Civil Engineering,* 2009, doi:10.1155/2009/312034.

[8] F. Moses (1979) 'Weigh-in-motion system using instrumented bridges', *ASCE Transportation Engineering Journal,* 105, 233-249.

[9] P. Kolakowski, J. Szelazek, K. Sekula, A. Swiercz, K. Mizerski and P. Gutkiewicz (2011) 'Structural health monitoring of a railway truss bridge using vibration-based and ultrasonic methods', *Smart Materials and Structures,* 20 (3), 035016.

[10] E.J. OBrien, M.J. Quilligan, R. Karoumi (2006) 'Calculating an influence line from direct measurements', *Proceedings of the Institution of Civil Engineers, Bridge Engineering,* 159(1), 31-34.

Development of a new generation Bridge Weigh in Motion System

Myra Lydon[1], Su Taylor[1], D Robinson[1], Ciaran Doherty[2]
[1]School of Planning, Architecture and Civil Engineering Queens University Belfast, Northern Ireland
[2]Amey Consulting, Rushmere House, Belfast, N. Ireland
email: mlydon01@qub.ac.uk, s.e.taylor@qub.ac.uk, des.robinson@qub.ac.uk, ciaran.doherty@amey.co.uk.

ABSTRACT: In recent years, Structural Health Monitoring (SHM) systems have been developed to monitor bridge deterioration and hence bridge safety. However, these systems are only telling half the story. A road bridge is only safe if the stresses caused by the passing traffic are less than the capacity of the bridge to resist them. Conventional SHM systems can be used to improve knowledge of the bridge capacity to resist stresses but give no information on the causes of increased stresses. The concept of in Bridge Weigh-in-Motion (B-WiM) is to establish axle loads, without interruption to traffic flow, by using strain sensors at a bridge soffit and subsequently converting the data to real time axle loads or stresses. Recently a system has been developed whereby strain sensors are installed to the underside of the bridge, these systems are commonly known as Nothing-On-Road (NOR). A data acquisition system is used in conjunction with the sensors to detect and record a passing axle which is recognised by a peak in strain. Fiber Optic Sensors (FOS) are commonly used for SHM, this paper looks at the suitability of using FOS sensors for B-WIM. The study investigates fixing methods, durability, scanning rate and accuracy range. This will result in an accurate method of assessing existing bridges, providing safer assessments and reducing unnecessary repairs. The finite element package Abaqus has been used to develop a model of the existing underpass bridge at the Loughbrickland exit on the A1 in Northern Ireland. The FE model has been used to locate the sensors in the critical locations; this has been done under numerous loading conditions while also taking into consideration varying transverse position of the axle.

KEY WORDS: Bridge Weigh-in-Motion, Fibre optic sensors, Structural Health Monitoring

1 INTRODUCTION

Conventional bridge health monitoring systems can improve knowledge of the bridge capacity but give no information on the causes of increased stresses. The solution to the bridge safety problem is twofold: control of overloaded trucks and safety assessment/monitoring of bridges. The concept of in Bridge Weigh-in-Motion (B-WiM) is to establish real axle loads, without interruption to traffic flow and in the case of this research to extend the life of concrete bridges in the UK and Ireland [1]. In order to achieve this, a very high scanning rate of the sensors, is required to capture the peak strains induced in the bridge structure by the moving vehicles. Additionally, the sensors can measure the velocity and axle configuration of the vehicle by applying a suitable algorithm in the post processing of the measurements from the data acquisition. This system has the potential to provide an inexpensive portable method of rapidly retrieving unbiased traffic information. The deployment of such a system would be desirable as it would enable the collection of data for planning and economic surveys and would be of great benefit to the network asset owners [2]. This research explores beyond the current state of the art technology to recommend concepts and potential additional sensor technology which would overcome the existing limitations of the current technology. Expanded use of alternative sensor technology will be considered coupled with the concepts for solution algorithms, data pattern recognition and information processing.

The research work reported in this paper presents an innovative approach to amplify the strain signal using fibre optic strain sensors which have been developed using Fibre Bragg Grating (FBG) technology. Their performance was examined and compared with the performance of more conventional electric resistant strain (ERS) sensors and vibrating wire (VW) strain sensor. The overall aim of this research programme is to detect strains and related changes in the bridge structure caused by an axle moving at speed. This experimental study investigated strain transfer mechanisms and amplification techniques. Amplification was required to improve the accuracy below one microstrain.($\mu\varepsilon$) A typical medium span reinforced concrete bridge will show very low levels of strain under typical axle load and the B-WiM algorithms require a distinct change in strain to accurately determine axle weights. Additionally, an accurate sensor network with the capability of high scanning rates, can provide a 'early warning' to damage and allow for the planning and implementation of remedial action to the structure at a point where it is less expensive and invasive than when visible surface signs of deterioration have been observed.. Conclusions on the suitability of the fibre optic sensors for long-term structural health monitoring of reinforced concrete bridge structures have been made.

2 SENSOR SYSTEMS FOR B-WIM

2.1 Fibre Bragg Grating sensors

Tensile and compressive strains, measured at a bridge soffit can be used as a means of detecting axle position, configuration and weights using suitable post-processing as described earlier. To measure the tensile and compressive strains, FBG sensors can be adapted from other industrial monitoring applications

[3]. Previous work on the use of Fibre Bragg Grating sensors for strain measurement has been extensively documented in the literature, e.g. [4,5] and such sensors have been developed for measuring rapid, dynamic changes and long-term performance of concrete bridges and composite steel-concrete box structures [6,7] but FBG technology has not been used for sub microstrain measurements needed for accurate Bridge Weigh-in Motion under dynamic moving loads. Three types of FBG's sensors were compared, focusing on site suitability, fixing methods and accuracy. FBG1 was a non-metallic strain sensor based on FBG technology which could be quickly and easily mounted in place using a specialized two component low viscosity modified amine epoxy. The epoxy develops 90% of its cure properties at 24 hours, the full cure time is 72 hours. When fully cured the epoxy inherits a tensile strength of 31N/mm^2, tensile modulus of 6,700 N/mm^2 and a compressive strength of 80 N/mm^2. The sensor has a self-adhesive backing which holds it in place while the epoxy is injected and encapsulates the fibre thus fixing the sensor; this sensor has a gauge length of 10mm and a packaged sensor length of 20 mm. Temperature compensation is carried out using an additional temperature sensor which is attached to the structure. One temperature sensor can be used for temperature compensation of numerous strain sensors but this is not essential for B-WiM as the algorithm utilises the change in strain under a moving axle load. FBG2 had a 50 mm gauge length, it is a temperature compensated strain sensor based on FBG technology and has a packaged sensor length of 136 mm. A more accurate long-term strain measurement can be provided due to the close proximity of the individual strain and temperature FBGs in one sensor. The sensors rugged design makes it suitable for long term monitoring in harsh weather conditions, [8] and armoured cables lead from the sensors protecting the fibre cable. FBG3 has a gauge length of 250 mm and a packaged sensor length of 300 mm; it is surface mounted sensor based on FBG technology and is also internally temperature compensated. Each end of the sensor is attached to the structure via rigid brackets that are welded, doweled, epoxied, or grouted to the surface of a material or structure. The optical sensors can be multiplexed along very long lengths of fibre, are well suited to large structures and can be set accurately by placing the FBGs at pre-determined points along a configured optical sensor network. The two-fold nature of the sensor system is designed to ensure (i) a greater region (length) of coverage by the monitoring system whilst (ii) allowing a greater number of B-WiM sensors to be placed in the areas predicted to be most sensitive. In the case of B-WiM, these positions are based on peak stress areas established using finite element analysis (FEA).

2.2 ERS Sensors

Electrical resistance strain sensors with gauge lengths of, 5 mm (ERS1) and 30 mm (ERS2) were trialled, the surface was prepared as recommended [9]. As the material is strained the foil is deformed causing the electrical resistance to change, which is calibrated to the equivalent change in strain by the gauge factor (GF)

2.3 VW Sensors

Vibrating Wire sensors are surface mounted; a change in strain on the surface causes a change in tension in the wire which results in a change in the resonant frequency of oscillation of the wire. This change is calibrated to the equivalent change in strain between the fixings. If the VW is perpendicular to a crack in concrete it can be assumed that all of the strain change is caused by the cracking opening and the VW sensor is a thus measuring crack width. In this test a 100 mm sensor was used.

2.4 Data Collection and Logging

Data from the FBG, VW and ERS sensors were obtained and recorded during the progress of the series of experiments carried out and described below. Data acquisition was carried out using commercially available software and interrogation units for each of the sensor types. The scanning rate capability of the sensors is a critical factor in selecting an appropriate sensors, the data from the Phase 1 tests, as detailed below (3) was recorded at different scanning rates. The scanning rate was limited to the maximum scanning rate of the slowest sensor included in the test. Hence, the scanning rate of each sensor included in an individual test was all set the same allowing ease of comparison when considering the results.

Each testing Phase included only short term tests therefore the data from all sensors was continually monitored during the full test process.

Additionally load was recorded directly from the direct tension testing machine with its accompanying software. This ensured effective comparisons between the performance of the fibre optic sensor and conventional strain sensors.

3 EXPERIMENTAL PROGRAM

The aim of the work was to conduct a series of sequential tests in which a number of different fixing techniques, with representative conditions of a concrete bridge deck soffit, were evaluated. The bridge structure selected for this B-WiM research consisted of 27no. pre-stressed precast concrete Y4 beams and a cast in-situ concrete deck. The bridge spans 19 m and has an angle of skew of 22.7°. Accurate B-WiM requires sensors to be attached to the longitudinal members and deck soffit of the bridge structure. The beam sensors can be fixed directly to the soffit of the concrete beams. However, the bridge deck had been cast using permanent non-structural Glass Fibre Reinforced concrete (GFRC) formwork. A site survey revealed the formwork could not be removed without damage to the structural concrete deck slab. Hence, the proposed method of fixing involved attaching the sensors to a stainless steel plate which could then be fixed to the structural element. The testing phases detailed where carried out in order to determine a suitable sensor, plate geometry for amplification and fixing method.

3.1 Phase 1: Performance Comparison of sensors for B-WiM

The initial testing was aimed at providing a performance comparison between two types of FBG's, VW and ERS1 sensors and inform on the type of sensor which was most suitable for SHM for B-WIM applications. All four sensors

were fixed onto a 200 x 100 mm stainless steel plate. The test was carried out using a direct tension testing machine with a load capacity of 100 kN. Load was applied, under stroke control, at a rate of 0.01 mm/min. The scanning rate was varied but the highest scanning rate for the data acquisition of the VW was 0.2 Hz for accurate strain readings. Therefore, for comparison purposes, the scanning rate for all sensors was set the same at 0.2 Hz. The length of the temperature compensated FOS was incompatible with the maximum settings of the test rig cross-heads and affected plate clamping which resulted in some slip at an applied load of ~80 N. The loading rate was increased to 1mm/min which was sufficient to ensure full clamping of the plate and then only limited slip occurred during loading. Data acquisition/FOS interrogation was carried out using three separate systems, to enable comparison of the results for the different sensors, the time stamps for each system were synchronised.

3.2 Phase 2: FBG/ERS sensors with modified plate geometry for strain amplification

It had already been determined that a fixing plate was required in order to measure the change in strain in the concrete bridge deck under live traffic loading. The critical sensor locations were established using finite element analysis (FEA) of a full 3D model of the bridge. The results from the FEA indicate the change in strain in the bridge deck would be low even under heavy loading. The largest change in strain was 30 microstrain and less than 5 microstrain for most typical traffic loading. In order to amplify the strain at the sensor location on the plate, the area in the central region of the plate was reduced. Assuming that the change in strain in the plate is consistent, the section with the reduced area gives a higher stress and hence amplified changes in strain under a set change in load (or axle load). The following theory was used to select a suitable geometry for the plate. Considering:

$$\varepsilon = {}^{\sigma}/_{E} \quad \text{and} \quad \sigma = {}^{F}/_{A} \quad \text{then } \varepsilon = {}^{F}/_{EA} \tag{1}$$

Where E= young's modulus, σ= Stress, A= cross sectional area, a reduction in cross sectional area results in an inversely proportional increase in strain. Consider the plate shown in Fig. 1, the plate geometry was such that the cross sectional area of the central region was one third of that of the outer regions. Therefore the change in strain in the centre of the plate would be three times that of the change in strain in the outer edges of the plate (ε_1). The following theory was then applied to establish the relationship between the change in strain in the plate compared to the actual change in strain (ε_T) in the structural element (in this research the concrete bridge):

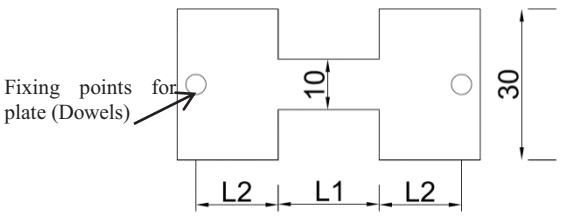


Figure 1. Geometry of plate proposed for amplification. all dimensions in mm.

Change in strain:

$$\varepsilon = {}^{\Delta L}/_{L} \text{ so } \Delta L = \varepsilon L\,, \tag{2}$$

Actual change in strain in the concrete:

$$\Delta L = \varepsilon_T(2L_2 + L_1) \tag{3}$$

Next consider the change in strain in each individual area of the plate, from (1) we know the change in strain is inversely proportional to the cross sectional area, therefore if the strain in the outer regions is ε_1 the strain in the central region is $3\varepsilon_1$:

$$\Delta L = (L_2\varepsilon_1 + L_1 3\varepsilon_1 + L_2\varepsilon_1) \text{ so } \Delta L = (2L_2 + 3L_1)\varepsilon_1 \tag{4}$$

Amplification factor:

Equating (3) & (4) $$\varepsilon_1 = \frac{\varepsilon_T(2L_2+L_1)}{(2L_2+3L_1)} \tag{5}$$

Where L1 and L2 are the lengths as shown in Fig. 1 and ΔL= change in length.

Based on this theory, a spread sheet was used to calculate the optimum geometry of the plate in order to amplify the change in strain by a factor of three. The final geometry is shown in Fig. 2 and stainless steel dowels were used to replicate the fixing to the concrete surface. The three sensors were attached, two ERS1 sensors, one attached each side of the plate to take account of bending strain and FBG1 attached to one side of the plate. The plate and sensors were tested in a similar manner to Test 1 but with a stroke control rate of 1 mm/min and a scanning rate of 5 Hz for all sensors. The scanning rate was limited by the data acquisition for the ERS sensors as the FBG sensors can be interrogated at 2000 Hz.

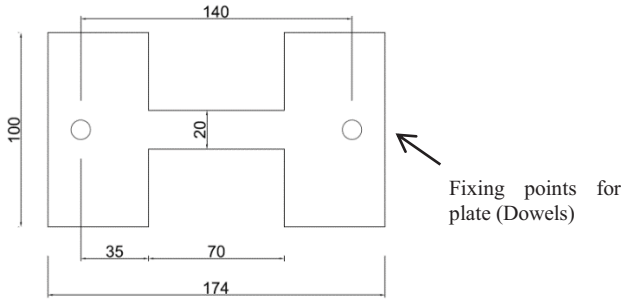


Figure 2. Geometry of Dogbone plate, Phase 2, (mm)

3.3 Phase 3:ERS sensors with further modified plate geometry and fixed to an equivalent concrete bridge surface.

Following the results of Phase 2 (as discussed in more detail in section 4), the geometry of the plate was modified to reduce the effect of stress concentration. This test was also carried out to determine a suitable method of fixing the steel plate to a concrete structure. The plate was mounted to a concrete section which represented a real concrete bridge. Hence, allowing a comparison to be made between the actual strain in the concrete and the amplified strain in the central region of the plate. This test used ERS sensors as it is more cost effective in testing the fixing method as a high scanning rate was not required. ERS1 sensors were attached to both sides of the plate and one ERS2

sensor was attached to the surface of a 3.5 m long by 200 mm deep by 120 mm wide reinforced concrete beam directly below the plate (see Fig. 3).

The plate was fixed to the bottom surface of the concrete beam at the midspan, the position of maximum bending moment. Dowels were welded to the plate to provide a fixing mechanism. A two-part thixotropic epoxy adhesive was used to fix the 10 mm diameter dowels which were embedded in 12mm diameter holes to allow for a 1 mm adhesive line around the dowels. The plate was positioned 5 mm from the surface of the concrete giving 40mm embedment length.

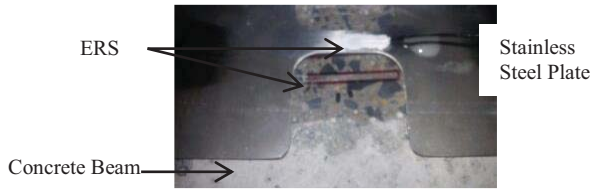


Figure. 3. Phase 3: testing layout

The concrete beam was simply supported under the test rig and load was applied at the third spans to enable pure flexure in the central region of the beam, as shown in Fig. 4. Load was applied incrementally using an accurately calibrated 600 kN capacity hydraulic actuator. Load was applied in 1 kN increments under load control with strain readings recorded at each increment of load. A maximum load of 8 kN was applied to the beam. The test was repeated three times.

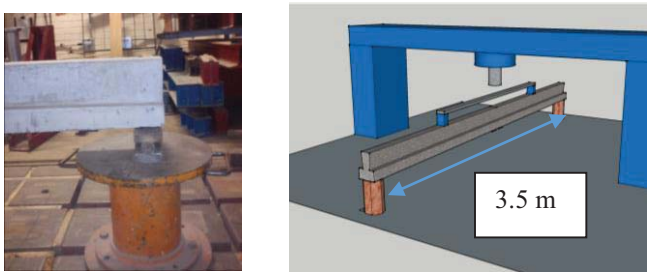


Figure. 4. Phase 3: Load test arrangement

A 3D Finite Element analysis (FEA) of the test arrangement was carried out to predict the behaviour of the elements in the test arrangement. The concrete beam was modelled using C3D8R 8-node linear brick elements. The bond between the steel dowel and the concrete beam was modelled using a tie constraint(ABAQUS n.d.). The elements were meshed so the nodes on the beam match those on the dowel as closly as possible. The modulus of elasticity of the concrete was defined as 26.6 x 10^3 N/mm^2 with a density of 2.3 x 10^{-9} t/mm^3. The steel was assigned a modulus of elasticity of 205 x 10^3 N /mm^2, a density of 2.3 x 10^{-9} t/mm^3

In order to save on computational time the planes of symmetry in the elements are exploited and only one quarter of the actual structure is modelled. As the model is symmetrical about two planes a quarter model was developed and the proper restraints are applied at the symmetry planes.

3.4 Phase 4: Plate sensitivity analysis and testing

Due to further problems with stress concentration in the central region of the plate caused by the use of a single dowel for fixing, the amplification of the strain signal was low, as discussed in more detail in the results section. Hence, an additional FEA was then required to determine the effect fixing the plate to the beam via two dowels at either end of the plate. This was done to attempt to utilise the full cross-sectional area of the wider section of the plate to ensure maximum amplification at the narrow section. The FEA was then used to carry out a sensitivity analysis to determine most efficient and practical plate geometry. The following factors were considered, the dowel offset, the thickness of the plate, the dowel diameter and the width of the tapered area. The dowel offset refers to the distance the plate is offset from the concrete surface and all dowels had the same embedment length of 50 mm. The control values for the in the FEA predictions were; dowel diameter: 10 mm, dowel offset: 10 mm, width at centre: 10mm plate thickness: 2 mm. The variables were dowel diameter: 5-20 mm, dowel offset: 10-100 mm, width at centre: 10-85 mm plate thickness: 1-10 mm, with only one parameter changing at any one time. Six stainless steel plates were fabricated, which were fixed to concrete section in a similar manner as in phase 3, the test was carried out to validate the FEA predictions. Table 1 details the variables in this phase of testing. As the magnification of strain is related to the difference in the cross-sectional areas, Plate 5 was fabricated with a tapered thickness as shown in Fig. 5.

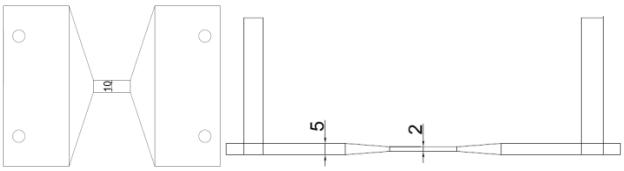


Figure. 5. Phase 4: Geometry of Plate 5, all dimensions in mm

Table 1 Phase 4: Plate Geometry

Test no.	*1*		*2*		*3*	
Plate no.	**1**	**2**	**3**	**4**	**5**	**6**
Thickness (mm)	2	2	5	5	5 to 2*	8
Dowel Length (mm)	60	100	60	100	100	100
Plate offset from concrete (mm)	10	50	10	50	50	50

**tapered thickness in order to further reduce ratio of cross sectional area,*

4 RESULTS OF TEST PHASES 1 TO 4

4.1 Phase 1: Performance Comparison of sensors for B-WiM

For accurate B-WiM predictions, a minimum scanning rate of 200 Hz is required but more typically about 500 Hz. In these tests, VW, FBG and ERS sensors were tested in direct tension on a steel plate at various scanning rates. The results in Fig. 6 show that the sensors gave reasonably accurate predictions of the tensile strain, when the strain between the cross-heads (equivalent to the strain in a concrete deck), or 'test-rig' strain was 42 με, the strains in FBG1, FBG2, VW and ERS1 were 59

με, 25 με, 66 με and 61με respectively. However, the results indicate bending occurred in the plate which increased the tensile strain on one face and decreased the tensile strain on the other face. The VW debonded at a strain value of 75 με, this coupled with a maximum accurate scanning rate 0.2 Hz for the VW data acquisition deems this type of sensor unsuitable for dynamic strain measurement and B-WiM applications.

The axial tensile strain can be determined from the average of FBG1 and FBG2 which will remove the strain due to bending. This showed that both sensor types gave reasonably good accuracy when compared to the data acquisition from the tension testing machine, which has an accuracy of +-1microstrain. At a 'test-rig' strain of 71 με, the strain averaged from FBG1 and FBG2 was 73 με compared with the average strain from ERS1 and FBG2 which was 74 με.

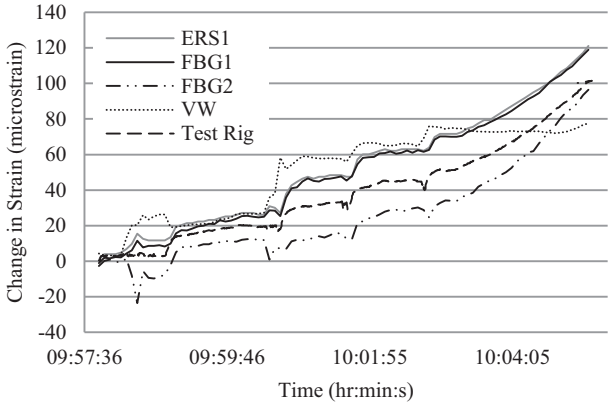


Figure 6. Phase 1: Strain vs. time results at 0.2Hz scanning rate for three types of sensor

In order to further compare the accuracy of the ERS and FBG's, the test was repeated without the VW and the sensors interrogated at a higher scanning of 5 Hz. However when the results were averaged to present only the axial strain, the FBG provided better accuracy, at a 'test-rig' strain of 64 με, the strain averaged from FBG1 and FBG2 was 64 με compared with the average strain from ERS1 and FBG2 which was 60 με.

. Some of the advantages of using the FOS are they can be multiplexed, this means the possibility of hundreds of sensors along the length of a single fibre. The equivalent for ERS would be then 100s of wires being run back to a single interrogation point, which can lead to potential complications and confusion, again for an inexperienced user. Should an issue arise with the hardware interrogating the equipment for FOS this can be easily replaced with minimal setup, once the configuration file is developed the interrogating unit can be replaced in seconds which is not the case for ERS.

The environmental conditions on site also needed to be considered when choosing an appropriate sensor, the damp weather conditions in the UK and Ireland require a durable sensor, ERS have the potential to corrode, as they are metallic, this is not an issue for FOS which are silica based. ERS have the advantage of being easily repaired if they are fractured on site, however with the increasing technology in portable splicers this is becoming less of an issue for FOS. FOS also allow for connectors to be added between each sensor so if one sensor in a series is damaged it can easily be replaced. Multiplexing options for FOS include wavelength multiplexing, time division multiplexing (TDM), frequency division multiplexing (FDM) etc, which are tried and tested and allow for this use of multiple sensors per fibre FOS have been used in real-life conditions over multiple kilometres of fibre,

A further issue encountered in relation to the ERS sensors was the difficulty in fixing the sensor to the surface compared with the ease of fixing the packaged non-metallic optical sensor. There is not the same need for surface preparation and thereby the skill of the person installing them has less of an impact on the potential accuracy of the results obtained.

In order to install the B-WiM system on site road closures were required these closures were costly and disruptive and it was vital that the chosen system could be easily and quickly installed so as to provide minimum disruption to the road network. Therefore, ERS sensors with the current data acquisition were not deemed suitable for the practical development of a full B-WIM system. However, the results show ERS provide accurate results and therefore they were used for subsequent tests for comparing fixing methods for the plate and for the development of a plate for geometry for maximum strain amplification The use of FBG's for all tests would have substantially increased to cost of the project and as the tests were carried out in a controlled environment and the sensors were not to be exposed to harsh weather conditions durability was not an issue. As well as this the time allowed for accurately fixing the sensors was not governed by road closures and multiplexing would be of little benefit as only a small number of sensors were required.,

FBG1 was found to be the most suitable as it was easily mounted and quick to adhere to both steel and concrete surfaces. FBG2 has a higher gauge length and an overall packaged length of 136 mm which made it impractical for fixing directly at the concrete slab soffit. Additionally, to enable amplification, the plate would be much larger and could lead to lower accuracy in detecting the absolute peak strain under a moving axle load as the strain would increase over a longer period of time.

4.2 Phase 2: FBG/ERS sensors with modified plate geometry for strain amplification.

As discussed in section 3, the geometry of the plate was adjusted in order to amplify the strain in the central region of the plate compared to that in the concrete bridge deck. FBG and ERS sensors were used and strains were recorded in a similar way to Phase 1 with a scanning rate of 5 Hz. The results, indicate strain amplification was not successful. When the strain between the cross-heads (equivalent to the strain in a concrete deck), or 'test-rig' strain was 87 με, the strains in FBG1, ERS1 and ERS2 were 104 με, 74 με and 67 με respectively. Additionally, when taking into account the bending in the plate, ERS1 appears to be inaccurate and corroborates the findings in Phase 1. An FEA of the test configuration was carried out and it showed that a stress concentration occurred at the corners of the plate due to the sharp change in cross-section. Hence, the plate geometry was adjusted to give a smoother transition when reducing cross sectional area.

4.3 *Phase 3: ERS sensors with further modified plate geometry and fixed to an equivalent concrete bridge surface.*

As discussed in section 3, the geometry of the plate was further adjusted to enable amplification of strain in the central region of the plate and the plate was mounted to an equivalent concrete bridge surface. The results in Fig. 7 show that the plate did not provide the expected amplification. For example, at an applied load of 8 kN, the change in strain measured at the tension face of the concrete beam was 121 με and change in strain measured in the plate, was 156 με, hence providing an amplification factor of 1.29.

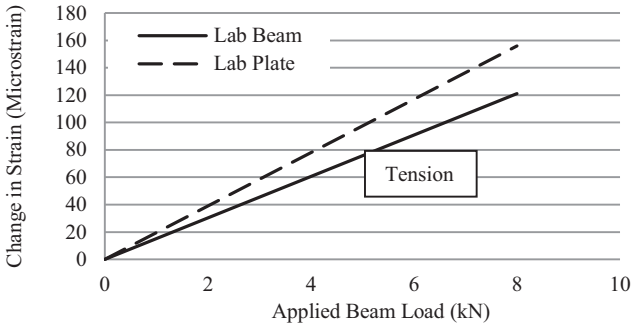


Figure. 7. Phase 3: Change in Strain vs. Applied Load (laboratory)

The results from the FEA corroborate the actual test results, at an applied FEA load of 8 kN the predicted change in strain in the plate was 184 με and the predicted change in strain in the concrete was 144 με equating to an amplification factor of 1.28 for B-WiM applications, a factor of at least 2 was desirable. It was determined the issue with the stress concentration in the central region of the plate caused by the use of a single dowel for fixing, the amplification of the strain signal was low. Hence, an additional FEA was then required to determine the effect fixing the plate to the beam via two dowels at either end of the plate. This was done to attempt to utilise the full cross-sectional area of the wider section of the plate to ensure maximum amplification at the narrow section. This provided a significantly improved strain distribution and hence indicated that it was more effective to have a double dowel system.

4.4 *Phase 4: Plate sensitivity analysis and testing*

The findings of the FE sensitivity analysis indicated the optimum plate thickness was 8 mm. However, the 5 mm gives similar results and was far most cost effective. Also, the shorter the offset the more amplification occurred and this was tested in the laboratory trials. The bolt diameter had little effect and 10mm was used as a practical and economical solution. The optimum width in the central region was 10 mm and this could not be reduced further due to the sensor geometry.

4.4.1 Phase 4: Test 1 Results

Phase 4 tests involved the testing of 6 plates with variables as given in Table 1. In order to compare the strain amplification in Plates 1 and 2, the change in strain recorded by the plate sensors is shown in Fig. 8. Test 1 showed that the shorter dowel length gave a higher amplification of strain and confirmed the predictions from the FEA sensitivity analysis. When a load of 29 kN was applied, the measured changes in strain from the Plate sensors were -16 με and -8 με in Plate 1 and 2 respectively. However, it was found that by removing the bending strains, a reduced amplification was achieved. Hence by including the bending strain a higher amplification of strain can be achieved provided the sensor system is correctly calibrated. In practice, when using this sensor technology for B-WiM, the calibration will be under a known axle load and gross vehicle weight. This amplified reference strain can then be used to calculate unknown axle loads from the subsequent recorded peak strains. Therefore, if the bending strain is utilised to amplify the strain signal, the system is calibrated using this change in strain for each peak in strain under the crossing axle load.

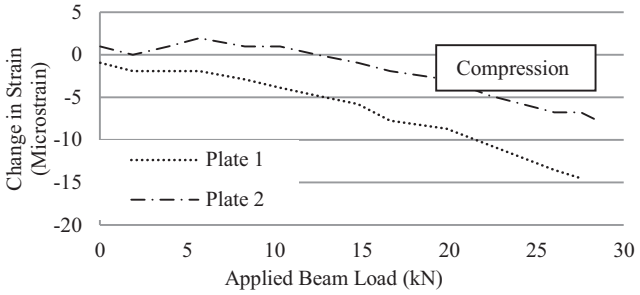


Figure 8. Phase 4- Test 1: Comparison of Plate sensors

4.4.2 Phase 4 : Test 2 Results

Test 2 confirmed that greater amplification was achieved when the plate was located closer to the surface of the concrete; the shorter dowel length gave a higher amplification of strain and confirmed the predictions from the FEA. When a load of 29 kN was applied, the measured change in strain from the Plate sensors on Plates 3 & 4 were -50 με and -29 με respectively. Therefore, the optimum location of the plate was as close as possible to the surface of the concrete structure whilst allowing for curvature of the concrete section under live traffic loading. The results from Test 1 & 2 were used to determine a suitable thickness of plate between 2 mm & 5 mm. At an applied load of 29 kN, the measured change in strain (from the Plate sensors) was -16 με, - 8 με, -50 με and -29 με for Plates 1, 2, 3 and 4 respectively (Fig. 9). This indicated that Plate 3 gave the highest amplification of strain as the strain in the concrete surface was similar for all tests at the same applied load.

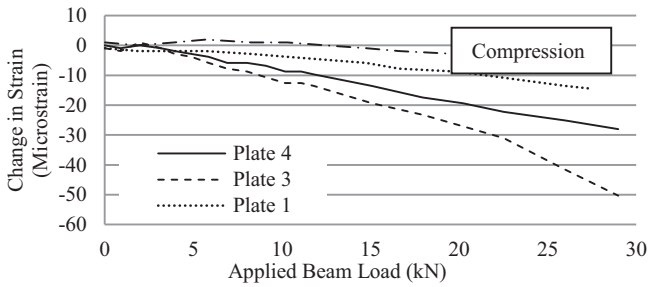


Figure 9. Phase 4 - Tests 1 & 2: Comparison of Plates 1 to 4

4.4.3 Phase 4 Test 3 Results

Tests 1 & 2 showed that the most suitable fixing for the plate was at a minimum offset. However, the plates in this

test had been fabricated and embedded in the concrete prior to completing Tests 1 & 2 and the offset for Plates 4 & 5 was 50 mm. Test 3 was carried out to provide a further comparison of the effect of plate thickness by testing plates 5 & 6. A maximum load of 12 kN was applied as this was below the concrete tensile cracking load in beam 2. The change in strain at the concrete surface was measured using FBG and ERS sensors. At an applied load of 12 kN, the ERS and FBG sensors measured a change in strain of 40 με and 39 με respectively) and there was no evidence of debonding in these sensors. Fig. 10 shows the change in strain for all plates with an offset of 50 mm to determine the most effective plate thickness for strain amplification. This test confirmed that the optimum thickness for the plate was 5 mm. However, the strain readings show that the plate did not amplify the induced strain at the concrete surface but the tapered plate (in plan) does give higher strain values than a straight plate. At an applied load of 12 kN, the maximum change in strain recorded by the Plate senor was 10 με compared with a concrete surface strain of 40 με recorded by the FGB. Further FEA showed that this was due to the fixing method as the dowels may not provide adequate strain transfer and the method of fixing was adjusted for site applications. Fig. 11, shows the adapted plate where the blocks were fixed directly to the concrete surface giving an offset of 10 mm and Plate 3 geometry was used to give maximum strain.

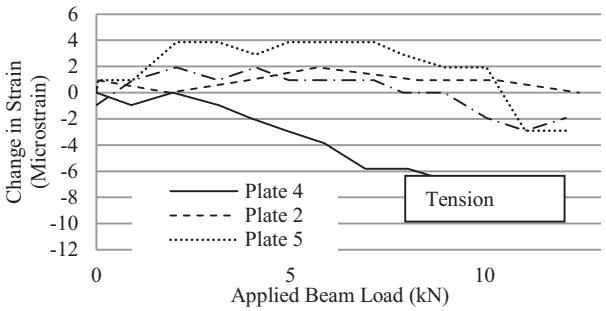


Figure 10. Phase 4: Comparison of Plate sensors from all tests.

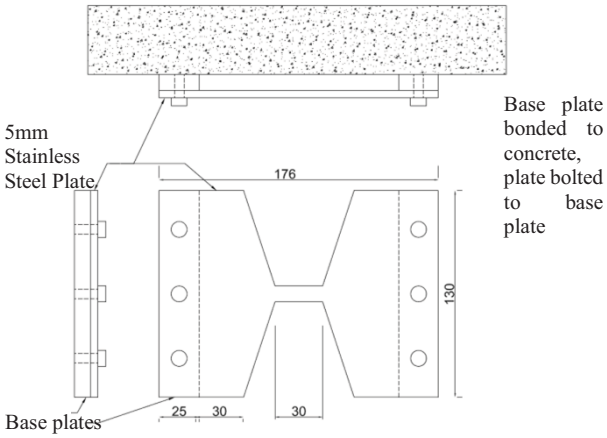


Figure 11. Geometry of final proposed plate.

5 INSTALLATION AT BRIDGE STRUCTURE

The optimum plate geometry as determined from Phase 4 was trialled on a real bridge site to test the amplification in strain under live traffic loading. The plate was instrumented with an FBG1 sensor and fixed to the underside of the longitudinal concrete beam. Another FBG1 sensor was fixed directly to the concrete surface of the beam. Both sensors were orientated to measure a change in longitudinal strain in the beam as shown in Fig.12. The base plates were fixed to the concrete beam using a two part filled epoxy adhesive system, both surfaces were cleaned and prepared to remove any grease or lose dirt. The surface of the base plate was roughened to ensure a strong grip was obtained.

The data shown in Fig. 13 confirms that strain amplification was successful under live axle loading. The sensor measuring strain directly from the surface of the beam recorded a change in strain of 11 με and the sensor fixed to the plate measured a change in strain of 20 με under the same load. The vehicle in this example was a typical 5 axle heavy good vehicle and the results show an amplification factor of ~2. This means that lower axle loads can be measured with increased accuracy than by measuring the direct strain in the concrete surface.



Figure 12. Arrangement of sensor installed for site trial.

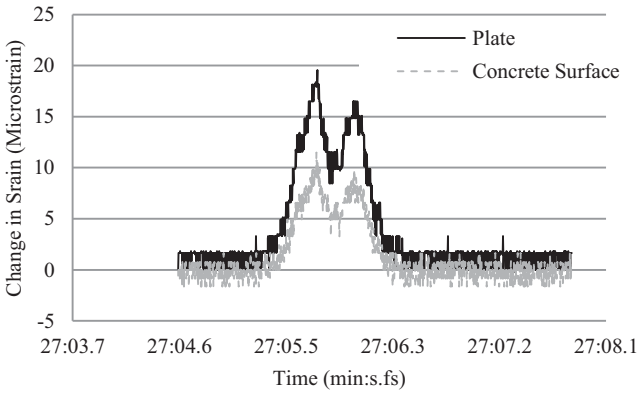


Figure. 13. Strain amplification obtained in field trial

6 DISCUSSION AND CONCLUSIONS

The overall aim of this research was to find as sensor suitable for use in field trials of a new generation B-WiM system. A series of sequential test programmes have been carried out to determine the most suitable type of sensor and then develop a suite of sensors for B-WiM applications. ERS, VW and FBG-based fibre optic sensors and different fixing techniques were compared.

Phase 1 was a performance comparison of the sensors types and showed that the FBG based sensors to be the most suitable sensor to provide accurate readings at a high scanning rate. The reasons for this are principally associated with capability of existing interrogation units, which can provide scanning rates up to 2000 Hz. The maximum scanning rate for the VW sensors was 0.2 Hz which made them unsuitable for B-WiM application. In a field environment it is important that the system can be easily and accurately installed, hence difficulties associated with the method of attachment of the ERS sensors regarded them as unsuitable for the proposed system. By contrast, the FBG sensors were quick and easy to install and demonstrated the ability to measure change in strain at high scanning rates. This gave confidence in the sensor type and subsequently the FBG1 sensor type was determined as the most suitable due to its size and ease of fixing. ERS sensors were found to provide results which corresponded well with those obtained from the FBG sensors. As the limiting factor of the ERS sensors was the scanning rate they were suitable for testing fixing methods and strain amplification at low scanning rates. Phase 2 testing aided in the development of a modified plate which could be used as a means of fixing the sensors to the deck soffit and amplifying the strain readings. The FEA indicated that the geometry of the plate resulted in a stress concentration in small regions of the plate which reduced the strain amplification at the sensor location.

The actual amplification was truly quantified in phase 3 testing; although some amplification was achieved it did not correspond to the amplification anticipated from the theory used to design the plate. The results whilst an improvement from the previous Phase 2 tests did not correlate with the predicted amplification. It was evident from the predicted strain distribution of a further FEA that, the full geometry of the plate was not utilised. The FEA sensitivity analysis worked well to provide an indication to a suitable fixing plate the results from this were then corroborated in the laboratory trials. Test 1 & 2 of Phase four was carried out using only ERS sensors. However even in the final Phase of testing an issue with strain transfer to the plate still existed, this loss of strain transfer is thought to be due to the use of dowels as a fixing mechanism.

The final plate design was installed at the bridge site with an adjusted fixing method to provide improved strain transfer between the concrete element and the instrumented plate. The results from live traffic loading at the bridge structure in Fig. 16 show successful strain amplification was achieved. The figure shows the strain was almost doubled; hence the sensor is sensitive to a 0.5 microstrain change making it capable of detecting light axle loads. One issue for further investigation is the possibility of further strain amplification and hence increased sensitivity to lower changed in strain.

In summary, the work carried out in four sequential test series has shown the value of the FBG-based sensors and formed the basis for the design of a fixing plate for the sensors which has been proved to provide strain amplification for monitoring both tensile and compressive strains for applications of this type. On-going research is aimed at evaluating and optimizing the plate design and the overall sensor system.

REFERENCES

[1] J Kalin, A Žnidarič, I Lavrič, Practical Implementation of Nothing-On-The- Road Bridge Weigh-In-Motion System Practical Implementation Of Nothing-On-The- Road Bridge Weigh-In-Motion System. *Proceedings: 9th International Symposium for Road Transport Technology*, Penn State State College, Pennsylvania, USA, 2006.

[2] T Deesomsuk, T Pinkaew, Effectiveness of Vehicle Weight Estimation from Bridge Weigh-in-Motion. *Advances in Civil Engineering*, vol. 2009, Article ID 312034, 13 pages, 2009. doi:10.1155/2009/312034, 2009

[3] K T V Grattan and T Sun, Fiber optic sensor technology: an overview, *Sensors and Actuators* 82 40–61, 2000

[4] Y M Gebremichael, W Li, B T Meggitt, W J O Boyle, K T V Grattan, B McKinley, L F Boswell, K A Aarnes, S E Aasen, B Tynes, Y Fonjallaz and T Triantafillou, A Field Deployable, Multiplexed Bragg Grating Sensor System Used in an Extensive Highway Bridge Monitoring Evaluation Tests, *IEEE Sensors Journal*, Volume 5, No. 3, 2005

[5] J R Casas and P J S Cruz, Fiber optic sensors for bridge monitoring, *Journal of Bridge Engineering* (December), 2003

[6] E Rivera, D J Thomson and D Polyzois, Structural Health Monitoring of Composite Poles Using Fiber Optic Sensors, Proceedings of the 2002 *IEEE Canadian Conference On Electrical & Computer Engineering*, IEEE, 2002

[7] D Inaudi, Overview of 40 bridge structural health monitoring projects, *International bridge conference*, IBC, 2010

[8] R M Measures, Structural Monitoring with Fiber Optic Technology, Academic Press, 2001

[9] M Lydon , S Taylor , C Doherty, S Grattan, P Camon, Structural monitoring of the restoration of Titanic's Dry Dock, *Civil Structural Health Monitoring (CSHM-4): SHM systems supporting extension of the structures' service life.* Vol. 1 Berlin, 2012.

ACKNOWLEDGMENT

The authors would like to thank Prof E O Brien and Mr. K. McDonald for their advice and support in this work.

Next generation Structural Health Monitoring using Wireless Sensor Network Technology

Brendan O'Flynn[1], Holger Wörsching[2], David Boyle[3]
[1]Tyndall National Institute, University College Cork, Cork, Ireland
[2]Solexperts. Mettlenbachstrasse 25, 8617 Mönchaltorf, Switzerland
[3]Dept. of Electrical and Electronic Engineering, Imperial College London, UK
email: brendan.oflynn@tyndall.ie; holger.woersching@solexperts.com; david.boyle@imperial.ac.uk

ABSTRACT: As wireless sensor network (WSN) technology matures, many applications are emerging that demand systems to operate autonomously for decades or more. The FP7 Green sEnsor NEtworks for Structural monItoring (GENESI) project developed a new generation of "green" wireless sensor networks, which can be embedded in civil infrastructures at the time of construction, and continue to provide monitoring and control capabilities for the structures' lifetime. The project developed and deployed a number of technologies that contribute to a new generation of wirelessly networked microsystems for industrial applications. A combination of state-of-the-art low- power processing and communication components with a variety of heterogeneous structural health monitoring sensors (e.g. strain gauges, displacement transducers, inclinometers, pressure sensors, temperature sensors, moisture sensors, etc.) and a smart energy system, in tandem with software advances, have contributed to delivering significant improvements over the current generation of WSN and SHM systems. Energy is scavenged from the environment by a multi-source energy harvester, complemented by a variety of local storage options, which may be supplemented with a small hydrogen fuel cell. Testing of the overall system in a real deployment was undertaken using two test-beds (a Metro Line excavation in Rome, and cable-stayed bridge construction project in Switzerland). This paper presents an overview of the technology developed, and showcases its application in a major infrastructure project: the *Pont de la Poya* cable-stayed bridge in Fribourg, Switzerland. Complementary technology was developed, such as a deployment tool for simplified in field hardware commissioning (i.e. dynamic firmware synthesis and installation), also providing network management and reprogramming capabilities. Critical parameters, indicative of the structural integrity of the infrastructure, are periodically sampled and transmitted (in real time) to a web-based visualisation platform. The bridge has been monitored by the GENESI system since construction began, and it is expected to continue delivering structural integrity information throughout the bridge's operational lifetime.

KEY WORDS: Structural Health Monitoring, Wireless Sensor Networks, Cyber-physical Systems.

1 INTRODUCTION

Autonomous, wireless structural health monitoring (SHM) for civil engineering structures is a growing market with significant potential for economic impact. This is predicated on increased value and economic relevance to new infrastructure constructions. Simultaneously, existing constructions are kept operational for longer periods, where maintenance and repair costs are required to be kept as low as possible during the lifetime of the infrastructure. Furthermore, new projects in urban areas are often constructed in close proximity to existing infrastructure, which implies stricter and more complex safety requirements.

New sensing technologies, better data acquisition systems, more sophisticated data transmission and data management are some of the driving forces behind the growing trend towards autonomous SHM as part of the management process in the monitoring of infrastructure throughout its lifetime – from the construction phase through to end-of-life and decommissioning.

1.1 Structural Health Monitoring

Civil engineering structures are an integral part of daily life. In particular traffic routes, rail and road, bridges as well as buildings in urban areas are of high economic value to the public. The OECD estimates the sum for infrastructure investments worldwide, to 2030, at 70,000bn USD. SHM is the process method used to observe the condition of infrastructure and structural systems to detect changes in material conditions and physical properties over time.

The SHM process involves the observation of a system over extended periods, monitoring a range of parameters and identifying any changes in those parameter values. This can be done by a combination of optical inspections, by taking samples and tests in laboratories (e.g. concrete), by field tests and increasingly the taking of regular measurements with various types of electrical sensors (displacement, strain, tilt, etc.).

SHM is important during the construction of new structures as well as during their operational lifetime. It can reduce the risk of significant failures by detecting changes in structures' physical integrity. These may be indicative that additional checks or repair measures are required. SHM can help to optimize overall Risk Management (RM, e.g. Figure 1), where timely alerts can lead to preventative maintenance, thus leading to reduced overall cost, and ensuring citizen safety.

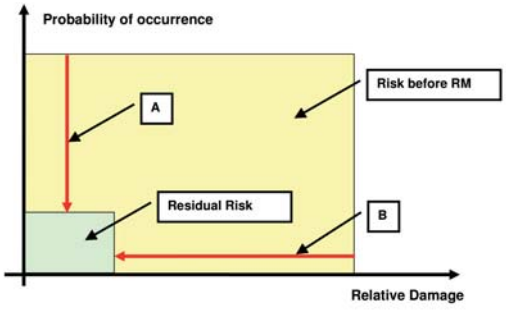


Figure 1. SHM contributes to reducing Residual Risk.



Figure 2. Bridge collapse in Minneapolis, August 2007[1].

1.2 The Importance of SHM

One of the most tragic and well-known examples in recent years is the collapse of the Mississippi River Bridge in Minneapolis in 2007, when 13 people were killed. The collapse was caused by the sudden failure of under-sized and corroded gusset plates. Contributing to that design, or construction error was the fact that additional concrete was an increased dead load after rebuilding measures. This, combined with an insufficient check of safety functions and bridge deformation [1], resulted in catastrophic failure of the system.

The impending collapse of the bridge could have been identified, and possibly prevented, using an early warning alert. This would have been achievable if the strains and deformations of the supporting elements of the bridge had been monitored regularly. This could have allowed repair actions to be taken, e.g. the improvement of the stability of the construction, before it became a critical situation. In addition, with an automated SHM system *in situ*, at least traffic could have been stopped before the collapse. Thus, loss of life could have been prevented, and repair costs minimised.

2 GENESI TECHNOLOGY

Green sEnsor NEtworks for Structural monItoring (GENESI) is a recently developed autonomous wireless data acquisition system for SHM and monitoring the effects of natural risks (e.g. landslides) [2, 3]. It was a collaborative project funded by the European Commission under the Seventh Framework Programme.

With partners from two leading international industrial SHM practitioners and several academic partners, the system was designed to serve companies and authorities as the most modern, flexible and economically viable automated SHM system.

Integrated microsystems combining computation, energy harvesting, and wireless transceivers were designed to accommodate interfaces to a range of analogue and digital sensor types [2, 4]. Given the rugged nature of the deployment environment, miniaturization of the system was ignored, as robust connectors and packaging are required for deployment in the field. An example of the final prototype deployed is shown in Figure 3.

Wireless networking allows for flexible installation and modification (e.g. extending the network to included additional nodes, or dynamically adapting to fewer networked

[1] Image courtesy of Mike Wills under CC BY-SA 2.0

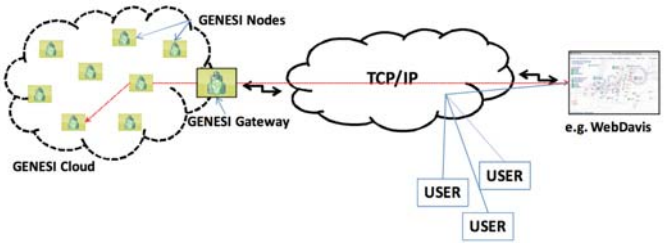


Figure 3. Conceptual Architecture of a GENESI Network.

nodes) [5]. The system was designed to monitor a structure, and it's immediate environment, for the full lifecycle, i.e. pre-, during, and post-construction. An objective was to achieve monitoring capabilities approaching the operational lifetime of the structure (i.e. decades, or more), by leveraging multi-source energy harvesting techniques, multiple energy storage facilities, low-power electronics, networking protocols and allowing adaptive, and reconfigurable, sampling and reporting intervals depending upon the criticality of the situation. In this manner, it may be achievable to detect irregular patterns of behaviour in the system, and its environment, efficiently and over a longer term than has been previously achieved.

2.1 GENESI Operation

The GENESI system operates by communicating sensor readings to a back end storage system. It achieves this by periodically sampling sensors connected to each device before wirelessly transmitting the data across the network towards a gateway device. The gateway device collects and formats the sensor readings, and transmits the data to a networked server, over which the data may be visualised using a web application. In the first instance, and for the purposes of demonstration, a script, implementing FTP was used to demonstrate the end-to-end connection (periodically transferring formatted CSV). For the purposes of demonstration, WebDavis (a proprietary web-enabled visualisation tool that operates over the database) allows authorised users to visualise and explore the data. The conceptual architecture of the system and its operation is illustrated in Figure 3.

2.2 GENESI Hardware

A modular design approach was taken in the development of the GENESI hardware. Three distinct architectural layers, namely the sensor, main and power layers, were used to facilitate concurrent development. The reference high-level architecture is shown in Figure 4, and the initial prototype (each layer implemented as a discrete PCB with appropriate physical connectors) is shown in Figure 5.

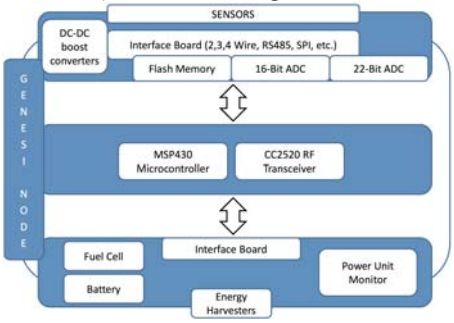


Figure 4. GENESI Hardware Architecture.



Figure 5. First GENESI Hardware Prototype [2].

2.3 Energy Harvesting: the GENESI Smart Power Unit

Long term operational SHM requires extending deployment lifetime by many years over what was traditionally possible [2]. One of the most challenging problems faced in WSNs is energy consumption. When a device has depleted its energy storage, it can no longer execute its function unless the energy storage is replenished, or becomes dynamically ambient-available. Communication above all else was traditionally considered to be the primary energy consumer in wireless networks. In SHM systems that integrate trusted sensors, this is no true in some cases [4]. Therefore, finding a solution to the energy problem is even more important than in traditional WSNs predicated on cheap sensors.

Figure 6 shows the architecture of the GENESI Smart Power Unit (SPU) designed to meet the energy requirements for the system [3]. Considering the need for flexibility in the field, the design included the appropriate conditioning circuitry to accommodate numerous harvesters and storage devices. Solar and wind harvesting are possible, where storage is provided by Li-Ion battery and supercapacitors. An interface was also constructed to allow interfacing with a hydrogen fuel cell, which could be used to replenish storage up to 4 times during critical times where transmission requirements are high and scavenging impossible.

The SPU design includes a low-power (TI MSP430) microcontroller that is primarily used for managing the selection of the appropriate supply source and harvester, based on the implementation of Maximum Power Point Tracking (MPPT) algorithms for each. This allows support for dynamic changes in operating frequency, and thus minimum achievable duty cycle.

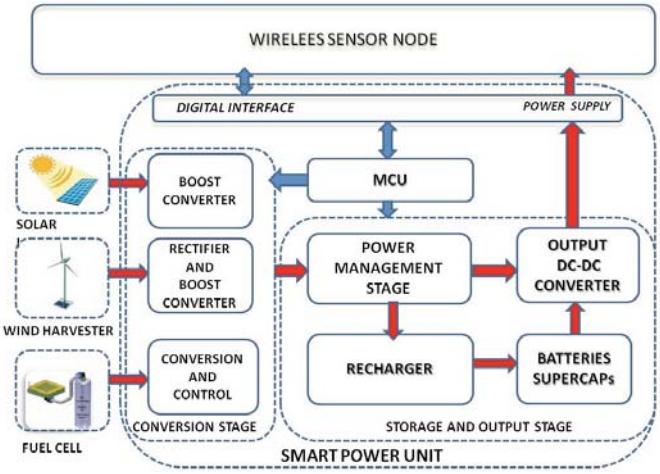


Figure 6. GENESI Hardware Prototype [3].

3 SHM AT 'PONT DE LA POYA'

The *Pont de la Poya* bridge is a large suspension bridge that underwent construction between 2009 and 2013 to bypass (for road traffic) the historic city of Fribourg, Switzerland. The overall length of the bypass is approximately 1.5 km, of which 300 m is a tunnel and 850 m is the bridge. The bridge structure spans the River Saane, passing above at an average height of 70 m above the valley floor. It is based on 10 pillars, and has two pylons that reach a maximum height of 110 m. The distance between the pylons is 196 m.

The prototype GENESI networks were installed at *Pont de la Poya* in 2012–2013. The following parameters were sampled during the construction phase, and may continue to be periodically sampled during the operational phase:

- Strains in auxiliary stiff bars for the tunnel construction (excavation pit)
- Inclination of the pylons and pillars
- Bearing displacements (e.g. due to temperature variations)
- Environmental parameters: temperature, wind, air pressure, ground water levels and soil moisture

The network can easily be extended to include additional sensors to accommodate unforeseen monitoring requirements and additional use cases.

3.1 Deployment: Software and Networking

Monitoring *Pont de la Poya* using GENESI technology commenced during the construction phase of the project. A number of complementary technological advances facilitated simple and fast deployment of the hardware on the structure. Reducing the complexity of commissioning these types of systems was another key factor in the design of the overall system, whilst the use of wireless communications technology ensured that traditional cabling of SHM sensors to data-loggers was no longer required. This ensures that significant savings are made in terms of installation time, and interference with construction works (i.e. cabling).

A key advantage was the development and availability of a software tool to assist non-WSN specialists to dynamically synthesise and upload the firmware that runs on each node on the fly [5]. This means that the devices can be installed stepwise in the field, i.e. node-by-node, without the need for significant pre-configuration or embedded systems expertise.

Dynamic and autonomous network formation also allows for flexible deployment in the field. The embedded firmware for the prototype deployment was developed using TinyOS, following a substantial 'porting' effort to accommodate an incrementally performance-improved architecture comprising a recent MSP430 (F5437) MCU and CC2520 RFIC (illustrated in Figure 5). TinyOS allowed standard library implementations of dynamic network formation and discovery protocols to be used. The initial deployment at *Poya* used a standard implementation of CTP (for network formation, traffic routing and management) [6] over BoX-MAC-2 (the *de facto* TinyOS Medium Access Control protocol). One of the key factors in the decision to use TinyOS in the prototype deployment was the availability and maturity of Deluge, providing the ability to remotely and wirelessly reprogram devices in the field. Whilst TinyOS was used in the deployment, the Contiki OS has also been used during development [2].

Table 1. SHM at *Pont de la Poya* – Summary.

Element	Measurements	Purpose During Construction	Purpose during Operation
Stiff bars (in tunnel section)	Strain (VW strain gauges)	Detecting Critical Loads	Stiff bars are removed in final construction
Pylons	Inclination	Check and verify bridge behaviour. Detect critical situations due to possible construction and design faults	Detect irregular behaviour during operation, possibly caused by/after impacts (storm, earthquakes and traffic accidents). Detect deformation/bending due to aging/long term settlements.
Pillars	Inclinations	Check and verify bridge behaviour. Detect critical situations due to possible construction and design faults	Detect irregular behaviour during operation, possibly caused by/after impacts (natural and traffic accidents). Detect deformation/bending due to aging/long term settlements.
Bearings	Deformations	Not installed	Verify design values and detect irregular behaviour (e.g. due to corrosion and settlements)
Bridge Section/Carriageway	Acceleration	Not installed	Detect impacts and irregular behaviour in oscillations
All Sections	Environmental Parameters: Temperature, Wind, Air Pressure, etc.	Detect environmental influence on bridge and on sensing elements	Detect environmental influence on bridge and sensing elements



Figure 7. GENESI Node deployed at *Pont de la Poya*. External components visible include a solar energy harvester, inclination sensor and RF antenna

Figure 7 illustrates a packaged GENESI node deployed on the bridge at Poya. The electronics (i.e. PCBs) are enclosed in an appropriately IP-rated polymer enclosure. The external components include the physical sensors, the energy harvester and the antenna. The final PCB is designed for easy sensor attachment in the field using robust screw terminal blocks. In this way, cables to sensors can be easily measured and cut to allow various distances from the sensing points to the device(s). This added flexibility allows the electronics to be installed at appropriate locations, as may be required to assist RF propagation, or ensure accessibility when the sensors may become embedded (e.g. in concrete).

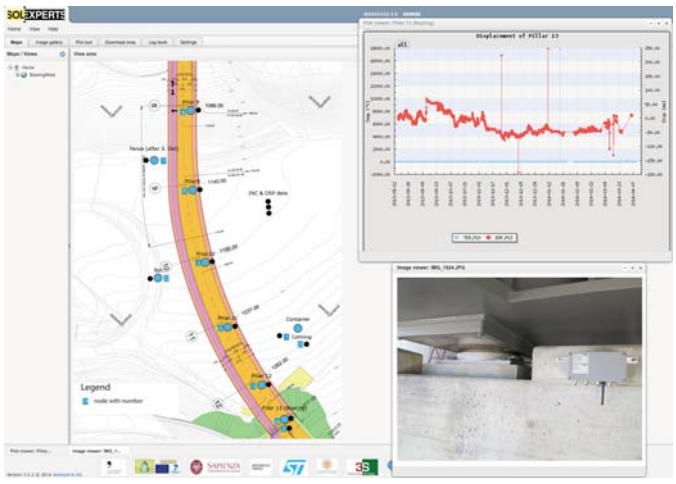


Figure 8. The GENESI Network monitoring the West Bearing at *Pont de la Poya*, visualised online using Solexperts' WebDavis tool. The inset: graph plots displacement and temperature over time; the image shows the physical device.

4 SHM DATA ANALYSIS AND VISUALISATION

4.1 Web-based Visualisation

Authorised persons have continuous access to (near) real time data from the monitoring system via the Solexperts WebDavis application (shown in Figure 8). Web-based visualisation allows remote access to the deployment from anywhere the Internet can be accessed using a web browser. Individual devices and sensors can be selected from a map or plans of the bridge, and timeline graphs of the resultant data can readily be

generated. Typical calculations, temperature compensation for example, can be performed automatically.

Using these tools, Engineers can see the immediate reaction of the construction, and/or individual constituent elements, during construction phases and beyond. When irregular or extraordinary events (e.g. earthquake, storm, impact, etc.) occur, it is of interest to ensure that no lasting effects have occurred. In the *Poya* deployment, it was most interesting to monitor the bending of the pylons due to asymmetric loading conditions during construction. This allowed the verification of design values, and to establish if irregular behaviour(s) occurred.

5 ADVANTAGES OF GENESI TECHNOLOGY

Compared with currently available SHM systems on the market, GENESI has a number of advantages. It combines features of traditional cabled SHM systems (high reliability, trust, quality of service) with the possibilities of autonomous, wireless, and low maintenance systems.

Wireless data transfer, a feature of GENESI technology, saves on the commissioning costs of cables, and associated labour costs for installation. The risk of failure due to broken cables (e.g. vandalism, animals or construction works) is significantly reduced, and for existing structures (i.e. retrofit installations) long cable are unnecessary, and thus do not affect the aesthetics of the construction (e.g. in historical and/or touristic sites). Depending on site conditions, this can lead to installation cost reductions in excess of 50%.

GENESI nodes self-configure in the formation of networks, and allow dynamic addition and removal new nodes without disruption to data collection. State of the art communications protocols (e.g. CTP [6] and DISSense [7] are currently implemented at *Pont de la Poya* and the Rome Metro, respectively) are used to connect devices, form a network, and route information to the gateway. The gateway then feeds the WebDavis system. Given that the software in use is based on contemporary open source initiatives, it will be reasonably straightforward to deploy improved networking and communications capabilities, particularly as standards emerge (e.g. the IPv6 stack over IEEE 802.15.4) and are made to operate efficiently and effectively.

In conjunction with software tools developed, it is easy to deploy and remove additional nodes and sensors. This makes the system flexible, opening good possibilities to implement the system during construction phases and adapt the systems' functionality later for long term monitoring without additional hardware and reprogramming costs. Thus the system does not only address the two phases "construction" and "end-of-life" of a structure.

GENESI PCBs offer connectivity to a large number of standard SHM sensors on market. Due to their wide flexibility for analogue and digital sensors (providing appropriately conditioned power and high accuracy reading), also many other "generic" sensor types in addition to the ones listed on the bridge scenario can be connected to each node as required by specific monitoring needs. Those tested to-date include: displacement, inclination, strain, temperature, pressure, moisture, wind and various other types (given a number of standard analogue and digital electrical interfaces) [2, 3, 4].

The system is "green and sustainable", and optimized in its energy use. GENESI technology can easily operate 5 to 10 times longer than standard systems available on the market. With good energy harvesting possibilities, this can be significantly extended. This saves on long-term maintenance costs for SHM itself, as the number of periodic regular field trips and access to nodes to change batteries is significantly reduced or eradicated. The system can be reconfigured remotely, saving costs to access the nodes in hard to reach deployments or dangerous sensing fields.

The graphical user interface developed to assist with in field programming and deployment of sensing nodes is straightforward and easy to use. It was designed such that any person with a basic knowledge of computer systems and SHM can learn to set up and maintain the relevant features of the GENESI system in just one or two days [5].

Data upload for online web-based visualisation has a latency ranging from seconds to minutes (depending on network size (connection and settling time) and system configuration) providing near real time data sets for analysis. It is worth noting that the implementation is easily extensible to exploit contemporary data representation, formatting and transfer methods, such as xml, JSON and REST, respectively. Therefore, any data collection platform can be used to store, manage and explore the resultant data.

Complementary in-network data processing and adaptive sampling mechanisms have also been developed and are available to help in reducing the power usage, and assist in analysing the data, and/or adjusting the sampling intervals as required [8, 9, 10].

6 ECONOMIC CONSIDERATIONS

Table 2 provides an overview of estimated prices for a typical SHM system. As research and development costs are very high for GENESI technology, and would not prominently feature in a market model, they are not taken in account. To achieve economic feasibility and create realistic market uptake, devices must be in the range of less than 200 to 300 EUR per piece. This is considered to be realistic.

Currently the overall cost (producing devices in small volumes, e.g. hundreds) for a GENESI node sums to about 1100 to 1500 EUR (selling price). This is well within the range of competitive technologies. This does include development cost, however, which, when subtracted more than halves, and additional significant cost savings are possible with respect to commissioning and maintenance of the system in the field.

Shown in Table 2 are the estimated costs associated with GENESI SHM in comparison with COTS SHM systems. This

Table 2. Cost Comparison with COTS SHM Systems.

	Standard Cabled	Standard GPRS	GENESI
System Hardware	45000	55000	40000
Installation	25000	12000	12000
Maintenance (15 years)	20000	25000	10000
Overall	90000	92000	62000

considers a typical deployment of 15-20 nodes monitoring a bridge or tunnel. The table shows that savings in excess of 33% are immediately possible over standard configurations.

Fieldwork during the prototype system installation at *Pont de la Poya* demonstrated that a new node, including sensors, could be completely installed in approximately 20 minutes by a single person (including programming the device). This is the same time that is normally to interface a COTS sensor, but, due to wireless communication, no further cabling is required. This saves a significant amount of time and material (cables, connectors, cable protection, mounting material, equipment to reach the mounting positions). Furthermore, instrumentation as described above would not be possible with a cabled system.

In existing networks, the most significant maintenance costs are incurred due to broken cables (damaged by works, animals or vandalism) or lightning problems (more critical due to long cables). Other costs arise due to replacement of nodes, or when cables have to be rearranged due to the fieldwork. Therefore, actual operational costs will be greatly reduced as a result of the wireless nature of communications and ease of reconfiguration of the network.

7 CONCLUSION

The GENESI SHM system was described as applied to the monitoring of the cable-stayed bridge, *Pont de la Poya*, in Switzerland. Wireless and 'green', GENESI technology exhibits significant technological and economic advantages over existing SHM systems. Some of the economic benefits include savings via low installation costs, lower maintenance costs, fewer tools and materials for scaffolding, installation, etc. Depending on the monitoring scenario, a cost saving of 30 – 50% is realistic, depending on deployment scenario.

The system is sufficiently flexible to be installed during construction, needing minor changes for extended monitoring. Cabled systems usually do not offer this flexibility, often break, and/or have to be removed. GENSESI technology can be used to monitor structural integrity in areas where it was not previously possible (e.g. in tunnel constructions behind tunnel boring machines), and in locations where no energy or cellular (and/or other infrastructure communications) networks are available. This is particularly attractive in, for example, new tunnels, remote environmental monitoring in mountainous regions, traffic ways, etc.

The market for SHM systems continues to grow rapidly through major infrastructure investment in transportation infrastructure, bridges, power plants, water networks, oil and gas pipelines, etc. Existing structures are increasingly reaching critical ages (30 or 40 years in operation). Society's attitude towards protecting these investments, old and new, in addition to reduced acceptance of unmitigated risk in a technological age, suggests that there is enormous market potential for technologies with characteristics similar to those developed in GENESI.

7.1 Future Directions

Notwithstanding the potential of the technology, there remain a number of technical and operational challenges that must be overcome before the system can be considered complete and market ready. There is a need to find an energy efficient gateway to achieve connectivity to the Internet and ensure consistent bi-directional availability. Contemporary gateway implementations require significant energy, particularly those connecting via cellular networks (1-4 Watts). Methods to achieve more granular control over the devices in the network are essential. Existing reconfiguration methods involve flooding the network with broadcast messages, and consider systems that monitor distributed phenomena across the sensing field. Very little work has been done that considers heterogeneous sensors, particularly those that detect highly localised phenomena (e.g. cracks detected using displacement transducers), where addressing of discrete devices (and individual sensors) is essential. Finally, there is a need to further field test the system. This is needed to fully understand residual challenges and emergent behaviours, including reliability, data quality and system trustworthiness. Acquiring sufficient quantities of data from the deployed system, over time, is of importance to SHM practitioners to allow for meaningful interpretation of the structure's dynamics.

ACKNOWLEDGMENTS

The authors appreciate support of the European Commission under the Seventh Framework Programme (FP7), assistance from authorities, planners and construction companies of Rome Metro B1 and Pont de la Poya (Fribourg, Switzerland). The authors acknowledge all GENESI project partners for their contribution to this work. The authors also acknowledge continued support from EIT ICT Labs and the Research Council UK's Digital Economy Programme (EPSRC Grant No. EP/I038837/1).

REFERENCES

[1] Frommer, F. J. (Associated Press) "NSTB: Design Errors Factor in 2007 Bridge Collapse" [Online] Available: http://usatoday30.usatoday.com/news/world/2008-11-13-628592230_x.htm. [Accessed 22 July 2014]

[2] Boyle, D., Magno, M., O'Flynn, B., Brunelli, D., Popovici, E., Benini, L. (2011) 'Towards Persistent Structural Health Monitoring Through Sustainable Wireless Sensor Networks', *in Proc. IEEE ISSNIP 2011*. 6–9 December 2011. Adelaide, Australia.

[3] Magno, M., Boyle, D., Brunelli, D., O'Flynn, B., Popovici, E., Benini, L., (2014) 'Extended Wireless Monitoring Through Intelligent Hybrid Energy Supply,' *Industrial Electronics, IEEE Transactions on*, vol.61, no.4, pp.1871-1881, April 2014.

[4] Boyle, D., Srbinovski, B., O'Flynn, B., Popovici, E. (2012) 'Energy analysis of industrial sensors in novel wireless SHM systems'. *In Proc. IEEE Sensors 2012*. Taipei, Taiwan.

[5] Barta, L., Boyle, D., O'Flynn, B., Popovici, E. (2013) 'Simplified Commissioning and Maintenance for Wireless Sensor Networks'. *In Proc. Architecture of Computing Systems (ARCS), 26th International Conference on*, 19-22 Feb. 2013.

[6] Gnawali, O., Fonseca, R., Jamieson, K., Moss, D., Levis, P. 'Collection Tree Protocol', *In Proc. ACM SenSys, 2009*. California, USA.

[7] Colesanti, U.M., Santini, S., Vitaletti, A, (2011) 'DISSense: An adaptive ultralow-power communication protocol for wireless sensor networks,' *In Proc. DCOSS 2011.* 27-29 June 2011. Barcelona, Spain.

[8] Masoum, A., Meratnia, N., Havinga, P.J.M. (2013) 'A distributed compressive sensing technique for data gathering in Wireless Sensor Networks'. *4th International Conference on Emerging Ubiquitous Systems and Pervasive Networks (EUSPN-2013)*, Niagara Falls, Canada.

[9] Taghikhaki, Z. and Meratnia, N., Havinga, P.J.M. (2013) 'A Trust-based Probabilistic Coverage Algorithm for Wireless Sensor Networks.' *2013 International Workshop on Communications and Sensor Networks (ComSense-2013)*, Niagara Falls, Canada.

[10] Masoum, A. and Meratnia, N., Havinga, P.J.M. (2013) 'An energy-efficient adaptive sampling scheme for wireless sensor networks'. *In Proc. IEEE ISSNIP 2013*, 2-5 April 2013, Melbourne, Australia.

Application of output-only modal method to the monitoring of bridges using an instrumented vehicle

Abdollah Malekjafarian, Eugene OBrien
School of Civil, Structural and Environmental Engineering, University College Dublin, Belfield, Dublin 4, Ireland
email: abdollah.malekjafarian@ucdconnect.ie, eugene.obrien@ucd.ie

ABSTRACT: In this paper, a well-known output-only modal analysis method called Frequency Domain Decomposition (FDD) is tested in simulation of the monitoring of bridge frequency. The modal data can be obtained from a passing instrumented vehicle and used for bridge health monitoring. Three measurement strategies are suggested to collect the acceleration responses from the vehicle axles for FDD. It is shown that using multiple axles leads to better results in comparison to using just one. The effect of ambient excitation to all parts of the bridge is also discussed. In addition, the use of FDD to distinguish bridge frequency from vehicle frequency is investigated.

KEY WORDS: Vehicle Bridge Interaction; FDD method; Instrumented vehicle; Health monitoring.

1 INTRODUCTION

Structural health monitoring of bridges is becoming increasingly common for their maintenance and for decisions on repair and rehabilitation. Many damage detection methods are based on the concept that damage involves changes in bridge structural properties such as stiffness, which cause detectable changes in modal properties of the structure. These methods involve modal testing to identify the modal properties of the structure before and after damage [1]. For a structure such as a bridge, output-only modal testing in which only the response of the bridge is required, is more common than forced-vibration modal testing methods that requires the history of applied force. However, with these methods, the structure should ideally be excited artificially at different points using a controlled or ambient force and responses should be measured at many points [1 and 2]. Although these methods are currently being used in practice, they need considerable effort, specialist, equipment and the analysis of great quantities of data.

Recently, the possibility of using vehicle bridge interaction (VBI) data measured on a vehicle to estimate the dynamic properties of a bridge has gained considerable interest [3]. The method is based on installing sensors on the vehicle instead of the bridge which is a low cost alternative to conventional structural health monitoring [3 and 4]. This method is generally based on the Fast Fourier Transform (FFT) of the measured response that is the basic frequency analysis tool for such a response. The natural frequencies of the bridge can be obtained using the FFT spectrum of the measured response from the travelling vehicle. In addition to Yang et al's work, an increasing number of authors have proposed bridge health monitoring based on the dynamic response of the passing vehicle over the bridge [5, 6, 7, 8 and 9].

In these methods, the modal properties of the bridge are extracted from the vehicle response passing over the bridge. Therefore, they can be considered as output-only modal analysis. In output-only modal analysis (or ambient modal analysis) modal data can be obtain using only measured responses, i.e. ,there is no need to measure or control the input forces [2]. While using output-only data simplifies the damage detection setup, it is still required to attach sensors to the bridge structure.

In this paper, the concept of bridge natural frequency monitoring based on output-only modal analysis methods is investigated using the response from sensors installed on the vehicle. Vehicle bridge dynamic interaction is modelled using the finite element method (FEM). Frequency Domain Decomposition (FDD) method which is one of the most well-known output-only methods in the frequency domain [10], is used in this paper. FDD method is applied to the vehicle acceleration response during the passage of the vehicle over the bridge. Three strategies are suggested to provide data for application of the FDD method. In the first strategy, measured acceleration response from one passing instrumented axle is used as a single measurement channel. In the second strategy, vehicle responses are obtained from repeating the same simulation of a passing axle over the bridge for different ambient excitation forces. In the third strategy, two following axles equipped with accelerometers are simulated crossing the bridge. For all strategies frequency analysis using FFT and FDD methods are applied to the measured response of the vehicle to monitor the first natural frequency of the bridge. The obtained results show that application of the FDD method for monitoring bridge frequency has many advantages in comparison to the classical FFT method.

2 VEHICLE BRIDGE INTERACTION MODEL

In order to assess the application of the FDD method, the dynamic response of the instrumented vehicle is generated using numerical simulation (FEM). The FE model and procedure of calculating the vehicle dynamic responses are explained in the following.

The model of vehicle bridge interaction, which is used in this study, is shown in Fig. 1. The vehicle consists of a sprung mass m_v with a single degree of freedom (DOF), supported with an elastic spring k_v. The bridge is modelled as a simply supported beam of length L, flexural rigidity EI and mass per unit length m^* using 20 beam type (4 degrees of freedom) elements. A road profile is included in the simulations and the irregularities of this profile are randomly generated according to the ISO standard [11] for a road class 'A' (very good profile, as expected in a well maintained highway).

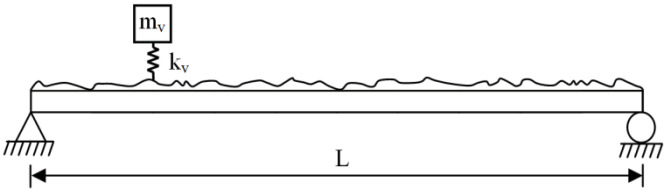


Figure 1. Vehicle bridge interaction model.

A FE vehicle-bridge interaction model explained in the literature [12], is used to represent the vehicle travelling over the bridge. The dynamic equations of motion of the VBI system are solved using the Wilson-θ method. The optimal value of the parameter, θ =1.42, is used for unconditional stability in the integration scheme [9].

3 OUTPUT-ONLY MODAL METHODS

In the past few years, output-only modal analysis (or operational modal analysis) has received considerable attention. The most important advantage of these methods is that only the response signals are measured and the test structure is only excited by the ambient forces [2]. Therefore, there is no need to measure the excitation forces. This method is mostly used for large structures such as buildings, bridges and towers in which it is not possible to excite the structure artificially as to measure excitation forces [2].

3.1 Frequency Domain Decomposition (FDD) method

FDD is an output-only modal analysis method in the frequency domain that was first proposed by Brincker et al. [10]. It is assumed that the input force to the structure is a white noise signal. For low damping, the power spectral density matrix of outputs of the structure can be defined as $G_{yy}(j\omega)$. The dynamic behaviour of a structure is dominated by one of its modes close to the corresponding natural frequency. Therefore, the response of structure is similar to its mode shape close to each natural frequency. In order to obtain the natural frequencies and mode shapes, the power spectral density matrix of the response for each frequency is decomposed by applying Singular Value Decomposition (SVD) to the matrix [10]:

$$\hat{G}_{yy}(j\omega_i) = [U]_i[\Sigma]_i[U]_i^H \quad (1)$$

where the matrix $[U]_i = [\{u\}_{i1}, \{u\}_{i2}, \cdots, \{u\}_{im}]$ is the unitary matrix including the singular vectors $\{u\}_{ij}$ and $[\Sigma]_i$ is a diagonal matrix including singular values σ_{ij}. Therefore, if singular values obtained from outputs of the structure are plotted, dominant peaks belong to natural frequencies of the structure and the corresponding singular vectors are mode shapes of the structure. If an improved version of FDD called Enhanced FDD (EFDD) is used, damping ratios of the structure can be estimated as well [10 and 13].

4 NUMERICAL ASSESSMENT

In this section, a frequency analysis of the bridge is carried out on the vehicle response using both FFT and FDD methods.

4.1 Case study

A VBI system, as shown in Fig. 1, is used in this study. The bridge properties are listed in Table 1.

Table 1. Properties of the bridge.

Properties	Unit	Symbol	value
Length	m	L	30
Mass per unit	kg/m	m^*	2000
Modulus of elasticity	GPa	E	27.5
Second moment of area	m^4	I	0.175

The first three natural frequencies of the bridge, obtained from the FE method, are given in Table 2.

Table 2. First three natural frequencies of the bridge.

Mode No.	1	2	3
Natural frequency (Hz)	2.70	10.82	24.36

A typical vehicle model of sprung mass is used in this study to represent the behaviour of the vehicle interacting with the bridge. The vehicle properties are listed in Table 3. It travels over the bridge at a constant speed of 2 m/s.

Table 3. Properties of the vehicle.

Properties	Unit	Symbol	Value
Mass	kg	m_v	1000
Stiffness	N/m	k_v	170×10^4
Frequency	Hz	ω	6.56

When a road profile is used in the simulation, the vehicle frequency is excited and consequently is dominant in the measured acceleration response of the vehicle [14]. Therefore,

sometimes it is hard to detect the bridge frequency from the vehicle response. As was suggested by [14], in order to improve the bridge response portion of the measured response of the vehicle, random excitation are applied to other parts of the bridge to improve the bridge frequency content in the vehicle acceleration.

The simulation is carried out using the FE method programmed in the MATLAB software environment. The sampling time interval is selected to be 0.0005 to provide enough data for accurate identification. Therefore, the total length of the acceleration response of the vehicle is 15 s. The simulated acceleration response of the vehicle while it travels over the bridge is shown in Fig. 2 against vehicle distance measured from the left side of the bridge.

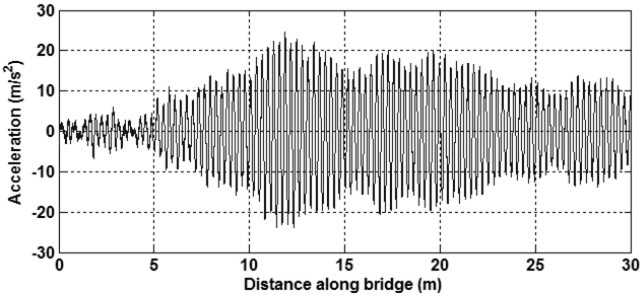


Figure 2. Acceleration response of the vehicle.

In order to analyse the vehicle response, a FFT is performed on the simulated vehicle response. The obtained FFT spectrum of the vehicle response is shown in Fig. 3.

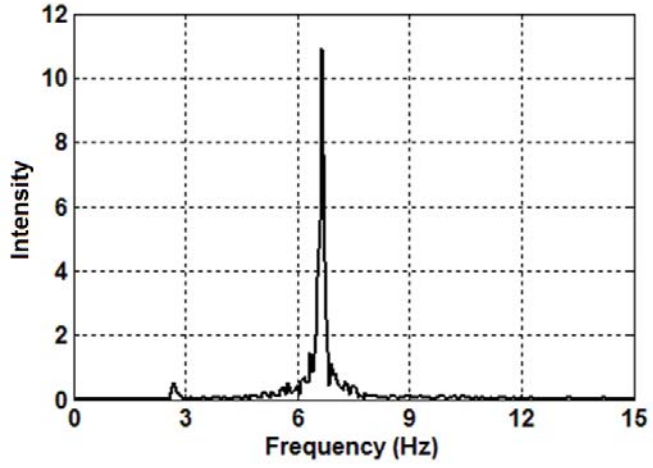


Figure 3. FFT spectrum of the vehicle acceleration response.

As expected, the dominant peak of the spectrum corresponds to the vehicle frequency around 6.56 Hz that is mentioned in Table 3. In addition, a peak corresponding to the first natural frequency of the bridge is detectable around 2.7 Hz.

As observed in Fig. 3, when the raw intensity of the spectrum is used for plotting the spectrum, it is hard to pick out the peak that corresponds to the bridge frequency. Therefore, it is suggested to plot intensity on a log scale. The FFT spectrum of the vehicle response is plotted again on semi-log plot in Fig. 4. It can be seen that peak picking of the frequencies is obviously simpler in this view. In comparison to Fig. 3 in which a small peak corresponded to for the bridge frequency, a sharp and clearly detectable peak is visible on a log scale.

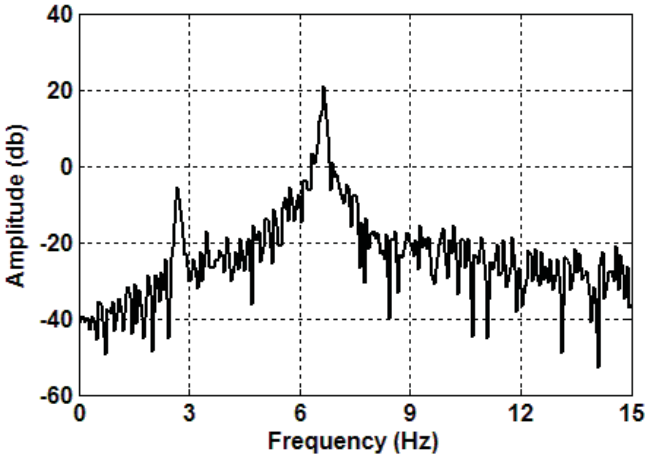


Figure 4. FFT spectrum of the vehicle acceleration response in db.

4.2 Strategy 1: Application of FDD method using single vehicle measurement

In this section, the FDD method is performed on the same simulated signal shown in Fig. 2.

As explained in section 3.1, the power spectral density matrix is first constructed from the simulated response. As a first strategy, the FDD method is applied to the same simulated vehicle response that was used in section 4.1. Then singular values are extracted using SVD of the power spectral density. The SVD diagram obtained is shown in Fig. 5.

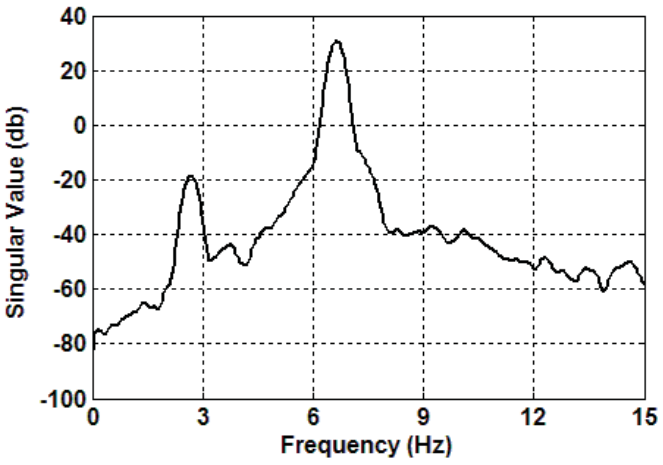


Figure 5. SVD diagram of the vehicle acceleration response.

In Fig. 5 both vehicle and bridge frequencies can be detected using the FDD method. Therefore, it is recommended to use the FDD method instead of using FFT to identify of bridge frequency from a measured vehicle response.

4.3 *Strategy 2: Application of FDD method using multiple vehicle measurements*

As explained before, FDD is an output-only modal analysis method. This method is usually used as a multi-channel method and rarely operates using only one signal. This means that in the classical use of the method, several responses that are measured from installed sensors at several points on the structure, would be used as input to the FDD method.

In this section, the test of section 4.2 is repeated four times and the response of the vehicle is measured separately each time. The only difference in these four simulations is that different random excitations are applied to the bridge each time. Using multiple signals from the vehicle leads to some advantages. First, more data can be provided which gives more accurate results. This is particularly so, when the speed of the vehicle is high and consequently the length of the time history is not large enough for a successful analysis. In addition, using multiple signals with the FDD method, gives a multi-signal SVD diagram that includes peaks at the natural frequencies. These extra peaks can be very useful in the case that the operator is not sure about the existence of a particular frequency. If a peak occurs in all SVD curves, then it can be configured as a frequency of the system with high assurance. Particularly, in the case where the vehicle frequency is close to the bridge natural frequency, the availability of more data can be helpful for accurate identification of the frequencies.

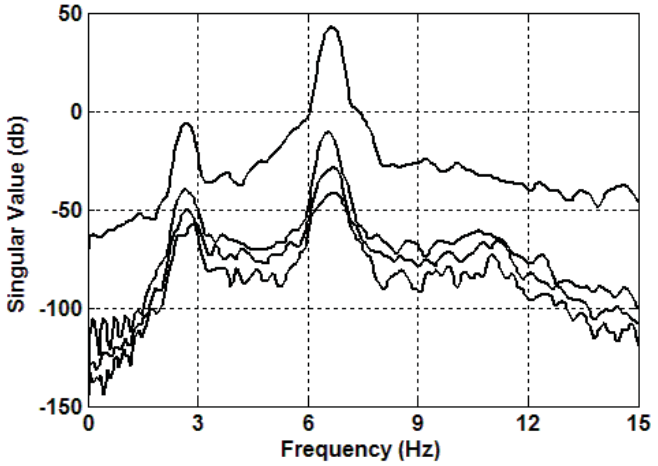


Figure 6. SVD diagram for four vehicle acceleration responses.

The SVD diagrams obtained from performing an FDD on the four simulated responses is shown in Fig. 6. It can be observed that all four curves have peaks at the vehicle and bridge frequencies. It can be concluded that using multiple measurements leads to more data that is useful in the more complicated situations.

4.4 *Strategy 3: Application of FDD method using measurements from two following axles*

As mentioned in the previous section, the responses obtained from repeating the same simulations, are approximately the same, except in their random ambient excitations. Although four different responses is useful, but it would be more desired if totally different signals could be used. In this section, measured signals from following axles with the same properties are used as proposed by Keenahan et al. [8] and Yang et al. [15]. An axle spacing of s = 6 is used in the configuration illustrated in Fig. 7. Using different axle properties would result in two different frequencies and would make it harder to investigate the spectrum. Thus, in this section, the properties of the axles are considered to be same as given in Table 3. It is assumed that the simulation starts when axle 2 is at the left end of the bridge and finishes when the axle 1 arrives at the right end of the bridge when they travel at constant speed of 2 m/s. Therefore, the total path that each vehicle travels in the simulation is L-s = 24m and the time length of the response is 12 s. The simulated responses obtained for the two axles are shown in Fig. 8.

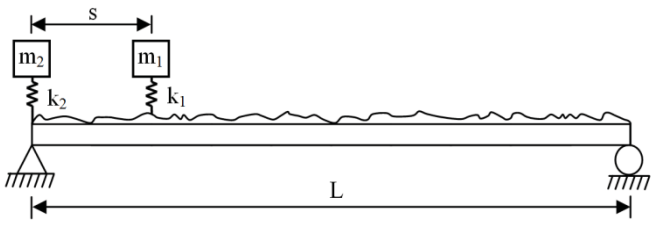


Figure 7. Two following axles travelling over the bridge.

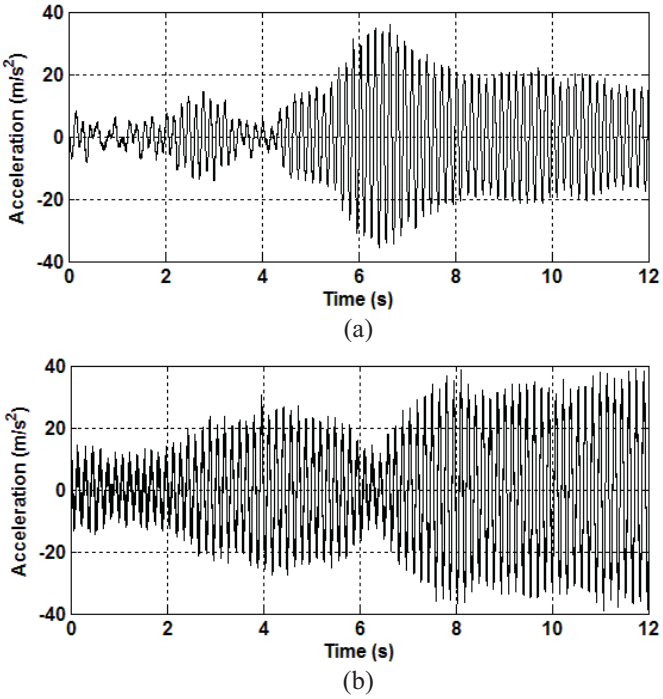


Figure 8. Acceleration responses of the two connected axles; a: axle 1, b: axle 2.

The FDD method is applied to the vehicle responses. The SVD diagram is shown in Fig. 9. It is observed that there are two SVD curves, are for each axle, and both have peaks at bridge and vehicle frequencies. It can be seen that the level of the second curve is improved at the frequency peaks in comparison with Fig. 6. This is because of using totally

different data in FDD method. In order to take advantages of the FDD method, it is recommended to use strategy 3. This strategy can be extended to use more than two axles in a multi-axle vehicle that is practical.

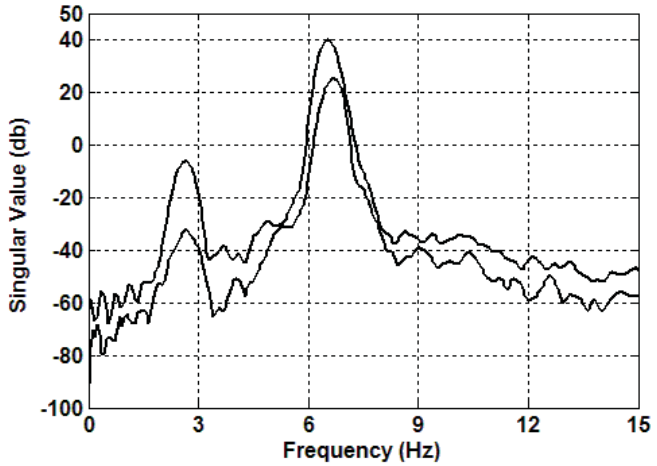


Figure 9. SVD diagram of the two connected axles.

4.5 *Application of FDD in case of closeness of vehicle frequency to the bridge frequency*

One challenge of estimation of bridge frequency using passing vehicle responses is the existence of a close vehicle frequency [16]. The vehicle frequency usually appears dominant in the spectrum. When the frequency of the vehicle is close to the bridge frequency, it causes a useful excitation of the bridge frequency in the spectrum, but several peaks tend to merge in the spectrum while makes it hard to process it and identify the frequencies. On the other hand, the FDD method can deal with closely-spaced modes [17].

Table 4. Properties of the new vehicle.

Properties	Unit	Symbol	Value
Mass	kg	m_v	4000
Stiffness	N/m	k_v	170×10^4
Frequency	Hz	ω	3.28

A new axle with properties given in Table 4 is used in this section to decrease the frequency of the vehicle. The properties of the new axle are selected so that axle frequency is close to the bridge first natural frequency. Strategy 3, using two connected axles, is used in this simulation.

The FFT spectrum of the measured response of the first axle is shown in Fig. 10. The closeness of the vehicle and bridge frequencies results in an unsmooth spectrum curve and it is hard to detect proper peaks.

The simulated responses obtained from the two connected axles are used within the FDD method in a similar procedure to that of section 4.4. The SVD diagram obtained using the FDD method is shown in Fig. 11. The FDD method gives a smooth diagram, even for this case of closeness of vehicle and bridge frequencies.

It is notable that previous studies [6] have shown that the estimation of bridge dynamic properties from a passing vehicle is not significantly sensitive to noise, since the responses are measured at the same location as the excitation.

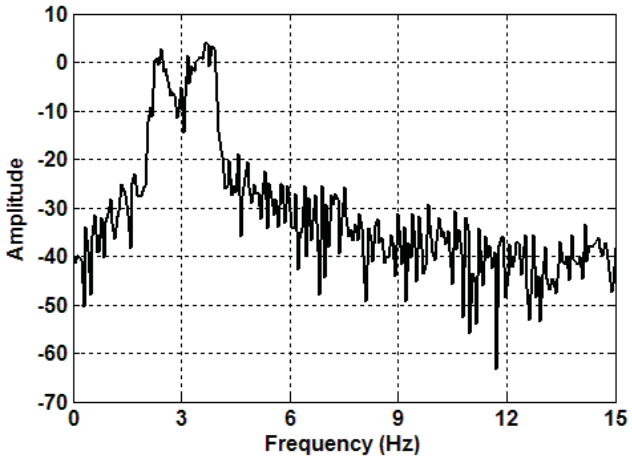


Figure 10. FFT spectrum of the axle acceleration response for close bridge and vehicle frequencies.

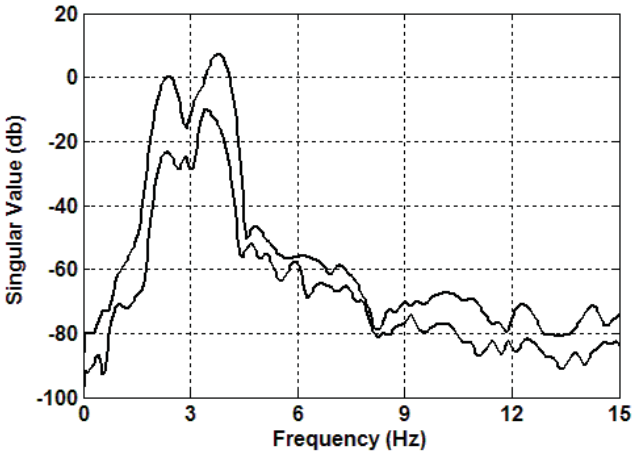


Figure 11. SVD diagram of the two connected axles acceleration responses in the case of close bridge and vehicle frequencies.

5 CONCLUSION

In this paper, the potential of application of the FDD method in identification of bridge frequency using the response of a passing vehicle is investigated. Several strategies tested to take advantage of the FDD method. It is shown that using measured responses from different axles gives better results in comparison with repeating the same simulations with different random excitation of bridge. In addition, the effectiveness of the FDD method in the case of closeness of bridge and vehicle frequencies is investigated. It is shown that the FDD method can identify both bridge and vehicle frequencies in this case, while the classical FFT analysis does not reveal the frequencies clearly. Therefore, it can be concluded that the FDD method can be an effective alternative to the FFT for bridge identification using vehicle response.

ACKNOWLEDGMENTS

The authors wish to express their gratitude for the financial support received from Science Foundation Ireland towards this investigation under the US-Ireland Partnership Scheme

REFERENCES

[1] Carden, E. P. and Fanning, P. (2004), 'Vibration based condition monitoring: a review', *Structural Health Monitoring*, 3 (4), pp. 355–377

[2] Zhang, L., Brincker, R. and Andersen, P. (2005), 'An Overview of Operational Modal Analysis: Major Development and Issues', *Proceeding of the 1st International Operational Modal Analysis Conference (IOMAC)*, Copenhagen, Denmark

[3] Yang, Y. B., Lin, C. W. and Yau, J. D. (2004), 'Extracting bridge frequencies from the dynamic response of a passing vehicle', *Journal of Sound and Vibration,* 272, 471–493.

[4] Lin, C. W. and Yang, Y. B. (2005), 'Use of a passing vehicle to scan the fundamental bridges frequencies: an experimental verification', *Engineering Structures,* 27, 1865–1878.

[5] Bu, J. Q., Law, S. S. and Zhu X. Q. (2006), 'Innovative bridge condition assessment from dynamic response of a passing vehicle', *Journal of Engineering Mechanics,* 132,1372–1379.

[6] Xiang, Z., Dai, X., Zhang, Y. and Lu, Q. (2010), 'The tap-scan method for damage detection of bridge structures', *Interaction and Multiscale Mechanics*, 3, 173–191.

[7] Kim, C. W., Kawatani, M. and Hao, J., (2012), 'Modal parameter identification of short span bridges under a moving vehicle by means of multivariate AR model', *Structure and Infrastructure Engineering*, 8(5): 459-472.

[8] Keenahan, J., OBrien, E.J., McGetrick, P.J. and Gonzalez, A. (2013), 'The use of a dynamic truck-trailer drive-by system to monitor bridge damping', *Structural Health Monitoring*, DOI: 10.1177/1475921713513974

[9] Gonzalez, A., OBrien, E.J., and McGetrick, P.J. (2012), 'Identification of damping in a bridge using a moving instrumented vehicle', *Journal of Sound and Vibration*, 331 (18), 4115-4131

[10] Brincker, R., Andersen, P., and Zhang, L. (2000), 'Modal identification from ambient responses using frequency domain decomposition', *Proceedings of the 18th International Modal Analysis Conference (IMAC),* San Antonio, TX, pp. 625–63.

[11] ISO 8608:1995, Mechanical Vibration-road Surface Profiles-reporting of Measured Data', *International Standards Organisation,* 1995.

[12] J.W. Tedesco, W.G. McDougal and C.A. Ross, *Structural Dynamics, Theory and Applications*, Addison-Wesley, 1999.

[13] Khatibi, M. M., Ashory, M. R., Malekjafarian, A., and Brincker, R. (2012), 'Mass–stiffness change method for scaling of operational mode shapes', *Mechanical Systems and Signal Processing*, Volume 26, Pages 34–59

[14] Yang, Y. B., and Chang, K. C. (2009), 'Extracting the bridge frequencies indirectly from a passing vehicle: parametric study', *Engineering Structures,* 31, 2448–2459.

[15] Yang, Y. B., Li Y. C., and Chang, K. C. (2012), 'Using two connected vehicles to measure the frequencies of bridges with rough surface – a theoretical study', *Acta Mechanica*, 223(8):1851–61.

[16] Yang, Y. B., Chang, K. C., and Li Y. C. (2013), 'Filtering techniques for extracting bridge frequencies from a test vehicle, moving over the bridge', *Engineering Structures*, 48, 353–362

[17] Malekjafarian, A., Ashory, M. R., Khatibi, M. M. (2009), 'Double Modes Determination of a Gearbox Shaft Using Operational Modal Analysis', *Proceeding of the 2nd International Operational Modal Analysis Conference (IOMAC)*, Italy, Pages 127-133.

Ceramic Waste Sludge as a Partial Cement Replacement

Francis Kenna[1], Paul Archbold[2]
[1] John Gannon Concrete Ltd., Split Hill Quarries, Ballinagore, Co.Westmeath, Ireland
[2]Department of Civil Engineering, Athlone Institute of Technology, Dublin Road, Athlone, Co.Westmeath, Ireland
Email: [1] frankkenna@gmail.com, [2] parchbold@ait.ie

ABSTRACT: In this research study, waste ceramic sludge derived from orthopaedic implant mass finishing processes were employed as a supplementary cementitious material (SCM) in the partial replacement of ordinary Portland cement (OPC).The cement was replaced by dried ceramic sludge in powder form accordingly in ranges up to 50%wt. The results demonstrate that the addition of ceramic sludge powder as an active addition to OPC can enhance the mechanical strength of concrete when incorporated in the range of 15-20%. Furthermore, results show improved cohesiveness and a reduction of bleed waters in the concretes fresh phase. The results also show that the overall durability of the concrete was improved through a reduced water absorption capacity. The waste ceramic sludge employed constitutes a significant volume of the source factory's waste stream. This waste is traditionally disposed of in landfill, incurring significant economic and environmental costs. As such, there is demand for research into potential re-use of the material.

KEY WORDS: Waste ground ceramic; Pozzolan; Supplementary cementitious material; Concrete compressive strength.

1 INTRODUCTION

1.1 Cement production and the environment

The environmental impact of cement production has been well documented [1]. Large volumes of virgin raw materials such as limestone and clays are consumed along with the significant greenhouse gas emissions which can be attributed to the production of cement clinker. It has been estimated to take 1.7 tonnes of finite virgin material to produce 1 ton of cement clinker. Cement production facilities also consume enormous amounts of fossil fuels, making cement production an extremely carbon intensive industry [2].

The cement and concrete industry has recognized the environmental impact of cement production which has prompted much research into more sustainable cement production alternatives. The need for research has been further exacerbated by the necessity to comply with Kyoto Protocol driven emission targets [3].

1.2 Alternative materials for concrete and cement

There has been a great volume of studies concerning the replacement of virgin material aggregates for concrete and cement production with non-hazardous post consumer and industrial wastes [4]. Alternative concrete aggregate studies have utilized such materials as construction and demolition wastes [5,6], glass [7,8], plastics [9], rubber [10], municipal incinerator bottom ash [11] and ceramics [12], to mention but a few. Each of these alternative aggregates presents their own unique advantages/disadvantages to the properties of fresh and hardened concrete. The variety of properties affected along with issues relating to the consistency of supply, heightened quality control requirements and conformity related problems [13] have led to reluctance to implement wide scale production of concrete products containing many of these wastes.

Similarly there has been wide scale research into the use of end of life wastes as supplementary cementitious materials otherwise known as pozzolans, for the partial replacement of ordinary Portland cement as a binder for concrete. These studies have considered the replacement of OPC through either, incorporating wastes with virgin materials in the production of cement clinker prior to milling or through the blending of preprocessed wastes with OPC. The latter of these techniques is generally regarded as being the most efficient in terms of the environmental impact.

A wide range of waste materials have been considered, mainly due to their chemical composition being similar to that of known pozzolanic materials. The waste materials which have been considered through these studies vary greatly and include well known SCM's such as silica fume [14], fly ash [15] and granulated blast furnace slag [16]. Other studies have considered potential SCM's such as glass [17,18], rice husk ash [19], municipal sewage sludge ash [20] and fine ground ceramics [21-28].

1.3 Hydraulic reactions in cement

The hydration of cement is an exothermic chemical reaction between cementitious minerals and water which leads to setting and eventual hardening of concrete. In its anhydrous state, cement consists of four main minerals alite, belite, aluminate and ferrite. Of these, alite (C_3S or tricalcium silicate) and belite (C_2S or dicalcium silicate) are the main reactive minerals contributing to concrete strength. In the presence of moisture these minerals will react and produce calcium silicate hydrate C-S-H which is the main strength component phase of the cement reaction. The chemical formula for these reactions can be seen in equations 1 and 2 below.

$$2C_3S + 6H \rightarrow C_3S_2H_3 + 3CH \quad (1)$$

$$2C_2S + 4H \rightarrow C_3S_2H_3 + CH \quad (2)$$

Where;
C= CaO (calcium oxide); S= SiO_2 (silicon dioxide); H= H_2O
CH= $Ca(OH)_2$ (calcium hydroxide)

Calcium hydroxide or lime is a by-product of these reactions which has no cementing or strength giving properties and is prone to chemical attack and leaching. The strength of concrete is very much dependent upon the hydration reaction

of which water plays a critical role. The hydration reaction itself consumes a specific amount of water. Typically more water is added to concrete than is needed for full cement hydration. This excess water will remain in the microstructure pore space, ultimately weakening the concrete [29].

1.4 Pozzolanic reactions of SCM's

Natural pozzolanic materials such as volcanic ash and pumicite have been used in hydraulic binders for thousands of years with examples found which date between 5000-4000B.C. [30]. Pozzolanic materials are best defined as siliceous or alumino-siliceous material that, in finely divided form and in the presence of moisture, chemically reacts at ordinary temperatures with calcium hydroxide released by the hydration of Portland cement to form compounds possessing cementing properties [31].

$$\text{Pozzolan} + \text{CH} + \text{H} \rightarrow \text{C-S-H} \quad (3)$$

The pozzolanic chemical reaction with calcium hydroxide can be seen in equation 3. This reaction is much slower than the reactions of alite and belite but has the benefit of replacing porous CH with C-S-H. A well designed cement blend incorporating pozzolanic materials will produce a denser and ultimately stronger and more durable concrete.

1.5 Waste ceramic as a SCM

This preliminary study into the possible pozzolanic characteristics of fine ground waste ceramics, utilizes spent ceramic media which is a waste stream product of mass finishing processes. Mass finishing is a term used to describe a group of abrasive industrial processes by which large lots of parts or components made from metal or other material are processed to achieve a variety of surfaces finishes such as deburring and surface smoothing [32].

Ceramic media is formed through the extrusion and vitrification of wet clay with the addition of abrasives such as aluminium oxide, silicon carbide, quartz or others usually ranging between 80-200um in diameter. In the finishing process the media becomes ground, spent grinding metals are then recovered from the media and the process ultimately produces a fine ceramic sludge waste product. This waste is traditionally then disposed of in landfill, incurring significant economic and environmental costs. Mass finishing processes are used throughout the world in industries such as automotive, aerospace, jewelery, medical and firearms to mention but a few. Instances of ceramic media waste in Ireland are mainly from the medical industry with in excess of 1000 tonnes/annum being produced between two of the larger orthopaedic implant manufacturers. As such, there is demand for research into potential re-use of the material.

Several authors have indicated the potential for the incorporation fine ground ceramic waste as an SCM, these studies are varied in terms of the type and origin of ceramic wastes utilized. One common theme throughout these studies is the indication that the chemical composition of various waste ceramics is favorable in terms of potential Pozzolanicity owing to high SiO_2 and Al_2O_3 content [21-28 and 33].

The waste from ceramic media used in mass finishing is highly controlled at source and therefore a homogenous waste product is produced. The economic benefits that would accrue from the utilization of ceramic media sludge waste as a SCM are listed below;

- Payment to receive this raw material at or above current landfill rates (exceeds the cost of cement per ton due to current landfill tax charges which can only increase in the future).
- Minimal reprocessing costs (Drying at low temperature and minimal milling required)
- Energy and emissions savings for the cement producer
- Reduced extraction and use of virgin materials

The aim of this study is to conduct initial testing to determine various fresh and hardened state concrete characteristics of concrete utilizing supplementary cementitious ceramics (SCC)/cement blends, which may indicate the potential for ceramic media sludge to be used as a SCM and justify further more extensive research. The use of the acronym SCC in this paper should not be confused with the acronym for self-compacting concrete.

2 EXPERIMENTAL PROCEDURE

2.1 Materials

2.1.1 Waste ceramic sludge

As previously mentioned, the pozzolanic material utilized in the study was ceramic waste sludge derived from mass finishing processes. Mass finishing is a wet process which produces a ground ceramic sludge with moisture content up to and above 50%.

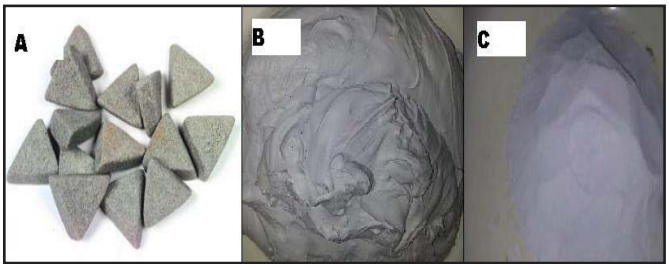


Figure 1: SCC production process (A) ceramic media prior to mass finishing process (B) ceramic waste sludge (C) dry milled SCC

In order to produce a dry powdered SCC, the ceramic sludge was dried at $T=105^0C$ for a period of 48hours.The dried sludge forms a cake like solid in static drying conditions. This ceramic cake was subsequently milled until a ceramic powder was created with a particle diameter passing a 150µm sieve. The production process of SCC from orthopedic mass finishing media can be seen in Figure 1.

2.1.2 Water

The water used in the making of concrete samples was of drinking quality with a pH of 7.8. The water cement ratio used in the design of the concrete reference mix was 0.5. The actual volume of mix water was maintained constant for all mixes despite reductions in OPC content. The decision to maintain the water content was taken in order to make direct comparison between the mixes in their fresh state, and to

avoid the use of water reducing admixtures which may have influenced the results.

2.1.3 Aggregates

The sand and coarse aggregate used to make concrete samples were extracted from a limestone sand/gravel quarry. The aggregates consisted of a well graded limestone sand, 14mm and 10mm nominal sized aggregate. These aggregates had a sub angular to rounded particle shape and moderately smooth surface texture. The aggregate particle size distribution can be seen in Figure 2.

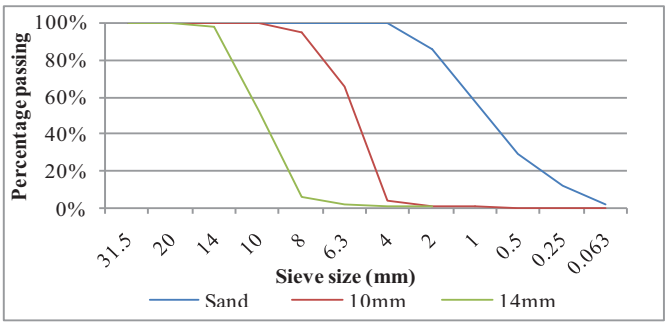


Figure 2: Aggregate grading used for concrete samples

2.1.4 Cement and SCC compositional properties

The reference cements used in the study were CEM I 42.5R and CEM II A/L 32.5N type cements according to EN 197-1:2011 Standard [31]. The chemical composition of these cements and SCC powders used in this study are shown in Table 1.

Table 1: Chemical composition of cement binders and SCC powder

	Materials		
Chemical Constituent %	CEM I 42.5R	CEM II A/L 32.5N	SCC powder
SiO_2	19.6	18.63	68.8
Al_2O_3	4.41	5.41	18.4
Fe_2O_3	3.3	2.9	4.6
CaO	63.21	62.42	1.5
MgO	4.2	3.2	0.72
Na_2O	0.3	0.3	2
K_2O	0.5	0.4	1.62
SO_3	1.4	2.86	0.06
Loss on ignition	1.4	3.68	0.5

2.2 Sample preparation

The present investigation studied the partial replacement of cement with ground ceramic powder by adding several combinations of SCC powder. Cement blend binders were prepared by dry mixing the powdered SCC with CEM II A/L 32.5N in the range of 20, 35 and 50wt% and CEM I 42.5R in the range of 15, 20, 25, 30, 35, 40 and 50wt%. The percentage SCC was set on the basis of the typical compositional range for Portland composite cement blends as suggested in EN 197-1:2011 [31]. A cement type utilizing ceramic pozzolana would be considered a pozzolanic cement type with the notation CEM IV in EN 197-1 and would contain Portland cement clinker in the range of 45-90%.

Table 2: Concrete mix proportions using CEM II A/L 32.5

Mix Ref.	Kg		Litres	Kg			
	Cement	SCC	Water	Sand	10mm	14mm	w/c ratio
Control (OPC)	320	-	160	885	440	440	0.5
20% SCC	256	64	160	885	440	440	0.5
35% SCC	208	112	160	885	440	440	0.5
50% SCC	160	160	160	885	440	440	0.5

The cement blend mixing procedure was carried out in a mixer for 15 min to ensure repeatability of the blend. The reference binder was 100% OPC CEM II A/L 32.5N in the first instance and 100% OPC CEM I 42.5R in the second instance. Concrete samples were prepared by mixer for characteristic compressive strength f_c= 20N/mm^2 according to the Building Research Establishment (BRE) mix design procedure [34]. The mix proportions for concrete samples using cement blends with CEM II A/L 32.5N are shown in Table 2 and CEM I 42.5R blends in Table 3.

Table 3: Concrete mix proportions using CEM I 42.5R

Mix Ref.	Kg		Litres	Kg			
	Cement	SCC	Water	Sand	10mm	14mm	w/c ratio
Control (OPC)	280	-	140	885	440	440	0.50
15% SCC	238	42	140	885	440	440	0.50
20% SCC	224	56	140	885	440	440	0.50
25% SCC	210	70	140	885	440	440	0.50
30% SCC	196	84	140	885	440	440	0.50
35% SCC	182	98	140	885	440	440	0.50
40% SCC	168	112	140	885	440	440	0.50
50% SCC	140	140	140	885	440	440	0.50

In the case of compressive strength tests, prepared concrete samples were placed in 100x100x100mm cube molds in three layers using a vibrating table for compaction (vibration time ≈ 1min per layer). The concrete samples were de-molded after 24h and placed in a curing tank for (7, 28, 91 days) at T=20^{0}C and relative humidity of 65%.

2.3 Fresh state testing

In order to determine the fresh state characteristics of blended cement concrete using SCC, slump [35], degree of compactability [36] and sieve segregation tests [37] were conducted on samples produced using CEM I 42.5R and SCC as binders. The tests were conducted for the blended cement concrete samples in the range of 0%, 20%, 30%, 40% and 50%wt cement replacement with a water/cement ratio of 0.5. The addition of 15.7L/m^3 of Plasticement® 186 was added to mixes in order to increase the consistence prior to conducting sieve segregation tests.

2.4 Hardened state testing

2.4.1 Density and water absorption

The density [38] and water absorption [39] of SCC blended cement concrete samples were determined for all cement replacement ranges produced using CEM I 42.5R. The samples were cured in a curing tank for 28 days at T=20^{0}C and relative humidity of 65% prior to conducting the tests.

2.4.2 Compressive strength

For each mix using SCC and CEM II A/L 32.5N blends, samples were tested to determine the compressive strengths at 7, 28 and 91 days of curing. Mixes utilizing SCC and CEM I 42.5R were tested to determine compressive strength development at 7 and 28 days only. The compressive strength for each mixture was obtained from an average of five sample specimens for each curing time interval. A 2000-kN capacity uniaxial compressive testing machine was used to test the specimens at a constant loading rate of 0.6N/mm2.S in accordance with EN 12390-3:2009[40].

3 RESULTS AND DISCUSSION

3.1 Fresh state characteristics

The results of slump tests shown in Figure 3 show a decrease in concrete consistence as the percentage of SCC increases. Recent studies [22, 23, and 26] have shown that this is a common phenomenon with fine ground ceramic waste blended cements. This is most likely due to a higher water absorption rate of the ground ceramic particles. It is likely that low water/cement ratio concretes would require a water reducing agent or superplasticizor when incorporating SCC blended cements.

An increase in the percentage SCC also had a decreasing effect on the degree of compactability of the concrete which can be seen in Figure 3. The addition of SCC blended cement had a noticeable decreasing effect on the amount of bleed water which appeared on the concrete surface during the test. This effect can be attributed to both the water absorption rate of the SCC powder and to its particle packing effect. The specific gravity of the fine ground SCC is substantially less than that of the cement and therefore when added by %wt, a larger volume of fines are incorporated in the mix.

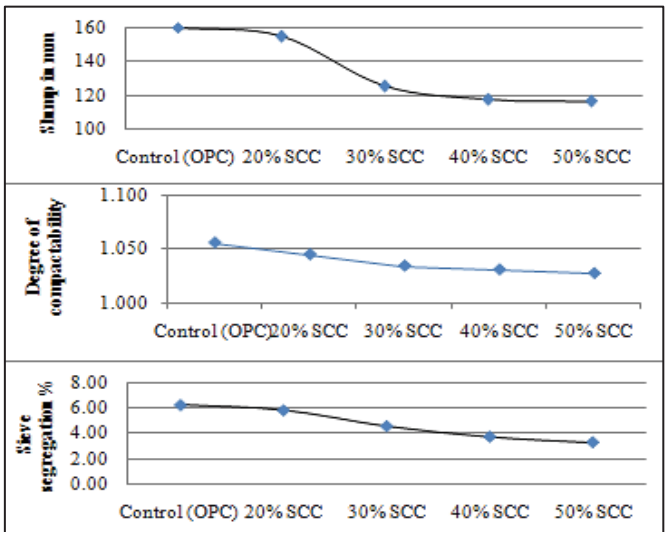


Figure 3: Fresh SCC concrete test results

Sieve segregation tests were conducted on the samples as a means to assess the cohesive nature of SCC concretes. The results shown in Figure 3 illustrate a decrease in segregation as the percentage of SCC increases. These results represent an increase in the cohesiveness of the concrete as SCC content is increased. This increase in cohesion would be of benefit to pumped or self-compacting concrete applications.

3.2 Density and water absorption

The density of SCC blended cement concretes were only slightly reduced from that of the reference concrete with the largest reduction in the order of 7%. Figure 4 shows that in terms of water absorption, SCC concretes have a lower water absorption capacity than the reference concrete even as early as 28 days. A low water absorption capacity is analogous to low permeability, which is a crucial factor in the overall durability of concrete. Less permeable concrete's are more resistant to the ingress of water and salts which can be deleterious to concrete and steel reinforcement.

The largest water absorption reduction was recorded for the 30% SCC concrete with an approximate 24% reduction, all other SCC concretes displayed a reduction when compared to the reference concrete, however, a gradual increase occurred in the SCC concretes above 30% cement replacement.

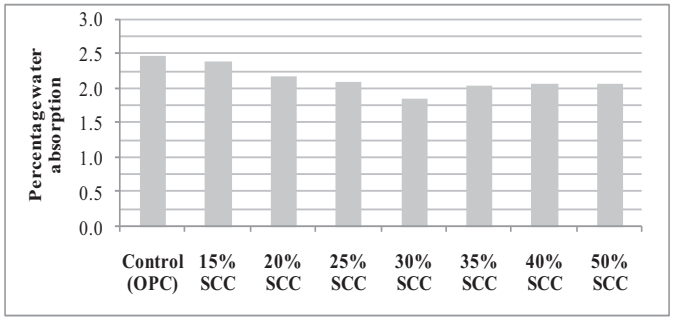


Figure 4: Water absorption

These results reflect those of a study carried out after 90 days using fine ground ceramic tiles, where all concretes using up to 40% cement replacement recorded lower absorption capacities [18]. It would be expected that as pozzolanic reactions continue, the water absorption of SCC concretes would decrease further due to the formation of void filling C-S-H.

3.3 Aesthetics of SCC blended cement concrete

Blended cements incorporating pozzolans as a cement replacement tend to have an effect on the color of the hardened concrete they produce. This color change is generally accepted as a positive aesthetic characteristic. Well known pozzolans such as GGBS and metakaolin generally produce concretes with a lighter surface finish than OPC concretes.

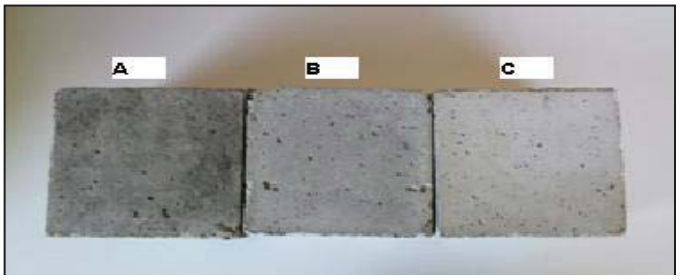


Figure 5: Concrete color variation (A)100% CEM I OPC (B) 20% SCC (C) 50% SCC

It is apparent from the concrete samples produced in this study that the color of hardened concrete produced from ground ceramic media, also produces a lighter surface finish. Figure 5 shows the gradual lightening of the concrete color with increased %wt cement replacement with SCC material.

3.4 Compressive strength

3.4.1 CEM II A/L 32.5N/SCC blended cement

The results obtained from compressive strength testing indicate significant strength development reductions ≈ 36% at early curing ages between the control sample and all of the SCC samples. This result was expected as all pozzolans with the exception of highly reactive pozzolans exhibit this mechanical strength behaviour. Early strength of both pastes and concretes decreases while ultimate strength is often found to exceed that of the reference Portland cement. If cements contain small amounts of very active pozzolana (silica fume, for example), both early and ultimate strengths may be higher than those of the substituted cement [30].

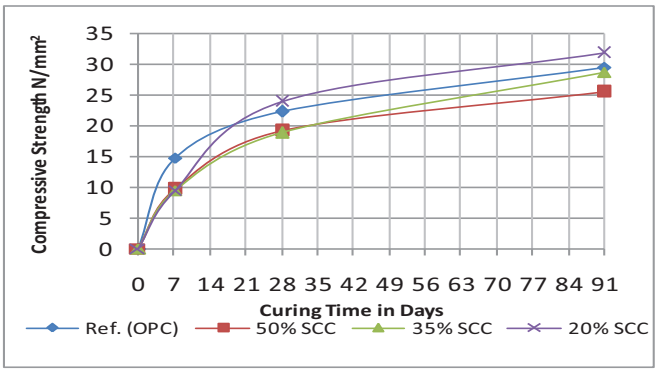


Figure 6: Compressive strength of CEM II A/L 32.5N/SCC samples

All three SCC sample mixes exhibited similar strength development characteristics up to 7 days which is most likely an indication of delayed pozzolanic reaction in the concrete. The reaction between alite and belite in the presence of a reduced cement content would limit the formation of calcium hydroxide ($Ca(OH)_2$) in the concrete matrix [29]. Therefore it is reasonable to assume that early compressive strength reductions are due to inhibited reactions between ceramic pozzolana and a limited early supply of $Ca(OH)_2$.

Results showed that strength decreased with an increase in SCC cement replacement with the lowest strength occurring for an SCC cement replacement of 50%. However, the strength reduction with 50% cement replacement was within 15% of the OPC reference mix at 28 and 91 days. Similarly with a SCC cement replacement of 35%, a 15% strength reduction was recorded at 28 days and a mere 3% at 90 days. Both of these mixes failed to meet the mix design characteristic strength of 20N/mm^2 at 28 days, however, both were found to be well above 20N/mm^2 at 90 days. The SCC 20% sample recorded a marginal strength increase of approximately 7.5% when compared to the OPC reference mix at 28 and 91 days.

In terms of emulating the characteristic compressive strength (f_c) performance of CEM II A/L 32.5N cements, the optimal range for SCC cement replacement would be in the order of 15-20%wt. However with careful design consideration it may be possible to incorporate SCC produced from ceramic mass finishing media at higher ratios.

3.4.2 CEM I 42.5R/SCC blended cements

The results obtained from CEM I 42.5R/SCC sample compression tests are shown in Figure 7. These results indicate a gradual and significant decrease in early compressive strength as the %SCC is increased. These findings are consistent with other research using fine ground ceramics [23, 25]. The early age strength is contrary to the results obtained from CEM II blends where 7 day strengths were approximately equal. The availability of free lime at an early age in CEM II A/L cements would have initiated pozzolanic reactions and therefore would influence early age strength.

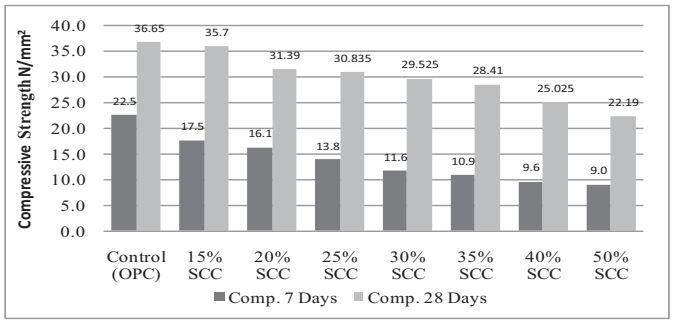


Figure7: Compressive strength of CEM I 42.5R samples

A gradual decrease in compressive strength was also recorded as SCC content increased for sample characteristic compressive strengths after 28 days. The lowest recorded strength was found in 50%SCC samples representing a 40% reduction.

The optimal cement replacement range indicated by CEM I/SCC samples correlates with the results from CEM II/SCC samples at 15-20%. Reductions in compressive strength in 20%SCC samples were 28% and 14% after 7 and 28 days of curing respectively. At a 15%SCC content, early age strength was reduced by 22% and only 3% after 28 days. Based on the results from CEM II/SCC samples it is expected that both 15%SCC and 20%SCC samples would exceed or at least match the compressive strength of the reference concrete after an extended period of curing.

4 CONCLUSIONS

The potential of using fine ground ceramic media sludge derived from mass finishing processes as a blended cement replacement has been investigated in this study. The results demonstrate this potential and the following conclusions can be drawn from the study:

I. The workability of SCC cement concretes reduce as the percentage SCC is increased, however, less energy would be required for compaction of the concrete when compared to OPC concrete.

II. SCC cement concretes display improved cohesion characteristics and are less prone to segregation.

III. The durability of SCC cement concretes would be improved in comparison to OPC concretes due to a reduction in water absorption capacity.

IV. SCC cement concretes lighten in color as the percentage SCC is increased which presents aesthetic benefits.

V. The optimal range for the incorporation of SCC has been found to be in the order of 15-20%. At this cement replacement rate SCC concretes display reduced early age strength, however, 28 day characteristic strengths are similar to those of OPC concretes. The long term strength of SCC concretes would be expected to exceed that of OPC concretes.

If sufficient volumes of waste ceramic media sludge were available, its use as a cement replacement would be potentially lucrative for re-processors.

ACKKNOWLEDGEMENTS

This research programme was realized through the funding and support of John Gannon Concrete Ltd.

REFERENCES

[1] Chen, C., Habert, G., Bouzidi, Y. & Jullien, A. (2010) Environmental impact of cement production: detail of the different processes and cement plant variability evaluation. *Journal of Cleaner Production,* 18 (5) pp. 478-485.

[2] Puertas, F., García-Díaz, I., Barba, A., Gazulla, M.F., Palacios, M., Gómez, M.P. & Martínez-Ramírez, S. (2008) Ceramic wastes as alternative raw materials for Portland cement clinker production. *Cement and Concrete Composites,* 30 (9) pp. 798-805.

[3] Dhir, R.K., Dyer, T.D. & Halliday, J.E. (2002) *Sustainable Concrete Construction: Proceedings of the International Conference Held at the University of Dundee, Scotland, UK on 9-11 September, 2002.* Thomas Telford

[4] Siddique, R. (2010) *Waste Materials and By-Products in Concrete.* Springer

[5] Rao, A., Jha, K.N. & Misra, S. (2007) Use of aggregates from recycled construction and demolition waste in concrete. *Resources, Conservation and Recycling,* 50 (1) pp. 71-81.

[6] Wagih, A.M., El-Karmoty, H.Z., Ebid, M. & Okba, S.H. (2013) Recycled construction and demolition concrete waste as aggregate for structural concrete. *HBRC Journal,* 9 (3) pp. 193-200.

[7] De Castro, S. & De Brito, J. (2013) Evaluation of the durability of concrete made with crushed glass aggregates. *Journal of Cleaner Production,* 41 (0) pp. 7-14.

[8] Park, S.B., Lee, B.C. & Kim, J.H. (2004) Studies on mechanical properties of concrete containing waste glass aggregate. *Cement and Concrete Research,* 34 (12) pp. 2181-2189.

[9] Saikia, N. & De Brito, J. (2012) Use of plastic waste as aggregate in cement mortar and concrete preparation: A review. *Construction and Building Materials,* 34 (0) pp. 385-401.

[10] Issa, C.A. & Salem, G. (2013) Utilization of recycled crumb rubber as fine aggregates in concrete mix design. *Construction and Building Materials,* 42 (0) pp. 48-52.

[11] Müller, U. & Rübner, K. (2006) The microstructure of concrete made with municipal waste incinerator bottom ash as an aggregate component. *Cement and Concrete Research,* 36 (8) pp. 1434-1443.

[12] Halicka, A., Ogrodnik, P. & Zegardlo, B. (2013) Using ceramic sanitary ware waste as concrete aggregate. *Construction and Building Materials,* 48 (0) pp. 295-305.

[13] Cen (2013) *EN 12620:2013 Aggragates for concrete*. European Community for Standarization.

[14] Yajun, J. & Cahyadi, J.H. (2003) Effects of densified silica fume on microstructure and compressive strength of blended cement pastes. *Cement and Concrete Research,* 33 (10) pp. 1543-1548.

[15] Bouzoubaâ, N., Zhang, M.H. & Malhotra, V.M. (2000) Laboratory-produced high-volume fly ash blended cements: compressive strength and resistance to the chloride-ion penetration of concrete. *Cement and Concrete Research,* 30 (7) pp. 1037-1046.

[16] Kolani, B., Buffo-Lacarrière, L., Sellier, A., Escadeillas, G., Boutillon, L. & Linger, L. (2012) Hydration of slag-blended cements. *Cement and Concrete Composites,* 34 (9) pp. 1009-1018.

[17] Idir, R., Cyr, M. & Tagnit-Hamou, A. (2011) Pozzolanic properties of fine and coarse color-mixed glass cullet. *Cement and Concrete Composites,* 33 (1) pp. 19-29.

[18] Shi, C., Wu, Y., Riefler, C. & Wang, H. (2005) Characteristics and pozzolanic reactivity of glass powders. *Cement and Concrete Research,* 35 (5) pp. 987-993.

[19] Chao-Lung, H., Anh-Tuan, B.L. & Chun-Tsun, C. (2011) Effect of rice husk ash on the strength and durability characteristics of concrete. *Construction and Building Materials,* 25 (9) pp. 3768-3772.

[20] Pan, S.-C., Tseng, D.-H., Lee, C.-C. & Lee, C. (2003) Influence of the fineness of sewage sludge ash on the mortar properties. *Cement and Concrete Research,* 33 (11) pp. 1749-1754.

[21] Bignozzi, M.C. & Bonduà, S. (2011) Alternative blended cement with ceramic residues: Corrosion resistance investigation on reinforced mortar. *Cement and Concrete Research,* 41 (9) pp. 947-954.

[22] Bignozzi, M.C. & Saccani, A. (2012) Ceramic waste as aggregate and supplementary cementing material: A combined action to contrast alkali silica reaction (ASR). *Cement and Concrete Composites,* 34 (10) pp. 1141-1148.

[23] Heidari, A. & Tavakoli, D. (2013) A study of the mechanical properties of ground ceramic powder concrete incorporating nano-SiO2 particles. *Construction and Building Materials,* 38 (0) pp. 255-264.

[24] Katzer, J. (2013) Strength performance comparison of mortars made with waste fine aggregate and ceramic fume. *Construction and Building Materials,* 47 (0) pp. 1-6.

[25] Pacheco-Torgal, F. & Jalali, S. (2010) Reusing ceramic wastes in concrete. *Construction and Building Materials,* 24 (5) pp. 832-838.

[26] Pereira-De-Oliveira, L.A., Castro-Gomes, J.P. & Santos, P.M.S. (2012) The potential pozzolanic activity of glass and red-clay ceramic waste as cement mortars components. *Construction and Building Materials,* 31 (0) pp. 197-203.

[27] Sánchez De Rojas, M.I., Marín, F., Rivera, J. & Frías, M. (2006) Morphology and Properties in Blended Cements with Ceramic Wastes as a Pozzolanic Material. *Journal of the American Ceramic Society,* 89 (12) pp. 3701-3705.

[28] Tydlitát, V., Zákoutský, J., Volfová, P. & Černý, R. (2012) Hydration heat development in blended cements containing fine-ground ceramics. *Thermochimica Acta,* 543 (0) pp. 125-129.

[29] Winter, N.B. (2012) *Understanding Cement: An Introduction to Cement Production, Cement Hydration and Deleterious Processes in Concrete.* WHD Microanalysis Consultants

[30] Massazza, F. (1993) Pozzolanic cements. *Cement and Concrete Composites,* 15 (4) pp. 185-214.

[31] Cen (2011) IS *EN 197-1:2011 Cements-Part 1: Composition, specification and conformity criteria for common cements*. European Community for Standardization.

[32] Davidson, D.A. (2007) Mass finishing processes. *Metal Finishing,* Volume 105 (Issue 10) pp. Pages 72-83.

[33] Medina, C., Banfill, P.F.G., Sánchez De Rojas, M.I. & Frías, M. (2013) Rheological and calorimetric behaviour of cements blended with containing ceramic sanitary ware and construction/demolition waste. *Construction and Building Materials,* 40 (0) pp. 822-831.

[34] Telchenné, D., Franklin, R. & Erntroy, H. (1988) Design of Normal Concrete Mixes (Second ed.). Watford: Building Research Establishment Ltd.

[35] Cen (2009a) IS *EN 12350-2:2009 Testing fresh concrete-Part 2: Slump-test*. European Community for Standardization.

[36] Cen (2009b) IS *EN 12350-4:2009 Testing fresh concrete-Part 4: Degree of compactability*. European Community for Standardization.

[37] Cen (2010) IS *EN 12350-11:2010 Self compacting concrete -Sieve segregation test*. European Community for Standardization.

[38] Cen (2000) IS *EN 12390-7:2000 Testing hardened concrete-Part 7: Density of hardened concrete*. European Community for Standardization.

[39] Bsi (2011) *BS 1881-122:2011 Testing concrete-Part 122 Method for determination of water absorption*.

[40] Cen (2009c) IS *EN 12390-3:2009 Testing hardened concrete - Part 3:Compressive strength of test specimens*. European Community for Standardization.

Impact of hydration on the properties of hemp-lime concrete

Walker_R, Pavia_S
Department of Civil, Structural and Environnemental Engineering, Trinity College, Dublin, Ireland
email: walkerro@tcd.ie, pavias@tcd.ie

ABSTRACT: Hemp-lime concrete is a low-embodied energy, carbon-negative, sustainable building material made with a lime-based binder and hemp aggregate. The material properties depend on several factors including: binder and hemp type and their ratio, water content, density, manufacturing method and curing conditions. This paper investigates hydration of a commercial binder which includes significant hydraulic additions. During curing, hydraulic binders compete for water with the (high suction) hemp particles. This competition can trigger a shortage of water for binder hydration which can undermine the performance of the concrete.
The paper investigates the effect of saturating the concrete in water following an initial curing period. It concludes that hydration restarts following the reintroduction of water: the Scanning Electron Microscope evidenced a significant increase in the amount of hydrates filling pores in the concrete following re-immersion. The results also evidenced that the increase in the amount of hydrates results in a compressive strength enhancement and a reduction in permeability and capillary absorption of the concrete. This paper highlights the importance of considering mixing water content and drying conditions (including time of demoulding, curing humidity and temperature and sample size) to ensure full hydration of hydraulic binder in hemp concrete and obtaining optimum performance of the material.

KEY WORDS: Hemp-lime concrete; Hydration; Microstructure; Strength; Permeability; Capillary absorption

1 INTRODUCTION

Hemp-lime concrete is an alternative to conventional construction materials. It is a low-embodied energy, carbon-negative, sustainable building material made of a lime-based binder and hemp aggregate. It was developed in France in the 1990s and has since been used in hundreds of houses in Europe. Although an innovative material, organic matter has been added to building materials since antiquity.
Hemp-lime concrete is light-weight (average wall density 275-400kg/m^3) and non-structural, typically used in combination with load-bearing frames. The material properties depend on several factors including: binder type, binder:hemp ratio, mixing water content, density, hemp shiv properties, manufacturing method, curing conditions and age.
It typically exhibits low strength and a ductile compressive failure between 0.2-1.2 MPa [1-7] and an open pore structure (70.6% porosity [8]). Hemp-lime concrete has excellent thermal performance: a high thermal capacity (1000 J/kgK [9], 1240-1350 J/kgK [10], 1560±30 J/kgK [11]) coupled with a medium density and a low thermal conductivity (0.05-0.12 W/mK [12]) provide the material with good insulation capabilities.
The hemp-lime concrete comprises of hemp shiv (approximately 5-30mm in length) coated by a binder that forms a matrix that holds the concrete together. Evrard and de Herde (2010) identified three types of pores; 1-10mm air voids that are interconnected and separated from the shiv by a binder coating, micro pores in the hemp shiv c.10um and smaller pores in the lime matrix c.1um [13]. Hydrates in the binder further reduces the pore size.
The binder is typically lime based with hydraulic additions to facilitate setting and early strength development. Commercial binders specially formulated for use with hemp are also available in the market. Their formulation are not accurately known but may contain hydraulic additions including Portland cement, hydraulic lime and pozzolans.
The hydraulicity of the binder should be low to avoid competition for water with hemp particles. Furthermore, strongly hydraulic binders can lead to trapping residual moisture in hemp particles [1].
Following an investigation of hemp concrete durability (freeze:thaw and salt exposure) which involved saturating the concrete in water after 9 months curing, it was evident that exposing hemp concrete made with a commercial binder to water following curing increased binder hydration [7]. Such an increase in hydration was not evident for less hydraulic binders. This research investigates the effect of this additional binder hydration on compressive strength, permeability and capillary action of hemp concrete made with commercial binder.
Additional hydration of hemp-lime concrete, following initial curing has not yet been investigated although De Bruijn et al. (2009) observed an increase in compressive strength of samples with cement binder following freeze/thaw cycling and attributed this to the immersion in water for 24 hours prior to testing [14]. However, Evrard (2003) does not contemplate re-hydration, stating that an initial lack of water for hydration causes the concrete to powder and this is irreversible [1]. In cement mortars, hydration restarts following reintroduction of water however, the material may not achieve its full compressive strength due to cracking and to the formation of

different hydrates which may not contribute as much to strength [15].

In relation to mortar properties, increasing hydraulicity enhances pore size distribution and this is partly attributed to hydrates filling pores [16]. Increasing hydraulicity in lime mortars, increases strength, reduces water vapour permeability [17] and reduces capillarity [16]. However, these effects may not be directly comparable to hemp-lime concrete due to the macroporosity of its interparticular spaces [18].

As aforementioned, this research investigates strength development, permeability and capillary action. The concrete develops early strength due to the hydrates in the binder forming a continuous network [19] and it then gains strength more slowly due to carbonation [2]. The effect of the binder's hydraulic strength on hemp concrete has yielded varying opinions. Hirst et al. (2010) found that the strength of the concrete is not directly related to the strength of the binder [5]. Nguyen (2010) however claims that stronger binders can increase the strength of the concrete, provided that their hydraulicity is not compromised by a shortage of water [20]. De Bruijn et al. (2009) and Murphy et al. (2010) also showed that compressive strength of hemp concrete increased with increasing binder hydraulicity [4, 14]. Walker and Pavía (2014) investigated the strength of hemp concrete with a range of binders including calcium-lime/pozzolan; calcium-lime/hydraulic-lime/cement and commercial binder. The authors found that strength development was a function of binder hydraulicity up to 6 months but, at 1 year, all hemp concretes displayed a similar compressive strength (0.32-0.41MPa) [7]. It is evident that the commercial binder did not fully hydrate as discussed in this paper.

Hemp-lime concrete is commonly described as having good water vapour permeability. The common industry figure of water vapour diffusion resistance factor (μ) is 4.85 ± 0.24 [11, 21] in accordance with EN 12572 for samples with a binder:hemp:water ratio of 2:1:3 and density of c.400kg/m^3. Collet et al. (2009) measured water vapour permeability for moulded hemp samples with a binder:hemp ratio of 2:1 and density of c.420kg/m^3 and obtained a value 1.7x10^{-11} kg.m^{-1}.s^{-1}.Pa^{-1}[22]. Le Tran (2011 referring to Grelat 2005) observed that the binder strongly influences hemp concrete permeability with less hydraulic binders having a lower water vapour diffusion resistance factor however, like-with-like was not compared as the density varied between samples [23 referring to 24].

Walker and Pavia (2014) observed a vapour diffusion resistance factor between 5.42 and 5.71 for a range of binders including calcium-lime/pozzolan; calcium-lime/hydraulic-lime/cement and commercial binder for a density of c.360kg/m^3[10]. A trend of decreasing vapour permeability with increasing binder hydraulicity was established although not statistically significant. The lack of significance was attributed to the relatively small variation in binder hydraulicity amongst the concretes (as the commercial binder initially did not fully hydrate as discussed in this paper).

Hemp-lime concretes have high capillarity on account of their open pore structure and ability to hold water in their capillaries. Evrard (2008) measured a water absorption coefficient of 4.42 ± 0.27 kg/m^{2}h$^{1/2}$ for a concrete made with proprietary binder and density c. 487kg/m^3 in accordance with DIN 52617 [11]. Evrard (2003) states that concretes with higher hydraulicity have a lower capillary absorption [1]. Conversely, De Bruijn et al. (2009) observed no significant difference between the capillarity of concretes of varying hydraulic content and calculated the water sorption coefficient at 0.15kg/m^{2}s$^{1/2}$ for concrete with density ranging from 587 to 733 kg/m^3 [14]. In contrast, Walker and Pavía (2014) evidenced a relationship between decreasing permeability and increasing binder hydraulicity measuring water sorption coefficients between 2.65 and 3.37kg/m^{2}h$^{1/2}$ over the first 24 hours for a range of binders including calcium-lime/pozzolan; calcium-lime/hydraulic-lime/cement and commercial binder with density c.360kg/m^3 [10].

2 MATERIALS AND METHODS

2.1 Materials

The concrete was made using a commercial binder whose composition is not accurately known but has been formulated specially for use with hemp and contains hydraulic additions. Industrial hemp shiv was supplied by La Chanvrière De L'aube in central France. The water content was determined by the expertise of a skilled building practitioner, Henry Thompson to produce a suitable workability and was lower than that recommended by the manufacturer. The hemp:binder:water content (by weight) was 2:1:2.9.

2.2 Mixing, Curing and Compaction

Mixing was carried out on site in a large pan mixer at 2 batches per mix. The binder and ¾ of the water were mixed for 2.5 minutes to form a slurry. The hemp was then gradually added as well as the remaining water. The total mixing time was 7 minutes. After mixing, the concrete was put into cling-film lined, 100mm cubic moulds in a single layer. The mould was removed and the samples transferred to a curing room at temperature of 16°C±3°C and 55±10% RH.

2.3 Immersion after curing

For the compressive strength testing; 9 month cured 100mm cubes were immersed in water for 2 days and wrapped in plastic for 2 weeks. They were then allowed to dry for 2 months and then tested at 1 year. The results were compared against control samples that remained in the curing room until testing, also at 1 year. The initial dry density of the concrete was 360kg/m^3 and following saturation c.385kg/m^3.

The permeability and capillary action samples were similarly treated however, they were immersed at 1 year and tested at 1 year and 2.5 months. Their initial dry density was c.400kg/m^3 and c.428kg/m^3 following saturation. Four 100mm hemp-lime concretes cubes were tested for each property.

2.4 Microstructure

The microstructure of the binder and the surface of the hemp were investigated using a Tescan MIRA Field Emission Scanning Electron Microscope. The samples were freshly fractured and covered with a gold coating in an 'Emscope SC500' plasma coating unit. Individual hemp particles were

extracted from fractured surfaces and mounted on pin stubs prior to coating.

2.5 Strength

Compressive strength was measured on 100mm cubes using a Zwick Testing apparatus. No standards currently apply to hemp-lime concrete thus the testing procedures of EN459-2 [25] and EN196-1 [26] were used to guide the testing. The samples did not break but continuously deformed in a plastic manner. Failure strength was considered as the point at which the stress/strain curve departs from linear behaviour. The compressive strength (at 1 year) of concretes that were exposed to salt water spray in a SC1000 Open Lid Salt Fog Chamber [7] for 1 month followed by two months of drying is also discussed.

2.6 Permeability

The water vapour permeability was guided by EN 12086:1997 [27]. The specimens were placed on a dish with a small lip with one side exposed to the humid environment of the curing room (20±1°C and 50±5% RH) and the underside exposed to the dish containing 75g of calcium chloride, a desiccant that maintains the RH at 0%. The sides of the specimen are sealed by means of a rubber sleeve and sealant to ensure that water vapour transfer only occurs through the exposed surface of the specimen. The test was continued for 9 weeks and samples weighted at weekly intervals. The samples stabilised during three weeks and the readings from the subsequent six weeks provided the results to determine water vapour permeability.

2.7 Capillary Action

The water absorption coefficient by capillarity was guided by EN 1925:1999 [28]. The standard was altered in order to adapt it to the hemp-lime concrete. On account of the highly porous nature of the concrete, the duration of the test was 10,000 minutes. The samples were placed on a wire grill, in a container of water so that the water covered the lower 5mm of the samples, and weighted at intervals over time. The coefficient is a measure of the water sorption as a function of the surface area of the specimen and time.

3 RESULTS

3.1 Morphology

SEM evidenced abundant hydrates at the hemp-lime interface as shown in Figure 1. However, a large increase in the quantity of hydrates in the commercial binder as a result of water saturation is observed (Figure 2). Abundant needle-shaped hydrates are evident growing into the pores suggesting a reduction in pore size.

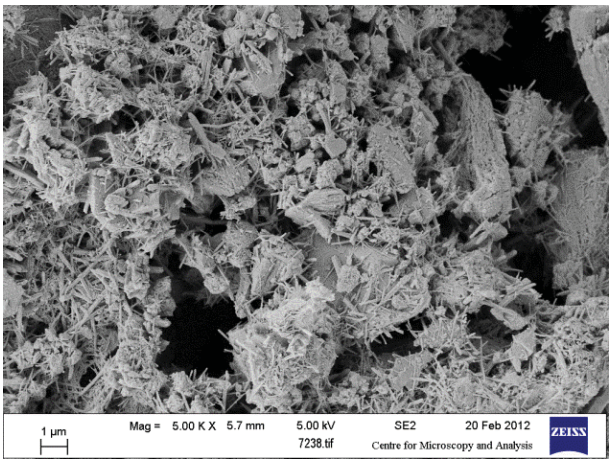


Figure 1. Hydrates in hemp-lime concrete made with commercial binder.

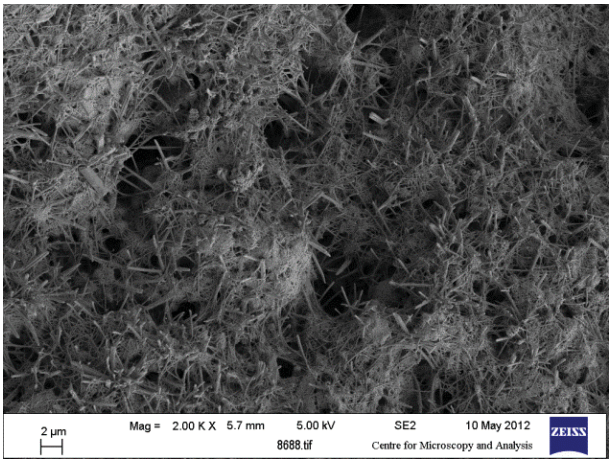


Figure 2. Increased quantity of hydrates in the binder of hemp concrete saturated with water for 2 weeks.

A weight gain of approximately 7% in the concretes immersed after curing further supports the evidence of an increased hydration: water was likely incorporated in additional hydrates resulting in weight gain of the hemp-lime concrete.

3.2 Strength

As aforementioned, the strength of 1 year concrete (immersed after curing) and 1 year (control) concrete was compared to the strength of 1 year concrete exposed to a salt spray solution at regular intervals for 1 month.

Compressive strength increased by 77% and 127% following saturation in water for 2 weeks and salt water spraying for 4 weeks respectively, as shown in Figure 3. This further suggests that the re-introduction of water into the concrete bearing hydraulic binder allows further hydration to occur. The high hydraulic component of the commercial binder clearly did not fully hydrate during initial curing. Re-introducing water allows additional hydration and clearly increases concrete strength (compared to the initial partially-hydrated concrete). The formation of new hydrates leading to strength increase is likely facilitated by a combination of the high water storage and outstanding water transfer properties

of the hemp concrete which allow water to penetrate; and the concrete's ductility which reduces the likelihood of cracking.
It was also observed that, when the concrete is exposed to water for longer (1 month spray test as opposed to 2 weeks water saturation), it exhibits an even higher compressive strength.

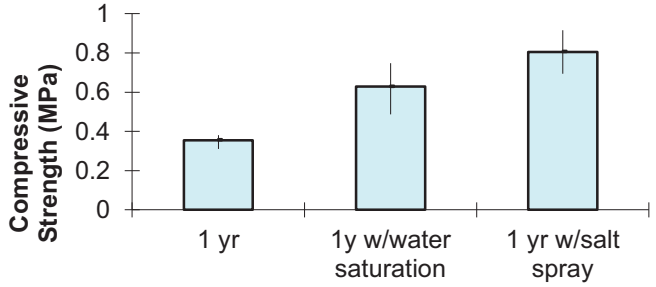


Figure 3. Compressive strength of concrete at 1 year.

3.3 Water Vapour Permeability

The water vapour permeability is initially very low, with a water vapour diffusion factor at 1 week of 11.5 and 16 for the control and saturated concretes respectively as shown in Figure 4. The permeability rate stabilised from about 3 weeks and it is observed that it takes longer for the water saturated concrete to achieve a constant permeability rate. There is a significant difference in the average water vapour diffusion factor of 6.1 for the concrete (curing room) and 7.6 for the concrete (water saturated) achieved between weeks 3 and 9. The results show a strong relationship between increasing binder hydraulicity and decreasing permeability. The results agree with Le Tran (2011 referring to Grelat 2005) who observed that the binder strongly influences the permeability of the concrete with less hydraulic binders having a lower water vapour diffusion resistance factor [23 referring to 24].

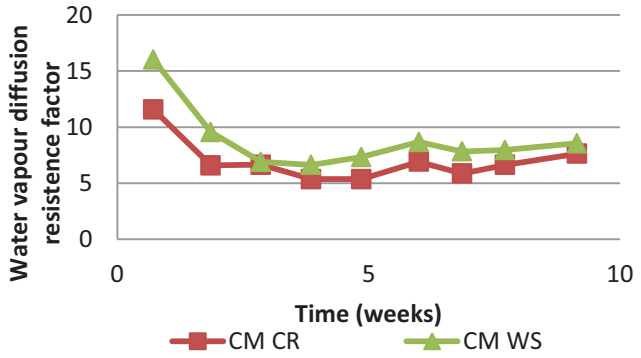


Figure 4. Water vapour permeability of concretes. CM CR – control concrete (curing room); CM WS concrete saturated in water for 2 weeks. Concrete tested at 14.5 months.

3.4 Capillary Action

The control and saturated concretes reached water sorption coefficient (slope of the line) of 2.14 and 3.88 respectively. The results further suggest that additional hydration due to reintroduction of water after initial curing reduces the sizes of the capillary pores and pore connectivity thereby reducing the water absorption due to capillary uptake at early ages (Figure 5). (Walker and Pavia 2014) also observed a relationship between decreasing capillary action and increasing binder hydraulicity in hemp-lime concrete with different binders [10].

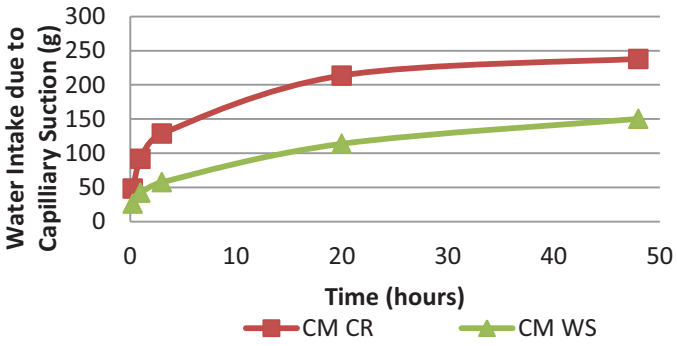


Figure 5. Water absorption due to capillary uptake over time. CM CR – control concrete (curing room); CM WS concrete saturated in water for 2 weeks. Concrete tested at 14.5 months.

4 DISCUSSION

The commercial binder is marketed as a lime based binder and therefore the high level of hydration recorded in this research was not expected. Evidently, there is a competition for water between the binder and hemp and the binder did not have enough water to fully hydrate. It appears that re-introducing water restarts the hydration process for unreacted binder. This disagrees with the assertion by Evrard (2003) that the lack of water for hydration causes the concrete to powder and this is irreversible [1].
In this research, there was insufficient water available for the full hydration of the concrete made with the commercial binder. This is due to either or both: low mixing water content or fast drying which will reduce the quantity of water available for binder hydration. However, the concrete was mixed and cured in a similar manner to other authors using commercial binders suggesting that it achieved similar hydration. The compressive strength reached by the concrete is similar to that reported by other authors which suggests similar hydration.
The water content slightly varied from the recommended quantity however it provided a suitable workability as determined by a skilled practitioner. The quantity of mixing water was 49% (by weight) which is within the range of other authors 42.4%-50.9% [19], 43%-48% [5] and similar to 50% [29]–all using commercial binders.
The curing conditions were also similar to those by other authors: 16°C±3°C and relative humidity 55%±10% which would result in similar drying conditions to 20±1°C and 60±5% RH [5] and 20°C and 65% used by [29]. Furthermore, Arnaud and Gourlay (2012) found that the ideal curing conditions for hydraulic lime and a commercial binder to achieve optimum compressive strength at 28 days is 20°C and 50% RH and that high relative humidity (98% and 75%) reduces the 28 day strength of a commercial and hydraulic lime binder [19].
The small specimen size (100mm cube) compared to the cylinders used by [5 and 19] likely hastened drying. Drying may also have been further hastened on account of directly demoulding the samples, which differed from demoulding at 6

days [5] and 5 days [29]. However, the duration of drying of the samples (c. 40 days) is longer than c. 30 days observed by [29]

In relation to mixing, prewetting the hemp may prove beneficial for hydraulic commercial binder. Cerezo (2005) and Nguyen (2010) prewet the hemp to avoid competition for water between binder and hemp shiv, this could enhance hydration of an eminently hydraulic binder [2, 20].

However, as aforementioned, irrespective of mixing and drying conditions, the compressive strength achieved by the concrete in this research suggests a similar level of hydration to other authors. The average compressive strength of the concrete at 28 days is 0.21MPa which is similar to 0.18MPa ([5] density 375kg/m^3) and 0.15-0.3MPa [19]. Furthermore, the compressive strength achieved following salt water spray for 1 month is 0.81MPa at 1 year for an initial concrete density of c.360kg/m^3. This is at the upper end of the compressive strength range achieved for hemp-lime concretes by other authors, and suggests that this quantity of hydrates is rarely achieved in the concrete.

It is evident that the binder did not fully hydrate, and this illustrates the importance of considering the binder's hydraulicity when selecting optimum mixing water content and curing conditions to ensure full hydration.

5 CONCLUSION

- Water saturation can restart hydration in partly hydrated hydraulic binders of hemp concretes. Weight gain is attributed to incorporating water in the formation of new hydrates.
- Additional hydration reduces pore sizes in the binder.
- Additional hydration increases compressive strength and reduces permeability and capillary action.
- Mixing water content and drying conditions (including time of demoulding, curing humidity and temperature and sample size) must be carefully controlled to ensure full hydration of the concrete binder.

ACKNOWLEDGMENTS

The authors wish to thank the Environmental Protection Agency for funding this research. The authors also thank the Traditional Lime Company, Clogrennane Lime and Ecocem for the provision of materials and also Dr Heath Bagshaw (Centre for Microscopy and Analysis) for his help with the SEM.

REFERENCES

[1] Evrard, A. (2003), *'Hemp Concrete- A synthesis of physical properties',* Construire en Chanvre, France.

[2] Cerezo, V. (2005), *'Propriétés mécaniques, thermiques et acoustiques d'un matériau à base de particules végétales: approche expérimentale et modélisation théorique'*, PhD thesis, L'Institut National des Sciences Appliquées de Lyon, France.

[3] De Bruijn, P. (2008), '*Hemp Concretes - Mechanical Properties using both Shives and Fibres',* Licentiate Thesis, Swedish University of Agricultural Sciences, Sweden.

[4] Murphy, F., Pavia, S., Walker, R. (2010), 'An assessment of some physical properties of limehemp concrete', *Proceedings of the Bridge and Concrete Research Ireland (BCRI),* University of Cork, Cork, 431 – 438.

[5] Hirst, E., Walker, P., Paine, K., and Yates, T. (2010), 'Characterisation of Low Density Hemp-Lime Concrete Building Materials under Compression Loading', *Proceedings of the 2nd International Conference on Sustainable Construction Materials and Technologies,* Italy.

[6] Gourlay, E., and Arnaud, L. (2010), 'Comportement hygrothermique des murs de béton de chanvre', *Proceeding of Société Française de Thermique*, Le Touquet, France.

[7] Walker, R., and Pavia, S. (2014), 'Mechanical properties and durability of hemp-lime concretes', *Construction and Building Materials, in press.*

[8] Collet, F., Bart, M., Serres, L., and Miriel, J. (2008), 'Porous structure and water vapour sorption of hemp-based materials', *Construction and Building Materials*, 22(6), 1271-1280.

[9] Tran Le, A. D., Maalouf, C., Mai, T. H., Wurtz, E., and Collet, F. (2010), 'Transient hygrothermal behaviour of a hemp concrete building envelope', *Energy and Buildings*, 42(10), 1797-1806.

[10] Walker, R., and Pavia, S. (2014a), 'Moisture transfer and thermal properties of hemp-lime concretes', *Construction and Building Materials, in press.*

[11] Evrard, A. (2008), *'Transient hygothermal behaviour of hemp-lime material',* PhD thesis, Universite catholique de Louvain, Belgium.

[12] Daly, P., Ronchetti, P. and Woolley, T. (2012), *'Hemp Lime Bio-concrete as a Construction Material',* Enivoronmental Protection Agency, Ireland.

[13] Evrard, A., and de Herde, A. (2010). "Hygrothermal Performance of Lime-Hemp Wall Assemblies." *Journal of Building Physics*, 34, 5-25.

[14] De Bruijn, P. B., Jeppssona, K.-H., Sandin, K., and Nilssona, C. (2009), 'Mechanical properties of lime–hemp concrete containing shives and fibres', *Biosystems Engineering*, 103(4), 474-479.

[15] Takeshi, I., and Taketo, U. (2003), 'Effect of curing condition at early age on microstructure of hardened cement', *Japan Society of Civil Engineers*, 17-26.

[16] Arandigoyen, M., and Alvarez, J. I. (2006), 'Blended pastes of cement and lime: Pore structure and capillary porosity', *Applied Surface Science,* 252(23), 8077-8085.

[17] Svennberg, K. (2006), *'Moisture Buffering in the Indoor Environment',* PhD thesis, Lund University, Sweden.

[18] Wilkinson, S. (2009), *'A study of the moisture buffering potential of hemp in combination with lime and clay based binders',* MSc thesis, Centre for Alternative Technology, UK.

[19] Arnaud, L., and Gourlay, E. (2012), 'Experimental study of parameters influencing mechanical properties of hemp concretes', *Construction and Building Materials,* 28(1), 50-56.

[20] Nguyen, T. (2010), *'Contribution à l'étude de la formulation et du procédé de fabrication d'éléments de construction en béton de chanvre',* PhD thesis, Université de Bretagne-Sud, France.

[21] Evrard, A., and de Herde, A., (2005), 'Bioclimatic Envelopes made of lime and hemp concrete', *Proceedings of CISBAT,* Ecole Polytechnique Federale de Lausanne, Switzerland.

[22] Collet, F. (2009), 'Hydric characterization of sprayed hempcrete', *Proceedings of the 4th International Building Physics Conference,* Istanbul, Turkey.

[23] Tran Le, A. (2011), *'Etude des transferts hygrothermique dans le beton de chanvre et leur application au batiments',* PhD thesis, University of Reims Champagne-Ardenne, France.

[24] Grelat, A. (2005), *'Utilisation des matériaux renouvelables en parois de maisons individuelles à ossature bois',* Rapport final de l'Annexe 3- Expérimentations en laboratoire, Instrumentation in situ. Fédération Française Du Bâtiment, France.

[25] EN 459-1:2010 Building lime. Definitions, specifications and conformity criteria.

[26] EN 196-1-2005 Methods of testing cement. Determination of strength.

[27] EN 12086:1997 Thermal insulating products for building applications — Determination of water vapour transmission properties.

[28] EN 1925:1999 Natural stone test methods - Determination of water absorption coefficient by capillarity

[29] Evrard, A. (2006), "Sorption behaviour of Hemp-lime Concrete and its relation to indoor comfort and energy demand', *Proceeding of PLEA2006 - The 23rd Conference on Passive and Low Energy Architecture,* Geneva, Switzerland.

A Study on Cement Grout Rheology: Optimum Dosage of Superplasticisers Related to their Composition and Interaction with Mineral Additions

E. García-Taengua[1], M. Sonebi[1], S. Taylor[1], L. Ferrara[2], P. Deegan[3], A. Pattarini[4]
[1]Department of Civil Engineering, Queen's University, Belfast, Northern Ireland
[2]Department of Structural Engineering, Politecnico di Milano, Milan, Italy
[3]Banagher Precast Concrete, Banagher, Ireland
[4]Azichem, Goito (Mantova), Italy
email: e.garcia-taengua@qub.ac.uk, S.E.Taylor@qub.ac.uk, m.sonebi@qub.ac.uk, liberato.ferrara@polimi.it, peterd@bancrete.com, a.pattarini@azichem.it

ABSTRACT: The effect of different superplasticisers is closely related to the type of cement and also to the properties and amounts of different mineral additions. As a consequence, the optimum superplasticiser dosage is not the same in all cases, and is not the same for all superplasticisers. This study is framed on the basis of real working conditions in a precast concrete company, and represents the first step towards the optimisation of the self-compacting concrete (SCC) mixes. To study the effect that mineral admixtures have on superplasticisers performance, the rheology of different grouts with a water/solids ratio of 0.40 has been studied using the Marsh cone. All results have been analysed by means of multiple linear regression. Optimum dosages for selected superplasticisers currently used in a particular precast concrete company are determined as a function of the composition and amounts of different mineral additions. This makes it possible to optimise grout composition to be applied to the optimisation of the cement matrix of SCCs. As a result, real production conditions can be adjusted and take advantage of these findings for continuous improvement.

KEY WORDS: cement grouts; superplasticisers; mineral additions; self-compacting concrete.

1 INTRODUCTION

The use of mineral admixtures such as limestone powder or filler (LSP), fly ash, silica fume or ground granulated blast furnace slag (GGBS) affects the interaction between superplasticiser (SP) and cement, mainly in terms of SP adsorption [1]. The interaction between mineral admixtures and cement is also modified by the type and SP dosage. As a result, the effect of admixture-cement interactions on the properties of fresh concrete are difficult to rationalise, specially in the case of systems including mineral admixtures [5]. However, the rheology of fresh grouts and cement pastes is directly linked to the development of mortar and concrete microstructure [1], and hence the convenience of their study.

The Marsh cone test measures grout or paste fluidity, as the inverse of the flow time. Though the cone geometry and volume to be tested varies between countries and authors, the principle is always the same. The flow time is directly related to fresh behaviour parameters such as yield stress and plastic viscosity [9, 3]. Therefore, besides being a workability test aimed at specification and quality control of cement pastes and grouts [9], and considering its simplicity and highly visual interpretability of the outcome, it has been extensively used for research and is the test selected to be used in this research.

The proliferation of high performance concretes in the last two decades has drawn attention to fine materials used to partially replace cement [7]. LSP usually has a positive effect on the rheology of fresh concrete, mainly improving cohesion and reducing yield stress, and therefore allows the reduction of SP dosage to enhance good workability levels [6]. However, this is not the case for all mineral admixtures, not even for all LSPs: mineral admixtures improve concrete performance but sometimes reduce workability, since the addition of a fine powder is likely to increase the water demand [4]. As a result of the complex interaction between different mineral admixtures and between them and the SP, the concept of compatibility between admixtures and SPs arises [1, 2, 3].

All the aforementioned aspects highlight the convenience of further research dealing with mineral admixtures and SP in grouts. Accordingly, the research reported in this paper proposes a new approach to analyse Marsh cone test results and explores the compatibility between two particular mineral admixtures (LSP and GGBS) and two SPs (SP1 and SP2).

2 EXPERIMENTAL PROGRAMME

2.1 Materials

The materials used to produce the grouts have been: cement, LSP, GGBS, in addition to water and SP. The chemical composition of cement, LSP and GGBS has been obtained by means of XRF and is summarised in Table 1.

Cement is CEM I 42.5R produced by Irish cement. LSP has an average particle size (d_{50}) of 9.1 microns, and GGBS has an average particle size of 13.8 microns. Their particle size distribution is shown in Figure 1.

Fluidity of cement pastes and grouts depends on the composition and effectiveness of the SP, which varies from one product to another [3]. Hence the convenience of considering more than one product. Accordingly, two polycarboxylate ether-based SPs have been used, SP1 and SP2. Their densities are 1.06 g/cm^3 and 1.08 g/cm^3 respectively. Both superplasticisers are similar in terms of water content (65% and 60% respectively) and composition, as can be observed by looking at their DTGA curves in Figure 2. Two significant differences are noticed: one extra peak at approx. 250ºC reveals a component of SP2 which is not found in SP1, and the first peak does not occur at exactly the same temperature in both cases.

Table 1. Chemical composition of the powders used.

	Cement	LSP	GGBS
SiO_2	19.61	1.74	35.65
TiO_2	0.336	0.011	0.735
Al_2O_3	5.02	0.09	11.53
Fe_2O_3	3.14	0.11	0.96
MnO	0.097	0.048	0.210
MgO	2.67	0.54	7.22
CaO	63.79	55.24	41.26
Na_2O	0.22	<0.003	0.26
K_2O	0.469	0.026	0.396
P_2O_5	0.077	0.132	0.008
SO_3	3.04	<0.002	2.33
L.O.I.	2.40	42.71	-0.86

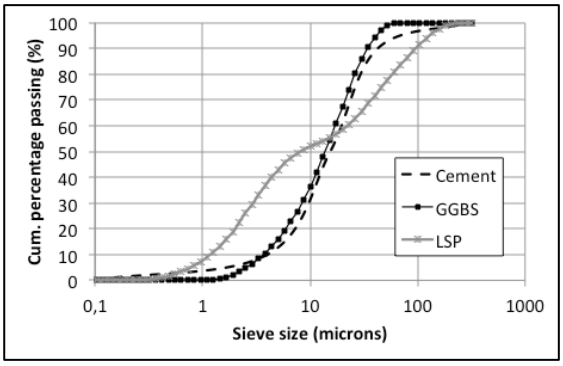


Figure 1. Particle size distributions of powders.

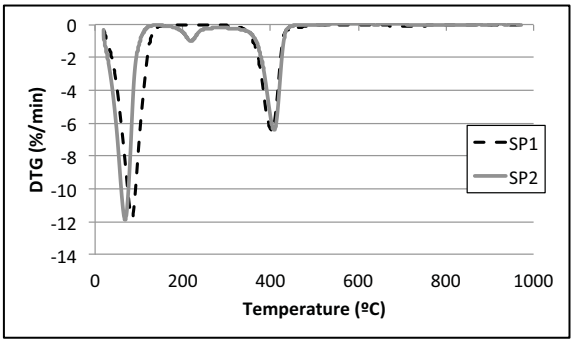


Figure 2. DTGA curves obtained for SP1 and SP2.

2.2 Composition of Grouts

The fundamental objective of this research was to study the effect that different percentages of LSP and GGBS have on Marsh cone flow times of the corresponding cement grouts. To do so, grouts with different weight percentages of their solid components have been produced and tested, according to the combinations shown in Table 2.

Since the effect of LSP and GGBS might differ depending on SP, these combinations have been produced and tested twice, using SP1 in a first series and SP2 in a second series.

The water/binder and water/solids ratios have a direct impact on Marsh cone flow times, as well as SP content [3]. In this research, the water/solids ratio was kept at 0.40 for all grouts. According to the recommendations of Aïtcin[10], the water/solids is usually assumed 0.35 for initial reference as long as the flow time for a SP dosage of 1% over binder weight falls between 60 and 90 seconds. If not, the possibility of varying this value must be considered. In the case of this research, after some preliminary tests where the flow time was higher than 90 seconds, it was decided to increase the reference water/solids ratio to 0.40 instead of 0.35.

Table 2. Percentages of solids in the combinations tested.

Grout ref.	Cement	Limestone	GGBS
G-0	100%	0%	0%
G-30L	70%	30%	0%
G-25G	75%	0%	25%
G-50G	50%	0%	50%
G-30L35G	35%	30%	35%

2.3 Grouts Production and Testing

Water has been used at a temperature between 15ºC and 18ºC in all cases. Since the sequence used to incorporate the different components into the mixer can significantly affect workability [3, 14], grouts production and testing has followed the same sequence of operations in all cases. The SP is dilluted in water and both are poured into the mixer. The mixer is started at low speed and all solids are gradually poured during 1 min 30 sec approx. After that, the grout adhered to the mixer is returned to the mix and then the mixer is operated again at medium speed. One minute before testing the mixer is operated at high speed.

The flowability of all grouts has been evaluated through the Marsh cone 7-min flow time, according to the standard EN 445: the time it takes for 1.2 litres of grout to pass the 10 mm opening of the cone has been measured for all grouts after 7 minutes mixing.

3 ANALYSIS OF RESULTS: METHODOLOGY

3.1 Flow Times and Flow Curves

7-min flow times obtained for different dosages of SP1 or SP2, expressed in terms of SP weight referred to the total binder weight, are given in Tables 3 and 4 respectively.

Table 3. Marsh cone test results for mixes made with SP1.

	SP content (% over binder weight)					
	0.6	0.8	1.0	1.2	1.4	1.6
	7-min flow times (seconds)					
G-0	70	60	56	50	51	56
G-30L	51	54	39	42	38	-
G-25G	77	75	65	64	61	63
G-50G	84	68	70	71	69	65
G-30L35G	34	32	32	31	-	-

Table 4. Marsh cone test results for mixes made with SP2.

	SP content (% over binder weight)					
	0.6	0.8	1.0	1.2	1.4	1.6
	7-min flow times (seconds)					
G-0	174	90	87	-	72	59
G-30L	77	37	38	33	37	-
G-25G	141	-	97	95	89	89
G-50G	161	132	114	110	-	111
G-30L35G	63	46	38	-	39	-

In each case, exponential curves have been fitted to the experimental results by means of nonlinear regression (using

the "Fitting curves" toolbox in Matlab 2014a), according to the following expression:

$$t(x) = a\ exp\left(1/_{bx+c}\right) \quad (1)$$

where: x is the SP content expressed in percentage over binder weight, $t(x)$ is the 7-min flow time, and a, b, and c are parameters to be obtained when fitting the equation. Table 5 shows the values obtained for these parameters.

This approach offers potential advantages when compared to other methodologies proposed to determine the saturation point [3]: it allows further interpretation of the experimental results because the three parameters a, b, and c define the position and shape of the flow curve. Parameter a is the asymptotic flow time and therefore informs of the maximum effect that the SP might have on a grout with a certain composition. Parameters b and c define the shape of the curve.

Table 5. Coefficients fitted (eq. 1).

	Grout ref.	a	b	c	x^*	$t(x^*)$
SP1	G-0	47.9	7.98	-2.01	0.73	62
	G-30L	31.6	2.69	0.493	0.68	48
	G-25G	56.2	7.49	-1.562	0.77	71
	G-50G	60.1	6.07	0.447	0.62	76
	G-30L35G	29.22	10.98	0.008	0.26	41
SP2	G-0	52.42	4.01	-1.56	1.78	63
	G-30L	23.37	2.63	-0.47	1.22	33
	G-25G	82.38	10.29	-4.31	1.26	93
	G-50G	104.4	20.35	-9.91	1.02	114
	G-30L35G	32.18	4.66	-1.01	1.00	43

3.2 Definition of Saturation Point

The saturation point, or optimum dosage, of a superplasticiser is the point beyond which additional superplasticiser is of no benefit [11]. This point is often determined visually, and there are a number of definitions based on the slope of the flow curve [3]. However, all these previous definitions are usually based on geometrical criteria and not on SP efficiency.

The authors have thought it convenient to introduce a more explicit definition for the saturation point, and therefore have attempted a new definition based on the efficiency of increasing amounts of superplasticiser. Once the exponential curve following eq. (1) has been fitted to experimental data, the saturation point or optimum SP dosage, x^*, is defined as the point beyond which no time reduction higher than 10 seconds is possible by adding SP at a dosage of 1% over binder weight. This criterion is exemplified in Figure 3. This value can be obtained from the following equation:

$$t(x^*) - t(x^* + 1) = 10 \quad (2)$$

Values for the optimum dosages, x^*, obtained for SP1 and SP2 together with the corresponding 7-min flow times, $t(x^*)$, are shown in Table 5.

4 RESULTS AND DISCUSSION

4.1 Effect of SP1 and SP2 on the reference grouts

The reference grouts in this research are those with no mineral admixtures, i.e. 100% cement. Figure 4 shows the flow curves obtained for the reference grouts using SP1 and SP2. It is observed that the asymptotic time is very similar for both admixtures (a is 48 seconds for SP1 and 53 seconds for SP2), and therefore their ideal, maximum performance on cement grout would be very similar. However, the shape of these curves clearly shows that SP1 is more efficient than SP2, because flow times for a certain superplasticiser dosage are lower for SP1 than for SP2. Furthermore the saturation point of SP1 corresponds to a lower dosage than that of SP2, and therefore the optimum performance is achieved in a more cost-effective way for SP1 than for SP2.

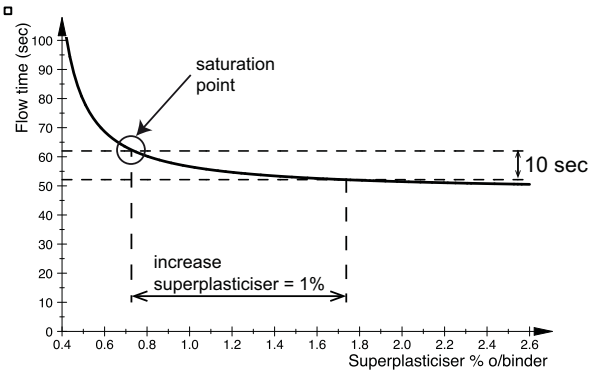


Figure 3. Definition of Saturation Point.

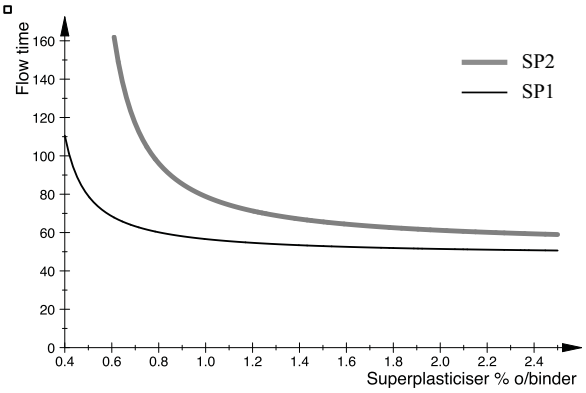


Figure 4. Flow curves for reference grouts (100% cement).

4.2 Effect of Limestone Filler (LSP)

It has been previously found that the use of LSP at contents higher than 20% improves the dispersion of all solid particles and enhances compatibility between cement and SP [2]. The term 'compatibility' has been used in literature to qualitatively describe the interaction between a cementitious material and a superplasticiser: the more compatible they are, the more flowable is the resulting grout, or paste. When cement replacement materials or inert powders are used, the compatibility between cement and SP is likely to be modified.

The results herein reported are coherent with previous findings. Figure 5 shows the flow curves obtained for grouts with 30% LSP and 70% cement, compared to those obtained for the reference grouts. It is observed that using LSP implies a general reduction of flow times.

This reduction is especially important when the superplasticiser used is SP2, which has been identified as the less performant in reference grouts. As a result, the performance of both superplasticisers is very similar for dosages above 0.75 % over binder weight when 30% of the solids in the grout is replaced by LSP. Therefore, the addition of LSP is positive not only from the point of view of the grout

fluidity but can also counterbalance a possible lack of efficiency of the superplasticiser.

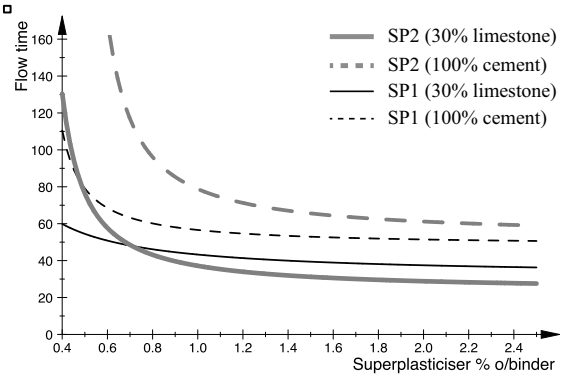


Figure 5. Flow curves for grouts G-30L.

This is due to the fact that limestone powders complement the deficiency in fine particles of the cement, enhancing stability of fresh grout and playing a lubricating role between the relatively coarser cement grains [6]. Indeed it can be seen in Figure 1 that the limestone filler used in this research has a wide particle size distribution (ranging from d_{10} = 1.19 microns to d_{90} = 96.4 microns). Generally, the use of LSP increases yield stress and reduces plastic viscosity, implying better stability and flowability [8].

It is true that in some cases limestone powders have been found to have quite the opposite effect, but this has been attributed to fillers with high MgO contents [6]. This is not the case, because the limestone filler used in this research has a negligible MgO content (see Table 1).

4.3 Effect of GGBS

Figure 6 shows the flow curves obtained for grouts with GGBS contents of 25% and 50%, compared to those obtained for the reference grouts.

It is observed that replacing cement with GGBS has a negative impact on grout flowability, implying a general increase of flow times, especially when the superplasticiser used is SP2, which has been identified as the less performant.

In this case, it is clear that the replacement of cement with GGBS causes a severe loss of compatibility between cement and superplasticiser SP2.

Generally, the use of GGBS has been reported to improve flowability and mix cohesion [11, 12, 15]. However, it has been sometimes detected that using mineral admixtures can reduce workability, and when this happens, the most recurrent explanation found by other authors involves an increase in water demand [4] due to a higher surface to volume ratio.

A final explanation for this has not been found by the authors yet. However, there are several aspects that can explain the negative impact of GGBS on flow times reported here. First, the flaky shape of GGBS particles might be increasing the friction close to the cone orifice when the grout is flowing out of the Marsh cone. Second, as can be observed in Figure 1, the size distribution is rather narrow when compared to that of the limestone filler (d_{10}-d_{90} range is 3.67-34 microns): this can mean an inefficient lubricating role of GGBS particles. Third, it is possible that differences between SP1 and SP2 include the fact that some fraction of SP2 is adsorbed onto the GGBS particles while this does not happens with SP1. This could be a consequence of the different composition of SP1 and SP2 (see Figure 2) and needs to be further explored, for instance by looking for possible changes in the zeta potential [16]. And fourth, having only 50% of cement in the grout increases the average interparticle distance between cement particles and SP molecules. All these aspects may be at operation together.

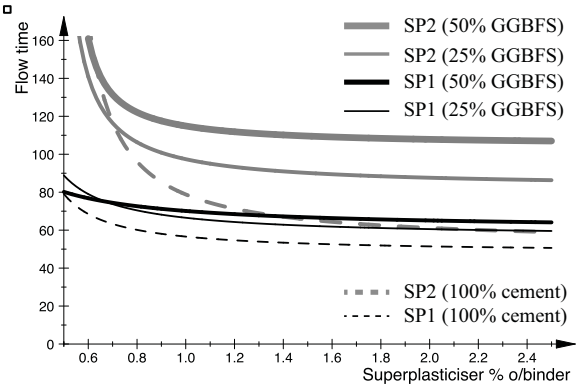


Figure 6. Flow curves for grouts G-25G and G-50G.

4.4 Interaction between Limestone Filler and GGBS

Following the results presented in sections 4.2 and 4.3, it can be concluded that the use of LSP implies a general reduction of flow times, while the use of GGBS has proved to have a contrary effect. Therefore, it would be reasonable to expect that these effects are someway counterbalanced when both mineral admixtures are used simultaneously.

However, this is not the case. Flow curves obtained for grouts when both filler limestone and GGBS are used together with cement (35% cement, 35% GGBS and 30% limestone filler) are shown in Figure 7. It can be observed that a general reduction in flow times is achieved when both mineral additions are used, regardless of the superplasticiser used. As a matter of fact, the flow curves obtained under these circumstances are quite similar to those corresponding to grouts with 30% LSP and no GGBS.

This behaviour can be explained in terms of the particle size distribution of these powders. Figure 8 shows the size distribution obtained when LSP and GGBS are blended in the same proportion. It is observed that this size distribution is not only wider than that of GGBS alone but also more continuous than that of LSP. This, and the fact that only 35% of grout solids is cement, explain the behaviour observed.

Therefore, it can be concluded that the effect of these mineral additions on flow times is not simple: they not only interact with the cement and superplasticiser but also between themselves. This interaction has turned out to be advantageous for the flowability of the grout. However, the problem is not trivial and cannot be generalised, since there are many conflicting cases that can be found in previous literature [4]. It is therefore of paramount importance to carry out preliminary tests to study the compatibility between mineral admixtures and superplasticiser rather than relying in general assumptions.

4.5 Optimum Superplasticiser Dosage

The relationship between the optimum superplasticiser dosage (saturation point), the type of superplasticiser, and the

percentages of LSP and GGBS over solids content has been modelled by means of multiple linear regression.

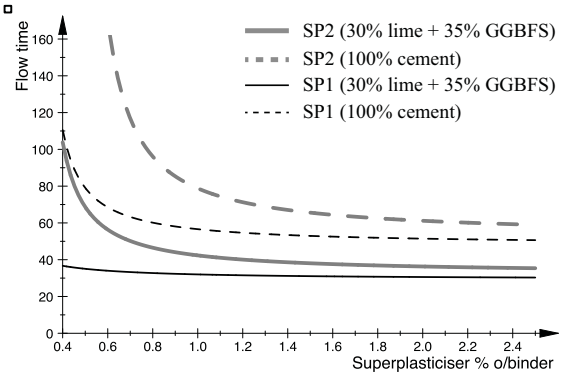


Figure 7. Flow curves for grouts G-35G30L.

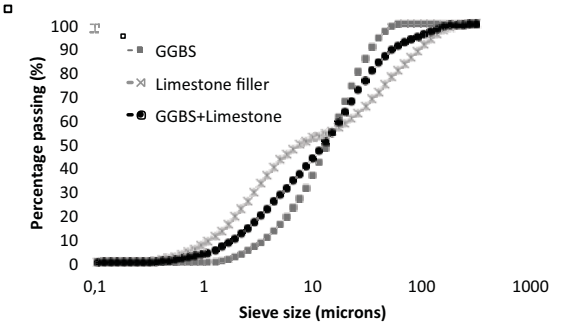


Figure 8. Particle size distribution for blend LSP+GGBS.

After fitting the experimental data, a highly accurate model (R-squared 91.6%) has been found for the SP saturation point, given by equations (3) and (4) for SP1 and SP2 respectively:

$$x^* = 0.929 - 0.0102L - 0.00885G \quad (SP1) \qquad (3)$$

$$x^* = 1.573 - 0.0102L - 0.00885G \quad (SP2) \qquad (4)$$

Where: x^* is the saturation point of the superplasticiser expressed in percentage over binder weight; L is the LSP percentage over total solids weight (between 0 and 30); and G is the GGBS percentage over total solids weight (between 0 and 50).

The model as given by equations (3) and (4) can be used to estimate the optimum dosage of either SP1 or SP2 in different scenarios as long as they fall within the ranges tested (LSP percentages between 0% and 30%, and GGBS percentages between 0% and 50%).

Figure 9 shows the effects plots for this model, together with the 95%-confidence intervals or bands. Black lines show the average trends. It can be observed that, in average, the saturation point for SP2 is twice as much as for SP1, in other words: SP1 is twice as efficient as SP1, in average.

With respect to LSP and GGBS, their use reduces the saturation point of the superplasticiser, either SP1 or SP2. This must not be misunderstood: this is advantageous only if the flow time corresponding to this optimum dosage is also reduced, as happens with LSP but not with GGBS, as will be discussed in the following section. As shown by these plots, using 30% of limestone filler causes an average reduction of 30% in the saturation point, and the use of GGBS causes an average reduction of 40%.

All aforementioned aspects lead to conclusions which are remarkable from the point of view of the superplasticisers cost-effectiveness. If both SP1 and SP2 have a similar cost per unit volume, choosing SP1 implies a reduction in superplasticiser consumption costs up to 50% at optimum dosage, and the use of LSP makes it possible to further reduce costs without compromising performance as long as the cost generated by consuming LSP is not greater than the cost reduction in SP consumption. On these grounds, economic optimisation for grouts and, by extension, for self compacting concrete is possible.

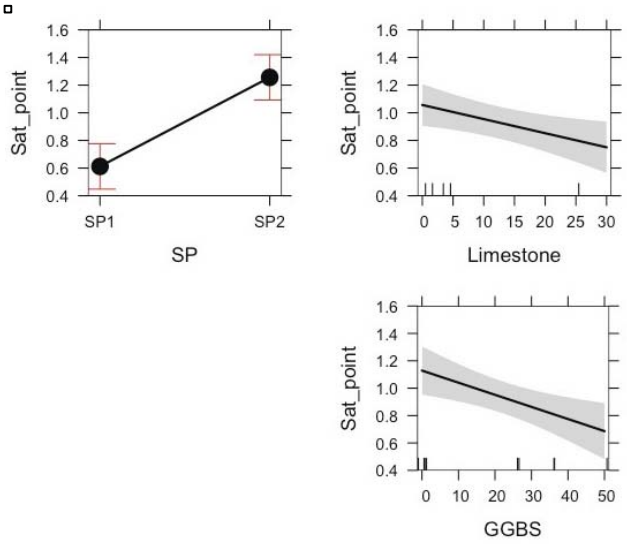


Figure 9. SP saturation point related to SP, LSP and GGBS.

4.6 Optimum Flow Time

The flow time corresponding to the SP saturation point stands for the maximum level of performance aimed at, because it is not reasonable to use higher SP dosages. It has been related to the type of superplasticiser and the percentages of LSP and GGBS over solids content by means of multiple linear regression. Equations (5) and (6) have been obtained:

$$t(x^*) = 63.58 - 0.447L + 0.282G - 0.02LG \quad (SP1) \quad (5)$$

$$t(x^*) = 63.58 - 1.092L + 1.017G - 0.02LG \quad (SP2) \quad (6)$$

Where: *t(x*)* is the flow time corresponding to the saturation point of the superplasticiser, expressed in seconds.

The model is highly accurate: R-squared is 99.3%. This model proves highly consistent with all previous discussion of experimental observations. In this regard, two particular aspects of this model have to be highlighted.

The first important aspect is that the type of superplasticiser modifies the effect of mineral admixtures on flow time: the constants multiplying L and G in equations (5) and (6) are different depending on whether SP1 or SP2 is used. The favourable effect of LSP on flow time is always significant, but specially when SP2 is used. Since this has been identified as the least performant SP in this research, it can be concluded that LSP introduces compatibility in the cement-SP system.

Figure 10 reflects that the use of GGBS up to 50% introduces no significant differences with respect to the reference grout when SP1 is used, which has turned out to be highly compatible with cement. On the contrary, if SP2 is

used, a replacement of 50% cement with GGBS implies that the flow time at the optimum SP dosage is twofold increased.

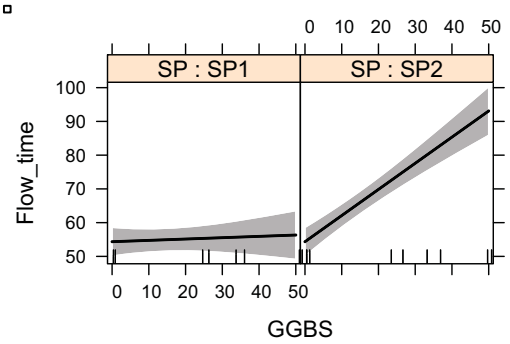


Figure 10. Flow time *t(x*)* related to SP and GGBS.

The second important aspect regarding this model is that the interaction between limestone filler and GGBS percentages has a significant effect on this flow time. Such interaction is represented by the term multiplying *L G* in equations (5) and (6). Figure 11 shows the average trends of flow time vs GGBS content for the two amounts considered for limestone filler (0% and 30% replacement). It can be seen that, when the grout solids are 30% limestone filler, the GGBS content has no significant effect on flow times. On the contrary, when the grout is produced without limestone filler, increasing GGBS content clearly increases flow times at optimum superplasticiser dosage. This reinforces the idea that the use of limestone filler at 30% introduces compatibility in the cement-admixture system.

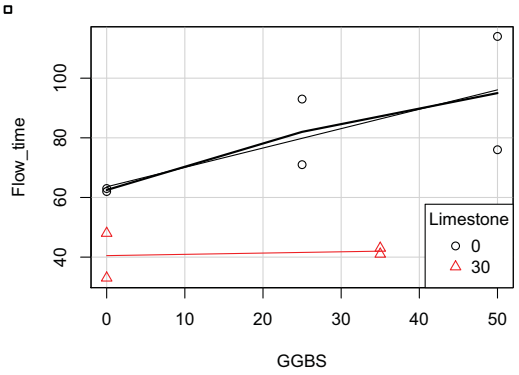


Figure 11. Flow time *t(x*)* related to LSP and GGBS.

5 CONCLUSIONS

- The compatibility between rapid cement, two mineral additions (LSP and GGBS) and two SPs (SP1 and SP2) has been studied in grouts using the Marsh cone.
- An exponential expression to analytically define the flow curves obtained from the Marsh cone has been proposed.
- A new definition based on SP efficiency has been proposed for the saturation point or optimum SP dosage.
- The ideal, maximum performance of SP1 and SP2 is similar. However, SP1 is more efficient and more compatible than SP2 with the mineral additions considered.
- Adding LSP is beneficial: it not only improves flowability but also counterbalances a possible lack of SP efficiency.
- Replacing cement with GGBS has a negative impact on flowability, implying a general increase of flow times, especially when SP2 is used.
- The addition of 30% LSP together with 35% GGBS has been proved to be a far better option than adding only GGBS, regardless of the SP used.
- The effect of mineral additions like LSP and GGBS on grout flowability is not simple: they not only interact with the cement and SP but also between themselves.

ACKNOWLEDGEMENTS

The research herein reported has been made possible by the funding received from the European Union, as part of the FP7-PEOPLE-2012-IAPP project "EiroCrete: Development of sustainable, lower carbon, pre-cast concrete infrastructure". The authors wish to thank their industrial partners as well: Banagher Precast Concrete (Ireland) and Azichem (Italy).

REFERENCES

[1] Burgos-Montes, O., Palacios, M., Rivilla, P., and Puertas, F. (2012). "Compatibility between superplasticizer admixtures and cements with mineral additions." *Construction and Building Materials*, 31, 300–309.

[2] Jolicoeur, C., and Simard, M. A. (1998). "Chemical Admixture-Cement Interactions: Phenomenology and Physico-chemical Concepts." *Cement and Concrete Composites*, 20, 87–101.

[3] Agulló, L., Toralles-Carbonari, B., Gettu, R., and Aguado, A. (1999). "Fluidity of cement pastes with mineral admixtures and superplasticizer - A study based on the Marsh cone test." *Materials and Structures*, 32, 479–485.

[4] Sonebi, M. (2001). "Factorial design modelling of mix proportion parameters of underwater composite cement grouts." *Cement and Concrete Research*, 31, 1553–1560.

[5] Nehdi, M., and Mindess, S. (1996). "Optimization of high strength limestone filler cement mortars." *Cement and Concrete Research*, 26(6), 883–893.

[6] Nehdi, M. (2000). "Why some carbonate fillers cause rapid increases of viscosity in dispersed cement-based materials." *Cement and Concrete Research*, 30, 1663–1669.

[7] Ferraris, C. F., Obla, K. H., and Hill, R. (2000). "The influence of mineral admixtures on the rheology of cement paste and concrete." *Cement and Concrete Research*, 31, 245–255.

[8] Hallal, A., Kadri, E. H., Ezziane, K., Kadri, A., and Khelafi, H. (2010). "Combined effect of mineral admixtures with superplasticizers on the fluidity of the blended cement paste." *Construction and Building Materials*, 24, 1418–1423.

[9] Aïtcin, P.C. (1998), *High Performance Concrete*, ed. by CRC Press, 624 pp.

[10] Fernandez-Altable, V., and Casanova, I. (2006). "Influence of mixing sequence and superplasticiser dosage on the rheological response of cement pastes at different temperatures." *Cement and Concrete Research*, 36(7), 1222–1230.

[11] Neville, A.M. (2011), *Properties of Concrete* (5th edition), ed. by Pearson, 846 pp.

[12] Hewlett, P.C. (2004), *Lea's Chemistry of Cement and Concrete* (4th edition), ed. by Elsevier, 1057 pp.

[13] Svermova, L., Sonebi, M., and Bartos, P. J. M. (2003). "Influence of mix proportions on rheology of cement grouts containing limestone powder." *Cement and Concrete Composites*, 25, 737–749.

[14] Bapat, J.D. (2012), *Mineral Admixtures in Cement and Concrete*, ed. by CRC Press, 310 pp.

[15] Plank, J., and Hirsch, C. (2007). "Impact of zeta potential of early cement hydration phases on superplasticizer adsorption." *Cement and Concrete Research*, 37(4), 537–542.

An assessment of some properties of Roman cement.

S. Pavía and M. Durcan
[1,2] Department of Civil, Structural and Environmental Engineering. Trinity College Dublin. Ireland.
email: pavias@tcd.ie, mickdurcan@gmail.com

ABSTRACT: Roman cement is a rapid natural cement produced by burning, below the melting point, limestone bearing abundant clay. Despite its name it has little to do with the lime-pozzolan binders the Romans used. Patented in 1796, it quickly became popular for several reasons. It perfectly imitates stone at lower cost so it was widely used for architectural decoration and sculptures and its fast setting allowed application to water structures. Furthermore, Roman cement led to the establishment of the prefabrication industry, as it produced water pipes with superior resistance than existing ones based on the first Portland cements (PC). Current uses include restoration, fast masonry, water proofing applications and rendering. Despite its fast setting and significant early strength, Roman cement does not reach (near) maximum strength within 28 days, as it is the case with PC materials, but continues to harden over several years, a time scale closer to that of lime mortars. As Roman cement does not contain free lime, this is due to the slow hydration of di-calcium silicate (belite-Ca_2S) which begins soon after the rapid initial set and continues rising strength slow and steady up to 10 years. This paper intends to contribute to the knowledge of Roman cement by comparing the density, porosity, capillary suction, mechanical properties and thermal output of Roman cement mortars with those of eminently hydraulic natural lime (NHL5) and PC mortars (CEMI). The mechanical and hygric performance of the Roman cement mortars studied are similar to those of NHL5 mortars. The water/binder ratio (close to 0.50), produced weaker, more porous and permeable Roman cement materials than equivalent PC mixes. Shrinkage and cracking are difficulties associated with binders in construction. However, the results evidenced that Roman cement undergoes slight, near-linear contraction when curing conditions are constantly at 20 ^{o}C and 65% relative humidity. This highlights its potential as a rendering material however, the shrinkage measured is lower than site shrinkage. The results also evidenced that Roman cement generates moderate temperatures when curing, and this can avoid problems associated with temperature gradients and heat dissipation on hydration. Roman cement has a wide and varied potential in the field of construction. Although extremely rapid setting, a low-cost, readily available product (citric acid) can retard hydration predictably.

KEY WORDS: Roman cement; Compressive and Flexural Strength; Shrinkage; Capillary suction; Porosity.

1 INTRODUCTION

In 1796, Parker filed a patent on the burning of marl nodules (septaria) [1]. The cement produced represented a major step forward in building because it was an emminently hydraulic binder with faster setting and hardening than the first Portland cements and the lime and lime/pozzolan mixtures of the past. The cement was produced by burning at low temperature (below the melting point) a clayey limestone or marl with a proportion of clay varying approximately from 22 % to 35%, using the simple technology traditionally used for lime furnaces [2]. The cement is simply ground and it does not need to slake due to the almost total lack of quick lime. The low quenching together with no slaking and easy grinding made production simple. As a result, in the early 19th century, production spread throughout Europe.

This cement was called “Roman cement”, an incorrect and confusing name as it has very little to do with the hydraulic, lime-pozzolan binders the Romans used. Other names include rapid natural cement, quick setting and prompt cement.

Roman Cement had many uses up until the early 20th century when Portland cement overtook construction. The material quickly became very popular for a number of reasons. Due to its ultra-fine grain size, Roman cement can produce accurate castings and was used to imitate carved stone. It perfectly imitates stone at a lower cost [1] so it was widely used for prefabricated mouldings, architectural decoration and sculptures (Figure 1). In addition, its fast setting allowed application to structures in contact with water. Furthermore, it led to the establishment of the cement-based prefabrication industry, as it was used to produce water outlet pipes of superior resistance to aggressive water than the existing pipes based on the first Portland cements. In Ireland and the UK, it was often used as a facade material in renders, run mouldings and prefabricated mouldings (Figure 1). Today, Roman cement is produced in several countries in Europe and current uses include restoration of facades and sculptures, fast masonry, water proofing applications and rendering.

As a result of the chemical composition of the raw material and the burning at low temperature (600 to 1200°C, slightly higher than that of hydraulic limes), the minerals produced are different to those in modern Portland cements but identical to those in natural hydraulic limes although in different proportions (Figure 2). Part of the raw stone does not heat enough to transform and it simply dehydrates while other parts are transformed into amorphous or low crystalline phases including aluminates (C_4AF, C_3A, $C_{12}A_7$, C_4A_3S and C_2AS) responsible for quick setting and hardening during the first hours of hydration; and silicates in the form of belite

(C_2S) which are slow strength raisers and increase resistance over several years [2]. There is only seldom clinkerization (melting) in local areas forming a small quantity of alite (C_3S), as this clinker begins to form at temperatures around 1200°C hardly reached in the Roman cement making process.

Due to these mineral components, Roman cement builds strength in two distinct phases over a very long period. Initially, on hydration, the aluminates formed at low temperature produce a quick set (at 2 to 3 minutes) which constitutes the first phase. Later, when belite is hydrated, the second strength building phase begins extending over many months. According to the The Louis Vicat Technical Centre [2], a 1:1 mix (by weight) with a water /cement ratio of 0.38 achieves a compressive strength of 14 N/mm^2 at 1 day of curing; 30 N/mm^2 at 1 month; and 45 and 65 N/mm^2 at 1 and 10 years respectively. The strength of the material varies according to mix proportions and water/cement ratio. Roman cement can be used in a very wide range of mix proportions (from 10 to 50% of the dry mortar weight and even 100% in the case of grouting and slurry). In general, water/cement ratios under 0.50 are required for high strength applications that require fast setting and low permeability such as waterproofing whereas water/cement ratios over 0.50 produce weaker, more porous and permeable materials with mechanical and hygric performance closer to those of natural hydraulic lime mortars [2].



Figure 1. Borris House, County Carlow, a 19th century building with Roman cement mouldings.

This paper investigates Roman cement mortars, retarded with citric acid, with water/cement ratios of 0.47. These conditions were set to make the material workable and compatible with original Roman cement and hydraulic lime mortars and thus more suited to repair a wide range of substrates. Ideal curing conditions for Roman cements require a constant relative humidity > 90% as this enhances hydration, reducing porosity and permeability due to a greater amount of hydrates filling pores. In this paper, curing conditions were ambient temperature and humidity in order to make the curing process comparable to site curing. On site, a more or less intensive drying takes place initially which works against hydration. A site produced mortar will have greater porosity and capillarity than the same mortar having undergone an ideal cure in the laboratory. This paper compares the density, porosity, capillary suction, compressive/and flexural strength and thermal output of Roman cement mortar with those of eminently hydraulic natural lime (NHL5) and cement mortars (CEMI).

2 MATERIALS AND METHODS

2.1 Materials and mixing

The cement was delivered as a dry-hydrate. All mixes were 1/3 binder to sand ratio by weight. The overall ratio of binder /sand/water was calculated as approximately 1: 3: 1/2 in accordance with EN 196-1 [3]. The Roman cement mortars were fabricated with high water /cement ratios (0.47) to achieve mechanical and hygric properties closer to those of historic Roman cement specimens. The water demand of industrial binders raises with the amount of free lime. The three binders include similar water/binder ratios as these are eminently hydraulic binders with little or no free lime (Table 1). In general, high water/binder ratios lead to greater voids and lower ultimate strength. As aforementioned, Roman cement requires water/cement ratios under 0.50 for high strength applications that require fast setting and low permeability such as waterproofing whereas water/cement ratios over 0.50 produce weaker, more porous and permeable materials.

The PC and NHL materials were mixed in accordance with EN 196-1 [3]. With regard to the Roman cement, citric acid was used as a retardant. As the manufacturer's dosage was vague, experiments were conducted to measure the initial set with varying amounts of citric acid to select the correct amount of retarder.

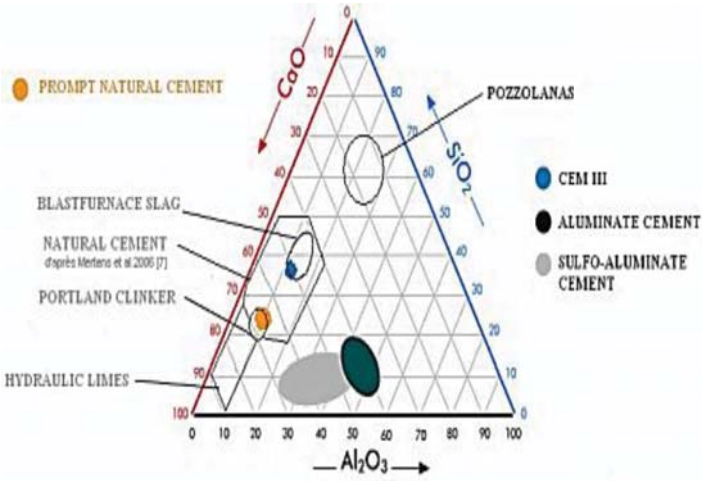


Figure 2. Composition of Roman (prompt) cement compared with other cements in Europe [2].

Table 1. Mortar composition. (*)+8 g. (0.7%) citric acid.

Binder	Binder (g)	Aggregate (g)	Water/binder
Roman cement(*)	1100	3300	0.47
PC	700	2100	0.52
NHL5	700	2100	0.44

2.2 Permeability

The permeability was measured with an Autoclam apparatus on 100mm cubes. The apparatus is assembled over one of the faces of the cube ensuring the seal is not exposed at the edge.

The Autoclam maintains an even head of water upon the face of the cube while simultaneously measuring the amount of water that permeates the surface. The test lasts 15 minutes and pressure readings and quantity of water penetrated are recorded every minute. The values reported are the arithmetic mean of three tests.

2.3 Capillary absorption

The dry specimens were weighed and placed 2 mm deep into water according the RILEM [4] recommendations. The weight was recorded after 15 and 30 minutes and one, three, eight and twenty-four hours. The weight of water absorbed was plotted against the square root of time. The values reported are the arithmetic mean of three tests.

2.4 Densities and porosity

The bulk (δ) and real (δr) densities and porosity were determined according to RILEM recommendations [4] with the equations below; where md is the dry mass; mh the hydrostatic mass and ms the water saturated mass at atmospheric pressure. The values reported are the arithmetic mean of three tests.

$$\delta = \frac{m_d}{m_s - m_h} \quad \delta_r = \frac{m_d}{m_d - m_h} \qquad (1,2)$$

The open porosity was calculated according to the following equation.

$$p = \frac{m_s - m_d}{m_s - m_h} \text{x} 100 \qquad (3)$$

2.5 Compressive and flexural strength

The compressive strength Rc (MPa=N/mm^2) was measured using equation 4 [5]; where A (mm^2) is the sectional area and (F) the load at which failure occurred.

$$Rc = F / A \qquad (4)$$

The flexural strength (MPa) was calculated using equation 5 [6]; where Ff is the peak load (N); b the side of the prism (mm) and l the distance between supports (mm).

$$Rf_f = {1.5 x Ff x l}/{b^3} \qquad (5)$$

The values reported are the arithmetic mean of three/six tests.

2.6 Shrinkage

The decrease in length of the specimens (40x40x160mm), measured along the longitudinal axis, when the decrease is caused by any factor other than applied forces was measured with gauges accurate to 0.002 mm, on a daily basis for the first two weeks and then regularly for a month [7].

2.7 Thermal output

The thermal output generated by the Roman cement on hydration was recorded. This is an indirect measurement of strength development as hydration produces the cementing hydrates responsible for strength development. Nine thermocouples (K-type) were arranged along the central vertical and horizontal axes inside a cubic mould (250mm side), with one thermocouple placed outside to represent the ambient temperature. They were connected to a computer with a data recorder. After the mortar was poured into the mould and vibrated to remove air voids, recording of data began. As Roman cement reaches the initial set fast (even with a retardant), it was expected that the maximum thermal output will be reached relatively quickly so readings were taken every second for two and a half hours and every ten seconds for the subsequent 11 hours.

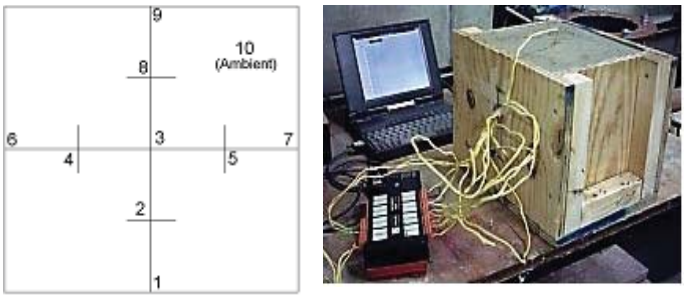


Figure 3. Thermocouple arrangement and orientation (left) and thermal output recording of uninsulated Roman cement.

3 RESULTS

3.1 Retardation

As aforementioned, experiments were conducted to measure the initial set when 0, 2, 4, 6, 8 and 10g of citric acid were added. As expected, the initial setting time rises linearly with the amount of acid. Following testing, 8 grams (0.7% of the cement weight) were selected to ensure approximately 45-60 minutes workability.

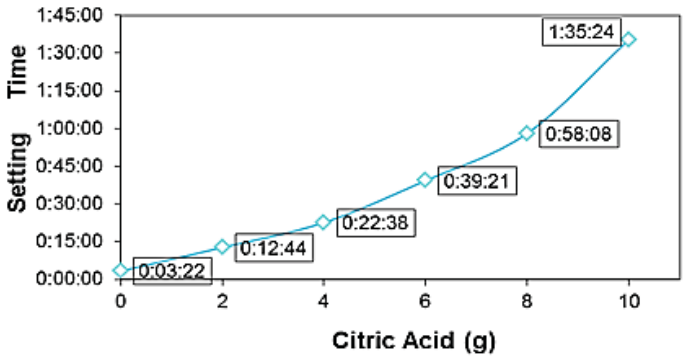


Figure 4. Influence of varying amounts of citric acid retarder on initial set of Roman cement.

3.2 Densities and porosity

According to the results, the Roman cement and NHL5 mortars have similar densities and porosity. The Portland cement mortar is slightly denser and contains less voids, exhibiting higher bulk density and similar real density which agree with its lower porosity. The porosity of the Roman cement mortar produced is similar to the porosity reported for the historic range (Table 2): an extensive analysis of historic Roman cements across Europe indicates porosity ranging from 20-45% (most common 22-32%) [8]. The Roman cement porosity obtained is at the higher end of equivalent laboratory specimens cured in optimum hydration conditions (>90% RH) which lie in the range 18–22% (Table 2).

The PC and NHL porosities agree with those previously reported on equivalent mixes. According to table 2, the porosities of PC and Roman cement are similar, closer than previously stated (according to Kozłowski et al. [8], the porosity of equivalent PC mixes is lower at 11%).

Table 2. Densities and porosity of the mortars in this paper and comparison with other authors [2,8,9,10].

Binder	Porosity %	Bulk density kg/m3	Real density kg/m3
RC	22.07	1946.00	2508.59
NHL 5	21.97	1933.00	2474.44
PC	17.63	2069.00	2511.32
RC (90%RH) [8]	18 - 22	-	-
RC (ancient) [2]	23 - 40	-	-
NHL 5 [9]	23 - 25	1879-1916	-
PC [9,10]	20-23	1840-2048	-

3.3 *Capillary suction*

The results evidenced a higher capillarity for the Roman cement. The Roman cement initially absorbs more water at a faster rate than the NHL5 mixes however, after approximately 8 hrs, they have absorbed a similar amount of water and suction stops. The PC mortars absorbed water at a lower rate and showed lower overall suction. These agree with the porosity results. The Roman cement capillarity is comparable to that reported by previous authors ranging from 4 –10 $kg/m^2/hr^{0.5}$ [8]. The Louis Vicat Technical Centre [2], for Roman cement bearing a higher water/binder ratio (0.95) however cured in optimum hydration conditions, reports a capillary suction of 1.4 $Kg/m^2.min^{0.5}$(at 3 hours) and 12.54 $Kg/m^2.min^{0.5}$(24 hours). The higher capillarity of the Roman cement in this study can be attributed to the existence of more abundant and coarser pores developed as a result of restricted hydration (due to curing in ambient conditions rather than in constant humidity over 90% which enhances hydrate formation). The lower values of the PC and NHL5 mortars also agree with the range reported by previous authors for PC (2 $kg/m^2/hr^{0.5}$ [8] and 0.055 $kg/m^2/s^{0.5}$ [9] and NHL5 (14$kg/m^2/hr^{0.5}$[8] and 0.25-0.30$kg/m^2s^{0.5}$ [9].

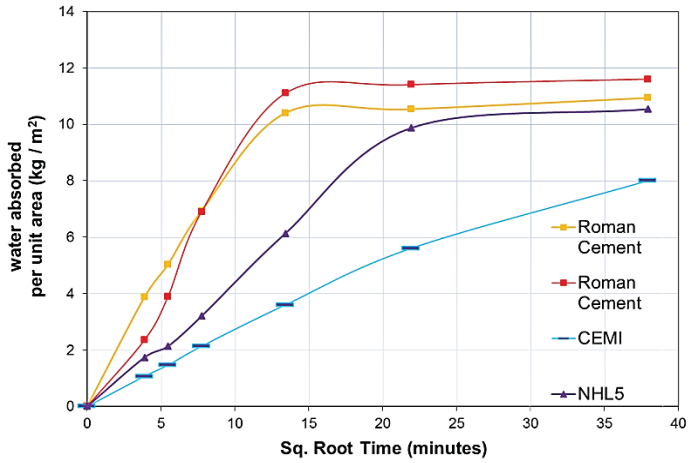


Figure 4. Water absorbed by capillarity over time (at 15 and 30 minutes and 1, 3, 8 and 24 hours).

3.4 *Permeability*

Two experiments were carried out both producing approximately linear results. However, the older specimens (10 days older) were more permeable. According to Kozłowski et al. [8], Roman cements initially display a coarser pore structure which is a function of the production of hexagonal hydrates (AFm phases) on aluminate hydration. These coarse pores later refine as a result of their infill with calcium silicate hydrates (CSH) formed on belite hydration which yields a final refined pore structure. The higher permeability of the older mortars can be due to the existence of coarser pores developed as a result of restricted hydration (due to curing in ambient conditions rather than in 90% humidity which refines the pore system by enhancing hydrate formation). In addition, some porosity can be related to microcracking induced by shrinkage at late stages. The Roman cement permeability values are higher than those reported for equivalent PC mixes [11].

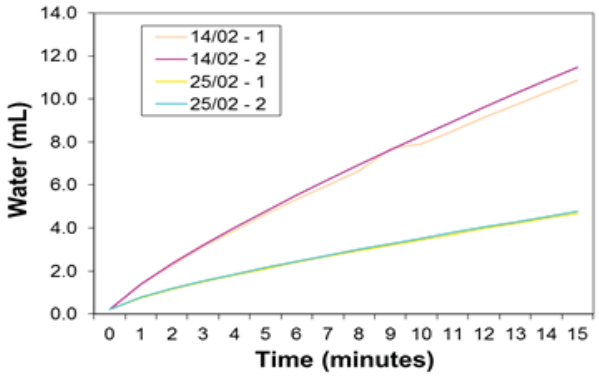


Figure 5. Permeability of Roman cement mortars: water intake over time during Autoclam experiment.

3.5 *Compressive and flexural strength*

The Roman Cement strength measured was compared with equivalent NHL and PC mortars (Table 3). Values (at 28 days) are average of 3 and 6 tests for compressive and flexural strength respectively. Most COVs ranged from 4.1 to 22. As expected from the water/binder ratio of 0.47, the mechanical performance of the Roman cement is close to that of the natural hydraulic lime mortars. The Roman cement has strength slightly superior than the NHL5 mortars but lower than the PC mortar. The values are comparable with those of PC/lime mixes typically used in construction (Table 3).

The strength results agree with several authors however, they are lower than other values reported. The compressive strength recorded is comparable with the 5-7 N/mm^2 at 28 days reported by Kozłowski et al. [8] and the 3.8 N/mm^2 (for equivalent mixes with higher w/b (0.95) cured in optimum hydration conditions) reported by [2]. However, a 1/3 mix (by weight) with a water /cement ratio of 0.50 can achieve a compressive strength of 16 N/mm^2 at 1 month; and 35.16 N/mm^2 at 1 year [2]. The lower values in this study (6-9 N/mm^2 at 1 month) are probably due to the higher dosage of retarder used to achieve a specific workable life (it is well

known that citric acid delays clinker hydration therefore retarding strength development), a lower humidity during curing and a slightly higher water/cement ratio.

Table 3. Compressive and flexural strength of Roman cement and comparable NHL and PC/lime mortars.

Mix composition	Compressive strength (MPa)	Flexural strength (MPa)
Roman Cement	6.3-9.1	1-2.5
NHL5 (2.5:1) [12]	3-4	1
NHL5 [9]	9	1.9-2.4
NHL5 [13]	6	1.4
NHL5 [14,15]	4.4	1.5-1.9
NHL5 [16]	3.8-4.4	1.3
NHL5 [17]	5.7-6.1	1.3-1.6
PC [18]	15	-
PC [9]	16-24	2.9
PC/lime/sand 1/ 0 /6 [19]	9.8	3.5
PC/lime/sand 1/0.25/6 [19]	12.7	4.4
PC/lime/sand 1/0.50/4 [20]	11-14	3-3.5

3.6 Thermal output

Despite its rapid set, Roman cement does not exhibit a strong exothermic output during curing. This is due to the absence of alite, whose reaction is highly exothermic. In Roman cement, the clinker that initially hydrates (responsible for the setting) is aluminate, whose hydration is not as highly exothermic as that of alite. As aforementioned, the retardant provided approximately 35 minutes workability. The end of the workable life is represented on the graph by the beginning of the accelerated thermal output after 20 minutes.

The maximum temperature reached was 29.51°C after 174 minutes (2.9 hrs). Subsequently, the material cools down and reaches ambient temperature after 900 minutes (15 hrs.) This thermal output is lower than that of Portland cement and the heat dissipation seems faster. For example, the surface of a 100cm cube of CEM I reaches 25°C at 10 hours (600 min) and 38°C at 20 hours [21] while the superficial gauge (gauge 9) of the Roman cement investigated reaches approximately 19°C at 10 hours and, after 15 hours, it has already reached ambient temperature. The maximum temperature recorded by the central gauge of the Roman cement investigated (gauge 3) is nearly 29°C after 107 minutes (1.78 hours) and approximately 23°C at 10 hours; after 15 hours, it has reached ambient temperature. In contrast, typical values reached at the centre of a 100 cm cube of CEM I are 30°C at 10 hours and 54°C at 20 hours [21]. As aforementioned, the lower heat evolution and faster heat dissipation of Roman cement when compared to Portland cement is due to its lack of alite. The temperature evolution at different locations remained consistent- the only gauge slightly incongruent is gauge 9 which was located at the top of the specimen and reflects the cool ambient temperature over the course of the night.

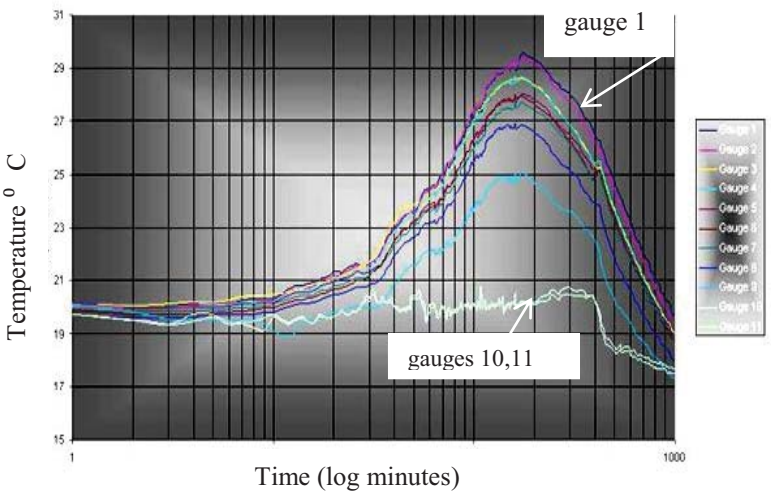


Figure 7. Thermal output of Roman cement over time. Gauges 10 and 11 record ambient temperature.

3.7 Linear shrinkage

The shrinkage readings are consistent, running relatively uniformly over the duration of the experiment. As it can be seen from figure 8, shrinkage ranges from approximately 86 to 100 µm. The maximum shrinkage is 100µm (625µm per meter) 0.062% of the original length of 160mm. The large increase in the rate of shrinkage for specimen [28/02 – 3] between the 24th and 28th day deviates excessively from all the other results and is probably due to a flawed reading.

The shrinkage values obtained agree with those reported by former authors [2] for similar mixes at 28 days (260 µm per meter). The shrinkage is lower than that reported by Wilk et al. [22]: 2310µm per meter at 28 days (520 at 14 days) in mixes with higher water content (w/b=0.65).

The shrinkage recorded is low, probably lower than site shrinkage. Drying shrinkage lowers with slower drying and increasing aggregate content and humidity, but it is however enhanced with increasing water/binder ratio. The mortars investigated are 1/3 mixes produced in the laboratory, in controlled ambient humidity. However, on site, curing conditions are uncontrolled and drying is often faster (at least initially). Furthermore, castings often use binder rich mixes which are more susceptible to shrink (as it is the cement binder what shrinks while the aggregate remains insensitive to drying). According to Wilk et al. [22], networks of fine cracks are characteristic of Roman cements both historic and new; and this prevents broader acceptance of Roman cement by the construction sector.

The NHL5 and PC shrinkage are comparable, although greater, than those previously reported (110 and 90 µm per meter for NHL5 and PC respectively at 28 days [9]). Generally, Roman cement materials show higher shrinkage than those based on the Portland cement [22]. A 5-month cured Portland cement paste produced at w/c = 0.5 reaches a total shrinkage of approximately 3000 µm/m at 45% RH (Rougelot et al. in [22]).

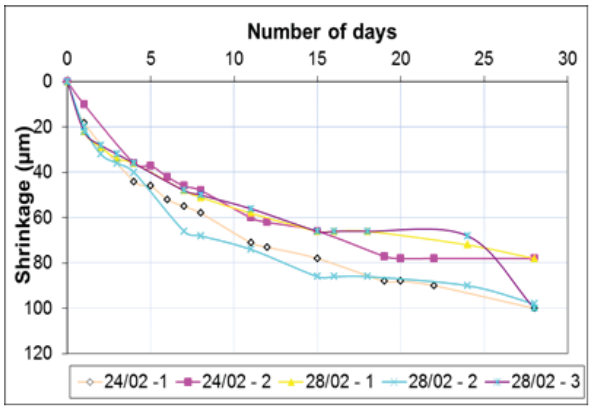


Figure 8. Linear shrinkage of Roman cement prisms over 28 days.

4 CONCLUSION

The mechanical and hygric performance of the Roman cement mortars studied are close to those of natural hydraulic lime mortars. This is probably due to the fact that they were fabricated with water/cement ratios close to 0.50, and as a result they are weaker, more porous and permeable than equivalent PC mixes.

Despite their fast setting and significant early strength Roman cement mortars do not reach their (near) maximum strength within 28 days, as it is the case with PC materials, but continue to harden over several years, a time scale closer to that of lime mortars. As Roman cement does not contain free lime, this is due to the slow hydration of di-calcium silicate (belite-Ca_2S) which begins soon after the rapid initial set and continues rising strength slow and steady- up to 10 years [2].

Shrinkage problems and cracking are difficulties associated with the use of binders in construction. According to the linear shrinkage experiment, Roman cement undergoes slight, near-linear contraction over a 28 day time period when curing conditions are constantly at approximately 20 degrees centigrade and 65% relative humidity. This highlights its potential as a rendering material.

Finally, Roman cement generates moderate temperatures when curing, and this can avoid problems associated with temperature gradients and heat dissipation during hydration.
Roman cement has a wide and varied potential in the field of construction. Although it is extremely rapid setting, a cheap and readily available natural product, citric acid, can retard hydration predictably.

ACKNOWLEDGMENTS

The authors wish to thanks the Chief Technician in the Department, Dr Kevin Ryan, and technical staff Patrick Veale, Michael Grimes and Eoin Dunne.

REFERENCES

[1] Parker and Co. (1796) Roman cement, artificial terras, and stucco. (Southwark, England)
[2] Groupe Vicat Liants Spéciaux (2007) Technical Specification for Prompt natural cement. The Louis Vicat Technical Centre, Laboratoire Materiaux et Microstructures.
[3] EN 196-1 (2005) Methods of testing cement Part 1: Determination of strength. European Committee for Standardization. Brussels.
[4] Commission 25-PEM, RILEM 'Essais recommandés pour mesurer l'alteration des pierres et évaluer l'efficacité des méthodes de traitement', *Materiaux et Constructions*, Bull. Rilem, **13** (75) (1980) 216-220.
[5] EN 459-2 (2010) Building lime, Part 2: Test methods. European Committee for Standardization. Brussels.
[6] EN 197-1(2011) Cement: Composition, specifications and conformity criteria for common cements. European Committee for Standardization. Brussels.
[7] ASTM C 596-96 Standard test method for drying shrinkage of mortar containing hydraulic cement.
[8] R. Kozłowski G. Hilbert C. Gurtner D. Hughes J. Weber Eds. (2012) Manual On Best Practice In The Application Of Roman Cements. Roman cement, past and present. Conservation theory and practice. Eu-Project No. 226898 | Rocare Fp7-Env-2008-1.
[9] K. Cosgrove & S. Pavía Mechanical and fluid transfer properties of some lime and Portland cement mortars. *Proceedings of PROHITEC 09* – Mazzolani editor, 2009, Taylor and Francis Group, London, 1603-1607.
[10] S. Pavía, B. Fitzgerald and E. Treacy (2006) An assessment of lime mortars for masonry repair, *Concrete Research Ireland, December, 2005*, University College Dublin, 101 – 108
[11] S. Pavía and E. Condren , A study of the durability of OPC vs. GGBS concrete on exposure to silage effluent, *Journal of Materials in Civil Engineering, ASCE*, 20, (4), 2008, 313 – 320
[12] Hanley R, Pavía S, (2008) A study of the workability of natural hydraulic lime mortars and its influence on strength, Materials and Structures, 41 (2) 373 – 381
[13] O'Donohue, N. (2008) *Influence of preparation and curing on physical properties of lime mortar.* Research thesis, unpublished, Dept of Civil Engineering, Trinity College Dublin.
[14] Duignan, P. (2009) *An assessment of the elasticity of hydraulic lime mortars*. Research thesis, unpublished, Dept of Civil Engineering, Trinity College Dublin.
[15] A. Costigan and S. Pavía (2010) Mechanical properties of clay brick masonry bound with hydraulic limes and hydrated calcium lime. *8th International Masonry Conference*, *Dresden*, edited by W. Jäger, B. Haseltine, A. Fried, 903 – 914
[16] A. Costigan and S. Pavia (2013) Influence of the mechanical properties of lime mortar on the strength of brick masonry in, editor(s) Jan Valek, John J. Hughes and Caspar J.W.P. Groot , *RILEM bookseries Vol. 7. Historic Mortars: Characterisation, Assessment and Repair*, Springer New York, 2013, 359 – 372.
[17] R. Patterson and S. Pavía (2012) Influence of loading rate and specimen geometry on lime mortar strength, *Bridge and Concrete Research in Ireland (BCRI) Conference.* Dublin Institute of Technology.
[18] Condren E. and Pavía S, A comparative study of the moisture transfer properties and durability of PC and GGBS mortars, *International Conference on Concrete Platform*, *Queen's University, Belfast*, *2007*, edited by Eds M.I. Russell and P.A.Muhammed Basheer , 2007, 468 – 478
[19] S. Pavia and O. Brennan (2013) Portland cement-lime mortars for conservation, *3rd Historic Mortars Conference (HMC13) University of the West of Scotland Glasgow, September 2013*, edited by J Hughes.
[20] A. Costigan and S. Pavia (2014) Effect of mortar water content in the properties of masonry. *9th International Masonry Conference Guimarães.* Escola de Engenharia. Universidade do Minho.
[21] PCA (Portland Cement Association) 1997 Portland Cement, Concrete and Heat of Hydration. Concrete technology today. Volume 18/Number 2 Skokie, Illinois USA, 1-7.
[22] Wilk, D, Bratasz, Ł., Kozłowski, R. Shrinkage cracking in Roman cement pastes and mortars. Cement & Concrete Research. 2013, Vol. 53, 168-175.

Real-time monitoring and performance of retaining structures

Eugene Baily[1], Bryan Mc Cabe[1], Jamie Goggins[1], Paul Kieran[2]
[1]Department of Civil Engineering, College of Engineering and Informatics, NUI Galway
[2]Shell Exploration and Production Ireland Limited
email: e.baily1@nuigalway.ie, bryan.mccabe@nuigalway.ie, jamie.goggins@nuigalway.ie, paul.kieran@shell.com

ABSTRACT: The advent of reliable real-time monitoring devices has changed the way we monitor the construction of geotechnical infrastructure. This paper presents a case study where Shaped Accel Arrays (SAA) were employed as part of the real-time monitoring regime for the construction of two retaining structures that utilised a combination of secant and sheet piles. To improve their structural rigidity, a capping beam and horizontal props were employed. The retaining structures were erected to facilitate the launching and retrieval of a Tunnel Boring Machine (TBM). The monitoring regime detected structural sway and toe movement of the sheet pile walls. Adjustment methods for these effects are discussed within this paper, along with a comparative study between manual and real-time monitoring. Adjusting for the effects of sway and toe movement can considerably change the maximum deflection from that registered by an SAA, therefore, it is important to account for these effects when employing SAAs to monitor the movement of a retaining structure. Furthermore, a cost comparison of using real-time monitoring in place of manual monitoring suggests that for a project of this nature where monitoring is required for more than 6 months, real-time monitoring becomes more cost effective.

KEY WORDS: Retaining structures, real time monitoring, shaped accel arrays.

1 INTRODUCTION

The Corrib Gas Field is located approximately 83km off the west coast of Ireland. It was originally discovered by Enterprise Energy in 1996, which was bought by Shell E&P Ireland Limited in 2002. Shell E&P Ireland Limited will operate the field on behalf of its Partners, Statoil and Vermilion. The field is one of only three gas fields discovered in Ireland and is classified as a medium-size gas field, estimated to yield approximately one trillion cubic feet of natural gas over an operating life of fifteen to twenty years. At peak production, Corrib will supply up to 60% of Ireland's natural gas needs.

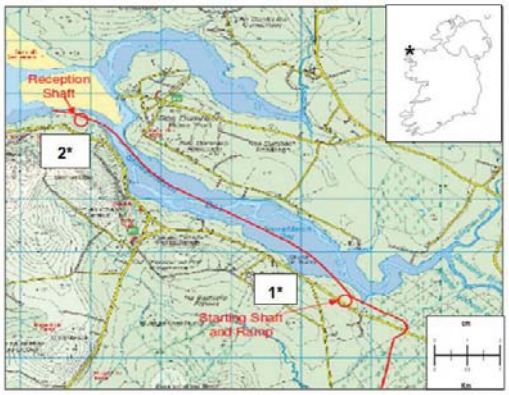
As part of the onshore pipeline link to the Bellanaboy Bridge Gas Terminal, a 4.9km long tunnel was constructed to allow the installation of the pipeline under Sruwaddacon Bay (Fig.1). To facilitate the installation and extraction of the TBM, a launch shaft was constructed to the east of the bay at Aughoose and a reception shaft to the west at Glengad. Each shaft was formed by constructing a secant pile wall, orthogonal to the longitudinal axis of the tunnel and sheet piles along the shaft boundaries (Fig.2). Inclinometers, Shaped Accel Arrays (SAAs), optical surveying equipment and piezometers were employed as part of the monitoring regime during and after construction.

Real-time monitoring of wall movements enabled by the SAAs is the focus of this paper. There is very limited experience of SAA use in Ireland, so the paper serves as a source of information on the devices. In addition, the SAA data attained is presented and interpreted. The launch shaft retaining structure experienced nominal toe movement and sway during its construction. Methods for incorporating these movements into the deflected shape of the retaining structure are discussed. The final section of this paper will serve as an aid to assist engineers in the appraisal of real time and manual monitoring options.

2 LAUNCH AND RECEPTION SHAFTS

2.1 General

The launch shaft consisted of two zones, a start pit and ramp section, measuring approximately 9.5m wide by 17.6m long and 6.2m wide by 74.2m long, respectively (Fig. 2). The overburden was retained on the west face (i.e. orthogonal direction to the longitudinal access of the tunnel) by a male-female secant pile wall with piles of 1.2m diameter which incorporated Glass Fibre Reinforcement (GFR) to create a "soft eye" through which the TBM was launched. The remaining walls were constructed of interlocking U-section sheet piles, with toe depth between approximately 9.0m and 14.0m below ground level (bgl). Constructed on the top of the start pit walls was a 1.4m wide by 1.0m deep reinforced concrete capping beam, to which horizontal steel props were fixed. The props and capping beam were installed prior to excavation of overburden within the start pit. To maximise the amount of unrestricted space in the ramp section, post-tensioned ground anchors and waler beams were placed 2m bgl.



*1*Aughoose site, 2*Glengad site*
Figure 1. Sruwaddacon Bay, Mayo (Ireland)

Similarly, the reception shaft was constructed with a soft eye GFR secant pile wall to the east and the remaining retaining walls were constructed using interlocking U-section sheet piles. The reception shaft measured approximately 17.0m by 10.0m on plan with an average sheet pile toe depth of approximately 14.0m (Fig. 2). Horizontal props and a capping beam were also used in this shaft to enhance structural rigidity.

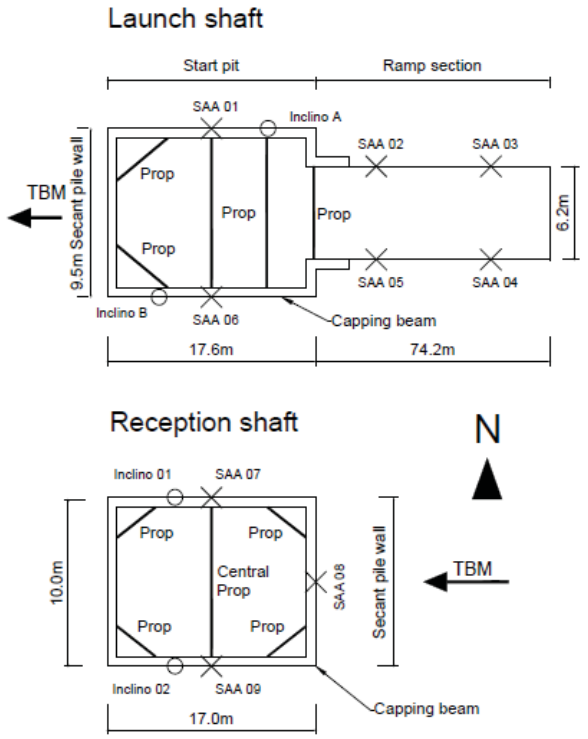


Figure 2. Plan views of launch and reception shafts, which are located at Aughoose and Glengad sites, respectively.

2.2 Ground conditions

The soil profile at the Aughoose site consisted of peat, silty sands and gravels overlying bedrock (Table 1). The peat layer was excavated and replaced with Clause 804 aggregate prior to construction of the shaft. The ground water table within the Aughoose site varied in depth from 0.8m to 2.8m bgl. Falling head permeability tests found the overburden layer had an average permeability of 6.35×10^{-6} m/s and well pumping tests established the bedrock had a permeability ranging between 3.0×10^{-6}m/s to 5×10^{-5} m/s. A number of Standard Penetration Tests (SPT) were conducted on the site, with the SPT N value of the sand layer ranging from 10 to >50. Shear box tests results indicated that the sand layer had an angle of internal friction in the range 36^{o} to 41^{o}.

The soil profile at Glengad site consisted of sandy topsoil, silty sands and gravels overlying bedrock (Table 2). The average SPT N of the gravel layer was 46 with a range from 21 to >50 blows. The ground water table varied from 0.84m to 1.47m bgl, with an average bedrock permeability of 6.5x10-6 m/s, which was calculated from a well pumping test. During the construction stage of the shafts, well pumping was employed to reduce the ground water levels.

Table 1. Aughoose soil profile

Depth (m bgl)	Soil Profile
0-4.6	PEAT (*replaced with Clause 804 aggregate)*
4.6-6.5	Silty very gravelly SAND & sandyGRAVEL
6.5-7.5	Highly weathered, weak to moderately strong MICA SCHIST
> 7.5	Moderately weathered, strong to very strong PSAMMITE

Table 2. Glengad soil profile

Depth (m bgl)	Soil Profile
0-0.2	Sandy topsoil
0.2-3.5	Silty gravelly SAND/sandy GRAVEL with cobbles
>3.5	Moderately weathered, moderately strong to very strong PSAMMITE

3 SHAPED ACCEL ARRAY

3.1 Shaped accel array configuration

A SAA is an articulate chain of sensors installed inside a water-tight casing, which includes a microprocessor and temperature sensor every 8 segments. The rigid segments are either 305mm or 500mm in length and contain a tri-axial Micro Electro Mechanical System (MEMS) accelerometer. The MEMS accelerometer measures the static tilt of each segment relative to gravity and adjusts for temperature [1]. A composite joint connects the rigid sections together. This joint permits two degrees of freedom between segments, while preventing torsion. The MEMS also permits the measurement of vibrations up to ± 2g [1]. SAAs can measure either the 2D or 3D deflected shape of a structure, depending on how they are installed. Installing an SAA vertically permits 3D monitoring, while horizontal installation only permits 2D monitoring. They have an accuracy of ± 1.5mm non-grouted and ± 0.5mm grouted over a length of 32m and can operate within a temperature range of -45^{0}C to 85^{0}C with a maximum length of 100m [1], [2]. Unlike their predecessors (i.e. analog sensors), SAAs only require one cable per instrument, which significantly reduces the installation cost in large scale projects [3]. The SAA is factory-calibrated and completely sealed; therefore, no field calibration is required. However, careful consideration must be given to the required length of SAA, as no field adjustments are possible on the instrument. SAA installation and data acquisition can adopt a number of different formats.

3.2 SAA installation and data acquisition

An SAA can either be connected to a computer or a data acquisition system for remote monitoring, rendering them an ideal instrument for real time monitoring. SAAs have been successfully employed to monitor slope stability/movements, settlement, structural stability of deep excavations, mines, quarry faces and have become an important part of structural health monitoring regimes globally. At the planning stage of the project, careful consideration should be given to the installation of deflection monitoring equipment. For example, when installing an inclinometer or SAA to monitor the cumulative deflection of a retaining structure, a decision is required as to whether the base of the instrument should be

anchored into a stationary soil layer beneath the proposed structure or fixed at the toe depth of the proposed structure. Fixing the base of the instrument into a stationary soil layer beneath the proposed structure requires installation within a dedicated borehole to ensure cumulative displacement is measured. However, if the base of the instrument is not firmly anchored into the soil layer, then alternative means are required to measure the cumulative displacement of the instrument. Adjustment to the deflected shape can be made by measuring displacement at the top of the instrument using optical surveying equipment [2].

SAAs are typically installed inside a special plastic conduit of 27mm internal diameter, which reduces the tendency of the instrument to try to twist and to facilitate installation or extraction of the instrument. This conduit is typically grouted into place, prior to installing the device. In the case of the sheet pile retaining structures at the Corrib Tunnel site, the conduits were grouted into hollow steel sections, which were pre-welded to the back of a sheet pile prior to its installation. An alternative to this method of installation is to grout the plastic conduit into a borehole, drilled adjacent to the retaining structure before inserting the instrument.

4 MONITORING REGIME

4.1 Overview

The monitoring regime for the construction of the launch and reception shafts at the Corrib Tunnel site consisted of piezometers, conventional inclinometers and SAAs and the use of optical surveying equipment. Eight SAAs were employed at the Aughoose site and three at the Glengad site, one of which was placed into the GRF secant pile wall (Fig.2). All SAAs were placed into plastic conduits, which were grouted in place, thereby improving the accuracy of the results produced. The inclinometers (at Glengad) were regularly monitored manually (up to twice daily), by an inclinometer probe, whereas the SAAs and their data acquisition systems recorded the deflected shape of the retaining structures every 30 minutes. In addition to the SAAs employed as part of the real time monitoring regime for the construction of the launch and reception shafts (the subject of this paper), SAA's have been successfully used elsewhere on the Corrib project to monitor the construction of the onshore pipeline.

4.2 Data acquisition

Data acquisition systems installed at both shafts allowed for the continuous monitoring of the retaining structures, during and after their construction. This information was available to the relevant personnel via an internet portal. Deflection (magnitude and rate) thresholds were set by the designers, based upon predictions from finite element models. Should these thresholds be exceeded, appropriate contingency measures (such as halting excavation, opening of the weep holes and ceasing well pumping within the shaft) could be considered.

The SAAs at either shaft were not anchored into the bedrock beneath the retaining structures. Therefore, as alluded to in Section 3, a total of 16 benchmarks were needed to monitor the movement at the top of the structures. Thus, 8 were placed on the capping beam of the launch shaft and a further 8 were placed on the capping beam of the reception shaft. The benchmarks were surveyed on a regular basis using optical surveying equipment, which had an accuracy of ± 3mm. Results of the optical surveying and SAA monitoring regime were amalgamated to calculate the cumulative deflection of the retaining structures.

5 RESULTS AND DISCUSSION

This discussion focuses primarily on how to adjust the deflected shape produced by an SAA to incorporate the sway and toe movement of a retaining structure. This adjustment could equally be applied to the inclinometer results. Furthermore, the results from an inclinometer and SAA, located in close proximity, are compared.

5.1 Unadjusted deflection

The unadjusted deflected shape of SAA 01 is presented in Figure 3, as a function of the excavation depth. As outlined in Section 2, the capping beam and horizontal props were installed prior to the excavation of the overburden from within the shafts. Therefore, it is assumed that once the props were installed, the distance between opposite walls of the retaining structure at the capping beam level remained relatively unchanged. The base of the SAA was not anchored into the subsoil strata beneath the retaining structure. Hence, it is reasonable to assume that as the overburden was excavated from within the retaining structure, the toe of the sheet pile wall rotated into the excavation, bringing with it the base of the SAA; this has been observed by other studies [2]. Two adjustments to the deflected shape of the SAA 01 are necessary when in the above configuration. These adjustments are:

(i) Adjustment of the deflected shape of the SAA for the movement of its base.

(ii) The retaining structure as a unit may sway because of unequal earth and/or hydrostatic pressures on opposite walls. Sway will also affect the deflected shape of the SAA.

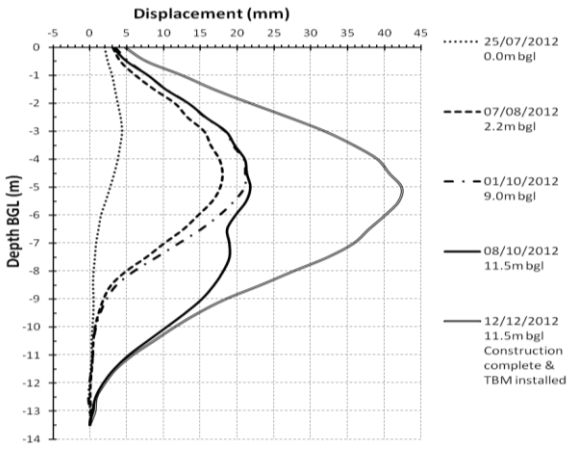


Figure 3. SAA 01 unadjusted deflected shape

5.2 Adjustment for base movement

To remove the error generated by the movement of the SAA's base, it is sufficient to consider the top of the SAA as stationary and all displacements are relative to the top rather

than the base of the instrument. The adjusted-for-base-movement deflected shape of the SAA 01 is presented in Figure 4. It can be seen from this graph that the toe of the sheet pile moves away from the excavation, rather than into the excavation. Temporary horizontal props were placed within the start pit during its construction and may account for the outward movement of the sheet pile toes. Excess toe movement of the retaining wall can be a precursor to the onset of failure of the structure and warrants monitoring. For example, during the construction of the Tottenham Court Road Station (London), excess inward toe movement of a retaining wall during the excavation phase prompted the early installation of a floor slab section [2].

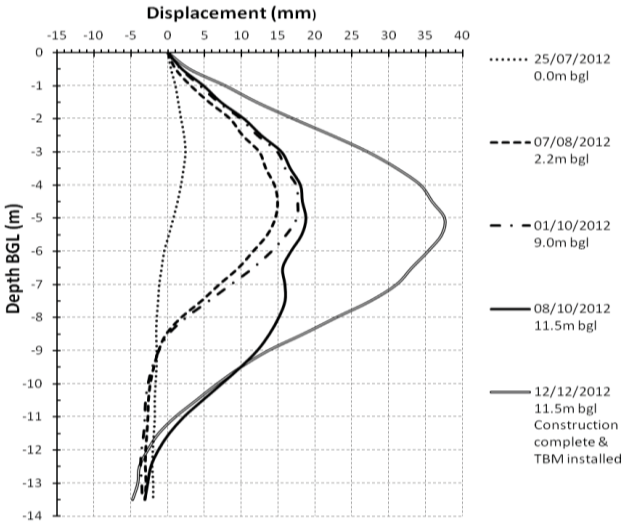


Figure 4. SAA 01 Adjusted-for-base-movement

5.3 Adjustment for sway

The sway effect may be monitored through the regular surveying of the capping beam benchmarks, and then accounted for by adjusting the deflected shape. Regular optical surveying of the capping beam found that, at the end of the construction phase, the launch shaft's north side retaining wall had swayed approximately 10mm (± 3mm) to the north. To remove the effect of sway from the deflected shape of the SAA, a correction (C) was applied as follows (C>0 represents inward sway, i.e. toward the excavation):

$$C = \pm \text{Total sway} \times (1 - \text{depth considered/total depth}) \quad (1)$$

$$\text{Corrected deflection} = \text{deflection at point considered} + C \quad (2)$$

The adjusted-for-sway and adjusted-for-base-movement deflected shape of SAA 01 is presented in Figure 5, from which it can be seen the maximum recorded deflected is reduced by approximately 5mm. Sway adjustment can have a significant effect on the deflected shape of a SAA. The adjusted deflected shapes of SAA 06 are presented in Figure 6. A survey of the benchmarks closest to the SAA 06 indicated that this wall of structure had swayed approximately 13mm (± 3mm) to the north during its construction. Applying the sway correction to the already adjusted-for-base-movement deflected shape of SAA 06 increased the maximum deflection by approximately 9mm. In some circumstances adjusting for sway may cause the deflected shape of the retaining structure to approach or exceed the threshold limits imposed within the monitoring regime [2]. Therefore, when using an unanchored SAA to monitor the construction of a retaining structure, the effect of sway and instrument movement should be incorporated into the deflected shape of the SAA, to produce a more rigorous monitoring regime.

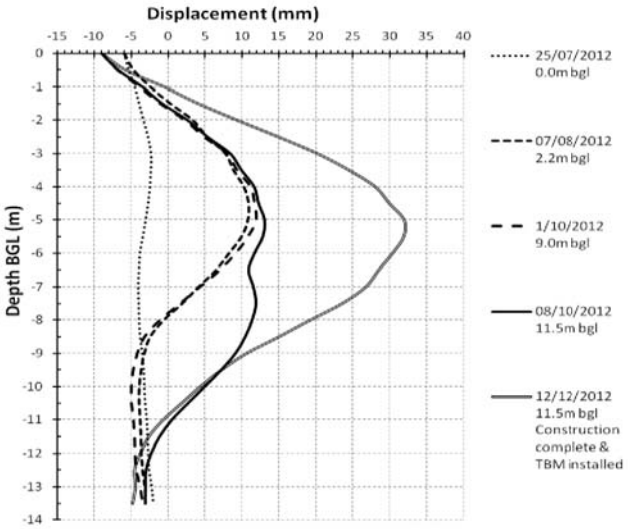


Figure 5. SAA01 adjusted-for-sway and base-movement

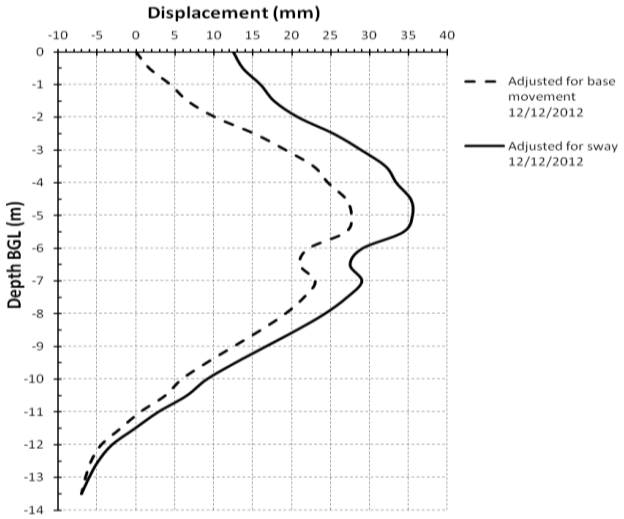


Figure 6. SAA 06 adjusted-for-sway and base-movement

5.4 Inclinometer/SAA comparison

The movement profiles measured by devices SAA 07 and inclinometer 01, located 1.25m apart in the reception shaft, are compared in Fig. 7. As can be seen from this plot, there are slight differences between the deflected shapes, which may be due to the difference in position of the instruments along the capping beam (Fig. 2); SAA 07 is located closer to the central prop. The additional stiffness provided by the central prop at capping beam level may be reducing the extent of deflection in this region. Notwithstanding this, the deflected shapes of both instruments are in good agreement.

Other research which compared the results of inclinometers and SAAs during the construction of Tottenham Court Road Station (London) also found slight differences between SAAs and inclinometer deflected shapes [2]. The authors of that research suggested that the difference may have been due to the inclinometer probe, which was not fully stabilised during its reading.

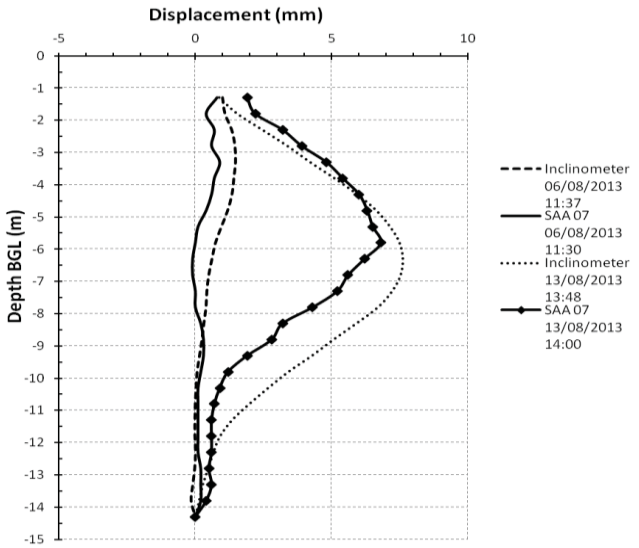


Figure 7. Inclinometer 01 and SAA 07 deflected shapes

6 COST ANALYSES AND COMPARATIVE STUDY

A cost analysis study comparing SAAs and manual inclinometer monitoring is presented in this section. Also outlined are some of the monitoring and practical considerations, which may assist when choosing between these monitoring regimes.

6.1 Cost analyses assumptions

The cost analyses study was based on using either 3 inclinometers or 3 SAAs, each measuring 10m in length, to monitor the movement of a retaining structure during construction. The assumptions of the study are as follows:

(i) Instrument costs for the inclinometers consisted of the 30m of inclinometer casing. The instrument costs for the SAAs consisted of the 3 SAAs plus a data logger necessary for remote monitoring. The cost of powering the data logger was not included in the study.
(ii) Installing the SAAs was deemed to take an extra day's labour, compared to the inclinometers, because of the additional time required to connect and program the data logger. Both methods require similar consumables for installation (such as grout). It is worth noting that when toe fixity is required, costs associated for boreholes are common to both methods, therefore, they are excluded from the comparison.
(iii) The inclinometer monitoring cost was calculated using the following assumptions; the monitoring regime was 7 days a week and 1 hour was required to read the 3 inclinometers. The time required to report the findings of the inclinometer monitoring were not included. The rental cost of the inclinometer probe was included within the monitoring cost. The maximum monitoring frequency was limited to 4 times a day.
(iv) The SAA monitoring cost consisted of a monthly subscription fee to access the monitoring data via a secure website, where the information is readily available to download in graphical format. This subscription fee does not change irrespective of the frequency of the monitoring.

6.2 Cost analyses

Table 3 compares the instrument and installation cost of both methods; the results are normalised relative to the cost of the inclinometer casing.

Table 3. Cost comparison of real-time monitoring relative to manual monitoring

Category	Inclinometer	SAA
(i) Instrument cost	1	26
(ii) Installation cost	3.3	5.7

The findings of this cost analyses are:

(i) The instrument and installation costs associated with 3 SAAs is approximately 7.5 times that of 3 standard manual inclinometers (excluding the inclinometer probe)
(ii) As the monitoring frequency and duration of the project increase, the real time monitoring becomes more economically advantageous relative to the manual monitoring (Fig. 8).

Therefore, careful consideration should be given to the duration of the project and the monitoring frequency required during its construction. Moreover, if the retaining structure is of a permanent nature, where the construction monitoring regime instrumentation can be incorporated into the structural health monitoring regime.

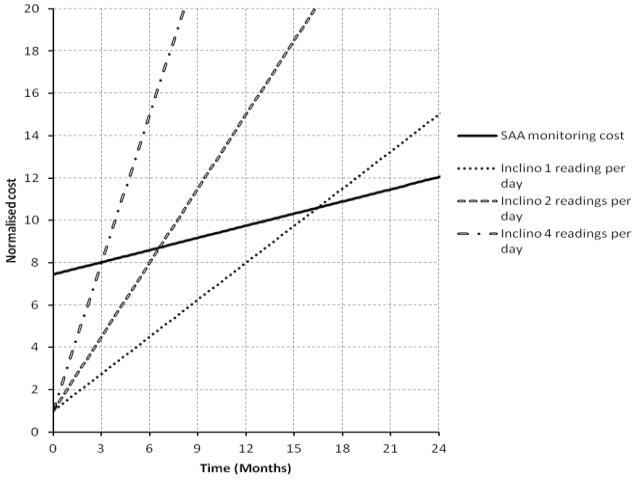


Figure 8. Monitoring comparison graph

6.3 Monitoring considerations

Apart from the monetary cost of the monitoring regime other considerations are presented in Table 4. This table is based on the authors' experiences, where high represents either a higher level of consideration, outputs or suitability.

Table 4. Comparison of real-time and manual monitoring

Category	Real time	Manual
(i) Design consideration	High	Low
(ii) Accuracy/reliability	High	High
(iii) Monitoring frequency	Very high	Low
(iv) Speed of alert	High	Low
(v) Remote location	High	Low

(i) At the design stage, real time monitoring requires more consideration: issues such as communications coverage, power supply (solar panels and batteries or mains), length of the SAA and data logger location must all be considered. Whereas, the major design consideration for manual inclinometers are length of the casing and location of the instrument, for ease of access during the construction stage.

(ii) Both instruments are highly reliable. The real time monitoring system requires a power supply and data logging system, unlike the inclinometer, thereby, making them more susceptible to power failures and surges etc. However, a back-up battery can be employed.

(iii) SAAs can monitor and log an average of a 1000 readings every 10 seconds and can measure vibrations of ±2g. This renders them particularly suitable for monitoring urban development adjacent to sensitive structures. Inclinometer readings are generally taken twice daily unless the rate of excavation warrants more monitoring.

(iv) The time taken to issue an alert can be a crucial consideration when selecting a monitoring system. Typically, the delay between the data-logger recording the information and its availability on the web portal depends on the frequency at which this information is uploaded from the data-logger. In isolated locations, to preserve battery life and reduce satellite connection costs, the monitoring system is typically configured to store a number of hours of monitoring data before uploading. In the aforementioned configuration the system can no longer be considered as real-time monitoring. SAA monitoring coupled with ground water monitoring can be used to provide important information for value engineering, for example in the Tottenham Court Road Station development, the use of SAA monitoring permitted the propping layout to be modified and reduced by one level of props, which subsequently reduced the schedule by 26 days [2].

(v) The use of real time monitoring is particularly suited to monitoring landslide prone zones, seismic zones or remote locations, where access can prove difficult or hazardous [4]. They reduce the requirement for physical presence on site, therefore improving health and safety and negate the need for lone working.

7 CONCLUSION

(i) Where the base of the SAA (and inclinometer) is not anchored and horizontal props are used at the top of the structure, then additional monitoring must be put in place to track the sway movement of the retaining structure. The results of which should be incorporated into the deflected shape of the SAA as soon as available, to provided a more holistic view of the deflection profile

(ii) It has been shown (in this instance) that SAA instrument and installation costs are typically more expensive. However, as the life span of the projects increases this cost reduces in comparison to manual monitoring.

(iii) Real time monitoring is particularly suited to monitoring remote structures or locations, where instant feedback is essential and can reduce the number of personnel required on site during construction. Their usage is likely to play an ever increasing role in efficient management of geotechnical risk.

On the Corrib project, a total of 11 SAAs were successfully employed as part of the real time monitoring regime, which monitored the construction of two retaining structures (shafts). Despite the value added for this project, they should not be seen as the panacea for all projects, sometime the time span and cost constraints of a project render them unsuitable as a monitoring solution.

ACKNOWLEDGEMENTS
The authors would like to thank the following companies, AGL Consulting Geotechnical Engineers, BAM Civil/Wayss & Freytag Joint venture and Geotechnical Observations Ltd. The authors would especially like to thank, Shell E&P Ireland Limited for its financial support and technical assistance provided during this research.

References

[1] D. Abdoun, T. Danisch.T. Ha, "Advanced sensing for real-time monitoring of geotechnical systems," *Geo-Frontiers*, vol. GSP 138, no. 518, 2005.

[2] P. Lipscombe, R. Carter, C. Perkins, O. Guerrero, S. Thurlow, "The Use of Shape Accel Arrays (SAAs) for Measuring Retaining Wall Deflection," 2012. [Online]. Available: http://www.getec.uk.com.

[3] A. J. Hyett, "Innovative Digital Instrumentation for Geotechnical Monitoring Systems." [Online]. Available: http://www.yieldpoint.com.

[4] D. D. Dasenbrock, "Automated Landslide Instrumentation Programs on US Route 2 in Crookston MN," no. Barr, 2006.

The Use of 3D Laser Scanning Technology for Bridge Inspection and Assessment

M.J. Minehane[1], R. O'Donovan[1,2], K.D. Ruane[1], B. O'Keeffe[3]
[1]RPS Group Ltd., Innishmore, Ballincollig, Cork, Ireland
[2]University College Cork, College Road, Cork, Ireland
[3]Murphy Surveys Ltd., Cityview, Castletreasure, Donnybrook, Douglas, Cork, Ireland
email: michael.minehane@rpsgroup.com, ross.odonovan@ucc.ie, kieran.ruane@rpsgroup.com, bokeeffe@murphysurveys.ie

ABSTRACT: Bridge inspectors require as-built survey data in order to undertake a bridge inspection and structural assessment. In some instances, bridges are located in difficult terrain where access using conventional methods is expensive and potentially unsafe. Where traditional survey methods require either the installation of extensive access platforms or specialist roped access, laser scanning offers the ability to safely and remotely acquire comprehensive information without direct contact. Using several instrument set-ups over a project site, 3D laser scanning enables the collection of dense 3D point clouds, which accurately capture detailed geometries, member imperfections and details of damage/settlement. The data obtained is readily applicable to Building Information Modelling (BIM) and can assist with current and future bridge inspections and assessments.

This paper provides an overview of recent applications of laser scanning to bridge inspection and assessment. Case Study 1 describes the iconic Chetwynd Viaduct, a four-span cast iron under-arch structure constructed in 1851. The Viaduct is located on the outskirts of Cork City over a busy national road. In the 1960s the Viaduct was decommissioned and the superstructure was partly dismantled. It is proposed to restore the Viaduct as a pedestrian/cycle bridge to form part of a 36km greenway along the disused railway line. Few as-built records exist, and the nature of the site made traditional survey methods difficult. 3D laser scanning was successfully undertaken and the data enabled the development of a finite element model for structural assessment. Case Study 2 describes a masonry arch river bridge in Killorglin, Co. Kerry. Over time, foundation settlement caused noticeable deformations. The deformations had been monitored using traditional survey methods, with limited success. 3D laser scanning was undertaken and allowed for accurate monitoring of the bridge during underpinning works and provided valuable data for future monitoring of the bridge.

KEY WORDS: 3D laser scanning; Bridge assessment; Bridge inspection, Bridge rehabilitation, Heritage.

1 INTRODUCTION

Three-dimensional (3D) terrestrial laser scanners are instruments that are capable of remotely recording precise surface data of objects without direct contact. An oscillating mirror enables a continuous scanning process to take place between the desired range of tilt. A pan mechanism allows the scanner to be re-orientated for a new line of scan. Mounting the laser scanner on a tripod provides the simplest configuration (static 3D terrestrial laser scanning) [1]. Data acquisition is performed at a user-defined density and can range from a coarse ground contour level of detail to fine-detail modelling, such as nuts and bolts on a steel latticed element.

Laser scanning has, in recent years, rapidly established a significant and diverse range of applications in areas including engineering, construction, architecture and heritage. There are numerous studies in the literature highlighting recent and potential applications for 3D laser scanning in these fields and offering comparisons with alternative forms of data acquisition [2-6]. The following provides some sample documented applications of 3D laser scanning in the discipline of civil engineering, with particular emphasis paid to bridge engineering:

- As-built records of infrastructure [7-8];
- Damage assessment [9-12];
- Structural Health Monitoring (SHM) [13-14];
- Deformation/settlement monitoring [15-17];
- Scour assessment [18];
- Surface flatness/texture assessment [19-20];
- Bridge inspection and assessment [21-28].

Significant industry transformations in the use of Building Information Modelling (BIM) present remarkable opportunities for clients and engineers to employ the use of laser scanning in the context of holistic, collaborative workflows grounded in three-dimensional model-based design [29].

This paper presents two case studies in the field of bridge inspection and assessment where 3D terrestrial laser scanning was successfully implemented.

2 CASE STUDY 1: CHETWYND VIADUCT

2.1 Background and History

Chetwynd Viaduct is a listed heritage structure and well-known landmark located on the abandoned Cork – Bandon and South Coast Railway. Cork County Council proposes to reuse the abandoned railway line as a 36km dedicated off-road cycle and walking route from Cork City to Kinsale. The greenway will incorporate two major viaducts at Chetwynd and Halfway. RPS Consulting Engineers were appointed in 2013 to carry out a feasibility study on the proposed reuse of these structures including inspections, structural assessments, preliminary remedial works and costings. Chetwynd Viaduct (Figures 1 & 2) is located approximately 5km south of Cork

City, spanning over the Glasheen River valley and the N71 Cork-Bandon Road. The viaduct was designed by Charles Nixon, a former pupil of Isambard Kingdom Brunel. Construction of the viaduct took place between 1849 and 1851 by contractors Fox, Henderson & Co., who also built the Crystal Palace in London. Measuring 500ft (152.4m) from abutment to abutment, the viaduct was considered to be the largest of its kind in Ireland at the time of construction [30].



Figure 1. Chetwynd Viaduct.

The structure suffered damaged during the Irish Civil War in 1922 and was subsequently repaired [31]. The rail line was officially closed on the 31st March 1961. The entire decking and parapets were subsequently removed to preclude pedestrian access.

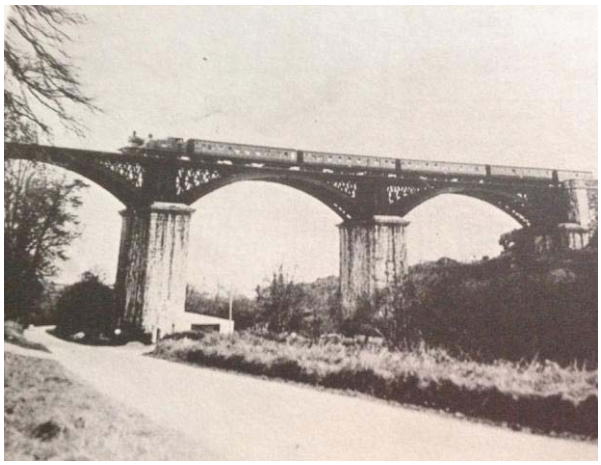


Figure 2. Chetwynd Viaduct in service [31].

2.2 *Description of Structure*

Chetwynd Viaduct is a four-span cast iron under-arch railway bridge supported on tall masonry piers and abutments. Each span consists of four prefabricated cast iron arch ribs, cast on site in sections and subsequently spliced and lifted into position. Cast iron bracing connected to the top and bottom flanges of the arch ribs provide lateral restraint and transfer wind and other transverse loading to the abutments. Prefabricated cast iron latticed spandrel walls comprising cruciform-shaped struts support the deck from the arch ribs. The original deck comprised cast iron covering plates, flanged and bolted together and supported on cast iron transverse beams. Wrought iron transverse tie-rods connect the node points of the cast iron latticed spandrel walls at mid-height. This form of hybrid construction combining wrought iron and cast iron components was common at the time of construction as the limited tensile capacity of cast iron became recognised. Wrought iron, which possesses a much higher tensile strength than cast iron, was frequently substituted as tension members. The photograph in Figure 3 gives a view of the bridge soffit, showing the primary members.



Figure 3. View showing primary members.

2.3 *3D Terrestrial Laser Scan*

A 3D terrestrial laser scan of the structure was carried out in September 2013 using a Leica P20; a pulse based terrestrial laser scanner (Figure 4). In total, 28 individual scans were executed from various positions around the Viaduct. Each scan took approximately 7 minutes to complete and points were surveyed at a rate of approximately 1 million points per second. The maximum operating range of the P20 Scanner is up to 120m ensuring that sufficient detail of the structure could be safely captured without the need to access the deck level or to use Mobile Elevated Work Platforms (MEWPs).



Figure 4. 3D terrestrial laser scanner in operation.

The accuracy of the laser scanner is given as 3mm at 50m, and decreases to 6mm when the distance to the structure increases to 100m. The height of the viaduct is approximately 28m above ground level, meaning the range from each scan set-up never exceeded 50m. The well-defined planes of Chetwynd Viaduct were analysed and modelled using a best fit with respect to the point cloud. This is a sophisticated feature of the modelling component of Leica Cyclone Software, which was used to create the 3D AutoCAD model. Individual features within the database, such as an arch rib, are isolated by the modeller. The software subsequently analyses this portion of the point cloud and creates a best-fit

solid for export to AutoCAD. At this time the modeller has the opportunity to tweak the dimensions of the solid if more reliable information exists.

In addition to the accuracy of the scanner and processing tools, all scan positions were co-ordinated using a Leica 1201+ Total Station in order to ensure that the greatest accuracy was achieved when registering the scans. The database was referenced to Irish National Grid and Malin Head Datum. Once registered, the scans were coloured using imagery obtained from a Nikon D200 camera mounted on a Nodal Ninja bracket in order to create high resolution 360° panoramic images (Figure 5).

The scan database was unified, or gridded, to 5mm in order to make the point cloud more regular and the database more manageable. This process reduced the point cloud from 3,633 million points to 298 million points. Using Leica Cyclone and Cloudworx for AutoCAD software, a solid 3D model was generated in dwg format (Figure 6). All irregularities in the structure were modelled individually as there was a degree of variation across the key member pieces. Similarly, the masonry piers were found to be of varying sizes and were also modelled individually.

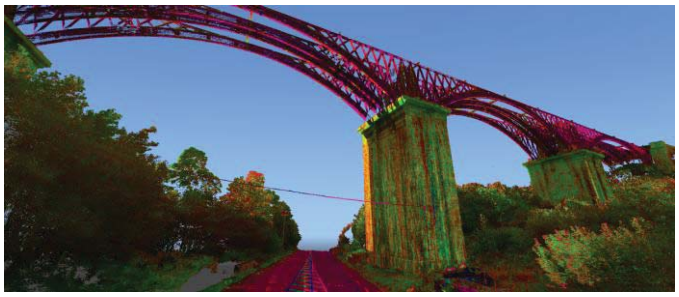


Figure 5. 3D laser scan output.

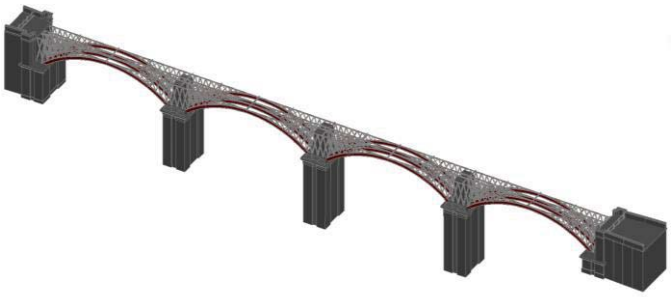
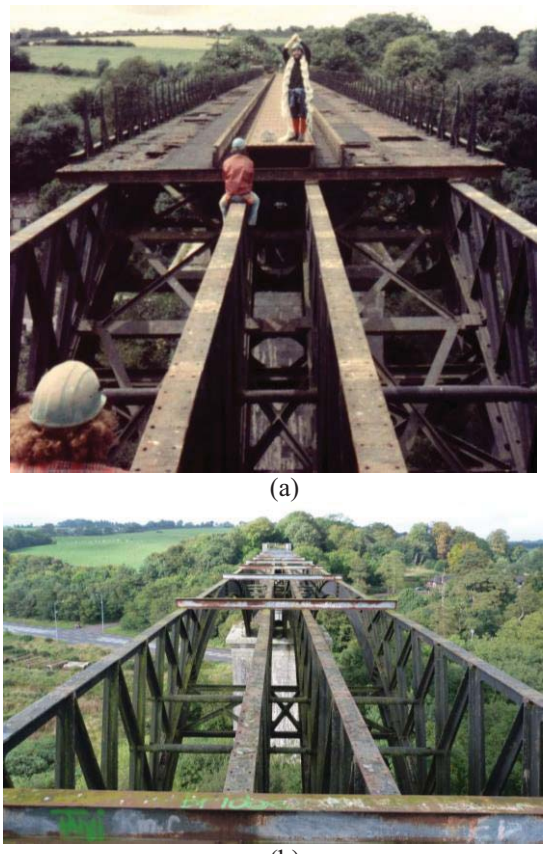


Figure 6. 3D solid model of Chetwend Viaduct.

2.4 Inspection

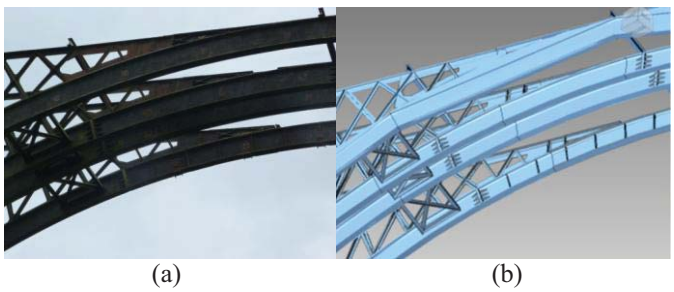
An inspection of Chetwynd Viaduct was carried out in September 2013. On-site measurements confirmed the accuracy of the 3D terrestrial laser scan. Considering Chetwynd Viaduct is in excess of 160 years old, and has not received any maintenance in over 50 years, the structure is in remarkably good condition. This section briefly highlights some of the primary defects encountered during inspection:

- Numerous wrought iron transverse tie-rods have failed and will require replacing to adequately restrain the spandrel walls;
- Failure of protective paintwork system has occurred;
- Figure 7 gives a photographic comparison of the topside of the structure at the time of inspection and the structure during deck removal during the 1960's. The comparison reveals that, in addition to the decking and parapets, a significant proportion of the original cast iron cross bracing has also been removed during the 1960's. This compromises the structure's out-of-plane stability and its implications are discussed later;
- Figure 8 shows the repaired section of the structure following the damage sustained in the Irish Civil War in 1922. Repair works comprise solid spandrel infill plates, gusset plates and supplementary plate stiffeners.



(a) (b)

Figure 7. Deck during deck removal (a) [32] and during 2013 inspection (b).



(a) (b)

Figure 8. Photograph of repaired section (a) and laser scan solid model of repaired section (b).

2.5 Finite Element Model

A full three-dimensional linear elastic finite element model was developed for Chetwynd Viaduct using LUSAS v14.7

Finite Element Software. With minimal post-processing, it was possible to import the 3D laser scan data into a finite element (FE) program to carry out a structural assessment of Chetwynd Viaduct for its proposed reuse as a pedestrian/cycle bridge. Importing the data directly enabled the as-built geometry to be modelled and saved time tediously generating the geometry manually.

A view of the three-dimensional FE model is given in Figure 9. Additional members were introduced to replicate the loading imposed by a replacement deck. The web and flanges of the arch ribs were modelled as thick shell elements. All other elements were modelled as thick beam elements.

A linear eigenvalue buckling analysis of the structure was also undertaken to investigate the influence of the bracing removal on the out-of-plane stability. It is prudent to include geometric imperfection in any buckling analysis as the buckling load is often sensitive to deviations from the true geometry. The data imported from the 3D laser scan incorporated all imperfections including bow imperfections, member crookedness and damaged/repaired sections.

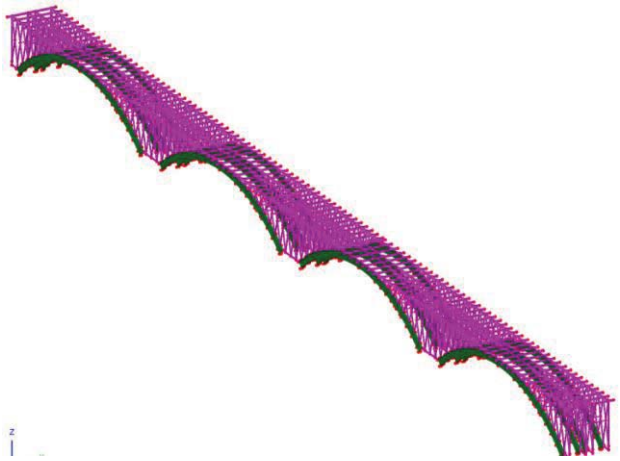


Figure 9. Fleshed view of 3D finite element model.

2.6 *Basis of Assessment*

The structural assessment of the superstructure was carried out in accordance with BD21/01 [33]. For the cast iron components, a permissible stress assessment (Serviceability Limit State) was carried out, whereas, for the wrought iron components, an Ultimate Limit State approach was adopted. BD 21/01 [33] compliant material properties used in the analysis and assessment are given in Table 1.

Table 1. Material properties for assessment.

Material Property	Cast Iron Components	Wrought Iron Components
Unit weight	7200 kg/m^3	7700 kg/m^3
Modulus of elasticity	105000 N/mm^2	200000 N/mm^2
Coefficient of thermal expansion	10.2 x 10^{-6} C^{-1}	12.0 x 10^{-6} C^{-1}
Material partial factor	1.0	1.2
Compressive stress limit	154 N/mm^2	-
Tensile stress limit	-46 N/mm^2	-
Shear stress limit	46 N/mm^2	-

2.7 *Assessment Results*

For the cast iron components, the assessment demonstrated the members to have sufficient capacity to carry the loads imposed from its proposed reuse as a pedestrian/cycle bridge. A contour of direct stress in the cast iron arch ribs is provided in Figure 10. The wrought iron components also demonstrated sufficient capacity for the applied loading at Ultimate Limit State.

Regarding the linear eigenvalue buckling analysis, the observed mode of buckling for Chetwynd Viaduct, based on the reduced bracing provisions, is given in Figure 11. In the absence of sufficient bracing, the critical mode of buckling is global out-of-plane buckling of the cast iron arch ribs. Although the load corresponding to instability was higher than the loading imposed, the re-introduction of supplementary lateral bracing was included with bridge remedial works proposals in order to provide adequate lateral restraint and to cater for wind loading.

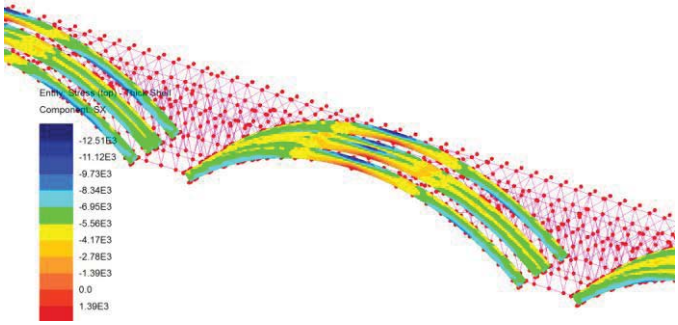


Figure 10. Contour of direct stress in cast iron arch ribs (kN/m^2).

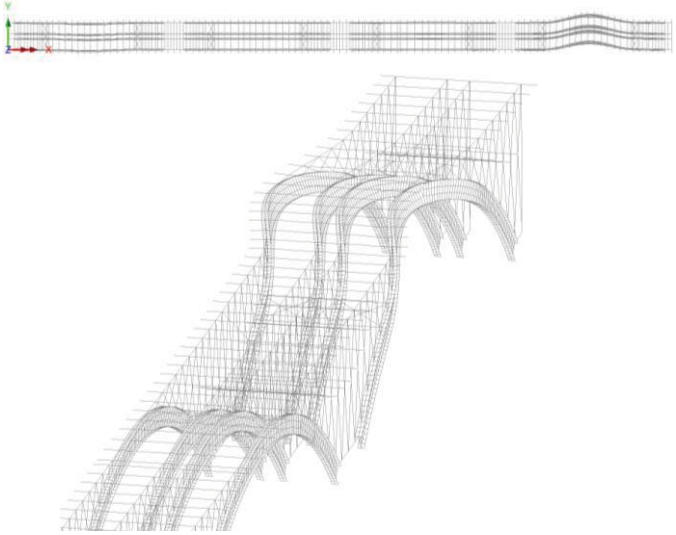


Figure 11. Plan and close-up view of observed mode of out-of-plane buckling of cast iron arch ribs in end span.

3 CASE STUDY 2: LAUNE BRIDGE

3.1 *Background and History*

Laune Bridge, opened in 1885, is an eight-span masonry arch bridge carrying the N70 over the tidal river Laune in Killorglin, Co. Kerry. The bridge is a registered protected

structure. The existing structure (Figure 12) comprised of limestone ashlar voussoirs and rock-hewn rounded cut-waters.

There had been concerns raised over a number of years regarding noticeable settlement at several piers located on the western end (Killorglin side) of the river Laune. A number of studies had been undertaken to evaluate and continuously monitor the settlement and any associated defects. The studies typically involved the use of traditional level surveys using fixed survey studs on the bridge parapet. Over time the survey records had been misplaced and the permanent studs damaged. In 2009, RPS was commissioned to investigate, design and manage a permanent solution for the bridge.



Figure 12. Laune Bridge.

3.2 3D Terrestrial Laser Scan

3D laser scanning of the bridge was undertaken in June 2009. Using a Leica Scan Station 2; a pulse based Laser Scanner, the bridge was scanned from 6 individual locations. The accuracy of the laser scanner is given as +/- 6mm. Three scans were at deck level capturing road and parapet wall detail, while three more scanning points were established on the adjacent banks, both upstream and downstream. The Scan Station 2 had a maximum operating range of 300m, which particularly suited the task due to site logistics. The maximum scan rate of the scanner was 50,000 points per second with individual scans requiring up to 1.5 hours in order to complete a full 360° scan. As a result of these times, the surveyors were able to focus the scanner on particular areas of the bridge by defining survey windows, for example, by scanning one pier at a time. This enabled a higher scanning resolution or point density, to be selected for the key pier areas, whilst reducing the resolution on the less important contextual detail surrounding the bridge.

Imagery of the bridge was also captured using the laser scanner's on-board camera. Each 360° scan was complimented by colour imagery comprising of 111 individual 64 megapixel images. Subsequently, the images were automatically stitched by the scanner in order to create a full panoramic image (Figure 13). The final registered and unified point cloud consisted of 9.8 million points. The database was referenced to Irish National Grid and Malin Head Datum, the co-ordinates of which were established using Leica 1200 Series GPS Bases.

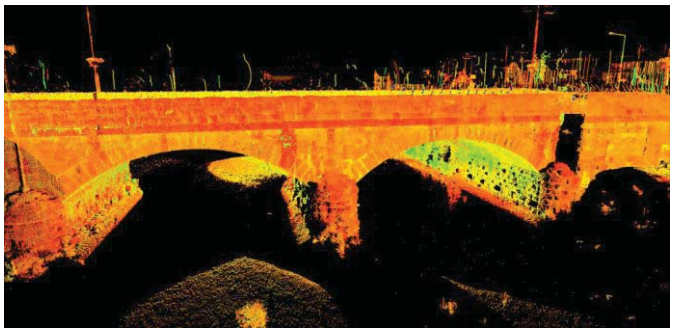


Figure 13. Sample 3D laser scan output for Laune Bridge.

2D AutoCAD drawings were extracted from the database using Leica Cloudworx software. Individual stone detail on each of the piers was digitised and represented in both elevation and cross section. This detail further confirmed the extent of the settlement which is visually evident on site. A TruView presentation of the dataset was also provided, enabling point measurement from a full colour panoramic photo viewer.

The point cloud database provides a comprehensive digital record of the structure for both heritage and monitoring purposes. Further scans from the permanent control points established on site will enable future monitoring of any movement or settlement greater than 5mm that may occur on the bridge.

3.3 Rehabilitation Works

Rehabilitation works consisted of micro piling to the three western piers from road level. Eight micro piles were provided per pier and are capable of supporting an axial load of 475kN per pile. Each micro pile comprised of a 63mm diameter Dywidag Gewi steel threaded bar in a 192mm diameter casing, which was subsequently fully grouted. The piles extended approximately 7.5m below the base of the piers, where they were terminated in a 1.5m long socket in the mudstone bedrock. All piling works were carried out at night in order to minimise disruption (Figure 14).



Figure 14. Pile installation from road surface level.

Scour protection to the piers was provided in the form graded rip-rap. The bull-nosed cutwaters, which were damaged and locally dislodged due to the historic settlement, were subsequently taken down and re-constructed following piling works.



Figure 15. Graded rip-rap scour protection and reconstructed bull-nose cut-waters.

4 CONCLUSIONS

This paper presented two case studies in the field of bridge inspection and assessment where 3D laser scanning was successfully implemented. In the case of Chetwynd Viaduct, laser scanning provided accurate modelling of intricate cast iron members, captured member imperfections, details of historic damage/repair and provided the geometry for direct integration into a finite element model to perform a structural assessment. In the case of Laune Bridge, 3D laser scanning was used effectively to assess and monitor settlement, capture detailed geometry including individual stones and provided valuable information in arriving at the optimum rehabilitation solution. In both instances, 3D laser scanning offered added value to the clients for the future management of each historic asset.

REFERENCES

[1] Schofield, W., and Breach, M., *Engineering Surveying*, sixth edition, Elsevier Ltd., Oxford, UK, 2007, 634p.

[2] Fuchs, P.A., Washer, G.A., Chase, S.B., and Moore, M. (2004), 'Applications of Laser-Based Instrumentation for Highway Bridges', *Journal of Bridge Engineering*, ASCE, November/December, pp. 541-549.

[3] Zhu, Z., and Brilakis, I. (2009), 'Comparison of Optical Sensor-Based Spatial Data Collection Techniques for Civil Infrastructure Modeling', *Journal of Computing in Civil Engineering*, ASCE, May/June, pp. 170-177.

[4] Slattery, D.K., and Slattery, K.T., *Evaluation of 3-D Laser Scanning for Construction Application*, Research Report ICT-10-068, Illinois Center for Transportation, Illinois, USA, 2010, 97p.

[5] Jaselskis, E.J., Gao, Z., and Walters, R.C. (2005), 'Improving Transportation Projects Using Laser Scanning', *Journal of Construction Engineering and Management*, ASCE, March, 131, pp. 377-384.

[6] Chang, P.C., and Liu, S.C. (2003), 'Recent Research in Nondestructive Evaluation of Civil Infrastructures, *Journal of Materials in Civil Engineering*, ASCE, May/June, 15, pp. 298-304.

[7] Ross, R.J., Bradshaw, B.K., and Anderson, S.J., *Use of Laser Scanning Technology to Obtain As-Built Records of Historic Covered Bridges*, Research Paper FPL-RP-669, United States Department of Agriculture, Washington, USA, 2012, 21p.

[8] Foltz, L.B. (2000), '3D Laser Scanner Provides Benefits for PennDOT Bridge and Rockface Surveys', *Professional Surveyor*, May, pp. 22-28.

[9] Laefer, D.F., Truong-Hong, L., Carr, H., and Singh, M. (2014), 'Crack detection limits in unit based masonry with terrestrial laser scanning', *NDT & E International*, 62, pp. 66-76.

[10] Li, H., Dong, S., El-Tawil, S., and Kamat, V.R. (2013), 'Relative Displacement Sensing Techniques for Postevent Structural Damage Assessment: Review', *Journal of Structural Engineering*, ASCE, September, pp. 1421-1434.

[11] Olsen, M.J., Kuester, F., Chang, B.J., and Hutchinson, T.C. (2010), 'Terrestrial Laser Scanning-Based Structural Damage Assessment', *Journal of Computing in Civil Engineering*, ASCE, May/June, pp. 264-272.

[12] Yong-bo, Y., Wan-heng, L., Jin-quan, Z., and Jian-guo, N. (2013), 'Three-Dimensional Detection Method for Bridge Surface Defects Based on Line-Shaped Lasers', *Journal of Highway and Transportation Research Development*, 7(2), pp. 69-72.

[13] Vaghefi, K., Oats, R.C., Harris, D.K. *et al* (2012), 'Evaluation of Commercially Available Remote Sensors for Highway Bridge Condition Assessment', *Journal of Bridge Engineering*, ASCE, November/December, pp. 886-895.

[14] Modares, M., and Waksmanski, N. (2013), 'Overview of Structural Health Monitoring for Steel Bridges', *Practice Periodical on Structural Design and Construction*, ASCE, August, pp. 187-191.

[15] Nevling, D.L., Linzell, D.G. (2011), 'Curved Girder Deformation Prediction Effectiveness Using First-Order, Linear Geometric Finite-Element Models', *Practice Periodical on Structural Design and Construction*, ASCE, May, pp. 56-61.

[16] Gordon, S.J., and Lichti, D.D. (2007), 'Modeling Terrestrial Laser Scanner Data for Precise Structural Deformation Measurement', *Journal of Surveying Information*, ASCE, May, pp. 72-80.

[17] Zogg, H.M., and Ingensand, H. (2008), 'Terrestrial Laser Scanning for Deformation Monitoring – Load Tests on the Felsenau Viaduct (CH)', *The International Archives of the Photogrammetry, Remote Sensing and Spatial Information Sciences*, Volume XXXVII, Part B5, pp. 555-562.

[18] Tafarojnoruz, A., Gaudio, R., and Calomino, F. (2012), 'Evaluation of Flow-Altering Countermeasures Against Bridge Pier Scour', *Journal of Hydraulic Engineering*, ASCE, March, pp. 297-305.

[19] Tang, P., Huber, D., and Akinci, B. (2011), 'Characterization of Laser Scanners and Algorithms for Detecting Flatness Defects on Concrete Surfaces', *Journal of Computing in Civil Engineering*, ASCE, January/February, pp. 31-42.

[20] Santos, P.M., and Júlio, E.N. (2010), 'Comparison of Methods for Texture Assessment of Concrete Surfaces', *ACI Materials Journal*, 107(5), pp. 433-440.

[21] Werner, T., and Morris, D. (2010), '3D Laser Scanning for Masonry Arch Bridges', Proceedings of *FIG Congress 2012:Facing the Challenges*, Sydney, Australia, pp. 1-15.

[22] Morer,P., Arteaga, I., Armesto, J., and Arias, P. (2011), 'Comparative structural analyses of masonry bridges: An application to the Carnadela Bridge', *Journal of Cultural Heritage*, Volume 12, pp. 300-309.

[23] Herráez, J., Denia, J.L., Navarro, P., Bosch, L., and Bosch, I. (2013), 'Design and calibration of a drill-guided system by laser for structural strengthening of historic bridge', *Journal of Cultural Heritage*, Volume 14, pp. 248-253.

[24] Lubowiecka, I., Armesto, J., Arias, P., and Lorenzo, H. (2009), 'Historic bridge modelling using laser scanning, ground penetrating radar and finite element methods in the context of structural dynamics', *Engineering Structures*, Volume 31, pp. 2667-2676.

[25] Fuchs, P.A., Washer, G.A., Chase, S.B., and Moore, M. (2004), 'Laser-Based Instrumentation for Bridge Load Testing', *Journal of Performance of Constructed Facilities*, ASCE, November, pp. 213-219.

[26] Solla, M., Lorenzo, H., Riveiro, B., and Rial, F.I. (2011), 'Non-destructive methodologies in the assessment of the masonry arch bridge of Traba, Spain', *Engineering Failure Analysis*, Volume 18, pp. 828-835.

[27] Riveiro, B., Morer, P., Arias, P., and Artega, I. (2011), 'Terrestrial laser scanning and limit analysis of masonry arch bridges', *Construction and Building Materials*, Volume 25, pp. 1726-1735.

[28] Arteaga, I., and Morer, P. (2012), 'The effect of geometry on the structural capacity of masonry arch bridges', *Construction and Building Materials*, Volume 34, pp. 97-106.

[29] Randall, T. (2011), 'Construction Engineering Requirements for Integrating Laser Scanning Technology and Building Information Modelling', *Journal of Construction Engineering and Management*, ASCE, October, pp. 797-805.

[30] Illustrated London News, *Opening of the Cork and Bandon Railway*, Vol. XIX, 1851, pp. 733.

[31] Cox, R., and Gould, M., *Ireland's Bridges*, Wolfhound Press, Dublin, Ireland, 2003, 169p.

[32] Mahers Sports, *Chetwynd Viaduct*, [Online] Available from: http://mahersoutdoor.blogspot.ie/2010/12/chetwynd-viaduct.html, [Accessed 3rd March 2014].

[33] Highways Agency, *The Assessment of Highway Bridges and Structures*, BD 21/01, Highways Agency, London, UK, 2001.

UNDERWATER ACOUSTIC IMAGING FOR BRIDGES AND MARINE INFRASTRUCTURE

Terence M. Browne, CEng, MIEI[1], Thomas J. Collins, CEng, MIEI[2]
[1]CEI Collins Engineers Ltd, Northern Ireland Science Park, Queen's Road, Belfast BT39DT, Northern Ireland
[2]CEI Collins Engineers Ltd, Riverview Business Park, Unit G6, Nangor Road, Dublin 12, Ireland
email: tbrowne@collinsengr.com, tjcollins@collinsengr.com

ABSTRACT: One of the most difficult locations to design, construct, and assess infrastructure is under the water surface. The marine environment provides many challenges in the river, coastal, and offshore environments. The ability to observe the submerged surroundings and underwater infrastructure (e.g., bridge foundations, water facilities, marine renewable energy structures, etc.) with imaging provides tremendous value in design, condition assessment, and construction quality control process. There is always an element of risk associated with bridges and marine infrastructure located in the aggressive water environment. However, innovative underwater imaging technology can reduce risks associated with diving and risks of facility owners. Underwater acoustic imaging can enhance underwater observations at any time, but its true value is most often demonstrated during flood events and extreme depths where divers and other technologies are not feasible.

Underwater imaging technologies have be utilized to supplement diving inspections at a variety of submerged structures over the past two decades, but the latest advancements in range and resolution provide infrastructure managers with a diverse set of tools. Some underwater imaging technologies are better–suited to use in certain circumstances depending on the need. Therefore, this paper will provide lessons learned to date at various locations with underwater imaging based on Knowledge-Transfer-Program research at Queens University in Belfast and research in the USA, as well as worldwide implementation of this technology. Information will be provided on using both 2-D and 3-D images with positive conclusions on the effectiveness when used by qualified personnel.

KEY WORDS: Underwater, Marine, Bridges, Infrastructure, Assessment, Inspection, Sonar, Acoustic Imaging

1 INTRODUCTION

Being involved in marine structures and bridge projects around the world allowed Collins Engineers to first utilize underwater imaging for infrastructure assessment and documentation of submerged components in 1991. In 2010, Collins embarked on a Knowledge Transfer Partnership with Queens University for the research and development of various underwater imaging techniques. Work was undertaken to investigate as many different forms of underwater imaging as possible and then their potential was evaluated using a Strengths, Weaknesses, Opportunities and Threats (SWOT) analysis tool.

The Queens University study then focused on the use of ground penetrating radar (GPR), in conjunction with a hydrographic sonar survey system, for the purpose of identifying scour and scour infill around the submerged structures. Additionally, the study included a comprehensive listing of commercially available acoustic imaging devices that used sonar instead of radar.

The report concluded that GPR has several useful applications for underwater inspections, but it was limited to fresh water with a maximum depth of only around 10 metres. Unlike GPR, sonar could be used in fresh, brackish, and salt water with unlimited depth depending on the deployment method.

Sonar technologies can be classified into two broad categories based on the type of data that they produce. Some systems produce two-dimensional data while others produce three-dimensional data. Two-dimensional sonar systems take a three-dimensional space and plot it on a two-dimensional screen. Three-dimensional data consists of many data points each with unique x, y, and z coordinates. When discussing three-dimensional data such as that produced by single or multi-beam hydrographic survey sonar, the amount of detail that can be generated is dependent upon how small of an area the beam can focus on and also upon the number of points that are obtained. The number of data points obtained in an area is referred to as data density. If a particular sonar system has more beams, or a faster ping rate, the ability to obtain more dense data coverage becomes possible in less time. The accuracy of the data and correctness of the evaluation is also improved when point locations are distinguished. Refer to Figure 1 for an example of a false echo return with an echosounder sonar cone projection instead of a sonar imaging acoustic fan projection.

For several reasons determined over years of use, 2-D sector scanning and 3-D multi-beam sonar are considered the best solutions for generating images of the vertical components of submerged structures and adjacent channel bottom although there are many additional types of other sonar devices that are available but space has limited their discussion herein.

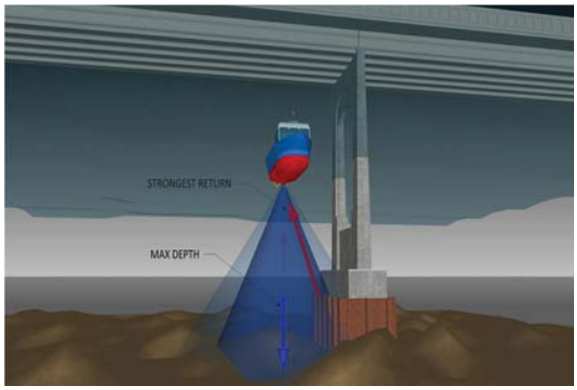


Figure 1. False sonar echo return near a bridge pier.

1.1 2-D Imaging Sonar Systems

Two-dimensional imaging sonar systems have oblong, fan-shaped beams. They essentially work by recording the full range of returns from the wide dimension of the cone angle and plotting them on a two-dimensional drawing.

Sector scanning sonar emits fan-shaped acoustic pulses through the water and requires the vessel to remain stationary while the head is mechanically rotating. The acoustic images are recorded in a series of "slices" generated by a ping after each rotation of the transducer. Scanning sonar operating frequencies usually range between 330 kHz and 2.25 MHz, with a common frequency used for channel bottom and structural imaging of 675 kHz.

Although sector scanning sonar was used to investigate submerged structures more than 20 years ago, it was not until circa 2000 that higher resolution imaging devices became readily available at cost effective prices. Since 2000, numerous structures have been scanned to document underwater conditions. Refer to Figures 2 and 3 for example images of an undermined bridge and quaywall having offset blocks, respectively.

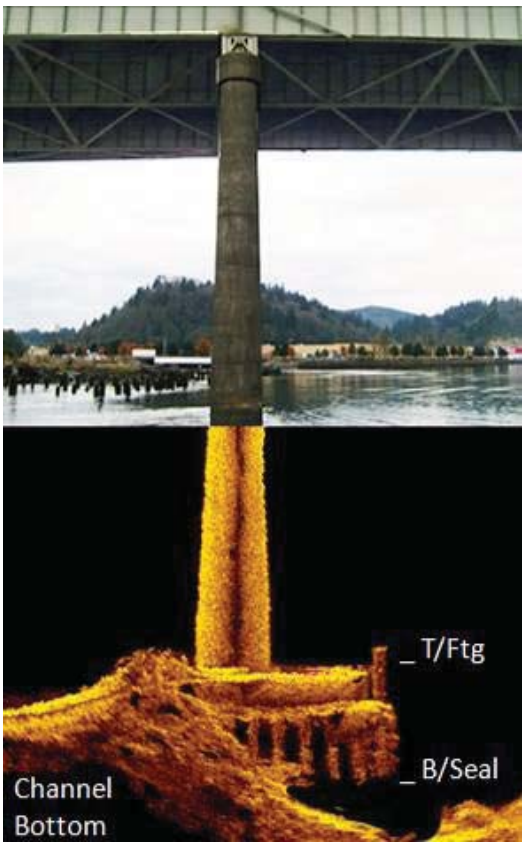


Figure 2. 2-D image of undermined bridge pier.

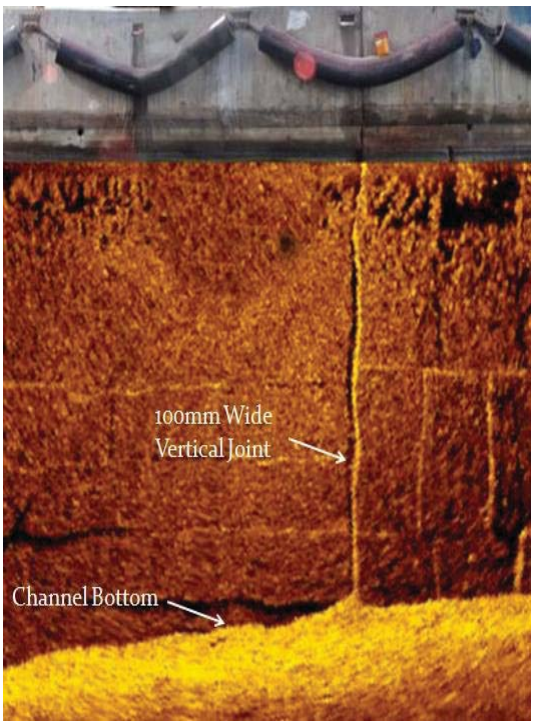


Figure 3. 2-D image of offset joints in quaywall.

1.2 3-D Imaging Sonar Systems

1.2.1 Fathometers/Echosounders

Sonar is the most common method for conducting hydrographic surveys to obtain basic water depths and determine obvious navigational hazards or overall dredging needs. Fathometers and echosounders are single-beam sonar systems that gather three-dimensional data when connected to a GPS or other geographical coordinate collection system. Fathometer frequencies typically range between 24 kHz and 340 kHz, with higher frequencies yielding higher resolution, but little or no channel bottom penetration. More advanced fathometer systems are compatible with GPS receivers or robotic total stations and allow geographic coordinates to be associated with each depth reading. When a fathometer is coupled with one of these devices, water depths can be post-processed and referenced to a horizontal coordinate system. This allows for very accurate channel bottom surveys, which can be easily compared to future surveys. When water conditions allow, a boat-mounted transducer allows efficient data collection. A fathometer survey conducted during a typical underwater inspection around a structure may include recording channel bottom profiles along the sides and a set distance interval or grid away from the structure.

The primary benefit of a fathometer is the ability to obtain geo-referenced channel bottom profiles. The profiles can be used to locate and quantify apparent scour depressions, areas of aggradation, and channel bottom objects such as exposed pier footings or debris accumulation. Overlaying and comparing channel bottom profiles from successive underwater bridge inspections can alert engineers to possible channel-related problems. Foundation information from as-built plans can be superimposed onto the channel cross-sections and profiles for reference purposes.

The primary limitation of a single-beam echosounder is its inability to collect data outside the path of the vessel transporting the transducer. For this reason, the functionality of fathometers is limited to obtaining channel bottom depth information only and imaging of vertical structure faces is not feasible.

Because sonar footprints can become quite large at depth, the sonar operator must be careful not to confuse an exposed bridge footing or other submerged obstruction as the channel bottom. With single-beam sonar, the exact location of the return echo is not always known due to the cone angle. Likewise, fathometers will not provide information about the channel bottom elevation located directly below a footing and cannot provide undermining dimensions.

Data density is typically low in comparison to data obtained by multi-beam sonar collection methods. For instance, a single-beam fathometer survey will typically cover only 5 to 10 percent of the total channel bottom area. This limitation prevents detection of channel bottom irregularities or scour holes unless the vessel passes directly over the top of the interested area with a narrow beam. Additionally, contour maps created from single-beam sonar rely heavily on interpolation between data points. In other words, data obtained from these systems doesn't possess good enough resolution to detect small irregularities. For channel bottoms that are relatively flat, or that have a gentle slope, this method works well. Low data density and the presence of steep or irregular surfaces can cause data interpolation to show an inaccurate representation of actual conditions.

1.2.2 Multi-Beam Sonar

Multi-beam swath sonar consists of a line of numerous narrow circular beams. The beam arrangement allows detailed mapping of a very thin transverse section with each sonar pulse. Most systems are boat mounted and require forward progress of the boat to advance the position of the send/receive the sound signal. Multi-beam swath sonar systems (also referred to as swath echosounders) function similar to single-beam echo sounders except, they have multiple sonar beams acting simultaneously allowing for much more dense data coverage in a shorter period of time. This swath system uses a fanned array of sound beams that typically give near 100 percent coverage of the seafloor or channel bottom. For instance, a typical multi-beam survey may have a fanned array that is capable of a "swath width" of seven times the water depth. Refer to Figure 4 for an illustration of the survey fan.

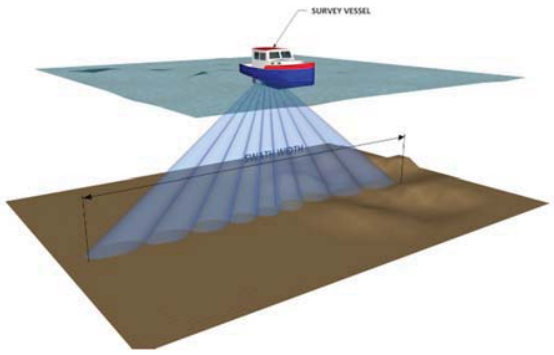


Figure 4. Multi-beam swath sonar beam pattern.

For vertical imaging applications, the same theory applies but the swath width is dependent upon the distance between the transducer and the vertical face of the structure. Since the direction and angle of the beams can change with the heave, pitch, and roll of the survey vessel, it is necessary to have motion compensators and a gyrocompass that account (in real-time) for the motion and relay correction factors back to the on-board processor.

Another form of multi-beam sonar is three-dimensional mechanical scanning sonar, which is essentially a multi-beam sonar unit fitted with a mechanical stepping motor on a stationary tripod or otherwise deployed stationary object. The mechanically scanning sonar needs to remain stationary while performing scans, but data can be collected within range.

The primary benefit of multi-beam swath sonar is the ability to quickly obtain large quantities of three-dimensional data. Multi-beam swath sonar produces a three-dimensional still image that is often referred to as a point cloud. For bridge inspection applications, the production of three-dimensional data would allow an inspector to document and assess the depth of spalling, scaling, or possibly even foundation undermining. By using multiple or overlapping passes, the sonar operator is able to obtain greater data density and 100 percent bottom coverage of the area.

The primary limitations of multi-beam swath sonar are that the vast quantities of data produced can be cumbersome and time consuming to post process. Because of the additional sensors required and the complexity of the relationship between these sensors, a portable multi-beam installation is significantly more complex and time consuming than a comparable single-beam installation or mechanically scanning multibeam setup. Both field operation and data post processing require a greater deal of training and skill to master than other imaging sonars used without motion compensation or GPS positioning. Additionally, all multi-beam sonar systems are considerably more expensive than other sonar devices.

The final limitation of multi-beam swath sonar as it pertains to underwater inspection is the difficulty of such systems to smoothly transition from acquiring data on the channel to the vertical face of a bridge support when they are in a downward looking configuration. This occurs because swathe multi-beam systems are finely tuned through power and gain adjustments to detect the channel bottom and thus don't always accurately record returns from dissimilar materials and locations. Additionally, the data often requires a large amount of manual post processing to weed out the acoustic noise. In the hands of a skilled technician multi-beam swath sonar can yield high quality surveys but the relative complexity compared to single-beam systems is a definite disadvantage. It should also be noted that a swathe multi-beam systems would be a poor choice for shallow waterways with relatively simple bottom topography. However, in areas with certain characteristics (e.g., deep water, complex bottom topography, limited visibility, strong currents, large areas, etc.) swath offers some efficiency. Nonetheless, the stationary sonar provides a number of unique benefits relative to any other existing technologies. Refer to Figures 5 through 8 for examples of the 3-D point cloud data collected with a stationary channel bottom deployed tri-pod with mechanically scanning multi-beam sonar head.

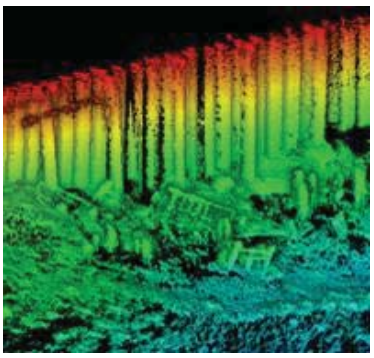


Figure 5. 3-D point cloud of channel debris at quaywall.

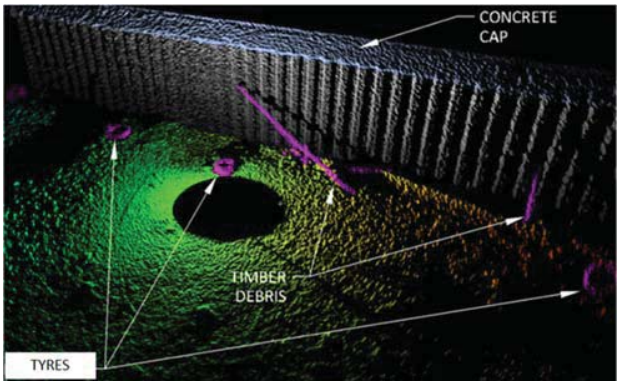


Figure 6. 3-D point cloud image of steel sheeting quaywall.

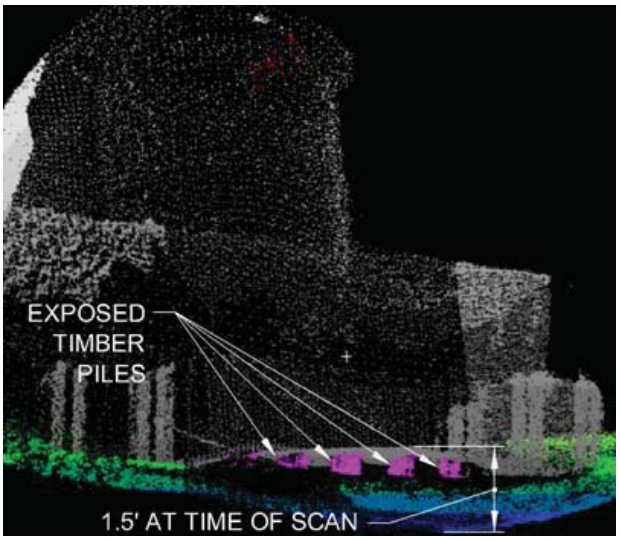


Figure 7. 3-D point cloud image of undermined foundation.

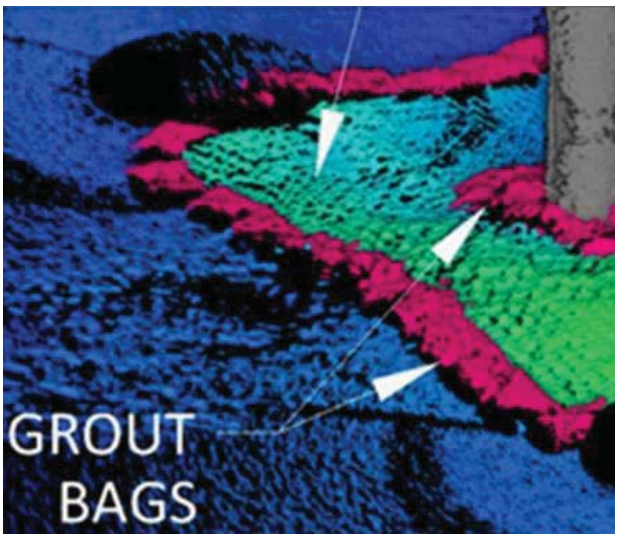


Figure 8. 3-D point cloud image of scour protection mat.

2 FIELD IMPLEMENTION OF TECHNOLOGY

Traditional underwater inspection field techniques and procedures are well documented. Yet some inspectors and owners have increasingly been turning to acoustic imaging technology to enhance inspection and documentation procedures. This trend has been accelerated based on the special needs of some bridge owners with structures located in adverse site conditions such as zero visibility, high velocity currents, heavy debris, and extreme depth. Urbanisation and climate change are two reasons these special needs are occurring more frequently worldwide. Because these factors can limit a diver's ability to thoroughly inspect a bridge below water, enhancements such as acoustic imaging have been used as a supplement to ensure a thorough inspection. To date, acoustic imaging has been used at thousands of sites around the world. Potential applicability of acoustic imaging for underwater inspections are outlined in the below sections:

- Rapid condition assessment.
- Scour detection and documentation.
- Underwater construction inspection.
- Security threat assessment.
- Documented visual representation of the entire underwater structure.
- Enhancing diver safety and efficiency at challenging dive sites.

2.1 Rapid Condition Assessment

Both natural disaster and man-made events can cause the need for emergency structural assessment. Natural disaster events include floods, earthquakes, and tsunamis. Man-made events can include vessel impacts and dam breaks. Rapid condition assessment is often required immediately following an emergency event.

Emergency events can threaten the structural stability of a structure, and decisions often cannot wait for adverse conditions to become more favorable for a dive inspection. The immediate need for a decision can result in overly conservative closures requiring unnecessary lengthy detours or economic consequences. With acoustic imaging technology owners can get important information about a structure during or soon after an event, whereas a dive inspection might have to wait weeks or months for floodwaters to recede or for conditions to otherwise become favorable.

2.2 Scour Detection and Documentation

The number one cause of bridge failure is scour. Likewise, scour is a significant issue for other marine infrastructure such as port, harbour, and offshore structures including wind turbines and other energy producing structures. This makes it paramount for owners to be able to efficiently and safely be able to assess the presence of scour at their sites. The presence of scour can often be difficult for an inspection diver or ROV to detect for a variety of reasons and this makes underwater imaging technologies extremely useful.

In addition to hydrographic surveys, fixed scour monitoring systems can be established for continuous scour monitoring at a specific site. A fixed scour monitoring system means that it is permanently or semi-permanently attached to a structure to repeatedly monitor a specific area. However, it is difficult and expensive to obtain complete coverage of the entire structures at every site with a fixed system. The portability of a 2-D sector scanning sonar or a 3-D mechanically scanning multi-beam sonar provides a tremendous value.

2.3 Underwater Construction Inspection

Underwater imaging technologies can be used in all phases of construction; from pre-construction planning, through the construction phase, to verifying as-built information and construction verification.

Another construction related business that heavily utilizes sonar technology is the dredging industry. Everything from single-beam fathometer surveys to side-scan sonar and multi-beam swath surveys have been used to quantify and classify river channels and the sea-bed. The primary uses a stationary acoustic imaging device includes the detection of obstacles that could damage the dredging head; the ability to map the composition and distribution of the seabed sediments; and the increased accuracy in calculated volumes under structures. Careful consideration needs to be given to the deployment and location of the different acoustic imaging systems to guarantee the best results as part of any construction operation.

2.4 Security Threat Assessment

The ability to image underwater structures has obvious security implications for marine infrastructure and maritime vessels. The potential applications are numerous and include

scanning for explosives and detecting intruders. Various types of commercially available imaging sonar have been used for this purpose and there are several cases showing that acoustic imaging technologies have proven to be an efficient and reliable way to accomplish this task. Therefore, military and law enforcement agencies are also using these technologies for non-engineering purposes.

2.5 Visual Representation of Submerged Structure

One of the main advantages of underwater imaging technology is the ability to image a structure regardless of water clarity. Where other optical technologies, ROV, or a diver might allow an inspector to visualize parts of a structure, several types of sonar allow an owner to see images of a structure in its entirety. After all, areas could be missed unless sonar is used to ensure 100% coverage.

2.6 Enhancing Diver Safety and Efficiency

As described in the cases above, underwater imaging technology has a large impact on diver safety and efficiency. As previously stated, many acoustic imaging technologies have the ability to generate data that can then be used to track a diver's location or direct a diver to or away from a specific area.

3 CONCLUSIONS

The technology exists to obtain "photographic-like" 2-D acoustic images, as well 3-D acoustic point cloud data models of infrastructure below the water for documentation and assessment purposes. Similar to other underwater work (e.g., diving and ROV video work), acoustic imaging professionals must have training and experience to ensure safe operations and the collection of high quality accurate data.

Lessons learned over the years include appropriate deployment methods to increase quality and reduce issues such as slant range distortion, acoustic shadows, false indications, wrong terminology of findings, poor situation evaluations, and data registration errors. It has been the authors' experience that the lead acoustic imaging professional should have formalised training in both sonar and underwater inspections with sufficient experience to allow proper identification of defects and the ability to make critical assessments. Since assessments must be completed with certainty, an engineer-diving team may need to be deployed if there is any uncertainty about submerged conditions. Also in some cases, ROVs that have traditionally relied on optical video documentation and navigation can benefit from being equipped with various sonar imaging technologies in poor visibility conditions.

ACKNOWLEDGMENTS

The authors would like to thank the individuals at Queens University for their research efforts, as well as the staff at CEI Collins Engineers Ltd, who have been implementing acoustic technologies in the field, continuing research on this topic, and obtaining the images provided herein.

REFERENCES

[1] Browne, T., et.al., "*Reliability of Underwater Acoustic Imaging and Underwater Ultrasonic Testing",* ASNT Proceedings of the Structural Materials Conference, 2014.

[2] Browne, T., "*Underwater Acoustic Imaging Devices for Portable Scour Monitoring",* Proceedings of the International Conference on Scour and Erosion, 2010.

[3] Cambell, K., et al., "*Ground Penetrating Radar as an Innovative Tool for Identifying Areas of Scour and Scour Infill Around Bridges*", Proceedings of the International Bridge Conference, 2010.

[4] Tomlinson B, et.al., "*Emerging Acoustic Techniques for Monitoring the Condition and Performance of Underwater Structures",* Paper 28 in Proceedings of the ICE Conference on Breakwaters, Coastal Structures and Coastlines, Ed. Allsop N.W.H. ISBN 0 7277 3042 8, pp 345-357, Thomas Telford, London. 2001.

The hydraulics and resulting bed scour within the vicinity of submerged single span arch bridges.

Donal Ryan[1], Gerard A Hamill[2], John McRobert[3], William Smyth[4]
[1]School of the Built Environment, University of Ulster, Shore Road Newtownabbey. BT37 0QB
[2]School of Planning, Architecture & Civil Engineering, Queen's University Belfast, David Keir Building, Stranmillis Road, Belfast. [3]DRD Roads Service, Highway Structures Unit, County Hall, Galgorm Road, Ballymena. Co. Antrim.
[4]South West College, Dungannon Campus, Circular Road, Dungannon. Co. Tyrone.
email: d.ryan@ulster.ac.uk, g.a.hamill@ulster.ac.uk, john.mcrobert@drdni.gov.uk, william.smyth@swc.ac.uk

ABSTRACT: As a consequence of climate change there is now a more frequent occurrence of extreme rainfall events where, with higher rates of urbanisation, the built environment has become increasingly affected by flooding. This is of particular importance in relation to the stability of bridge structures that span rivers and canals etc. In November 2009, the UK and Ireland were subjected to extraordinarily severe weather conditions for several days. The rainfall was logged as the highest level of rainfall ever recorded within the UK, and as a direct consequence, unprecedented flooding occurred in Cumbria. This flooding led to the collapse of three road bridges which were generally 19th century masonry arch bridges, with relatively shallow foundations. In the UK, knowledge of the combined effect of bridge scouring and inundation has been not been particularly widely studied. Recent research carried out considered the hydraulic analysis of single arch bridges under flood conditions, but no consideration was given towards the likely damage to these structures due to scouring. Other work was done to predict the discharge downstream of an inundated arch, focussing on predicting afflux as opposed to bridge scour, under both pressurised and free-surface flows, but no predictive equation for scour under pressurised conditions was ever considered.

This paper will present initial findings from an experimental investigation into the effects of surcharged flow and subsequent scour within the vicinity of single span arch bridges. Velocities profiles will be shown within the vicinity of the arch, in addition to the depth of clear water scour, for a series of flows and model spans. The data will be presented, where results will be correlated to the most recent predictive equations. The accuracy of these equations will be presented, and the findings will present a basis for developing further studies in relation to arch bridges.

KEY WORDS: Scour, pressurised flow, sediment, bridge.

1 INTRODUCTION

In November 2009, the UK and Ireland were subjected to extraordinarily severe weather conditions for several days. The rainfall recorded at Seawaith Farm, Borrowdale, was in excess of 316mm over a 24-hour period, and was the highest level of rainfall ever recorded within the UK. As a consequence, unprecedented flooding occurred in Cumbria. Due to a combination of rainfall, and the terrain, the flooding led to the collapse of three road bridges and the same number of footbridges around Cockermouth and Workington and resulted in considerable negative economic, social and environmental impacts. The bridges were generally of masonry arch construction, built in the 19th Century and with relatively shallow foundations. The causes of these collapses are likely to be related to a combination of factors, including (1) Foundation Scouring (2) Upwards pressure on the arch soffit, causing separation of the arch stones (3) Lateral water pressure and (4) Debris impact.

Highways Agency published a revision to BA 74/06 "Assessment of Scour at Highway Bridges" in 2012. The new revision (i.e. BD 97/12 [1]) advises on how to determine the level of risk associated with scour effects. However, no advice was given on how to carry out design for this risk. Highways Agency also refers to BA59/94 "The Design of Highway Bridges for Hydraulic Action" [2] provides design guidance based on references from publications prior to 1994. The significance BA59/94 reference date is that this Advice Note does not take into account the current situation in relation to climate change, nor does it consider neither submerged decks nor arches.

In the UK, the above standards clarify that the recommended design guidance documentation for highway bridges does not provide advice on predicting/designing to reduce scour under pressurized flow conditions. The rationale behind this paper is to address the current knowledge gap when looking at pressurized flood flows/inundation on existing structures, with particular emphasis on structures with limited spans. The impact of this research will become significant to stakeholders and designers, where the findings will inform maintenance guidance and provide design advice to engineers.

2 BACKGROUND RESEARCH

2.1 Bridge Hydraulics

Several Authors have investigated the hydraulics of flow in the vicinity of an arch bridge. The majority of that work was carried out for normal flow conditions, where arch inundation was not considered. Previous authors were also interested in the prediction of afflux and discharge through the bridge structure. However, when the soffit of a bridge is submerged there were two specific conditions that can exist, (1) Sluice Flow and (2) Orifice flow, where Equations 1 to 3 were proposed by Bradley [3] proposed below:

$$Q = C_d a_w \left[2g\left(Y_u - \frac{Z}{2} + \frac{\alpha_u V_u{}^2}{2g}\right)\right]^{1/2} \quad (1)$$

$$Q = C_d a_w (2g\Delta H)^{1/2} \quad (2)$$

where C_d (= 0.35 to 0.6) is the discharge coefficient, a_w is the total area of the opening flowing full (m^2), Y_u is the upstream depth (m) and Z is distance between the soffit and the bed level (m). Equation 3 defines ΔH as:

$$\Delta H = \left[\left(Y_u - \frac{Z}{2} + \frac{\alpha_u V_u{}^2}{2g}\right) - \left(Y_d - \frac{Z}{2} + \frac{\alpha_d V_d{}^2}{2g}\right)\right] \quad (3)$$

The subscripts u and d denote upstream and downstream respectively. The above equations have never been tested for arch bridges, and the most application equation for predicting Discharge was proposed by Biery & Delleur [4] as:

$$Q = C_d\sqrt{2g}\ \frac{17}{24}\ y_1{}^{3/2} b \left[\begin{array}{c} 1 - 0.1294\left(\frac{y_1}{r}\right)^2 \\ -0.0177\left(\frac{y_1}{r}\right)^4 \end{array}\right] \quad (4)$$

where y_1 is the depth of flow at the section of maximum backwater (m), b is the span width at the spring line of the arch (m) and r is the radius of curvature of the arch (m). The limitation of Equation 4 is that the C_d value must be determined from Tables within the publication itself, and the same equation determines discharge for both sluice and orifice conditions, where no clear evidence from tests is demonstrated within the publication. Equations 1 to 3 cannot be used due to the fact that the constriction is not an arch.

The above equations have been widely used to predict bridge afflux and have also been utilised to determine the flow through the bridge constriction and hence the average flow velocity through the same. As the velocity increase within a bridge constriction, formulae were developed to determine scour depth as a function of the relationship between upstream average velocity (v_u) and the average velocity through the constriction (v_B). A value for v_B is determined from Equation 4 for an arch bridge.

2.2. Bridge Scour

Shan et al [5] suggested the following equations to predict pressurized clear water scour under vertical contraction only:

$$y_2 = \left[\frac{k_u Q^2}{D_m^{2/3} W^2}\right]^{3/7} \quad (5)$$

And

$$\frac{t}{h_b} = 0.5\left(\frac{h_b h_t}{h_u{}^2}\right)^{0.2}\left(1 - \frac{h_w}{h_t}\right)^{-0.1} \quad (6)$$

Where h_b is the vertical size of the bridge opening prior to scour (m), t is the maximum height of the separation zone (m), h_u is the upstream normal depth (m), D_m is the median grain diameter (m), W is the upstream channel width (m), k_u is a dimensionless parameter (0.025), Q is the upstream flow (m^3/s) and y_2 is a measurement related to scour depth (m). The value for h_b is subtracted from (y_2 + t) to get the total depth of scour (y_s). Q is calculated using Equations 1, 2 and 4. V_{uc} and V_b are the velocities upstream and through the bridge respectively.

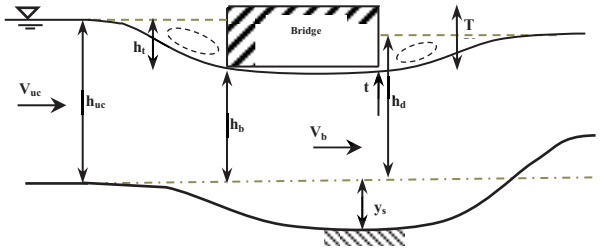


Figure 1: Parameter Definitions for Maximum Scour

The limitations to the above relationship are that the constriction is only vertical. With an arch bridge, the constriction is both vertical and horizontal and the validity of the above equations has yet to be tested.

3 EXPERIMENTAL SET-UP & DATA ACQUISITION

3.1 Velocity Testing

Previous Authors, including Arneson & Abt [6], Richardson & Davis [7] and Gou [8] carried out extensive physical modelling on sediment scouring. However, there was no evidence of attempting to understand the flow velocities within the vicinity of the bridges. Each author cited the work of early authors such as Laursen [9] and in relation to examining critical velocity of sediment (V_c), but made little attempt to carry out any work in establishing a relationship between scour depth and velocity within the vicinity of the bridge, under pressurised low. There seems to be an emphasis on upstream average critical velocity (V_{uc}) and the average velocity through the bridge (V_b). These are averaged, based on continuity equation, and using Equations 1-4, depending on the physical conditions.

The present investigation considers the nature of these velocities through an arch bridge, in order to gain a better understanding of the nature of flow through a pressurized arch. Velocity measurements are taken by using a SonTEK 2D Acoustic Doppler Anemometer (ADV), with a sampling frequency of 50Hz. Measurements were taken for an initially flatten bed, stabilized by using an Epoxy Resin treatment. Following this, the scour holes were allowed to fully develop to an approximate equilibrium stage of erosion (approx. 80 mins), and measurements taken for the purposes of making comparisons with the flat bed condition.

A grid system is used both upstream and downstream of the arch models, where the grid density for velocity measurement (ADV probe) was increased within the vicinity of the higher velocities to that of a 20 x 20mm Grid. Outside the confines of the arch, the grid was increased to a density of 50 x 50mm.

Velocity measurements were taken on the XY plane at three positions (1) 500mm upstream of the flow entering the arch, (2) at 20mm upstream of the flow entering the bridge arch and (3) 20mm downstream of the flow exiting the bridge arch. The data was then analysed to determine how the velocity profiles varied with distance through the arch.

3.2 Bridge Model & Scour Tests

All of the uPVC model bridge experiments have been carried out within a 10-metre long Perspex channel of dimensions 760 mm × 250 mm. The overall depth at the recess section was 480 mm. Water is supplied via a reservoir and 2 No. impeller pumps and is capable of supplying 100 L/s to the upstream supply reservoir. A recess is constructed within the channel for the purposes of these experiments to a total depth of 230 mm. A bridge model structure was inserted half way down the channel and is illustrated in Figure 2. The abutment length (i.e. model road width) is 280mm for these experiments.

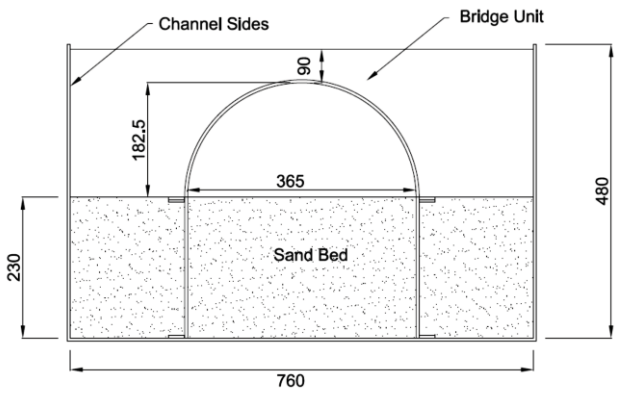


Figure 2: Scale Model of Bridge Cross-Section for Typical Arch.

Figure 3 shows the model in the channel after a typical experimental run of 80 minutes, and where the flow was 32 l/s. The sediment used in the test had a d_{50} of 1.1 mm.



Figure 3: Experimental Setup after test run at 32 l/s.

4 RESULTS AND DISCUSSION

4.1 Velocity Measurements

From the XY measurement for velocities on the flat bed, Surfer™ was used for the purposes of visualising the velocity distributions as the flow progressed through the arch. Figure 4 shows a plot of a 23 L/s flow passing through a bridge under flood conditions.

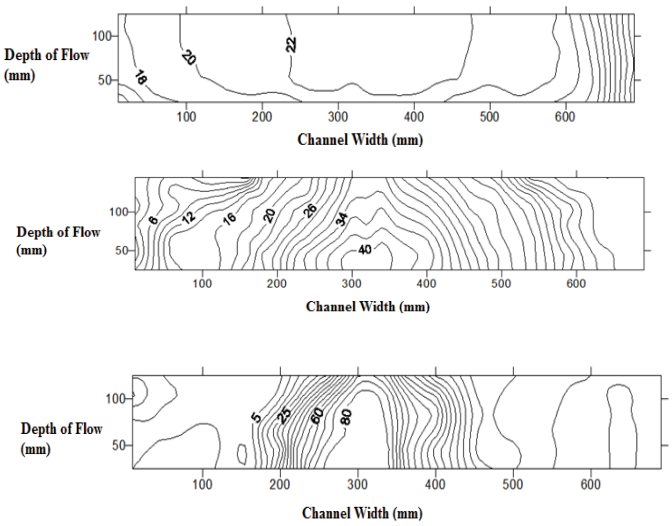


Figure 4: Contour Plot of Flatbed velocities at 500mm upstream, 20mm upstream and 20mm downstream of Arch Bridge unit at 23 L/s.

The velocity contour plot clearly shows that the velocity gradient and peak value increase as the flow passes through the arch bridge. The arch is not drawn on these contours, however it can be clearly seen that there is a concentration of high velocities at the position of the arch, which is centred at 300mm on the contour plots. The velocities also increase four-fold as the flow passes through the arch.
Considering these velocities in a 2-Dimensional Plane, these are shown on Figure 5 along the axis of the Arch Centreline.

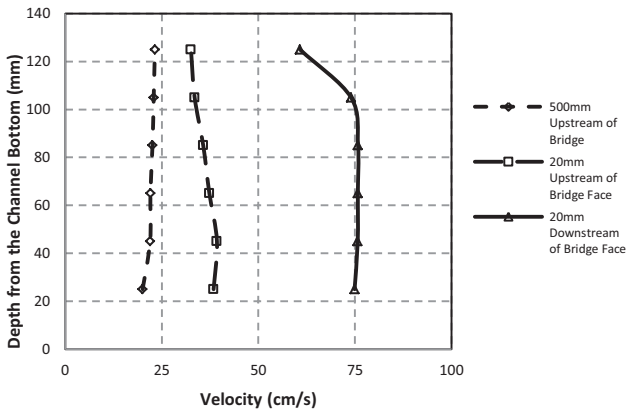


Figure 5: Flatbed velocities at 500mm upstream, 20mm upstream and 20mm downstream of bridge unit at 23 L/s.

From Figure 5 it can be demonstrated that, from the upstream to downstream face of the arch bridge, there is an acceleration provided by the upstream head where the maximum velocity within the profile increases from 39 to 76 cm/s. This is an increase of almost two-fold. By examination of additional tests, with the same physical conditions, but with flow increases from 26 to 32 L/s, similar changes in velocity occur. Therefore, it calls into question whether or not it can be assumed that the velocity through the bridge (V_b) is constant, as per the findings of previous authors such as Biery & Delleur [4]. This is especially the case for vertical constriction only, and should be further investigated.

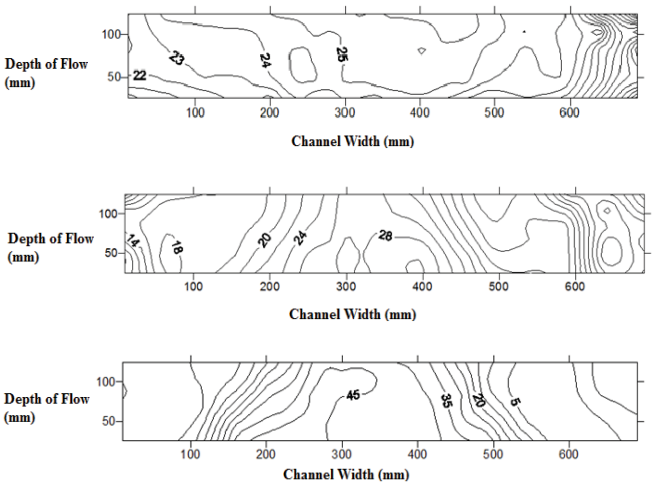


Figure 6: Contour Plot of scour hole velocities at 500mm upstream, 20mm upstream and 20mm downstream of Arch Bridge unit at 23L/s.

When considering the characteristics of the flow contours within a fully developed scour hole, the contours are shown in Figure 6. The flow, in this case is for 23L/s, as previously discussed.

In this case, the velocity contours are less pronounced, and the magnitude of these velocities is less pronounced. This is expected as all of the erosion has taken place. However, worth noting is the fact that velocities (some 22mm above the bed) are still in the order of 45cm/s (0.45m/s), which would still exceed the critical velocity of most small to medium sands. It would be expected that the slope of the scour hole may play a part in the scouring process ending, but the velocities still remaining above their threshold values.

4.2 Development of Scour within the vicinity of the Bridge.

For the purposes of this study, each scour test was allowed to run for a total of 80 mins at a constant flow, which was determined as a reasonable estimate of the near asymptotic/equilibrium state where 95% of scouring has occurred. The 3D Scanner was utilised to determine the overall scour hole profile and Mountains Software was used to create the surface. Figure 7 shows the 3D Scanner used for the current investigation.



Figure 7: 3D Scanner Equipment for measuring scour depth.



Figure 8: 3D Photo of Scour Hole with reference points (bridge unit removed).

All 3-D profiles were carried out as described above, with the use of a network of reference points (circular plastic stickers) placed over the initially flat bed. A second scan is then carried out at 0.5mm resolution after the placement of new reference points placed, as shown on Figure 8. It can also be seen that the main bridge superstructure has been removed in this case, for the purposes of measurement. Figure 9 shows the scanned image.

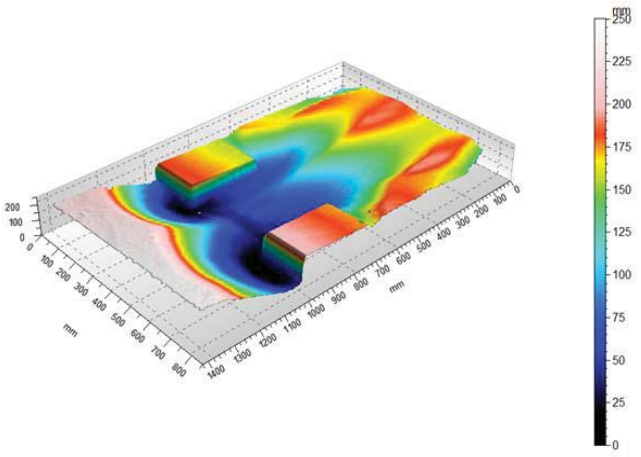


Figure 8: 3D Plot from laser scan produced using "Mountains" Software.

From the above plot, it is possible to determine all depths of scour, position of maximum scour and deposition, volumes of scour and deposition using the software at the end of every test. The line of maximum depth of scour can be determined and to the accuracy of 0.5mm. These plots confirmed that the maximum depth of scour always occurred at the upstream face of the abutment/foundation. This relationship held for all tests completed during this investigation.

4.3 Scour Depth as a function of time

The maximum depth of scour is a function of several experimental parameters that include flow, width of bridge span, sediment characteristics, level of afflux, abutment length, time etc. The key parameter is scour depth, but it is also critical to understand how quickly the maximum depth of scour is reached within a flood situation.

Measurements of the depth of scour, with respect to time, were made for each test and presented with Scour Depth (mm) versus Time (mins) as shown in Figure 9. Each measurement was carried out using a vertical probe, in still water, as the flow pump was switched off. It is clear that the rate of development of scour is high at the early stages of each test, and subsequently decreases after 8 to 10 minutes, where the depth begins to level out as the time approaches 80 minutes.

4.3 Afflux as a Function of Time.

McGahey et al et al [10] carried out a significant amount of work in determining how to predict afflux levels on the upstream side of many bridges throughout the UK and Abroad. The purpose of this work was focussed on predicting the level of afflux and its effect on upstream conditions (i.e. potential for flooding etc.).

From Figure 10, it is reasonable to understand that the initial levels of afflux increase with the rising discharge. However, this is not a linear relationship as the afflux values for 23 and 26 L/s are reasonably close.

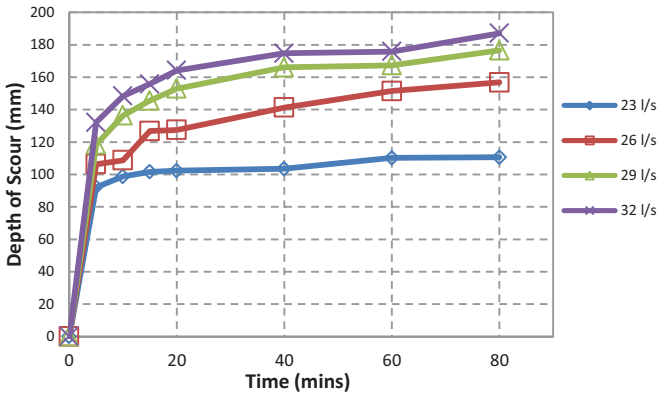


Figure 9: Scour Depth vs Time for Bridge Abutment.

During the present investigation, the afflux level was measured with time, to determine if there may be a relationship between afflux level and the development of the scour hole. Figure 10 shows the results for 4 No. flows through a model arch bridge, carried out at the same time as the scour test shown in Figure 9.

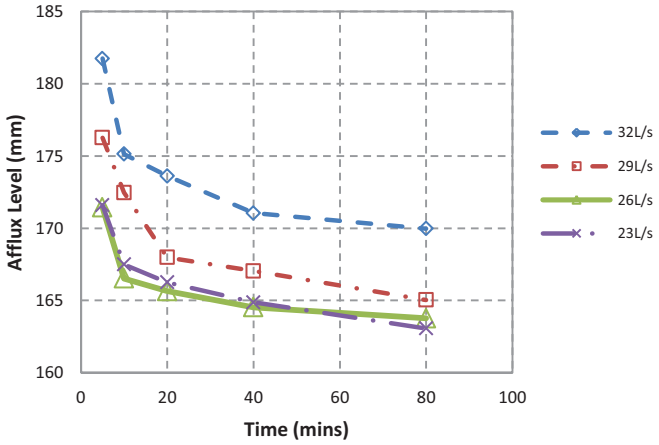


Figure 10: Afflux Level v_s time

However, considering Figure 9, the same flows demonstrate that scour depth is more sensitive to the small change in flow and, as these flows increase, the scour depth becomes less sensitive. This is the opposite of what is shown in Figure 10, where the difference in afflux is more pronounced between 32 L/s and 29 L/s when compared to the lower discharges. This is not what would normally be expected within pressurised flow conditions and is worth investigating further. It would also suggest that the upstream head may have a more limited effect on scour depth than expected.

4.4 Calculation of Theoretical Scour Depth and comparison with Laboratory Results.

The average velocity was determined by using the velocity area method to calculate the measured flow for each individual experiment, and then dividing the flow result by the total area of that flow (i.e. width × depth). It was found that the error between the metered flows and the measured values were less than 1%. These measured discharges were then compared with the predicted values by Biery & Delleur

[4]. Each of these values was, in turn, used to make a prediction of the final depth of scour as a function of the experimental conditions. The results are shown in Table 1.

Measured Flow (L/s)	Flow by Biery & Delleur(L/s)	Measured Scour Depth (mm)	Theoretical Scour Depth (mm)	% Error Scour
23.02	20.6	111	183.3	40%
26.5	21.3	157	218.8	28%
30.1	22.3	177	254.1	31%
33.2	24.3	187	289.1	35%

Table1: Comparison between Theoretical & Actual Discharges/Scour Depths.

It can be seen from Table 1 that there are two key observations. Firstly, the error between the actual measured discharges (hence velocities) varies from 10 – 24% as these values increase from 23 L/s to 33.2 L/s. In addition to this observation, scour depth is plotted against discharge is shown in Figure 11. In this case, the theoretical depth of scour is up to 40% in overestimation when compared to the actual scour depths. This would suggest that the existing equations do not predict pressurised scour for an arch bridge particularly well.

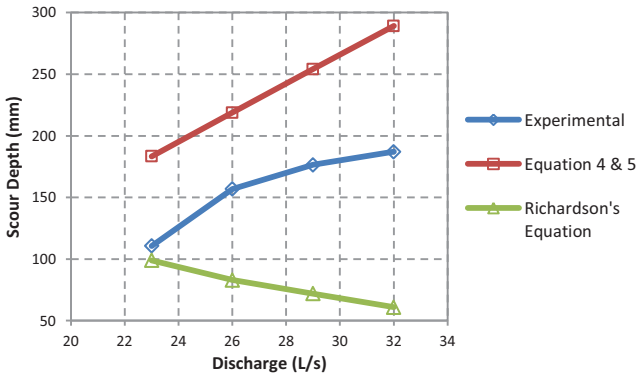


Figure 11: Comparison of Experimental Scour Depths with Existing Equations.

An equation was proposed by Richardson et al [6] to predicts pressurised flow as:

$$\frac{y_s}{y_1} = -5.08 + 1.27\left(\frac{y_1}{H_b}\right) + 4.44\left(\frac{H_b}{y_1}\right) + 0.19\left(\frac{V_a}{V_c}\right) \qquad (7)$$

Where y_1 is the upstream depth (m), V_a is the average velocity through the bridge opening (m/s) and V_c is the critical velocity for incipient motion (m/s). When the predictions from Equation 7 are plotted against the current experimental data it is clear that the scour depth from the present data is reasonably close to Equation 7 at the lowest velocity, but rapidly begins to move well above these predicted values as the discharge is increased. However, it is a concern Equation 7 presents that the depth of scour decreases with a rise in discharge/velocity. This is something that cannot physically occur within the current experimental set-up, where scour depth is expected to increase with a rise in discharge. What can be confirmed is that the work of Richardson et al [7] is not applicable to submerged flow in the vicinity of an arch bridge.

5 CONCLUSIONS

For the range of tests carried out for the present investigation, it has been found that there is a clear mathematical relationship between scour depth and time. As time increases, the rate of development of scour also decreases to an asymptotic (almost zero) value. When considering the afflux levels with time, there is also a decrease in upstream afflux level with time, as scouring progresses. The development of scouring, and the drop in afflux value are directly related and further testing is currently underway in order to determine if the relationship between scour depth and afflux can be ascertained.

Current methods from Biery & Delleur [4] also over predict discharge through the bridge units. This is possibly due to the fact that the abutment length was not considered to any great detail within those studies. This will therefore require further investigation as the current model utilised an abutment length of 280mm whereas, the work of Biery & Delleur [4] used much shorter lengths, where the arches almost behaved like flat plates. This is possibly the reason for the acceleration of the water under the bridge, where the increase in velocity is significant as the flow enters and exits the arch. Further work is underway to investigate the length of the abutment and how it may affect the under bridge flow velocities, in addition to determining the actual flow through the arch.

Following on from the above observations, this study will be further developed in order to propose a new range of semi-empirical equations to predict scour depth in the vicinity of a submerged arch bridge structure.

REFERENCES

[1] Design Manual for Roads & Bridges, “The Assessment of Scour and Other Hydraulic Actions at Highway Structures”, BD 97/12 (2012). Department for Transport (UK).

[2] Design Manual for Roads & Bridges, “The Design of Highway Bridges for Hydraulic Action”, BA59/94 (1994). Department for Transport (UK).

[3] Bradley, J.N., (1978) “Hydraulics of Bridge Waterways”. U.S. Dept Transportation/Federal Highways Administration, Washington, D.C., 2nd Edition.

[4] Biery P. F. and Delleur. W. Hydraulics of single-span arch bridge constrictions. Proc. Am. Soc. Civ. Engrs, J. Hydraulics Div, 1962, 88, HY2, March, 75-108.

[5] Shan, H., Xie, Z., Bojanowski, C., Suaznabar, O., Lottes, S., Shen, J., Kerenyi, K. (2012). “Submerged Flow Bridge Scout under Clear Water Conditions”. U.S. Department of Transportation, Federal Highway Administration (FHWA), Report No: FHWA-HRT-12-034.

[6] Arneson, L.A. and Abt, S.R., (1998). "Vertical contraction scour at bridges with water flowing under pressure conditions." Transportation Research Record. 1647, 10-17.

[7] Richardson , E.V., Davis, S.R., (2001) Evaluating Scour at Bridges, HEC-18, FHWA-NH-01-001, 4th Edition. US. D.O.T. Washington. DC.

[8] Guo, J., Kerenyi, K., Paga-Ortiz, J.E. “Bridge Pressure Scour for Clear Water Conditions”. (2009) Report No: FHWA-HRT-09-041. U.S. Department of Transportation, Federal Highway Administration (FHWA).

[9] Laursen, E.M., 1960, “Scour at bridge crossings” Journal Hydraulic Division, American Society of Civil Engineering, v. 89, no. HY3.

[10] McGahey, C. Lambe, R. Knight, D.W. “Practical Channel Hydraulics: Roughness, Conveyance and Afflux”, Taylor & Francis Group.

Numerical simulation of fluid flow around an array of cylinders at low Reynolds number

William Finnegan[1], Jamie Goggins[2]
College of Engineering and Informatics, National University of Ireland, Galway, Ireland
Ryan Institute for Environmental, Marine and Energy Research, National University of Ireland, Galway, Ireland
email: [1] william.finnegan@nuigalway.ie, [2] jamie.goggins@nuigalway.ie

ABSTRACT: Fluid flow past a cylinder is a problem in fluid mechanics which has been investigated for decades. The flow of a fluid around an array of structures is found in a number of engineering applications. Two examples of this include the flow of water around oil and gas pipelines and air flow around tall buildings. With the advances in computational fluid dynamics, it is now possible to explore the wake characteristics, in particular the phenomena of vortex shedding, in much more detail. In this paper, the flow around an array of eight cylindrical structures in a staggered configuration is explored at a Reynolds number of 100. The commercial computational fluid dynamics software, ANSYS CFX, is used to model the analysis.
In this study, particular interest is given to the wake interactions and the forces on the individual structures within the array. The flow pattern around the structures is displayed using the velocity contours of the flow, for a number of spacing configurations. The drag and lift coefficients and Strouhal number are calculated and compared for each structure within the array at each spacing configuration. In addition, a validation study is performed on this numerical model using two geometries, which are similar to the cylinder array of interest. Within this validation study, results are also compared to experimental data.

KEY WORDS: Array; Computational fluid dynamics; Cylindrical structures; Fluid flow; Low Reynolds number; Wake interaction.

1 INTRODUCTION

The flow of a fluid around an array of structures is found in many engineering applications, including around oil and gas pipelines, offshore structures, tall buildings, wastewater treatment systems and in heat exchangers. The wake interference within the array is of particular interest as a result of its practical importance in these applications.

The classical fluid mechanics problem of fluid flow past a single circular cylinder has been explored for decades. Results from experimental studies have been compiled by Wieselsberger [1], Tritton [2] and Van Dyke [3]. However, only in recent years, with the use of computational fluid dynamics, has it been possible to really understand the wake characteristics as a result of vortex shedding. Therefore, a large number of numerical simulations of fluid flow past a single circular cylinder at low Reynolds number, *Re*, have been performed [4, 5, 6, 7, 8, 9, 10].

Numerical simulations have also been employed to explore the flow field around arrays of circular cylinders. In general, studies have been restricted to a small finite number of cylinders within the array, usually less than four. Ding et al. [11] used a mesh-free least square-based finite difference method to numerically study the flow field around two circular cylinders at $Re = 100$ and 200. Similarly, Harichandan [12] employed an unstructured grid consistent flux reconstruction technique to solve the Navier-Stokes equations in order to explore the flow past two and three cylinders at $Re = 100$ and 200. Lam et al. [13] experimentally explored the flow pattern and velocity field distribution around an array of four cylinders in a square configuration at $Re = 200$. This study was subsequently used to validate the models developed for the numerical investigation of flow around an array of four cylinders. This numerical investigation was performed, in two-dimensions, by Lam et al. [14] and, in three-dimensions, Lam and Zou [15]. Huang et al. [16] investigated the flow around two rows of unequal-sized cylinders at $Re = 65$. Furthermore, the velocity upstream of the cylinder array was explored.

In this paper, commercial computational fluid dynamics (CFD) software is used to explore fluid flow past a large array of circular cylinders. The CFD software used is ANSYS CFX [17], which solves the Reynolds-averaged Navier-Stokes equation using the finite-volume method. In this study, the flow around an array of eight cylindrical structures in a staggered configuration is investigated with particular interest given to the wake interactions and the forces on the individual structures within the array. The analysis is performed at $Re = 100$ with three spacing configurations explored of $T = 1.5D$, $3D$, $4.5D$, where D is the diameter of a cylindrical structure. Furthermore, the numerical model developed to perform the necessary analyses is validated using two geometries, which are similar to the cylinder array of interest: a single cylinder and two side-by-side cylinders.

2 METHODOLOGY

In order to perform the numerical CFD analysis detailed in this paper, ANSYS CFX [17] is utilized. The governing equations, flow parameters and the numerical model associated with the analysis are detailed in this section.

2.1 Governing equations

The method on which the solver in ANSYS CFX is based on is the finite volume technique [17]. This technique divides the region of interest into sub-regions and discretises the

governing equations in order to solve them iteratively over each sub-region. Therefore, an approximation of the value of each variable at points throughout the domain is achieved.

The governing equations that need to be solved by the ANSYS CFX [17] solver is the mass continuity equation [18], which is given as:

$$\frac{\partial \rho}{\partial t} + \frac{\partial (\rho u_1)}{\partial x} + \frac{\partial (\rho u_2)}{\partial y} = 0 \quad (1)$$

and the Navier-Stokes equations [18], which are given as:

$$\rho\left(\frac{\partial u_1}{\partial t} + u_1\frac{\partial u_1}{\partial x} + u_2\frac{\partial u_1}{\partial y}\right) = -\frac{\partial p}{\partial x} + 2\mu\frac{\partial^2 u_1}{\partial x^2} + \frac{\partial}{\partial y}\left(\mu\left(\frac{\partial u_1}{\partial y} + \frac{\partial u_2}{\partial x}\right)\right) + F_1 \quad (2)$$

$$\rho\left(\frac{\partial u_2}{\partial t} + u_1\frac{\partial u_2}{\partial x} + u_2\frac{\partial u_2}{\partial y}\right) = -\frac{\partial p}{\partial y} + 2\mu\frac{\partial^2 u_2}{\partial y^2} + \frac{\partial}{\partial x}\left(\mu\left(\frac{\partial u_1}{\partial y} + \frac{\partial u_2}{\partial x}\right)\right) - \rho g + F_2 \quad (3)$$

where t is time, x is the horizontal distance from the input boundary, y is the vertical distance from the lower boundary, ρ is fluid density, u_1 is the horizontal flow velocity, u_2 is the vertical flow velocity, F_1 is the body force on the fluid in the horizontal direction, $F_2 - \rho g$ is the body force on the fluid in the vertical direction, p is pressure, μ is viscosity and g is acceleration due to gravity.

2.2 Definition of flow parameters

In this study, the forces on each structure within an array and how they differ as a result of wake interaction is of particular interest. Therefore, the flow parameters which are of most interest are the drag and lift coefficients, as well as the Strouhal number.

In order to characterise the flow and predict flow patterns, the Reynolds number, *Re*, which is calculated based on the diameter of a cylindrical structure, *D*, within the array, is used. It is defined as the ratio of inertial forces to viscous forces and, for a circular cylinder, is given by:

$$Re = \frac{\rho U_\infty D}{\mu} \quad (4)$$

where, U_∞ is the far-field horizontal velocity and D is the diameter of the circular cylinder.

In viscous flow, the drag, or horizontal, F_d, and lift, or vertical, F_l, forces are determined from the pressure distribution and friction at the surface of the structure. Therefore, the non-dimensional drag coefficient, C_d, is given by:

$$C_d = \frac{F_d}{\rho U_\infty^2 A} \quad (5)$$

and the non-dimensional lift coefficient, C_l, is given by:

$$C_l = \frac{F_l}{\rho U_\infty^2 A} \quad (6)$$

where, A is the reference area. For clarity in the presenting of the results, a time-averaged value is given for the drag coefficient, while both a time-averaged value and a range is given for the lift coefficient.

The Strouhal number is used as a measure of the oscillating fluid flow phenomenon in the wake region and is defined by:

$$St = \frac{f_s D}{U_\infty} \quad (7)$$

where, f_s is the shedding frequency. A fast Fourier transform (FFT) of the lift coefficient is used to calculate the shedding frequency.

2.3 CFD model set-up

The set-up for the CFD model is divided into three stages: (1) the geometry setup, which defines the physical dimensions of the model, (2) the mesh setup, where the computational domain mesh is created and (3) the wave-water, or physics, set-up, which defines the analysis type, the domain setup and the boundary conditions. A schematic which details the model domain, including definition of spacing, *T*, and overall domain dimensions is shown in Figure 1.

The overall geometry of the model is rectangular in plan with a thickness less than the size of the smallest element, which is *D*/20. Two symmetry boundaries are utilised, so the model is infinitely wide. The cylindrical structures which comprise the array are fixed and, thus, are simply 'cut' from the computational domain. The spacing between the array and the adjacent walls is set to a constant 5*D* throughout the study. Similarly, the distance from the array to the inlet and outlet boundaries is set to 5*D* and 20*D*, respectively. This is similar to the spacing used by Rahman [8].

A maximum mesh size is set throughout the computational domain of *D*/10. However, additional refinement is defined near the wall of the cylindrical structures and, also, within the immediate wake region behind the structure. This refinement is set to *D*/20. The total number of mesh elements for the validation studies was approximately 51,000. This figure increased to approximately 66,000 for the larger array of eight cylindrical structures.

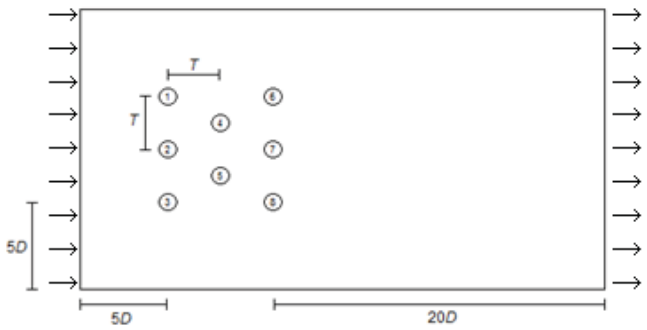


Figure 1. Schematic of the model domain, including definition of spacing, *T*, and overall domain dimensions.

Since the flow is unsteady at Re = 100, it is necessary to perform a transient analysis. Therefore, an analysis with a maximum non-dimensional time-step of 0.02 for a non-dimensional total time of 40 is specified, where non-dimensional time is defined as:

$$\frac{U_\infty t}{D} \quad (8)$$

This maximum non-dimensional time-step was also observed by Lam et al. [14]. An inlet boundary with the far-field horizontal velocity defined as the flow velocity and an outlet boundary with a pressure of 0 Pa are also specified. The adjacent walls have been defined with a free-slip condition and the cylindrical structures are specified as a wall boundary with a no-slip condition. During the solver run, the drag and lift forces on each cylindrical structure within the array are recorded.

3 MODEL VALIDATION

In order to ensure the accuracy of the numerical model, it is necessary to perform a validation study by comparing the results to previously published data, ideally obtained from physical experimental studies. In this paper, two validation studies are undertaken: fluid flow past a single cylinder and fluid flow past two side-by-side cylinders.

Initially, the fluid flow past a single cylinder is explored. This study not only provides a method for validating the model but, also, gives the opportunity to explore a number of model properties, including mesh refinement, overall domain dimensions and optimum time-step. This analysis ensures the development of an accurate model, the details of which are given in Section 2.3. In this analysis, a range of low Reynolds number were investigated, which were Re = 20, 40, 60, 80, 100, 200. For $Re \leq 40$, a steady state analysis was performed as vortex shedding does not occur at such a low Reynolds number. However, once this value is exceeded, it is necessary to perform a transient analysis as the flow becomes unsteady and the vortex shedding phenomenon may be overlooked in the calculations. A summary of the drag coefficients obtained from this analysis is shown in Figure 2. In this graph, the results from the present study are compared to experimental findings, presented by Wieselsberger [1]. The two sets of results are in good agreement, which is evident from the Figure 2. In addition, the drag and lift coefficient and Strouhal number, which are 1.3655, ± 0.0751 and 0.1474, respectively, are compared to independent numerical and experimental observations for the fluid flow around a single cylinder at Re = 100. This comparison is displayed in Table 1 and the results from the present study are consistent with the independent observations.

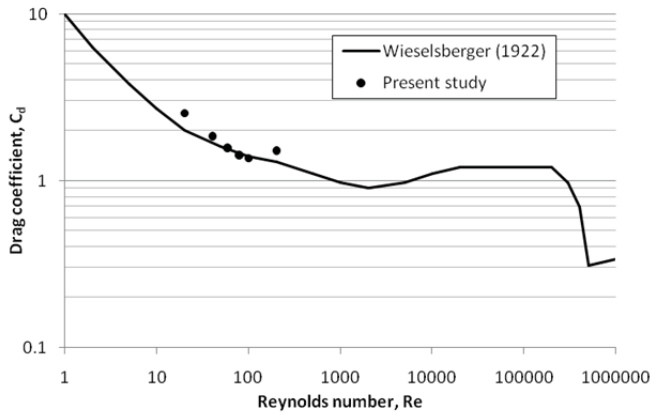


Figure 2. Comparison of the drag coefficient on a single cylinder with the experimental findings of Wieselsberger [1] at $20 \leq Re \leq 200$.

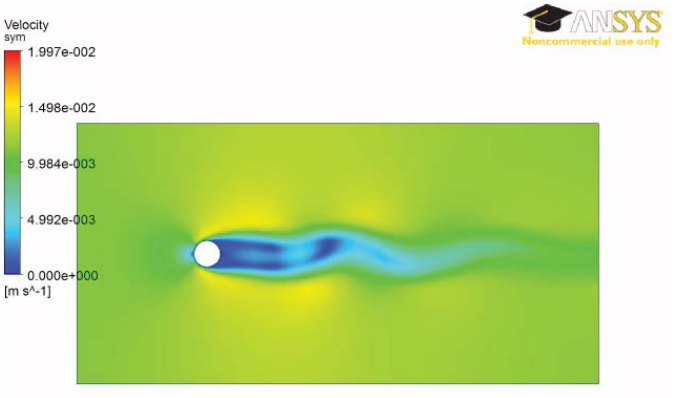


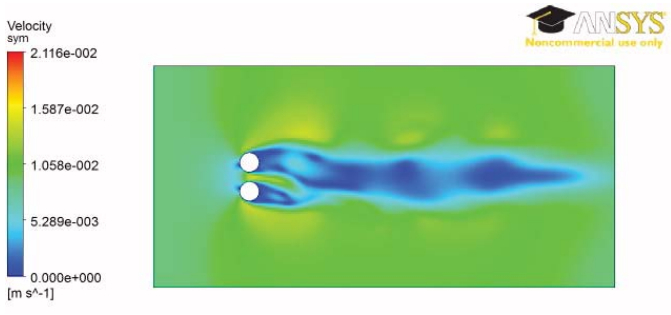
Figure 3. Magnitude of absolute velocity contours of the fluid flow around a single cylinder at Re = 100.

Table 1. Comparison of the drag and lift coefficients and Strouhal number with independent numerical and experimental observations for the fluid flow around a single cylinder at Re = 100.

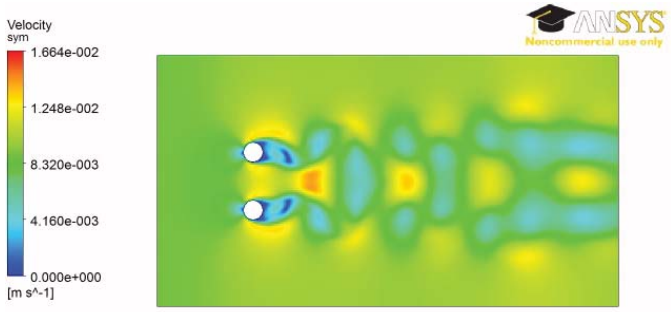
	C_d	C_l	St
Wieselsberger [1]	1.326		0.1608
Tritton [2]	1.32		0.16
Ding et al. [11]	1.356	±0.287	0.166
Lam [14]	1.36	±0.105	0.16
Rajani [9]	1.3353	±0.0896	0.1569
Harichandan [12]	1.352	±0.278	0.161
Present study	1.3655	±0.0751	0.1474

The next stage of the model validation is to investigate fluid flow over a pair of side-by-side cylinders. Two configurations, which have a spacing of $T = 1.5D$ and $T = 3D$, are used. For the purpose of this validation, the Reynolds number is held constant, where Re = 100.

The drag and lift coefficients and Strouhal number are compared to the independent numerical observations of Ding et al. [11] and Harichandan [12]. These results are given for $T = 1.5D$ and $T = 3D$ in Table 2 and Table 3, respectively. It is evident that the results of the present study predict a larger force for both the drag and lift coefficients than the previously observed results. However, they are still in reasonable agreement. A noteworthy outcome from these analyses is the wake patterns behind the two cylinders, which can be seen from the velocity contours shown in Figure 4. In the first instance, when $T = 1.5D$, the two cylinders begin to act a single body with a single wake. As a result of this, it is very difficult to accurately estimate the shedding frequency of each structure and, therefore, the Strouhal number is omitted from the analysis, which can be seen in Table 2. While, in the second instance, when $T = 3D$, there are two parallel vortex streets which are approximately 180° out of phase causing the overall flow to be symmetric between the two cylinders. This is the same observation as Huang et al. [16], Ding et al. [11] and Harichandan [12].



(a)



(b)

Figure 4. Velocity contours of the fluid flow around two cylinders at Re = 100 and a spacing of (a): T = 1.5D and (b): T = 3D.

Table 2. Comparison of the drag and lift coefficients and Strouhal number with independent numerical observations for the fluid flow around two cylinders at a spacing of T = 1.5D at Re = 100.

	C_d	C_l	St
Upper cylinder:			
Ding et al. [11]	1.53	-0.46	-
Harichandan [12]	1.58	-0.41	-
Present study	2.05	-0.639	-
Lower cylinder:			
Ding et al. [11]	1.51	0.47	-
Harichandan [12]	1.52	0.41	-
Present study	1.78	0.518	-

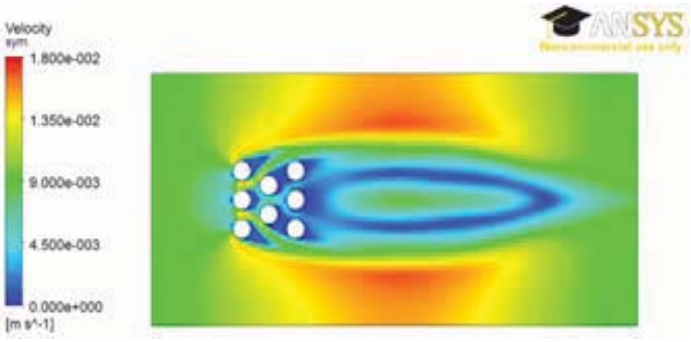
Table 3. Comparison of the drag and lift coefficients and Strouhal number with independent numerical observations for the fluid flow around two cylinders at a spacing of T = 3D at Re = 100.

	C_d	C_l	St
Upper cylinder:			
Ding et al. [11]	1.56	-0.131 ± 0.253	0.182
Harichandan [12]	1.45	-0.1 ± 0.025	0.181
Present study	1.827	-0.1734 ± 0.6559	0.208
Lower cylinder:			
Ding et al. [11]	1.56	0.131 ± 0.253	0.182
Harichandan [12]	1.45	0.1 ± 0.025	0.181
Present study	1.821	0.1803 ± 0.6529	0.207

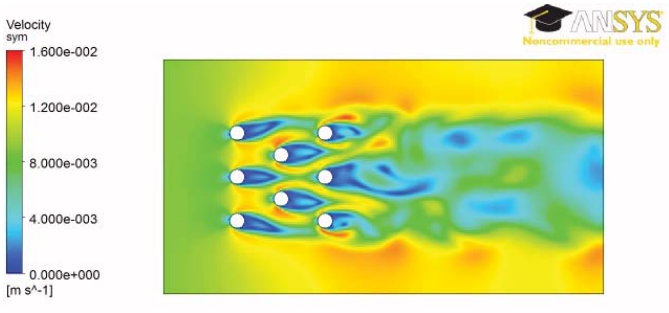
4 RESULTS AND DISCUSSION

In order to explore the effects of the wave interaction on the forces on each structure within a large array of structures, fluid flow around an array of eight cylindrical structures in a staggered configuration is numerically simulated using the CFD model. Since, the wake interaction is of particular interest, unsteady flow at a low Reynolds number is studied. Therefore, the analysis is performed at Re = 100, where the phenomenon of vortex shedding is occurring. Furthermore, the effects of the spacing between cylinders is explored by using three spacing configurations explored of T = 1.5D, 3D, 4.5D. Figure 1 illustrates how the geometry is characterised and, also, defines the spacing parameter, T.

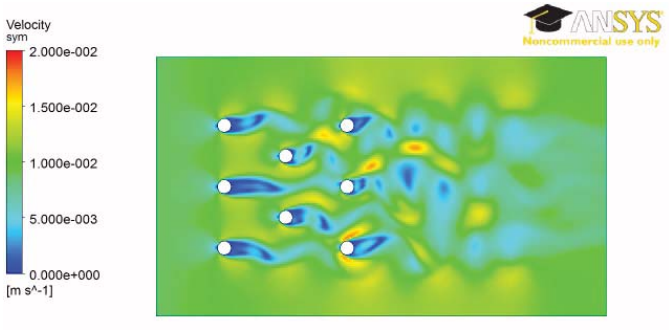
The wake interactions between the cylindrical structures within the array can be seen from the absolute velocity contours of the fluid flow around the array, which is displayed in Figure 5. For all three spacing configurations it is evident that there is a degree of symmetry of the flow pattern about the centreline of the model. Although, it is not fully symmetric, the flow patterns of the wake of the outer cylindrical structures tend to mirror each other for the closer spacing configurations of T = 1.5D and 3D (i.e. Cylinder 1 mirrors cylinder 3 and cylinder 6 mirrors cylinder 8). For the case of T = 4.5D, symmetry of the flow pattern of the wakes does seem to be present for the first row (cylinders 1 and 3) but this symmetric is lost when the flow reaches the third row. Similar to the what was observed in the validation study described in Section 3 for the flow past two side-by-side cylindrical structures at T = 1.5D, the cylinders within the array act as a single body with a single wake. The flow patterns seen in Figure 5(a) are similar to what would be seen for an analysis performed of flow around a single body at a Reynolds number of approximately 400. In addition, a vortex has formed behind the array. Here, the absolute velocity appears to have slowed down as the fluid flow changes direction. For the other two spacing configurations individual wakes develop for each structure within the array and their oscillating features interact with each other. It is clear to see from Figure 5(b), at the closer spacing of T = 3D, the interaction between the fluid flow around the structures is greater. Therefore, at a closer spacing there are additional forces on each structure as a result of this interaction. These forces are less evident at a spacing of T = 4.5D, seen in Figure 5(c), where the drag force on each structure are of a similar magnitude.



(a)



(b)



(c)

Figure 5. Velocity contours of the fluid flow around an array of eight cylindrical structures at Re = 100 and a spacing of (a): $T = 1.5D$, (b): $T = 3D$ and (c): $T = 4.5D$.

In order to analyse the force on each individual structure within the array, two of the flow parameters, which are discussed in Section 2.2, are used: the drag and lift coefficients. The drag and lift coefficients for each structure are calculated and displayed in Table 4 and Table 5, respectively. For a spacing configuration of $T = 1.5D$, it can be seen that the drag coefficient is significantly larger for the first row and that, essentially, each row partially blocks the flow for the subsequent row. For a spacing configuration of $T = 3D$, the drag coefficient is reasonably constant for each structure with the exception of cylinder 7, which is the middle cylinder in the third row. There is significant decrease in the drag coefficient, and therefore, the horizontal force on the structure. This is also evident from Figure 6 (a), where the drag force is shown graphically in the time-domain. For a spacing configuration of $T = 4.5D$, the wake interactions have less of an effect on the individual structures as there are no significant increases or decreases in drag coefficients.

Table 4. Drag coefficients, C_d, on each cylinder for the fluid flow around an array of 8 cylinders at Re = 100.

Cylinder No.	$T = 1.5D$	$T = 3D$	$T = 4.5D$
1	2.2738	1.797	1.6375
2	2.2356	1.715	1.5564
3	2.258	1.781	1.6144
4	0.9595	1.702	1.9237
5	0.9747	1.67	1.8378
6	0.3234	1.793	1.5386
7	0.2924	1.036	1.6425
8	0.3187	1.797	1.8175

For a spacing configuration of $T = 1.5D$ and $3D$, the symmetry characteristics of the flow pattern are also evident from the lift coefficients, where the lift coefficient of cylinder 1 is the negative of the lift coefficient of cylinder 3, similarly for cylinder 6 and cylinder 8. This is as a result of the vortex streets, which are approximately 180° out of phase. In addition, the lift force is shown graphically in the time-domain in Figure 6 (b). For a spacing configuration of $T = 4.5D$, as expected, similar to the flow pattern, symmetry is seen for the first row, where the lift coefficient of cylinder 1 is the negative of the lift coefficient of cylinder 3. However, this symmetry is lost by row three and this is evident from the lift coefficients.

Table 5. Lift coefficients, C_l, on each cylinder for the fluid flow around an array of 8 cylinders at Re = 100.

Cylinder No.	$T = 1.5D$	$T = 3D$	$T = 4.5D$
1	0.8566 ± 0.0015	0.2708 ± 0.0999	0.1333 ± 0.325
2	-0.014 ± 0.0006	0.0264 ± 0.021	-0.0097 ± 0.1453
3	-0.8286 ± 0.0015	-0.2616 ± 0.0639	-0.1335 ± 0.2408
4	0.1728 ± 0.0024	0.0337 ± 0.2028	0.0447 ± 1.1857
5	-0.1598 ± 0.0036	-0.0148 ± 0.1779	-0.1561 ± 1.3176
6	0.197 ± 0.041	-0.1331 ± 0.4224	0.1151 ± 0.985
7	0.0041 ± 0.0049	0.0012 ± 0.1206	-0.176 ± 1.662
8	-0.1879 ± 0.0354	0.0862 ± 0.5668	-0.2098 ± 1.6587

5 CONCLUSIONS

A systematic study of fluid flow around a large array of structures is presented. Particular interest is paid to exploring the effects of the wake interaction and the difference in the forces on each structure within the array. Furthermore, in order to validate the CFD model which will perform the numerical analysis, two geometries, which are similar the array of interest were explored: a single cylinder and a pair of side-by-side cylinders.

In this paper, the flow around an array of eight cylindrical structures in a staggered configuration at Re = 100 with three spacing configurations of $T = 1.5D$, $3D$, $4.5D$ was explored. It is evident from the analyses that the flow pattern, wake interactions and forces on the individual structures within the array are a function of the spacing configuration.

Although the flow pattern about the centreline of the model is not fully symmetric, the flow patterns of the wake of the outer cylindrical structures tend to mirror each other for the closer spacing configurations of $T = 1.5D$ and $3D$. For the case of $T = 4.5D$, symmetry of the flow pattern of the wakes does seem to be present for the first row, but this symmetric is lost when the flow reaches the third row. This is further evident when the drag and lift coefficients on each cylindrical

structure within the array are explored. In addition, for a spacing configuration of $T = 1.5D$, the cylinders within the array act as a single body with a single wake. The flow patterns seen here are similar to what would be seen for an analysis performed of flow around a single body at a Reynolds number of approximately 400. For the other two spacing configurations individual wakes develop for each structure within the array and their oscillating features interact with each other.

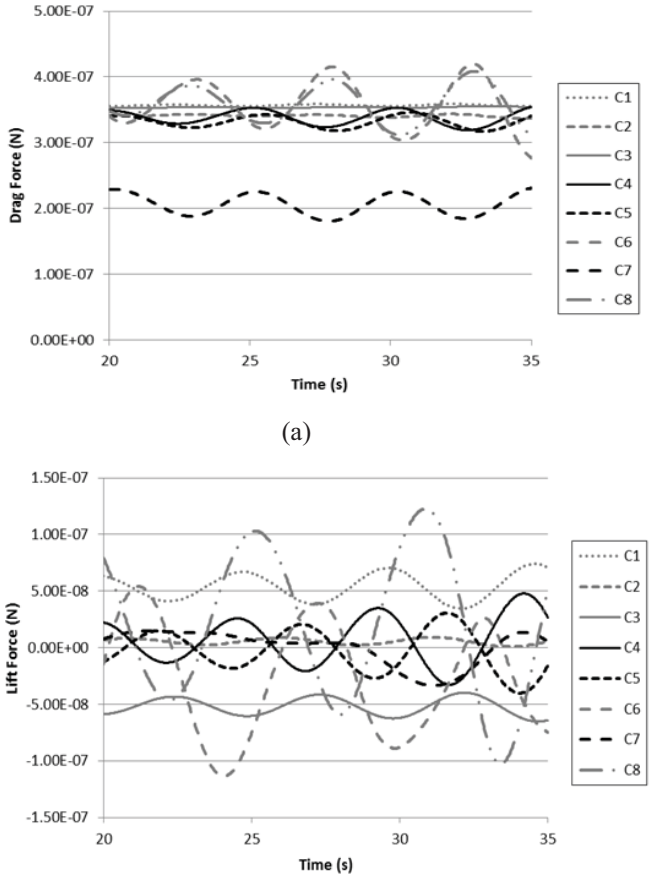


Figure 6. Forces on each cylindrical structure within the array of eight structures at $Re = 100$ and a spacing of $T = 4.5D$, (a): drag force and (b): lift force.

When the structures within the array are closer together, $T = 1.5D$, it can be seen that the drag coefficient is significantly larger for the first row and that, essentially, each row partially blocks the flow for the subsequent row. For a spacing configuration of $T = 3D$, the drag coefficient is reasonably constant for each structure with the exception of cylinder 7, where there is a significant decrease in the drag coefficient. For a spacing configuration of $T = 4.5D$, the wake interactions have less of an effect on the individual structures as there are no significant increases or decreases in drag coefficients.

These significant differences in the drag force between the structures within the array would have an impact in the design considerations for a number of engineering applications, in particular in the design of offshore structures, oil and gas pipelines. In these cases, the structural loadings are quite substantial and is, therefore, increasingly important to ensure that the structures are not unnecessarily overdesigned. On the other hand, for systems such as wastewater treatment systems, the effects of the wake interaction and the difference in the forces on each structure within the array should be considered for efficient operational of these systems.

ACKNOWLEDGMENTS

The first author would like to acknowledge the funding provided by the Department of Agriculture, Food and the Marine (Ref.: 13-F-507).

REFERENCES

[1] C. Wieselsberger, *New data on the laws of fluid resistance citation*, in *National Advisory Committee for Aeronautics: Technical Note No. 84*. 1922.

[2] D.J. Tritton, Experiments on the flow past a circular cylinder at low Reynolds numbers. *Journal of Fluid Mechanics*. 6(04) (1959) 547-567.

[3] M. Van Dyke, An album of fluid motion. *USA: The Parabolid Press*. (1982).

[4] S.C.R. Dennis, G.-Z. Chang, Numerical solutions for steady flow past a circular cylinder at Reynolds numbers up to 100. *Journal of Fluid Mechanics*. 42(03) (1970) 471-489.

[5] R. Gautier, D. Biau, E. Lamballais, A reference solution of the flow over a circular cylinder at Re=40. *Computers & Fluids*. 75(0) (2013) 103-111.

[6] M. Sato, T. Kobayashi, A fundamental study of the flow past a circular cylinder using Abaqus/CFD in *SIMULIA Community Conference* 2012.

[7] J. Park, K. Kwon, H. Choi, Numerical solutions of flow past a circular cylinder at Reynolds numbers up to 160. *KSME International Journal*. 12(6) (1998) 1200-1205.

[8] M.M. Rahman, M.M. Karim, M.A. Alim, *Numerical investigation of unsteady flow past a circular cylinder using 2-D finite volume method*, 2008. Vol. 4.

[9] B.N. Rajani, A. Kandasamy, S. Majumdar, Numerical simulation of laminar flow past a circular cylinder. *Applied Mathematical Modelling*. 33(3) (2009) 1228-1247.

[10] M. Yousefifard, P. Ghadimi, R. Zamanian, Unstructured Grid Solutions for Incompressible Laminar Flow over a Circular Cylinder Using a Particular Finite Volume-Finite Element Method. *Journal of Engineering*. 2013 (2013) 9.

[11] H. Ding, C. Shu, K.S. Yeo, D. Xu, Numerical simulation of flows around two circular cylinders by mesh-free least square-based finite difference methods. *International Journal for Numerical Methods in Fluids*. 53(2) (2007) 305-332.

[12] A.B. Harichandan, A. Roy, Numerical investigation of low Reynolds number flow past two and three circular cylinders using unstructured grid CFR scheme. *International Journal of Heat and Fluid Flow*. 31(2) (2010) 154-171.

[13] K. Lam, J.Y. Li, K.T. Chan, R.M.C. So, Flow pattern and velocity field distribution of cross-flow around four cylinders in a square configuration at a low Reynolds number. *Journal of Fluids and Structures*. 17(5) (2003) 665-679.

[14] K. Lam, W.Q. Gong, R.M.C. So, Numerical simulation of cross-flow around four cylinders in an in-line square configuration. *Journal of Fluids and Structures*. 24(1) (2008) 34-57.

[15] K. Lam, L. Zou, Three-dimensional numerical simulations of cross-flow around four cylinders in an in-line square configuration. *Journal of Fluids and Structures*. 26(3) (2010) 482-502.

[16] Z. Huang, J.A. Olson, R.J. Kerekes, S.I. Green, Numerical simulation of the flow around rows of cylinders. *Computers & Fluids*. 35(5) (2006) 485-491.

[17] ANSYS Inc., *ANSYS CFX, Release 12.1*. 2009.

[18] H.K. Versteeg, W. Malalasekera, *An Introduction to Computational Fluid Dynamics, The Finite Volume Method*, 1995. Essex, England: Prentice Hall.

Contact mechanics for fretting in flexible marine risers

S.M. O'Halloran[1], A.D. Connaire[2], S.B. Leen[1], A.M. Harte[3]
[1]Department of Mechanical Engineering, National University of Ireland, Galway, Ireland
[2]Wood Group Kenny, Galway Technology Park, Parkmore, Galway, Ireland
[3]Department of Civil Engineering, National University of Ireland, Galway, Ireland
Email: s.ohalloran1@nuigalway.ie, adrian.connaire@woodgroupkenny.com, sean.leen@nuigalway.ie, annette.harte@nuigalway.ie

ABSTRACT:
The objective of this study is to develop analytical solutions for fretting fatigue in the pressure armour wire of flexible marine risers. Analytical and finite element based solutions for bodies in contact and under tangential displacement are presented, with a view to application to in-service loading of the contact area of the pressure armour wire. The analytical solution for substrate stress components is compared to finite element solutions for two cylinder-on-flat cases: gross sliding and partial slip. The analytical and FE solutions are generally in agreement for trailing edge tensile stresses and stick-slip interface shear stresses, which control crack initiation and early crack propagation. The analytical method presented has the potential to form the basis for computationally inexpensive prediction of fretting fatigue and wear in marine risers.

KEY WORDS: Fretting, fatigue, contact mechanics

1 INTRODUCTION

Flexible marine risers are a key component in the delivery of offshore hydrocarbons from the seabed to sea level, typically to a floating structure, such as a platform or vessel. Flexible risers are comprised of a large number of layers (see Figure 1) with different functions. The research presented focuses on the interlocked metallic layer, the pressure armour wire; the primary function of this layer is to contain internal pressure and resist hoop stress. Fretting is a wear damage mechanism that occurs in the contact region between two materials under combined normal load and micro-scale cyclical relative tangential motion. These geometrical and loading conditions are present, for example, in the nub and groove valley regions of the pressure armour wires in flexible risers (as shown schematically in Figure 2).

Fretting can cause local cracking and damage of the pressure armour layer, thus reducing the service life of the riser. At present, fretting behaviour in the pressure armour layer of flexible marine risers is a subject which requires further research. The American Petroleum Industry (API) design codes recommends a safety factor of 10 for fatigue design of pressure armour layers [1], to account for the uncertainties associated with fretting, for example.

Fretting can be divided into three slip regimes [2], depending on the slip amplitude: (i) gross slip, (ii) partial slip and (iii) mixed slip regime. Because of this, the contact mechanics of two bodies in contact under combined normal and tangential loading is important for fretting behaviour. Hertz, e.g. [3], solved the problem of elastic contact between two elastic half spaces in terms of semi-ellipsoidal geometries with an elliptical contact area. Cattaneo [4] and Mindlin [5] independently combined solutions for normal and tangential loading of Hertzian contact to develop a solution for the partial slip case.

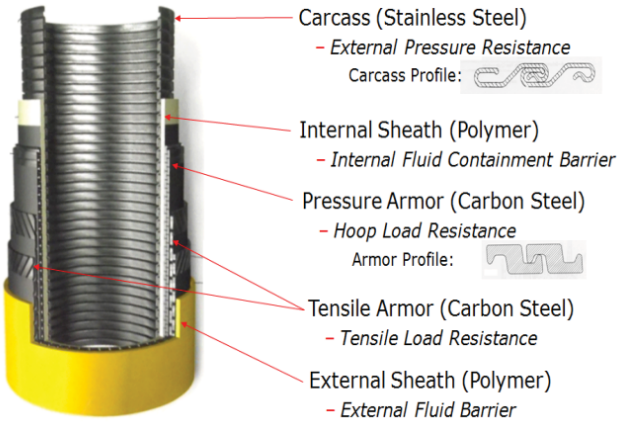


Figure 1. Cross section of a flexible marine riser (Wood Group Kenny).

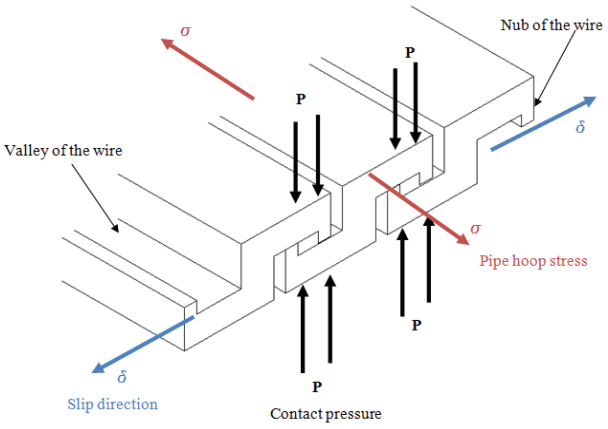


Figure 2. Schematic of loading on the pressure armour layer of a flexible marine riser.

The majority of work carried out on fretting fatigue has focused on other areas of engineering such as spline couplings used in aerospace engineering, [6] and [7]. Research has been carried out to a lesser extent on fretting fatigue of flexible marine risers, in particular, the pressure armour layer. Perera, [8], has carried out experimental work on the fretting behaviour of the pressure armour layer of unbounded flexible pipes; however, this study did not compare experimental data with any computational or analytical models.

2 ANALYTICAL METHODS

2.1 Contact mechanics

When two elastic bodies come into contact under normal loading, elastic deformation takes place which results in a contact area in the three-dimensional case and a contact width in the two-dimensional case.

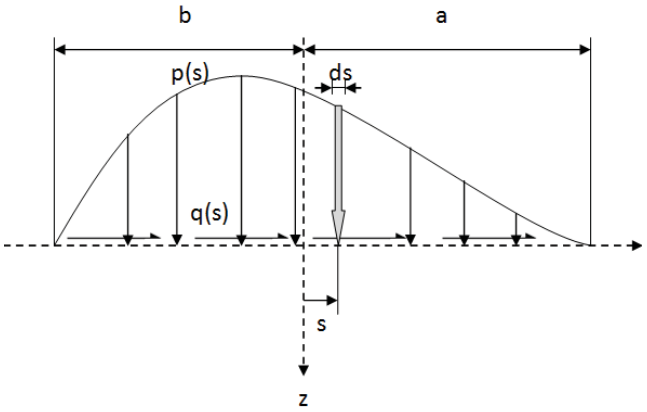


Figure 3. Definition of terms for integration of general normal and tangential traction distributions.

2.2 Distributed normal and tangential loading

In general, contact stresses are transmitted through normal pressure and shear loading. For both normal pressure distribution (*p(s)*) and tangential load distribution (*q(s)*) the sub surface stress components at a point (*x, z*) are given by integrating over the loaded region. Superposition can be used to calculate stresses in a sliding contact problem.

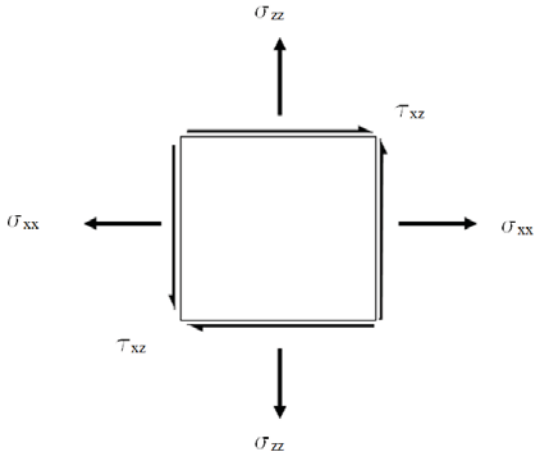


Figure 4. Cartesian two-dimensional stress components.

Substrate stresses are obtained through the application of elasticity theory for concentrated normal and tangential loads and integration over the contact region for distribution of normal and shear traction. The two-dimensional Cartesian stress components are given by [3]:

$$(\sigma_{xx})_n = -\frac{2z}{\pi}\int_{-b}^{a}\frac{p(s)(x-s)^2\,ds}{\left\{(x-s)^2+z^2\right\}^2} \tag{1}$$

$$(\sigma_{zz})_n = -\frac{2z^3}{\pi}\int_{-b}^{a}\frac{p(s)\,ds}{\left\{(x-s)^2+z^2\right\}^2} \tag{2}$$

$$(\tau_{xz})_n = -\frac{2z^2}{\pi}\int_{-b}^{a}\frac{p(s)(x-s)\,ds}{\left\{(x-s)^2+z^2\right\}^2} \tag{3}$$

where *a, b, z, s, ds* and *x* are illustrated in Figure 3.

A similar procedure is applied in order to calculate the stress components due to tangential traction. For a case of pure sliding, and assuming Coulomb-Amontons' Law for sliding friction:

$$q(s) = \mu p(s) \tag{4}$$

where μ is the coefficient of friction (COF).

Substrate stresses due to the tangential traction distribution can thus be obtained from:

$$(\sigma_{xx})_t = -\frac{2}{\pi}\int_{-b}^{a}\frac{q(s)(x-s)^3\,ds}{\left\{(x-s)^2+z^2\right\}^2} \tag{5}$$

$$(\sigma_{zz})_t = -\frac{2z^2}{\pi}\int_{-b}^{a}\frac{q(s)(x-s)\,ds}{\left\{(x-s)^2+z^2\right\}^2} \tag{6}$$

$$(\tau_{xz})_t = -\frac{2z}{\pi}\int_{-b}^{a}\frac{q(s)(x-s)^2\,ds}{\left\{(x-s)^2+z^2\right\}^2} \tag{7}$$

2.3 Sliding cylinder-on-flat

Closed form solutions for the substrate stresses for the two-dimensional case of a pair of elastic half-spaces, and for two contacting spheres have previously been published [3].

The contact pressure distribution for a 2D case for contact between two infinitely long cylinders under normal loading conditions is given by:

$$p(x) = p_o\sqrt{1-\left(\frac{x}{a}\right)^2} \tag{8}$$

where a is the contact semi-width and p_o is the maximum pressure, given by:

$$a = \sqrt{\frac{4PR}{\pi E^*}} \tag{9}$$

$$p_o = \frac{2P}{\pi a} \tag{10}$$

where P is the applied normal load, and E^* and R^* are the compound Young's modulus and radius of curvature of the contacting bodies, given by:

$$\frac{1}{E^*} = \frac{1-\nu_1^2}{E_1} + \frac{1-\nu_2^2}{E_2} \tag{11}$$

$$R^* = \frac{1}{R_1} + \frac{1}{R_2} \tag{12}$$

where ν_i, E_i and R_i are Poisson's ratio, Young's modulus and radius of curvature of body i respectively.

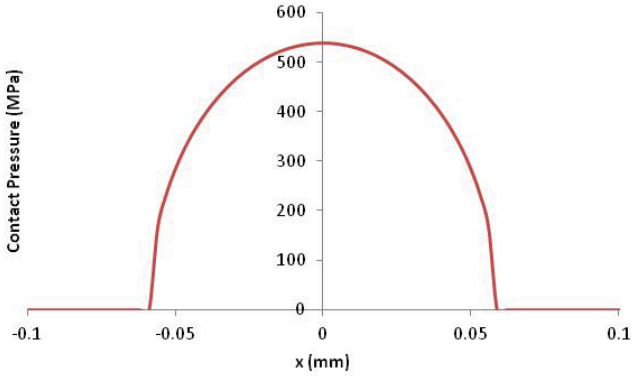


Figure 5. Contact shear distribution for a cylinder-on-flat sliding case.

2.4 *Partial sliding: Cattaneo – Mindlin solution*

When a tangential force with magnitude less than the limiting frictional force is applied to two bodies in contact under normal loading, no gross sliding motion takes place. For the stick region ($-c \le x \le c$) $\tau(x) < \mu p(x)$, resulting in no relative motion between the bodies within this region; slip occurs at the edges of contact $c \le |x| \le a$, i.e. $\tau(x) = \mu p(x)$.

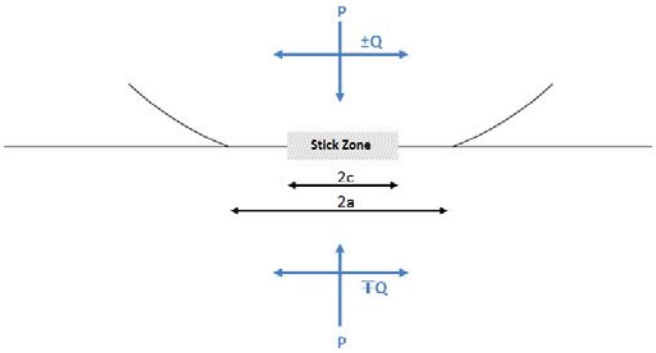


Figure 6. Stick and slip regions for cylinder-on-flat partial slip contact.

The magnitude of the tangential force (Q) determines the size of the stick region. The stick region for partial slip of contacting cylinders is given by:

$$\frac{c}{a} = \sqrt{1 - \frac{Q}{\mu P}} \tag{13}$$

where c is the contact semi-width of the stick region.

The contact pressure due to the tangential force can be obtained using superposition of the load distributions for the stick region ($q''(x)$) and the slip region ($q'(x)$).

$$q''(x) = -\frac{c}{a}\mu p_o \sqrt{1 - \frac{x^2}{c^2}} \tag{14}$$

$q''(x)$ acts in the stick region $-c \le x \le c$.

$$q'(x) = \mu p_o \sqrt{1 - \frac{x^2}{a^2}} \tag{15}$$

$q'(x)$ acts at the edges of contact $c \le |x| \le a$.

$$q(x) = q''(x) + q'(x) \tag{16}$$

Eqs 14 and 15 ensure that the stick-slip conditions for partial slip are satisfied.

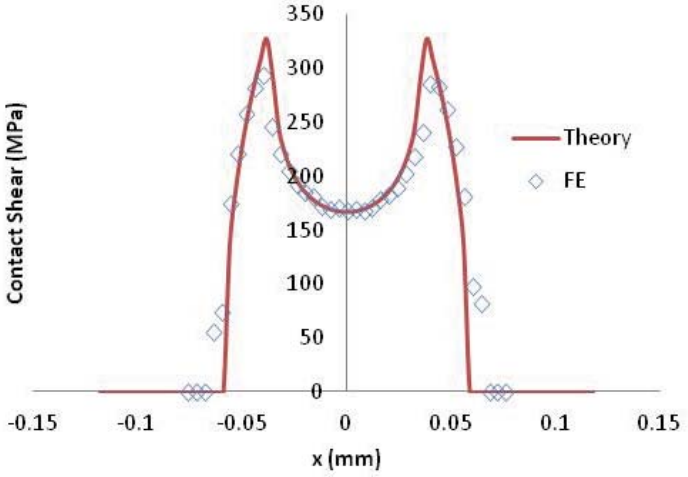


Figure 7. Contact shear distribution for a cylinder-on-flat partial sliding case.

2.5 *Stress calculation*

This load distribution for each case (Eq 8 for sliding and superposition of Eqs 8 and 16 for the partial slip case) are used in conjunction with Eqs 1 to 3 and Eqs 5 to 7 to calculate the stress components for each case using superposition of the stresses due to the normal pressure distribution and the shear distribution.

Some assumptions are made in order to calculate the pressure distribution for both the sliding and partial sliding contact problem [3]:

- Surfaces are continuous and non-conforming;
- The strains are small;
- The bodies are infinite elastic half-space i.e. the dimension of the contact is small in comparison to the dimensions of each body and the radii of the curvature of the surfaces.

3 COMPUTATIONAL MODELLING

3.1 Finite Element Modeling

Finite element models have been developed in Abaqus for both gross slip and partial slip cylinder on flat contact cases. The loading conditions are as shown in Tables 1 and 2.

Table 1. Loading conditions: Gross slip case

Normal Load (kN/mm)	Stroke
50	0.01 mm

Table 2. Loading conditions: Partial slip case

Normal Load (kN/mm)	Stroke
50	25 kN

A two-dimensional, plane strain assumption has been assumed for each case. The material used is a carbon steel, with a Young's modulus of 200GPa and a Poisson's ratio of 0.3. The radius for the cylinder case is 6 mm (based on test specimen dimensions used for the fretting fatigue test rig in [9]).

A coefficient of friction of 0.8 was used, based on the assumption that after a sufficient number of cycles, that surface modifications within the slip zone will raise the local COF from an initial value of approximately 0.3 to between 0.7 and 0.9, as described in [10].

Since the analysis is a frictional contact problem, two-dimensional, four noded, quadrilateral, plane strain elements were used due to their accuracy and stability for these loading conditions [11]. A mesh sensitivity study was used to establish the mesh which is highly refined in the contact region, becoming coarser further from the contact area (see Figures 8 and 9). The contact element size is approximately 4µm x 4µm. The transition between fine mesh and coarse mesh is achieved by reducing the mesh density through an unstructured mesh between the fine and coarse meshes (see Figure 9).

The master-slave algorithm for finite sliding contact was used to define the surface interaction for both models. The maximum allowable penetration depth between master and slave nodes was set to 1 µm. The adjustment tolerance for the initial geometry was set to 0.001 µm. Since Coulomb-Amontons' Law is assumed for sliding friction, the exact stick condition is ensured by implementing Coulomb friction based on the Lagrange multiplier contact algorithm.

The dimensions of the substrate material were made significantly larger than the contact area so that the assumption of an elastic half-space remained valid. The bottom edge of the substrate was restrained in the z direction and the left and right edges were restrained in the x direction.

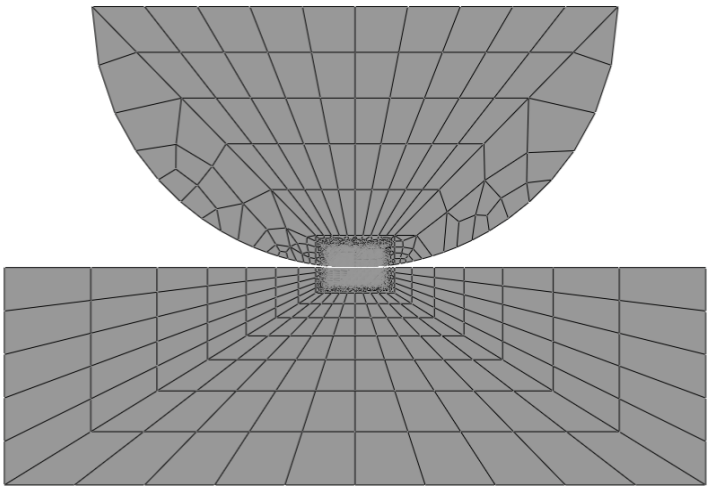


Figure 8: Mesh used for cylinder on flat contact.

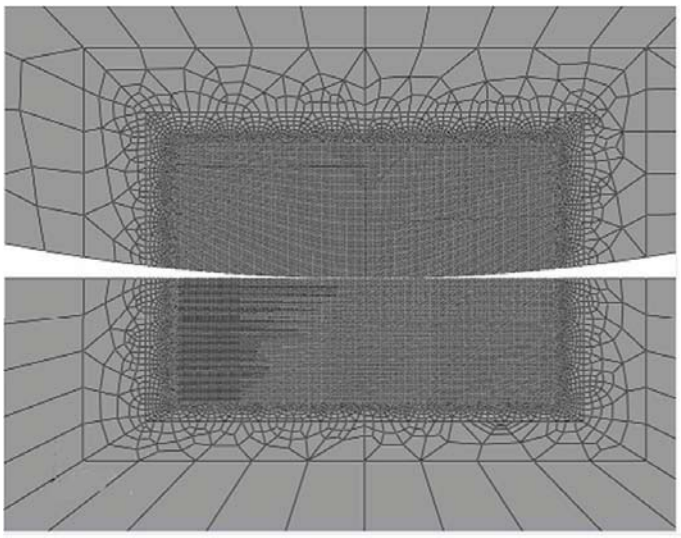


Figure 9. Mesh refinement in contact area.

3.2 Loading history

The normal load P is applied to the cylinder, and then a cyclic tangential load (Q) or displacement (Δ) is applied in a similar manner to shown in Figure 10.

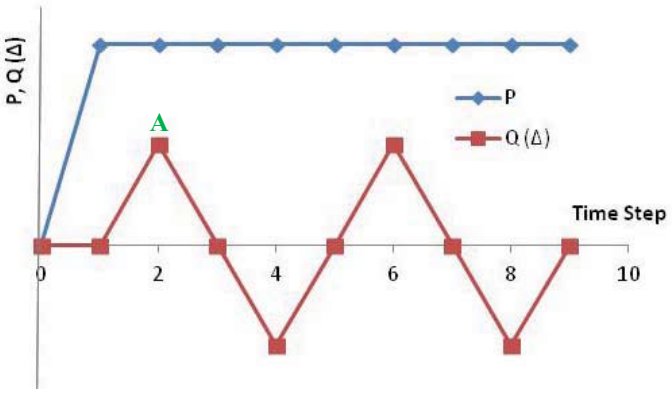


Figure 10. Stroke and loading history.

4 RESULTS

4.1 Loading cycle

For both the sliding and partial sliding cylinder-on-flat contact cases, the results for the FE model are obtained from point A on the loading cycle (see Figure 10). The analytical model used does not give results for mid-cycle tangential loading. The results are taken from a depth of z = 4.845 μm (this depth is along a set of integration points).

4.2 Sliding cylinder-on-flat results

Both theoretical and FE results for the cylinder on flat sliding contact case are presented in Figures 11 and 12. Qualitatively, the FE solution produces trailing edge tensile stress at the same location as the analytical solution. The location of maximum shear stress differs by 1% between the two models. The FE solution predicts trailing edge tensile stress and maximum shear stresses that are 1% and 7% lower respectively than the analytical solution.

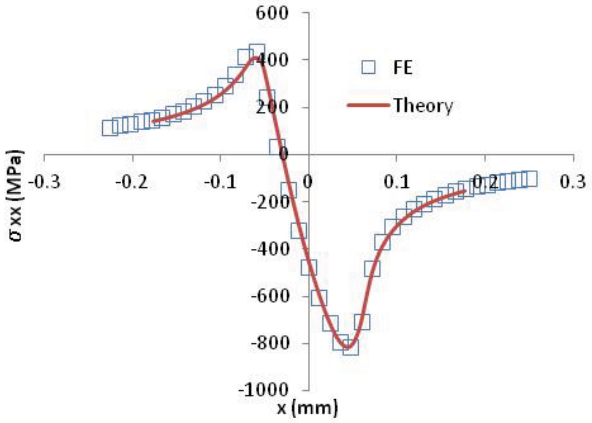


Figure 11. Comparison of σ_{xx} stress results from FE to the analytical solution for sliding case.

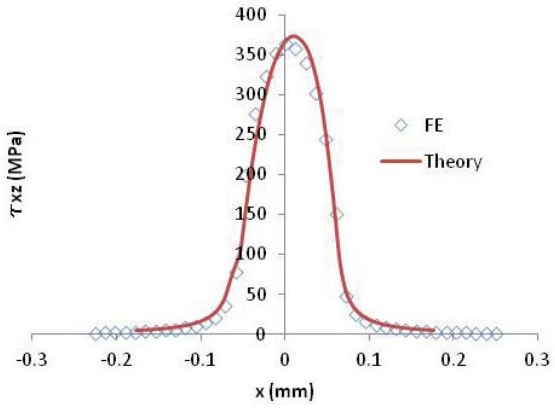


Figure 12. Comparison of τ_{xz} stress results from FE to the analytical solution for sliding case.

4.3 Cylinder-on-flat partial slip results

Figures 13 and 14 show the comparison between analytical and FE solutions for the partial slip case. The FE solution produces trailing edge tensile stress at the same location as the analytical solution. The location of maximum shear stress differs by 10% between the two models. The FE solution produces the same trailing edge tensile stresses, however the maximum shear stress is 14% lower than the analytical solution. This is because the contact shear distribution produced by the FE model does not correspond exactly with the theoretical distribution (see Figure 7).

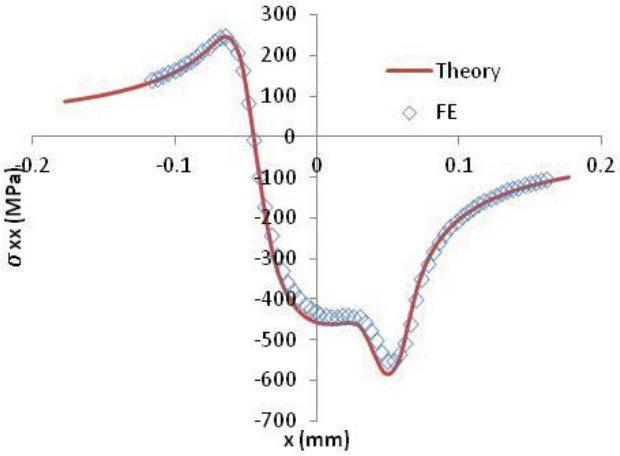


Figure 13. Comparison of σ_{xx} stress results from FE to the analytical solution for partial slip case.

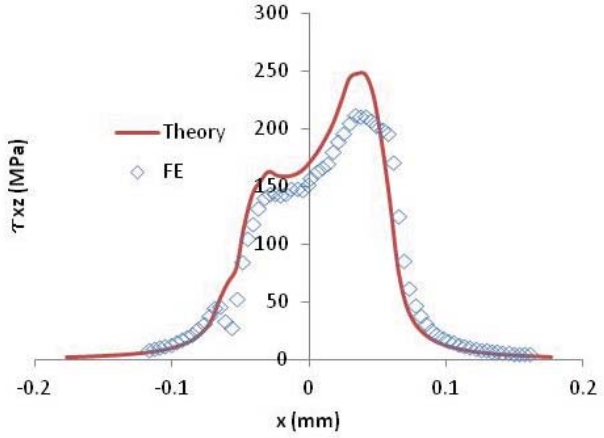


Figure 14. Comparison of τ_{xz} stress results from FE to the analytical solution for partial slip case.

5 FRETTING FATIGUE

5.1 Crack growth and wear

For fretting fatigue cracks, the stress range is of importance for the calculation of fatigue life. High shear stress (τ_{xz}) ranges cause crack initiation, and high tangential (trailing edge) stress (σ_{xx}) ranges cause Mode I crack propagation. Since the loading is cyclical, a material point can experience high shear stresses and low tangential stresses followed by high tangential stresses and low shear stresses in the next stage of the cycle; this behaviour increases the possibility of crack formation and growth. Crack growth can occur for both low and high cycle fatigue.

Fretting wear can be beneficial by removing material affected by the crack initiation prior to crack propagation. Previous work has shown the importance of modelling wear due to its influence on crack initiation and propagation [12].

A Smith-Watson-Topper (SWT) critical plane approach [13] fatigue parameter can be used to predict crack nucleation. A modified SWT approach [14] was developed to incorporate the effects of slip on crack initiation and surface wear damage, using a fretting fatigue damage factor, D_{fret}.

$$\sigma_{\max}\Delta\varepsilon_a D_{fret} = \frac{(\sigma'_f)^2}{E}(2N_f)^{2b} + \sigma'_f\,\varepsilon'_f\,(2N_f)^{b+c} \qquad (17)$$

where σ_{max} is the maximum normal stress on the critical plane, $\Delta\varepsilon_a$ is the maximum normal strain amplitude on the same plane, E is Young's modulus σ'_f and b are fatigue strength coefficient and exponent, ε'_f and c are the fatigue ductility coefficient and exponent, and N_f is the number of cycles to failure.

D_{fret} is a fretting fatigue damage factor given by [14]:

$$D_{fret} = (1-\tau\delta)^m \left|1 - \frac{\tau\delta}{(\tau\delta)_{th}}\right|^n \qquad (18)$$

where m, n and $(\tau\delta)_{th}$ are material constants to be determined experimentally.

The modified SWT parameter gives more accurate predictions for fretting fatigue life and locations.

6 DISCUSSION AND FUTURE WORK

6.1 Discussion

An analytical solution for substrate stress has been presented; this has been compared to FE solutions for gross slip and partial slip of a cylinder on flat contact.

The analytical solution relies on known or assumed contact pressure distributions; therefore, assumptions made for the pressure distribution must remain valid for the FE model for accurate comparison. An elastic half-space requires accurate representation within Abaqus; this was achieved by ensuring that the substrate dimensions were large enough with respect to the contact width to avoid effects due to the boundary conditions (the substrate width was 20 mm in comparison to 60 μm contact semi-width).

The integration for the theoretical model was calculated using the trapezoidal rule; a sensitivity study was carried out to ensure convergence. All stress component results were taken from integration points, to avoid nodal averaging of results.

Computation time is a major factor when choosing model type; the run time for the theoretical solution is a few seconds in comparison to about 45 minutes for the FE model. At present, a limitation of the theoretical model is that results are only calculated for one time instant in the tangential cycle. It is important for the calculation of surface (fatigue) damage to know the stress range rather than just the maximum stress at a point. The modified SWT approach using D_{fret}, fretting fatigue damage factor, can be implemented into an FE model using user subroutines.

The FE model can potentially include plasticity effects which can be significant in fretting [9], particularly due to wear effects [15].

6.2 Future work

Geometries closer to those of the pressure armour wire of flexible marine risers will be modeled, such as rounded punch on flat and wedge on flat contacts.

Experimental testing will be carried out on pressure armour wire material to identify coefficient of friction and wear coefficient; results from experimental testing will also be used to validate the computational and numerical models.

Fretting fatigue damage will be implemented in the computational and theoretical models, using the modified SWT approach, for example.

ACKNOWLEDGMENTS

The authors would like to thank the Irish Research Council and Wood Group Kenny for funding of this project through the Enterprise Partner Scheme.

REFERENCES

[1]. *API Recommended Practice for Flexible Marine Risers, 17J*, American Petroleum Industry

[2]. Hannel, S., et al., *The fretting sliding transition as a criterion for electrical contact performance.* Wear, 2001. **249**(9): p. 761-770.

[3]. Johnson, K.L., *Contact Mechanics.* 1985: Cambridge : Cambridge University Press

[4]. Cattaneo, C., *Sul Contato di Due Corpo Elastici.* Atti Accad. Naz. Lincei, Cl. Sci. Fis., Mat. Nat., Rend., 27, pp. 342–348, 434–436, 474–478., 1938.

[5]. Mindlin, R.D., *Compliance of Elastic Bodies in Contact* ASME Trans. J. Appl. Mech., 16, pp. 259–268., 1949.

[6]. Wavish, P.M., et al., *A Multiaxial Fretting Fatigue Test for Spline Coupling Contact.* Fatigue & Fracture of Engineering Materials & Structures, 2009.

[7]. Ding, J., I.R. McColl, and S.B. Leen, *The application of fretting wear modelling to a spline coupling.* Wear, 2007. 262(9–10): p. 1205-1216.

[8]. Perera, S.D.R., et al., *An Investigation into Fretting Behaviour in Pressure Armor Wires of Unbonded Flexible Pipes*, in *ASME 26th International Conference on Offshore Mechanics and Artic Engineering, OMAE 2007*. 2007: San Diego, California, USA.

[9]. McCarthy, O.J., J.P. McGarry, and S.B. Leen, *Microstructure-sensitive prediction and experimental validation of fretting fatigue.* Wear, 2013. 305(1–2): p. 100-114.

[10]. Hills, D.A. and D. Nowell, *Mechanics of Fretting Fatigue*. 1994: Dordrecht ; London : Kluwer Academic Publishers

[11]. McColl, I.R., J. Ding, and S.B. Leen, *Finite element simulation and experimental validation of fretting wear.* Wear, 2004. 256(11–12): p. 1114-1127.

[12]. Madge, J.J., S.B. Leen, and P.H. Shipway, *A combined wear and crack nucleation–propagation methodology for fretting fatigue prediction.* International Journal of Fatigue, 2008. 30(9): p. 1509-1528.

[13]. Smith, K.N., P. Watson, and T.H. Topper, *A stress-strain function for the fatigue of metals.* Wear, 1996. 198: p. 93-107.

[14]. Ding, J., et al., *Fretting fatigue predictions in a complex coupling.* International Journal of Fatigue, 2007. 29(7): p. 1229-1244.

[15]. Mohd Tobi, A.L., et al., *A study on the interaction between fretting wear and cyclic plasticity for Ti–6Al–4V.* Wear, 2009. 267(1–4): p. 270-282.

A Comparison of Techniques to Determine Surface Texture Data

Grainne McQuaid[1], Phillip Millar[2] & David Woodward[3]
[1]Built Environment Research Institute, University of Ulster,Shore Road, Newtownabbey, Antrim, BT37 0QB, Northern Ireland
[2]Built Environment Research Institute, University of Ulster,Shore Road, Newtownabbey, Antrim, BT37 0QB, Northern Ireland
[3]Built Environment Research Institute, University of Ulster,Shore Road, Newtownabbey, Antrim, BT37 0QB, Northern Ireland
email: mcquaid-g@email.ulster.ac.uk, p.millar@ulster.ac.uk, wdh.woodward@ulster.ac.uk

ABSTRACT: Surface texture at a range of scales is important as it relates to how a tyre interacts with a road surface material. Surface texture is measured using the volumetric patch method, commonly known as the sand patch test. It is also measured using line laser techniques to generate 2D profiles. However, a patch of sand and a 2D profile is limited in their ability to understand how tyre tread interacts with road surface texture. This paper reports a study of chipped Hot Rolled Asphalt (HRA). This is the most common type of asphalt surfacing material in Ireland and is relatively simple in terms of its texture. Close Range Photogrammetry (CRP) and High Resolution Scanning (HRS) were used to create 3D models of the HRA surface texture. A vinyl cast was made and also assessed. The vinyl cast technique results in a permanent record of the asphalt surface texture and allows for time based studies showing its evolution. The 3D meshes were analysed for a 2D and 3D areal parameters using Digital Surf MountainsMap6. Analysis of the findings show how sand patch, 3D photogrammetry and laser techniques data may be used to better understand road surface textures.

KEY WORDS: Close range photogrammetry; High resolution scanner; Abbott-Firestone curve.

1 INTRODUCTION

Surface texture is an important pavement characteristic. It has been found to relate to a number of performance requirements such as surface noise, water drainage, rolling resistance, skid resistance and surface spray. There is a need to better understand texture, the factors that influence it and how it affects these surface parameters.

Primarily distinguished as either positive or negative, surface texture can be divided according to its wavelength. With a wavelength in the range of 0.5 mm – 50 mm, macro-texture will be the focus of the research presented in this paper. The macro-texture is regarded as one of the most significant texture bands in relation to the behaviour of various surface properties. This secures its place of interest in highway engineering [1]. The principle purpose of macro-texture is to provide adequate drainage of water away from the pavement surface. This avoids film/pockets of water forming on the surface, which can interfere with the tyre-pavement interface, risking driver safety.

The volumetric patch technique is widely accepted in highway engineering as a measurement of surface macro-texture. This traditional methodology has been modified in recent years with the replacement of sand by glass spheres as detailed in BS EN 13036-1 [2]. The efficiency and economy of the method is ideal for industry. However the mean texture depth (MTD), derived from the volumetric patch technique merely provides a one dimensional representation of the texture. This limits its use for measurement of macro-texture, particularly in the research field. Non-contact 3D capture of the surface texture enables the possibility of a more extensive texture analysis to be carried out.

In recent years static and dynamic laser based devices have become popular for the 3D capture of pavement surface texture. In previous use laser devices typically relied on surface profiling for texture analysis. Kane [3] used laser profiling in a laboratory setting to chart changes in surface texture through testing procedures. Across England the Highways Agency (HA) has implemented the Traffic Speed Condition Survey (TRACS) which utilises surface profiling. TRACS incorporates the use of a laser mounted vehicle carried out along with other data collection at highway speeds of up to 60 miles per hour [4]. The assessment of data collected by TRACS allows monitoring of surface deterioration.

Similar to dynamic, static laser devices have also been used to understand surface texture. Sangiorgi [5] collected a 3D model of a specimen surface texture using a static laser device. Analysis was carried out on the captured surface which included roughness parameters, mean profile depth (MPD) and the Abbott-Firestone curve (AFC). Sangiorgi concluded the use of roughness parameters enabled the characterization of the surface.

Image capture as an alternative for 3D modelling of surface texture is a growing trend. Dunford [6] investigated non-contact measurement of micro-texture through image analysis using pixel intensities. Progression of the original methodology by Dunford [7] saw the use of an Alicona 'InfiniteFocus' microscope at the National Physics Laboratory (NPL), Teddington, UK. By adjusting the lens vertically, whilst continuously capturing the surface, a three dimensional representation of a stone was achieved. This methodology worked on a micro-scale; however it may not be feasible on the scale necessary in industry. Chandler et al [8] began to realise the potential of low budget cameras to capture and model objects. El Gendy and Shalaby [9] worked with photogrammetric stereo techniques proposed by Woodham [10]. This entailed using multiple images to create a stereoscopic image of the surface. A 3D map was formed in

image processing software using the changes in surface illumination created by artificial lighting. Millar [11] utilised photogrammetric software to create a Triangular Irregular Network (TIN) from a stereo image pair. With the produced TIN 3D model, Millar [12] demonstrated the scope of Close range photogrammetry (CRP) for both positive and negative textured surfaces. Millar [13] demonstrated a strong agreement with the use of CRP across a variety of surface textures with the reference volumetric patch technique.

The use of physical replication of a surface texture allows a record of the surface to be created. It enables processing to be carried out in a more suitable timeframe. This process of replication ensures minimum interruption to construction and traffic. The Transport Research Laboratory (TRL) has previously used a compound to create replications of aggregate surfaces which underwent accelerated polishing on the Wehner-Schulze machine [14]. After investigating the visual and surface texture change of the actual surface and replicate, Dunford concluded better results were obtained from the actual surface. It was found that the replication compound was affecting the specimen surface. This demonstrated the need to fully understand the effect compound application has on the original surface under investigation.

This paper investigates the 3D capture of specimen surface texture using both CRP and High Resolution Scanner (HRS) methodologies. The methodologies were applied to asphalt specimens and their corresponding casts. McQuaid [15] investigated the use of a negative textured SMA slab and its corresponding vinyl cast using both HRS and CRP methodologies. The aim was to assess the usability of both surfaces and methods to achieve optimum surface recovery.

Surface recovery comprises reconstruction of an area of surface texture in the form of a digital model. In CRP for example this requires cross matching of at least one stereo image pair within a prescribed control framework to provide scale and orientation. The digital surface is then generated typically using the Delaunay triangulation algorithm in the form of a triangular irregular network (TIN). Scanning generates the surface as a point cloud captured within a prescribed framework also. The surfaces generated with either of the two methods may be exported to other surface analysis systems for evaluation.

This paper will continue to make comparisons between the two methods of 3D modelling and the use of surface replication for analysis with a positive textured surface. Concluding a good comparison with the real asphalt surface, the replication surface could provide a more efficient means of capturing and recording surface texture.

2 METHODOLOGY

2.1 Specimen assessed

A hot rolled asphalt (HRA) with 20 mm chippings at spread rate 12 kg/m² slab specimen was used for the 3D modelling and analysis discussed in this paper. The specimen had dimensions 305 x 305 x 50 mm and had undergone compaction by a Cooper roller compactor. The specimen underwent 10, 000 wheel passes of accelerated wet trafficking on the University of Ulster's Road Test Machine (RTM). The RTM is used to assess the wear characteristics of high friction surfacing for British Board of Agrément (BBA) accreditation, for usage within the UK [16]. The RTM consists of a 2.1 mm diameter table which holds up to ten specimens, rotating at 10 rpm. Two Federal 195/70R14 tyres are positioned vertically above the table, allowing transverse trafficking across the width of the specimen. The simulation of real trafficking is encouraged by the application of a 5 kN load through each tyre onto the specimen. The RTM trafficking is operated in a controlled environment with a temperature of 10 $\pm$ 2 °C and is used in accordance with Appendix H of TRL Report 176 [17].

2.2 Asphalt specimen surface cast

A red vinamold material was used to create a cast of the HRA slab specimen surface texture. This vinyl compound was red, flexible, durable and non-toxic. The vinamold material was melted to form a viscous fluid at 150°C. Using a restricting template the fluid was poured over the surface, whilst the self levelling nature of the fluid ensured even coverage. Following sufficient cooling the cast was removed. The HRA slab specimen required care for cast removal due to the textured nature of the surface.

White paint was applied to the vinamold cast to disguise the uneven colouring which has occurred due to localised bitumen staining. The addition of paint maximises the recovery of surface texture in the HRS methodology. The paint application was carried out sparingly, offering maximum recovery whilst ensuring minimum addition to the specimen surface texture.

2.3 CRP procedure

A Canon EOS 400D SLR camera, with a 10Mp CCD array and an attached calibrated 60 mm macro lens was used for the capture of the stereo image pair. All images were captured normal to the surface under natural environmental conditions. With the camera tripod mounted and a remote shutter release, possible camera shake was minimized.

A calibrated aluminium framework of control points, as shown in Figure 1 was used to allow the recovery of surface elevation and orientation. The framework control points were calibrated using a digital micrometer, forming a control calibration file.

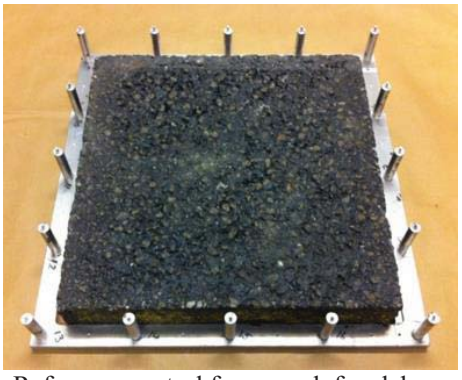


Figure 1. Reference control framework for slab specimen, allowing recovery of surface elevation and orientation for CRP procedure.

The stereo image pair, control calibration and camera calibration files were imported into Topcon ImageMaster photogrammetric software [18]. All control points were cross matched with additional tie points added to reduce the level of redundancy. The TIN was created at a mesh resolution of 0.5 mm. No filtering was applied to the TIN as to avoid possible removal of surface roughness. The resultant Cartesian coordinates of the TIN were exported in a comma separated value (CSV) file format allowing successful import into Digital Surf MountainsMap Version 6 surface analysis software [19].

2.4 HRS procedure

A ZScanner 800 high resolution 3D laser scanner (HRS) which has a stated resolution of 50 µm was used for the research presented in this paper. A combination of scan resolution was used to ensure the maximum point cloud was obtained for the specimen surface. This involved an initial coarse scan of 2 mm followed by a fine resolution scan of 0.5 mm. During scanning a reference framework, as shown in Figure 2 was used. This was constructed of a plastic mesh of proprietary control points, which secured in place was draped over the specimen. The use of the mesh allowed the accompanying ZScan 3D digitising software to recovery surface elevation and orientation. Post scanning and prior to export the point cloud facets were edited, to remove any redundant data points. The facet resolution was set to 0.5 mm, allowing a comparable 3D model with that produced though the CRP procedure. With editing complete the point cloud was exported in a TXT file format, allowing import into Digital Surf MountainsMap Version6 surface analysis software [19].

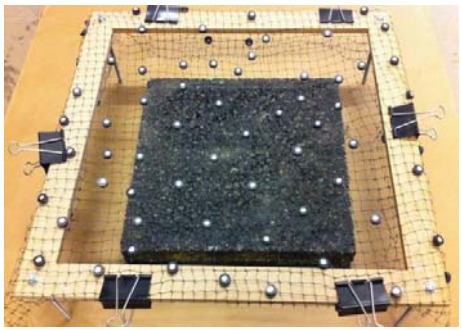


Figure 2. Reference control framework allowing recovery of surface elevation and orientation in HRS procedure.

2.5 Post processing

All spatial analysis was carried out in accordance with BS EN ISO 25178-2 [20]. With the import of the corresponding Cartesian coordinates, MountainsMap operators were applied to prepare the surface for analysis. This included levelling of the surface to a least squares plane. Figure 3 shows the levelled 3D model for the slab specimen, captured using the CRP procedure. The cast 3D models (Figure 4) underwent an additional operator to mirror the surface elevation, z axis. This inversion of surface elevations allowed the cast surface texture to be converted to form the original slab surface texture. An Area of Interest (AOI) was chosen for analysis which represented the most heavily trafficked area of the slab, as depicted in Figure 5. This AOI has dimensions 265 x 215 mm (Figure 6).

Following the application of initial operators linear, square and volumetric analysis was carried out on the 3D models. This included investigation of functional parameters, height parameters, depth distribution and the Abbott-Firestone curve (AFC).

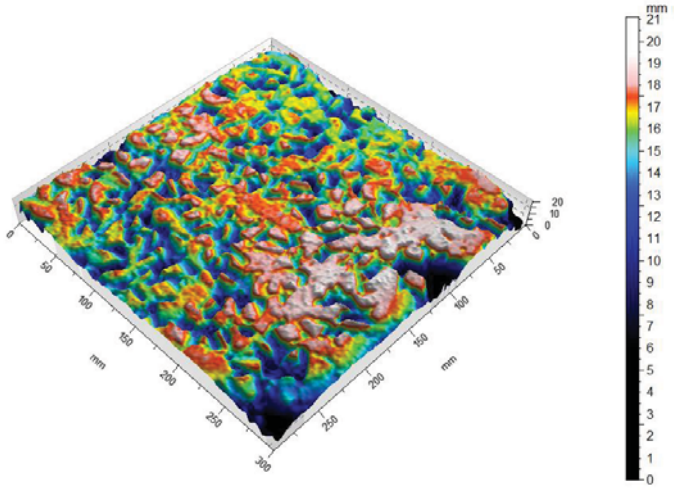


Figure 3. Depth classified 3D model of asphalt slab created with CRP and displayed in MountainsMap

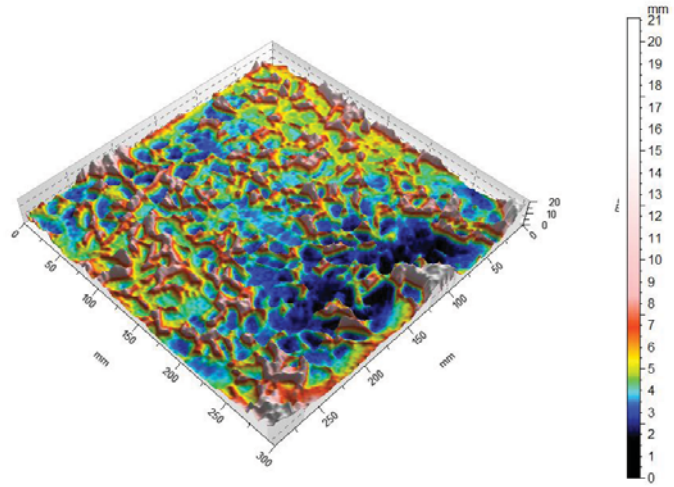


Figure 4. Depth classified 3D model of vinyl cast created with CRP and displayed in MountainsMap, prior to inversion.

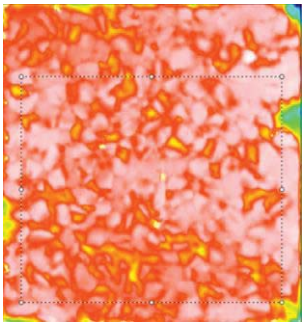


Figure 5. Selection of the AOI representing the most trafficked area of the slab specimen.

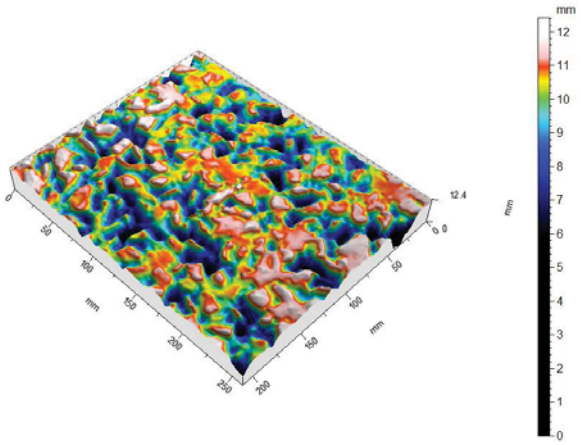


Figure 6. Area of interest (AOI) selected for analysis.

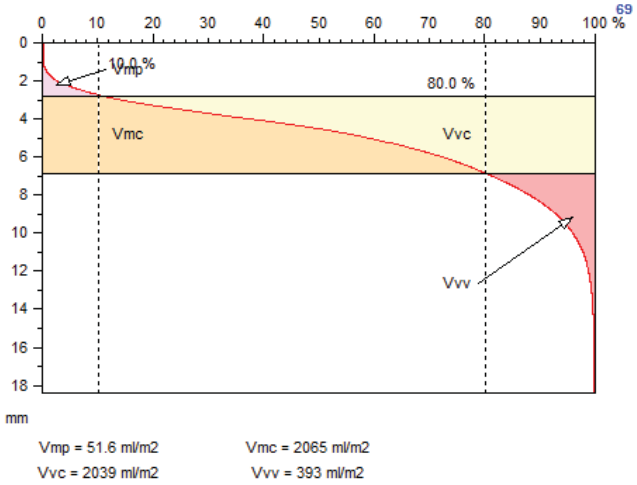


Figure 8. Example AFC for the cast CRP model.

3 RESULTS

Digital Surf MountainsMap software allowed 2D and 3D parameters to be measured in accordance with BS EN ISO 25178-2 [20]. Initial 2D profiles were taken across the 3D model surface at determined intervals. Figure 7 shows a series of five profiles taken across the slab 3D model, captured using the HRS methodology. It also displays the average (red) profile for the entire surface. Despite the small size of the surface, the profiles behave differently. This suggests that a 2D analysis carried out on a single or average profile may not be representative for the surface as a whole.

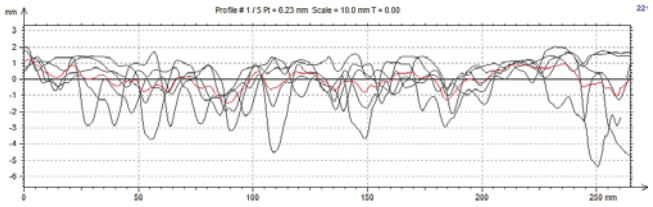


Figure 7. Series of five profiles including an average (red) profile for slab HRA 3D model.

Abbott Firestone curves (AFC) were obtained for each 3D model. The AFC is a volume ratio based curve whereby four volume parameters are identified on a texture profile. The four volume parameters are the volume of peak material (Vmp), volume of core material (Vmc), volume of core voids (Vvc) and volume of valley voids (Vvv). Figure 8 shows the AFC for the cast CRP 3D model. As detailed in Figure 8, MountainsMap software adopts a default lower (10%) and upper (80%) Areal Material Bearing Ratio (AMBR). For analysis in this paper the lower (10%) limit was adjusted to investigate the development of the surface texture. The Areal Material Bearing Ratio expresses the percentage of flat surface created by a cut line set at a defined depth. In Figure 8 for example the cut line is located at approximately 2.8mm into the surface equivalent to an AMBR of 10%.

Of particular interest in Figure 8 is the volume of material in the peaks as they comprise those elements of the surface texture that are in contact with the tyre. The volume of core and valley voids can offer additional insight into storage and drainage properties of a given surface.

Figure 9 displays analysis of the AFC used to investigate the development of the 3D model surface texture with depth into the surface. The graph plots Vmp against the AMBR for the HRA slab and its corresponding vinyl cast using both HRS and CRP methods. If the Vmp is used as a measure of the recovery of surface texture, it can be concluded that maximum recovery was achieved using the vinyl cast and CRP methodology. Therefore the slab 3D model obtained with the HRS methodology showed the lowest recovery of surface texture.

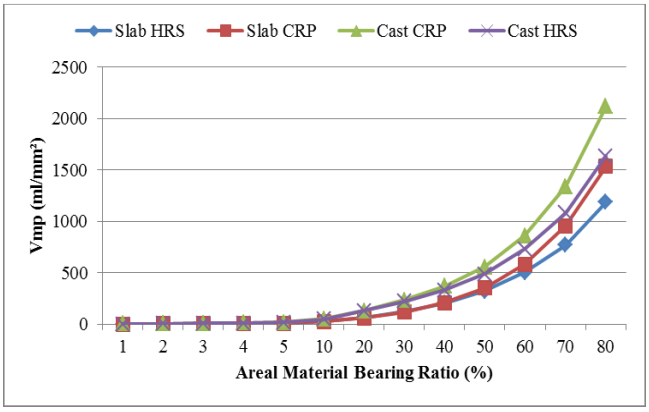


Figure 9. Vmp plotted against AMBR data, derived from the AFC.

Figure 10 plots the slab Vmp against the cast Vmp for both HRS and CRP methods. A strong linear trend is found for both methods. This suggests an approximate additional surface texture recovery of 38% for the cast 3D model compared to that of the actual slab specimen.

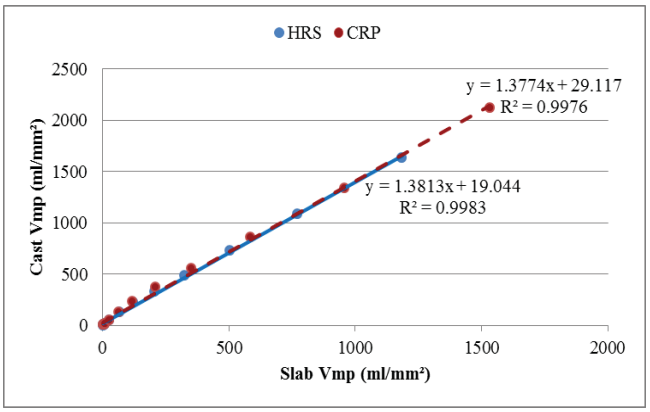


Figure 10. Comparison of slab Vmp against cast Vmp for both CRP and HRS methods, derived from the AFC.

The HRS and CRP methods are compared in Figure 11 for both the slab and corresponding cast. Again, a strong linear correlation was found. The graph suggests an additional recovery of approximately 27% of surface texture for the CRP method compared to that of the HRS method.

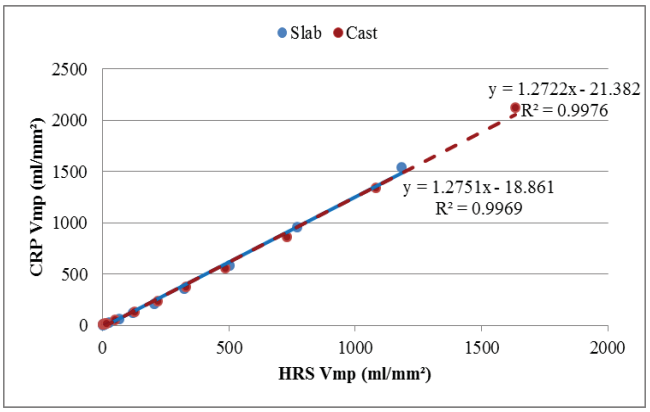


Figure 11. Comparison of HRS Vmp against CRP Vmp for both slab and cast 3D models, derived from the AFC.

Figure 12 displays further volume parameters derived from the AFC. The graph shows an additional recovery of approximately 63 – 72% Vvc for the cast compared with the slab specimen. Therefore it suggests the cast provides better representation of possible voids for retention of water and surface drainage.

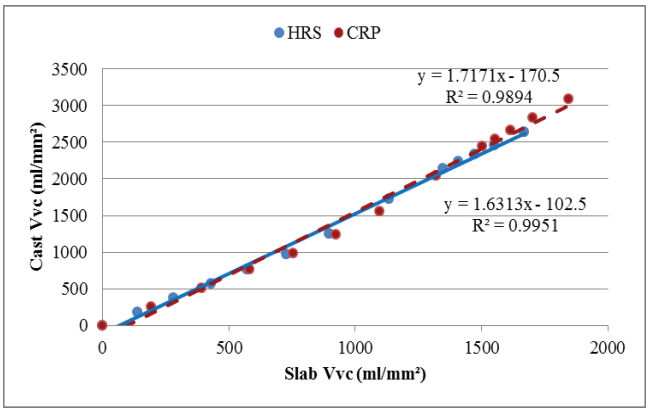


Figure 12. Comparison of slab Vvc against cast Vvc for both CRP and HRS methods, derived from the AFC.

Height parameters for each 3D model were determined in accordance with BS EN ISO 25178-2 [20]. These are displayed in Table 1. The height parameters presented are defined as:

Sq - Root mean square height of the scale-limited surface.
Sa - Arithmetical mean height of the scale limited surface.
Sp - Maximum peak height of the scale limited surface.
Sv - Maximum pit height of the scale limited sur-face.
Ssk - Skewness of the scale-limited surface.
Sku - Kurtosis of the scale-limited surface.

Sp and Sv are measured using the mean reference plane. The mean reference plane is used during initial levelling of the 3D models and is therefore assumed consistent across the data sets. By representing the highest point in the surface, Sp can be used to investigate the wear of material peaks and in the application of sliding contact. Representing the lowest point, Sv can give an insight along with the AFC Vvc to valley depths and the retention of fluids on the surface.

Sq and Sa parameters are independent of the mean reference plane. If disputes arise regarding the mean reference plane, these height parameters can be used to investigate the two specimen surfaces and methods of 3D capture.

Ssk and Sku relate to the skewness and kurtosis of the 3D surface texture respectively. For a normal distributed surface a Ssk of 0 and a Sku of 3 would be expected. Ssk and Sku are based on the symmetry and deviation from a normal distribution on a histogram of the heights of all measured points. With an Ssk > 0 a predominance of peaks is assumed and an Ssk < 0, a predominance of valleys is assumed. In terms of kurtosis a Sku > 3 suggests extreme high peaks or deep valleys.

A mean model texture depth (MMTD) was also recorded for each model. These are presented in Table 2.

Table 1. Height parameters for the 3D models.

3D Surface	Sq	Sa	Sp	Sv	Ssk	Sku
Slab HRS	1.26	0.99	1.94	-3.88	-1.02	3.63
Slab CRP	1.62	1.28	2.07	-5.14	-1.2	3.96
Cast HRS	1.65	1.31	2.58	-5.23	-0.94	3.54
Cast CRP	2.15	1.70	3.18	-6.98	-1.11	3.86

Table 2. MMTD for the 3D models.

3D Surface	MMTD
Slab HRS	1.8
Slab CRP	2.18
Cast HRS	2.23
Cast CRP	2.83

4 DISCUSSION

The results displayed in Figure 9 suggest the Vmp recovery was greatest for the cast CRP followed by cast HRS, slab CRP and finally slab HRS. This ranking for the HRA surfacing correlates with that produced in McQuaid [15] for the SMA surfacing. Therefore this volumetric relationship is consistent across the two asphalt materials despite the differing negative and positive surface textures. The Vmp spreads across a larger range for the HRA models when compared to the SMA 3D models [15]. This could be due to the more textured and at times occlusive nature of the HRA.

The investigation into the recovery of Vmp for slab/cast surface and HRS/CRP method was presented in Figure 10 and 11. The consistent correlations in both figures confirm the cast surface and CRP methods to maximise the recovery of surface texture material. Again this is in agreement with McQuaid [15] for the SMA material.

Investigating the drainage paths of asphalt surfacing is restricted by the 3D modelling methods ability to capture the surface with depth. This is particularly challenging when working with an occlusive surface texture. Figure 12 shows the cast to give greatest recovery of Vvc. This highlights the effective use of the cast to investigate surface drainage and retention of water.

Figures 13 and 14 show the depth distribution for the slab 3D models and the cast 3D models respectively. Visual examination of these figures suggests both CRP models may have surface noise. In Figure 13 this is apparent by the extended leading tale in the slab CRP. The extended end tale for the slab CRP also suggests the method is recovering to a greater depth into the surface than the HRS method. Both cast HRS and cast CRP demonstrate in Figure 14 the greatest extension in the end tails. This confirms the use of the vinyl cast enables the recovery of texture to greater depths into the surface. As Figure 14 details the cast depth distributions, it must be reminded that the cast 3D models underwent inversion. Therefore surface noise for the cast CRP model also contributes to the extended end tail. Following inspection of the AFC, surface noise was again confirmed in the CRP models. This is apparent by the extended Vmp depth (at the top) in the AFC for the cast CRP in Figure 8. This surface noise has negligible effect on the volume parameters derived from the AFC. However the presence of surface noise will have a more influencing effect on the height parameters for the surface.

Successful correlation of height parameters would suggest the 3D models to be the same. By consulting Table 1 this is not the case. When previously investigating an SMA material, McQuaid [15] found any variation was related to the method used to create the model, i.e. HRS or CRP. It was also concluded that the presence of surface noise could be responsible for deviation in height parameters. Through analysis of the AFC and depth distribution it was suggested that surface noise was present in the CRP 3D models. McQuaid [15] discussed, as suggested by Michigan Metrology [21], the removal of 1% areal material bearing ratio (AMBR) to the peaks and valleys, i.e. top and bottom of the 3D model, would aid removal of any outlier points such as surface noise. The AOI for CRP 3D models in this paper were therefore threshold to only include data points within the AMBR range of 1% - 99%. This should offer enough correction to eradicate any problems. Less deviation from the mean was evident as a result across all assessed height parameters. HRS models are less susceptible to surface noise and therefore did not require a similar correction.

The cast CRP and cast HRS recorded the largest Sp and Sv valleys, suggesting that the use of the cast for 3D capture of surface texture recovered to a greater depth into the surface when compared with the slab 3D models.

The skewness parameter Ssk for all models are less than zero, suggesting a similar relationship across all 3D models, the predominance of valleys. The kurtosis parameters for all models are greater than three. As discussed previously this suggests extreme high peaks/valleys are present, which agrees with the deep textured chipped HRA surface used for the 3D models.

The chipped HRA asphalt surface recorded a MTD (derived from the volumetric patch technique) of 1.83 during testing. Following this the user variability of the technique for a number of surfaces was investigated. With ten sets of operator data a deviation (1.69 – 2.01 MTD) from the mean of 0.09 mm was found for the HRA surface in this paper. Table 2 details the MMTD for all four 3D models. They are not consistent and fall outside the deviation determined from the user variability study on the volumetric patch technique. However the vinyl cast offers recovery of surface texture to a greater depth into the surface compared with the slab, therefore a variation in MMTD would be expected.

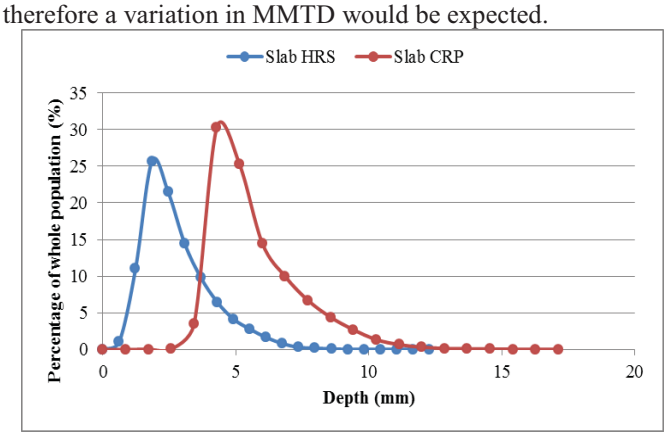


Figure 13. Depth distribution of data points for the slab 3D model using both HRS and CRP methods.

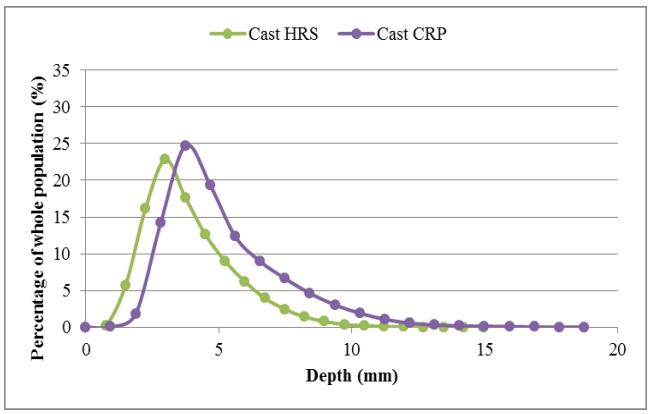


Figure 14. Depth distribution of data points for the cast 3D model using both HRS and CRP methods.

5 CONCLUSION

A chipped HRA asphalt surface and its corresponding vinyl cast were used to create four 3D models. This entailed using both CRP and HRS methods for 3D capture of the surface texture. Further analysis and comparison with previous work was made to determine the similarity between the models.

The height parameters, Sq, Sa, Sp and Sv showed consistently higher values for the use of the cast compared to the slab. The same relationship occurs when the CRP method is compared with the HRS. The Ssk and Sku values also correlated well with each other for all four 3D models. This is more conclusive than that found by McQuaid [15] when investigating a SMA surfacing. The comparison of methods was more complex when investigating the SMA material, primarily due to the presence of surface noise.

Similar to McQuaid [15] the AFC and percentage depth distribution data was able to confirm the presence of surface noise in CRP derived 3D models. As with the SMA analysis this had negligible effect on the volumetric analysis (AFC) but did influence the height parameters. As suggested previously, the removal of 1% AMBR to the peaks and valleys (AMBR 1% - 99%) was used to offer adequate correction. This eradicated any outlier data which may have been due to surface noise. As a result better correlation between the height parameters was found across all four 3D models.

The ability for the vinyl cast to recover to greater depths into the surface confirm the potential of the tool for analysing the surface voids and therefore possible retention/drainage of surface water.

In the SMA analysis, it was concluded that the cast HRS provided the most reliable method of surface 3D capture. This was primarily due to the effect of surface noise on the CRP 3D models. The HRA analysis provided in this paper has incorporated details which address this issue. Therefore it can be concluded that the cast still remains the most reliable surface for 3D capture. However both HRS and CRP offered good surface recovery post removal of any surface noise. It would be expected that the CRP method would perform better again if the application of white paint was eliminated. White paint was used on the vinyl casts to maximise surface recovery for the HRS method. Therefore the removal of this application from the CRP method would optimize its surface recovery further. With CRP methods economy and efficiency also taken into account, it can be concluded that the CRP method offers the best 3D capture of surface texture for the HRA material investigated in this paper.

Findings presented in this paper are based on static capture of surface parameters. Although recovery of the surfaces at the resolutions adopted is computationally demanding, development of new algorithms and increasing processing power would in principle commend the methods to mobile surface recovery.

REFERENCES

[1] Flintsch, G. W., de Leon E, McGhee K. K. and Al-Quadi, Imad L. (2003), 'Pavement Surface Macrotexture Measurement and Application'. Transportation Research Record, *Journal of the Transportation Research Board, TRB,* National Re-search Council, Washington D.C., Vol 1860, 201-209.

[2] British Standards Institution. (2010(d)), BS EN 13036-1: 2010: Road and Airfield Surface Characteristics. Test Methods: Measurement of Pavement Surface Macro-Texture Depth using a Volumetric Patch Technique, 2nd edn. London: BSI.

[3] Kane, M., Artamendi, I. and Scarpas, T. (2013), 'Long-term skid resistance of asphalt surfacings: Correlation between Wehner-Schulze friction values and the mineralogical com-position of the aggregates', *Wear,* Vol. 303 (1-2). 235-243.

[4] Design Manual for Roads and Bridges, (2008), Volume 7, 'Pavement Maintenance Assessment', Section 3, Part 2, London: Highways Agency.

[5] Sangiorgi, C., Bitelli, G., Lantieri, C., Irali, F. and Girardi, F. (2012), 'A study on texture and acoustic properties of cold laid microsurfacings'. *5th International Congress of Sustain-ability of Road Infrastructure,* Rome, Italy 29-31 October.

[6] Dunford, A. (2008), 'PPR538. Measuring skid resistance without contact; 2006-2007 progress report', Crowthorne, TRL.

[7] Dunford, A.M., Parry, A.R., Shipway, P.H. and Viner. H. E. (2012), 'Three-dimensional characterisation of surface texture for road stones undergoing simulated traffic wear', *Wear*, 292-293, 188-196.

[8] Chandler, H., Fryer, J. G. and Jack, A. (2005), 'Metric Capabilities of Low Cost Digital Cameras for Close Range Surface Measurement', *The Photogrammetric* Record, Vol. 20, 109, 2-26.

[9] El Gendy, A., Shalaby, A., Flintsch, G. (2011), 'Stereo-vision applications to reconstruct the 3D texture of pavement surface', *International Journal of Pavement Engineering*, 12, 3, 263-273.

[10] Woodham, R. (1980), 'Photometric method for determining surface orientation from multiple images', *Optical Engineering*, 19, 139–144.

[11] Millar, P. (2013), 'Non-Contact Evaluation of the Geometric Properties of Highway Surfacing Textures Using Close Range Photogrammetry', PhD Thesis, School of Built Environment, University of Ulster.

[12] Millar, P., Woodward, D. (2010), 'Application of Digital Elevation Models to Delineate Areas of Residual Water in Highway Surfaces', Irish Transport Research Network. Dublin.

[13] Millar, P., Woodward, D. and McQuaid, G. (2012), 'Close up and Dirty, an Evaluation of the Character of Asphalt Surfacings in-situ Using Close Range Photogrammetry', *MAIREPAV7, 7th International Conference on Maintenance and Rehabilitation of Pavements and Technological Control,* Auckland, New Zealand, August 28-30.

[14] Dunford, A. (2010), 'PPR538. Measuring skid resistance without contact; 2009-2010 progress report', Crowthorne, TRL.

[15] McQuaid, G., Woodward, D. and Millar, P. (2013), 'Comparison of surface parameters for a 10 mm SMA without contact', *3rd International Conference on Transportation Infrastructure*, University of Pisa, Pisa, Italy.

[16] British Board of Agreement, The Highway Authorities Product Approval Scheme (HAPAS), (2009), BBA Datasheet 04/06, Issue 3.

[17] Nicholls J.C. (1997), 'Laboratory tests on high-friction surfaces for highways', TRL Report 176, Crowthorne: TRL Limited

[18] Topcon, (2010), ImageMaster: Release 2.7, Livermore, California.

[19] Digital Surf, (2012), Mountains Map: Release 6, Besançon, France.

[20] British Standards Institution, (2012), 'BS EN ISO 25178-2: 2012 Geometric product specifications (GPS) – Surface texture: Areal terms, definitions and surface texture parameters', London: British Standards Institution.

[21] Michigan Metrology, (2013), '*3D* Surface Roughness and Wear Measurement, Analysis and Inspection', Available: http://www.michmet.com/, Last accessed 3rd Aug 2013.

Bond coats and asphalt durability under freeze thaw conditions

Philip McManus, David Woodward and Alan Strong
School of the Built Environment, University of Ulster, Jordanstown, Co. Antrim, Northern Ireland
email: wdh.woodward@ulster.ac.uk, wa.strong@ulster.ac.uk

ABSTRACT: This paper considers potential problems with the use of bond coats in composite asphalt materials under freeze thaw conditions when water is present or trapped in the lower asphalt material. This could simulate conditions during new highway pavement construction, or planned maintenance when it rains prior to application of bond coat and the final surfacing layer. Bond coat is applied to bond the surfacing and lower asphalt layers together, to seal the structure from the ingress of water during in-service life and create a composite layer with increased structural contribution to the pavement. The traditional method of assessing the effect of a bond coat is shear strength testing. Despite many years of development there are still problems with this approach. Given the apparent increased frequency of asphalt surfacing failures such as potholing and ravelling in recent years it was decided to investigate whether trapped water in the lower asphalt layer was a concern. The paper suggests that the presence of a bond coat between asphalt layers that restricts the flow of water up from lower layers may result in forces that contribute to separation of the asphalt layers during freeze thaw conditions leading to premature failure.

KEY WORDS: Bond coat, Durability, Premature failure, Freeze thaw.

1 INTRODUCTION

Problems being blamed on climate change need to be better understood by those involved in civil engineering. For example, unexpected asphalt failures that happen after extreme cold events.

This is particularly relevant given the implications of the Construction Products Regulation [1] and the emphasis now being placed on performance and durability over the in-service life of construction products.

Highway pavements are constructed in layers with bond coat used to bond the surfacing and lower asphalt layers together. This has been shown to have many benefits i.e. it provides shear resistance, assists in the transfer of traffic loading, seals the structure from the ingress of water during in-service life and creates a composite layer with increased structural contribution to the pavement.

Bond coats are considered to act as an impermeable layer. Under ideal conditions they are sprayed onto a dry surface. Given Ireland's climate these ideal conditions may not always be met. Whether new construction or as part of a maintenance resurfacing programme, it may rain prior to application of the bond coat and the surfacing course.

This can lead to the underlying base course becoming damp or even saturated with water. If a bond coat is then laid over this damp or saturated course the impermeable nature of the bond coat may then trap the water for quite considerable periods of time.

With the onset of winter freezing conditions this trapped water may expand and could initiate the separation of the two upper pavement courses and lead to the premature failure of the pavement surface. Localised problems may initiate the onset of smaller scale problems such as alligator cracking or pot-holing.

Research into highway material freeze thaw typically consider failure mechanisms related to water absorbed in either the aggregate and / or the asphalt mix.

This paper adopts a different approach and aims to illustrate what may happen if water is trapped within or under asphalt layers subject to deep penetrating frost.

The reason for this study are the recent winters in Ireland with prolonged periods of cold weather that led to conditions of deep penetrating frost. After the thaw there was a noticeable increase in asphalt durability problems and premature failure well before expected design life. Of the different reasons proposed, the freeze thaw action of water was considered a culprit.

Freezing water expands by approximately 9%. Therefore, if constrained and not allowed to expand it can create expansive pressure. In the context of this paper, the constraint to expansion is caused by the use of a bond coat trapping water below the surface course either at the interface or within the structure of lower courses.

2 TEST METHODOLOGY

A simple experiment was designed to illustrate what may be happening with the use of bond coat in the proposed scenario [2]. The experiment removed most of the variables associated with the lower asphalt layer and focused on the impact of the bond coat interface with an overlying asphalt layer as water freezes in a confined environment.

The lower asphalt layer was replaced by a thick walled metal cylinder of internal diameter 100mm and internal depth of 60mm. The cylinder is shown in Figure 1. This had a bevelled rim that provided a sharp edge for the asphalt sample to rest onto and prevented it from freezing to the metal cylinder.



Figure 1. Test cylinder used for freezing tests.

Two types of asphalt mix were assessed i.e. 10mm Stone Mastic Asphalt (SMA) and 20mm Asphalt Concrete (AC). These were 150mm in diameter and had been compacted to 200 gyrations to their Conventional Refusal Density using a gyratory compactor. Figure 2 shows a test specimen with applied bond coat.



Figure 2. Test specimen with bond coat.

The test setup consisted of the metal cylinder filled with water, the asphalt test specimen resting on its rim with a 15kg weight placed on top. This was setup was placed in a chest freezer at -25^{0}C for 24 hours. The thick base and walls of the cylinder and the weight on top ensured that any expansion of the water was restricted to the vertical direction only i.e. the interface with the asphalt test specimen.

3 TEST OBSERVATIONS

Initial testing assessed how water in a cylinder would freeze. As expected this found an approximate 9% increase in volume. Figure 3 shows z-direction expansion of water freezing in a cylinder.

It was observed that water initially froze from the top and sides at the same time. This left a central core of water within the ice. Initially the freezing process left a flat top to the ice block. As the remaining water froze, it expanded creating a distinctive cone shape on top of the ice block as shown in Figure 3.



Figure 3. Expansion of unrestrained ice.

Figure 4 shows an example of a 10mm SMA with no bond coat and a 15kg weight after being frozen. Initially, as the freezing cylinder of water became pressurized it forced its way out through the gaps between the cylinder rim and the asphalt test specimen surface texture.



Figure 4. A 10mm SMA specimen, no coat and 15kg weight after freezing.

When this froze, the pressurized water was forced up through interconnected air voids within the test specimen. This resulted in the formation of ice on the surface of the test specimen and formed small stalactites on the outside edge and

underside of the test specimen. Figure 5 shows frozen water emerging out of 10mm SMA specimen. In places these had formed small icicles.



Figure 5. Frozen water emerging out of 10mm SMA specimen

Located directly under the icicles were ice stalagmite features indicating that a flow of water had passed through the SMA test specimen before the water in the internals channels within the test specimen finally froze. The 15kg weight was lifted by about 7 mm. As the water had frozen up through the test specimen it took a considerable force to separate the two.



Figure 6. Vertical uplift of 10mm SMA test specimen with bond coat and 15 kg weight

Figure 6 shows a 10mm SMA test specimen that had bond coat applied. This shows the 15kg weight placed on top of the test specimen resting at angle. It was observed that water began freezing from the edges leaving a water core within the ice block. With continued freezing, expansion caused the surface to rise vertically. A cone developed and only a small amount of water spilled out of the metal cylinder.

This lifted both test specimen and 15kg weight, as shown in Figure 6. The test specimen could easily be detached from the ice indicating little if any bond.

The bond coat did not allow the freezing water to penetrate into the SMA indicating that it had formed an effective waterproof barrier to the underside of the specimen preventing the flow of pressurized water. Similar conditions were observed as for 10mm SMA test specimens treated with tack with the 15kg weight lifted by approximately 22mm.

When the test was repeated using a 20mm AC with no bond or tack coat, freezing developed similar to the 10mm SMA test specimens causing up to 8mm of uplift. However, there was no evidence of water having been forced through the test specimen during the freezing process.

This suggested that this AC mix, when compacted to its conventional refusal density, is more resistant to freezing water penetration. Water did escape through gaps left between the cylinder rim and the rougher textured underside of the test specimen.

It took a hammer to separate the ice from the asphalt concrete. A large amount of ice remained attached to the AC suggesting a bond between ice and asphalt had developed. Freezing of 20 mm asphalt concrete, bond coat and 15kg weight resulted in uplift similar to that for the SMA. Again, there was poor bond between test specimen and ice. The same occurred when tack coat was used.

4 DISCUSSION

The investigation into how water freezes in a confined cylinder found that it is influenced by confining pressures from the walls of the cylinder and from the block of ice freezing from the outside in. This can lead to increased pressure and in the case of this simple experiment vertical forces.

Placing a loaded SMA or AC test specimen on top of the water container within the cylinder changed its freezing pattern. Pressurized water initially escaped through gaps between the textured base of the test specimen and the rim of the cylinder. This subsequently froze; pressure increased and forced water through an internal network of voids.

The internal void network for the AC was less well developed than the SMA which allowed water to reach its edges and top surface. Freezing eventually results in a strong bond between ice and test specimen. The application of bond coat created a smooth surfaced waterproof barrier.

Ice could not penetrate through this layer causing uplift. The test specimen could be easily separated from the ice. The same was found the test specimens with tack coat.

5 CONCLUSIONS

A very simple test was designed to assess the interaction of water freezing under an asphalt test specimen. The laboratory test is highly idealized and is a simplification of real-life. It was found that the application of a bond or tack coat caused a different phenomenon to occur compared to no coating.

Both bond and tack coats restricted the flow of ice formation within the test specimen during freezing. This

caused uplift of the test specimen and 15kg weight. Similar freezing conditions with no coating found much less uplift as the water was found to flow within the test specimen.

There was more internal flow observed for the SMA. The findings of what is a simplistic laboratory study suggest that the use of bond coat may be having unexpected effect on the bonding of asphalt layers and durability of the asphalt pavement.

This may be weakening the pavement structure and the surface layer. This reduction of the life span of the pavement surface not only increases the cost of maintenance of the pavement but also leads to a poorer quality pavement surface for drivers that could lead to damage of their vehicle and the possibility of increased road accidents.

6 REFERENCES

[1] *Construction Products Regulation* (2011) Regulation (EU) No 305/2011, European Parliament and of the Council.

[2] McManus, P. (2012), *Bitumen bond coat durability under cyclic freeze thaw conditions*. MSc Infrastructure Dissertation, University of Ulster, Northern Ireland.

Development of a method to predict the durability of warm mix asphalt

Karen Kennedy, Ruth Mitchell, David Woodward and Phillip Millar
School of Built Environnent, University of Ulster, Jordanstown, Shore Road, Newtownabbey, Northern Ireland
email: wdh.woodward@ulster.ac.uk

ABSTRACT: Hot Mix Asphalt (HMA) has been the main type of material used in road construction around the world for many years. The use of Warm Mix Asphalt (WMA) technologies allow asphalt production and compaction temperatures to be reduced. This has obvious implications ranging from reduced energy use in manufacture, allowing compaction at lower temperatures to less fumes giving safer working conditions. However, the issue of its longer term durability is still relatively unknown particularly in Ireland. This paper considers a new method to predict the durability of asphalt materials. Roller compacted 14mm Stone Mastic Asphalt test specimens were subjected to simulated accelerated trafficking using a modified wheel track test equipment. This had been fitted with a pneumatic tyre and modified to drag the test tyre across the test specimen in one direction. This can exploit weaknesses of the surfacing causing it to ravel and breakup. 3D models of the test specimen before and after simulated trafficking were made using a hand held ZScanner 800 3D laser. Change in the 3D models were analysed using DigitalSurf MountainsMap6 Premium software. In developing this new test method it was found that test temperature and compaction were important factors in causing the asphalt surface to ravel. After testing at 30^0C it was concluded that addition of the 4 additives used did not detrimentally affect the durability of WMA SMA14 asphalt in comparison to the HMA control. Based on the findings of this new test method it is concluded that if properly compacted, the use of additives will result in a WMA SMA that is comparable to HMA SMA in terms of durability.

KEY WORDS: Asphalt, Durability, Warm Mix Asphalt, Compaction, Dragged ravelling test, 3D modelling.

1 INTRODUCTION

This paper describes the use of a test method designed to assess the durability of road surface asphalt materials. The method is called the Dragged Ravelling Test (DRT). It was developed to assess factors such as compaction, temperature and presence of moisture on asphalt mix durability [1, 2]. The DRT is based on the Immersion Wheel Track Test originally developed by the Road Research Laboratory in the 1950s [3].

In the original method a bituminous specimen is immersed in water at 40^0C for 1 hour. A hard rubber tyre reciprocates across its surface causing stripping of the bitumen and rutting of the test specimen. It was subsequently modified with a braking system to increase contact stress during testing [4].

The latest development, detailed in this paper, replaces the solid rubber tyre with a treaded pneumatic tyre to increase contact with the textured asphalt test specimen. The damage caused to the test specimen is quantified using 3D modelling. This paper summarises the DRT test methods and uses a case study to show how it may be used. The asphalt used in the case study was a 14mm Stone Mastic Asphalt (SMA14) made with four different additives.

2 THE DRAGGED RAVELLING TEST

The Dragged Ravelling Test (DRT) was developed to simulate conditions at the tyre / asphalt interface. It accelerates a range of failure mechanisms experienced at this interface including ravelling, secondary compaction and moisture sensitivity, loss of adhesion / cohesion. 3D modelling is used to quantify any change in the surface of the test specimen.

The test method assesses roller compacted specimens 305 x 305 x 50 mm in size. The first stage of the test involves securely fitting the test specimen in an aluminium reference mould. This is scanned using a hand held ZScanner800^{TM} High Resolution 3D Scanner. The test specimen and reference mould is then submerged in water for a predetermine time, typically 1 hour. A reciprocating tyre traffics the test specimen for a defined period of time. The pneumatic tyre moves freely forward before being locked and dragged backwards across the test specimen.

The tyre and braking mechanism is shown in Figure 1. Factors such as test specimen compaction, test duration, type of pre-conditioning and water test temperature can be altered depending on what is being considered. After testing the bituminous specimen is rescanned. The 3D model is cleaned using ZScan software, as shown in Figure 2 and then imported into Digital Surf MountainsMap6 (MountainsMap) for analysis.



Figure 1. The DRT braking system.

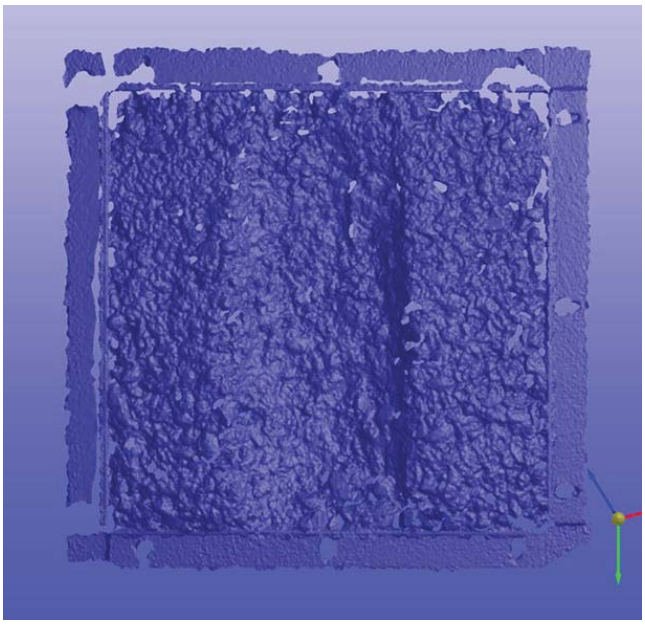


Figure 2. Example of a cleaned 3D model.

The contact between the test tyre and the specimen surface was considered to be important. The change in contact area at different tyre inflation pressures and loads was determined. Figure 3 shows the lever arm assembly of the DRT resting on a high resolution XSensor pressure pad to measure its contact patch. Tyre inflation pressure ranged from 0 to 56 psi. Three static loading conditions were assessed i.e. 9.59 kg (A), 18.86 kg (B) and 28.06 kg (C).

Figure 4 shows an example of the contact patch for the pneumatic tyre with inflation pressure 18.5 psi and loading condition C. Figure 5 plots the pressure pad data for the 3 loading conditions at different tyre inflation pressures. This indicates that contact area increases as tyre inflation pressure decreases and increases with load. Loading condition C was used for DRT testing.

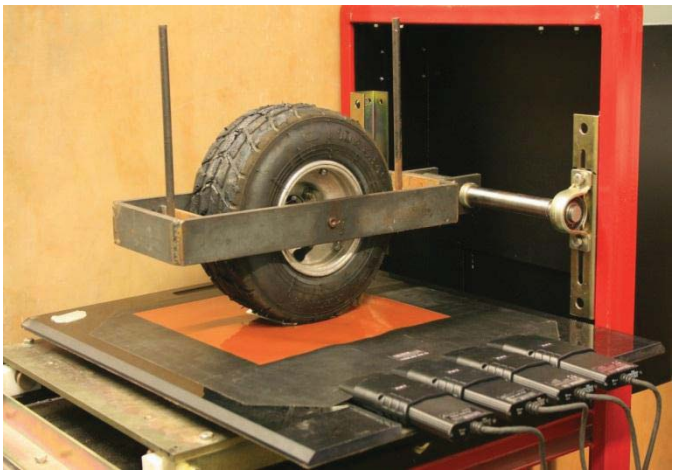


Figure 3. Measurement of test tyre contact patch using a high resolution XSensor pressure pad.

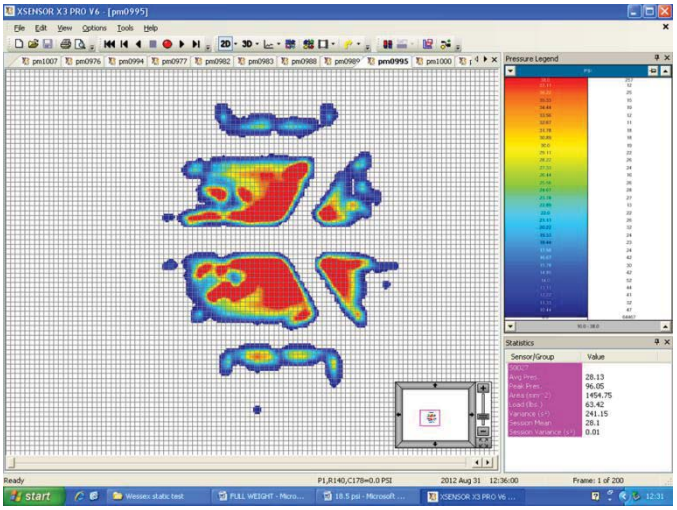


Figure 4. Example test tyre contact patch.

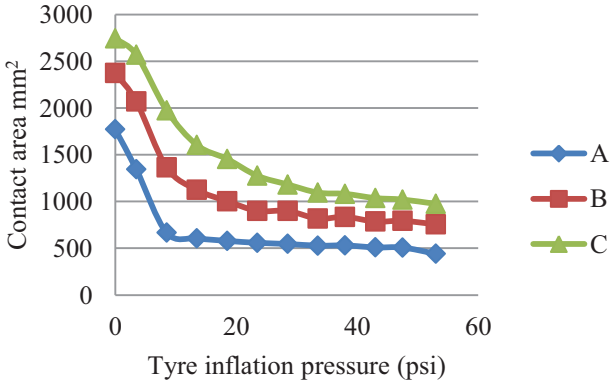


Figure 5. Contact area v. tyre inflation pressure for the 3 loading conditions.

The aluminium reference mould is important for aligning 3D models of the test specimen before and after testing.

Figure 6 shows the test specimen in the reference mould with a mesh of control dots required for laser scanning. The test specimen remains in the reference mould throughout all stages of DRT testing. This allows the 3D models to be accurately aligned in MountainsMap and the pre and post-test specimens to be compared.

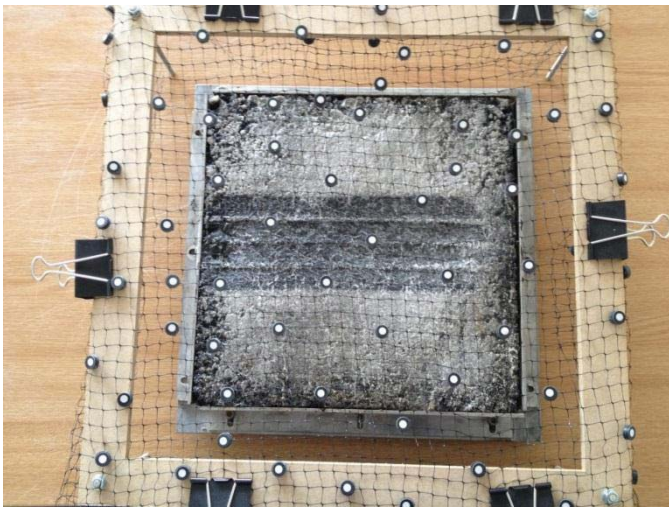


Figure 6. Test specimen in reference mould ready for 3D laser scanning.

Figure 7 and 8 show 3D models for a poorly compacted test specimen before and after testing. These have been produced in MountainsMap. Colour is used to emphasise the z-scale. In this example, the dragged tyre caused the poorly compacted test specimen to suffer considerable material loss.

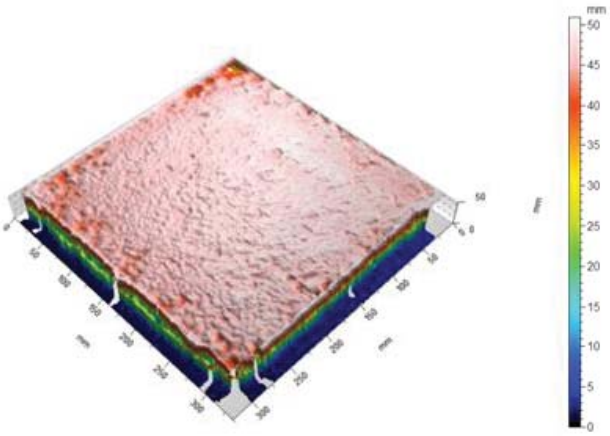


Figure 7. Example of poorly compacted test specimen 3D model prior to testing.

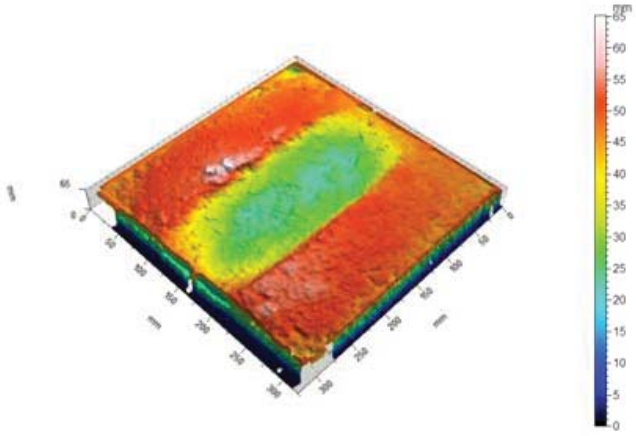


Figure 8. Example of poorly compacted test specimen 3D model after testing.

Initial analysis of the 3D model considered the entire test specimen (1, 2). To simply the analysis, his was reduced to just that part of the test specimen that was subject to trafficking. Figure 9 shows an example Area of Interest (AOI) selected for analysis. In this example the dimensions were 155 x 200 mm in size. However, once the 3D model is created, any part of it can be analysed.

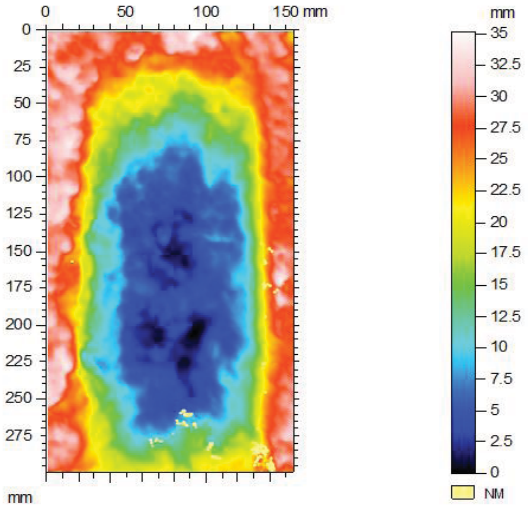


Figure 9. Example of defined Area of Interest used for volumetric analysis.

3 USE OF DRT TO ASSESS THE DURABILITY OF A WARM 14MM STONE MASTIC ASPHALT

The following case study shows how the DRT test has been used to assess the durability of a warm 14 mm Stone Mastic Asphalt (SMA14). The aggregate was a Silurian greywacke mixed with 70/100 penetration grade and 0.3% cellulose fibres. The following mixtures were assessed: standard hot mix SMA14 (HMA), warm mix SMA14 with no additive (WMA N), warm mix SMA14 with additive Product A (WMA PA), warm mix SMA14 with additive Product B (WMA PB), warm mix SMA14 with additive Product C (WMA PC) and warm mix SMA14 with additive Product D (WMA PD). The mixing temperature was reduced by 30^0C from 160^0C to 130^0C for all the warm SMA14 test specimens. The test specimens were compacted using a Copper roller compactor. Table 1 details the bulk density of each specimen.

Table 1. Bulk density for SMA14 test specimens.

Test Specimen	Bulk Density (kg/m^3)
HMA	2136
WMA N	2132
WMA PA	2125
WMA PB	2120
WMA PC	2134
WMA PD	2113

In this case study, the test specimens were preconditioned by soaking in water at 30^0C for 60 minutes and then tested for 60 minutes with a 28 kg load. 3D models were made before and after testing and analysed in MountainsMap. The depth profile of the AOI after testing depth was measured using a Step Height Measurement procedure in MountainsMap. Transverse profiles were measured at 7 locations in the AOI i.e. P40, 80, 120, 160, 200, 240 and 280. Profile P40 was measured at 40 mm from the top edge of the AOI. An example profile using Step Height Measurement is shown in Figure 10.

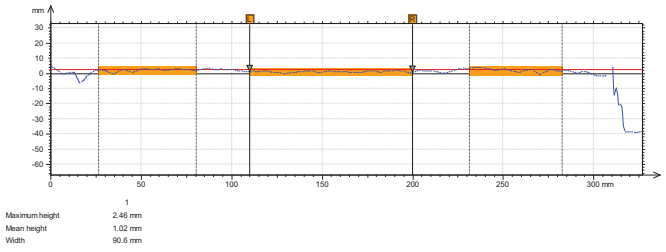


Figure 10. Example of Step Height Measurement.

The profile data for each of the test specimens is summarised in Table 2. This also shows the profile average depth. The average profile depths are plotted in Figure 11. The profile data show all of the test specimens to be similar. The profile depths taken from the 3D models are all less than 1 mm indicating the warm mix SMA14 mixtures to be durable.

Table 2. Comparison of profile depths.

	Rut Depths (mm)					
Profile	HMA	WMA N	WMA PA	WMA PB	WMA PC	WMA PD
P40	0.29	0.29	0.23	0.26	0.62	0.50
P80	0.83	1.50	1.43	0.97	0.38	1.74
P120	0.83	0.5	0.57	0.03	0.74	0.93
P160	0.63	0.66	1.25	0.66	0.23	0.99
P200	0.56	0.38	0.29	0.23	0.22	1.37
P240	1.04	1.10	0.22	0.67	0.72	1.19
P280	0.53	0.63	0.64	0.21	0.69	1.24
Average	0.67	0.72	0.66	0.43	0.52	1.14

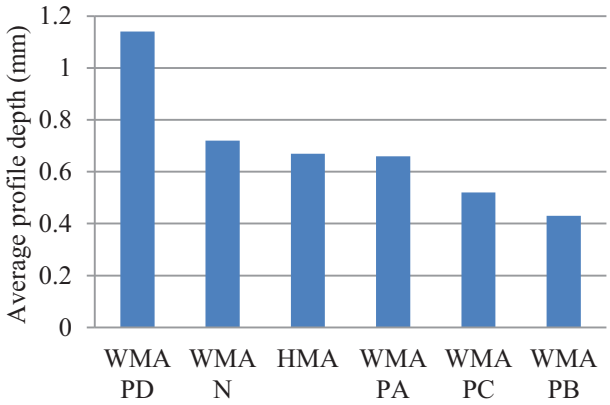


Figure 11. SMA14 mixtures ranked according to average profile depth.

The 3D models were assessed to determine difference in surface volume using the Volume of a Hole procedure in MountainsMap. Figure 12 shows the difference in volume for the test specimens i.e. the amount of material lost during testing.

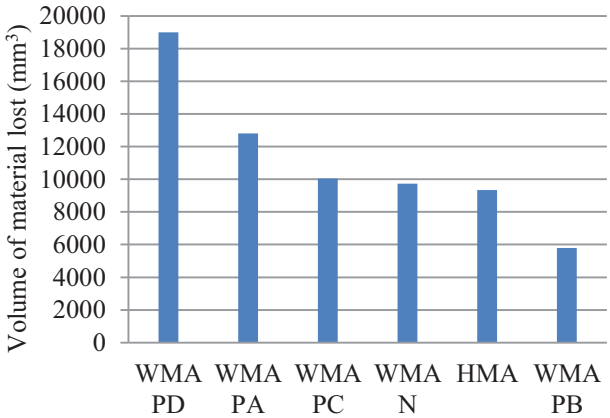


Figure 12. SMA14 mixtures ranked according to volume of material lost.

Both the profile and the volume loss data show that the warm mix SMA14 test specimens had comparable

performance to the hot mix SMA14 test specimen. This indicates that the reduction in temperature combined with the use of WMA additives does not have a negative effect on the durability of the SMA14 assessed in this case study. Although WMAPD had a slightly larger amount of both rutting and volume loss this is not considered significant.

4 CONCLUSION

This paper summarised the Dragged Ravelling Test that has been developed to better predict the durability of asphalt mixtures. The use of a reference mould to accurately place the scanned specimens for 3D analysis was discussed. A case study was used to show how the DRT test can be used to assess the durability of warm mix Stone Mastic Asphalt modified with 4 different additives. As part of a larger study into the use of warm mix asphalt in Ireland, the main finding of this case study is that there is no significant difference in durability of the warm mix and hot mix mixtures assessed.

ACKNOWLEDGMENTS

The research presented in this paper was funded by the National Roads Authority of Ireland through the NRA Research Fellowship Programme. The views expressed are not necessarily those of the National Roads Authority.

REFERENCES

[1] R.K. Mitchell. *Durability of Warm Mix Asphalt*, PhD Thesis University of Ulster, 2014.

[2] R.K. Mitchell, W.D.H. Woodward and C. Maguire, (2014), 'Development of a durability test procedure using a Dragged Immersion Wheel Track Test'. *ICTI Conference*, Pisa, Italy, April 22-25th .

[3] Mathews. D.H. and Colwill. D.M. (1962), 'The Immersion Wheel Track Test'. *Journal of Applied Chemistry*, November, 505-509.

[4] McKibben. D.M, *A Study of the Factors Affecting the Performance of Dense Bitumen Macadam Wearing Courses in Northern Ireland*, PhD Thesis University of Ulster, 1987.

Non-contact Evaluation of Geometric Properties of Highway Surfacing Materials

Phillip Millar, David Woodward, Grainne McQuaid
School of the Built Environnent, University of Ulster, Jordanstown Road, Newtownabbey, BT32 0QB, Northern Ireland
email: p.millar@ulster.ac.uk, wdh.woodward@ulster.ac.uk, g.mcquaid@email@ulster.ac.uk

ABSTRACT: The volumetric patch test remains the sole contractually binding standard for estimation of texture depths of highway surfaces in the United Kingdom. As the test reports a single geometry only it contributes little to knowledge of the geometric properties of the road surface material and hence the nature of the tyre-surface interface and interaction. This paper compares and contrasts three dimensional models of surfacing materials using two non-contact methods of highway surface recovery i.e. close range photogrammetry and high definition laser scanning. A range of areal geometric properties are derived from the 3D models and aligned with current international standards not normally applied within the highway engineering context. The study demonstrates that non-contact surface recovery offers additional insight to the tyre-surface interface as compared with current accepted standards. This has wide ranging implications for the study of tyre-surface phenomena including safety, noise, water storage, wear and three dimensional contact area.

KEY WORDS: Close range photogrammetry; Non-contact evaluation; Geometric properties; Surface Modelling; Laser Scanning.

1 INTRODUCTION

The volumetric patch technique, commonly known as the sand patch method, remains the sole contractually binding standard for estimation of texture depth of a highway surface within the United Kingdom in the event of a contractual dispute [1]. The test has been extensively researched and is for example a harmonized European Standard test method [2]. Although a volumetric technique, the character of the highway surface is reported at the macrotexture scale as a single measurement of texture depth known as Mean Texture Depth (MTD).

From this single measure inferences are drawn in respect of a range of surface phenomena. This paper compares and contrasts 3D models of highway surfacing materials using two non-contact methods of recovery i.e. close range photogrammetry and high definition laser scanning. This paper aims to illustrate that 3D modelling has wide ranging implications for the study of tyre-surface phenomena including safety, noise, water storage, wear and three dimensional contact area.

2 BACKGROUND

The understanding of surface texture has evolved over time [3, 4, 5]. The extremes of texture likely to be found on highway surfaces is illustrated in Figure 1 [5]. It is complex physically, materially and mechanically [6]. Different studies have considered 12 main factors [7] whilst others have identified more than 40 in a study of dynamic pavement behaviour using fuzzy sets [8]. This complexity explains to some extent the range of techniques and technologies that have been developed to evaluate the character of highway surfacing textures. This paper considers the texture in three dimensions as recovered using two non-contact methods, Close Range Photogrammetry (CRP) and High Definition Laser Scanning (HDLS).

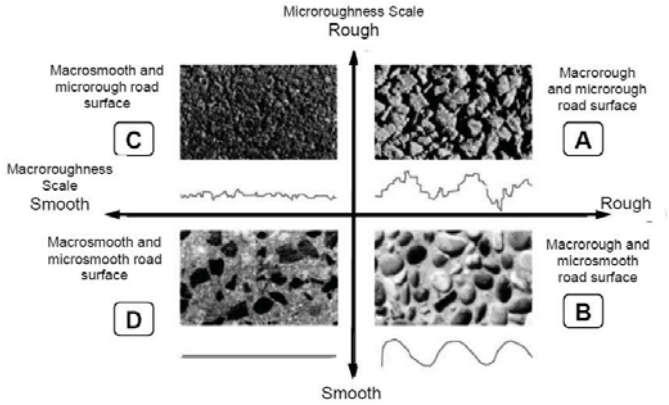


Figure 2. Extremes of texture likely to be found on highway surfaces [5].

Non-contact techniques such as laser scanning and photogrammetry are preferred by researchers for saving time and labour and for the ability of these methods to construct a three dimensional (3D) vision of the soil surface [9]. The laser based apparatus known as the Circular Texture Meter (CTM) [10, 11] reports texture depth as a mean profile depth (MPD). Close Range Photogrammetry (CRP) is an alternative non-contact technique used to evaluate the rate of wear of asphalt concrete surfacings subject to accelerated trafficking in the laboratory [12]. Figure 2 shows the relationship between volumetric patch MTD and a new parameter, Mean Model Texture Depth (MMTD) based on meshes recovered from stereo images taken at 80 locations [13] in the eastern seaboard of the United States of America, the United Kingdom and areas of mainland Europe. The surfacings ranged from asphalt concrete, hot rolled asphalt, stone mastic asphalt to surface dressing.

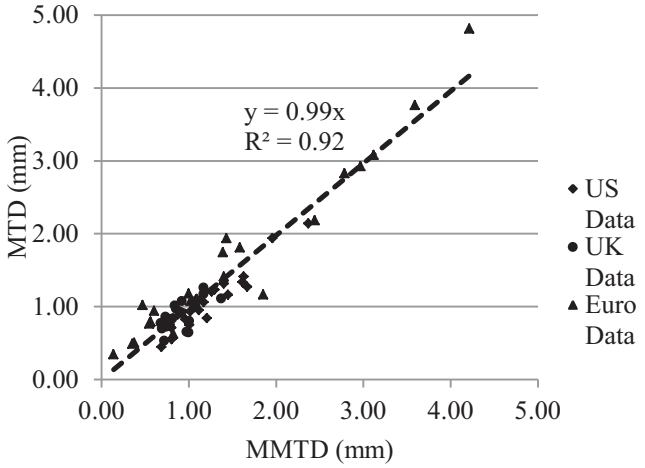


Figure 2. Correlation of MMTD and MTD [13].

3 SURFACE PARAMETERS CONSIDERED IN THIS PAPER

The surface parameters considered in this paper are based on definitions in BS EN ISO 25178-2 [14]. This standard is normally associated with the areal properties of mechanical products. However, many of its definitions are analogous to the characteristics of highway surfacing textures. Only three Functional Surface Parameters (FSP) are considered in this paper i.e. the volume of material in the peaks (Vmp), the volume of material in the core (Vmc) and the volume of voids in the core (Vvc). These are illustrated with respect to a profile as shown in Figure 3.

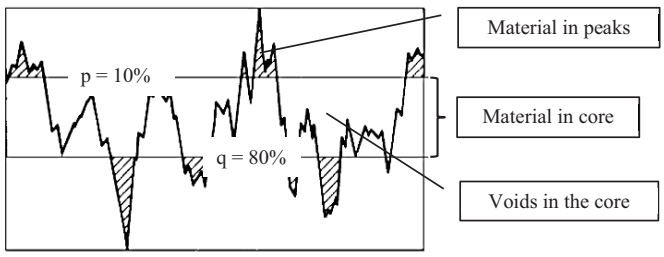


Figure 3. Illustration of regions corresponding to functional surface parameters Vmp, Vmc and Vvc.

The cut level values 'p' and 'q' correspond to 10% and 80% Areal Material Bearing Ratio (AMBR) and are the defaults specified in BS EN ISO 25178-3. The 'p' value for example would represent the depth at which the bearing area is 10% of the entire sample area.

4 METHODOLOY

4.1 Sample selection

Seven asphalt materials were selected for evaluation. These comprised Stone Mastic Asphalt (SMA) SMA6, SMA10 and SMA14 where the numerical suffix indicates the nominal aggregate size, and Hot Rolled Asphalts (HRA), HRA0, HRA10, HRA12 and HRA16. The numerical suffix for each of the HRA materials indicates the chip application rate in kg/m^2. Collectively, these materials represent a range of texture scales from the SMA6 negatively textured to the HRA16 positively textured surfacings and as such they present a comprehensive range of challenges to non-contact surface recovery.

4.2 Sample conditioning

Test specimen slabs of each material 305mm x 305mm x 50mm deep were manufactured and compacted using a roller compactor and mounted on the Road Test Machine (RTM). The RTM with slabs in place is shown in Figure 4. The slabs were conditioned by subjecting them to accelerated trafficking equivalent to 10,000 wheel passes. This exposed the aggregate and minimised surface noise in the 3D models arising from glare caused by refracted light from fresh binder. Each test specimen slabs was assessed for wet friction using the pendulum test and texture depth using the volumetric patch method.



Figure 4. University of Ulster Road Test Machine (RTM) with sample slabs in place

4.3 Surface recovery using Close Range Photogrammetry

Images were captured within a rectangular array of control points. The control framework with an asphalt sample in place is shown in Figure 5. The Cartesian (x,y,z) coordinates of each of the sixteen control points was measured before image capture using a digital micrometer. Only four points are required for image cross matching. Hence the framework contains many levels of redundancy allowing the points that give the best stereo orientation to be selected. Stereo image pairs were then processed using ImageMaster photogrammetric software and used to construct surface meshes at defined mesh spacings of 0.5mm and 0.2mm. The mesh vertices were exported in comma separated values CSV format for analysis in DigitalSurf Mountains Map® Premium (Mountains) surface analysis software.

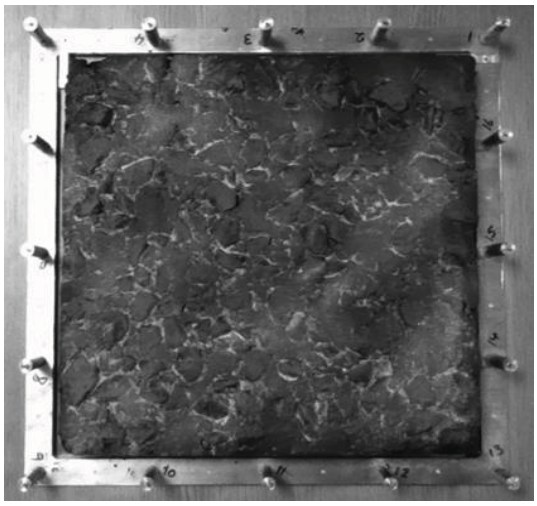


Figure 5. Control framework with asphalt sample in place for CRP.

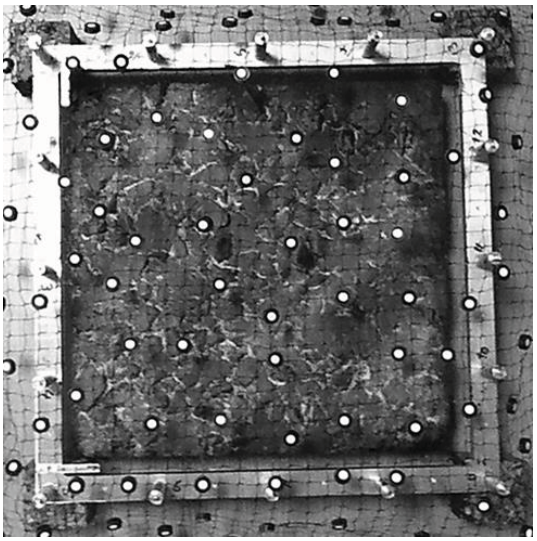


Figure 6. Arrangement of control points with asphalt sample in place for HDLS.

4.4 Surface recovery using 3D laser scanning

Following the photogrammetric work the surface of each test specimen was subject to scanning using a portable high definition 3D laser scanner (HDLS) having a stated resolution capability of 50 microns. Scanning at this resolution is computationally demanding therefore surfaces were scanned at a resolution of 0.5mm at the limit of the microtexture scale corresponding to the 0.5mm mesh spacing of the CRP models. This allowed a direct comparison to be made of the datasets for each surface.

The portability of the 3D laser scanner allows it to be manipulated such that the emitted light is incident normal to the plane of the surface element being scanned so far as is reasonably possible. This optimises recovery of surfaces that vary considerably such as highly textured surface dressings and chipped HRA. Recovery of the test specimen surface using HDLS requires a network of control points to be draped over the rectangular control framework used for the CRP process as shown in Figure 6.

The scanned surface was modelled by surface facets. It is inevitable that laser scanning will recover surface elements of all objects within its range and within the scope of the control points. This results in a large amount of redundant data that is not pertinent to the asphalt surface and might include elements of the CRP framework, the material supporting it and the table that the whole arrangement rests on. On completion of the scan this redundant data was highlighted and removed prior to surface analysis. Smoothing filters were not applied to the data. The coordinates of triangular facets' vertices were exported in CSV format for subsequent analysis and comparison with the CRP data.

4.5 Reconstruction and reorientation of the surfaces

The CRP models are based on images captured within a prescribed grid of control points consequently there is no explicit requirement to re-orientate the surface to a level plane to facilitate depth measurement. The network of control points for the HDLS technique is flexible and the scanner orientation of the raw scan data is therefore arbitrary. This results in an initial display of surface data as shown in Figure 7.

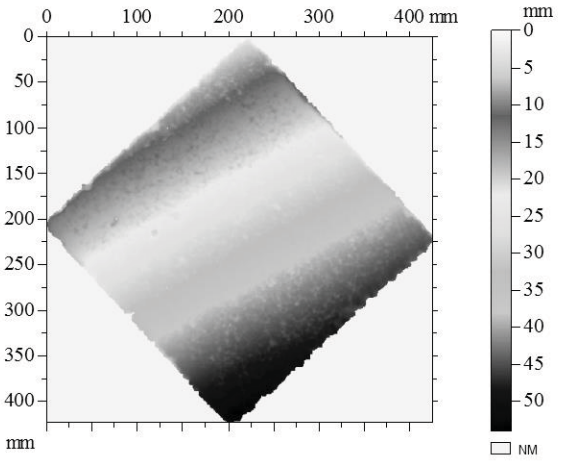


Figure 7. Initial plot of vertex points from laser scan.

This shows the plot of HDLS raw data points of the vertices of the SMA6 surfacing before levelling with respect to a best fit least squares plane. After applying a least squares levelling operator the surface appears as shown in Figure 8. Following leveling, the FSPs were generated for AMBR in increments from 0% up to the default BS EN ISO 21758:2 AMBR of 80%.

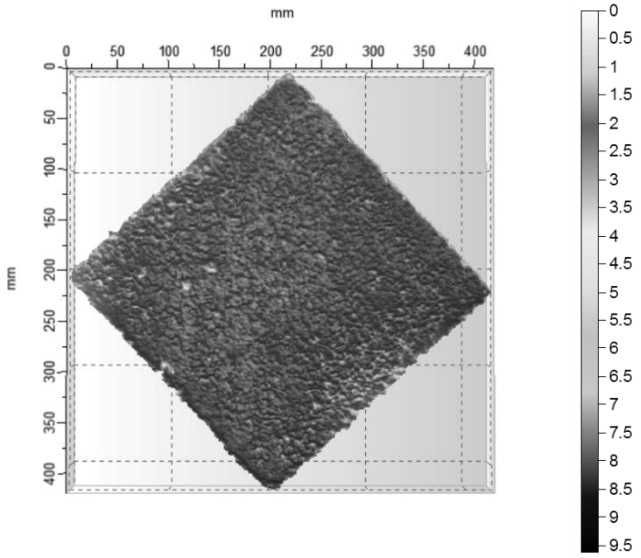


Figure 8. HDLS dataset after application of the leveling operator.

Table 1. Summary of FVP outputs.

Surface Type	FVP	R^2	Trend line Equation	Difference in surface recovery between HDLS and CRP methods (%)
SMA6	Vmp	0.997	y = 1.166x	16.6
	Vmc	0.997	y = 1.117x	11.7
	Vvc	0.994	y = 1.214x	21.4
SMA10	Vmp	0.999	y = 1.104x	10.4
	Vmc	0.999	y = 1.108x	10.8
	Vvc	0.999	y = 1.124x	12.4
SMA14	Vmp	0.999	y = 0.875x	-12.5
	Vmc	0.999	y = 0.897x	-10.3
	Vvc	0.997	y = 0.842x	-15.8
HRA0	Vmp	0.998	y = 680.04x	680.4
	Vmc	0.997	y = 704.13x	704.1
	Vvc	0.997	y = 697.66x	697.6
HRA10	Vmp	0.998	y = 0.88x	-12
	Vmc	0.907	y = 0.907x	-9.3
	Vvc	0.999	y = 0.891x	-10.9
HRA12	Vmp	0.992	y = 1.053x	5.3
	Vmc	0.993	y = 1.128x	12.8
	Vvc	0.971	y = 0.910x	-9
HRA16	Vmp	0.999	y = 1.142x	14.2
	Vmc	0.999	y = 1.166x	16.6
	Vvc	0.999	y = 1.124x	12.4

5 RESULTS AND DISCUSSION

Correlation analysis was carried out for the found data. This is summarised in Table 1. Figure 9 plots Vmp for the HDLS and CRP methods for 6mm SMA sample. This example shows strong R^2 correlation coefficient of 0.99. The plot shows that the CRP method has under-recovered the surface compared to the HDLS method by approximately 16%. However, this is not consistent across all surfaces as there is a declining trend for the SMA samples to an apparent over-recovery of the peak material for the 14mm SMA of 12.5% as compared to the HDLS data.

The un-chipped HRA shows an increase in surface recovery of 680.4% as compared with CRP. The texture of the un-chipped HRA is exceptionally low and shifting the cut level even fractions of a millimetre into the model results in substantial increases in the values of the FVP. The smooth and relatively featureless surfaces are not consistently recovered well using the CRP method as there is insufficient surface texture on the dark and relatively uniform surfaces from which to create the surface mesh. Although the general data trend is similar resulting in a strong correlation between the two datasets for this surface the CRP method did not capture the surface adequately for the small increments of depth for which the FVP data were generated. For the purposes of some types of further analysis and discussion therefore this surface has been treated as an outlier.

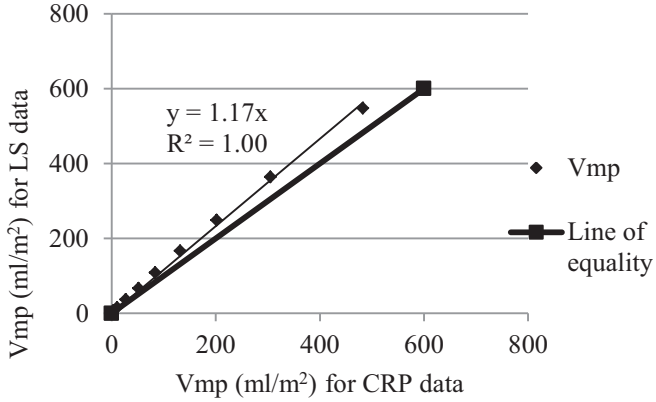


Figure 9. Plot of Vmp for CRP data against Vmp for LS data.

The FVP values derived from each method are strongly correlated with nominal aggregate size and rate of chip spread for the SMA and HRA surfaces respectively as shown in Figure 10. There is a reversal of trends between the SMA and HRA surfaces.

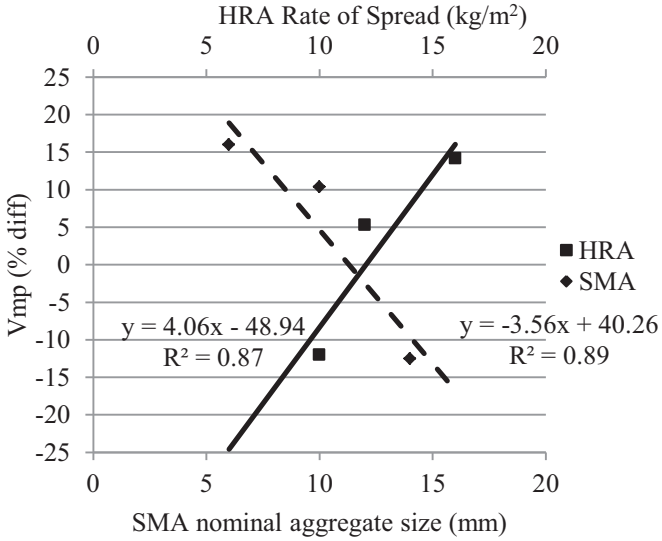


Figure 10. Comparative plot of nominal aggregate size and rate of chip spread against difference in Vmp recovery.

Figure 11 shows MTD values to have a strong correlation with nominal aggregate size for SMA and rate of chipping for the HRA.

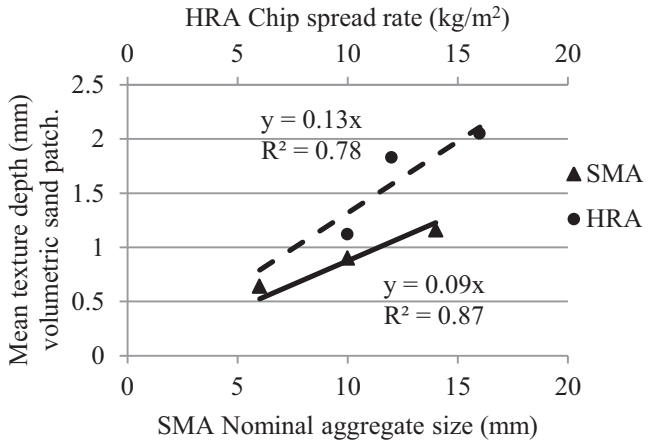


Figure 11. Plot of test specimen and mean texture depth by material type.

It would be reasonable therefore to expect a relationship between the percentage difference in surface recovery and MTD. This is demonstrated in Figure 12 which plots volumetric sand patch MTD against percentage difference in surface recovery between the 2 non-contact techniques. This shows Figure 12 and 10 to have a similar character. The plots demonstrate relationships between surface recovery, material type and texture configuration.

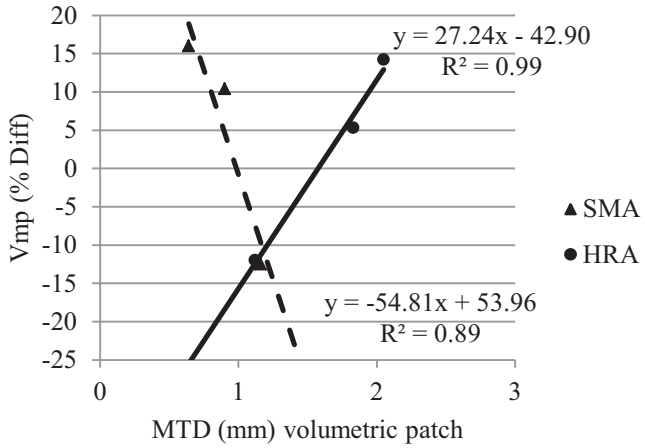


Figure 12. Plot of MTD and percentage difference in recovery of Vmp

6 CONCLUSIONS

This paper has considered the use of geometric parameters derived from 3D models of seven asphalt surfacing materials obtained using two non-contact methods. Only three parameters are considered in this paper. With the exception of smooth unchipped hot rolled asphalt, strong correlations were found for the materials assessed. The authors have already found good correlation between MMTD and MTD based on the CRP method. It is concluded in this study that 3D laser scanning is also a robust method of modeling asphalt materials. Both methods offer greater insight to the characterization of the tyre / asphalt interface. It is acknowledged that the dataset reported in this paper is small and more work is required.

REFERENCES

[1] Road Surface Treatments Association (2011), '*RSTA: Guidance Note on Surface Dressing Aggregates'*. RSTA ADEPT Code of Practice for Surface Dressing Part 3.

[2] British Standards Institution, BS EN 13036-1: 2010: *Road and Airfield Surface Characteristics. Test Methods: Measurement of Pavement Surface Macro-Texture Depth using a Volumetric Patch Technique*, 2nd edn. London: BSI, 2010.

[3] Henry, J. J. (1996), 'Overview of the International PIARC experiments to compare and harmonise texture and skid resistance measurements'. *Proceedings of the 3rd International Symposium on Pavements Surface Characteristics.*

[4] Design Manual for Roads and Bridges (2006). *Surfacing Materials for New and Maintenance Construction. Volume 7: Pavement Design and Maintenance*.

[5] Kane, M. and Scharnigg, K. (2009), *Deliverable D10: Report on different parameters influencing skid resistance, rolling resistance and noise emissions.* EU Project TYROSAFE, Brussels: FEHRL.

[6] Chelliah, T., Stephanos, P., Shah, M.G., and Smith, T. (2003), Developing a Design Policy to Improve Pavement Surface Characteristics. *TRB 82nd Annual Meeting.* Washington, D.C., January 12-16

[7] Hall, J., Smith, K. & Titus-Glover, L., 2009. *Guide for Pavement Friction*. National Cooperative Highway Research Program

[8] Ivanov V., Shyrokau, B., Augsburg, K. and Algin, V. 2010. 'Fuzzy evaluation of tyre-surface interaction parameters'. *Journal of Terramechanics*, 47(2), 113-130.

[9] Mohamed, A.M., Elbasit, Abd., Anyoji, H., Yashuda, H. and Yamamoto, S. (2009), 'Potential of low cost close-range photogrammetry system in soil microtopography quantification'. *Hydrological Processes*, 23, 1408-1417.

[10] Abe, H., Henry, J.J., Tamai, A., and Wambold, J. (2000), 'Measurement of Pavement Macrotexture Using the CTMeter'. *Transportation Research Record 1764*, Transportation Research Board, TRB, National Research Council, Washington, D.C.

[11] Noyce D.A., Bahia, H.U., Yambó, J.M., and Kim, G. (2005), 'Incorporating Road Safety into Pavement Management: Maximizing Asphalt Pavement Surface Friction for Road Safety Improvements'. *Midwest Regional University Transportation Center Traffic Operations and Safety (TOPS) Laboratory.*

[12] Millar, P., Woodward, D. and Woodside, A. (2009), 'Use of close range terrestrial photogrammetry to assess accelerated wear of asphalt concrete surface course mixes'. *Sixth International Conference on Maintenance and Rehabilitation of Pavements and Technological Control*, Politechnico di Torino, Italy July 8-10.

[13] Millar, P. (2013), *Non-Contact Evaluation of the Geometric Properties of Asphalt Surfacings Using Close Range Photogrammetry,* PhD Thesis, University of Ulster, United Kingdom.

[14] British Standards Institution BS EN ISO 25178-2:2013 *Geometrical product specifications (GPS) - Surface texture: Areal - Part 2: Terms, definitions and surface texture parameters*. BSI: London.

The Performance of a Cathodic Protection System in Reinforced Concrete Structure: Monitoring and Service Life Modelling

Cillian Ward[1], Sreejith Nanukuttan[2], John McRobert[3]
[1]4th Year Civil Engineering, School of Planning Architecture and Civil Engineering, Queens University Belfast
[2]School of Planning Architecture and Civil Engineering, Queens University Belfast, Northern Ireland, BT9 5AG
[3]Roads Service Highways Structures Unit, County Hall, 182 Galgorm Road, Ballymena, Northern Ireland, BT42 1QG
Email: cward24@qub.ac.uk, s.nanukuttan@qub.ac.uk, john.mcrobert@drdni.gov.uk

ABSTRACT: The use of cathodic protection in reinforced concrete is becoming increasingly common with such systems being installed on a number of structures throughout the United Kingdom and Ireland. However the prescribed design lives (or service life) of each cathodic protection system vary widely. The aim of this project was to assess the effectiveness of a sacrificial anode cathodic protection system and to predict its design life through a series of laboratory based experiments. The experimental plan involved casting a number of slabs which represented a common road bridge structure. The corrosion of the steel within the experimental slabs was then accelerated prior to installation of a cathodic protection system. During the experiment corrosion potential of the steel reinforcement was monitored using half-cell measurement. Additionally the current flow between the cathodic protection system and the steel reinforcement was recorded to assess the degree of protection. A combination of theoretical calculations and experimental results were then collated to determine the design life of this cathodic protection system. It can be concluded that this sacrificial anode based cathodic protection system was effective in halting the corrosion of steel reinforcement in the concrete slabs studied. Both the corrosion current and half-cell potentials indicated a change in passivity for the steel reinforcement once sacrificial anodes were introduced. The corrosion current was observed to be sensitive to the changes to the exposure environment. Based on the experimental variables studied the design life of this sacrificial anode can be taken as 26 to 30 years.

KEY WORDS: CONCRETE DURABILITY; CATHODIC PROTECTION; HYBRID ANODES, SACRIFICIAL ANODES; CONCRETE REPAIR, HIGHWAY STRUCTURES, MONITORING, DESIGN LIFE.

1 INTRODUCTION

Reinforced concrete is one of the most versatile and high performance construction materials and has been in use for hundreds of years. There are vast arrays of civil engineering structures that incorporate reinforced concrete such as bridges, water retaining structures, multi storey buildings and maritime structures. Many of which have been in service for decades, leaving the civil engineers of today with an ageing infrastructure that must be maintained.

In many cases reinforced concrete structures have met and surpassed their design lives with no significant signs of deterioration. However it has been observed that the onset of corrosion of steel reinforcement has led to deterioration in many structures much earlier than expected. As discussed by Burke [1] deterioration of reinforced concrete due to corrosion of reinforcing steel is more prevalent in saline environments, this means that marine and highway structures such as jetties and bridges are particularly at risk of premature deterioration.

Based on the factors that have been found to affect corrosion all new build structures are designed with corrosion mitigation in mind, so that onset of corrosion is delayed as much as possible. Nevertheless, repair is essential for those structures that are actively corroding. The most commonly used method of corrosion control is cathodic protection which can be retrofitted to degrading structures relatively un-invasively. A large variable of cathodic protection is its effective design life (or service life after installation) which can have major cost implications; the prediction of this design life formed the key objective of this project. As such the effective design life of cathodic protection is an area of interest to all utilities involved in the maintenance of reinforced concrete structures. One such agency is the "Road Service of Northern Ireland" which is responsible for the maintenance of hundreds of reinforced concrete road bridges and other reinforced concrete structures. For the purposes of this project an idealised scenario was created with input from Road Service to examine the effectiveness of a specified cathodic protection system and predict the design life of such a system. The Road Service provided details of "CP-Tech Duo guard 500 Hybrid Sacrificial Anode System," which was of interest to them for the protection of concrete road bridges.

1.1 Outline of the experimental plan and project objectives

A number of concrete slabs were created with similar mix design as that of an ageing road bridge. Corrosion in the steel reinforcement was accelerated using anode/cathode system and an external current source. A "CP Tech duo guard 500 sacrificial anode system" [2] was then installed as per the supplier's recommendations and current flowing to the anode and the change of half-cell values of the steel, etc were assessed to study the performance of the sacrificial system. The main objectives of the project were:

1. To determine whether the corrosion of steel reinforcement can be halted by the installation of sacrificial anodes.

2. To predict the design life of a sacrificial anode based on the mass loss of the anode over the period during which it is operational.
3. To compare the effect of placement/location and quantities of sacrificial anodes on the corrosion mitigation behaviour.

2 CATHODIC PROTECTION SYSTEM

In cathodic protection, a weak metal (known as a sacrificial anode) is electrically connected to an existing useful metal such as structural steel or rebar [1]. The weak metal becomes the anode of the system and corrodes readily, while the existing structural metal becomes the cathode and remains protected. Cathodic protection is dependent on the flow of current between anode and cathode and consequently there will be an ionic flow from anodic region to cathodic region. The current flow is maintained through an electrical connection, whereas the ionic flow relies on the presence of a conductive media such as concrete pore water. The most common use of cathodic protection in reinforced concrete is as a retrofitted system used to prevent further corrosion of steel reinforcement. This project will focus on retrofitted system that is installed on steel reinforcement which has already begun to corrode with the aim of controlling further corrosion.

2.1 Duoguard 500 Hybrid Anode

The anode used in this study was "CP-Tech Duo guard 500 Hybrid Sacrificial Anode" which is designed to act as impressed current anode in the short term and galvanic anode in the long term with the aim of offering the advantages of both types of cathodic protection.

During the impressed current phase an external direct current power supply is connected between the anodes and steel reinforcement in order to control the polarity of steel reinforcement (to make it negative). The anode is used here as the sacrificial metal that offers free electrons to suppress the corrosion reaction in reinforcement steel. This stage lasts for one week for these particular anodes. After the impressed current phase the anodes are electrically connected to the steel without an external power supply and therefore act in a galvanic manner and provide a long term protection. The assumptions here are: (1) The conductivity of concrete is sufficient to allow ionic mobility between cathode and anode, (2) The sacrificial anode goes into solution to release electrons which act to protect reinforcing steel. (3) The deposition of reaction products on the surface of sacrificial anode does not affect the long term performance of the anode.

The anodes used in this project were installed by drilling into a concrete surface; the anode is inserted and grouted in place. An advantage of probe style anodes is that the pathway between the galvanic anode and the cathode reinforcement is quite short resulting in an increased rate of current flow which in theory provides better protection while it also causes accelerated consumption of the galvanic anode. A general arrangement drawing for a probe style galvanic anode is shown in Figure 1.

3 EXPERIMENTAL REPORT

3.1 Phase 1: Production of slabs representative of an ageing highway bridge

The first stage of experimental programme was the design of the steel reinforcement to initiate rapid corrosion. 10mm and 40mm rebar were used to create a large cross sectional area ratio 1:16 to ensure that the 10mm steel positioned closed to the surface would readily become the anode during the forced corrosion stage while the 40mm steel acts as the cathode. Detail of the layout is given in Figure 2.

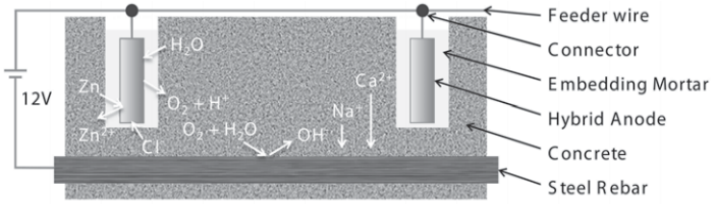
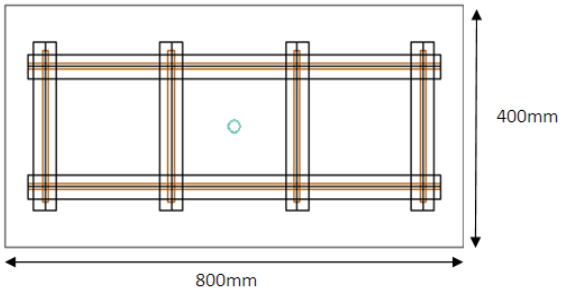
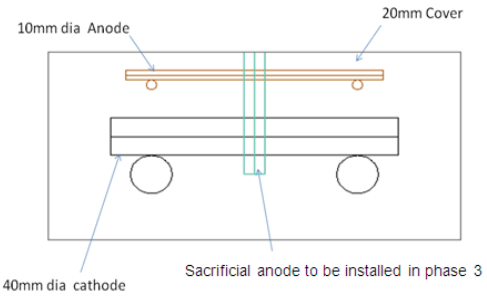


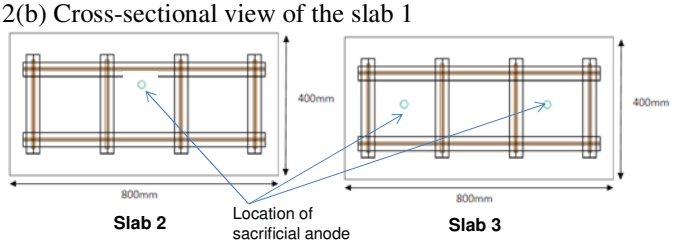
Figure 1. Diagram of probe impressed current arrangement and reactions that occur (Concrete Preservation Technologies, 2012)



2(a) Plan view of slab 1 showing position of anodes/cathodes Light green circle shows the location at which the sacrificial anode was installed in Phase 3.



2(b) Cross-sectional view of the slab 1



2(c) Plan view of slabs 2 and 3 showing the location of sacrificial anodes.

Figure 2. Layout of a slab showing anodes and cathodes with provision for the installation of sacrificial anode in the middle.

Horizontal spacings of 240mm centre to centre were chosen for both the 10mm and 40mm rebar, the perpendicular stirrups were also to be spaced at 240mm centres which are reasonably comparable dimensions with bridge deck design, the rebar had a length of 720mm so that the slabs would have a rectangular shape.

The vertical spacing between the top (anode) and bottom (cathode) steel was reduced to 95mm in order to ensure that the rate of corrosion of steel reinforcement could be accelerated. A minimum cover of 40mm was provided to all rebar except for the anode which had only 20mm cover to the top of the concrete surface.
Three slabs of identical reinforcement layout were created. The only change between the slabs is the location and number of sacrificial anodes installed during the corrosion protection stage. "Slab 2" had the sacrificial anode installed closer to the steel reinforcement and "slab 3" had two sacrificial anodes installed refer to Figure 2c for further details.

A concrete mix design was carried out in accordance with D.O.E Mix design [4]. The final mix details are shown in Table 1.

Table 1 Concrete mix details

	Mass of materials for 1m^3 concrete		
Material	**kg/m^3**	**Ratio by mass**	**Equivalent Ratio**
Portland Cement	305	0.127	1.000
Dry Sand	650	0.270	2.131
Basalt Aggregate	1290	0.537	4.229
Water	155	0.064	0.508
Calcium Chloride	0.5	0.001	0.002
Total	2400.5	1	7.870

The cement content of the mix was kept deliberately low (305kg/m^3) as this would have been a common cement content in historical mixes. Also the calcium chloride content was 1% by weight of cement; this would have been a typical quantity of admixture in the past and also aids the acceleration of corrosion. For monitoring and impressed current purposes a number of electrical wires were to be connected to the rebar; the method for installation of these is as follows:

1. A 6mm diameter 8mm deep hole was drilled into the 40mm steel at its midpoint. On the 10mm diameter rebar a 2mm diameter hole was drilled.
2. Titanium wire was cut into lengths and separate wires were inserted individually into the drilled holes.
3. On the 40mm diameter rebar a 5mm diameter pop rivet was inserted in order to secure the wire to the rebar. On the 10mm rebar the titanium wire was wrapped around the rebar and secured using insulating tape.

All electrical wire connections to the rebar were insulated by either coating with silicone (40mm rebar) or wrapping with insulating tape (10mm rebar) to prevent induction of corrosion at the electrical connection sites. The concrete for the slabs was mixed and poured on the 11/12/2012. The concrete surface was finished by hand float. After 5 days the slabs were removed from their formworks and moved outside to begin the accelerated corrosion phase of the project.

3.2 Phase 2: Acceleration of corrosion of steel in slabs

The accelerated corrosion schedule is shown in Table 2.

Programme of Accelerated Corrosion	
Date	**Activity**
20/12/2012	Slabs Moved Outside (No External Voltage)
20/12/2012 – 03/01/2013 (14 days)	Passive Corrosion Phase
03/01/2013 – 07/01/2013 (4 Days)	Impressed Current Corrosion Phase (7V External Voltage)
07/01/2013 – 17/01/2013 (11 Days)	Impressed Current Corrosion Phase (12V External Voltage)
17/01/2013 – 14/02/2013 (28 Days)	Passive Corrosion Phase 2 (No External Voltage)

Table 2. Schedule of activities to initiate corrosion in test slabs

After 11 days it was found that significant surface cracking had occurred along the lines of the rebar, these cracks had been developing throughout the impressed current corrosion phase. Rust staining was also observed weeping from the surface cracks on the slabs. A picture of the corroded slabs is shown in Figure 4. After it became clear that extensive corrosion was occurring, the power supply was switched off and the slabs were left ready for the installation of a cathodic protection system. During the accelerated corrosion phase half cell readings were taken at regular intervals to confirm whether corrosion was occurring.



Figure 4. Slabs undergoing accelerated corrosion

3.3 Phase 3: Installation of cathodic protection system and impressed current

The sacrificial anodes were installed in accordance with the manufacturer's instructions. The 12v power supply was connected one day after the installation of anodes and remained connected for seven days. The 12v supply should have induced enough current flow to effectively halt the corrosion of the 10mm anode steel causing it to become a protected cathode steel which is protected by the corrosion of the sacrificial anode. At the end of impressed current phase the external voltage was removed and sacrificial anodes were left to act passively within the slabs. Current flow between the

sacrificial anode and steel was monitored during this phase to study the activities. This is explained in Phase 4.

3.4 Phase 4: Galvanic cathodic protection and monitoring phase

Phase 4 of the project involved monitoring the sacrificial anodes while they acted in their passive galvanic capacity (no external voltage was applied during this phase).
An automated data recording system was set up to record the voltage difference between the sacrificial anode and 10mm steel reinforcement. In theory if the sacrificial anode is corroding to provide protection to the reinforcement steel there will be a current flow between the two. Therefore by recording the voltage the effectiveness of the cathodic protection can be assessed.

Current measurements were taken at 15 minute intervals between the dates of 22/02/2013 and the 19/04/2013. After a number of readings had been recorded in the lab it was decided that the slabs should be moved outside to test the effects of the increased moisture present in an external environment. The slabs were moved outside on 26/03/2013 and remained outside until the end of the monitoring phase. The sacrificial anodes were removed from the slabs by drilling a 50mm core hole at each anode location and the anodes were weighed to quantify the mass loss.

3.5 Phase 5: Data Analysis

Data analysis involved collating the recovered data from the automated recorder and the half-cell measurements to produce a set of test results. This is explained further in the next section.

4 RESULTS AND ANALYSIS

4.1 Half Cell Monitoring

Half cell monitoring was carried out over the duration of the project to determine the degree of reinforcement corrosion occurring within the slabs at a given moment.
Figure 5 shows an overview of the average half-cell results obtained during the key phases during this project. The three slabs performed in a similar fashion; all three corrode at a rapid rate during the accelerated corrosion phase (phase 2) and experience a sharp rise in half cell potential during the impressed current cathodic protection phase (phase 3).
Figure 5 also shows that during the application of an external current the average half cell potentials declined to between -300mv and -400mv which suggests that there was a high risk of corrosion of the reinforcing steel. The graph also shows that the largest drop in average half-cell potential occurred during the passive corrosion period before the impressed current was applied. During this period the potential value declined to between -680 and -700 indicating a severe degree of corrosion.

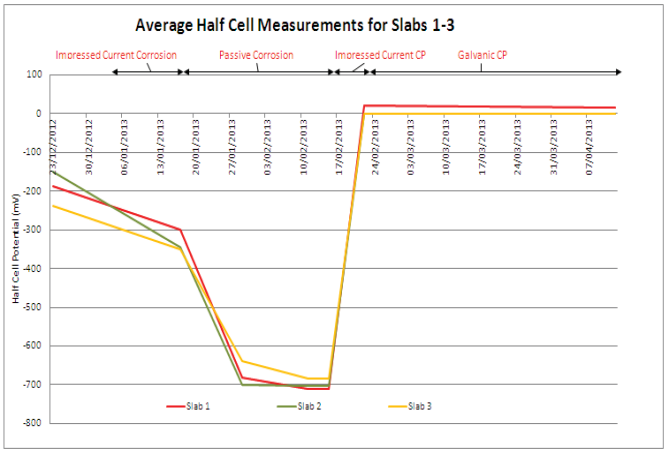


Figure 5 Half-cell measurements from each slab during different phases of corrosion

The half cell results complement the laboratory observations to confirm the presence of extensive corrosion on the reinforcing steel prior to the installation of the cathodic protection system. It can also be seen that the average half cell potentials increased exponentially after the commencement of the impressed current cathodic protection phase from between -650 and -700 to between 0 and 20. This massive increase in half cell potential suggests that the corrosion of the 10mm steel reinforcement had been halted. A number of subsequent half cell tests taken during phase 4 of the project showed that there had been no significant further drop in half cell potential. These results suggest that the corrosion of the steel reinforcement was indeed halted by the cathodic protection system and that the system continued to protect the reinforcement while acting in its galvanic capacity.

However it was also important to assess the pattern of the half-cell results to determine whether any areas in the slabs were experiencing much lower or higher half cell potentials than the others. Large variations in potential from one reading to the next may indicate that only localised corrosion is occurring as opposed to the desired wide spread corrosion of the 10mm rebar. It was possible to assess the pattern of corrosion within the slabs by generating a number of contour plots of the half-cell results. From contour plots it was found that steel positioned closer to the sacrificial anodes had higher half-cell potentials which may be further evidence that the corrosion of steel reinforcement was halted and subsequently protected by the cathodic protection. This data is available in the full project report [5].

4.2 Monitoring corrosion current

The sacrificial anode and reinforcement steel was connected electrically and the current flow in this circuit was measured by noting down the voltage values (Figure 6) across a known electrical resistance. This is a common procedure adopted in studying the corrosion of steel in laboratory based concrete specimens. The voltage difference relates directly through Ohm's law to the current flow between the sacrificial anode and reinforcement steel and as such should indicate the degree of protection offered to the steel by the cathodic protection system. If the readings remain above zero an ionic current will

be present and as a result the steel reinforcement can be considered to be protected. However if there is no voltage difference or a negative reading there will be no ionic flow between the sacrificial anode and steel reinforcement, this would mean that the steel could once again begin to corrode.

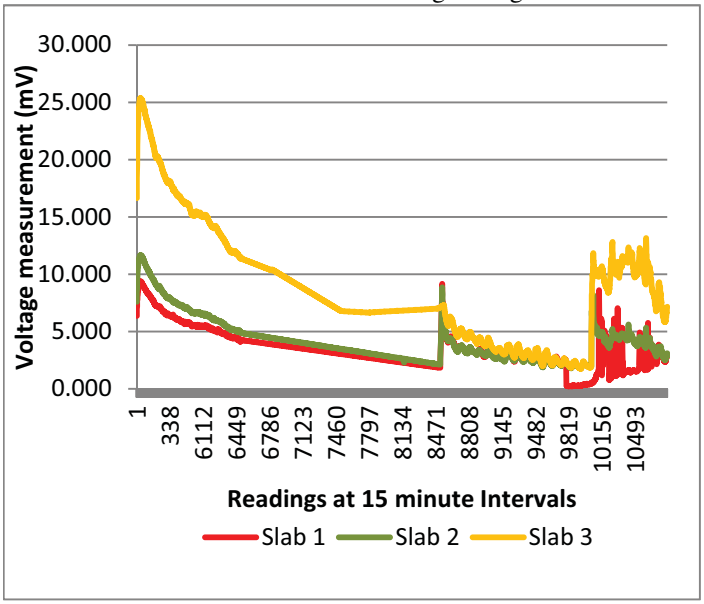


Figure 6. Potential difference between sacrificial anode and steel reinforcement measured on all 3 slabs.

From Figure 6, it can be see that the voltage peaks quite early near the beginning of monitoring with slabs 1, 2 and 3 peaking at 26mV, 12mV and 9mV respectively. An explanation for this is that voltage monitoring began immediately after the end of the impressed current cathodic protection phase, the externally applied current from this phase will have generated a high current flow between the sacrificial anode and reinforcing steel. This current may not have dissipated immediately, resulting in slightly higher voltage readings during the early stages of monitoring.

The trend of the voltage readings in each of the three slabs shows that as time progresses the level of activity decreases significantly. This indicates either that the level of residual corrosion activity is low or that the effectiveness of the system reduces over time. However it can be seen that once the slabs were moved outside (time = 9819) the voltage readings in all three immediately increased this is most likely due to the ingress moisture which increases ionic flow. This observation also suggests that the reason for the declining effectiveness may have been due to the low moisture environment of the laboratory.

During the period that the slabs are outside the voltage readings appear to fluctuate frequently, it can also be seen that at one point the voltage in slab 1 drops very close to 0. The primary reason for these variable results is weather; during the period where the slabs were stored outside there was an unseasonal drop in temperature and heavy snow for 6-7 days. During the period of snow any water present both inside and outside the slabs is likely to have frozen to form ice, ice is a less useful electrolyte than free water and as a result the current flow in the slabs is likely to have been inhibited. The low temperatures that were experienced by the slabs are likely to have reduced the overall ionic flow between the sacrificial anodes and the steel. The small fluctuations that are visible are due the daily changes between night and day where a freeze-thaw cycle occurs. These conditions were unexpected at the time of year when the experiment took place however they are none the less useful in assessing the performance of the cathodic protection system under varying weather conditions.

4.3 Design Life prediction using mass loss and voltage monitoring

In order to assess the design life of each of the sacrificial anodes it was necessary to calculate the total mass of material lost during their operational lives. There are two ways to do this, theoretically using Faraday's law or experimental by weighing the anodes and recording the variation in weight.

The theoretical process uses Faradays law which relates the charge passed to the mass lost. The calculated values of cumulative charge for slabs 1, 2 and three are 1677.212, 2023.722 and 4222.068 respectively. This computed by integration of the cumulative current graphs shown in figure 7 to determine total charge passed.

An example of the calculation for slab 1 is shown below:

Faradays Law states that:

$$\text{Mass Loss (M)} = \frac{\text{Charge Passed (Q)}}{\text{Faradays Constant } (\frac{\text{Q}}{\text{mol}})} \text{ x } \frac{\text{Molecular Mass of Material } (\frac{\text{g}}{\text{mol}})}{\text{Valency of Material}}$$

Faradays Constant = 96500 Q/mol

Molecular Mass of Zinc (anode material) = 65.382 g/mol

Valency of Zinc = 2

For Slab 1: Charge passed = 1677.212 Coulombs

Substituting values in the above equation gives a theoretical mass loss value of 0.568g for the sacrificial anode installed in slab 1.

Table 2 presents the actual mass loss calculated from experiments. It can be seen that for the anodes recovered from slabs 1 and 2 the mass losses were 0.7 and 0.9 grams respectively. Unfortunately both of the anodes from slab 3 were damaged during removal resulting in additional mass loss making their weights useless for the purpose of prediction of design life as a consequence they have been omitted from Table 3.

Table 2 Actual mass loss and experimental rate of consumption of anodes/day

Sacrificial anode reference	Weight Prior to installation (g)	Mass loss (g)	Rate of consumption (per day)	Predicted design life (Years)
Slab 1: Anode 1	187.8	0.7	0.0125	26.783
Slab 2: Anode 2	188.1	0.9	0.0161	20.831

For example, design life of Slab 1 Anode 1 is:

Design life = 65% of {(187.8g ÷ 0.0125 g/day)/365}=26.783

The value of 65% is widely used in the design of sacrificial anodes and refers to the estimated percentage of the anode that is expected to be consumed during its design life.

As given in Table 3, the theoretical mass loss (based on charge passed) for slab 1 and slab 2 were found to be 0.568 and 0.686g, respectively. Both values are comparable to the actual mass loss determined from experiments. The design life in Table 2 is calculated by assuming a constant rate of consumption of anodes for the entire service life. This shows a design life of 20-26 years. Such linear decay is not realistic for most structures. After the initial increase in consumption of charge, the charge required to maintain the passivity of reinforcement steel is likely to be low. If the latter phase is considered separately a more accurate service life can be estimated. This is referred to hereafter as variable decay approximation. To generate a more accurate prediction the cumulative charge measurements was split into two groups; the mass loss during impressed current phase (1 week) and the galvanic phase when voltage readings appear to plateau. This is termed as variable approximation and in summary this was made by treating the mass loss during the early stages of the experiment as an initial consumption and using the charge recordings during the less variable final 10 days of the experiment to generate a long term picture.

Variable Approximation of Design Life of Anodes				
Slab Reference	**Theoretical Mass Loss (g)**	**Mass loss per Anode (g)**	**Mass loss per day (g)**	**Variable approximation of Design Life (Years)**
Slab 1	0.063	0.063	0.006	52.861
Slab 2	0.113	0.113	0.011	29.524
Slab 3	0.245	0.122	0.012	27.249

Table 3 Design life estimated assuming a variable decay of sacrificial anodes over time

There are significant variations in the two sets of design life predictions. The weight change prediction assumes a linear decay of anode per design life and hence it is not comparable to the design life predicted using variable decay method.

Other notable observations are:

The design life's for the anodes in slabs 1 and 2 are very different although both slabs have the same steel arrangement and 1 sacrificial anode each. The location of installation of anode is the only variable between the slabs. The design life in Table 1 and Table 3 is estimated based on data observed for 56 days and the duration may not be sufficiently long to study the effect of this variable.

Slab 3 contained two sacrificial anodes as opposed to 1 anode each installed in slab 1 and 2. The increased anode configuration may have resulted in a more rapid protection offered for the reinforcement steel. This may justify the higher charge flow observed in Figure 7 for slab 3. A design life estimated based on the higher charge flow will always give a conservative estimate. In order to accurately estimate the design life of anodes in this configuration a long term study is required.

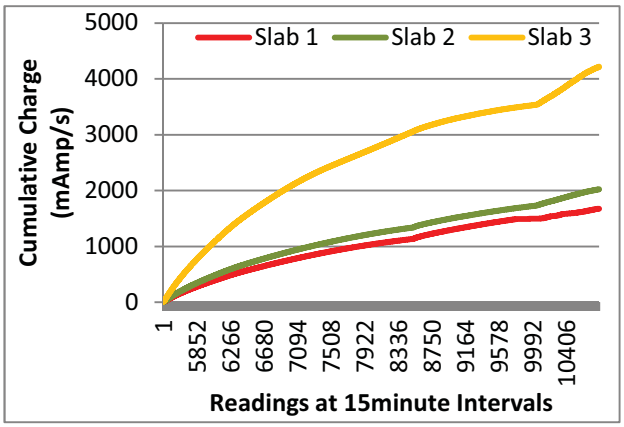


Figure 7 Cumulative charge flow for the 3 slabs quantified from the voltage measurements.

The experimental programme had limitations in terms of number of replicate specimens studied. Therefore, a long term study is recommended to validate the procedure/protocol outlined here for estimating the design life.

6.0 Concluding remarks

The results indicate that the CP-Tech sacrificial anodes have effectively controlled corrosion of the steel. The current (voltage) flow recorded shows the level of activity of steel reinforcement and also gives an opportunity to estimate the design life. Half-cell values confirm the findings deduced from the current measurements.

The current measurement indicates that the position of sacrificial anode does have a positive effect on the current flow during initial stages of CP system. This suggests a faster mitigation of corrosion or higher degree of protection of steel. However, the long term effect of the position of installation needs to be studied further. A similar positive effect was observed for slab 3 where 2 sacrificial anodes were installed.

Half-cell or corrosion current can be used to monitor the effectiveness of corrosion protection systems in real structures. The data seems to be sensitive to external weather events and moisture condition of the structure.

A simpler method for determining the design life of CP system was put forward using Faraday's law and current/voltage measurements. This needs to be validated based on long term data.

The following key variables should be given consideration for further work: (1) conductivity of the concrete, (2) changes in resistivity value between anode and cathode interface, (3) temperature effect and (4) role of corrosion residue that forms on the surface of sacrificial anodes on the working of anodes.

REFERENCES

[1] Burke, N. S., 1994. Corrosion Activity of Steel Reinforced Concrete Structures. 1 ed. Baltimore: ASTM Publishing.

[2] Concrete Preservation Technologies, 2012. *DuoGuard Hybrid Anode System.*http://cp-tech.co.uk/wp-content/uploads/2012/06/DuoGuard-Datasheet-R2.pdf

[3] Cotis, Bob; University of Manchester, 2003. *Performance of Sacrificial Anodes for use in Reinforced,* Manchester: s.n.

[4] Department of the Environment; 1988. Design of Normal Concrete Mixes, London

[5] Ward, Cillian S.N. J.M., 2013. Monitoring the Performance of a Cathodic Protection System in Reinforced Concrete. Queens University Belfast

A New Performance Based Method for Design and Maintenance of Reinforced Concrete Structures

C. Green[1], S. Nanukuttan[1], M. Basheer[1]
[1]Department of Civil Engineering, Queen's University Belfast
email: cgreen12@qub.ac.uk, s.nanukuttan@qub.ac.uk, m.basheer@qub.ac.uk

ABSTRACT: Research has shown that the cost of managing structures puts high strain on the infrastructure budget, with estimates of over 50% of the European construction budget being dedicated to repair and maintenance. If reinforced concrete structures are not suitably designed and adequately maintained, their service life is compromised, resulting in the full economic value of the investment not realised. The issue is more prevalent in coastal structures as a result of combinations of aggressive actions, such as those caused by chlorides, sulphates and cyclic freezing and thawing.
It is a common practice nowadays to ensure durability of reinforced concrete structures by specifying a concrete mix and a nominal cover at the design stage to cater for the exposure environment. This in theory should produce the performance required to achieve a specified service life. Although the European Standard EN 206-1 specifies variations in the exposure environment, it does not take into account the macro and micro climates surrounding structures, which have a significant influence on their performance and service life. Therefore, in order to construct structures which will perform satisfactorily in different exposure environments, the following two aspects need to be developed: a performance based specification to supplement EN 206-1 which will outline the expected performance of the structure in a given environment; and a simple yet transferrable procedure for assessing the performance of structures in service termed KPI Theory. This will allow the asset managers not only to design structures for the intended service life, but also to take informed maintenance decisions should the performance in service fall short of what was specified. This paper aims to discuss this further.

KEY WORDS: performance-based specification, diffusion coefficient, service life modelling, durability testing, *in situ* testing

1 INTRODUCTION

The prediction of possible durability problems in a structure would enable timely intervention for repair and maintenance and extend the service life of a structure. A premeditation of failures would not only give time for resource allocation but may also enable simple and relatively inexpensive repair procedures to be taken as opposed to regular cyclical repairs which cost more in the long term (Figure 1).

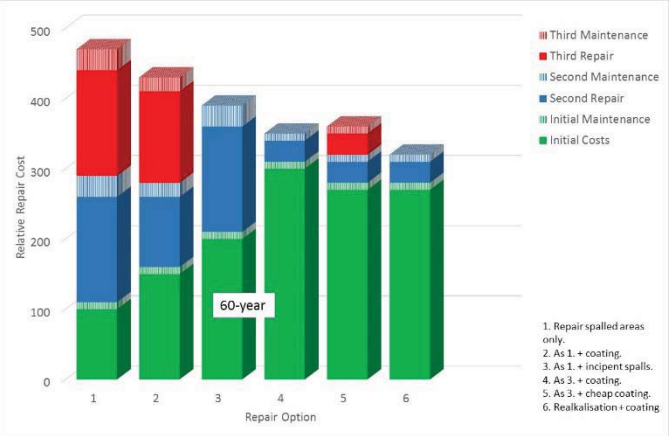


Figure 1: Cost implications of various repair methods. (Adapted from P. Robery)

The structures which undergo deterioration are generally the most crucial to society and the economy; for example shipping ports and main commuter carriageways. If this infrastructure was placed out of action for a period for extensive repair/maintenance/rebuilding it would have large cost implications across a region. These costs can be allocated to several areas: government costs, environmental costs (carbon emissions), commuter costs (extra fuel used in diversions) and time costs (wasted hours). Therefore it is important to examine the methods of concrete specification of new structures in order to examine if value for money is being achieved.

This paper aims to introduce the theory/reasoning behind Key Performance Indicators (KPI's), the concept of which is to reduce the numerous Performance Indicators (PI's) to the several most influential aspects/characteristics of a reinforced concrete structure which when analysed together produce a viable indication of the performance/service life of the structure.

2 CONCRETE SPECIFICATIONS

2.1 BS8500 and EN206

BS8500 was the original concrete specification; this specified concrete based solely on the strength of the concrete. The current concrete specification was introduced in the year 2000, titled BS EN206:2000. This specification is a step in the right direction in terms of taking into consideration other factors apart from concrete strength into the design process. However this standard is very prescriptive in nature and

details the minimum requirements for structures to reach either 50 or 100 years i.e. strict boundary conditions. In reality these structures are not guaranteed these service lives and premature deterioration often occurs. The next section details the process of concrete specification using the existing standards:

- To begin with; the structure is classified in regards to the exposure setting of which there are 18 these however can be categorised into 6 main areas:

X0: No risk of corrosion or attack
XC: Corrosion induced by carbonation
XD: Corrosion induced by chlorides other than from sea water
XS: Corrosion induced by chlorides sea water (see Table 1)
XA: Chemical Attack

- Define the slump class S1-S5 which will depend on the workability required and the structural form of the structure,
- Define a service life of either 50 or 100 years,
- Define a concrete cover depth which correlates with the exposure class,
- The combination of exposure class and concrete cover specifies the designer with a cement type, compressive strength, w/b ratio and minimum cement content,
- The last combination also has an associated maximum aggregate size.

Table 1: Exert from EN206 – Coastal Structures

Exposure Condition	Class Designation	Note
Corrosion induced by chlorides from sea water	XS1	Exposed to airborne salt but not in direct contact with sea water & Structures in coastal areas
	XS2	Permanently submerged & Concrete below mid-tide level
	XS3	Tidal splash and spray zones & Concrete in the upper tidal zones and the splash and spray zone

This process is very clinical with little room for innovation or diversion from the standards in addition it does not account for the influence of other mix components such as admixtures[1].

The exposure classes while there are many (18) in terms of those in the XS and XD chloride classes they are not specific enough in terms of chloride concentrations to which the structures will be exposed. Sea water salinity which affects coastal structures can range between 2-40g/l these ranges cause drastic differences in the service life of a RC coastal structure. These specifications have also led to the notion that a higher cement content results in a more durable concrete when in-fact this is not the case. Henderson (1998) has also highlighted that the only checks for durability performance are:

- concrete cover
- w/b ratio
- cement content

2.2 Performance Based Specifications

In the past 5-6 years there has been acknowledgement within industry of the need for performance based concrete specifications due to the apparent inadequacies with the existing prescriptive concrete specifications. BS EN 206 has begun to encourage the performance specifications with the addition of ‘‘Annex J: Performance-related design methods with respect to durability" this annex is rather vague in its allowances and requires long term data to reinforce any choices. In short the guidelines provided in Annex J seem to put the liability of the concrete mix with the designer and does not provide information about which durability properties are the most influential and therefore the durability parameter which should be monitored/measured. BS EN 206 while it mentions performance based concrete specifications it does not actively promote it or infer confidence within a designer to opt for the performance based method.

3 ASSET MANAGEMENT

The Highways agency identifies the holistic approach which should be taken with the management of structures:

"to maintain the structural integrity and safety by preserving and where necessary upgrading bridges and other structures to adequate standards at minimum cost over the life of the structure [2]*"*

While this approach is what the management agencies strive towards many fall short. America is an example of a country struggling to manage their infrastructure, In America every four years the American Society of Civil Engineers (ASCE) produces a report card detailing the state of the country’s infrastructure; the 2013 report card has given the country a D+/Poor across all infrastructure while also estimating a required investment of $3.6 Trillion by 2020.

3.1 Bridge Management Strategy (BMS)

The main RC infrastructure for most countries are bridges therefore the best way to evaluate the condition assessment strategies in various countries is to examine their Bridge Management Systems (BMS). The BMS are obviously focussed on bridges but often include the assessment of retaining walls and coastal structures as well. The next section goes into further detail on the BMS used in Ireland and the UK.

Ireland Condition Assessment Strategy

Ireland's National Roads Authority (NRA) adopted Eirespan as their chosen BMS in 2001 which is a customisation of the Danish DANBRO system (In Ireland the major arterial routes are managed centrally from Dublin, all other structures are managed by each counties individual Co. Council without the use of Eirspan) [3]. The strategy adopted by Ireland consists of a series of principal inspections which will produce a condition rating between 0-5 where; 0 relates to little damage and 5 relates to a high risk structure in need of maintenance. A special inspection is deemed necessary to determine the cause

of damage, the extent of the damage or the best repair method to be adopted [3].

DANBRO is a database system with the goal of assisting in the management of bridges by putting together a comprehensive report of the important information. DANBRO does not make decisions it consists of guidelines and management tools for use by inspectors [4].

Ireland's NRA have recently added the inclusion of GGBS to the specification of concrete structures in order to increase durability. The M4 motorway which opened in 2005 was one such road; at 34km in length all structural concrete consisted of 50% GGBS replacement. Along this stretch of road there were 19 over-bridges, 7 under-bridges and 3 underpasses [5]. The NRA aims to use GGBS replacement in any structural concrete which undergoes chloride exposures as a means of actively enhancing durability. The NRA have also developed performance criteria in the form of limiting diffusion values for a number of cements used in a harbour project in Ireland (Table 2); this shows that there is the possibility of further development of this performance based measurement to the wider structure community once a performance based strategy is fully investigated.

Table 2: Diffusion limits for various concrete types in a harbour project in Ireland [6]

Cement Type	Diffusion Coefficient ($x10^{-12}m^2/s$)
CEM I	7-18
CEM II/A	7-17
CEM II/B	5-10
CEM III/A	2-5
CEM III/B	0.9-3.5

Northern Ireland

In Northern Ireland (NI) the Roads Service is responsible for the maintenance of infrastructure. The current condition assessment strategy adopted with NI has been the same as Scotland; however the Road Service is currently in the process of implementing a new strategy which has been carried over from England [7]. This strategy is titled Bridge Condition Indicators (BCI) although it can also encompass other structures such as retaining walls. The ethos behind this strategy came from the County Surveyors Society (2000) as detailed in the quotation below:

"... essential to have a numerical indicator which could be used to determine whether the overall condition of road structures is deteriorating or not, in order to assess whether sufficient is being spent on bridge maintenance."

While this may seem like a step in the right direction further investigation shows this method is in fact a very indepth visual inspection which uses a factor based method to generate a condition value. This factor based method revolves around the severity and extent of deterioration which is then combined with the importance of the element.

3.2 Summary of Asset Management in N. Ireland and Ireland

The BMS used within the UK and Ireland do not facilitate/encourage forward planning required to ensure maximum economic benefit from their RC structures. They rely on condition assessment evaluations carried out by man not machine which in its nature can be subjective and speculative. The outputs of the reports do not produce a long term maintenance plan or quantify the performance of the structure it merely provides the next inspection date. However Ireland are beginning to understand the benefits of a performance based approach with the inclusion of diffusion limits for a variety of concrete mixes, these limits are still very general and do not seem to be linked to prediction of service life.

The best condition assessment strategies should incorporate service life modelling as a means of developing the appropriate and most cost effective maintenance plans. A convenient approach has yet to be developed in the UK and Ireland.

Through research into condition assessment strategies is can also be determined that may countries take a reactive approach as opposed to a proactive approach.

4 OVERVIEW OF CHLORIDE INDUCED DETERIORATION

The service life of a concrete structure is defined as the time from construction until a critical limit of a user defined technical property is reached. In the case of structures in chloride environments this user defined property is the corrosion of the reinforcement. This deterioration of a RC structure consists of two phases; the initiation phase and the propagation stage as illustrated in Figure 2.

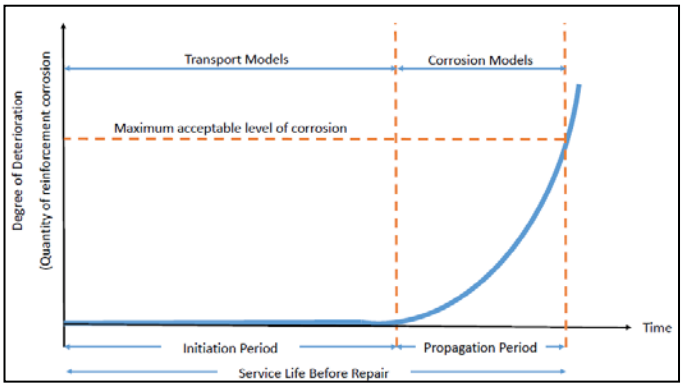


Figure 2 Conceptual Service Life Model adapted from Tuutti (1982)[8]

The initiation phase begins with the construction of the structure and is the period from initial construction until the point whereby the steel reinforcement loses its passivity as a result of the exposure environment of the structure. The depassivation of the reinforcing steel initiates the corrosion process also known as the propagation phase, the propagation phase continues until the structure is no longer deemed functional [9]. This paper focusses upon the initiation phase of the service life of a RC structure i.e. from the construction of the structure to the point where the reinforcing steel becomes depassivated.

Chloride ions may be introduced to a structure in a number of ways; for example through the use of contaminated marine aggregates, de-icing salts or direct exposure to a marine environment.

The failure of a RC structure can be attributed to two main groups of factors; failure due to the workmanship or a failure due to the materials used. These factors are elaborated below.

1. Workmanship: Concrete workmanship refers to the construction processes in placing the concrete. Workmanship can cause a number of durability problems such as inaccurate concrete cover to reinforcement and alteration of a concrete mix once it reaches site; in some areas it is common practice to add water to the concrete to make it more workable.
2. Material Failure: The failure of the concrete is a major durability problem and can be caused by multiple mechanisms both external and internal of the concrete.

The workmanship of a structure is difficult to define; the only measurable factor related to the workmanship of a RC structure is the concrete cover to the reinforcement. Alternatively material failure is a broad subject area with many interconnected factors. There is much literature in the area and therefore Figure 3 summaries the interconnectivity of the main influencing aspects of material failure due to chloride induced corrosion.

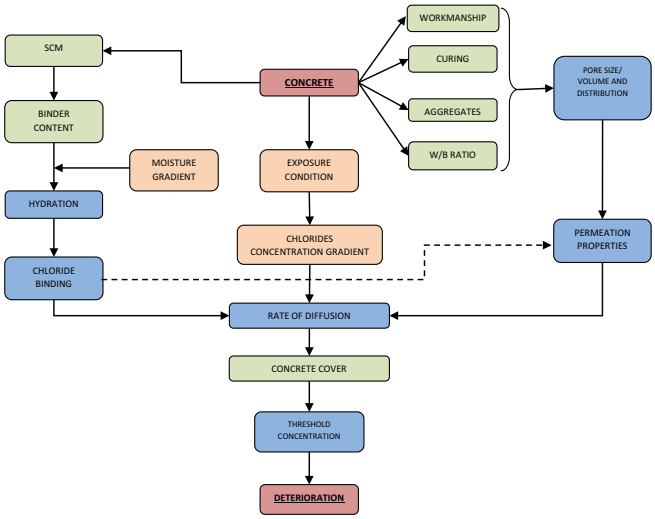


Figure 3: The links between the factors/variables which have a significant influence on the performance of RC concrete in chloride exposure environments

5 KEY PERFORMANCE INDICATORS (KPI'S)

The factors/variables in Figure 3 are Performance Indicators (PI's), they can give an indication of the state-of-health of the structure however for many of these indicators it is not feasible or possible to quantify these on existing structures. The PI's are numerous and not all of the PI's can be used to predict the service life of a structure.

Service life models vary and different models can use upwards of 10 PI's to produce their models. Figure 3 illustrates the multiple aspects of concrete which affect the rate of deterioration for a structure in a chloride environment. The figure demonstrates the major areas of PIs: they are the transport mechanisms, the environment, the mix details, the rate of corrosion and the chloride threshold for reinforcement corrosion.

The KPI's would provide information about the structure which is useful for either the designer or the asset owner for determining the service life (for new structures) or state-of-health of their asset (for existing structures). These KPI's will not necessarily be the same for both the asset owners and the designers as the information available to each group varies. Therefore the KPI's need to be tailored to the user.

For example the designer will have information on the concrete mix, i.e. w/b ratio, binder content etc., while the asset owner may not have this information. The asset owners will however have information on the current condition of the structure, i.e. surface chloride concentration, diffusion coefficient, etc through carrying out tests and inspections and from previous inspection reports/test data of the structures.

6 SENSITIVITY ANALYSIS

An in depth parametric study was carried out on the ClinConc service life model to reduce the number of PI's to a select few KPI's. A full analysis of the model identified the following parameters to have the most influence over concrete performance i.e. KPI's:

1) Porosity (which encompasses the concrete mix parameters),
2) Chloride binding parameters,
3) Chloride diffusivity,
4) Cover depth, and
6) Exposure conditions - temperature, surface chloride and initial chloride concentration,

The diffusion co-efficient was the most influential parameter and easily measurable by a number of different tests therefore it is examined next in term of usability by Asset Managers. The remainder of the KPI's will be analysed in subsequent papers.

7 DIFFUSION CO-EFFICIENT

A sensitivity analysis of the Clinconc service life model identified diffusion as the main driving parameter [10]. It should be noted that the diffusion coefficient of concrete mixes are not detailed in BS8500 or EN 206. There are several methods to measure the diffusion coefficient of concrete which vary in complexity, destructive nature and time consumption. The next section examines two tests available to measure the diffusion coefficient and their applicability to the asset management sector. To compare the tests a set of 12 concrete mixes have been examined using each test method. These concrete mixes are detailed in Table 3 (The mixes highlighted are those which are available for use in the European concrete standards).

Table 3: Concrete mixes which were tested

Binder	w/b		
CEM I	0.35	0.45	0.65
CEM I +35% GGBS	0.35	0.45	0.65
CEM I +65% GGBS	0.35	0.45	0.65
CEM I +35% PFA	0.35	0.45	0.65

7.1 Non-steady state diffusion co-efficient NTBuild 492

The non-steady state migration test is the EU industry accepted method of the determination of the diffusion coefficient within a concrete structure. However the test is destructive requiring a core to be taken form the structure and also is very time consuming in terms of man hours (30hrs).

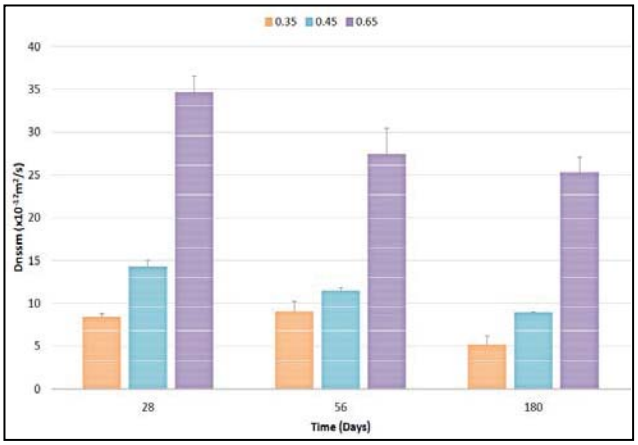


Figure 4: CEM I concrete tested over a 180 day period for the 3 different w/b ratios

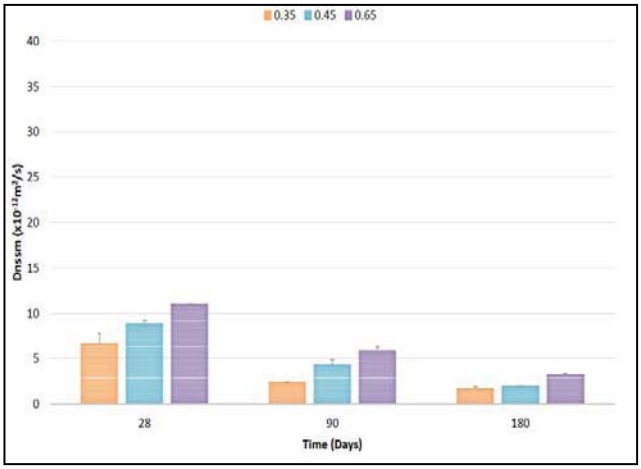


Figure 5: CEM I +35%GGBS concrete tested over a 180 day period for the 3 different w/b ratios

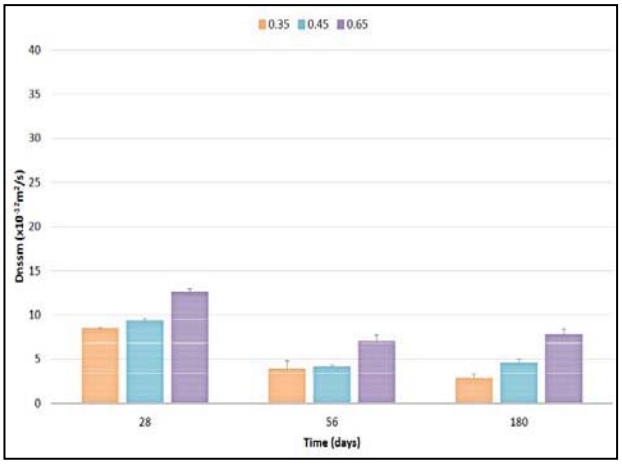


Figure 6: CEM I +65%GGBS concrete tested over a 180 day period for the 3 different w/b ratios

The results provide the expected trends of an increase in diffusion coefficient along with an increase in the w/b ratio. The graphs also detail the reduction in diffusion over the 180 day test period. When comparing the CEM I concretes and the CEM I plus GGBS concrete binder combinations it can be seen that the addition of GGBS provides a significant decrease in the diffusion coefficient compared with the CEM I concrete. When the CEM I concrete is compared with the CEM I plus PFA concrete, the PFA combination is actually higher in diffusion coefficient in the early stages however the decrease in diffusion coefficient over time is much sharper in the PFA concrete than the CEM I concrete.

It should be noted that these differences in diffusion are not visible in the concrete design codes.

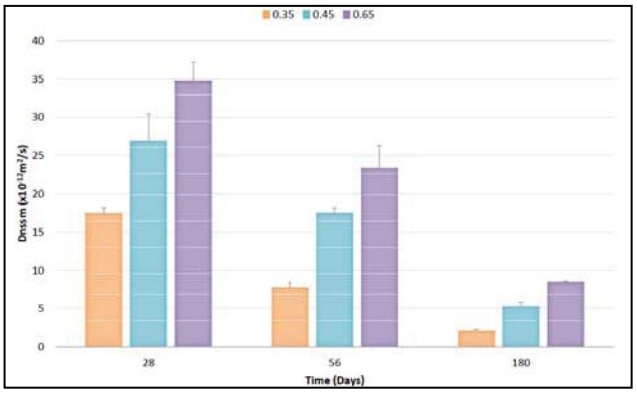


Figure 7: CEM I +35%PFA concrete tested over a 180 day period for the 3 different w/b ratios

7.2 Permit Ion Migration Test

The Permit Ion Migration Test (Permit) was developed at Queen's University Belfast; it is a site based test of the concrete diffusivity. The Permit test is a non-destructive test which mimics the lab based NTBuild 492 non-steady state migration test to provide an *insitu* diffusion co-efficient ($D_{(insitu)}$) over a shorter test period of between 6-8 hours depending on the concrete [11]. This test would also prove less expensive than the NTBuild 492 due to the lack of coring, laboratory analysis and materials required. The same 12 concrete mixes were tested using the Permit Ion Migration test.

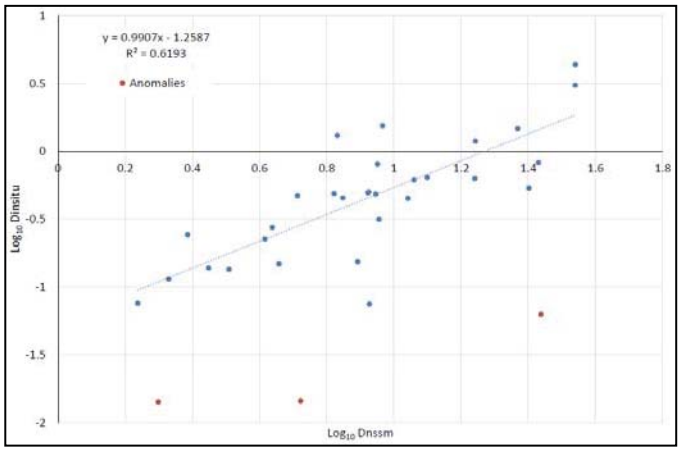


Figure 8: Comparison between D_{nssm} and $D_{(insitu)}$

Figure 8 illustrates results in comparison with the $D_{nssm.}$.The results show a reasonable level of fit (R^2=0.6193) after the

removal of the highlighted anomalies; there is also a defined relationship of:

$$y = 0.9907x - 1.2587 \quad (1)$$

7.3 Summary of Diffusion Tests

The three tests detailed in this paper have varying uses to asset managers. While the NTBuild 492 test is the most accurate and the accepted industry standard it is a destructive, expensive and time consuming test. As is industry standard to take cube samples to test for concrete strength, it could also be considered to take a small concrete slab sample to carry out the NTBuild 492 migration test to understand the base line of concrete diffusivity using this test.

The Permit test is shorter in duration and with a few units multiple tests could be carried out simultaneously over the course of a day, there is also a good relationship between the Permit and NTBuild 492.

This analysis has shown that there are feasible methods of quantifying the most influential of the durability characteristics in order to provide some sort of condition assessment of existing structures or quality control of new structures.

8 DEVELOPMENT OF KPI GUIDELINES

Table 4 is the beginning of a KPI database for 12 concrete mixes from BS 8500. The remaining KPI's would also have to be incorporated into a database. The result of which would be a practical method of determining the concrete performance which is able to be carried out with tools which are less destructive and time consuming.

Table 4: NTBuild 492 diffusion coefficients ($x10^{-12}m^2$) of the laboratory test concrete at t=180days

	w/b ratio		
Cement Type	0.35	0.45	0.65
CEM I	5.162425	8.933755	25.23595
CEM I+35%GGBS	2.8049	4.547653	7.797228
CEM I+65%GGBS	1.72698	1.986667	3.230447
CEM I+35%PFA	2.134321	5.277593	8.455914

9 CONCLUSIONS

This paper has begun the development of the KPI strategy by focusing firstly on the diffusion coefficient. The paper has shown how the diffusion coefficient should be a factor to take into consideration in the design of concrete structures due to the large variations in values across a range of cement combination types which the designers may not be aware of the range in variations. The use of the diffusion coefficient as both a factor to use in the design of RC structures and as a means of evaluating newly built and existing structures should be more apparent.

The diffusion coefficient is just one a number of KPI's, The next stage is to introduce the remaining KPI's in combination with the diffusion coefficient to produce a method of quantifying the remaining service lives of the RC structure under investigation as opposed to visually determining the service life of a structure.

References

[1] H. Beushausen, "The use of performance-based specifications to prevent repair of rein- forced concrete structures," in *Concrete Solutions*, 2012.

[2] Department for Transport, "The Department of Transport's Road Business Plan," 1988.

[3] L. Duffy, "Development of Eirspan: Ireland's bridge management system," *ICE Bridg. Eng.*, no. BE3, pp. 139–146, 2004.

[4] J. Lauridsen and B. Lassen, "The Danish bridge management system DANBRO," in *Management of Highway Structures*, 1999, pp. 61–70.

[5] ECOCEM, "ECOCEM GGBS: Case Studies, M4 Motorway Bridge Structures.," 2013. [Online]. Available: http://www.ecocem.ie/about,case_studies,6.htm. [Accessed: 22-Aug-2013].

[6] S. Srinivasan, A. S. Silva, S. V Nanukuttan, and M. M. Salta, "DuratiNET Concrete Strucutres: Durability factors and requirements," 2012.

[7] S. V. Nanukuttan and C. Green, "Conversation detailing the condition assessment strategies adopted by Northern Ireland Roads Service," 2013, p. N/A.

[8] B. Martin-Perez, "Service life modelling of R.C. highway structures exposed to chlorides," Toronto, 1999.

[9] C. L. Page, "Basic principles of corrosion," in *Corrosion of Steel in Concrete RILEM Report 60-CSC*, P. Schiessl, Ed. 1988.

[10] C. Green, S. Nanukuttan, M. Basheer, and D. Robinson, "The introduction of Key Performance Indicators (KPI) for predicting the state-of-health of reinforced concrete structures in chloride environments," in *International Congress on Durability of Concrete*, 2012.

[11] S. Nanukuttan, "Development of a new test protocol for the Permit Ion Migration Test", PhD thesis, Queen's University Belfast, 2007.

Opportunities for Innovation in Offshore Geotechnical Engineering

Robert, B. Gilbert[1], David Bruton[2]
[1]The University of Texas at Austin
[2]Crondall Energy
email: bob_gilbert@mail.utexas.edu

ABSTRACT: Geotechnical engineering for offshore facilities has consistently advanced in developing new methods of design, techniques for site characterization and types of foundations. Fortunately, there are still ample opportunities to make further advancements through innovation:

1. Providing for foundations to move in a controlled manner rather than remain fixed. Flowlines in deepwater provide a great application for this approach. Trying to keep flowlines from moving as they expand and contract due to operational changes in temperatures and pressures can require significant restorative forces from foundations. However, allowing flowlines to move in controlled ways that maintain their functionality can be accomplished with much smaller and less expensive foundations. Can we develop technologies and design methods to accommodate foundations that move?
2. Developing foundations that rely more on the forces of nature versus man to be installed. A driven pile requires much more energy to be installed than will likely be applied in its service life under the most severe loading condition. Conversely, drag embedment anchors provide an example of a foundation that is essentially installed to its final penetration and capacity as it is loaded in service by nature. Can we conceive new foundation types that capitalize on this concept?
3. Predicting minimum possible capacities for foundations. Existing design methods focus on the mean or most likely value for the capacity and then utilize factors of safety or resistance factors to accommodate uncertainty. However, the reliability of a foundation is governed by the minimum possible capacity. Can we formulate methods to predict the minimum possible capacity and establish more reliable or efficient designs on this basis?
4. Improving understanding of the mechanisms that trigger debris flows. Submarine debris flows can run out for hundreds of kilometers and pose significant risks to offshore facilities. While advances have been made in mapping ancient debris flows, it is still difficult to predict what will cause them and how far they will go in the future. Can we establish soil properties and conditions leading to debris flows to better manage their risk?

Case histories and research will be used to illuminate these opportunities and hopefully motivate ideas for future research.

Concrete – Making an Impact

Roger P. West, Associate Professor, Department of Civil, Structural and Environmental Engineering, Trinity College, University of Dublin, Ireland
email: rwest@tcd.ie

ABSTRACT: Against a background of the economic depression and the decimation of the construction industry in Ireland, the academic sector has experiences very significant cut-backs for over five years, leading not only to re-structuring, but swinging commercialism and managerialism. This impacts heavily on the nature of the work which academics undertake in an engineering sector in which an additional integrated postgraduate year has had to be added to accredited courses. This has meant less not more time has been available for deep and meaningful research despite promises of innovation and entrepreneurship at the highest levels. More positively, in reviewing almost twenty years of Concrete Research in Ireland Colloquia/Symposia, the number and quality of papers presented remains by and large consistently high. In an area really only taught on advanced level courses, in this keynote paper an insight is provided into some practical examples of concrete impact research which summarises work undertaken in Trinity over the last two decades.

KEY WORDS:GRP, Impact, Steel Fibres, Waste Paper

1. BACKGROUND

At conferences, an audience rightfully expects a keynote speaker to provide sage advice on a technical subject, graphically illustrated, usually in overview, and I will try to do so in due course. A keynote paper can also be written in the first person and I shall use this latitude to express some opinions, as a career academic, which, hopefully, may stimulate some debate. It would be disingenuous of me to deliver a keynote without making observations on the climate in which we all make our contribution to the concrete legacy in Ireland. The emergence of "green shoots" in the bottom of the steep canyon does not mean we see green pastures when viewed from above.

To begin with, the financial cuts in third level education have been equally as savage as elsewhere and, against a background of Croke Park and Haddington Road commitments, bludgeoning commercialisation and managerialism has infiltrated the third level sector. Where heretofore one may have thought of education and research as being client driven, it has now become customer driven – a subtle change in which, instead of service with integrity, minimum standards of satisfaction are promised, measured and delivered, without full recognition of the effects on thoroughness and, more importantly, research. While this may seem harsh or vague, I will give some specific examples to illustrate how the ability to provide leadership in education, research and innovation is being seriously compromised, in my opinion.

2. CONCRETE RESEARCH COLLOQUIA/SYMPOSIA HISTORY

But first, let me review the series of research gatherings which have taken place since its inception at the 1995 decennial "Concrete Practice in Ireland" symposium [1] so ably organised by UCD every decade over thirty years since 1965. A review of the statistics is given in Table 1 of the concrete research events instituted, particularly for younger researchers. It may be observed that so far as concrete is concerned almost 145 out of 350 papers delivered have been on concrete as the main theme at 8 events [2 – 9] in the intervening 20 years, organised on an entirely voluntary basis. For much of these two decades, papers were predominantly delivered by students and academics from QUB, NUIG, TCD and UCD but in recent years eight of the Institutes of Technology (CIT, DIT, AIT in particular) and an increasing number from industry have made contributions as lead authors. The evolution of the series, with its amalgamation with the bridge research community in 2008, has meant that other materials, particularly timber and soils, and structures other than bridges, have had their own parallel sessions and, indeed, Keynote addresses in recent years. Hence, the recent significant name change to a more inclusive, though unpopular in some sectors of the various constituencies, "Civil Engineering Research in Ireland", or CERI. This leaves the door open for other specialisms, such as environmental, energy or transport engineering to have an opportunity to put forward their own themes at future events, with full respect for extant strong research streams in these areas. In any case, there continues to be a very positive encouragement for young researchers to cut their conference

Table 1: Locations and paper themes for the bi-annual research events since 1995.(Legend: A: Concrete; B: Bridges; C: Geotechnical; D: Materials; E: Structures)

Event	Organiser	A	B	C	D	E	Total
CRI 97	TCD	16	NA	NA	NA	NA	16
CRI 01	NUIG	19	NA	NA	NA	NA	19
CRI 03	QUB	21	NA	NA	NA	NA	21
CRI 05	UCD	15	NA	NA	NA	NA	15
CRI 08 BRI 08	NUIG	15	24	8	NA	NA	47
BCRI 10	UCC & CIT	28	30	11	4	NA	73
BCRI 12	DIT & TCD	15	30	19	10	11	85
CERAI 14	QUB	15	16	9	21	10	71

teeth at the dais at the CERI event, as was the intentions of the early organisers.

What to expect in the future may well be determined by how the Institutes of Technology respond to their osmosis towards Technical Universities and how they strategise as to their role in higher education in Ireland. But behind all of this promise, is an unspoken and proverbial elephant in the room for all third level institutions, tectonic plates moving slowly towards earthquake events.

3. CHANGING LANDSCAPES IN ACADEMIA

The multi-faceted role of an academic has become more than the stereotype of teaching and undertaking research. Administration of courses (admissions, continuous assessment, evaluations, accreditation, examinations, etc), project managing research projects, pastoral care of students, performing safety audits, quality assurance, public relations for visitors against a background of swelling globalisation have all accumulated to the extent that volunteerism on, for example, national committees has diminished. But the longer term effect on the aspect of the job which always seems to be tagged on at the end of a busy day, namely research, is the overwhelming concern.

The tertiary education sector has been inculcated by managerialism and commercialisation, both necessary responses to savage cut backs in State support, which has led to quite inadequate funds to run previously successful degree courses. By way of example, I shall briefly describe just two areas where improvements have been delivered in the absence of additional resources on the ground as exemplars of the reality that is modern academic life. These surely comes at a cost.

3.1 Post Bologna Agreement Evaluation

An agreement between the States of Europe to harmonise education has led to the introduction of integrated year-long Bachelors/Masters courses added to Bachelors' degrees in engineering in Ireland, unwisely spearheaded by Engineers Ireland. For engineering degree courses to be accredited, this five year model is now the entry point into the profession. I say unwisely because the Institution did not have to fund the extra (level 9) year and while students must pay tuition fees, little if any of this is returned to the laboratories or in recruitment of staff to deliver the Masters courses. In fact quite the opposite – the moratorium on replacement of academic and technical staff, save for those posts funded by "non-exchequer" funding, persists to the detriment of the concrete research and teaching community. Due to the need to deal with ongoing deficits in-house, as a consequence of the continuing cut-backs in state support, the local funds to run materials and structural laboratories, for consumables and basic equipment renewal have all but disappeared. The persistent and on-going annual cutbacks means that inevitably the traditional concrete laboratories will struggle to modernise, and to adapt to new European stsndards, never mind to provide well-equipped laboratories for advanced teaching, research and commercial work.

So while a suite of additional modules of level 9 courses are being provided throughout the country for few extra resources, with attendant admissions, QA and examination, inevitably less time is available for deep thinking, ideas and inspiration in research. While the applied nature of the research projects demanded at a higher level by the Masters programmes is to be welcomed, the students do not have sufficient time for the depth, detail or complexity necessary to develop a deep understanding of topics.

While undoubtedly the introduction of Bologna-style courses into engineering will be good for graduates and for the profession of engineering as a whole in the long term, it will be just another facet of the marginalisation of research in universities and ITs.

3.2 Quality costs

A second example is the introduction of better quality assurance, accountability, transparency and health and safety, which are all of themselves laudable and inherently beneficial to the education sector. However, as educationalists argue for less examinations and more continuous assessment, this creates much more administration. As we have to prove that coursework has been submitted in case of legal dispute on failure of a subject, the hundreds of weekly reports, essays and tutorials all have to be signed in and checked prior to marking. Missing coursework has to be forensically sought. Furthermore, and rightly, students are entitled to feedback on their work in a timely fashion, all to protect the rights of the customer, the student, by imposed ubiquitous managerialism.

I am not suggesting that any of this is not desirable, but one needs to resource such activities, which of course, does not eventuate. If this was a facet of work imposed by legislation in the private sector, the cost would have to be inevitably borne by the customer – but in education, the fees we charge students are strictly controlled by the very government who is imposing these changes. Of course, academics execute these changes as fast as the dictates arrive, with as much efficiency and thoroughness as one can muster. However, the administrative staff, themselves hugely overburdened, simply informs academic what has to be done and so the belief in the existence of seemingly infinite elasticity of time of academics to undertake these new and ever-increasing list of tasks means that ultimately less time is spent on research. It may

seem that one has a reluctance to embrace change, to deny that quality of education must be delivered yet, in fact, none of these tasks of itself is unachievable or undesirable. But they all take time, time which means even less time for deep thinking and reflective contemplation on research matters. Inspiration should not be confined to moments waiting for a bus or at 4am when one wakes to scribble a note on the pad on the bed side locker.

Similar examples could be cited for exam procedures, postgraduate admissions, grant applications, PhD supervision, financial control of projects, etc, etc . Undoubtedly, procedures are much more regularised in line with best practice but at what cost?

There is practically no recruitment following loss of retiring or resigning staff and expertise in concrete technology is lost. This is partly because, unlike in the private sector, academics are solitary and isolated with no ongoing professional responsibility to clients when a senior member, academic of technician retires. Furthermore, few capital equipment grants have existed for engineering for 5 years because Colleges, I suspect, would be in deficit if cuts were not transferred to cost centres – hard commercialism - such that not enough funds reach the departments to run laboratories and courses, even postgraduate taught courses with high student numbers. That has raised an awkward question on the provision of third and fourth level education in a country of just 5 million people which has 7 universities and 14 Institutes of Technology – the emergence of amalgamated Technical Universities is rational in this sense. Indeed Prof Eugene O'Brien of UCD has raised this matter of rationalisation several times in the newspapers. However, in a customer-driven sector, choice where differences exist is preferable to uniformity and blandness.

3.3 Conclusion

No doubt there is the ability to perform the aforementioned tasks efficiently, with well thought out schemes. Indeed, if one agrees that none of these specific managerial imperatives is anything other than good news for the customer – the fact is that it is inevitable that there will be less time for reflection, deep thinking, inspiration, which leads to world-class research. We are being less than honest in fulfilling our roles as academics in the true sense of the term if we do not observe and discuss this.

Expertise takes decades to develop through focussed research, experiential learning and hard work. Research has to be deep, detailed and will usually be complex - there should be no quick fix despite what the customer might like to see honoured. Research is an absorbing journey for those who are lucky enough to have the opportunity to undertake it. But inspiration, "truthful thoughtfulness" [10], and deep thinking should not be corralled into the short gaps between one meeting and the next, one lecture and the next. Obtaining the depth of understanding that leads in due course to concrete expertise is not best served by the persistent and swelling imposition of the instruments of managerialism.

4. IMPACT ON CONCRETE

Having dealt with the impact of changing scenarios on concrete research, let me turn now to the main research topic – impact on concrete. Prof Simon Perry, the 8th incumbent of the 1842 Chair of Civil Engineering at Trinity College, brought substantial expertise in the impact resistance of concrete to Ireland. Indeed, in fundraising for the now aptly named Simon Perry Building, he had the ambition to drop objects through trap doors over four floors of the building onto a heavily reinforced basement floor! However, it emerged that constructing concrete elements that could resist more than an 8m drop height was beyond the technology of the day.

So far as impact strength is concerned, the fixation with 28 day compressive strength of concrete is dissolved when one realises that the strain rate on testing is vital in determining strength, that is, strength is not an absolute mechanical property of concrete (Figure 1) .

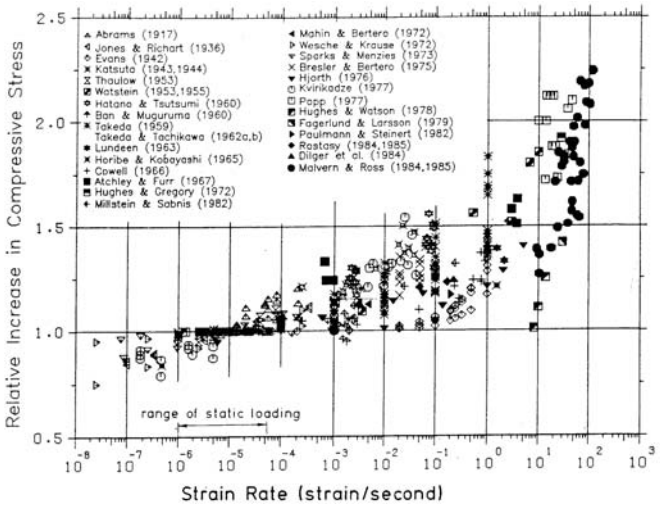


Figure 1: Relative concrete compressive strength with strain rate

The natural intuition when confronted with an impact loading scenario is to make something stronger to resist that action. Perry realised that confining concrete, passively or actively, enhanced its apparent strength considerably (Figure 2). In contrast, by researching novel lightweight blocks made with only polystyrene beads as aggregate, he was able to show how weak deformable concrete can also be a benefit when energy needs to be absorbed – peak loads can be reduced and impact durations can be extended, resulting in bearing crushing rather than explosive tensile reflective wave failure (Figure 3).

Having been inspired by this at an early age, this author subsequently undertook research into impact response on a variety of new materials, with the privilege of working with several gurus in industry. The balance of this paper will be devoted to giving just a few examples which expound the Perry principles in more modern materials.

4.1 Recycled Paper Waste concrete

Long before plastic fibres became so fashionable, a paper mill in Dublin was disposing of tons of plastics left over after paper had been recycled (Figure 4). Concrete made with 20% plastic waste as an additive crushes under impact (Figure 5), softened the damage on a structure below giving rise to lower but longer impact forces (Figure 6), much as the polystyrene concrete had done previously. This potential fender material

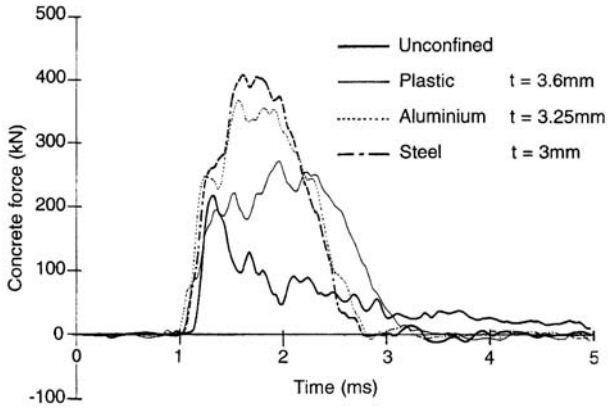


Figure 2: Strength improvement when cylinders with plastic, aluminium or steel sleeves confine the concrete



Figure 3: Footprint of impactor in Polystyrene concrete

never developed as the paper recycling industry collapsed at the time.

4.2 Glass reinforced concrete planks

Inland and Coastal Marina Systems in Banagher sell marina systems (Figure 7) around Europe and the distinctive feature is durable, thin and non-slip GRC planks. However, the



Figure 4: Recycled paper waste, mostly plastic fibres



Figure 5: Crushing failure of RPW concrete due to impact

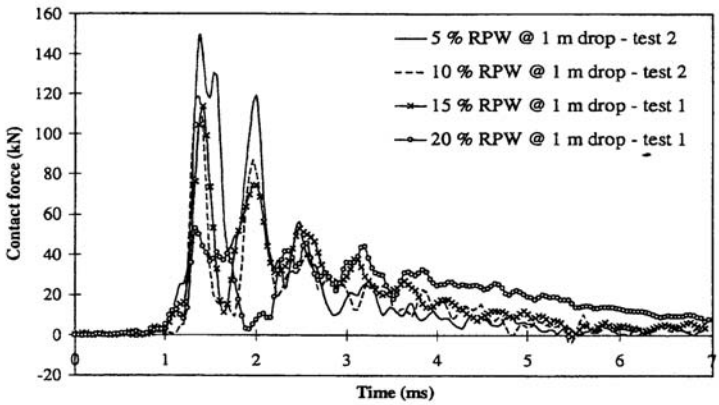


Figure 6: Reduction in peak stress with increasing RPW content

consequence of an impact due to an inadvisable jump off a boat, or the dropping of an empty gas cylinder could lead to the catastrophic shear failure seen in Figure 8. However, the addition of non-corrosive GRP bars allowed an unsafe impact failure to be developed into a safe one (Figure 9), where, while the concrete is still damaged by an impact, it retains sufficient residual strength to support a static load. The flexibility provided by the composite was parallel to timber planks, thus rebound after initial impact was also a feature of the dynamic response.



Figure 7: Marina pontoon systems with GRC planks

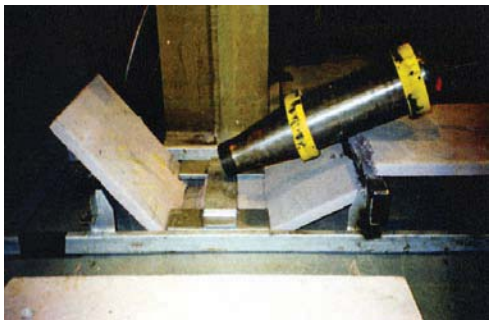


Figure 8: Shear failure of unreinforced GRC planks under simulated loading of a person jumping from 2m height

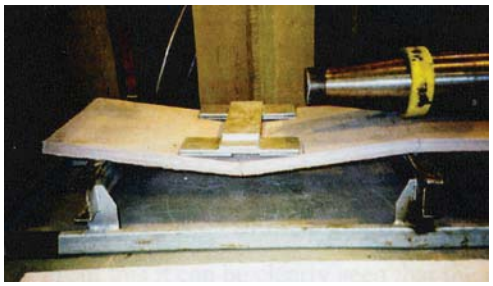


Figure 9: Safe failure of a GRC plank reinforced with GRP bars under impact

4.3 High Performance Fibre Reinforced Concrete

A 300mm square 63mm thick paving slab will disintegrate under an impact from a 70kg solid steel impactor dropped from just 0.5m (Figure 10). Even reinforced concrete slabs will exhibit classic shear plug failure under higher velocity impacts (Figure 11). Testing of very high dosage fibre concrete (100kg/m^3 of 50mm hooked steel fibres) improves the impact resistance substantially such that it will not perforate a similar slab when the impactor is dropped from 6m (travelling at approximately 50km/hr). The fibres not only bind the crack (Figure 12), utilising the pull-out resistance of the hooked end of the fibres, but due to the high tensile strength of the fibres, no fibres fail in tension, unlike their macro polypropylene equivalents.

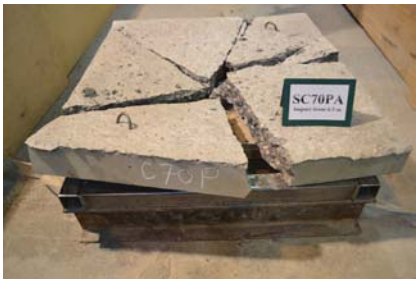


Figure 10: Classic flexural failure of plain concrete under just 0.5 drop of a 70kg solid steel mass

4.4 Fibre in paving slabs

An extension of this concept, developed in the laboratory, is the regular damage, and consequent trip hazard, created on many of our streets through the delivery of beer barrels (Figure 13). If the cork bag, acting as a sacrificial fender material, is missed when dropping an aluminium beer cask, the paving slabs will inevitably crack



Figure 11: Typical shear plug failure under a mesh reinforced slab subject to a 2m drop of 70kg mass



Figure 12: Crack pattern under a high dosage steel fibre concrete slab under 6m drop of a 70kg mass

under as little as one such impact. With illegal parking, the cracked slabs can no longer distribute the load down to the subgrade and a pot hole develops. By testing potential solutions in the laboratory one can identify the characteristic pattern of an inclined barrel impact (Figure 14 and 15), in which, incidentally, the edges of the barrel suffer some plastic distortion, a softer impact in which the missile as well as the target absorbs some of the impact energy. By using high dosage fibre concrete mixes it can be shown that although it is not possible for the fibres to prevent cracking (as the concrete has to crack to transfer the tensile stress into the fibres), they do provide residual load capacity by bridging the cracks. Thus, subgrade failure does not occur as it does in the unreinforced case and the pull out capacity of the fibres prevents a trip hazard from developing, allowing replacement in due course under resular maintenance. This solution would be easy for local authorities to implement at little additional expense. Incidentally, if one were to align the fibres in the slabs to lie on the horizontal plane, novelly using permanent magnets (Figure 16), the efficacy of the fibres improves and impact resistance capacity increases.



Figure 13: The use of a cork bag as a fender material normally prevents impact damage to paving slabs

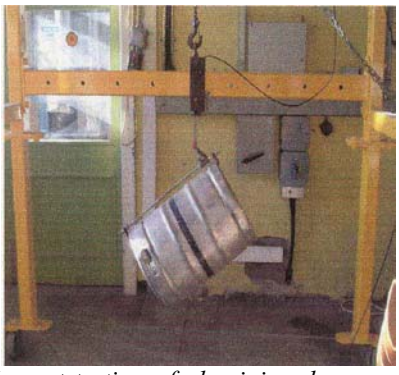


Figure 14: Impact testing of aluminium beer cask on paving slabs at different angles of inclination

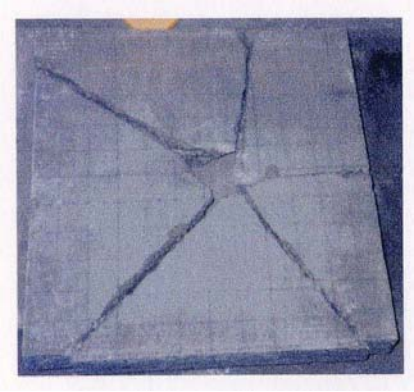


Figure 15: Typical impact pattern on paving slab under aluminium beer cask impact

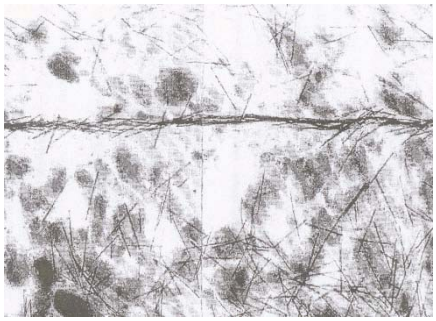


Figure 16: X-ray of thin slice of concrete slab showing how magnets successfully aligned steel fibres

4.5 GRP

The cases above show the resilience and capability of concrete, suitably reinforced, to resist low velocity hard impact loading. But a new composite product (GRP, Figure 17) produced by Relinea from Belfast, which is non-cementitious, has shown the way with regard to resilience during an impact. Using the same impact as described above at similar higher velocities, the response of a 38mm open grating is remarkably resilient – instead of the signature brittle puncture of concrete, or indeed the buckling of steel, GRP's response is highly energy absorbing (Figure 18) with minimal damage (Figure 19), maintaining structural integrity with significant rebounding of the impactor by as much as 3m with re-transferred kinetic energy. The ability of alternative materials such as fibres, high performance cements and GRP is transforming the impact resistance of structural elements.

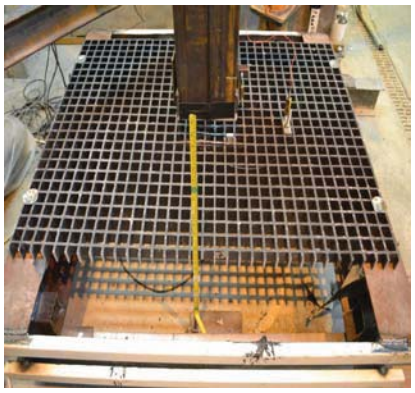


Figure 17:GRP gratings

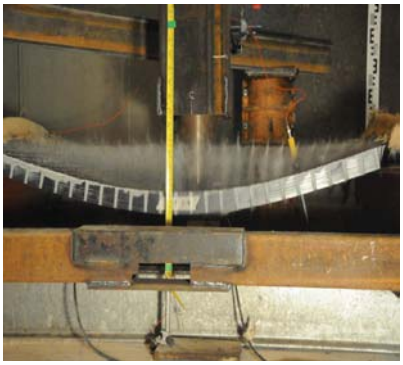


Figure 18: Maximum displacement of GRP grating under 6m drop height impact of 70kg mass



Figure 19: Minor tensile tearing of GRP fibres on the bottom surface post 6m impact by 70kg mass

5. TEACHING IMPACT

In conveying an understanding of the nature of the impact response in a conventional structural dynamics course, usually at postgraduate level, it is important not to focus on the mathematics unduly (though capability to the extent of being comfortable with maths is essential) but on the inherent characteristics of systems under impact loading. The fundamental equation for the response of a single degree of freedom structure shown in Equation 1 below can not only be easily modelled using software individually developed, but can also be observed in a simple well-designed experiment in the laboratory, showing the relative influences of stiffness, mass, damping and impact energy.

Formal examination of this understanding can be undertaken by allowing the students to bring with them into the examination hall a signed stamped A4 crib sheet on which they have extracted from the lecture notes the essential equations of dynamics – no examples, no text, no diagrams, just two sides of raw equations. In this way, as the student

selects these equations and writes them on to the sheet by hand, in advance the student subliminally develops an understanding of symbols and equations and an interpretation of dynamic behaviour for all aspects of the course naturally follows. Furthermore, more challenging and realistic exam questions can be asked, including an examination of the importance of energy transfer and damping rather than resonance in the response to impact loading on concrete.

$$u(t) = \frac{1}{m\omega_D}\int_0^t P(\tau)e^{-\xi\omega_n(t-\tau)}\sin\omega_D(t-\tau)d\tau \qquad \text{Eqn. 1}$$

6. CONCLUSIONS

If one does not see a growing child for a while, one is surprised to see how much has changed, change which is not seen if one is a regular acquaintance. The changes we are witnessing in third level education have occurred in steps over the last eight years or so, but this has come about not through some cataclysmic announcement for change – it is creeping and pernicious. Managerialism and commercialisation are stymieing research and innovation.

In a hypothetical academic concrete mix, if one likens academic staff to water and students to cement, water facilitates the growth and strength development of the cement. If technical staff is analogous to coarse aggregates, they form a substantial part of any strong concrete and reducing stone is detrimental to strength. And if equipment is representative of sand, a well graded sand makes concrete flow. But what makes concrete more efficient and perform at a high level is adequate finance, the admixture in the academic mix. If you reduce the w/c ratio to try to achieve higher performance without increasing the admixture dosage one ends up with unworkable concrete and much weaker strength. If one watches a concrete cube being tested in compression, one cannot see any cracks until it fails brittlely. Microcrack growth is creeping and pernicious. But, using acoustic monitoring, one can hear the cracks developing and growing. One does not need an impact load to get a catastrophic failure, but if one does not listen to concrete being stressed one will not be warned of unstable crack propagation. The academic mix is highly stressed – listen and observe.

REFERENCE

1. *Proceedings of Concrete Practice in Ireland*, UCD, Ed. M. Richardson, 1995 pp. 177.

2. *Proceedings of Concrete Research in Ireland Colloquium 1997*, TCD, Eds. R. West and D. O'Dwyer, pp.148.

3. *Proceedings of Concrete Research in Ireland Colloquium 2001*, NUIG, Eds. E.Cannon, pp. 146.

4. *Proceedings of Concrete Research in Ireland Colloquium* 2003,QUB, Eds. P. Basheer and M.Russell, pp.194.

5. *Proceedings of Concrete Research in Ireland Colloquium 2005*, UCD, Ed. C.McNally, pp.147.

6,.*Joint Symposium Proceedings of Concrete Research in Ireland and Bridge Research in Ireland 2008*, NUIG, Eds. E. Cannon, R. West and P. Fanning, pp. 460.

7. *Proceedings of Joint Symposium Bridge and Concrete Practice in Ireland 2010*, UCC and CIT, Eds. N. Ni Nuallain, D. Walsh and R.West, pp. 671.

8. Proceedings of Bridge and Concrete Research in Ireland Conference 2012, DIT & TCD, Eds. C. Caprani and A. O'Connor, pp. 533.

9. *Proceedings of Civil Engineering and Research Association of Ireland 2014*, Eds S. Nanukuttan and J. Goggins.

10. Gallagher, M, Academic Armageddon – An Irish requiem for higher education, The Liffey Press, Dublin, 2012.

ACKNOWLEDGEMENTS

Thanks are due to the many postgraduate students who were closely involved with the research projects described.

Thanks are due to Peter Deegan of Banagher Concrete and Karen Maguire of Relinea for support for two of the research programmes

Without the ingenuity of the technical staff at Trinity, many of these projects would have been unviable. Thanks in particular to: Chief Technicians Chris O'Donovan and Dr Kevin Ryan and technicians Sean Downey, Eoin Dunne, Michael Grimes, George Jones, David McAuley, and Barry McElhinney.

.

Ultimate Structural Capacity of Very High Dosage Steel Fibre Concrete Beams

Andrew Donnelly, Roger West, Abbas Kasim Mohammed, Michael Grimes
Department of Civil, Structural and Environmental Engineering, Trinity College Dublin, Ireland
email: rwest@tcd.ie

ABSTRACT: There is a perception that the addition of steel fibres to concrete beams confers enhanced flexural strength and ductility. However both of these contentions are misleading because, for normal dosage rates, the peak strength is determined by the uncracked concrete and fibres only provide post-cracking toughness (that is, the residual load resistance after concrete cracks) when they are loaded by imposing a displacement, which is not often the case in practice. Even then, pull-out of these high tensile fibres, not their ductility, causes a subsequent reduced load resistance. Furthermore, recently published research suggests that fibres can provide full structural action on their own, without any reinforcing bars, in cases of suspended beams. This project sets out to investigate whether, under high dosage rates, fibre reinforced concrete suspended beams tested under load and displacement control, offer additional flexural strength and a controlled failure mechanism in the different flexural responses, in the absence of any conventional longitudinal or shear reinforcing bars. The paper will describe a series of controlled tests on simply supported beams, which will demonstrate the veracity of these claims, thereby improving our understanding of the structural capacity contribution of random fibres in concrete.

KEY WORDS: Flexural behaviour; Steel Fibres; Steel Fibre Reinforced Concrete.

1 INTRODUCTION

Steel fibres have been used for crack prevention, predominantly associated with long-term drying shrinkage, since the 1970s and 1980s. They are commonly used in concrete slabs or pavements as these elements have a large surface area and drying shrinkage can be problematic. Steel fibres are added to the concrete mix in the batching plant. The steel fibres resist the non-structural tensile stresses created by the drying shrinkage issues. The use of steel fibres as a crack prevention method is well established. Research emanating from different parts of the globe [1, 2] suggests that equivalent longitudinal and shear performance can be attained using steel fibres as the exclusive source of reinforcement. While shear resistance in slabs on grade is well known, shear and flexural resistance is now suggested for suspended slabs and beams. This paper investigates these claims by testing concrete beams in flexure, with varying combinations of traditional reinforcement and steel fibres.

1.1 Steel Fibres

There are many different types of steel fibres which vary in length, shape, aspect ratio and diameter. Millions of tonnes of steel fibres are used successfully every year in the construction industry. Steel fibres have a high tensile strength which resists the drying shrinkage tensile stresses. In flexural testing the steel fibres rarely yield as they pull out before their tensile capacity is reached due to their relatively short length. Steel fibres are added to the fresh concrete mix during batching but care must be taken to avoid balling of the fibres, especially at high dosage rates. Typical dosage rates range from 30kg/m^3 to 60kg/m^3. In this testing, a dosage rate of 100kg/m^3 was used to test if equivalent reinforcing bar (rebar) flexural and shear performance could be achieved.

1.2 Concrete Mix

The addition of steel fibres to a concrete mix introduces a number of issues which affect the design of the concrete mix. The inclusion of high dosages of steel fibres decreases the workability of the concrete significantly so that the use of super-plasticizer must be considered along with a number of other changes to the design mix. To increase the bond between the concrete and the steel fibres, supplementary cementitious materials such as Ground Granulated Blastfurnace Slag (GGBS) can be used. The fineness of GGBS and the higher packing allows for a better bond between the steel fibres and the concrete paste.

1.3 Test Specimens

Five different test specimens were designed so a comparison between traditional reinforcement and fibre reinforced beams could be made [3]. The beam compositions can be seen in Fig.1. There is a plain concrete beam, a beam solely reinforced with steel fibres, a beam with U shaped longitudinal reinforcing bars, a beam with U shaped longitudinal reinforcing bars and steel fibres and finally a fully reinforced concrete beam with longitudinal steel bars and shear links. The fibres were 50mm long hooked fibres. The beams were tested using both load controlled and displacement controlled test methods with rates of 10kN/min and 1mm / min respectively. The two types of test method were used to differentiate ductility/toughness and pull out and to investigate the failure loads and modes of each specimen.

Serviceability conditions were not examined and the test regime was bespoke for the test programme.

2 METHODS

2.1 Experimental program

Five concrete beams were designed and ten were made, where each type was tested using load controlled and displacement controlled testing methods. In load control, the head of the actuator is moved to such an extent that the next increment in load is applied, a rate of kN/min. In contrast, in displacement control mode, the head of the actuator was moved at a particular rate (in mm/min) and the load resistance offered by the beam is measured. The beams in Fig. 1 were designed so that a comparison could be made in performance between the different beam types. It was not expected that full RC equivalence would be achieved by a fibre reinforced beam but the fibre and cement matrix choice were such as to optimize the fibre beam's performance. The plain beam and the beam with longitudinal reinforcement were chosen as upper and lower bounds so that the performance of the fibre reinforced beam could be put in perspective. Another expectation was that if steel fibres were added to a beam with longitudinal steel bars without links, the fibres would resist the shear forces to some degree.

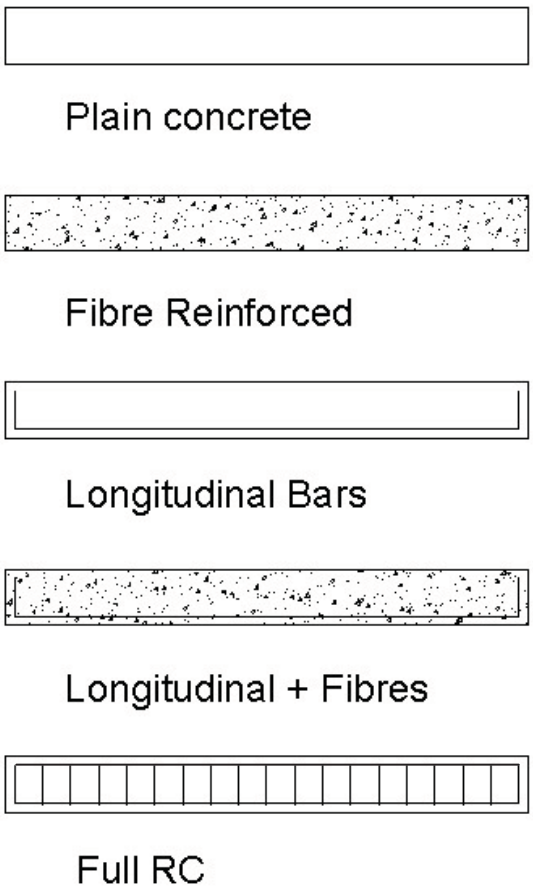


Fig.1 Beam test types

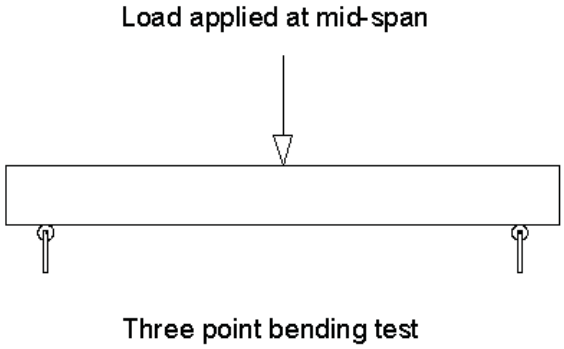


Figure 2: Load application arrangement

2.2 Experimental setup

The beams were tested using a three-point bending test (Fig. 2). This is unusual for fibre reinforced beam testing (normally four point bending is used to reduces shear in the middle third) and was selected to encourage the flexural cracks to occur close to the beam's centre. Maximum bending occurs at the mid-span and there is a lesser variability in the position of failure when compared with a four point bending test.

The beams were tested using a Zwick testing machine (Fig.3). which provided fine control on the application and measurement of load and deflection. Additional Linear Variable Displacement Transducers (LVDT's) were also used to measure the deflections of the beam. One LVDT was placed under each side of the test specimen to allow for eccentricities. An average value for deflection was used in the analysis.

Displacement controlled testing is the norm when testing steel fibre reinforced concrete beams [4, 5, 6]. This test allows the post cracking toughness to be evaluated. The displacement controlled test moves the actuator downwards at a set displacement rate. As the beam moves down the resistance to the displacement increases until cracking occurs. Once the concrete cracks the resistance offered by the beam to the displacement drops off. The actuator head moves down with much less resistance than it did prior to the crack, but at the same rate of displacement and so the beam does not fail suddenly. At this stage, pull-out of the fibres occurs slowly which is often misinterpreted as ductility. It is not ductility but rather post cracking toughness. However, the relative merits of different fibre shapes, aspect ratio and dosage can be observed in the study of this toughness and residual strength on pull-out.

In load controlled testing the actuator applies an increasing load at a constant loading rate. The actuator head moves down at the rate necessary to deliver the next load increment. When the beam begins to fail, the actuator tries to impose the next increment in load but as it cracks load capacity is reduced, it cannot reach the next load increment and the head moves

downwards rapidly, chasing the load and sudden failure can occur in the absence of post cracking strength. This test offers a more realistic outcome than the displacement controlled test because when a high load is applied to a real structure only redundancy and moment re-distribution prevent the structure from collapsing in the absence of ductility..



Figure 3: Load application in the Zwick beam test

3 RESULTS AND ANALYSIS

The performance of the fibre reinforced beams will be described in this section in comparison to baseline beams.

3.1 Steel Fibre Reinforced Beam

Fig.4 shows the load against deflection plot for the fibre reinforced beam in both displacement-controlled and load-controlled testing.

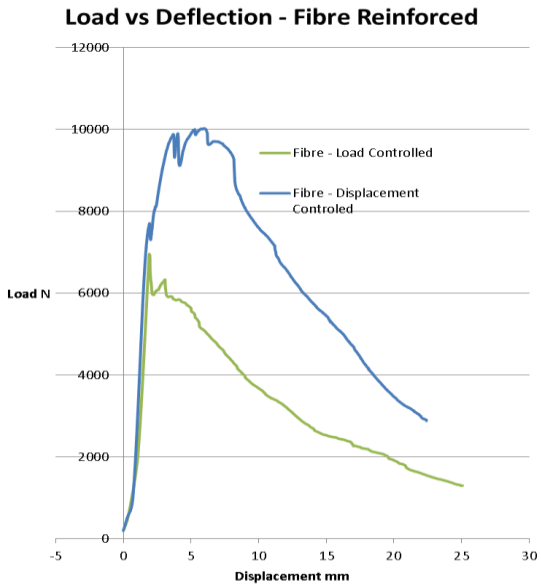


Fig 4: Load and displacement controlled fibre beams

Different behaviour can be seen from two typical fibre beams, one load, one displacement controlled. . Cracking occurs at approximately 7kN for both beams. For the displacement controlled test, post cracking toughness can be seen. As the concrete cracked the resistance of the beam dropped and the load offered to reach the next displacement increment also dropped off. Considering Fig. 5, the time against displacement plot, it can be seen that a gradual failure occurs, in the case of displacement control, with fibre pull-out offering the residual load capacity, not fibre ductility (see Figure 6) – the fibres are very high strength (of the order of 1200MPa) and their length does not allow them to reach their elastic limit.

The same beam, tested using a load controlled test, behaves differently. Post cracking, fibre pull-out occurs very rapidly (see Fig. 5) and a sudden failure was experienced, though the load displacement plot is misleading in this regard as few data

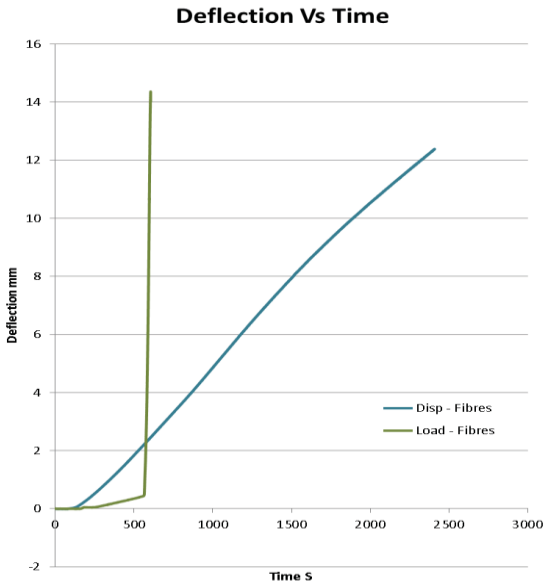


Fig.5 Beam central displacement over time for load and displacement control fibre beams



Figure 6: Pull-out of fibres in fibre reinforced beam only, in load control test

points exist on the graph post cracking, unlike the previous case.

3.2 Longitudinal Steel + Fibres

Fig.7 shows the load against displacement plot for the beam type with both longitudinal steel and steel fibres in both displacement controlled testing and load controlled testing.

Both beams performed very similarly. Similar ultimate loads of approximately 53kN were achieved. This beam contains longitudinal steel and steel fibres but it behaves like a fully reinforced concrete beam. There are no sudden failures, as can be seen in Fig.8. The steel fibres appear to be successfully taking the shear stresses in the concrete. This is a notable

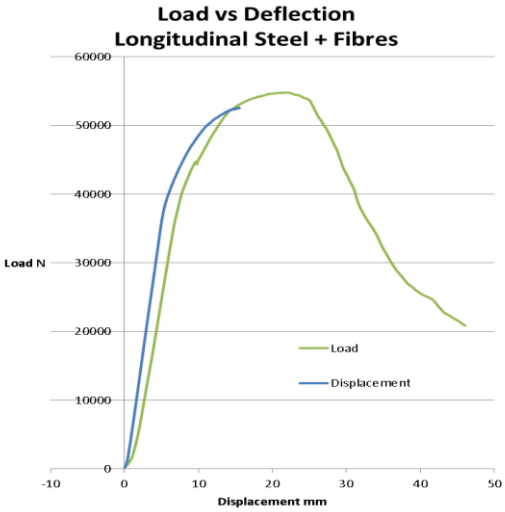


Fig.7: Load against displacement in load and displacement control for longitudinal with fibre beams

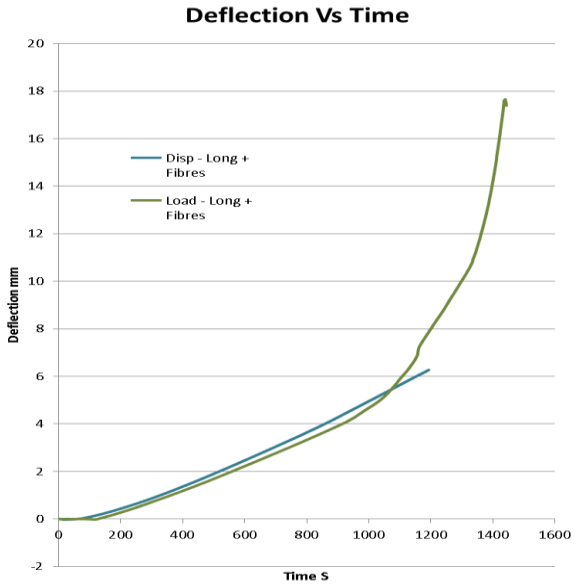


Fig. 8: Displacement against time in load and displacement control for longitudinal with fibre beams

result as shear failure was evident in the beams with longitudinal bars only.

3.3 Comparison of Beams

Fig.9 shows the plots for the plain, fibre reinforced and longitudinally reinforced beams for displacement controlled testing. The plain concrete beam failed suddenly at 4kN, as expected.

The fibre reinforced beam reached a post cracking ultimate load of 10kN. The fibre reinforced beam failed due bending but did not fail suddenly. The increase in ultimate load compared to the plain concrete can be attributed to the steel fibres. The gradual failure is related to the method of testing. The fibre reinforced beam fails slowly in the displacement controlled test. It is important to note that this is not due to ductility. The fibres pull out of the concrete due to a lack of anchorage and this pull-out behaviour is often attributed to additional ductility which is incorrect. This can be shown in the load controlled test as pull out occurs suddenly (Fig. 5). The longitudinally reinforced beam reached an ultimate load of 45kN with a ductile failure. Although the addition of the steel fibres increased the peak load it is not comparable to the longitudinal steel bars. This improved behaviour in

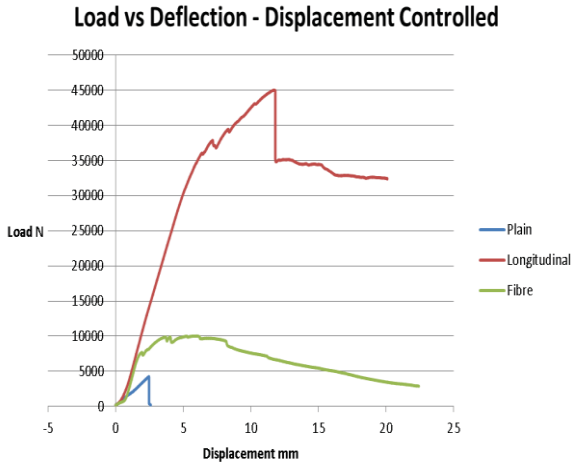


Fig. 9: Load against displacement plot for plain, fibre and fully reinforced beams in displacement control tests

comparison to plain concrete is often promoted but in reality plain concrete beams are rarely, if ever used to support structural loads so it is not significant. The fibre reinforced concrete beam does not perform nearly as well as the longitudinal steel bars.

Fig.10 shows the plots for the same three beams using load controlled testing. As before, the plain concrete beam failed suddenly at 4kN. This time the fibre reinforced beam also fails suddenly with an ultimate load of 7kN. This is noticeably lower than the same beam using displacement controlled testing, but it is still an improvement on the plain concrete beam. During the load controlled test, the fibre reinforced beam behaves quite similarly to the plain concrete beam – the apparent post cracking toughness is actually the recording of a

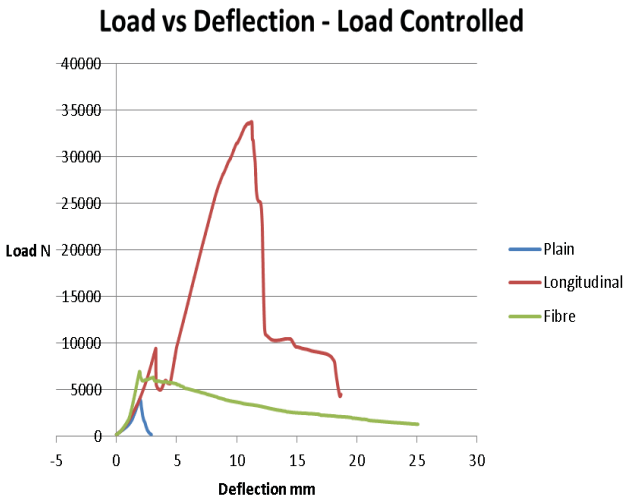


Fig.10: Load against displacement plot for plain, fibre and fully reinforced beams in load control tests

sudden failure. There is no ductility and a small increase in ultimate load. The longitudinally reinforced bar reaches an ultimate load of 34kN then fails suddenly in shear (see Fig 11). All three beams failed suddenly which is due to the nature of the test. The longitudinally reinforced beam clearly performs best. The fibres failed to perform as well as the longitudinal steel bars in terms of strength and failure behaviour.



Fig. 11: Failure mode of longitudinal beam with no shear reinforcement, in load control

Using steel fibres as the sole form of tension reinforcement does not achieve performance comparable to an RC beam. However the use of steel fibres provides shear resistance when used in conjunction with longitudinal steel bars. Fig.12 shows the load against deflection plots for the longitudinal, longitudinal + fibres and fully reinforced beams for displacement controlled testing. The beam which contained longitudinal steel failed in shear and reached an ultimate load of 45kN. With the addition of steel fibres the beam sustained a greater ultimate load of 53kN. The failure mechanism with the addition of fibres was due to excessive deflections. Both shear and bending cracks appeared but no sudden failure occurred. This improvement in shear performance is due to the addition of the steel fibres. The fully reinforced beam, containing

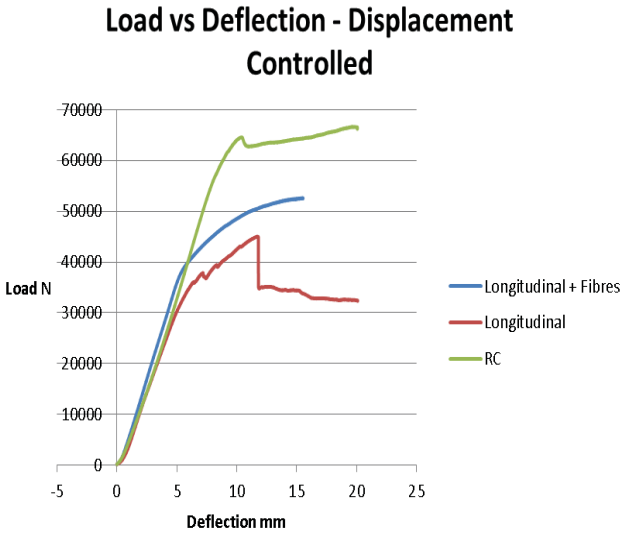


Fig.12: Ductile response of reinforced beams with and without shear links, in displacement control mode

longitudinal steel and shear links performed (failure load 66kN) better than the longitudinal and longitudinal with steel fibre beams as expected. The beam with longitudinal steel and fibres behaved similarly to the fully reinforced beam with reduced sustained loads. No sudden failures occurred and both beams failed in bending.

Fig.13 shows the equivalent tests to Fig 12 except where load control is used. The behaviour of those beams with shear reinforcement (either as links or fibres) are not much different in nature, with ductility evident. However, the onset of the elastic limit observed in Fig 13 is followed by sudden collapse, unlike Fig. 12, where some residual load resistance is seen post cracking. As previously explained, this is because the actuator seeks to impose the next load increment which the beam does not have to capacity to provide, the head moves quickly chasing the load and the beam collapses suddenly, initially by de-bonding the main rebar, then in shear.

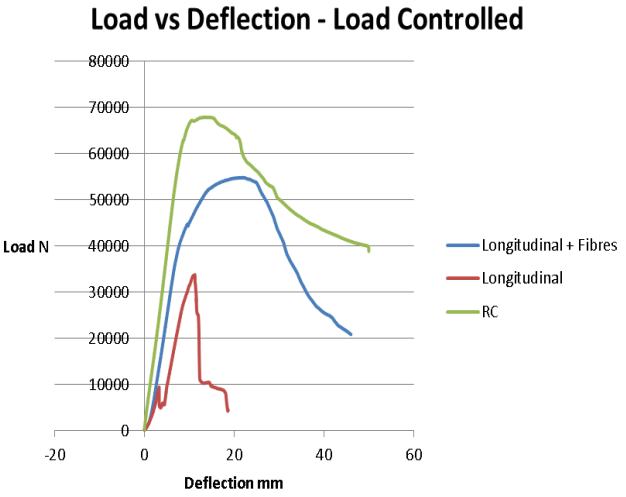


Fig.13: Response of reinforced beams with and without shear links, in load control mode – Longitudinal beams fail in shear

The addition of fibres allows for some increase in load capacity and allows rebar ductility. The fully reinforced beam outperforms the fibre reinforced beam significantly and failure is ultimately by crushing of the concrete after considerably flexural cracking and rebar ductility (see Fig. 14), as might be expected.
These graphs show that it is not possible to replace traditional longitudinal steel reinforcing bars with high dosages of steel fibres to resist the structural tensile force. Even with provision made for high steel dosages, improved bond due to GGBS and the use of C40/50 concrete, the fibres did not achieve RC equivalence. Additional load can be sustained in comparison to plain concrete but the fibres cannot sustain large tensile forces. The fibres themselves can sustain large tensile loads but they pull-out before they have a chance to become ductile. This result was expected as the fibres would have to have an equivalent cross sectional area in the tension zone as the steel bars. The cross sectional area of one fibre is approximately $1mm^2$. The number of fibres required in the tension zone, even if preferentially aligned, would be impractical for applications in the construction industry. Even high dosage rates ($100kg/m^3$) cannot provide equivalent cross sectional area. Even if this could be achieved, the fibres pull out due to inadequate anchorage / bond would dominate and further increased dosages would cause insuperable workability issues in placing the concrete.



Fig. 14: Crushing of concrete failure mode post ductility in displacement controlled test on RC beam.

4 CONCLUSION

The use of steel fibres as the exclusive source of structural tensile resistance does not achieve equal flexural behaviour, when compared to conventional reinforced concrete beams. Reduced ultimate loads and sudden failures occurred with the use of steel fibres.

Steel fibres do not add ductility to beams; rather they provide increased post cracking toughness when tested in displacement control only, evidence of fibre pull-out, not plasticity. The failure behaviour of beams greatly depends on the test methods.

There was evidence of enhanced shear capacity due to the fibres, though shear tests were not specifically conducted. The beams containing steel fibres instead of shear links performed similar to fully reinforced concrete beams. The addition of the steel fibres prevented sudden failures and bridged the shear cracks. Although a reduction in ultimate load compared to a fully reinforced concrete beam was recorded, the steel fibres added some structural shear capacity.

ACKNOWLEDGMENTS

The authors would like to thank the technical staff at the Department of Civil, Structural & Environmental Engineering at Trinity College Dublin.

REFERENCES

[1] Michels.J, Waldmann.D, Maas.S, Zurbes.A (2011) Steel fibres as only reinforcement for flat slab construction – Experimental investigation and design, *Construction and Building Materials*, 26, pp 145-155.

[2] Destrée, X. Concrete free suspended elevated slabs reinforced with only steel fibres: Full scale testing results and conclusions- Design examples. *International RILEM Workshop on High Performance Fiber Reinforced Cementitious Composites in Structural Applications*. Eds. G. Fischer, and V. C. Li. RILEM Publications SARL, 2006.

[3] American Society for Testing Materials. C293/C293M- *Standard Test Method for Flexural Strength of Concrete*.

[4] Pajak, M and Ponikiewski, T. (2013) "Flexural behaviour of self-compacting concrete reinforced with different types of steel fibers", *Construction and Building Materials*, volume (47), pp. 397-408.

[5] Meda, A. Minelli, F and Plizzari, G. (2012) "Flexural behaviour of RC beams in fibre reinforced concrete", *Composites: Part B*, volume (43), pp. 2930-2937.

[6] Conforti, A. Minelli, F and Plizzari, G. (2013) "Wide-shallow beams with and without steel fibres: A peculiar behaviour in shear and flexure", *Composites: Part B*, Volume (51), pp. 282-290.

Effect of fibre type and dosage on early age tensile strength of bedding mortar

J. Backus[1,2], M. Sonebi[1], T. Moore[2], D. Hughes[1]
[1]School of Planning, Architecture and Civil Engineering, Queen's University Belfast, Belfast, UK
[2]Larsen Building Group, Westbank Road, Belfast, Northern Ireland
email: j.backus@qub.ac.uk

ABSTRACT: This paper reports the results of a comprehensive study on the effect of the type and dosage of fibres on the early-age direct tensile strength of bedding mortar. Five types of fibres were used in mortar including polypropylene fibres (PPF), basalt fibres (BF), glass fibres (GF), polyvinyl acrylic fibres (PVAF) and polyacrylonitrile fibres (PACF) at varying percentage for a given binder composition. The direct tensile strength was determined at the age of 3 hours. The effect of these fibres on the workability of bedding mortar was also measured. The results showed that PVA and glass fibres increased the early-age direct tensile strength up to 2% dosage with PVAF exhibiting the best performance. The other fibres PACF, PPF and BF when the dosage increased above 0.5% led to a reduction of the direct tensile strengths and forming of clumps

KEY WORDS: Fibres, mortar, tensile

1 INTRODUCTION

The reinstatement of ironworks (manhole covers, access covers etc) creates a unique development of stresses in the bedding material that requires a tensile strength of 5 MPa and compressive strength of 30 MPa after 3 hours [1]. Inadequate bedding materials crack under these stresses making the ironwork unsafe and needing to be reinstalled. These reinstatements cost the UK an estimated £207 million per year [2].

Concrete and other cement based materials are the most widely used construction material [3] in spite of their poor performance in tension. As the tensile strength of concrete is normally only 10% of the compressive strength, fibres were incorporated to address this deficiency.

The introduction of fibres into concrete and mortars creates a composite material that has many desirable attributes. The fibres bridge micro-cracks that form by plastic and drying shrinkage thus allowing tensile loads to be transferred over these cracks and increasing performance. The downsides include increased costs, decrease in workability and limited strength gain. Furthermore, the physical and mechanical properties of the fibres such as length, diameter and bond also have an effect on the performance of the composite material.

The composition of rapid setting mortars is such as to reduce the likelihood of shrinkage and potentially reduce the formation of cracks, thus limiting the effectiveness of this attribute of fibre reinforcement. Therefore, the experiment discussed in this paper looks more at the contribution of fibres to direct tensile strength.

The addition of fibres can result in improvements of flexural strength, toughness, impact strength and resistance to fatigue [4] [5]. The reduction in micro-cracking may also improve the durability of concrete [5].

2 MATERIALS, MIX PROPORTIONS AND EXPERIMENTAL PROGRAM

The basic mortar mix consisted of a blend of CEM II in a proprietary rapid setting cement binder system, fine sands and a liquid polymer that created a w/b ratio of 0.16 to give a stiff mix. A defoaming agent, plasticiser, retarder and accelerator were added to reduce air voids content, maintain sufficient workability and control the open and setting times, respectively. This remained the same for all mixes with various additional fibres added at quantities according to Table 1 with approximate bulk densities shown in Table 2.

Table 1- Fibre percentages

Fibre percentages	0%	0.2%	0.5%	2%

Table 2- Fibre bulk densities

Fibre types	Glass	Basalt	PP	PVA	PAC
Bulk density[1] (approx.) g/cm^3	36	30	8	7	7
Specific gravity[2] g/cm^3	2.68	2.67	0.91	1.3	1.18

[1] measured [2] from company literature

2.1 Mixing and testing methods

The mix was placed in a mortar mixer (Figure 1) along with the liquid and mixed for 1 minute. The mortar was then placed in three dumb-bell shaped briquette moulds each fibre dosage (Figure 2) for in accordance with BS 6319-7 (British Standards, 1983) and kneaded into the moulds and the surface finished with a palette knife. The specimens were removed from the moulds after 1 hour and allowed to cure at laboratory



Figure 1 - Matest automatic mortar mixer



Figure 2 – Dumb-bell moulds

temperature (20±1°C and 55±1% relative humidity (RH)) until testing after 3 hours.

Tensile tests using dumb-bell specimen were carried out in accordance with BS 6319-7 (British Standards, 1983) with the specimens weighed and measured before being loaded at 1 mm/min until failure (Figure 3). The tensile force was then calculated using the maximum force and the area of the specimen.

3 RESULTS AND DISCUSSION

3.1 Effect of polypropylene fibres (PPF)

Figure 4 presents the variation of the mean tensile strength against the percentage of PPF fibres. It can be observed that an initial drop in mean tensile strength from 5.6 to 5.1 MPa at 0.2% fibre dosage occurs. This could be a result of air entrapment from the fibres [5] or due to the variability of testing. However, there is then an increase up to a mean strength of 6.1 MPa at 0.5% fibre dosage. At 2%, the volume



Figure 3 – Tensile loading of dumb-bell specimen

of fibres became dominant due to the low specific gravity which results in a drop of the workability with the mix became very dry. At this percentage of fibres, the mix was unworkable with a corresponding drop in mean tensile strength to 4.4 MPa.

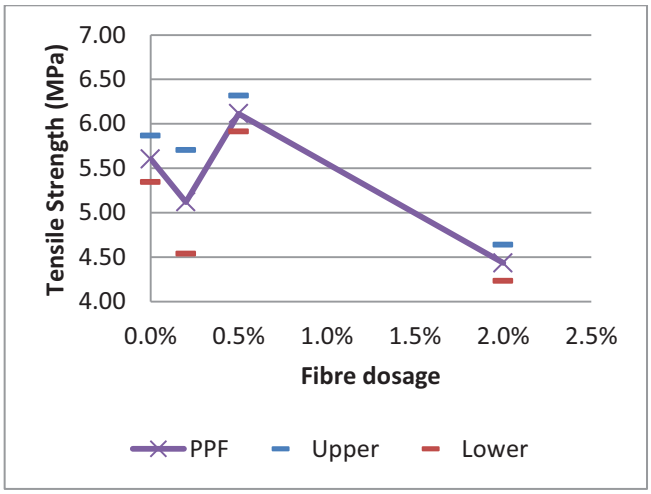


Figure 4- Variation of the tensile strength versus the percentage of polypropylene fibres

3.2 Effect of basalt fibres (BF)

Figure 5 presents the variation of the mean tensile strength with the percentage of basalt fibres. It can be seen that after an initial increase in tensile strength from 5.6 to 6.0 MPa, the mortar with more basalt fibres exhibited a loss of tensile strength. Continuing increase of the basalt fibres up to 2% led to a reduction of tensile strength to value of 5.5 MPa (Figure 5).

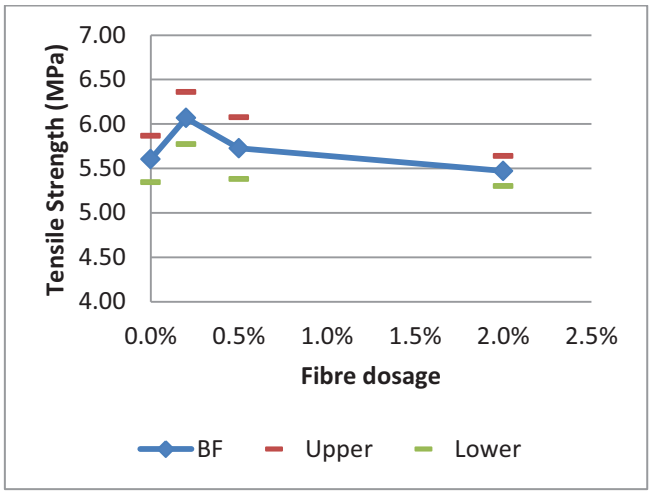


Figure 5- Variation of the tensile strength versus the percentage of basalt fibres

3.3 *Effect of glass fibres (GF)*

From Figure 6 it can be observed that adding glass fibres at 0.2% led to an initial drop in tensile strength, which again could be variability of the testing or may be an effect of air entrapment caused by the fibres [5]. The inclusion of more glass fibres brought an increase in tensile strength. From an initial tensile strength of 5.6 MPa with no fibres, the strength increased to a maximum of 6.1MPa with 2% fibre dosage.

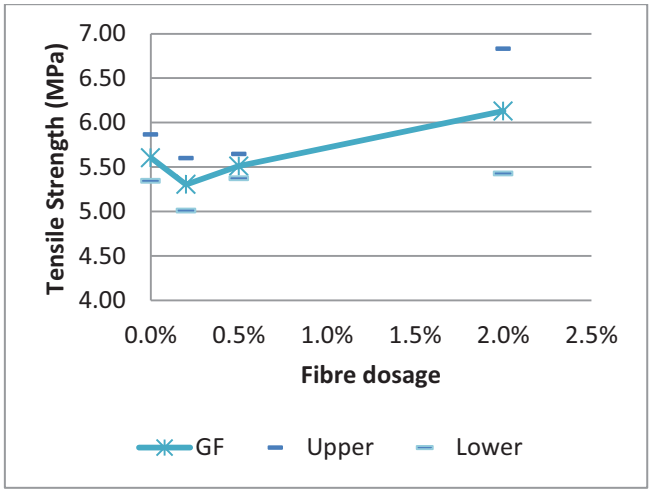


Figure 6- Variation of the tensile strength versus the percentage of glass fibres

3.4 *Effect of PAC fibres (PACF)*

The addition of PAC fibres contributed little to overall mean tensile strength with the strength at 0.5% and 2% fibre dosages (5.7, 5.5 MPa, respectively) remaining within the margins of error of the control sample (5.6 MPa with a standard deviation of 0.3 MPa) as shown in Figure 7. The addition of 0.2% fibres resulted in a loss of strength to 5.3 MPa similar to that experienced by the PP (Figure 4) and glass fibres (Figure 6).

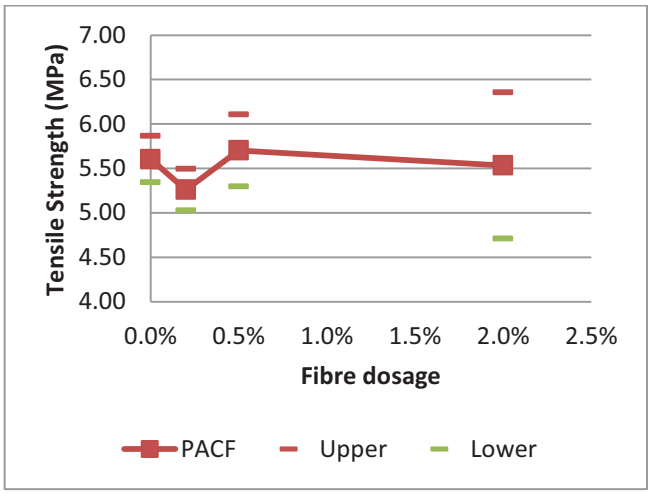


Figure 7- Variation of the tensile strength versus the percentage of PAC fibres

3.5 *Effect of PVA fibres*

The PVA fibres exhibited (Figure 8) a significant improvement in tensile strengths with increasing dosages of fibres and unlike the PP, glass and PAC fibres did not exhibit an initial reduction in strength with the addition of fibres. The tensile strength gain experienced by the PVA from 5.6 to 6.6 MPa was the greatest of any of the fibres with the strength gain (1 MPa) at 2% fibres double that of the glass fibres (0.5 MPa). Similarly, with the exception of basalt at 0.2% dosage, the PVA fibres out performed every other fibre at each fibre dosage due to their hydrophilic nature creating a better bond between the fibres and binder [6, 7].

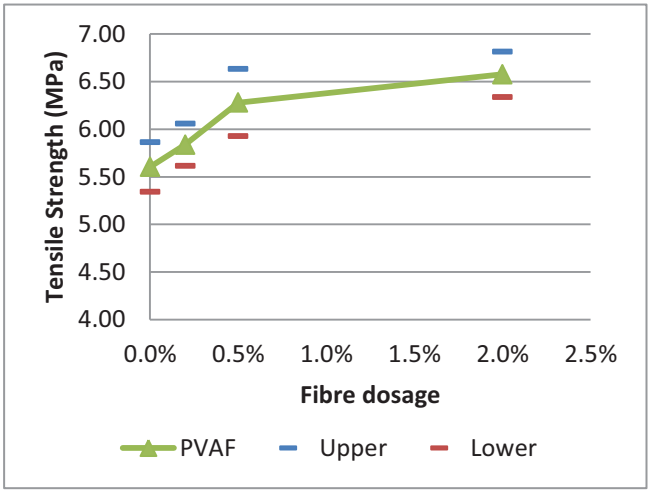


Figure 8- Variation of the tensile strength versus the percentage of PVA fibres

4 DISCUSSION

With the exception of PAC fibres which had a minimal increase of 0.1 MPa, all the fibre types brought about an increase (>0.5 MPa) in tensile strength as shown in Table 3 at different level of percentage of fibres.

Table 3 - Ultimate strength of various fibres

Fibre type	Glass	Basalt	PP	PAC	PVA
Mean ultimate strength (MPa)	6.1	6.1	6.1	5.7	6.6
Standard deviation	0.7	0.29	0.2	0.41	0.24
Mean strength gain (MPa)	0.5	0.5	0.5	0.1	1.0
Mean strength gain (%)	9	9	9	2	18
Optimum dosage (%)	2.0	0.2	0.5	0.5	2.0

Only basalt and PVA did not exhibit an initial loss of strength from the addition of fibres into the mix (Figure 5 and Figure 8). This loss of strength could be attributed to air entrainment [8] that is more significant that the contribution of strength from the fibres and therefore with PP, glass and PAC fibres, a minimal fibre dosage may be necessary before an increase in strength occurs. Similarly, the PAC, PP and basalt fibres all had an optimum dosage of fibres after which additional fibres contributed to a reduction in workability that impaired the compaction of the samples and resulted in a loss of tensile strength.

5 CONCLUSIONS

This paper reports the investigation of the effect of 5 types of fibres mixed in mortar including polypropylene fibres (PPF), basalt fibres (BF), glass fibres (GF), polyvinyl acrylic fibres (PVAF) and polyacrylonitrile fibres (PACF) by varying percentage of fibres up to 2%. With minimal fibre dosages (0.2%), PVAF fibres followed by basalt fibres demonstrated the best performance vis-à-vis of the tensile strength, while an increase in the dosage of PVAF showed continuous improvement of the tensile strength compared to other fibre types. The use of small dosages (0.2%) of polypropylene, polyacrylonitrile and basalt fibres proved to be detrimental to early age tensile strength and the ideal dosage should be considered.

ACKNOWLEDGMENTS

The authors would like to thank Knowledge Transfer Partnerships for the financial support of this industrial project with Larsen Building Group.

REFERENCES

[1] P.-C. Aitcin, "Cements of yesterday and today: Concrete of tomorrow," *Cement and Concrete Research,* vol. 30, no. 9, pp. 1349-1359, September 2000.

[2] ACI Committee 544, "State-of-the-Art Report on Fiber Reinforced Concrete," American Concrete Institute, 2002.

[3] K. M. Hossain, M. Lachemi, M. Sammour and M. Sonebi, "Strength and fracture energy characteristics of self-consolidating concrete incorporating polyvinyl alcohol, steel and hybrid fibres," *Construction and Building Materials,* no. 45, pp. 20-29, 2013.

[4] C. J. Brown, *The Performance of Road Ironwork Installations,* Nottingham: University of Nottingham, 1997.

[5] ABC Polymer, "Concrete Fibres," [Online]. Available: http://www.abcpolymerindustries.com/concrete-fibers.php. [Accessed 17th June 2014].

[6] T. Kanda and V. C. Li, "INTERFACE PROPERTY AND APPARENT STRENGTH OF HIGH-STRENGTH HYDROPHILIC FIBER IN CEMENT MATRIX," *Journal of Materials in Civil Engineergin,* vol. 10, no. 1, pp. 5-13, 1998.

[7] E. M. Bezerra, A. P. Joaquim and H. Savastano Jr, "SOME PROPERTIES OF FIBER-CEMENT COMPOSITES," in *Conferência Brasileira de Materiais e Tecnologias Não-convencionais: Habitações e Infra-estrutura de Interesse Social Brasil - NOCMAT 2004*, Pirassununga, Brazil, 2004.

[8] M. Pigeon, R. Pleau, M. Azzabi and N. Banthia, "Durability of microfibres-reinforced mortars," *Cement and Concrete Research,* vol. 26, no. 4, pp. 601-609, 1996.

[9] British Standards, *BS 6319-7 Testing of resin compositions for use in construction - Part 7: Method for measurement of tensile strength.*

Real-time monitoring of a hybrid precast and in-situ concrete flat slab system

Jamie Goggins[1,2,3], Shane Newell[1,4], Daniel King[1], Magdalena Hajdukiewicz[1,2,3]
[1] College of Engineering & Informatics, National University of Ireland, Galway, Ireland
[2] Ryan Institute, National University of Ireland, Galway, Ireland
[3] Informatics Research Unit for Sustainable Engineering (IRUSE), National University of Ireland, Galway
[4] Galway Mayo Institute of Technology, Galway, Ireland.
email: Jamie.Goggins@nuigalway.ie

ABSTRACT: This paper presents a scheme developed for instrumentation and monitoring of the structural performance of a hybrid precast and in-situ concrete flat slab system employed in an educational building. The system contains a precast plate flooring slab, which is composed of a thin reinforced concrete plate incorporating a steel lattice girder and all reinforcement required by design. A top mat of reinforcement is placed on site, as well as reinforcing stitching bars across the precast slab joints to ensure shear transfer and two way bending action. The concrete topping is then placed on site. Preliminary data obtained from the instrumented building are discussed. Continuous monitoring of the data will allow long term effects, such as creep, to also be monitored and compared with design guidelines.

KEY WORDS: Structural health monitoring; reinforced concrete flat slab; real-time monitoring; vibrating wire gauges.

1 INTRODUCTION

This project focuses on monitoring the structural performance of innovative building structural precast elements designed and manufactured by Oran Pre-Cast Ltd., and evaluating their effectiveness. This is done using vibrating wire gauges embedded in concrete elements of the newly built Life Course Studies Institute (LCSI) building at the National University of Ireland, Galway (NUI Galway).

At the first stage of the project, the vibrating wire gauges, as well as thermistors, were embedded in the concrete precast elements of the LCSI building. The structural monitoring started at the production stage of the precast elements, through the on-site installation and will continue during the building operation. Following this, measured data will be analysed and used to (i) develop and calibrate numerical models that predict building structural performance; and (ii) validate/develop design guidelines for hybrid precast and in-situ concrete flat slab systems.

This paper presents the instrumentation and monitoring strategy utilised to determine the structural performance of a hybrid precast and in-situ concrete flat slab system employed in an educational building, as well as some preliminary results from the project.

2 LIFE COURSE STUDIES INSTITUTE (LCSI) BUILDING

The construction of the LCSI building at NUI Galway commenced in July 2013 by JJ Rhatigan & Company Limited and is expected to be completed by May 2014. It was a design and build contract. The building was designed by Simon J. Kelly and Partners architects with Arup Consulting Engineers acting as consulting engineers and Alan Lipscombe as transport consultant. The building is part 3 storey and part 2 storey with a gross floor area of 3633 sqm (Fig. 1). It is predominately a precast concrete building with the precast elements designed, manufactured and installed by Oran Pre-Cast Ltd. The building will host the newly established Life Course Studies Institute (LCSI) and comprises of single occupant offices, open plan offices for researchers, a 150-seater lecture hall, and auxiliary spaces and services, including an atrium. The floor plate used for the superstructure of the building is a hybrid precast and in-situ concrete flat slab system. A reinforced concrete twin wall system is the primary lateral resisting system in the building, as well as transferring gravity loads to the ground. The twin wall system consists of two plates of 65mm thick concrete connected by means of cast-in lattice girders to form a core between the plates. The cavity between the plates is filled with concrete on site after the panel has been erected to complete the composite wall. Precast reinforced concrete columns and downstand beams are also employed in the building. A number of different cladding systems have been employed in the building, as seen, for example, in Figure 1.



Figure 1. Photomontage of the Life Course Studies Institute building © Simon J Kelly Architects.

3 INSTRUMENTATION OF THE LCSI BUILDING

3.1 Introduction

The scheme developed and implemented for the Life Course Studies Institute building is similar to that deployed in the

Engineering building at NUI Galway. Previous papers [1-5] have illustrated the overall instrumentation of that building and its development as a research tool. Lessons learnt from that project were taken forward into the new project. The vibrating wire (VW) strain gauges (Gage Technique model TES/5.5/T) embedded in the concrete elements in the Engineering building to monitor both temperature and longitudinal strains were found to be robust and reliable. Thus, these were also used in the LCSI building. The VW gauges have a range of greater than 3000 microstrain with a resolution of better than 1 microstrain. In addition to the VW gauges, a number of electrical resistance strain gauges were also installed on the reinforcement bars in the void form flat slab of the Engineering building. However, it was found that over time, the data obtained from these sensors may not be reliable due to the harsh environment that the sensors are located in. Thus, it was decided not to use this type of sensor in the LCSI building. In addition to the VW strain gauges (Fig. 2), a large number of thermistors were also embedded in concrete elements in the building, which will allow the influence of heat transfer and storage in structural precast building components on indoor environments to be investigated [6].

3.2 Data acquisition system

To collect data from the sensors, a data acquisition system containing CR1000 data loggers, AVW200 vibrating wire interface and AM16/32B multiplexers obtained from Campbell Scientific were employed. This system has been automatically logging data from the sensors embedded in the reinforced concrete flat slab system since their initial installation. During the construction phase, data is being stored on a flash memory card, which is manually downloaded onto a laptop weekly and backed-up on a server. However, data communication relay through the use of Campbell Scientific's NL115 Ethernet and Compact Flash Module will allow data to be collected over a local network after this is set up on commissioning of the building.

3.3 Instrumented flat slab

The 300 mm deep flat slab forming the first floor of the East block of the LCSI (Fig. 3) has a total of 59 vibrating wire (VW) gauges installed over 29 designated sections, as shown in Figure 4. The slab has a long span of 8.14 m and is the third bay out of a total of six in this direction (Fig. 3). It has two spans in the orthogonal direction of 5.808 m and 4.213 m with the outside edge supported on a 215 x 1180 mm deep downstand beam spanning between 800 x 215 mm precast reinforced concrete columns on grid line intersections and the interior of the slab supported by 600 x 215 mm reinforced concrete columns (Fig. 4). A plan view and typical cross-section indicating the locations of the VW gauges embedded in the concrete flat slab system are shown in Figure 4. The VW gauges are numbered in Figure 4, with 'Lx' and 'Ly' indicating strain measurements in the long and short span directions, respectively; 'H1', 'H2', 'H3' and 'P' indicating the depth within the slab that the sensor is located, as given in Table A1 in the appendix (i.e. near the top, middle, bottom of the in-situ component and plate, respectively). In total, 59 number VW gauges were employed. This includes:

- 10 no. on Grid Line 3 (centre of column strip) in the short span direction;
- 4 no. on Grid Line 3 + 1500 mm (edge of column strip) in the short span direction;
- 17 no. on Grid Line 3.5 (middle strip) in the short span direction;
- 9 no. on Grid Line A + 2800 mm (middle strip) in the long span direction;
- 4 no. on Grid Line B (centre of column strip) in the long span direction;
- 10 no. on Grid Line B + 1300 mm (edge of column strip) in the long span direction;
- 5 no. in the precast element located at in the longitudinal span direction at the edge of the column strip 1300 mm from Grid Line B.

Preliminary results from the sensors located on Grid Line 3.5 are presented in Section 5. However, in order to interpret this data, material properties are first required. These were determined through a material testing programme, which is described in Section 4.



Figure 2. Vibrating wire gauge installed in the plate element.

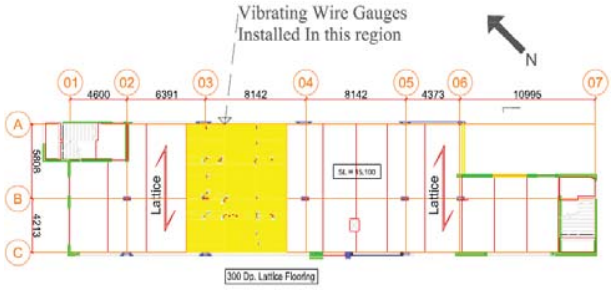


Figure 3. Plan of first floor of the East block of LCSI with instrumented area highlighted (dimensions in mm).

4 MATERIAL TESTING

In order to have accurate representation of the properties of the concrete used in the structural elements in this building, a comprehensive material testing campaign is currently underway. The data obtained for these tests will be used in interpreting the data from the sensors installed on site (see Section 3), in codified approaches and in material models employed in finite element analyses studies to determine the short and long term structural performance of reinforced concrete hybrid precast and in-situ concrete flat slab systems.

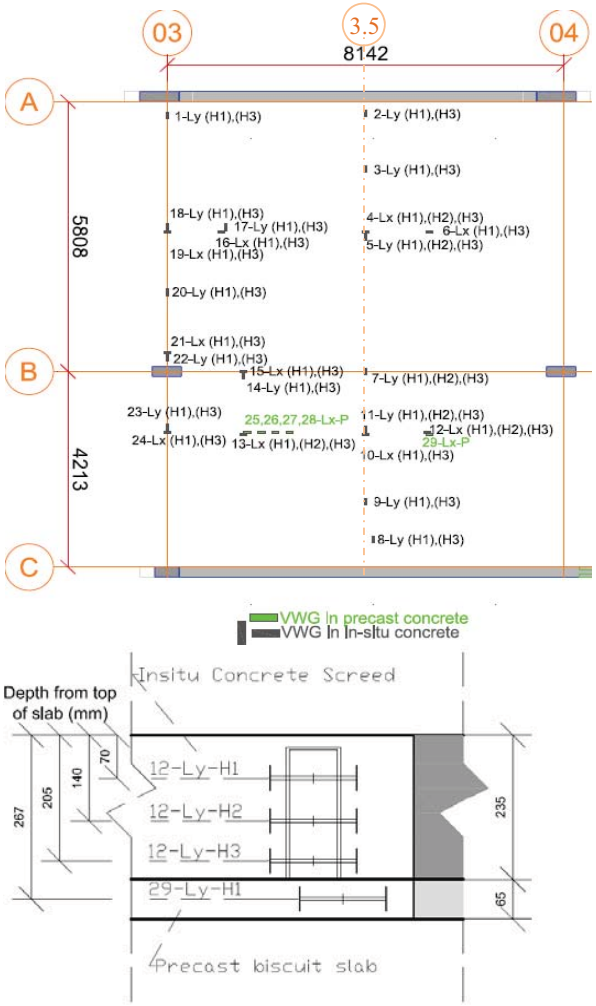


Figure 4. (a) Plan view and (b) typical section showing locations of vibrating wire gauge installed in the flat slab system (dimensions in mm).

Two mix designs were employed in the hybrid precast and in-situ concrete flat slab system – (1) a C40/50 D10 concrete mix with 370 kg/m^3 of CEM II-A/L for the precast plate and (2) a C28/35 D20 concrete mix (slump S2) with 195 kg/m^3 of CEM II-A/L and 85 kg/m^3 of (i.e. 30%) GGBS for the in-situ topping. Cylinder, cube and prism specimens were obtained from these concrete mixes to determine the various properties of the mixes used [7]. These included specific gravity, density, compressive strength [8], modulus of elasticity [9] and tensile strength of the concrete [10]. The tests have been/will be carried out at various concrete ages including 3, 7, 14, 28, 56, 112 and 365 days, as shown in Table 1. The coefficient of thermal expansion is also a useful property, which will be determined in the laboratory using the AASHTO T336-11 standard [11]. The apparatus used to measure this is shown with the calibration specimen in Figure 5. As a comprehensive material testing programme had already been undertaken on the concrete mix design for the precast plate element[12], a more condensed testing programme is undertaken in this project on this mix design.

Table 1. Testing schedule for Roadstone in-situ concrete mix

Materials testing carried out	100 x 100mm cubes	150 mm dia x 300 mm high cylinders
Compressive strength test (3,7,14,28,56,112, 365 days)	Y	Y
Tensile splitting test (28 days)	-	Y
Modulus of elasticity (7, 28,56, 112 days)	-	Y
Coefficient of thermal expansion (2 specimens)	-	Y
Specific gravity and density (All specimens)	Y	Y
Specimen left on site with embedded thermistor to measure temperature	-	Y



Figure 5. Apparatus used to measure the coefficient of thermal expansion.

The concrete compressive strengths for both the in-situ and precast concrete at different curing times, determined in accordance with IS EN 12390-3 [8], are given in Table 2. The 28 day minimum characteristic compressive strengths specified for both mixes have being met. The precast mix was specified as C40/50, but achieved average compressive cube strengths of 51.2 N/mm^2 and 71.9 N/mm^2 at 3 and 28 days of age, respectively. The associated characteristic cube strengths were 36.6 N/mm^2 and 60.5 N/mm^2, respectively. The associated characteristic cylinder strengths were 26.0 N/mm^2 and 43.5 N/mm^2, respectively. The in-situ concrete mix, specified as a C28/35, reached an average compressive cube strength of 40.9 N/mm^2 at 28 days of age. The associated characteristic cube strength was 30.2 N/mm^2, which is lower than the minimum value specified. On the other hand, the characteristic cylinder compressive strength was 29.8 N/mm^2 at 28 days of age, which exceeds the minimum value of 28 N/mm^2 specified. Figure 6 shows the development of the mixes' compressive strengths over time. The rate of strength gain between the cylinder and cubes for each mix is similar.

Figure 7 shows the development of the elastic modulus for both concrete mixes over time. The elastic modulus tends to

an average value of approximately 45 GPa for both mixes. However, at 7 days of age, the elastic modulus of the precast concrete mix is approximately 40% higher than that of the in-situ concrete mix, as would be expected with its early compressive strength gain (Table 2). The different rates of elastic modulus development would have impacts in terms of stiffness and the deflections of the flat slab.

Table 2. Average compressive strength (N/mm^2) results

Specimen	Cubes		Cylinders	
Age (Days)	In-situ	Precast	In-situ	Precast
3	18.61	51.15	-	36.36
7	27.86	62.74	23.45	45.10
14	32.04	66.55	-	50.52
21	-	72.49	-	53.95
28	40.89	71.88	33.89	52.76
56	44.43	78.95	35.35	52.92
112	47.59	75.66	37.02	-

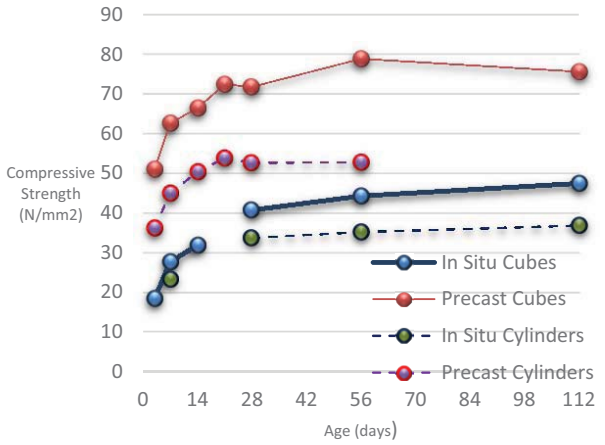


Figure 6. Development of average compressive strength with age

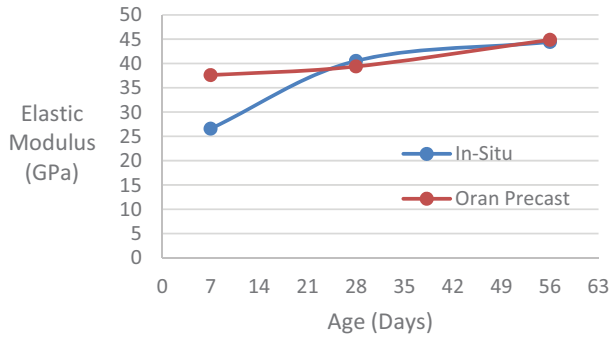


Figure 7. Development of elastic modulus with age for concrete mixes

5 PRELIMINARY RESULTS

The instrumentation installed in the LCSI building is generating real time data in relation to the strain and temperature in the first floor hybrid concrete flat slab system in the two storey section (East zone) of the LCSI building. The data will be analysed and interpreted continuously during both the construction and operational phase of the building. Unfortunately, no data was received from ten of the VW strain gauges. The majority of these gauges are located in the bottom of the in-situ element of the slab and it is suspected that they were damaged during the concreting operation. The location and reference for the installed VW gauges are given in Table A1. Two or three VW gauges (H1, H2 and H3) were located in the depth of the in-situ element of the slab to allow measurement of strain through the section to be recorded.

The 300 mm deep hybrid concrete flat slab at first floor consists of a 65 mm thick precast lattice girder plank and 235 mm thick in-situ concrete (Fig. 4(b)). The precast planks at first floor were installed on the 16-18th October 2013 and the in-situ concrete slab was poured on the 24th October 2013. Data relating to strain and temperature in the concrete slab has been continuously recorded since the 28th October 2013. The precast planks were propped prior to pouring the in-situ slab at first floor and subsequently a similar propping arrangement was used to support the roof slab overhead (similar hybrid concrete flat slab system). On the 3rd December 2013, props were removed from the roof slab first, followed by the first floor.

A number of load tests were undertaken on the first floor slab in late December 2013 and early January 2014 using bagged cement which was available on site, prior to fit-out. The load tests consisted of applying concentrated loads and uniformly distributed line loads similar to the design variable imposed load allowed for the slab (Figure 8).



Figure 8. Load test on first floor slab

The results presented in this paper are based on the VW gauges installed along Grid Line (GL) 3.5. VW gauges were installed at seven locations along GL3.5 and were positioned in both the long and short span directions. GL3.5 is located along the joint between two of the precast lattice girder units. All VW gauges have built-in thermistors, which monitor temperature in the concrete section. This is important as it ensures that the measured strain takes account of the difference in the coefficient of thermal expansion of the gauge and surrounding concrete. In the literature, there are varying

recommendations for the coefficient of thermal expansion of concrete [13], [14]. The coefficient of thermal expansion is taken as 10 microstrain/°C, as specified in EN1992-1-1 [14] for the measured strains presented in this paper. It is envisaged that the proposed testing programme (described in Section 4) will determine specific properties related to the concrete, such as the coefficient of thermal expansion of the in-situ concrete in the floor structure and this will enhance the accuracy of the recorded strain data from the VW gauges.

The measured changes in strain through the in-situ section of the first floor structure along GL 3.5 (in the two-span direction) are shown in Figure 9. 'H1' and 'H3' refer to the first and third strain gauge at a specific location in the slab, measured from the top of the slab, respectively. The changes in strain relate to the period 28th October 2013 (commencement of recordings) until the 12th December 2013, which was 9 days after the props were removed from the first floor and the floor structure supported its self-weight. Until the props were removed, the floor structure was supported by five lines of continuous supports at maximum 2.4 m centres (as required by the precast lattice girder designer) and, therefore, it was expected that flexural strain in the slab would be limited. Prior to removal of props, the slab was subject to strain due to a number of factors such as creep, shrinkage (autogeneous and drying) and temperature change. The measured strains along GL 3.5 suggest that for the initial phase of curing (first 10 days) that the top portion of the slab (H1 gauges) was predominantly subject to tensile strains (negative) and the portion of the slab adjacent to the precast plank (H3 gauges) was subject to compressive strains. However, after the props were removed, the in-situ slab along GL3.5 was subject to compressive strains through the section. This suggests that the expected flexural strains along GL 3.5 are minimal and that the principal strains are from other sources other than flexure.

Figure 10 shows the measured change in strains through the in-situ portion of the slab at one location (gauge ref: 7-Ly) along GL 3.5 and the corresponding air temperature. The air temperature readings are from the NUI Galway weather station which is located approximately 1.5 km from the site [15]. The three strain measurements relate to gauges located approximately in the top (H1), middle (H2) and bottom (H3) section of the in-situ slab. The peak strains recorded in the three gauges correlate to the peak air temperature (12th December 2013), which suggests that strain due to temperature is a significant factor. It is also noted that following the removal of props, compressive strains are recorded at this location through the section of the slab, which indicates that flexural strains are not the dominant source of strain.

The prediction of strains (or deflections) for suspended concrete slab systems is difficult to estimate accurately. The behaviour of a slab at service loads varies with time and depends on the extent of cracking, stiffness of the slab, creep, shrinkage and degree of restraint. A range of +15% to -30% between calculated and actual deflections is suggested in some publications [16].

It is proposed to use BS EN 1992-1-1 [14] to determine predicted strains for the first floor slab in the LCSI building. Eurocode 2 [14] uses a distribution factor coefficient (ζ) to determine deformation parameters such as strain or curvature. The factor ζ allows tension stiffening at a section to be accounted for in calculations as the actual behaviour of a slab will be a combination of the member in its uncracked and fully cracked state.

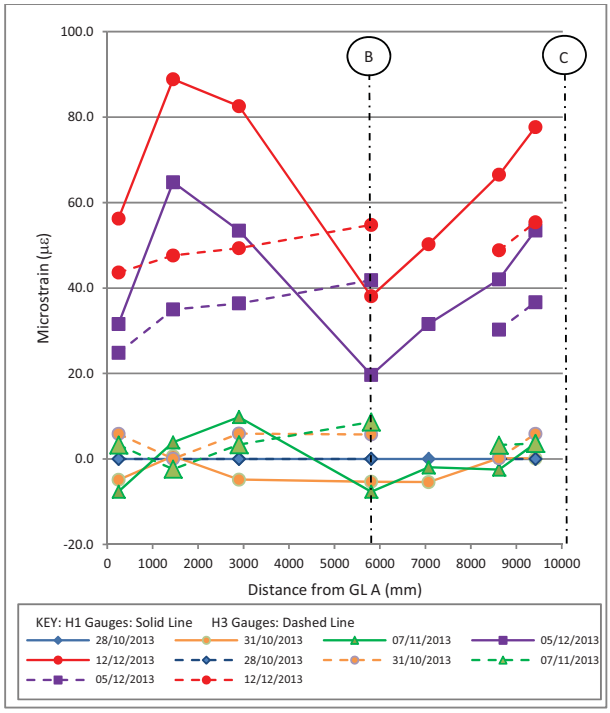


Figure 9. Changes in measured strain along GL 3.5

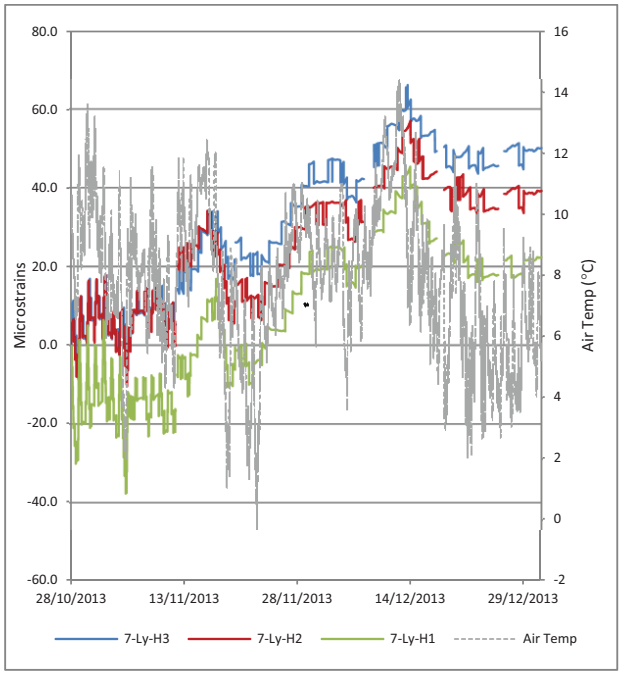


Figure 10. Measured strain (7-Ly) and air temperature

6 CONCLUSIONS

This paper presents a real-time monitoring campaign of a hybrid precast and in-situ reinforced concrete flat slab system installed in an educational building at NUI Galway. The preliminary results presented in this paper are at an early stage and it is expected that the measured data will be used to compare actual behaviour with predicted behaviour using structural codes, such as the Eurocodes. The material testing programme will complement this process because calculated methods for behaviour of concrete slabs at service loads are most sensitive to values of concrete properties (creep coefficient, elastic modulus etc.). Continuous monitoring of the data will allow long term effects in the structural performance of the slab to be monitored and compared with design guidelines.

ACKNOWLEDGMENTS

A great debt of gratitude is owed to all members of the project team involved in the design and construction of the Life Course Studies Institute building who have facilitated our work throughout the project. A special mention is also owed to the technical staff at NUI Galway for their assistance during the instrumentation process.

REFERENCES

[1] Cannon, E and Goggins, J, (2010), 'The new Engineering building at NUI Galway as a teaching tool for structural engineering," *BCRI 2010*, Cork, Ireland, September 2010.

[2] Goggins, J; Byrne, D; Cannon, E (2012) 'The creation of a 'living laboratory' for structural engineering at the National University of Ireland, Galway'. *The Structural Engineer*, 90 (4):12-19

[3] Byrne, D, Goggins, J, and Cannon, E (2012), 'The analysis of time dependent effects of reinforced concrete systems through in-situ structural health monitoring,' *IABSE Conference – Global Thinking in Structural Engineering: Recent Achievements*, Egypt, July 2012.

[4] Byrne, D, Goggins, J, Cannon, E (2012), 'Assessing the performance of structural elements within the Engineering building at NUI Galway,' *BCRI2012*, Dublin, September 2012.

[5] Byrne, D. and Goggins. J. (2013) 'Evaluating the structural capacity of concrete elements through in-situ instrumentation.' *Key Engineering Materials* 569 (2013): 382-389

[6] Hajdukiewicz, M, Goggins, J, (2014), 'The influence of heat transfer and storage in structural precast building components on indoor environments,' *Civil Engineering Research of Ireland 2014 Conference*, Belfast, August 2014.

[7] I.S. EN 12390-2 (2009), 'Testing hardened concrete - Part 2: Making and curing specimens for strength tests', NSAI, Dublin.

[8] I.S. EN 12390-3 (2009), 'Testing Hardened Concrete – Part 3 Compressive Strength of Test Specimens' NSAI, Dublin.

[9] I.S. EN 12390-13 (2013), 'Testing hardened concrete - Part 13: Determination of secant modulus of elasticity in compression', NSAI, Dublin.

[10] I.S. EN 12390-6 (2006), 'Testing Hardened Concrete – Part 6 Tensile Splitting of Test Specimens' NSAI, Dublin.

[11] AASHTO (2011). 'T 336-111, Standard method of test for coefficient of thermal expansion of hydraulic cement concrete', American Association of State and Highway Transportation Officials, Washington, USA.

[12] Mollohan A. and Crossan C. (2013), 'Investigating the concrete characteristics of the new Engineering building', BE thesis, College of Engineering & Informatics, NUI Galway, May 2013.

[13] Neville A.M. (2012). 'Properties of concrete', 5th Ed., Trans-Atlantic Publications, Inc

[14] CEN (1992), 'EN 1992-1-1, Eurocode 2: Design of concrete structures. General rules for buildings,' ed. Brussels, Belgium, 1992.

[15] IRUSE, (2011) 'IRUSE weather website,' [Online]. Available: http://weather.nuigalway.ie/.

[16] The Concrete Society (2005), 'Technical Report No. 58. 'Deflections in concrete slabs and beams', Cromwell Press, UK

APPENDIX

Table A1. Location of VW gauges.

ID	X (mm)	Y (mm)	Z (mm)
1-Ly-H1	0	300	75
1-Ly-H3	0	300	187
2-Ly-H1	4071	250	67
2-Ly-H3	4071	250	180
3-Ly-H1	4071	1450	75
3-Ly-H3	4071	1450	207
4-Lx-H1	4071	2800	55
4-Lx-H2	4071	2800	110
4-Lx-H3	4071	2800	210
5-Ly-H1	4071	2900	60
5-Ly-H2	4071	2900	135
5-Ly-H3	4071	2900	200
6-Lx-H1	5371	2800	75
6-Lx-H3	5371	2800	190
7-Ly-H1	4071	5808	65
7-Ly-H2	4071	5808	140
7-Ly-H3	4071	5808	200
8-Ly-H1	4221	9421	50
8-Ly-H3	4221	9421	200
9-Ly-H1	4071	8621	75
9-Ly-H3	4071	8621	200
10-Lx-H1	4071	7171	65
10-Lx-H3	4071	7171	215
11-Ly-H1	4071	7071	70
11-Ly-H2	4071	7071	140
11-Ly-H3	4071	7071	205
12-Lx-H1	5321	7171	90
12-Lx-H2	5321	7171	125
12-Lx-H3	5321	7171	210
13-Lx-H1	1553	7171	85
13-Lx-H2	1553	7171	125
13-Lx-H3	1553	7171	205
14-Ly-H1	1553	5908	75
14-Ly-H3	1553	5908	205
15-Lx-H1	1553	5808	80
15-Lx-H3	1553	5808	200
16-Lx-H1	1103	2800	50
16-Lx-H3	1103	2800	200
17-Ly-H1	1203	2700	90
17-Ly-H3	1203	2700	200
18-Ly-H1	0	2700	70
18-Ly-H3	0	2700	205
19-Lx-H1	0	2800	75
19-Lx-H3	0	2800	185
20-Ly-H1	0	4100	75
20-Ly-H3	0	4100	205
21-Lx-H1	0	5400	80
21-Lx-H3	0	5400	210
22-Ly-H1	0	5500	80
22-Ly-H3	0	5500	200
23-Ly-H1	0	7021	70
23-Ly-H3	0	7021	195
24-Lx-H1	0	7121	70
24-Lx-H3	0	7121	205
25-Lx-P	1643	7121	267
26-Lx-P	1933	7121	267
27-Lx-P	2223	7121	267
28-Lx-P	2513	7121	267
29-Lx-P	5321	7121	267

Notes: 1) Depth (Z) measured from top of slab to centre of VW gauge.
2) H1, H2 & H3 refer to gauge at specific location measured from top of slab respectively. P refers to gauge in precast plank.
3) Origin taken as intersection of grid lines A and 3.

Impact Resistance of High-Dosage Steel Fibre Reinforced Concrete Slabs

Roger P. West, Mohammad Reza Dousti
Department of Civil, Structural and Environmental Engineering, Trinity College Dublin, Ireland
email: rwest@tcd.ie, doustim@tcd.ie

ABSTRACT: It is acknowledged that the provision of steel fibres in high strength concrete assists in reducing brittleness and improves abrasion and impact resistance. In particular, the fibres bridge the macrocracks as they begin to arise and restrict crack opening and, thus, propagation. In this context, this paper examines the dynamic response of fibre reinforced slabs to a low velocity hard impact under different momentums at impact. By comparing FRC with plain and mesh reinforced slabs, it is shown how, under different drop heights, a global flexural or punching shear response is prompted, leading to classic spalling, scabbing, shear plug formation and ultimately perforation to varying degrees. In particular, it appears that while the high dosage fibre reinforced high strength concrete cannot prevent crack formation under such a severe impact, it does prevent total collapse, thereby confirming their efficacy in confining damage and protecting property.

KEY WORDS: Impact Resistance; Steel Fibres; Steel Fibre Reinforced Concrete.

1 INTRODUCTION

Issues with poor fracture toughness of concrete could possibly be reduced to a large extent by reinforcing it with steel fibres. The resulting material, having a random distribution of short and discontinuous fibres, is referred to as fibre reinforced concrete (FRC), which is gradually becoming an appreciated common construction material. Considerable development has been made within the last three decades in comprehending the short and long-term performances of fibre reinforced cementitious materials, and this has led to a variety of novel and revolutionary applications (Bentur and Mindess, 2007). Cracks and their propagation are among the most crucial issues concerning concrete specimen and concrete structures all over the world. It might not be possible to prevent the concrete from cracking, but there are several methods to prevent their propagation. Crack propagation might result in severe structural damage anywhere at any time. Steel fibres are usually employed to prevent this crack propagation. In the hardened condition, when fibres are appropriately bonded and attached, they interact with the matrix in the state of micro-cracks and efficiently bridge these cracks thus slowing down their coalescence and unstable development (Banthia et al., 2004). Steel fibres come in different types in terms of geometry and aspect ratio. Different dosages are used according to the application of the structure. The dosage of the fibre is either expressed in percentage or kg / m^3 terms. This experimental project was designed to investigate the degree of damage on steel fibre reinforced concrete slabs, under an impact test (drop weight test).

As in any fibre reinforced composite, fibre-matrix bond in FRC is of crucial importance. Nevertheless, in contrast to fibre reinforced polymers (FRPs) employed in aerospace and automobile industries where fibres are used to improve strength and elastic modulus, in FRCs, toughness or energy absorption ability is of primary interest. Consequently, inelastic bond failure mechanisms like interfacial crack development, crack tortuosity and fibre slip are more important. Fibre pull-out tests are usually executed to evaluate fibre effectiveness in FRC and in these kinds of tests fibre bond and slip are monitored at the same time (Bindiganavile and Banthia, 2001).

1.1 SFRC Impact

The impact test, as executed on SFRC, has significantly better characteristics under impact loading compared to plain concrete, with regards to both strength and fracture energy. The function of the fibres is, basically, the control of cracking by bridging when they propagate within the matrix. A number of high strain rate experiments were conducted to assess the characteristics of SFRC, such as instrumented drop weight tests, missile impact and explosive loading. Nonetheless, it is hard to relate the outcomes of these experiments and find an exact relationship between them, as the high strain rate properties of SFRC seem to be strongly influenced by the details of the specimen geometry and the test set up. For example, the mass of the drop hammer, the height, from which it has been dropped (Banthia and Bindiganavile, 2002), or the specimen size and the specimen support conditions, all influence the numerical data. Furthermore, Solomos and Berra (2004) discovered that under compressive impact, SFRC shows a unique size effect: the impact strength of 40 mm cubes was as much as 25% greater than that of 60 mm cubes. Almost the same outcomes are seen in flexure. Banthia et al., (2003) discussed the influence of specimen size on the toughness factor for four various drop elevation of the impact hammer. The size influence seems to be more noticeable at higher elevations.

The impact tests described here are bespoke tests designed to demonstrate the principles being investigated and as such do

not follow any code of practice.

1.2 Test Specimens

The impact test was executed on plain concrete as well as fibre reinforced concrete and conventional rebar (A393 mesh 25mm from the lower face) reinforced concrete slabs with a dimension of 700 mm x 700 mm x 68 mm in each case. Plain and fibre reinforced cylinders with a length of 300 mm and a diameter of 150 mm were also cast to study the axial response of the specimen. Specimens were designed either as a normal strength concrete (35 MPa) or a high strength concrete (70 MPa). Plain concrete was considered as the upper boundary in terms of degree of damage and rebar reinforced concrete was presumed to be the lower boundary. Steel fibres were added to some of the pours in order to check the influence of them on the concrete specimen, under an impact loading from different heights. The results of this project could be categorised as a qualitative results, although some quantitative results were obtained as well. Fibre reinforced concrete slabs are compared with the plain and the rebar reinforced concrete slabs in order to comment on the fibre's influence on the concrete specimen's ductility and its effect on crack propagation.

1.3 Steel FIbres

Based on the application of a structure, different types of steel fibres are used nowadays. In this research, hooked-end steel fibres with a length of 35 mm and also a diameter of 0.5 mm were utilized at a very high dosage of 80 kg/m^3, selected to reduce the risk of balling. The fibres were added gradually to the mix while mixing. In order to have a better and more desireable fibre distribution, the steel fibres were added in small batches. After each batch was added, the mixer would stir the concrete mix and then, the following batch of fibre was added.

1.4 Objective

The objective of these experiments was to investigate the flexural and axial response of steel fibre reinforced concrete specimens (slabs and cylinders in this case) under impact loading by performing a dynamic test. The main objective could be expressed as checking the influence of steel fibres on the ductility of concrete specimens. If the concrete‘s ductility increases significantly (compared to the plain concrete specimens) with fibres, a shear failure is also expected.

1.5 Concrete Mix Design

These experiments consist of two different strengths for concrete and thus two different mix designs. The normal strength concrete was designed to have a 35 MPa characteristic strength at the age of 28 days of curing, however, the high strength concrete was designed to have 70 MPa after 28 days of curing. The design was based on the British Research Establishment (BRE) method for both 35 MPa and 70 MPa concrete specimens. A water/cement ratio of 0.5 was adopted for the normal strength concrete whereas a water/cement ratio of 0.35 was selected for the high strength concrete. The coarse aggregates consumed were a combination of 20 mm aggregates and 10 mm aggregates. In order to address the water demand of the mix, superplasticiser was used (0.8% v/wt cement for normal strength concrete and 1.4% v/wt cement for high strength concrete). Where shown, 70% GGBS was used in lieu of the CEM IIA-L cement.

2 METHODS

2.1 Experimental Programme

Nine different types of specimen were cast in this experiment, with a total of 64 slabs undergoing the impact test. All slabs were tested after 28 days of curing. Prior to the impact testing, the compressive strength of each mix was identified (compression test on control cubes were performed). A 76 kg steel billet with a 100mm nose cone impact surface diameter is dropped under gravity, onto the centre of the concrete specimens to see the specimen's impact resistance. During the impact test, the steel billet was dropped from 4 different heights of 0.5 m, 1 m, 2 m and 6 m on to the slabs, chosen to display the range of response types seen in this paper..

2.2 Test Setup

For the impact test on the slabs, a metal frame with a dimension approximately the same as the slabs was built and prepared prior to the testing and it was placed exactly under the impact rig. Then, the concrete slabs were placed on top of the metal frame to be tested. This metal frame was also centralised under the impact rig, so that the steel billet would make an impact approximately on the centre of the slabs. The impact testing performed on the slabs illustrated the flexural, and, if possible, the shear response on the concrete specimen within the experimental work. Since this project was a qualitative project and not a quantitative one, visual comparison was the most ideal method to establish a conclusion. Therefore, after each drop test on each specimen, a large number of photographs were taken from different angles to the specimen in order to demonstrate the extent of damage and local penetration and global response of the specimen.

Thus photographs were also employed to demonstrate the axial response of the concrete cylinders, the flexural and possibly shear response of the concrete slabs. These photos also illustrated the bending and the displacements of the slabs, after the impact test was performed on them. After each impact test, the width of the cracks noticed on the specimen, were measured with a digital caliper. These measurements were as precise as possible and are tabulated further in this paper. Aside from the crack widths on the slabs and cylinders, the diameter and length of the cylinders were measured after the impact, in order to observe and understand the difference and the influence of the impact intensity, and the specimen's axial response throughout the experiment.

3 RESULTS AND ANALYSIS

3.1 Slump Test Results

The slump value for each pour and mix design was recorded. No significant difference was observed in the slump value of

the pours with the same designed strength and composition. This showed the consistency of the mix designs throughout the experimental project. However, as expected, a dramatic decrease in the slump value was witnessed in the pours containing the high dosage of steel fibres. The fibres had reduced the workability of the concrete in both normal and high strength concrete pours, though no balling occurred.

3.2 Compression Test Results

Cubes were cast in this project for compressive strength along with cylinders and slabs under impact. They were tested after twenty-eight days and a comparison between the strengths of different types of concrete is illustrated in the Figure 1. The fibre concrete mixes were marginally higher in strength.

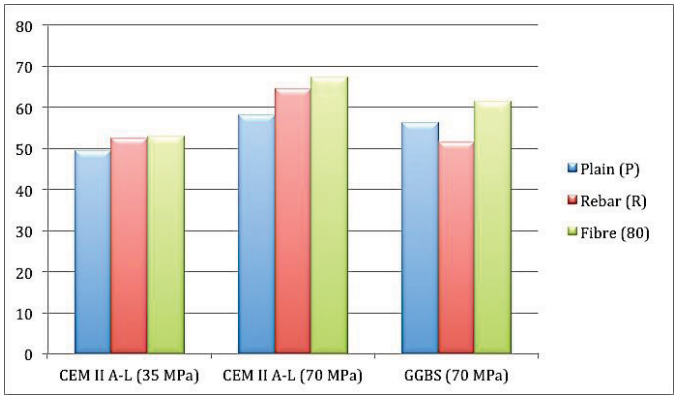


Figure 1: Compressive strength (cube, in MPa) of specimens after 28 days of curing

Note that the cubes labeled and allocated in the rebar reinforced concrete group, are not actually reinforced, but are a duplicate of the plain concrete cubes. Generally, it is not expected that steel fibres enhance concrete's compressive strength since they come into action only where tension and cracking is involved. As it was observed, the steel fibres did not influence the compressive strength of the concrete significantly.

3.3 Impact (Drop Weight) Test Results

Research performed by Li et al. in 2005 suggested that seven phenomena are associated with impact and impact effects on concrete targets (such as slabs). These seven phenomena could be expressed as follows (Figure 2):

(1) *Penetration*: Tunneling into the target by the projectile. Note that the length of the tunnel is known as the penetration depth.

(2) *Shear plug (cone cracking)*: Formation of a cone-like crack under the projectile and the possible subsequent punching shear plug.

(3) *Spalling*: Ejection of target material from the proximal face of the target.

(4) *Radial cracking*: Global cracks radiating from the impact point and appearing on either the proximal or distal face of the concrete slab or both, when cracks develop through the target thickness.

(5) *Scabbing*: Ejection of fragments from the distal face of the target.

(6) *Perforation*: Complete passage of the projectile through the target with or without a residual velocity.

(7) *Overall structural responses and failures*: Global bending, shear and membrane responses as well as their induced failures throughout the target.

All of the above mentioned impact effects are illustrated schematically in Figure 2.

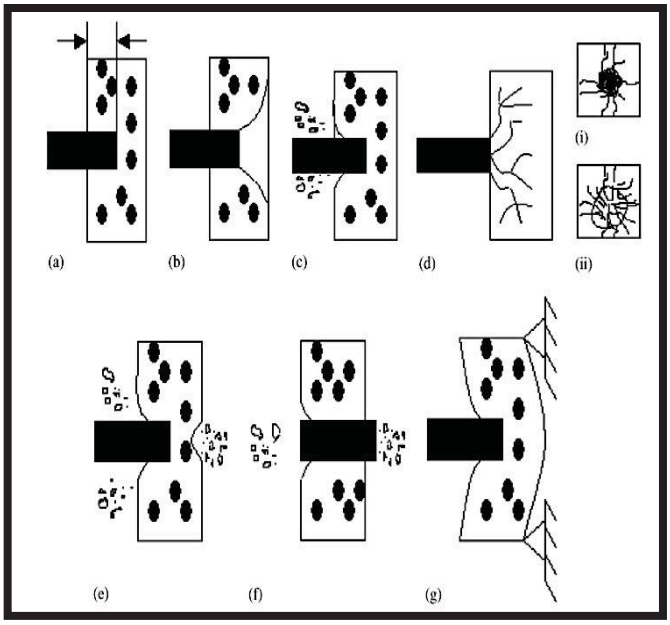


Figure 2. Impact effects on concrete targets: (a) Penetration, (b) Shear plug (cone cracking), (c) Spalling, (d) Cracks on (i) proximal face and (ii) distal face, (e) Scabbing, (f) Perforation and (g) Overall target response (Li et al., 2005)

The impact test results are demonstrated via photographs in this section. Different comparisons have been done. Figure 3 demonstrates the impact test results on the plain concrete from four different heights while Figure 4 shows the equivalents for SFRC.

As observed in Figure 3, the 35 MPa (CEM II A-L) plain concrete slabs demonstrate absolutely no resistance to the impact testing, not even from the lowest height (0.5 m). However, the 35 MPa (CEM II A-L) steel fibre reinforced slabs are witnessed to show a completely different behaviour after the impact loading (Figure 4).

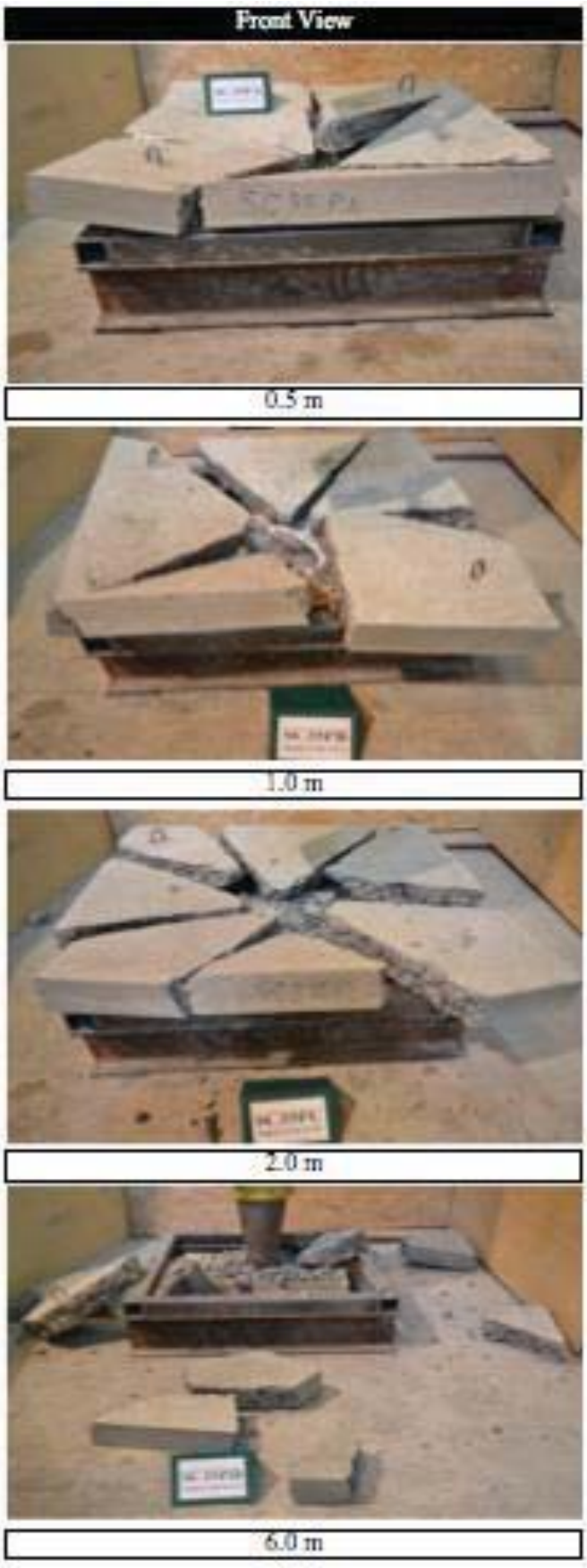


Figure 3: Impact resistance of 35 MPa (CEM II A-L) plain concrete slabs

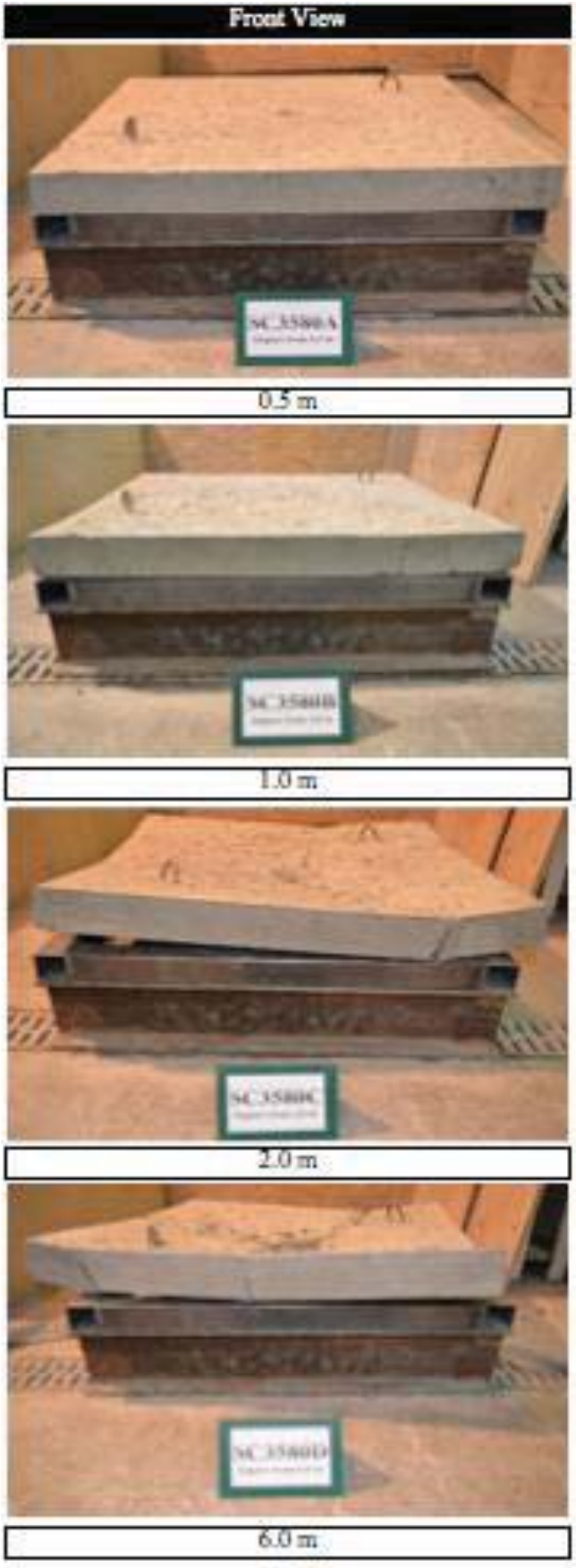


Figure 4: Impact resistance of 35 MPa (CEM II A-L) steel fibre reinforced concrete slabs

The steel fibre reinforced 35 MPa concrete slabs even resisted the impact test from 6 m and the specimen did not break into pieces. While significant flexural bending was observed, steel fibres bridged through the cracks and held the concrete segments together while preventing the crack propagation.

The same test was executed on the conventional rebar (mesh) reinforced concrete slabs. No significant damage was witnessed after impact from 0.5 m and 1 m, but after an impact test from 2 m height, a shear punch, with perforation was observed on the rebar reinforced slab, along with surface spalling and scabbing. However, the rebar reinfroced concrete slab was completely destroyed after an impact from a height of 6 m. This is clearly shown in Figure 5.

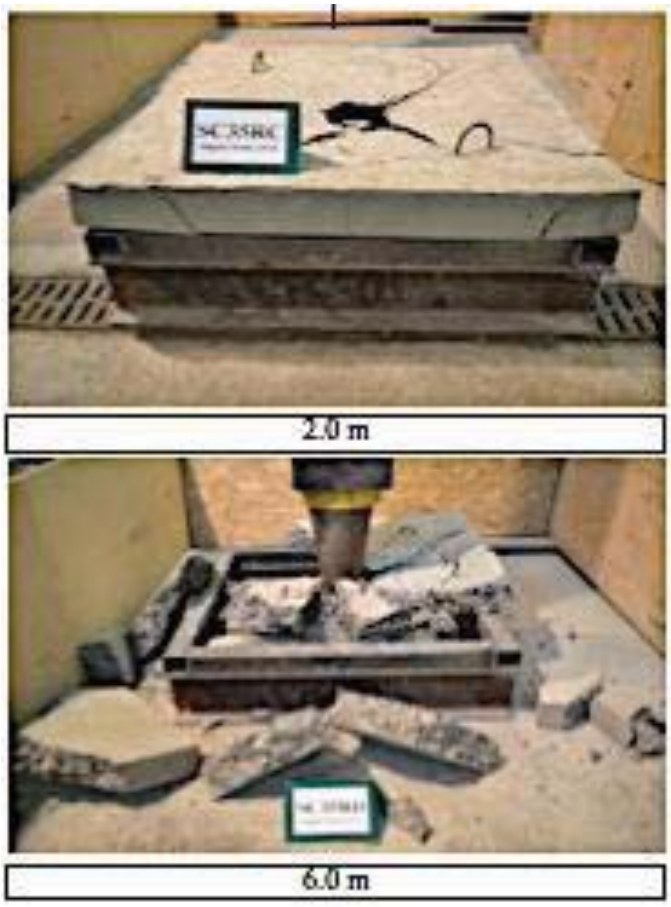


Figure 5: Impact resistance of 35 MPa (CEM II A-L) rebar (mesh) reinforced concrete slabs (shear punch and complete failure was observed after impacts from 2 m and 6 m respectively)

This test was also performed on the high strength concrete (70 MPa) containing CEM II A-L. Due to the higher strength (higher amount of cementitious material) the concrete was more brittle and, therefore, surprisingly the degree of damage was larger than the ones designed with a compressive strength of 35 MPa. The 35 MPa (CEM II A-L) fibre reinforced concrete slab did not fail under an impact from 6 m, however, the FRC slabs with the higher strength broke into pieces and the fibres were not capable of holding the concrete sections together. An impact from 2 m and 6 m on a 70 MPa (CEM II A-L) SFRC is demonstrated in Figure 6.

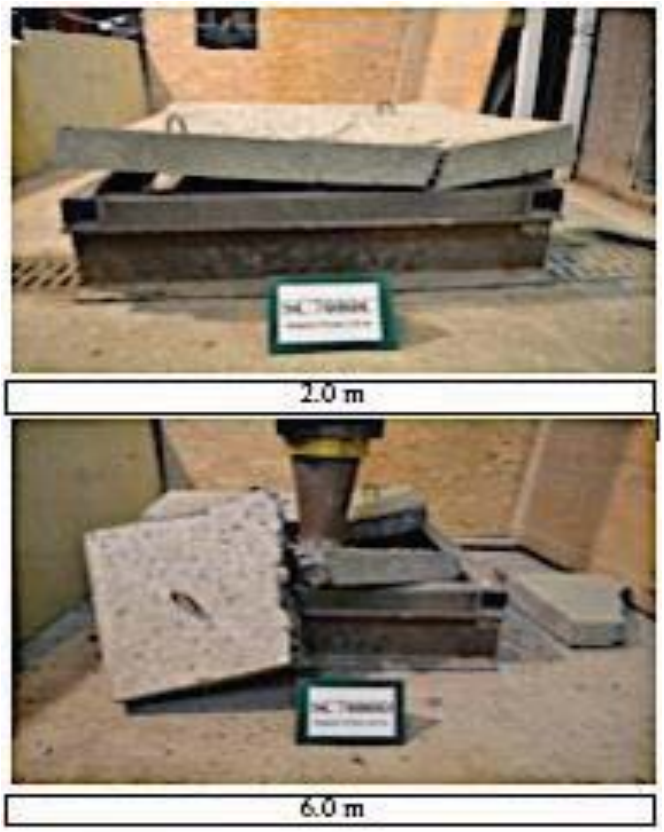


Figure 6: Impact resistance of 70 MPa (CEM II A-L) steel fibre reinforced concrete slabs

3.4 Crack Widths

After each impact test was performed, the widths of the cracks identified on the slabs were measured and recorded, in order to have a better quantitative comparison. A comparison between the average crack widths at the bottom of the rebar reinforced slabs and the steel fibre reinforced slabs is shown in Figure 7.

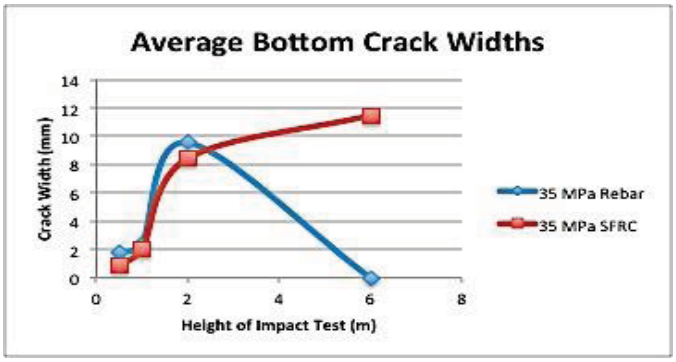


Figure 7: Average bottom crack widths of 35 MPa rebar reinforced concrete slabs vs. 35 MPa steel fibre reinforced concrete slabs

As observed in Figure 7, the crack widths are increased when the steel fibres are added to the concrete specimens. After an

impact from 6 m on to the rebar reinforced concrete slab, there is literally no crack width since the concrete has broken into pieces whereas the SFRC slab will remain serviceable after such an impact. The average crack width on the 35 MPa SFRC slab, after an impact from 6 m, is approximately 12 mm, which is high, but the slab stays in tact.

Basically, as for the 35 MPa concrete slabs, the steel fibre reinforced concrete slab performed better than the rebar reinforced concrete slab, according to the photographs and based on the measured crack widths. This demonstrates the ability of steel fibres in bridging through the concrete sections. The same scenario is again witnessed for the specimens with the higher compressive strength. Figure 8 illustrates the average bottom crack widths of 70 MPa rebar reinforced concrete slabs compared to the ones of the 70 MPa steel fibre reinforced concrete slabs.

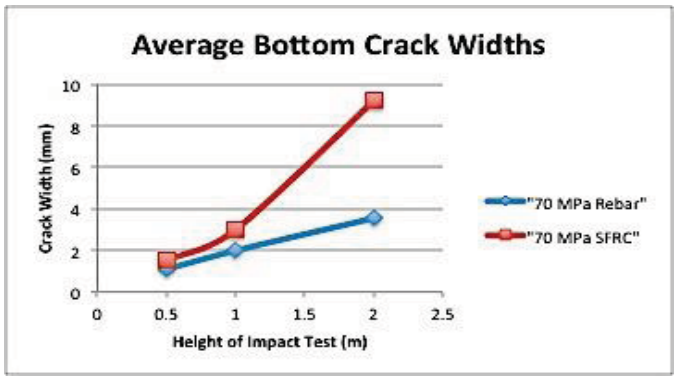


Figure 8: Average bottom crack widths of 70 MPa rebar reinforced concrete slabs vs. 70 MPa steel fibre reinforced concrete slabs

4 CONCLUSION

The slabs were tested to demonstrate the flexural and shear response of the concrete to impact. As expected, the plain concrete slabs did not display any resistance to the drop weight test (not even from 0.5 m). The rebar reinforced concrete slabs and the fibre reinforced concrete slabs did not fail under an impact from 0.5 m and 1.0 m in this project.

As for the 35 MPa specimens, the slabs reinforced with steel fibres demonstrated a better resistant to the impact loading. While the plain concrete slabs shattered and were destroyed under impact, the rebar reinforced and the fibre reinforced concrete slabs displayed better resistance. After dropping the billet on the rebar reinforced concrete slabs from 2.0 m, the billet penetrated through and a shear plug occurred (shear punch) along with the flexural response of the slab. The degree of damage was higher when the billet was dropped from 6.0 m, but a shear punch was still the outcome. Interestingly, the slabs reinforced with steel fibre, were much more resistant under the impact loading. The billet did not incur significant damage, even when it was dropped from 6.0m and neither perforations nor penetrations were witnessed. On the other hand, significant cracking was observed on these fibre reinforced concrete slabs.

As for the 70 MPa concrete specimens, the fibre reinforced concrete slabs also performed better in impact resistance, compared to the rebar reinforced concrete slabs. However, the steel billet did penetrate through the fibre reinforced concrete slab this time, when dropped from a height of 6.0 m. Generally, the degree of damage in all high strength concrete (70 MPa) slabs was more than the degree of damage in the normal strength (35 MPa) concrete slabs. This is probably due to the fact that higher strength concretes are more brittle because of the amount of cementitious material present inside the concrete.

ACKNOWLEDGMENTS

The authors would like to thank the technical staff at the Department of Civil, Structural & Environmental Engineering at Trinity College Dublin.

REFERENCES

[1] Bentur, A. and Mindess, S. (2007) '*Fibre reinforced cementitious composites*', 2nd edition, Modern concrete technology series.

[2] Banthia, N., Gupta, R. and Mindess, S. (2004) '*Developing crack resistant FRC overlay materials for repair applications*', NSF conference, Bergamo, Italy.

[3] Bindiganavile, V. and Banthia, N. (2001) '*Polymer and steel fibre-reinforced cementitious composites under impact loading – Part 1: Bond-slip response*'. ACI Mater. J. 98, 10–16.

[4] Bindiganavile, V. and Banthia, N. (2001) '*Polymer and steel fibre reinforced cementitious composites under impact loading'*, Part 2: Flexural toughness, American concrete institute, Materials journal, Vol. 98(1): pp. 17-24.

[5] Banthia, N. and Bindiganavile, V. (2002) '*Fibre reinforced cement based composites under drop weight impact loading: Test equipment and material influences'*, in P. Balaguru, A. Naaman and W. Weiss (eds) Concrete: Material science to applications – A tribute to Surendra P. Shah, SP-206, American concrete institute, Farmington Hill, MI, pp. 411–428.

[6] Solomos, G. and Berra, M. (2004) '*Compressive behaviour of high performance concrete at dynamic strain-rates'*, in M. di Prisco, R. Felicetti and G.A. Plizzari (eds) Fibre-reinforced concretes, BEFIB 2004, RILEM proceedings PRO 39, RILEM publications, Bagneux, Vol. 1, pp. 421–430.

[7] Banthia, N., Bindiganavile, V. and Mindess, S. (2003) '*Impact resistance of fibre reinforced concrete: A progress report*', in A.E. Naaman and H.W. Reinhardt (eds) High performance fibre reinforced cement composites (HPFRCC 4), RILEM proceedings PRO 30, RILEM publications, Bagneux, pp. 117–131.

[8] Li, Q. M., Reid, S. R., Wen, H. M. and Telford, A. R. (2005) '*Local impact effects of hard missiles on concrete targets*', international journal of impact engineering 32, 224-284.

Strength and Deformation Characteristics of Concrete Containing Recycled Aggregate Fines

Dr David Collery[1], Dr Philip McKenna[2], Dr David Dunne[3], Dr Kevin Paine[4]
[1]Mott MacDonald, Mott MacDonald House, 8-12 Sydenham Road, Croydon, CR0 2EE
[2]CH2M HILL, City Park, 368 Alexandra Parade, Glasgow, Scotland, G31 3AU
[3]Aecom, Colmore Plaza, 20 Colmore Circus Queensway, Birmingham, West Midlands B4 6AT
[4] University of Bath, Claverton Down, Bath, North East Somerset BA2 7AY

email: David.Collery@mottmac.com, Philip.McKenna@ch2m.com, David.Dunne@aecom.com, K.Paine@bath.ac.uk

ABSTRACT: The recycling of construction, demolition and excavation waste (CDEW), makes it inevitable that a sand-like by-product is generated during the crushing and screening processes when producing coarse recycled aggregate. It is estimated that between 25% and 50% of initial CDEW after processing can be classified as fines, depending on the type, source and quality of the CDEW. Recycled aggregate fines (RAF) have an uncertain composition because of their sources, along with a potentially high clay and gypsum content. Given the possible multiple sources of RAF, it is vital to assess their suitability for use in concrete with respect to both engineering properties and environmental impact. In this paper the relationships given in national design codes between compressive strength and other strength and deformation characteristics are assessed in regards to recycled aggregate fines. The results suggest that whilst use of recycled aggregate fines may reduce strength at a given water/cement ratio (w/c ratio), compared to natural aggregates, that in the main, other characteristics are proportional to this loss in compressive strength.

KEY WORDS: recycled materials, aggregates, concrete, sustainability

1 INTRODUCTION

The recycling of construction, demolition and excavation waste makes it inevitable that a sand-like by-product is generated during the crushing and screening processes when producing coarse recycled aggregate. It is estimated that between 25 and 50% of initial CDEW after processing can be classed as fines, depending on the type, source and quality of the CDEW [1, 2]. Recycled aggregate fines have an uncertain composition because of their sources, along with a potentially high clay and gypsum content. Given the possible multiple sources of RAF, it is vital to assess their suitability for use in concrete with respect to both engineering properties and environmental impact.

A number of researchers have presented findings that the use of RAF as a natural sand replacement typically reduces the engineering properties of the RAF concretes to varying degrees. However, the use of RAF for replacement of natural aggregates fines by 30% does not seem to affect the compressive strength of the concrete. At higher percentages of RAF, a reduction in the compressive strength was observed [3,4].

Research with RAF concretes has found that RAF did not affect the ratio of flexural strength to compressive strength: as the compressive strength decreased with RAF, so too did the flexural strength [5]. The use of RAF was shown to decrease the modulus of elasticity of concrete by up to 18% with 100% replacement of natural sand [4].

The drying shrinkage of RAF concretes has been reported to increases in some cases up to 50%, compared to similar natural aggregates (NA) concrete [6]. Similar findings regarding the creep of concrete made with RAF, have shown there to be 35% to 45% higher creep strain in RAF concrete to that of natural sand concretes [7,8].

Research indicates that as RAF replacement levels increase a corresponding deterioration in the engineering properties of concrete is reported. In Japan [9] use of RAF is classify by particle aggregate density and water absorption and or formed, example, ≥2500kg/m3 and ≤ 3,5% water absorption is class H, indicating that no limitations are put on the type and segment for concrete and structures with a nominal strength of 45 MPa or less. Research into improving recycled aggregate fines before being used as fines aggregate in concrete as been undertaken by Ogawa [10,11]. The research focused on removing the components such as gypsum plaster and asphat and using different crusher to access which produced fine aggregate with lowest level of brittle defective part (cracks pore and voids), so to reduce the effects of RAF have on concrete.

However, in many cases it was difficult to ascertain the RAF characteristics within these studies. As the characteristics of any aggregate in concrete has an effect on concrete performance, it is important to understand what these parameters are and how these can affect concrete performance.

This paper reports on findings of research carried out at the University of Dundee to determine, whether; (i) concrete made with RAF differs from reference concretes made with natural aggregate, and(ii) the strength and deformation characteristics given in Eurocode 2 [12] (Table 1) are applicable to concretes made with RAF. This research forms part of a larger study undertaken to assess the applicability of a “Performance Base Approach” of normal weight aggregates

(natural, recycled and manufactured aggregate) for use in concrete.

In addition, this paper aims to increase knowledge regarding the use of RAF in concrete, highlighting potential benefits and concerns, so if engineers do get the opportunity to specify RAF in concrete, this paper will aid in their decision making process and possibly help increase the use of RAF concrete in the correct application. In turn, this will lead to an increase in the use of sustainable materials within the industry.

Table 1 Stress and deformation characteristics based on Eurocode 2

MATERIAL PROPERTY	ANALYTICAL RELATIONSHIP
Cylinder Strength, f_{ck}	
Cube Strength, $f_{ck,cube}$	$f_{ck} \approx 1.25\ f_c$
Compressive Strength, f_{cm}	$f_{cm} = f_{ck} + 8$
Tensile Strength, f_{ctm}	$f_{ctm} = 0.3\ f_{ck}^{(2/3)} \leq$ C50/60 $f_{ctm} = 2.12\ \ln((1+(f_{cm}/10)) >$ C50/60
Flexural Strength, $f_{ct,fl}$	$f_{ctm,fl} = 1.5\ f_{ctm}$
Tensile Splitting strength, $f_{ct,sp}$	$f_{ctm,sp} = (1/0.9)\ f_{ctm}$
Elastic Modulus, E_{cm}	$E_{cm} = 22\ [f_{cm} / 10]^{0.3}$ (f_{cm} in N/mm^2)

2 MATERIALS AND METHODOLOGY

The geometrical, physical and chemical characteristics of RAF, natural river sand and natural coarse aggregates were determined in accordance with BS EN 12620 [13]. The type, description, location, particle size distribution and aggregate characteristics of the aggregates are presented in Table 2 & 3 and Figure 1.

Table 2 Aggregates description and location

Aggregates type	Location	Production description
Natural Sand	Fife	Uncrushed, Grading 0/4mm
Natural Gravel	Fife	Uncrushed, Grading 4/10mm and 10/20 mm
RAF	Carnousie	Mobile cone crusher, crushed CDEW material, a mixture of materials, grading 0/4mm

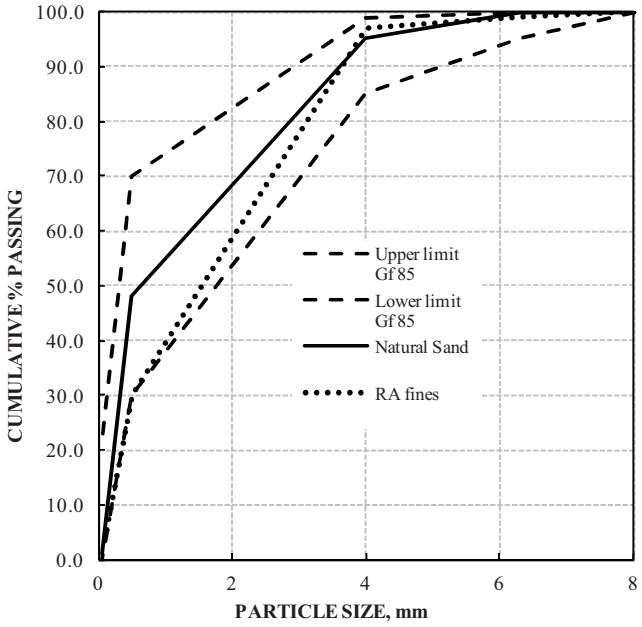


Figure 1 Particle Size Distribution for Natural Sand and Recycled Aggregate fine

This paper reports on characteristics of these aggregates and their effect on the main engineering properties of concrete at three w/c ratios (0.35, 0.50 and 0.70). RAF was used to replace natural sand at 25%, 50% and 100% for all three w/c ratios. Three natural sand based mixes were used as the reference concretes, giving a total of 12 concretes presented within this paper.

Concrete mixes in this research were designed in accordance with the Building Research Establishment (BRE) method. The BRE method is used for designing normal concrete mixes and is an established mix design method in the UK [14]. The method bases its designs on the required compressive strength, consistency, and durability requirements of the concrete. In the mix design, durability is specified by the maximum w/c ratio, minimum cement content, and minimum compressive strength. In this research, the main parameters controlling the mix design were the w/c ratio, the water content, and consistency. The BRE mix design was therefore implemented in the following steps:

- Select the required water content, with varieties for crushed and uncrushed aggregates: Table 3 in the BRE mix design.
- Calculate the cement content (water content divided by the w/c ratio).
- Calculate the total aggregate content. This requires an estimation of the wet density of the concrete, which is a value that reflects the relative density of combined fine and coarse aggregates on saturated surface dry (SSD) values and the free-water content of the concrete mix. The cement and water content values are subtracted from the concrete density to give the total aggregate content.

- The proportion of sand was determined by a percentage of the total aggregates content, and was estimated from the percentage of sand passing through 600μm sieves. This value was used for the BRE mix design (interpolation was necessary), along with information on the maximum aggregates size and the required consistency, to obtain the percentage of the fines in the total aggregates content.
- The coarse aggregates content was calculated by subtracting the sand content from the total aggregates content. This content was then divided by a ratio of 2:1 to give 20mm and 10mm coarse aggregates contents.

Table 3 Fine aggregates characteristics

Characteristics	Natural Sand	RAF
Density, kg/m^3 (i) SSD (BS EN 1097-6) [15]	2600	2540
(ii) Loose bulk (BS EN 1097-3)[16]	1580	1290
(iii) Compacted bulk	1660	1380
Compaction (BS EN 1097-3)	0.65	0.64
Water Absorption, % (BS EN 1097-6)	1.00	2.50
Drying Shrinkage, % (BS EN 1367- 4)[17]	0.03	0.067
Loss of Ignition, % (BS EN 1744-1) [18]	3.50	9.0
Aspect ratio (Slide gauge)	0.72	0.73
Convexity (voids)	0.91	0.92
Sphericity (Irregular shape)	0.87	0.86
Shape (BS EN 933-4) [19]	Round	Angular
Chloride total (BS EN 1744-1)	0.012	0.050
Chloride water (BS EN 1744-1)	0.001	0.004
Sulfate water (BS EN 1744-1)	ND	0.030

ND = Not Detected

Strength and deformation characteristics investigated included: (i) compressive strength, (ii) tensile splitting strength and flexural strength, (iii) static modulus of elasticity, and (iv) basic/drying creep.

3 AGGREGATE CHARACTERISTICS

The RAF and natural sand aggregate characteristics are presented in Table 3. BS and EN standards were used to characterise these aggregates (Table 3), other than the aspect ratio, convexity and sphericity of the fine aggregates which were determined by QICPIC Image Analysis System, which uses a helium-neon pulsed laser light source, an adaptable beam expansion unit, an imaging lens and camera to analyse fine particles as they pass the camera by means of a gravity disperser unit.

4 MEASUREMENT OF CONCRETE PROPERTIES

4.1 Compressive strength

The compressive strength of all concretes were determined by testing 100mm cube specimens in accordance with BS EN 12390-3:2002 [20]. Compressive strength tests were carried out at 3, 7, 28, 90 and 180 days. The 28 day characteristic compressive strengths for the three w/c ratios and replacement levels are presented in Figure 2. It was shown that as the replacement level of RAF increases, a reduction in the compressive strength of concrete was recorded. The strength for 100% RAF was approximately 6N/mm^2 to 12 N/mm^2 lower than the natural sand concrete, which represent on average a 25% reduction in the characteristic strength compared to natural concrete.

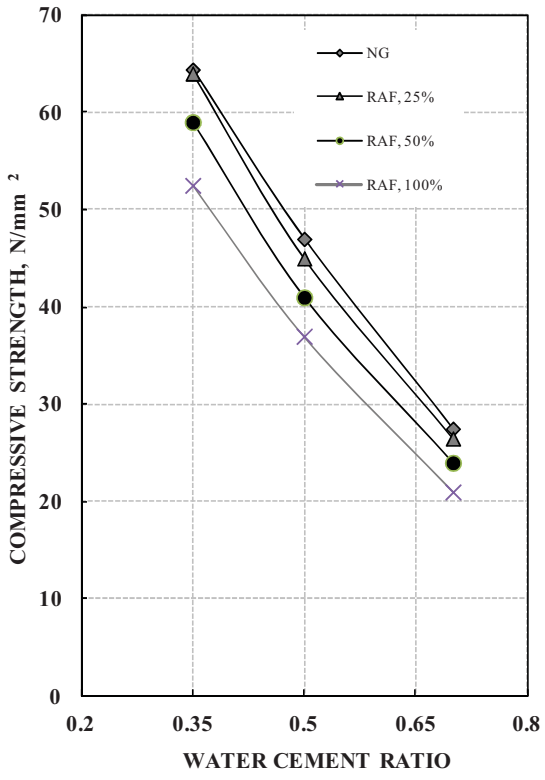


Figure 2 Relationship between w/c ratio and compressive strength for RAF concrete at different replacement levels

4.2 Tensile Strength

Tensile splitting strength was tested in accordance with BS EN 12390-6:2000 [21], using an Avery Denison machine to

test cylinders of 150mm diameter and 300mm length at 28 days. The cylinders were placed horizontally between the plates with hardboard strips. The results were rounded to the nearest 0.05N/mm². The relationship between mean cube strength ($f_{cm,cube}$) and mean tensile splitting strength ($f_{ctm,sp}$) is shown in Figure 2.

The results presented in Figure 2, indicate that the tensile strength reduced as the RAF replacement level increased. However, in general all the results lie on or above the 95 % confidence curve, suggesting that the Eurocode 2 relationship is reasonable. At high strengths there is a kink in the Eurocode 2 relationship to reflect a potential decrease in the gain in tensile strength with increased cube strength. Insufficient results were obtained at high strengths to verify whether this relationship is adequate for RAF concrete at high strength.

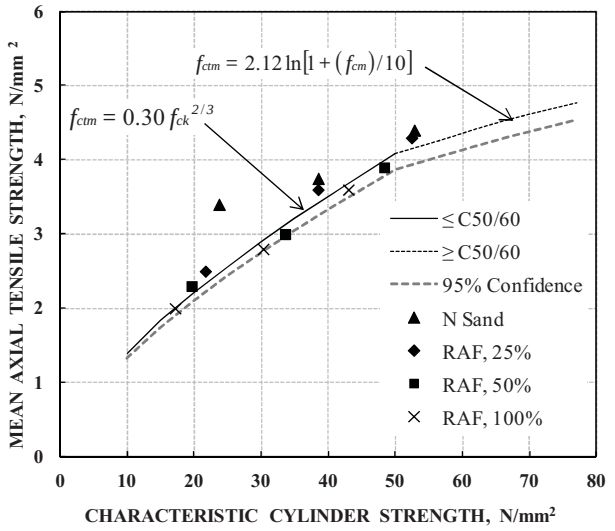


Figure 2 Relationship between characteristic cylinder strength and mean axial splitting strength

4.3 Modulus of Elasticity

Tests for calculating the modulus of elasticity were carried out at 28 and 90 days, using specimen cylinders measuring 150mm in diameter and 300mm long. The procedure was essentially as prescribed in BS 1881: Part 121 1983[22], which calculates the modulus from the stress/strain relationship.

The relationship between mean elastic modulus (E_{cm}) and mean cube strength ($f_{cm,cube}$) for all concretes are shown in Figure 3. In relation to the relationship given in Eurocode 2 (Table 1) there was a degree of scatter of results, which would be expected due to the known effect of aggregate type on the elastic modulus of concrete. This is acknowledged in Eurocode 2 which states that the values in Table 1 are applicable to quartzite aggregates, and should be reduced by 10% and 30% for limestone and sandstone aggregates respectively, and increased by 20% for basalt aggregates. These lines are indicated in Figure 3.

In general recycled aggregate concretes fell below the equation in Table 1, but were within the reduction limits permitted for sandstone aggregates, the exception of RAF 100%. This concrete was below the sandstone design line. In general, natural sand and RAF 25% and 50% concrete tended to have elastic modules 25% lower than those given in Table 1 for a given compressive strength.

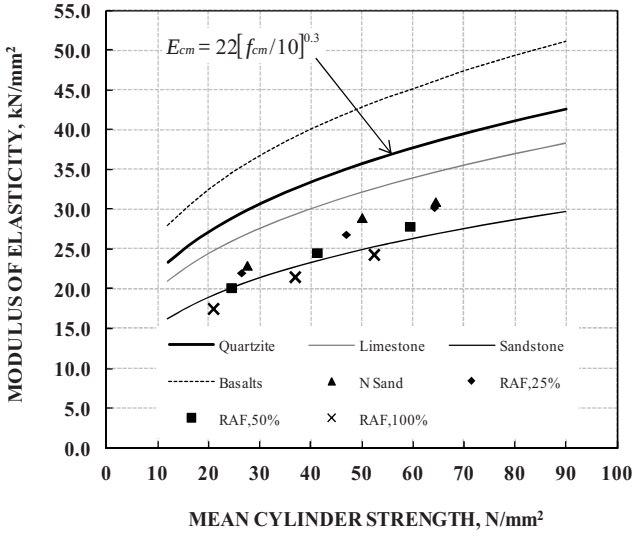


Figure 3 Relationship between mean cylinder strength and mean modulus of elasticity

4.4 Creep

Creep tests were carried out using a cylinder specimen of 100mm diameter and 300mm in length, in accordance with a procedure developed at the University of Dundee [23], due to no current standard European test method. At the age of 28 days, the specimen was capped at each end, as described in the procedure for testing the modulus of elasticity. Two demec points were then glued 200mm apart on a vertical line of each cylinder (50mm from both of the specimen), and the cylinders were covered with wax to seal them and to prevent shrinkage effects from drying. The specimens were subjected to a constant compression stress of 40% of the compressive strength of the concrete.

With this preparation, measurements were taken daily during the first week of loading, and then at three-day intervals for 12 weeks. Similar measurements were taken on sealed unloaded specimens. Concrete creep was calculated by comparing changes in the length of the specimen under constant load to changes in the length of the unloaded specimen in a similar environment.

Due to the limitation of creep rigs within the laboratory and the time constraint of the creep experiment, only RAF 100% at 0.5 w/c concrete was examined. Thus a degree of caution is required regarding these creep results.

Figure 4, shows the development of creep coefficient of natural sand and RAF at 100% replacement. RAF 100% had a

higher creep coefficient than natural sand concrete. Figure 5 shows how the experimental values for creep coefficient (after 90 days) compares to creep coefficient as calculated by Method 1 (given in the body of Eurocode 2) and Method 2 (in Annex B to Eurocode 2). The results are above the Method 2 line and below Method 1 line, indicating that caution is required when determining creep coefficient with the use of Method Two.

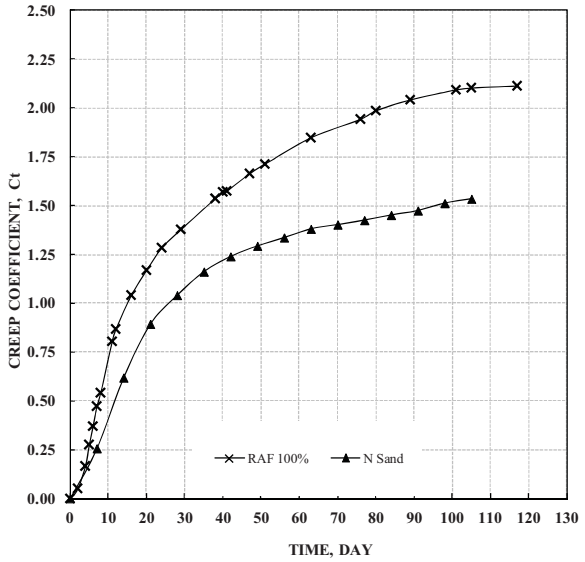


Figure 4 Creep coefficient of concrete made with natural sand and RAF at 100% replacement (w/c ratio = 0.5)

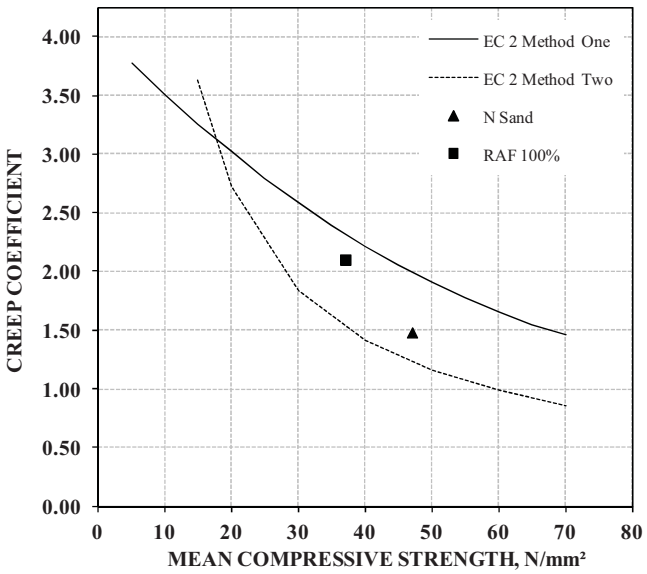


Figure 5 Relationship between creep coefficient given in Eurocode 2 and that experimentally measured at 90 days (w/c ratio = 0.5)

5 PRACTICAL IMPLICATIONS

Recent moves towards greater sustainability in concrete have led to greater interest in use of recycled aggregate fines in concrete. However, there has been concern that these aggregates may produce concrete that are not compatible with commonly accepted structural design rules.

The work reported has shown that the use of RAF may result in significant differences in compressive strength at a given w/c ratio when compared to natural aggregate concretes. However, differences in strength between natural aggregate concretes and RAF concretes are in the main proportionally carried over to other aspects of engineering performance (i.e. tensile splitting strength, elastic modulus and creep).

From these initial results, it can be suggested that there is no need for any review of general design procedures relating to the use of recycled aggregate fines, on account of differences in behaviour between these and normal aggregate concretes.

However, for the design parameter modulus of elasticity, it is recommended that trial mixes and testing be undertaken for replacement levels greater than 50%, as the sandstone design relationship is likely to overestimate the value. For tensile splitting strength and creep coefficient, criteria in Eurocode 2 may be used without modification.

As RAF has an uncertain composition because of their sources, along with a potentially high clay and gypsum content, it is recommended that chemical analysis be undertaken on all sources of RAF (similar to natural aggregate). If the RAF is from a washing plant, research has indicated that the majority of RAFs are suitable for use in concrete in regard to their chemical composition [24] .

This information should help engineers and designers to have more control and flexibility in their approach to the concrete they use. This is in terms of choice of RAF, with knowledge that compressive strength is appropriate for assessing other stress and deformation characteristics of a concrete mix.

6 CONCLUSION

The research presented in this paper was part of a much wider and more comprehensive study into the use of recycled and manufactured aggregates in structural concrete. Based on the work in this paper using recycled aggregate fines at three w/c ratios, and three replacement levels, it can be concluded that recycled aggregates fines may be used effectively within the framework of current design procedures. In particular it was observed that:

- Concrete made with natural, recycled aggregate fines will have different strength and deformation characteristics at a given w/c ratio.
- Changes in the strength and deformation characteristics when using recycled aggregate fines are proportional to the changes in compressive strength.
- Accepted and assumed relationships between engineering properties and compressive strength as used in most design codes are valid. The exception

was which respect to the modulus of elasticity of concrete with a 100% replacement of natural sand with recycled aggregates fines.

ACKNOWLEDGMENTS

The author's would like to thank the University of Dundee for facilitating and supporting this study, which formed part of a larger research project into the use of recycled and manufactured aggregates in concrete.

REFERENCES

[1] Van der Wegen G and Haverkort R. (1998); Recycled Construction Demolition Wastes as a Fine Aggregate for Concrete, Sustainable Construction: Proceeding of the international Symposium organised by the Concrete Technology Unit, University of Dundee and held at the Department of Trade and Industry conference centre, London, pp 333-345

[2] WBCSD. *Concrete Recycling: The cement sustainability initiative* http://www.wbcsdcement.org/pdf/CSI RecyclingConcrete-FullReport.pdf. (2009)

[3] Poon C.S, Kou S, Wan H, Etxeberria M (2009); Properties of concrete blocks prepared with low grade recycled aggregates, Waste Management Vol. 29 pp 2369-2377

[4] Evangelista L and Brito J.de. (2007); Mechanical behaviour of concrete made with fine recycled concrete aggregates. Cement and Concrete Research Vol. 29, pp 397-401

[5] Ravindrarajah, R.S and Tam T.C. (1987); Recycled concrete as fine and course aggregates in concrete. Magazine of Concrete Research, Vol. 39, pp 214-220

[6] Hansen T.C (1992); Recycling of Demolished Concrete and Masonry. Report of Technical Committee 37-DRC Demolition and Reuse of Concrete. RELIM (The international union of Testing and Research Laboratories for Materials and Structures)

[7] Ajdukiewicz A, Kiliszczewicz A. (2002); Influence of recycled aggregates on mechanical properties of HS/HPC. Cement and Concrete Research, Vol. 24, pp 269-279

[8] Evangelista. L. [a] & De Brito[b] .J (2013) Concrete with fine recycled aggregates: a review, European Journal of Environmental and Civil Engineering, vol 18, issue 2 pp 129-132

[9] JIS. (2011) Recycled aggregates for concrete – class H (JIS A5021:2011). Tokyo: Japan Concrete Institute (in Japanese)

[10] Ogawa, H., Nawa, T, Yamamoto K and Ohya K (2011). Research on a method for improving the quality of recycled fine aggregates by selectively. Dobokuggakkai Ronbunshuu E 67, 213-227

[11] Ogawa, H., Nawa, T,(2011) Improving the quality of Recycled Fine Aggregates by Selective Removal of Brittleness Defects. Journal of Advance Concrete Technology, volume 10, pp 395-410

[12] British Standard Institution (2004) BS EN 1992-1 Eurocode 2: Design of concrete structures – Part 1-1: General rules and rules for building.

[13] British Standard Institution (2008) BS EN 12620: Aggregates for concrete. British Standards Institution

[14] Marsh B, (1998); Design of normal concrete mixes, Second edition. Building Research Establishment

[15] British Standard Institution (2000) BE EN 1097-6, Test for mechanical and physical properties of aggregates – Part 6: Determination of particle density and water absorption

[16] British Standard Institution (1998) BS EN 1097-3, Tests for mechanical and physical properties of aggregates Part 3: Determination of loose bulk density and voids

[17] British Standard Institution (1998) BS EN 1367- 4 Test for thermal and weathering properties of aggregates – Part 4: Determination of drying

[18] British Standard Institution (1998) BS EN 1744-1, Test for chemical properties of aggregates – Part 1: Chemical analysis

[19] British Standard Institution (2001) BS EN 933-4 Tests for geometrical properties of aggregates - Part 3: Determination of particle shape - Shape index

[20] British Standard Institution (2000) BS EN 12390-4 Testing hardened concrete - Part 4: Compressive strength – Specification for testing machines

[21] British Standard Institution (2000) BS EN 12390-6 Testing hardened concrete - Part 6: Tensile Splitting strength of test specimens

[22] British Standard Institution (1983) BS 1881-121, Testing concrete - Part 121: Method for determination of static modulus of elasticity in compression

[23] DHIR, R.K., MUNDAY, J.L. & ONG, L.T., 1986. Investigations of the engineering properties of OPC/Pulverized-fuel ash concrete: Deformation properties. The Structural Engineer, vol 64(2), pp.36-42

[24] RK Dhir, KA Paine and JE Halliday, (2008) Facilitating the Wider Use of Coarse and Fine Recycled Aggregates from Washing Plants, WRAP Report, AGG-105-003

Assessing the reliability of pile driveability predictions from wave equations

Farrell E.R._1[1], Gill D.R._2[1] Farrell N._3[1]
AGL Consulting, Suite 2, The Avenue, Beacon Court, Sandyford, Dublin 18, Ireland
email: eric.farrell@agl.ie, david.gill@agl.ie, niamh.farrell@agl.ie,

ABSTRACT: Dynamic wave analysis methods are increasingly being used to predict pile performance from geotechnical parameters, replacing the old Hiley and Engineering News Formulae. Such analysis methods can be used to select an appropriate hammer, to assess drivability and driving stresses and to predict the static pile capacity for a particular set.

This paper discusses the relationship between standard geotechnical test parameters and those relevant to the 'dynamic' response of soils, with particular reference to Irish conditions. The recorded pile driving records for a site in Ireland is compared to those computed using dynamic wave analysis predictions from geotechnical parameters using two different software programs, PDPWave and GRLWeap. The findings of these studies are used to develop recommendations on the use of dynamic wave analysis methods in Ireland.

KEY WORDS: piles; dynamic analysis; case history

1 INTRODUCTION

Pile dynamic analysis (PDA) methods are increasingly being used to predict pile performance from geotechnical parameters, replacing the old Hiley and Engineering News formulae. Pile performance parameters predicted using these methods includes driveability (blows per unit penetration), time to drive a pile to its required depth and the dynamic stresses induced during driving. These methods use the same fundamental equations as those applied in the analysis of Dynamic Load Testing of piles (DLT) using wave matching methods but require the input of energy parameters, pile construction and the dynamic properties of the ground.

This paper looks at the background to the development of these methods of analysis and examines their reliability by using a recent case history of a pile driven to support a crane rail as part of the Alexandra Quay East (AQE) refurbishment project. The AQE is being constructed by BAM Civil and is expected to be completed in 2015. The analyses are carried out using two industry standard software programs, PDPWave and GRLWeap in order to compare the different soil models available.

The comparison between predicted and recorded driveability results are used to show that standard geotechnical relationships can be used when developing the soil resistance models.

2 BACKGROUND TO DYNAMIC PILE ANALYSIS

2.1 Basic Equations

The basis of all wave mechanics in piles is that the pile responds to impact in accordance the one-dimensional wave equation. Smith [1] developed a method of using numerical solutions to investigate the dynamic behaviour of piles during driving which could include the properties such as ram weight, ram velocity, cushion, pile properties and dynamic behaviour of the soil. In the Smith model, the piling system is modelled by a series of masses and springs and the pile itself is divided up into discrete 'lumped' masses interconnected by springs and dashpots which can be formulated into a computer algorithm. The pile-soil interface is modelled using elasto-plastic springs to represent static resistance and a quasi linear dashpot to model the damping resistance. The spring constant assigned to a soil (k) is determined by dividing the resistance assigned to a pile section by the maximum elastic deformation or Quake (i.e., Quake has a linear dimension). The dashpot represents the resistance to motion assuming a viscous behaviour of the soil and is termed the dynamic resistance (R_d). Smith [1] determined the dynamic resistance using the static resistance (R_s) of the pile, the velocity of the pile tip (V) and the Smith damping factor (j) – as given in Eq 1.

$$R_d = j\, R_s\, V \tag{1}$$

The total soil resistance to pile driving (R_t) is therefore given by Eq. 2. The total resistance must consider both the shaft and toe resistances.

$$R_t = R_s\,(1+jV) = (\Delta_p - \Delta_p')k(1+jV) \tag{2}$$

where k is determined by dividing the resistance assigned to a pile section by the value of the soil quake and Δ_p and Δ_p' are displacement and permanent displacement of the pile tip [2]. The resistance is constant for displacements beyond the quake.

Different expressions may be used for the damping resistance. The units of j in the Smith relationship (see Eq. 1) are s/m. The damping resistance may be represented by $R_D(t)= Jv(t)$ in which case the damping factor has units of kN

s/m, or by $R_D(t)= j_c(EA/c)v(t)$, where j_c is the Case damping factor and is dimensionless. Middendorp [3] lists other relationships, including the form $R_sJ_sV^{\alpha}$, which is an option available in PDPWave. Goble and Rausche [4] state that the general experience with CAPWAP analyses indicates that none of these relationships gives fundamental soil properties and further research is necessary in this area.

The resistance can also be modelled as acceleration dependent, in which case it is treated by simply adding to the mass of the pile [3].

The fundamental relationship used in dynamic pile behaviour is conservation of energy, which is expressed in Eq. 3 and is that energy applied by the hammer minus energy lost in pile (E_{pl}) and minus the energy lost in soil (E_{sl}) is equal to the total driving resistance times (R_t) times the permanent set of the pile under one blow (S).

$$e_d e_h E_r - E_{pl} - E_{sl} = R_t S \qquad (3)$$

where e_d = energy loss in piling system
e_h= hammer efficiency
E_r = rated energy given by manufacturer

The wave equation approach differs from the old energy formula in that the parameters e_d, E_{pl} and E_{sl} are computed through numerically modelling the driving system, pile and soil behaviour. Only the hammer efficiency is estimated. The total resistance to driving comprises the shaft driving resistance and the toe driving resistance.

2.2 Static resistance to driving (SRD)

The Static Resistance to Driving (SRD) is the resistance mobilised during driving and is derived from the long-term shaft resistance (derived using standard static geotechnical procedures), which are reduced by factors to allow for the reductions in shaft resistance and long-term end bearing from the standard static values due to the driving. The terminology of the reduction factors vary, the most common being the setup factor but also adjustments are by gain/loss factors or by fatigue factors. Typically the long-term shaft resistance is in terms of kPa and the total resistance is obtained by multiplying this resistance by the pile perimeter and pile segment length and multiplying the end bearing by the area of the pile tip. The setup factor is usually only applied to shaft resistance and not to end bearing. The SRD at the toe can be higher than the long term static resistance where relaxation is possible. Cessations in driving can be considered by the use of a setup time, which is the time that the static resistance to driving reverts back to the long-term shaft resistance.

2.3 Dynamic parameters

The basic dynamic parameters required in the analyses are the quake for shaft and toe resistance, and damping factors for both. More complicated analyses can require other parameters.

The skin quake for impact driven piles is normally taken as 2 or 2.5mm. Toe Quake for unplugged piles is generally 2.5mm and is adjusted for plugged piles according to the size of the pile; the rule of D/120 (inches) is typically used for very dense or hard soils, and D/60 for all other soils.

2.4 Methods of analysis

The one-dimensional elastic propagation of the wave along a pile can readily be formulated using finite difference or finite element methods. PDPWave solves the wave equation by using the method of characteristics [3].

3 THE PROJECT, LOCATION, GEOLOGY

3.1 The Project

The pile driving record analysed in this report was from a tubular pile installed as part of the Alexandra Quay East Phase 3 works which included the refurbishment of an existing quay. The former quay was constructed using 16 to 17m high concrete caissons (including a 3m high concrete cap) with a plan area of about 15m by 8m, which were placed at about -13 mAOD. The surface level was about 3 to 3.5m AOD. The refurbishment work was required to allow dredging works below the formation level of the caissons to accommodate larger vessels. This is achieved by forming a combi-wall in front of the caissons which is tied into the caissons themselves. This included driving H section piles to refusal at 1.9m centres and infill AZ-17-700 sheet piles. This paper discusses the resistance to driving of a static test pile (STP) which was put down to support a crane rail.

3.2 Location

Alexandra Quay East (AQE) is located on the north side of the River Liffey in Dublin Port as shown on Figure. The approximate location of the Static Load Test Pile (STP) is shown on this figure.

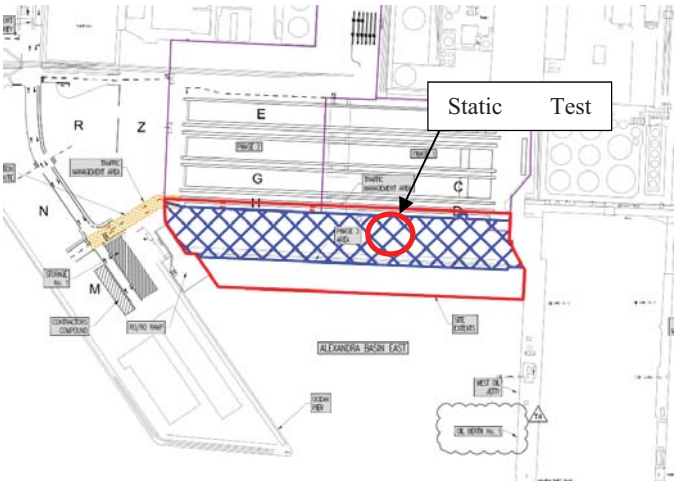


Figure 1. Location of Alexandra Quay East refurbishment

3.3 Geology

The Dublin Port area is on land reclaimed from the sea over the years, expanding out from the City Quays with the creation of the Great South Wall and North Bull Wall in the

Dublin estuary. The Liffey River deposits material within this bay as does, to a lesser extent, the Tolka and Dodder Rivers. The limestone bedrock is at a significant depth in the Dublin Bay area due to the presence of a preglacial channel. The depth to bedrock at the AQE is indicated to be between -40 and -30mAOD (Malin). The stratification at AQE is made up of:-

- Made Ground
- Recent estuarine and alluvial deposits which comprise soft estuarine silts/clays and post glacial sands and gravels.
- Port Clay, which is discussed in the following sections.
- Glacial deposits
- Limestone bedrock.

4 GROUND CONDITIONS AND PARAMETERS

The expected stratification at the AQE at the location of the Pile SPT is summarised in Table 1. The ground parameters are best appreciated from the plot of the values from the standard penetration tests – see Figure and from the undrained shear strength values interpreted from the CPTu probes – see Figure . Atterberg limits measured on samples from the site are shown on Figure .

The driving resistance of the Port Clay is of particular interest as a significant depth of this stratum underlies the Dublin Bay area, including the Dublin Port area, Ringsend and Sandymount. The presence of fine sand and silt layers with this deposit has caused rapid release of suction pressures in undisturbed samples recovered from this stratum and an underestimation of its in-situ strength [5]. With reference to the values of c_u interpreted from the CPTu results put down for the AQE, which are shown on Figure , a lower value could be interpreted below -25mOD and it is of interest to determine if this is evident in the pile driving records.

Table 1. Typical stratification at location of STP

Stratum	Description	mOD (T)*	Summary of properties
Made Ground	Loose to medium dense or dense silty sandy Gravel or gravelly Sand with cobbles and boulders and brick and concrete, sometimes with Clay or Silt lenses	3m (16)	N_{SPT} = 7 to refusal- see Figure q_c = 5 to 15 MPa, ave 5MPa at top, 7MPa at base. c_{uave} of soft ≈30kPa
Estuarine/ Alluvial Sands & Gravels	Medium dense and dense sandy Gravels or slightly silty sandy Gravel with occ. cobbles	-13m (4)	N_{SPT} = 12 to 36, ave. 22- see Figure
Port Clay	Firm, becoming stiff, laminated sandy Clay, locally silt.	-17m (12)	See Figure c_{uk}=120kPa above -25mOD c_{uk}=100kPa below -25mOD ϕ'_k=32°
Glacial till	Very stiff and hard slightly sandy slightly gravelly CLAY with occasional to many cobbles and boulders	-29m (2.5)	N_{SPT} = refusal c_{uk} taken as 400kPa
Rock	Limestone	-31.5 (-)	UCS = 30MPa

*approx.. mAOD of top of stratum/(T=Thickness)

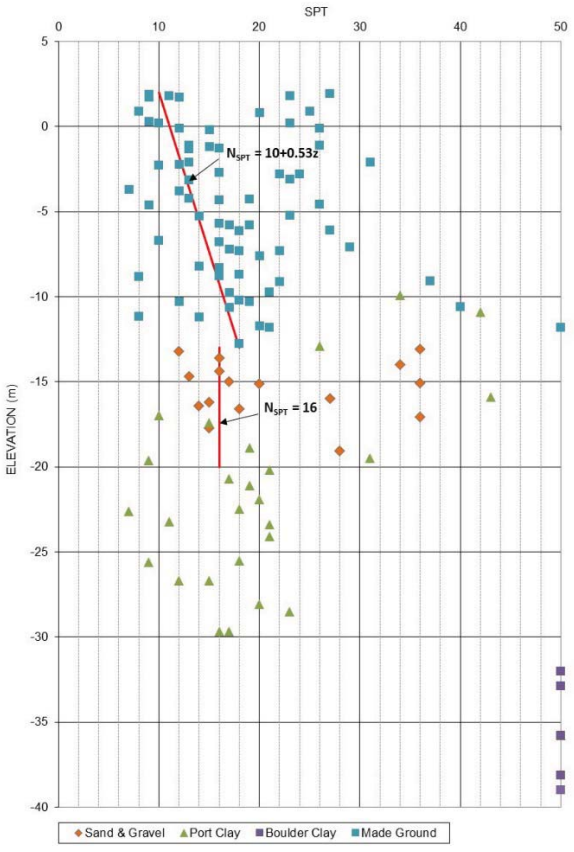


Figure 2. N_{SPT} values versus elevation

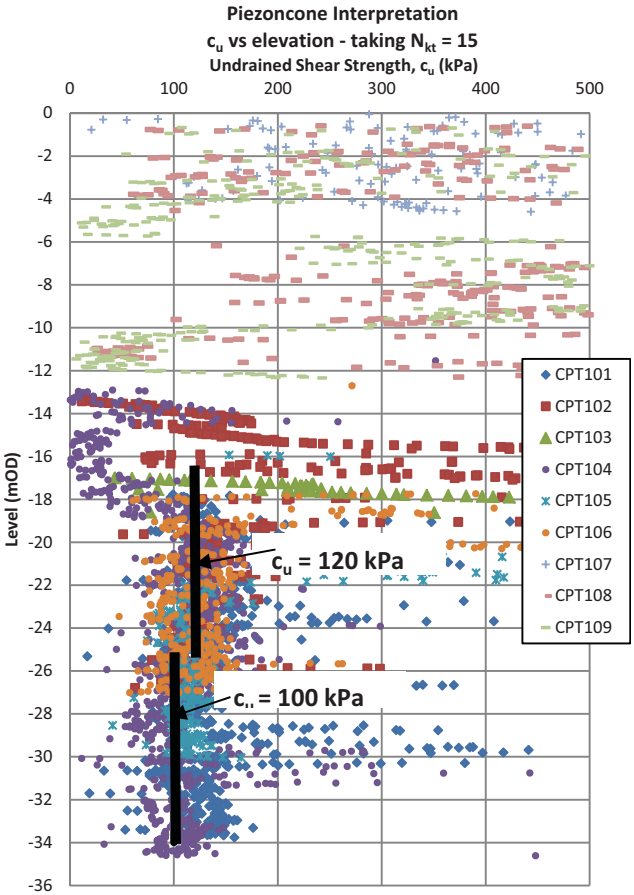


Figure 3. c_u interpreted from CPT data

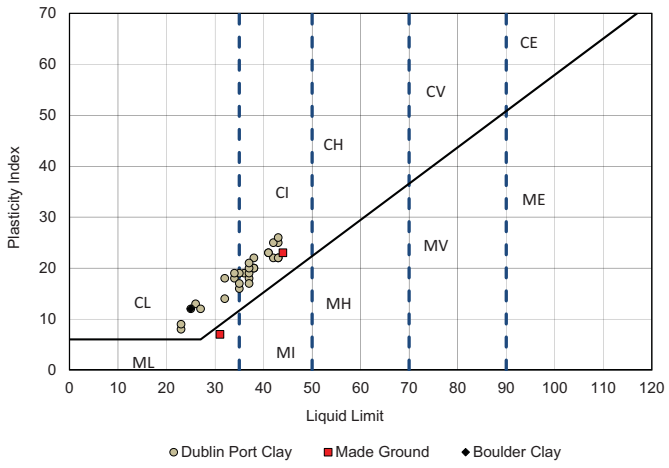


Figure 4. Atterberg limits recorded at AQE

5 DETAILS OF PILE AND PILE DRIVING

Pile STP was a 406mm diameter and 14.3mm thick open steel tube which was driven in two sections to accommodate the capacity of the pile leader. The first 22m long section was driven to 20.25m using a Delmag D22 hammer. The upper 0.25m of the pile was then burnt off and a section welded on to give a total pile length of 38m. This was driven to a set using a BSP HH9 hammer which was achieved at about 33m penetration. A set of 12 blows per 12.5mm was achieved at that depth.

The ground elevation at the location of Pile STP was about 3m OD.

The driving records of Pile STP are shown on Figure 5 as blows per 250mm penetration. Site inspection indicated that the pile plugged during driving.

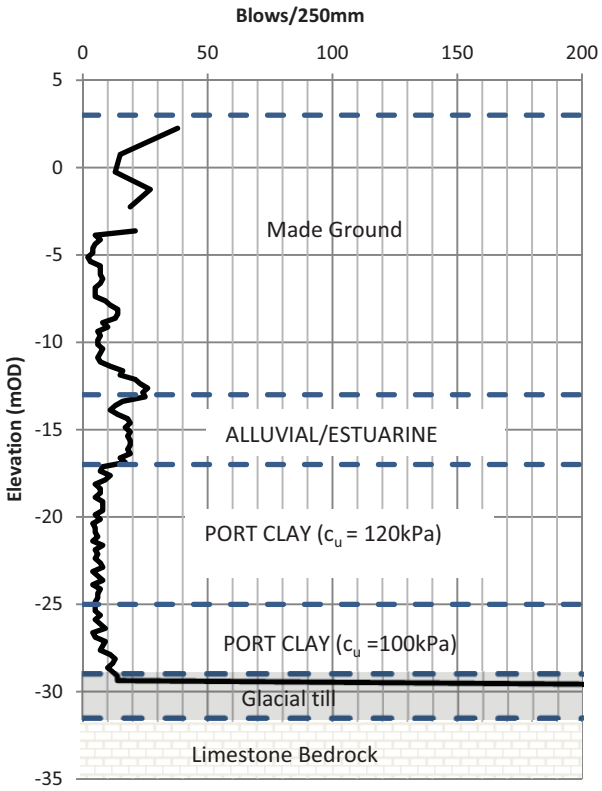


Figure 5. Driving records of Pile STP.

6 DRIVEABILITY ANALYSIS

6.1 Methods of analysis

The pile driveability analyses were carried out using two industry standard software packages, namely PDPWave and GRLWeap. The hammer characteristics were obtained from the library details or from the hammer manufacturer's website. The pile was modelled as plugged, which is consistent with the site observations and is to be expected for a 406mm tubular pile.

6.2 Soil parameters

The soil parameters used in the analyses are given on Table 2 to Table 5. The yield stress for the different strata were determined using standard soil parameters. For example, the static yield stress in the Dublin Port Clay was determined from the c_u values illustrated on Figure using shaft yield stress = α c_u with α =0.5 which is in line with typical empirical correlations used in practice. The toe yield stress was estimated as 9 c_u.

The choice of the appropriate c_u value for driveability analysis would be expected to differ from a characteristic value used, for example, in an overall stability analysis, an average or higher bound value may have to be considered.

Table 2. PDP Wave - Shaft

Stratum	Yield Stress kPa	Quake mm	Yield Factor	B	Damping Constant NMS/m^3	α
Made Ground	60	2.5	1	1	0.006	1
Alluvial/ Estuarine	66	2.5	1	1	0.007	1
DPC (1)	60	2.5	1	1	0.024	0.2
DPC (2)	50	2.5	1	1	0.02	0.2
BC	400	2.5	1	1	0.2	0.2
Rock	4000	2.5	1	1	0.4	1

Table 3. PDP Wave - Toe

Stratum	Yield Stress MPa	Quake mm	Yield Factor	B	Damping Constant NMS/m^3	α
Made Ground	1.2	6.7	1	1	0.452	1
Alluvial/ Estuarine	1.3	6.7	1	1	0.465	1
DPC (1)	1.08	6.7	1	1	0.331	0.2
DPC (2)	0.9	6.7	1	1	0.313	0.2
BC	7.2	3.4	1	1	0.555	0.2
Rock	135	1	1	1	1.735	1

Table 4. GRLWeap - Shaft

Stratum	Yield Stress kPa	Quake mm	Setup factor	Damping Constant s/m
Made Ground	60	2.5	1.5	0.16
Alluvial/ Estuarine	66	2.5	1.5	0.16
DPC (1)	60	2.5	1.5	0.65
DPC (2)	50	2.5	1.5	0.65
BC	400	2.5	1.5	0.65
Rock	4000	2.5	1.5	0.65

Table 5. GRLWeap - Toe

Stratum	Yield Stress MPa	Quake mm	Setup factor	Damping Constant s/m
Made Ground	4	6.7	1.0	0.5
Alluvial/ Estuarine	4	6.7	1.0	0.5
DPC (1)	1.08	6.7	1.0	0.5
DPC (2)	0.9	6.7	1.0	0.5
BC	3.6	3.4	1.0	0.5
Rock	36.0	1	1.0	0.5

7 RESULTS

The driveability predictions of the 406mm diameter by 14.3m thick plugged tubular pile which was initially driven to 20.25m penetration using the Delmag D22 and then extended to 38m total length and driven to a set at a depth of 33m using the BSP HH9 hammer, are shown on Figure and Figure as blows per 250mm penetration for PDPWave and GRLWave respectively. These figures also show the site recorded driving history.

The comparison between predicted and recorded blows/250mm penetration is excellent apart from that for the Delmag 22 from ground level to 20.25m penetration using GRLWeap, which is the drive of the first section of the pile. Inspection of the computed details indicates that this disparity is probably due to the modelling of the Delmag D22 hammer rather than an error in modelling the soil properties as the results indicate a significant reduction in energy supplied to the top of the pile with increased penetration. The properties of the hammer were taken from the databank included in the program. This requires further investigation. Interestingly, the PDPWave analysis gives a correct prediction for both sections.

The prediction of both PDPWave and GRLWeap was excellent in the Port Clay. Comparing the predicted and recorded results, the driving records do not indicate the reduction in undrained shear strength of the Port Clay below -25m OD which could be inferred from the CPTu results.

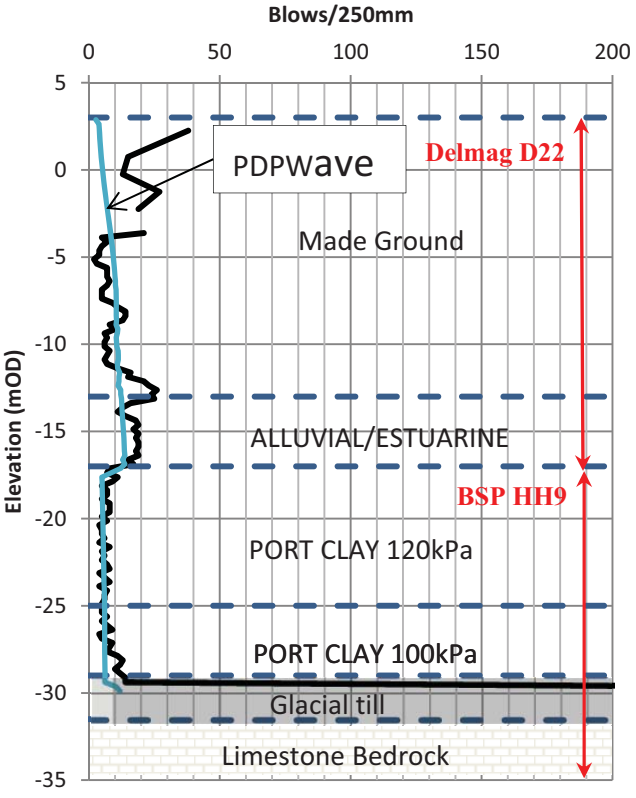


Figure 6. PDPWave Driveability predictions

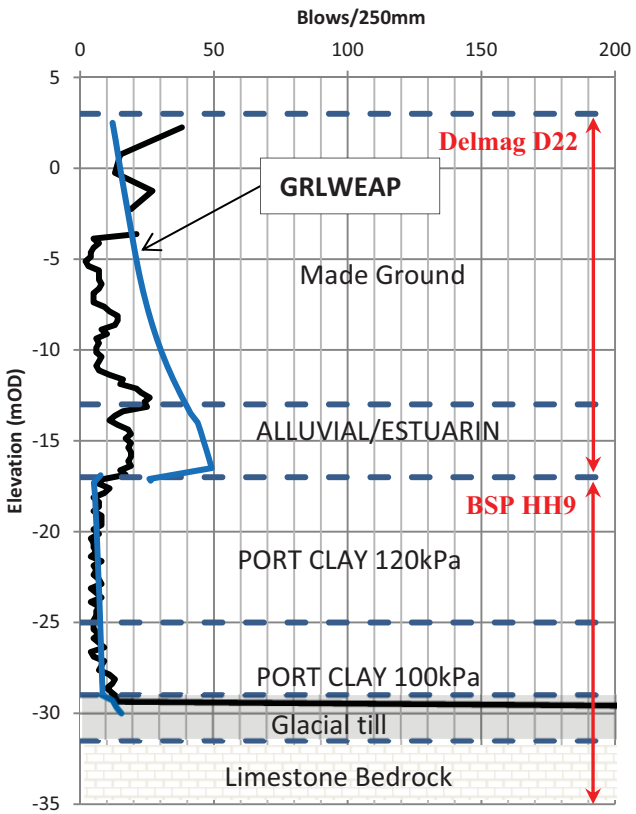


Figure 7 GRLWeap Driveability predictions

8 CONCLUSIONS

The good comparison obtained between the recorded driving records on the AQE site and those predicted using wave analysis methods, together with standard geotechnical soil parameters for determining yield stresses, shows that these methods can be a useful tool both in the selection of the appropriate hammer for a project but also in backanalysing soil properties from driving performance.

The driving prediction of one analysis for the upper 20.25m penetration was poor, however this is considered to be related to a model used for the hammer and requires further research.

Contrary to a possible interpretation of the CPTu test results on this site, the driving records do not indicate a drop off in undrained shear strength in the Port Clay with depth.

ACKNOWLEDGMENTS

The authors would like to thank BAM Civil for their assistance and for permission to publish this case record.

REFERENCES

[1] E.A.L Smith (1960) Pile driving analysis by wave equation, *Jnl. Of Soil Mechanics and Foundation Division, Proc. ASCE,2574*.

[2] M C McVay and C L Kuo (1999) Estimating damping and quake by using traditional soil testings, Dept. of Civil Engineering, Uni.of Florida, submitted to the Florida Dept. of Transport.

[3] S. Middledorp (2004), Thirty years of experience with the wave equation solution based on the method of characteristics., 7th Int. Conf. on the Application of Stress Wave Theory to Piles, Kuala Lumar, Malaysia.

[4] G.G. Goble and F. Rausche F, (1980), Pile driveability predictions by Capwap, *Numerical methods in offshore piling*, ICE, London, 29-36.

[5] E R Farrell and D Wall, (1990) The soils of Dublin, *Trans. Instn. Engrs. Ireland*, 115, 1990, 78-97

Finite element analyses of the installation of offshore spudcan foundations in clay

Sogol Fallah and Ken Gavin
Scgool of Civil, Structural and Environnemental Engineering, University College Dublin, Belfield, Dublin, Ireland
email: sogol.fallah@ucdconnect.ie, kenneth.gavin@ucd.ie

ABSTRACT: Jack-up rigs are used in offshore construction, drilling and maintenance projects. Once positioned at an offshore site the rig is jacked into the operating position by deploying steel legs supported by large pad foundations called spudcans. Depending on the sea bed soil conditions the spudcan, which can be up to 20 m wide, can penetrate many metres into the soil. Design guidelines recommend conventional bearing capacity approaches to estimate the penetration depth of spudcans, however, the appropriate bearing capacity factors for this large-deformation problem are difficult to determine. In this paper, the continuous penetration of spudcans is modelled using the Coupled Eulerian Lagrangian method. The effect of soil strength on the backflow mechanism which develops during installation is highlighted.

KEY WORDS: Spudcan; Clay; CEL Analysis; Installation

1 INTRODUCTION

Offshore jack-up rigs are widely used for oil and gas well drilling, site exploration, wind farm construction and for maintenance projects. The rigs, see Figure 1 typically consist of three or four legs resting on large conical footings with diameters in the range of 10-20 meters, known as spudcans. During installation, the hull of the jack-up is ballasted with water and the leg is lowered until the bearing capacity of the spudcan is equal to the dead-weight of the rig. When the legs are all in place the ballast is removed and the rig operates on effectively preloaded foundations. The spudcan penetration problem is a complex, large deformation geotechnical problem for which numerical modelling is particularly suited.

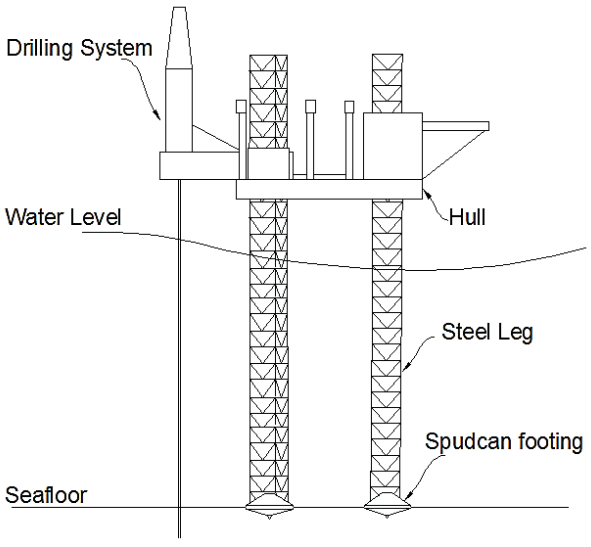


Figure 1. Schematic spudcan footing for jack-up rig

2 LARGE DEFORMATION FINITE ELEMENT ANALYSIS

Because of the numerical difficulties associated with performing large deformation analyses, early work on finite element analysis of spudcans assumed the foundations to be wished-in-place and the stress field around the pile was defined by making some simplifying assumptions [1]. Recent developments in finite element analyses allow large deformation analyses including Cone Penetration Testing (CPT) and pile installation to be modelled.

There are two approaches which can be adopted, the Lagrangian approach and the Eulerian approach. The difference between the approaches is illustrated in Figure 2. In the traditional Lagrangian approach, shown in Figure 2 (a), the elements are filled with material and they deform as the material deforms. In the Eulerian approach, the elements are fixed and the material flows through the elements as shown in Figure 2 (b). As a result, there is no mesh distortion in the Eulerian approach.

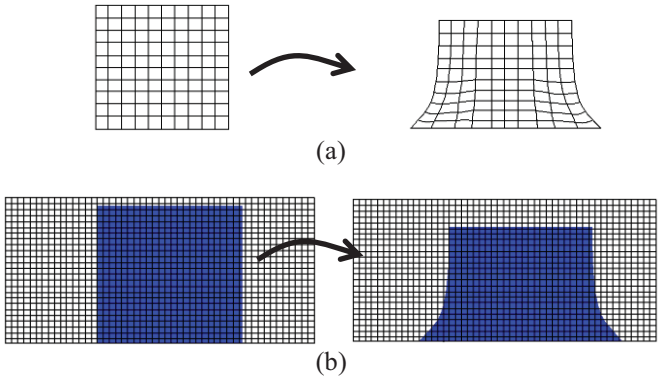


Figure 2. Lagrangian Vs Eulerian technique

When performing large deformation problems such as spudcan penetration excessive mesh distortions may lead to difficulty with convergence or inaccurate results during numerical modelling. To overcome these problems, different techniques have been introduced such as Arbitrary Lagrangian-Eulerian (ALE) and Coupled Eulerian Lagrangian (CEL) techniques. The ALE technique aims to reduce the distortions by remeshing the domain at a certain frequency. The field values are interpolated and transferred from the old mesh to a new improved mesh. In this method, the number of elements and the connectivity of the nodes do not change during the remeshing process. Instead the nodes are moved to find a new position in order to reduce the distortion of elements. The Coupled Eulerian Lagrangian (CEL) method provides an environment in which both Lagrangian and Eulerian materials can be used. This method of analysis avoids excessive mesh distortions although it has limitation on defining the material boundaries. As shown in Figure 2 (b), multiple materials can exist in an Eulerian element. Since the boundaries between the materials are approximate, the boundary surface is discontinuous in this approach. In this study the CEL method is adopted.

The large deformation finite element analysis of spudcans has been addressed in the recent studies [1]–[4]. Previous work on large deformation finite element analysis of spudcans has been performed by Qiu et al. [5] who investigated the capabilities of the CEL method by performing benchmark tests on strip foundation. Two case studies considered in the analyses showed very good agreement with analytical solutions. The application of CEL for simulating pile installation and the effects of a ship running aground were also considered. Tho et al [6] performed three dimensional Eulerian analyses to investigate the effect of spudcan penetration on adjacent piles. The results were compared to experimental data from a centrifuge good agreement was obtained. The above studies suggest that the CEL technique is a reliable approach to solve large deformation problems such as spudcan installation.

The mechanism of failure during deep penetration in soft and stiff clay will be different. In this paper CEL analyses were performed to investigate the failure mechanism which develops during continuous spudcan penetration into soft and stiff clay using Abaqus/Explicit [7]. The flow pattern of the soil in the area surrounding the spudcan (including backflow) is compared for the two cases.

3 FINITE ELEMENT MODEL

A three dimensional finite element model was developed to simulate the continuous penetration of the spudcan. Considering the symmetry of the problem, only a quarter of the domain was modelled. The soil domain was chosen as 7.5 spud can diameters, D in the horizontal direction and 8D to the bottom boundary. Given the concentration of large deformations, the Tresca constitutive model was adopted for the soil. The flow of the material normal to boundary planes was restricted by applying velocity boundary conditions to the planes. All the analyses were undertaken assuming undrained conditions. The soil was assumed to have a Poisson's ratio of 0.495, friction and dilation angles were set to zero and a soil stiffness of E/s_u = 500 was adopted where s_u is the undrained shear strength of the soil and E is the soil stiffness. Analyses were carried out for a spudcan with a conical angle of 150^0 as shown in Figure 3. The steel leg was not considered in this analysis as it has been shown to have a relatively small influence on the results. The spudcan was modeled as Lagrangian rigid element. The soil-structure interface was assumed to be frictionless.

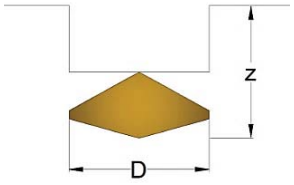


Figure 3. Geometry of the spudcan in simulation

During installation a large volume of soil is displaced to accommodate the spudcan. This will cause heave at the seafloor level. In order to allow the material to move upward, a void layer was defined above the seafloor level as illustrated in Figure 4. The red area indicates the void layer and the blue area indicates the soil layer. The initial location of the spudcan is also shown in this figure. The initial stress field is defined using the submerged unit weight of the soil.

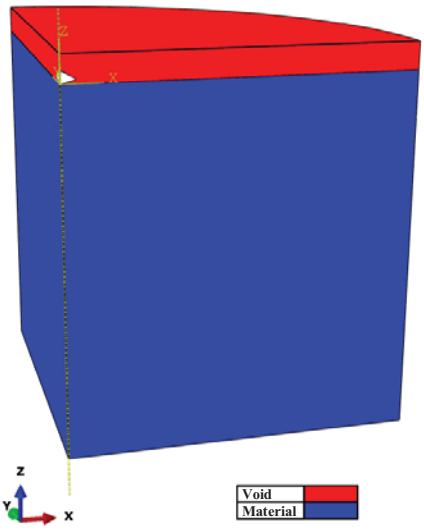


Figure 4. The quarter symmetry representation of the model

3.1 Influence of loading rate

The influence of loading rate on the soil contact pressure mobilised during spudcan penetration was investigated by performing analyses with loading rates of 0.25 m/s, 0.5 m/s and 1.0 m/s respectively. The load-penetration curve shown in Figure 5 reveals that the results were not significantly dependent on the loading rate. The bearing capacity of the spudcan q_n in Figure 5 was obtained by dividing the reaction force by projected area of the spudcan. A loading rate of 0.5 m/s was therefore selected for remaining analyses presented in this paper.

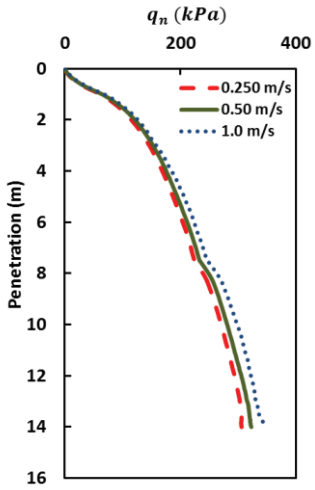


Figure 5. Load- penetration curves for spudcan penetration subjected to different loading rates

3.2 Influence of Mesh Density

A set of simulations was performed to study the effect of mesh density on the bearing capacity of the spudcan. Rather than considering a maximum available vertical force, all penetration analyses were performed to a fixed spudcan penetration depth of 15 m. The soil domain was therefore divided into two regions. The upper region with a depth of 20 m (where strains were concentrated) had a fine mesh. The soil below 20 m had a coarser mesh in order to increase computational efficiency. A uniform soil profile, with a constant s_u of 20 kPa was assumed. The effect of mesh element size (for the upper region) was investigated by varying the smallest element size in Fine Mesh (0.75 m or 0.075D), Medium Mesh (1.25 m or 0.125D) and Coarse Mesh (2.5 m or 0.250D) as shown in Figure 7.

The load-penetration response of the three analyses is shown in Figure 6. This figure illustrates that the medium mesh provided a reasonable compromise between numerical accuracy and simulation times.

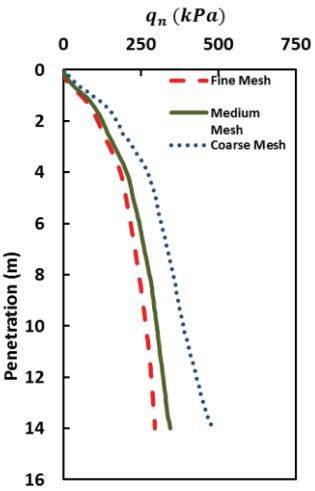
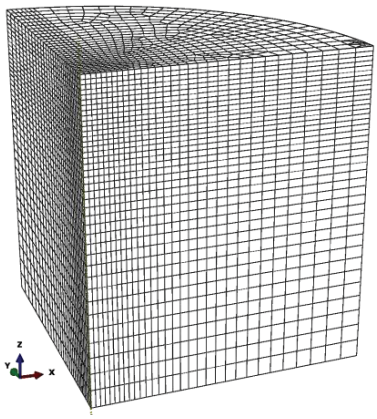
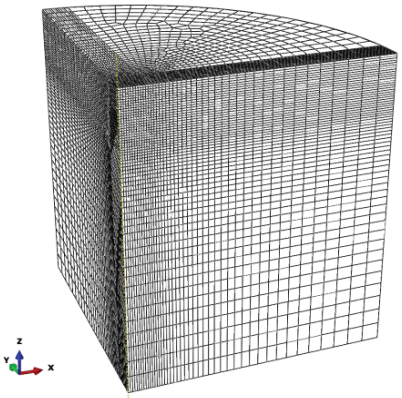


Figure 6. Load- penetration curves for spudcan penetration subjected to different mesh densities

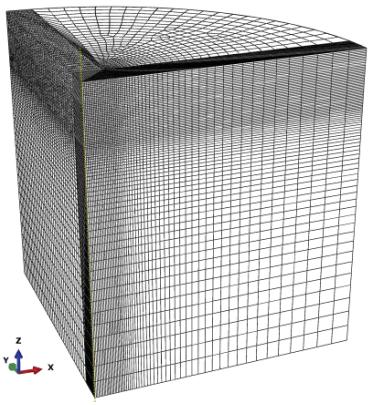
.



Coarse Mesh



Medium Mesh



Fine Mesh

Figure 7. Finite element meshes used to study the influence of mesh density

3.2 Results

Finite element analysis of spudcan penetration in soft (s_u = 10 kPa) and stiff clay (s_u = 100 kPa) were performed to investigate the failure mechanism which developed during deep penetration of the spudcan. The bearing pressure mobilised in the two soil profiles shown in Figure 8.

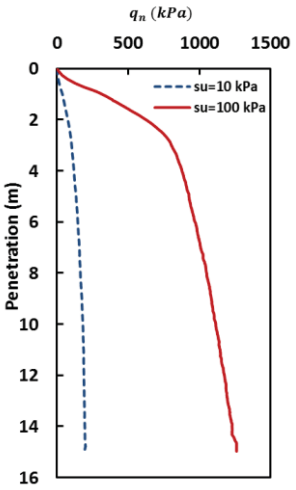


Figure 8. Load-penetration response for soft and stiff clay

As noted in the Eulerian domain flow of material is allowed. The ratio by which each Eulerian element is filled with material is defined by a parameter known as the Eulerian Volume Fraction (EVF). Figure 9 (soft clay) and Figure 10 (stiff clay) show the EVF values developed at a depth of 9, 12 and 15 m during penetration of the spudcan. The upper layer, shown by the red colour, is a void layer which is empty of material and the blue areas represent elements filled with material. The elements that are partly filled with material are represented in the colour spectrum. It is clear from the figures, that the material boundaries are not defined precisely. This is one of the weaknesses of the CEL approach compared to the Lagrangian approach. However, the efficiency of the CEL approach in terms of time, computational cost and also avoiding the excessive mesh distortions, makes this method very practical for solving the large deformation problems.

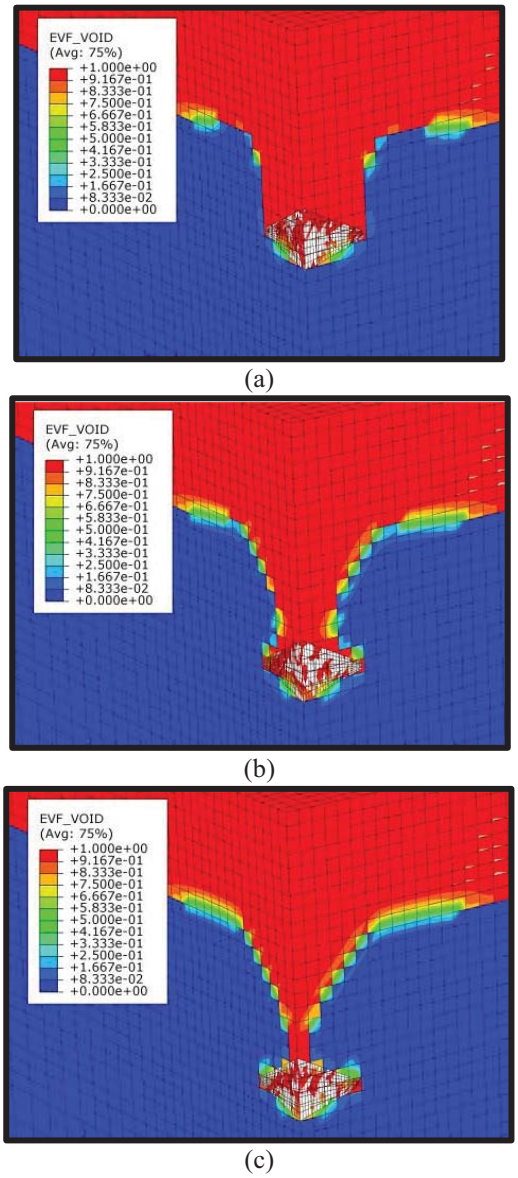


Figure 9. Eulerian volume fraction plot for spudcan penetration into soft clay at depth of (a) 9 m (b) 12 m (c) 15 m

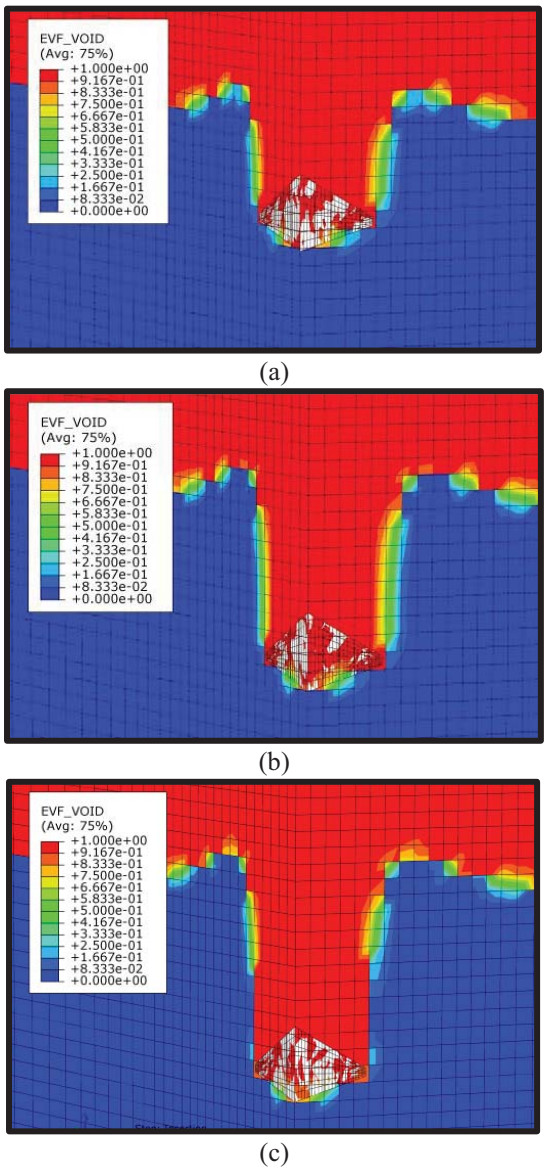


Figure 10. Eulerian volume fraction plot for spudcan penetration into stiff clay at depth of (a) 9 m (b) 12 m (c) 15 m

Figure 9 and Figure 10 illustrate the displacements of the soil during the installation of the spudcan in soft and stiff clay. As it can be seen in the Figure 9 (a) and Figure 10 (a), a large cavity (with similar width to the spudcan) is formed during the initial stages of installation of the spudcan. With further penetration (figure 9b and 10 b), the soil surrounding the spudcan moves in the upward direction causing heave for both the soft and stiff clay layers. The amount of heave is significantly lower for the soft clay. This is because partial backflow of the soil into the cavity occurs in the soft clay. The backflow of the soil into the cavity becomes larger as the installation proceeds in soft clay as illustrated in Figure 9 (b). However, the cavity wall remains vertical and stable in the stiff clay as shown in Figure 10 (b).

Figure 9 (c) shows that at the end of installation, the spudcan is buried under the backflow soil in the soft clay while the cavity walls remained stable in the stiff clay as shown in Figure 10 (c). Since spudcans are temporary foundations, when the operation period ends, the spudcans are extracted to move the jack-up rig to another drilling location. The backflow of the soft soil together with the development of suction at the bottom of the spudcan can make it very difficult to extract the spudcans. Failures and time delays are common. In order to ease the extraction of the spudcan different techniques are used such as bottom water jetting [8].

In order to demonstrate the soil movement in more details, the velocity vector plot of the soil surrounding the spudcan is shown at the penetration depths of 9, 12 and 15 m in Figure 11 (soft clay) and Figure 12 (stiff clay). For the soft clay, before the start of backflow, the dominant movement of the soil is upward. As the penetration proceeds, a transitional movement of the soil from vertical to lateral is observed around the spudcan as illustrated in Figure 11 (b). This is when backflow starts. With further penetration the movement of the cavity wall soil is completely directed toward the spudcan and a local soil flow is formed around the spudcan as shown in Figure 11(c).

The flow pattern on the soil around the spudcan in stiff clay mainly remains the same throughout installation. Figure 12(b) indicates that at depth of 9 m, the movement of the soil is still upward and the walls remain vertical. At depth of 15 m, as shown in Figure 12 (c), the velocity vectors are still upward while a slightly lateral movement can be observed around the spudcan that is not significant.

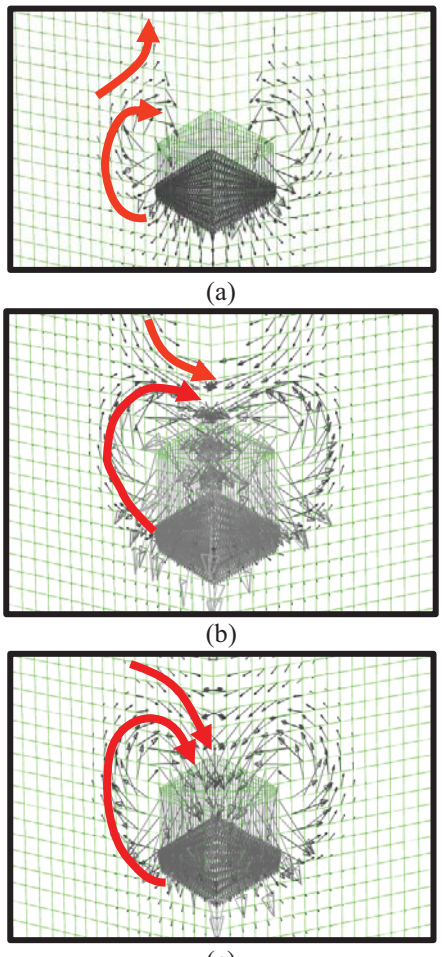


Figure 11. Velocity vector plot for spudcan penetration into soft clay at depth of (a) 9 m (b) 12 m (c) 15 m

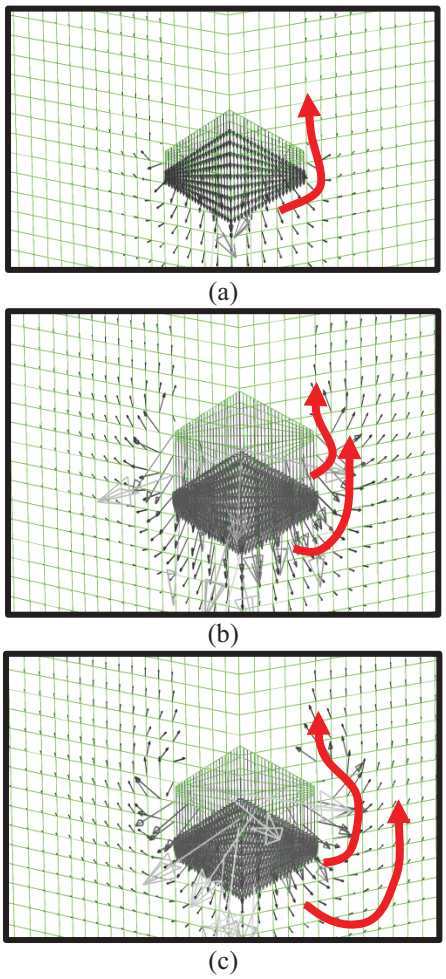


Figure 12. Velocity vector plot for spudcan penetration into stiff clay at depth of (a) 9 m (b) 12 m (c) 15 m

4 CONCLUSION

The Coupled Eulerian Lagrangian method is shown to be a reliable method to simulate large deformation problems in geotechnical engineering. The analysis of problems involving large deformation, such as spudcan installation, using the traditional Lagrangian approach is a significant challenge. However, using the CEL technique it is possible to undertake the numerical analysis of the problems involving large deformations.

Three dimensional finite element analyses can be very expensive in terms of computation and time. It is important to find an efficient mesh density which is accurate enough and practically fast. It is also important to also to adopt a representative loading rate for these analyses. A set of sensitivity analyses were performed to find the appropriate mesh density and loading rate required for this study.

The continuous penetration of the spudcan into the soft and stiff clay with undrained shear strengths of 10 kPa and 100 kPa, respectively was simulated. The continuous load-penetration response of spudcans for the two cases was recorded and the failure mechanism was assessed.

It was shown that the cavity with a diameter equal to the spudcan forms at start of installation. With further penetration, upward movement of the soil surrounding the spudcan continued and led to the formation of the heave surface at the seafloor. In the soft clay, as the spudcan penetrated to larger depths, lateral movement of the soil toward the cavity was observed. In contrast the upward flow pattern remained the same for the stiff clay. Finally, for the soft clay the spudcan became buried under the backflow of the soil in the soft clay and large heaves were observed in the stiff clay.

The results of this study show that large deformation finite element analyses can produce realistic predictions of the behaviour of soil during foundation installation. In the future more realistic soil profiles (including models which account for the variation of the shear strength of soil with depth) and more complex soil models will be considered. Furthermore, to have a better understating of the behaviour of the soft clay and obtain the resistance force during extraction of the spudcan (which is an important stage in the life-cycle of the foundation), it is important to consider the pore pressures generated and in particular to model the generation of suctions at the bottom of the spudcan.

REFERENCES

[1] X. X. Zhou, Y. K. Chow, and C. F. Leung, "Numerical modelling of extraction of spudcans," *Géotechnique*, vol. 59, no. 1, pp. 29–39, Jan. 2009.

[2] L. Kellezi and H. Stromann, "FEM analysis of jack-up spudcan penetration for multi-layered critical soil conditions," *... bga Int. Conf. ...*, 2003.

[3] M. S. Hossain, M. F. Randolph, and D. J. White, "Limiting cavity depth for spudcan foundations penetrating clay," *Géotechnique*, vol. 55, no. 9, pp. 679–690, Jan. 2005.

[4] M. S. Hossain and M. F. Randolph, "Deep-penetrating spudcan foundations on layered clays: centrifuge tests," *Géotechnique*, vol. 60, no. 3, pp. 157–170, Jan. 2010.

[5] G. Qiu, S. Henke, and J. Grabe, "Application of a Coupled Eulerian–Lagrangian approach on geomechanical problems involving large deformations," *Comput. Geotech.*, vol. 38, no. 1, pp. 30–39, Jan. 2011.

[6] K. K. Tho, C. F. Leung, Y. K. Chow, and S. Swaddiwudhipong, "Eulerian Finite-Element Technique for Analysis of Jack-Up Spudcan Penetration," *Int. J. Geomech.*, vol. 12, no. February, pp. 64–73, 2012.

[7] R. I. SIMULIA, Providence, "ABAQUS." 2010.

[8] C. Gaudin, B. Bienen, and M. J. Cassidy, "Investigation of the potential of bottom water jetting to ease spudcan extraction in soft clay," *Géotechnique*, vol. 61, no. 12, pp. 1043–1054, Dec. 2011.

Reassessing Foundation Reuse Assessment Tools

Debra F. Laefer[1], Kelly-Ann Farrell[2]
[1]Urban Modelling Group, School of Civil, Structural, and Environmental Engineering, University of College Dublin, Dublin, Ireland
email: debra.laefer@ucd.ie, farrell.kellyann@gmail.com

ABSTRACT: A greater emphasis on sustainability and increased ground congestion in urban areas has made foundation reuse increasingly important. While several decision-making aids and assessment tools have been developed, none have been independently assessed. The aim of this project is to analyse three prominent assessment tools through their application to five cases. Through the comparison and analysis of the five case studies and the applied assessment methods, benefits and difficulties associated with their usage became apparent. Observations were made and which led to recommendations on how these difficulties could be overcome.

KEY WORDS: Foundation Reuse, Urban, Deep Foundations.

1 INTRODUCTION

With increased interest in foundation reuse, have come various proposals for assessment tools (e.g. [1,2]). To date, however, there has not yet been a critical assessment of the effectiveness and appropriateness of these systems. As such, this paper provides a preliminary assessment of three of these system using five previously published cases histories.

2 SYSTEMS

The following systems were considered: (1) the Modified SPEAR method; (2) the RuFUS assessment method; and (3) the CIRIA method.

2.1 Modified Spear Method

The Sustainable Project Appraisal Routine (SPeAR) was a quadrant-based bull's eye chart originally intended for the design of infrastructure, master-plans, and individual buildings. Strauss et al. [3] then applied it for assessing foundation reuse using the quadrants of environment, societal, economic and natural resources to represent the universal indicators/main drivers [4]. Each was sub-divided into two sub-categories and seven levels. Shading closer to the centre indicated higher drivers for sustainability [5]. McGregor et al. [4] lists the advantages of the SPeAR method as allowing the sustainability of a project to be evaluated and illustrated in all stages of a project, with inter-relationships visible between indicators. Laefer [6] then proposed to make this visual assessment tool quantitative. The original 8 sub-categories were used but with 6 quantitative levels, instead of 7 qualitative ones. These are explained briefly below.

1. Site location relates to the percentage of unprotected greenfield sites in a community.
2. Archaeology and historical constraints focus on whether individual properties have an architectural designation and are protected structures or in historical areas.
3. Geological conditions depend on the difficulty of building on the existing materials.
4. Sustainability and material reuse are determined by the amount of construction material that is installed within the ground, which reflects the existing embodied energy.
5. Land value and cash flow projections are determined by monthly rent for a ground floor retail unit within the area and the median monthly household income.
6. Construction costs are determined using a variant of the Big Mac Index [7] with the cost of a Big Mac closest to the site being divided into the cost of a cubic meter of ready-mix concrete.
7. Consistency relates to how long a company has been at that location.
8. Approvals and development risk are linked to the average planning application length.

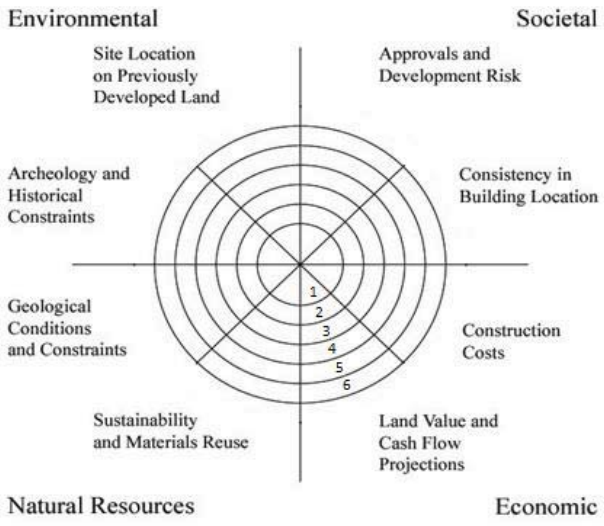


Figure 1. Modified SpeAR assessment method.

Each factor is divided into a six-point scale (compared to the seven-point scale of the original SPeAR model) [3]. The

revised method can be used to compare foundation reuse and its drivers in different cities. The first level is for the worst-case scenario, the risks and effects reduce as the level increases and moves away from the target centre.

Laefer [6] also recognized that the drivers used within the model focus mainly on the planning and environmental aspects. The drivers used do not include some major aspects that should be considered such as the quality and condition of the existing foundations. These have been recognized as important considerations in the RuFUS guide and in the above sections, when determining whether foundation reuse is a viable option for a project.

2.2 RuFUS assessment method

A flow chart was established to aid in the decision process of reusing deep foundations (figure 2). Step 1 establishes whether foundations already exist. Step 2 determines the extent of geometric compatibility of the existing foundations and the proposed superstructure. Partial compatibility and partial reuse may be a viable option. Step 3 determines the acceptability of the proposed foundation reuse solution. Desk studies and site investigations are performed to obtain the required information to move forward with foundation reuse. Stage 4 compares the proposed reuse design solution with alternative design solutions to show that the proposed solution is the most appropriate option. A final in-depth assessment is required to verify information and to perform thorough site investigations where required.

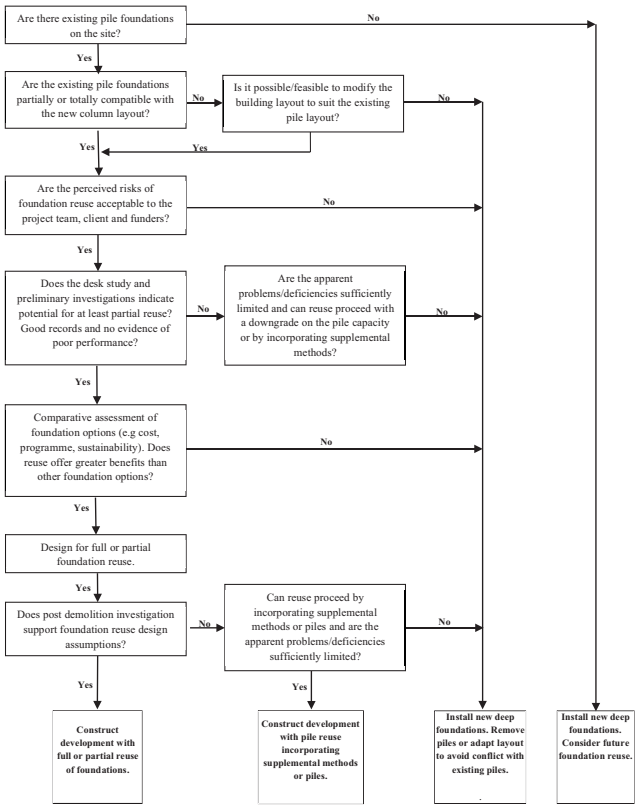


Figure. 2. RuFUS flow chart assessment process

2.3 CIRIA assessment process

The CIRIA guide proposed a simplified version of the RuFUS flow chart, figure 3 [8]. Key questions are recognized that must be answered in order to enable reuse. If all the key questions can be answered 'yes' then it is reasonable to assume foundation reuse is feasible. However, if the majority of the key questions cannot be answered successfully, then foundation reuse may not be a viable solution. Subsequently the decision must be made as to whether it is appropriate to design the foundations for reuse in the future.

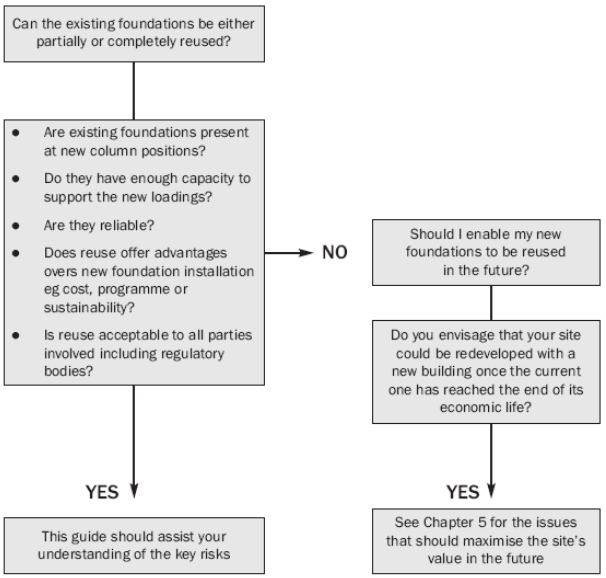


Fig. 3. Modified CIRIA Assessment Method

3 CASE STUDY SUMMARIES

Five case studies were chosen from the 'Reuse of foundations for urban sites- Proceedings of the international conference', Butcher et al. [9]. These case studies include the construction of a new three storey office block in South Gyle, Edinburgh, the construction of a new office block at Belgrave House, London, the redevelopment of ARUP's head office in Lon-don, the construction of a new museum, 'The Collection' in Lincoln and the redevelopment of the site of the Magistrates Court building in Manchester.

Case 1 – A new three-story office block to be constructed on the site of an original two-storey office structure in South Gyle, Edinburgh [10].

Case 2 – Belgrave House, a redevelopment project which began with the demolition of the existing seven storey office structure and construction of a new six storey, composite steel and concrete office building in London. Main constraints were underground metro lines [11,12].

Case 3 – Refurbishment of ARUP's head office in London. The existing building was a six storey concrete structure with a single storey basement. For the refurbishment, the building was stripped back to its original structural frame and a new extension was added requiring an additional 31% load on a number of piles. New foundations were necessary only for the extension.

Table 1. Drivers and difficulties for foundation reuse.

Case	Drivers	Difficulties
1	Using original building footprint	Risk with the future performance of the piles- who will take responsibility /insure the new design
	Original contractor was available - took responsebility for testing and verification of existing piles and the construction of the new piles	Capacity of foundations- difficult to consider under RuFUS flow chart
	Good quality as-built records available with pile logs and pile load tests	
	Potential savings in construction costs and program and energy	
	Redundant piles available and used for pile testing, testing to failure was possible	
2	Ground congestion- must follow London Underground & Crossrail regulations. Under reamed piles also existing on site	Damage during demolition of the original structure causing some cracking to existing piles
	Thorough inspections and risk assessment performed on site- both visual and laboratory inspections con-firmed condition of the foundations and supported pile reuse	Incompatibility between existing and new layouts- required transfer structures to support the necessary loads
	Savings - construction time/costs/risks	
	Client wanted the potential for future development on site so wanted to limit the elements to be placed in the ground	
	Drawings were available, which enabled the assessment of the piles and the site	
3	Refurbishment project- compatibility with new design, pre-existing skeleton of structure remained	Inaccurate information- poor quality records and conflicting information
	Past records- ground investigations, design drawings and pile tests were available, however they did not indicate geometry or layout sufficiently	Limited space available for ground investigations as foundations and building frame remained on site
	Investigations supported reuse- therefore reduced the risks associated with the previous lack of information	Gravel pits recognized on site- although in places that did not require an increase in capacity to carry the increased loads on from the new structure
	Conditions of foundations confirmed through testing	Increased capacities on foundations required due to new structure- supplemental foundations originally thought to be required however reserve capacity utilized with roof plant moved to an alternative position
4	Protected ground - archaeological remains present on site, reuse would avoid intrusions and damage to the remains in the ground	Incompatibility between existing layout and proposed new structural layout
	Historic surrounding - cathedral views	Iconic design required-did not want to follow strict car park grid
	Drawings and records from original construction	Reuse was not considered originally as the tender was won on competition basis as there was a requirement for a unique and iconic design
	Feasibility study supporting reuse of foundations- shows great potential for reuse.	Existing archaeology on site – although good documentation on the archaeology of the site was available and the design team determined that the installation of new piles would not cause a significant impact on the preservation of the site
5	Foundation plan and section obtained - standard and quality of drawing not known i.e. design, as-built etc	Uncertainties with depth of bedrock and pile lengths
	Foundations found to be in good condition- layout confirmed from testing	Depth of bedrock differed from past records, uncertainty and accuracy of the existing information
	Conservative pile designs at time of construction therefore extra capacity was available to take increased loads where necessary	Strict boundary constraints - not possible to alter placement of the new structure, the site was part of a larger Master Plan

Case 4 – New Collection Museum in Lincoln, UK had very tight site constraints including the surrounding historical area and archaeological remains. Reuse was not originally considered but alterations were made to avail of foundation reuse opportunities [13].

Case 5 – New Magistrates Court building in Manchester involved a detailed site investigation but foundation reuse was not deemed possible due to missing and unreliable information, as well as grid alignment incompatibilities [14,15].

3.1 Results of the assessment of the case studies

Table 1 summarizes the findings from assessing the five case studies. The main drivers for reuse in each case and the associated difficulties are highlighted.

Table 2 shows the main advantages and disadvantages of the RuFUS flow chart assessment. One of the main disadvantages was that the capacity of the foundations was not assessed independently in this process. This has been found as one of the most important aspects when considering and assessing foundations for their reusability. Without sufficient capacity for the foundations to sustain the loads of the proposed new structure, reuse is not a viable solution. Another important consideration is the ground congestion on the site and within the site surroundings. It is important that the ground congestion on site be thoroughly investigated on site as each site is unique, there are numerous types of ground congestion that can exist.

Table 2. Advantages and disadvantages of RuFUS assessment.

Advantages	Disadvantages
Notes the importance of compatibility.	Lack of information on surrounding area.
Staged approach/ checklist assessment process for foundation reuse.	Capacity not assessed independently.
Considers ground congestion.	Ground congestion should be assessed in overall assessment process, not in a separate flow chart process.
Illustrates the foundation solutions available for a project.	Does not consider quality of records available- has major implications on a project.

Table 3 was compiled for ease of assessment when conducting the RuFUS assessment and to compare the assessments of the five case studies. The table illustrates the important factors that were present in all cases. These include the existence of foundations on site, the compatibility of the foundations, the acceptability of a reuse solution, the importance of site investigations, the importance of comparing foundation solutions and ensuring a reuse solution is beneficial for a project. Although post demolition investigations are illustrated as an important stage, certain assumptions were made in assessing the foundation case studies. For a reuse solution, the pile foundations will be tested for reliability and capacity after the demolition of the original structure. As such, this is not considered to be a determining factor.

The CIRIA assessment seemed to consider all the major points such as compatibility of existing foundations and proposed new structure, the capacity of the foundations, the reliability of the foundations and the alternative foundation solutions available. However, the CIRIA guide does not readily consider the main site constraints when considering foundation reuse, which include ground congestion, site boundaries and archaeology. This assessment process also does not consider the specific foundation solution to be adopted, in comparison to the RuFUS process. The advantages and disadvantages of the CIRIA assessment observed can be seen in table 4 below.

Table 3. Comparing RuFUS assessments

	Case 1	Case 2	Case 3	Case 4	Case 5
Are there existing foundations on site?	**X**	**X**	**X**	**X**	**X**
Are existing pile locations compatible with new structure?	**X**	**X**	**X**	**X**	**X**
Possible/Feasible to modify the building layout to enable reuse?				**X**	**X**
Acceptable risks and reuse solution?	**X**	**X**	**X**	**X**	
Desk study and preliminary investigations support reuse?	**X**	**X**	**X**	**X**	
Possible to reuse with downgrade on capacity or incorporating supplemental methods?	**X**		**X**		
Comparative assessment of foundation solutions. Does reuse offer benefits over other options?	**X**	**X**	**X**	**X**	
Post demolition investigations support reuse?	**X**	**X**	**X**	**X**	
Can reuse proceed by incorporating supplemental methods?		**X**			
Construct with partial or total reuse.	**X**		**X**	**X**	
Construct with reuse incorporating supplemental methods or piles.		**X**			
Install new deep foundations. Remove or avoid existing piles.	**X**				
Install new deep foundations. Consider future foundation reuse.					

Table 4. Advantages and disadvantages of CIRIA assessment

Advantages	Disadvantages
Notes the importance of compatibility.	Does not consider the main site considerations e.g. Ground congestion, site boundaries, archaeology.
Recognizes the importance of the foundations capacity.	Does not supply the type of foundation solution to be adopted
Considers the reliability of the foundations clearly and independently	
Compares foundation solutions to ensure reuse has advantages over alternative approaches.	

4 OVERVIEW OF ASSESSMENT METHODS

The modified SPeAR diagram method illustrated the main drivers for reuse in a particular area and may be used to convince the parties involved in a project's early stages, that foundation reuse is a feasible and appealing solution. While the resulting diagram was beneficial in the assessment of the reuse capabilities for an area, it may not be appropriate as a standalone assessment method for a particular site/project. In contrast, the RuFUS flow chart assessment process [17] included a clear layout and staged approach to assessment. It also supplied alternative foundation solutions. The flow chart either recommends a reuse solution, reuse with supplemental elements, or installing new foundations. However, it does not clearly define site specifics such as the foundation properties and site constraints. The CIRIA simplified 5-point method determined the applicability of foundation reuse to a particular project. The capacity and reliability of the existing foundations were two of the most important factors. This question-based approach was more direct than the RuFUS flow chart.

5 CONCLUSIONS

The assessment of five case studies via three assessment methods showed that although each of the assessment methods provided some insights, none of the above were fully comprehensive. The SPeAR method proved successful as a preliminary assessment approach. In comparison the RuFUS and CIRIA assessments better consider the particulars of a site; namely the compatibility between existing structures and new structures, the quality of the records available, and the capacity and reliability of the foundations. Without all of these components, the possibility of achieving a foundation reuse solution is limited. Therefore, it is recommended that the modified SPeAR method should be performed in the first stage and a second process should be performed to assess foundation capacity, information availability, main site considerations, constraints, and alternative solution options.

REFERENCES

[1] Norman, J. Starzec, P. Anderson, S.A. and Chapman, T. J. P. (2006) 'Foundation reuse decision model part 2: Results and sensitivity analysis for an idealised case study'. Proc. of inter-national conference on reuse of foundations for urban sites. Watford, UK, 19-20 October 2006. Butcher, A. P. Powell, J. J. M. Skinner, H.D. (eds.) pp. 35-46.

[2] Laefer, D. F. and Manke, J. P. (2008) 'Building reuse assessment for sustainable urban reconstruction'. Journal of Construction Engineering and Management, 134(3): pp. 212-217.

[3] Strauss, J. Nicholls, R. Chapman, T. and Anderson, S. (2007) 'Drivers affecting frequency of foundation reuse and relevance to U.S. cities'. Geo-Denver 2007: New Peaks in Geotechnics. Denver, 18-21 February, 2007. Geotechnical Special Publication: American Society of Civil Engineers n 158. DOI http://dx.doi.org/10.1061/40902(221)20.

[4] McGregor, A. I. And Roberts, C. (2003) 'Using the SPEAR Assessment tool in sustainable master planning'. Available at: http://www.arup.com/_assets/_download/download129.pdf (Accessed 10 January 2011).

[5] Misra, A. and Basu, D. (2011) Sustainability in geotechnical engineering. Internal Geotechnical Report. Dept. of Civil and Environmental Engineering, University of Connecticut.

[6] Laefer, D. F. (2011) 'Quantitative support for a qualitative foundation reuse assessment tool', Geo-Frontiers 2011: Advances in Geotechnical Engineering, Proc. of the Geo-Frontiers 2011 Conference. March 13-16, 2011. American Society of Civil Engineers (ASCE), n 211 GSP, pp. 113-121.

[7] The Economist (2012), The Big Mac Index. Available at: www.economist.com (accessed March 2012)

[8] Chapman, T. Anderson, S and Windle, J. (2007) Reuse of Foundations. London: CIRIA.

[9] Butcher, A. P. Powell, J. J. M, Skinner, H.D. (2006a) Reuse of foundations for urban sites-A best practice handbook. United Kingdom: IHS BRE Press.

[10] Lennon, D. J. Irving, D. A. C. and Boyd, P. J. H. (2006) 'Investigation and reuse of piled foundations at South Gyle, Edinburgh'. Proc. of international conference on reuse of foundations for urban sites. Watford, UK, 19-20 October 2006. Butcher, A. P. Powell, J. J. M. Skin-ner, H.D. (eds.) pp. 347-356.

[11] Vaziri, M and Windle, J. (2006a) 'Strategy for the reuse of existing piles: Case study at Belgrave house, London.' Proc. of international conference on reuse of foundations for urban sites. Watford, UK, 19-20 October 2006. Butcher, A. P. Powell, J. J. M. Skinner, H.D. (eds.) pp. 47-58.

[12] Vaziri, M and Windle, J. (2006b) 'Testing strategy for the reuse of existing piles: Case study at Belgrave house, London.' Proc. of international conference on reuse of foundations for urban sites. Watford, UK, 19-20 October 2006. Butcher, A. P. Powell, J. J. M. and Skinner, H.D. (eds.) pp. 59-67.

[13] ARUP (2011). ARUP. Available at: http://www.arup.com/Projects/SPeAR.aspx (Accessed January 2012).

[14] Williams, J. (2006b) 'Pile reuse at The Collection, Lincoln: Lessons learnt' Proc. of international conference on reuse of foundations for urban sites. Watford, UK, 19-20 October 2006. Butcher, A. P. Powell, J. J. M. and Skinner, H.D. (eds.) pp. 303-307.

[15] Carillion PLC (2011), Manchester Magistrates Court. Available at: http://www.carillionplc.com/private_finance/assets/documents/mancheste r.pdf (Accessed March 2012).

[16] Curtis, D.C and Lowe, C.R. (2006) 'Investigation of under-reamed piles in sandstone to as-sess potential reuse', Proc. of international conference on reuse of foundations for urban sites. Watford, UK, 19-20 October 2006. Butcher, A. P. Powell, J. J. M and Skinner, H. D. (eds.) pp. 339-345.

[17] Butcher, A. P. Powell, J. J. M, Skinner, H.D. (2006b) Reuse of foundations for urban sites- Proceedings of the International Conference. Watford, UK, 19-20 October 2006. United Kingdom: IHS BRE Press.

Soil nailing optimisation: lost opportunities in current practice

Debra F. Laefer[1], Conor McGroarty[2], Oisín Ó Murchú[3]
[1]Urban Modelling Group, School of Civil, Structural, and Environmental Engineering, University of College Dublin, Dublin, Ireland
[2]RPS Consulting Engineers
[3]Jacobs Engineering, Ireland

email: debra.laefer@ucd.ie, conor.mcgroarty@gmail.com, oisinomurchu1@gmail.com

ABSTRACT: This paper analyses 127 cases histories in the US and Europe to evaluate the current state of soil nailing practice with respect to soil nail lengths and density, wall heights, wall inclination, and shotcrete thickness, as well as applications. When the cases are considered by project size and soil type, certain inefficiencies appear. Namely, smaller projects exhibit conservatism in nail density and shotcrete thickness, and use only a fully vertical wall. In contrast on larger projects, there appears to be an optimization of these factors. What is evident is that for smaller projects and/or shorter walls, contractors are adopting conservative rules of practice instead of actually designing the projects in accordance with published design manuals. A single, small case is reconsidered using the Geotechnical Engineering Circular No.7, GEC 7 design guide resulting in an estimated 7.2% savings.

KEY WORDS: Soil Nailing, Codes, Design, Optimisation.

1 INTRODUCTION

Soil nailing is primarily used to stabilise slopes and excavation faces. The technique comprises of the installation of reinforcing 'nails', sub-horizontally, into a soil mass, which improves soil coherency. The method originated from rock bolting and multi-anchorage systems [1,2,3]. Methods vary with soil type but generally consist of the following [4]:
1) Initial excavation of 1-2 m deep;
2) Nail installations (driving or placement into a pre-drilled, grouted borehole).
3) Facing construction (to support open-cut before the next lift of soil is excavated).

Europe's first documented soil nail wall was constructed in Versailles in 1972 and grew in popularity over the next two decades, culminating in Clouterre [1], a comprehensive document detailing construction methods. This paper explores inconsistencies since this publication and provides insight into cost savings measures.

2 BACKGROUND

The first major research program on soil nailing (Bodenvernagelung) was undertaken in Germany 1975-81 [3]. Prior, Mason filed a US patent in 1970, having constructed several projects using the technique [3]. The French national research program Clouterre [1] in 1991 was the first comprehensive document, which detailed construction, design codes, and analysis on full-scale models.

The FHWA Manual for design and construction monitoring of soil nail walls [3] was published in 1999 and was an outcome of Demonstration Project 103 (DP103), which commenced in 1992 as an American equivalent to Clouterre [1]. DP103 aimed at introducing soil nailing to American State Departments of Transportation. The focus was for permanent installations. In 2003, Geotechnical Engineering Circular No.7 Soil Nail Walls (GEC7) [4] was published, which essentially up-dated the FHWA Manual [4]. Following the UK's Construction Industry Research and Information Association's (CIRIA) ground engineering Research Project 674, a best practice guidance [2] was published in 2005. In 2008, the Hong Kong government's Civil Engineering Department published Geoguide 7: guide to soil nail design and construction [5].

2.1 Design manuals, standards and guidelines

In the US, GEC7 is used in the public sector [6] with additional widespread private sector usage. Some European countries developed their own soil nailing standards, such as Clouterre [1] and the Nordic handbook of reinforced soils and fills [7]. However, since 2010, European countries under European standards' jurisdiction must conform to Eurocode 7: geotechnical design [8].

3 METHODOLOGY

Over the past 20 years soil nailing has moved from proprietary techniques to a standardised approach adoptable on public projects. To what extent this is actually adopted is the main consideration herein. A database of 127 case studies was compiled from contractor websites, journal papers, and conference proceedings issued by the Deep Foundations Institute [9], the Chinese Institute of Soil Mechanics and Geotechnical Engineering [10], the Construction Industry Research and Information Association [2] the American Society of Civil Engineers [11], the USDOT [12] and Hong Kong's CEDD [13].

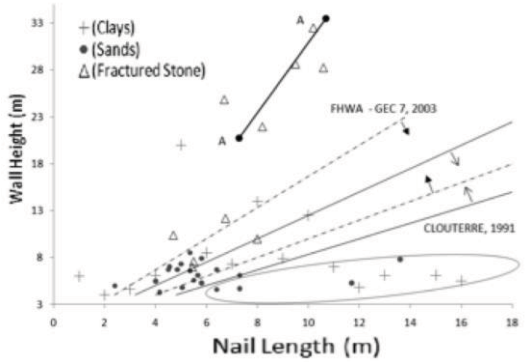
4 ANALYSIS AND RESULTS

Some results indicate that well-designed and cost-efficient methods are not being followed consistently. Instead, on smaller scale projects (<≈10m), a "rule-of-thumb" approach was commonly applied. Nail densities were calculated using two approaches: dividing the total number of nails by the

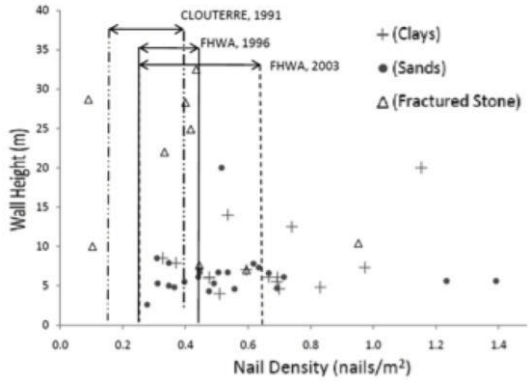
total area of soil nailing works or multiplying the horizontal by the vertical spacing and then taking the inverse.

4.1 Nail length vs wall height

Design is largely related to the ratio of the nail length (L) to the wall height (H). Values of less than 0.5H were generally not accepted as they do not satisfy sliding or overturning requirements [3]. For bored and grouted soil nails, L/H ratios generally ranged from 0.6 to 1.3 depending on ground conditions, [2] but 0.7-0.85 was most common. Clouterre [1] specified the L/H ratio for bored and grouted nails as 0.8-1.2, which was also adopted by CIRIA [2]. This ratio was modified for U.S. practice to 0.6-1.0 [3.4]. Figure 1 show significant scatter for walls less than 10m high, thereby suggesting less consistent designs than for taller walls; potentially over-designed walls are circled in Fig. 1a. Cases along line A-A are predominantly in fractured stone and above 20m. The increased friction angle of fractured stone allows a reduced L/H ratio for these walls.



a) Nail length vs. wall height



b) Nail density vs. wall height

Figure 1. Nail Installation Characteristics

4.2 Nail Density vs Wall Height

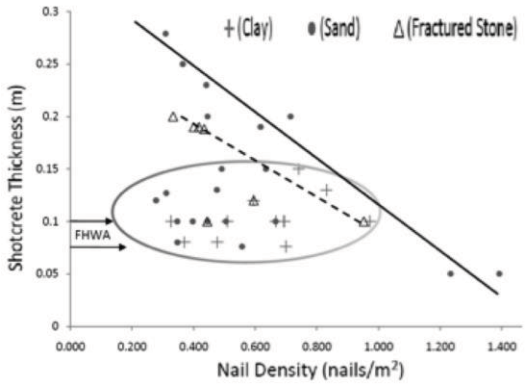
With consideration of nail density versus wall height, the principle that earth pressures are directly related to depth is important. From this, intuition would dictate that the higher a soil nail wall, the larger the earth pressures acting on it would be and therefore, require more soil nails. As can be seen in Fig. 1b, there is no immediately discernible trend in nail density versus wall height. On closer inspection, large walls (> 20m) in fractured stone seem to follow an almost linear relationship between 0.33 and 0.44 nails/m^2, suggesting optimized design. Although a linear trend in nail density would be intuitive, the major design publications refer to acceptable nail spacing, irrespective of wall height. Clouterre [1] lists spacing grids of 2.5-6m^2 for bored and grouted nails, corresponding to nail densities of 0.4-0.16 nails/m^2. The Manual [3] suggests standard grids of 2.25-4m^2 (0.44-0.25 nails/m^2), GEC7 [4] adopts a slightly more conservative approach, specifying grids of 1.56-4m^2 (0.64-0.25 nails/m^2).

CIRIA [2] proposed grid options similar to the other manuals, while Geoguide 7 [5] does not recommend any grid sizes but notes that in Hong Kong, grids of 2.25-4m^2 (0.44-0.25 nails/m^2) are commonly used. Each major, subsequent, design publication has increased both the minimum and maximum nail densities. This increase could be attributed to a growing understanding as to the range of effective densities. Few correlations exist in design manuals relating nail densities and wall heights. This coupled with the explicit proposal of various standard grid dimensions, is likely to continue non-optimized design.

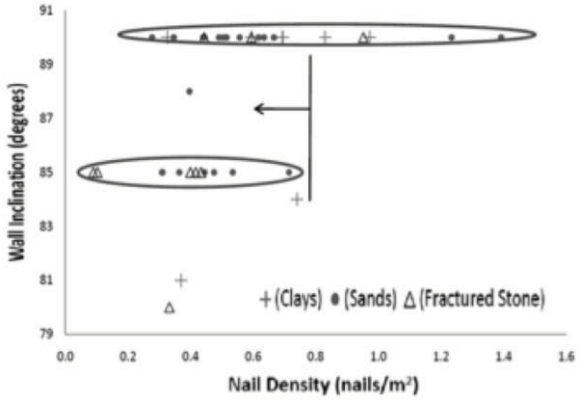
4.3 Nail Density vs. Shotcrete Thickness

When analyzing shotcrete depth versus nail density, an increase in span (the distance between two consecutive nails), generates an increased tributary area, which would suggest a needed increase in shotcrete depth. This relationship appears as a linear trend in Fig. 2a for many cases in sand and fractured stone. However, for the majority of cases shotcrete depths range from 75-150mm regardless of soil type (Fig. 2a).

This standardization could be an extension of the FHWA [3,4] recommendations. The earlier Clouterre [1] and later Geoguide 7 [5] recommend calculating shotcrete depth in a project specific manner. Instead, Clouterre [1] suggested standard ranges and ratios for nail density and nail length. Clouterre [1] relates the facing depth to the tensile forces at the nail head. The tensile forces depends primarily on nail spacing (i.e. nail density). Therefore, decreasing shotcrete depths with increasing nail densities would be expected.



a) Nail density vs. shotcrete thickness



b) Nail density vs. wall inclination

Figure 2. Wall characteristics

4.4 Nail Density vs. Inclination

Clouterre [1] and GEC 7 [4] discuss the structural benefits of inclining a soil nail wall. The active earth pressure acting on the wall face will decrease, as the wall slope flattens [4], in turn allowing a reduction in nail density/length. Those in sands and clays showed no variation in nail density with inclination, indicating non-optimized design. This contrasts strongly with cases in fractured stone, (Fig. 2b) where a clear 'step down' in nail densities occurs between inclinations of 90° and 85°. When analyzed regardless of soil type a clear drop is evident from nail densities of 0.22-1.4 nails/m^2 for vertical walls to only 0.1-0.575 nails/m^2 for walls inclined 15° from vertical. For a 1000m^2 wall, a 0.1 nails/m^2 reduction would save 100 nails. With a minimum nail length of 2.4m, saving 240m in nail material and related transportation and installation costs. Possible reduction in nail densities by reducing wall inclination is not well documented compared to information on nail length. Other explanations for not reducing nail densities or for not inclining the wall could be the acceptance of a standard approach or project requirements. A vertical wall is generally chosen for two main reasons [3]: (1) maximize space of a given project and (2) ease of constructability.

5 COST BENEFIT ANALYSIS

The redesign of the soil nail wall, to illustrate the cost implications of non-optimized walls, is presented below. The permanent soil nail wall constructed at Pearsall, Texas in 1995 was originally designed by DP 103 as 4.6m high and 152m long wall to retain an existing highway embankment, in a predominately sandy ground with SPT values of 10-40. The design grout-ground bond was 62kPa was selected for the vertical wall with 1.3m horizontal and 1.1m vertical nail spacing (corresponding to a nail density of 0.7 nails/m^2). The average nail length was 4.7m. Shotcrete for the temporary facing was 76mm; 229mm for permanent.

5.1 Design Calculations

The redesign of this project was carried out in accordance with GEC 7 [4].

Step 1: Initial Soil Nail Wall Considerations

1) Wall Layout: Wall height (H), wall length (L_e), and face batter (α) are as follows: H = 4.6 m; Wall Length, $L_e >> H$; Face batter, $\alpha = 10$
2) Soil Nail Horizontal and Vertical Spacing, S_H and S_V:
   a) Select Sv = 1.8 m
   b) Select S_H = 1.8 m. $S_H \times S_V = 3.24\ m^2 \leq 4\ m^2$
   c) Values of vertical spacing near top /toe of the wall S_{V0} and S_{VN} = 0.5m
3) Soil Nail Pattern on Wall Face
4) Select Rectangular Pattern
5) Soil Nail Inclination, i:
   a) Select i = 15 for all nails except top row
   b) Select i = 20˚ degrees for top row
6) Soil Nail Length Distribution: Select a uniform nail length
7) Soil Nail Materials:
   a) Select threaded solid bars
   b) Yield tensile strength, f_y = 520MPa = 0.52 kN/mm^2 (Grade 75)
8) Soil Properties: Φ' = 30 degrees; c' = assumed conservatively as 0; γ = 17 kN/m^3
9) Drillhole Diameter = 0.15m
10) Bond Strength: Design bond strength = 62 kPa
11) Safety Factors:
   a) Nail bar tensile strength factor, F_{st} = 1.8
   b) Facing flexure factor, F_{sff}(temp) = 1.35, F_{sff}(perm) = 1.5
   c) Pullout resistance factor, F_{sp} = 2.0
   d) Global stability factor, F_{sg} = 1.35

Step 2: Preliminary Design

1) Uncorrected Uniform Nail Length:
   a) Design bond strength q_a = 62 kPa
   b) Normalized pullout resistance, μ, $\mu=(q_a D_{DH})/(\gamma S_H S_V)$ $= (62\times0.15)/ (17\times1.8\times1.8) = 0.17$
   c) Normalized cohesion $c^*= c'/\gamma H = 0$
   d) μ = 0.17 produces a normalized L/H=0.77
   e) Charts used in GEC 7 (FHWA 2003) were developed for: Drill hole diameter = 150mm; Normalized cohesion = 0.02; Global Stability Factor, F_{sg} = 1.35; Drillhole diameter C_{1L} = 0.83; Soil Cohesion C_{2L} = 1.09; Safety Factor C_{3L} = 1.08
   f) Adjusted normalized nail length: $L/H=C_{1L}\times C_{2L}\times C_{3L}\times L/H=0.83\times1.09\times1.08\times0.77=0.75$
   g) The following corrections to L/H are necessary:
      i) To account live load surcharge, increase wall height to 5.2m
      ii) L = 0.75 × 5.2 = 3.9m
      iii) For the needed 3 rows, total nail length, $L_{TOT}=3L=3\times3.9=11.7m$

2) Nail Maximum Tensile Force:
   a) Max design nail force, $t_{max\text{-}so}$, 0.18 from Figure 5.3
   b) Apply Corrections: Drill hole diameter: C_{1F}=1.47; cohesion: C_{2F}=1.09
   c) The corrected normalized maximum nail force is: $t_{max\text{-}s}= C_{1F} \times C_{2F} \times t_{max\text{-}so} = 1.47 \times1.09\times0.18 = 0.29$
   d) Maximum design nail force: $T_{max\text{-}s}=g\times H\times S_V\times S_H\times t_{max\text{-}s}=17\times5.2\times1.8^2\times0.29 = 83.06$

kN

e) Nail tensile capacity, R_T = Fst × T_{max-s} = 1.8 × 83.06 = 149.5 kN

f) Necessary nail bar cross-sectional area, $A_T=(T_{max-s} \times Fst)/f_y = R_T/f_y$ = 145.5/0.52=288mm^2

g) Area of 25mm diameter threaded bar = 510 mm^2

3) Facing Design:

a) Design the nail head tensile force: $T_o = T_{max-s}$ [0.6 + 0.2(S_V – 1)] = 83.06[0.6+0.2(1.8 – 1)] = 63.13 kN

b) Temporary Facing: Shotcrete thickness (h) = 76 mm; f'$_c$ (compressive strength) = 21MPa; and Welded wire mesh reinforcement, f'$_y$ = 420 MPa

c) Permanent Facing: CIP concrete thickness (h) = 100mm; d = 50mm; f'$_c$ = 21MPa; f'$_y$ = 420MPa

i) Limiting reinforcement ratios, r_{min} (%) = = 0.175; r_{max}(%) = = 1.09

ii) Considering the width of the analysis section as 1 m, a_s = rd; $a_{s\ min}$ = 66.5 mm^2/m; $a_{s\ max}$ = 414 mm^2/m

iii) Select reinforcement; use a mesh 300 × 300 of (12 mm bars) – Area per unit length at midspan a_{sm} = 377 mm^2/m

iv) Reinforcement ratios along each section and the total reinforcement ratio are: $r_{hm} = r_{hn} = r_{vm} = r_{vn}$ = ((377)/(1000×100))×100 = 0.38% r_{tot} = .76 %

v) Select Factor C_f = 1, Table 2 R_{FF} = × (377+ 377) (mm^2/m) × 0.1 (m) × 420 (Mpa) = 123 kN

vi) Ultimate loads (kN) $FS_{FF} \times T_o$, FS_{FF} = 1.5 for Permanent Facings 1.5 × 63.13 = 94.7 ≤ 123 kN

d) Punching Shear Resistance (R_{FP}) for temporary facing: Calculate R_{FP} for temporary facing: The punching shear failure consists of the failure of a truncated cone of mean diameter D'$_c$ = L_p+ h, where L_p is the bearing plate length. The resisting shear force on this cone, V_f, is V_F =330× ×π ×D'$_c$(m)×h(m); V_F=330××π×(0.225+0.1)×0.1= 154

Resistance against punching shear failure is: $R_{FP} = C_pV_F$ where C_p =1

R_{FP} = 154.4 ≥ 85 kN – (FS × T_o), (1.35 × 63.13)

e) Punching Shear Resistance (R_{FP}) for permanent facing: D'$_c$ is defined for permanent facing as D'$_c$ = minimum of S_{HS} +h_c or 2h_c where S_{HS} is the headed-stud separation and h_c the effective headed-stud length (Table 3).

$h_c = Ls + t_p – t_{SH}$ = 105+25–7.9 = 122.1

where, Ls, t_p and t_{SH} are the stud length, plate thickness and stud thickness, respectively D'$_c$ = min (150 + 122.1 or 2×122.1) = 244; V_F=330× ×π ×D'$_c$(m)×h(m); V_F=330××π×(0.244)×0.122= 141.4

Resistance against punching shear failure is: $R_{FP} = C_pV_F$, where C_p =1

R_{FP}=141.4≥94.7kN–(FS×T_o), (1.5× 63)

f) Headed-Stud tensile resistance (R_{FS}): Nail headed-stud tensile capacity: R_{FS}= $4A_H \times f_y$ = 4 × (($\pi \times d^2$)/4) × .420 = 213 kN ≥ 126 kN–(FS×T_o), (2×63.13) where A_H is the headed-stud area.

This resulted in the data shown in Table 1, which meets all of the design criteria and the redesign shown in Table 2.

Table 1. Bearing plates and headed studs (from [4])

Bearing plate	Type	4 headed-studs 0.5 x 4.125
	Steel	250 MPa (Grade 420)
	Dimensions	Length; L_p = 225 mm and Thickness t_p = 25mm
Headed studs	Dimensions	Nominal length; L_n=105mm; head diameter; D_h= 25.4mm; shaft diameter; D_s=12.7mm; head thickness t_H =7.9mm; spacing; S_{SH} =150mm

Table 2. Design and Redesign Parameters

Parameter	Original Design	Redesign
Inclination	90°	80°
Nail spacing grid	1.3m h x 1.1m v (1.43m^2)	1.8 x 1.8m (3.24m^2)
Permanent facing depth	229mm	100mm

5.2 Cost Savings

Using a cost of \$125/m^3 for concrete and 12.25/m for reinforcing, total cost savings totaled \$22,006 (Table 3) represents a 7.2% cost reduction. These figures do not include the potential savings in drilling, grouting and labour, associated with smaller nail lengths and facing depths. The estimated cost was \$393/m^2 of soil nail wall × 539m^2 of wall = \$211,827 in 1995. Using an inflation factor of 1.447 [14], the total 2011 cost was \$306,513 USD.

Table 3. Cost savings from redesign

	Actual design	Re-design	Savings	Costs (\$USD)	Savings (\$USD) = (savings x costs)
Nails (m)	2,199.6 m	994.5 m	1,205 m	12.67/m	15,268.62
Shotcrete	76 mm	76 mm	NA	NA	NA
Concrete	123.4 m^3	69.5 m^3	53.9 m^3	125/m^3	6,737.5
				Total Savings	22,006

6 CONCLUSIONS

This paper examined data from over 100 case studies, and uncovered potential trends related to non-optimal design of soil nailing projects. These designs appear to be due to a tendency to build as a standard instead of to a standard. This default approach to design may be due to the proprietary nature in which the technology evolved with a lack of harmonization across design manuals. The ratios of length to height decreased with every major research report published. This change shows a progression in design practices with increased knowledge and/or confidence. The redesign of a relatively small project (539m^2) saved \$22,000 (7.2%) on just materials.

ACKNOWLEDGMENTS

Thanks to Dr. Mike Long of UCD for sharing advise and experience.

REFERENCES

[1] Clouterre (1991). French National Research Project: Recommendations CLOUTERRE 1991 - Soil Nailing Recommendations. Presses de l'Ecole Nationale des Ponts et Chaussees, Paris.
[2] CIRIA (2005). Soil nailing - best practice guidance. CIRIA, London.
[3] Federal Highway Administration (FHWA) (1999) US Department of Transportation FHWA, http://www.fhwa.dot.gov [Accessed 5 Jan. 2011].
[4] FHWA (2003). Geotechnical Eng. Circular (GEC) No.7 Soil Nail Walls. Washington D.C.
[5] GEO (2008). Guide to Soil Nail Design & Construction. Geotechnical Eng. Office, Hong Kong.
[6] Deep Foundations Inst. (DFI) (2010). Soil nailing guide specification, Hawthorne, NJ.
[7] NCC (2002) Nordic handbook of reinforced soils and fills. Nordic Geosynthetic Group, Stockholm.
[8] CEN (1999). Eurocode 7: Geotechnical design. NSAI, Dublin.
[9] DFI (2011), http://www.dfi.org/ [Accessed 5 Mar. 2011]. FHWA (1999). FHWA/SA-96/069: Manual for design and construction monitoring of soil nail walls, Washington, D.C.
[10] CISMGE (2011), http://www.cismge.org.cn/ [Accessed 6 Jan 2011].
[11] ASCE (1996-2011), http://www.asce.org/ [Accessed 15 Nov. 2010].
[12] United States Department of Transportation (USDOOT) (2009), FHWA, http://www.fhwa.dot.gov [Accessed 5 Jan. 2011].
[13] CEDD (2010), http://www.cedd.gov.hk/ eng/index.htm [Accessed 7 Jan 2011].
[14] Sahr, R.C. (2011), Consumer price index con-version factors 1800 to 2015, http://oregonstate.edu/.cla/polisci/faculty-research/sahr/sahr.htm [Accessed 26 Mar 2011].

The effect of scour on the dynamic response of an offshore wind turbine

Luke J. Prendergast[1], Kenneth Gavin[1], Paul Doherty[1]
[1]School of Civil, Structural & Environmental Engineering, University College Dublin, Dublin 4,Ireland
email: luke.prendergast@ucdconnect.ie, kenneth.gavin@ucd.ie, paul.doherty@ucd.ie

ABSTRACT: Wind turbines are dynamically sensitive structures, with excitation forces arising from the rotor spinning at a specific angular velocity and the blade passing the turbine tower at a set frequency. It is critical that the structural design of the turbine is undertaken in such a way that the system natural frequency resides away from the resonant excitation bands. This will become increasingly important over the next decade as turbines evolve and the operational frequency bands change. The system natural frequency is governed by the structural properties of the turbine tower and the nacelle weight, combined with the stiffness of the soil-foundation elements. An accurate estimate of the soil stiffness is crucial to ensure a realistic model of the overall turbine behaviour. Over 75% of offshore wind turbines currently have monopile foundations, which are designed as a soft-stiff system, with the functional design frequency of the turbine structure falling between the upper and lower excitation frequency bands. The dynamic stability of the foundation is provided by the interaction between the monopile shaft and the adjacent soil strata. In this paper, the effect of scour on the frequency response of an offshore wind turbine is investigated numerically for a range of different soil densities. The turbine system is modelled using simple numerical modelling techniques. Euler-Bernoulli beam elements are used to model the tower. Altered versions of these elements are used to model the monopile, with an extra node and degree of freedom to allow the input of lateral soil stiffness into the model. The nacelle and rotor system is modelled as a lumped mass at the top of the turbine tower. In-situ CPT-based approaches are used for modelling the soil stiffness. The effect of scour is investigated for each design case.

KEY WORDS: Scour; Wind Turbines, SHM, Frequency

1 INTRODUCTION

Wind turbines are dynamically sensitive structures, with excitation forces arising from the rotor spinning at a specific angular velocity and the blade passing the turbine tower at a set frequency, known as the 1P and 3P frequencies respectively for a three-bladed turbine system. LeBlanc et al. [1] give details that state typical turbine 1P frequencies tend to be between 0.17 to 0.33 Hz and 3P frequencies tend to be between 0.5 to 1 Hz. It is critical that the structural design of the turbine is undertaken in such a way that the system natural frequency resides away from the resonant excitation bands. The system frequency is governed by a combination of the wind turbine structural properties and the stiffness of the foundation soil strata. Over 75% of offshore wind turbines currently have monopile foundations, which are designed as a soft-stiff system, with the functional design frequency of the turbine structure falling between the upper and lower excitation frequency bands [2]. In conventional design of offshore structures such as oil and gas platforms, an over-estimation of the soil stiffness leads to a conservative design but has no major implications for safety. In the case of offshore wind turbines, however, due to the upper and lower-bound resonant frequency bands, an over or underestimation of foundation stiffness can be detrimental to the safety and integrity of these structures in operation. The dynamic stability of the foundation is provided by the interaction between the monopile shaft and the adjacent soil strata. Any changes in the interaction process will lead to changes in the dynamic stability of the structure.

Scour can be defined as the excavation and removal of material from around foundation elements as a result of the erosive action of flowing water (Hamill, 1999). This phenomenon has been widely studied with respect to bridges spanning rivers, where the magnitude of the scour affecting the structure is limited to the flow properties of the channel at the location of the bridge and the boundary conditions of the cross-sectional flow area. In the case of coastal environments, the lack of a fixed boundary condition in respect of a riverbank means that equilibrium flow conditions may not manifest themselves and scour could be very detrimental to structures at mobile sand sites. Scour has the effect of rapidly reducing the system stiffness of foundation elements and can lead to structural failure. The scour process of reducing the soil support and hence increasing the free length can result in larger losses in stiffness than an equivalent loss of stiffness arising from soil stiffness degradation or other mechanisms. In the case of offshore wind turbines, changes in the design frequency caused by losses in foundation stiffness as would occur with scour can lead to the generation of resonant effects, which can be very detrimental to the design life of these structures in operation and lead to the generation of fatigue effects in the structural members. The design scour depth is usually taken as 1.3 pile diameters, which in the case of large diameter monopiles can add significant costs to foundations if this design is deemed too conservative. For example, for a 6 m

diameter monopile, the design scour depth is 7.8 m, which means that the monopile has to have this extra length to account for the scour process.

In this paper, a parametric study on the effect of scour on the frequency response of an offshore wind turbine is detailed. The parametric study involves varying soil stiffness profiles and depths of scour to assess the effect of each on the frequency response of a simple turbine model. Realistic turbine properties and offshore soil stiffness is hypothesised for the purpose of this analysis. Offshore site conditions corresponding to loose, medium dense and dense sand are generated for the purpose of the analysis and scour to a design depth of 1.3 pile diameters is applied to ascertain realistic frequency shifts to be expected for this magnitude of scour.

2 SOIL-STRUCTURAL MODELLING

2.1 Turbine Structure

The structural model employs a 2D beam-type modelling procedure to ascertain the frequency response of a standard 3.6 MW turbine for a range of different soil stiffness regimes. The properties of a 3.6 MW turbine are modelled because this is currently one of the most common systems being installed offshore; hence it is of interest in this study. The modelling is undertaken in the MATLAB programming environment. Standard geometric properties are used to model the wind turbine superstructure, which consists of a tubular steel tower tapered from its base to the top with a lumped mass to represent the combined mass of the rotor and nacelle elements. The sub-structure consists of a monopile embedded 30 m into "soil", with a free cantilevered length of 45 m above the ground line. The depth of water surrounding the turbine foundation may have a small effect on the natural frequency through added mass, but its influence is not modelled in this study. The interface power system is represented as a lumped mass at the transition between the monopile and the tower. The tower elements are modelled as standard 4-DOF Euler-Bernoulli beam elements with mass and stiffness matrices as defined in [3]. These are shown in Equation (1).

$$K_{BEAM} = \begin{bmatrix} \frac{12EI}{L^3} & \frac{6EI}{L^2} & -\frac{12EI}{L^3} & \frac{6EI}{L^2} \\ \frac{6EI}{L^2} & \frac{4EI}{L} & -\frac{6EI}{L^2} & \frac{2EI}{L} \\ -\frac{12EI}{L^3} & -\frac{6EI}{L^2} & \frac{12EI}{L^3} & -\frac{6EI}{L^2} \\ \frac{6EI}{L^2} & \frac{2EI}{L} & -\frac{6EI}{L^2} & \frac{4EI}{L} \end{bmatrix} \quad (1a)$$

$$M_{BEAM} = \frac{\rho AL}{420}\begin{bmatrix} 156 & 22L & 54 & -13L \\ 22L & 4L^2 & 13L & -3L^2 \\ 54 & 13L & 156 & -22L \\ -13L & -3L^2 & -22L & 4L^2 \end{bmatrix} \quad (1b)$$

where K_{BEAM} = standard beam element stiffness matrix, M_{BEAM} = standard beam element mass matrix, E = Young's modulus of steel (kN m^{-2}), I = moment of inertia (m^4), ρ = density of steel (kg m^{-3}), A = cross-sectional area (m^2) and L = length of element (m).

The discretisation of each element is set at 0.5 m, which means that each beam element has a length of 0.5 m. This is deemed adequate to represent effectively changes in the global dynamic response (overall frequency changes) of the structure to changes in boundary conditions (scour). The monopile is modelled using modified Euler-Bernoulli beam elements, where the 4-DOF beam elements are combined with 2-DOF spring elements to create a 5-DOF spring-beam element. The stiffness contribution from the soil is modelled using this linear spring contribution (2-DOF element) as shown in Equation (2).

$$K_{SPRING} = k_s\begin{bmatrix} 1 & -1 \\ -1 & 1 \end{bmatrix} \quad (2)$$

where k_s is the small-strain stiffness coefficient of the combined soil-structure system at that depth. A schematic of the numerical model is shown in Figure 1. The individual elemental mass and stiffness matrices are assembled together to create global mass and stiffness matrices representing the entire system. The frequency response of the structure can be obtained by manipulating these matrices.

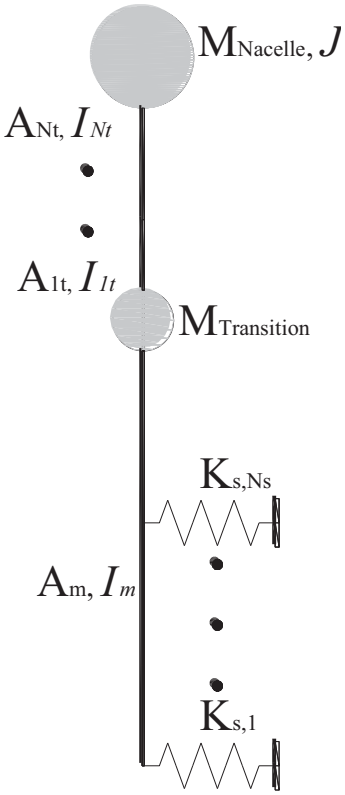


Figure 1. Numerical schematic of turbine system.

The main turbine structural properties are outlined in Table 1.

Table 1. Turbine Properties.

Property	Value
Tower length (m)	70 m
Tower diameter (m)	3.5 – 5 m
Nacelle mass (kg)	230,000 kg
Monopile diameter (m)	6 m
Pile wall thickness (m)	0.09 m
Monopile length (m)	75 m
Embedded depth (m)	30 m

2.2 Soil Properties

Three different soil stiffness profiles are created for the purpose of the analysis within this paper. Profiles correspond to loose, medium dense and dense sand, typical of those found at offshore sites where wind farms are often constructed. In the first instance, soil stiffness values were assigned using soil classifications based on the American Petroleum Institute design code [4], which describes sand behaviour based on relative density (D_r). From the API code, to consider the range of sands typically encountered in the offshore environment, uniform soil deposits 30 m deep with D_r values of 30%, 50% and 80% were considered, corresponding to loose, medium dense and dense sand. The relative density values were assumed constant over the entire penetration depth. Synthetic Cone Penetration Test (CPT) profiles were generated corresponding to these Dr values and linearly increasing effective stress profiles using the empirical relation available in [5]. A plot of these CPT q_c profiles is shown in Figure 2.

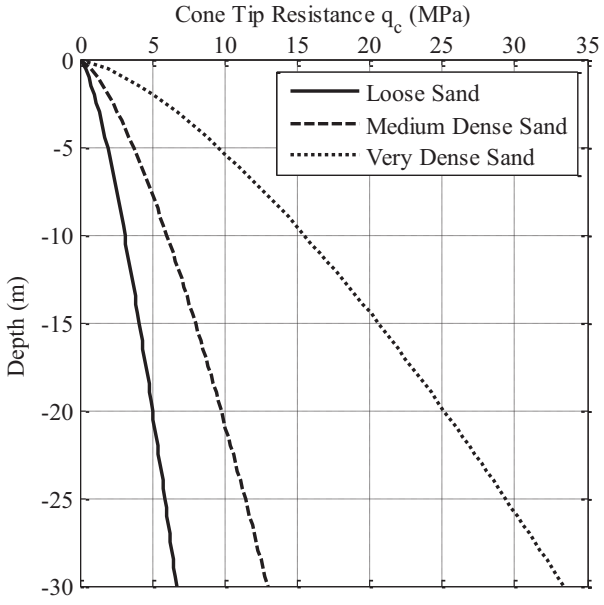


Figure 2. Synthetic CPT Profiles

These CPT q_c profiles were converted to profiles of the small-strain shear modulus G_0, for the given relative density value considered. The purpose behind converting to G_0 is due to the fact that very small strains are imparted into the soil mass during operational dynamic conditions; hence the small strain shear modulus of the soil is a particularly useful parameter in terms of dynamic modelling of soil-structure interaction. The G_0 profiles can be converted to profiles of the modulus of subgrade reaction, K for the soil-structure system using the procedure outlined in [6], [7]. The K formulation is modified from Vesic [8] who derived an expression coupling the beam and soil properties in the elastic continuum. This K value represents the system stiffness and depends on the structural properties of the monopile and the stiffness properties of the foundation soil. This K value is converted into individual lateral spring stiffness moduli by multiplying the value at each spring depth (depth into the ground) by the soil spring spacing (spacing between springs in the model, in this case 0.5 m).

3 ANALYSIS & RESULTS

The design depth of scour around a monopile is 1.3 times the pile diameter. For a 6 m diameter monopile, this corresponds to a depth of scour of 7.8 m. The frequency response of the numerical model is obtained by performing an eigenvalue analysis on the structural system matrix **[D]**. An eigenvalue analysis involves obtaining the eigenvalues and eigenvectors of this **[D]** matrix, which is a function of the mass and stiffness of the entire system. The eigenvalues correspond to the natural frequencies and the eigenvectors correspond to the mode shapes. The system matrix is defined in Equation (3).

$$[\mathbf{D}] = \frac{[\mathbf{K}]}{[\mathbf{M}]} \tag{3}$$

where **[K]** is the global stiffness matrix, created by assembling together the tower beams and monopile spring-beam elements and **[M]** is the global mass matrix, obtained in the same way. The eigenvalues are obtained by using MATLAB's in-built 'eig' function. Eigenvalue analyses are undertaken for the case of zero scour and full design scour, where scour is modelled as the removal of springs from the numerical model.

The results are obtained for each different soil stiffness profile (loose, medium dense and dense sand). These are presented in Table 2. The change in frequency for the loose sand profile over the design depth and beyond is shown in Figure 3. The 1P nominal frequency at 0.22 Hz is the frequency associated with the rotation of a rotor for a 3.6 MW turbine.

Table 2. Analysis Results.

Case	Freq zero scour (Hz)	Freq 7.8 m scour (Hz)	% Change
Loose	0.295	0.2705	8.4 %
Medium Dense	0.301	0.278	7.7 %
Dense	0.306	0.285	6.96 %

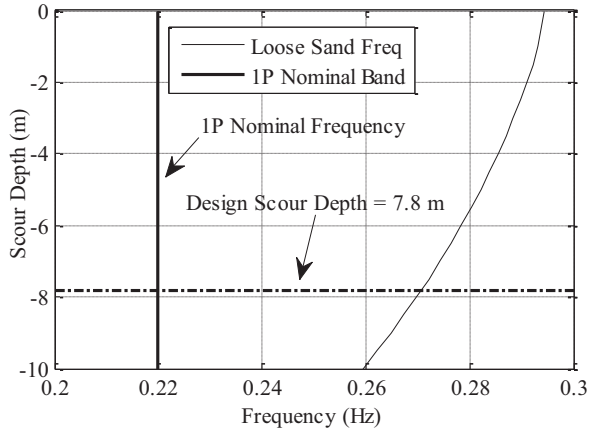


Figure 3. Frequency change in loose sand

4 DISCUSSION & CONCLUSION

The loose sand profile exhibits the largest relative changes in frequency due to scour with changes of 8.4% over 7.8 m as compared to changes of 6.96 % for the dense sand case. From the results, it is evident that significant changes in frequency can occur due to scour and this should be explicitly accounted for in the design process of large scale offshore wind turbine foundations. These changes are higher than those predicted using conventional design codes (such as API) to model the soil stiffness, which consider the soil stiffness profile as linearly varying with depth. The profiles considered in this paper are non-linearly varying with depth and are arguably more realistic. As a result of the non-linear nature of the profiles considered within this paper, higher stiffness is encountered at shallower depths relative to a linearly increasing stiffness profile with other design methods such as API. Due to this higher relative stiffness at shallower depths as hypothesised in this paper, larger variations in frequency result from scour.

ACKNOWLEDGEMENTS

The authors would like to acknowledge the support of the Earth and Natural Sciences (ENS) Doctoral Studies Programme, funded by the Higher Education Authority (HEA) through the Programme for Research at Third Level Institutions, Cycle 5 (PRTLI-5), co-funded by the European Regional Development Fund (ERDF).

REFERENCES

[1] C. LeBlanc, G. T. Houlsby, and B. W. Byrne, "Response of stiff piles in sand to long-term cyclic lateral loading," *Géotechnique*, vol. 60, no. 2, pp. 79–90, Jan. 2010.

[2] P. Doherty and K. Gavin, "Laterally loaded monopile design for offshore wind farms," *Proceedings of the ICE - Energy*, vol. 165, no. 1, pp. 7–17, Feb. 2012.

[3] Y. W. Kwon and H. Bang, *The Finite Element Method using MATLAB*. Boca Raton, FL: CRC Press, Inc., 2000, pp. 237–244.

[4] API, "RP2A: Recommended practice for planning, designing and constructing offshore platforms - Working stress design," Washington, DC, 2007.

[5] T. Lunne and H. P. Christopherson, "Interpretation of Cone Penetrometer Data for Offshore Sands," in *Offshore Technology Conference OTC4464*, 1983.

[6] L. J. Prendergast, D. Hester, K. Gavin, and J. J. O'Sullivan, "An investigation of the changes in the natural frequency of a pile affected by scour," *Journal of Sound and Vibration*, vol. 332, no. 25, pp. 6685–6702, 2013.

[7] S. A. Ashford and T. Juirnarongrit, "Evaluation of Pile Diameter Effect on Initial Modulus of Subgrade Reaction," *Geotechnical and Geoenvironmental Engineering*, vol. 129, no. 3, pp. 234–242, 2003.

[8] A. B. Vesic, "Bending of beams resting on isotropic elastic solid," *Journal of Soil Mechanics and Foundation Engineering*, vol. 87, pp. 35–53, 1961.

Mechanical Resistance Characteristics of GGBS Concrete in Fire

Ted McKenna[1], Mark G. Richardson[2], Brian O'Rourke[1]
[1]Department of Civil, Structural and Environmental Engineering, Cork Institute of Technology, Bishopstown, Cork, Ireland
[2]School of Civil, Structural and Environmental Engineering, University College Dublin, Belfield, Dublin 4, Ireland
email: ted.mckenna@cit.ie, mark.richardson@ucd.ie, brian.orourke@cit.ie

ABSTRACT: Fire can have a devastating effect on life, property and the environment. Concrete is considered an effective material in protecting against the detrimental effects of fire on common structures. However, concrete exposed to high temperatures experiences physical and chemical transformations resulting in detrimental effects on performance. Past studies indicate that binder type influences the ability of a particular concrete to resist deterioration in mechanical strength.

The current study investigates the load bearing resistance (i.e. strength) characteristics of concrete consisting of varying binder types. Four mix types were selected, with the binder content varying from 100% CEM II/A-L to containing Ground Granulated Blastfurnace Slag (GGBS) replacement quantities ranging from 30% to 70%. An experimental programme was developed to investigate the residual compressive strength of normal strength concrete of varying binder type subjected to elevated temperatures of 300˚C, 600˚C and 900˚C. The study considered both short-term and long-term progressive deterioration.

Exposure to 300˚C resulted in reduction in relative strength for the 100% CEM II concrete, while the 70% GGBS exhibited an increase in relative strength. Exposure of concrete specimens to elevated temperatures of 600˚C and 900˚C resulted in residual compressive strengths, which were 60% and 15% respectively of the strength of the unheated concrete. It was concluded that the inclusion of GGBS as a binder material does not influence the performance of concrete in fire in terms of load resistance.

KEY WORDS: Fire; Elevated temperature; Concrete; Ground granulated blastfurnace slag (GGBS); Compressive strength.

1 INTRODUCTION

The aim of this research was to establish whether the use of Ground Granulated Blastfurnace Slag (GGBS) as a binder replacement in concrete results in improved performance at elevated temperatures. Compressive strength is typically the critical material property/characteristic for structural concrete. An objective of the proposed research was to substantiate previously conducted research which postulated the following:

i. Ground Granulated Blastfurnace Slag (GGBS) concrete retains greater strength following exposure to fire/elevated temperature when compared with CEM I concrete.
ii. Residual strength of GGBS concrete, when compared with CEM I concrete, is greater over time following a fire/elevated temperature event.

Furthermore, the research aimed to establish whether these trends were identifiable in CEM II/A-L GGBS combination concretes now commonly used in Irish practice.

2 LITERATURE REVIEW

A state-of-the-art review entitled, "Ground Granulated Blast Furnace Slag (GGBS) as a concrete additive" [1], by Aβbrock et al. (2007) highlighted potential beneficial effects of using GGBS as a binder replacement to increase the fire resistance of concrete. This postulation was based on a document published in 2001 entitled "Series of Publications on Special Stresses, Volume 4: Mass Concrete – Fire Concrete" by Kollo and Lang [2]. This document refers in turn to research completed in 1936 by Rustschuk in Leningrad (now St. Petersburg) [3].

Based on the earlier research by Rustschuk, it was reported that increased replacement of Portland cement clinker with GGBS as the binder material leads to increased stability following exposure to elevated temperatures such as during a fire. The inclusion of GGBS as a binder replacement results in a significantly lower reduction in compressive strength [3]. This research lists the significantly lower portlandite content in the hardened cement paste of hydrated cement pastes containing GGBS, when compared with hydrated Portland cements, as a prime contributor to improved performance at elevated temperature. While not definitive, from the terminology used in reporting the research, it is likely that the experimental programme was completed using binder pastes. Kollo and Lang [2] indicate that the material strength continues to deteriorate with time following an elevated temperature event. While the deterioration in strength varies depending on binder type, with blastfurnace cement demonstrating improved relative performance, this may mean that the inclusion of GGBS in the mix may only serve to delay an inevitable decrease in strength.

The influence of binder type on concrete has been considered in a number of other research studies. Balazs and Lubloy [4] reported that the reduction in compressive strength due to elevated temperature decreases with increased slag content. This outcome is consistent with that of Sullivan and Sharshar [5] who reported superior performance of slag pastes at temperatures up to 600˚C. Research on the behaviour of self-compacting concrete produced with GGBS and Fly Ash (FA) additives concluded that neither significantly influence residual compressive strength or weight loss [6]. Khoury [7] has reported a similar view, stating that his research finds GGBS to provide the best performance at high temperatures. In a study of GGBS concrete incorporating steel fibre and polypropylene fibre, it was concluded that using GGBS as a binder replacement can improve splitting strength both before and after exposure to elevated temperature [8]. Poon et al [9] also concluded that the use of GGBS as a binder replacement in concrete improved strength retention at elevated temperatures, however if relative strengths are considered there is no discernible difference.

Numerous studies have considered binder pastes or mortars exclusively in terms of elevated temperature effect. For example, an investigation of the effects of high temperature on mortars, containing both OPC and GGBS, concluded that GGBS improves mechanical strength when a comparison of the relative residual strength is considered [10]. However, if the actual compressive strengths reported in the research are compared, there is little discernible difference for temperatures up to 600˚C with the exception of mortar containing 50% GGBS which performs markedly better throughout. Mendes et al [11] considered the long-term progressive deterioration following fire exposure and concluded that the rehydration of lime (CaO) following heating results in severe deterioration in the structure of OPC paste compared with no deterioration on OPC/GGBS blended specimens.

An investigation of the effects of elevated temperature on cement paste containing varying amounts of GGBS and of varying water/binder ratio again reported benefits to GGBS inclusion and in particular at temperatures of 1050˚C [12].

3 RESEARCH SIGNIFICANCE

While many studies exist that compare the performance of GGBS/Portland cement clinker combination concrete with concrete containing cements of high clinker content (i.e. Ordinary Portland Cement (OPC), CEM I), studies comparing GGBS concrete with CEM II/A-L concrete are not as prevalent. Information on the performance of such concretes at elevated temperature is very limited and hence the influence of GGBS on concrete performance at elevated temperature requires investigation.

4 EXPERIMENTAL

4.1 Overview

The experimental programme comprised:

- Manufacture of 68 cube specimens for the four respective mix types, with each mix containing varying levels of GGBS as binder replacement (i.e. 272 cubes in total);
- Exposure of cubes to elevated temperatures;
- Recording mass variations both pre- and post-heating;
- Compressive strength testing on completion of cooling stage as well as 28 and 56 days after exposure to elevated temperatures.

4.2 Aggregates

The aggregates used in the manufacture of the concrete test specimens consisted of single sized 20mm limestone aggregate, single sized 10mm limestone aggregate and sandstone sand. Properties of the aggregates are given in Table 1.

Table 1. Aggregate Properties

	Coarse		**Fine**
Type	Crushed		Uncrushed
I.S. EN 12620 Designation	10/20	4/10	0/4
Maximum size (mm)	20	10	4
Water Absorption (%)	0.5	0.7	2.0
Relative Density	2.66	2.66	2.58

The aggregates were graded and their conformity to I.S. EN 12620 confirmed. The combined particle size distribution was plotted for the aggregate proportions proposed for the concrete mix to ensure conformity with industry advised upper and lower limits.

4.3 Mix Proportions

The mix proportions used for the experimental programme are given in Table 2.

Table 2. Mix Proportions.

	Mix Type			
	GO	**G3**	**G5**	**G7**
% CEM II/A-L binder	*100%*	*70%*	*50%*	*30%*
% GGBS binder	*0%*	*30%*	*50%*	*70%*
CEM II/A-L (kg/m^3)	320	224	160	96
GGBS (kg/m^3)	0	96	160	224
Water	175	175	175	175
20mm Aggregate (kg/m^3)	755	750	750	745
10mm Aggregate (kg/m^3)	470	470	470	465
Sand (kg/m^3)	640	635	635	635
Binder Content (kg/m^3)	320	320	320	320
W/B Ratio	0.547	0.547	0.547	0.547

No additives were included in the concrete mixes.

4.4 Test Specimen Manufacture, Curing & Drying

A rotating drum mixer was used for the mixing of the concrete. Cube specimens, 100mm x 100mm x 100 mm in size, were made and cured in accordance with I.S. EN 12390-2. Specimens for each respective mix type were taken from a single batch of concrete. The test specimens remained in the steel moulds for approximately 22 hours and protected against shock, vibration and dehydration at a temperature of 20 (± 5) °C.

4.5 Compressive Strength at 28 days

Compressive strength tests were carried out on a selected number of concrete cube specimens after 28 days of curing. The compressive strength tests were completed in accordance with I.S. EN 12390-3 using calibrated test equipment. A summary of results for cube compressive tests for concrete aged 28 days is given in Table 3.

Table 3. Compressive Cube Strengths at 28 days

Mix Type			
GO	**G3**	**G5**	**G7**
51 MPa	46 MPa	45 MPa	33 MPa

4.6 Heating and Cooling Methodology

A single kiln was used to apply all heating regimes. The kiln used is a Ramsell Naber N41 Furnace with internal dimensions of 500mm long, by 350mm wide and 290mm high. The kiln was electrically heated with heating elements located on the longer sides of the kiln. The cube specimens were heated and tested under unsealed conditions, thus allowing moisture and gases to be released to and from the cubes. The cubes were placed in two layers within the kiln.

Recording the typical strength behaviour of concrete following exposure to elevated temperature can be misleading unless the specific mix and environmental conditions are specified [13]. While the mix proportions and specimen manufacture are detailed in the preceding sections, the following aims to provide explanation for the heating regimes undertaken. Khoury identifies the following distinct stages of the heating cycle:

1) First heating,
2) Constant temperature,
3) Cooling,
4) Post-cooling stages.

First-time heating is the most complex period, with as many as 20 factors potentially contributing to either increase or decrease in strength at various stages during the period. Little change in strength can be expected during the constant temperature stage with the exception of processes not completed during the period of first heating. The effect of thermal and inter-particle stress-induced cracking becomes more significant during the cooling stage. The chemical and physical effects of absorption of moisture dominate the post-cooling stage [13].

For the research relevant to this paper the specimens were exposed to three constant (maximum) elevated temperatures, namely 300°C, 600°C and 900°C. Firstly, the rate of heat increase within the kiln is dictated by the capacity of the kiln. The rate of heating achieved during kiln trials is illustrated in Figure 1, with the standard fire curve in accordance with I.S. EN 1992-1-2 included for comparison purposes.

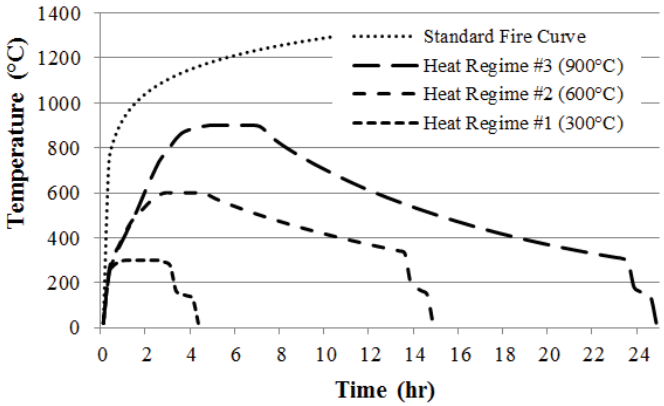


Figure 1. Heating regime time-temperature profiles.

The kiln atmospheric temperature is then maintained at the respective maximum temperatures for a set period of time to allow thermal equilibrium to be reached within the kiln and within the concrete cubes. Due to the low thermal conductivity of the concrete, the cube specimens were 'soaked' at maximum temperatures of 300˚C, 600˚C and 900˚C for two hours to ensure that a uniform temperature was achieved across the cube section (i.e. the core temperature was equal to the surface temperature of the cube specimen).

On completion of each respective constant temperature period, the cooling phase adopted was similar for all maximum temperatures. The cooling was not controlled, but was monitored. To minimise the effects of thermal shock, the temperature at which the door was opened varied between 300°C and 330°C. The test specimens remained in the kiln for a period of one hour after the kiln door was opened. The cube specimens were then removed with the average temperature within the kiln at 130°C. On removal from the kiln, the cube specimens were stored in laboratory conditions (i.e. approximate temperature of 20°C and relative humidity of 50%) until required for testing.

It is considered that this approach to the first heating, constant maximum heat exposure, cooling and post-cooling storage would minimise environmental factors adversely affecting the experimental data as recorded. A summary of the relevant periods for each of the heating regimes is illustrated in Figure 1 and recorded in Table 4.

Table 4. Heating Regime Time Periods

Maximum Temperature	First Heating	Constant Temperature	Cooling in Kiln
300°C	0.5 hrs	2 hrs	0.5hrs
600°C	2.5 hrs	2 hrs	9 hrs
900°C	5.0 hrs	2 hrs	14 hrs

4.7 Residual compressive strength tests following exposure to elevated temperatures

As well as considering the residual strength immediately following the cooling phase, the residual strength at both 28 days and 56 days after heating were also considered to determine potential further deterioration over time. The residual strength recorded at the end of the cooling phase is conservatively indicative of the concrete strength during the fire event and can therefore be used in the design of a structure for fire. The long term residual strength will influence the appropriate timing and approach to a structural assessment of a fire damaged reinforced concrete structure.

Compressive strength tests were completed on test specimens of each mix type and each maximum temperature exposure. The test specimens were stored in laboratory conditions (i.e. approximate temperature of 20°C and relative humidity of 50%) pending compressive strength tests at periods of 28 days and 56 days following the heating regime. Compressive strength tests were completed in accordance with I.S. EN 12390-3.

4.8 Visual Inspection

The response of these specimens during the post-cooling phase was visually observed and recorded.

5 RESULTS AND DISCUSSION

5.1 Compressive Strength

The residual strengths immediately following the cooling phase of each respective heat regime are illustrated in Figure 2.

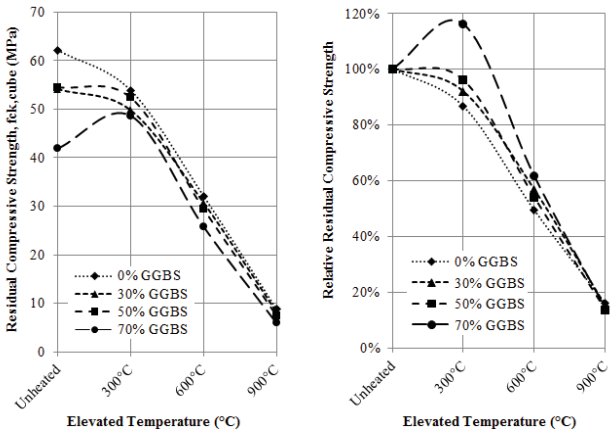


Figure 2. Residual and relative compressive cube strengths for concretes of varying binder type at 1 day post-heating.

While the compressive strengths of the unheated concrete for respective mix types vary, when heated to 300˚C the magnitude of strengths converge as illustrated in Figure 2(a). At temperatures above 300˚C the strength reduction is linear and comparable for different mix types. In Figure 2(a) concrete containing 0% GGBS performed best while the concrete containing 70% GGBS is the worst performing. However, if the results are compared in terms of relative strength (i.e. residual strength of heated concrete relative to the unheated concrete), the concrete containing 70% GGBS is the best performing concrete, while concrete containing 0% GGBS is the worst performing as illustrated in Figure 2(b). These results are consistent with the findings of Uysal et al [6] but are up to 20% less strength than findings reported by Seleem at al [14], which was based on a lower strength concrete (i.e. 28MPa unheated compressive strength).

A comparison of the relative strengths as presented in Figure 2(b) with the reduction factors published in I.S. EN 1992-1-2 [15] is illustrated in Figure 3. The overall profiles are comparable demonstrating consistency with I.S. EN 1992-1-2. With the exception of the mix containing 70% GGBS at an elevated temperature of 300°C, the reduction in strength from assessment of experimental data is comparable to the reduction factors specified in I.S. EN 1992-1-2 [15]. The aggregate used in the manufacture of the concrete for the experimental programmes was limestone and is therefore calcareous; however the results of the experimental programme indicate lower performance when compared with that of concrete containing calcareous aggregate as specified in I.S. EN 1992-1-2. Research on the influence of aggregates on the mechanical characteristics of concrete exposed to fire found that siliceous aggregate performed better that limestone aggregate, which is contrary to I.S. EN 1992-1-2 charts [16].

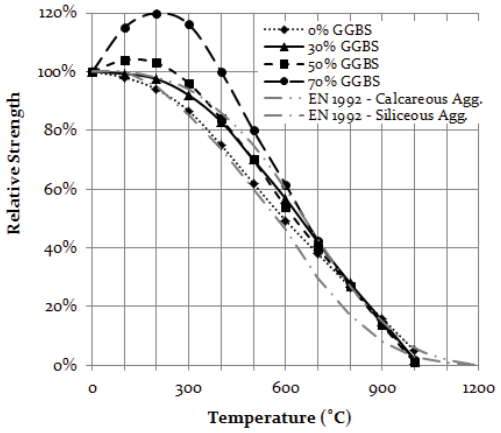


Figure 3. Comparison relative compressive cube strengths derived from experimental data with I.S. EN 1992-1-2 data.

When compared with research by Hertz [17], which was based on a significant amount of test data, and forms the basis for I.S. EN 1992-1-2 [15], the experimental data from the current research should be comparable with Hertz's data in the cold condition. The experimental data, as illustrated in Figure 4, appear to compare more readily with the data from the upper limit of concrete tested in the cold condition and the design curve based on concrete tested in the hot condition.

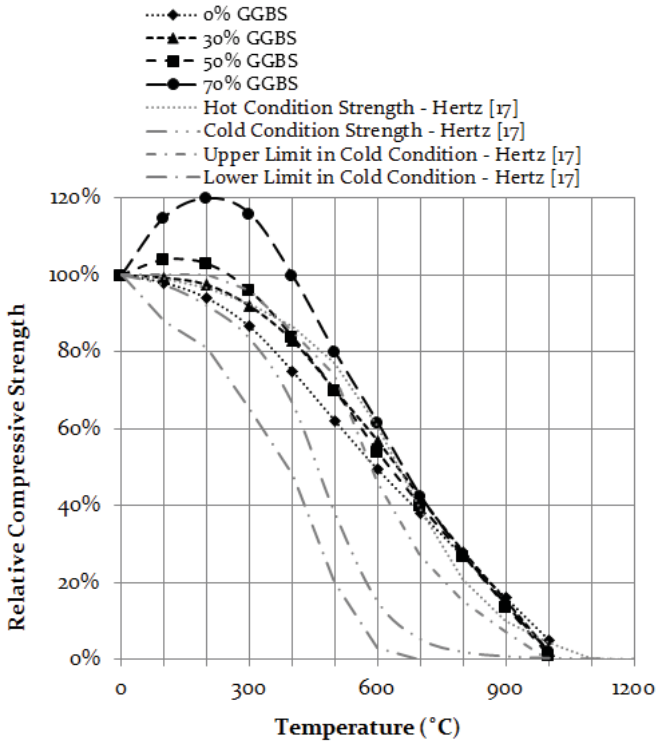


Figure 4. Comparison relative compressive cube strengths derived from experimental data with Hertz design curves [17]

The long term residual strength of concrete following a fire event is an important consideration. It provides an indication of the appropriate minimum time lapse required between a fire event and the commencement of an assessment of the long term condition of a fire damaged structure. The residual compressive strengths for concrete subject to varying elevated temperatures, at completion of the cooling phase, 28 days after heat regime and 56 days after heat regime are illustrated in Figure 5. The associated relative strengths are illustrated in Figure 6.

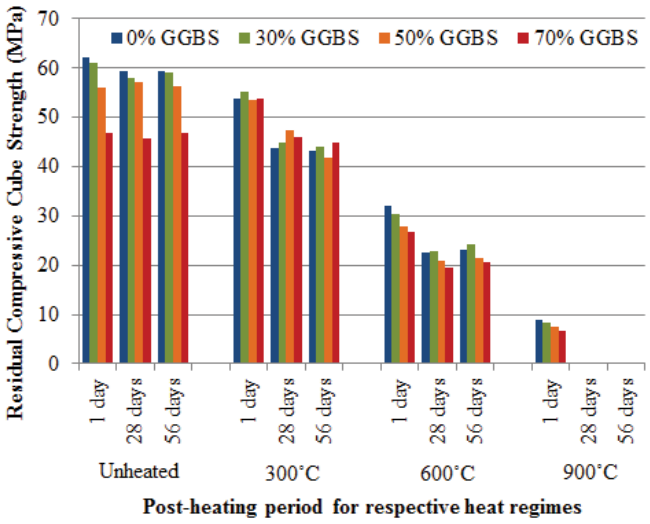


Figure 5. Residual compressive cube strengths of concrete with varying elevated temperature

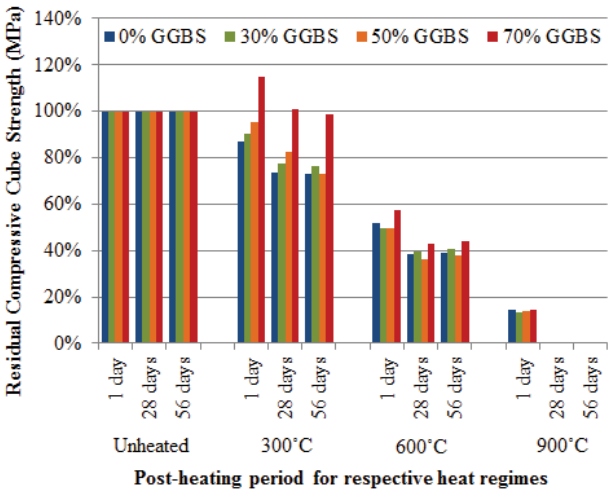


Figure 6. Relative compressive cube strength of concrete with varying elevated temperature

From the data illustrated in Figure 5 and Figure 6 it is clear that continued deterioration of the compressive strength continues for a time after the initial cooling phase. However, this deterioration would appear to be almost complete within 28 days as there is little difference, and even some increases, in the strength for the specimens tested at 56 days after heating compared to those tested 28 days after heating. These results are consistent with similar research by Sarshar and Khoury [18] and Papayianni and Valiasis [19], which reported a rise of strength in the time between 28 days and 180 days after heating. The deterioration in strength is not influenced by the type of binder used.

In summary, it is recommended that if tests are to be carried out on fire damaged concrete in order to assess its condition, such testing should not be carried out until at least 28 days after the fire event.

5.2 Visual Inspection

It should be noted that the specimens heated to 900˚C could not be compressive strength tested at 28 days or 56 days after heating as they had disintegrated as a result of the rehydration process. This progression of specimen deterioration is illustrated in Figure 7 and Figure 8. In research on the influence of aggregate on behaviour of concrete subject to elevated temperatures, it was concluded that the decarbonation of calcite in the calcareous aggregate between 600˚C and 750˚C resulted in reaction with ambient atmospheric humidity upon cooling, thus forming portlandite by multiplying its volume by 2.5 [20]. Such an increase in volume leads to disintegration of the concrete. As the current research was conducted using limestone aggregate, this could also explain the disintegration of the test specimens.



Figure 7. Specimen condition 4 days after heating.



Figure 8. Specimen condition 9 days after heating.

In summary, the use of GGBS as a binder replacement ranging from 30% to 70% does not appear to result in a discernible difference in terms of compressive strength performance of concrete. However, this is not consistent with published research based on comparisons of binder mortars. This is most likely due to the volume of aggregate and hence is not a result of binder quality.

6 CONCLUSIONS

The findings of this research are:

1) Short-term residual strength
   There is no notable difference in performance between concrete containing 100% CEM II and that consisting of GGBS binder material at replacement levels ranging from 30% to 70%.
2) Long-term residual strength
   There is no notable difference in performance between concrete containing 100% CEM II and that consisting of GGBS binder material at replacement levels ranging from 30% to 70%.
3) If the actual residual strengths of the mortar are considered instead of the relative strengths, the variability of results would make such a conclusion ambiguous.

7 RECOMMENDATIONS

A significant obstacle encountered during this research was the lack of clear and established practice in determining the properties of concrete in fire. Reported research offers varying and often contradictory conclusions. A method of determining the properties of concrete at elevated temperatures, which is both accurate and economic, should be established to allow assessment of concretes with varying constituents with a view application of data to design methods.

ACKNOWLEDGMENTS

Cork Institute of Technology for establishing the fire test facilities used during the experimental element of this research. Ecocem (Ireland) for supply of binder materials.

REFERENCES

1. Aβbrock, O., W. Brameshuber, and D. Droll, *Ground Granulated Blast Furnace Slag (GGBS) as a concrete additive - Current situation and scenarios for its use in Germany*. 2007.
2. Kollo, H. and E. Lang, *Specialstresses Volume 4: Mass Concrete, Fire Concrete*. 2001.
3. Rustschuk, G.M., *Comparison of the cements, taking into account exposure to high temperatures (including pozzolanic cement)*. 1936: Leningrad.
4. Balazs, G.L. and E. Lubloy, *RC Structures in and after fire.* Hungarian Group of FIB - Concrete Structures Annual Technical Journal, 2012. **13**: p. 72-80.
5. Sullivan, P.J.E. and R. Sharshar, *The performance of concrete at elevated temperatures (as measured by the reduction in compressive strength).* Fire Technology, 1992. **28**(3): p. 240-250.
6. Uysal, M., K. Yilmaz, and M. Ipek, *Properties and behavior of self-compacting concrete produced with GBFS and FA additives subjected to high temperatures.* Construction and Building Materials, 2012. **28**(1): p. 321-326.
7. Khoury, G.A., *Effect of fire on concrete and concrete structures.* Progress in Structural Engineering and Materials, 2000. **2**(4): p. 429-447.
8. Gao, D., D. Yan, and X. Li, *Splitting strength of GGBFS concrete incorporating with steel fiber and polypropylene fiber after exposure to elevated temperatures.* Fire Safety Journal, 2012. **54**(0): p. 67-73.
9. Poon, C.-S., et al., *Comparison of the strength and durability performance of normal- and high-strength pozzolanic concretes at elevated temperatures.* Cement and Concrete Research, 2001. **31**(9): p. 1291-1300.
10. Delhomme, F., J. Ambroise, and A. Limam, *Effects of high temperatures on mortar specimens containing Portland cement and GGBFS.* Materials and Structures, 2012. **45**(11): p. 1685-1692.
11. Mendes, A., J. Sanjayan, and F. Collins, *Long-term progressive deterioration following fire exposure of OPC versus slag blended cement pastes.* Materials and Structures, 2009. **42**(1): p. 95-101.
12. Wang, H.Y., *The effects of elevated temperature on cement paste containing GGBFS.* Cement and Concrete Composites, 2008. **30**(10): p. 992-999.
13. Khoury, G.A. *Compressive strength of concrete at high temperatures: A reassessment*. Magazine of Concrete Research, 1992. **44**, 291-309 DOI: 10.1680/macr.1992.44.161.291.
14. Seleem, H.E.D.H., A.M. Rashad, and T. Elsokary, *Effect of elevated temperature on physico-mechanical properties of blended cement concrete.* Construction and Building Materials, 2011. **25**(2): p. 1009-1017.
15. NSAI, *I.S. EN 1992-1-2:2005 Eurocode 2: Design of Concrete Structures - Part 1-2: General Rules - Structural Fire Design (including National Annex)*. 2005b, National Standards Authority of Ireland.
16. Robert, F. and H. Colina *The influence of aggregates on the mechanical characteristics of concrete exposed to fire*. Magazine of Concrete Research, 2009. **61**, 311-321.
17. Hertz, K.D. *Concrete strength for fire safety design*. Magazine of Concrete Research, 2005. **57**, 445-453.
18. Sarshar, R. and G.A. Khoury *Material and environmental factors influencing the compressive strength of unsealed cement paste and concrete at high temperatures*. Magazine of Concrete Research, 1993. **162**, 51-61.
19. Papayianni, J. and T. Valiasis, *Residual mechanical properties of heated concrete incorporating different pozzolanic materials.* Materials and Structures, 1991. **24**(2): p. 115-121.
20. Xing, Z., et al., *Influence of the nature of aggregates on the behaviour of concrete subjected to elevated temperature.* Cement and Concrete Research, 2011. **41**(4): p. 392-402.

Shear Behaviour of Prescast Prestressed Hollowcore Slabs

Cian Twomey[1], Brian O'Rourke[2], David Hodge[2]
[1]Cronin & Sutton Consulting, 45 Fitzwilliam Place, Dublin 2, Ireland
[2]Department of Civil, Structural and Environmental Engineering, Cork Institute of Technology, Bishopstown, Co. Cork, Ireland
email: cian.twomey@csconsulting.ie, brian.orourke@cit.ie, david.hodge@cit.ie

ABSTRACT: The aim of this research was to examine the structural behaviour of precast prestressed hollowcore slabs subject to shear actions. There is a lack of consensus presented in the literature and published guidance regarding the appropriateness of various shear resistance determination methods.
Full scale load tests were carried out on hollowcore slabs. The laboratory tests were modelled using the LUSAS Finite Element Analysis (FEA) package and the results subsequently compared. Three precast prestressed hollowcore slabs were tested to failure in the Heavy Structures Laboratory at Cork Institute of Technology. These tests provided real physical data, as well as validation data to compare with finite element models generated after the physical testing.
The study found that IS EN 1992-1-1:2005 [1], or Eurocode 2 (EC2) is conservative for shear resistance. Close agreement between the physical tests and the LUSAS finite element model tests was achieved. The analysed data showed that the results of both the linear elastic and non-linear finite element models compared well with the test results. A sensitivity analysis on the effect of varying three design variables, namely the concrete strength, the level of prestress force and the slab cross-sectional area was carried out using calibrated FEA models. This sensitivity analysis found that the tensile strength of concrete was the most significant factor of the three in influencing the determination of the shear capacity of the slab.
It was concluded that the data analysed in this study were more consistent with shear capacity determination methods presented by research and guidance publications than by the guidance given in EC2. The study also showed that FEA is suitable for non-linear prestressed concrete modelling and analysis.

1 INTRODUCTION

The aim of this research was to examine the structural behaviour of precast prestressed hollowcore slabs subject to shear actions. The primary objectives of the study were to:

- Carry out a review of the published research literature and codes of practice on shear behaviour of hollowcore slabs.
- Carry out laboratory tests on the shear behaviour of hollowcore slabs.
- Generate and calibrate finite element analysis (FEA) models to study shear behaviour of hollowcore slabs.
- Compare full scale laboratory tests with the FEA models.
- Establish the suitability or otherwise of finite element analysis as an analysis tool for shear behaviour of hollowcore slabs in the general case.
- Examine the validity of published design guidance formulae for shear behaviour of hollowcore slabs in the general case.

2 CODES & LITERATURE REVIEW

In total two design codes IS EN 1992-1-1:2005 (EC2) and IS EN 1168:2005 [2] and 17 research papers were reviewed.

2.1 Guidance Codes & Documents

2.1.1 EC2

According to EC2, there are two scenarios under which a member must provide shear resistance. When the section is cracked, possibly due to the effects of flexure, and when a section is un-cracked, as a result of low flexural stresses, or applied prestress preventing the formation of cracks. For sections considered to be cracked in flexure, Expression 6.2(a) as shown in Equation 1 applies:

$$V_{Rd,c} = [C_{Rd,c}k(100\,\rho_l f_{ck})^{1/3} + k_1\,\sigma_{cp}]\,b_w d \quad (1)$$

The parameters for the equations can be found after section 7 of the paper. Where the flexural tensile stress in the section is less than $f_{ctk,0,05}/\gamma_c$ (where $f_{ctk,0,05}$ is the lowest five percentile characteristic axial tensile strength of concrete, as specified in Table 3.1of EC2 and γ_c is the partial factor for concrete as a material, the value for which comes from Table 2.1N of EC2), Expression 6.4 as shown in Equation 2 must be used:

$$V_{Rd,c} = \frac{I \cdot b_w}{S} \sqrt{(f_{ctd})^2 + \alpha_l \sigma_{cp} f_{ctd}} \quad (2)$$

The section is considered to be un-cracked based on the low tensile stresses due to the applied prestress.

2.1.2 IS EN 1168

Specific guidance and the requirements for the testing of precast hollowcore members, for the verification of shear capacity, are given in Annex J of IS EN 1168 [2]. An amended version of IS EN 1168:2005, I.S. EN 1168:2005 + A3:2011 (IS EN 1168) [3], containing suggested refinements is subject to commentary, prior to publishing, at the time of writing. The more recent revision includes a number of changes. The changes applicable to this study are the inclusion of a shear resistance formula, shown by Equation 3 and a revised physical testing methodology. This is discussed further in Section 3: Laboratory Testing & Results.

$$V_{Rdc} = \frac{I b_w(y)}{S_c(y)}\left(\sqrt{(f_{ctd})^2 + \sigma_{cp}(y) f_{ctd}} - \tau_{cp}(y)\right)$$

where

(3)

$$\sigma_{cp}(y) = \sum_{t=1}^{n}\left\{\left[\frac{1}{A} + \frac{(Y_c - y)(Y_c - Yp_t)}{I}\right] \times P_t(l_x)\right\} - \frac{M_{Ed}}{I} \times (Y_c - y)$$

$$\tau_{cp}(y) = \frac{1}{b_w(y)} \times \sum_{t=1}^{n}\left\{\left[\frac{A_c(y)}{A} - \frac{S_c(y) \times (Y_c - Yp_t)}{I} + Cp_t(y)\right] \times \frac{dP_t(l_x)}{dx}\right\}$$

The equation is discussed further in Section 2.2: Research Papers.

2.2 Research Papers

Yang [4] published a paper in 1994 containing "Equation 10" for the calculation of the shear resistance of precast prestressed hollowcore slabs. It is presented in Equation 4.

$$V_t = V_{z,max} = \frac{bI_y}{S_{cp}}\left\{\frac{b}{2S_{cp}} f_{ct} x_{cp} z_{cp} + \frac{S_{cp}}{b}\left(\frac{e}{I_y} - \frac{A_{cp}}{AS_{cp}}\right)\frac{dN_p}{dx} + \left[\left(\frac{b}{2S_{cp}} f_{ct} x_{cp} z_{cp}\right)^2 + \left(\frac{e}{I_y} - \frac{A_{cp}}{AS_{cp}}\right) f_{ct} x_{cp} z_{cp} + \left(\frac{1}{A} - \frac{z_{cp} e}{I_y}\right) N_p f_{ct} + f_{ct}^2\right]^{1/2}\right\} \quad (4)$$

Equation 4 used a theory of a critical point in a section. This is important to note as the most recent draft of the quality control standard, I.S. EN 1168:2005 + A3:2011 (IS EN 1168), suggests the implementation of a shear resistance formula different to that of EN 1992-1-1 (EC 2), based on the concept of a critical point.

In 2000, Pajari [5] published a study, which compared the results of previously carried out tests with theoretical data generated by Eurocode 2 and Yang.

It can be seen in Figure 1 that while the data generated by Yang's Equation 10 show closer correlation between calculated and observed resistance than that generated by EC2, neither dataset could be considered as accurate.

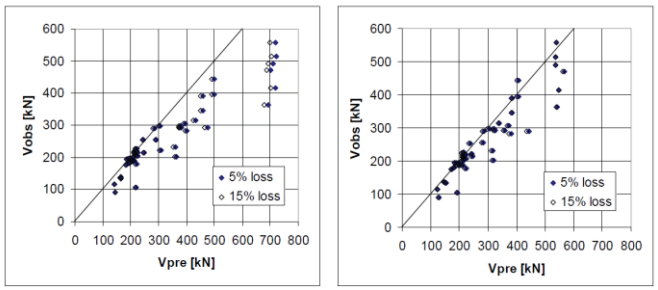


Figure 1 – Predicted vs Observed Failure Loads [5]

From the works of Pajari and Yang, amongst others, there was an apparent lack of consensus regarding to the appropriateness of design formulae for shear resistance. It has been shown that FEA can be applied to correctly model shear behaviour of slabs. Numerous studies have documented and discussed various laboratory tests and their respective approaches and observations. These were taken into consideration to inform a methodology for this study.

3 LABORATORY TESTING & RESULTS

Three tests were carried out on hollowcore slabs provided by Ducon Concrete Ltd. of Kanturk, County Cork. Slabs of depth 150mm, 200mm and 250mm were tested.

A cross-section of a 150mm depth slab is shown in Figure 2. The testing was carried out in the Heavy Structures Laboratory in Cork Institute of Technology.

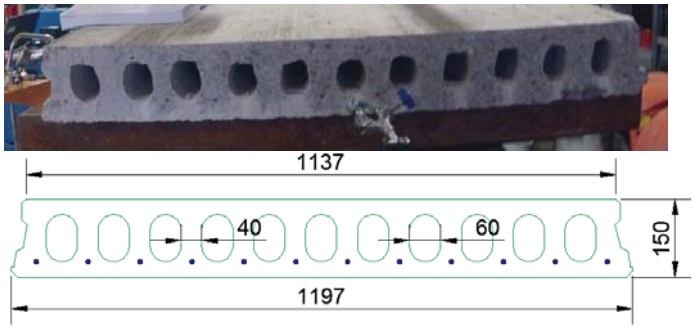


Figure 2 – 150mm Deep Slab Cross-Section

A roller and a pinned bearing were set-up as supports for the shear test. The slab supports were supported on two load-cells at each end of the slab. A spreader beam for the load application was placed at 2.5*h* from the edge of the top plate of the support. The shear test setup is shown in Figure 3. The arrangement was as specified in IS EN 1168.

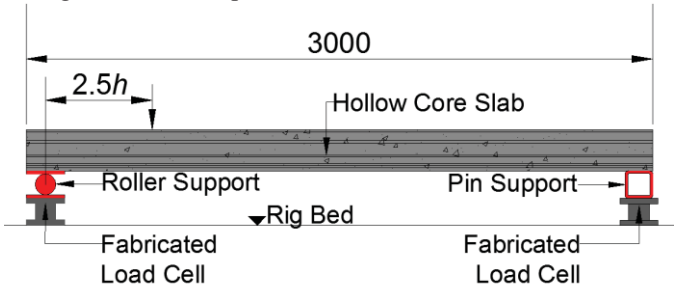


Figure 3 – Shear Test Set-up as per IS EN 1168

Strain gauges were attached at number of specific locations on each slab to measure and record the strain experienced throughout the course of the test. The strain at each location would later be compared to the strain at the corresponding locations in the finite element model.

The failure modes of the three slab depths are shown in Figure 4. Shear failure was not achieved for the 150mm slab as flexure was critical, but shear failure was achieved for the 200mm and 250mm deep sections.

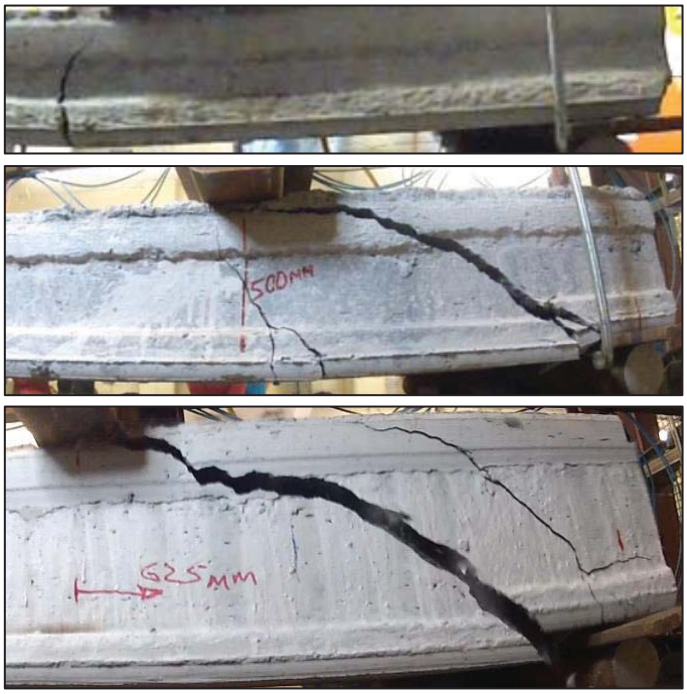


Figure 4 –Failure of 150mm, 200mm, 250mm slabs

It can be seen in Figure 5 that EC2 under-estimated the shear resistance of the two slabs where a shear failure was achieved.

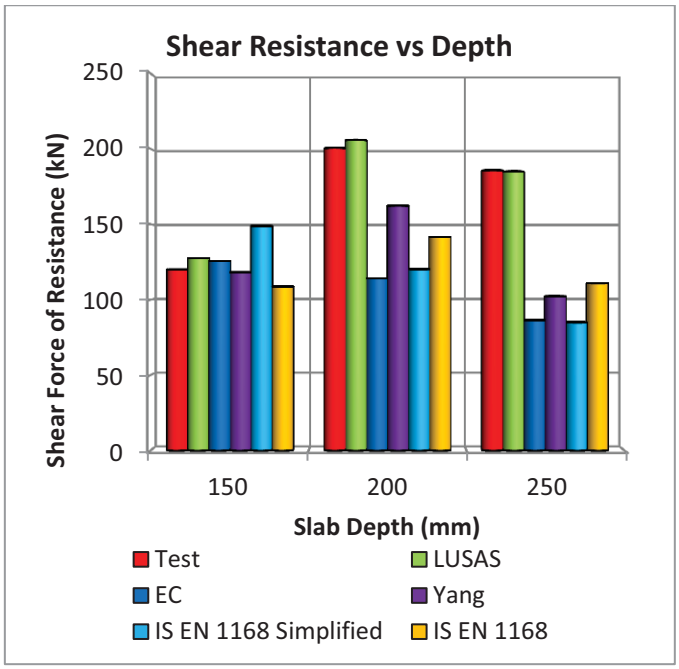


Figure 5 – Failure Loads, Observed vs Calculated

In Figure 5, "Test" refers to the laboratory tests, "LUSAS" refers to the results of the FEA model to be discussed in the next section, "EC" is generated using EC2 expressions as appropriate, "Yang" is produced using Yang's Equation 10 and IS EN 1168 provides its two formulae, simplified and otherwise.

Nearly all of the formulae under-estimated the shear capacity across the range of slabs tested, which is desirable. What the graph suggests is that Yang's Equation 10 and IS EN 1168 are more representative of the real shear behaviour.

4 FINITE ELEMENT MODELLING

Following the laboratory testing, a finite element analysis was undertaken. Following the initial running of the various LUSAS models, a number of refinements were carried out and models were re-run.

4.1 Finite Element Modelling

Three dimensional solid volume models were generated to simulate the shear tests carried out on the various slabs. Models were generated using elastic material properties and linear solvers. This allowed for quick solving times with a view to model refinement. Models were later run with non-linear concrete cracking properties as provided by Concrete Model 94 within LUSAS.

The accuracy of each model can be examined by comparing the shear failure load of the physical test with that of each finite element model. These are shown in Table 1 which shows close agreement between physical test data and FEA data. The table presented suggests that the finite element models trend towards a closer solution with increased depth.

Table 1 – Failure Loads (kN), Physical Test vs FEA Test

Slab Depths	150mm	200mm	250mm
Physical Test	120	200.48	185.72
LUSAS	127.6	205.77	184.98
% Difference	6.33%	2.64%	0.40%

The failure patterns observed from the LUSAS models are shown in Figure 6. They are similar to the failures of the tests carried out in the laboratory. The FEA failures do not show the same extent of failure as the physical model as once significant openings are generated, the FEA model ceases to iterate any further as the member is deemed to have failed.

Cracking can be observed by the red lines in Figure 6. Some limited cracking can be seen at each support. As the shear failures shown in Figure 4 showed cracking originating at the supports. A more refined mesh at the support locations would have shown this more clearly and provided insight as to the extent of cracking at the support immediately prior to failure.

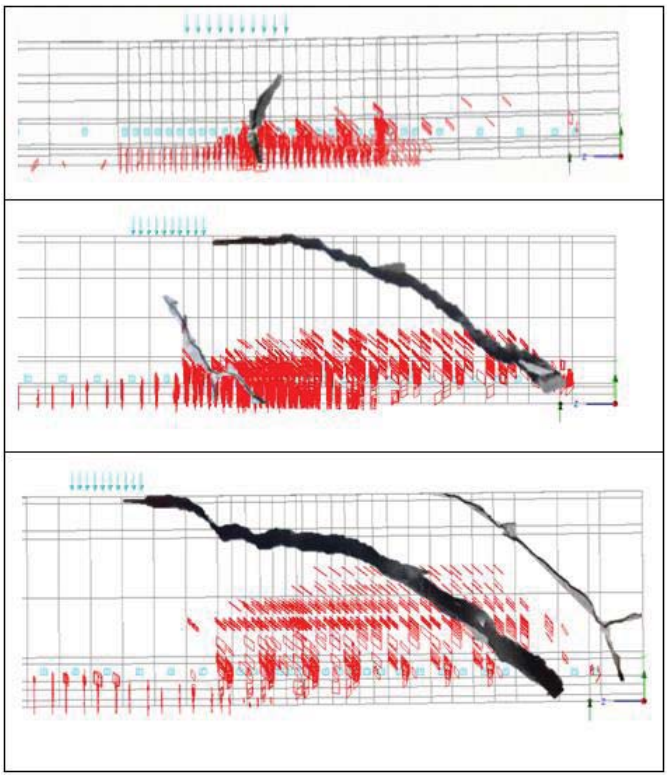


Figure 6 – Tension Cracks in Non-Linear Model with Physical Test Cracks Overlaid

To confirm the calibration of the shear models, strain comparisons were carried out. The strains recorded in the physical tests were consistent with the strains measured in the finite element models as shown in Figure 7, which presents the results from the 150mm, 200mm and 250mm deep slab as examples.

For a selection of corresponding points, the solid lines represent various strains measured and recorded in the laboratory, while the dashed lines represent strain outputs from LUSAS.

The similarities between the solid and dashed lines of corresponding colours can be seen to follow the same trend and, hence, the finite element models were deemed to be adequately calibrated. The slight variations shown were dismissed as a combination of insufficient mesh refinement in the FEA strain gauge locations and local anomalies in the physical test.

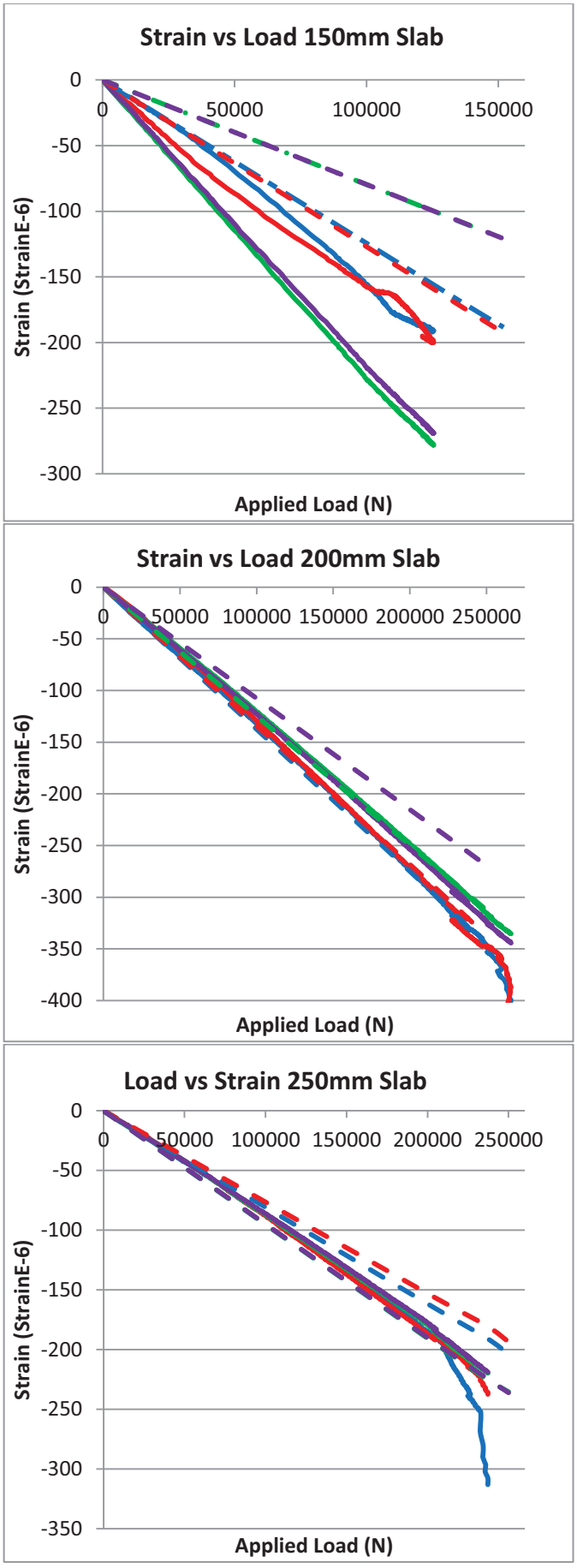


Figure 7 – Strain Measured, Laboratory Tests vs LUSAS FEA

5 SENSITIVITY ANALYSIS

Three sensitivity analyses were carried out using the non-linear shear models, which were deemed to be calibrated satisfactorily based on the data presented in Section 4.1. In order to maintain the calibration, only one aspect of each model was varied at any one time.

Three variables were examined:

- Concrete of reduced tensile strength was applied; $f_{ctk0.05}$ = 1.5MPa vs 2.5MPa,
- The level of prestress force in the section,
- The cross-sectional area of the slab.

Each model was run and the failure load increment noted for each. The failure load was then compared to various calculated resistances using the corresponding altered section and material properties as appropriate. The trends noted throughout the sensitivity analysis can be clearly seen and compared in Figure 8.

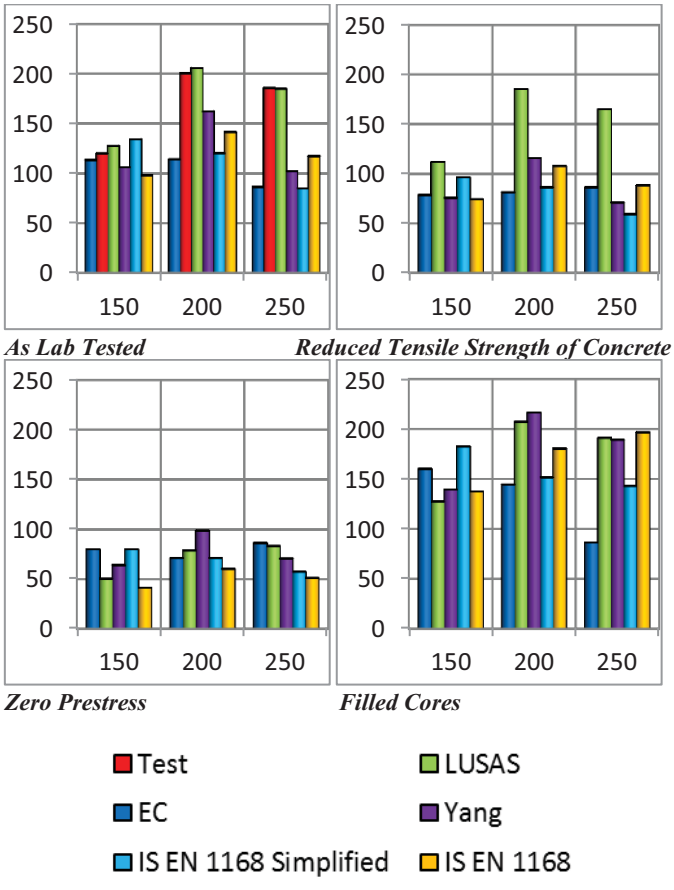


Figure 8 – Sensitivity Analysis

The sensitivity analyses suggest that tensile strength of the concrete is a significant factor that influences the shear resistance of the slabs. In seeking a more accurate solution, the tensile strength of concrete within the various formulae should be considered as a good point of focus.

6 DISCUSSION

It is clear that EC2 under-estimates the shear capacity for deeper sections. Two shear formulae are presented in IS EN 1168:2005 + A3:2011. It can be deduced from this study that the more intricate of the two formulae gives a better estimate of shear capacity.

The EC2 design formulae for members subject to shear forces were found to be safe, and in fact, could be considered as over-conservative for deeper members.

7 CONCLUSIONS

For the shear testing carried out, a good correlation between physical laboratory testing and the FEA study was achieved.

The study revealed that the design formulae given in EC2 are valid, but may be considered as conservative.

The sensitivity analysis carried out on the shear models suggests that the tensile strength of concrete is the main influence on shear resistance.

For the design of precast prestressed hollowcore slabs subject to shear, it is recommended that IS EN 1168:2005+A3:2011 be employed as an industry standard.

The study has shown that FEA is suitable for non-linear prestressed concrete modelling and analysis.

EQUATION PARAMETERS

Equation 1

$V_{Rd,c}$ in Newtons
f_{ck} in MPa
k $(1+(200/d)^{0.5}) \leq 2.0$
ρ_1 $(A_{sl}/b_w d) \leq 0.02$
A_{sl} area tensile reinforcement that extends $\geq (l_{bd}+d)$ beyond the section considered
b_w smallest width of cross-section in the tensile area [mm]
σ_{cp} $N_{Ed}/A_c < 0.2 f_{cd}$ [MPa]
N_{Ed} axial force in the cross-section due to prestressing,
A_c area of concrete cross-section [mm^2]
($C_{Rd,c}$, v_{min} and k_1 can be found in the National Annex)

Equation 2

I second moment of area
b_w width of cross-section at the centroidal axis allowing for ducts
S first moment of area above and about the centroidal axis
α_1 $l_x/l_{pt2} \leq 1.0$
l_x distance of section considered from the starting point of the transmission length
l_{pt2} upper bound value of the transmission length
σ_{cp} concrete compressive stress at the centroidal axis due to prestressing = N_{Ed}/A_c.

Equation 3

I second moment of area of the cross section
$b_w(y)$ web width at the height y
Y_c height of the centroidal axis
$S_c(y)$ first moment of the area above height y and about the centroidal axis
y height of the critical point on the line of failure
l_x distance of the considered point on the line of failure from the starting point of the transmission length (x)
$\sigma_{cp}(y)$ concrete compressive stress at the height y and distance l_x
n number of tendon layers
A effective cross section surface
$P_t(l_x)$ prestressing force in the considered tendon layer at distance l_x. The transfer of prestress shall be taken into account according to EN 1992-1-1:2004, 8.10.2.2
M_{Ed} bending moment due to the vertical load
$\tau_{cp}(y)$ concrete shear stress due to transmission of prestress at height y and distance l_x
$A_c(y)$ the area above height y
$C_{Pt}(y)$ factor taking into account the position of the considered tendon layer
C_{Pt} = -1 when $y \leq Y_{Pt}$
C_{Pt} = 0 when $y > Y_{Pt}$
Y_{Pt} height of the position of considered tendon layer

Equation 4

x_{cp} horizontal distance between the critical point and the centre of support
N_p effective prestress in strands at the critical point
e vertical distance between the centroid of pretensioned strands and the centroid of the whole cross-section
$M_y(x_{cp})$ bending moment at the critical point
$V_z(x_{cp})$ shear force at the critical point
A area of whole cross-section
$b(z_{cp})$ total web width of slab at the critical point
$S_y(z_{cp})$ first moment of area of cross section
I_y moment of inertia
dN_p/dx gradient of the effective prestress force at support
A_{cp} area above the critical point
S_{cp} first moment of area above the critical point
f_{ct} tensile strength of concrete

REFERENCES

[1] NSAI, "Eurocode 2: Design of concrete structures - Part 1-1:General Rules and rules for buildings (Including Irish National Annex)," NSAI, Dublin, 2004.

[2] B.S.I., "BS EN 1168:2005 Precast concrete products - Hollow core slabs," B.S.I., Brussels, 2005.

[3] B.S.I., "I.S. EN 1168:2005+A3:2011 Precast concrete products - Hollow core," B.S.I., Dublin, 2011.

[4] L. Yang, "Design of Prestressed Hollow Core Slabs with Reference to Web Shear Failure," vol. 120, no. 9, 1994.

[5] M. Pajari, "Resistance of Prestressed Hollow Core Slabs Against Web Shear Failure," VTT Technical Research Centre of Finland,, Espoo, 2005.

The Behaviour of Connections in Segmental Precast Concrete Pile Systems

Evan Causer[1,2], Kieran Ruane[1,2]
[1]Department of Civil, Structural & Enviromental Engineering, Cork Institute of Technology, Bishopstown, Cork, Ireland
[2]RPS Consulting Engineers Ltd, Innishmore, Ballincollig, Cork Ireland
email: evan.causer@rpsgroup.com, kieran.ruane@rpsgroup.com.

ABSTRACT: Segmental driven precast concrete piles are a popular form of piled foundation. This is due to time and cost savings that can achieved over traditional forms of replacement piles because of efficient use of material, economies of scale and speed of installation. A number of problems can arise with the driving of piles that may result in an unforeseen moment being induced in the pile. Segmental pile systems incorporate connections in the pile and it is important that the strength of the connection be comparable to that of the pile cross-section. The design of segmental precast concrete pile systems is presented in a number of guidance documents. When these documents were examined it was found that the design of connections for combined axial and bending forces was not covered in detail. A program of laboratory testing and a nonlinear finite element analysis were undertaken to establish the competence of connections under the combined actions. A series of destructive tests was carried out on a pile incorporating a commonly available pile connection. The laboratory testing involved the application of a constant axial load across the connection and a uniform bending moment that was increased until failure. Failure loads and failure modes determined from the laboratory testing were compared to the results obtained from the finite element analysis. The results from the laboratory testing and the finite element analysis indicate that the failure mode of the pile segment was attributed to the concrete cross-section. The laboratory testing also indicated that exposure of the reinforcement at the connection as the bending moment approached the ultimate limit state, may be cause for concern with regard to durability.

KEY WORDS: Segmental driven piles, precast concrete, connections, 3D nonlinear finite element analysis, laterally loaded pile.

1 INTRODUCTION

Designers and contractors are continually aiming to reduce costs and increase the speed of installation across all areas of a project. One of the areas that this can be achieved is in the substructure. In cases where a deep foundation is required, segmental driven piles are often the favoured solution. These piles comprise a number of precast concrete segments that are joined together mechanically to achieve the required depth of foundation (see Figure 1).

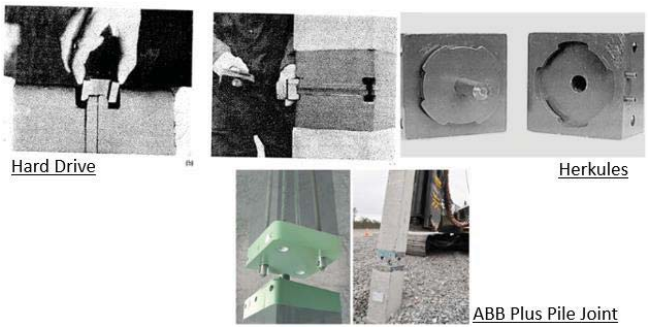


Figure 1. Proprietary pile joints [1]

There are a number of benefits to segmental piles:

- Speed of installation;
- No open excavation;
- Ease of handling;
- Good quality control over concrete and efficient use of material due to factory production.

A segmental precast concrete piling solution recently developed by a leading UK contractor can achieve the installation of a multi-segment 20m pile in just 20 minutes [2] (see Figure 2).



Figure 2. Installation of segmental precast concrete pile [2]

However, as with all piled foundations, it is difficult to examine the integrity of the pile once it is in place. In addition, financial constraints often limit the scope of pile testing to the minimum requirements specified in design standards. Consequently, while the requirements of the design standards may be satisfied, it is difficult to be assured of the integrity of every pile installed due to the variations of geotechnical conditions across a site.

Problems can arise with the driving of piles under certain conditions:

- Rock head is at a significant slope (Figure 3);

- Underlying strata are transitioning rapidly from weak to strong strata;
- There are obstacles present in the ground e.g. boulder clays.

In these situations the pile may deviate from the prescribed driving alignment and a moment can be generated in the pile resulting in failure of the pile. As segmental piles incorporate connections into the pile it is important that the strength of the connection be comparable to the pile cross-section.

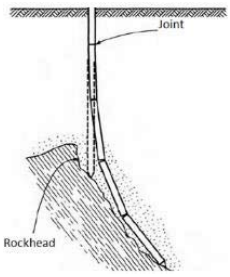


Figure 3. Pile failure [1]

Failure of the pile segment cross section due to combined axial load and moment is unlikely under normal loading conditions as design of combined effects is well documented. However, as the pile is made up of a number of segments it is possible that the joint may fail due to the combined effects. *Tomlinson et al* [1] and *Fleming et al* [3] both note that failure of the joint is a significant cause for concern. Consequently, it can be seen that verification of the robustness and rigidity of the pile joint to provide full transfer of moments and forces between segments is important.

2 DESIGN GUIDANCE

There are a number of design codes that give guidance on the design of segmental precast concrete pile systems for structural and geotechnical actions:

- IS EN 12794: 2005 + A1: 2007 – Precast concrete products – Foundation Piles [4];
- IS EN 1992-1: 2005 - Design of concrete structures: General rules for buildings [5];
- IS EN 1997-1: 2005 Geotechnical design: General rules [6];
- CIRIA 103 - Design of laterally loaded piles [7].

The design of joints in segmental pile systems is governed by IS EN 12794. It outlines the definition of a pile joint: '*Pile joints shall locate and maintain a coaxial connection between pile segments'* [4]. It also provides design guidance by means of a physical test, to verify the robustness and rigidity of the pile joint. The test procedure requires a separate axial and lateral load test on the pile joint. The axial test involves the driving of a section of pile incorporating a joint in an area where geotechnical parameters are well understood. The lateral test involves applying a uniform bending moment across the pile joint in the form of a two point bending test. There are four different classes of pile joints based on their performance under the test regime (see Table 1).

Table 1. Pile Joint Classification [4]

Class [2]	Capacity	Performance	Verification	Methods Impact load test
A	Compression/tension and bending	Robustness and rigidity	Static calculations to be verified by impact testing and subsequent bending test.	Impact load test with 1 000 impact blows having stress level 28 N/mm^2. [1]
B	Compression/tension and bending	Robustness and rigidity	Static calculations to be verified by impact testing and subsequent bending test.	Impact load test with 1 000 impact blows having stress level 22 N/mm^2. [1]
C	Compression/tension and bending	Robustness and rigidity	Static calculations to be verified by impact testing and subsequent bending test.	Impact load test with 1 000 impact blows having stress level 17 N/mm^2. [1]
D	Compression	Robustness and rigidity	Static calculations to be verified by impact testing.	Impact load test with 500 impact blows having stress level 17 N/mm^2. [1]

[5] *deleted text* [6]

[1] Stress level means: compressive stresses around the pile joint caused by impact blows.

[2] Pile joint class (i.e. the dynamic stress level during Impact load test) is chosen according to national provisions to correspond the target geotechnical capacity of the segmental pile.

3 LABORATORY TESTING

Given that that IS EN 12794 does not make allowance for the testing of joints under combined actions it was decided to develop a test programme for a common type of joint subjected to combined actions. The testing involved subjecting two pile segments jointed together using a *Hard Drive* pile joint to a constant axial load and applying a lateral load that provided a uniform bending moment across the pile joint that was increased until failure. The *Hard Drive* joint comprises two square steel end plates that are connected together with four I shaped locking pegs located in the corners of the plates (see Fig 1). The testing was conducted in the Heavy Structures Laboratory (HSL) at Cork Institute of Technology (CIT).

3.1 Test specimen

Four sets of test specimens were fabricated. The first was used as a trial to work out any fabrication issues and assess the performance of the test setup. The remaining three were used to undertake a robust test regime and form a body of test data. In order to ensure that scaling issues would not be an issue a one to one scale representation of the smallest commercially available joint was fabricated - a 200mm x 200mm square joint.

Fabrication drawings were unavailable for a 200mm joint and the only available drawings were for a 270mm joint. These drawings were used as the basis for the design of the test segment and the dimensions modified to result in a 200mm square joint. The overall length of the test specimen was limited by the maximum working length available within the lateral test rig, approximately 1600mm. It was decided that the overall length of the specimen should be no more that 1500mm, resulting in two pile segments with length 750mm each. This also allowed for a single pile segment to be cast from one concrete mixer with eight standard 100mm x 100mm x 100mm concrete cubes (see Table 2). Each half of a test specimen comprised an endplate with 4 No. H12 reinforcing bars welded to it. Shear links were also provided at 75mm c/c. After the first test, the welds were visually inspected, no signs of plastic deformation or yielding were observed (see Figure 4).

Table 2. Concrete strength of test specimens

Test No.	Segment on LHS of Test Rig	Concrete Strength (N/mm^2)	Segment on RHS of Test Rig	Concrete Strength (N/mm^2)
1	A	32.43	B	34.97
2	A1	37.48	A2	31.06
3	B1	31.18	B2	36.92
4	X1	45.75	X2	42.29

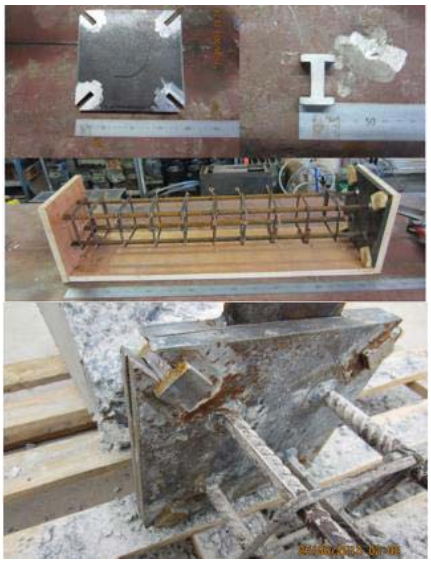


Figure 4. Test specimen

3.2 Test setup

In order to undertake the laboratory testing an apparatus capable of providing a reaction in two directions was required. This was achieved using a combination of the large test rig and the lateral test rig. The initial test set up comprised a pair of pile segments enclosed in the lateral test rig and simply supported with the pile joint located at midspan. The axial load was generated using 1 no. 55 tonne hydraulic jack and the reaction provided by the lateral test rig. In order to develop a uniform bending moment 2 no. 25 tonne hydraulic jacks were located either side of the joint along the centreline of the pile segment with the large test rig providing the reaction. After the initial test a number of faults were identified, that required the test setup to be modified (see Figure 5).

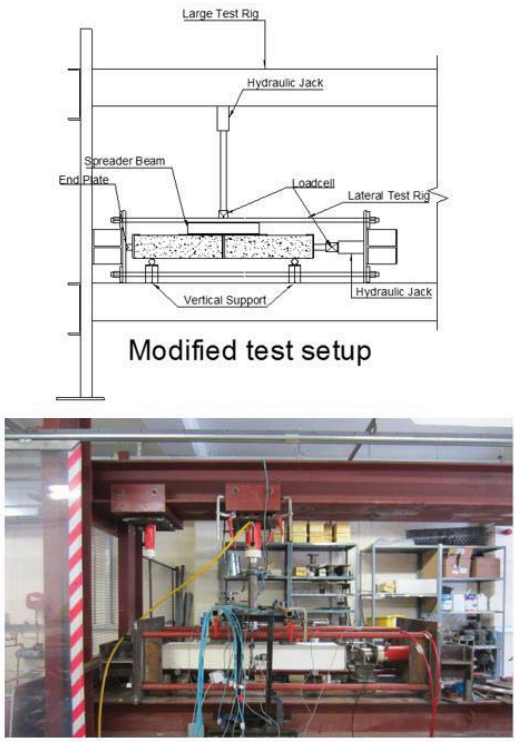


Figure 5. Modified test setup

After the first test it was found that the one of the load cells was incorrectly calibrated, as a result the first set of test results were disregarded. This resulted in the 2 no. 25 tonne hydraulic jacks providing the bending moment being replaced by 1 no. 55 tonne hydraulic jack and a spreader beam.

The pile segment butted against the left hand side of the test rig provided a support that was neither pinned nor fixed but somewhere in between. The stiffness of the support would be difficult to quantify for the finite element analysis. Consequently, a removable end plate that could act as a roller was fabricated (see Figure 6).



Figure 6. Removable end plate

3.3 Test data

A system 7000 data logger was used to record all the key data during the testing. This apparatus can record 10 readings per second from multiple measuring devices. The main results that were recorded during the testing were displacements at various locations, strains on the locking peg and on the reinforcement. The displacement gauges were primarily used to ensure that the test specimen was deflecting as expected and to ensure that no out of plane movement was occurring. The use of strain gauges on the web of the locking pegs was a limited success. This was due to a number of them being damaged as the locking pegs were being hammered into place.

3.4 Test results

The prescribed axial loads of 150kN, 300kN and 425kN were chosen based on the capacity of the available hydraulic jack and the desire to achieve axial loads that would result in an under reinforced failure, over-reinforced failure and balanced failure of the cross-section. Once the specimens were bedded and it was verified that all data recording instruments were working correctly the prescribed axial load was applied. The bending moment was then applied in increments until failure of the specimen occurred (see Table 3).

Table 3. Failure loads

Test No.	Prescribed axial load (kN)	Axial load at failure (kN)	Bending moment at failure (kNm)	Segment Failure
1	---	---	---	B(RHS)
2	150	191	11.8	A2(RHS)
3	300	307	27.5	B1(LHS)
4	425	424	26.5	X2(RHS)

4 FINITE ELEMENT ANALYSIS

A 3D non-linear Finite Element Analysis (FEA) was undertaken using the software LUSAS (Version 14.7-10). The procedure for FEA undertaken was similar to that used in the laboratory testing where the prescribed axial load was applied and the bending moment applied incrementally until failure of the model. The analysis utilised plastic material properties for both the steel and concrete. Slidelines were also utilised to model the contact surfaces in the analysis. A number of methods were used to reduce the time taken to solve the model:

- A plane of symmetry was used to half the model in the vertical plane;
- Elastic material properties were retained in parts of the model away from areas of interest;
- It was assumed that the welds were of uniform cross-section and had similar material properties to the bar (see Figure 7).

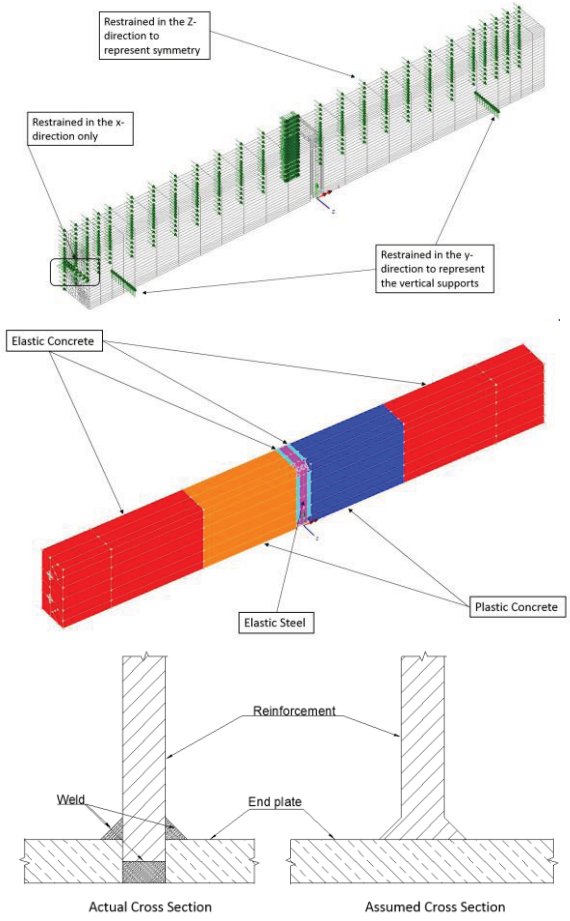


Figure 7. Boundary conditions for FEA

The model was meshed using an 8-node 3D solid continuum element using linear interpolation. This element was selected as it allowed for the use of both plastic material models and slidelines. Failure of the analysis was governed by the plastic material properties. The *Multi-Crack Concrete Model* [8] was used to model failure of the concrete while a *Von Mises* model was used to set the yield criterion for the steel (see Figure 8).

Material properties used in the analysis were based on the results of material sampling from the laboratory testing.

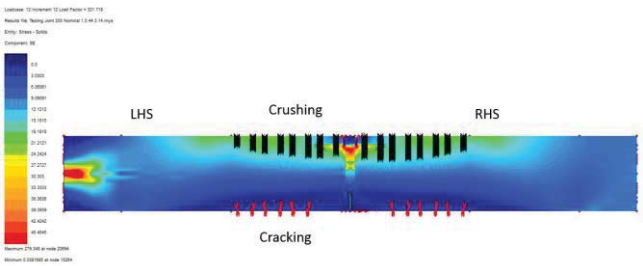


Figure 8. Contour plot of Von Mises stress and crack crush pattern at failure of Test 4

The results of the FEA indicated that failure of the concrete cross section was the main factor that governed failure of the model. The FEA indicated that as the axial load was increased the stress developed in the locking peg due to the application of the bending moment reduced (see Figure 9). The FEA also demonstrated that the locking peg did not yield plastically in any of the analysis and the maximum stress developed occurred in test 2 and was less than 20% of the yield stress.

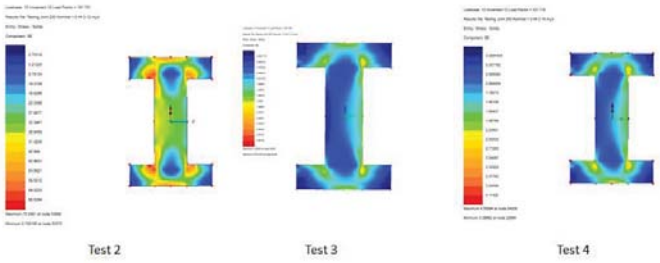


Figure 9. Stress contours in lower locking peg at failure

5 RESULTS

The results of the laboratory testing and the FEA indicated that the configuration of the pile joint tested was structurally sound and it did not deform plastically. Failure of the concrete cross section was the primary mode of failure (see Figure 10).



Figure 10. Failure of pile cross section for Test 4

The results of both the FEA and the laboratory tests display similar trends however the magnitude of the failure load varied significantly. Hand calculations based on moment axial force interaction theory for reinforced concrete indicate that the results from the laboratory tests and the FEA are following a similar trend (see Figure 11. Note: Test 4 was omitted for clarity as the concrete strength was significantly stronger than that of the other tests). It can be seen that the LUSAS models failed at lower loads than both the laboratory test and the hand calculations.

The failure mode in the laboratory testing was failure of the concrete cross section by means of concrete cracking and corresponding yielding of reinforcing steel. The results of the LUSAS model indicated a similar mode of failure, however there was not the same level of yielding of the reinforcing steel as in the laboratory testing. The concrete cracking in the LUSAS model was causing the analysis to terminate before complete yielding of the reinforcement.

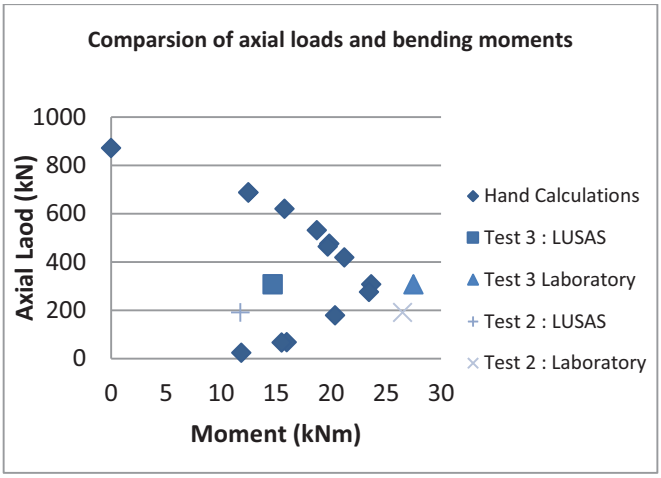


Figure 11. Comparison of test results

It was observed during the laboratory testing that the effects of the bending moment on the connection caused exposure of the reinforcing steel at the connection (see Figure 10).

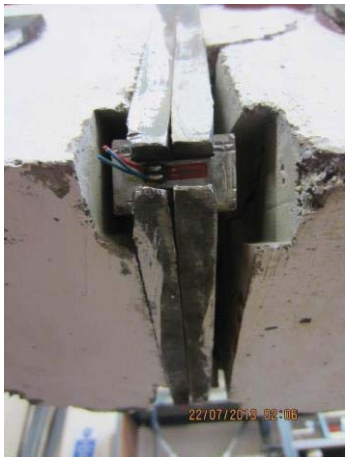


Figure 12. Exposure of the joint due to bending moment

6 CONCLUSIONS

Based on the literature review undertaken it was found that the structural competency of the connections in segmental piles is a cause for concern. The literature review established that limited scientific data is available. The results of the laboratory testing indicate that the configuration of the pile joint that was tested is structurally sound and the failure of the concrete cross section was the primary mode of failure. Neither the end plate nor the locking peg in the joint configuration that was tested exhibited any sign of yielding or plastic deformation. The FEA and hand calculations support the results of the laboratory testing. However, it was observed in the laboratory testing that the effects of the bending moment on the connection and the resulting deflections caused exposure of the reinforcing steel at the connection as the magnitude of the bending moment approached the ultimate limit state. This may be a cause for concern for the long term durability of the connection. Further research would be required for confidence in the joint in all configurations.

ACKNOWLEDGEMENTS

The authors would like to thank Mr Jim Morgan and Mr Liam Jones for their assistance with the laboratory testing.

The research reported in this paper was conducted as part of the taught MEng (Structural Engineering) programme at Cork Institute of Technology.

REFERENCES

[1] Tomlinson M, Woodward J. Pile Design and Construction Practice. Fifth Edition. Taylor& Francis Group, United Kingdom, 2008.
[2] Hayward D. Economy Down Under. New Civil Engineer, Volume 47, pages 16- 17, November 2012.
[3] Flemming K, Weltman A, Randolph M, Elson K. Piling Engineering Third Edition. Taylor& Francis Group, United Kingdom, 2009
[4] British Standards Institution, BS EN 12794:2005 including amendment A1:2007, Precast Concrete Products – Foundation Piles. BSI , London, July, 2007
[5] National Standards Authority of Ireland, IS EN 1992-1-1:2005, Eurocode 2: Design of concrete structures - Part 1-1: General rules and rules for buildings (Including Irish National Annex), NSAI, Dublin, April, 2005
[6] National Standards Authority of Ireland, IS EN 1997-1:2005, Eurocode 7: Geotechnical design - Part 1: General rules (Including Irish National Annex 2007), NSAI, Dublin, April, 2007.
[7] Construction Industry Research and Information Association, CIRIA 103, Design of laterally loaded piles. CIRIA, London, 1984.
[8] London University Stress Analysis System, Theory Manual Volume 1. Version 14.7-10, pages 208-222, LUSAS, United Kingdom, 2008.

Shear Capacity of Insulated Precast Concrete Façade Panels

Kinnane, O., West, R., Grimes, M., Grimes, J.
Department of Civil, Structural and Environmental Engineering, Trinity College Dublin, Ireland
email: oliver.kinnane@tcd.ie, rwest@tcd.ie, mgrimes@tcd.ie, jogrimes@tcd.ie

ABSTRACT: Pre-cast concrete external cladding panels have in the past had difficulty in avoiding thermal bridging and one way of preventing this is to embed the insulation in a sandwich between the load-bearing internal panel and the external leaf at the precast factory. However, steel plated shear connectors, for example, are still required to support the outer leaf vertically and the optimum design of these must allow for both thermal and strength capacity constraints. The ends of these plates, which are embedded in the wall panels, are anchored by small diameter longitudinal rebar. In this paper the shear testing of 24 full scale concrete panels will be described, where the coupling plate parameters included their depth, thickness and length by virtue of the insulated cavity width. Different load capacities, stiffnesses and failure modes were observed leading to a better understanding of structural behaviour, where in some cases several phases of non-linear response with different degrees of ductility are observed before the ultimate load is experienced. In particular, the dominant failure types appear to be either compressive or shear buckling, or plate slip arising from concrete spalling and local distortion of the embedded longitudinal rebar. The causality of failure mode with geometry is examined.

KEY WORDS: Precast Concrete Cladding; Sandwich Panels; Shear Connectors.

1 INTRODUCTION

Precast concrete became a popular cladding material in the 1950s and 1960s, with the increase in medium to high-rise building for residential and office use. Nowadays, in the age of building energy efficiency, precast concrete remains a highly desirable solution for building cladding and recladding with advantages over other systems including excellent inherent thermal, acoustic and fire resistance properties. Significantly precast cladding is virtually maintenance free and can last as long as the structure to which it is attached. Panels are precast in the factory and transported to site for installation, enabling increased construction efficiencies. Traditionally precast cladding consisted of a single layer of concrete. Growing in popularity is the precast concrete sandwich panel consisting of multiple layers. This paper is concerned with the evaluation of the structural integrity of precast sandwich panels and particularly their shear capacity.

1.1 Sandwich Panels

Sandwich panels (Figure 1) are a popular facade cladding as systems contain all function layers; weather layer, thermal layer, and structural layer, in one precast panel. The sandwich panel configuration embeds high performance insulation between a structurally salient inner concrete wall layer, or wythe, and an external weather resistant thinner wythe. Panels can be configured to achieve low U-values specified by national and European building regulations, by including a large thickness of insulation between the wythes. The interior and exterior concrete layers are tied together using shear ties.

1.2 Shear Ties

Shear ties provide integrity between the interior and exterior wythes of concrete. Shear ties exist in a wide range of materials and configurations. They are produced as plates, trusses, pins, rods, and grids [1]. For composite action they act against gravity or shear displacement, by transferring the dead load due to the outer wythe of concrete onto the inner load bearing wythe. The requirement for the sandwich panel to act in composite or non-composite will generally direct the form of the tie and the material used. Stainless steel is commonly used for the highest strength tie systems. Other tie types will interact with the reinforcing bar in the concrete and tie into this mesh to enhance composite action. They are placed strategically within the sandwich panel to ensure suitable suspension of the outer leaf.

1.3 Flat Plate Ties

When designing precast sandwich panels it is important to ensure that no constraints are placed on the outer wythe of concrete. In a robust and commonly used sandwich panel configuration, a pair of separated flat plate anchors serve as load bearing and torsional anchors simultaneously. Given the pair of ties act together, lateral displacment due to eccentricity is prevented. Additonal retaining ties are positioned close to the perimeter of the sandwich panel to aid against tensile and compressive wind loads and possible damage due to demolding.

Flat plate connectors (Figure 2) have the advantage over other types of connectors that they allow the outer wythe of concrete freedom to expand and contract within its plane. Hence, they do not constrain relative movement while ensuring composite action.

This study investigates the flat plate connector through an extensive experimental program. Maximum and yield loads are documented for plates of different geometries. The mode of failure of different plate types is investigated

2 TESTING

2.1 Experimental program

Twenty four concrete sandwich panels were tested with various flat anchor plate dimensions and panel cavity widths. All of the sandwich panels tested measure 1m x 1m. Different combinations of the parameters listed in Table 1 configure the 24 panels listed in Table 2. The panels are assigned a 'test group code' to identify the matching parameters - *A,B,C,D,E,F* represent different size cavity width (w_c); *a,b* represent plate thicknesss (t); *1,2,3* represent plate depths (d) and aspect ratios are also given (w_p/d).

Table 1. Sandwich panel parameters

Parameter	No. of	Types (mm)
Plate thickness (t)	2	2 (*b*), 3 (*a*)
Plate depth (d)	3	80 (*1*), 240 (*2*), 400 (*3*)
Cavity width (w_c)	6	240 (*A*), 160(*C*), 90(*F*), 110 (*E*), 120 (*D*), 180 (*B*)
Plate width (w_p)	5	350, 260, 200, 225, 280

Table 2. Sandwich panel configurations

Test No.	Cavity Width w_c (mm)	Plate Thick-ness t (mm)	Plate Depth, d (mm)	Plate Width, w_p(mm)	Aspect Ratio (w_p/d)	Test group code
1	240	3	80	350	4.375	*Aa1*
2	240	3	80	350	4.375	*Aa1*
3	240	3	80	350	4.375	*Aa1*
4	240	3	240	350	1.46	*Aa2*
5	240	3	240	350	1.46	*Aa2*
6	240	3	240	350	1.46	*Aa2*
7	240	3	400	350	0.875	*Aa3*
8	240	3	400	350	0.875	*Aa3*
9	240	3	400	350	0.875	*Aa3*
10	160	2	80	260	3.25	*Cb1*
11	160	2	240	260	1.08	*Cb2*
12	160	2	400	260	0.65	*Cb3*
13	90	2	80	200	2.5	*Fb1*
14	90	2	240	200	0.83	*Fb2*
15	90	2	400	200	0.5	*Fb3*
16	110	2	80	225	2.82	*Eb1*
17	110	**3**	240	225	0.94	*Eb2*
18	110	2	400	225	0.56	*Eb3*
19	120	3	80	225	2.82	*Da1*
20	120	3	240	225	0.94	*Da2*
21	120	2	400	225	0.56	*Da3*
22	180	3	80	280	3.5	*Ba1*
23	180	3	240	280	1.17	*Ba2*
24	180	3	400	280	0.7	*Ba3*

2.2 Experimental setup

An experimental setup was developed to evaluate the shear response of the flat plate ties. The setup, shown in Figure 1, applies a load with a hydraulic jack, into the steel spreader beam and through the concrete of the outer wythe to the plates within. Each sandwich panel was loaded beyond its expected yield load with many of the panels being brought to overload, so as to assess the failure modes of the plates. Six Linear Differential Variable Transducers (LVDTs) are used in each test; two LVDTs monitor movement on the face, a second pair monitor horizontal movement along the side of the panel, a third pair were positioned underneath to monitor vertical displacement.



Figure 1. (left) Panel installed on rig

An example of a flat plate tie is shown in Figure 2. The rebar is threaded through the circular holes, the elongated/eliptical holes are included for the concrete to bond to the plate, as it does with the rebar.



Figure 2. Image of shear plate with threaded rebar [2]

Figure 3 shows a section, and elevation view, of a test panel, with 400mm deep plate installed. The panels contain two plates for torsional stability, and they act to minimize eccentricity during evaluation.

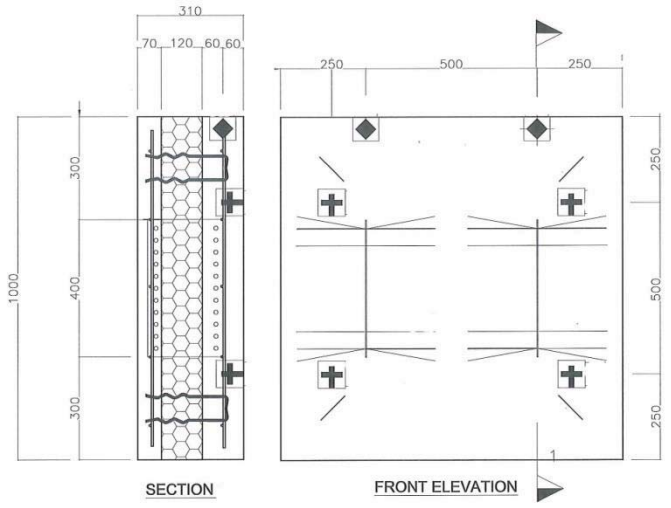


Figure 3. Sandwich panel configuration [3].

3 RESULTS

The performance of the different sandwich panel configuration with different plate dimensions are listed in Table 2.

Table 3. Sandwich panel test results

Test No.	Test code	Design load *	Approx yield load	Approx max load	Stiffness K33%	Failure mode
1	Aa1	9.6	16	26.1	12	Plate slippage
2	Aa1	9.6	14	25.6	15	Plate slippage
3	Aa1	9.6	15	25.4	11	Plate slippage
4	Aa2	62.4	90	103.7	49	Concrete face cracking
5	Aa2	62.4	85	95.0	37	Concrete face cracking
6	Aa2	62.4	80	97.5	84	Concrete face cracking
7	Aa3	159	205	209.5	57	Concrete face cracking
8	Aa3	159	162	164.3	48	Concrete face cracking
9	Aa3	159	140	144.6	100	Concrete face cracking
10	Cb1	19.8	16	30.0	34	Plate buckling
11	Cb2	72.0	98	102.2	79	Plate buckling
12	Cb3	156	170	171.6	120	Plate buckling
13	Fb1	22.2	45	80.1	3	Plate buckling
14	Fb2	118.8	145	163.2	36	Plate buckling
15	Fb3	227.4	230	241.7	110	Plate buckling
16	Eb1	14.4	35	36.8	6	Plate buckling
17	Ea2	108	205	207.4	31	Plate buckling
18	Eb3	205.8	224	229.4	11	Plate buckling
19	Da1	24.6	39	50.0	28	Plate buckling
20	Da2	102	135	144.0	110	Plate buckling
21	Db3	205.8	190	197.7	130	Plate buckling
22	Ba1	19.2	48	66.7	67	Plate slippage
23	Ba2	78.0	130	134.1	83	Concrete face cracking
24	Ba3	196.8	240	240.1	70	Concrete face cracking

*The design loads are those specified by the plate manufacturer.

3.1 Shear response of plates of different plate depth

So as to assess the effect of the plate depth parameter Tests 1-9 are the focus of this section - three sets of three panels with plate depths 80mm (Aa1), 240mm (Aa2) and 400mm (Aa3) are analysed. Cavity width, plate width and plate thickness are constant across these test groups (240mm, 350mm and 3mm respectively). However, the variance in plate depth implies aspect ratios for test groups Aa1, Aa2, Aa3, of 4.375, 1.46 and 0.875 respectively.

The average strength of the panels are 25.7kN, 98.7kN and 172.8kN for plates of depths 80mm (Aa1), 240mm (Aa2) and 400mm (Aa3). Associated deflections and stiffness values are listed in Table 4. Average deflections range from 10.3mm for the shallow 80mm deep plates to an average of 4mm and 3.5mm for the 240mm and 400mm deep plates respectively.

Figure 4 displays the shear-deformation performance of three Typical panels, with 80, 240 and 400mm plates. The panels with different plate depths display significantly different shear tie performances.

Table 4. Performance of 3mm plates of different depths (Tests 1-9). * marks those tests that were stopped before max load was reached.

	Loads (kN)		**Stiffness**			**Deflection (mm)**	
Test	**Max**	**@1mm**	**K 33%**	**K 75%**	**K max**	**@ 33% load**	**@ max load**
1	**26.1**	**11.31**	**12**	**22**	**2.3**	**0.75**	**13.1**
2	**25.6**	**15.35**	**15**	**19**	**3.7**	**0.8**	**7.6**
3	**25.4**	**9.82**	**11**	**19**	**2.3**	**0.83**	**10.8**
4	103.7	40.15	49	78	30	0.76	3.8
5	94.9	36.46	37	71	23	0.86	4.9
6	97.5	62.02	84	73	35	0.33	3.2
7	**209.5**	**54.66**	**57**	**157**	**58**	**1.17**	**4.2**
8	**164.3**	**49.07**	**48**	**123**	**55**	**1.14**	**3.6**
9	**144.6**	**77.22**	**100**	**108**	**68**	**0.47**	**2.6**

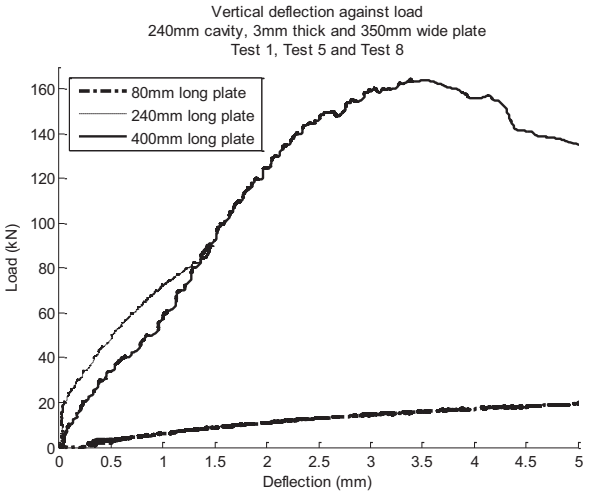


Figure 4. Shear-deformation performance of plates of different depths (Example from test group *Aa1-Aa3*).

The 80mm plates display a smooth response which might be approximated to three distinct regions of movement (i) elastic, (ii) elastic and plastic and (iii) plastic regions. The response of the three panels with 80mm plates are shown in Figure 5.

In contrast the 240mm plates display a stiffer elastic region and an acutely, almost platteauing plastic region (Figure 4).

The 400mm plates display the stiffest response to increasing load, evidenced by the steep slope, a plastic region and an almost instant loss of load capacity.

The responses of the different plated depths are associated with different modes of failure are discussed in the subsequent section.

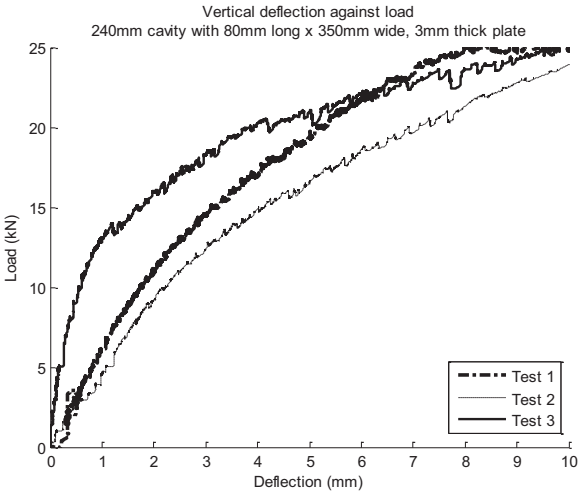


Figure 5. Response of 80 mm plates in panels with 240mm cavity. (Test group code *Aa1*)

The elastic stiffness is calculated as the slope of the graph up to 33% of the ultimate load. The stiffness varies from an average of 12.7kN/mm^2 for the 80mm set of plates to 56.7kN/mm^2 for the set of 240mm deep plates and 68.3kN/mm^2 for the set of 400mm deep plates, although there is large variance between individual plates. Other authors describe the elastic branch as the secant of 75% of the ultimate load [1]. As shown in Table 4, in this study, stiffness values vary significantly in the 33% to 75% of maximum load range.

3.2 Shear response of plates of different plate thickness

Among the 24 panels tested, plates with two different thicknesses are investigated. 15 panels with 3mm plates and 9 panels with 2mm plates are tested.

The 2mm plates yield at a significantly lower load than similar panels with 3mm plates when all other parameters are comparable.

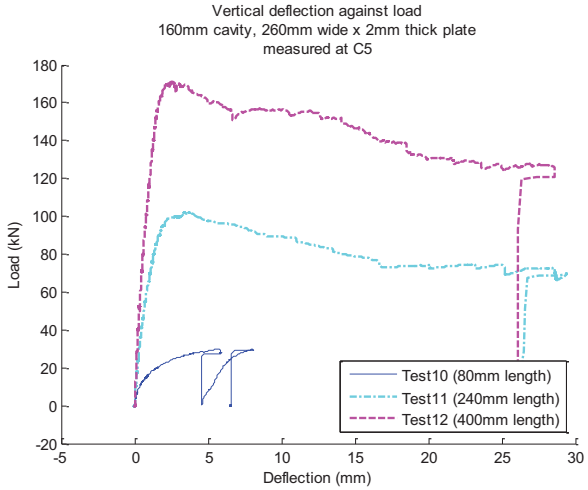


Figure 6. 2mm thick plates.

3.3 Shear response of plates of different insulation width

The width of the insulation layer was varied in panels with different combinations of plate depth and thickness. Figure 7 shows the response of Tests 1-3 already shown in Figure 5, relative to Tests 19 and 22 which are panels of thinner cavity widths. Tests 19 and 22 include plates of 80mm depth, and 3mm thickness, however the cavity widths are 120mm and 180mm respectively, corresponding to plate widths of 225mm and 280mm respectively.

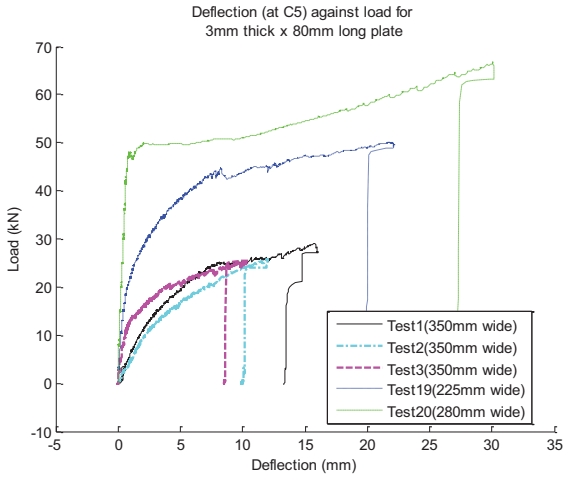


Figure 7. Tests 1-3 compared to panels of different cavity width and hence plate width.

The panel stiffness in the main increases with decreasing cavity width. In the samples shown in Figure 7 the stiffness of the 280mm panel (180mm cavity) is however greater than the stiffness of the panel with a 225mm panel (120mm cavity).

Average maximum strength varies from 80.1kN to 25.7kN for cavity widths of 90mm to 240mm, for 80mm deep plates. Also average strengths vary from 241.7kN to 172.8kN for

insulation layer widths of 90mm depth to 240mm depth respectively, for 400mm deep plates.

4 DISCUSSION

This section focuses on the failure modes of the different plate types. The variation in shear-deformation response is directly related to the variability in plate dimension. The dominant failure types appear to be plate slip arising from concrete spalling and local distortion of the embedded longitudinal rebar (for the 3mm thick plates), and either compressive or shear buckling (for the 2mm thick plates).

4.1 Failure mode related to plate depth

The three plate depths display very different modes of failure. In the case of the thicker (3mm) plates, the,

1. 80mm deep plates displaying slippage (group Aa1, Figure 8),
2. 240mm deep plates display cracking on the face of the outer wythe of concrete, and evidence of pull-out of the rebar (group Aa2), and,
3. 400mm deep plates display significant cracking and pullout and in some cases distortion of the rebar (group Aa3, Figures 9, 10 and 11).



Figure 8. Insulation removed to show slippage of 80mm plate.

The panels with 240mm and 400mm deep plates consistently show cracking on the front face in a horizontal line corresponding with the top of the plates within (Figure 9). Figure 10 shows evidence of associated concrete spalling where the plate has rotated anticlockwise in the plane of the plate, and direction of applied load, creating pull out of the top portion of plate and associated cracking on the front face of the panel

The 3mm thick plates do not generally show evidence of buckling unlike their 2mm counterparts (except when brought well beyond the design load to overload (*e.g.* Test 17)).

The concrete on the panel face was excavated to identify the impact of the load testing on the plate within, as can be seen in Figure 9.



Figure 9. Horizontal face cracking that occured during testing, and excavation work carried out after to identify mode of plate failure (Test 8).

The insulation was removed from the panels to view the movement of the plate during testing, and the resulting concrete spalling, as shown in Figure 10.



Figure 10. Evidence of concrete spalling (Test 8).

The concrete around the plate was then excavated away to display the embedded portion of the plate and the impact of testing on the rebar, which displayed rebar bending in a number of situations.





Figure 10. (Left) Pull out of top portion of the (3mm thick, 400mm deep) plate. (Right) Close up of top portion of plate displaying pullout and rebar embedment (Test 8).

4.2 Failure mode related to plate thickness

Plate thickness is perhaps the most salient parameter in defining the failure mode of the panels. The thinner (2mm) plates in contrast to the thicker (3mm) plates display consistent failure through plate buckling (Figure 12).

The 2mm and 3mm thick plates are not directly comparable as, unfortunately, no two panel configurations share the same dimensions otherwise. However ultimate loads for 2mm plates are consistently considerably lower for panels of similar insulation widths.



Figure 11. Example of buckling in 2mm thick, 400mm deep plate (Test 21, left) insulation removed post test, (right) rebar arrangment and bearing on hole.

4.3 Failure mode related to cavity width

Panels of various cavity widths do not show a common failure mode. Plates installed in the slender cavity range (90 - 120mm) and wide cavity range (160mm - 240mm) show various modes of failure which are more associated with the plate thickness than correlated with the cavity widths.

5 CONCLUSION

This paper documents the results of an extensive experimental study of 24 precast concrete sandwich panels. The approximate yield load and ultimate load were identified.

The shear response of the panels vary considerably for different plate dimensions principally plate thickness, plate depth and plate width which is dependent on the width of insulation. The performance of Test Group Cb1-3 can be compared with the performance of Test Group Aa1-3, with similar yield and ultimate loads. Based on this similarity, it might be proposed that an 80mm increase in cavity width can be likened to a 1mm reduction in plate thicknesss. However, these same panels differ in their modes of failure.

Several different modes of failure were evident for plates of different parametric configuration, with the thinner plates buckling and the thicker plates causing concrete spalling and local distortion of the embedded longitudinal rebar. Based on the results of the extensive experimental testing undertaken it is proposed that a minimum of 3mm thick plates should be used to avoid premature plate buckling.

ACKNOWLEDGMENTS

The authors would like to thank Fixinox, Belgium for allowing publication of this test and data. The authors would also like to thank Techrete, Ireland for manufacturing the panels and for their continued support of Façade Engineering research at Trinity College Dublin.

REFERENCES

[1] C. Naito, J. Hoemann, M. Beacraft, and B. Bewick, “Performance and Characterization of Shear Ties for Use in Insulated Precast Concrete Sandwich Wall Panels,” *J. Struct. Eng.*, vol. 138, no. 1, pp. 52–61, 2012.

[2] “Fixinox - Fixing solutions and anchors for heavy claddings.” .

[3] “Techrete - Architectural Precast Concrete Cladding.” [Online]. Available: http://www.techrete.ie/. [Accessed: 03-Feb-2014].

An Investigation into the Capabilities of Design Codes to Determine the Load Capacity of RC Deep Beams

Daniel Shinnick[1,2], Des Walsh[1], Kieran Ruane[1, 3]
[1] Department of Civil, Structural & Environmental Engineering, Cork Institute of Technology, Cork, Ireland
[2] Mott MacDonald Ireland, 5 Eastgate Avenue, Eastgate, Little Island, Cork, Ireland
[3] RPS Consulting Engineers Ltd., Innishmore, Co. Cork, Ireland
daniel.shinnick@mottmac.com, des.walsh@cit.ie, kieran.ruane@rpsgroup.com

ABSTRACT: The publication of fib Bulletin 55: CEB FIP Model Code 2010[(1)] (MC2010) in 2012 provides additional guidance for the design of deep beams. The deep beams can be analysed using plastic analysis or non-linear analysis. Plastic analysis design can be conducted in the form of the Strut-and-Tie Method (STM), where the internal forces in the deep beam are idealised as a series of struts and ties. Non-linear design is conducted with the aid of FE software where the concrete material properties are entered into the software to resemble the deep beam. This study investigates the ability of MC2010 to determine the load capacity of deep beams using both forms of analysis. Other design standards such as EN1992-1-1Design of Concrete Structures General Rules and Rules for Buildings (EC 2) [(2)], ACI 318-11 Design Code Requirements for Structural Concrete (ACI) [(3)] and CSA A23.3 Design of Concrete Structures (CSA) [(4)] were also considered in order to make a comparison. Fourteen reinforced concrete deep beams were modelled using plastic analysis and twelve reinforced concrete deep beams were modelled using non-linear analysis. The results from the plastic and non-linear analysis were compared to that of the actual test data conducted by Foster and Gilbert [(5)]. The results showed that for plastic analysis, MC2010 provides a conservative design in predicting the load capacity for deep beams. It was also found that in order to model deep beams using non-linear analysis with plane stress elements a larger mesh was required to obtain a comparable result to the test data. Possible limitations in the applicability of non-linear finite element analysis with plane stress elements to analyse deep beams were identified. Further investigations may be required as this investigation only considered plane stress elements.

KEY WORDS:
Deep beams; High strength concrete; FE analysis; LUSAS; Model Code 2010; Strut-and-Tie Model; Span to depth ratio (L/D)

1 INTRODUCTION

Deep beams are generally defined as structural members with a span to depth ratio of less than three. Practical applications of deep beams include transfer girders in tall buildings, foundations, offshore structures and bridge diaphragms. Bernoulli's beam theory that plane sections remain plane is not valid for deep beams as shear deformation become significant and cannot be ignored. As a result deep beams have an irregular stress distribution which varies greatly depending on the L/D ratio. Therefore deep beams are usually designed either by non-linear or plastic analysis.

This investigation considers deep beams with the following L/D ratios: 1.2, 2.0 and 3.0. This paper investigates the ability of MC2010 to predict the load capacity of fourteen high strength concrete deep beams using plastic analysis and twelve high strength concrete deep beams using non-linear analysis tested by Foster and Gilbert[(5)].

2 RESEARCH SIGNIFICANCE

The publication of CEB-FIP Model Code 2010 [(1)] gives designers new criteria for the design of deep beams using plastic analysis by means of the STM and non-linear analysis using FE software. The STM is the lower bound theory of plasticity and therefore, it should always under-predict the load capacity. The aim of this investigation was to determine whether the design provisions in MC2010 [(1)] result in a more efficient design compared to other design codes.

3 FOSTER AND GILBERT [(5)]

This investigation utilizes research conducted by Foster and Gilbert [(5)]. They investigated the load capacity of a number of high strength deep beams, which were tested to failure. Their research was based on the provisions and guidance given in CIRIA Guide 2 [(6)], ACI 318-89 [(7)] and Strut-and-Tie model (STM) proposed by Rogowsky and MacGregor [(8)]. Rogowsky and MacGregor's method [(8)] which is similar to that of CEB-FIP Model Code 1990 [(9)] which uses the efficiency factor proposed by Warwick and Foster [(10)]. Many of these codes are now considered outdated or have been subsequently replaced, but Foster and Gilbert's test data remains a contribution to engineering.

The study by Foster and Gilbert [(5)] considers three variables: concrete strength, L/D ratio and secondary reinforcement. The concrete strength varied between 77 and 120 MPa. The research conducted by Foster and Gilbert[(5)] may not be fully representative for all deep beams as the study only considered high strength concrete and they did not vary the amount of primary reinforcement significantly.

The paper by Foster and Gilbert [5] was chosen for the following reasons:

1. The test procedure was clearly defined and the beams could be modelled from the available data;
2. Additional concrete material properties other than the compressive strength of the concrete on were given for all test specimens, such as: indirect tensile strength, density and initial elastic modulus;
3. The failure load for each beam was known along with a description of failure mode and crack pattern;
4. Steel reinforcement yield data were provided;
5. The concrete was supplied by ready-mix truck therefore its properties were likely to be consistent;
6. The authors seemed to be a credible source from their biographical description.

3.1 Test Data from Foster and Gilbert [5]

Foster and Gilbert's paper [5] provided enough test data to eliminate any requirement to conduct laboratory testing. The test arrangement is presented in Figure 1. The concrete cylinder strength, the failure load of the beam and the mode of failure are given in Table 1.

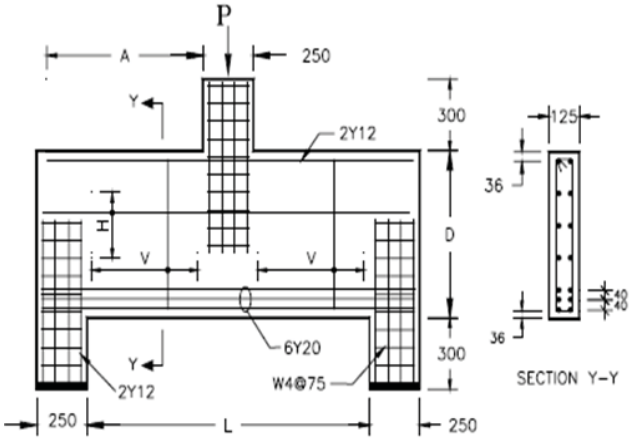


Figure 1 Reinforcement detail [5]

Table 1 Compressive strength and failure load [5]

Test Beam	f_{cm} (MPa)	Failure Load (kN)	Failure Mode
1	91	2000	Crushing of column*
2	96	2000	Crushing of column*
3	80	2600	Balanced failure
5	83	1590	Balanced failure
6	120	1650	Tension failure
7	78	1400	Tension failure
9	89	1170	Tension failure
10	93	1460	Tension failure
12	80	1020	Tension failure
13	120	1050	Tension failure
14	77	1050	Tension failure
16	89	870	Tension failure

* Test abandoned

The reinforcement details for the beams are also given in Figure 1 along with the beam thickness, cover and reinforcement spacing. The location and quantity of the tensile reinforcement was found to be important as these parameters determined the position of the tie (tensile member) in the idealize STM. This in turn determined the size of the nodal region.

The various beam geometry tested by Foster and Gilbert [5] which was used as part of this investigation are presented in Table 2 along with the quantity of secondary reinforcement used in each test beam specimen.

Table 2 Beam dimension and reinforcement [5]

Test Beam	L mm	A mm	D mm	V	H
1-3	1450	850	1200	8*2W6@75	5*2W6@175
5-7	1400	825	700	8*2W6@75	3*2W6@135
9	1400	825	700	None	None
10	1400	825	700	11*2W6@50	None
12-14	2100	1175	700	13*2W6@75	3*2W6@135
16	2100	1175	700	None	None

Further information regarding the test procedure conducted by Foster and Gilbert is contained in their paper *Experimental Studies on High-Strength Concrete Deep Beams* [5].

4 PLASTIC ANALYSIS (STM)

The design of deep beams in accordance with MC2010 [1] using the STM is stated in Clause 7.3.6 of the code. The allowable compressive stress of a strut and the various nodal regions is given by Equation 1, where k_c is a reduction factor to account for a reduced compressive strength.

$$f_{cd} = \frac{k_c f_{ck}}{\gamma_c} \quad (1)$$

4.1 Strut Design

For strut design the reduction factor is given by Equation 2.

$$k_c = 0.55\,(\frac{30}{f_{ck}})^{1/3} \leq 0.55 \quad (2)$$

4.2 Node Design

The reduction factor for nodal design depends on the idealized stress applied to a particular node. There are three types of node: CCC, CCT and CTT. A CCC node consists of a node fully in compression from three lines of idealized force. A CCT node has one side where there is a tensile force while a CTT node has two sides in tension. CTT nodes were not considered as part of this investigation.

4.2.1 CCC Node

For CCC node design, k_c is given by Equation 3.

$$k_c = 1.0\,(\frac{30}{f_{ck}})^{1/3} \leq 1.0 \quad (3)$$

4.2.2 CCT Node

For CCT node design, the k_c is given by Equation 4.

$$k_c = 0.75\,(\frac{30}{f_{ck}})^{1/3} \leq 1.0 \quad (4)$$

4.3 Tie Design

Tie design is given by Equation 5.

$$f_{yd} = \frac{f_{yk}}{\gamma_s} \quad (5)$$

5 PLASTIC ANALYSIS RESULTS

The failure criterion used for plastic analysis was taking the load capacity as the lowest load to cause the deign stress in the strut, nodes or the tie to exceed the allowable stress limits. Table 3 shows the percentage of the predicted load capacity for each beam to that of the failure load.

Comparing the predicted load capacity to that of the actual load it can be seen that the provisions of MC2010 underestimates the load capacity with a mean predicted load capacity of 34.7% of the actual applied load. This equates to an average factor of safety (FoS) of 2.9 applied to the design.

Table 3 Percentage of actual load capacity

Test	L/D	MC 10[(1)]	EC 2[(2)]	ACI[(3)]	CSA[(4)]
1	1.2	40.4	60.9	76.7	88.9
2	1.2	41.9	62.3	76.7	88.9
3	1.2	37.1	57.3	59.0	68.4
4	1.2	31.1	47.8	52.0	60.3
5	2.0	38.4	51.8	50.0	58.1
6	2.0	45.2	61.1	59.0	68.4
7	2.0	40.6	62.9	70.6	81.9
9	2.0	35.5	53.8	56.6	65.6
10	2.0	37.1	55.6	57.4	66.5
11	2.0	21.3	32.9	56.9	31.1
12	3.0	26.9	36.4	55.2	45.0
13	3.0	23.6	36.6	55.2	34.0
16	3.0	31.1	47.1	66.7	47.0
Mean		34.7	51.3	60.9	61.9
St Dev		7.3	10.4	8.9	18.8
FoS		2.9	2.0	1.6	1.6

The results from this investigation suggest that the provisions in CSA A23.3 give the most reliable load predictions for beams with an L/D ratio of less than or equal to 2.0, while ACI 318 provides a better solution for beams with an L/D ratio of 3.0.

The predicted load capacity is dependent on the percentage and location of the main reinforcement provided, as this influences strength of the tie and the size of the nodal zones. The test specimens conducted by Forster and Gilbert [(5)] didn't vary the percentage of reinforcement for each L/D ratio; Beams 1-4 had 1.3% while Beams 5-16 had 2.2%.

The predicted load capacities for the beam with varying concrete compressive strength are shown in Figure 2 to 4. It can be seen that the yield criterion of the tie becomes the governing factor for ACI and CSA designs. There is no increase in the load capacity for an increase in concrete compressive strength. Designs are considered safe if the predicted load capacity is below the actual tested load. Figures 2 to 4 show that the design provisions of ACI and CSA give a better approximation of the load capacity.

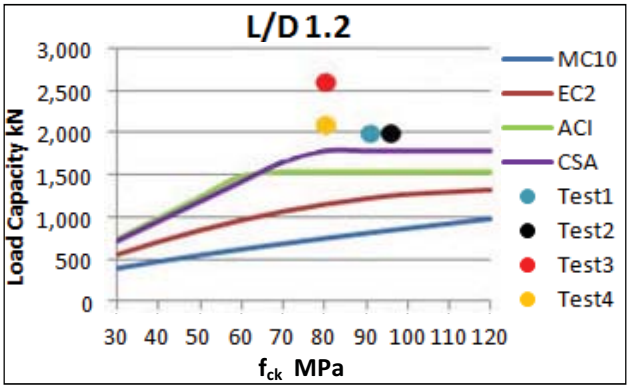


Figure 2 – Predicted load capacity for L/D = 1.2

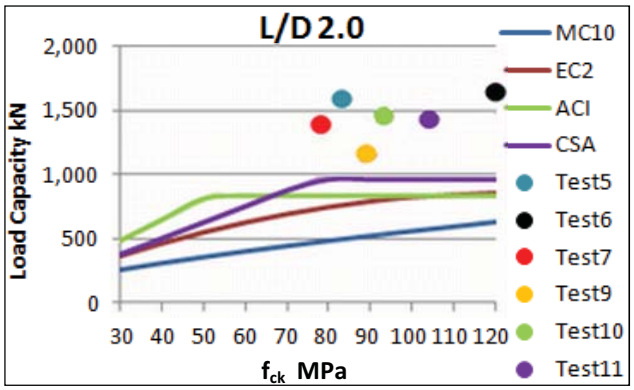


Figure 3 – Predicted load capacity for L/D = 2.0

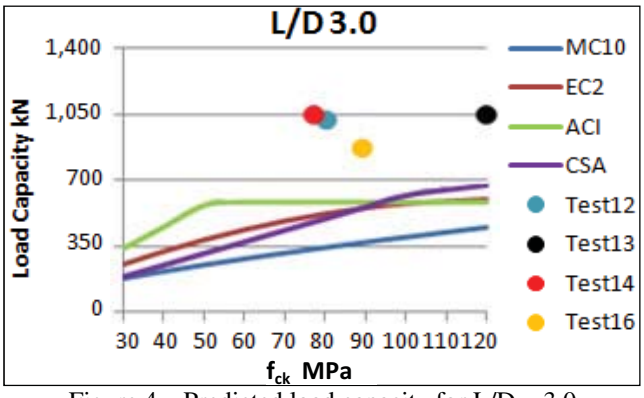


Figure 4 – Predicted load capacity for L/D = 3.0

6 NON-LINEAR FE ANALYSIS

In order to model a deep beam using FE software, concrete non-linear properties are required as inputs. Input properties such as modulus of elasticity (E), strain at maximum compression force (ε_c) and ultimate strain ($\varepsilon_{c,lim}$) are required as part of the failure criterion. MC2010 [1] allows these parameters to be determined based on the compressive strength of the concrete. Figure 5 shows a typical stress-strain curve for concrete and how the stress-strain relationship varies with the compressive strength of the concrete.

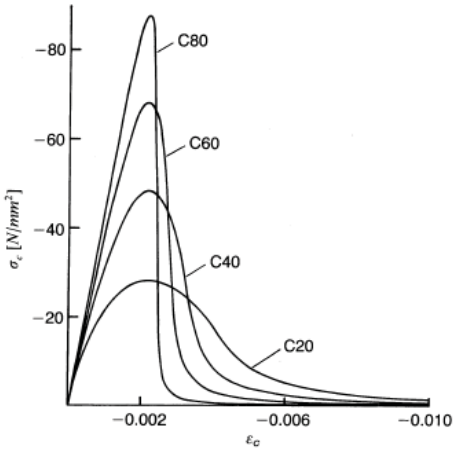


Figure 5 Stress - strain curve with concrete strength [9]

Generally a strain of 0.002 (ε_{c1}) is assumed at the maximum uniaxial compressive force, and increasing to 0.0035 at ultimate limit (ε_{cu1}).

6.1 MC2010 Concrete material properties [1]

The value for elastic modulus (E_{ci}) at 28 days can be obtained given by Equation 6.

$$E_{ci} = E_{c0}\alpha_E\left(\frac{f_{cm}}{10}\right)^{1/3} \qquad (6)$$

where

- E_{c0} = 21.5x10^3 MPa
- α_E = 1.0 for quartzite aggregate (or refer to Table 5.1-6 of the code)

Table 5.1-8 of the code gives the elastic modulus (E_{ci}) and the strain at maximum compression force (ε_c) and ultimate strain ($\varepsilon_{c,lim}$) for the different concrete strengths. Table 4 gives the values for high strength concrete from MC2010.

Table 4 Elastic modulus & strains [1]

Concrete grade	C70	C80	C90	C100	C110	C120
E_{ci} [GPa]	42.6	44.4	46.0	47.5	48.9	50.3
E_{c1} [GPa]	28.9	31.4	33.8	36	39.3	42.7
ε_{c1} [‰]	-2.7	-2.8	-2.9	-3.0	-3.0	-3.0
$\varepsilon_{c,lim}$ [‰]	-3.2	-3.1	-3.0	-3.0	-3.0	-3.0
k	1.47	1.41	1.36	1.32	1.24	1.18

The values for the elastic modulus (E_{ci}) used in the models were obtained from Equation 6, while the value for strain at maximum compression force (ε_c) and ultimate strain ($\varepsilon_{c,lim}$) were obtained by linear interpolation using Table 4.

6.2 Comparison of non linear properties

The actual E value for the beams was known as it was determined from cylinder testing. The actual E value of the concrete is not always available to the designer and as a result the designer must rely on the code provisions to determine variable properties such as E. The values for E are obtained for the relationship defined in the code based on the compressive strength of the concrete. ACI gives two equations to determine E_c as a result both equations were uses.

Table 6 gives the percentage of the determined E value to that of the actual measure E value from test data. It can be seen that ACI 318 (2), gives the closest approximation to the value of E_0 determined from the experimental data with a mean value of 98%.

Table 6 Percentage of actual E value

Beam	MC10 E_{ci}/E_0	EC2 E_{cm}/E_0	ACI318(1) E_c/E_0	ACI318(2) E_c/E_0
1	0.86	0.82	0.84	0.99
2	0.88	0.83	0.87	1.02
3	0.83	0.79	0.79	0.90
5	0.84	0.80	0.81	0.95
6	0.94	0.88	0.97	1.14
7	0.82	0.78	0.78	0.89
12	0.83	0.79	0.79	0.93
13	0.94	0.88	0.97	1.14
14	0.82	0.78	0.78	0.89
Standard Deviation	0.05	0.04	0.08	0.10
Mean	0.86	0.82	0.84	0.98

6.3 Modelling

Twelve deep beams were modelled using LUSAS FE software, each model took account of symmetry and therefore only half the model needed to be modelled. All beams were modelled as 2D Plane Stress Continuum Elements along with the actual quantity of reinforcement shown in Figure 1 and the secondary reinforcement given in Table 2. The reinforcements were modelled as 1D bar elements.

The beams were analysed using Multi-Crack Concrete (Model 94) failure criteria within LUSAS. This is a plastic damage contact model where damage planes occur according to the principal stress. The basic softening curve can be controlled by a fixed softening curve, which is dependent on the element size.[11] The fixing of the softening curve is controlled by the specified strain values ε_{c1} and ε_{cu1} therefore the varying values for ε_{c1} and ε_{cu1} should have an effect on the load capacity determined by LUSAS. As ACI (2) gives the best approximation for the E_0 it was expected to give the best results for the non-linear analysis.

The element size was found to have a significant effect on the ability of LUSAS to accurately solve for the load capacity. A large element size was found to be more suitable to predict a closer approximation of the load capacity.

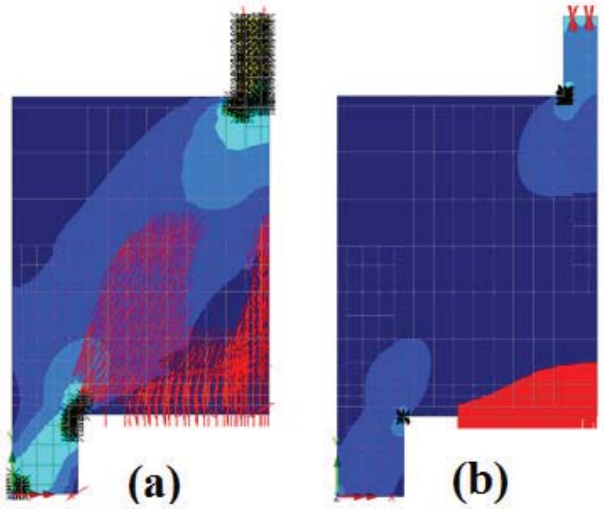


Figure 6 Effect of element size on load capacity

Figure 6 shows two identical models with the only difference being the element size defined in LUSAS. The effect the element size has on the model can be seen where: (a) consists of a model with an element size of 100mm and solved to 98.9% load capacity while (b) consists of the same model with an element size of 10mm and solved to 49.4% load capacity.

It can be seen that the beam in Figure 6 (a) suffers from extensive cracking at mid span and cracking along the line of the idealised strut along with crushing of the concrete at the point of load application and support. Figure 6 (b) only exhibits a minor degree of cracking in the mid span. The reason for this may be an ill conditioned stiffness matrix.

Ill conditioning is where a small error in the data results in a large error in the solution. This inevitably results in the failure in the ability of the FE software to determine the load capacity giving the last converged load step of the analysis as the load capacity.

When extensive cracking occurs in a FE model, this results in a degradation of the stiffness matrix which can lead to ill-conditioning of the stiffness matrix.[12] A sensitivity analysis should be carried out in order to determine the appropriate approach to model deep beams.

7 NON-LINEAR FE ANALYSIS RESULTS

The load capacities determined from non-linear analysis for the twelve beams modelled in accordance with the provision of the stated design codes are given in Table 7. The values are presented as a percentage of the actual applied load achieved during testing. The results show that the provision of ACI 318 gives the most reliable mean load capacity of 81.0% of the actual applied load.

Little variation was found for the design load capacity of deep beam using non-linear analysis in accordance with the code provisions as a number of FE models exhibited signs that they may have failed due to ill-conditioning.

Table 7 Percentage of actual load capacity

Beam	MC10	EC2	ACI (1)	ACI (2)
1	100	94	100	102
2	103	101	103	105
3	95	76	98	78
5	72	61	71	87
6	93	93	93	85
7	73	70	72	84
9	66	79	83	81
10	58	58	58	73
12	70	63	50	66
13	81	75	76	75
14	74	65	57	74
16	64	63	63	62
Mean	79.2	74.8	75.0	81.0
St Dev	15.1	14.5	18.4	12.9

It can be seen that Beams 1-3 with an L/D of 1.2 give the closest load approximation. It is suspected that the locations of the secondary reinforcement had an influencing effect on the element size. As indicated in 6.3 the element size has a significant effect on the capability of LUSAS to determine the load capacity. The large deviation in the predicted load capacity is a likely result of a number models suffering from degradation of the stiffness matrix.

8 CONCLUSION AND RECOMMENDATIONS

8.1 Plastic Analysis

Plastic analysis in accordance with MC2010 [1] produces conservative designs with an average FoS of 2.9 for the fourteen beams considered as part of this investigation.

This investigation shows that for deep beams with an L/D of 2.0, or less, design in accordance with CSA A23.3 [4] give a more efficient design. For deep beams with an L/D greater than 2.0, design in accordance with ACI 318 [3] provides the most efficient design.

Figures 2 to 4 show that the yield criterion of the tie becomes the governing factor with increased concrete compressive strength. While in comparison, the design in accordance with MC2010 [1] and EC 2 [2] shows the node or strut failing before the steel tie yields.

The load capacity of deep beams is largely dependent on the size of the nodal zone and the strength of the tie; therefore it is recommended that a minimum and maximum area for steel should be specified in each code specifically for the design of deep beams to prevent sudden failure of the beam.

8.2 Non Linear FE Analysis

As part of the investigation it was noticed that the element size has the most significant effect on the ability of LUSAS to solve for the load capacity. It is recommended that when modelling deep beams using LUSAS and using Plane Stress Analysis that larger element sizes should be used. This will reduce the risk of the model failing prematurely due to ill-conditioning of the stiffness matrix.

It is recommended that a sensitivity study should be undertaken on the effect element size has on deep beams. The location and quantity of the reinforcement has a significant effect on the element size. The locations of reinforcement reduce element size in location of high stress and this may result in premature failure of the model as a possible result of an ill-conditioned stiffness matrix.

The design of deep beams using FE analysis in accordance with ACI 318[3] gives the most accurate results in comparison to that of the test data. Using the design provision of ACI 318 (2), the mean load capacity of 81% was obtained for all the beams considered. MC2010 [1] in comparison gives a mean load capacity of 79.2%. The comparison of the results showed little variation between the different design codes in the prediction of the load capacity using non linear analysis.

9 ACKNOWLEDGEMENTS

The research reported in this paper was undertaken as part of the taught MEng (Structural Engineering) programme at Cork Institute of Technology.

SYMBOLS AND NOTATION

A	Shear span
CCC	Compression node without ties
CCT	Compression node with one ties
CTT	Compression node with two ties
D	Depth of section
FE	Finite Element
FoS	Factor of Safety
E, E_{c0}, E_{ci}, E_{cm}, E_c	Modulus of elasticity from design code considered
E_{c1}	Secant modulus from the origin to the peak compressive stress
E_0	Initial modulus of elasticity obtained by Foster and Gilbert from testing
H	Quantity of horizontal web reinforcement used in each test specimen
I	Second moment of area
L	Clear span
L/D	Span to depth ratio
P	Applied axial load
STM	Strut-and-Tie Method
V	Quantity of vertical web reinforcement used in each test specimen
W	Web reinforcement consisting of hard drawn wire with a yield strength of 451MPa.
Y	Main reinforcement consisting of deformed bars with a yield strength of 400 MPa
f_{ck}	Characteristic value of cylinder compressive strength
f_{cm}	Concrete compressive strength given by Foster and Gilbert
f_{yd}	Design yield of tension yielding stress of non-prestressing reinforcement
f_{yk}	Characteristic yield of tension yielding stress of non-prestressing reinforcement
k	Plasticity number
k_c	Reduction factor accounting for tensile stress parallel to the direction of the strut
α_E	Coefficient for different types of aggregates
γ_s	Partial safety factor for the material properties of reinforcement
ε_c	Concrete compression strain
$\varepsilon_{c,lim}$	Ultimate strain
ε_1	Strain at maximum compressive stress

REFERENCES

[1] CEB-FIP. CEB-FIP Model Code 2010. Comite Euro-International Du Beton/Federation Internationale de la Precontrainte; 2012

[2] CEN European Committee for Standardization, EN 1992-1-1, Design of concrete structures general rules and rules for buildings; 2005

[3] American Concrete Institute ACI 318 Building Code Requirements for Structural Concrete; 2011

[4] Canadian Standards Association A23.3-04 Design of Concrete Structures; 2004

[5] S. Foster and I Gilbert, ACI Technical Paper No.95-S34, Experimental Studies on High-Strength Concrete Deep Beams. 1998

[6] Ove Arup & Partners. The design of deep beams in reinforced concrete. London, CIRIA. 1977

[7] American Concrete Institute ACI Building Code Requirements for Structural Concrete ACI 318-89, American Concrete Institute, Farmington Hills, MI, 1989

[8] Rogowsky D. M. and MacGregor J. G. "Shear Strength of Deep Reinforced Concrete Continuous Beams," Structural Engineering Report No. 110, Dept. Of Civil Engineering, University of Alberta, Edmonton, Alberta, Canada, Nov. 1983, 178 pp.

[9] CEB-FIP Model Code for Concrete Structures 1990, Comite Euro-International Du Beton/Federation Internationale de la Precontrainte; 1993

[10] Warwick W.B. and Foster S.J., "Investigation into the Efficiency Factor Used in Non-Flexural Reinforced Concrete Member Design," UNICIV Report No. R-320, School of Civil Engineering, The University of New South Wales, July 1993, 81 pp.

[11] LUSAS Solver Reference Manual LUSAS Version 14.5, Surry, UK. 2010

[12] Structural Concrete Finite-element Analysis for Limit-State Design, p163-164, M.D. Kolsovos & M.N. Pavlovic, Thomas Telford, London, 1995

The overconsolidation ratio of the Dublin Port Clay

David Gill_1[1], Eric Farrell_2[1]
[1]AGL Consulting, Suite 2, The Avenue, Beacon Court, Sandyford, Dublin 18.
email: david.gill@agl.ie, eric.farrell@agl.ie

-ABSTRACT: The Dublin Port Clay (DPC) extends below much of the Dublin Port and Docks area and is a significant stratum for many of the infrastructure developments in the area. The DPC comprises a stiff clay with silt laminations and sand layers. The origin of the deposit is uncertain but it was probably laid down as a lacustrine or glaciomarine deposit during a warm interglacial period. The silt and sand laminations make the stratum susceptible to disturbance during borehole drilling and this can affect some in-situ and laboratory tests. This has caused the stratum to be misinterpreted as a post-glacial normally consolidated clay. This paper presents an interpretation of the typical undrained shear strength, overconsolidation ratio (OCR) and K_0 profile of Dublin Port Clay obtained from detailed ground investigations carried out for some recent large projects in Dublin Port and Ringsend. Due to sample disturbance it has not been possible to identify a preconsolidation pressure for oedometer tests. Therefore OCR, which is an important parameter in geotechnical analysis, has been estimated from cone penetration tests (CPT) and is shown to be consistent with the interpreted profile of undrained shear strength.

KEY WORDS: Dublin Port Clay, undrained shear strength, OCR, cone penetration tests, CU triaxial test, K_0

1 INTRODUCTION

The Dublin Port Clay (DPC) extends below much of the Dublin Port and Docks area as well as Ringsend and can be up to 20m thick. It is a significant stratum for many of the infrastructure developments in the area. The geotechnical characteristics of the Dublin Port Clay presented herein are based on the results of detailed ground investigations that have been carried out for the refurbishment of the quay wall at Alexandra Quay East (AQE) in Dublin Port and for the Ringsend Waste Water Treatment Works. The locations of the sites are shown Figure 1.



Figure 1. Site location plan

The typical succession of strata in the Dublin Port area is:

- Made Ground.
- Recent estuarine and alluvial deposits which comprise soft estuarine silts/clays and sands and gravels.
- Dublin Port clay.
- Glacial deposits (boulder clay and glacial gravels).
- Limestone bedrock.

The Port Clay is a stiff, often thinly to thickly laminated slightly sandy CLAY, locally SILT and with rare gravel. Sand is fine and laminations, where present, range from <1mm to 10mm of silty/fine sand and are typically 10 to 25mm apart.

The silt and sand laminations make the stratum very susceptible to disturbance softening during borehole drilling and can be the cause of low strengths measured in Standard Penetration Tests (SPT's) and certain laboratory tests. In the past this has resulted in an underestimation of the strength and stiffness of the stratum and its interpretation as a post-glacial normally consolidated clay.

The origin of the deposit is uncertain. Naylor [1] described the stratum to be post-glacial and laid down as intertidal mud flats, possibly estuarine during a period of submergence. However, based on the interpreted overconsolidation ratio (OCR) and shear strength it appears more likely that the stratum is a glaciolacustrine or glaciomarine deposit laid down during a warm interglacial period that was subsequently overlaid with other material which has since been eroded.

The focus of this research is the OCR of the stratum, which provides its stress history in a dimensionless form. This is an important parameter for geotechnical design as underestimating OCR can cause the magnitude of consolidation settlements to be overestimated and lead to expensive geotechnical solutions.

2 CLASSIFICATION TESTS

The classification of the DPC is typically that of a low and intermediate plasticity Clay (CL-CI) when plotted on a Casagrande Plasticity Chart as shown on Figure 2. The results fall on the T-line which has been identified by Boulton and Paul [2] as typical of glacially derived deposits and would not be typical of marine deposits.

The liquid and plastic limits (w_L and w_p) are plotted against depth on Figure 3. The plastic limit is typically in the range 13 to 21 and generally increases with depth from 20 to 30m and is reasonably constant below 30m. The liquid limit is in the range 22 to 48, also generally increasing with depth. A plot of plasticity index, I_p vs depth on Figure 4 shows that I_p is in the range 4 to 30. The average I_p generally increases from about 10 to 20 from a depth of 20m to 30m and is approximately constant below this to the base of the stratum.

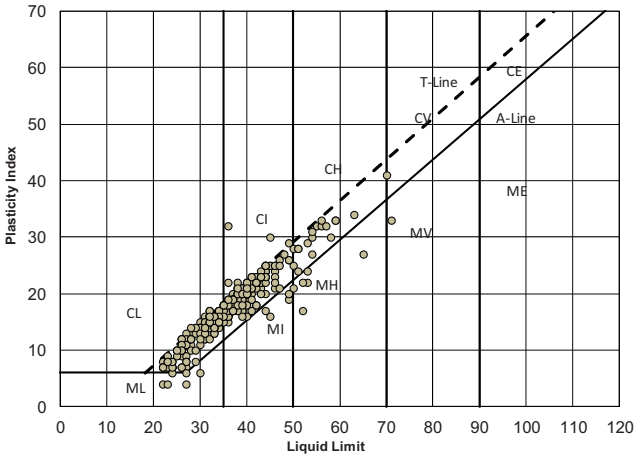


Figure 2. Casagrande plasticity chart

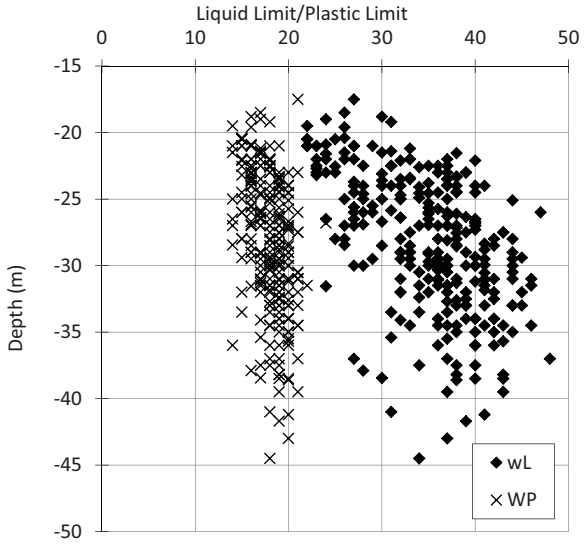


Figure 3. Plastic limit and liquid limit vs depth

The natural moisture content, w_n vs depth is plotted on Figure 5. The moisture content was typically in the range 17 to 31%, generally increasing with depth from 15 to 30m and is approximately constant from 30m to the base of the stratum. Normally the moisture contents of a uniform stratum would be expected to reduce with depth due to the increase in effective stress. However this is not so for the Port Clay but it is consistent with the liquid limit and plasticity index variation, with higher plasticity clay found to be present at depth.

Particle size distribution curves are presented on Figure 6. Almost 100% material from samples passed the 425µm sieve. The composition of the Port Clay shows a significant silt size particle content and is in the range 50 to 80%.

The bulk density was measured to be in the range 1.96 to 2.27 Mg/m^3.

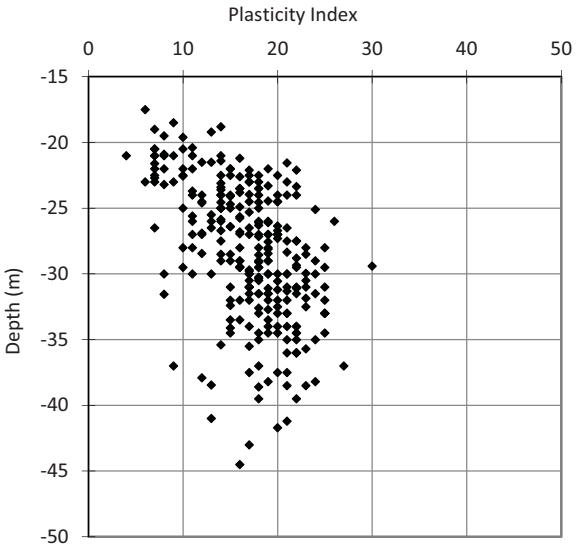


Figure 4. Plasticity Index vs depth

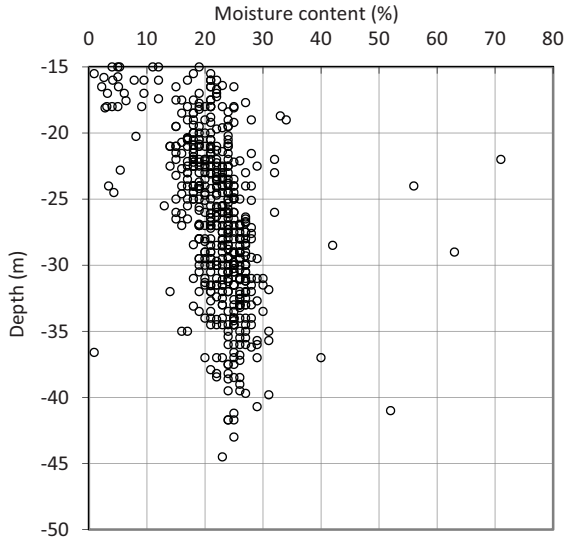


Figure 5. Moisture content vs depth

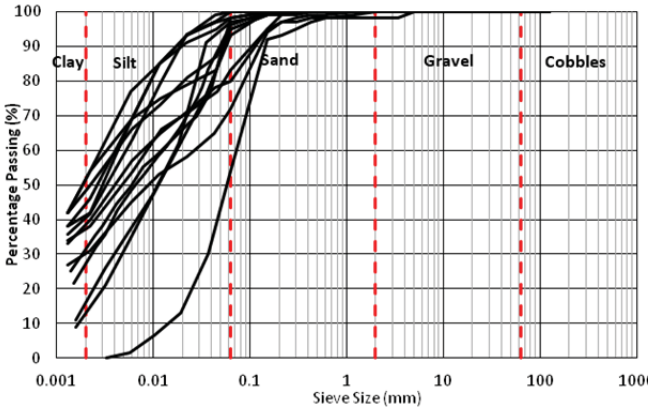


Figure 6. Particle size distribution

3 UNDRAINED SHEAR STRENGTH

3.1 Testing methods

The undrained shear strength measured in unconsolidated undrained (UU) and consolidated undrained (CU) triaxial compression tests and interpreted from SPT and CPT field tests are presented. It should be noted that no single undrained shear strength, c_u exists and the parameter is dependent on the mode of failure, strain rate, anisotropy and stress history. The c_u value to be used in design therefore needs to consider the mode of failure expected. An additional factor to be considered is the effect of drilling/sampling disturbance. For the DPC the undrained shear strength determined from SPT's and from unconsolidated undrained (UU) triaxial tests has been found to be adversely affected by sample disturbance giving unrepresentatively low values.

3.2 UU Triaxial Tests

The undrained shear strength measured in traditional UU triaxial tests are presented on Figure 7. Sampling was by U100 methods and from 102mm diameter triple barrel rotary coring. It can be seen that strengths as low as 40kPa were measured at depths of over 40m. This gives an undrained shear strength ratio c_u/σ'_v that is less than 0.2 below 30m depth, which is lower than would be expected for a normally consolidated clay. The UU triaxial results are therefore considered to grossly underestimate the undrained shear strength, probably due to loss of suction pressures and softening during sampling.

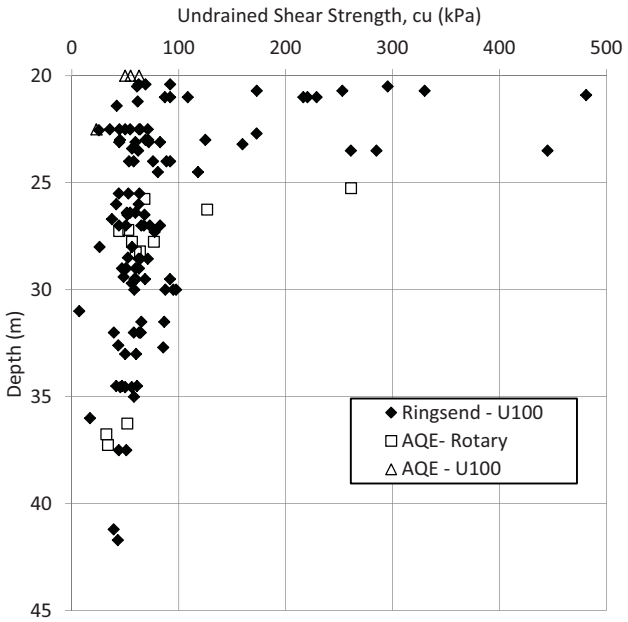


Figure 7. UU triaxial c_u vs depth

3.3 CU Triaxial Tests

In order to overcome the loss in effective stress suffered by the soil during sampling, triaxial compression tests were carried out on specimens that were consolidated to their in situ stress condition. The undrained shear strength results of samples consolidated isotropically and anisotropically to different pressures are shown on Figure 8. The anisotropic tests were consolidated to give ratios of horizontal effective stress to vertical effective stress (K_0) in the range 0.5 to 0.75. There is a considerable scatter in the results which is to be expected in samples consolidated to the different pressures.

For a vertical effective stress range of approximately 200 kPa to 400 kPa, which approximates in situ conditions, the CU triaxial tests give a lower bound undrained shear strength of 100 kPa. The average c_u for the anisotropically consolidated tests is 180 kPa and is 230 kPa for the isotropically consolidated tests for the in situ stress range.

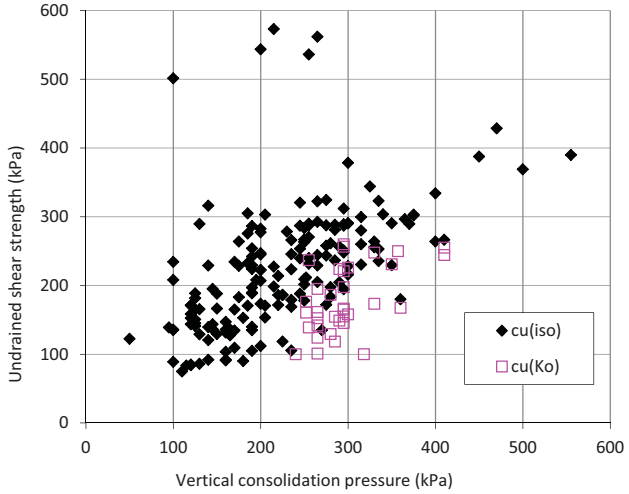


Figure 8. CU triaxial c_u vs vertical consolidation pressure

3.4 SPT

A plot of SPT N-values vs elevation are presented on Figure 9. Values as low as N_{SPT} = 7 were recorded, which using the relationship c_u = 5 N_{SPT} kPa from Stroud [3] gives a lower bound undrained shear strength of 35 kPa. The test results are considered to be affected by drilling disturbance due to high pore pressures in the silt and sand laminations.

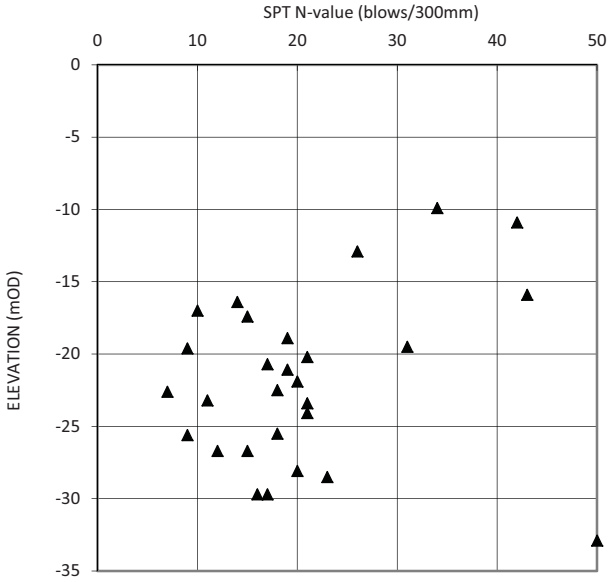


Figure 9. SPT N-values vs elevation

3.5 CPTu

A typical profile of corrected cone resistance, q_t and porewater pressure, u_2 for the Port Clay is presented on Figure 10. The presence of sand layers is indicated by the spikes in cone resistance and a corresponding reduction in excess pore pressure. The undrained shear strength can be obtained from CPTu's in fine grained soil using the following equation:

$$s_u = (q_t - \sigma_{vo})/N_{kt}$$

Where N_{kt} is an empirical cone factor and σ_{vo} is the total in situ vertical stress. For a low plasticity fine grained soil with I_p = 20, N_{kt} is the range 13 to 18 from Aas et al. [4] for average undrained shear strength (i.e., the average of triaxial compression, triaxial extension and direct simple shear). Typical undrained shear strength profiles interpreted from individual CPTu tests at AQE and Ringsend are shown on Figure 10. These are based on N_k = 15 which is appropriate for comparison with *average* undrained shear strength. This gives c_u to be typically in the range 100 to 160 kPa. The reduction in c_u with depth below 34m that is evident on Figure 11 for the Ringsend CPT is typical of the profiles for tests carried out at both Ringsend and AQE.

The N_k factor for equivalent compressive undrained shear strength would be about 11 and this gives c_u to be in the range 135 to 220 kPa. This is noted to be similar to the strength range obtained for the anisotropically consolidated undrained triaxial tests of 100 to 265 kPa.

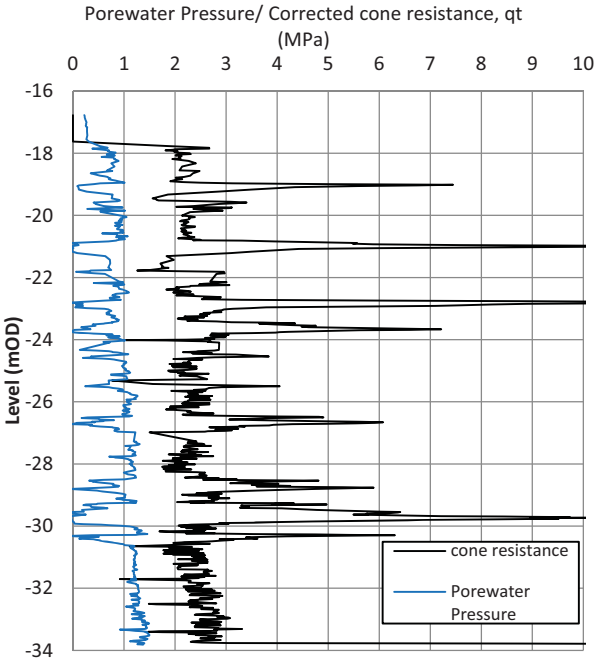


Figure 10. Typical CPTu profile for DPC

The ratio of undrained shear strength to vertical effective stress (c_u/σ'_v) interpreted typical tests at AQE and Ringsend are presented on Figure 12. Typically c_u/σ'_v is 0.3 to 0.6, reducing with depth.

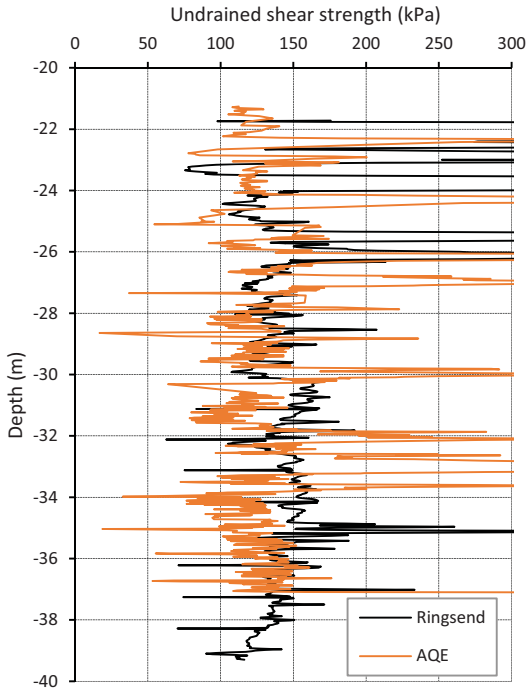


Figure 11. Undrained shear strength from CPT with N_{kt} = 15

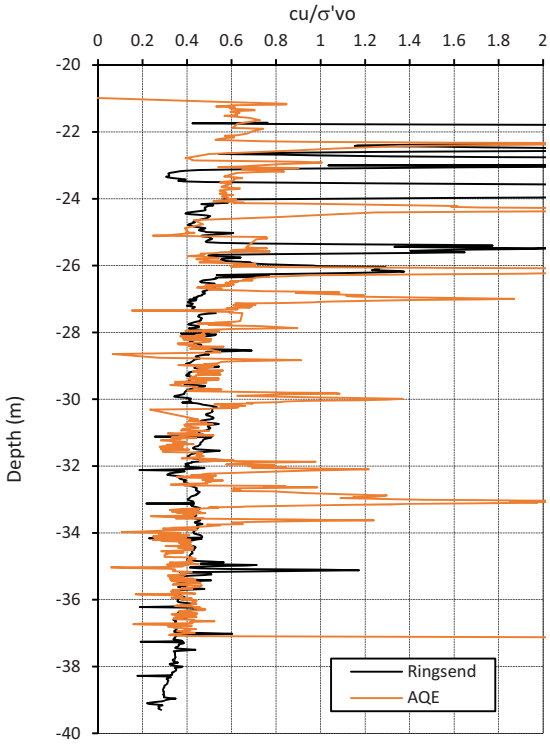


Figure 12. Undrained shear strength ratio c_u/σ'_v vs depth from CPT

4 OVERCONSOLIDATION RATIO

Overconsolidation ratio (OCR) is typically defined as the ratio of maximum past effective consolidation stress and the current effective overburden stress. This can be obtained from the preconsolidation pressure identified from the initial

loading in oedometer tests. However due to sample disturbance it has not been possible to identify this for the DPC. Therefore an estimate of OCR has been made using CPTu profiles.

The OCR can be interpreted from CPTu data using the following equation by Lunne et al. [5]:

$$OCR = 0.3(q_t-\sigma_{v0})/\sigma'_{v0} \quad (1)$$

The calculated OCR vs depth for typical CPT probes carried out at AQE and Ringsend are plotted on Figure 13. This shows a trend of decreasing OCR with depth. Overall it is considered reasonable to assume that OCR is about 2 to 3 to a depth of 32m and is about 1.7 to 2.0 at lower depths.

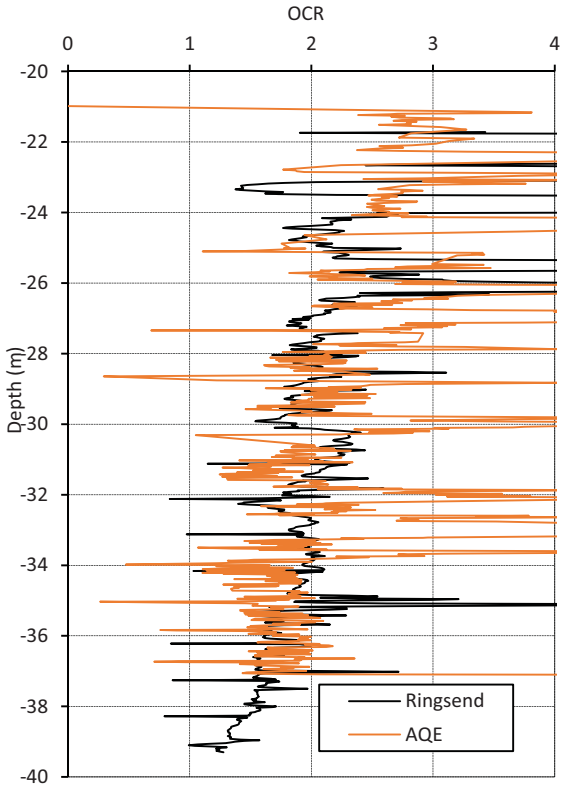


Figure 13. OCR (Lunne [5]) vs depth from CPT

An alternative method for obtaining OCR, by Mayne [6] is given by the following equation and is plotted on Figure 14:

$$OCR = 2\left[\frac{1}{1.95M+1}\left(\frac{q_t-u_2}{\sigma'_{v0}}\right)\right]^{1.33} \quad (2)$$

Where M is the slope of the critical state lines and is given by

$$M = \frac{6\sin\varphi}{1+\sin\varphi} \quad (3)$$

This gives a higher OCR than Equation 1 and is about 6 at the top of the stratum reducing to 2 at the base.

The OCR can also be estimated based on index properties and undrained shear strength. According to Ladd, et al. [7] OCR can be estimated using the normalised undrained shear strength from the equation:

$$OCR^{0.8} = [(c_u/\sigma'_v)_{OC}/(c_u/\sigma'_v)_{NC}] \quad (4)$$

Where $(c_u/\sigma'_v)_{NC}$ is typically 0.22 for I_p = 20 and the average of triaxial compression, extension and direct simple shear. For $(c_u/\sigma'_v)_{OC}$ of 0.3 to 0.6 this gives OCR = 1.5 to 3.5. This is consistent with the OCR obtained from Equation 1 and plotted on Figure 13.

Relationships between c_u/σ'_v, OCR and I_p by Andresen et al [8] give c_u/σ'_v = 0.4 to 0.7 for the OCR profile obtained from Equation 1 and 0.5 to 1.3 for the OCR profile obtained from Equation 2. Equation 1 therefore also gives a closer fit to the c_u/σ'_v profile on Figure 12.

It has therefore been concluded that for a depth range of about 20 to 40m the OCR of the DPC is considered to be in the range 1.7 to 3, reducing with depth.

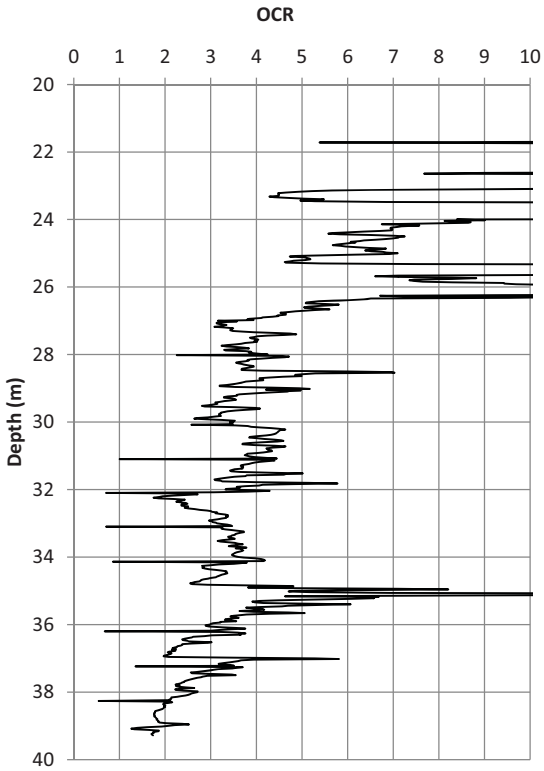


Figure 14. OCR (Mayne [6]) vs depth from CPT

5 IN SITU HORIZONTAL STRESS RATIO, K_0

The in situ horizontal stress can be estimated using the relationship between K_0, OCR and I_p presented by Brooker and Ireland [9]. Taking the OCR profile given by Equation 1 gives K_0 = 0.6 to 0.75, reducing with depth.

Kulhawy and Mayne [10] suggested the following relationship to estimate K_0 from CPT measurements based on pressuremeter test results, although considerable scatter was reported so is considered by them to be only a guide:

$$K_0 = 0.1\left(\frac{q_t-\sigma_{v0}}{\sigma'_{v0}}\right) \quad (5)$$

This gives K_0 to be typically in the range 0.5 to 0.9, reducing with depth. This is generally consistent with the interpretation of K_0 from the interpreted OCR range and the relationship by Brooker and Ireland [9].

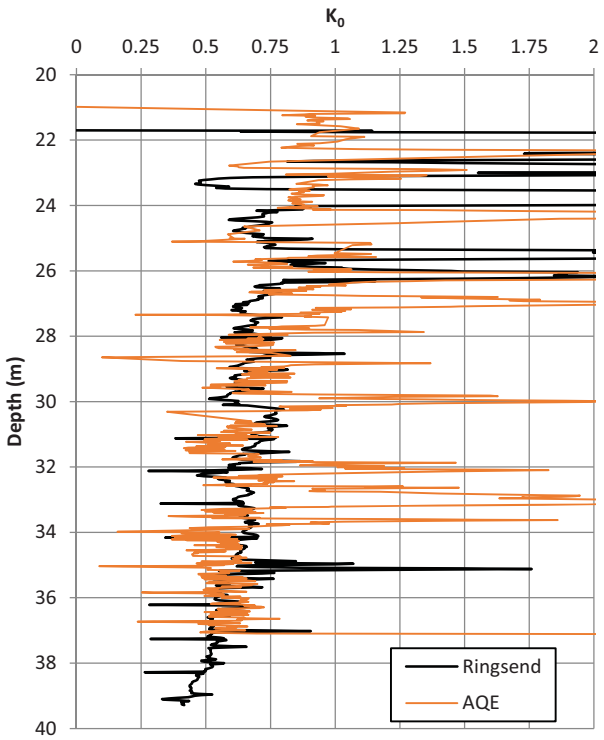


Figure 15. K_0 (Mayne [10]) vs depth from CPT

6 CONCLUSIONS

The Dublin Port Clay has been misinterpreted in the past as a normally consolidated post glacial clay due to its silt and sand laminations which make the stratum very susceptible to sample disturbance. This sample disturbance has also made it difficult to reliably identify a preconsolidation pressure from oedometer tests.

The overconsolidation ratio has been interpreted from typical CPT profiles at two sites to be in the range 1.7 to 3, reducing with depth. This OCR range has been found to be consistent with undrained shear strength measured in consolidated undrained triaxial compression tests and also with values interpreted from the CPT's, which typically classifies as stiff or very stiff in the range 100 to 200 kPa. The OCR is also found to be consistent with estimates for K_0, which are considered to be typically range of 0.6 to 0.75, reducing with depth.

ACKNOWLEDGMENTS

The author's would like to acknowledge the use of soils data from the AQE refurbishment and Ringsend Waste Water Treatment projects.

REFERENCES

[1] Naylor, D. (1965). 'Pleistocene and post-pleistocene sediments in Dublin Bay'. *Scientific Proceedings of the Royal Dublin Society*, Series A, Vol 2, No.11.

[2] Boulton, G.S. and Paul, M.A. (1976), 'The influence of genetic processes on some properties of glacial tills', *Quaterly Journal of Engineering Geology* Vol. 9 (No. 3) 159-194.

[3] Stroud, M.A., (1989), 'The standard penetration test – its application and interpretation', *Geotechnology Conference on Penetration Testing in the UK,* ICE.

[4] Aas, G., Lacass, S., Lunne, T. and Hoeg, K. (1986), 'Use of in situ tests for foundation design on clay', *Proceedings of the ASCE Specialyt Conference In Situ '86: Use of In Situ Tests in Geotechnical Engineering,* Blacksburg, 1-30 American Society of Engineers.

[5] Lunne, T., Robertson, P.K. and Powell, J.J.M, *Cone Penetration Testing in Geotechnical Practice,* Spon Press, 1997.

[6] Mayne, P.W. (1991), 'Determining OCR in clays by piezocone tests unsing cavity expansion and critical state concepts', Japanese Society of of Soil Mechanics and Foundation Engineering, *Soils and Foundations* – Vol. 31, No. 2, 65-76.

[7] Ladd, C.C., Foot, R., Ishihar, K., Schlosser, F and Poulos, H.G. (1977), 'Stress – deformation and strength characteristics. State of the Art Report, *Proceedings 9th International Conference on Soil Mechanics and Foundation Engineering*, Tokyo.

[8] Brooker, E.W. and Ireland, H.O. (1965),'Earth pressure at rest related to stress history'. *Canadian Geotechnical Journal* 2(1), 1-15.

[9] Kulhawy, F.H and Mayne P.H. (1990), 'Manual on estimating soil properties for foundation design', *Electric Power Research Institute*, EPRI, August 1990.

[10] Andresen, T., Berre, T, Leven, A. and Lunne, T., (1979), 'Procedures used to obtain soil paramters for foundation engineering in the North Sea', *Marine Geotechnology*, 3(3), 201-66.

A novel triaxial testing procedure to model the action of lubricants in pipe jacking

Ciaran C. Reilly[1], Trevor L.L. Orr[2]
[1] J. B. Barry & Partners, Dublin, Ireland (Formerly: Department of Civil, Structural and Environmental Engineering, Trinity College Dublin, Dublin 2, Ireland)
[2] Department of Civil, Structural and Environmental Engineering, Trinity College Dublin, Dublin 2, Ireland
Email: creilly@jbbarry.ie, torr@tcd.ie

ABSTRACT: Pipe jacking and microtunnelling are important trenchless construction techniques that are seeing increasing application around the world. The maximum length achievable with a single pipe jacking drive depends largely on the resistance to the jacking force that develops over the pipeline surface due to skin friction resistance between the advancing pipe and the soil. Often, bentonite or polymer slurries are injected into the soil from ports on the surface of the pipe with the intention of reducing the skin friction resistance. Field studies have shown that this procedure can achieve reductions in skin friction resistance of up to 90%, however the exact mechanism by which these slurries act is not fully understood. This paper presents the results of a series of experiments carried out using a novel triaxial testing apparatus, where a lubricant was injected into the interface between a coarse-grained soil and a rough concrete surface, similar to that of a concrete jacking pipe, while the soil was shearing against the rough concrete surface. The testing procedure is described, selected results are presented and recommendations towards practice arising out of the research are suggested.

KEY WORDS: Pipe jacking; Microtunnelling; Lubrication; Jacking force; Triaxial testing; Interface friction; Physical modelling.

1 INTRODUCTION

Pipe jacking, or microtunnelling, is a trenchless construction technique that allows for the installation of long horizontal distances of pipeline with a minimum of vertical intrusions to the ground surface. The product pipes to be installed are driven through the ground using the force developed by a jacking frame installed in a fixed shaft, while the spoil at the front of the pipeline is removed via a pipe jacking shield and mechanically transferred to the surface for disposal. A typical equipment configuration for slurry shield pipe jacking is shown in Figure 1.

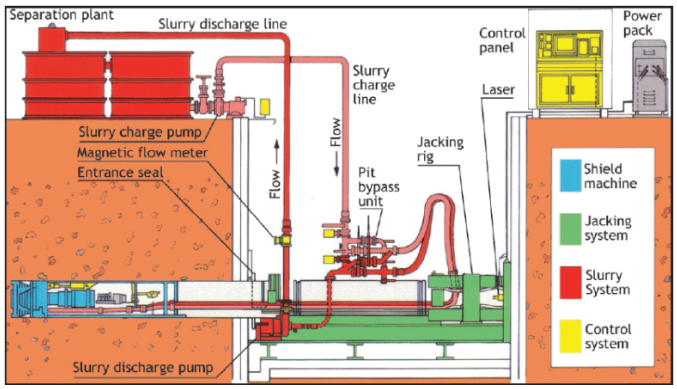


Figure 1. Typical pipe jacking site configuration (Source: Iseki Microtunnelling).

The skin friction resistance is the resistance developed over the surface of the pipeline as it advances through the ground. This is an important consideration in pipe jacking, as the magnitude of the skin friction resistance force typically dictates the maximum drive length possible without the use of unwieldy and time-consuming intermediate jacking stations. The provision of an overcut, which is an annular gap around the product pipes created through the use of a pipe jacking shield of a diameter greater than that of the product pipes, is the primary means of reducing the skin friction resistance on a pipeline. Further significant reductions are possible through the injection of a lubricant through ports in the skin of the product pipes. By the injection of lubricants, reductions in skin friction resistance of greater than 90% are commonly achieved in the field [1, 2].

The physical modelling of the lubricant injection process in pipe jacking has been mainly conducted in direct shear apparatus or small-scale tank testing devices [3-5]. However, shortcomings have been identified in terms of accurately representing field conditions and the ability to continuously control and monitor the pore fluid pressure. It is considered that pore pressure plays a very important role in the reduction of skin friction resistance, as lubricant slurries applied to an interface and not subject to pressurisation were found to have negligible benefits in reducing interface shearing resistance [3, 6, 7].

The present paper presents the results of a series of tests carried out using a modified triaxial compression testing apparatus to model the interface shearing resistance of a coarse-grained soil against a rough concrete surface while lubricants are injected into the interface. The roughness of the concrete surface was similar to that of a commercially available jacking pipe.

2 SKIN FRICTION AND LUBRICATION IN PIPE JACKING

Pipe jacking lubricants are typically injected through ports on the pipeline surface into the surrounding soil, as shown in Figure 2.

Pipe jacking lubricants in common usage are bentonite- or polymer-based slurries, mixed in a grout mixer on the surface and delivered through a network of pipes by semi-automated or automated delivery systems (Figure 3). Injection quantities are usually controlled on the basis of "common sense and experience" [8] or prescribed injection volumes [9].

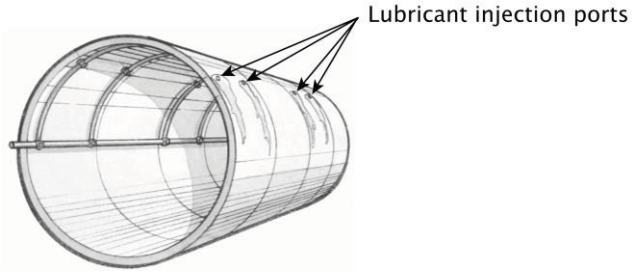


Figure 2. Typical arrangement of lubricant injection ports (Source: Pipe Jacking Association).

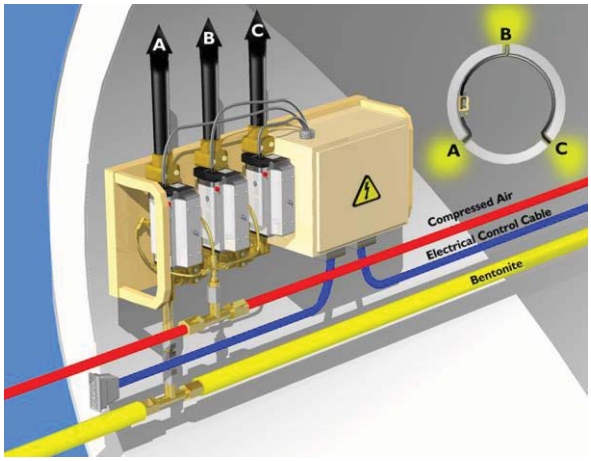


Figure 3. Automatic lubricant injection system (Source: Herrenknecht AG).

3 EXPERIMENTAL APPARATUS AND PROCEDURE

This paper presents the results of a series of novel triaxial tests carried out to model the injection of lubricants into the interface between a coarse-grained soil and a jacking pipe and identify the beneficial mechanisms of the lubricant. A two-part triaxial test specimen was utilised that incorporated a preformed interface along which shearing took place, together with a system for injecting lubricants into the interface under controlled conditions of pressure and volume. The tests were carried out in a triaxial cell intended for the compression testing of 38mm diameter specimens that was modified by the fitting of a laterally-translating top cap and a system to allow for the injection of lubricant slurries, as shown schematically in Figure 4.

3.1 Interface shear testing in triaxial compression

Previous research carried out to determine the residual shear strength of clay specimens which contained precut failure planes was investigated [10-13] and it was found that the residual angle of friction was obtained when the precut failure plane was at an inclination θ as follows:

$$\theta = 45° + \frac{\phi'_r}{2} \qquad (1)$$

When choosing the inclination of the preformed concrete failure surface for the tests with sand, to achieve the minimum friction angle, which is the constant volume friction angle, ϕ'_{cv}, it was decided to determine the inclination using Equation 1, with ϕ'_{cv} replacing ϕ'_r. The constant volume angle of friction of the test sands was approximately 30°, so the inclination of the preformed failure plane, θ, was set to 60°.

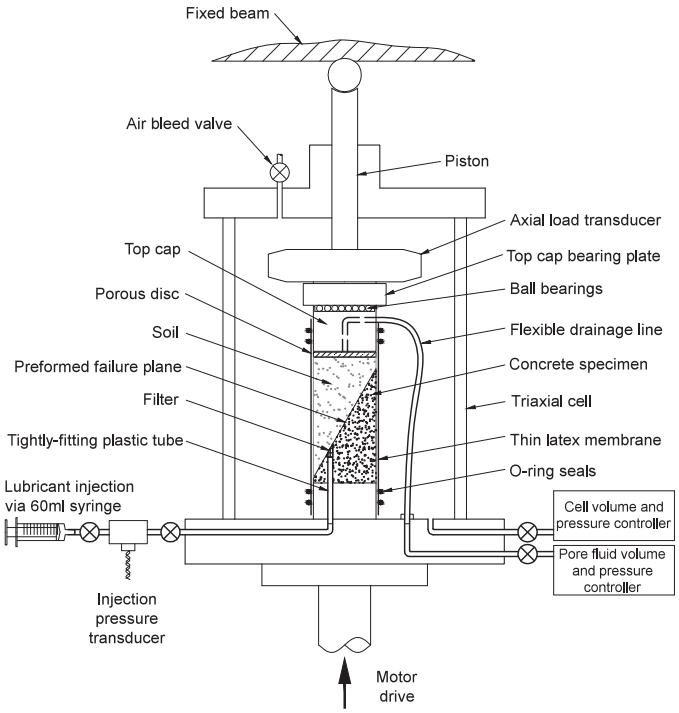


Figure 4. Triaxial testing apparatus.

3.2 Concrete test specimens

A number of 38mm diameter microconcrete test specimens were manufactured. The mix design was 2 parts fine to medium sand, 1 part Ordinary Portland Cement and 0.7 parts potable water by mass. A mould to form the concrete specimens with a preformed failure surface was fabricated from a PVC drainage pipe of suitable diameter, cut off at θ = 60°. Following casting and when the concrete had reached an initial set, a rough surface finish was created on the preformed failure plane using a steel trowel. Specimens were cured for at least 7 days before an opening, to allow lubricant injection, was bored using a pillar drill and jig. Views of one finished specimen are shown in Figure 5.

The surface roughness of the concrete specimens and a number of samples taken from typical jacking pipes available on the market in Ireland were characterised using a white light interferometer. The average surface roughness (R_a) of the concrete test specimens was 22.8μm while the average roughness of the jacking pipes measured was 24.2 μm. These values are close and so confidence was established in the ability of the physical model to reflect field conditions accurately.



Figure 5. Views of finished concrete specimens.

3.3 Pipe jacking lubricants

Two lubricants, one bentonite- and one polymer-based, were used in this study. Each was mixed with potable water at concentrations typically used in practice. The bentonite-based slurry was CETCO Hydraul-EZ, which is anecdotally the most commonly used pipe jacking lubricant in the UK and Ireland. The Hydraul-EZ slurry was mixed at 4% concentration and had a Marsh Funnel time of 50 seconds.

The polymer slurry utilised was MX Liquid Polymer produced by Mudtech Ltd. Although the mix ingredients are proprietary, its light tan colouring, like milky tea, may indicate that it contains an active polymer suspended in an oil/water emulsion. It is marketed as having a high gel strength and cuttings carrying capacity. For testing, a concentration of 0.5% was chosen and when mixed the resulting slurry was clear in colour with a Marsh Funnel time of 40 seconds.

3.4 Test soils

Two types of sand were used for testing, denoted as IGB sand and Banagher sand. IGB sand is a fine to medium white silica sand, while Banagher sand is the fraction passing a 2mm sieve of the concrete-making sand used in the TCD labs. It is medium to coarse, grey, sand with variable grain shapes.

The grading curves of these sands are shown in Figure 6 while the main properties are presented in Table 1.

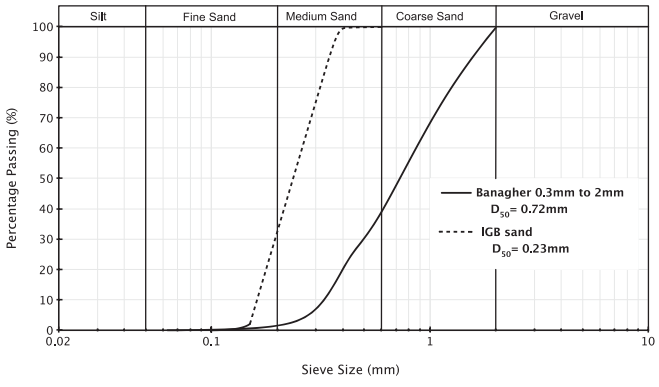


Figure 6. Particle size distribution of test sands.

Table 1. Test sand properties.

Sand	$\gamma_{d,min}$ (kN/m^3)	$\gamma_{d,max}$ (kN/m^3)	D_{10} (mm)	D_{50} (mm)	C_U
IGB	14.2	16.4	0.164	0.23	1.60
Banagher	14.1	17.3	0.33	0.72	2.64

3.5 Testing procedures

In order to model the various phases of the pipe jacking process, interface shear testing was carried out in four phases:

1. Unlubricated tests to calibrate the testing apparatus with direct shear testing carried out [7, 14].
2. Static lubricant injection, carried out to simulate the injection of lubricant before restarting a pipe jack following a stoppage.
3. Dynamic lubricant injection, carried out to simulate the injection of lubricant while a pipe jack is being advanced.
4. Constant pressure lubricant injection, carried out to simulate continuous lubrication during a pipe jack.

Results for phases 1 and 2 are discussed in this paper. The results of phases 3 and 4 are presented elsewhere [7].

3.6 Interpretation of results and application of corrections

From the results of the initial unlubricated tests, it was seen that the failure mode was the block slippage of the sand specimen over the rough concrete interface and failure in shear was accompanied by a reduction in the contact area along the interface, as shown in Figure 7.

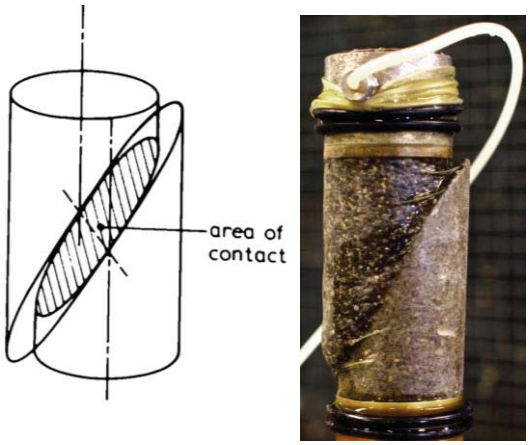


Figure 7. Schematic (left) and photograph (right) of sheared two-part triaxial specimen.

3.6.1 Non-linear deviator stress response

The deviator stress responses with strain observed during unlubricated tests (as shown in Figure 8 for example) were non-linear and proved difficult to interpret.

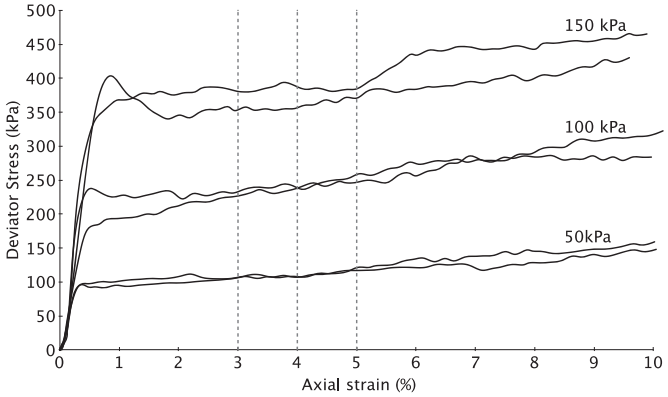


Figure 8. Deviator stress response with axial strain for unlubricated tests on IGB sand showing non-linear response.

Visual observations made during testing and finite element modelling (Figure 9) showed that shear displacement was concentrated in a narrow band adjacent to the interface, consistent with the behaviour expected if the specimen was shearing along the interface [15].

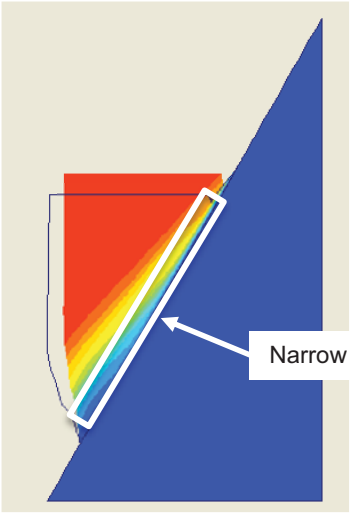


Figure 9. Total displacements in finite element model after imposition of 10% axial strain on IGB specimen shearing against rough concrete interface.

The Mohr circles of stress for a number of axial strains were produced and the resulting interpreted angles of interface friction were compared with the results of direct shear testing carried out to model the shearing behaviour of pipe jacking pipes against the test sands (Figure 10 and Figure 11).

The Mohr circles of stress and interpreted angles of interface friction resistance for IGB sand, assuming that the Mohr Coulomb failure condition controlled the behaviour of the specimen and that the shear strength envelope passed through the origin, are shown for 3%, 4% and 5% axial strain in Figure 12.

It was found that at 4% axial strain the interpreted angle of interface friction of 34.2° provided the best match with the expected constant volume angle of interface friction of IGB sand determined in direct shear of 34.0° degrees. Therefore, the principal stresses recorded at 4% axial strain are used to calculate the constant volume angle of interface friction for IGB sand in the novel triaxial testing apparatus.

Unfortunately, the same procedure did not provide a good match between the expected direct shear angle of interface friction and that determined in the triaxial compression apparatus for the Banagher sand, with a much lower angle of interface friction being interpreted along with an unexplained apparent cohesion intercept [7]. For this reason, it was decided that experimental results would be interpreted using deviator stress as a parameter for the comparison of interface shearing resistance, rather than the angle of interface shearing resistance which would be more conventionally used.

3.6.2 Corrections for changing contact area

As the soil specimen displaced relative to the concrete specimen, as shown in Figure 7, the contact area between the two changed. In order to correct for this it was assumed that

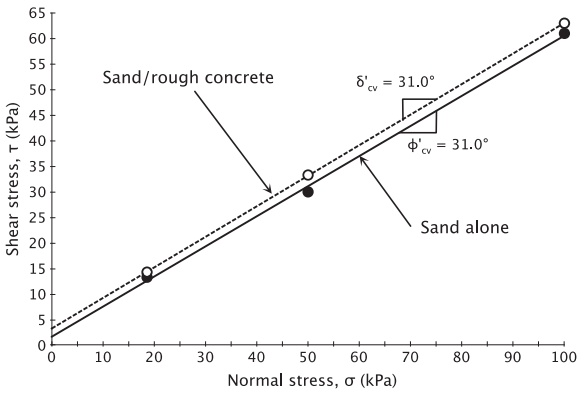


Figure 10. Direct shear testing results for IGB sand shearing internally and against a rough concrete interface.

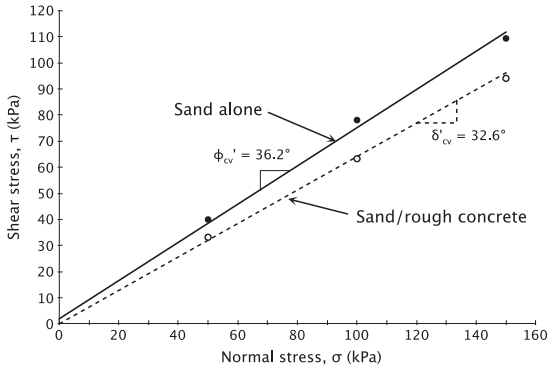


Figure 11. Direct shear testing results for Banagher sand shearing internally and against a rough concrete interface.

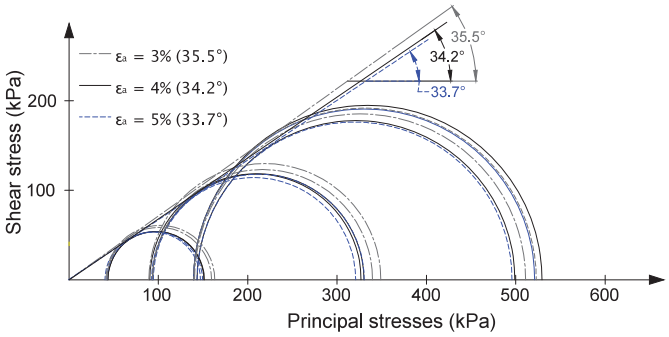


Figure 12. Mohr circles for triaxial tests with IGB sand and rough concrete showing stress at 3, 4 and 5% axial strain.

the final shear plane formed an elliptical shape [16]. The lengths of the major and minor axes, d_a and d_b, were measured after testing and the corrected area, A_C, was calculated as follows:

$$A_C = \frac{\pi}{4} d_a d_b \qquad (2)$$

From an initial circular cross section of diameter 38mm and area 1134.1mm^2, the lengths of the major and minor axes of typical failure surfaces at 10% axial strain were measured as d_a = 39mm and d_b = 34mm, giving a final area of 1071.7mm^2, i.e. a 5.5% reduction in contact area. This correction was applied linearly across the range of axial strain from the start to the end of the test, so that the contact area steadily

decreased from the known original area to the measured final area.

3.6.3 Corrections for membrane restraint

As the soil specimen translated relative to the preformed failure plane, the confining membrane was stretched significantly and in effect took up a portion of the load transmitted to the specimen by the loading ram. Therefore, it was necessary to correct for the restraint offered by the membrane as sliding took place. Dummy tests were performed on a 38mm diameter specimen made up of a rigid plaster base cut at 60° to the horizontal with soft Plasticine moulded to shape and used to make the specimen up to the correct height. To minimise friction along the preformed failure plane two sheets of thin polythene, each coated with a thick film of petroleum jelly, were used to separate the materials. It was observed that by taking these measures, friction between the plaster preformed failure plane and the Plasticine was reduced to negligible levels. Several interface friction tests were carried out in triaxial compression at cell pressure levels between 50 and 150 kPa. A single curve was then fitted to all the experimental data to give a membrane correction with strain, σ_m, as follows:

$$\sigma_m = 12.5 - 12.5 \times 0.825^{\varepsilon} \quad (3)$$

This correction was applied to all deviator stress responses before analysis.

3.7 Results

The test results presented below were derived following the application of area and membrane corrections, while deviator stress is quoted at 4% axial strain as specified in Section 3.6.1. The results are presented in terms of (i) deviator stress against strain and (ii) deviator stress ratio against normalised lubricant pressure. The deviator stress ratio is the ratio of the deviator stress obtained from the lubricated shearing divided by the average deviator stress response from unlubricated testing of the same sand. The normalised lubricant pressure is the pressure measured in the lubricant circuit (shown on the lower left of Figure 4) divided by the cell pressure within the triaxial cell. Lubricant pressures are measured at three instances:

1. The highest pressure achieved during the injection phase – denoted as the *highest injection pressure.*
2. The pressure at the injection port at the start of shearing, which was delayed until the pore pressure at the top of the specimen had dissipated to 10 kPa, – denoted as the *initial injection pressure.*
3. The pressure at the injection port at 4% axial strain, when the strength of the interface is measured – denoted as the *4% strain injection pressure.*

The results of four static injection tests where Hydraul-EZ slurry was injected into the interface between IGB sand and rough concrete prior to shearing are shown in Figure 13 and Figure 14, and results of six static injection tests where Hydraul-EZ slurry was injected into the interface between Banagher sand and rough concrete prior to shearing are shown in Figure 15 and Figure 16. The pore pressure at the top of the specimen was allowed to reach equilibrium with the pre-set back pressure prior to shearing commencing.

In each case it is seen that the deviator stress ratio reduces with increasing normalised lubricant pressure. The minimum deviator stress ratio is 0.53 with IGB sand and 0.06 with Banagher sand, i.e. a 47% and a 94% reduction in deviator stress ratio, respectively. Results for the injection of MX Polymer are not shown, however smaller magnitudes of effects were observed, i.e. a reduction of deviator stress ratio of 7% in IGB sand and 78% in Banagher sand.

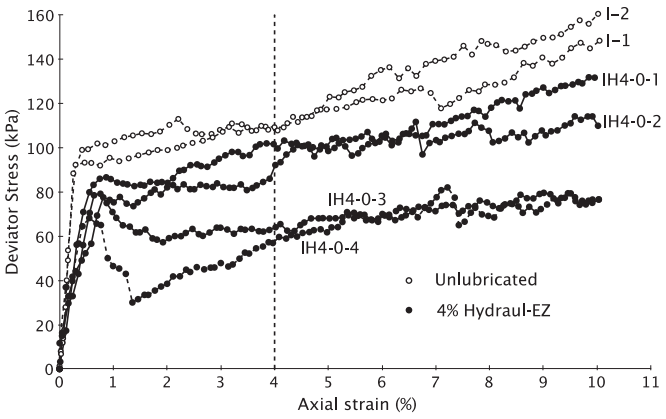


Figure 13. Deviator stress plot for testing where 4% Hydraul-EZ was injected into IGB sand prior to shearing.

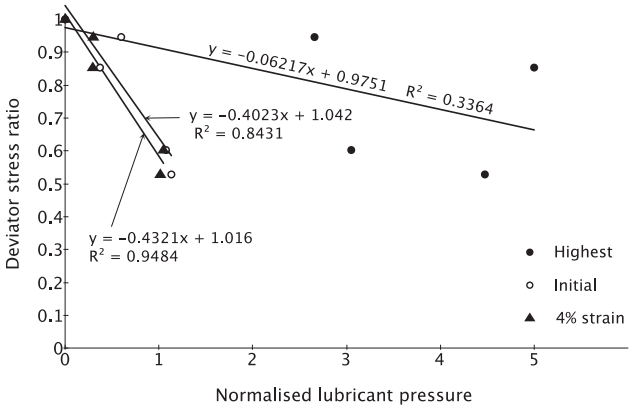


Figure 14. Deviator stress ratio against normalised lubricant pressure for tests where 4% Hydraul-EZ was injected into IGB sand.

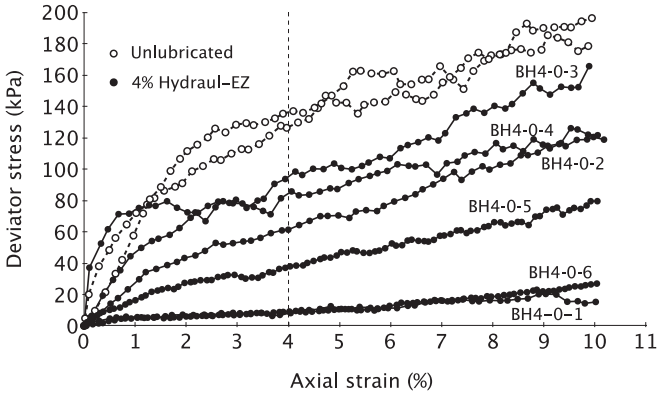


Figure 15. Deviator stress plot for testing where 4% Hydraul-EZ was injected into Banagher sand prior to shearing.

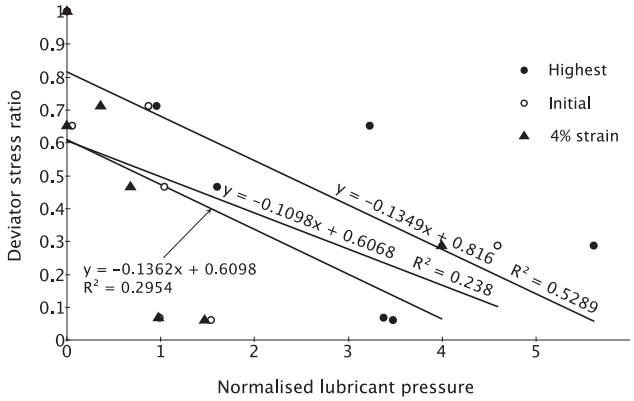


Figure 16 - Deviator stress ratio against normalised lubricant pressure for tests where 4% Hydraul-EZ was injected into Banagher sand.

3.8 Comments on results

In the static injection tests using IGB sand, reductions in the deviator stress ratio of 47% and 7% were observed with Hydraul-EZ and MX Polymer lubricants respectively. In the case of Banagher sand, the reductions of the deviator stress ratio obtained were 94% for Hydraul-EZ and 78% for MX Polymer. This showed that the bentonite-based Hydraul-EZ was the more effective lubricant in the case of both sand types and that the lubrication process worked more effectively within the Banagher sand than the IGB sand. Experimental reductions in skin friction resistance of up to 94% were achieved, which is in line with the magnitude of reductions observed in the field [1, 2]. Unfortunately it was not possible to explain the different responses between the two types of sand.

4 CONCLUSION

The results show that adequate pressurisation of the lubricant applied to the interface between the soil and the jacking pipes is required to bring about the magnitude of skin friction reductions observed in the field.

The proposed mechanism of action is that of effective stress reduction. The slurry blocks the pores in the soil, and with the pores blocked, the fluid pressure within the slurry is transferred to the soil skeleton, reducing the effective stress acting on the interface. Through the Mohr-Coulomb relationship, the shear stress is also reduced in proportion to the effective stress, since it is not considered that the angle of interface friction is altered to a significant extent by the presence of the slurry.

The ability of a particular lubricant to form a filter cake in the soil close to the pipe surface was shown to be beneficial in retaining an elevated pore pressure when the source injection pressure was reduced. The research demonstrates that, when designing for the use of pressurised lubricants in the field, close attention should be paid to the properties of the lubricant with regard to the formation of a filter cake and to the properties of the filter cake in the soil. This is an area in which further research is required, as it was not possible to explain the different response to lubricant injection observed in the two test sands.

The main conclusion and recommendation towards practice deriving from the research is that pipe jacking lubricants should be applied under controlled pressure rather than controlled volume to gain the maximum beneficial reduction in skin friction resistance.

ACKNOWLEDGMENTS

The Authors wish to acknowledge the support received from the Irish Research Council. The assistance of Martin Carney and Eoin Dunne in the Geotechnical Engineering laboratory at Trinity College Dublin is gratefully acknowledged, as is the helpful input received from Prof. Stephan Jefferis.

REFERENCES

[1] Pellet-Beaucour, A.-L. & Kastner, R. (2002), 'Experimental & analytical study of friction forces during microtunneling operations'. *Tunnelling and Underground Space Technology*, 17(1), pp. 83-97.

[2] Staheli, K. (2006), *Jacking Force Prediction: An Interface Friction Approach Based On Pipe Surface Roughness.* PhD thesis, Georgia Institute of Technology.

[3] McGillivray, C. (2009), *Lubrication mechanisms and their influence on interface friction during installation of subsurface pipes.* PhD thesis, Georgia Institute of Technology.

[4] Shou, K., Yen, J. & Liu, M. (2010), 'On the frictional property of lubricants and its impact on jacking force and soil-pipe interaction of pipe-jacking'. *Tunnelling and Underground Space Technology*, 25(4), pp. 469-477.

[5] Phelipot, A., Dias, D. & Kastner, R. (2003), 'Influence of overcut and lubrication during microtunneling', In: *ISTT International No-Dig 2003*, Los Angeles.

[6] McGillivray, C. & Frost, D. (2010), 'Influence of bentonite slurry on interface friction', In: *Characterization and Behavior of Interfaces - Proceedings of Research Symposium on Characterization and Behavior of Interfaces*, Atlanta, GA.

[7] Reilly, C. C. (2014), *The influence of lubricant slurries on skin friction resistance in pipe jacking.* PhD thesis, Trinity College Dublin.

[8] Borghi, F. X. (2006), *Soil conditioning for pipe-jacking and tunnelling.* PhD Thesis, University of Cambridge.

[9] Ulkan, A. (2013), 'Development in trenchless technologies at Herrenknecht', In: *GSTT 1st No Dig Berlin 2013*, Berlin. 2A-1-1 - 2A-1-6.

[10] Skempton, A. W. (1964), 'Long-term stability of clay slopes'. *Géotechnique*, 14(2), pp. 75-102.

[11] Chandler, R. J. (1966), 'The measurement of residual strength in triaxial compression'. *Géotechnique*, 16(3), pp. 181-186.

[12] Muir, A. J. (1971), *Effect of shear strength parameters on slope stability analyses in the Winnipeg area.* MSc thesis, University of Manitoba.

[13] Meehan, C., Tiwari, B., Brandon, T. & Duncan, J. (2011), 'Triaxial shear testing of polished slickensided surfaces'. *Landslides*, 8(4), pp. 449-458.

[14] Reilly, C. C. & Orr, T. L. L. (2012), 'Analysis of interface friction effects on microtunnel jacking forces in coarse-grained soils', In: *Bridge and Concrete Research in Ireland Conference. 6-7 September 2012.* , Dublin. 121-126.

[15] Uesugi, M., Kishida, H. & Tsubakihara, Y. (1988), 'Behaviour of sand particles in sand-steel friction'. *Soils and Foundations*, 28(1), pp. 107-118.

[16] La Rochelle, P., Leroueil, S., Trak, B., Blais-Leroux, L. & Tavenas, F. (1988), 'Observational approach to membrane and area corrections in triaxial tests', In: *Advanced Triaxial Testing of Soil and Rock, ASTM STP 977*, Philadelphia, PA.

A systematic review of common correlations between unconfined compressive strength and point load index for Dublin Calp Limestone

Patrick Casey[1], Marie Fleming[2]
[1]Geotechnical Group, Arup, Dublin, Ireland
[2]Geotechnical Group, Arup, Dublin, Ireland
email: patrick.casey@arup.com, marie.fleming@arup.com

ABSTRACT: The Calp formation covers a large part of central and eastern Ireland and is composed of inter-bedded Limestones, Mudstones and Shales of Carboniferous age. Difficulties can frequently be encountered in recovery of rock core samples suitable for unconfined compressive strength (UCS) testing due to fracturing of the rock resulting from folding and uplift of the formation and the weak nature of some rock layers. This has led to the adoption of UCS values predicted from point load index results in many civil engineering design problems. This paper sets out the results of a systematic review of measured UCS and point load index results from several hundred individual boreholes carried out across the Dublin region and an assessment of the suitability of commonly used UCS and point load index correlations is presented. The findings of this study have been further refined by carrying out point load index testing on the cut off ends of rock core arising from the preparation of rock core for UCS testing. On a number of large civil engineering projects point load tests have been carried out on the cut off ends of rock core arising from the preparation of rock core for UCS testing allowing direct analysis of the relationship between the results of the two tests to be undertaken. The compiled data demonstrates a poor correlation between UCS values and point load index test results from typical industry projects. The data shows that result from the limestone and mudstone sub-units have to be separated in order to use UCS-point load index correlations.

KEY WORDS: Uniaxial compressive strength; Point load Index; Calp Formation; Limestone; Mudstone.

1 INTRODUCTION

The point load and uniaxial compressive strength (UCS) tests are accecpted rock mechanics testing procedures. The point load index (Is_{50}) obtained from the point load test and UCS test results are widely used in designing surface and underground structures. The UCS test requires a sample to be prepared from a length of intact rock core however suitable sections of core are not always readily available for testing, particularly on smaller scale site investigation programmes. Where direct UCS data is not available for a project it is common practice to predict the UCS from Is_{50} results obtained on the project. Industry practice in Ireland has been to adopt a conversion factor of 21 to 24 to predict UCS values from Is_{50} measurements in Calp Limestone. This range is consistent with findings by other authors on Limestone within Ireland [1] outside of Ireland [2], [3] and is consistent with the suggested ISRM conversion factor of 20 to 25 [4].

It has been observed that there is a very wide scatter in both the Is_{50} and UCS results for the Calp Limestone and that UCS values predicted from Is_{50} using a conversion factor of 21 to 24 can vary widely from actual UCS results from nearby samples.

It was decided to investigate the scatter in the results obtained with the goals of determining a reason for this scatter and obtaining a higher level of confidence in the conversion factors being applied. This paper sets out the results of this investigation. The test methodology that was adopted in order to provide a large data set with both UCS and Is_{50} results from immediately adjacent pieces of rock core is described and the results are presented and discussed.

2 CALP LIMESTONE

The Calp limestone (also known as the Lucan Formation) was deposited during the Dinantian Epoch (approximately 325 to 363 million years ago) of the Carboniferous Period. The Geological Survey of Ireland (GSI) describe the Calp as an interbedded sequence of dark grey massive limestones, shaley limestones and massive mudstones and cherts. The Calp was deposited in a basinal and ramp environment in deeper water with limited fauna. The widespread presence of graded bedding suggests that much of the limestone was deposited by turbidity currents [5].

The main discontinuities within the Calp are in the form of the distinct bedding planes which lie between the limestone and mudstone beds as indicated on Figure 1 (down hole optical teliviewer image from Project D). The spacing of bedding planes range typically between 100 mm and 300 mm but may be thicker.

Due to the thick cover of glacial till overlying much of the Calp bedrock, very little information is available on faulting within the Calp but the overall fault pattern observed in the vicinity of Dublin indicates the predominance of strike directions NE-SW, with subordinate faults striking NNW-SSE and ENE-WSW to E-W [6].

The multi-layer sequence of beds with differing competence in strength (limestone, and mudstone beds) is susceptible to folding with related shearing along bedding planes coinciding with interfaces between materials of varying competence.

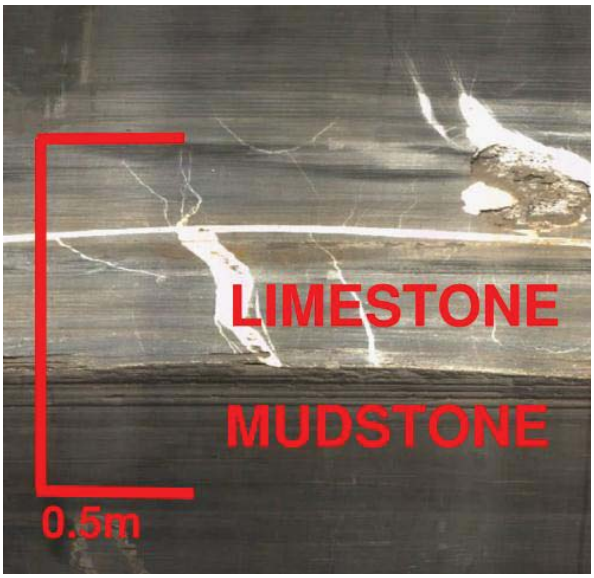


Figure 1. Clear bedding plane between Limestone and Mudstone within Calp

Exposures of the Calp in quarries show that faulting and folding within the rockmass can occur over short distances, <1.0m, as well as on a macro scale of many tens of meters.

Recovery of Calp limestone through conventional rock coring techniques is generally good although it has been observed that mudstone layers can disintegrate into black clay material along fault zones and in weathered zones. Further discontinuities in the form of orthogonal joint sets which are predominantly vertical to sub-vertical in relation to bedding, can result in poor core recovery when encountered during coring.

3 ROCK STRENGTH TESTS

3.1 Uniaxial compressive strength test

Specimens from drill cores are prepared by cutting them to the specified length and are thereafter grinded and measured. There are strict requirements on the flatness of the end surfaces in order to obtain an even load distribution across the sample. Recommended ratio of height/diameter of the specimens is between 2 and 3. The specimens are loaded axially up to failure and the UCS value calculated from the failure load.

3.2 Point load index test

The point load index test is performed by subjecting a rock specimen to an increasingly concentrated load until failure occurs by splitting the specimen. The concentrated load is applied through coaxial, truncated conical platens. The failure load is used to calculate the point load strength index.]. As the point load test can be carried out on irregular rock samples or on cores of different diameter the result must be corrected to the standard equivalent diameter of 50mm. This corrected number is referred to as the Is_{50} for the sample.

4 TEST METHODOLOGY

Previous studies on the prediction of UCS values from Is_{50} have made use of statistical analysis of large data bases of UCS and Is_{50} results. Generally these studies have used linear regression to obtain correlations between the results from the two tests.

At the outset of this study a similar assessment was applied to existing data sets from in house records however this resulted in a level of inaccuracy which was considered too great for rocks which were either considerably stronger or weaker than the mean rock strength. It was theorised that this inaccuracy may be as a result ofcomparing UCS and Is_{50} results from pieces of rock that are too distance from each other within the rock mass and that the natural variability of the Calp rock mass, even within a single borehole, meant that the UCS and Is_{50} results were not directly comparable. It was also acknowledged that the direction of the testing(parallel to or perpendicular to the axis of borehole) and the results obtained may also be influenced by the relationship between the test direction and the direction of natural bedding planes within the rock.

In an effort to control these variables it was decided to specify point load tests on the cut off pieces of rock produced when the UCS test samples were being trimmed with point load index tests being carried out both axially and diametrically.

5 RESULTS

Test results have been collated from a number of sites around Dublin and County Kildare. The full database contains over 3,700 individual Is_{50} results and over 600 UCS measurements. Within this database over 300 UCS measurements have corresponding Is_{50} measurements from the cut off pieces produced in UCS sample preparation.

The UCS measurements range from 1MN/m^2 to 200MN/m^2 with a numerical average of 55MN/m^2. Figure 2 shows the actual frequency of all UCS measurements for core from the Calp formation.

The Is_{50} measurements range from <1MN/m^2 to 12MN/m^2 with a numerical average of 3MN/m^2. Figure 2 shows the actual frequency of all Is_{50} measurements for samples from the Calp formation. The x axis in Figure 3 is truncated to 10MN/m^2 in order to have the same scale on all such plots within this paper. Only one Is_{50} result is > 10MN/m^2

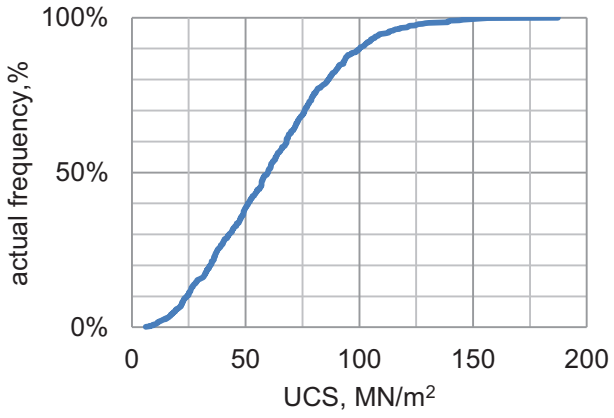


Figure 2. Actual frequency of all UCS measurements.

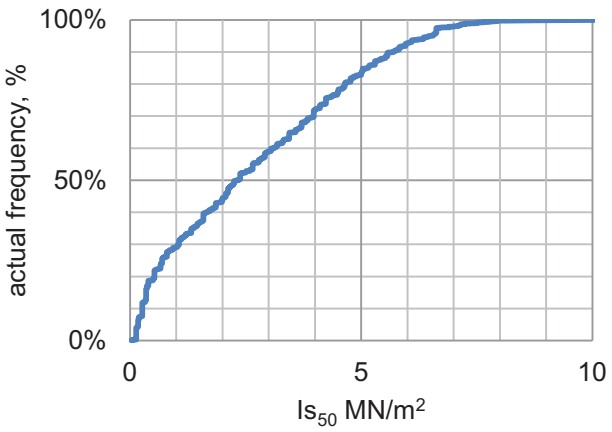


Figure 3. Actual frequency of all Is_{50} measurements.

The subset of Is_{50} measurements carried out on the UCS sample cut offs has been compared to the overall data set. Measurements within this subset range from <1MN/m^2 to 8MN/m^2, with a numerical average of 3MN/m^2.

Figure 4 presents the data where UCS and Is_{50} measurements have been recorded on adjacent pieces of rock. The ordinate on the x axis is the Is_{50} measurement on the cut off piece and the ordinate on the y axis is the UCS measurement from the main core sample in each case.

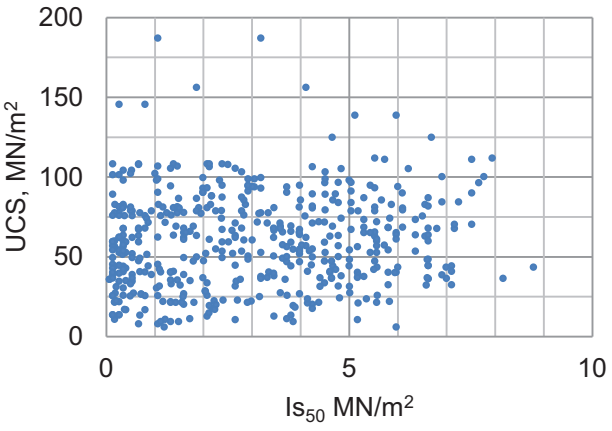


Figure 4. UCS and Is_{50} measurements on adjacent rock samples.

Figure 4 includes results for all samples taken within the Calp formation with no filtering for rock type applied. It is clear that there is no meaningful linear correlation to convert Is_{50} measurements to UCS values within the data in Figure 4.

Efforts have been made in recent times by site investigation contractors to improve the detail and accuracy of rock core logs in the Calp formation. Historically rock core from within the Calp formation has been simply described simply throughout as *Limestone.* Detailed core logs are now expected to clearly identify limestone and mudstone sub-units within the boreholes. This clear separation of Limestone and Mudstone within the core log allows for rock strengths to be assessed for each sub-unit.

Figures 5 and 6 shows the actual frequency of UCS and Is_{50} measurements from boreholes where the core logging carefully identified and recorded the separate Mudstone and Limestone units within the Calp. Data is presented form a single project (Project D) where considerable effort was undertaken by the contractor to log the Limestone and Mudstone sub-units within the core.

It should be noted that there were no UCS tests carried out on Mudstone samples on Project D and all the test results on Figure 4 are in fact from Limestone.

Two Is_{50} lines are plotted on Figure 6, one for the data set of results for results from Limstone and one for results from Mudstone. This data suggests that the Mudstone is, on average, 50% weaker than the Limestone.

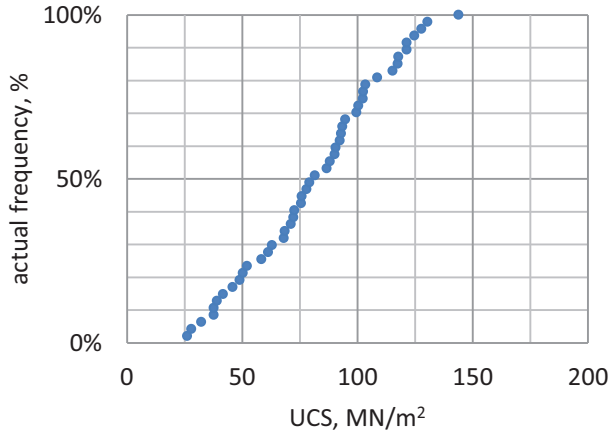


Figure 5. UCS measurements from Project D.

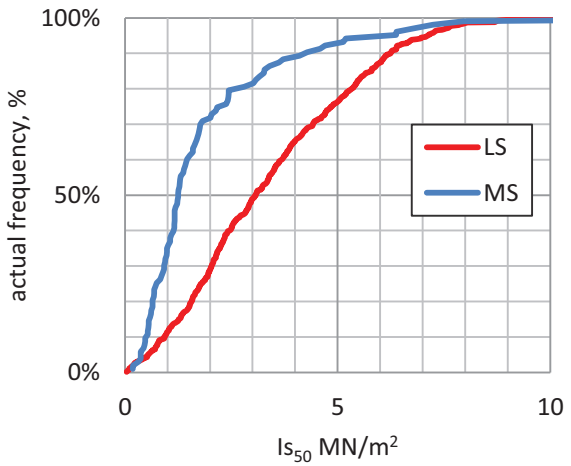


Figure 6. Is_{50} measurements mudstone (MS) and limestone (LS) samples from Project D.

Figure 7 presents the data from Project D where UCS and Is_{50} measurements have been recorded on adjacent pieces of Limestone.

Two lines are plotted on Figure 7, one representing UCS values predicted from Is_{50} measurements using a correlation factor of 21, (f = 21) and the second representing a correlation factor of 31, (f = 31). It can be seen from figure 6 that the

commonly used industry factor of 21 represents a lower bound of the actual UCS values for the Limestone. The data suggests that the f = 21 correlation will almost always under predict the UCS value for the Limestone. Using an Is_{50} measurement of $3MN/m^2$ as an example the UCS values predicted by the f = 21 correlation is almost 1/3 lower than the value predicted by the f = 31 correlation.

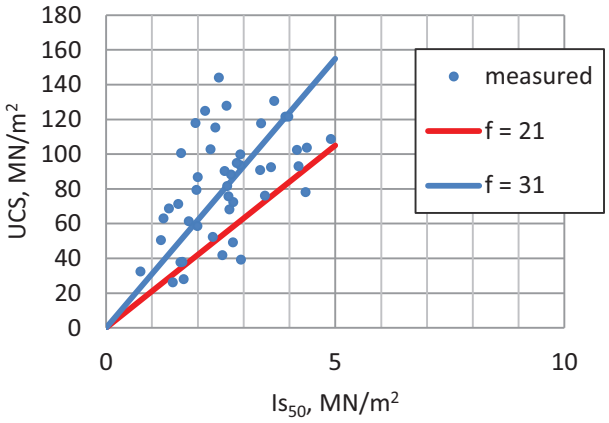


Figure 7. UCS and Is_{50} measurements on adjacent rock samples from Project D.

It should be noted that there are no UCS samples from rock which has been described as Mudstone within the data set on Project D. This means that there is little evidence to allow the f = 31correlation factor to be used for converting Is_{50} measurements to UCS values for Mudstone.

The absence of UCS values for the Mudstone may be as a result of the Mudstone being too weak to withstand the drilling process to allow suitable intact core to be recovered for testing. This theory is born out to some extent by the data in Figure 5 which shows that the Mudstone typically shows only half the strength recorded in the Limestone

The level of core logging detail achieved on Project D is not yet replicated across the industry. Figure 7 presents the data from another project, Project B, where UCS and Is_{50} measurements have again been recorded on adjacent pieces of rock. Figure 8 and 9 show the actual frequency of Is_{50} and UCS measurements recorded on this site

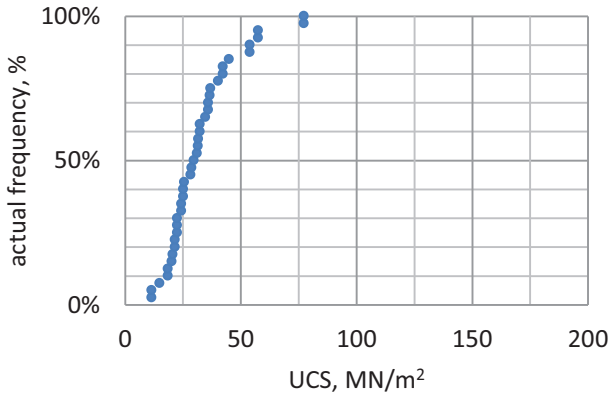


Figure 8. UCS measurements from Project B

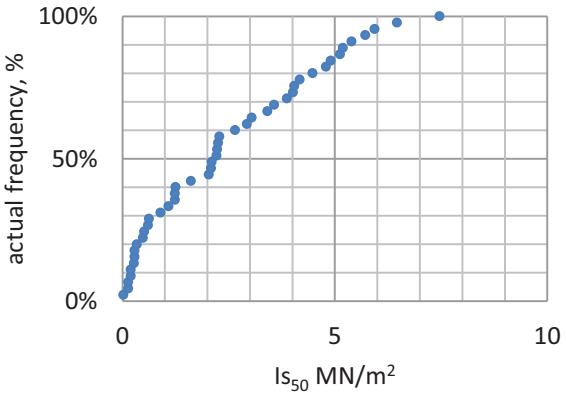


Figure 9. Is_{50} measurements from Project B

Figure 10 presents the data where UCS and Is_{50} measurements have been recorded on adjacent pieces of rock from UCS samples and the cut offs. For the purpose of comparison with the f = 21 and f = 31 correlations a 'best fit' line through the origin has been drawn for this data. The equation for this line is 'y = 9 x'.

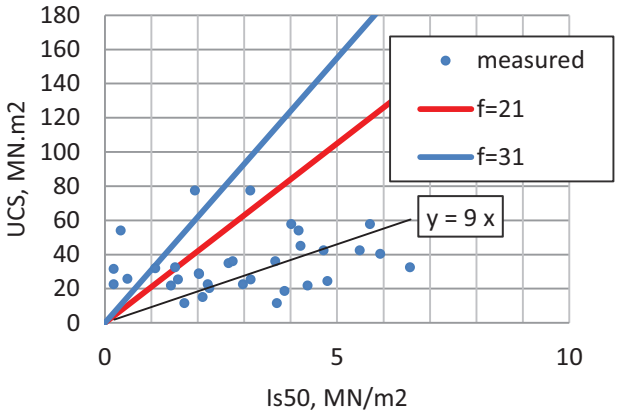


Figure 10. UCS and Is_{50} measurements on adjacent rock samples from Project B.

Corehole logs on Project B describe the rock as Limestone throughout. It is clear however that the data does not fit the general f = 21 correlation or the f = 31 correlation produced using the larger data set from Limestone in the Calp formation. The actual UCS measurements for the rock on this site are also lower than the normal range of strengths recorded for Limestone within the Calp formation. While this data set shows UCS values which are significantly lower than typical values from figure 2 or 5, Is_{50} values from the data are within the typical ranges from figure 3 and 6. This suggests an f correlation factor lower than the 21 or 31 values discussed in this paper.

One possible reason for this result is that part (or all) of the rock from the site has been incorrectly logged as Limestone when it should have been described as Mudstone. Figure 6

shows that where correctly logged the Mudstone sub-units within the Calp formation are normally much weaker that the Limestone sub-units.

6 DISCUSSION

The point load index tests used in compiling the data base were carried out, axially, diametrically and on irregular pieces of rock. Review of the Is_{50} measurements obtained shows that the results do not appear to be significantly affected by the direction of the test. While this study has made use of samples obtained from vertical and inclined boreholes, the micro and macro folding and reorientation of the Calp formation means that the axis of the borehole, (the reference by which the direction of the test is measured), is rarely perpendicular to the natural bedding planes within the Calp formation. It is considered that almost all of the point load tests, irrespective of the description, have been carried out at a random angle to the natural bedding planes and that strength trends based on the direction of the Is_{50} test are inconclusive.

In carrying out this work significant strength variations have been demonstrated between the Limestone and Mudstone sub-units within the Calp formation with average Is_{50} strengths in the Mudstone typically only half average strengths in the Limestone. The f = 31 correlation developed for the Limestone should not be used to predict UCS values from Is_{50} results on Mudstone samples without further study and justification.

Some of rock core from Project B has been interpreted to have been logged incorrectly. If it is considered that the majority of this data set could represent UCS and Is_{50} measurements on Mudstone then the data on figure 10 allows an f correlation to be developed for the Mudstone. Using simple linear regression with a zero intercept results in the trendline shown on figure 10 and an f = 9 correlation for Mudstone within the Calp formation.

Figure 6 suggests that the average Is_{50} value for the Mudstone is in the region of 1 to 2MN/m^2. An f = 9 correlation suggests an average UCS value for the Mudstone of 10 to 20MN/m^2, considerably weaker than the average UCS Value for the Limestone, 50 to 60MN/m^2.

Whilst correlations based on this type of linear regression are common in literature its application here can be questioned. Forcing the trendline to pass through zero completely underestimates the UCS for rocks with a low Is_{50}. Removing the requirement for a zero intercept gives a trendline with a correlation of for the Mudstone in Figure 10 of UCS = 2 x Is_{50} + 30. While this trend line deals with the unrealistic issue of the correlation predicting zero or very low UCS values at low Is_{50} values, it does so by having a lower limit on the UCS in built in the equation; 30MN/m^2. Adoption of such a limit is questionable and does not appear to be consistent with observed UCS results from Project B. Questions raised by both these issues, the forced zero intercept or the forced minimum UCS value, suggest that the UCS:Is_{50} correlation may not be linear at very low UCS values. Study of this point is outside the scope of this paper.

A key finding of this study is the reliance on accurate logging of the rock from the Calp formation prior to the application of any correlation factor. It has been shown that there can be significant variation within the Calp itself and proper logging of the rock core as Limestone or Mudstone is crucial in being able to properly interpret the rock strength tests.

Using a correlation factor to predict the UCS value should only be done in the full knowledge of the ultimate engineering application of the UCS values. This also applies when selecting any design parameter from a dataset which has a wide scatter of results. In selecting a UCS value equal to the numerical average value, or using the f = 31 correlation which effectively equates to the numerical average, the engineer is accepting that fully 50% of the material to be encountered will be weaker than allowed for in their design. This level of variation in a material parameter is not accounted for by the use of material partial factors in design calculations and, as with all geotechnical design, care should be exercised in selecting design parameters from data sets.

7 CONCLUSION

Based on the datasets analysed, it has been demonstrated that point load test results can be used to predict the UCS value for the Limestone sub-unit of the Calp formation. This study suggests that commonly used correlations of 21 – 24 will generally under predict the UCS value and that a correlation factor of 31 may better predict the average UCS value based on UCS test results and Is_{50} results from tests carried out on the cut off ends produced in sample preparation.

The inability of linear correlations to produce satisfactory UCS results at very low strengths suggests that the relationship may not be linear at very low strengths. Along with this there is insufficient data available to verify any correlation factor to convert Is_{50} results to UCS values for Mudstone. There is some data that could suggest a correlation factor for Mudstone as low as 10 and while more work is required in this area there is evidence that the correlation factors for Limestone and Mudstone are significantly different. This factor is critical when trying to assess results in historical data sets which may not differentiate between tests on Limestone and Mudstone.

Future studies which focus on producing a significant data set of results for the Mudstone unit will help in determining an accurate correlation factor for that sub-unit. Such work may also investigate if the difference between the f = 21 – 24 and f = 31 correlations actually results from the effect of averaging results and correlations across the two rock types.

The reliability of using a correlation factor to convert Is_{50} results to UCS values relies on the proper description of the rock core and the linking of Is_{50} measurements to either Limestone or Mudstone.

Thorough logging of recovered Calp rock core has been highlighted as essential in understanding the heterogeneity of the rockmass, and subsequent strength variations.

ACKNOWLEDGMENTS

The author would like to acknowledge the work done by IGSL in improving the level of detail provided on Calp rock core logs and Brian Byrne of IT Carlow for providing the results from undergraduate work in this area.

REFERENCES

[1] Walsh, K. (2011), *An Investigation into the Correlation between the Point Load Index and Uniaxial Compressive Strength,* BEng Thesis, Institute of Technology, Carlow, Ireland.

[2] Kahraman, S., (2001) Evaluation of simple methods for assessing the uniaxial compressive strength of rock, *International Journal of Rock Mechanics and Mining Sciences* 38;981-994.

[3] Bieniawski, Z., (1974) Estimating the strength of rock materials, *Journal of the South African Institute of Mining and Metallurgy*;312-320.

[4] ASTM D 5731-08, Standard Test Method for Determination of the Point Load Strength Index of Rocks and Application to Rock Strength Classifications, 2008.

[5] McConnell, B., Philcox,M. and Geraghty, M.(2001) Geology of Meath A geological description to accompany the bedrock geology 1:100. 000 scale map series, Sheet 13, Meath, Geological Survey of Ireland.

[6] Nolan, S.C. (1986) *The Carboniferous geology of the Dublin area*. Unpublished PhD Thesis, University of Dublin.

Some geotechnical characteristics of a soft soil deposit along the Foyle Valley

Paul Quigley[1], Mike Long[2], Sergio Solera[3], Dan Raynor[3] and Corrado Ruta[3]
[1]Arup, 50 Ringsend Road, Dublin 4, Ireland
[2]University College Dublin, Ireland
[3]Arup, 4 Pierhead Street, Capital Waterside, Cardiff, CF10 4QP UK
email: paul.quigley@arup.com, mike.long@ucd.ie, sergio.a.solera@googlemail.com,
dan.raynor@arup.com, corrado.ruta@arup.com

ABSTRACT: The proposed A5 Western Transport Corridor in Northern Ireland is approximately 85 km long and runs between the village of New Buildings and the border with the Republic of Ireland south of Aughnacloy. A section of the proposed route runs adjacent to the River Foyle where the ground conditions consist of very soft, compressible silts with occasional peat layers. There is some evidence to suggest that the silts are structured which is uncommon in Ireland. Staged construction using vertical drains and high strength geotextiles is being considered for the construction of high embankments. Previous ground investigation data suggested that the silts have very low undrained shear strengths. A supplementary ground investigation was carried out to further define the soil characteristics. Two cluster areas of boreholes with piston samples, shear vanes, cone penetration tests and piezoball tests were carried out to compare measurements. The data suggest that sample disturbance by traditional ground investigation methods significantly affects the strength measurement of the soil. Good correlations between strength measurements from piezoball, CPT pore water measurements and laboratory testing on piston samples were established.

KEY WORDS: Undrained shear strength, piezoball, CPT.

1 INTRODUCTION

Arup Atkins Joint Venture working as designers for the joint venture Balfour Beatty, Bam and McCann is developing the detailed design of the A5 Western Transport Corridor between Strabane and New Buildings in Northern Ireland. An extensive deposit of soft ground is located in the flood plain of the River Foyle and the River Glenmornan (Figure 1). Previous ground investigations suggested the presence of very soft ground. Cone penetration tests (CPT) recorded end resistances of close to zero. An additional ground investigation was commissioned to investigate the soft deposits more closely and to validate the preliminary design for the area. Two clusters of boreholes with piston samples, shear vanes, CPT and piezoball tests were carried out to compare measurements. The two cluster areas are situated either side of the River Glenmornan which flows into the nearby River Foyle.

2 GEOLOGY

The soft soils are described as post glacial Holocene deposits. The Foyle Valley would have been flooded by the sea during the early Holocene times as sea rise from the melting continental ice sheets outpaced isostatic rise of the land. Initially during this phase there was a phase of peat formation across the valley floor. By mid Holocene times (6000yrs BP) eustatic sea level rise was largely complete but isostatic uplift of the land continued, resulting in a fall in sea level by 6 to 8m. This uplift would have shrunk the Foyle Estuary to its present configuration with peat formation succeeding the estuarine deposits in places. The uplift is likely to have resulted in a change in groundwater conditions from a saline environment to a freshwater environment, resulting in a reduction of salt ions in the soil matrix.

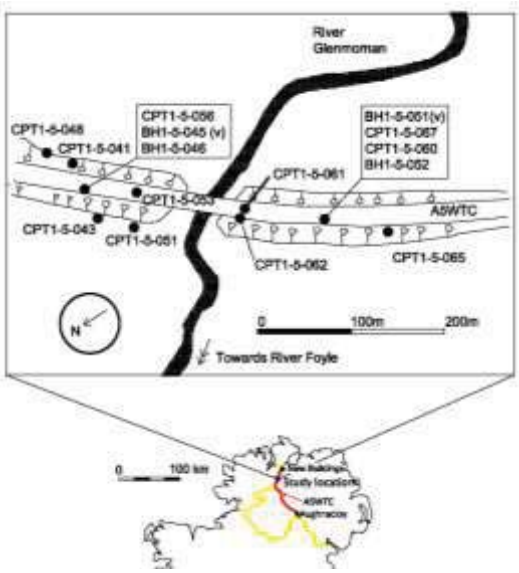


Figure 1. Site location and selected ground investigation locations.

3 MATERIAL PROPERTIES

The general stratification consists of topsoil with organic matter over 3 – 4m of very compressible silt over 3 – 6m of silt over glacial till. Groundwater was recorded typically 1 – 1.5m below existing ground level and the measurements suggest that a hydrostatic profile is present.

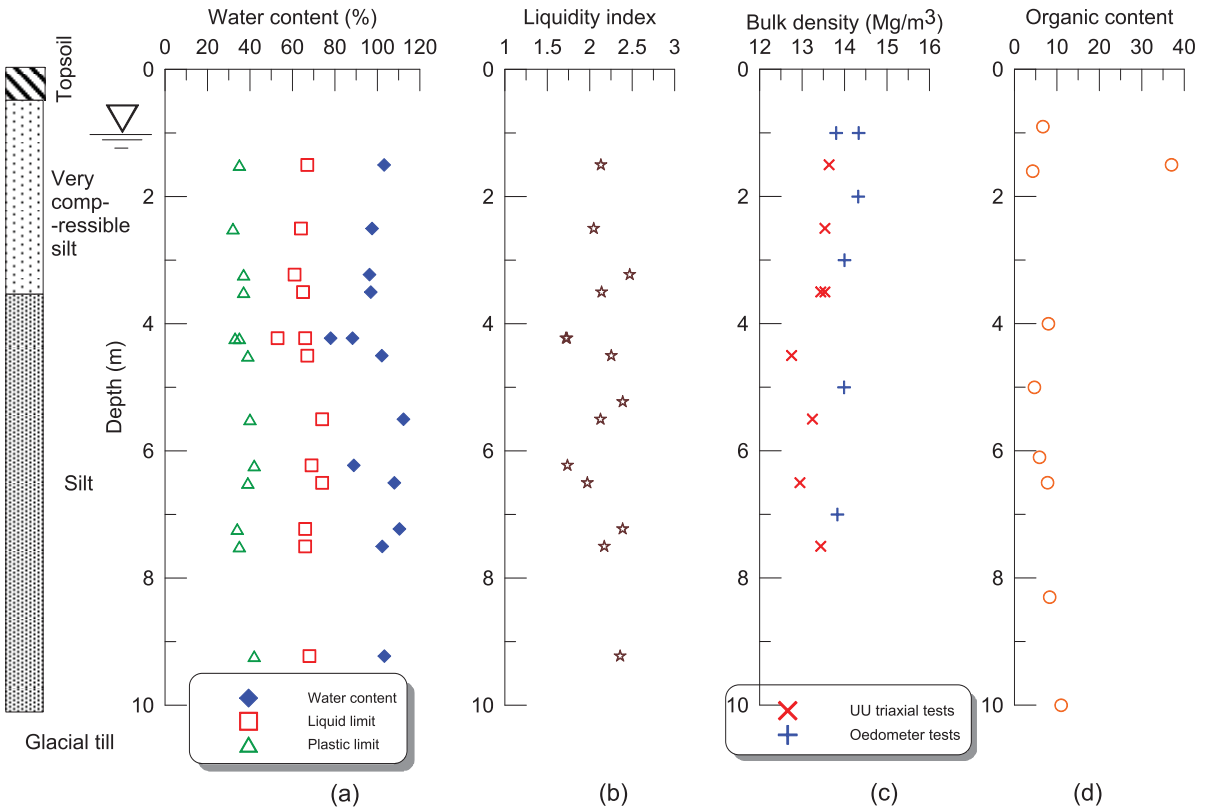


Figure 2 Soil indices (a), liquidity index (b) bulk density (c) and organic content (d) versus depth

3.1 Index tests

The distribution of moisture content (w_N), organic content and plasticity indices with depth is shown on Figures 2. The natural moisture content is considerably greater than the liquid limit (w_L) which is indicative of a structured soil or a slightly cemented soil. During the liquid limit test the soil is remoulded, destroying the structure between the grains and reducing the void space. When water is added it no longer occupies the larger void space in the structured soil and the corresponding liquid limit is lower than the natural moisture content. Similar results have been encountered in other structured soils such as in Canada, Sweden and calcareous deposits in Ireland. The organic content (measured using the total organic carbon method) varies between 3 and 7% and averages 5% through the deposit.

The moisture content is relatively consistent at about 100 – 110% with depth. This is not typical of a normally consolidated soil where the moisture content would be expected to decrease slightly with depth. Most of the data plots as a silt below the A line (Figure 3) although the structured nature of the soil suggests that classification based on liquid limit and plasticity index in isolation of the moisture content should be considered with caution. The particle size distribution curves are shown on Figure 4 and indicate a similar grading throughout the soft deposit. The proportions of clay and sand is pretty limited (<10% of either).

3.2 Bulk density

The bulk density results shown on Figure 2 (b) are taken from oedometer and triaxial results. The exact depth of the specimens was not reported on the test report, with only the depth ranges within the piston sample tubes from which the specimen was taken recorded.

The data on Figure 2 assumes that the depth corresponds to the midpoint in the piston sample. It is noted that differing bulk density values are measured between the oedometer and triaxial measurements from BH1-5-046 with the triaxial measurements being about 0.5 – 1.2 kN/m^3 less than the corresponding oedometer measurements. The results would be expected to be more closely aligned. The difference may be due to densification during the installation of the 75mm diameter oedometer ring over the sample. The triaxial samples were extruded directly from the piston tube and were not trimmed further. Variations in strength measurements between the sampling techniques are discussed later.

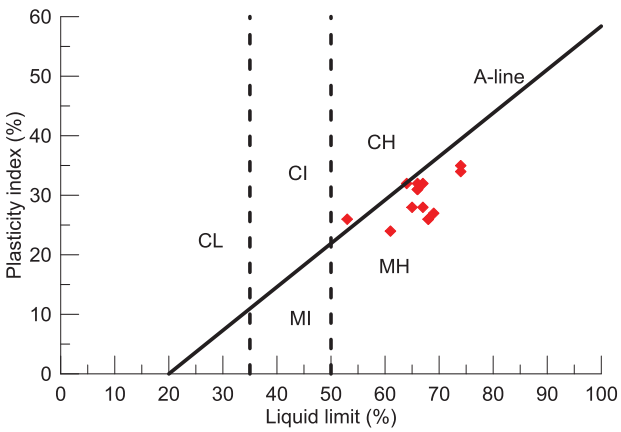


Figure 3. Classification chart

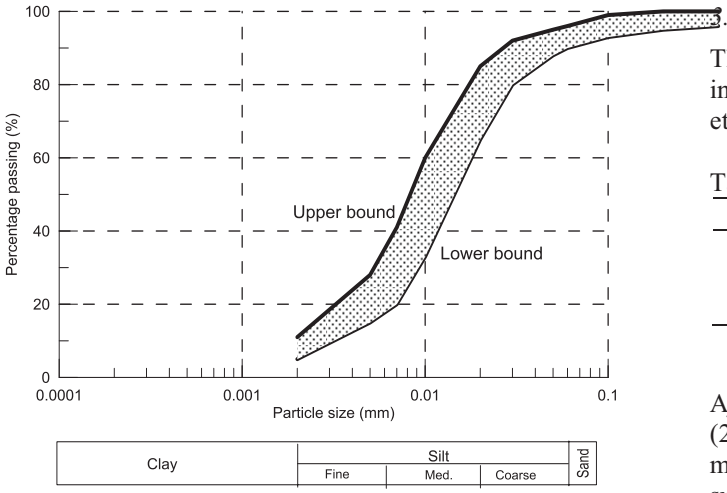


Figure 4. Particle size distribution

3.3 Consolidation tests

A series of oedometer tests (75mm diameter) were carried out on specimens from piston samples. The stress versus voids ratio (e_0), Janbu (1963) modulus (M) versus stress and coefficient of consolidation (c_v) versus stress graphs are shown on Figure 5.

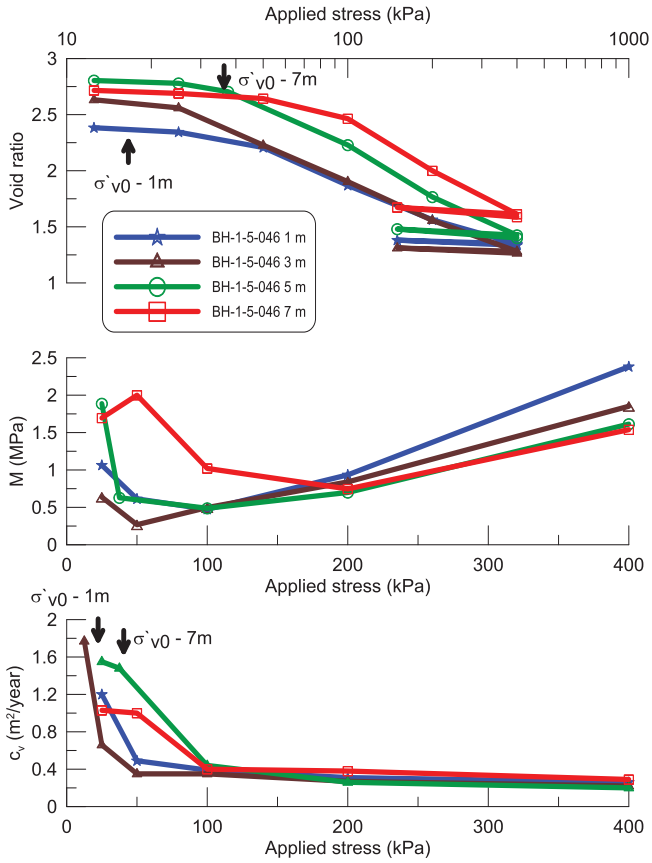


Figure 5. Consolidation test results at BH1-5-046

The coefficient of consolidation (c_v) values indicate that the values decrease significantly as the stress approaches post yield stress and continue to decrease slightly with increasing stress.

3.4 Compression indices

There are numerous correlations between the compression index (C_C) and various index properties for the soils (McCabe et al., 2014) and a limited number are outlined in Table 1.

Table 1. Some relationships between index parameters and C_C

Equation	Reference
$C_C = 0.5269e_0 - 0.2117$	Nath and DeDalal (2004)
$C_C = w_N/100$	Mesri and Ajlouni (2007)
$C_C = 0.0092(w_L - 0.13)$	Mayne (1980)

The relationship between C_C and w_N proposed by Mesri and Ajlouni (2007) was developed for peat but McCabe et al. (2014) show a reasonable correlation for Irish silts with a moisture content greater than 60%. The data in Figure 6 suggests that there is a reasonable correlation between water content and C_C, assuming that the soils are saturated and the specific gravity is constant. The Nath and DeDalal (2004) prediction is plotted assuming that:

$$w_N = \frac{G_s}{e} \quad (1)$$

where G_s is the specific gravity of the soil, which is assumed to be 2.65. The relationship proposed by Mayne (1980) based on the liquid limit significantly underpredicts C_C which is understandable considering the deconstruction of the soil structure during the liquid limit test. The data also suggests that the ratio of the compression index to the recompression index (C_C/C_S) value typically ranges from 8 to 10.

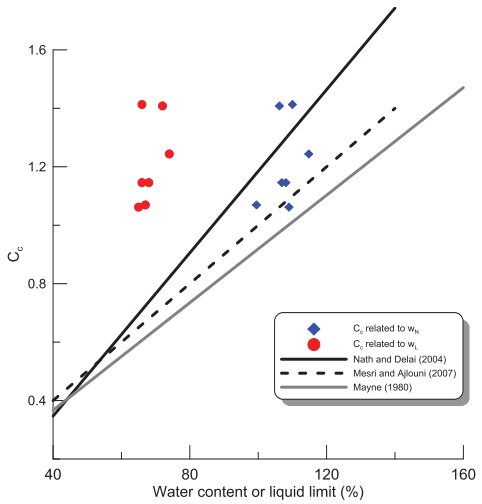


Figure 6. Comparison between Cc and soil indices

4 YIELD STRESS

For fine grained soils the in situ stress is usually defined in terms of the Overconsolidation Ratio (OCR), where the OCR is defined as the ratio of the maximum previous effective consolidation stress and the present effective overburden stress. For mechanically overconsolidated soils where the only change has been the removal of the overburden stress, this definition is appropriate. However, for cemented and (or) aged soils, the OCR may represent the ratio of the yield stress and the present effective overburden stress. The yield stress

will depend on the direction and type of loading (Robertson, 2009).

4.1 Laboratory methods

A number of methods were used to estimate the yield stress of the soil. Specimens from thin walled piston samples were tested in oedometer and the results were interpreted using a variety of methods. The traditional Casagrande consolidation plots suggested that the soil was lightly overconsolidated with a preoverburden stress (which is equal to the yield stress less the in situ effective stress) of 5 – 10kPa.

4.2 Field methods

Kulhawy and Mayne (1990) proposed estimating the preconsolidation or yield stress (σ'_p) from CPT measurements:

$$\sigma'_p = k(q_t - \sigma_{v0}) \quad (2)$$

where k is the preconsolidation cone factor, q_t is the corrected cone tip resistance and σ_{v0} is the total overburden stress. An average value of $k = 0.33$ with an expected range of 0.2 to 0.5 is commonly used. Robertson (2009) reports that the estimate is not strongly influenced by soil sensitivity.

The end resistances at the site were too low to be reliably used in the yield stress estimate. The piezoball end resistance was used in equation 3 to develop a reasonable correlation with the yield stress estimated from the oedometer tests (Figure 7) using the following equation:

$$\sigma'_p = k_{pb}(q_{ball} - \sigma_{v0}) \quad (3)$$

where k_{pb} is a factor relating to the piezoball and q_{ball} is the piezoball net end resistance.

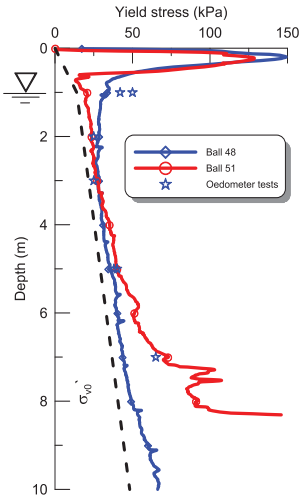


Figure 7 Correlation between laboratory and piezoball estimates of yield stress.

As the contact area of the piezoball is 10 times the area of a cone (100cm^2 versus 10cm^2) and mobilises a higher resistance than the CPT the k_{pb} factor is significantly lower than the k factor. The influence of the total overburden stress is also reduced as the ball resistance is significantly higher than the CPT end resistance. Good agreement was found between the consolidation tests and the piezoball tests using a k_{pb} factor of 0.018.

5 UNDRAINED SHEAR STRENGTH

5.1 Cone penetration tests

The end resistances in many of the CPTs were very low and close to zero. This may be due to temperature effects (and resulting zero load drift) as described by Boylan et al. (2008). The undrained shear strengths could not be reliably measured by the usual N_k or N_{kt} methods. The excess pore water pressure was used to estimate the undrained shear strength using the relationship:

$$s_u = \frac{\Delta u}{N_{\Delta u}} \quad (4)$$

where $\Delta u = u_2 - u_0$ and $N_{\Delta U}$ is a correction factor usually varying between 4 and 10 (Robertson and Cabal, 2010). A value of 8 is assumed for this project which is towards the conservative end of the scale and recommended by Karlsrud et al. (2005). Bihs et al. (2010) also found good correlation with this value for the Limerick Tunnel road.

5.2 Piezoball methods

Very low CPT end resistances were anticipated and piezoball tests were used to try to determine the undrained shear strength profile (Figure 8). The piezoball consists of a spherical ball threaded onto the load cell of the piezocone. The advantages of the piezoball are:

- The cross sectional areas is 100 cm^2 compared to 10cm^2 on a regular CPT. Consequently the load cell in the piezocone picks up much more load from very soft layers and the resolution is much better.
- The sphere does not deviate significantly if it hits organic matter such as twigs or cobbles, unlike a T – bar.
- Pore water pressure sensors can be placed in multiple locations.
- Theoretical solutions exist for inorganic deposits. Details on correlations used in Irish soils are described by Long et al. (2014).

The piezoball is pushed into the ground at the same rate as the CPTU (2 cm/sec.) and readings are taken of the penetration resistance (q_c) and the pore pressure generated (u). Net resistance (q_{ball}) is then calculated using the following equation (Chung and Randolph, 2004):

$$q_{ball} = q_c - [\sigma_{v0} - (1 - a)u_0]\frac{A_s}{A_p} \quad (5)$$

where a is a cone factor for correcting out of balance pore pressure effects, u_0 is the hydrostatic pore pressure and A_s/A_p is the ratio of the cross sectional area of the shaft to the projected area of the penetrometer. Often, this correction from q_c to q_{ball} is so small that there is little need to apply it. In cases where the pore pressure and overburden effects are large, such as in offshore conditions, it is necessary to apply the correction. Subsequently undrained shear strength can be determined using:

$$s_u = \frac{q_{ball}}{N_{ball}} \quad (6)$$

Good agreement was found between the undrained shear strength estimated from the piezoball (using N_{ball} =12 which is in the typical range for soft, cohesive soils) and CPT undrained shear strengths based on the pore water pressure (Figure 9). The data suggests that the undrained shear strength may approximate $0.5\sigma'_{v0}$ for triaxial compression.

The data shows two trends north and south of the River Glenmornan (Figure 9). North of the river the CPT profile shows very low shear strengths over the initial 2 – 3m. This is partly due to the inability of the piezocone to generate significant excess pore water pressure. The UU triaxial results from piston samples indicate much higher undrained shear strengths. South of the river the piezocone pore water pressure data close to the river is unsatisfactory as there appears to be saturation issues with the piezocone.

5.3 *Unconsolidated Undrained triaxial results*

Samples were taken using piston samples and U4/U100 samples. The data suggests that the U4/U100 samples are densified during the sampling process (Figure 10a). There is a marked difference between the strength measurements in the U4 samples and the piston samples in the upper 4m (Figure 10b). Long (2006) reported similar findings on other deposits in Ireland. It would seem prudent to disregard the shear strength measurements obtained from U4/U100 samples.

5.4 *Field vane results*

Figure 11 shows the variation in triaxial compression and the field vane results for the A5 site. The strength measurements are lower than recorded from the piezoball and triaxial results. Long and O'Riordan (2001) reviewed the operational field strength of the soft clays at the Athlone Bypass and concluded that the field vane strength underestimates the operational strength of the clays due to a combination of anisotropic and vane insertion disturbance effects.

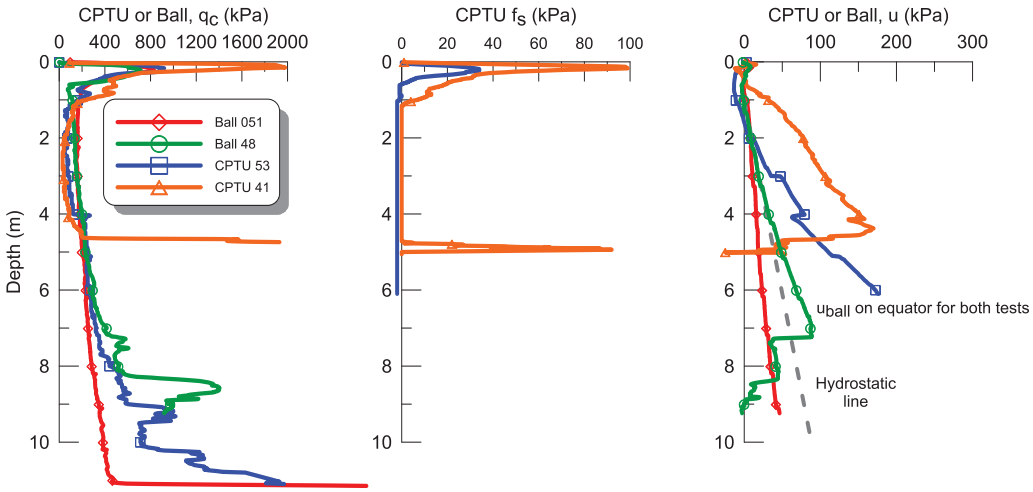


Figure 8 CPT and piezoball north of River Glenmornan

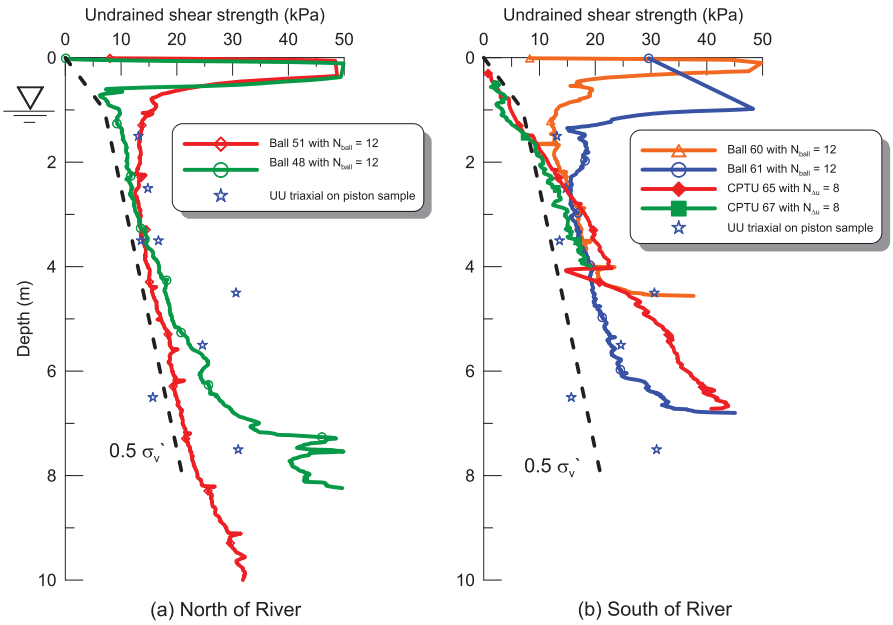


Figure 9 Undrained shear strength profiles north and south of the River Glenmornan

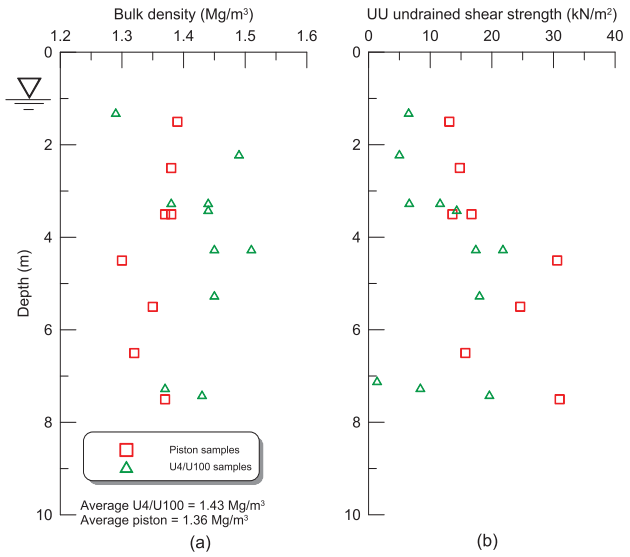


Figure 10 Variance in bulk density and strength with sampling technique

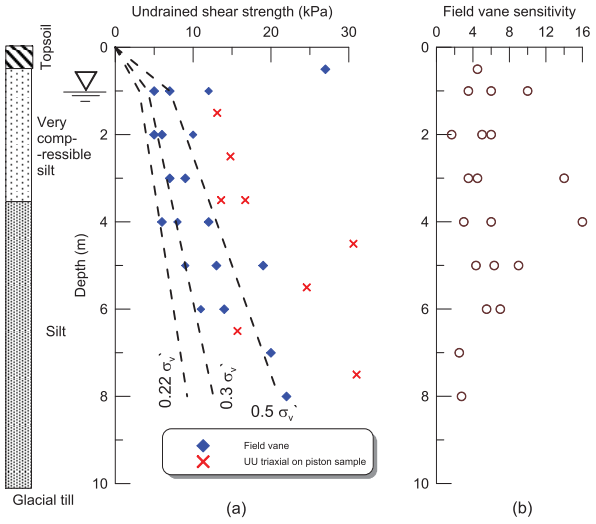


Figure 11 Shear vane results

6 CONCLUSIONS

(i) Soft soils present along the Foyle Valley appear to be structured which is uncommon in Ireland.

(ii) These soils are particularly sensitive to sample disturbance and U4/U100 samples should not be relied upon.

(iii) The compression index should be estimated using relationships based on water content or voids ratio rather than the liquid limit for this soft sensitive deposit.

(iv) A good correlation between the piezoball data and oedometers results for the yield stress of the soil was established for this site.

(v) Very low strength measurements were recorded. Good agreement was found between the triaxial results on piston samples and piezoball measurements. Good agreement was also found by correlating the excess pore water pressure during the CPT and the undrained shear strength from 3m below ground level.

(vi) Field shear vane tests measurements are not in agreement with piezoball, CPT and triaxial results, suggesting that soil disturbance during the installation of the vane may have occurred.

(vii) Further work should be carried out to establish the relationship between the gain in undrained shear strength and increases in effective stress, particularly at and just above the yield stress of the soil.

ACKNOWLEDGMENTS

The authors would like to thank the Roads Service of Northern Ireland and Balfour Beatty, Bam and McCann joint venture for permission to publish this paper. The opinions and conclusions in this paper are the authors' own. The authors would like to thank their colleagues for their contributions to this paper and in particular Aled Phillips, Flavia Cappelletti and Adrian Collings (all Arup). The authors are grateful to Darren Ward (In Situ SI) who arranged for the piezoball tests to be carried out.

REFERENCES

[1] Bihs, A., Long, M., Marchetti, D. and Ward, D. (2010), 'Interpretation of CPTU and SDMT in organic, Irish soils'. Proceedings of 2nd International Symposium on Cone Penetration Testing, Huntington Beach, CA, USA, May 2010.

[2] Boylan, N., Mathijssen, F.A.J.M., Long, M. and Molenkamp, F., (2008), 'Accuracy of Piezocone Testing in Organic Soils', 11th Baltic Sea Geotechnical Conference, Gdansk, Poland.

[3] Chung, S.F. and Randolph, M.F., (2004), 'Penetration resistances in soft clay for different shaped penetrometers', 2nd International Conference on Geotechnical and Geophysical Site Characterisation, ISC'2. Millpress, Porto, pp. 671-677

[4] Janbu, N. (1963), 'Soil compressibility as determined by oedometer and triaxial tests', Proc. ECSMFE, Wiesbaden, 1: 19-25.

[5] Karlsrud, K., Lunne, T., Kort, D.A. and Strandvik, S., (2005), 'CPTU correlations for clays', Proc. 16th International Conference on Soil Mechanics and Geotechnical Engineering, Osaka, pp. 693-702.

[6] Kulhawy, F.H. and Mayne, P.H. (1990), 'Manual on estimating soil properties for foundation design', Electric Power Research Institute, Palo Alto, USA, Report EL-6800.

[7] Long, M. (2006), 'Sample disturbance effects on medium plasticity clay/silt', ICE Geotechnical Engineering, April 2006 pp. 99-111.

[8] Long, M. M. & O'Riordan (2001), 'Field behaviour of very soft clays at the Athlone embankments', Géotechnique Vol. 51, No. 4, p.293-309.

[9] Long, M., Colreavy, C., Ward, D. and Quigley, P. (2014), 'Piezoball tests in soft Irish clays', Proceedings CPT14, May 2014, Las Vegas, USA.

[10] Mayne, P.W. (1980), 'Cam-Clay predictions of undrained shear strength', Journal of the Geotechnical Engineering Division, ASCE 106(GT11): 1219-124.

[11] McCabe, B.A., Sheil, B.B., Buggy, F.J., Long, M.M. and Farrell, E.R. (2014), 'Empirical correlations for the compression index of Irish soft soils', Paper in preparation for ICE Geotechnical Engineering.

[12] Mesri, G. and Ajlouni, M. (2007), 'Engineering properties of fibrous peats', Journal of the Geotechnical Engineering Division ASCE 133(7): 850-866.

[13] Nath, A. and DeDalal, S.S. (2004), 'The role of Plasticity Index in predicting compression behaviour of clays', EJGE http://ejge.com/2004/Ppr0466/Ppr0466.htm

[14] Robertson, P.K. (2009), 'Interpretation of cone penetration tests – a unified approach', Canadian Geotechnical Journal, Vol. 46, pp 1337 – 1355 (2009).

[15] Robertson, P.K. and Cabal, K.L. (2010), 'Guide to Cone Penetration Testing for Geotechnical Engineering', Gregg Drilling and Testing Inc. 4th Ed. July 2010.

Implications of geometrical variations on the pull-out capacity of plate anchors

Soroosh Jalilvand[1], Kenneth Gavin[2], Paul Doherty[3]

[1]School of Civil, Structural and Environmental Engineering, University College Dublin
[2]School of Civil, Structural and Environmental Engineering, University College Dublin
[3]School of Civil, Structural and Environmental Engineering, University College Dublin

Emails: soroosh.jalilvand@ucdconnect.ie, kenneth.gavin@ucd.ie, paul.doherty@ucd.ie

ABSTRACT: The growing interest in the wind energy has led to the development of large offshore wind farms. The demand for locating these developments in deep waters and in locations visually inaccessible from urban centres highlights the need for reliable foundation systems. In deep water (> 60 m), floating offshore platforms become an economically viable alternative. A range of mooring systems can be used to tether floating offshore platforms. However, central to the sustainability of all of these systems is the performance of the anchor points used. Plate anchors are a common solution used to secure offshore platforms. This study addresses the holding capacity of plate anchors through numerical modelling. Plate anchors with similar bearing area but of various shapes (square, circular and triangular) subjected to translational and rotational displacement are considered. Comparison of the yield behaviours of these anchors demonstrates the influence of anchor shape on the capacity of the anchors. The study is conducted using Finite Element Analysis implementing the Coupled-Eulerian-Lagrangian approach (CEL). The use of CEL assures numerical stability during the large strain problems considered. The plate is assumed to be a rigid body which is initially embedded in the seabed (wished-in-place). The plate's response to loading is assumed to be undrained. Small translational and rotational increments of displacement are applied to the plate and the corresponding forces and moments are measured. The results of the analyses provide insights into the effect of plate geometry on the yield behaviour of the plate anchors. The uplift capacities of anchors with various shapes (square, circular and triangular) are compared and their yield moment interaction responses are demonstrated.

KEY WORDS: Plate anchor, Capacity, shape effect, numerical methods.

1 INTRODUCTION

Sustainable development of deep water oil and gas facilities, as well as wind energy applications, requires an enhanced understanding of the performance of foundation systems for floating offshore platforms. Plate anchors are a key component of the mooring systems. The behaviour of plate anchor is controlled by a variety of factors including shape, bearing area, soil conditions and embedment depth. The effect of embedment depth and soil conditions on the capacity of plate anchor has been extensively investigated [1]–[7]. The effect of the shape on the plate behaviour has thus far received less attention despite the prominent work accomplished in [8]–[11].

The importance of the study of anchor shape effect is evident to the designers of mooring systems. Plate anchors in practice are offered in a variety of shapes from rectangles and circles to arbitrary polygons and therefore, insight into the influence of anchor geometry on its ultimate capacity is of great significance. A range of approaches from analytical [11], to numerical [10], to model scale tests [8], [9] have been employed in the literature to address this issue. In [11], plastic limit analyses conducted to obtain the lower bound solutions for the capacity ratio of circular and square anchors. The results demonstrated slightly larger capacities for circular anchors. In [10], a set of large deformation finite element analyses were performed on circular and rectangular plate anchors embedded in clay. The findings suggest that circular anchors had slightly higher capacity than square anchors of the same size. In [12], however, model scale tests on circular and square anchors showed similar uplift factors for the two anchor shapes. In [8], a series of model scale tests were conducted on circular and rectangular anchors demonstrated that rectangular anchors with larger length-to-width ratios mobilised the lowest resistance. The tests also provided correlations between the capacity ratio of rectangular and square anchors [8], which compared well with previous proposals [9], [13].

In order to extend the works cited in the literature, the current study addresses the influence of shape on the anchor capacity by comparing the uplift capacity of square, circular and triangular anchors, as well as, investigating the moment capacity of circular and square anchors. The anchor geometry was chosen such that all anchors considered had similar bearing area. Analyses were performed using the Finite Element (FE) method using a Coupled-Eulerian-Lagrangian (CEL) scheme, which is briefly introduced in Section 2. This section also includes information regarding model geometry and soil parameters employed in the analysis. In Section 3, the results of uplift analyses on the square, circular and triangular anchors are discussed. In Section 4, the effect of shape on the moment capacity of square, circular and triangular anchors is evaluated. Finally, Section 5 concludes by summarizing the findings in this study and discussing the direction for our future research.

2 NUMERICAL MODEL

2.1 Model definition

The domain size used for the analyses is shown in Figure 1. Domain size for the analysisThe domain involves two parts distinguished from each other by the dashed line: (1) the

lower part that is assumed to be filled with soil, and (2) the upper part that is a void. The existence of void allows for the formation of heave above the initial soil surface (dashed line) as the anchor is being pulled out.

The anchors were assumed to be rigid throughout the analyses and the soil flow through the bottom and side boundaries was constrained. The anchors were assumed to be "wished-in-place" at the depth $4B_{max}$, where B_{max} is the measure of largest anchor size employed. In order to obtain B_{max}, the anchor shapes are circumscribed by circles and the diameter of the largest circle is rounded up to the next integer to give B_{max}. The value of B_{max} is assumed to be 4 m for our analyses. The choice of $4B_{max}$ as the initial anchor depth allows for the development of maximum capacity in the anchors as the condition of deep embedment prevails (as demonstrated by finite element modelling [14] and model scale tests in [9]).

A reduced mesh size was used in locations close to the plate anchor. Mesh refinement is performed in directions both parallel and normal to the plate anchor (see Figure 1). The number of elements used in the study is 195,000.

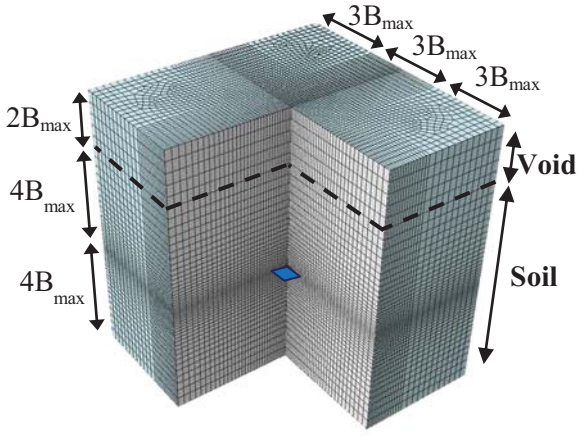


Figure 1. Domain size for the analysis. Anchor size is exaggerated for clarity purposes.

2.2 Coupled-Eulerian-Lagrangian approach

All analyses in this study were conducted using the Coupled-Eulerian-Lagrangian (CEL) technique. The use of CEL enables modelling of large deformations and therefore, is well-suited for our analysis. The soil in this technique is defined by the Eulerian concept and the plate is defined as a Lagrangian material. In the Lagrangian zone, the mesh and the material always coincide. In the Eulerian region, the material can flow from one element and enter another. By coupling the two concepts, the CEL technique allows for modelling large deformation plate-soil interactions without the need to deal with issues such as mesh distortion.

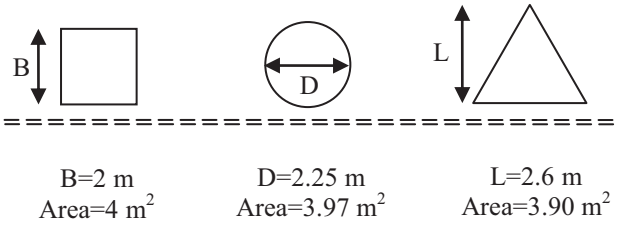
2.3 Soil condition

The soil is modelled as an elastic-perfectly plastic undrained material obeying a Tresca yield surface. The Poisson's ratio was set to 0.495 and the modulus of elasticity was chosen as $500s_u$, where s_u undrained shear strength of the soil was taken as the constant value of 20kPa in the analyses. The soil is considered to be weightless and the suction force at the bottom surface of the plate is zero ("breakaway" condition).

2.4 Plate anchor geometries

The dimensions of the plate anchors were adjusted (using the square anchor as a reference) so that all shapes had similar bearing areas, See Table 1.

Table 1. Plate anchor shapes and dimensions used in the study



The plate thickness for all the anchors was selected as 0.5 m to reduce the computational cost of meshing the domain in the direction of the thickness. Although the thickness value is large, it is shown by numerical experiment that the choice did not affect the ultimate uplift capacity calculations. The reason is because the interaction between the plate and the surrounding soil is only defined through normal forces (smooth surfaces), which is governed by the plate bearing area and soil flow mechanism. The plate bearing area does not change with an increase of the plate thickness and the soil flow mechanism is only slightly affected by the change in the plate thickness. Moreover, the plates were assumed to be rigid throughout the analysis, which also eliminated the effect of thickness on the plate deformation. Therefore, the overall capacity calculations remained valid.

3 EFFECT OF SHAPE ON THE UPLIFT CAPACITY

In the first stage of the analyses, the uplift capacity of plate anchors of various shapes (i.e. square, circular and triangular) but with different bearing areas was calculated. All of the anchors were initially embedded at a depth of $4B_{max}$. The uplift distance for each anchor is proportional to the anchor size as defined in Table 1. The uplift rate was set at B_{min}/sec for all tests, where B_{min} is the smallest anchor size used in the analysis (2 m). The relative uplift capacities (factors) of the three anchor shapes considered are shown in Figure 2. The uplift capacity was defined as the ratio of the pull-out load to the bearing area of each anchor. Only the relative capacity of anchors is important in this study; therefore, all values are normalized with respect to the maximum uplift factor obtained for all the three anchors. It should be noted, however, that the values shown in Figure 2 are the averaged responses, and the actual data obtained from the simulation involved fluctuations. This is demonstrated for the triangular anchor in Figure 3, where the dots show the actual output from the simulation and the solid line describes the calculated average response. Normalization is performed in Figure 3 in the same way as described for Figure 2. Figure 3 also demonstrates the trend for the uplift load; a sudden increase is observed at the start of the anchor displacement followed by a plateau region corresponding to the anchor ultimate capacity. The whole response is consistent with the elastic-perfectly plastic soil behaviour used in the analysis.

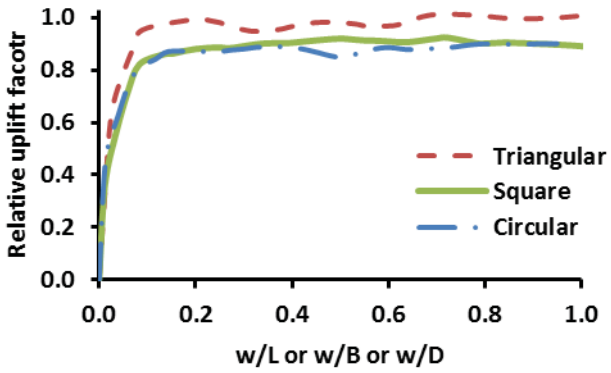


Figure 2. Comparison of the uplift factor of triangular, square and circular anchors. Uplift factor is defined as the ratio of the uplift load to the anchor bearing area. Anchor displacement (w) is normalized in terms of the plates' sizes (L, B and D used for triangular, square and circular anchors, respectively.).

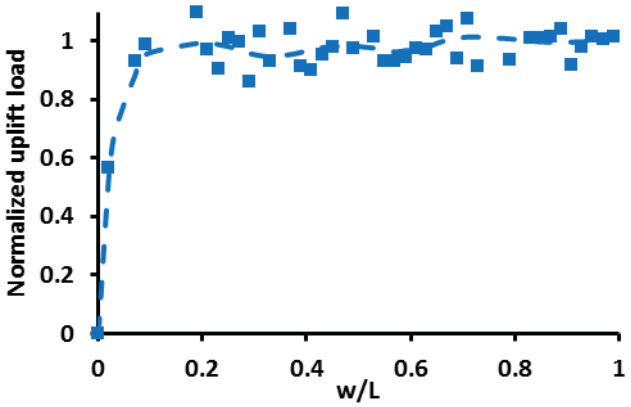


Figure 3. Moving average technique (dashed-line) is used to smooth the data obtained from the uplift simulation (dots). The results for the triangular anchor are shown as typical. Anchor displacement (w) is normalized with respect to the triangular anchor size (L).

Comparison of the data obtained from the uplift simulations shows that the triangular anchor developed the highest relative resistance. The square and circular anchors, on the other hand, developed roughly similar uplift capacities. The higher capacity of triangular anchor could be attributed to its larger dimension (L) compared to the square (B) and the circular (D) anchors, which is expected to mobilize a larger zone of influence for an equal bearing area. Earlier studies on square and circular anchors of similar size (but different bearing areas), suggested either equality of uplift capacities [12], or slightly larger capacities for circular anchors [10], [11]. No mention of triangular anchors was made in those studies.

4 EFFECT OF SHAPE ON THE MOMENT CAPACITY

In addition to considering the uplift capacity, we studied the effect of geometry on the moment capacity of square, circular and triangular anchors. Rotation was performed with respect to the pitch and the yaw axes and different combinations of them (see Figure 4 for the definitions). The pitch and yaw axes, as well as any combinations of them, are assumed to pass through the geometric centre of the plate anchor. Due to the symmetry, only the rotation axes that lie in the shaded area in Figure 4 were used in the simulations. The angular velocity was set at $\pi/2$ Rad/s in each case, and the simulation continued until the anchor made a complete $\pi/2$-degree. The moment-rotation response of the square, circular and triangular anchors (all normalized with respect to the circular anchor) are shown in Figure 5. As for the uplift simulation, the actual data (depicted by solid lines) involved fluctuations and averaged responses (dashed-lines) were used for the analyses. The data shows that the resistance developed rapidly at the start of the test followed by a plateau region at relatively small rotations suggesting that the ultimate moment capacity of the anchor was achieved.

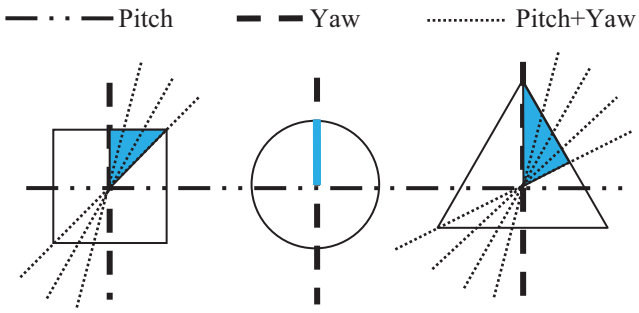


Figure 4. Definition of the pitch (horizontal) and the yaw (vertical) axes and various combinations of them for the square, circular and triangular anchors. All rotation axes go through the geometric centre of the plates. Due to the symmetry, only the rotation axes that lie in the shaded areas of the plates were used in the simulations.

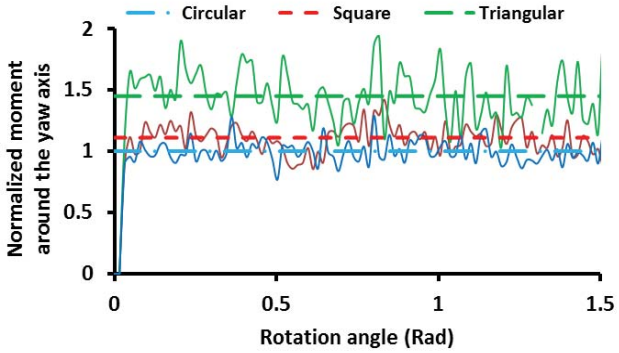


Figure 5. Moment induced on the square, circular and triangular plate anchors during the rotation around the yaw axis. All values are normalized with respect to the response of the circular anchor.

Simulation of the square and triangular anchors involved combinations of the pitch and yaw rotations. In each case, the moment-rotation diagram was derived and the average yield moment was calculated. To provide a framework for

comparison, the resulting values were then normalized with respect to the yield moment of the circular anchor. Figure 6 depicts the normalized yield moments of the square, circular and triangular anchors in various combinations of pitch and yaw rotations. The results show larger moment values for the triangular anchor compared to both square and circular anchors, when all anchors have similar areas. Furthermore, the yield moment for the square anchor obtained to be slightly larger than the circular anchor with the similar area. It is interesting to note that the yield moment in the triangular anchor (distance between the interaction diagram and the origin in Figure 6) does not change noticeably with respect to the axis of rotation. The yield moment in the square anchor, on the other hand, shows slightly more dependence on the rotation axis with the highest moment obtained when rotation performed around an axis lying between the pitch (or yaw) axis and the diagonal.

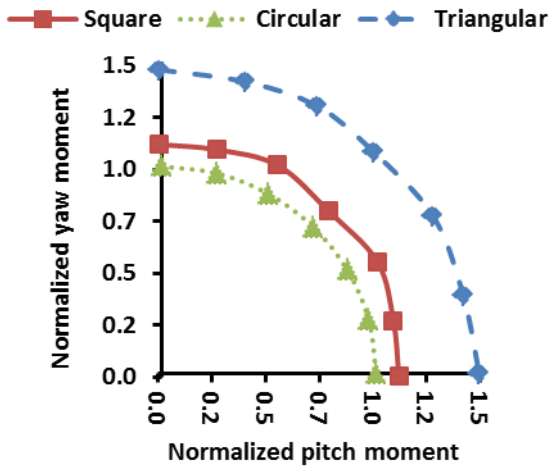


Figure 6. Interaction of pitch and yaw moment capacities. All values are normalized with respect to the moment capacity of the circular anchor. Moment capacity of the square anchor is maximum when the rotation axis is between the square diagonal and the pitch (or yaw) axis. The triangular anchor shows a more uniform response as compared to the square anchor.

5 CONCLUSION

A numerical analysis using the three-dimensional large-deformation Finite Element Method (CEL technique) was performed to study the effect of anchor shape on the yield behaviour of plate anchors in both translational and rotational loading conditions. The study was undertaken using weightless clay with a uniform undrained strength profile. The plate was assumed to be rigid.

In the first part of the analysis, the uplift behaviour of plate anchors with various shapes (triangular, square and circular) but similar bearing area was studied. All of the plate anchors were initially assumed to be embedded at the same depth ("wished-in-place") and positioned with their face up. Uplift simulations were performed on each anchor and the soil reaction was calculated. Simulations continued until the plate displaced a distance equal to its size (large enough for the anchor response to converge). The resulting force-displacement diagrams were then averaged in their converged region to yield the ultimate uplift load of the plate anchors. Uplift factors were subsequently obtained by dividing the converged values with the anchors bearing area. Comparison of the results for triangular, square and circular plate anchors (with similar bearing area) shows the triangular anchor developed the highest uplift factor while the square and circular anchor mobilised approximately the same capacities. This behaviour could be attributed to the larger dimension of the triangular anchor (2.6 m) compared to square (2 m) and circular (2.25 m) anchors, which spread out the effective anchor zone and mobilized a larger volume of soil.

In the second part of the analysis, the moment capacity of square, circular and triangular anchors with similar bearing area was studied. Again, both anchors were assumed "wished-in-place" and in a horizontal position. Rotation was performed with respect to plate anchors' pitch and yaw axes and various combinations of them. Soil reaction was recorded throughout the simulation in terms of pitch and yaw moments. Simulation continued until the plate made a full $\pi/2$-degree turn (large enough for development of anchor's moment capacity). The moment-rotation diagrams were then used to extract the yield moments of square, circular and triangular anchors in different combinations of pitch and yaw rotations. The interaction diagrams derived for pitch and yaw moments demonstrated the highest moment values for the triangular anchor and the lowest values for the circular anchor, when all anchor shapes have similar areas.

In summary, the comparison of plate anchors with various shapes (square, circular and triangular) but similar bearing area showed that the triangular anchor developed the highest uplift and moment capacities in comparison to the other two shapes, and in this regard, it could potentially be considered for development of more sustainable offshore foundation concepts. Further experimental and numerical investigations will improve our insight toward such developments.

ACKNOWLEDGMENT

This publication has emanated from research conducted with the financial support of Science Foundation Ireland under the US-Ireland R&D Partnership Program Grant Number SFI/12/US/E2479.

REFERENCES

[1] M. P. O'Neill, M. F. Bransby, and M. F. Randolph, "Drag anchor fluke-soil interaction in clays," *Can. Geotech. J.*, vol. 40, no. 1, pp. 78–94, 2003.

[2] R. S. Merifield, A. V Lyamin, and S. W. Sloan, "Stability of inclined strip anchors in purely cohesive soil," *J. Geotech. Geoenvironmental Eng.*, vol. 131, no. 6, pp. 792–799, 2005.

[3] Z. Song, Y. Hu, and M. F. Randolph, "Numerical simulation of vertical uplift of plate anchors in clay," *J. Geotech. Geoenvironmental Eng.*, vol. 134, no. 6, pp. 866–875, 2008.

[4] M. Yang, J. D. Murff, and C. P. Aubeny, "Undrained capacity of plate anchors under general loading," *J. Geotech. Geoenvironmental Eng.*, vol. 136, no. 10, pp. 1383–1393, 2010.

[5] Y. Hu, J. Liu, L. Yu, and X.-J. Kong, “Numerical study on plate anchor stability in clay,” *Géotechnique*, vol. 61, no. 3, pp. 235–246, Mar. 2011.

[6] A. M. Fahmy, J. R. de Bruyn, and T. A. Newson, “Numerical Investigation of the Inclined Uplift Behavior of Anchors Embedded in Clay,” *Geotech. Geol. Eng.*, vol. 31, no. 5, pp. 1525–1542, 2013.

[7] M. Jesmani, M. Kamalzare, and M. Nazari, “Numerical study of behavior of anchor plates in clayey soils,” *Int. J. Geomech.*, vol. 13, no. 5, pp. 502–513, 2013.

[8] S. P. Singh and S. V. Ramaswamy, “Effect of shape on holding capacity of plate anchors buried in soft soil,” *Geomech. Geoengin.*, vol. 3, no. 2, pp. 145–154, May 2008.

[9] B. M. Das, “Model tests for uplift capacity of foundations in clay,” *Soils Found.*, vol. 18, no. 2, pp. 17–24, 1978.

[10] D. Wang, Y. Hu, and M. F. Randolph, “Three-dimensional large deformation finite-element analysis of plate anchors in uniform clay,” *J. Geotech. Geoenvironmental Eng.*, vol. 136, no. 2, pp. 355–365, 2010.

[11] R. S. Merifield, A. V Lyamin, S. W. Sloan, and H. S. Yu, “Three-dimensional lower bound solutions for stability of plate anchors in clay,” *J. Geotech. Geoenvironmental Eng.*, vol. 129, no. 3, pp. 243–253, 2003.

[12] B. M. Das and G. Singh, “Uplift capacity of plate anchor in clay,” in *Proc. 4th Int. Offshore and Polar Engineering Conf., ISOPE, Golden, Colo.*, 1994, pp. 436–442.

[13] B. M. Das, “A procedure for estimation of ultimate capacity of foundations in clay,” *Soils Found.*, vol. 20, no. 1, pp. 77–82, 1980.

[14] L.-Z. Wang, Z. Guo, and F. Yuan, “Three-dimensional interaction between anchor chain and seabed,” *Appl. Ocean Res.*, vol. 32, no. 4, pp. 404–413, Oct. 2010.

Impact hammer testing on post-tensioned steel RHS sections; an investigation of the "Compression Softening" effect

D. Noble[1], M.Nogal[1], A.O'Connor[1], V.Pakrashi[2]
[1]Department of Civil, Structural & Environmental Engineering, Trinity College Dublin, Dublin 2, Ireland
[2]Dynamical Systems and Risk Laboratory, Civil & Environmental Engineering, School of Engineering, University College Cork, Ireland
email: nobleda@tcd.ie, alan.oconnor@tcd.ie

ABSTRACT:
The effect of pre-stress force magnitude (N) and eccentricity (e) on natural frequencies (NFs, ω_n) of pre-stressed concrete (PSC) structures has been widely debated. No agreement currently exists as to how pre-stress force magnitude and eccentricity affect natural frequencies of PSC structures. Some reports state that the NFs decrease with increasing N ("compression softening" effect); others suggest that NFs increase with increasing N. Finally, some claim that the NFs are unaffected by N. This paper describes and analyses a set of impact hammer tests conducted on externally axially loaded steel rectangular hollow sections (RHSs) at various levels of axial load. Impact hammer testing was also conducted on the same post-tensioned RHSs. The aim of the research is to investigate under which conditions the "compression softening" effect holds true, and whether the migration of the fundamental frequencies for an external axial load are analogous to that for a post-tensioned section. Two sections with differing slenderness ratios were tested. Experimental modal analysis has been conducted and the experimental natural frequencies were identified. The Fast Fourier Transform (FFT) was applied to the signal in the time domain to transform it into the frequency domain. This was repeated for varying values of axial force at different impact locations. The applications of the results are widespread. The Eurocode 2 (EC2) equation for pre-stress loss as a function of time is well established. If the relationship between pre-stress force and natural frequency for PSC structures can be established, then the variation of natural frequency over the design life of a PSC structure due to pre-stress loss can be estimated. This problem is particularly pertinent in the field of post-tensioned concrete wind turbine towers and in the field of pre and post-tensioned concrete bridge girders.

KEY WORDS: Compression softening; Dynamics; Fast Fourier transform; Impact hammer testing; Natural frequency; Post-tensioned steel; Pre-stress force; Pre-stressed concrete; Signal processing.

1 INTRODUCTION

The effect that the applied pre-stressing force has on the dynamic behaviour of pre-stressed concrete structures is a widely debated topic [1]. There are currently three distinct arguments found in the literature;

1. The natural vibration frequency (ω_n) decreases with increasing pre-stress force magnitude (N). This is known as the "compression softening" effect and is based on classical Euler-Bernoulli theory of an externally axially loaded homogeneous beam, Equation (1), Table 1 [2, 3].
2. ω_n is unaffected by N. This is based on a non-linear kinematic model which concludes that the final equation of motion for a vibrating beam is independent of pre-stress force magnitude [4].
3. ω_n increases with increasing N. This has found to be the case in numerous empirical studies [5-7] however, a satisfactory mathematical model has yet to be formulated, despite some attempts [7, 8].

Table 1 shows the main existing prediction models for the change in natural vibration frequency with pre-stress force magnitude for simply supported (SS) PSC beams. Figure 1 shows the percentage change in fundamental frequency of a SS PSC beam with varying N. The properties of a PSC beam outlined in Table 2 have been used to calculate the predicted change for each of the models outlined in Table 1. It should be noted that, in this case, the magnitude of the predicted change in natural frequency is very small for practical ranges of pre-stressing force, and could be considered to be negligible. For example, in this case the changes are reported to be in the region of ±1%.

Table 1. Existing prediction models for change in ω_n with N.

Author	Prediction Model	
"Compression Softening" [2, 3]	$\omega_n^2 = \left(\frac{n\pi}{l}\right)^4 \frac{EI}{m} - \left(\frac{n\pi}{l}\right)^2 \frac{N}{m}$	(1)
Kim et al. [8]	$\omega_n^2 = \left(\frac{n\pi}{l_r}\right)^4 \frac{E_c I_c}{m_r} + \left(\frac{n\pi}{l_r}\right)^2 \frac{N}{m_r}$	(2)
Saiidi et al. [5]	$\omega_n^2 = \left(\frac{n\pi}{l}\right)^4 \frac{\left(1+1.75\frac{N}{f_c'}\right)EI_g}{m}$	(3)
Zhang et al. [9]	$\omega_n^2 = \left(\frac{n\pi}{l}\right)^4 \frac{\left(1+\frac{mNl^2}{250E_0I_0}\right)E_0I}{m}$	(4)
Dall'Asta & Dezi [10]	$\omega_n^2 = \left(\frac{n\pi}{l}\right)^4 \frac{\left\lfloor\left(E_b - \frac{N}{A_b}\right)I_b + \left(E_c - \frac{N}{A_c}\right)I_c\right\rfloor}{m}$	(5)

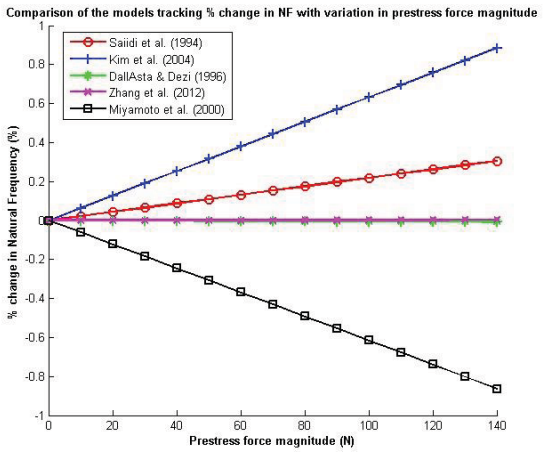


Figure 1. % Change in fundamental frequency with varying N according to the models outlined in Table 1.

Table 2. Properties of PSC beam to obtain Figure 1.

Property	Value	Unit
Breadth, b	150	mm
Height, h	200	mm
Span, L	2.0	m
Young's modulus, E	33	GPa
Density of reinforced concrete, ρ	24	kN/m^3

The importance of this research is widespread. The effect of pre-stress force magnitude on natural frequency of pre-stressed concrete structures has many implications, specifically in the pre-stressed concrete bridge industry and for pre-cast, post-tensioned concrete wind turbine towers. Pre-stress force decreases over time due to concrete creep, steel relaxation, anchorage pull in and other factors. Structural engineers should thus be able to monitor or estimate changes in the natural bending frequency of pre-stressed concrete structures over the course of their design life to ensure their safety and serviceability. As a result, prediction of change in natural frequency of pre-stressed concrete structures over time is of great importance.

In order to isolate this problem, a study must first be conducted into the validity of the "compression softening" effect. Subsequently, the aim of this paper is to report on the impact hammer testing and experimental modal analysis conducted on both externally axially loaded steel RHSs, and their post-tensioned counterparts. The purpose of the research is first to determine under what conditions the "compression softening" equation holds true. The assumption that an external axial load is dynamically equivalent to an internal post-tensioning force is investigated in this paper.

2 LITERATURE REVIEW

2.1 Frequency decreases with increasing pre-stress force

Many authors have argued that the natural vibration frequency of pre-stressed concrete structures tends to decrease as the magnitude of the pre-stressing force increases [2, 3, 11, 12]. Various mathematical models have been formulated, based on a linear kinematic framework. It considers small deflection theory only and does not take into account large displacements and moderate rotations about the axis of bending. This "compression softening" equation, is outlined in Equation (1), Table 1, where ω_n is the natural frequency of the beam in radians per unit time, n is the mode number, l is the span length, N is the axial compressive force, m is the beam mass per unit length, E is Young's modulus of elasticity and I is the second moment of area, with respect to the centroid of the cross section. l_r and m_r are the reduced span and mass per unit length due to axial shortening respectively. The "compression softening" argument is valid for externally axially loaded Euler-Bernoulli beams that are susceptible to buckling failure. The theory is based on Euler buckling theory and states that as the external axial load approaches its critical Euler buckling load, $P_{cr} = \left(\frac{n\pi}{l_e}\right)^2 EI$, the flexural rigidity of the beam decreases, and thus the natural bending frequencies of the beam are decreased. l_e is the effective length of the section based on its support conditions. In fact, the theory suggests that at the critical Euler buckling load, the fundamental frequency disappears to zero, i.e. $\omega_1 = 0$ when $N = P_{cr}$, as the beam has buckled in its first mode shape. This can be seen in Figure 2.

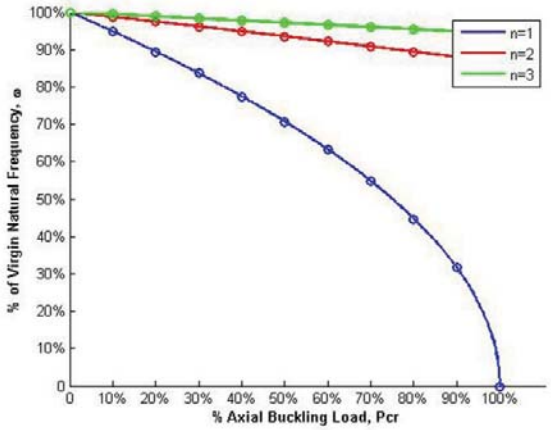


Figure 2. % Change in virgin ω_n with varying N according to the "compression softening" effect, Equation (1), Table 1.

There are arguments suggesting that this "compression softening" effect is not valid for pre-stressed concrete structures. Firstly, the main assumptions in [2, 3, 11, 12] take into account an external axial load being applied to a homogeneous, isotropic section. In the case of pre-stressed concrete, neither of these assumptions is valid. According to some authors [13, 14], "compression softening" is only applicable to external axial loads and the pre-stressing force cannot be considered as such as it is internal to the structure. Furthermore, as pointed out by Saiidi et al. [5], concrete is not a homogeneous material and is susceptible to cracks. Saiidi also showed experimentally that the application of Equation (1) to pre-stressed concrete beams is erroneous. Equation (1) is based on Euler buckling theory, which is only applicable to homogeneous externally axially loaded beams, such as steel beams. The main assumption of applying the "compression softening" effect is that the pre-stressing force in the strand is equivalent to an external axial load of equal magnitude applied to the beam ends. This has been refuted by many authors [12-15] who state that the pre-stressing force is not equivalent to an externally applied axial load as it is internal to the structure and as a result cannot cause Euler buckling to

occur. These authors consider that it is erroneous to treat a pre-stress load as an external axial load, and that it may only be valid in cases where the beam has been jacked against permanent abutments or when the pre-stressing force is induced by high-strength steel wires which are anchored to the end faces of the beam with extremely large internal voids compared to the area of the beam cross section [15].

2.2 Frequency independent of pre-stress force magnitude

Hamed & Frostig [4] presented a rigorous mathematical proof indicating that the magnitude of the pre-stressing force does not affect the natural frequencies of pre-stressed concrete beams. A non-linear kinematic framework was adopted, in comparison with the aforementioned linear kinematic framework presented in other studies [2, 3, 11, 12]. This enabled large displacements and moderate rotations to be accounted for. It was subsequently demonstrated that the governing equation of motion for the beam is independent of axial force, for bonded and unbonded pre-stressing tendons.

2.3 Frequency increases with increasing pre-stress force

Experimental evidence is relatively abundant to suggest that the natural frequency of PSC structures actually increases with increasing pre-stress force magnitude [5-7, 9, 16-18]. Experimental modal analysis has been conducted on a series of vibration tests, both in-situ and in the lab indicating that natural frequency increases with increasing pre-stressing force. Saiidi et al. [5], who initially assumed the "compression softening" argument to hold true for pre-stressed concrete beams, suggest the reason behind this is due to the effect of the pre-stressing force on the closure of micro-cracks that have been induced in the pre-stressed concrete section, and the subsequent increase in stiffness in the section as a result. However, this has not been proven conclusively, either experimentally or theoretically. Mathematical models have also been formulated indicating the increase in natural frequency with increasing pre-stressing force [8]. Furthermore, there is significant evidence to suggest the natural frequency of pre-stressed concrete structures is not only sensitive to the magnitude of the pre-stressing force but is also to the tendon profile within the section and the tendon eccentricity [3, 6, 12]. The profile and eccentricity alters the net second moment of area of the cross section, thus directly affecting the bending stiffness and hence natural frequency of the beam section. The models tracking an increase in natural frequency with increasing pre-stressing force tend to focus on stiffness alteration, or the increase in flexural rigidity of the section with increasing pre-stressing force.

3 METHODOLOGY

3.1 Dynamic Impact Hammer testing

Dynamic impact hammer testing was conducted on 4No. grade S235 steel RHSs, with a Young's Modulus of 205GPa. The properties of the steel sections are outlined in Table 3 and Table 4. Figure 3 shows the external axial load case (Case 1), where dynamic impact hammer testing was carried out on 2No. specimens, a RHS 50×30×3 (Beam 1) and a RHS 120×60×3 (Beam 2), respectively. Each section had a different slenderness ratio, as outlined in Table 4. The purpose of varying the slenderness ratio was to test the validity of Equation (1) for slender members, which are expected to fail, in compression, close to an Euler buckling condition, and stocky members, which show deviation from classical Euler buckling theory. Since Equation (1) is consistent with Euler buckling theory, it was expected that the dynamic results for the stocky section would deviate from the "compression softening" theory. The test specimen was placed in the small test frame and inserted into two pinned connection joints. One pin was fixed directly to the frame. The other was attached to a load cell, which was in turn connected to a 300 ton loading jack. The jack was mounted on the other side of the frame, as shown in Figure 3. A hydraulic hand pump was connected to the loading jack to vary the external axial load. Impact hammer testing was conducted on the 2No. test specimens at different axial load levels until failure had occurred.

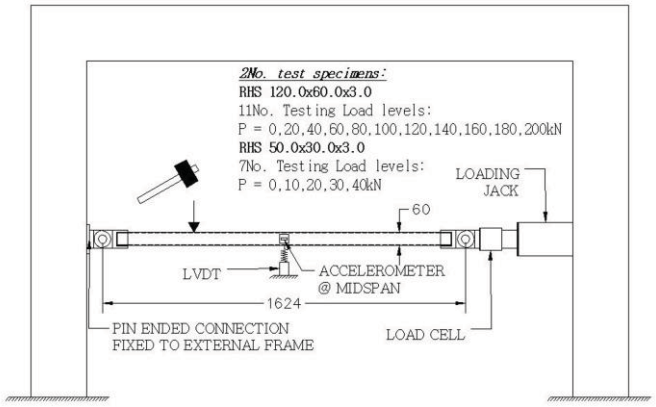


Figure 3. Case 1; External Axial Load Case.

Figure 4 shows the post-tensioned load case (Case 2) where impact hammer testing was carried out on the same RHSs. The sections were post-tensioned using a 15.7mm Freysinnet 7 wire concentric strand. The strand was anchored with the appropriate collets either side of 2No. 300 ton loading jacks. A load cell and a baseplate were positioned between the jack and the end of the steel RHS section, helping to evenly transfer the post-tensioning load into the section. 2No. jacks and 2No. load cells were used in order to balance the mass under vibration. Multiple load cells ensured an even distribution of post-tensioning load throughout the length of the section. The post-tensioned section was supported on either side by knife-edge supports that were a distance of 1.500m apart. One of the jacks was connected to a hydraulic hand pump to transfer a post-tensioning load into the section.

Table 3. Properties of steel RHS sections tested.

Property	RHS 50×30×3	RHS 120×60×3
Beam #	Beam 1	Beam 2
$m\ (kg/m)$	3.41	8.12
$A\ (cm^2)$	4.34	10.30
$I_{zz}\ (cm^4)$	5.94	65.50

Table 4. Some properties of each experimental case.

	Case 1	Case 2
Figure #	Figure 3	Figure 4
Span, L (m)	1.624	1.500
Slenderness Beam 1, λ_{zz_1}	139	128
Slenderness Beam 2, λ_{zz_2}	64	59
Beam 1; $\omega_{1_1}\ (Hz)$	36.0	42.2

Beam 2; ω_{1_2} (Hz)	77.5	90.9

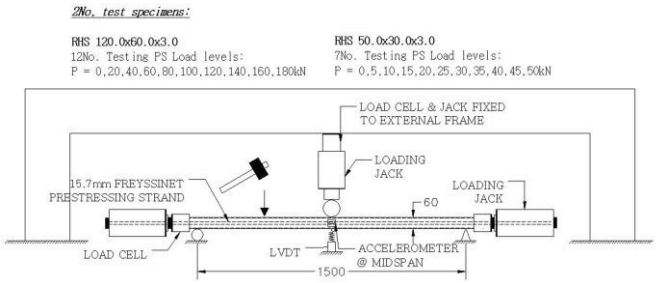


Figure 4. Case 2; Post-tensioned Load Case.

The Multiple Input, Multiple Output (MIMO) method was used in which there were multiple dynamic excitation points and multiple instrumentation response points. 5No. equally spaced input locations were used as both input points and response points as shown in Figure 5. Strain gauges were placed at each of the response points, labelled L1-L5, and an accelerometer was mounted at mid-span on each section, at location L3. 10No. strikes of the sledge hammer were applied at each input point for each load increment, giving a total of 50 frequency data points per axial load level.

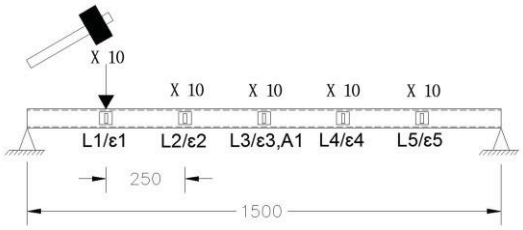


Figure 5. Instrumentation set-up.

The axial load increments varied in number from 5 to 12 depending on the Beam/Case combination, and can be seen in Figure 3 & Figure 4. The impact data was collected using a StrainSmart 6000 data acquisition system. The system collected the real-time strain, acceleration, load and deflection data for each of the four beam and load case combinations. The data was sampled at a rate of 10,000Hz.

3.2 Signal Processing

Following collection of the impact hammer data, the raw signal (acceleration-time data) was imported into Matlab. The Fast Fourier Transform (FFT) was then performed on the acceleration data in the time domain in order to convert into the frequency domain. A peak picking algorithm was then used to identify the peaks in the frequency domain.

The raw signal contained significant electrical noise. In some cases, a "zero drift" in the accelerometer was observed. Subsequently, the peaks in the frequency domain were difficult to determine. A signal processing algorithm was developed in Matlab and is outlined in Figure 6. The signals were processed to eliminate noise and remove the zero drift. The processed acceleration data was then smoothed in the time domain and the FFT was recomputed. Finally, the data was smoothed in the frequency domain. Following smoothing in the frequency domain, the peak picking algorithm was re-invoked and the peaks were again determined. The search bands for the fundamental frequency of each beam were defined as 20-60Hz for Beam 1 and 60-120Hz for Beam 2. The raw data and the processed data were compared, and following processing, the structural peaks were much easier to identify. The peaks in the frequency domain were identified as the natural frequencies of the structural system.

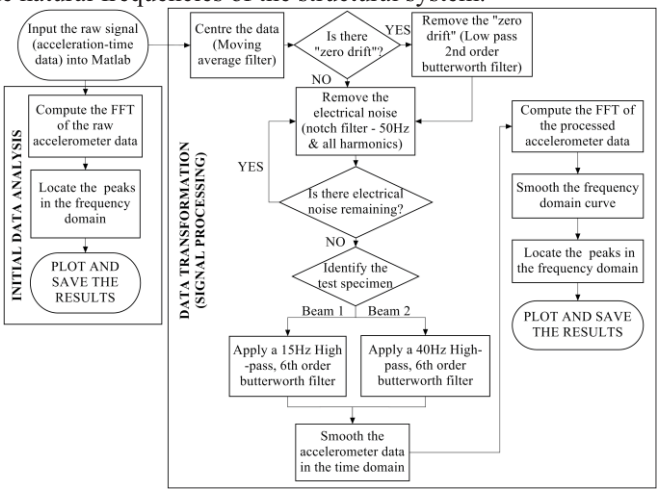


Figure 6. Initial data analysis & signal processing algorithm.

3.3 Static 3 point bending tests

Static three point bending tests were conducted on both post-tensioned beams. A point load was applied at mid-span of the beam at each post-tensioned load level. A LVDT recorded the corresponding deflection associated with each combination of point load and post-tensioning force. The corresponding equivalent static flexural rigidity for a simply supported beam could therefore be calculated as $EI' = \frac{PL^3}{48\delta}$. Natural frequencies could then be predicted using the following; ${\omega_n}^2 = \left(\frac{n\pi}{l}\right)^4 \frac{EI'}{m}$.

4 RESULTS

4.1 Accelerometer Data

Following application of the FFT to each signal, the fundamental natural frequencies of the structural systems were identified. Figure 7 shows the results of the impact hammer data for Beam 1, Case 1. It can be seen that there is a constant decreasing trend in the fundamental frequency with increasing external axial compressive load. The frequency decreases by approximately 15% over the range of external axial load of 0-30kN.

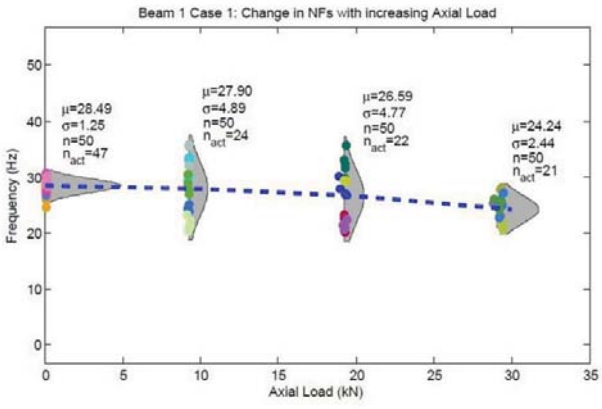


Figure 7. Beam 1, Case 1 – Change in first natural frequency with increasing external axial load (RHS 50×30×3).

Figure 8 shows the migration of the frequency of Beam 1, Case 2 with increasing post-tensioning load. No clear trend in fundamental frequency is observed over the range of post-tensioning force for a post-tensioned steel section. It can be clearly seen that the post-tensioned load case (Case 2) does not follow the trend predicted by Equation (1).

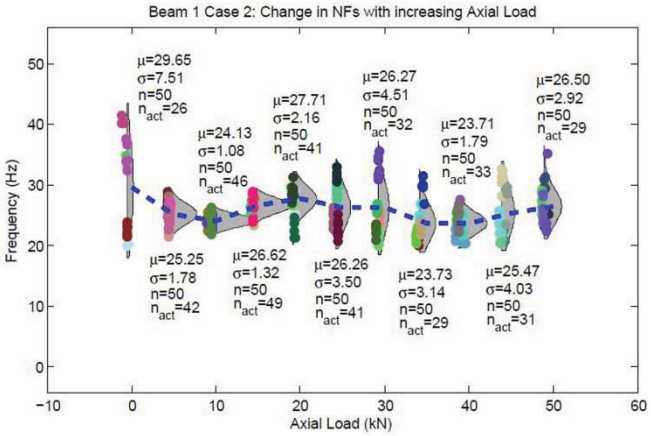


Figure 8. Beam 1, Case 2 – Change in first natural frequency with increasing post-tensioning force (RHS 50×30×3).

Figure 9 shows the change in fundamental frequency with increasing external axial load for Beam 2, Case 1. The slenderness ratio for Beam 2, Case 1 is $\lambda_{zz_1} = 64$ (Table 4). Euler buckling theory is a poor prediction for sections with a slenderness ratio under approximately 120. Since Equation (1) is based on Euler buckling theory, it was postulated that the migration in frequency for members with low and intermediate slenderness would deviate from that predicted by Equation (1). It can be seen from Figure 9 that despite an initial decrease in fundamental frequency for a seating load of 20kN, a steady increase was recorded thereafter. From 140kN onwards a decreasing trend was observed.

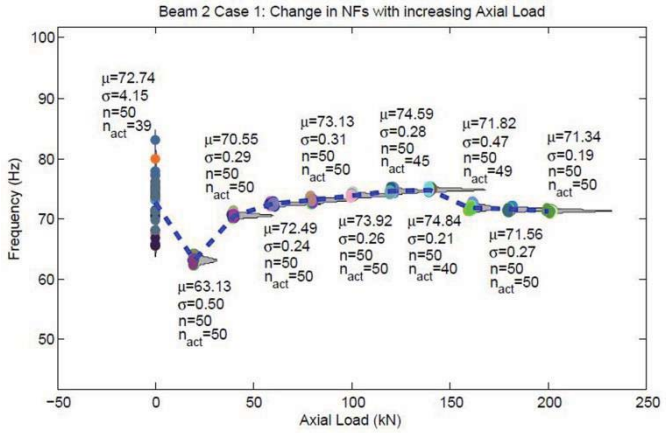


Figure 9. Beam 2, Case 1 – Change in first natural frequency with increasing external axial load (RHS 120×60×3).

Figure 10 shows the change in fundamental frequency with increasing post-tensioning force for Beam 2, Case 2. Similarities exist between Figure 8 (Beam 1, Case 2) and Figure 10. Again, an overall decreasing trend in fundamental frequency with increasing post-tensioning force is observed. Like Figure 8, the frequency is seen to increase and decrease in a waveform-like manner with increasing post-tensioning force.

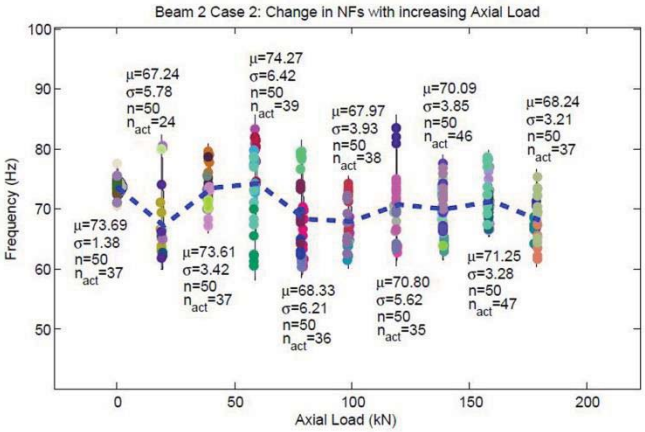


Figure 10. Beam 2, Case 2 – Change in first natural frequency with increasing post-tensioning force (RHS 120×60×3).

4.2 *Static 3 point bending data*

As outlined in Figure 11, it was found that there was an increase in equivalent static flexural rigidity (EI') of Beam 1 for a seating load of 2.5kN, and subsequently, the predicted frequency was increased from the virgin fundamental frequency over that range. Thereafter, a steady decrease in equivalent static flexural rigidity (EI') was reported, and the fundamental frequencies were therefore predicted to decrease. Neither the static, nor the dynamic data was found to follow the trend predicted by Equation (1). "Compression softening" theory for Beam 1, Case 1 suggests that the frequency should decrease, however, as outlined in Figure 11, the rate and magnitude of the decrease in frequency is not of the rate and magnitude predicted by "compression softening".

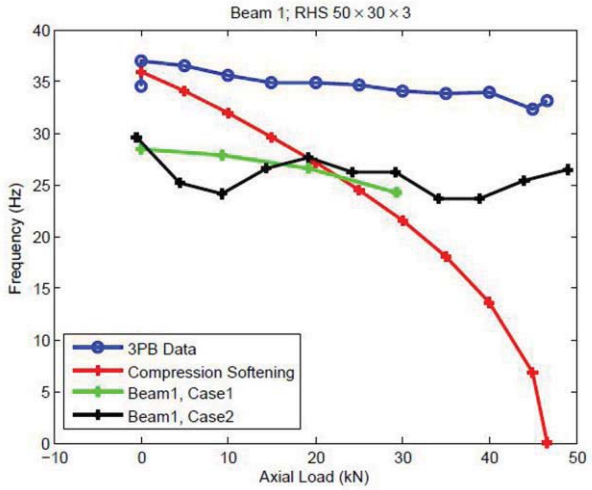


Figure 11. Beam 1 – Comparison of theoretical "compression softening" data to experimental results.

Figure 12 shows the comparison between static 3 point bending tests, the "compression softening" theory and both dynamic cases. Figure 12 seems to indicate that the externally axially loaded stocky section deviates from "compression softening" theory, and despite the initial drop off in frequency observed from 0-20kN, a general increasing trend in frequency is observed.

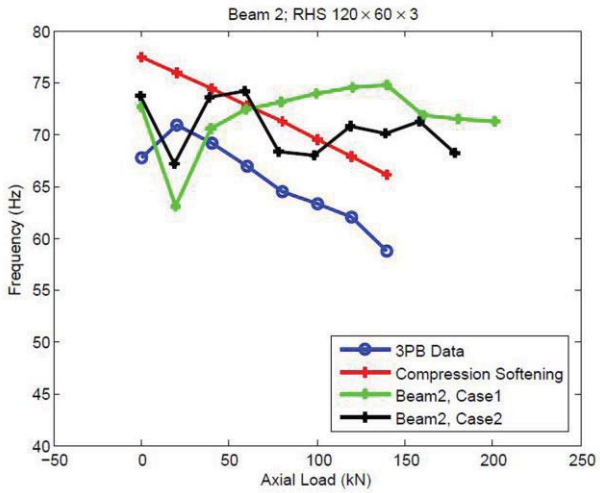


Figure 12. Beam 2 – Comparison of theoretical "compression softening" data to experimental results.

4.3 External Axial Failure Conditions

The predicted and reported failure loads of both sections are outlined in Table 5, taking the Young's Modulus of steel to be 210 GPa, and a yield strength of 235MPa.

Table 5. Predicted vs. reported failure loads.

Property	RHS 50×30×3	RHS 120×60×3
Beam #	Beam 1	Beam 2
$N_{b,Rd_{yy}}\ (kN)$	35.4	187.5
$P_{CR_{yy}}\ (kN)$	46.7	514.7
$N_{c,Rd}$	97.1	230.5
Failure Reported (kN)	40	260

The externally axially loaded slender section buckled in its first mode shape in the manner predicted by Euler buckling theory. Buckling was reported at a value of 40kN, which is 13% greater than the design value of 35.4kN, as predicted by Eurocode 3 ($N_{b,Rd_{yy}}$) and 14% lower than the critical Euler buckling load ($P_{CR_{yy}}$) of 46.7kN. The externally axially loaded stocky section failed by local buckling close to one of the supports. Failure was reported at 260kN, which is 13% greater than the design crushing load ($N_{c,Rd}$).

5 CONCLUSIONS

From analysing the results of impact hammer testing on both externally axially loaded steel RHSs and post-tensioned steel RHSs, it can be concluded that a post-tensioning load is not dynamically equivalent to an external axial load, and the migration of fundamental frequency for both cases is not analogous. Neither case has been found to follow the prediction of Equation (1). Furthermore, the dynamic properties are found to be different for slender and stocky sections. As a result, it can be concluded that Equation (1) is not a valid prediction for the change in natural frequency with increasing post-tensioning load magnitude for post-tensioned concrete structures. Concrete itself is a more variable material than steel. Its failure mode is also different to that predicted by Euler, as it is a brittle, highly non-linear material that is susceptible to cracking under relatively low tensile stress.

ACKNOWLEDGMENTS

The authors would like to acknowledge the financial support given by the Irish Research Council (IRC) under their Embark initiative. The authors would also like to sincerely thank Banagher Concrete, Heitons Steel, Roadstone, Fairyhouse Steel, and Freyssinet for their support in supplying testing materials throughout the duration of the project to date.

REFERENCES

[1] A. Quilligan, A. O'Connor, and V. Pakrashi, "Fragility analysis of steel and concrete wind turbine towers," *Engineering Structures,* vol. 36, pp. 270 - 282, 2012.

[2] F. S. Tse, I. E. Morse, and R. T. Hinkle, *Mechanical vibrations: theory and applications*: Allyn and Bacon, 1978.

[3] A. Miyamoto, K. Tei, H. Nakamura, and J. Bull, "Behavior of Prestressed Beam Strengthened with External Tendons," *Journal of Structural Engineering,* vol. 126, pp. 1033-1044, 2000.

[4] E. Hamed and Y. Frostig, "Natural frequencies of bonded and unbonded prestressed beams - prestress force effects," *Journal of Sound and Vibration,* vol. 295, pp. 28 - 39, 2006.

[5] M. Saiidi, B. Douglas, and S. Feng, "Prestress Force Effect on Vibration Frequency of Concrete Bridges," *Journal of Structural Engineering,* vol. 120, pp. 2233-2241, 1994.

[6] T. Hop, "The effect of degree of prestressing and age of concrete beams on frequency and damping of their free vibration," *Materials and Structures,* vol. 24, pp. 210-220, 1991.

[7] Y. Zhang and R. Li, "Natural Frequency of Full-Prestressed Concrete Beam," *Transactions of Tianjin University,* vol. 13, pp. 354-359, October 2007.

[8] J.-T. Kim, C.-B. Yun, Y.-S. Ryu, and H.-M. Cho, "Identification of prestress-loss in PSC beams using modal information," *Structural Engineering and Mechanics,* vol. 17, pp. 467-482, 2004.

[9] Y. Zhang, Y. Zheng, and H. Li, "A Dynamic Test of Fully prestressed Concrete Beams," *Advanced Materials Research,* vol. 368-373, pp. 2483-2490, 2012.

[10] A. Dall'Asta and L. Dezi, "Discussion of "Prestress Force Effect on Vibration Frequency of Concrete Bridges" by M. Saiidi, B. Douglas, and S. Feng," *Journal of Structural Engineering,* vol. 122, pp. 458-458, 1996.

[11] K. K. Raju and G. V. Rao, "Free Vibration Behavior of Prestressed Beams," *Journal of Structural Engineering,* vol. 112, pp. 433-437, 1986.

[12] A. Dall'Asta and G. Leoni, "Vibrations of Beams Prestressed by Internal Frictionless Cables," *Journal of Sound and Vibration,* vol. 222, pp. 1 - 18, 1999.

[13] Z. Bažant and L. Cedolin, "Discussion of "Free Vibration Behavior of Prestressed Beams" by K. Kanaka Raju and G. Venkateswara Rao (February, 1986, Vol. 112, No. 2)," *Journal of Structural Engineering,* vol. 113, pp. 2087-2087, 1987.

[14] G. Deák, "Discussion of "Prestress Force Effect on Vibration Frequency of Concrete Bridges" by M. Saiidi, B. Douglas, and S. Feng," *Journal of Structural Engineering,* vol. 122, pp. 458-459, 1996.

[15] F. Bartlett, "Discussion of "Free Vibration Behavior of Prestressed Beams" by K. Kanaka Raju and G. Venkateswara Rao (February, 1986, Vol. 112, No. 2)," *Journal of Structural Engineering,* vol. 113, pp. 2085-2087, 1987.

[16] M. S. Williams and S. Falati, "Modal testing of a post-tensioned concrete model floor slab," in *Proceedings of the International Modal Analysis Conference - IMAC* vol. 1, ed, 1999, pp. 14-20.

[17] D.-D. Ho, J.-T. Kim, N. Stubbs, and W.-S. Park, "Prestress-force estimation in PSC girder using modal parameters and system identification," *Advances in Structural Engineering,* vol. 15, pp. 997-1012, 2012.

[18] Z. R. Lu and S. S. Law, "Identification of prestress force from measured structural responses," *Mechanical Systems and Signal Processing,* vol. 20, pp. 2186-2199, 2006.

Stressing Geometry Control of Cable-stayed Bridges

James Barry[1], Kieran Ruane[1,2], John J. Murphy[1]
[1]Department of Civil, Structural & Environmental Engineering, Cork Institute of Technology, Bishopstown, Cork, Ireland
[2]RPS Consulting Engineers, Innishmore, Ballincollig, Co. Cork, Ireland
email: james.barry1@mycit.ie, kieran.ruane@rpsgroup.com, john.justinmurphy@cit.ie

ABSTRACT: Cable-stayed structures are used as an option for the construction of long span bridges. An important aspect of the design of such structures is the control of the stresses in the cables, which serves to ensure that deflections of the deck due to both dead and imposed loads are maintained within appropriate limits. This paper considers the stressing control of cable-stayed bridges using the Hibernian Road Footbridge in Cork City as the basis for the analysis.
A detailed analysis of the Hibernian Road Footbridge is undertaken to establish the required prestress in the cables and precamber of the deck. The analysis is undertaken using the stiffness method of structural analysis, incorporating the use of the Unit Load Method and taking account of the non-linear behaviour of the cables. Flow charts outlining the calculation procedure are presented. The non-linear behaviour and the need to avoid apparent compression in the cables, when the bridge is loaded unsymmetrically present a number of challenges in the calculations. The calculation algorithm to address these challenges is explained. The calculations are undertaken in a spreadsheet and the results are compared with the results obtained from a LUSAS finite element analysis of the bridge. The results from the spreadsheet compared well with the results obtained from the LUSAS analysis and the stressing procedure required for the bridge kept the deflections within the allowable limits when applied to the LUSAS model. This has highlighted the usefulness of a spreadsheet as it will exclude the need for finite element analysis at the preliminary design stage and can also be used to complement a software package, which does not incorporate the calculation of the cable stressing required.

KEY WORDS: Cable-stayed bridge; Spreadsheet; Cable stressing procedure; Finite element analysis; Preliminary design.

1 INTRODUCTION

Cable-stayed structures are used as an option for the construction of long span bridges. An important aspect of the design of such structures is the control of the stresses in the cables, which serves to ensure that deflections of the deck due to both dead and imposed loads are maintained within appropriate limits. This paper considers the stressing control of cable-stayed bridges using the Hibernian Road Footbridge in Cork City, Ireland as the basis for the analysis.

The development of a spreadsheet that analyses a bridge and outputs the appropriate stresses for each of the cables in the bridge is described in this paper.

2 STRESSING OF STAY CABLES

2.1 Cable interaction

If a cable-stayed bridge is to resist the forces correctly, the stay cables must be stressed to a predetermined value. The stress required varies from cable to cable, depending on the deflection of the deck under permanent loading. The aim when working out the required cable stresses is to create a deck profile that is as level as possible due to permanent loads; this process is often referred to as the stressing geometry control.

When calculating the required cable stresses, it is important to balance both the stress in the cable and the deflection and bending of the deck. The calculation of the stresses is an iterative process because as each cable is individually stressed the other cable stresses are modified. In Figure 1, the influence that stressing a single cable has on the other cables can be seen:

1) The cables without any prestress applied.
2) The far right cable is stressed so the deck at the connection point returns to its un-deformed position.
3) Next the cable second from the right is stressed so that its connection to the deck is brought back to its un-deformed position.

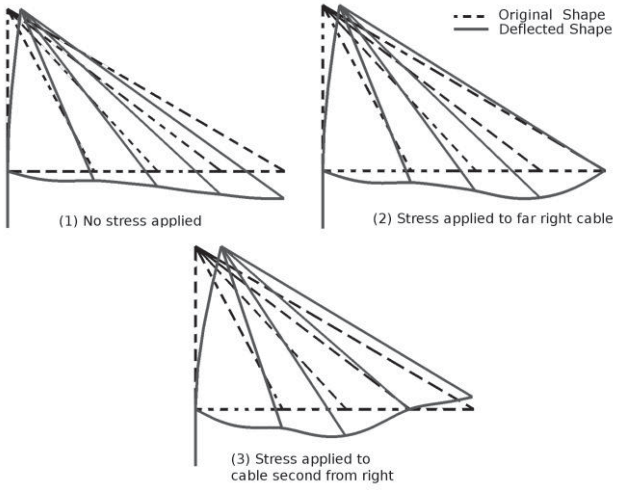


Figure 1. Cable interaction

It can be seen that the second stressing displaces the far right cable. It is this interaction between the cables that leads to an iterative approach being required to ensure that the final stressing levels produce a level deck.

Keeping the deck level is not the only consideration when stressing the stay cables; another factor is the magnitude of stress that is being applied. Each cable stay must be capable of resisting its required stress. It is recommended that the stay cables take stresses only up to 45 % of their breaking load. This limit is applied to keep the stay in a range that will minimise the irreversible strain that may arise from relaxation of the steel [1].

The required stress in the cables is initially calculated for the permanent loading situation. However, other loadcases also need to be considered as they may cause deflection of the deck leading to unacceptable geometry of the bridge and undesirable levels of stress in the cables.

2.2 Methods of applying cable prestress

The method and sequence of applying the prestress to the cable stays varies depending on the type of construction used. For instance, if the bridge is constructed on propped formwork the cables need not be stressed until the very end prior to removing the formwork. All of the cables are then stressed so that they are taut. Finally the formwork is removed and the weight of the bridge is transferred into the cables. When this method is used, it is common for the formwork to incorporate hydraulic jacks so that the transfer of weight onto the cable stays can be controlled by slowly lowering the jacks in a prescribed order.

Alternatively, if a construction method such as the balanced cantilever is used, it is important that the cables are stressed as the construction stages progress. It may be necessary to alter the stresses in a number of cables after any one stage so that the overall geometry of the bridge is kept within acceptable limits, predefined at the design stage.

When this method of applying cable stresses is used, measurements of the cable stresses, deck profile, pylon deflection and deck stresses are frequently taken during construction so that adjustments can be made to keep them within allowable limits.

3 CALCULATION OF THE REQUIRED CABLE STRESSES

3.1 Unit Load Method

The Unit Load Method is commonly used by software programs to calculate the required stress in the cable stays to meet given criteria, such as a maximum allowable bending moment or deflection. In this method a unit load is applied to all the cable stays and also a unit translation is applied to the end support (normally referred to as jacking in the calculations). This method calculates a required load factor for each cable stay, that when applied to the unit load gives the required stress for the cable. The load factor is calculated using an iterative process, whereby the load factors are all set as unknowns and the influence of a Unit Load on each cable stay is taken into account. By setting the load factors to an unknown, a series of simultaneous equations is produced and through solving these equations the load factors are calculated. Through the use of these load factors, the force required in each cable stay can be found by multiplying by the Unit Load that was initially applied to the cables. This force when applied to the cables leads to a stress that will allow the bridge to meet the given criteria, which were set out before the calculations commenced. If the criteria for the required stressing were that the bending moments had to be equal to predefined values the equations for a four cabled bridge (see Figure 2) would take the form of Equation 1 [2]:

$$\begin{aligned} M_A &= M_{PL} + (M_{LC1=1} \times ULF_1) + \dots \\ &+ (M_{LC4=1} \times ULF_4) + M_{Lj} \times ULF_j \\ &\vdots \\ M_E &= M_{PL} + (M_{LC1=1} \times ULF_1) + \dots \\ &+ (M_{LC4=1} \times ULF_4) + M_{Lj} \times ULF_j, \end{aligned} \quad (1)$$

where ULF_i = Unknown Load Factor of the i^{th} cable.

The Unit Load Method was used within the spreadsheet to calculate the required cable stresses.

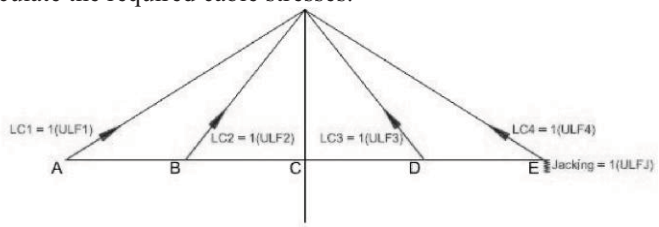


Figure 2. Example bridge with Unit Loads applied

3.2 Construction Stage Analysis

Depending on the method of construction used, the displacements and moments in the deck and pylon can exceed allowable limits during construction while remaining below the limits in its final state. For this reason, analysis must be carried out for each step of the construction process. The analysis allows for the calculation of the required cable stay stresses and deformations of the bridge structure at each stage of construction, which can then be compared with allowable limits. There are two methods that can be adopted for this analysis: - backward analysis and forward analysis. These analyses are often carried out using a finite element software program such as LUSAS.

3.2.1 Backward Construction Analysis

In backward construction analysis, the bridge starts in its final state and each step removes a structural element in reverse order to its real construction sequence. The analysis starts with the required deck profile and cable stay stresses applied for the fully constructed bridge [3]. For this analysis it is assumed that all age related deformations such as creep and shrinkage have taken place [4]. From there the bridge is unloaded of age related effects, and construction induced loading is then applied. Bridge elements are removed in the reverse order to the actual construction sequence, which allows the cable stresses required for each stage to be calculated using a method such as the Unit Load Method. The moments and deflections of the deck and pylon should also be checked at each stage. When the analysis is complete a series of stresses, which keep the deck and pylon profile and forces within allowable limits for each of the construction stages has been obtained.

3.2.2 Forward Construction Analysis

Forward construction analysis is similar to the backward construction analysis in what it can produce and what should be monitored. However, in this analysis the bridge is constructed in steps as it would be in the real situation. The effects of creep and shrinkage should be taken into account during the construction stage analysis [4]. Once analysis is complete a series of cable stay stresses will be obtained, which will satisfy the required limits of deflection and stresses in deck and pylon during each stage of construction.

There are disadvantages to both forms of construction analysis, which can lead to unsatisfactory results. For example, it can be difficult to estimate the age related deformations required at the beginning of the backward analysis. When using the forward analysis method, the required final profile may not be obtained without large changes to the cable stress during the final stage of construction. For these reasons both methods are often undertaken until convergence of the cable stresses at each stage occurs [4].

4 LUSAS CABLE-STAYED BRIDGE MODELS

4.1 Bridge template

The template for the bridge to be modelled was the Hibernian Road Footbridge (see Figure 3), which has four sets of cables per cable plane, as shown in Figure 4. The bridge is supported vertically at its ends, A and B. The pylon comprises two 450 x 450 x 10 mm RHS, one on each cable plane and the primary beams are 690 x 50 mm CHS.



Figure 3. The Hibernian Road Footbridge

For this analysis the end supports were removed; this fundamentally changed aspects of the structural behaviour of the bridge, necessitating an adjustment to the size of the pylon. As the bridge is a pedestrian bridge the variable load is taken as 5 kN/m^2 [5], the bridge is taken as 3 metres wide so the load on the primary beams is 7.5 kN/m. The permanent load was taken as 13 kN/m taking account of the self weight of both the primary and secondary beams, parapets, and decking. The loadcases are critically important when considering the cable stressing procedure; for this reason in addition to the permanent only loadcase, five variable loadcases were considered.

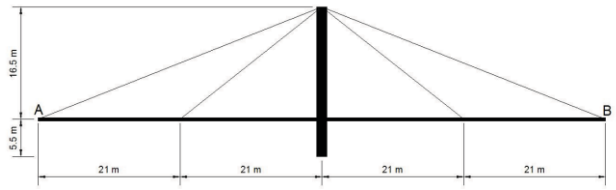


Figure 4. Model's main dimensions

4.2 Variable loadcases

The five variable loadcases considered for the analysis are depicted in Figure 5 and were as follows:

1) Maximum loading across entire span;
2) Minimum loading on right of pylon and maximum on left of pylon;
3) Maximum loading on right of pylon and minimum on left of pylon;
4) Maximum and minimum loading alternating across span;
5) Minimum and maximum loading alternating across span.

Minimum loading consists of permanent loading only. Maximum loading consists of both permanent loading and variable loading acting together.

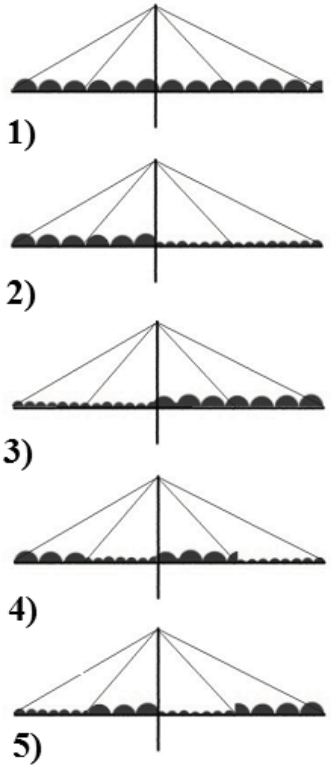


Figure 5. Variable loadcases considered

5 DEVELOPING THE SPREADSHEET

5.1 Advantages of a spreadsheet

Due to the repetitive nature of the calculations required to identify a suitable stressing sequence, a spreadsheet was deemed to be an appropriate method of undertaking the calculations. To verify the spreadsheet's results throughout the development, it was continuously compared with the finite element analysis performed on LUSAS.

5.2 Assumptions made

As the spreadsheet was developed for use at the preliminary stage of a bridge design, a number of assumptions were made to limit both the size of the spreadsheet and also the time required to calculate the desired results.
The main assumptions were:

- The pylon and beams would not undergo any axial deformations;
- The bridge was constructed on formwork with loading being applied to the cables after the bridge had been constructed.

Any assumption that was made when undertaking the spreadsheet calculations was reflected in the LUSAS model so that the comparison made would be correct.

5.3 Factors to be considered

5.3.1 Avoiding apparent compression

As a cable is not capable of resisting a compressive force, it was important to remove compressive cable forces from the analysis.

When calculating the minimum tensile force required in a cable there were two factors to be considered. The first was the maximum apparent compressive force in the cables due to the variable load analysis; the minimum tensile force must be greater than this. The second factor is the amount of tensile force required to remove sag from the cables; this can be specified in the inputs of the spreadsheet.

5.3.2 Non-linearity

Cables of a cable-stayed bridge tend to sag when the tensile force in them is not sufficient to keep them taut. When the cables sag, they act non-linearly and the stiffness of the cable reduces as the effective Young's Modulus changes. The change in the effective Young's Modulus leads to a large deflection in the deck due to a small force change. To simplify the calculations in the spreadsheet, an idealised stress-strain relationship was assumed giving rise to a bi-linear relationship. Using this relationship, a stress-stiffness graph as shown in Figure 6 is achieved.

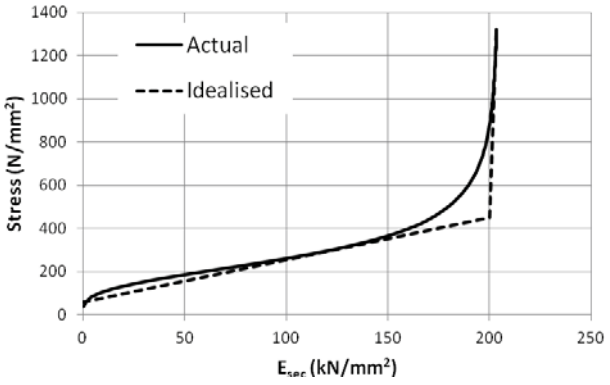


Figure 6. Idealised stress-stiffness curve of a cable

The effective Young's Modulus, E_{sec}, of a cable is a function of the following parameters:

- Axial stress prior to loading (σ_1);
- Axial stress after loading (σ_2);
- Specific weight of the cable (γ);
- Horizontal distance between the cable ends (a);
- Young's Modulus of a taut cable (E).

Equation 2 is used to calculate the effective Young's Modulus [6].

$$\frac{1}{E_{\text{sec}}} = \frac{1}{E} + \frac{\gamma^2 a^2}{24}\left(\frac{\sigma_1 + \sigma_2}{\sigma_1^{\,2}\sigma_2^{\,2}}\right) \qquad (2)$$

5.4 Input data

Data are input to the spreadsheet by means of a user friendly userform, which splits the information required into five categories: bridge dimensions, section properties, cable data, loading and constraints. The information required for the calculations include:

- the distances between the four cable to beam connections and the pylon height;
- Young's Modulus for the pylons, cables and beams;
- second moments of area for both the pylon and beams;
- cross-sectional area of cables;
- minimum force to remove cable sag;
- the permanent loading on the bridge;
- the variable loading on the bridge;
- the deflection criteria that should be met.

The userform also helps reduce the possibility of errors by ensuring the correct data type is entered into the spreadsheet such as positive numbers only for lengths, areas and strengths.

5.5 Calculation algorithm

The algorithm used in calculating the cable prestress required is an iterative calculation and is best described using a process flow shown in Figure 7.

5.6 Optimisation of cable stay stresses and construction precamber

The optimisation process undertaken by the spreadsheet to ensure that the results remain within the constraints alters the stay stresses and the precamber at construction. The constraints that must be met are:

- Cables should not exceed 45% of their ultimate breaking load;
- Cables should not be in compression;
- Deck deflections must remain within the allowable limits specified by the user.

The optimisation also involves a simplified non-linear analysis; the process of optimisation is shown in Figure 8. A situation can transpire where given the input data, a solution cannot be found as the constraints are too restrictive. To stop the spreadsheet from going into an infinite loop and becoming unresponsive, the calculations are set to stop after performing 20 iterations.

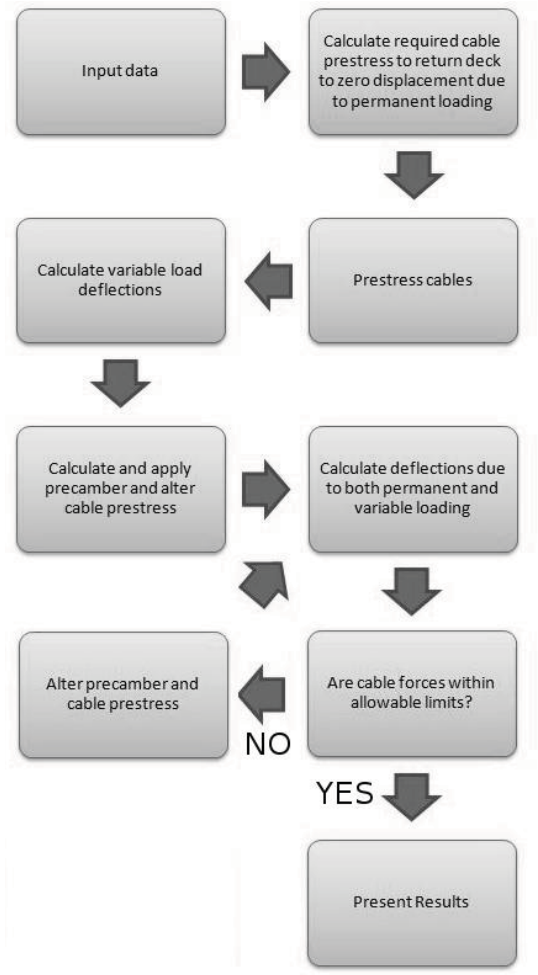


Figure 7. Spreadsheet calculation algorithm

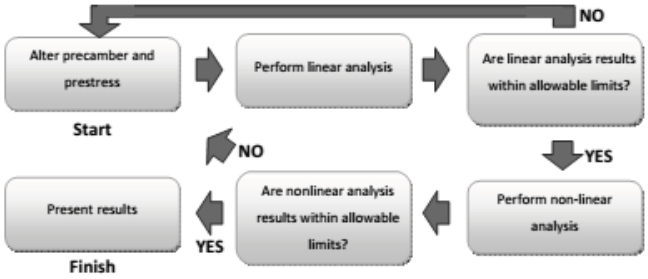


Figure 8. Process of optimising prestress and precamber

5.7 Calculation algorithm complications

A number of complications arose while introducing the non-linear calculations into the spreadsheet; the following describes the complications and the solutions, which were used to mitigate them.

5.7.1 Varying cable strengths

As the spreadsheet allows for the input of a different ultimate strength for each cable, the point at which the cables begin to sag also varies. This introduces a difficulty when deciding which cable governs the reduction in load required to bring all cables below the limit for changing their respective effective Young's Modulus values, as the one which has the highest or lowest force is not necessarily the correct choice. To mitigate against this, it was decided that the cable which has the largest difference between its force and respective limit would be the governing cable. To help evaluate the differences, each cable is first given two case numbers and from those is assigned a category number. The case numbers are assigned using the following rules:

1. Cable is in apparent compression;
2. Cable is in tension but sagging (below sagging limit);
3. Cable is in tension and taut (above sagging limit).

A case is applied for both before and after loading; using these case numbers the algorithm next assigns the cable a category number based on which number the cable has prior to loading and after loading. The following are the categories used:

- Cable goes from taut to sagging (Case 3 to Case 2);
- Cable goes from taut to apparent compression (Case 3 to Case 1);
- Cable goes from sagging to taut (Case 2 to Case 3);
- Cable goes from sagging to apparent compression (Case 2 to Case 1);
- Cable goes from apparent compression to taut (Case 1 to Case 3);
- Cable goes from apparent compression to sagging (Case 1 to Case 2);
- Cable does not change (both cases are the same).

Implementing this category system simplifies the algorithm and also allows the cable's effective Young's Modulus to be changed correctly, to the sagging modulus for a cable beginning to sag and a modulus of zero for a cable going into apparent compression.

5.7.2 Changing the effective Young's Modulus

As it is possible during the non-linear analysis, depending on the input data, for two cables of a bridge to meet their change point at the same percentage of loading, it is important that both cable's effective Young's Modulus are changed at the same time during calculations. This difficulty appeared when analysing a symmetrical bridge, with identical cables and a uniform loading. The cable forces at the end of the analysis were not matching and this raised concerns. This added to the fact that the cables might not necessarily have the same force in them due to varying cable strengths, requires a robust logic check. To combat this, the spreadsheet was programmed to identify a cable with the same difference as another cable, which is having its effective Young's Modulus changed and adjust each cable's properties at the same time.

6 SPREADSHEET AND LUSAS MODEL COMPARISONS

A vital part of the development of the spreadsheet was ensuring the results obtained were correct, for this reason a LUSAS model was developed in parallel and the results were continuously scrutinised. Linear and non-linear models were created with the non-linear model taking account of cable sag, while the linear model did not.

6.1 Linear comparison

The first step in the calculation is the linear analysis with the assumption that there is no axial deformation of the beams or pylon. Two LUSAS models were created for comparison with the spreadsheet results; the first took account of the

assumption and the second did not. The second model was used to verify that the results were not significantly affected by the assumptions made.

When the results were compared, it was observed that the spreadsheet and the model not taking account of axial deformations compared extremely well. The comparison of the spreadsheet and the model taking account of axial deformations also compared extremely well, but did, however, present a larger difference than the previous comparison. A comparison of cable forces due to variable loadcase five and the calculated stressing procedure being applied to the bridge can be seen in Table 1.

Table 1. Comparison of cable forces from linear analysis

Results from	Spreadsheet (kN)	LUSAS model (axial deformation neglected) (kN)	LUSAS model (axial deformation accounted for) (kN)
Cable 1	-293	-293.1	-293.1
Cable 2	-610.1	-610.0	-609.2
Cable 3	-651.4	-651.3	-650.7
Cable 4	-473.5	-473.5	-473.4

6.2 Non-linear comparison

As with the linear calculations, a comparison was also made between non-linear results obtained from the spreadsheet and a non-linear LUSAS model. In this case, the LUSAS model allowed axial deformations in the beam and pylon. A comparison of cable forces calculated in the non-linear analysis due to variable loadcase five and the calculated stressing procedure being applied to the bridge can be seen in Table 2.

Table 2. Comparison of cable forces from non-linear analysis

Results from	Spreadsheet (kN)	Non-linear LUSAS model (kN)
Cable 1	-290.6	-288.7
Cable 2	-618.3	-619.6
Cable 3	-659.5	-659.6
Cable 4	-470.9	-470.7

7 CONCLUSION

It has been shown that a spreadsheet can be created to undertake preliminary analysis and was proven to produce accurate results when compared with a time consuming finite element model. The paper has outlined the methodology required to complete the analysis of the stressing procedure of a cable-stayed bridge. This methodology provides a building block and can be expanded to cover other situations where there may be need for more cables or more spans. The development of this spreadsheet has proven that a spreadsheet is a suitable means of undertaking the design. Once created the spreadsheet can be manipulated quickly and easily without the need for finite element analysis software, saving both time and resources at the preliminary design stage of a bridge project. Time savings will vary depending on finite element software capabilities, but time savings of up to 70% have been achieved.

LINK TO SPREADSHEET

http://1drv.ms/1dRGbmk

ACKNOWLEDGMENTS

The research reported in this paper was conducted as part of the BEng (Hons.) in Structural Engineering at Cork Institute of Technology.

REFERENCES

[1] G. Parke and N. Hewson, Eds., *ICE Manual of Bridge Engineering*, Thomas Telford, London, UK, second edition, 2008.

[2] A. Bruer, H. Pircher, H. Bokan, Computer Based Optimizing of Cable-Stayed Bridges, in Proc. of IABSE Conference "Cable-Stayed Bridges – Past, Present and Future". Malmö, Sweden, 1999.

[3] S. Chatterjee, *The Design of Modern Steel Bridges*, Blackwell Science Ltd. Oxford, UK, second edition, 2003.

[4] W. F. Chen and L. Duan, *Bridge Engineering Handbook*, CRC Press, first edition, 1999.

[5] NSAI, *IS EN 1991-2:2009 Eurocode 1: Actions on structures - Part 2: Traffic loads on bridges*, National Standards Authority of Ireland, Dublin, Ireland, 2009.

[6] N. Gimsing and C. Georgakis, Cable Supported Bridges Concept and Design, Wiley, West Sussex, UK, third edition, 2012.

The Design of Moment Connections between Rectangular Hollow Sections

B. Allen[1,2], J.J. Murphy[2]
[1]Arup Consulting Engineers, 15 Oliver Plunkett Street, Cork Ireland
[2]Department of Civil, Structural & Environmental Engineering, Bishopstown, Cork, Ireland
email: billy.allen@arup.com, john.justinmurphy@cit.ie

ABSTRACT: Steel portal frames in the construction industry typically comprise I and H sections. The design procedures for the connections in these frames (base, eaves and apex) are well established. This research is based on using rectangular hollow sections (RHS) as the column and rafter members. The eaves connection of a rectangular hollow section pitched portal frame is investigated in this paper and includes a review of various experimental research relating to moment connections between rectangular hollow sections. Three eaves joints were considered in this research. The joints were physically tested in the laboratory and a finite element analysis (FEA) carried out. An initial design approach for predicting the moment-rotation relationship for the joints was formulated. Reasonable correlation between the laboratory, finite element analysis and initial design approach was found for the linear elastic behaviour of the connection, while further work is required to define the appropriate yield line mechanism to be considered in the non-linear section of the curve.

KEY WORDS: Rectangular hollow section; Moment connection; Finite element analysis; Steel connection; LUSAS.

1 INTRODUCTION

This paper investigates the design of moment connections between rectangular hollow sections (RHS). Bolted connections between such sections in portal frames, which generally comprise structural H and/or I sections, are typically not that common.

Connections using similar size rectangular hollow sections as column and rafter elements at the eaves location in a typical pitched portal frame are studied. Three joint types were considered for research and analysed using physical laboratory testing and finite element analysis. The focus of the research was to establish a moment-rotation relationship for rectangular hollow sections using the procedures set out in *IS EN 1993-1-8* (EC3) [1] for structural I and H sections as a template. An initial design approach was formulated, which is suitable for an approximation of initial joint stiffnesses.

1.1 Background

In general there is a lack of knowledge regarding moment connections provided in portal frames when using rectangular hollow section connections. From a review of research papers and design documents, guidance is available for connections where a universal beam is connected to a rectangular hollow section column by means of blind bolts, fin plates or a welded connection. A lack of research was found for bolted hollow section to hollow section connections other than tension splices.

2 PREVIOUS RESEARCH AND CURRENT SPECIFICATIONS

Section 7 of EC3 [1] details rules used to determine the static resistance of hollow section joints. The scope of the section deals with uniplanar and multiplanar joints in lattice structures only; no reference is made to frames, beams or columns. Section 6 of EC3 details design methods for connecting H or I sections that can be used in frames of any kind.

The only current design recommendations for using RHS in portal frames have been produced by CIDECT (Comité International pour le Developpement et l'Étude de la Construction Tubulaire), an international association of leading manufacturers of hollow sections and pipes. The design guides produced by CIDECT are based on research carried out on various aspects relating to hollow sections and their use mainly in structural applications.

Of interest to this research was work carried out by Mang et al. [2]. Mitred RHS knee joints at 90° were investigated for unstiffened and stiffened connections (see Figure 1).

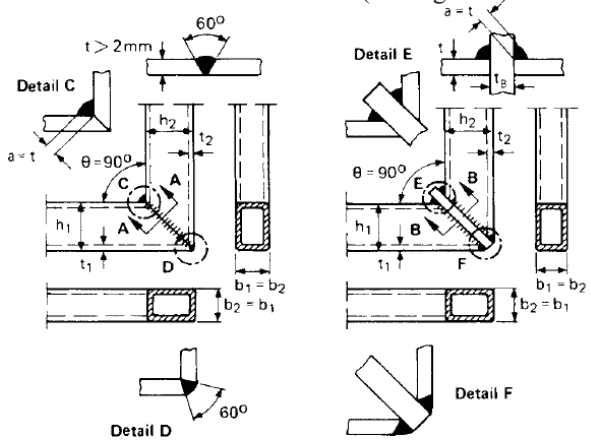


Figure 1. Knee joints researched by Mang et al. [2]

Packer et al. [3] investigated RHS connections bolted on two sides subjected to tension loading (see Figure 2), based on research carried out by Kato and Mukai [4]. The research determined that the limit states for such a connection are:

- Yield strength of the end plate,
- Tensile strength of the bolts, including prying action,
- Strength of the weld connecting the flange plate to the RHS.

It was found that the modified T-stub procedure in EC3 could be used to evaluate these limit states providing that the centre line of the bolts in the flange plate is not positioned beyond the corner of the RHS.

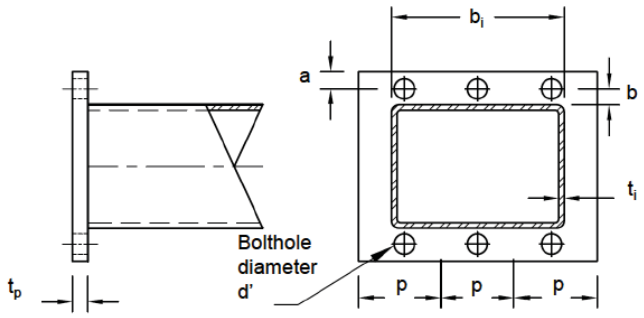


Figure 2. Rectangular flange plate joint. [5]

Design guide 3 produced by CIDECT [5] references flange plate joints, which are subjected to axial and moment loads. The design guidance set out for such a connection is based on a hypothetical "effective" axial load (see Equation 1). This is based on research undertaken by Kurobane et al. [6]. This procedure is conservative as "*it computes the maximum tensile normal stress in the RHS and then applies this to the whole member cross section*" [5].

$$\textit{Effective Axial Load} = \left(\frac{N_i}{A_i} \pm \frac{M_i}{W_i} \right) A_i \qquad (1)$$

where: N_i = Axial load,
M_i = Moment,
A_i = Cross sectional area of section,
W_i = Elastic section modulus of RHS.

Wilkinson and Hancock [7] undertook research on the use of cold formed hollow sections in portal frames. This research was funded in part by CIDECT with recommendations and observations obtained referenced in the CIDECT design guides. The overall aim of the research was to show that plastic design can be used in cold-formed rectangular hollow section portal frames.

The area of Wilkinson and Hancock's research of interest here is the investigation of plastic hinges occurring at the connection between column and rafter. Their research focused on identifying the most appropriate form of connection that could be formed at the knee joint. This connection should "*be capable of reaching the plastic moment (M_p) and maintaining the plastic moment for a suitable amount of plastic hinge rotation, to allow for redistribution of bending moments in a frame*" [7]. The forms of joints considered were:

- Unstiffened welded,
- Stiffened welded,
- Bolted end plate (see Figure 3),
- Internal sleeve.

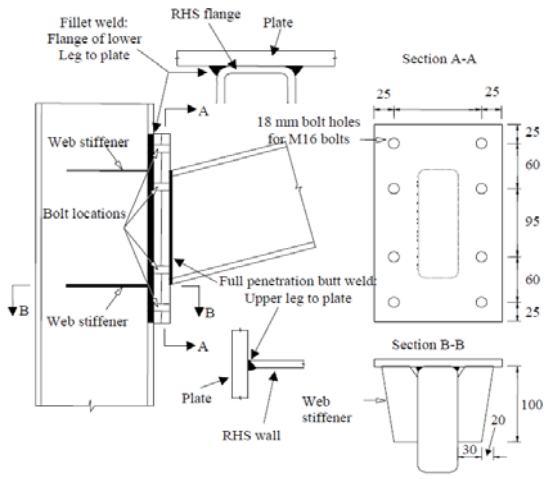


Figure 3. Bolted end plate knee connection. [7]

3 CONNECTION DETAILS

Three joint types were considered in this research. The general form of these joints is presented in Figure 4. The angle subtended between members was 120° for each joint splayed evenly between column and rafter.

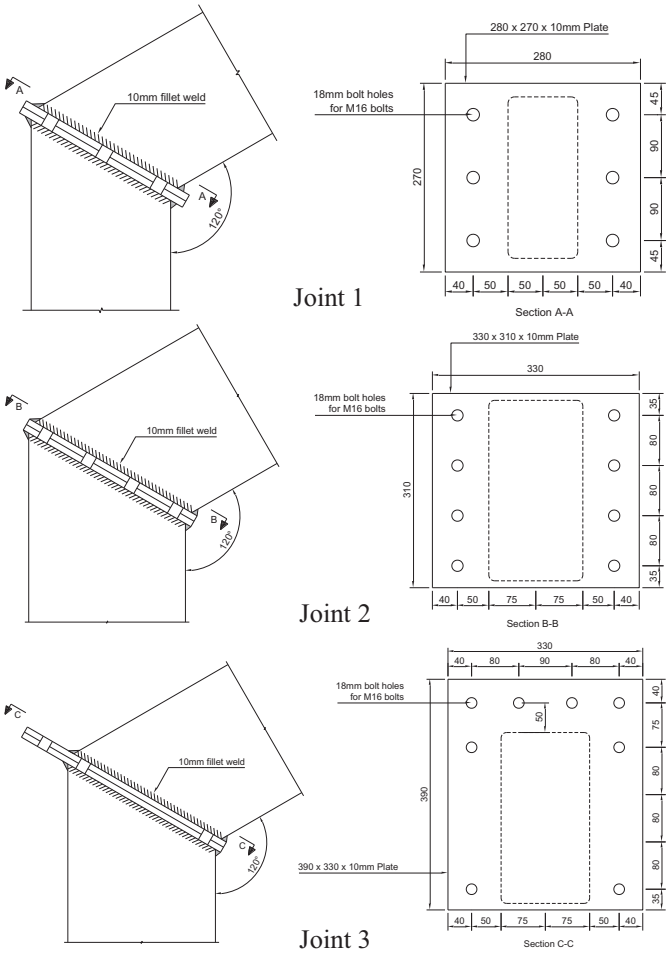


Figure 4. Connection details.

Table 1 outlines the details for each of the joints considered. A 10 mm thick end plate was used for all tests. Similarly a 10 mm fillet weld connected the hollow section with the end plate in all cases. The same size and specification of bolt, M16 x 50 mm grade 8.8 was used throughout.

Table 1. Joint overview.

	Joint 1	Joint 2	Joint 3
Joint type	Flush end plate	Flush end plate	Extended end plate
Beam	200 x 100 x 5.0	250 x 150 x 6.3	250 x 150 x 6.3
Column	200 x 100 x 5.0	250 x 150 x 6.3	250 x 150 x 6.3
Bolt size	M16 x 50 grade 8.8	M16 x 50 grade 8.8	M16 x 50 grade 8.8
Plate thickness	10 mm	10 mm	10 mm
Weld size	10 mm fillet	10 mm fillet	10 mm fillet
Plate yield stress (N/mm^2)	334	334	334
Hollow section yield stress (N/mm^2)	318	318	318

4 PHYSICAL TESTING

The general arrangement for the testing used the principles employed by Wilkinson and Hancock [7] to generate a moment at the joint. The centre of the joint was set up to be eccentric to the axis along which the load was applied and the joint was supported. It is this eccentricity that generates the lever arm to cause a moment to act on the joint.

4.1 Test arrangement

The test was set up to apply the load along a horizontal axis (see Figure 5). The ends of the rafter and column section were secured to the test rig by means of a pin joint. A web stiffening plate was provided to the plate to ensure that there was no local deformation of the hollow section. To apply the horizontal forces, a self-contained lateral test rig was used. It comprises two large stiffened end plates connected together using solid high yield RT550 Macalloy bars.

The left hand (column) end, of the test specimen was connected to the stiffened end plate by a pin joint bracket. A hydraulic jack, load cell, tilting cap and pin joint bracket were set up on the right hand (rafter) end. A roller support was provided at this end to allow translation in the direction of the applied load.

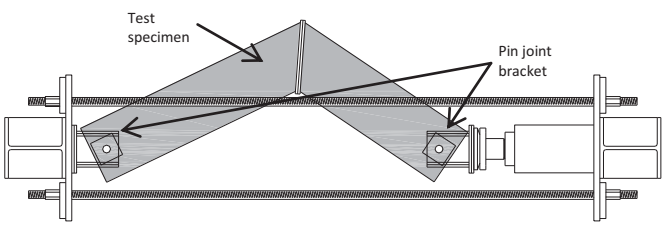


Figure 5. Lateral test rig.

4.2 Measuring devices

Inclinometers were used to measure the rotations of the column and rafter sections. The inclinometers were positioned along the centreline of the hollow sections a distance of $h/2$ from the centre of the joint, where h is the depth of hollow section. It had been identified from finite element analysis that this distance was sufficiently far away from the joint to ensure local deformations would not disrupt readings.

Displacement gauges were used to accurately record the displacements of the test specimen at specific locations. Vertical and horizontal gauges were positioned to measure the global movement of the specimen and used as a comparison with the finite element model. The vertical displacements recorded at the top of the connection were used for calculating 2nd order moments at the joint due to the change in joint eccentricity as the joint was loaded. A horizontal gauge was also positioned close to the joint end plate to record any out-of-plane displacements that may take place during the test.

4.3 Material properties

Tensile tests were carried out using a Denison Mayes material test rig in the Mechanical Engineering Department at Cork Institute of Technology to establish the material properties of the specimens being tested. Each specimen's yield strength was obtained and used in the FEA for more accurate modelling.

Each test comprised a sample of material subjected to an increasing tensile load until failure of the specimen. In total, two samples of rectangular hollow section, two samples of end plate and one sample of grade 8.8 M16 bolt were tested; the results are presented in Table 2.

Table 2. Tensile test results.

Specimen	Original Cross Section mm^2	Ultimate Tensile Strength N/mm^2	Yield Strength N/mm^2
10 mm Plate	600	459	337
10 mm Plate	555	451.7	331.5
Rectangular Hollow Section	251	366	313.6
Rectangular Hollow Section	255	381	322.9
Grade 8.8 Bolt	201.1	911.2	883.9

5 FINITE ELEMENT ANALYSIS

LUSAS v14.7 was used to model the joints tested in the laboratory using hexahedral volume mesh elements.

5.1 Boundary conditions

Symmetry of the joint was utilised to reduce the computational effort required to solve a model of the joints tested in the laboratory. The loading, support conditions and

bolt arrangement were symmetrical along the length of the test specimen. This was represented in the LUSAS analysis by splitting the connection along the central XY plane and assigning a restraint preventing translation in the Z direction as represented by the red surfaces in Figure 6.

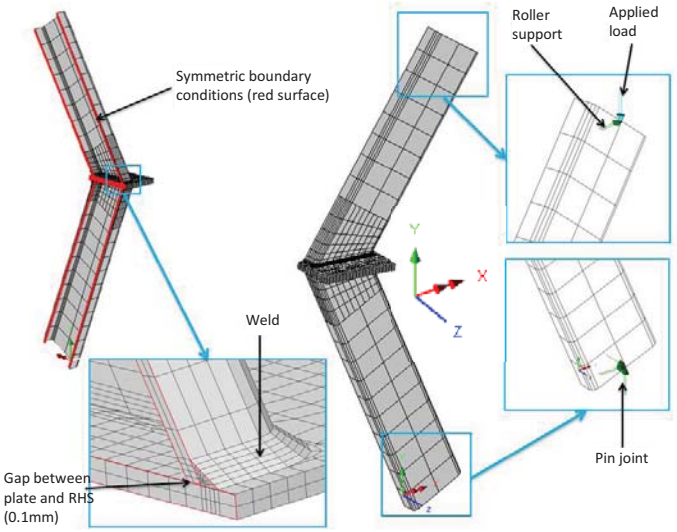


Figure 6. Boundary conditions.

All boundary conditions for the three models were kept constant with only the geometry changing between models. Features of the model include:

- The hollow section and plate were separated by a 0.1 mm gap; this ensured that all forces were to be transferred through the weld.
- A single pin joint was provided to the centre of the base, providing fixity in the vertical and horizontal directions with no rotational restraint.
- A roller support was provided to the rafter allowing displacement in one direction only.
- A single horizontal load was applied to the centre of the rafter spread over the thickness of the web. An initial load of 1 N was assigned and increased incrementally as the model solved.

5.2 Material properties

The "Von Mises stress potential model" was used to assign non-linear material properties to the finite element model. Within this, an initial uniaxial yield stress, which defines the stress at which the material would yield, was assigned. The material properties assigned for the models were informed from results obtained from the tensile tests undertaken.

5.3 Modelling of bolt

Due to the geometrical arrangement of the joint and application of the load, the primary force acting on the bolts is tension. How the bolts interact with the end plates influences the yield line pattern and thus the overall load carrying capacity of the joint. It is the effect that the bolt has on the plate rather than the bolt itself that is of interest in this research. It was determined that the bolt could be simplified as an elastic spring with similar stiffness properties to the bolt.

The stiffness of the bolt, k, along its longitudinal axis was calculated based on Equation 2:

$$k = EA/L \quad (2)$$

where: E = Young's modulus of bolt,
A = tensile cross sectional area of bolt,
L = length of bolt joint.

The stiffened length of bolt calculated is based on the assumption that the bolt head and nut provide additional deformation capacity to the joint along with the bolt shaft, thus reducing the stiffness (see Figure 7).

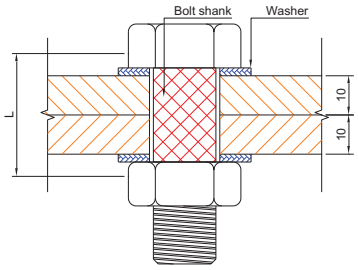


Figure 7. Bolt detail.

The spring stiffness was assigned to the areas enclosed in red in Figure 8. This area is representative of where the compressive forces due to the bolt-head and nut are applied. The area located in the centre is assigned a lower Young's modulus, half that of the plate. The material assigned to volumes "bolt inner" and "bolt outer" was kept elastic, preventing yielding from occurring at the bolt locations.

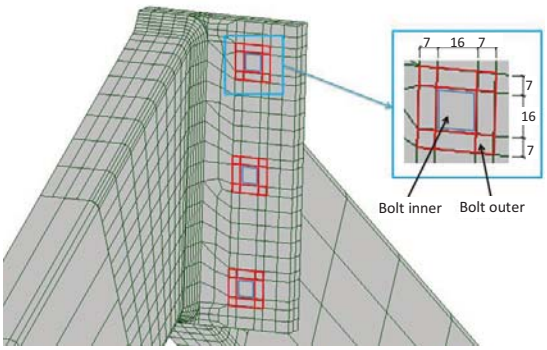


Figure 8. Modelling of bolt locations.

5.4 Slidelines

A slideline is an attribute within LUSAS that can be used to model contact between surfaces or tie dissimilar meshes together (see Figure 9).

A contact slideline was assigned to the surfaces between end plates, preventing penetration of the plates from occurring. A tied slideline was assigned along the length of both hollow sections to allow the application of different mesh sizes to the same member.

A second contact slideline was applied to the surfaces of the plate and hollow section separated by a 0.1 mm gap. The application of this slideline prevents any penetration that may occur between both surfaces due to high compressive loads.

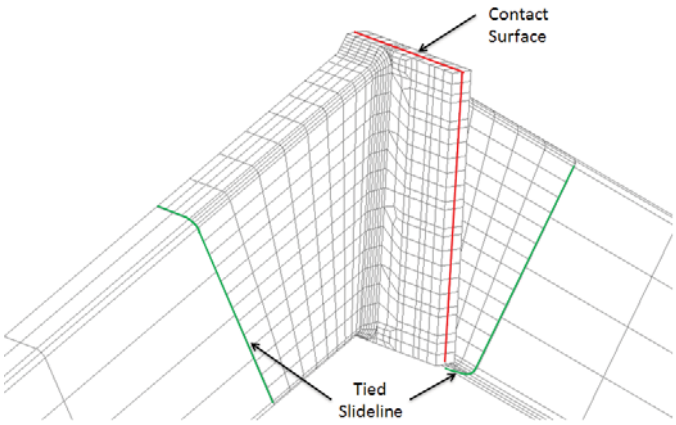


Figure 9. Slideline assignments.

6 PROPOSED DESIGN APPROACH

EC3 outlines an approach to analyse moment connections between I and H sections. This approach was used as a basis for developing both a moment-rotation relationship and establishing the moment resistance of connections between rectangular hollow section members. The results obtained were then compared with laboratory test and finite element analysis results.

Various modifications were made to certain parameters, in particular determining the effective length, l_{eff}, when using the equivalent T-stub analysis.

6.1 Design moment resistance $M_{j,Rd}$

The design resistance for each of the joints is based on the tension resistance of an equivalent T-stub flange. The three modes of failure set out in EC3 were checked:

- Mode 1, Complete yielding of the flange,
- Mode 2, Bolt failure with yielding of the flange,
- Mode 3, Bolt failure.

6.2 Joint stiffness

IS EN 1993-1-8 [1] provides two approaches to determine the moment-rotation relationship for joints. Method (a) uses the stiffness of the joint up to 2/3 the design moment resistance after which a modification, μ, is applied. Method (b) simplifies this curve based on a stiffness modification, η (see Figure 10).

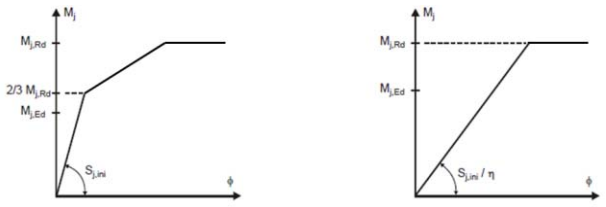


Figure 10a) and (b). Moment-rotation characteristic. [1]

For each component of the joint, a stiffness coefficient, k_i, was determined. These coefficients are specifically set up for joints between I and H sections formed at right angles; they were adjusted accordingly to account for the joint types tested. The stiffness coefficients considered are:

- Column web panel in shear, k_1
- Column web panel in compression, k_2
- Column web panel in tension, k_3
- End plate in bending, k_5

6.3 Yield Lines

The research undertaken focused on end plate in bending, k_5, which is given by equation 3.

$$k_5 = \frac{0.9 l_{eff} t_p^{\,2}}{m^3} \tag{3}$$

where: l_{eff} = the shortest effective length for an equivalent T-stub model,
t_p = end plate thickness,
m = geometrical plate property (centre of bolt to face of column).

Guidance for determining the yield line length, l_{eff}, was taken from EC3 and *Joints in Steel Construction – Moment Connections* [8]. These theoretical lengths were compared with yield patterns from both laboratory and finite element models. Figure 11 outlines the yield pattern for Joint 3. The shortest effective length calculated was then used in the calculations.

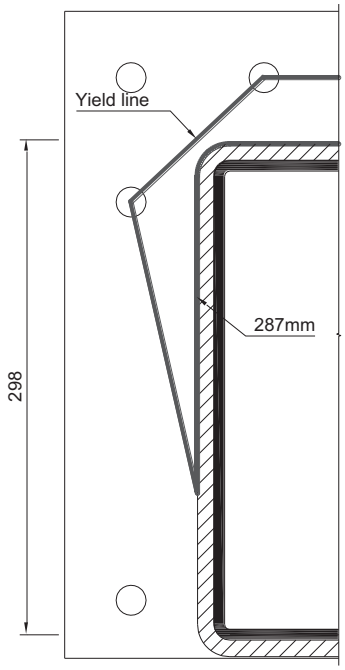


Figure 11. Yield line pattern – Joint 3.

7 RESULTS

The behaviour of each of the three joints was compared using moment-rotation curves generated from laboratory testing, finite element computer models and calculations based on a modified EC3 design approach.

The moment at the joint is the second order moment and includes the effect of changing eccentricity at the joint for both laboratory testing and finite element analysis. The rotation of the joint is determined as the difference between the column and rafter rotations.

Figure 12 outlines the moment-rotation curves for each of the tests carried out. As anticipated from the results of the three joints tested, Joint 1 is the weakest and least stiff while Joint 3 is the strongest and stiffest. That trend is reflected in

laboratory testing, finite element modelling and the proposed design approach based on EC3. It was noted that for the initial straight line portion for all joints, there was good correlation between the three approaches. For each joint, the laboratory test model was the first to deviate from the straight line portion of the curve. For the proposed design approach, the initial stiffness appears to correlate well with the test models.

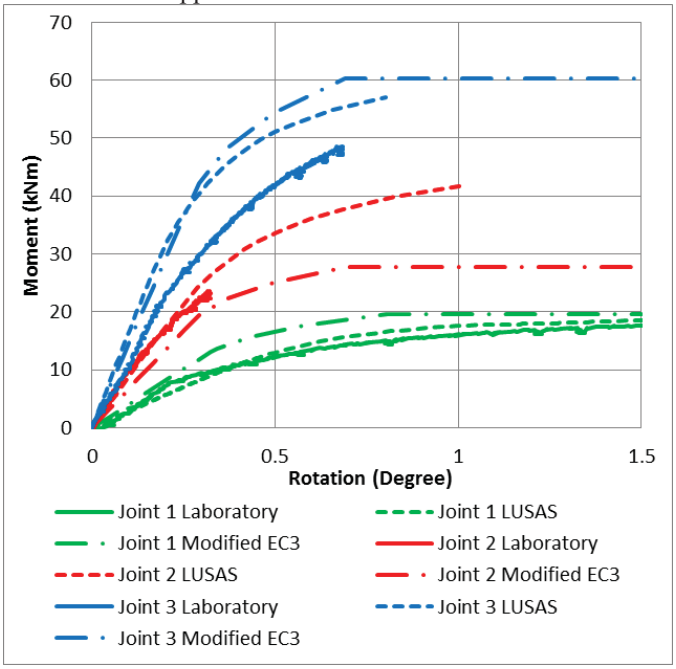


Figure 12 Combined moment-rotation curves.

8 CONCLUSION

Three separate joint types were considered in this research. Each was physically tested under laboratory conditions and modelled using finite element analysis. To establish a possible design approach for the joints, the procedures set out in *IS EN 1993-1-8* [1] and *Joints in Steel Construction – Moment Connections* [8] were modified to provide an approach for anticipating the moment-rotation relationship for eaves connections using rectangular hollow sections.

There was reasonable correlation of the moment-rotation curves for each of the joints researched. The initial stiffness calculated by using the modified EC3 approach provided a good approximation of what was established from computer modelling and laboratory testing. Less confidence can be placed in the anticipated behaviour of the joint beyond the linear elastic portion of the curve. While the Joint 1 moment-rotation curves are quite close for all three approaches, the FEA moment-rotation curve for Joint 2 is noticeably stiffer than the laboratory and EC3 curves and for Joint 3 the laboratory curve is less stiff than the other two. This indicates that further work is required to identify the appropriate yield lines that should be considered in the analysis.

8.1 Further research

The proposed design approach used in this research is a first attempt at generating a method of calculating the moment-rotation behaviour of rectangular hollow section connections at the eaves location. This research is based on guidance specifically designed for connections formed between I and H sections connected at right angles, where the behaviour of the connections is based on stiffness coefficients. For confidence in predicting the moment-rotation characteristic for a bolted hollow section connection, a new set of stiffness coefficients should be formulated and tested based on what is presented in Section 6 of *IS EN 1993-1-8* [1] for I and H sections

A particular area requiring further research is the use of the equivalent T-stub analysis for modelling the end plate behaviour, in particular calculating the effective length for a bolt row or bolt group. Other areas include analysing the behaviour of plates to generate failure modes other than Mode 1, altering the pitch of the rafter and modifying the angle of end plate relative to the column section.

By developing this research further it is hoped that moment connections between rectangular (and square) hollow sections will be made more economic both in terms of connection design and fabrication through improved understanding in the behaviour of such connections.

ACKNOWLEDGEMENTS

The authors would like to thank the staff of the Civil, Structural & Environmental Engineering Department at Cork Institute of Technology for their assistance, particularly Mr. James Morgan and Mr. Liam Jones for their assistance and advice during the testing phase of this research.

REFERENCES

[1] NSAI (2005), *IS EN 1993-1-8:2005, Eurocode 3: Design of steel structures – Part 1-8: Design of joints*. National Standards Authority of Ireland.

[2] Mang F., Steidl G. and Bucak O. (1980), *Design of welded lattice joints and moment resisting knee joints made of hollow sections*, International Institute of Welding, *Document XV-463-80*, University of Karlsruhe, Germany.

[3] Packer, J.A., Bruno, L., and Birkemoe, P.C., (1989) *Limit analysis of bolted RHS flange plate joints. Journal of Structural Engineering*, American Society of Civil Engineers, *Vol. 115*, No. 9, pp. 2226-2242.

[4] Kato, B., and Mukai, A., (1985) *Bolted tension flanges square hollow section members*. *CIDECT Program 8B Report*, University of Tokyo, Japan.

[5] J. A. Packer, J. Wardenier, X.-L. Zhao, G. J. van der Vegte and Y. Kurobane. (1995), *Design guide 3 – For rectangular hollow sections under predominantly static loading*. 1st edition, Verlag TUV Rheinland.

[6] Y. Kurobane, J. A. Packer, J. Wardenier, N. Yeomans. (2004), *Design guide 9 – for structural hollow section column connections.* 1st edition, Verlag TUV.

[7] Wilkinson T., Hancock G. (1998): *Tests of knee joints in cold-formed rectangular hollow sections*, research report no. R779. Department of Civil Engineering, University of Sydney, Sydney, Australia.

[8] SCI and BSCA (1997). *Joints in Steel Construction - Moment Connections*, 1st edition, Ascot & London: Steel Construction Institute and British Steel Construction Association.

Detailing & Curtailment of Steel Reinforcement to Eurocode 2

Brian O'Riordan[1], Ted McKenna[1], Donogh Coleman[1]
[1]Department of Civil, Structural and Environmental Engineering, Cork Institute of Technology, Bishopstown, Cork, Ireland.
email: brianoriordan00@gmail.com, ted.mckenna@cit.ie, donogh.coleman@cit.ie.

ABSTRACT: The now superseded British Standards (BS) design code BS8110-1:1997 provided simplified rules for curtailment of reinforced concrete elements. However, EN 1992-1-1 (EC2) does not provide any such rules and this has resulted in the simplified rules remaining applicable in most design practices as designers are reluctant to adopt the EC2 detailing rules because they are more complex when compared to BS. This research focuses on the simplified rules as these are predominantly applied each day in design offices and investigates the validity of this approach. The objectives were to compare the design codes used to produce RC drawings, namely BS 8110-1:1997 and I.S EN 1992-1-1 and demonstrate with worked examples the curtailment procedure in accordance with EC2 for solid slabs and beams.

The analysis conducted consisted of producing worked examples for anchorage and lap lengths and comparing the design approach outlined in both codes. Structural analysis models of continuous solid slab and beam elements were developed using proprietary analysis software. Spreadsheet solutions for anchorage and lap lengths were developed using Microsoft Excel. Drawings and sketches were produced using AutoCAD to illustrate the curtailment process.

Significant findings identify the bond condition and percentage of reinforcement at the lap location as significantly affecting anchorage lengths. EC2 provides two design approaches for the curtailment process, namely the tensile force method and the shift rule method. Both methods are explained within this research. A comparison of curtailment methods from previous design codes confirms that the BS simplified curtailment rules remain relevant. However, the anchorage and lap lengths produced in accordance with BS 8110 are not consistent with EC2.

KEY WORDS: Reinforced Concrete; Reinforcement; Anchorage-length; Lap-length; Curtailment; Tensile Force Envelope; Shift Rule;

1 INTRODUCTION

The British Standards design code BS8110-1:1997 [1] contained a comprehensive set of simplified detailing and curtailment rules for reinforced concrete elements. Tables and diagrams were produced making the detailing procedure a relatively quick and easy process. However, BS8110 has now been replaced with I.S EN 1992-1-1 [2]. EC2 has revised the design process by introducing longer more complex equations for calculating reinforcement curtailment, anchorage and lap lengths. This research aims to verify whether the BS approach complies with EC2. This research compares both BS8110-1:1997 and I.S EN 1992-1-1 and identifies similarities and differences.

2 ANCHORAGE LENGTHS

Essentially the tensile force in a bar must be less than the concrete anchorage force, otherwise the anchorage fails. Bars subjected to flexural (bending) forces must be anchored into the concrete [3]. EC2 has introduced three anchorage types.

The Basic Anchorage length ($l_{b,rqd}$) is the length of bar required to resist the maximum force in the reinforcement, assuming constant bond stress equal to the ultimate bond stress (f_{bd}) [4]. This accounts for location of reinforcement and bar diameter.

The Design Anchorage length (l_{bd}) is the design length and is used to determine the curtailment length of reinforcement in concrete elements. This accounts for bar shape and cover to reinforcement along with the effects of containment by any transverse reinforcement [5].

The Minimum Design Anchorage length ($l_{b,min}$) is also specified:

For anchorages in tension it is the greatest of:

- 0.3 times the basic anchorage length
- 10 times the bar diameter
- 100mm

For anchorages in compression it is the greater of:

- 0.6 times the basic anchorage length
- 10 times the bar diameter

The EC2 and BS anchorage lengths are shown in equations 1 to 3. Equation 1 and 2 are similar but with two significant differences. In the BS approach the design anchorage bond stress value (f_b) is equated to the ultimate design anchorage bond stress (f_{bu}) and the tensile stress in the bar is taken as the design yield value (i.e Characteristic yield strength (f_y) divided by material partial safety factor (γ_m)).

However, in EC2 the ultimate bond stress (f_{bd}) is dependent on whether good or poor bond conditions exist, and the bar size. EC2 also recommends that the design tensile stress (σ_{sd}) of the bar at the start of the anchorage should be determined. The third equation applies several reduction coefficients to the basic anchorage length to determine the design anchorage length.

BS 8110-1:1997 Design anchorage length:

$$\text{Length} = 0.95.f_y.\emptyset / (4.f_{bu}) \quad (1)$$

EC2 Basic anchorage length ($l_{b,rqd}$):

$$l_{b,rqd} = (\emptyset/4)\,(\sigma_{sd} / f_{bd}) \quad (2)$$

EC2 Design anchorage length (l_{bd}):

$$l_{bd} = \alpha_1.\alpha_2.\alpha_3.\alpha_4.\alpha_5.l_{b,rqd} \quad (3)$$

Where the coefficients are:

- **Coefficient α_1** - Shape of bars
- **Coefficient α_2** - Cover to bars
- **Coefficient α_3** - Transverse bars (not welded)
- **Coefficient α_4** - Transverse bars (welded)
- **Coefficient α_5** - Confinement by transverse pressure
- **Coefficient α_6** - Percentage of lapped bars

Design guidance on the coefficients is provided in Table 8 of EN 1992-1-1.

3 LAP LENGTHS

Due to manufacturing restrictions and ease of handling, bars longer than 12m are not recommended for use on site. Consequently, reinforcement bars often need to be lapped. At lap locations it is necessary to transfer the tensile or compression forces from one bar to the other, through the concrete so as to ensure no slippage of the reinforcement occurs [6]. The lapping of bars should be staggered and located away from areas of high stresses.

Guidance on lap lengths and locations is provided in clauses 3.12.8.9 to 3.12.8.15 of BS8110-1:1997. The significance of reinforcement location within the concrete was addressed and subsequently critical locations were identified. The solution was to increase the design lap length by a factor of 1.4 for reinforcement that was in the top of a concrete section [7] or in the corners where there is less confinement of the reinforcement [7]. Where laps occurred at both the top and corner of a member the design lap length was increased by a factor of 2.0. The design lap length formula used in BS 8110-1:1997 is given in equation 4:

$$\text{Length} = 0.95.f_y.\emptyset / (4.f_{bu}) \quad (4)$$

The EC2 design lap length procedure is similar to the anchorage length calculation in terms of using coefficients regarding bar shape, cover and confinement of transverse reinforcement. However, the percentage of lapped bars (α_6) in the section is now accounted for in equation 5.

EC2 Design lap length (l_0):

$$l_0 = \alpha_1.\alpha_2.\alpha_3.\alpha_5.\alpha_6.l_{b,rqd} \quad (5)$$

EC2 considers lap lengths in terms of the following:

- Main longitudinal reinforcement laps
- Transverse reinforcement in the lap zone

The arrangement of longitudinal bars needs to comply with Cl. 8.7.2 and figure 8.7 of EN 1992-1-1 as shown in Figure 1.

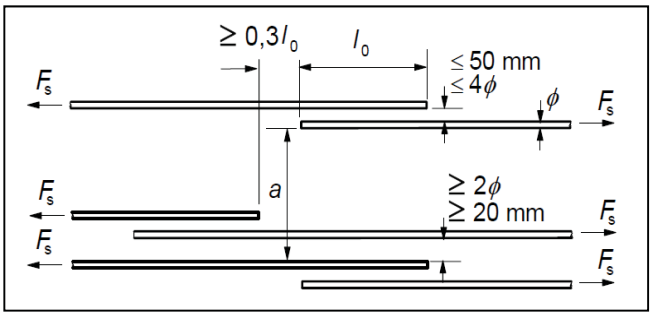


Figure 1. Adjacent Laps – fig 8.7.

The arrangement of transverse reinforcement in the lap zone needs to comply with clause 8.7.4 and figure 8.9 of EN 1992-1-1 as shown in Figure 2 and Figure 3.

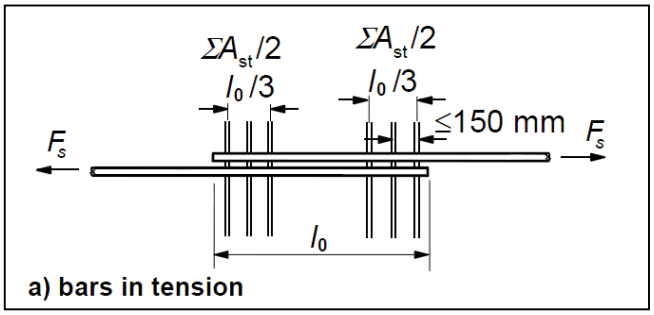


Figure 2. EN 1992-1-1 - Fig 8.9 (a)

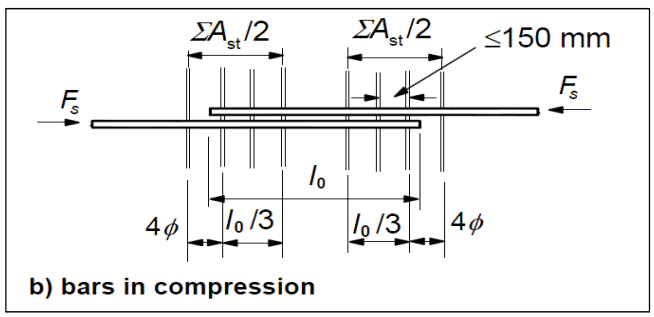


Figure 3. EN 1992-1-1 - Fig 8.9 (b)

4 CURTAILMENT

Reinforcement in concrete is primarily provided to resist tensile and compression forces acting on the section. However, these forces reduce significantly away from areas of concentrated stresses. Therefore at some point along the span of the member the amount of reinforcement may be reduced. This reduction is termed reinforcement curtailment. To determine the curtailment points, the theoretical point where the continuing bars provide sufficient tensile resistance must be identified. Figure 4 demonstrates the curtailment procedure. The diagram shows the end span of a continuous beam, the hatched area represents the resulting bending moment envelope from the applied loads.

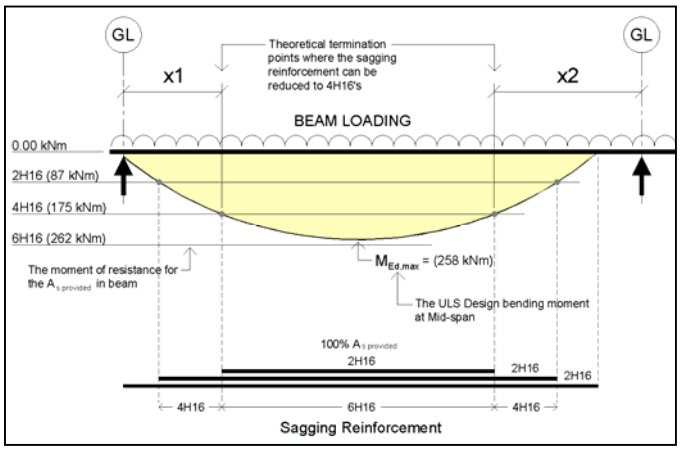


Figure 4. Typical beam curtailment diagram.

BS provided simplified rules for the curtailment of reinforcement in beams and slabs. The rules outlined in clauses 3.12.9 and 3.12.10 of BS8110 could be applied if certain loading arrangements and span lengths were achieved.

Clause 3.12.9 states that except for end supports, in every flexural member each bar should extend beyond the point at which in theory it is no longer needed, for a distance at least equal to the greater of:

- The effective depth of the member (d)
- 12 times the bar diameter

However in addition to the above, for a bar in the tension zone cl. 3.12.9.1 outlines other distances to consider:

a) A tension anchorage length beyond the theoretically point where reinforcement is not needed.

b) Distance to where the design shear capacity of the section is greater than twice the applied shear force.

c) Distance to where the continuing bars provide twice the required area of reinforcement to resist the bending moment.

Figure 5 shows a diagram of the curtailment process. Firstly the theoretical termination points 'x1' and 'x2' are calculated by using the moment of resistance (M_R) of the bars in the section. Then the additional distance from that point is applied using option: a), b) or c). Finally, the distances from either support to the curtailment points 1 and 2 (Cp1 and Cp2) are determined.

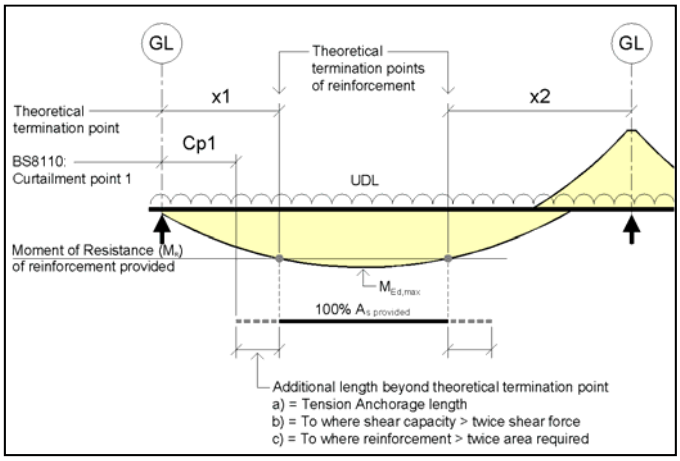


Figure 5. BS8110-1:1997 Curtailment diagram.

The use of these simplified rules meant that calculations identifying the exact curtailment points were unnecessary. Tension and compression anchorage and lap lengths were also simplified into tabular form and could be easily determined.

EC2 does not provide any simplified rules for curtailment, section 9 of EC2 – Detailing of members and particular rules sets out guidance for beams, solid slabs, flat slabs, columns, walls and foundations. This research focuses on beams and solid slabs. Clause 9.2.1.3 of EC2 provides guidance on the curtailment procedure for tension reinforcement. EC2 have introduced two new approaches for the curtailment process:

1. Tensile Force Envelope;
2. Shift Rule Method.

4.1 Tensile Force Envelope (TFE)

Clause 9.2.1.3 (1) of EC2 states that sufficient reinforcement should be provided to resist the envelope of the acting tensile force. This approach requires a tensile force envelope to be developed. It accounts for loading combinations but also the additional force ΔF_{td} resulting from concrete strut action. EC2 uses the variable strut inclination method for the design of shear reinforcement. This method takes account of an additional tensile force being applied to the tension reinforcement due to the concrete acting as a compression strut at the angle 'θ'. EC2 defines this additional force as 'ΔF_{td}'. The use of this variable strut inclination method may allow the designer to make savings on the amount of shear reinforcement provided in the section. However, it is important to note that any initial savings in shear reinforcement may be negated by the necessity for additional anchorage and curtailment lengths. Ultimately, the amount of shear reinforcement required in a section reduces as the angle of the concrete compression strut θ decreases. EC2 has set limits to the angle θ of between 21.8° and 45° to ensure excessive crushing of the concrete does not occur. The designer must strike a balance between the two to achieve a practical solution. For predominantly uniform loading the angle of 21.8° can be assumed for the compression strut angle θ [8].

The diagram shown in Figure 6 illustrates the tensile force method as outlined in EC2.

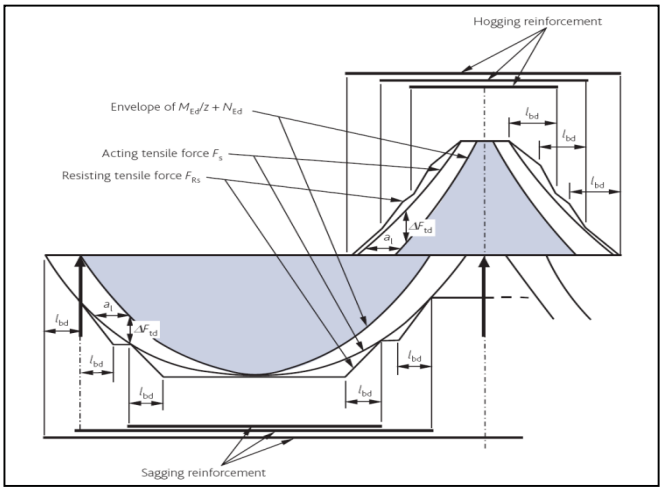


Figure 6. Illustration of the curtailment of longitudinal reinforcement (Concise Eurocode 2 – Figure 12.1)

In order to generate a tensile force envelope, equations 6, 7 and 8 are necessary.

Tensile force envelope $= (M_{Ed}/z + N_{Ed})$ (6)

Acting tensile force (F_s) $= (M_{Ed}/z + N_{Ed}) + \Delta F_{td}$ (7)

Resisting tensile force (F_{Rs}) $= A_{s\ provided}\,(f_{yk}/\gamma_s)$ (8)

where:

M_{Ed} = Ultimate Limit State design moment,
z = Lever arm (take as 0.9d),
N_{Ed} = Axial loading,
V_{Ed} = Ultimate limit State design Shear force,
ΔF_{td} = Additional tensile force due to strut action,
$A_{s,provided}$ = Area of reinforcement provided in section,
f_{yk} = Steel reinforcement characteristic strength,
γ_s = Partial safety factor for reinforcement,
a_1 = For solid slabs: $a_l = d$,
For beams: $a_l = z\,(\cot\theta - \cot\alpha)/2$,
l_{bd} = Design anchorage length.

The procedure to generate the TFE is as follows:

1. Produce bending moment and shear force envelopes.
2. Create spreadsheet and input bending moment and shear force values at equal intervals along the span.
3. Generate tensile force envelope using equation 6.
4. Calculate the additional tensile force (ΔF_{td}) values using the following expression: $(0.5 \times V_{Ed}\,(\cot\theta - \cot\alpha))$.
5. Generate acting tensile force (F_s) using equation 7.
6. Plot acting tensile force envelope to scale on a graph.
7. Calculate resisting tensile force (F_{Rs}) using equation 8.
8. Plot resisting tensile force values on the graph.
9. The curtailment points occur at the intersection of (F_S) and (F_{Rs}) plotted lines.

Figure 7 demonstrates the curtailment process executed on the end span of a continuous beam. The light shaded area represents the bending moment envelope. The darker shaded area is the tensile force envelope. The black curved line is the acting tensile force envelope and the horizontal lines indicate the resisting tensile force provided by the reinforcement.

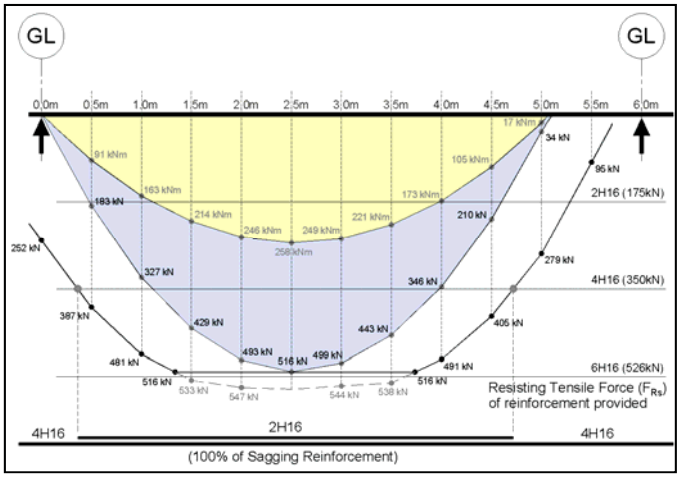


Figure 7. Typical TFE for end span of continuous beam

4.2 Shift Rule Method

EC2 provides an alternative option to producing a tensile force envelope for structural elements as outlined in clause 9.2.1.3 (2) which is known as the "Shift Rule".

a) For members that require shear reinforcement, the additional tensile force ΔF_{td} should be calculated in accordance with clause 6.2.3 (7);
b) For members that do not require shear reinforcement, the additional tensile force ΔF_{td} may be estimated by shifting the bending moment curve a distance $a_l = d$ in accordance with 6.2.2 (5) using the shift rule;
c) The shift rule may also be used as an alternative for members that require shear reinforcement where the additional tensile force ΔF_{td} may be estimated by shifting the bending moment curve envelope a distance $a_l = z\,(\cot\theta - \cot\alpha)/2$;

This shift rule can be used to estimate the additional tensile force applied to the reinforcement. The distance the moment curve is to be shifted is different for beams and slab members.

- Slabs: a_l = effective depth of the member (d)
- Beams: $a_l = z\,(\cot\theta - \cot\alpha)/2$

In the case of beams with predominantly uniform loading, the formula above may be simplified to 1.125d, where'd' is the effective depth of the beam. However, this simplification assumes that vertical links are used and that the concrete strut angle 'θ' is 21.8°. The Institution of Structural Engineers (IStructE) also provides guidance on the shift rule method, which states that the Designer should specify the curtailment length (l_{bd}) + a_l [9].

The procedure to execute the shift rule method is as follows:

Step 1: Produce a bending moment envelope and calculate the theoretical termination points of the reinforcement as shown in Figure 8. The distance the bars should extend

beyond the termination points should be confirmed with the Designer (depending on approach; EC2 or IStructE).

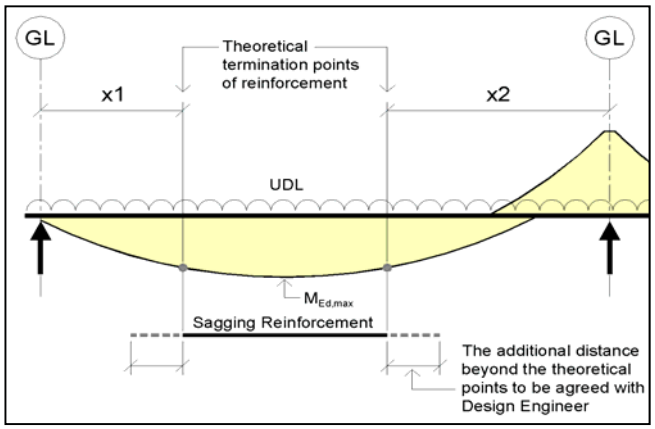


Figure 8. Step 1 (theoretical termination points)

Step 2: Shift the moment curve horizontally to the left and right a distance 'a_l' as indicated in Figure 9. The value of 'a_l' should be calculated in accordance with Cl. 9.2.1.3 (2) of EC2, ensuring that the value of the ULS maximum design moment ($M_{Ed,max}$) is not exceeded [2].

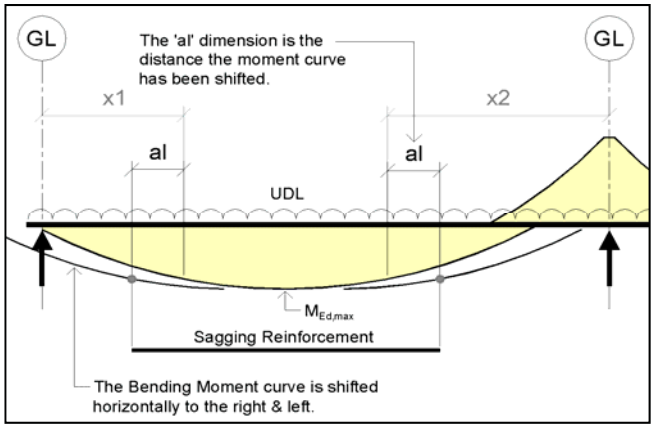


Figure 9. Step 2 (Shift moment curve a distance a_l)

Step 3: Calculate the distances from either the face of support or centre line of support to curtailment points (Cp) Cp1 & Cp2 as illustrated in Figure 10.

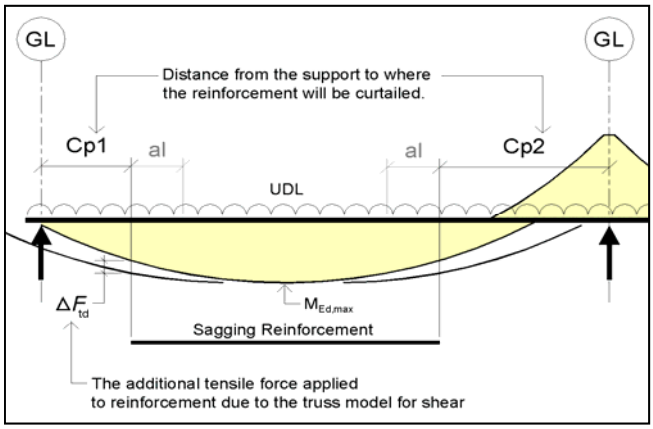


Figure 10. Step 3 (Determine distance from supports)

5 SPREAD SHEET SOLUTIONS

In the new design process there are six coefficients that require separate value inputs. The inclusion of these coefficients has made producing a tabulated system more complex. Therefore the use of a software solution is a far more effective tool. Decisions on coefficient inputs may be changed at ease with instant results, allowing the design to be optimised. Microsoft Excel was utilised to prepare the solutions for both anchorage and lap lengths. Figure 11 is an image taken from the spreadsheet. The spreadsheet was developed based on the formulae in sections 8 and 9 of Eurocode 2. The analytical explanations of the relevant values were taken from Table 3.1 of EC2.

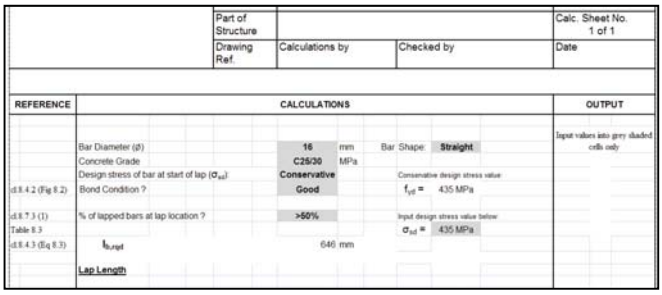


Figure 11. Spread sheet

6 WORKED EXAMPLE

As part of the research, worked examples were produced in accordance with EC2 to demonstrate the curtailment procedure for a continuous one way spanning solid slab and a continuous beam respectively. The shift rule method was used to determine the curtailment over the more complex tensile force method. The spans and loading arrangement for the slab and beam selected comply with the rules outlined in Cl. 12.8.9 and Cl. 3.12.8.15 of BS8110-1:1997. The structural analysis of the beam and slab was carried out using Staad-Pro which is proprietary software used for structural analysis and design. A series of loading combinations was applied to the structural members in accordance with I.S. EN 1991-1-1. The connections between beam and column were designed as simply supported. No account for the redistribution of moments was included in the analysis. The geometric properties are given in Table 1.

Table 1. Slab & Beam details

Element	Span (m)	Dimensions (m)	UDL (kN/m^2)
Slab	5.0	0.2h x 1.0w	14.93
Beam	6.0	0.65h x 0.25w	79.69

Several critical locations were identified and formed the focus of the comparison exercise; the areas selected are as follows:

- Anchorage of bottom bars at end supports,
- Lap length of bottom bars at end supports,
- Lap length of bottom bars at 1st interior support,
- Curtailment of bottom bars at end support,
- Curtailment of bottom bars at 1st interior support,
- Curtailment of top bars at 1st interior support,

The comparison results are listed in Tables 2 to 7.

Table 2. Anchorage of bottom bars at end support – measured from the face of support

Element	BS8110 (mm)	EC2 (mm)
Slab	*(12Ø+support width/2)* **245**	**108**
Beam	*(12Ø+support width/2)* **317**	**404**

Table 3. Lap of bottom bars at end support

Element	BS8110 (mm)	EC2 (mm)
Slab	**400**	**200**
Beam	**608**	**240**

Table 4. Lap of bottom bars at 1st interior support

Element	BS8110 (mm)	EC2 (mm)
Slab	**N/A**	**N/A**
Beam	*(38Ø)* **608**	**780**

Table 5. Curtailment of bottom bars at end support

Element	BS8110 (mm)	EC2 (mm)
Slab 100% rebar	*(0.1L)* **500**	**456**
Beam 100% rebar	*(0.1L)* **600**	**492**

Table 6. Curtailment of bottom bars at 1st interior support

Element	BS8110 (mm)	EC2 (mm)
Slab 100% rebar	*(0.2L)* **1000**	**1203**
Beam 100% rebar	(*0.15L)* **900**	**1396**

Table 7. Curtailment of top bars at 1st interior support

Element	BS8110 (mm)	EC2 (mm)
Slab 100% rebar	*(0.15L)* **750**	**652**
Slab 50% rebar	*(0.3L)* **1500**	**1250**
Beam 100% rebar	*(0.15L)* **900**	**745**
Beam 60% rebar	*(0.25L)* **1500**	**1680**

7 DISCUSSION

7.1 Anchorage Lengths

Table 8 outlines the key differences between each design approach. Notably it is the design stress in the bars and the bond conditions that are significantly different.

Table 8. Design approach key differences.

Design considerations	BS	EC2
Bond between reinforcement & concrete	Yes	Yes
Contact Area	Yes	Yes
Location of reinforcement in concrete	No	Yes
Steel characteristic yield strength (N/mm^2)	460	500
Partial safety factors (γ_m and γ_s)	1.05	1.15
Design yield strength (MPa)	438	435
Design stress at anchorage location (σ_{sd})	438	*T.B.C
Anchorage length measured from	Support centreline	Face of support

*T.B.C – To be calculated at start of anchorage point.

7.2 Lap lengths

Both design codes consider the location of reinforcement within the member when calculating lap lengths. However, the lap length calculation in EC2 also incorporates the percentage of reinforcement at the lap location. This is the only significant difference between both design codes. If lap locations could be staggered then small savings on materials could be achieved, but this is not always practical with short span members.

7.3 Curtailment

In the curtailment process both design codes provide comparable levels of information. Nonetheless, there are some notable exceptions. EC2 has addressed the issue of partial fixity of simply supported members and recommends providing 25% of the mid-span reinforcement in the top of the section. For bottom reinforcement at end supports, EC2 states that 25% of mid-span reinforcement should be provided. However, in the beam worked example it was revealed that 50% of the mid span reinforcement was necessary at end supports due the stresses in the 25% initially provided exceeding the allowable design yield strength of 435 MPa. It is interesting to note that this 50% is in line with the British Standards approach.

8 CONCLUSION

It is evident from the research undertaken that neither design code BS8110 or EC2 provide a comprehensive guide to detailing reinforcement. What is clear is that engineering judgment and good communication between RC Detailer and Designer must be exercised to ensure decisions made by the Designer are understood and applied to reinforcement drawings. The IStructE provides additional guidance on detailing best practice but their approach would appear to be conservative. The curtailment lengths calculated during this research to BS8110-1:1997, although somewhat conservative, do comply with EC2. However, the anchorage and lap lengths produced are not consistent with EC2. The results obtained show the calculated lengths well in excess or below the equivalent EC2 design lengths.

REFERENCES

[1] British Standards Institution (1997). BS 8110-1:1997 Structural Use of Concrete, Part 1: Code of practice for design and construction. London: British Standards Institution.

[2] Eurocode 2 (2005). I.S. EN 1992-1-1:2005 Design of concrete structures Part 1-1: General rules and rules for buildings (Including Irish National Annex) Ireland: The National Standards Authority of Ireland.

[3] W.H. Mosley, J.H. Bungey & R. Hulse (1999). Reinforced Concrete Design. 5th ed. New York: Palgrave MacMilan. P97.

[4] Chanakya Arya (1994). Design of Structural Elements. Great Britain: E & FN Spon. P245

[5] British Standards Institution (2004). EN 1992-1-1:2004 (E) Design of concrete structures Part 1.1 General rules and rules for buildings. London: British Standards Institution.

[6] W.H. Mosley, J.H. Bungey & R. Hulse (2007). Reinforced Concrete Design to Eurocode 2. 6th ed. New York: Palgrave MacMilan. p116.

[7] W.H. Mosley, J.H. Bungey & R. Hulse (2007). Reinforced Concrete Design. 5th ed. New York: Palgrave. p100.

[8] W.H. Mosley, J.H. Bungey & R. Hulse (2007). Reinforced Concrete Design. 6th ed. New York: Palgrave. p102.

[9] The Institution of Structural Engineers (2006). Standard Method of Detailing Structural Concrete. 3rd ed. London: The Institution of Structural Engineers. p75.

Performance of vinyl on concrete floors subject to pull off testing

N. Holmes[1], R.P. West[2]
[1]School of Civil & Structural Engineering, Dublin Institute of Technology, Bolton Street, Dublin 1, Ireland
[2]Department of Civil, Structural and Environmental Engineering, University of Dublin, Trinity College, Dublin 2, Ireland
Email: niall.holmes@dit.ie, rwest@tcd.ie

ABSTRACT: The application of impermeable floor coverings on concrete floor slabs when the surface achieves a relative humidity of 75% is not necessarily 'safe' as it does not consider the effect of accelerated drying which can result in significant residual moisture remaining through the slab at the time of covering. Accelerated drying can result in long term problems such as blistering of vinyls and rising of tiles due to excessive moisture and vapour pressure build-up underneath. This paper presents the findings after an impermeable floor covering was laid on a number of concrete slabs on which accelerated drying was employed. The results from subsequent moisture and vapour pressure measurements show that they do not cause direct failure of the covering. Indeed, after a series of pull-off tests carried out on the covering adhered to concrete specimens, the vinyl could not be removed. It is therefore concluded that the types of problems such as delamination and blistering, are caused by more than the build up of moisture and pressure but by the effects of glue solubility, poor workmanship, and salts (efflorescence etc) in the moisture.

KEY WORDS: Concrete floors; vinyl; adhesion; pull-off; vapour pressure

1 INTRODUCTION

Previous work in this area by the authors [1-4] has shown that when the concrete surface achieves a relative humidity (*rh*) of 75%, a residue of moisture exists through the depth of the slab, particularly so when accelerated drying is employed. BS 8203 [5] assumes that 75% *rh* is a safe value at which to apply floor coverings. However, this does not consider the effect of residual moisture through the slab at the time of covering and the long term problems that can occur. This residue of moisture is principally a function of the slab depth, w/c ratio and the drying environment and slowly equilibrates through the slab depth after the application of an impermeable covering. To investigate the effect of residual moisture on concrete floor coverings, *rh* and vapour pressure measurements were taken before and after application. The results demonstrate how moisture redistribution and vapour pressure build up under the impermeable covering following artificial drying with heaters and dehumidifiers.

Moisture migration in concrete floors plays an important role in the timely construction and finishing of buildings including warehouses, sports halls and other leisure facilities. In the UK, more than 6 million square metres of floors are constructed each year [6].

It is commonly believed that the build-up of vapour pressures and moistures are the main, even sole, cause of long-term problems to impermeable floor coverings such as delamination and blistering. Pull-off tests carried out on a number of concrete specimens with impermeable coverings will show that they, on their own, are not responsible for the problems mentioned above, at least not in the short term. It is concluded that they may also be due to glue solubility and moisture salts which combine to affect its ability to adhere the covering to the concrete.

This offers a real insight into the effect of premature laying of impervious coverings on concrete floors and how moisture builds up and ultimately leads to long-term problems.

2 BACKGROUND AND RESEARCH SIGNIFICANCE

The effect of on-going moisture migration following sealing of concrete floors and the long-term moisture and vapour pressure build-up is the cause of significant costs and inconvenience for clients and users. However, these issues may also occur as a result of poor laying practices, such as laying the covering on a dusty floor surface and with trapped air bubbles between the floor and the covering. Even if the dust and air bubbles are removed, problems such as inadequate glues, poor glue application and coverage and general poor workmanship can also lead to long-term issues.

When the covering was applied to the slabs for the tests here, it was firmly pressed down onto the concrete to ensure that no air pockets could develop between the covering and the concrete. If air bubbles are created at the time of covering, they may lead to future problems, as a single bubble can be spread by users walking on the covering and a larger area can be affected [7]. This causes the air bubble to spread and enlarge as it attaches to other nearby bubbles since air is

assumed incompressible in this situation. The existence of such bubbles can have further implications other than simply spreading over the surface. Since a void now exists between the concrete and the surface, evaporation from the surface will continue and moisture will accumulate within it over time, particularly if a large residue of moisture exists deep in the concrete at the time of covering. It has been shown [8] that conditions like these can cause the trapped moisture to squirt a meter into the air when burst and some floor manufacturers require that a heavy roller be passed over the covering a number of times to reduce this risk of multiple trapped air bubbles.

3 EXPERIMENTAL PROGRAMME

3.1 Mix Proportions

Concrete was manufactured with two w/c ratios (0.5 and 0.6) and a fixed water content of 195kg/m^3. The w/c ratios used were chosen as they represent the more typical range used in floor construction. Following a number of trial mixes, the final proportions were determined so that an average slump of 75mm was achieved. The mix proportions are summarised in Table 1.

Table 1. Mix proportions

Slab No.	w/c ratio	Mass of Ingredients (kg/m^3)				
		Water	CEM I	FA	CA	
					10mm	20mm
1	0.5	195	390	706	353	706
2	0.6	195	325	787	348	695

FA – Fine aggregate; CA – Course Aggregate

3.2 Materials

The cement type was CEM I grade 42.5 supplied by Irish Cement. The fine aggregate used was medium graded sand and the coarse aggregate (10 and 20mm) was pre-washed limestone with a maximum size of 20 mm. Before mixing, the water content of the sand was assessed using a Speedy moisture content apparatus and the free-water content added to the concrete was adjusted accordingly.

3.3 Preparation of samples

The concrete was manufactured using a pan mixer. Three slabs (700x700x150mm) and 12 concrete cubes (150x150x150mm) were manufactured. After mixing, the concrete was poured, in 50mm thick layers, into the timber moulds which had a release agent applied to ease de-moulding the following day. The concrete was vibrated on a vibrating table until no more air bubbles were visible on the surface. Curing of the concrete was provided by surrounding with with damp hessian and placing under polythene for 24 hours to trap moisture evaporating from the surface.

Each slab was drilled to depths of 15, 40, 65, 90, 115 and 135mm using a 15mm drill bit so that the *rh* at the depths could be monitored over time. Plastic tubes (Figure 1) were inserted into these holes and, with the arrangement of the rubber bung, an average *rh* reading was recorded approximately 5mm above the base. The four sides and base of the concrete slabs were then sealed with an impermeable epoxy paint to ensure drying took place in one direction only, namely upwards. Each face had three coats applied. Figure 2(a) shows a prepared slab prior to drying.

The slabs were transferred to a sealed control room to dry artificially where the average ambient temperature and humidity were 39.5^{0}C and 15.5% respectively. When the slabs reached a *rh* of 75% on the surface, they were covered with an impermeable floor covering (Figure 2(b)).

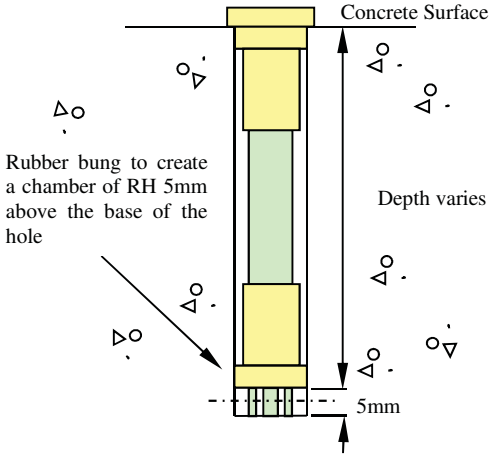
The covering, a standard floor vinyl with a sponge back, was applied using evo-stick super acrylic adhesive glue. Before application, the surface was gently 'smoothed' using a wire brush to remove all bumps with the resulting dust removed using a hand-brush and a heavy-duty industrial hoover. In addition, the heater and dehumidifier in the control room were turned off for 48 hours before the covering was applied and the door of the control room was left open to allow the heat to escape, as the manufacturer required that the vinyl was applied in normal conditions. The vinyl was cut into square pieces (720x720mm) and left for 24 hours to become acclimatised to the environment in which they would be kept.

The glue was applied with a V-notched trowel with serrated edges at 15mm intervals at an angle of 60^0 in accordance with the glue manufacturer's recommendations. When the glue became 'tacky' to touch, the covering was applied by laying it over the central area of the slab, removing it for a few moments and then re-laying it using direct pressure ensuring the covering was adhered evenly to the concrete surface. The holes for the humidity tubes, pressure gauge and lifting eyes were carefully cut out using a Stanley knife. Any cuttings made on the covering were sealed using silicone to ensure that the concrete surface was totally impervious to moisture loss and vapour pressure build up. The extra 10mm on all four sides was removed. Figure 2(b) shows a typical covered slab.

After the slabs were covered, the vapour pressure just under the covering at the centre of the slab, was monitored as shown in Figure 3. The vapour pressure was measured using PDCR 81 pore pressure gauges which are regularly used in soil mechanics. These probes are capable of measuring small changes in pressure and consist of a ceramic filter suitable for rugged construction. The standard specification for the gauge ranges from 1-35 bar (100-3500 kPa) and must be used in an airtight environment.

A rubber bung was used to cap the plastic tubes. The pressure gauge was inserted into the rubber bung and placed into a pre-drilled hole in the centre of the slab to a depth of 15mm. The pressure is measured as a function of the difference in voltage between the input and output.

As part of the vapour pressure measurement a Datascan 700 apparatus was used to record the voltage output. The Datascan apparatus is a series of intelligent measurement and data

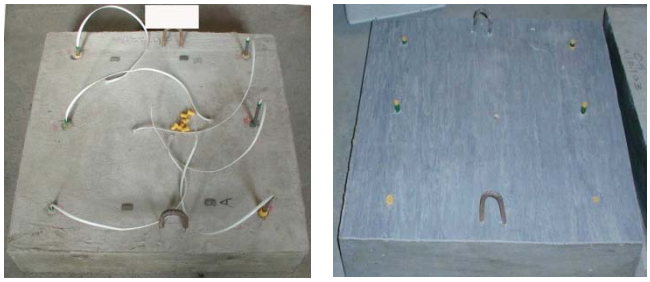


(a)



(b)

Figure 1. Plastic tube used to measure the *rh* in the slabs



(a) (b)

Figure 2. Prepared concrete specimens

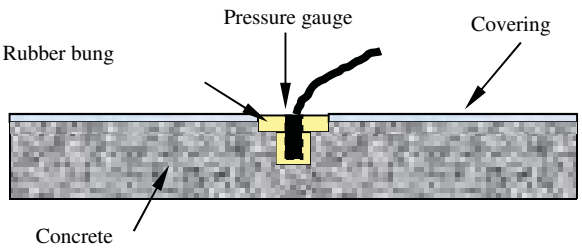


Figure 3. Set-up used to measure pressure under the covering

collection units developed for the industrial and scientific sectors [9].

Data measurement is made through measurement processor modules that contain an A/D converter microprocessor with a battery backup and power supply, along with a RS232 link capability to a host computer. The measurement processor used here is version 7221 that provides eight analogue inputs including channel excitation, as shown in Figure 4. A typical Datascan installation is shown in Figure 5 with the complete set-up in Figure 6.

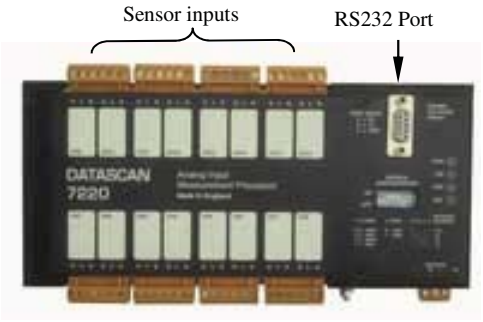


Figure 4. 7221 Measurement Processor

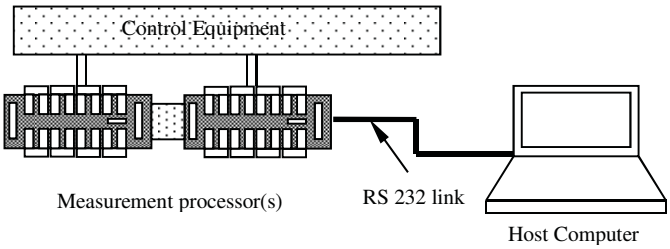


Figure 5. Typical Datascan installation

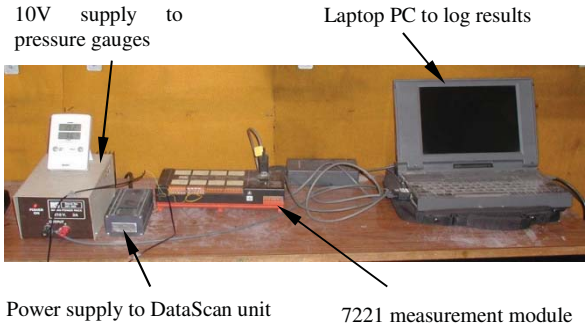
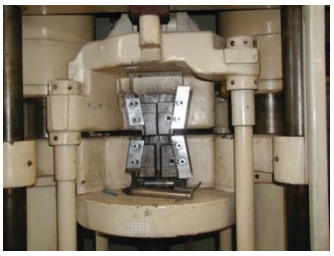
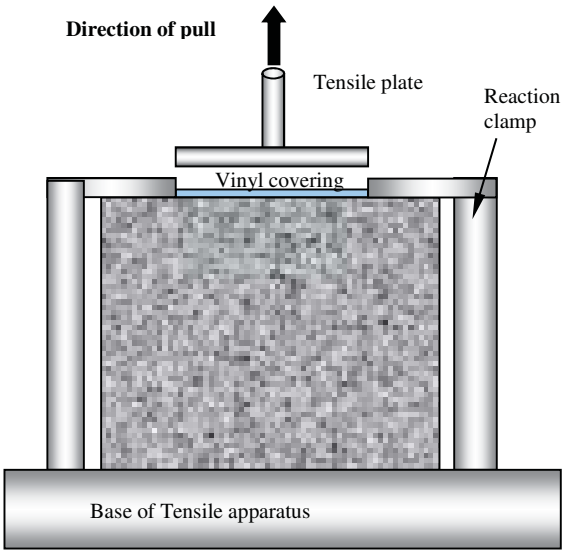


Figure 6. Complete vapour measurement set-up.

The 150mm concrete cubes were also allowed to dry in the artificial environment and sealed at the same time as the concrete slabs. The impermeable covering was applied to the top of the cube in an identical manner as to the slabs. These cubes were to be used to pull the vinyl off the concrete to assess the pull-off strength of the vinyl, as shown in Figure 7.



(a)



(b)

Figure 7. (a) Tensile testing apparatus and (b) schematic of the test set-up

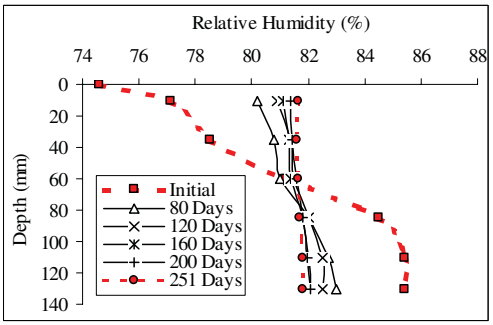
4 RESULTS AND DISCUSSION

4.1 rh / moisture build-up under the covering

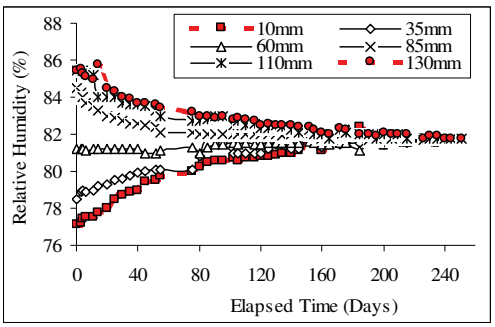
Figures 8-9 show the *rh* profiles in the two slabs previously dried in the control room after the impermeable covering was applied. As may be seen, the initial *rh* profiles with depth are non-linear which is due to the more onerous drying regime in which they were dried. The measured *rh* at 60mm, or 40% of the slab depth gives a good estimate of the long-term equilibrated *rh*. For example, in Figure 8(a), the measured *rh* at 60mm on sealing is approximately 81.5% at 251-days. In Figure 9(a), the measured *rh* initially at 60mm is 81% and at 240-days, the point of equilibrium, is 82%. The results give credence to the ASTM proposals to measure the *rh* at 40% of the depth for single face drying [10].

4.2 Vapour Pressure generation

Figure 10 shows the increase in vapour pressure underneath the covering for the two slabs. It is clear that slab 2 (w/c = 0.6) has a greater vapour pressure than slab 1 (w/c = 0.5) on average, approximately 250Pa over the 210-days. This is hardly surprising since slab 2 had a greater residue of moisture remaining in it at the time of covering.

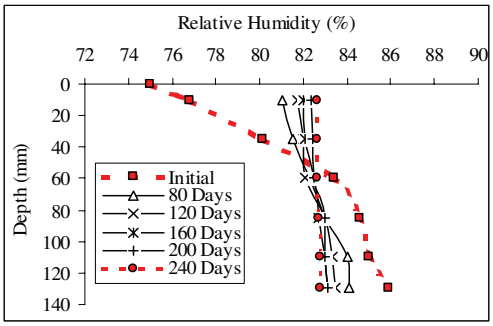


(a)

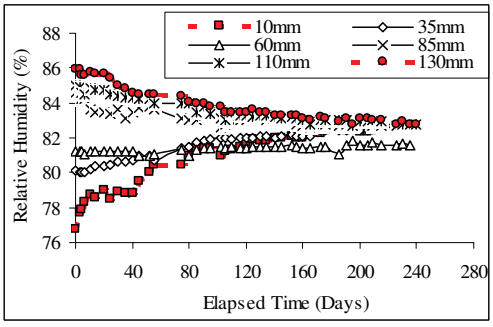


(b)

Figure 8. Experimental results for slab 1 showing the *rh* profiles (a) through the depth and (b) over time.



(a)



(b)

Figure 9. Experimental results for slab 2 showing the *rh* profiles through the depth (a) and over time (b).

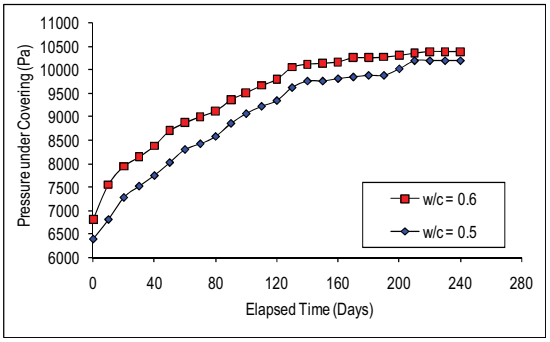


Figure 10. Experimental measurement of the vapour pressure increase in the slabs.

The importance of these tests is that along with an increasing build-up of moisture under the covering (see Figures 8-9), there would be a corresponding increase in vapour pressure and the combination of the two is partially responsible for the floor covering damage and problems mentioned above. This is particularly true for those slabs artificially dried where the vapour pressure is much higher than would be naturally. However, it is unlikely that, alone, the pressures here are likely to cause the problems reported earlier.

The maximum pressure recorded is approximately 10,500Pa, or 0.01MPa, which appears to be a small pressure in practical terms and corresponds to a vertical force applied under the covering, for the 700x700mm surface area, of 5.15kN. However, this force was not enough, in this instance to lift the vinyl as no damage was observed in the control room specimens.

It would be more likely in this instance that if damage did occur, it would be the combination of poor workmanship, poor glue strength or air bubbles being present at the time of covering and the effect of moisture build-up that would be the likely cause of any damage. Also, the possibility of salts in the migrating moisture reacting with the glue may also contribute to potential damage.

4.3 Pull-off tests

In order to assess what force is required to physically lift the covering, a number of pull-off tests were undertaken. This involved casting 12No. 150x150x150mm concrete cubes with w/c ratios of 0.5 and 0.6 (to match those above) and measuring the force required to pull off a 100x100mm piece of vinyl directly (see Figure 7) using a Denison tensile testing machine. The covering was applied in the same manner as it was to the concrete slabs. The mixes were designed with the same slump and compressive strength as before and were made in an identical manner as the slabs used for the drying experiments. After mixing, they were compacted in the moulds in two layers and cured for 3-days in a water-bath with an average water temperature of $20^0 \pm 2^0$. After curing, the cubes were air dried for the requisite number of days and then covered with the vinyl on one face as directed by the supplier.

The pull-off tests were conducted at 3, 28 and 56-days with the covering being applied 1-day prior to each test to investigate the effect the drying had on the pull-off loads required to remove the vinyl. The results from the tests are shown in Table 2 and Figure 11. As shown, the cubes with a w/c ratio of 0.5 have a greater pull-off force required as there is more cement than in those cubes with a w/c ratio of 0.6. Also, over time, the pull-off force increases for both w/c ratios as the cubes dry more and the glue adheres better to the drier concrete. The average tensile stresses exerted to remove the vinyl in Table 2 are 0.234MPa, 0.244MPa and 0.252MPa for the tests at 3, 28 and 56-days respectively. Comparing these to the measured vapour pressures in Figure 10 (0.01MPa), it is clear that they were not high enough to cause the vinyl to blister or rise from the concrete.

The results above show that sealing concrete when a significant amount of residual moisture exists deep in the concrete leads to a build-up of vapour pressures and moisture underneath over time. However, these problems alone are not responsible for delamination and blistering which are so common. Therefore, it is proposed here that the influence of the vapour pressures and moisture accumulation (including efflorescing salts) under the covering can cause solubility of the glue. This is an area which requires further research.

Table 2. Pull-off results

Age (days)	Cube No.	w/c ratio	Pull-off force (kN)	Tensile stress (MPa)
3	1	0.5	5.26	0.234
	2	0.5	5.34	0.237
	3	0.6	5.20	0.231
	4	0.6	5.24	0.233
Age (days)	**Cube No.**	**w/c ratio**	**Pull-off force (kN)**	**Tensile stress (MPa)**
28	5	0.5	6.00	0.267
	6	0.5	6.19	0.275
	7	0.6	5.40	0.240
	8	0.6	5.58	0.248
Age (days)	**Cube No.**	**w/c ratio**	**Pull-off force (kN)**	**Tensile stress (MPa)**
56	9	0.5	6.35	0.282
	10	0.5	6.30	0.280
	11	0.6	5.90	0.262
	12	0.6	5.92	0.263

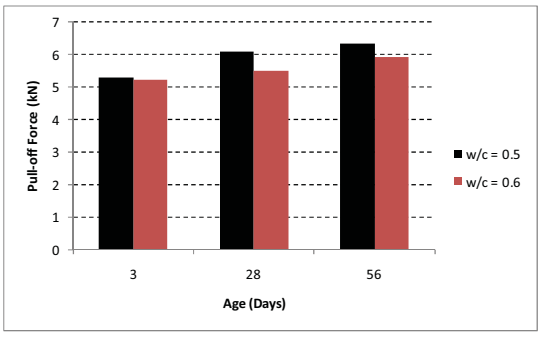


Figure 11. Pull-off test results

5 RESEARCH PROPOSAL

The above demonstrates that the vapour pressure alone is unlikely to cause delamination. However, in conjunction with the moisture resulting in a reduction in the glue's ability to adhere the covering to the concrete, the likelihood of long-term problems to the covering will be increased. As instances of covering failures are common with significant costs associated, it is proposed that further research be conducted. This should in the form of assessing the effect of efflorescing salts over time on the adhesive bond between the concrete and covering. XRD analysis could be used to monitor the creation of efflorescing salts over a similar time frame as shown here (> 250 days).

6 CONCLUSIONS

The results show that monitoring the moisture condition at the surface only is inadequate as damage to floor coverings is due to moisture and vapour pressure build-up as a result of residual moisture deep in the concrete at the time of covering. Surface moisture measurement offers little insight into the moisture condition deep in the slab.

While the internal moisture and vapour pressures under the covering are unlikely to cause delaminations, it is proposed that further research be carried out to monitor the effect that glue solubility and efflorescing salts have on the bond between it and the concrete.

The authors [1-4] have shown that forced drying leads to significantly larger residues of moisture deep in the concrete while the surface of the slab appears quite 'dry' on sealing. Only by measuring the rh at various depths in the concrete (or at least at 40% of the depth as suggested by the data presented here and as recently adopted by ASTM) at suitable intervals will one observe the actual moisture profile in the concrete

REFERENCES

[1] West, R.P. and Holmes, N. (2005), Predicting moisture movement during the drying of concrete floors using finite elements, Journal of Construction and Building Materials, Vol. 19 (9), 674-681.

[2] Holmes, N. and West, R.P (2013). Moisture Movement in Concrete during drying and after covering – A review, Magazine of Concrete Research – DOI 10.1680/macr.13.00142, July.

[3] Holmes, N. and West, R.P. (2010). Moisture Movement in Concrete during drying and after covering – A review, Proceedings of the Bridge and Concrete Research in Ireland (BCRI) Conference, University College Cork & Cork Institute of Technology, 73-82.

[4] West, R.P. and Holmes, N. (2003). Finite element modeling of moisture in concrete during drying, Proceedings of the 2003 Colloquium on Concrete Research in Ireland, Editors P.A.M. Basheer and M.I. Russell, Queen's University of Belfast, 157 – 165.

[5] British Standard Institution BS 8203 Part 1, (1996). Installation of Resilient Floor Coverings, London.

[6] Hulett, T (2002). What's new in floors - an overview of the key changes in TR34, *Proceedings of the International Symposium,* University of Dundee, Scotland, UK, Concrete Floors and Slabs, 101-108.

[7] Oman, P (2002). BIO-Vee Concrete Sealer, Waterproofer and Fortifier, Coating pre-treatment., Progressive Epoxy Polymers, Inc (http://www.epoxyproducts.com/vee4u.html).

[8] Floortest Case Studies (2002). www.floortest.com.

[9] *Datascan Users Manual*, Datascan Technology, 1995.

[10] ASTM F2170-02 (2002). Standard test method for determining relative humidity in concrete floor slabs using in-situ probes.

Combined chloride and carbon dioxide ingression in concrete exposed to cyclic wetting and drying

Jonathon Backus[1], Daniel McPolin[1], Niall Holmes[2] and Adrian Long[1]

[1]Queen's University of Belfast, Belfast, UK,
[2]Dublin Institute of Technology, Dublin, Ireland

email: jbackus01@qub.ac.uk

ABSTRACT: Carbonation and chloride ingress are the two of the main causes of corrosion in reinforced concrete structures. Combined effect of carbonation and chloride ingress was investigated during a 12 month wetting and drying exposure regime. This regime was chosen to simulate conditions in which multiple mode transport mechanisms are active and was conducted on a variety of binders. The penetration was evaluated using water and acid soluble chloride and pH profiles.

The results indicated that when chloride and carbon dioxide ingress together the effects can be adverse. The effect of carbonation on binding capability was observed with the subsequent release of free chlorides having a detrimental effect the corrosion resistance of the concrete due to the increased penetration of water soluble chlorides. The short fall of total chloride profiling as the sole method of analysis was also observed.

KEY WORDS: Durability, Fly Ash, Granulated Blast-Furnace Slag, Carbonation, Chloride

1 INTRODUCTION

Corrosion of reinforcing steel caused by the ingression of chlorides and carbonation is responsible for over 50% of the deterioration of concrete structures. In Europe it has been estimated that fifty percent of the total construction budget is spent on the inspection, maintenance and repair of concrete structures [1], while deterioration of structures as a result of corrosion of reinforcement required an annual expenditure of $8.3 billion in the United States [2].

The current European (EN 206) [3] and American (ACI 318) [4] standards provide guidelines for designing structures to combat each of these deterioration mechanisms individually but numerous scenarios exist where two or more of these mechanisms may occur simultaneously exist. Marine structures (Figure 1) or structures exposed to de-icing salts (Figure 2) are exposed to combinations of chloride and carbonation that are not specifically accounted for in the standards.

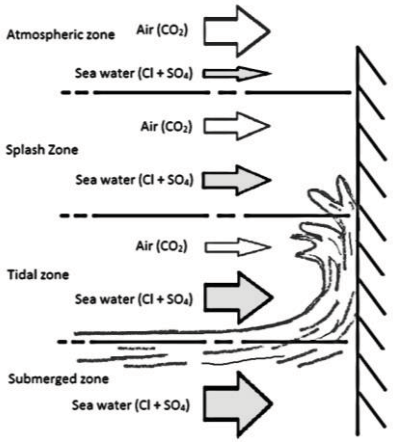


Figure 1- Coastal structure with representative exposure zones (adapted from [5])

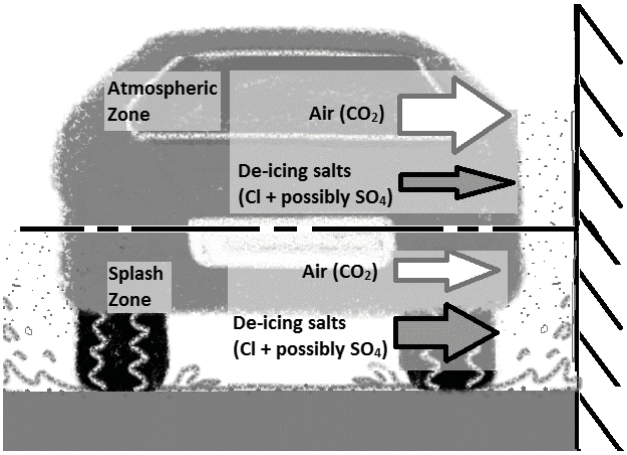


Figure 2 - Road structure exposed to de-icing salts and water

1.1 Chloride ingression

Chlorides occur naturally in seawater at concentrations between 4-20 g/l [6] depending on localized conditions and are also commonly present as sodium chloride used in de-icing salts.

Due to the structure of hydrated cement paste, chlorides within concrete can exist in two forms; free chlorides and bound chlorides. Free chlorides are dissolved in the concrete pore solution while bound chlorides are either physically bound (adsorbed onto the surface of the gel pores) or chemically bound (incorporated in the products of hydration), [7], [8]. It is

generally accepted that the free chlorides contained within the pore solution are those that can cause corrosion.

1.2 Carbonation

Carbon dioxide is a gas naturally existing in the atmosphere at a concentration of 0.03%. However, depending on localised conditions, concentrations may reach as high as 1% [7].

When carbon dioxide diffuses into the concrete, it dissolves in the pore fluid and then reacts with the alkaline calcium hydroxide ($CaOH_2$) to form calcium carbonate ($CaCO_3$) and water [9]. Calcium carbonate is less soluble in water than calcium hydroxide and has a greater volume than the original hydrate thus it has the potential to block the pores and reduce permeability [9].

The removal of calcium hydroxide from the pore fluid has the effect of reducing the pH of the concrete and when the pH of the concrete drops below 11.5 [10] the passive oxide film that protects the reinforcement becomes unstable and the reinforcement becomes susceptible to corrosion. The addition of supplementary cementitious materials (SCMs) affects the initial pH, the quantity of calcium hydroxide (Table 1) available for consumption and also the permeability of the concrete.

1.3 Interaction of chloride ingression and carbonation

Wetting and drying cycles are the most severe environments for corrosion caused by carbonation or chloride ingression and also the most likely scenario for combined deterioration to occur [11], [12]. The reason for this is the variation in relative humidity, which allows chloride ingression by both absorption and diffusion to occur. There is also the potential for outwards movement during parts of the exposure cycle. The variable relative humidity will also allow carbonation to occur during the periods of lower relative humidity.

The formation of calcium carbonate due to carbonation may result in a less permeable concrete and thus reduce rate of ingression of both carbon dioxide and chlorides; however, studies show that the reduction in pH also decreases the stability of Friedel's salt [13] as well as affecting the hydroxide content in the pore solution which brings about an increase in free chloride content. This increase in free chloride content may increase the concentration gradient and accelerate the ingress of chlorides or the increase of chlorides may result in the critical chloride threshold being reached at the reinforcement.

2 EXPERIMENTAL PROCEDURE

2.1 Specimen preparation

Three mixes were used in this study, incorporating Portland cement (PC), pulverised fuel ash (PFA) and ground granulated blast-furnace slag (GGBS) and details of the mixes are shown in Table 2. The chemical and physical compositions are shown in Table 1. A water-binder ratio of 0.5 was chosen for all mixes to give slump in the range of 10-50mm. The aggregate binder ratio was 5 for all mixes. Slabs of size 230 x 230 x 80 mm were cast for coring specimens along with ponding slabs of dimensions 230 x 230 x 100 mm and 100 mm cubes.

The slabs and cubes were manufactured according to EN 12390 [14] using a pan mixer, they were cast and removed from the moulds 24 hours after casting.

Table 1. Chemical composition and physical properties of binders

Chemical composition (%) and physical properties	PC	PFA	GGBS
SiO_2	19.88	59.01	35.2
Al_2O_3	6.03	22.8	13.96
Fe_2O_3	2.73	8.8	0.25
CaO	64.45	2.38	41.21
MgO	1.69	1.39	8.18
SO_3	3.14	0.27	-
K_2O	0.78	2.8	0.42
Na_2O	0.13	0.74	0.19
Cl	0.007	-	-
TiO_2	-	1.15	0.57
Mn_2O_4	-	0.08	0.55
MnO	-	-	0.49
P_2O_3	-	0.39	
Specific surface area (m2/kg)	322	340	600

2.2 Curing and preparation

After demoulding, the slabs were stored in a water bath (20±1°C) for three days. They were then removed and transferred to a constant temperature room with ambient conditions of 20±1°C and 55±1% relative humidity (RH) until they were 28 days old. At 28 days, a total of nine 60 mm cores were cut from each of the coring slabs manufactured for each of the mixes. Three cubes were tested at 28, 60 and 90 days to monitor hydration of the SCM mixes.

The cores were cut from the slabs with an external water source applied as a coolant during coring. If coring was carried out after exposure to the chloride environment, it would have affected the chloride distribution.

After coring, the cylinders and ponding slabs were applied with three coats of epoxy emulsion (Sikaguard 680) to form a barrier to prevent any lateral ingress of chloride ions or carbon dioxide. This was applied to all faces except for the ponding surface. To facilitate ponding, a 60 mm diameter pipe of length 50 mm was placed over the top of each core forming a reservoir in which the ponding solution could be contained. The joint between the pipe and the core was tight and silicone sealant was applied to ensure no leakage during ponding (Figure 3). The samples were then returned to the constant temperature and humidity room to for a minimum of 90 days to allow complete hydration of the SCM mixes.

Table 2. Mix design used in experiments to yield $1m_3$ of concrete (mass in kg)

Mix	Binder	PC	PFA	GGBS	Coarse Aggregate (max 10mm)	Fine Aggregate (max 2mm)	Water (excl. SSDS water)
PC	100% PC	370	-	-	1235	617	185
PFA	30% PFA	253	108	-	1206	603	181
GGBS	50% GGBS	184	-	184	1230	615	185

2.3 Exposure regime

To create an accelerated exposure regime that was representative of natural conditions while facilitating multiple mode deterioration, a wetting and drying regime was chosen. A similar regime has been used previously by Polder & Peelen [15] and is representative of the splash zone which Bamforth et al. [12] identified as the most severe in practice. The regime was optimised by monitoring the humidity development at depths within the concrete over a two week period while adjusting the temperature and humidity (Figure 4).



Figure 3 - Ponding specimens

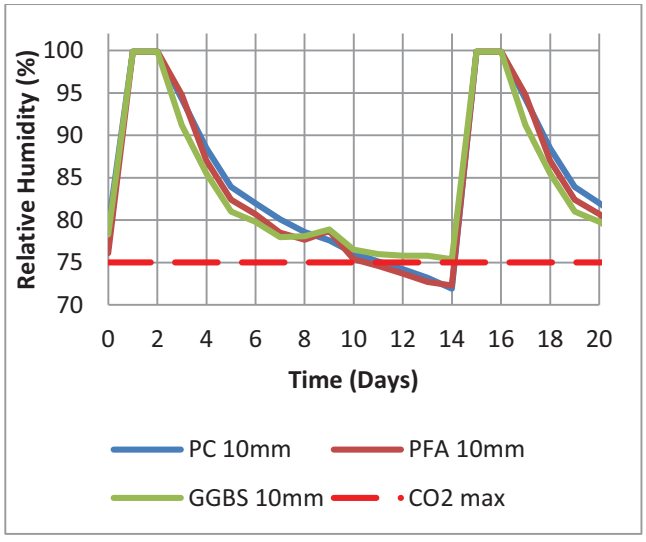


Figure 4 - Humidity development of samples

The selected ponding regime comprised of one day ponding in the deleterious solution followed by 13 days drying at 40°C and 20% relative humidity (RH) Figure 4. It is accepted that carbonation can occur below 80% with optimal carbonation occurring below 75% RH [16].

Two exposure regimes were selected for testing. These were 2.0% sodium chloride solution with atmospheric CO_2 and 2.0% sodium chloride with 5% CO_2. These cycles were repeated every fortnight until testing took place.

2.4 Testing

Testing of the samples was carried out after 4, 12, 24, 36 and 48 weeks. To monitor the ingress of the carbon dioxide and chloride along with their chemical and physical effects on the concrete a variety of tests were carried out.

2.4.1 pH profiles

Dust was obtained from a 60mm cylinder at depth increments of 0-1 mm, 1-2 mm, 2-3 mm, 3-4 mm, 4-5 mm, 5-7.5 mm, 7.5-10mm, 10-12.5 mm, 12.5-15 mm, 15-20 mm, 20-25mm and 20-30 mm; using a profile grinder. 1g of this dust was weighed into a small plastic bottle and 10 ml of deionised water was added [17]. The plastic bottles were then placed in a rotator and the solution mixed for 24 hours. After 24 hours, a Gelplas reference combination pH electrode was used to derive a pH value.

2.4.2 Water soluble chloride profiles

The samples that had been dissolved and agitated for the pH profiles were then placed in a centrifuge for 5 minutes at 5000 rpm to separate the solids from the solution. This 10 ml solution was then placed in 80 ml of deionised water and analysed using potentiometric titration with silver nitrate and a potassium nitrate reference electrode to obtain the water soluble chloride content.

2.4.3 Acid soluble chloride profiles

The acid soluble profiles were obtained with 1g of sample using nitric acid and potentiometric titration according to the procedure set out in BS EN 14629 [18].

3 PRESENTATION OF TEST RESULTS

3.1 Chloride and pH profiles

The 12 month acid soluble chloride profiles for PC, PFA and GGBS exposed to chloride only and chloride and carbon dioxide are shown in Figure 5 - Figure 7 as solid blue and black lines respectively lines with the 12 month chloride and carbon dioxide pH shown as a dashed black line. Although the shapes of the profiles alter, the general trend of a high surface concentration, followed by a dip, with an increase to a maximum concentration, at differing depths depending on the mixes and increasing depths with increasing exposure durations; before a final gradual decrease towards zero is present in all mixes. This profile is as would be expected from the external ponding source.

The chloride and carbon dioxide profiles all exhibit a greater drop in concentration between 0-15 mm which coincides with the decrease in pH level at these depths.

4 DISCUSSION

4.1 Chloride profiles

The most apparent effect of combined mechanisms can be observed in the chloride profiles of the chloride and carbon dioxide samples. The distinct plateau followed by an increase to a peak and then decrease to zero is most unlike what is seen in the chloride alone and not what would be expected from an external chloride source even accounting for the effects of

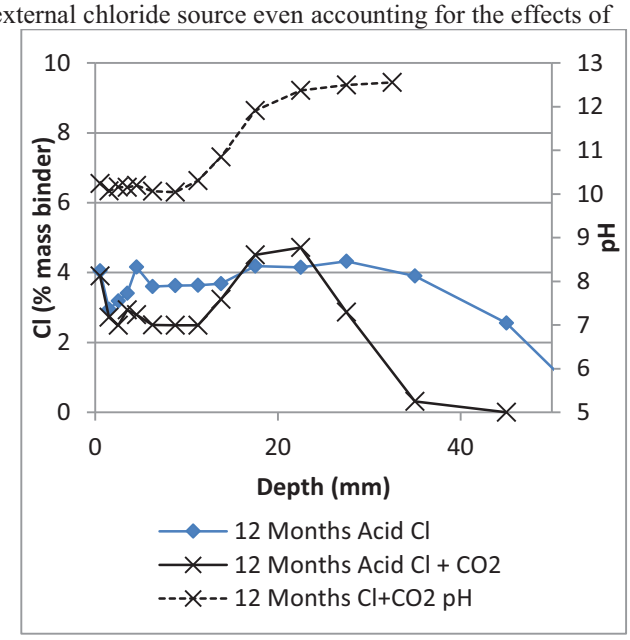


Figure 5 – PC acid soluble chloride and pH profiles

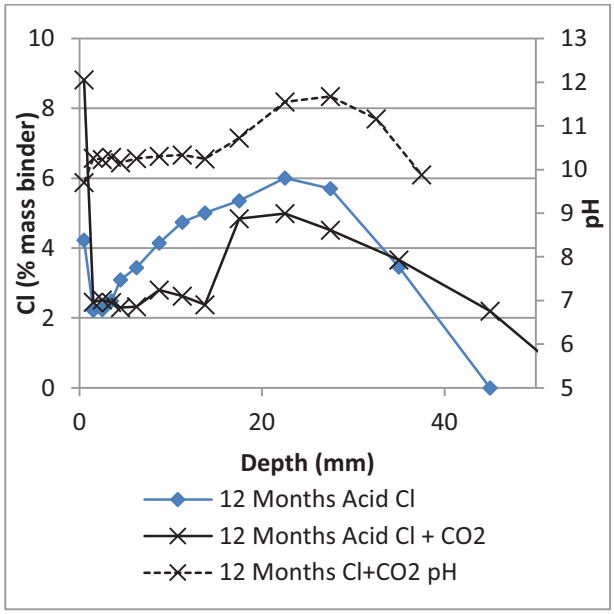


Figure 6 - PFA chloride only water and acid soluble chloride profiles

wetting and drying. The explanation for this unusual profile can be garnered by superimposing the pH profiles onto the chloride graphs as in Figure 5 - Figure 7 where it can be observed that in the case of the chloride and carbon dioxide exposures, there is a correlation between the pH and the chloride content. That is when the concrete is carbonated and the pH is low, the chloride concentration is correspondingly low; and when the

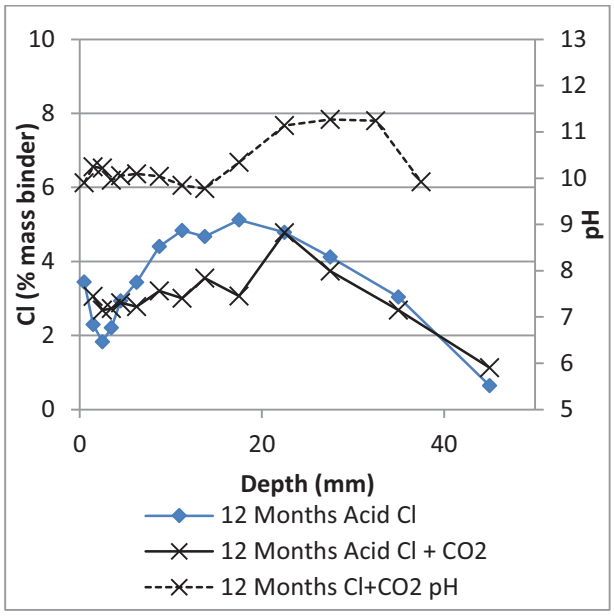


Figure 7 - GGBS chloride only water and acid soluble chloride profiles

pH begins to rise again as the carbonation front begins to reach its limit; the chloride concentration begins to rise also until it reaches its natural peak and decreases towards zero.

It is known [19] that Friedel's salts become unstable in carbonated concrete and chlorides are released, which would explain the lower total (acid soluble) chloride content. What this does not explain is why the water soluble content should also remain so low. There will remain some difference between the acid and water soluble content dues to residual Friedel's salts and some physically bound chlorides but if previously bound chlorides are released into the pore solution, the water chloride content should converge towards that of the acid soluble content.

Two possible explanations for this are that:

Calcium carbonate from carbonation is more voluminous than the calcium hydroxide that it consumed and would thus decrease the pore volume of the concrete. The decreased pore volume would hold less pore fluid and although the previously bound chlorides may increase the pore fluid chloride concentration, the decrease in volume means this is not reflected by an increase in chloride content in the free chloride profiles.

There remains a quantity of chlorides bound in the C-S-H phases of the concrete that are not released when the pH decreases.

4.1.1 Penetration and concentration of chlorides

The water soluble profiles were used to derive values for the maximum depth of penetration, maximum depth of penetration of the critical chloride threshold (taken as 0.5%) and the concentration at 25 mm depth. These values were then plotted on Figure 8 - Figure 13.

The water soluble concentrations at 25 mm are greater in the GGBS and PFA than the PC and similar in the chloride only and chloride and carbon dioxide exposures for the PFA and PC. In the GGBS, the presence of carbon dioxide has created a greater peak in water soluble chloride concentration in the

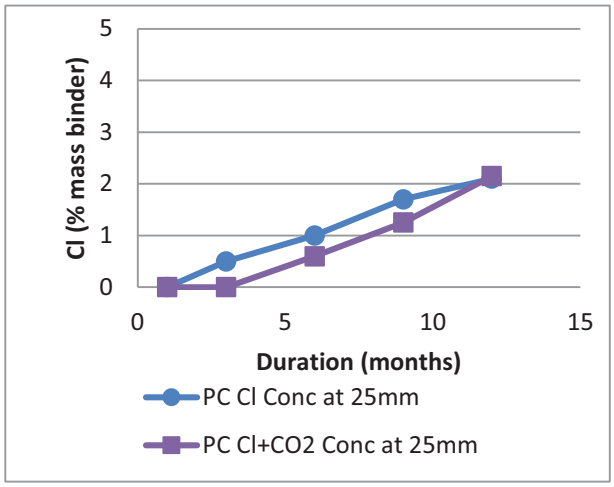


Figure 8 – PC concentration at 25 mm graph

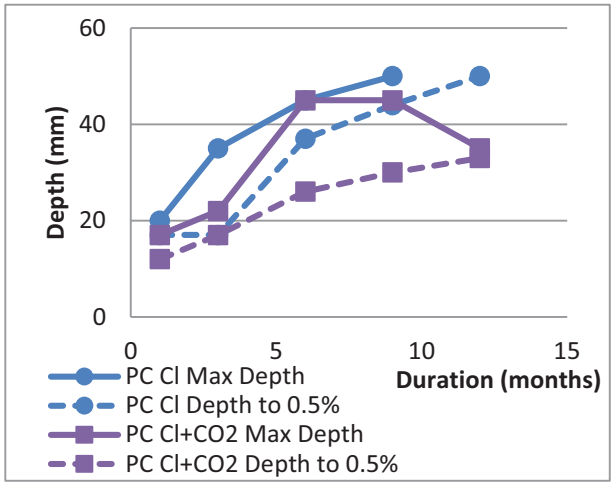


Figure 9 – PC penetration depths

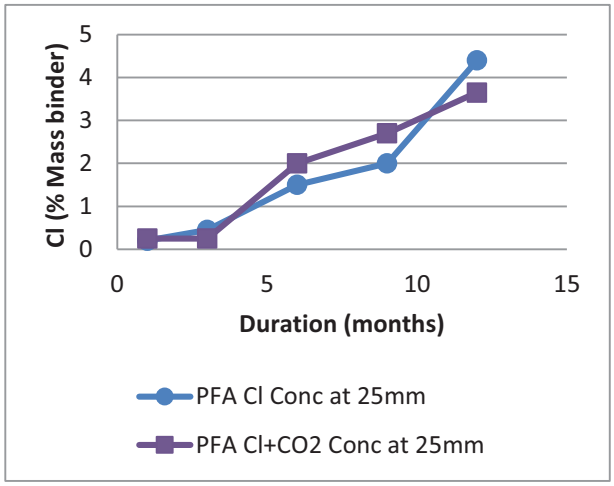


Figure 10 – PFA concentration at 25 mm graph

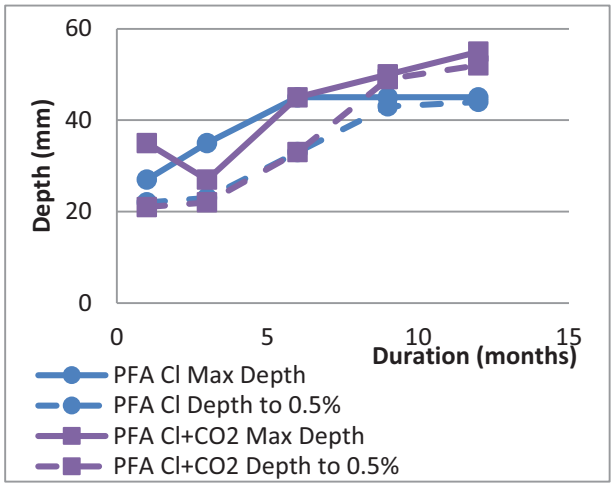


Figure 11 – PFA penetration depths

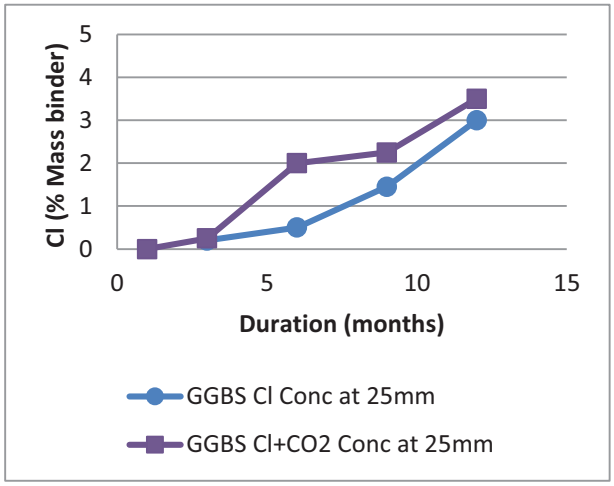


Figure 12 – GGBS concentration at 25 mm graph

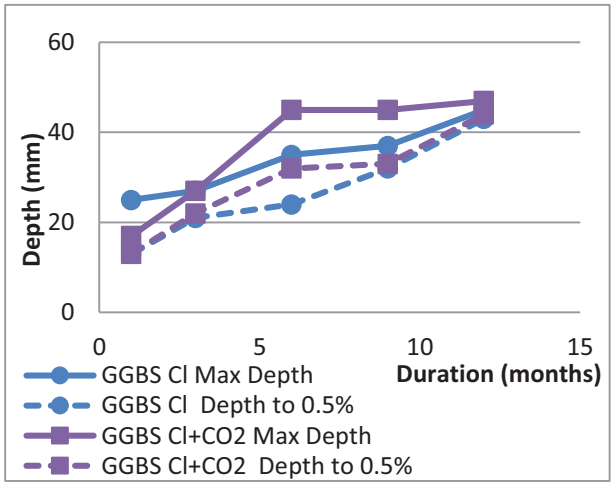


Figure 13 – GGBS penetration depths

combined exposure than the chloride only thus increasing the risk of corrosion.

Due to the peaks caused by the carbonation of the concrete and the subsequent release of additional free chlorides, the maximum depth of penetration is generally greater in the combined chloride and carbon dioxide samples as is the depth of penetration of the critical chloride concentration. There is less difference between the three mixes with GGBS allowing chloride to penetrate the least.

5 CONCLUSION

One of the most important factors affecting the corrosion of steel reinforcement is the concentration of free chlorides as they are responsible for active corrosion.

While the total chloride profiles here appear to have fluctuated more, the water chloride profiles generally followed a smoother curve. Although quantification of the water chlorides may be a more accurate way of assessing corrosion risk than total chlorides, it is a higher risk method as it does not account for the bound chlorides nor does it give an accurate representation of the actual 'free' chloride concentration. Should conditions arise where carbonation is also experienced leading to the liberation of additional bound chlorides, there is potential for an increase in free chloride concentration in the material.

When this information is considered in conjunction with a review by Angst et al. (2009) which highlights the large range of critical chloride concentrations that have been found to induce corrosion, it is apparent that a more accurate, comprehensive method of quantifying the corrosion potential of a structure is required.

The introduction of carbonation to a chloride environment appears to have the effect of reducing the chloride ingress over the duration of the exposure regime, despite an initial acceleration experienced in the GGBS.

REFERENCES

[1] G. P. Tilly and J. Jacobs, *Concrete Repairs: Performance in service and current practice*. Watford: Building Research Establishment, 2007.

[2] G. P. Tilly, "Durability of Concrete Repairs," in *Concrete Repairs*, M. Grantham, Ed. Oxford: Taylor and Francis, 2011, p. Chapter 14.

[3] British Standards, *BS EN 206-1:2000 Concrete — Part 1: Specification, performance, production and conformity*, vol. 3. British Standards Institution, 2005.

[4] ACI Committee 318, "Building Code Requirements for Structrual Concrete (ACI 318-05) and Commentary (ACI 318R-05)," American Concrete Institute, 2004.

[5] P. K. Mehta and P. J. M. Monteiro, *Concrete. Microstructures, Properties, and materials*, Third. McGraw-Hill, 2006.

[6] N. R. Buenfeld and J. B. Newman, "The permeability of concrete in a marine environment," *Mag. Concr. Res.*, vol. 36, no. 127, pp. 67–80, 1984.

[7] A. M. Neville, *Properties of Concrete*, Fourth. Harlow: Longman, 1995.

[8] J. Kropp, "RILEM Report 12. Performance criteria for concrete durability," London, 1995.

[9] L. J. Parrott, "A review of carbonation in reinforced concrete," Garston, 1987.

[10] P. Schiessl, *Corrosion of steel in concrete*. London: Chapman and Hall, 1988, p. 102.

[11] A. Neville, G. Wharf, H. Street, and U. K. The, "Chloride attack of reinforced concrete : an overview," *Mater. Struct.*, vol. 28, pp. 63–70, 1995.

[12] P. B. Bamforth, W. F. Price, and M. Emerson, "An international review of chloride ingress into structural concrete," Crowthorne, 1997.

[13] G. K. Glass, B. Reddy, and N. R. Buenfeld, "The participation of bound chloride in passive film breakdown on steel in concrete," *Corros. Sci.*, vol. 42, no. 2000, pp. 2013–2021, 2000.

[14] British Standards, *BS EN 12390-2:2009 Testing hardened concrete Part 2: Making and curing specimens for strength tests*. London: British Standards Institution, 2009.

[15] R. B. Polder and W. H. . Peelen, "Characterisation of chloride transport and reinforcement corrosion in concrete under cyclic wetting and drying by electrical resistivity," *Cem. Concr. Compos.*, vol. 24, no. 5, pp. 427–435, Oct. 2002.

[16] M. G. Richardson, *Fundamentals of durable reinforced concrete*. London: Spon Press, 2002.

[17] D. O. McPolin, P. A. M. Basheer, A. E. Long, K. T. V Grattan, and T. Sun, "New Test Method to Obtain pH Profiles due to Carbonation of Concretes Containing Supplementary Cementitious Materials," *J. Mater. Civ. Eng.*, no. November, pp. 936–946, 2007.

[18] British Standards, *BS EN 14629:2007 Products and systems for the protection and repair of concrete structures — Test methods — Determination of chloride content in hardened concrete*, vol. 3. London: British Standards Institution, 2007.

[19] A. K. Suryavanshi, J. D. Scantlebury, and S. B. Lyon, "Mechanism of Friedel's salt formation in cements rich in tri-calcium aluminate," *Cem. Concr. Res.*, vol. 26, no. 5, pp. 717–727, 1996.

[20] U. Angst, B. Elsener, C. K. Larsen, and Ø. Vennesland, "Critical chloride content in reinforced concrete — A review," *Cement and Concrete Research*, vol. 39, no. 12, Elsevier Ltd, pp. 1122–1138, Dec-2009.

A Study of Chlorides in a Reinforced Concrete Bridge

R. O'Donovan[1,2], B.D.O'Rourke[1], K.D.Ruane[1,3], J.J.Murphy[1]
[1] Department of Civil, Structural & Environmental Engineering, Cork Institute of Technology, Bishopstown, Cork, Ireland
[2]University College Cork, College Road, Cork, Ireland
[3]RPS Consulting Engineers Ltd, Innishmore, Ballincollig, Cork, Ireland

email: ross.odonovan@ucc.ie, brian.orourke@cit.ie, kieran.ruane@rpsgroup.com, john.justinmurphy@cit.ie

ABSTRACT: The current study investigates chloride deterioration of a 100 year old bridge located in a harsh marine environment. Constructed in 1908 – 1909 the Mizen Head Footbridge was one of the oldest reinforced concrete bridges in Ireland. The demolition of the bridge in 2009 provided a unique opportunity to examine its service life and to extract samples for analysis and investigation. Reinforcement corrosion due to chloride attack was identified. A focused study indicates that chloride contaminated constituents may have been used in the concrete mix. This research may provide valuable advice and guidance for the asset management of similar structures.

KEY WORDS: Chloride, Concrete Deterioration, Reinforced Concrete.

1 INTRODUCTION

Mizen Head and Cloghan Island are located on the south west coast of Ireland. The bridge was designed by Noel Ridley of Westminister. It was constructed in 1908-1909 to provide access to a fog signal station on Cloghan Island. In 1972 extensive remediation works were carried out on the bridge which consisted of cutting away defective concrete and coating all structural members with a bituminous membrane [1]. This may have been an attempt to repair visible defects and to seal exposed concrete surfaces from chloride ingress.

In 2002 following significant rust staining on the bridge, the bridge owners employed engineers to carry out an inspection and assessment of the bridge. High chloride levels were noted from dust samples taken from the bridge. Electrical continuity testing revealed that 86% of the reinforcement in the bridge was discontinuous and that the bridge was subject to brittle failure. The bridge was eventually demolished and replaced in 2009 – 2011 [2], [3]. Previous studies point to chloride attack on reinforcement as the cause of bridge deterioration [4], [5].

1.1 Initial Chloride Testing

As part of this study, initial chloride tests were carried out on concrete dust samples extracted at incremental depths of 25 mm from concrete drilled from the demolished bridge. These samples were tested in a commercial laboratory for the presence of chlorides. Test results are summarised in Table 1. In the absence of a known cement content, a 14% cement content by weight of concrete was selected to establish test results [6].

Analysis of initial chloride test results shows a uniform chloride profile in all of the concrete samples (Figure 1). This profile does not follow typical chloride ion transport behaviour theory (Figure 2) [7]. The recorded chloride levels are high with an average of 3.2%. This chloride profile warranted further investigation and testing.

Table 1. Initial chloride test results.

Sample No.	% Chloride*			Sample No.	% Chloride*		
	25 mm	50 mm	75 mm		25 mm	50 mm	75 mm
1	3.85	3.87	3.83	**7**	2.35	1.98	1.87
2	3.92	3.93	3.91	**8**	2.48	2.48	2.48
3	3.85	3.85	3.85	**9**	1.80	3.90	-
4	3.37	3.27	2.99	**10**	3.17	3.42	-
5	2.05	2.33	2.10	**11**	3.90	3.90	-
6	3.70	3.85	3.85				

* Chloride content by weight of cement (assumed 14% cement content by weight of concrete)

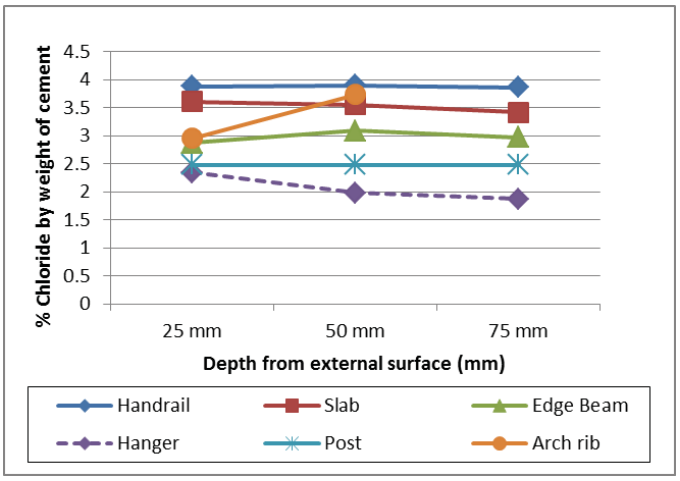


Figure 1. Initial chloride testing, chloride profile.

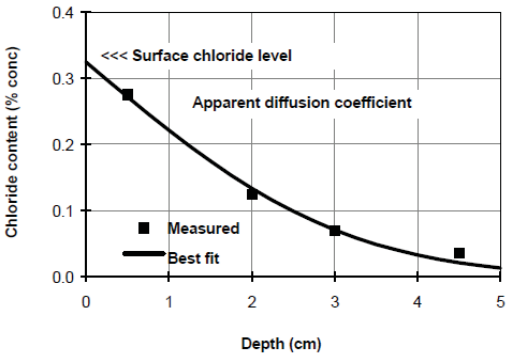


Figure 2. Typical chloride profile [7].

2 FURTHER CHLORIDE TESTING

Further chloride testing was carried out to identify possible causes for the uniform chloride profile, which was considered to be the result of one of the following mechanisms:

1. The use of admixtures such as calcium chloride in the concrete mix;
2. Leaching/dispersion of chlorides in reinforced concrete members after the bitumen membrane was applied in 1972;
3. The use of chloride contaminated aggregates or sea water in the concrete mix;
4. Ingress of chlorides from the marine environment over time.

The beneficial effects of calcium chloride admixtures had been known since 1885 [8]. However it is only since the 1920's that the use of calcium chloride in concrete has been the subject of research, investigations and reports [9]. Therefore, Mechanism 1 is ruled out as the use of admixtures in concrete is a relatively modern concrete practice and is unlikely to have been used in 1909. To investigate Mechanisms 2, 3 and 4, three series of tests were carried out.

2.1 Test Series 1 – Analysis of Concrete Dust Samples from Brow Head Quarry

Brow Head Quarry was established by Rowe brothers in the 1920's, at Castlemehigan near Crookhaven (Figure 3). The quarry was closed in 1939, following the outbreak of World War II [10], [11], [12]. Concrete from the reinforced concrete hoppers, which were constructed in 1927, was selected for this study. The reasons Brow Head Quarry was selected as part of the study are:-

1. It is located near the bridge (6 km);
2. It is of similar age as the reinforced concrete hoppers were constructed in 1927 only 18 years after the Mizen Bridge;
3. It may have contained locally sourced aggregates in the concrete mix similar to those used on the Mizen Bridge.

The quarry site is not as exposed as the bridge site, fronting a sheltered sea inlet. However, the concrete is exposed to chlorides from sea mists and seawater spray. The reinforced concrete hoppers show advanced signs of corrosion at road level. It is not known what concrete mix was used in the design and an assumed cement content of 14% by weight of concrete was used in the analysis [6]. The concrete had been exposed for a period of 85 years from 1927 to 2012. In contrast it is assumed that the concrete in the Mizen Bridge was exposed for a period of 63 years from 1909 to 1972 as after 1972 the bituminous membrane would have restricted chloride ingress into the concrete.

Dust samples were extracted from exposed concrete at two locations at road level where corrosion was most prevalent. The measured chloride profiles are presented in Figure 4.



Figure 3. Brow Head Quarry, 2012.

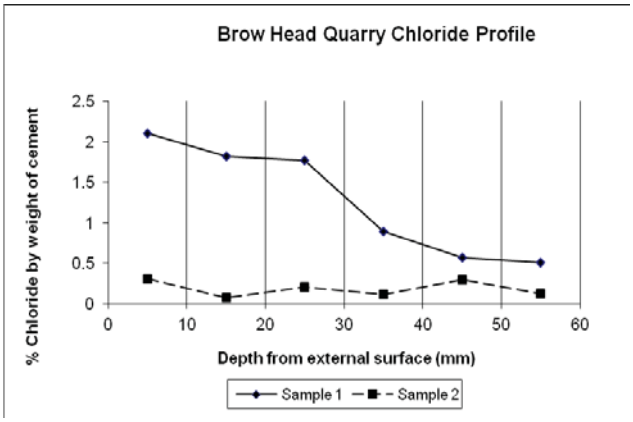


Figure 4. Brow Head Quarry chloride profiles.

Analysis of Test Series 1 Results

The chloride profiles are typical of what would be expected. Sample 1 shows a gradual decrease in chloride content from the surface indicating that chloride ingress has occurred at the surface with an average of 1.26% chloride. The slope of the graph is similar to a typical chloride profile (Figure 2).

Sample 2 is uniform with low chloride values having an average of 0.18% chloride. This may indicate that these values are the background chloride contents contained in the original concrete. This suggests that the Mizen Bridge concrete was different in some way that affected the observed chloride profile.

2.2 *Test Series 2 – Analysis of Concrete Dust Samples from Exposed Concrete on the Mizen Bridge Foundation*

There is no evidence that the exposed mass concrete foundation on the Mizen Bridge received the 1972 bituminous membrane. As a result, the foundations were exposed for a period of 103 years from 1909 to 2012. Chloride dust profiles were extracted from the horizontal surface of the west foundation at two locations. A third sample was taken from the surface in an attempt to ascertain the chloride level on the surface of the concrete. An assumed cement content of 14% by weight of concrete was used in the analysis [6]. The chloride profiles are shown in Figures 5 and 6.

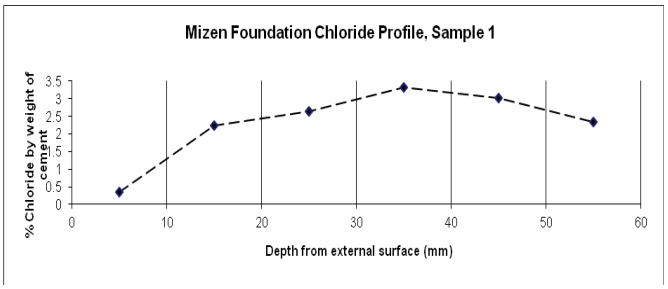


Figure 5. Chloride profile, Sample 1, Mizen Bridge foundation.

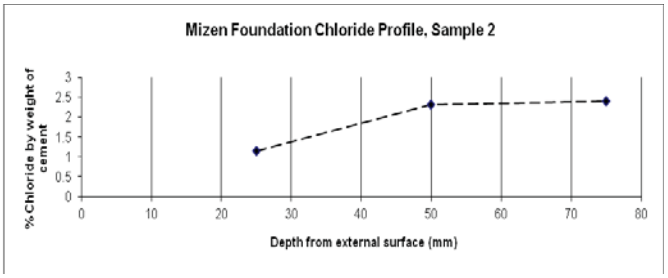


Figure 6. Chloride profile, Sample 2, Mizen Bridge foundation.

Analysis of Test Series 2 Results

Similar to the reinforced concrete bridge members, the chloride profiles in the foundation are uniform with depth. The chloride profile for Sample 1 shows a decrease in chlorides close to the external surface. This may be attributed to chloride leaching due to the presence of high levels of background chlorides. Again the high chloride levels are comparable with those that were found in the reinforced concrete bridge members with an average of 2.31% and 1.95% chloride content for Samples 1 and 2 respectively. It is also noted that the average chloride levels were much higher than those recorded at Brow Head Quarry.

2.3 *Test Series 3 – Recreation of Mizen Bridge 1908 Concrete Mix*

The objective of Test Series 3 was an attempt to re-create the 1908 concrete mix to ascertain whether chloride contaminated constituents might have been used in the concrete mix. The aim was to explain the abnormal chloride profiles recorded. Test Series 3 involved careful selection of mix constituents and the production of a number of trial mixes.

Cement

The 1904 British Standard for cement specified the grain size as follows:- *Residue on a sieve 76 x 76 = 5,776 meshes per square inch (aperture of 334 µm) shall not exceed 3 per cent. Residue on sieve 180 x 180 = 32,400 meshes per square inch (aperture of 141 µm) shall not exceed 10 per cent* [13].

In comparison, a modern IS EN 197, CEM I (Portland cement) with a Blaine fineness in the order of 400 m²/kg typically has 10% of particles larger than 50 µm and less than 10% smaller than 2 µm [14], [15].

Comparison of modern cement with the 1907 cement is notable for the following:-

1. Modern cement is a finer powder than the cement produced in 1907;
2. Finer cement results in a faster rate of hydration. The size of a cement particle has an important effect on the rate at which it hydrates when exposed to water. As the particle size increases, the rate of hydration slows down. A cement particle with a diameter of 12 µm reacts completely in about a day, whereas a particle with a diameter of 102 µm reacts completely in about a month [14];
3. Finer cements have lower values of loose densities. In the 1900's the weight of cement was taken as 100 pounds per cubic foot (1,604 kg/m³) [16], [17]. Modern cement has a settled bulk density of 1,375 kg/m³ and a particle density of 3130 kg/m³ [14].

The mix design for Trial Mix No.1 was derived by using a ratio 1:1.5:3 (cement: sand: aggregate) as described in the original bridge specification. CEM I (Portland cement) to IS EN 197-1 [18] was selected as it contains only 5% of minor additional constituents and is therefore more akin to early cement [14]. To account for the difference between loose densities for modern cements and cements of the 1900's, it was decided that the concrete constituents should be measured by weight rather than volume.

Aggregates

In the early days of reinforced concrete there was an understanding of the importance of the selection of suitable aggregates for use in concrete. For the purpose of Test Series 3, possible sources of the aggregate used in the Mizen Bridge were examined.

Fine Aggregates

Literature at the time stated "*Sea sand, if used should be free from salt, or concrete will effloresce. In marine reinforced concrete construction, this objection does not apply and sea sand is almost invariably used"* [19]. Petrographic testing identified fragments of shells, which proved similar to the type of shells found in nearby Barleycove Beach [3]. Therefore, it was decided to select Barleycove Beach sand as the fine aggregate for Test Series 3. The sand was extracted from the upper section of the beach, which is not subjected to wetting at high tides or from waves. Density tests to IS EN 1097-6:2000 [20] and grading analysis to BS 1377-2:1990 [21] were carried out on the sand.

An additional beach sand sample was prepared by washing it in potable water to reduce chloride content. The sand was mixed with potable water and agitated until suspended. The sand was then allowed to settle before the water was siphoned off. This process was repeated twice. The wet sand was then dried at room temperature.

Coarse Aggregates

The literature predominantly indicated that locally sourced broken rock/stone may have been used in the bridge. An examination of geological maps of West Cork, prepared by the Geological Survey of Ireland, indicates that Old Red Sandstone is common in the Mizen peninsula and surrounds [22].

Old Red Sandstone rock was extracted from Brow Head Quarry. The rock was broken by hand and subsequently, density tests to IS EN 1097-6:2000 [20] and grading analysis to BS 1377-2:1990 [21] were undertaken.

The Trial Mix was prepared using CEM I (Portland cement), Barleycove Beach sand, and Brow Head Quarry aggregates. A cut section of a concrete cube, from the trial mix, was then compared with samples from the Mizen Bridge (Figure 7).

It can be seen from a comparison of concrete sections, that locally sourced Old Red Sandstone was not used in the concrete mix for the reinforced concrete. There is a difference in colour of the two aggregates. The Old Red Sandstone is light brown and the Mizen aggregate is blue/green in colour. This observation may confirm the conclusion drawn from a petrographic analysis that aggregates used in the Mizen Bridge were derived from a number of sources [3].

The literature at the time stressed the importance of using good quality aggregates for reinforced concrete works [16], [17], [23].



Figure 7.– Visual comparison of a cut cube from Trial Mix No. 2 with actual concrete.

An examination of Ordnance Survey of Ireland maps and geological reports gave insight into possible alternative local sources for coarse aggregate [22], [24]. Local quarries and mines that were either abandoned or in operation around the time of construction were identified. These sites indicated sources of quartz and slate as shown in Figure 8.



Barleycove Beach

19th century copper mine

Bridge site

Brow Head Quarry

Durrus Slate Quarry

Schull – copper and slate, mines and quarries

Figure 8. Possible sources of local aggregates [22], [24].

Slate is a particularly poor material for use as aggregate for concrete and its use in concrete is precluded. Local quartz from the 19th century copper mine is a white stone and was not observed in the cut sections of the bridge. From this evidence it is speculated that imported coarse aggregates from an unknown source were delivered by boat to the bridge site for use in the reinforced concrete work.

An acid test on the Mizen aggregates indicated that the light blue/green aggregate is soluble. At this stage commercially available limestone aggregate was selected and used in the final concrete mix. The use of limestone aggregate would not adversely affect the chloride levels of concrete mixes prepared for Test Series 3.

The limestone aggregate was prepared by crushing to size, washing and carrying out density tests to IS EN 1097-6:2000 [20] and grading analysis to BS 1377-2:1990 [21].

Five batches of six cubes were made and air cured as indicated in Table 2. A water to cement ratio of 0.6 was used. The tests consisted of compressive strength tests, density testing and chloride testing.

Table 2. Test Series 3, Sources of concrete constituents, and mix design.

Batch No.	Sources of Concrete Constituents			
	Water	Fine Aggregate	Coarse Aggregate	Cement
	Typical Mix Design per m³ of Concrete			
	254 kg	545 kg	1098 kg	423 kg
1	Sea water	Unwashed Barleycove sand	Limestone	CEM I
2	Sea water	Washed Barleycove sand	Limestone	CEM I
3	Potable water	Unwashed Barleycove sand	Limestone	CEM I
4	Potable water	Washed Barleycove sand	Limestone	CEM I
5	Potable water	Commercial sand	Limestone	CEM I

Analysis of Test Series 3 Results

Results of Test Series 3 results are summarised in Table 3. The following observations are made:-

A The use of seawater and chloride contaminated Barleycove Beach sand (Batches 1 and 2) influenced the chloride content (1.18%, 1.60%, 1.26% and 1.31%);

B The higher chloride contents had the effect of giving lower slumps with slumps of 55 mm and 65 mm recorded for Batches 1 and 2 respectively and slumps in excess of 100 mm recorded for remaining batches;

C The mix containing potable water and chloride contaminated Barleycove Beach sand had chloride contents below the limit of 0.4% for concrete use with steel to IS EN 206-1 [25];

D The chloride contaminated concrete (Batches 1 and 2) had higher 28 day strengths of 28.4 N/mm² and 31.6 N/mm² respectively compared with the highest value of 23.6 N/mm² for the remaining batches.

Table 3. Test Series 3, test results.

Batch No.	Test Results			
	Concrete Slump (mm)	Average Concrete Cube Compressive Strength (N/mm²) at 28 days	Average concrete density (kg/m³)	% Chloride Content*
1	55	28.4	2310	1.18 & 1.60
2	65	31.6	2330	1.26 & 1.32
3	100	22.9	2320	0.12 & 0.17
4	125	23.2	2322	0.01 & 0.02
5	130	22.5	2382	0.01 & 0.02

* Chloride content by weight of cement (18.2% cement content by weight of concrete)

With reference to A, B and C, calcium chloride, sodium chloride and barium chloride have all been used with concrete as accelerating admixtures [14]. With references to Tables 2 and 3 it is noted that the high chloride levels in Batches 1 and 2 may have accelerated the set of the concrete, resulting in lower slumps and higher compressive strengths at 28 days.

3 DISCUSSION

In creating Test Series 3, a cement content by weight of concrete was calculated as 18.2%. It is possible to re-calibrate chloride data from the previous studies of 1989 and 2002, where assumed cement contents of 20% and 14% respectively were used.

The recalibrated chloride levels give average values of 1.65%, 2.04% and 2.40% for the studies carried out in 1989, 2002 and 2011 respectively. A comparison of these values with those in Table 3 indicates that seawater and possibly chloride contaminated aggregates may have been used in the original bridge. It may also be possible that a higher water to cement ratio than that used in Test Series 3 may have been used in 1908 in order to increase the concrete slump to achieve a more workable concrete. Test Series 3 does not account for chlorides present in the coarse aggregates. The use of seawater and marine sand in the mix would account for the high levels of chloride in the concrete and also the uniform chloride profile. This is further supported by Test Series 2 results and the observation of a white product in the concrete breakout (Figure 9).



Figure 9. Section of concrete breakout with possible cast-in chlorides shown as areas in white.

It is worth noting that in examining the chloride profiles for Brow Head Quarry, the average background chloride for Sample 2 was 0.18%. This compares well with the readings of 0.12% and 0.17% for Test Series 3, Batch 3. This similarity suggests that chloride contaminated sea sand may have been used in the Brow Head Quarry concrete mix.

3.1 Modelling of Chloride Ingress

Traditional chloride ingress models are not applicable in the case of the Mizen Bridge. The high chloride levels and uniform chloride profile are possibly accounted for by the use of chloride contaminated constituents such as seawater and untreated marine aggregates. Although some of the background chloride would have been taken up in the binder, a significant quantity of free chlorides would have remained inside the concrete.

In such circumstances the free chlorides contained in the fresh concrete would have initiated reinforcement corrosion. The presence of high levels of free chlorides in the concrete mix had the effect of reducing the initiation period. This would have reduced the service life of the reinforcement considerably. In this context, it is noted that there are reports of concrete repair being undertaken at Mizen Bridge in the late 1930's. It is also worth noting that the high levels of free chloride may have leached out at the concrete surface and may be the reason for the reduction of chloride levels observed near the concrete surface in Figure 9.

REFERENCES

[1] L.F. Stephens, *The Bridge at Mizen Head*, Irish Engineers, Volume 27, No.7, 1974.

[2] K. Ruane, R. O'Donovan, N. O'Keeffe, E. Lehane, M. Coleman, K. Power, B. Minihane, E. Collery, *The Design and Construction of the New Mizen Head Footbridge*, Proceedings of the Institution of Civil Engineers, 2013.

[3] K. Ruane and A. Healy, *Assessment Testing Mizen Head Footbridge Ireland*, Proceedings of the Institution of Civil Engineers, Bridge Engineering 157, Issue BE3, 2004.

[4] S. MacCraith, *Performance of an 80 year old Reinforced Concrete Bridge in an Extreme Environment*, Corrosion of Reinforcement in Concrete, Elsevier Applied Science, London, 1990.

[5] Private communication, K. Ruane, *Mizen Head Structural Evaluation,* RPS MCOS Consulting Engineers, 2005.

[6] M.H. Roberts, *BRE Information Paper 21/86, Determination of the Chloride and Cement Contents of Hardened Concrete,* Building Research Establishment, 1986.

[7] P.B. Bamforth, *Technical report no. 61, Enhancing reinforced concrete durability,* Concrete Society Publication, 2004.

[8] W. Millar and C.F. Nichols, *Improvements in means of accelerating the setting and hardening of cements,* Patent 2886, Patents Office, London, 1885.

[9] D.E. Tonini and S.W. Dean, (1977), *Corrosion of steel in concrete,* American Society for Testing and Materials, 1977.

[10] P. McCarthy and R. Hawkes, *Northside of the Mizen,* Mizen Productions, 4th Edition, 2007.

[11] A. Power, *Rock Island, Crookhaven,* Inspire Printing, 2006.

[12] D. Downey, *Next Parish America,* Inspire Printing, 2009.

[13] The British Engineering Standards Committee, *BS 12 British Standard Specification for Portland Cement*, Crosby Lockwood and Son, London, 1904.

[14] A.M. Neville, *Properties of Concrete*, Trans-Atlantic Publications, 5th Edition, 2011.

[15] Irish Cement, *Using Irish Cement, Cement Silos,* Irish Cement, 2005.

[16] C.F. Marsh, *Reinforced Concrete*, Butler & Tanner, 1904.

[17] F.W. Taylor and S.E. Thompson, *A Treatise on Concrete Plain and Reinforced*, J. Wiley and Sons, 1905.

[18] IS EN 197-1:2011, *Cement Part 1: Composition, Specifications and Conformity Criteria for Common Cements',* National Standards Authority of Ireland, 2011.

[19] A.L. Colby, *Reinforced Concrete in Europe*, The Chemical Publishing Co, 1909.

[20] IS EN 1097-6:2000, *Tests for Mechanical and Physical Properties of Aggregates, Part 6: Determination of Particle Density and Water Absorption,* National Standards Authority of Ireland, 2000.

[21] BS 1377-2:1990, *Methods of Tests for Soils for Civil Engineering Purposes, Particle size distribution*, British Standards Institution, 1990.

[22] Geological Survey of Ireland, http://www.gsi.ie/, 2014.

[23] J. de Courcy, *Concrete In Cork*, Paper presented to the Irish Concrete Society, Southern Region, 1989.

[24] Ordnance Survey of Ireland, http://www.osi.ie/, 2014.

[25] IS EN 206-1:2000, *Concrete Specification, performance, production and conformity,* National Standards Authority of Ireland, 2000.

Performance of Varies Cement Types in Acidic Wastewater Environments

Donogh Coleman[1], Ciaran McNally [2], Brian O'Rourke[1], Mark G Richardson[2]
[1]Department of Civil, Structural and Environmental Engineering, Cork Institute of Technology, Rossa Avenue, Bishopstown, Cork, Ireland.
[2]UCD School of Civil, Structural and Environmental Engineering, University College Dublin, Belfield, Dublin 4, Ireland.
e-mail: donogh.coleman@cit.ie, ciaran.mcnally@ucd.ie

ABSTRACT: Wastewater facilities are primarily constructed using concrete. Supplementary cementitious materials (SCM) such as Ground Granulated Blast Furnace Slag (GGBS) are being used in increasing quantities for technical, environmental, economic and aesthetic reasons. It has been shown that GGBS can increase the durability of concrete in wastewater environments. However, recent research has not demonstrated that this increase in durability is sufficient to prevent biodeterioration associated with acidic wastewaters. The literature has shown that the pH may vary from 1 to 5, leading to complex deterioration mechanisms that are not fully understood. The aim of this research is to investigate whether GGBS can increase the durability of concrete when subjected to acidic solutions. An experimental programme has been designed to compare performance of concretes manufactured using varying cementitious binders when subjected to acidic environments. Specimens were assessed for strength and deterioration, and the influence of mix parameters such as GGBS content. Three different concrete mixes were selected for the tests and the performance was monitored over a 52 week test duration to allow assessment of binder performance. The research showed the major role the pH of the solution plays in the deterioration of the concrete. It was also shown that CEM II has the highest neutralising effect on the acid.

KEY WORDS: Concrete durability; Concrete testing; Sulfate attack.

1 INTRODUCTION AND BACKGROUND

There exists a significant challenge internationally to provide durable wastewater treatment infrastructure. This is against a backdrop of infrastructural damage being reported in Belgium [1] USA [2], Germany [3], Japan [4] and Denmark [5]. In the USA, the annual investment to provide adequate wastewater infrastructure is estimated at $21 billion. This compares to an annual cost of $25 billion for the operation and maintenance of wastewater infrastructure [6]. The state of South Australia has an estimated budget of A$48 million per annum for maintaining existing wastewater infrastructure [7]. Although these structures are designed for a life span of up to 100 years, some are showing evidence of serious deterioration after less than 10 years in service [7].

The aim of this research is to investigate the effect that different types of cementitious binders have on the durability of concrete in wastewater treatment facilities subjected to sulfuric acid attack. The foremost prerequisite for durable concrete is that it is dense and impermeable to liquids and gases and possesses a high resistance to the penetration of ionic species [8]. Sulfuric acid attack is a combined acid-sulfate reaction. The dissolution effect is caused by the hydrogen ion and the corrosive effect is caused by the sulfate ion [9]. Ionization is the separation of a chemical into ionic species. This is what occurs in wastewater treatment facilities where sulfuric acid is broken down as; $H_2SO_4 \rightarrow H^+ + HSO_4^-$ and $HSO_4^- \rightarrow . H^+ + SO_4^-$. The SO_4^- ion can then react with components of the cementitious binder to form gypsum and ettringite. These compounds are very expansive and lead to tensile stresses and the formation of cracks and spalling [1].

Research on this topic has dated back to 1945 [10]. Progress had been made in understanding the attack mechanisms, the bacteria present and where the most vulnerable concrete occurs. However, little progress has been made to establish a cost effective solution to the problem. It is the structural engineer's responsibility to specify the concrete in wastewater treatment plants. From the estimated costs quoted previously, it is obvious that concrete specified based on design approaches using "XA3" exposure classes [11] is not adequate to deal with the harsh environment it is exposed to. The structural engineer has little choice but to specify this exposure class. A move to performance-based design that could be incorporated into a revised version of EN 206-1 [11] is required.

2 CHEMICAL & MICROBIOLOGICAL REACTIONS

Research has found that the corrosion of pipes and tanks in wastewater treatment facilities occurs just above the waterline. In 1945 Parker [10] was the first to discover that bacteria (Thiobacillus) was involved in the biogenic sulfuric acid corrosion process. Bacteria cannot grow on concrete surfaces as concrete exhibits a pH that is too high, in the range 11-13 [2]. When anaerobic conditions occur in raw sewage influent, sulfates are converted into sulfides (such as hydrogen sulfide) by the sulfate-reducing bacteria [7]. Hydrogen sulfide is released just above the water level due to turbulence and a pH decrease [12]. Elemental sulfur is produced when this gas reacts with oxygen and this is then deposited on the walls of the sewer structures. In the slime layer coating these walls, at a pH of around 4, aerobic sulfur-oxidizing bacteria (Thiobacillus sp.) metabolize the sulfur to sulfuric acid [1]. These can further reduce the surface pH to 1 or 2 and calcium sulfate is formed when sulfuric acid reacts with the free lime [$Ca(OH)_2$] in the concrete. The reaction is given in equation 1:

$$Ca(OH)_2 + H_2SO_4 \rightarrow CaSO_4 + 2H_2O \quad [1]$$

Calcium sulfate is subsequently hydrated to form gypsum ($CaSO_4 \cdot 2H_2O$). An increase in volume by a factor of 2.2 is associated with this reaction [1]. Gypsum can be identified by its white, mushy appearance which has no cohesive properties and has the consistency of "cottage cheese" [2]. If the pH is high enough the gypsum reacts with the calcium aluminate hydrate (C_3A) to form the less soluble but more expansive reaction product ettringite [10]:

$$3CaSO_4.2H_20 + 3CaO.Al_2O_3 + 26H_20 \rightarrow$$

$$(CaO)_3\,(Al_2O_3)\,(CaSO_4)_3.32H_20 \quad [2]$$

An increase in volume by a factor of up to 7 is associated with this reaction [12]. The flow of sewage accelerates the process by removing the degraded material.

There is evidence that using high proportions of polymer modified binders will reduce the attack from sulfuric acid [7]. However, at this time these materials are too expensive for the large scale surfaces associated with this problem; in this context the potential benefit of investigating different types of SCMs such as GGBS merits investigation.

3 PREVIOUS RESEARCH

Extensive research has been carried out into methods to reduce biogenic acid corrosion. The effects of polymeric materials [1], water/cement ratio [12], types of aggregates [7], cement type and SCM [7] & [14], have all been investigated. There are three types of tests that can be carried for sulfuric acid corrosion; microbial simulation tests, chemical tests and exposed in-situ tests.

Accelerated tests can be performed by increasing the concentration, increasing the temperature, using larger contact surfaces or by means of continuous wetting and drying cycles [15]. Most researchers increase the concentration to 1–5% sulfuric acid. The pH of the solution can be kept at a certain value by titration or by replenishing the solution at regular intervals. Mass loss and compressive strengths are the most commonly used parameters investigated.

De Belie *et al*. [13] carried out chemical tests using three different types of cements; CEM I 42.5 HSR/LA, CEM I 52.5 HSR/LA and blastfurnace slag cement CEM III/B 42.5 HRR/LA and two types of aggregates; gravel or porphyry (inert) and limestone (reactive). The pH of the chemical test was 0.9-1.0 (0.5% sulfuric acid). Concrete cylinders were subjected to 10 attack cycles. Each cycle lasted 5 days and consisting of rotating the samples in and out of the solution. After each cycle, they were then dried in air and brushed. The change in radius was recorded before and after brushing. The reason for this was to differentiate between a sample that undergoes large expansion, followed by equally large material loss by brushing and a sample that shows little expansion and material loss. If the samples were only measured after brushing, both types would show the same change in radius whereas the first one is more prone to degradation. The change in surface roughness was also measured. The solution was changed for each cycle. The pH of the solution increased from 0.9 to 1.6. The aggregate type had the greatest influence on the degradation of the concrete. The limestone aggregate outperformed the inert aggregates by neutralizing the acid. The reason given for this was the higher CaO content of the limestone aggregates (43-46%), compared with the gravel or porphyry aggregates (1-8%). Even though the pH of the acid increased to only 1.6, it is believed that a microenvironment with higher pH is created near the concrete surface by the limestone aggregates. The lowest water/cement ratio performed the best due to the lower water absorption values. The Portland cements outperformed slag cement. The CaO content of Portland cements (62-64%) is higher than the slag cement (48-49%).

Chang *et al*. [7] carried out chemical tests on six concrete mixes; four using calcareous limestone aggregates and two using siliceous aggregates. The cements used were: Portland cement, GGBS, two ternary cements containing slag and silica fume or pulverised fly ash (PFA) and silica fume. The samples were immersed in 1% sulfuric acid solution for 168 days. The pH was kept between 1.27 and 1.35 by weekly refreshing of the solution. The change in mass was recorded (samples were brushed), visual inspections were undertaken and the samples were tested for compressive strength. The samples were also examined under scanning electronic microscopy. The limestone aggregates outperformed the siliceous aggregates. The calcium carbonate in the limestone aggregate acted as a sacrificial medium near the concrete surface to neutralise the acid concentration and decrease the rate of deterioration of concrete subjected to acid attack. The cement types were ranked in the following order: (1) the ternary cement containing 7% silica fume and 33% PFA, (2) the Portland cement, (3) the ternary cement containing slag and silica fume, (4) GGBS. Chang *et al*. [7] considered load bearing capacity tests to be more reliable than mass change measurements.

O'Connell *et al*. [14] carried out chemical tests on six concrete mixes; 100% CEM II/AL, 50% CEM II/AL + 50% GGBS, 30% CEM II/AL + 70% GGBS, 100% CEM I, 30% CEM I+ 70% GGBS & 100% SRPC. Following the procedure recommended by Chang [7], the samples were immersed in 1% sulfuric acid (pH ≈1.5) for 168 days. The change in mass was recorded (the samples were brushed), visual inspections were undertaken and the samples were tested for compressive strength. The samples were also analysed using X-ray diffraction. The procedure was repeated but the second time the samples were not brushed. For both sets of results the GGBS outperformed all other mixes regardless of the binder type. However, the difference was not significant and the research concluded that none of the samples were capable of resisting the sulfuric acid attack at such a low pH value.

4 TESTING

4.1 Aggregates

Based on evidence from previous research, limestone aggregates were chosen for the experimental programme. Chang *et al*. [7] and De Belie *et al*. [13] showed that limestone aggregates improve the durability of the concrete subjected to sulfuric acid when compared to siliceous aggregates. For this reason 20mm single sized limestone aggregate, 10mm single sized limestone aggregate and limestone sand were used. The aggregates were graded and conformed to I.S. EN 12620:2002 [16].

The mix portions were adjusted to best fit inside the upper and lower boundary limits, chosen based on industry best practice. Figure 1 shows the combined grading of the 20mm limestone, 10mm limestone and the sand and the upper/lower boundary limits.

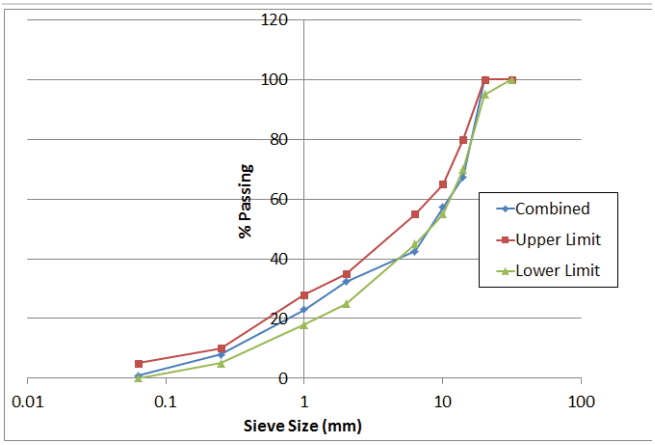


Figure 1. Combined Grading Curve.

4.2 *Binders and mix design*

Six mix designs were prepared. Table 1 gives a summary of the binder proportions:

Table 1. Binder Proportions (%).

	CEM I	CEM II/A-L	GGBS	SRPC
Mix 1	0	100	0	0
Mix 2	0	50	50	0
Mix 3	0	30	70	0
Mix 4	100	0	0	0
Mix 5	30	0	70	0
Mix 6	0	0	0	100

IS EN 206-1:2002 [11] sets out the main parameters for the mix design. For exposure class XA3 (>3000 mg/l and ≤ 6000 mg/l SO_4^{2-}; pH ≤ 4.5 and > 4) the water/binder (W/B) ratio is 0.45 and the binder content is 360kg/m^3. Moisture content tests were carried out on the 20mm single sized limestone aggregate, 10mm single sized limestone aggregate and limestone sand. The free water content was calculated and the mixes were adjusted accordingly. 0.03m^3 of each mix was prepared, making 20 cubes measuring 100mm.

4.3 *Mixing, Curing & Drying*

A rotating drum mixer was used to mix the concrete. Slump tests were completed in accordance with IS EN 12350-2:2009 [17]. The samples were cast using standard 100mm cube moulds and compacted on a vibrating table. 20 cubes were manufactured for each mix type. The cubes were covered in plastic sheeting and protected against shock, vibration and dehydration for approximately 20-24 hours, at which time they were demoulded. After removal from their moulds, the cubes were cured in water at a temperature of 20 (± 2) °C for 28 days.

4.4 *Test Procedure*

The purpose of this research is to investigate the effects of biogenic sulfuric acid deterioration on concrete, a biological phenomenon in wastewater treatment plants. As this is a difficult process to replicate in a laboratory environment and for practical reasons it is more suitable to mimic the corrosive effect using a purely chemical process. The active biofilm layer just above the waterline is crucial to the biological deterioration process. Previous research carried out by Monteny *et al.* [1] and Beeldens *et al.* [18], partially submerged the samples in sulfuric acid. O'Connell *et al.* [14] recommended fully submerging the samples in sulfuric acid as there was no bacteria in their research and hence no biofilm.

No standardized procedure for testing the resistance of concrete to sulfuric acid attack is currently available. Chang [7] determined that immersing the cubes in 1% sulfuric acid solution at pH ≈ 1.5 for up to 168 days provides the optimal balance between actual conditions and the need to accelerate the reaction process. After following this process, O'Connell *et al.* [14] determined that none of the tested samples could adequately address these exposure conditions.

For this experimental programme it was decided to adjust the pH recommended by Chang *et al.* [7] and increase the duration to 52 weeks. The mixes were immersed in solutions with a pH of 2 and a pH of 3.

Two cubes of each mix were crushed in accordance with I.S. EN 12390-3:2009 [19] after 28 days to provide baseline strength data. Of the remaining 18 cubes for each mix, six were placed in a solution of pH2, six in a solution of pH3 and the remainder were left in the curing tank. The cubes were removed from the acid tanks for assessment; once a week for the first four weeks and every second week thereafter.

Up to week 15 the samples were blotted with a paper towel and weighed. The samples were then brushed until all the loose material was removed. The samples were then blotted with a paper towel and weighed again. It was imperative that consistent brushing was undertaken for all specimens so a reliable comparison can be made. O'Connell *et al.* [14] recommended brushing until the water run-off was clear. For this experiment, no milky white run-off was present so brushing stopped once the loose material was removed.

The pH of the solutions was determined each week. The solutions were titrated back to a pH of 2 and 3 respectively at the time of assessment and the volume of acid required was recorded. The solution was refreshed in week 4, week 10 and every fifth week thereafter. The pH was measured using a calibrated digital pH meter.

5 RESULTS

5.1 *Mass loss of concrete specimens in pH2*

Figure 2 shows the percentage mass loss of each of the six mixes exposed to a sulfuric acid solution of pH2 for 52 weeks. The mass loss varied from 12.9% for Mix 6 to 16.1% for Mix 3.

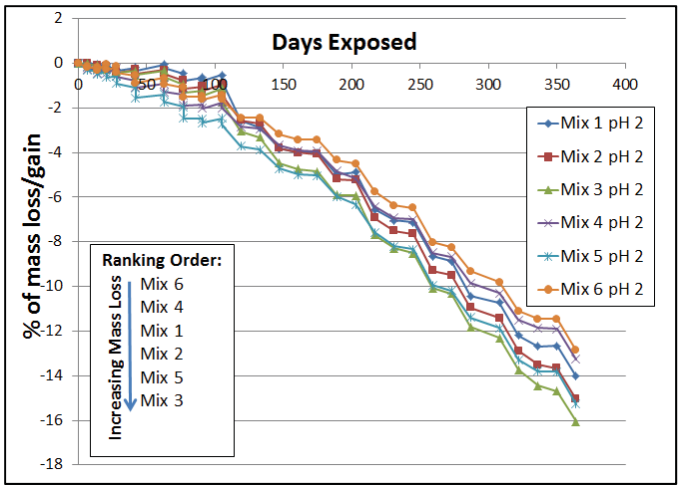


Figure 2. Mass loss of concrete cubes exposed to a pH2

5.2 *Mass loss of concrete specimens in pH3*

Figure 3 shows the percentage mass loss of each of the 6 mixes exposed to a sulfuric acid solution of pH3 for one year. The mass loss varied from 1.2% for Mix 6 to 2.7% for Mix 3.

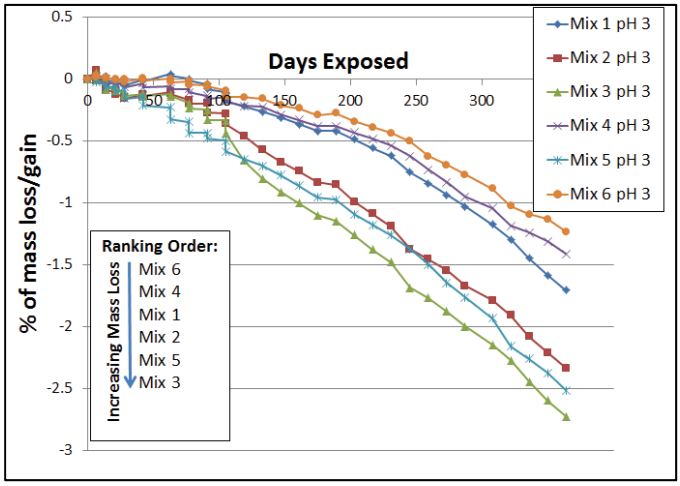


Figure 3. Mass loss of concrete cubes exposed to a pH3

5.3 *Compressive strengths of the mixes immersed in pH2 and pH3*

To compare the result of each of the six mixes, they are graphed together. The percentage strength of the concrete immersed in acid is measured against strength of concrete in curing tank (See Figure 4 & Figure 5)

Two cubes of each mix were crushed after 28 days in the curing tank. These results are the compressive strengths at day 0. Six cubes of each mix were placed in the following; water, a solution of pH2 and a solution of pH3. Two cubes were crushed on day 60, two on day 182 and the final two on day 364.

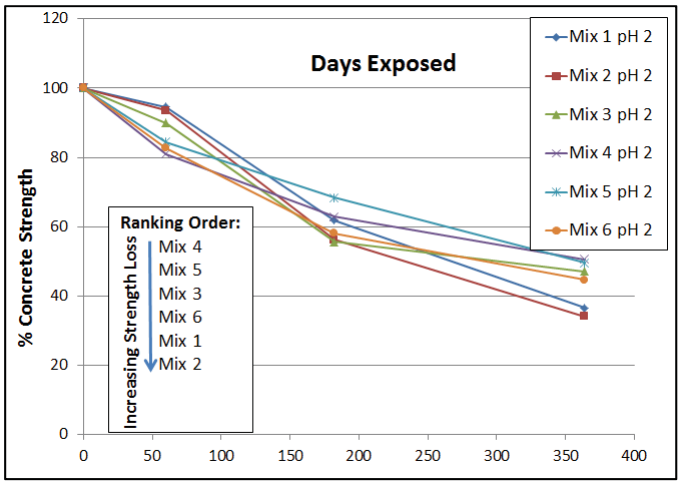


Figure 4. Compressive strengths of samples immersed in pH2 relative to the strengths of samples immersed in water for the same duration

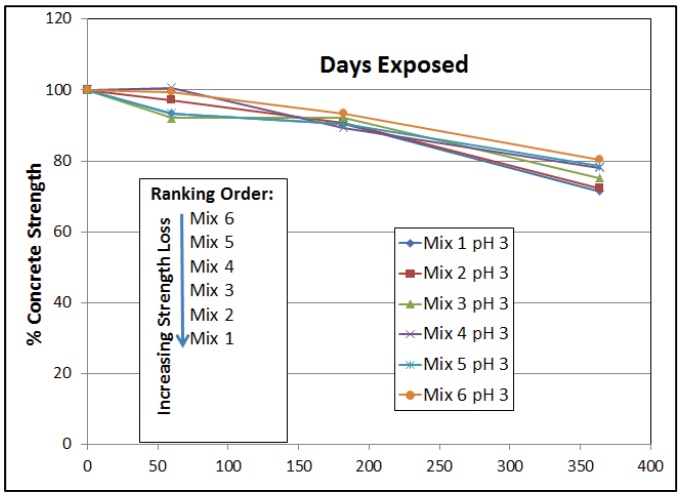


Figure 5. Compressive strengths of samples immersed in pH3 relative to the strengths of samples immersed in water for the same duration

5.4 *Volume of acid added to the solutions*

The solutions were titrated back to a pH of 2 and 3 respectively at the time of assessment and the volume of acid required was recorded. The solution was changed in week 4, week 10 and every fifth week after that. Figure 6 & Figure 7 show the percentage of mass loss versus the volume of 10% sulfuric acid added to the six mixes immersed in the pH2 and pH3 solution respectively.

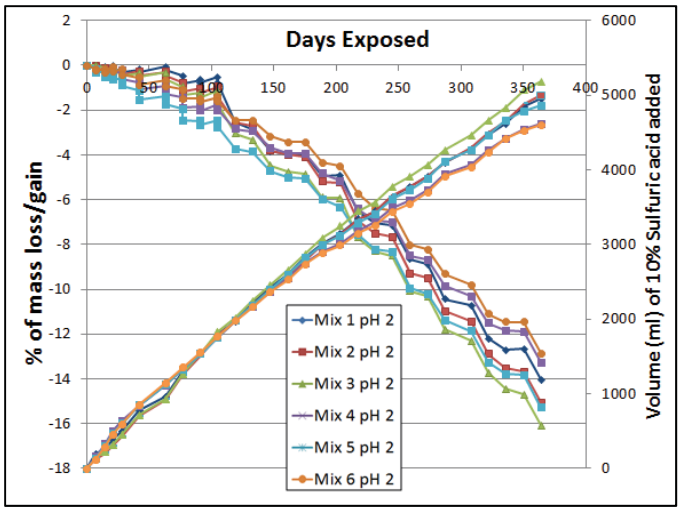


Figure 6. Percentage mass loss versus volume of acid added for cubes immersed in pH2 solution

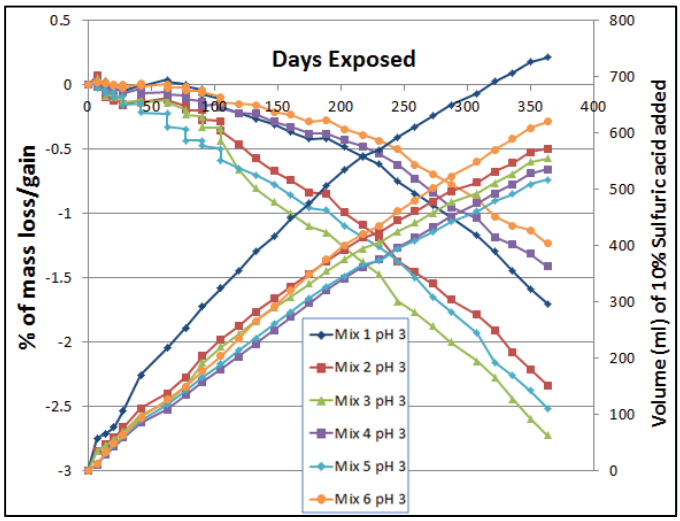


Figure 7. Percentage mass loss versus volume of acid added for cubes immersed in pH3 solution

6 DISCUSSION

6.1 Mass loss

The samples exposed to the pH2 solution experienced substantial mass loss, between 12.9% and 16.1% over the course of the experiment. The three mixes containing GGBS performed worse than those without, with SRPC performing the best. The samples exposed to the pH3 solution experienced very little mass loss; between 1.2% and 2.7%. The ranking order for both sets of results was identical.

The largest change in mass occurred after the solution was changed. Titrating back to the reference point of pH2 or pH3 did not have the same influence in terms of mass loss.

6.2 Compressive strength

The samples exposed to the pH2 solution, lost on average 57% of their strength relative to the control samples that were left in the curing tank. The two 70% GGBS samples were ranked second and third, however the 30% GGBS sample performed the worst. The samples exposed to the pH3 solution lost an average of 24% of their strength.

6.3 Volume of acid added

The volume of acid added is dependent on the neutralisation capacity of the sample. The volume of acid added is directly related to the mass loss. It can clearly be seen from Figure 6 that the more acid that was added, resulted in a higher mass loss. The three mixes containing CEM II had the highest volume of acid added to the solutions. This indicates that that the CEM II has the highest neutralising effect on the acid.

For the pH3, see Figure 7, the 100% CEM II mix had substantially more acid added than the other five mixes. This again indicates that CEM II has the highest neutralising effect on the acid.

7 CONCLUSIONS AND RECOMMENDATIONS

The question posed for these experiments was whether GGBS could increase the durability of concrete when subjected to acidic solutions. Based on these results, there is no evidence to suggest that there is a major difference between the mixes.

The pH of the solution plays a major role in the durability of concrete. On average the mixes immersed in pH2 experienced a mass loss of seven times that of the mixes immersed in pH3. The strength loss of the mixes in pH2 was on average 56% compared to 24% for the mixes immersed in pH3.

The results indicate that CEM II had the highest neutralising effect on the acid. This is most likely due to the buffering capacity of the additional limestone in CEM II.

The recommendations are to repeat the test procedure but to change the solution on a weekly basis rather than every 5 weeks. This will result in the same acid being added to all the mixes.

REFERENCES

[1] Monteny J, De Belie N, Vincke E, Verstraete W and Taerwe L. (2001), 'Chemical and microbiological tests to simulate sulfuric acid corrosion of polymer-modified concrete', *Cement and Concrete Research,* 31(9):1359–65.

[2] Davis JL, Nica D, Shields K and Roberts DJ. (1998), 'Analysis of concrete from corroded sewer pipe', *International Biodeterioration and Biodegredation,* 42(1):75–84.

[3] Sand W, Bock E and White D, (1987), 'Importance of hydrogen sulphide, thiosulfate, and methylmercatan for growth of Thiobacilli during simulation of concrete corrosion', *Applied and Environmental Microbiology*, 53(7):1645-1648.

[4] Moni, T, Koga, M, Hikosaka Y, Nonaka T, Mishina, Sakai Y and Koizumi J, (1991), 'Microbial corrosion of concrete sewer pipes, H_2S production from sediments and determination of corrosion rate', *Water Science and Technology*, 23(7-9):1275-1282.

[5] Vollertsen J, Nielsen AH, Jensen HS, Wium-Andersen T and Hvitved-Jacobsen T. (2008), 'Corrosion of concrete sewers – the kinetics of hydrogen sulfide oxidation' *Science of the Total Environment*, 394(1):162–70.

[6] Congressional Budget Office. Future investment in drinking and wastewater infrastructure. Congressional Budget Office; 2002. ISBN: 0160512433.

[7] Chang ZT, Song XJ, Munn R and Marosszeky M. (2005), 'Using limestone aggregates and different cements for enhancing resistance of concrete to sulfuric acid attack', *Cement and Concrete Research,* 35(8):1486–94.

[8] Osborne, G. J. (1999) Durability of Portland blast-furnace slag cement concrete. *Cement and Concrete Composites,* 21**,** 11-21.

[9] O'Connell, M, McNally, C and Richardson, MG. (2010), 'Biochemical attack on concrete in wastewater applications: A state of the art review', *Cement and Concrete Composites*, 32(7): 479-485.

[10] Parker, C. D. (1945a) The corrosion of concrete I. The isolation of a species of bacterium associated with the corrosion of concrete exposed

to atmospheres containing hydrogen sulphide. *Australian Journal of Experimental Biology & Medical Science,* 23**,** 81-90.
[11] National Standards Authority of Ireland. *IS EN 206-1:2002 Concrete - Part 1: Specification, performance, production and conformity.* NSAI, 2002.
[12] Bassuoni, M. T. & Nehdi, M. L. (2007) Resistance of self-consolidating concrete to sulfuric acid attack with consecutive pH reduction. *Cement and Concrete Research,* 37**,** 1070-1084.
[13] De Belie N, Monteny J, Beeldens A, Vincke E, Van Gemert D and Verstraete W. (2004), 'Experimental research and prediction of the effect of chemical and biogenic sulfuric acid on different types of commercially produced concrete sewer pipes', *Cement and Concrete Research,* 34(12):2223–36.
[14] O'Connell M, McNally C and Richardson MG, (2012), 'Performance of concrete incorporating GGBS in aggressive wastewater environments', *Construction and Building Materials* 27 (1):368-374
[15] Monteny J, Vincke E, Beeldens A, De Belie N, Taerwe L, Van Gemert D and Verstraete, W. (2000), 'Chemical, microbiological, and in situ test methods for biogenic sulfuric acid corrosion of concrete', *Cement and Concrete Research,* 30(4):623–34.
[16] National Standards Authority of Ireland. *IS EN 12620:2002+A1:2008 Aggregates for Concrete.* NSAI, 2002.
[17] National Standards Authority of Ireland. *IS EN 12350-2:2009 Testing fresh concrete - Part 2: Slump test.* NSAI, 2009.
[18] Beeldens A, Monteny J, Vincke E, De Belie N, Van Gemert D, Taerwe L and Verstraete W. (2001), 'Resistance to biogenic sulfuric acid corrosion of polymer-modified mortars', *Cement and Concrete Composites,* 23(1):47–56
[19] National Standards Authority of Ireland. *IS EN 12390-3:2009 Making and curing specimens for strength tests.* NSAI, 2009.

Influence of compressive loading on chloride ingress through concrete

Junjie Wang[1], P.A.Muhammed Basheer[1], Sreejith V. Nanukuttan[1], Yun Bai[2]
[1] School of Planning, Architecture and Civil Engineering, Queen's University Belfast, Northern Ireland, UK.d
[2]Department of Civil, Environmental and Geomatic Engineering, University College London, UK.
email: an u .ac.u . as eer u .ac.u s.nanu uttan u .ac.u yun. ai ucl.ac.u

ABSTRACT: Chloride-induced corrosion of steel in concrete is one of the most important durability and safety concerns for reinforced concrete structures. To study chloride ingress into concrete is thus very important. However, most of the researchers focus on studying chloride ingress through concrete samples without any loading. In reality concrete structures are subjected to different kinds of loads and therefore studying the effect of such loads on chloride transport is critical. In this work, 28 different concrete mixes were subjected to three levels of compressive load (0%, 50% and 75% of compressive failure load – *f*) for 24 hours. Further to unloading, these samples were subjected to non-steady state chloride diffusion test as per NT Build 443. The results were compared against the diffusion coefficient (*D)* obtained for concrete samples that had no previous loading. *D* value for concretes subjected to 75% *f* showed a significant increase compared to 0% loading condition, but the increase was insignificant for 50% *f*. The results indicate that the influence of concrete mixes variables on *D* is more significant than that of loading level. Surface chloride concentration also increased with the loading level, which might be due to the increased concrete surface area caused by micro cracking.

KEY WORDS: Chloride ions; Concrete; Durability; Diffusion; Loading.

1 INTRODUCTION

Chloride-induced corrosion of reinforced concrete structures is one of the most serious problems affecting economic growth and the safety of people's lives and properties. To study the processes of chloride transport in concrete is very important so that engineers can predict the service life of concrete structures. However, most of the studies have just focused on 'perfect' concretes which are usually not cracked or withstanding any structural loading. The existing service life prediction models, like Life-365 [1-2], AGEDDCA model [3] and DuraCrete [4], also do not consider any effect of loading or cracking. The predicted service life, based on the performance of concrete without considering the actual loading condition, may not be reliable. As a consequence, premature deterioration of structures in service is common. A field survey of 57 bridges in Kansas indicated that chloride concentration at a depth of 76 mm from the location of a surface crack can exceed the corrosion threshold amount within the first year [5]. Another survey of 15 marine structures in Florida showed that signs of corrosion could be seen at about 10 to 15 years since construction, with the average at about 11.5 years, meaning that corrosion has initiated much earlier than expected [6].

Few studies have been carried out on the influence of loading on chloride diffusion. A consistent decrease of chloride diffusion coefficient up to the loading level at 50% of concrete compressive strength was reported by Wang et al. [7], Li et al. [8] and Lim et al. [9]. The results at higher loading levels were not available. Also, most of the work focused only on pure Portland cement CEMI concrete, and the data on concrete with mineral additives is still limited.

This paper presents data from a test programme conducted to study the influence of loading on the chloride diffusion of concrete subjected to different stress levels. As shown in Table 1, different cement combinations were studied. The result of this study may aid in more accurate predictions of service life and in designing more durable concrete structures.

2 EXPERIMENTAL PROGRAMME

The coarse aggregate used was crushed and well graded basalt of size 5-20mm (size 5-10 mm/ size 10-20mm ratio is 33/67) and the fine aggregate was natural medium graded sand. Both aggregates were oven-dried at 100 ± 5 ℃ for 24 hours to remove the initial moisture and cooled down in air-tight containers before being used. Class 42.5N Portland cement (PC) CEMI conforming to BS EN 197-1:2011 [10] was used. Ground granulated blast-furnace (GGBS) complying with BS EN 6699: 1992 [11], pulverised fuel ash (PFA) complying with BS EN 450 [12] and silica fume (SF) EMSAC 500 S were used to replace part of CEMI in the mixes studied. The mix details and proportions for each mix are given in Table 1. The required quantities of the mix constituents were batched by mass and then mixed using a pan mixer in accordance with BS 1881-125: 1986 [13]. The test samples were cast according to BS EN 12390-2:2000 [14]. Slump of each mix is reported in Table 2. A vibrating table was used to compact the samples. The casting surface of concrete specimen was then smoothed and a thick black polythene sheet was used to cover the concrete. The curing regime was as follows: After demoulding, the specimens were placed in a water bath at 20 ℃ (± 1℃) for the first 3 days and then wrapped in wet hessian and thick black polythene sheets. They were then placed in a constant temperature room at 20 ℃ (± 1℃). A compressive strength test was conducted at an age of 28 and 56 days for each mix, and the results are shown in Table 2.

Table 1. Details of the concrete mixes studied including the mass of ingredients required to produce 1m^3.

Group	Portland Cement	GGBS	PFA	SF	Water	Superplasticiser	10 mm aggregate	20 mm aggregate	Sand
	kg/m^3								
0.45-CEMI,300	300	—	—	—	135	0.39	408	829	825
0.45-CEMI,360	360	—	—	—	162	0.47	384	780	776
0.45-35%GGBS,300	195	105	—	—	135	0.44	407	826	822
0.45-35%GGBS,360	234	126	—	—	162	0.52	382	776	772
0.45-65%GGBS,300	105	195	—	—	135	0.44	405	823	819
0.45-65%GGBS,360	126	234	—	—	162	0.52	371	752	769
0.45-5%SF, 300	270	—	—	15	135	0.44	399	810	821
0.45-5%SF, 360	324	—	—	18	162	0.52	376	762	773
0.45-10%SF, 300	270	—	—	30	135	0.52	406	824	820
0.45-10%SF, 360	324	—	—	36	162	0.63	381	774	770
0.45-17.5%PFA, 300	195	—	52.5	—	135	0.44	403	817	828
0.45-17.5%PFA, 360	234	—	63	—	162	0.52	380	770	781
0.45-35%PFA, 300	195	—	105	—	135	0.87	400	812	808
0.45-35%PFA, 360	234	—	126	—	162	1.04	374	759	755
0.65-CEMI,300	300	—	—	—	195	—	377	765	761
0.65-CEMI,360	360	—	—	—	234	—	346	702	690
0.65-35%GGBS, 300	195	105	—	—	195	—	375	762	758
0.65-35%GGBS, 360	234	126	—	—	234	—	344	699	695
0.65-65%GGBS, 300	105	195	—	—	195	—	374	759	755
0.65-65%GGBS, 360	126	234	—	—	234	—	342	695	692
0.65-5%SF, 300	270	—	—	15	195	0.10	368	747	758
0.65-5%SF, 360	324	—	—	18	234	0.13	339	687	697
0.65-10%SF, 300	270	—	—	30	195	0.22	374	760	756
0.65-10%SF, 360	324	—	—	36	234	0.26	343	696	693
0.65-17.5%PFA, 300	195	—	52.5	—	195	—	381	774	771
0.65-17.5%PFA, 360	234	—	63	—	234	—	352	714	710
0.65-35%PFA, 300	195	—	105	—	195	—	368	748	744
0.65-35%PFA, 360	234	—	126	—	234	—	336	682	679

After 56 days of curing, cores of size 100mm diameter and 80 mm thickness were cut from the blocks and the outermost, approximately 15 mm thick layer, was cut off from the two end surfaces using a water-cooled diamond saw. This was carried out to avoid the effects of the compaction influencing chloride transport and to ensure that results are indicative of mass concrete. The middle part of 50 ± 1 mm was thus used as test specimen. Three cores per mix were used to determine the failure compressive load, *f*. Based on this failure load, 9 other samples per mix were subjected to a compressive loading level of 0%, 50% or 75% *f* with three samples per load level. As shown in Figure 1, the load was applied and kept using a steel frame and a torque wrench which can show the load applied. After 24 hours of loading, all faces except the exposure face (one cut face) of the disc specimen were coated with epoxy. Samples were saturated in $Ca(OH)_2$ solution under vacuum conditions as specified in NT Build 443 [15].

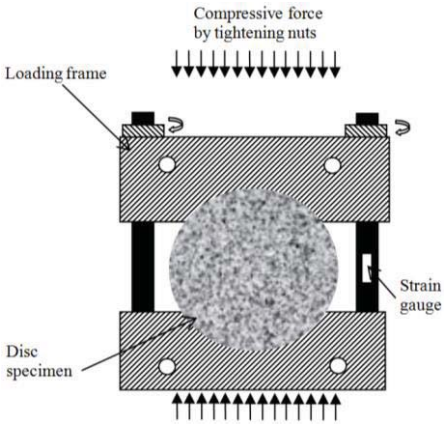


Figure 1. Schematic diagram of the loading set-up used for applying compressive loads on concrete cores.

Table 2. Slump and compressive strength of the different concretes

Mix ID	Slump (mm)	Compressive strength at 28 days			Compressive strength at 56 days		
		Mean (MPa)	SD (MPa)	CV (%)	Mean (MPa)	SD (MPa)	CV (%)
0.45-CEMI, 300	100	58.70	1.78	3.03	60.23	1.06	1.76
0.45-CEMI, 360	120	58.04	0.67	1.16	59.45	0.67	1.13
0.45-35%GGBS, 300	105	49.81	1.79	3.60	62.33	3.62	5.80
0.45-35%GGBS, 360	95	50.71	0.35	0.69	56.73	3.19	5.63
0.45-65%GGBS, 300	95	48.45	2.09	4.30	65.17	2.32	3.57
0.45-65%GGBS, 360	110	48.32	2.36	4.87	65.67	3.06	4.65
0.45-17.5%PFA, 300	110	53.10	1.80	3.40	60.50	0.92	1.51
0.45-17.5%PFA, 360	130	53.70	2.25	4.20	60.67	2.92	4.81
0.45-35%PFA, 300	90	49.22	2.31	4.70	60.40	1.10	1.82
0.45-35%PFA, 360	95	48.83	2.18	4.46	63.03	0.90	1.42
0.45-5%SF, 300	110	58.33	3.12	5.35	63.30	2.43	3.84
0.45-5%SF, 360	115	59.70	2.36	3.96	63.50	2.80	4.41
0.45-10%SF, 300	106	59.63	2.47	4.14	67.50	2.43	3.60
0.45-10%SF, 360	110	58.64	1.47	2.51	68.45	1.31	1.91
0.65-CEMI, 300	95	37.82	1.84	4.86	38.72	2.64	6.82
0.65-CEMI, 360	110	37.59	2.37	6.30	40.89	1.94	4.75
0.65-35%GGBS, 300	100	35.12	1.75	4.99	48.87	1.75	3.59
0.65-35%GGBS, 360	120	36.58	1.96	5.35	47.25	2.03	4.29
0.65-65%GGBS, 300	115	33.51	2.15	6.42	40.62	0.69	1.70
0.65-65%GGBS, 360	125	31.26	2.02	6.48	41.07	2.21	5.38
0.65-17.5%PFA, 300	110	32.04	1.82	5.67	37.05	3.16	8.54
0.65-17.5%PFA, 360	120	33.15	2.22	6.69	37.32	1.90	5.08
0.65-35%PFA, 300	120	29.24	1.23	4.20	38.34	2.40	6.25
0.65-35%PFA, 360	130	30.16	2.25	7.47	39.60	1.15	2.90
0.65-5%SF, 300	120	39.14	2.38	6.07	43.34	2.94	6.79
0.65-5%SF, 360	123	38.86	2.54	6.53	42.51	3.09	7.27
0.65-10%SF, 300	125	39.21	3.53	8.99	49.83	0.47	0.94
0.65-10%SF, 360	100	38.13	2.43	6.37	46.44	1.45	3.12

According to NT BUILD 443 [15], specimens were then immersed in an aqueous NaCl solution (containing NaCl 165 ± 1 g/dm^3) and kept for 35 days. The temperature of the solution was maintained at 23 ± 2 ℃. A profile grinder from Germann Instruments was used to grind the powder of concrete from the test specimens after ponding. The Preparation of filtrate containing chloride of each sample powder was conducted in accordance of a recommendation of RILEM TC 178-TMC [16]. The concentration of chloride ions in the filtrate was analysed using a commercial potentiometric titrator. The instrument was calibrated before each set of test by using standard chloride solutions with concentrations of 200ppm, 500ppm and 1000ppm. The principle of the automatic potentiometric titrator was: The solution containing chloride ions showed negative potential. 0.02 mol/L $AgNO_3$ was added to react with chloride ions, and AgCl (white crystalline solid) was formed. The negative potential was balanced. The sudden change of the potential of the solution from negative to positive was identified as the point of that all chloride ions had been reacted. Chloride concentration in the solution was calculated by Equation 1.

$$Cl^- = \frac{M_{Cl} C_{Ag} V_{Ag}}{V_{Cl}}$$

Equation 1

where, Cl^- is the chloride concentration in the tested solution, ppm; M_{Cl} is the molar mass of chloride, M_{Cl} = 35.453 g/mol; C_{Ag} is the molarity of the $AgNO_3$ solution used, mmol/L; V_{Ag} is the volume of the $AgNO_3$ solution used, L; V_{Cl} is the volume of the solution tested, L.

According to NT BUILD 443 [15], chloride diffusion coefficient and surface chloride concentration were determined by fitting Equation 2 to the measured chloride concentration at different depths of concrete. The initial chloride content was measured and can be taken as 0% by mass of concrete.

$$C_x = C_s (1 - erf(\frac{x}{2\sqrt{D_e t}})$$

Equation 2

where, C_x is the chloride concentration at depth x and time t, % mass of concrete; C_s is the chloride concentration at the surface, % mass of concrete; x is the depth, m; t is the time, s; D_e is the effective diffusion coefficient, m^2/s.

3 RESULTS AND DISCUSSION

As shown in Figure 2, chloride diffusion coefficient of concrete increased with the loading level. Up to 50% *f*, chloride diffusion coefficient (D) remained constant and did not change much. At 75% *f*, the D value for normal concretes increased by 50% of the unloaded 0%*f* value. For concretes with mineral additives this increase was around 30%. The increased micro cracking at 75% *f* combined with the residual strain that remains in the sample after loading is removed may help to explain the increase in D values observed. As shown in Figure 3, after unloading from 50% *f*, almost all induced strain is recovered, but a significant unrecoverable residual strain can be found after unloading from 75% *f*. The net result is that cracks induced by loading can shorten the effective distance of chloride diffusion in concrete, as shown in Figure 4.

D values for concretes with cement content 360 kg/m^3 were slightly higher than those of concretes with cement content 300 kg/m^3. Increased paste content in the former may help to explain the increase in D value. This is based on the assumption that paste volume is contributing to a larger proportion of the chloride transport in concrete.

Chloride diffusion coefficients of concretes with water/binder 0.65 were higher than those of concretes with water/binder 0.45 and this is due to the higher porosity. In summary, chloride diffusion coefficients of normal concretes can be reduced to 25% of the original values if mineral additives were added.

Surface chloride concentration was also derived from the regression analysis Equation 2. As shown in Figure 5, surface chloride concentration generally increased with the increase of loading level. This can be explained by more chloride ingress due to the cracks formed and the expansion of concrete volume caused by cracks, as shown in Figure 6. The decreased surface chloride concentration at 75% *f* in mix 0.45-5%SF-360 can be caused by the testing errors on chloride concentration.

As shown in Figure 5, concrete with more cement has a slight higher surface chloride concentration, but this trend is not very obvious for many mixes. The effect of loading on change of surface chloride concentration is more significant than the effect of cement content. Surface chloride concentration of concretes with water/binder ratio 0.65 was higher than that of concrete with water/binder ratio 0.45. More chloride ions were allowed to store on the concrete with higher water content because of higher porosity. GGBS and PFA seem to increase the surface chloride concentration as compared with ordinary cement. Slightly increased surface chloride concentration was found in Figure 5 when replacing cement with GGBS and PFA. This might be due to the higher chloride binding capacity [17] and more Friedel's salt formed because of higher alumina content [18]. Figure 5 shows that SF can slightly decrease the chloride surface concentration. SF was found to decrease chloride binding capacity by reduction in PH and dilution effect of C_3A [18].

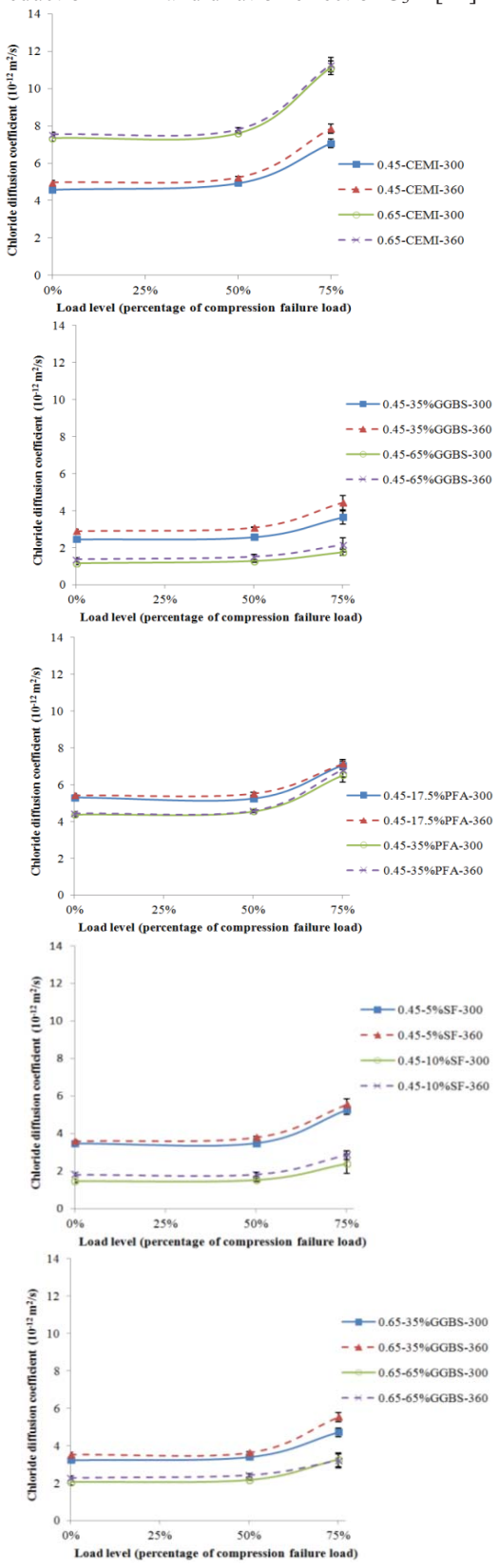
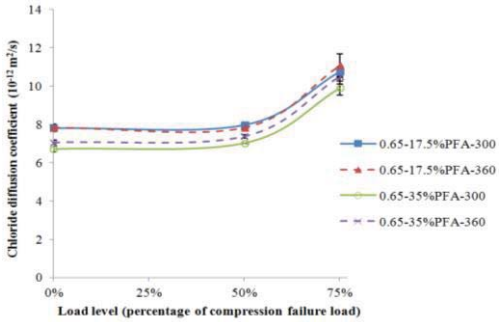


Figure 2. Chloride diffusion coefficient of each mix



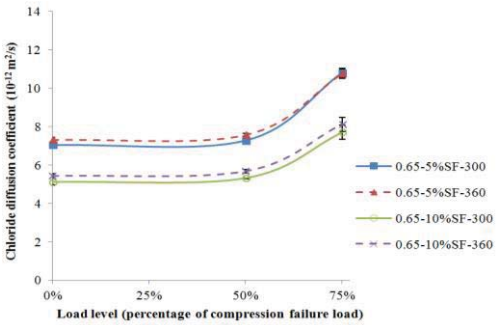


Figure 2. Chloride diffusion coefficient of each mix (continued).

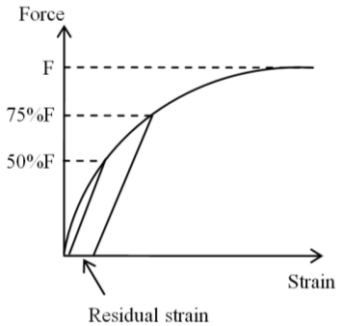
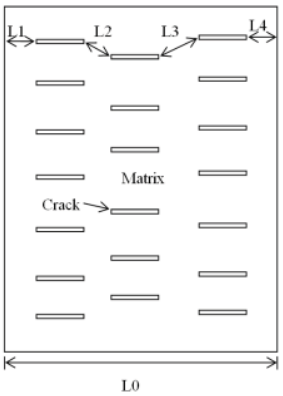


Figure 3. Schematic sketch of the residual strain after unloading.

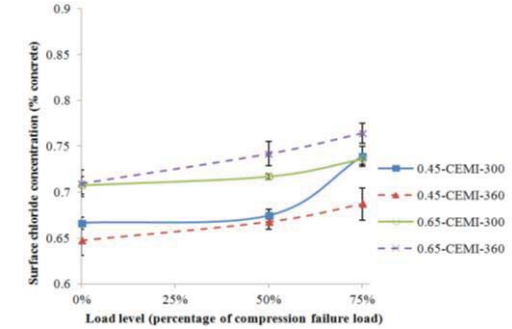


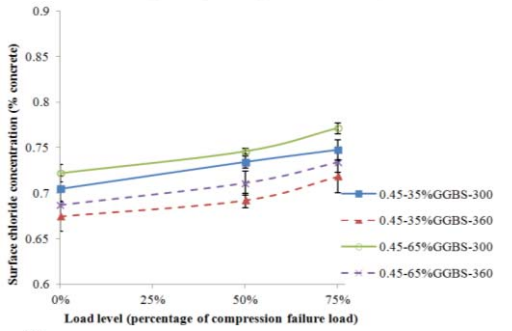
Original transport distance: L0

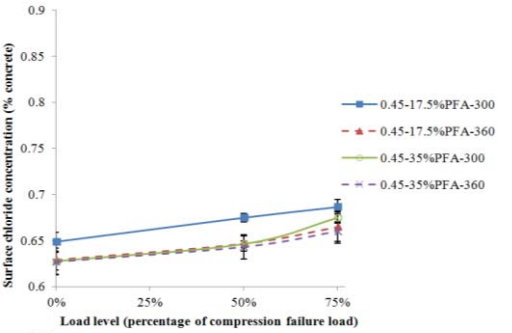
Effective transport distance in concrete with cracks: L1+ L2+ L3+ L4

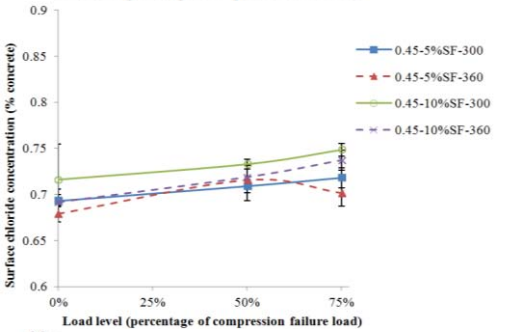
L1+ L2+ L3+ L4 < L0

Figure 4. Reduced chloride transport distance by cracks in concrete.









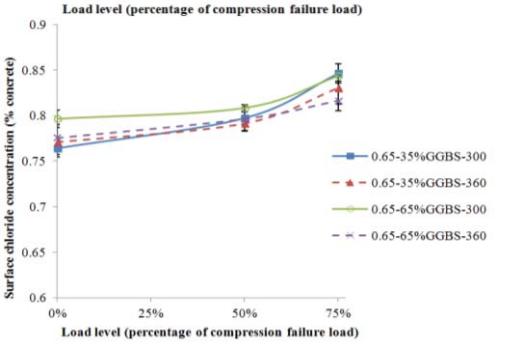


Figure 5. Surface chloride concentration of each mix.

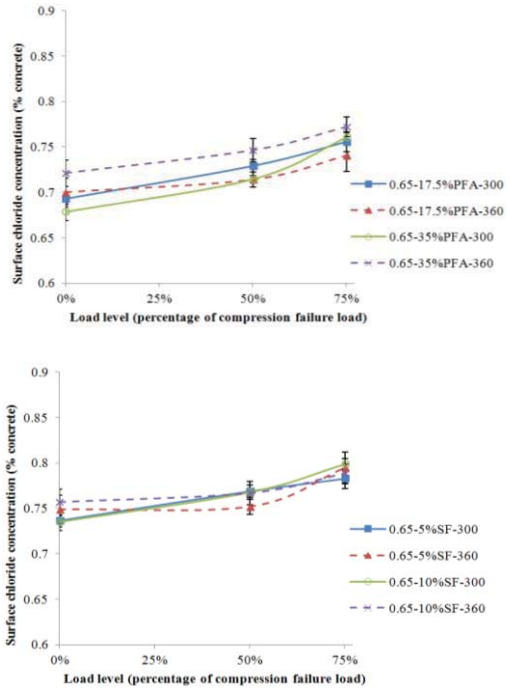


Figure 5. Surface chloride concentration of each mix (continued).

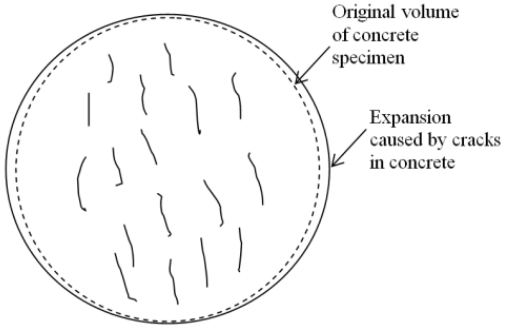


Figure 6. Expansion of volume caused by cracks in concrete.

4 CONCLUSIONS

From the above analysis, the following conclusions can be derived:

1) Loading can increase the chloride diffusion coefficient, the depth to which chloride ions ingress and the surface chloride concentration. There is little change of chloride diffusion coefficient of concrete after unloading from 50% *f*, but after unloading from 75% *f* a significant increase is observed. This increase is up to 50% for normal concrete and 30% for concrete with mineral additives.

2) The effect of cement content on chloride ingress is less significant compared to the effect caused by loading, water/binder or mineral additives.

3) Addition of mineral additives such as GGBS and PFA can slightly increase the surface chloride concentration but SF can slightly decrease chloride surface concentration. These mineral additives can significantly decrease the chloride diffusion coefficient and chloride ingress depth.

4) Lower water binder ratio and addition of mineral additives are the effective means for reducing the chloride ingress into concrete if the expected loading levels can reach up to 75% *f*.

REFERENCES

[1] Violetta, B. 2002, Life-365 service life prediction model, *Concrete International,* vol. 24, no. 12, pp. 53-57.

[2] Thomas, M. and Bentz, E. 2001, LIFE-365, service life prediction model, computer program for predicting the service life and life-cycle costs of reinforced concrete exposed to chlorides, *University of Toronto*.

[3] Bamforth, P. 2004, Enhancing reinforced concrete durability: Part two: Supplementary Technical Reports. *Concrete Society Technical Report 61*, Concrete Society.

[4] Siemes, T. and Edvardsen, C. 1999, Duracrete: service life design for concrete structures, Eighth International Conference on Durability of Building Materials and Components, 8DBMC. pp. 1343-1356.

[5] Lindquist, W.D., Darwin, D., Browning, J.A. and Miller, G.G. 2006, Effect of cracking on chloride content in concrete bridge decks, *ACI Materials Journal,* vol. 103, no. 6, pp. 467-473.

[6] Meletious, C. 1991. p 185., *Development of a field permeability test for assessing the durability of concrete in marine structures. PhD thesis.* University of Florida.

[7] Wang, H., Lu, C., Jin, W. and Bai, Y. 2011, Effect of external loads on the chloride transport in concrete, *Journal of Materials in Civil Engineering,* vol. 23, no. 7, pp. 1043-1049.

[8] Li, G., Hu, F., and Wu, Y. 2011, Chloride Ion Penetration in Stressed Concrete, *Journal of Materials in Civil Engineering,* vol. 23, no. 8, pp. 1145-1153.

[9] Lim, C., Gowripalan, N. and Sirivivatnanon, V., 2004. Microcracking and chloride ion diffusion of concrete under sustained uniaxial compression. Special Publication, 221, pp. 893-910.

[10] British Standards Institution, 2011. BS EN 197-1:2011, Cement Part 1: Composition, specifications and conformity criteria for common cements.

[11] British Standards Institution, 1992. BS 6699:1992 Specification for ground granulated blastfurnace slag for use with Portland cement.

[12] British Standards Institution. 2005. BS EN 450-2:2005 Fly ash for concrete. Part 2: Conformity evaluation.

[13] British Standards Institution, 1989. BS 1881-125:1986, Testing concrete — Part 125: Methods for mixing and sampling fresh concrete in the laboratory.

[14] British Standards Institution, 2003. BS EN 12390-2:2000, Testing hardened concrete — Part 2: Making and curing specimens for strength tests.

[15] Nordtest, 1995. NT BUILD 443 Approved 1995-11 Concrete hardened: accelerated chloride penetration.

[16] Andrade, C. and Castellote, M., 2002. Recommendation of RILEM TC 178-TMC: Testing and modelling chloride penetration in concrete: Analysis of total chloride content in concrete. *Materials and Structures*, 35(9), pp. 583-585.

[17] Mehta, P.K. and Monteiro, P.J.M. 2006. p 659. Concrete: microstructure, properties, and materials. McGraw-Hill, New York, 3rd edition.

[18] Yuan, Q., Shi, C., De Schutter, G. 2009, Audenaert, K., Deng, D., Chloride binding of cement-based materials subjected to external chloride environment - a review, *Construction and Building Materials*, vol. 23, no. 1, pp. 1-13.

Effects of Turbidity and Lighting on an Image Processing based Crack Detection Technique

Michael O'Byrne [1], Bidisha Ghosh[2], Vikram Pakrashi [3], Franck Schoefs[4]
[1,2] Trinity College Dublin, Department of Civil, Structural and Environmental Engineering, Dublin 1, Ireland
[3] University College Cork, Dynamical Systems and Risk Laboratory, Civil and Environmental Engineering, College Road, Cork, Ireland
[4] LUNAM Université, Université de Nantes-Ecole Centrale de Nantes, CNRS, GeM UMR 6183, IUML FR 3473, Institute for Research in Civil and Mechanical Engineering, 2, rue de la Houssinière BP 92208 44322 Nantes Cedex 3, France.
email: obyrnemj@tcd.ie, bghosh@tcd.ie, v.pakrashi@ucc.ie, franck.schoefs@univ-nantes.fr

ABSTRACT: The presence of cracks in a structure can be unsightly, may cause a loss in serviceability, or can lead to structural failure in more serious cases. Visible cracks provide an indication of the structural degradation and are an important factor when diagnosing the condition of a concrete structure. However, the identification and quantification of cracks is often a tedious, subjective and error prone task for visual inspectors. This paper presents an image processing approach to efficiently and objectively detect cracks. The approach employs a percolation based method which is applied to locations in the image where there is a large gradient, suggestive of edges or surface irregularities such as cracks. A new classification criterion is introduced which considers the pixel intensity values on either side of a crack. Detected regions that match the expected shape of a crack yet have disparate sides are rejected based on the assumption that they represent non-harmful edge boundaries.
The proposed technique is applied to images of a crack in an underwater setting. The performance of the technique is examined for varying conditions of turbidity and lighting. There were three set levels (low, medium, high) for each parameter. The influence and relative importance of these two environmental conditions which affect the crack detection process have been investigated, and the conditions that were conducive to good detection were isolated and ranked using the α-δ method as part of the Receiver Operating Characteristic (ROC) analysis. The technique is also extended to conventional, above water, images of cracks suffering from a variety of challenges that may be encountered during an inspection.

KEY WORDS: Crack Detection; Image Processing; Underwater; NDT; Lighting; Turbidity.

1 INTRODUCTION

A wide range of civil structures such as bridges, pavements, pipes, columns, etc. are affected by cracks. The detection of cracks is a costly yet crucial task for establishing a safe infrastructure network. Traditional monitoring methods often rely on regular visual inspections which require inspectors to travel to the location of a structure in order to determine its current state. As part of the inspection, observed cracks are often mapped, counted, quantitatively measured and photographed. Even with great diligence, measuring the true extent of cracks remains a difficult task for inspectors as their assessment is often subjective in nature and prone to error.

Adopting an image processing based approach to automatically count and quantify the length and width of cracks can enhance inspections, and in turn, lead to significant monetary savings or more frequent inspection cycles. Image processing methods use inexpensive and readily available equipment (i.e. a standard digital camera), and they do not require the inspector to undertake extensive training. Furthermore, advances in camera technology mean that rich detailed imagery of damaged components can be acquired. Additionally, visual inspections almost always capture photographs to include in the inspection report to corroborate the inspector's comments; however, these photographs are rarely exploited to their fullest potential in either a qualitative or a quantitative fashion. The primary limitations of image processing methods are the lack of penetration below the surface of the material and the requirement of good visibility and lighting conditions. Physical properties of the identified cracks, such as the length and width, may be extracted with knowledge of a real world scale. Possible ways of determining the scale factor include practical approaches such as placing an object of known dimensions alongside the crack or by using a stereo system to obtain 3D information. A calibrated stereo-rig which consists of two cameras viewing the scene from two slightly different vantage points is capable of providing a fully scaled metric scene reconstruction at the expense of greater algorithmic complexity and the requirement of an additional camera. Placing an object of known dimensions in the scene and reading the corresponding pixel dimensions in the acquired imagery is a straightforward solution, yet it may not suffice if the images are affected by linear perspective whereby far away objects appear smaller than objects that are closer to the camera. This issue limits the usefulness of known objects to only a local area in the vicinity of the known object, beyond which the scale loses meaning. This problem can be countered by having two or more known objects in the scene which provides scale factors at various points in the image. Interpolating between these points provides an improved estimate of the scale factor throughout the image that takes into account the effects of linear perspective. The quantitative nature of the data obtained from image analysis is important and naturally lends itself to numerous applications.

Given the pervasive nature of cracks and shortcomings of visual inspections, attempts to automate the crack detection

process have received a lot of attention. This has lead to the development of wide range of techniques such as wavelets [1], neural network approaches [2], statistical filters [3], and percolation based methods [4]. Zou *et al*. [5] have addressed the issue of challenging scene conditions by creating a robust three step algorithm involving shadow removal, tensor voting to create a crack probability map, followed by graph modelling. Wang and Huang [6] conducted a comparison of crack detection methods and identified percolation-based methods as being particularly suited to detecting ambiguous cracks. However, they also recognised that conventional percolation based methods are computationally expensive given that they operate on a local basis at each pixel location in the image. The percolation based method proposed in this paper addresses this issue by firstly applying the Sobel operator [7]. The Sobel operator gives an approximation of the image gradient. Sharp gradients usually correspond to object boundaries or surface irregularities, such as cracks. Thus, confining the percolation process to places with a large gradient magnitude leads to a concise search space which in turn leads to considerable computational savings.

While image based crack detection techniques are beneficial in terms of efficiency and convenience, knowledge of their performance levels for a host of operating conditions is crucial. This paper primarily considers underwater inspections of concrete structures, which often experience the lowest visibility due to poor light and/or turbidity. The effect of turbidity and lighting conditions has previously been investigated by [8] for detecting area based damages such as corroded regions. However, the extraction of cracks which are characterised by their fine, almost one dimensional structure follows a different methodology than that of area based damages and therefore requires separate consideration. The study has also been extended to consider above surface cracks in scenes suffering from a variety of challenges, such as bright spots, difficult viewing angles, road markings/ tyre marks, and low-contrast monochromatic scenes, all of which may mislead the crack detection algorithm. Receiver Operating Characteristic (ROC) analysis was used to assess the performance of the technique in the presence of such variability.

The methodology of proposed technique is discussed in the following section. Section 3 presents the images analyzed in this paper. Section 4 evaluates the performance of the proposed crack detection technique for the different operating conditions. Section 5 concludes the paper.

2 METHODOLOGY

2.1 Percolation based Crack Detection

Cracks are generally characterised by their narrow shape and their lower brightness in comparison to the surroundings. Percolation based methods take both of these characteristics into account.

The term 'percolation' refers to the natural phenomenon of fluids permeating through a porous material. This ideology is adapted for the purpose of crack detection, whereby the central pixel in a local window acts as the source of the fluid. The fluid gradually spreads outwards, favouring darker pixels which represent paths of less resistance, until it reaches the boundary of the window. At this point, the diffusion pattern of the fluid is analyzed. Cases where a narrow or linear path has been traced out are indicative of cracks, while irregular or radial diffusion patterns typically correspond to the non-cracked background.

The methodology of the proposed percolation based technique is illustrated in Figure 1.

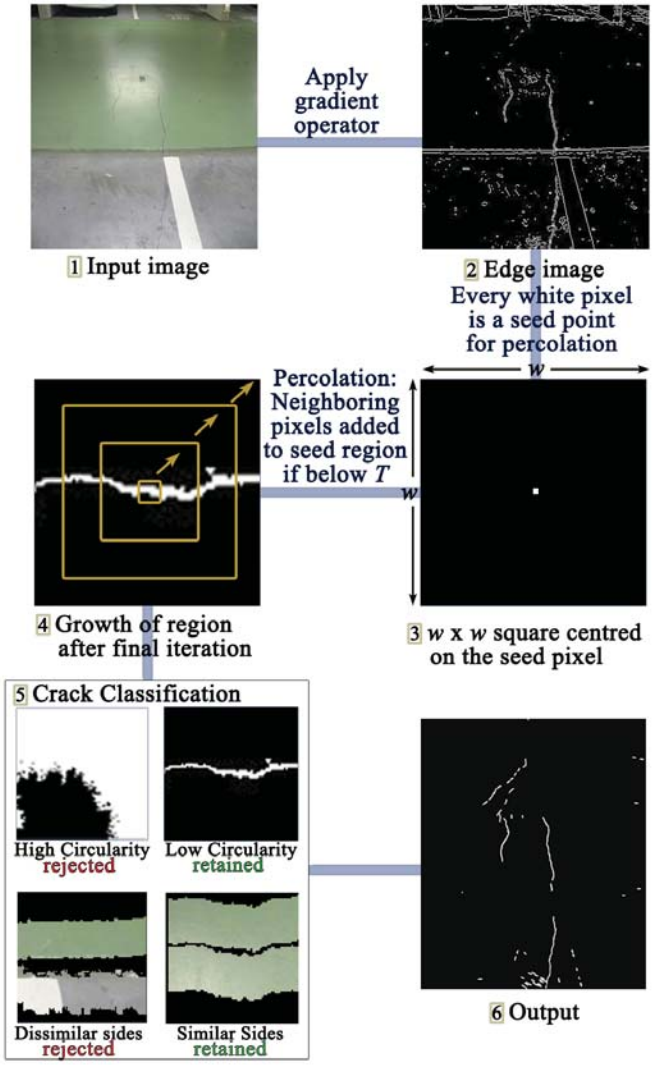


Figure 1. Methodology flowchart.

The proposed method is described as follows with reference to Figure 1:

Step 1: The input is a colour or greyscale image, *A*. The Sobel operator is applied to this image which gives an approximation of the image gradient. The output from this operation is a binary image, where white pixels represent locations that have a large gradient. In the case of colour images, the average gradient magnitude from the three colour channels is used.

Step 2: This binary image identifies points in the image where performing percolation would be relevant whilst overlooking points in the image where cracks are unlikely to be present. This cuts down on the computation time considerably. It is not essential that the entire crack is detected with the Sobel operator. Partial detection should be sufficient as the window will likely overlap with non-detected portions

of the crack. The detected pixels from this step are considered for percolation.

Step 3: A window of size w by w is centred on each detected pixel from the binary edge image. The pixel at the centre of the window, p_c, is the seed point of the percolated region, R_p. It has an intensity value of $A(p_c)$. Neighbouring pixels are added to the percolated region if they are equal to, or below, the Threshold, T, which is defined as:

$$T = \max(\text{mean}(R_p), \min(R_n)) \tag{1}$$

where R_n denotes pixels neighbouring the percolated region R_p. Essentially, T assumes the maximum value between either the mean intensity value of pixels already in the percolated region, or the minimum intensity value of the pixels neighbouring the percolated region. This ensures that there will always be at least one pixel added to the region following each iteration. Taking the mean intensity of the pixels in the percolated region is a meaningful action as it reduces the effect of outliers which could set the threshold to be unreasonably high, and it also allows the seed points obtained from the Sobel operator stage to be only loosely located near the dark crack for percolation to succeed. If the seed point is located just outside the crack, the percolated region should gravitate towards the interior of the crack and continue to proceed along the crack line.

Step 4: The process outlined in step 3 is repeated until the percolated region, R_p, reaches the boundary of the window. Percolation ceases and the resulting percolated shape is fed into the classification stage.

Step 5: The first stage of the classification phase involves evaluating the shape of the percolated region. This is done by calculating the circularity parameter C. The circularity is defined as:

$$C = \frac{4.P_{count}}{(\pi.P_{width}{}^2)} \tag{2}$$

where P_{count} is the total number of pixels in the percolated region and P_{width} is the maximum width of the percolated region. C can take values in the range 0 to 1. A value close to 1 corresponds to a circular shape, while a value close to 0 corresponds to a line segment that could represent a crack. With this in mind, percolated regions having a circularity lower than an arbitrary threshold are retained.

The second part of the classification phase involves checking the pixel intensity values on either side of the percolated region in order to discount cases where the perceived crack has an increased likelihood of being a false alarm, perhaps arising from some innocuous line boundary in the scene. This is achieved by dilating the percolated region in a perpendicular direction on both sides by a distance, d, and comparing the mean of the intensity values from the original image, A, on both sides, S_1 and S_2 respectively. A value of 20 pixels was taken as d throughout this paper. If the difference between the mean of the pixel values from both side, denoted as k, is greater than a preselected threshold than the percolated region is rejected. k is expressed as:

$$k = \left| \frac{1}{n_{S_1}} \sum A(u) - \frac{1}{n_{S_2}} \sum A(v) \right| \qquad u \in S_1,\ v \in S_2 \tag{3}$$

where n_{S_1} is the total number of pixels on one side of the crack while n_{S_2} is the number of pixel on the other side.

step 6: Retained percolated regions from the classification stage are added to the binary output image.

2.2 Error Analysis

The performance of the proposed crack detection technique is evaluated through the use of performance points in the ROC space. The ROC space allows for a convenient means of characterizing and comparing the performance of NDT methods in various conditions [9] and has been recently expanded to image detection [10]. For any NDT, the Detection Rate, *DR*, along with the accompanying Misclassification Rate, *MCR*, or alternatively known as Probability of Detection (PoD) and Probability of False Alarm (PFA) in the field of probability space and decision theory, are determined by comparing the detected cracks with a visually segmented image. The visually segmented image is created by a human operator who must manually identify the cracks in an image. This visually segmented image acts as the control as it is assumed it shows the true extent of cracking. The visually segmented image only needs to be created when it is wished to gauge the performance levels of the technique under scrutiny. The *DR* and *MCR* are represented as a percentage between 0% and 100%. Each (*MCR*,*DR*) pair formed a coordinate in the ROC space. The *DR* and *MCR* are defined as:

$$DR \approx \frac{Card(E)}{n_c} \text{ with } E = \left\{ g \in \Im ; \gamma_g = 1 \right\} \tag{4}$$

$$MCR \approx \frac{Card(F)}{n} \text{ with } F = \left\{ g \in \Im ; \gamma_g = -1 \right\} \tag{5}$$

where Card(.) indicates the cardinal of a particular set, $\Im = \{1, \ldots, n\}$, n is the total number of pixels in the image, n_c denotes the number of cracked pixels and γ_g is an instance label vector, where $\gamma_g = 1$ corresponds to correctly identified cracked pixels, i.e. true positives, and $\gamma_g = -1$ corresponds to incorrectly detected pixels and undetected damaged pixels, i.e. false negatives and false positives. F gathers situations of incorrectly detected pixels and undetected damaged pixels while E gathers the correctly detected ones.

3 DATA ANALYSIS

3.1 Underwater Crack Detection

The proposed crack detection technique is demonstrated on a cracked concrete specimen in an underwater setting (Figure 2) for varying controlled levels of turbidity and lighting. The quality of these photographs is assumed to be chiefly affected by luminosity, sharpness (focus accuracy), contrast and noise. These quality factors are directly related to the on-site operating conditions, of which lighting and turbidity are the

most influential. Turbidity is defined as the cloudiness in a liquid caused by the presence of suspended solids. These suspended solids scatter and absorb light and therefore reduce visibility. The level of turbidity may be exacerbated by interference during the inspection process, such as from a mechanical source like a boat or human contact with the river bed, which may aggravate and disturb sediment. Lighting also plays a pivotal role for achieving good visibility. Ambient light may be sufficient for near-surface inspections, however, it is unlikely to be sufficient at greater depths at which point artificial light sources become necessary. These artificial light sources may introduce luminous complexities such as 'bright-spots', whereby areas of high light intensity may be focused at a spot which may fool the crack detection algorithm. In this paper, three levels for turbidity were chosen (0 NTU (clear water), 6 NTU, and 12 NTU) and three lighting levels were used (100 Lux, 1000 Lux, 10000 Lux).

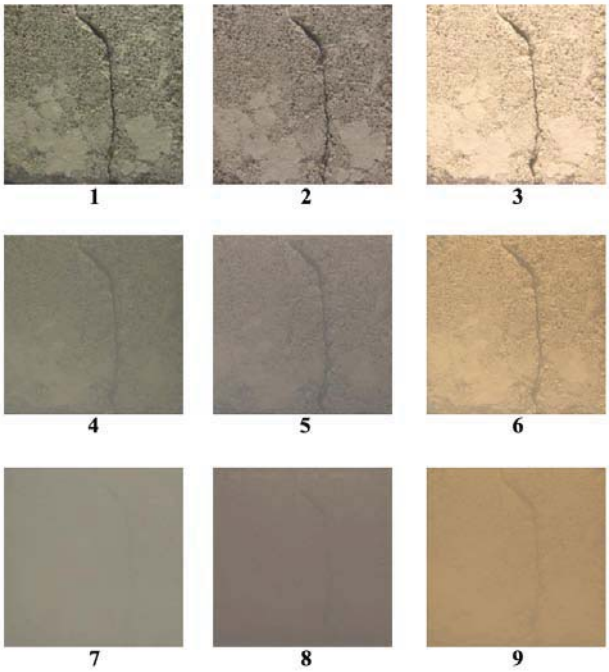


Figure 2. Cracked concrete specimen under vary lighing and turbidity conditions. **Columns**: Low, Medium, High Light. **Rows**: Low, Medium, High Turbidity.

3.2 Above-Water Crack Detection

Although underwater scenes generally provide some of the poorest visibility levels, interpreting images from above-water scenes can also be severely affected by some adverse conditions. It is thus important that the influence of some of the more common challenges for crack detection should be investigated. Figure 3 shows three image of cracks, each presenting one or more challenges, namely, (1) Road markings, (2) illumination complexities (i.e. bright-spots), (3) monochromatic scene with vague cracks.

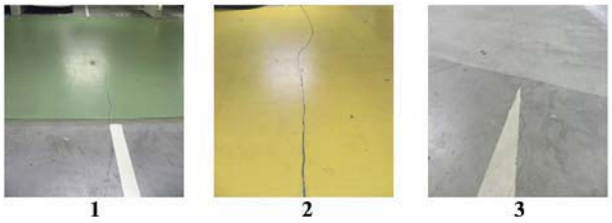


Figure 3. Cracks in a conventional above-water setting.

4 RESULTS

This section presents and discusses the results obtained following application of the crack detection technique on the underwater and above water images. The results for the underwater concrete specimen for changing lighting and turbidity levels is shown in Figure 4.

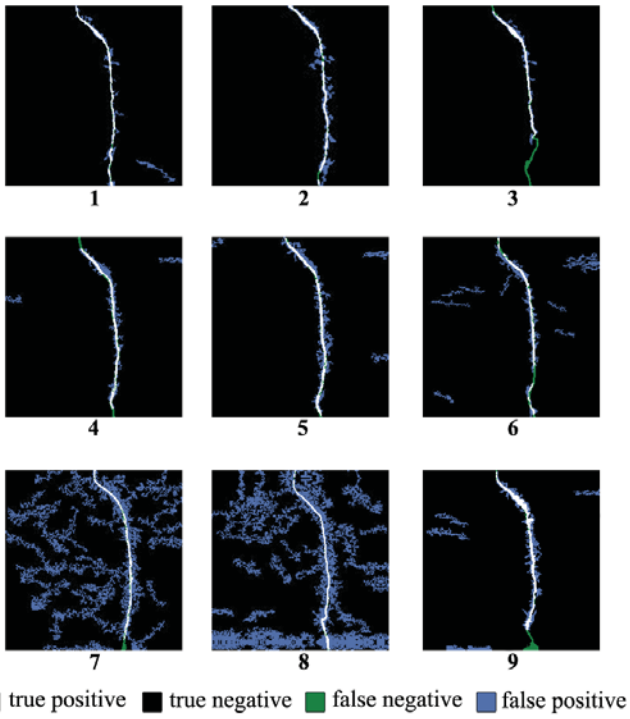


Figure 4. Detected cracks corresponding to the images in Figure2.

The results in the case of the above-water images are shown in Figure 5.

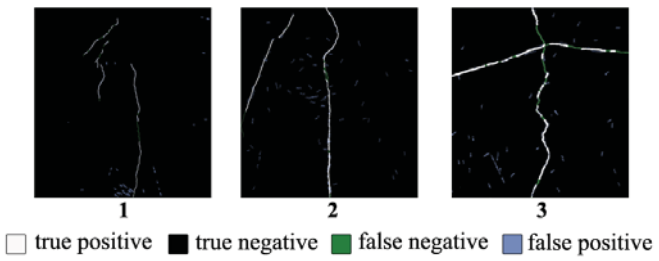


Figure 5. Detected cracks for the above-water images in Figure 3.

The performance of the crack detection technique applied to both the underwater and above-water images is quantified in

Table 1 and the associated performance points are plotted in the ROC space in Figure 6.

Table 1. Performance of the crack detection technique.

Image	Condition	(DR)	(MCR)	δ
Underwater cracks				
1	Low Light, Low Turbidity	89.8%	1.7%	0.10
2	Medium Light, Low Turbidity	87.4%	2.5%	0.13
3	High Light, Low Turbidity	62.6%	1.5%	0.37
4	Low Light, Medium Turbidity	76.3%	2.5%	0.24
5	Medium Light, Medium Turbidity	86.6%	3.7%	0.14
6	High Light, Medium Turbidity	68.6%	4.2%	0.32
7	Low Light, High Turbidity	80.0%	21.3%	0.29
8	Medium Light, High Turbidity	94.0%	26.8%	0.27
9	High Light, High Turbidity	78.1%	4.2%	0.22
Above-water cracks				
1	Road markings	73.0%	0.4%	0.27
2	Illumination complexities	69.2%	0.9%	0.31
3	Monochromatic scene	78.1%	0.6%	0.22

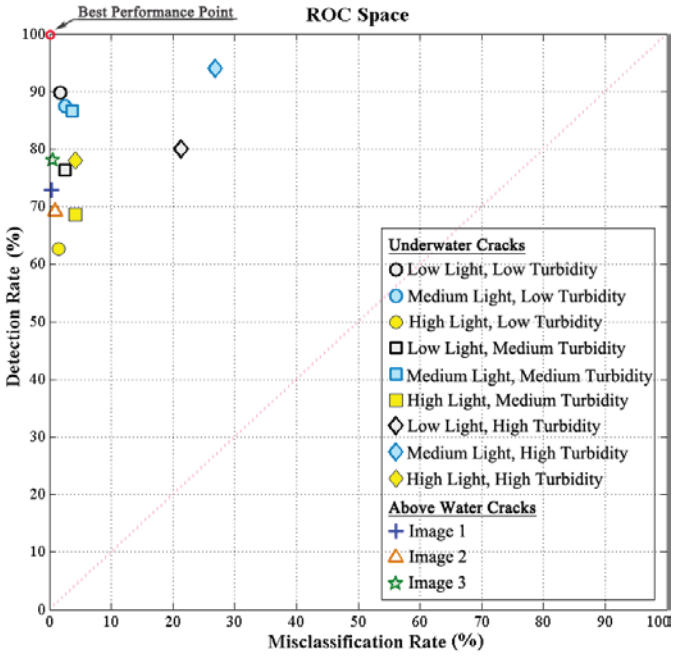


Figure 6. Evaluation of crack detection technique through the use of performance points in the ROC space.

4.1 Underwater Crack Detection

It may be observed from the detected regions in Figure 4 that the ability of the detection technique is strongly related to the degree of clarity in the original images (Figure 2). Unsurprisingly, images that feature poor visibility conditions produced poor performance levels, while on the other hand, images featuring clear and sufficiently lit scenes produced quite good detection results.

At the same time however, the results suggest that an overly bright light source can be harmful to the detection accuracy. The nature of underwater lighting means that an overly bright light source will induce a bright-spot at the centre of the light beam which will gradually fall-off, resulting in a non-uniform scene. It is this non-uniformity in lighting which the camera cannot effectively compensate for. An example of this can be seen in Figure 4(3) where the strong lighting creates a bright area on the surface of the specimen. This washes out some of the detail, thereby preventing a portion of the crack from being detected.

A clear trend that emerges from analysis of Table 1 is that the misclassification rate increases with increasing turbidity. However, the relationship does not appear to be linear. Instead, there is a gradual increase in *MCR* values from the low to the medium turbidity levels, while there is a pronounced increase between the medium and high turbidity levels. This suggests that as the turbidity approaches the operating limits there is a rapid deterioration in performance. This is especially evident for the high turbidity images in Figure 7 (7 and 8) where there is a high degree of false positives contributing to high *MCR* values in comparison to the lower turbidity levels.

An exception to the decline in performance associated with increasing turbidity and excessive lighting is in Figure 4(9). In this case, the high turbidity partially mitigates the high lighting through absorption and diffusion which limits the formation of a bright spot.

Overall, the best results are obtained for the low and medium light levels at the lowest turbidity, and the medium lighting level at the medium turbidity level (Figure 4, images 1, 2, and 5).

4.2 Above-Water Crack Detection

Analysis of the results in Table 1 and the corresponding performance points in the ROC space (Figure 6) reveal that each image performs quite consistently in spite of the varying challenges faced in each image. The first image (Figure 3(1)) demonstrates the usefulness of employing the classification criteria which rejects 'cracks' having dissimilar sides. It may be observed from the image of the detected cracks (Figure 5(1)) that there are very few false positives, even though the boundary between some road markings bears a resemblance to a crack (fine structured and darker than the surroundings).

The bright spot in Figure 3(2) has a deleterious effect on the detection accuracy as the crack remains partially undetected coinciding with this spot. This suggests that attempts to minimize the glare through careful choice of camera viewing angle/position during the on-site image acquisition stage would be worthwhile.

The cracks in Figure 3(3) appear quite vague at certain places. There are also numerous instances of staining on the floor which may mislead the crack detection algorithm. As such, it may be expected that the *DR* would suffer and there would be a high *MCR*, however the *DR* remains reasonably high and the *MCR* remains low. This may be attributed to percolation based methods which have been recognised as being well suited for detecting ambiguous cracks [6].

These results demonstrate the applicability of the crack detection technique to a wide range of scenarios.

5 CONCLUSION

A percolation based method for detecting cracks is proposed in this paper and applied to series of images under a host of varying conditions. The proposed method offers greater

efficiency than other percolation based methods, whilst still achieving good results, as the search space for cracks is confined to places where there is a sharp image intensity gradient as found by the Sobel operator. Furthermore, a new set of criteria is developed for the percolation stage and for the subsequent classification of the percolated regions.

Understanding how the operating conditions affect the performance of an image based crack detection technique is of great practical importance. This paper examines the effect of two parameters; turbidity and lighting, for an image processing based NDT tool for underwater structural health monitoring purposes. These parameters affect the underwater visibility which is crucial for an image based NDT to succeed. The influence and relative importance of these two environmental conditions have been investigated, and the NDT's sensitivity has been assessed through the use of performance points in the ROC space.

Although environmental conditions such as turbidity are generally uncontrollable in practice, lighting can be easily adjusted. Even in conventional above-water settings, consideration should be given to the lighting conditions in order to avoid bright spots. It is readily attainable to have appropriate lighting conditions which are conducive to structural health monitoring and damage detection. The results from this study may facilitate an inspector when deciding on the appropriateness and implementation of an image processing based crack detection technique, under a given set of environmental circumstances.

The α-δ method was used to measure performance. The performance levels obtained by the percolation based method shows that it remains effective even in less than optimal conditions.

ACKNOWLEDGMENTS

This work is funded by the Irish Research Council for Science, Engineering and Technology (IRCSET) and CAPACITES/IXEAD society under the Enterprise Partnership Scheme (EPS).

REFERENCES

[1] Khanfar, A., Abu-Khousa, M., and Qaddoumi, N. (2003), 'Microwave near-field non-destructive detection and characterization of disbonds in concrete structures using fuzzy logic techniques', *Composite Structures*, 62(3-4), 335-339.

[2] Choudhary, G., and Dey, S. (2012), 'Crack Detection in Concrete Surfaces using Image Processing, Fuzzy Logic, and Neural Networks', *2012 IEEE fifth International Conference on Advanced Computational Intelligence (ICACI)*, Nanjing, Jiangsu, China.

[3] Sinha, S.K., and Fieguth, P.W. (2006), 'Automated detection of cracks in buried concrete pipe images', *Automation in Construction*, 15(1), 58-72.

[4] Yamaguchi, T., and Hashimoto, S. (2008), 'Improved percolation-based method for crack detection in concrete surface images', *19th International Conference on Pattern Recognition*, Tampa, Florida, USA.

[5] Zou, Q., Cao, Y., Li, Q., Mao, Q., and Wang, S. (2012), 'CrackTree: Automatic crack detection from pavement images', *Pattern Recognition Letters*, 33(3), 227-238.

[6] Wang, P., Huang, H. (2010), 'Comparison analysis on present image-based crack detection methods in concrete structures', *3rd International Congress on Image and Signal Processing (CISP*, Yantai, China.

[7] Abdou, I.E., & Pratt, W. (1979), 'Quantitative design and evaluation of enhancement/thresholding edge detectors', *Proceedings of the IEEE*, 67(5), 753-763.

[8] O'Byrne, M., Ghosh, B., Pakrashi, V. and Schoefs, F. (2013), 'Effects of turbidity and lighting on the performance of an image processing based damage detection technique', *11th International Conference on Structural Safety & Reliability*, Columbia University, New York, USA.

[9] Rouhan, A. and Schoefs, F. (2003), 'Probabilistic modeling of inspection results for offshore structures', *Structural Safety*, 25(4), 379-399.

[10] Pakrashi, V., Schoefs, F., Memet, J.B. and O'Connor, A. (2010), 'ROC dependent event isolation method for image processing based assessment of corroded harbour structures', *Structure and Infrastructure Engineering: Maintenance, Management, Life-Cycle Design and performance (NSIE)*, 6(3), 365-378.

A research-based approach to promote the adoption of novel UK-based concrete test methods in Chinese construction standards

Bryan Magee[1], Muhammed Basheer[2], Sreejith Nanukuttan[2], Ting-Yu Hao[3] and Zhi-Gang Wu[3]

[1]Built Environment Research Institute, School of the Built Environment, University of Ulster, UK
[2]School of Planning, Architecture and Civil Engineering, Queen's University Belfast, UK
[3]Research Institute of High Performance Concrete, Central Research Institute of Building and Construction, China
Email : b.magee@ulster.ac.uk

ABSTRACT: As part of a UK-China Science Bridge project – a UK government funded initiative linking leading universities and businesses in selective partnering countries – in 2009 a collaborative research programme was initiated between Queen's University Belfast and the Research Institute of High Performance Concrete (part of the Central Research Institute of Building and Construction) in Beijing.

The focus of research was concrete permeability assessment; a key factor in determining the potential long-term durability of civil engineering infrastructure. More specifically, a programme of work was designed to allow comparisons between the related test method included in the Chinese construction standards (GB/T50082-2009) and a novel non-destructive test method, the Autoclam Permeability System, developed by researchers at Queen's University allowing both laboratory- and site-based measurement of air permeability, unsaturated water permeability and water absorption.

A programme of 14 concrete mixtures was investigated to assess the influence of water-binder ratio (in the range 0.36-0.60) and binder type (considered was cement, fly ash, slag and silica fume). All mixes were prepared and tested in China using local materials and assessed for slump and compressive strength, in addition to a suite of durability-related parameters using Chinese and UK test methods. Reported in the paper are the positive correlation coefficients attained between the various test methods and on-going work to secure adoption of the Autoclam test method in China.

KEY WORDS: Concrete permeability; Durability; Non-destructive testing; Autoclam; UK-China Science Bridge.

1 INTRODUCTION

Infrastructure is predicted to be the fastest growing sector in China's $5 trillion construction industry well beyond 2014, with growth fuelled by government initiatives to expand and upgrade the country's physical infrastructure; in particular its highways, railways and subway systems [1]. Associated consumption levels of steel, cement (700 million tons of cement were manufactured and consumed in China in 2002, representing about half of global output) and coal equates to China being one of the world's largest producers of greenhouse gas. In 2007, for example, CO_2 emissions in China were reported to be 1.8 billion tonnes, an increase of 105% from 1996 [2].

To combat this, sustainable development is an official government policy in China, with related investment and implementation far outstripping anything seen in Europe. Indeed, the Chinese 11th Five-Year Plan considers innovation and sustainability in the built environment to be crucial for achieving universal sustainable development [3]. Due to factors including material quality, worker competency and a focus on high-speed construction, however, premature deterioration of reinforced concrete structures in China is commonplace. A specific example includes the freeway concrete pavement between Shenzhen and Shantou in south China, which experienced considerable levels of cracking and deterioration after only 6-12 months service [4].

With direct links between attaining concrete durability and sustainable development well known [4], and with the built environment representing approximately 50% of China's national wealth, premature concrete durability problems are recognised has having serious economic consequences.

As such, the focus of the current research programme was to develop appropriate methodologies for assessing and ensuring adequate levels of concrete durability for Chinese infrastructure. More specifically, particular attention was placed on in situ concrete permeability; a property well known to represent cover concrete quality and durability performance more generally [5].

2 RESEARCH CONTEXT

2.1 UK-China Science Bridge initiative

In 2006, the UK government introduced financial support for UK institutions with existing research links to world-class universities and high-tech businesses in selective partnering countries. The remit of funded collaborations, or Science Bridges, has been to accelerate deployment of research knowledge, deepen and strengthen current research links, undertake proof-of-concept studies, enable acquisition of new skills, and encourage wealth creation by improving the transfer of research and expertise from the research base to businesses and other users.

With an initial focus on partnerships between the UK and US, the most recent round of Science Bridge awards extended to include the emerging super-economies of China and India. In 2008, three awards apiece were funded with the US and India and four with China. With 42 applications, compared to 26 and 20 for the US and India respectively, competition for UK–

China Science Bridge awards was intense. Selected in collaboration with the Chinese Ministry of Science and Technology, the four winning UK-China bridges received funding totaling £4.412 million over 3 years from the Research Councils UK.

2.2 Project partners

Led by research teams from the Schools of Electronics, Electrical Engineering and Computer Science and Planning, Architecture and Civil Engineering, a team from Queen's University Belfast successfully secured one of the four UK–China Science Bridge awards. With a dual focus of developing innovative and sustainable solutions relating to energy production and the built environment, this was the sole Science Bridge project, from all 10 awarded between China, India and the US, with a construction focus.

In terms of the construction-related area of the project, a diverse range of UK- and Chinese-based academic and industry partners were involved. The work undertaken as part of the research programme reported in this paper involved Queen's University Belfast, the Central Research Institute of Building and Construction and Amphora NDT Ltd.

2.3 Construction focus of Science Bridge

The primary concurrent aims of the construction-focused element of the Science Bridge project were to assist Chinese partners address infrastructure-related issues in a sustainable manner and enhance benefits for the UK/Ireland partners through uptake of established technologies, knowledge and expertise. Against this background, the scope of the project consisted of the following five principal activities:

- Activity 1: Proof-of-concept testing
- Activity 2: Technology transfer activities
- Activity 3: Training programmes
- Activity 4: Thematic workshops
- Activity 5: In depth UK–China forum delivery

With full details of the project available elsewhere in the literature [6], the focus of the current paper is work undertaken as part of activities 1 and 2 only.

3 RESEARCH AIM

Due to documented durability problems of concrete structures in China, demand exists for simple, reliable laboratory and in situ tests to assess/improve quality control. To this end, work undertaken in Science Bridge activities 1-2 focussed on demonstrating the appropriate application in China of non-destructive test methods developed at Queen's University. Test methods assessed included Autoclam [7], Permit [8] and Limpet [9], with related research undertaken predominantly in China in collaboration with the Central Research Institute of Building and Construction (CRIBC) and Tsinghua/Zhejiang Universities respectively.

The aim of the work reported in this paper was to: assess the reliability of the Autoclam test; develop relationships with existing laboratory-based tests covered by Chinese Standards; and prepare documents to support Autoclam's acceptance and standardisation in China. As such, the ultimate aim of the work was to encourage widespread workmanship, concrete quality and long term performance improvements throughout the Chinese construction sector.

4 RESEARCH BACKGROUND

Prior to the UK-China Science Bridge project in 2005, the Research Institute of High Performance Concrete (RIHPC) in Beijing (a unit of CRIBC) provisionally reviewed the Autoclam test method for the first time in China. Initial attraction to the method included its: potential suitability for both laboratory and on site use; ability to measure air and water permeability, as well as water absorption (sorptivity); ease of use by non-skilled operatives; and non-destructive nature. The method is also well-established, with more than 30 countries using it for a range of applications.

While various research studies followed [e.g.10-12], no previous work has been undertaken to establish correlations between Autoclam results and standard Chinese test methods. This research progression was deemed essential as part of the Science Bridge project for the potential introduction of the Autoclam as a standard test method in China.

5 METHODOLOGY

5.1 Materials

All materials used were sourced locally by CRIBC in Beijing. Ordinary Portland cement (PC) produced in Tangshan, Hebei, just outside Beijing and a local source of natural sand and gravel coarse aggregate was used throughout. In terms of cement additions, Beijing-sourced fly ash (FA), blast-furnace slag (GGBS) and silica fume (SF) were also used. A polycarboxylate superplasticizer produced in-house by CRIBC was used throughout to maintain concrete consistence.

5.2 Mixture proportions

A total of twelve concrete mixtures was considered as part of the research as shown in Table 1. The philosophy adopted was to assess a wide range of potential binder combination types for high-performance concrete (HPC) using two relatively low water/binder ratios (0.36 and 0.40). Binder combinations considered at these two water/binder ratios included: PC only; PC:FA; PC:GGBS; PC:SF and PC:FA:GGBS. In this way, the intention was to assess HPC mixes currently being considered for civil engineering infrastructure in China and aggressively challenge potential relationships between Chinese and Autoclam-based test methods. To provide a control reference point, a PC only control concrete with a water/binder ratio of 0.60 was also considered as part of the work.

5.3 Consistence and compressive strength testing

Concrete consistence was assessed in terms of slump and slump flow in accordance with BS EN 12350:2009 [13-14]. Compressive strength was measured using 100mm cubes in compliance with Chinese standard GB/50107-2009 [15].

5.4 Water penetration depth testing

The established Chinese method of assessing concrete permeability is the hydraulic pressure method to GB/T50082-2009 [16]. For each concrete considered, the test involved manufacturing six 150mm high truncated cone specimens with a top/bottom diameter of 175/185mm. After standard curing (20±2, 95%) for 28 or 90 days, water penetration depth

(WPD) under a constant pressure head (12bar for 24 hours) was manually measured to assess water permeability. As such, the test is similar to the water penetration test in BS-EN: 12390-8 2009, albeit this test uses a pressure of 5 bars applied over 72 hours. An indication of the testing apparatus and specimens used is provided in Figure 1.

5.5 Autoclam testing

Autoclam testing was carried out as specified in the literature [7] using standard 50mm diameter base ring apparatus. Three 230×230×100mm specimens for each concrete mixture were prepared and preconditioned by standard moist curing for 28 or 90 days followed by drying at 50°C for two weeks. After undertaking air permeability measurements initially, specimens were dried for at least one hour before water absorption and permeability testing. The average value of three measurements was selected as the final value of air permeability index (API), water absorption index (WAI) and water permeability index (WPI).

Due to potential sensitivity of air permeability readings due to surface moisture effects, a Kett moisture meter was additionally used to assess all concrete prior to testing. This instrument was accurate in the 0-12% by mass moisture content range to a precision level of ±0.5%.

6 RESULTS

6.1 Fresh and hardened properties

In terms of fresh concrete performance, relatively high levels of consistence were maintained throughout via the use of a superplasticizing admixture. By limiting slump and slump flow ranges to 170-190 and 390-450mm respectively (see Table 2), the intention was to eradicate any influence of concrete compaction on subsequent durability testing.

Compressive strength results for all mixtures at 7, 28 and 90 days are given in Figure 2. While results generally followed expected trends in terms of increasing strength with both age and reduced water/binder ratio, evident from Figure 2 is the wide variety of values resulting from the different binder combinations considered. For the 0.40 water/binder ratio concrete (mixes 2-6), for example, 28- and 90-day strengths ranged from 36-53MPa and 44-61MPa respectively. For the 0.36 water/binder ratio concrete (mixes 7-12), corresponding ranges were 34-59MPa and 45-66MPa respectively. Not considering the control concrete (mix 1), highest and lowest strengths were recorded for PC:SF (mixes 5 and 10) and PC:FA (mixes 3 and 8) respectively.

Additionally confirmed from Figure 2 is attainment of a desired wide range of concrete qualities from which to undertake subsequent concrete permeability test comparisons.

6.2 Concrete permeability/sorptivity testing

Provided in Table 3 are the results obtained from both Autoclam and water penetration depth testing, with 28- and 90-day values of WPI, WAI, API and WPD given.

While a range of values were obtained for the various concrete mixes considered, from Table 3 it can be seen that results followed expected general trends of increasing performance with both decreasing water/binder ratio and increasing age. For WPD data at 28 days, for example, a measured depth of 141mm for the PC control reduced to an average of 73 and 66mm for the 0.40 and 0.36 concretes respectively. Corresponding values at 90 days were 105, 36.8 and 22.6mm. Similarly for WPI data, a 28-day result of $11.70 \times 10^{-7} m^3.min^{-0.5}$ reduced to average values of 4.9 and 2.9 $\times 10^{-7} m^3.min^{-0.5}$ for the 0.40 and 0.36 concretes respectively. Corresponding 90-day values were 7.73, 1.8 and 1.2 $\times 10^{-7} m^3.min^{-0.5}$ respectively.

6.3 Moisture contents

Also given in Table 3 are values of concrete moisture content which were recorded prior to air permeability testing. Despite the variation of concrete mixture types and strengths at time of testing, it is clear from the data that moisture contents were fairly constant (ranging from 3.7-4.2 and 2.6-4.2% by mass at 28 and 90 days respectively) and that no obvious trends existed. As such it was provisionally concluded that the specimen pre-conditioning regime adopted had minimized any potential moisture-effects on subsequent permeability testing.

7 DISCUSSION

7.1 Permeability vs. strength relationships

As shown in Figure 3, initial data analysis focused on relationships between compressive strength and WPI and WPD results. While it is recognized that strength is not directly correlated to ultimate concrete durability, the aim was to compare the ability of the different test methods to distinguish between the various concrete types and qualities considered.

Analysis of all data points collectively (i.e. 28- and 90-day results for both the control and HPC mixes), as shown in Figure 3(a), suggested relatively strong relationships between compressive strength and both WPI and WPD (R^2 values of 0.66 and 0.72 respectively). By removing the PC control data points from the analysis and considering the low water/binder ratio HPC mixes exclusively, these relationships strengthened considerably for 28-day data with corresponding R^2 values of 0.89 and 0.80 (see Figure 3(b)). This analysis confirmed similar, strong capabilities of both the water permeability and water penetration tests to identify and rank a range of concrete in terms of their relative micro-structural quality and/or maturity.

Considering 90-day data for the HPC mixes however (see Figure 3(c)), these relationships diminished considerably, in particular for the water permeability test. Values of R^2 for the relationships between compressive strength and WPI and WPD were 0.63 and 0.00 respectively. This suggests that as HPC quality levels inherently increased with age, the ability of the test methods to accurately assess performance decreased. This was clearly particularly the case for the Autoclam-based water permeability test method, which produced very low results in the narrow range 0.97-3.35$\times 10^{-7}$ $m^3.min^{-0.5}$. This finding most likely reflects the lower operating pressure used by the water permeability test (0.5 bar) compared to the water penetration depth test (12 bar).

7.2 Water permeability vs. penetration depth relationships

With the central focus of the research being to establish potential correlations between Autoclam and Chinese test methods, the next analysis step involved comparisons of WPI and WPD data (see Figure 4).

As shown in Figure 4(a), analysis of all data points collectively (i.e. 28- and 90-day results for both the control and HPC mixes) confirmed a strong positive relation between WPI and WPD results (R^2 value = 0.81). Given the disparity of correlations between strength and WPI/WPD data at 28 and 90 days noted previously, WPI versus WPD relationships were re-analyzed for each age separately as shown in Figure 4(b). While strong correlations were maintained (R^2 values of 0.86 and 0.80 for 28 and 90-day data respectively), evident from Figure 4(b) was a disproportionate influence of the PC control concrete results, particularly for the 90-day data. To remove this effect, the data was reanalyzed considering the HPC mixes only as shown in Figure 4(c). Considered to be a truer reflection of the relationship between the two test methods, a relatively strong relationship (R^2 value of 0.75) was evident for the 28-day data set. Given the aforementioned inability of, in particular, the Autoclam-based water permeability test to assess the performance of low water/binder ratio HPC at 90 days, the relationship at this age was significantly weaker (R^2 value = 0.16).

7.3 Autoclam vs. water penetration depth relationships

While not a central focus of this study, relationships between WPD and both WAI and API were also analyzed. A summary of the R^2 values obtained is given in Table 4. Perhaps not surprisingly, given the differing natures of transport mechanisms being tested, relationships between WPD and both WAI and API were much weaker than with WPI. As such, these results were not considered further.

8 CONCLUSIONS

The overarching conclusion drawn from this research is that a relatively strong correlation (R^2 value = 0.75) exists between results obtained by water permeability (Autoclam) and penetration depth (GB/T50082-2009) testing. As such it was concluded that potential certainly exists for introducing Autoclam-based testing in China as a standard method for rapidly assessing concrete durability.

The caveat to this statement, however, is that in this research programme the same positive relationship did not exist for all data sets considered. It is recognized, for instance, that the analysis undertaken was based on a relatively small number of concrete mixes. Additionally, with the exception of the control concrete (mix 1), all mixes considered were low water-binder HPCs, meaning that the correlation relationships presented are based on a skewed set of experimental data.

A further significant impact on the conclusions drawn is the Autoclam test's recognized inability to distinguish performance differences between various HPC mixes; particular after prolonged periods of moist curing. This is perhaps not surprising given that the Autoclam test was originally developed to assess the relative performance of normal concretes.

Against this background, further research in this area is certainly required. For example, work is needed to establish relationships for a broader range of normal and high-performance concrete mixes at different test ages and possibly curing conditions. This would help to distinguish limitations of both test methods to accurately assess relative concrete performance.

Table 1. Concrete mixture proportions

Mix	W/B	Concrete constituents (kg/m^3)								Binder proportions (% by mass)
		Water	Total binder	PC	FA	GGBS	SF	Sand	Agg.	
1	0.6	225	375	375	0	0	0	720	1080	100:0
2	0.36	135	375	375	0	0	0	755	1130	100:0
3	0.36	135	375	225	150	0	0	755	1130	60:40
4	0.36	135	375	187	0	187	0	755	1130	50:50
5	0.36	135	375	355	0	0	20	755	1130	95:5
6	0.36	135	375	200	95	80	0	755	1130	55:25:20
7	0.40	185	465	465	0	0	0	750	1125	100:0
8	0.40	185	465	280	185	0	0	750	1125	60:40
9	0.40	185	465	233	232	0	0	750	1125	50:50
10	0.40	185	465	440	0	0	25	750	1125	95:5
11	0.40	185	465	245	120	100	0	750	1125	55:25:20
12	0.40	185	465	235	185	45	0	750	1125	50:40:10

Table 2. Consistence and compressive strength results

Mix	W/B	Consistence (mm)		Compressive strength (MPa)		
		Slump	Slump flow	7 day	28 day	90 day
1	0.60	180	410	20	32	37
2	0.36	175	405	45	55	64
3	0.36	185	420	24	34	46
4	0.36	170	390	40	56	65
5	0.36	175	405	52	60	66
6	0.36	180	410	35	46	55
7	0.40	175	395	37	48	57
8	0.40	185	425	22	36	44
9	0.40	190	410	32	52	59
10	0.40	185	415	40	53	62
11	0.40	185	400	25	43	51
12	0.40	175	390	20	44	51

Table 3. Permeability results at 28 (and 90) days

Mix	Moisture content, (% by mass)	Autoclam results			WPD (mm)
		API (ln(mbar)/min)	WPI	WAI	
			(x10^{-7} m^3.min$^{-0.5}$)		
1	3.8 (4.0)	0.84 (0.62)	11.70 (7.73)	3.50 (3.01)	141 (105)
2	4.2 (4.2)	0.27 (0.13)	1.79 (1.62)	2.48 (1.38)	54 (16)
3	3.9 (4.0)	0.19 (0.10)	6.32 (0.97)	2.03 (0.87)	95 (33)
4	3.8 (2.6)	0.16 (0.09)	1.29 (0.95)	1.67 (0.73)	58 (14)
5	4.1 (3.8)	0.23 (0.12)	1.37 (1.45)	2.32 (1.21)	60 (17)
6	4.0 (3.9)	0.13 (0.08)	3.82 (0.98)	1.36 (0.42)	62 (33)
7	4.1 (3.4)	0.67 (0.37)	3.49 (3.35)	3.42 (2.89)	69 (41)
8	4.0 (3.2)	0.43 (0.18)	8.17 (1.78)	3.12 (2.34)	87 (4.6)
9	3.9 (3.1)	0.39 (0.16)	3.28 (1.65)	2.90 (1.69)	69 (40)
10	3.7 (3.1)	0.54 (0.31)	3.25 (1.42)	3.21 (2.73)	63 (17)
11	4.1 (4.2)	0.33 (0.14)	5.73 (1.58)	2.55 (1.48)	81 (43)
12	4.1 (4.0)	0.37 (0.14)	5.52 (1.31)	2.79 (1.57)	67 (34)

Table 4. Correlation coefficients (R^2 values) for data sets

Test parameters:		CS	WPI	WAI	API
WPD	All concrete (All data)	0.72	0.81	0.43	0.56
	All concrete (28-day data)	0.68	0.86	0.18	0.38
	All concrete (90-day data)	0.69	0.80	0.29	0.61
	HPC concrete (All data)	0.64	0.65	0.34	0.28
	HPC concrete (28-day data)	0.80	0.75	0.03	0.01
	HPC concrete (90-day data)	0.63	0.16	0.08	0.03
WPI	All concrete (All data)	0.66	-	0.41	0.57
	All concrete (28-day data)	0.86	-	0.21	0.34
	All concrete (90-day data)	0.33	-	0.45	0.87
	HPC concrete (All data)	0.57	-	0.32	0.27
	HPC concrete (28-day data)	0.89	-	0.07	0.03
	HPC concrete (90-day data)	0.00	-	0.57	0.64

CS: Compressive strength
WPD: Water penetration depth WAI: Water absorption index
WPI: Water permeability index API: Air permeability index

(a) Specimen preparation



(b) Water penetration front on split specimens



Figure 1. Indication of hydraulic pressure method testing to GB/T50082-2009

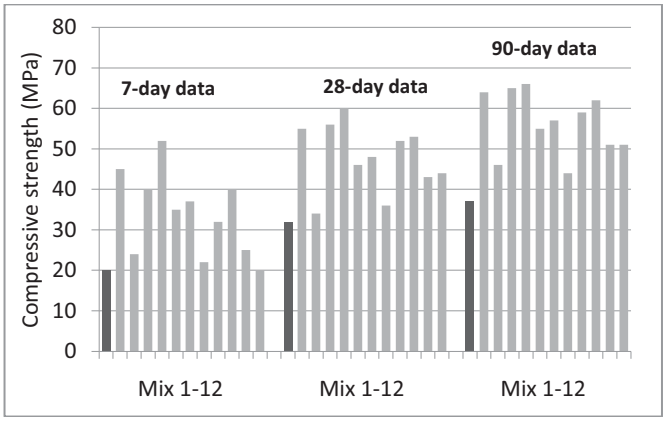


Figure 2. Compressive strength results

With respect to the Autoclam test's ability to assess HPC, it should be noted that recent concurrent research [17-19] has focused on enhancing and optimizing the sensitivity and repeatability of the test method when dealing with high quality, low water/binder materials. This involved, for example, modifying surface moisture conditions as well as applied pressures and areas of exposure during testing.

Taking this recent research and the aforementioned limitations of the reported testing programme into account in future research, the expectation is that relationships between WPI and WPD can be strengthened, thereby furthering the likelihood of Autoclam adoption in China.

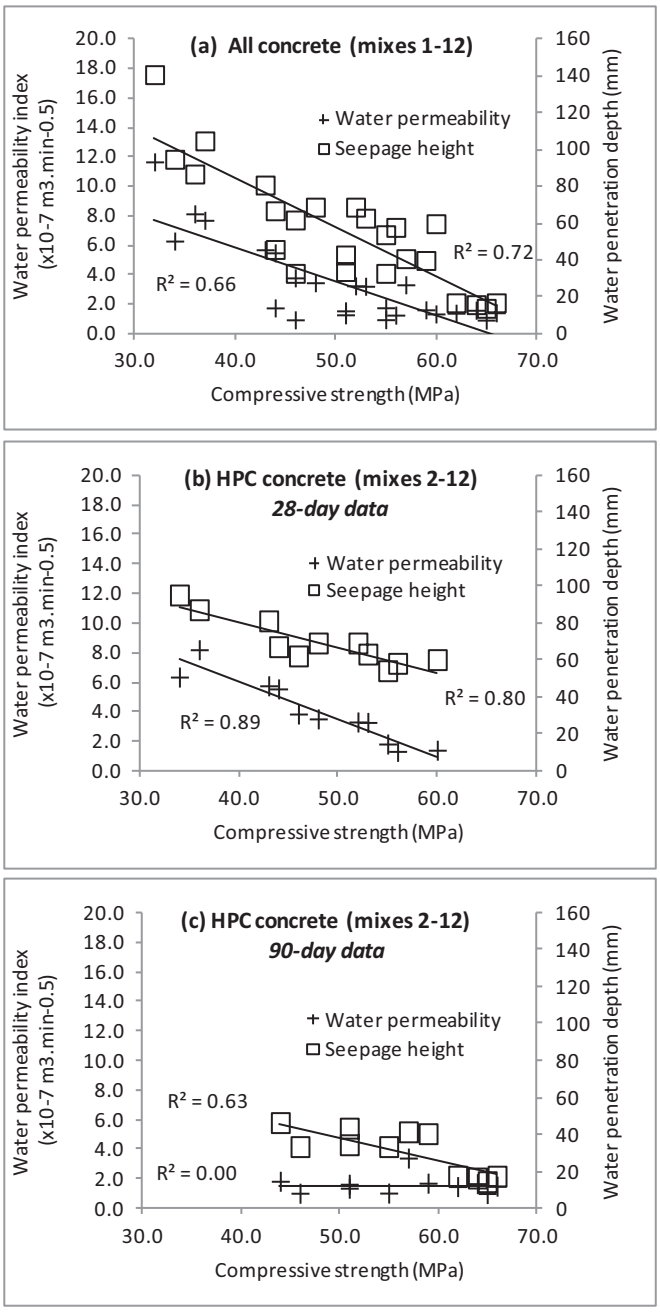


Figure 3. Permeability data versus compressive strength relationships

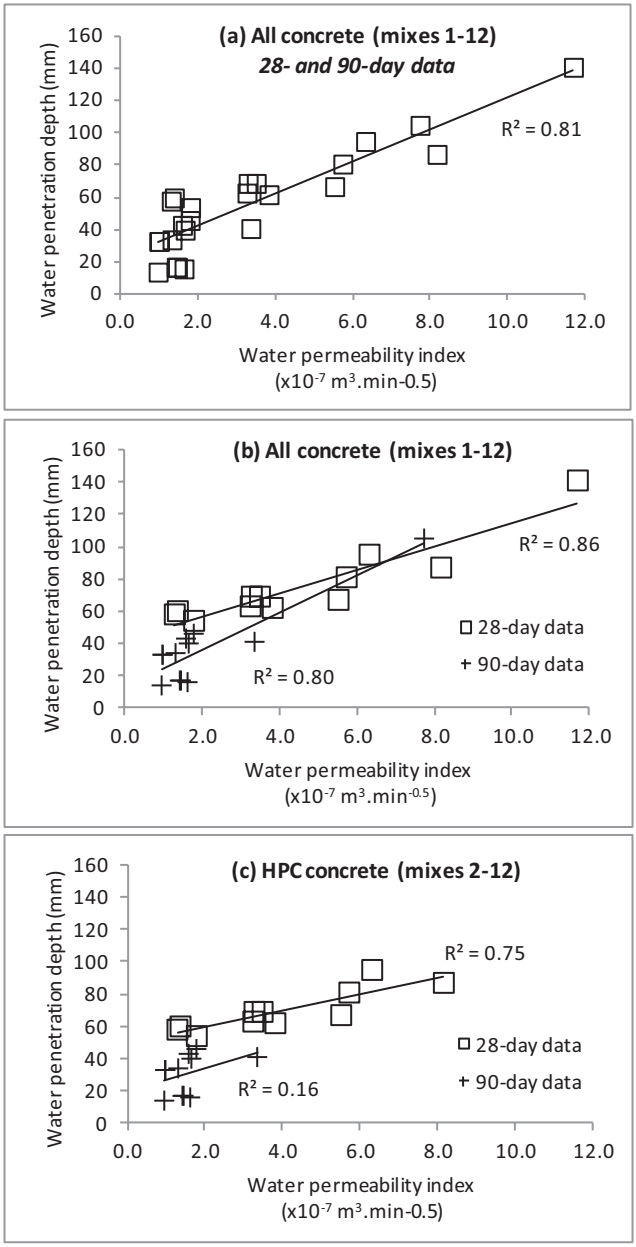


Figure 4. Water permeability versus water penetration relationships

ACKNOWLEDGMENTS

The financial support provided by both Research Councils UK (Grant EP/G04259411) and Queen's University Belfast is gratefully acknowledged.

REFERENCES

[1] Freedonia Group. Construction outlook in China, industry forecasts for 2012 and 2017, Product Code FED00019. Freedonia Group; 2008. p. 221.

[2] Malhotra VM. Sustainable issues and concrete technology. In: 11th International Conference on Recent Advances in Concrete Technology and Sustainable Development, May 9–12, Jinan, PR China, 2010.

[3] Yan Y. Facts and figures: China's main targets for 2006–2010. Official Web Portal. Chinese Government, <http://english.gov.cn/2006-03/06/content_219504.htm>. [accessed 15.10.2010].

[4] Qin W. What role could concrete technology play for sustainability in China?. In: International Workshop on Sustainable Development and Concrete Technology. Beijing; 2009. p. 35–43.

[5] Concrete Society Technical Report NO.31, Permeability testing of site concrete-a review of method and experience, 1987, pp 15-25

[6] Magee B.J., Basheer M, Bai Y, Long AE, McCarter WJ, Jin WL, Zhao YX, UK–China Science Bridge – Sustainable solutions for the built environment, Construction and Building Materials 47 (2013) 20–28.

[7] Basheer PAM, Long AE, Montgomery FR. The Autoclam – a new test for permeability Concrete. Journal of the Concrete Society 1994(July/August):27–9.

[8] Nanukuttan SV, Basheer PAM, Robinson DJ. Further developments of the Permit ion migration test for determining the chloride diffusivity of concrete. In: Forde MC, editor. Structural Faults and Repair-06, Edinburgh, June, vol. CD Rom. Engineering Technic Press; 2006. p. 14.

[9] Long AE. A review of methods of assessing the in-situ strength of concrete. Proc Intl Conf. on non-destructive testing. London, Edinburgh: Eng Technics Press; 1983. p. 56–78.

[10] Ting-Yu, Hao, Evaluating concrete permeation using Autoclam in China. In: Mark I, Russell, P.A.M. Basheer eds. Proceedings of Concrete Platform 2007, Belfast, UK, 19-20th April, 2007, 189-196

[11] Ting-Yu, Hao, Zhi-Gang, Wu. Assessment of Concrete Permeability by a Nondestructive Method. Key Engineering Materials Vols. 405-406 (2009) pp 309-314.

[12] Hao T, Wu Z, Su B. On-site permeability test of prestressed concrete containment of nuclear power stations, in proceedings of 13th International Conference of Structural Faults and Repair, Edinburgh, UK, 2010, pp. 84.

[13] BS EN 12350-2:2009, Testing fresh concrete, Part 2: Slump-test, British Standard Institute, 2009.

[14] BS EN 12350-5:2009, Testing fresh concrete, Part 5: Flow table test, British Standard Institute, 2009.

[15] GB/T 50107-2010, Standard for Evaluation of Concrete Compressive Strength Ministry of Housing and Urban-Rural Development, 2010.

[16] GB/T 50082-2009, Standard for test methods of long-term performance and durability of ordinary concrete, Ministry of Housing and Urban-Rural Development, 2009.

[17] K Yang, PAM Basheer, Y Bai, B Magee and AE Long, Development of a new insitu test method to measure the air permeability of high performance concretes, NDT&E International, 64, 2014, p. 306-314.

[18] K Yang, M Basheer B Magee and Bai Y, Investigation of moisture condition and Autoclam sensitivity on air permeability measurements for both normal concrete and high performance concrete, Construction and Building Materials 48 (2013) 306–314.

[19] K Yang, PAM Basheer, Y Bai, B Magee and AE Long, Assessment of the effectiveness of the guard ring in obtaining a uni-directional flow in an in situ water permeability test, Materials and Structures, DOI 10.1617/s11527-013-0175-5, 2013.

PD6694-1 and the Design of Gravity Retaining Walls

B. Solan[1], S.Orr[1], L.J. Whitworth[2] & P. McMenamin[3]
[1]School of the Built Environment, University of Ulster, Shore Road, Newtownabbey, Co Antrim, Northern Ireland
[2]The Annex Field View Halls Lane, Norton, Bury St Edmunds, Suffolk, England
[3]The Department of Regional Development, Roads Service, County Hall Ballymena, Co Antrim, Northern Ireland

email: b.solan@ulster.ac.uk

ABSTRACT: A wide range of Design Guidelines and Standards (CP2, BD30/87, BD37/01, BS8002) have evolved to reflect the various forms of retaining wall used in practice. Each new standard reflects changes in engineering understanding of soil structure interaction and how traffic loads are applied to the various structure types. Traditionally, traffic loadings, irrespective of the underlying design code, have been modelled using standard surcharge pressures. These surcharges are converted into horizontal thrusts by the application of a suitable coefficient of earth pressure, which reflects wall stiffness and the anticipated wall movements. The work of Shave et al. rejects the traditional surcharge model, stating that 'the uniform pressure method of BD37/01 does not realistically represent the distribution of pressures on walls due to vehicle loading'. They further suggested that the traffic 'pressures should be more concentrated towards the top of walls'. However, interestingly, many historic retaining walls still remain standing. To investigate Shave et al. rationale, this paper reviews the implications of PD6694-1 on the design of gravity retaining walls. This study compares wall thrust forces generated by the new standards for a range of wall heights with Terzaghi's simplified line load model, Culmann's wedge analysis, CP2 and the now redundant surcharge method. In addition, a parametric study was undertaken to investigate the implication of PD6694-1 on the design of walls. The variables included the strength of the backfill, the height of the wall and the offset distance 'a' between the 'lines of action' of the strip load and the retained face. A review of PD6694-1 suggests that there are anomalies regarding the application of the new traffic models, which is significant for wall design. This new method does not consider the use of wall friction and the use of the analogous virtual face when assessing the thrust intensity on walling elements.

KEY WORDS: Retaining Wall, Earth Pressure, Traffic Loading, Surcharge Model, PD6694-1 (PD), & Normal Vehicle Model.

1 INTRODUCTION & BACKGROUND TO PD6694-1

The need to retain material to create a level platform for agriculture or protective purposes has been common practice for centuries. Thus, from a societal perspective retaining structures irrespective of their construction forms (*gravity, embedded etc*.) are an integral part of work that historically military engineers, and in more recent time civil engineers, design and construct. One of the key problems that has hindered development is the assessment of the earth pressure that exists within the retained mass. Unlike traditional engineering materials like steel, concrete and timber, the nature of soils (*fine and coarse grained*) and their respective behaviour (*short and long term*) adds a depth of complexity to the design process. This must be fully understood by the designer, for a safe and sustainable structure to be developed. Traditionally, the design process has been governed by plastic analysis with designers opting for either a lower bound solution or an upper bound solution. Critical to the respective methods is the approach adopted regarding the boundary between the fill and the retaining surface and the ability to develop a frictional interface. The nature of this 'wall friction' has a radical effect on the magnitude and orientation of the resultant soil thrust. Incidentally, the inclusion of the wall frictions adds significantly to the complexity of the assessment process. As a result there is almost universal adoption of the Rankine method [1], where a smooth wall with no wall friction has become the standard design. The result is an oversized wall which has typically large reserves of strength. However, such oversizing cannot continue, given the current drive for economical designs and sustainable construction. As our engineering understanding of the earth pressure associated with retaining structures has evolved, a number of design methodologies have become popular (*Rankine 1857 & Coulomb 1776*) [1]. CP2 [2] was the first UK attempt to quantify the engineering assessment of earth pressures. This standard allowed the use of both approaches for design purposes. At that stage, the design methodology was underpinned by global Factors of Safety which worked reasonably well. While the work of Akroyd [3] subsequently asserted that CP2 [2] was antiquated in its approach to wall design, it did however provide a uniform basis for design and recognised the influence of external loading (*traffic surcharges, railway loading etc*.) on both the stability and operation of walling systems.

The subsequent replacement BS8002 [4] was a radical departure from CP2 [2]. It was the first real attempt to bring a limit state philosophy to soil mechanics (Bolton [5]), where both the in service and failure limit states were addressed. Perhaps the most radical part of the new standard was the use of structural equilibrium at both limits states and the concept of a Mobilisation Factor (M) which must be applied to both undrained and drained soil properties. Like its predecessor CP2 [2], it specified loading levels for the influence of external loading on walling systems. It also retained the use of a uniform surcharge as the means of representing traffic loadings. This same ethos was adopted by BD37/01[6] (*Highway Loading*), the bridge loading standard where the normal traffic loading (*HA*) and abnormal traffic loading (*HB*)

were represented by standard surcharges. While BS8002 [4] was heralded as a breakthrough within the profession, there remained many engineers that stuck with the familiarity of CP2 [2]. This resulted in design and checking problems on projects that were adopted by public bodies. The situation was complicated by the failure of the Highways Agency to update BD30/87 [7] which advocated a strange combination of CP2 [2] and BS8002 [4] when designing retaining wall and bridge abutments. With the formal adoption of Eurocodes as the means of design in April 2010, all publically procured works must now conform to these new standards. The Highways Agency and Professional Institutions such as the Institution of Civil and Structural Engineers have prepared the UK for this 'phase shift' in our approach to design. In the majority of cases, the transition has been relatively smooth and the majority of dominant structural forms e.g. bridges & buildings are being designed to the new standards. Many publications have been made available on the new codes and much of this work has focused on problems such as earth pressure assessment for integral bridge design, whereas the design of retaining walls has largely been ignored due to its perceived simplicity. Thus the new standards have been adopted and taken 'as given' despite the radical nature of the change associated with Eurocode 7 [8] and the new traffic loading model (*Normal Vehicle BSEN 1991-2:2003 [9] & its associated National Annex [10]*). Thus the traditional surcharge model which has, been successful to date, with few recorded failures has been replaced with a vehicular loading arrangement. The work of Shave et al. [11] asserts that the '*validity of the BD37 surcharge loading is somewhat questionable'*. In many respects, this could be viewed as a valid argument, but the replacement model is cumbersome, difficult to apply, is based on a methodology designed for relatively flexible walling systems, and, leaves many questions unanswered in terms of application.

2 NORMAL VEHICLE ASSESSMENT MODEL

Clause NA2.32 of the UK National Annex (NA) to BS EN 1991-2 [10] defines the vehicular model (*See Figure 1*) which must be used for the design of wing and retaining walls. The arrow labelled '1' in the diagram shows the direction of travel. Hereafter this vehicle shall be referred to as the Normal Vehicle (NV). For bridge design reference should be made to Clause 7.6 of PD6694-1 [12] where this model is used instead of Load Model 1 (Shave et al. [11]). The total weight of the vehicle is 320kN, which equates to an equivalent surcharge of 19.61kPa before the application of associated factors. The basic arrangement is subject to an Overload Factor (OF) of 1.5. Only the NV is subject to this factor and is reflective of the inherent variability of the recorded traffic masses on the UK road networks (Atkins Highway & Transport [13]). Finally, the new code has included a Dynamic Amplification Factor (DAF) to account for the real nature of traffic loading. Rattigan et al. [14] defined the DAF as the ratio between the maximum load effect when a bridge is loaded dynamically, and the maximum load effect when the same load is applied statically to the bridge. The DAF ranges from 1.4 at ground level to 1.0 at a depth of 7.0 m below ground level.

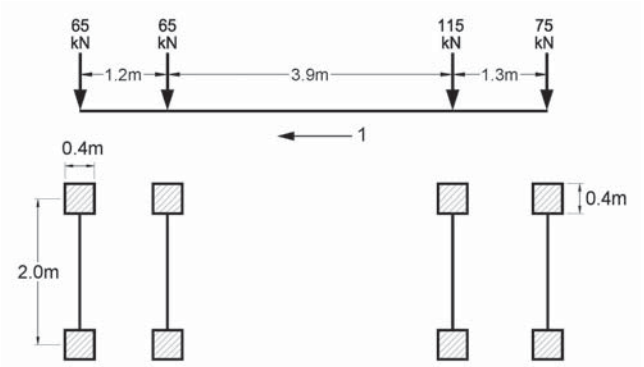


Figure 1 Vehicle model for Normal Traffic extracted from NA to BS EN 1991-2

Shave et al. [11] have noted the conservative nature of this approach compared with Canadian practice, which reduces the DAF to unity at a depth of 1.5m. The UK NA [10] permits detailed modelling to moderate the profile; however, most practitioners will use the suggested values. The NV is permitted within three notional lanes, with the axles of the vehicle in lane three being factored by a value of 0.5. The restriction of the vehicle to the notional lanes is similar to the HA and HB surcharge approach of BD37/01 [6]. For design situations, consideration shall be given to a single vehicle in each lane or a convoy of vehicles in each lane. In the convoy or 'traffic jam' case the DAF is reduced to unity and a maximum space of 3m is permitted between vehicles within the convoy. Laterally a minimum distance of 1m is permitted between vehicles. In all cases, the placing of the NV within the notional lanes longitudinally and transversely must ensure the maximum effect on the structure. However, what is somewhat surprising is that the PD gives no guidance on erring vehicles like the Accidental Wheel Load case of BD37/01 [6]. Therefore, beyond the limits of the notional lanes, only pedestrian loading (Load Model 4) and the Load Model 2 (LM2) case (*Clause 4.3.3 BSEN1991-2 [9]*) apply on the verge or footway. Presumably, the application of LM2 would be as per Clause 7.6.3 of the PD but without the use of an Overload factor.

3 PD6694-1 TRAFFIC SURCHARGE MODEL

Clause 7.6.3 of the PD outlines a suggested model for the assessment of lateral thrusts generated by NV and Special Vehicles (SV) on non-bridge abutment structures. The model is a derivative of one of the suggested methods of assessing vertical live loading e.g. line loads etc. in CIRIA C580[15]. The suggested method in the PD has been amended to allow for the suggested axle configurations in the NA to EC1 Part 2 [10], the notional lane widths and the influence of the friction angle of the material (Shave et al. [11]). Figure 2 outlines the general format of the method that is used as part of the analysis. The parameters shown in the diagram are explained in the next section. The same clause suggests that the method is applicable to other loading forms e.g. patch or wide strip loads provided the variable action can be replicated using the superposition of a series of parallel line loads. Perhaps the most interesting comment in Clause 7.6.3 of the PD is a passing mention of undefined 'short walls' subject to local

effects. Presumably a 'short wall' is a structure which is shorter than the loaded length of the NV, SV or other variable action impacting on the wall. The PD suggests two analysis methods that can be used to assess the influence of external actions on a retaining structure. Each will be addressed in turn.

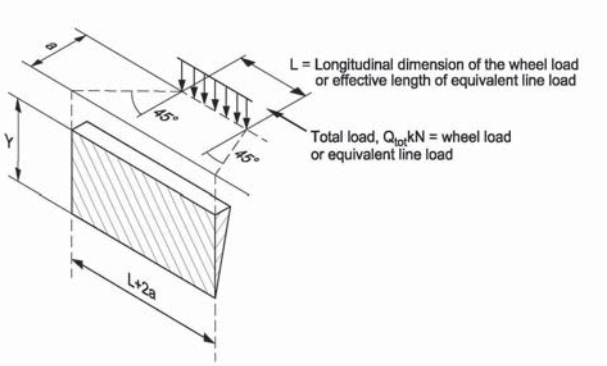


Figure 2 Basic Line Load Model extracted from PD6694-1 [12]

4.1 MODE 1 ACTIONS REMOTE FROM THE WALL

Figure 3 shows the mechanism for assessing the wall thrust for a semi-infinite strip load, where the line of application is not close to the wall. Thus for a > H tan(45 + φ'$_d$/2), where 'a' is the offset distance from the wall to the line of action of the wheel, 'H' is the height of the wall and φ'$_d$ is the design effective stress or drained friction angle (*constant volume*) of the retained material. The total thrust per m run on the wall resulting from the Mode 1 case is

$$\text{Thrust} = Q_L \tan(45 - \varphi'_d/2) \text{ kN/m} \qquad (1)$$

where (45 - φ'$_d$/2) is the standard Rankine earth pressure coefficient which assumes a wall friction (δ) = 0 (Azizi [16]). The term Q_L is the magnitude of the line load, where Q_L = Q_{tot}/(L+2a) , where Q_{tot} = weight of the vehicle and L is the length of the vehicle. Once the distance 'a' is less than a value of H tan(45 + φ'$_d$/2), then the Mode 2 method shown in Figure 4 applies.

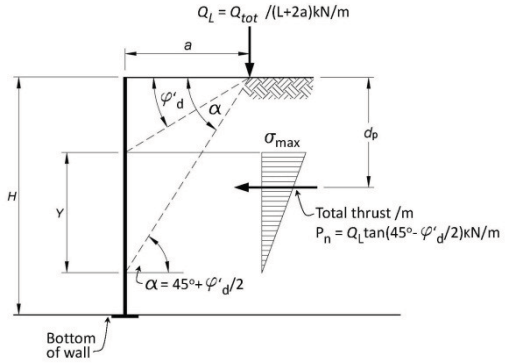


Figure 3 Mode 1 Model extracted from PD6694-1 [12]

4.2 MODE 2 ACTIONS CLOSE TO THE WALL

Figure 4 deals with the situation where a < H tan(45 + φ'$_d$/2). Shave et al. [11] suggested that the application of the Mode 1 method, in this case, was unrealistic and that the Mode 2 method was a rational alternative. In the Mode 2 case, the angle α is adjusted to match the geometry of the situation. Thus the total thrust on the wall per m run can be assessed as follows;

$$\text{Thrust} = Q_L \tan(\alpha - \varphi'_d) \text{ kN/m} \qquad (2)$$

In this instance α = tan^{1}(H/a).

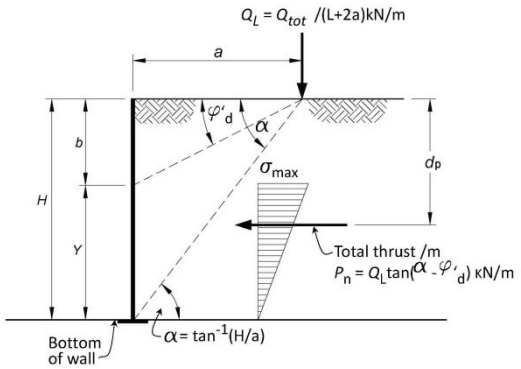


Figure 4 Mode 2 Model extracted from PD6694-1 [12]

4.3 COMPARISON OF MODES 1 & 2

Comparing the two modes of assessment confirms that the key factors for the assessment of the thrust on a structure are wall height (H), friction angle of the material (φ'$_d$) and the offset distance (a). Interestingly, the influence of wall friction is ignored despite the work of Clayton et al. [1] and O' Sullivan et al. [17] proving its veracity. Figure 5 illustrates the relationship between the two assessment modes for a range of wall heights over a typical range of backfill strengths. For the purpose of this analysis, only the overload factor was included in the vehicle loading assessment (Q_L) and a minimum footway width of 1.8m assumed. Wheel 1 is located 2.0m from the wall and wheel 2 is located 4m from the wall. At this stage, the DAF has been omitted for ease of understanding. As detailed in the PD, a comparison of the two modes is undertaken and where (α - φ'$_d$), is the smallest value, this is the governing criteria. Note α is either tan^{-1}(H/a) or (45 + φ'$_d$/2) as stated above. Figure 5 reveals a number of interesting observations. At shallow depths of wall (~ *1.5m*) the new NV model, has no impact on the wall design irrespective of the backfill strength. While most Technical Approval Authorities view walls less than 0.9m as exempt from technical approval, a normal prerequisite surcharge load of 10kPa (*BS8002 [4]*) would typically apply. Akroyd [3] did suggest this value is too high for a 'low wall'. However, the new traffic model will result in many minor walls being built which have minimal spare capacity in the event of accidental loading (*Load Model 2 EN1991 Pt 2 [9])* on the footway. In many cases, these low walls are constructed from brittle materials (*brick or block*) using rules of thumb, with minimum quality control, thus making them vulnerable in the event of unexpected loadings. What is also interesting is the influence of increasing material strength on the wall thrust and the magnitude of the loading. Poor quality backfill will result in significantly higher wall thrust irrespective of the design situation and this is before the application of partial loading

factors, associated with Eurocode 7 [8]. In general, the new NV will result in significantly higher lateral thrusts on the wall, compared with traditional UK practice. This is further developed in the next section of the paper.

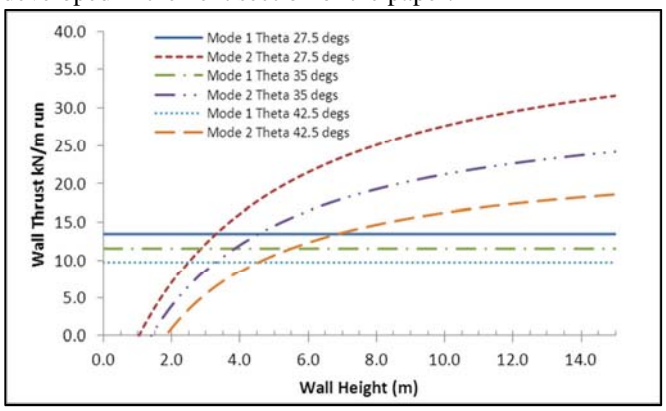


Figure 5 Comparison of Mode 1 & 2 thrust for a range of wall height

5 PARAMETER SENSITIVITY

As part of this study, it was necessary to determine how different input values for the PD method influence the lateral thrust on the wall. For this study it was decided to adopt a standard wall with a 1.8m wide footway with a carriageway width of 5m. Within the study, the primary variables were the wall height (H), the offset distance (a) and the strength of the back fill (φ'_d). In this case, both the DAF and the OF factors were applied to the analysis. The NA to BSEN1991-2 [10] is not specific in relation to the application of the DAF. Shave et al. [11] have suggested two alternative methods of applying the DAF. For the purpose of this study, an average DAF was applied to line loads associated with Modes 1 and 2; this was deemed reasonable given that the thrust on the wall is significantly above the values associated with BD37/01 [6] for the common range of walls. Based on a study of Figure 5 and the recommendation of BS8002 [4] Clause 4.3.1.2, a height range between 2 – 8m was considered typical for conventional gravity walling systems. The method of application was as per the PD [12] with 'a' being assessed from the retained face. Thus the impact of wall friction (δ) was ignored, despite its almost universal acceptance within soil mechanics (CIRIA C580 [15] & EC7 Part 1 [8]). Figure 6 shows the relationship between the two wheels of the NV and the impact the DAF has on the magnitude of the wall thrust. In this case the φ'_d chosen was 30°. The graph clearly demonstrates that the inclusion of the DAF dramatically increases the magnitude of the thrust from the NV between 1 and 7m.

The relationship between wall height and the resulting thrust for both conventional surcharges and the new Eurocode NV are shown in Figure 7. The results demonstrated that in conventional situations for walls up to 2m, the old design approach was satisfactory, irrespective of the surcharge intensity. Interestingly, improving the strength of the backfill raises the height of wall, which is not directly impacted upon by the new NV model. Therefore the traditional surcharge model was satisfactory for design purposes up to a maximum of almost 2.5m. Beyond a wall height of ~10.5m the new model stops imparting thrust to the wall, hence affording potential engineering savings. However the height is prohibitive for conventional gravity structures. This point of no loading is a function of axle configuration/location and the strength of the backfill material. Considering an average wall height of 5m, for the suggested strength ranges, this means the new traffic model thurst being on average 1.75 times higher than the 10kPa surcharge of BS8002 [4].

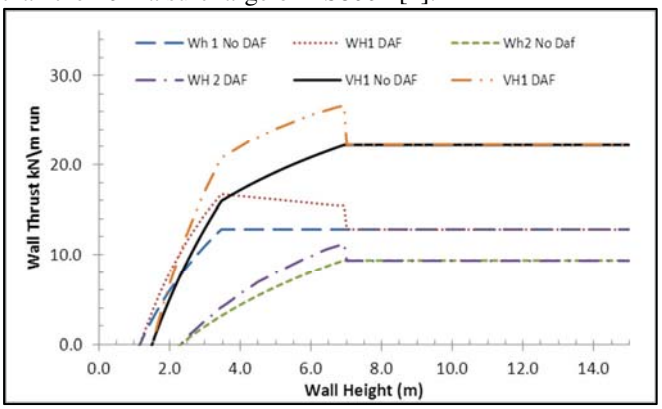


Figure 6 Relationship between wheel configuration and the wall thrust with and without the DAF.

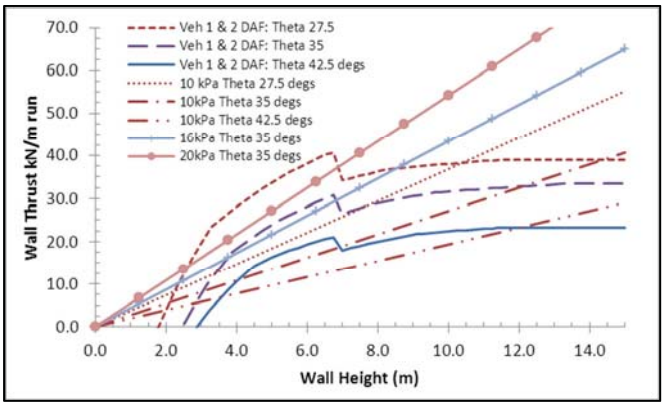


Figure 7 Relationship between wall thrust and height comparing the NV and traditional surcharge values.

If the same comparison is made for the 16 and 20kPa HB surcharges (BD37/01 [6]) then the ratio of (BS/PD) is 1.10 and 0.8775 respectively. Therefore, retaining structures supporting 'A' and 'B' class routes were potentially designed for comparable loading intensities provided the backfill strength was greater than 27.5°. However this ignores the application of the partial factor sets associated with Design Approach 1 (*DA1*) in EC7 Part 1 [8].

Figure 8 shows the relationship between the two wheels of the NV and the impact the DAF has on the magnitude of the wall thrust, with the variation of 'a', the offset value. In this example, a wall height of 4.0m was chosen and the φ'_d of the backfill material is 27.5°. For the purpose of understanding, the NV has been allowed to come within 0.2m of the edge of the structure; this equates to half the width of the contact area. As expected the new model confirms that the proximity of the axle configuration to the retained face has a significant impact on the wall thrust. As the individual wheels of the respective vehicles increase in distance from the retained face, their impacts dramatically reduces. Effectively, once the 'a' values of an individual wheel exceeds a value of H tan(φ'_d), there is

no impact on the structure. This would account for the tailing away of the Vehicle 1 curve shown in Figure 8. A point of particular interest is the impact of the wheels of the NV, if it is allowed to mount the kerb. In this case the thrust increases by a factor of 1.69 across the width of the verge.

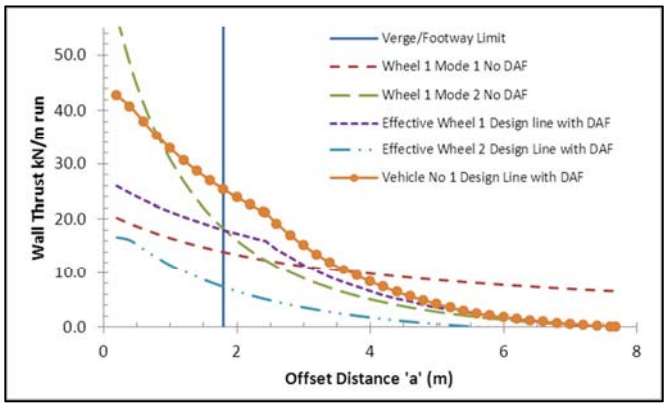


Figure 8 Comparison of Mode 1 & 2 thrust with the variation of 'a' with and without the DAF.

To further understand the influence of the offset distance 'a' on the value of the wall trusts, it was decided to vary the strength of the backfill material used in Figure 8. The same height of wall was used to facilitate the comparison. Backfill strengths of 35° and 42.5° were adopted which were deemed reflective of stone quality in Northern Ireland (Touahamia et al.) [18]. The results of the analysis are shown in Figure 9. As expected, with the improvement of the backfill strength the magnitude of the thrust on the wall reduced. At the edge of the verge/footway, there was approximately a 31% reduction in thrust between the respective friction angles. The diagram also compares the results of the new traffic model with the traditional surcharge loads associated with BS8002 [4] (10kPa) and the HB values (16 & 20kPa) used in BD37/01 [6]. To avoid congestion within the figure, the results are only shown for respective surcharges used in conjunction with a 35° friction angle. The results show the new models reducing the level of thrust on the wall when compared with the traditional UK practice with increasing values of 'a'. Whereas, if the NVs are permitted, to 'mount the kerb', then the values of thrust increases significantly. A similar magnitude of thrust would result, if a designer adopted the use of a virtual wall (Simpson [19]) at the back of a conventional stem cantilevered retaining wall. The PD traffic model does not provide guidance on the use of virtual wall and its potential effect on the magnitude of wall thrust. Interestingly in overall terms the PD [12] suggests the use of a cautious value of δ in any analysis. Comparing the results of the NVs at the kerb line, for a 35° friction angle, with the traditional design surcharges, the 20kPa model yields almost identical results. However the 16 & 10kPa models yield values which are ~ 19% and 49% smaller, respectively.

6 COMPARATIVE ANALYSIS

To allow working engineers to evaluate the impact of EN1991-2 [9], the associated NA [10] and the PD on the design of conventional retaining walls, it was necessary to compare the results of the new standards with a range of historic design methods. The methods adopted for this part of the study were CP2, Culmanns method and the Terzaghi [16] simplified strip analysis [20]. Figure 10 shows the simplified analysis suggested by CP2 (Clause 1.443) for the assessment of line loading. The model was based on the work of Terzaghi and was deemed acceptable given the 'unwieldy' nature of a wedge analysis (McMenamin [21]).

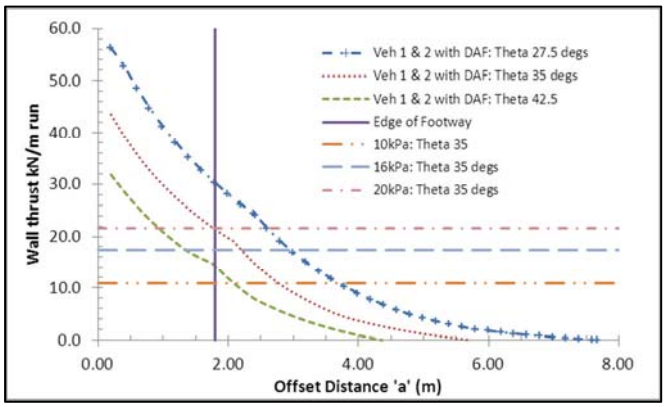


Figure 9 Relationship between wall thrust and the variation of 'a' comparing the NV and a traditional surcharge values.

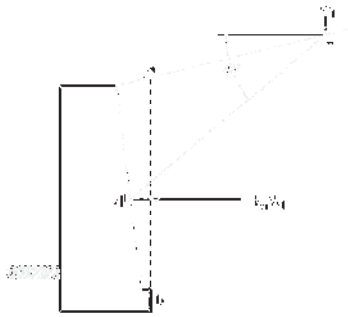


Figure 10 CP2 [1] Simplified Line Load Analogy

Based on a study of arching action within soils and using a modified Boussinesq analysis, Terzaghi suggested the formulas shown in Figure 11 for the assessment of pressure distributions behind rigid unyielding walls (Puller [20]). To allow ease of comparison of each method, the magnitude of the strip loads applied to each wall was as per Clause NA2.32 of the National Annex to BS EN 1991-2 [10]. A number of the comparative methods allow for the implications of wall friction (δ) within the analysis. Where possible, this has been included and presented in the comparison (See Tables 1 & 2).

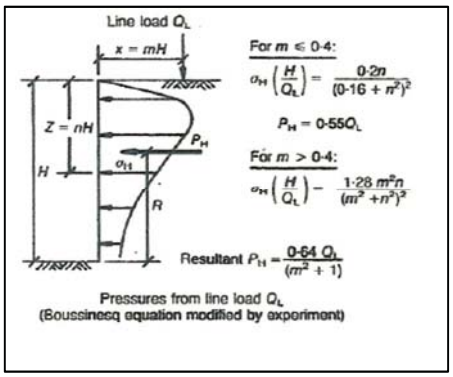


Figure 11 Terzaghi Simplified Strip Analysis Model [20]

Height (m)	Theta φ'_d (degs)	Culmann $\delta = 0$ (kN/m)	Culmann $\delta = 2/3\Phi$ (kN/m)	Terzaghi (kN/m)	CP2 $\delta = 0$ (kN/m)	CP2 $\delta = 2/3\Phi$ (kN/m)	PD6691 (kN/m)
2	27.5	9.40	9.40	14.70	11.04	9.00	3.97
	35.0	5.30	5.30	14.70	8.06	15.14	0.00
	42.5	1.30	1.30	14.70	5.82	13.01	0.00
5	27.5	23.90	19.60	31.80	24.52	18.51	33.67
	35.0	18.10	15.40	31.80	17.90	13.12	23.82
	42.5	13.30	12.00	31.80	12.92	9.25	16.25
8	27.5	27.40	23.40	30.93	23.78	22.56	36.24
	35.0	20.40	18.10	30.93	17.35	15.99	28.91
	42.5	14.70	13.60	30.93	12.53	11.28	19.94

Table 1 Comparison of Wall Thrust with historic assessment methods

Height (m)	Theta φ'_d (degs)	PD6691 (kN/m)	BS8002 10kPa (kN/m)	BD37/01 16kPa (kN/m)	BD37/01 20kPa (kN/m)
2	27.5	3.97	7.36	11.78	14.72
	35	0.00	5.42	8.67	10.84
	42.5	0.00	3.88	6.21	7.76
5	27.5	33.67	18.40	29.44	36.80
	35	23.82	13.55	21.68	27.10
	42.5	16.25	9.70	15.52	19.40
8	27.5	36.24	29.44	47.10	58.88
	35	28.91	21.68	34.69	43.36
	42.5	19.94	15.52	24.83	31.04

Table 2 Comparison of NV Thrusts with historic surcharge values

Both CP2 and the Culmann assessment provide similar results which are lower bounds to the PD method. However, if the OL & DAF factors were removed from the PD results, the results should be very similar. Both the Terzaghi [20&21] analyses and the PD model yielded comparable results aside from the very small wall (*2m*). However, a limitation of the Terzaghi analogy is there is no direct allowance for the backfill strength, despite calibration against field results. Comparing the PD with CP2 and the wedge analysis, the new method is inconsistent for shallow wall depths and thereafter produces thrusts significantly greater than those suggested by traditional methods. Ignoring the simplicity of the CP2 method (*40^o line of application*), the comparison with the Culmann analyses, clearly shows the new method is returning higher thrusts than established/historic methods. Incidentally the inclusion of a model factor described in Cl. 4.7 of the PD and the partial factor set associated with DA1 combination 2 would further elevate the thrust intensity. In Table 2, a comparison is drawn between the new normal traffic model and the traditional surcharge models used in the UK. The new model performance is poor for walls up to 2.5m (Figure 7). However, when compared with walls designed to BD37/01 [6], the model provides comparable results for mid height walls (5m) for the 16kPa surcharge. For higher walls, the old assessment method yields higher results. In terms of the 10kPa surcharge suggested by BS8002 [4], Shave et al. [11], assertion is correct that the new model provides a 'more realistic and also more onerous' results. However, as this paper has suggested the new traffic model needs refinement when considering smaller domestic type walls.

7 CONCLUSIONS

Based upon this initial review of PD6694-1 [12], the authors are of the opinion that the new traffic loading model is more onerous for the design of gravity retaining structures. This will have direct financial and environmental impact on future retaining wall design which adopts this methodology. This preliminary work has uncovered a range of small wall heights (domestic) which potentially could fall outside the area of influence of the new loading model, thus affording limited reserve capacity in the event of an overloading case. This hypothesis will be further developed in a paper currently under preparation for future publication. The new PD does leave some questions unanswered regarding the use of virtual walls, vehicles leaving the notional lanes and the possibility of using wall friction on the virtual face to reduce the magnitude of the wall thrust. Finally, there is the possibility that engineers using this new traffic surcharge methodology will focus on the intricacies of the traffic model, rather than the fundamental soil mechanics that underpin the design of walling systems. Therefore more work is needed to explore the impact of PD6694-1 [12] on design and education of those unaccustomed to Eurocode design.

REFERENCES

[1] Clayton, C. R. I and Milititsky, J. (1986) *Earth pressure and earth retaining structures*, 2nd Edition, Blackie Academic & professional London, 1993

[2] CP2 *Earth-retaining structures*, London, Institution of Structural Engineers, 1951

[3] Akroyd, T.N. W, *Earth-retaining structures: introduction to the Code of Practice*, The Structural Engineer, Vol 74, No 21, 5th Nov 1996, p360

[4] BS8002 *Code of practise for earth retaining structures,* London, British Standard Institute, 1994

[5] Bolton, M.D, *Geotechnical design of retaining walls,* The Structural Engineer, Vol 74, No 21, 5th Nov 1996, p365

[6] BD37/01 *Loads for Highway Bridges*, Highways Agency, London, TSO, 2001

[7] BD30/87 *Backfilled retaining walls and bridge abutment*, Highways Agency, London, TSO, 1987

[8] BS EN 1997-1:2004 Eurocode 7: Geotechnical design – Part 1: General rules, Incorporating corrigendum February 2009, BSi, London, UK

[9] BS EN 1991-2:2003 Eurocode 1: Actions on structures – Part 2: Traffic loads on bridges, Incorporating Corrigenda December 2004 and February 2010, BSi, London UK

[10] NA to BS EN 1991-2:2003 UK National Annex to Eurocode 1: Actions on structures – Part 2: Traffic loads on bridges, Incorporating Corrigendum No. 1, BSi, London, UK

[11] Shave, J, Christie, T. J. C, Denton, S. and Kidd, A. *Development of traffic surcharge models for highway structures*, in Proceedings of Bridge Design to Eurocodes – UK Implementation, Ed. by S. Denton, Nov 2010, ICE, London.

[12] PD 6694-1 Recommendations for the design of structures subject to traffic loading to BS EN 1997-1:2004 London, British Standard Institute, May 2011

[13] Atkins Highways & Transportation, *Background to UK National Annexes to EN1990 Annex A2 and EN1991-2*, London, Highways Agency, 2011

[14] Rattagin, P.H, OBrian, E.J, & Gonzalez. A, The Dynamic Amplification on highway bridges due to traffic flows, UCD, Dublin

[15] CIRIA *Report C580 Embedded retaining walls – guidance for economic design*, CIRIA, London 2003

[16] Aziza, F., Applied analysis in geotechnics, Spon press, London, 2000

[17] O`Sullivan, C.O., Creed. M., *Using a virtual back in retaining wall design,* Proceeding of the institution of civil engineers –geotechnical engineering, Vol 160, July 2007, p147

[18] Touahamia, M., Sivakumar, V. & McKelvey, D. *Shear strength of reinforced recycled material*, Construction and building materials, Vol 16, 2002 pg

[19] Simpson, B., *Design and construction of retaining walls to the new BS8002 and EC7*, CPD seminar, Institution of structural engineers, Stirling, 9th Jan 1997

[20] Puller, M., Deep excavation: a practical manual, 2nd Edt, Thomas Telford publishing, London, 2003

[21] McMenamin, P, Traffic loading on retaining walls – a comparative study, BEng degree dissertation, University of Ulster, Jordanstown, 2012

Vibration based seismic damage identification procedure for a steel concentrically braced frame structure

Daniel McCrum[1] & Andrea Staino[2]
[1]School of Planning, Architecture & Civil Engineering, Queen's University Belfast, BT9 5AG
[2]Department of Civil, Structural & Environmental Engineering, Trinity College Dublin
email: d.mccrum@qub.ac.uk

ABSTRACT: An approach for seismic damage identification of a single-storey steel concentrically braced frame (CBF) structure is presented through filtering and double integration of a recorded acceleration signal. The approach is aimed for use with readily available recorded acceleration signals to analyse the health of a structure. A band-pass filter removes noise from the acceleration signal followed by baseline correction being used to reduce the drift in velocity and displacement during numerical integration. The pre-processing achieves reliable numerical integration that predicts the displacement response accurately when compared to the measured lateral in-plane displacement of the CBF structure. The lateral displacement of the CBF structure is used to infer buckling and yielding of bracing members through seismic tests. The level of interstorey drift of the CBF during a seismic excitation allows the yield and buckling of the bracing members to be identified and indirectly detects damage based on exceedance of calculated displacement limits. The calculated buckling and yielding displacement threshold limits used to identify damage are demonstrated to accurately identify initial buckling and yielding in the bracing members.

KEY WORDS: Damage Detection, Seismic, Steel Braced Frame, Band-pass Filter, Baseline Correction

1 INTREODUCTION

Seismic damage detection in building structures enables engineers to assess the safety and allowable occupancy of a building directly after an earthquake event. Damage identification in building structures after an earthquake event also reduces the humanitarian impact on occupants and reduces the economic losses suffered by businesses and insurers. Accurate assessment of the damage state of a building allows insurers to assess claims more quickly and perform required maintenance or retrofitting in a manner that could reduce business interruption or allow faster re-occupation of homes.

After a seismic event, damage can be difficult to observe through visual inspection unless the structure is exposed and significant damage/deformation exists. In steel concentrically braced frame (CBF) structures the buckling of the bracing members is typically visually detectable, however, it may not be obvious if the bracing has yielded, and to what extent. If buckling alone exists, the frame may have adequate capacity for moderate aftershocks as long as the residual interstorey drift is sufficiently low. If such a state of damage exists, the structure could be deemed to be safe to be occupied until repair or retrofitting could be performed.

Existing damage identification methods can be separated into local and global methods that essentially track changes in structural parameters. Local methods identify damage in individual structural components. Acoustic or ultrasonic evaluation can be used as a non-destructive form of post-damage detection to identify localised damage, but such methods are labour intensive and time consuming. However, more popular continuous monitoring methods have also been developed to detect local damage in a structural health monitoring (SHM) approach. A local identification method using displacement and distributed strain measurements to detect the location and severity of structural damage in a simply supported beam was developed by [1]. [2] developed wireless dynamic strain sensors detection of damage that can be used for SHM of a steel moment resisting frame structure subjected to wind or loading. [2] used dynamic strain sensors to extract local damage information by evaluating the relative redistribution of the bending moments in the steel moment resisting frame structure pre- and post-earthquake.

Global methods of damage detection that track model parameters such as; mode shapes [3] & [4] interstorey drift [5], storey stiffness [6], finite element model updating [7] and purely statistical approaches [8] have been shown to be successful. The most common global method of damage detection is interstorey drift tracking because the double integration of readily available acceleration data can be performed. Changes in physical properties such as mass, stiffness or damping will result in detectable changes in modal properties such as frequency, mode shapes or modal damping [9]. Extensive literature reviews on vibration based methods exist [10]-[12].

In this paper, a strategy is presented to assess global damage in a single-storey steel CBF structure using a single relative acceleration signal. Using relative storey acceleration signals, which are readily available and easily recorded by accelerometers, the structural damage due to buckling and yielding, is assessed. The acceleration signal is filtered using a band-pass filter and baseline-corrected using a least-square curve fitting technique. The corrected acceleration response is then integrated twice to provide a reliable predicted in-plane lateral displacement response. In-plane lateral displacement thresholds based on calculated buckling and yielding displacement limits are then used to identify buckling and

yielding in the CBF structure. Test results of measured in-plane lateral displacement and brace member strains are compared to lateral displacement limits and successfully demonstrate the accuracy of the strategy.

2 CONCENTRICALLY BRACED FRAME STRUCTURAL DETAILS

The structural frame investigated in this paper was designed using the lateral pushover method of analysis in Eurocode 8 [13] as part of a larger three-storey CBF structure to resist an earthquake with a peak ground acceleration, a_g = 3.5m/s^2. The test frame is a ground-storey frame of the larger structure and comprises of a 356x140x36mm UB beam and two 203x203x46mm UC columns (as per Figure 1). Two sets of bracing was tested; 30x30x3mm SHS with normalised slenderness, $\overline{\lambda}$ = 1.68 and 50x30x3mm RHS with $\overline{\lambda}$ = 1.57. The brace sizes are within the Eurocode 3 [14] normalised slenderness limits of 1.3 < $\overline{\lambda}$ ≤ 2.0. The steel properties are; f_y = 235N/mm^2, and E = 210,000N/mm^2. The 203x203x46mm UC stub column sections located at the support and beam column connections were used to replicate pinned connections. The strain gauges are located on the front and top face of the bracing sections at locations of suspected buckling as shown in Figure 1 i.e. strain gauge (SG) 4 is located on the front face of the brace section and SG 5 is located on the top face of the brace section. The location of the LVDT's, load cell and numerically modelled lumped masses can be seen in Figure 1. LVDT A measures the in-plane lateral frame displacement and LVDT B measures the out-of-plane brace displacement.

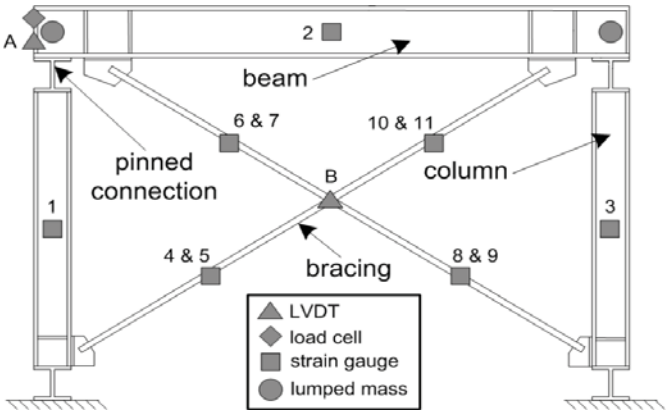


Figure 1. Steel concentrically braced test frame and instrumentation details.

3 TEST PROCEDURE

A series of hybrid tests were performed on the test structure in which physical testing is combined with simultaneous numerical modelling [15] & [16]. In the hybrid test method, it is conventionally assumed that the structure can be represented by lumped masses. At the location of the lumped masses, actuators are provided to apply the dynamic loading to the structure in the form of target displacements. Structural properties such as the inertia and damping are numerically modelled. The equations of motion of the structure are solved by numerical integration. The equation of motion in Equation 1 is solved over a series of time steps Δt, i.e. at the (i+1)th step of:

$$M\ddot{x}_{i+1} + C\dot{x}_{i+1} + R_{i+1} = F_{i+1} \quad (1)$$

in which $\ddot{x}_{i+1}$ is the nodal acceleration vector, $\dot{x}_{i+1}$ is the nodal velocity vector, R_{i+1} is the restoring force vector and F_{i+1} is the external excitation force applied to the system. If the excitation is an earthquake ground acceleration of $\ddot{x}_g$, then $F_{i+1} = -M\ddot{x}_g$. The target displacement x_{i+1} is calculated by the numerical component and sent to the experimental test structure. The displacement command for the current time step for the idealised structure is applied to the structure by the actuator (see Figure 2). The measured restoring force, R_{i+1} is then fed back to the numerical model where the displacement for the next target displacement command is calculated. The slow loading rate of the test structure is required so as not to induce damping or inertia response, because these have already been accounted for numerically

The single-storey CBF structure was supported off a reaction frame as shown in Figure 2 and therefore the measured displacements and thus accelerations are absolute. The test frame is located between two side-by-side reaction frames. During a test the actuator applies the command displacement to the frame as shown in Figure 2. The lumped masses were numerically modelled at the ends of the beams (refer to Figure 1). The inertial displacement resulting from the excitation was applied to the structure in a displacement controlled test using closed looped proportional integral derivative control. The MTS actuator has a 150kN capacity with a stroke of +/-125mm. An internally mounted LVDT provides the actuator displacement and an internal load cell provides the force feedback. Tests are performed at an expanded timescale (essentially a pseudo-dynamic test [17], with the acceleration and velocity numerically calculated from the equation of motion using the measured force and displacement from each time step of the time history.

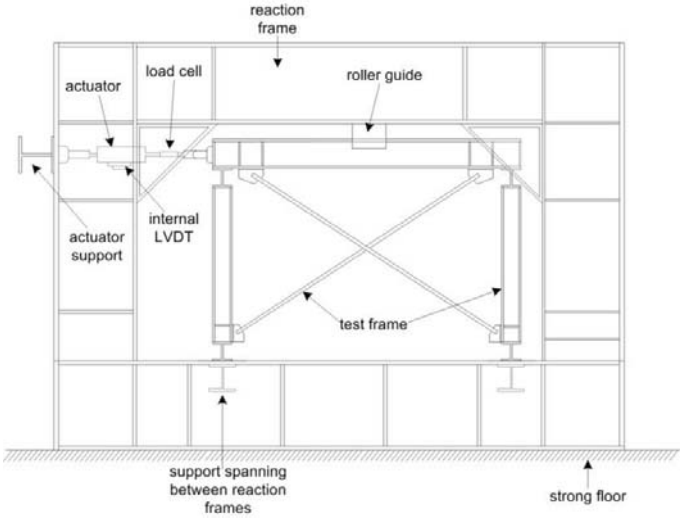


Figure 2. Experimental set-up showing side-by-side reaction frames and test structure

Table 1. Experimental programme and details.

Test No.	*Test type*	*Scaling Factor*	*Brace Size (mm)*	*Nodal Masses (kg)*	*Stiffness (N/mm^2)*
1	Elastic	0.4	30x30x3	45634	9805
2	Inelastic	1.0	30x30x3	45634	9846
3	Inelastic	2.0	30x30x3	45634	9379
4	Elastic	0.4	50x30x3	46924	11408
5	Inelastic	1.0	50x30x3	46924	11157
6	Inelastic	2.0	50x30x3	46924	10733

The scaled Taiwan (1986) earthquake time history was used as the input ground acceleration. The Taiwan earthquake had a magnitude of 7.3, was recorded a distance of 39km from its epicentre and had a peak ground acceleration (PGA) of 0.153*g*.

4 DAMAGE IDENTIFICATION

4.1 Damage identification procedure

The damage detection procedure is outlined as follows;

1. Filter recorded acceleration signal using a band-pass filter to remove noise from the relevant frequency band of interest.
2. Perform a polynomial baseline correction on the acceleration signal and numerically integrate the corrected acceleration twice to yield the predicted displacement.
3. Compare predicted displacement with measured test displacement and ensure within acceptable error bounds.
4. Calculate the buckling displacement and compare to predicted displacement to identify buckling. The Euler buckling capacity, N_{cr} is calculated from;
$$N_{cr} = \pi^2 EI/L_{cr}^2 \quad (2)$$
where; I is the Young's Modulus, I is the second moment of area of the section and L_{cr} is the effective length of the compression member. The brace member end connections are assumed as pinned-pinned. N_{cr} = 37.4kN for 30x30x3mm SHS and N_{cr} = 41.61kN for 50x30x3mm RHS. These forces correspond to a lateral frame displacement calculated as follows;
    a. The tension force in the tension bracing member, F_t and compression force in the compression bracing member, Fc are assumed to be equal up until buckling i.e. $F_c = F_t$. Therefore, the lateral frame force, P (actuator force) corresponding to yield is equal to;
    $$P = (F_c + F_t)\cos\theta \quad (3)$$
    & as $F_c = F_t$
    $$P = (N_{cr} + N_{cr})\cos\theta = 2N_{cr}\cos\theta \quad (4)$$
    where; θ is the angle of inclination of the bracing to the horizontal axis.
    b. Using Equation 4, the lateral frame force, P = 41.47kN for the 30x30x3mm SHS frame and P = 66.46kN for the 50x30x3mm RHS frame. Knowing the lateral frame stiffness, K (from Table 1) and using; $\delta = P/K$, the lateral displacement inducing buckling can be calculated. For example, the expected buckling displacement for TEST 3 is 4.44mm and TEST 6 is 6.19mm.
5. The first yield displacement of the frame can be calculated in a similar manner to Step 4, however, the tension and compression forces in the bracing cannot be assumed to be equal as the yield capacity of the brace member is greater than its buckling capacity. The initial buckling capacity of the brace member reduces during subsequent load cycles as a result of residual out-of-plane deformation. The maximum compressive force in the bracing members therefore reduces in subsequent load cycles. In [18], cyclic tests were performed on similar brace members 1.1m long of section size 20x20x2.0mm SHS ($\overline{\lambda}$ = 1.6, r_y = 0.727cm), 50x25x2.5mm RHS ($\overline{\lambda}$ = 1.2, r_y = 0.994cm) and 40x40x2.5mm SHS ($\overline{\lambda}$ = 0.8, r_y = 1.52cm); where r_y is the radius of gyration about the weak axis. The average buckling capacity in subsequent load cycles of the 20x20x2.0mm SHS (total of 22 cycles), 50x25x2.5mm RHS (total of 14 cycles) and 40x40x2.5mm SHS (total of 12 cycles) was approximately 52%, 58% & 67% that of the initial buckling capacity, respectively. These values were then used as a guide to estimate the reduced buckling capacity of the bracing members in this paper. Therefore, for the 30x30x3mm SHS sections and 50x30x3mm RHS used in these tests, the buckling capacity was reduced by an average estimated 50% and 60% for the 30x30x3mm SHS ($\overline{\lambda}$ = 1.68 & r_y = 1.08cm) and 50x30x3mm RHS ($\overline{\lambda}$ = 1.57 & r_y = 1.16cm), respectively. For example, $F_c = 0.5N_{cr}$ for 30x30x3mm SHS and the lateral frame force corresponding to yield is;
$$P = (F_c + F_t)\cos\theta \quad (5)$$
& as $F_c = 0.5N_{cr}$
$$P = (0.5N_{cr} + F_t)\cos\theta \quad (6)$$
Using Equation 6, the lateral frame force, P = 69.37kN for the TEST 3 for the 30x30x3mm SHS frame and P = 101.4kN for TEST 6 for the 50x30x3mm RHS frame. Knowing the lateral frame stiffness, K (from Table 1) and using; $\delta = P/K$, for TEST 3 for example, the 30x30x3mm SHS bracing tension yielding occurs at 7.38mm corresponding to a brace tension force of 73.8kN. Similarly, for TEST 6 the 50x30x3mm RHS bracing tension yielding occurs at 9.45mm corresponding to a brace tension force of 101.99kN.
6. Compare predicted displacements with displacement limits for buckling and yielding in order to infer the existence of structural damage.

4.2 *Reconstruction of displacement response from acceleration signal*

The recorded in-plane lateral acceleration signal is firstly filtered and baseline corrected to eliminate random high frequency noise and low-frequency trends. The corrected in-plane lateral acceleration is then integrated twice to retrieve the corresponding displacement signal. Subsequently, we show that a scaling gain can be conveniently applied to cater for numerical integration errors and further improve the agreement between the measured and the predicted in-plane displacement.

Measurement noise in the acceleration signal results in inaccurate integration of undesired components of vibration which are associated with intrinsic instrument error and nonlinearities. In order to mitigate the effect of low-frequency drift and high-frequency measurement noise, a band-pass filter with appropriate cut-off frequencies is designed and applied to the acceleration signal. The frequency content of the recorded waveform is analysed to select the cut-off frequencies of the filter. A band-pass filter with cut-off frequencies of 0.01Hz and 25Hz was applied to all acceleration signals. This filtering is beneficial for the reconstruction of the in-plane displacement time history from the measured in-plane acceleration signal as it allows the useful signal to be separated from the noise and a linear frequency response to be obtained.

In general, linear filtering alone is not sufficient to correct recorded acceleration signals that are integrated to give displacement. It is well-known that direct integration of acceleration data may lead to unrealistic results for velocity and displacement, due to initial baseline errors [19]-[22]. [21] discuss different sources of errors that can be identified to explain the drifts in velocities and displacements computed by directly integrating raw acceleration records, including digitization errors, low-frequency instrument noise, low-frequency background noise and mechanical or electrical hysteresis in a sensor. Baseline errors in particular have been shown to cause severe drifts if appropriate pre-processing schemes are not adopted [23].

Table 2. Peak and RMS error between measured and FCI displacement.

Test No.	*Peak Disp. Meas. (mm)*	*Peak Disp. Filtered (mm)*	*Peak Disp. Error (%)*	*RMS Disp. Meas. (mm)*	*RMS Disp. Filtered (mm)*	*RMS Disp. Error (%)*
1	3.92	4.44	13.46	0.59	0.68	15.22
2	9.94	11.41	14.77	1.95	2.25	15.20
3	19.59	22.77	16.23	2.97	3.42	15.24
4	4.03	4.51	12.03	0.78	0.88	11.58
5	10.24	11.57	12.99	1.93	2.17	12.10
6	20.24	22.69	12.09	3.53	3.95	11.82
		Mean	13.60		**Mean**	13.53
		COV	2.24		**COV**	2.89

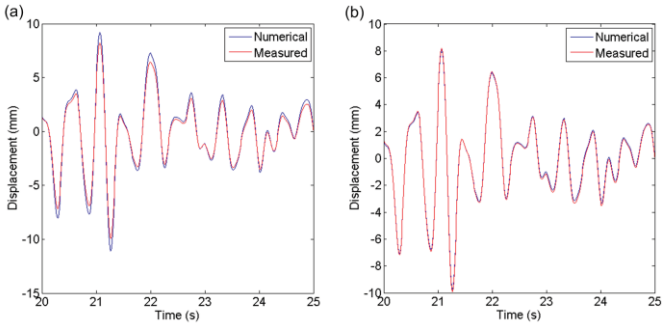


Figure 3. Lateral in-plane frame displacement versus time in TEST 6 from 20 to 25s (a) without scaling gain (FCI) and; (b) with scaling gain (FCIG)

For the purpose of illustration, the numerical (predicted) and the measured lateral in-plane frame displacement in TEST 6 are plotted in Figure 3(a). A high level of agreement between the predicted and the measured response is observed. For the six tests considered in this paper, the results of the application of the proposed methodology, denoted as Filtered Corrected Integrated (FCI) scheme, are illustrated in Table 2. By comparing the measured and the FCI reconstructed displacement, a mean peak displacement error of 13.6% and a mean rms displacement error of 13.5% are attained. The proposed scheme is therefore capable of providing a realistic prediction of the actual displacement response of the structure. On-line implementation of the FCI scheme is also straightforward, as the data can be filtered during acquisition and a windowed baseline correction operation can be easily performed.

Table 3. Peak and RMS error between measured and FCIG displacement.

Test No.	*Peak Disp. Meas. (mm)*	*Peak Disp. Filtered (mm)*	*Peak Disp. Error (%)*	*RMS Disp. Meas. (mm)*	*RMS Disp. Filtered (mm)*	*RMS Disp. Error (%)*
1	3.92	3.91	0.15	0.59	0.60	1.39
2	9.94	10.04	1.00	1.95	1.98	1.38
3	19.59	20.04	2.28	2.97	3.01	1.41
4	4.03	3.97	1.40	0.78	0.77	1.80
5	10.24	10.18	0.56	1.93	1.90	1.34
6	20.24	19.96	1.35	3.53	3.48	1.59
		Mean	1.12		**Mean**	1.49
		COV	0.46		**COV**	0.03

Observation of the results in Table 2 indicates that a slight overestimation of the response is obtained using the FCI method for the cases considered. This observation suggests the presence of an error in the numerical integration of the acquired acceleration samples. In fact, the use of a finite time step for the numerical integration causes an approximation in the solution which depends on the size of the integration time step with respect to the time constants of the system. The time step during the tests was 0.01s and a smaller time step would have resulted in improved accuracy of the numerical integration. To this end, a constant scaling gain is applied to the FCI reconstructed displacements to further improve the agreement between the measured and the predicted numerically computed response. As shown in Figure 3(b),

excellent improvement of the performances can be achieved by appropriately scaling the integrated displacement. By comparing the measured and the FCIG reconstructed displacement (Table 3), a mean peak displacement error of 1.1% and a mean rms displacement error of 1.5% are attained.

4.3 Verification of damage identification strategy

4.3.1 Identification of brace member buckling

Figure 4(a) shows the first 6.5s of the lateral in-plane displacement response of TEST 6. The actuator load versus in-plane lateral displacement of the cycles for the first 6s is shown in Figure 4(b) (up to the point of unloading after Point D in Figure 4(a)). The Euler buckling load is highlighted in Figure 4(b). The hysteresis plot of Figure 4(b) indicates buckling at displacements of 6.19mm corresponding to a lateral in-plane (actuator) force of 66.46kN. The negative displacement at Point D of -6.72mm is slightly larger in amplitude than the displacement at Point C, hence the skewed appearance of the hysteresis plot. No buckling is observed in the hysteresis plot at Points A & B as the structure remains linear. For cycles containing in-plane lateral displacements above ±6.19mm (Point D), slight nonlinearity in the hysteresis plots can be seen in the unloading phaseafter the peak at point D. No yielding was observed in the strain gauge measurements (SG 4-11) during the first 6s of TEST 6. Hence, the nonlinearity in the hysteresis plot indicates buckling of the bracing members.

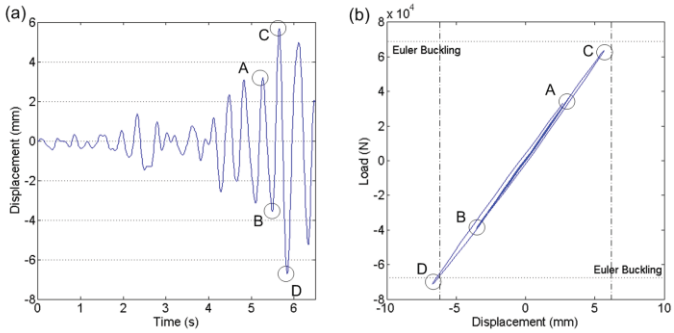


Figure 4. (a) Lateral in-plane displacement versus time for TEST 6 from 0-6.5s and; (b) lateral in-plane load (actuator) versus displacement hysteresis plot for TEST 6 from 0-6s

4.3.2 Identification of brace member yielding

Figure 5(a) shows the lateral in-plane displacement response of TEST 6 from 13-16s of the time history. Figure 5(b) shows the hysteresis plot for the E to F displacement cycle occurring at approximately 12s. The yield displacement was calculated at 9.45mm. Point E corresponds to a displacement of 12.31mm and is above the predicted yield displacement as can be seen in Figure 5(b). Point F corresponds to a displacement of -19.49mm and is shown to exceed yield displacement as can be seen in Figure 5(b). During the negative displacement cycle yielding can be seen to occur as the hysteresis plot becomes highly nonlinear. The hysteresis plot straightens on load reversal.

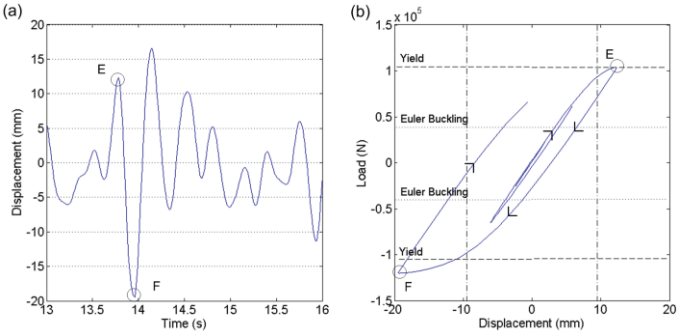


Figure 5. (a) Lateral in-plane displacement versus time for TEST 6 from 13-16s and; (b) lateral in-plane load (actuator) versus displacement hysteresis plot for first yield cycle in TEST 6 at approximately 13-14s

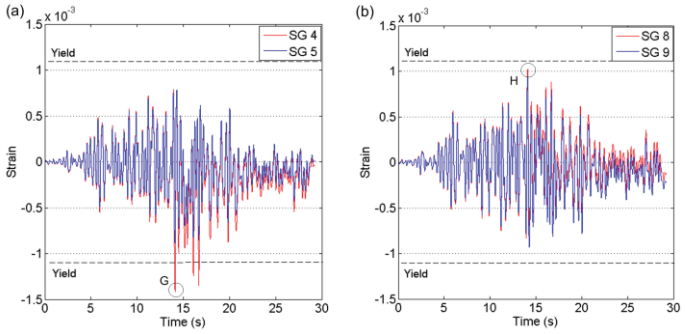


Figure 6. Strain versus time for TEST 6 for; (a) strain gauges 4 & 5 and; (b) strain gauges 8 & 9

Strain results are shown for SG 4, 5, 8 & 9 for TEST 6 in Figure 6 because these sections of the bracing members have a slightly larger effective length than the upper portion of the bracing (refer to Figure 1 for strain gauge locations). The effective length of the bracing between the column and central connection is greater than the effective length of the bracing from the central connection to the beam. First yielding was observed in the hysteresis plot for TEST 6 at approximately 14s (see Figure 5). From Figures 6(a) & (b), it can be seen that the peak strain is significantly above yield at this point in time at Point G and close to yield at Point H in Figures 6(a) & (b), respectively). The strain gauge results in Figure 6(a) indicate no error in predicting the yielding of the bracing members.

Table 4. Qualitative and quantitative summary of test results

No.	*Calc. Buckle Disp. (mm)*	*Damage Observation*	*Peak Test Disp. (mm)*	*Calc. Yield Disp. (mm)*	*Meas. First Yield (mm)*	*First Yield Error (%)*
1	±4.25	None	-3.94	±7.07	-	-
2	±4.24	Buckle (c.11s)	-10.01	±7.05	10 (14s)	3.4
3	±4.44	Buckle (c.6s)	-19.69	±7.39	9.1 (12s)	8.1
4	±5.82	None	4.53	±8.89	-	-
5	±5.96	Buckle (c.15s)	-10.28	±9.09	-10.3 (15s)	0.0
6	±6.19	Buckle (c.6s)	-19.49	±9.45	11.9 (14s)	0.0
					Mean	2.9
					COV	11.0

The qualitative and quantitative summary of the results of all six tests is shown in Table 4. Qualitatively, the first visual observation of buckling during the tests was observed and

recorded during each test and coincided with the predicted buckling displacement. Quantitatively, the predicted yield displacement is compared to strain gauge data and shown on average to predict first yield with an error of 2.9% as can be seen in Table 4. No error was observed in TEST 5 or TEST 6 as the measured yield strain coincided with the expected yield displacement.

5 CONCLUSIONS

This paper has presented a vibration based seismic damage detection strategy for a single-storey steel concentrically braced frame structure. A band-pass filter was used to remove noise from the in-plane lateral acceleration signal followed by baseline correction being applied to reduce the drift in velocity and displacement during numerical integration. This pre-processing resulted in reliable numerical integration that predicts the in-plane lateral displacement response accurately when compared to the measured in-plane lateral displacement of the CBF structure. A constant scaling gain can also be applied to the predicted in-plane lateral displacement to improve the accuracy of the prediction compared to the measured in-plane lateral displacement. Threshold limits of buckling and yielding in-plane displacement of the concentrically braced frame were calculated using the initial stiffness of the frame and are used to identify if buckling and/or yielding have occurred in the bracing members. Observation of the nonlinearity in the hysteresis plot is used to verify the successful predictions of buckling in the bracing members. Strain data from seismic tests is used to verify the successful prediction of the tension yielding in the bracing members. The strategy was shown to be successful at predicting buckling and yielding in the single-storey concentrically braced frame structure.

ACKNOWLEDGMENTS

The testing in this paper was funded as part of an Irish Research Council for Science, Engineering and Technology scholarship. The author would like to acknowledge the technical staff in the Structures Laboratory at Trinity College Dublin for their help in undertaking the tests.

REFERENCES

[1] Adewuyi, A.P., Wu, Z. and Kammrujaman Serker, N.H.M. (2009) Assessment of vibration-based damage identification methods using displacement and distributed strain measurments. Journal of Structural Health Monitoring, 8 (6) 443-461.

[2] Kurata, M., Fujita, K., He, L. and Yamaguchi, M. (2013) PVDF piezo film as dynamic strain sensor for local damage detection of steel frame buildings. Proc. SPIE 8692, Sensors and Smart Structures Technologies for Civil, Mechanical, and Aerospace Systems 2013. doi:10.1117/12.2009554.

[3] Hearn, G. & Testa, R.B. (1991) Modal analysis for damage detection in steel structures. Journal of Structural Engineering, 117(10):3042-3063.

[4] Yao, G.C., Chang, K.C. and Lee, G.C. (1992) Damage diagnosis of steel frames using vibrational signature analysis. Journal of Engineering Mechanics. 118: 1949-1961.

[5] Skolnik, D. and Wallace, J. (2010) Critical assessment of interstory drift measurements. Journal of Structural Engineering. 136 (12), 1574–1584.

[6] Koh, C.G., See, L.M. and Balendra, T. (1992) Damage detection of buildings: numerical and experimental studies. Journal of Structural Engineering. 121: 1155-1160.

[7] Wu, J.R. and Li, Q.S. (2006) Structural parameter identification and damage detection for a steel structure using a two-stage finite element model updating method. Journal of Constructional Steel Research. 62, 231-239.

[8] Krishnan Nair, K., Kiremidjian, A. S. and Law, K. H. (2006) Time series-based damage detection and localization algorithm with application to the ASCE benchmark structure. Journal of Sound and Vibration. 291, 349-368.

[9] Fan, W. and Qiao, P. (2011) Vibration-based damage identification methods: a review and comparative study. Journal of Structural Health Monitoring. 10 (1) 83-109.

[10] Doebling, S.W., Farrar, C.R., Prime, M.B. and Shevita, D.W. (1996) Damage identification and health monitoring of structural and mechanical systems from changes in their vibration characteristics: a literature review. Los Alamos National Laboratory Report.

[11] Sohn, H., Farrar, C.R., Hemez, F.M., Shunk, D.D., Stinemates, D.W. and Nadler, B.R. (2003). A review of structural health monitoring literature: 1996–2001. Los Alamos National Laboratory Report, LA-13976-MS.

[12] Carden, P.E. and Fanning, P. (2004) Vibration based condition monitoring: a review. Structural Health Monitoring, 3(4), 355–377.

[13] CEN (2004) Eurocode 8: Design of structures for earthquake resistance – Part 1: General rules, seismic actions and rules for buildings. BS EN 1998-1:2004. BSi, United Kingdom.

[14] CEN (2005) Eurocode 3: Design of steel structures – Part 1-1: General rules and rules for buildings. BS EN 1993-1-1:2005. BSi, United Kingdom.

[15] McCrum, D.P. and Broderick, B.M. (2013) Evaluation of a substructured soft-real time hybrid test for performing seismic analysis of complex structural systems. Computers and Structures. 129: 111–119.

[16] McCrum, D.P. and Broderick, B.M. (2013) An experimental and numerical investigation into the seismic performance of a multi-storey concentrically braced plan irregular structure. Bulletin of Earthquake Engineering, Volume 11, Issue 6, pp 2363-2385.

[17] Shing, P.B. and Mahin, S.A. (1984) Pseudodynamic test method for seismic performance evaluation: theory and implementation. Report UCB/EERC-84/01. Earthquake Engineering Research Center, University of California, Berkeley.

[18] Goggins, J. (2004) Earthquake resistant hollow and filled steel braces. PhD Thesis, Department of Civil, Structural & Environmental Engineering, Trinity College Dublin.

[19] Trifunac, M.D. (1971) Zero baseline correction of strong-motion accelerograms. Bulletin of the Seismological Society of America, v. 61, p. 1201-1211.

[20] Wang, L. J. (1996) Processing of near-field earthquake accelerograms. Earthquake Engineering Research Laboratory, California Institute of Technology. Technical Report, Caltech EERL:1996.EERL-96-04.

[21] Chiu, H.C. (1997) Stable baseline correction of digital strong-motion data. Bulletin of the Seismological Society of America, v. 87, p. 932-944.

[22] Boore, D.M. (2001) Effect of baseline corrections on displacements and response spectra for several recordings of the 1999 Chi-Chi Taiwan Earthquake. Bulletin of the Seismological Society of America, v. 91, p. 1199-1211.

[23] Yang, J., Li, J.B. and Lin, G. (2006) A simple approach to integration of acceleration data for dynamic soil–structure interaction analysis. Soil Dynamics and Earthquake Engineering, Volume 26, Issue 8, Pages 725-734.

Resistance of Plated Concrete to Impact Loading

Dr David Dunne[1], Dr David Collery[2], Dr Philip McKenna[3]
[1]AECOM, Colmore Plaza, 20 Colmore Circus Queensway, Birmingham, West Midlands, B4 6AT
[2]Mott MacDonald, Mott MacDonald House, 8-12 Sydenham Road, Croydon, CR0 2EE
[3]CH2M HILL, City Park, 368 Alexandra Parade, Glasgow G31 3AU
email: David.Dunne@aecom.com, David.Collery@mottmac.com, Philip.McKenna@ch2m.com

ABSTRACT: The current research programme was designed to extend the understanding of steel plated concrete for use in new construction activities. This is achieved by assessing the behaviour of two structural forms of walls to in-plane static and impact loading. These two forms include: (i) a steel plated concrete composite (S-P-C) and; (ii) a conventionally reinforced (C-R) wall. Research works undertaken into the area of concrete impact resistance demonstrate that the impact resistance of concrete is improved when utilizing alternative reinforcement techniques. This is in comparison to conventional reinforcement systems. In S-P-C, the conventional reinforcement is replaced by external steel plates. Advantages are obtained from the systems inherent robustness, derived from the composite action obtained between the steel plates on the outside and the hardened infill concrete core on the inside. Epoxy resin was deployed to provide a shear transfer mechanism, and to achieve composite action between the steel plates and concrete core. Static testing was deployed to assess the elastic behaviour of the walls under constant loading. Impact testing was performed by dropping impact loads (weights) onto the wall. Experimental results were obtained under static loading through deflection and strain measurements, impact loading results were obtained by observations of deflections, crack distributions, failure modes and ultimate load capacities of both systems. This study demonstrated that S-P-C provides for a stiffer construction form with reduced overall deflections to that of a conventionally reinforced concrete system. The S-P-C system sustained higher magnitudes of loading in both experiments. The system demonstrated a reduced and more even distribution in crack development, indicating an increase in energy absorption characteristics and stiffness of the C-R system.

KEY WORDS: Steel plates; Conventional reinforcement; Impact loading; Static loading; Cracking.

1 BACKGROUND

External steel plate bonding involves attaching reinforcement to the external faces of concrete members. The success of the system is dependent on the method of shear transfer used between the concrete and steel [1]. Whilst the use of anchored shear connectors is commonplace, epoxy resins are also deployed in retrofitting construction activities. The technique of strengthening concrete structures by bonding steel plates to the external faces, using epoxy adhesive, was pioneered in the late 1960s [2, 3].

The use of carbon fibre and fibre reinforced polymer (FRP) strengthening systems are commercially available [4, 5]. However, these are not covered within the context of the current research and no technical, practical application or economic comparisons are made.

2 STEEL-PLATED-CONCRETE

Concrete as a construction material is extensively used in structures. It provides protection for life, property and the environment. S-P-C is a robust form of construction in which composite action can be achieved in a number of ways, such as: the use of shear studs, overlapping shear studs, overlapping J-hooks; bi-steel welded stud systems and; epoxy resin plate bonding [6]. Applications include beams in common structures, wall panels, tunnels and aircraft hangars to name but a few [6].

Retrofitting of reinforced concrete using external steel plates has been applied to both beams and slabs in bridge and building construction over the decades. In the UK, the load carrying capacity of a number of concrete bridge structures have been increased by the technique of bonding steel plates with the use of epoxy adhesive [7]. This technique can be applied with a minimal increase in the cross-sectional dimensions of the bridge member.

In new S-P-C composite construction the conventional reinforcement is replaced by external steel plates. The main advantage of this is its robustness, derived from the composite action obtained between these steel plates on the outside and the concrete core on the inside. The scope of the current research programme was to investigate the behaviour of two different structural forms of walls: a conventionally reinforced wall and an S-P-C wall. It was considered that the S-P-C system would fully utilise the properties of both the steel and concrete, making it a more efficient, robust and durable system, which would performing better under variable loading conditions.

An experimental study was carried out using one of each of the two systems. These were then subjected to static and impact in plane loading. The main conclusion from this preliminary study was that the S-P-C composite system possesses a higher degree of stiffness and thus a greatly reduced degree of deflection, when compared to the conventionally reinforced wall. Other noteworthy design parameters such as strain development, crack patterns and their effects are also improved and discussed within this paper.

3 EXPIREMENTAL MODEL

The model depicted in Figures 1 and 2 and detailed in greater detail elsewhere [6], consists principally of two walls of the same size 900mm × 40mm × 300mm. One is conventionally reinforced with the second containing a S-P-C form of construction, consisting of two external plates as reinforcement. The reinforcement is illustrated in Figure 3. Both walls were cast into a specially designed concrete block (Figure 6), which provided a rigid foundation for testing the model.

The conventional reinforcement consisted of 6mm diameter mild steel plain bar. Allowing for a 280 anchorage into the anchor block, the walls were 1180mm long, placed longitudinally in the block and spaced at 23mm centres. Additionally, two horizontal reinforcement bars were placed at the top and bottom of the wall in their tensile and compressive zones. Finally, 6mm diameter link bars at 50mm centres and at lengths of 260mm were placed at staggered centres either side of the main horizontal steel. These acted to vertically fasten the reinforcement together.

The second form of reinforcement to be employed was that of steel plates. Placed on both sides of the externally reinforced wall, these measured 1180mm × 0.7mm × 300mm in size.

There was also reinforcement required for the concrete block which consisted of a steel cage of eight links of 10mm diameter steel bar.

The final element in the steel reinforcement was the addition of four reinforcing plates along the top of each wall, 50mm × 40mm × 10mm in size. Each plate had two number 100mm lengths of 6mm diameter steel bar welded to their base. These plates which can be seen in Figure 1 and in greater detail elsewhere [4], were placed at four number loading locations along the top of both walls. Their purpose was to distribute the applied loads and to reduce local damage.

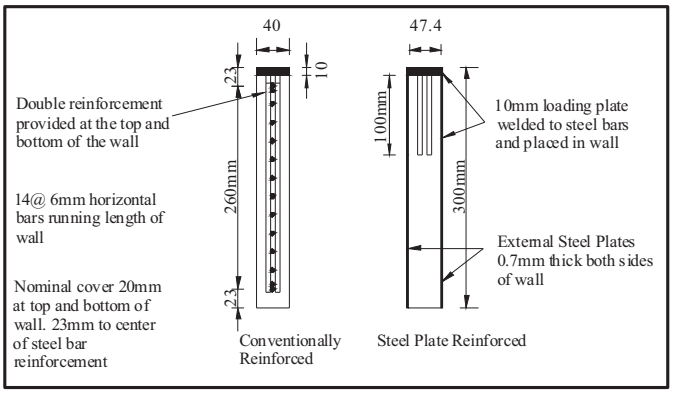


Figure 1. Shear walls cross sections.

4 MATERIAL PROPERTIES AND TEST PROCEDURES

The material properties were chosen to be representative of full size structures. The apparatus required to perform the concrete property testing was a Denison cube crushing machine and an Avery tensile testing machine was used to obtain the steels tensile properties. The standard testing setups and apparatus for the concrete and the steel can be seen in Figures 4 and 5.

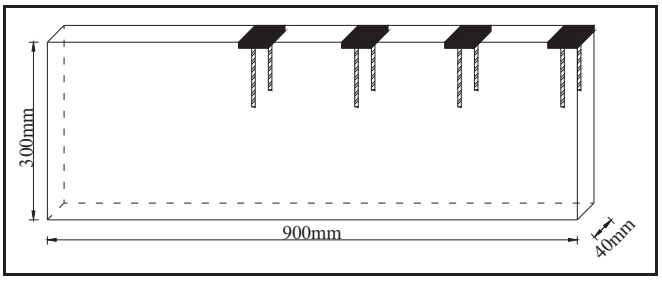


Figure 2. Reinforcing plate locations.



Figure 3. Wall steel bar and plate reinforcement.

4.1 Concrete and steel

Concrete

Two different grades of concrete were used. The concrete used in the restraint block was a standard RMC Ready-Mix design C50/60 grade concrete. Secondly, the concrete in the walls was a specially designed micro-concrete mix 1:2:6 (water:cement:aggregate), with a w/c ratio of 0.40. Two cubes and two cylinders, one from each wall, were tested for strength development at designated periods up to the day of testing as outlined in Table 1. The average of two test results is presented.



Figure 4. Concrete property testing arrangement.

Steel

Tensile testing of the steel bar and plate reinforcement was performed by an Avery testing machine. Two standard 0.7mm grade S275 mild steel plate and 6mm sections diameter bars

were tested. Reinforcing steel test properties are provided in Table 2.



Figure 5. Steel plate and bar property testing arrangement.

Table 1. Concrete properties.

Day Strength	Concrete		
	f_{cu}	f_{ct}	E_c
	(N/mm^2)		(kN/mm^2)
7	48.0	Not Tested	31.1
28	52.0	Not Tested	32.4
44	Not Tested	3.9	Not Tested
Test day	54.0	4.0	33.1

Table 2 Steel properties.

Steel		
Materials	f_y (N/mm^2)	E_s (kN/mm^2)
6.0 mm bar	490.0	Not Tested
0.7 mm plate	373.5	225.0

4.2 Epoxy resin

A two part cold cure epoxy resin, commonly used for structural bonding purposes in the UK, was employed to attach the steel plates to the concrete surface.

4.3 Instrumentation

Strain in the steel plates was measured through the use of linear strain gauges. These gauges were attached either side of the steel plates. A single dial indicator gauge was employed to record end wall deflections, to an accuracy of 0.01mm. Penny and Giles LVDT transducers were used to measure mid-span and end-span wall deflections under static loading. The mid-span and end-span test locations can be seen in Figure 6.

4.4 Static and impact testing methods

The static and impact testing apparatus is shown in Figures 6 and 7.

The static testing procedure consisted of a number of weights 1, 2, 5 and 10 kilograms applied manually to the walls at designate impact locations. These locations were located at the end and quarter points along the wall where 10mm thick steel loading plates were located as indicated in Figures 1 and 9-13 respectively. The measurements consisted of deflection from the transducers and the dial gauge positioned beneath the front of each wall and strain readings from the strain gauge.

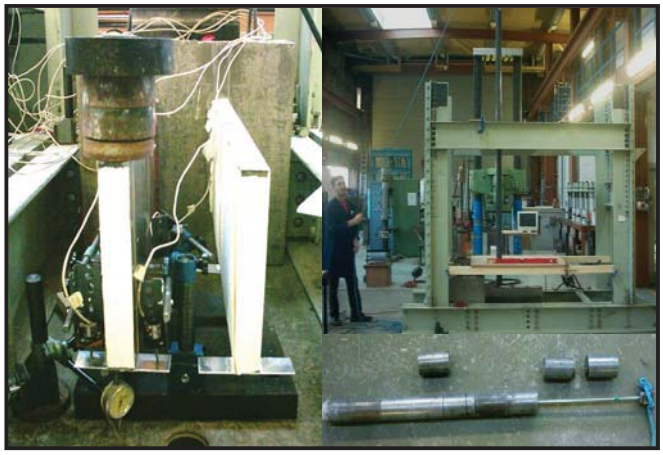


Figure 6. Static and impact test setup.

The main piece of equipment required in the impact test was an impactor. This consisted of a cylindrical steel section of 2.5kg weight which was manually placed onto a threaded bar. This allowed incremental increase in weights to be applied.

The first steel section had a domed end as this impacted the wall. The remaining sections were cylindrical in shape, 100mm long and 63.5mm in diameter as can be seen in Figure 7.

A hook located on the top of the bar allowed a rope to be threaded and a pulley mechanism to be employed. Finally, a guidance tube was used to guide the impactor over the loading plate locations. The testing mechanism layout is illustrated in Figure 6.



Figure 7. Impactor and weight sections.

5 RESULTS AND DISCUSSION

Plots of the deflection readings for both systems are shown in Figure 8. The load cycles represent the load values from 1kg up to 40kg. It is clear from the figure that the deflections of the S-P-C wall are considerably lower to that of the C-R system as well as linear over the span.

The conventionally reinforced wall demonstrated a greater mid-span deflection and greater end-span deflection. The main finding from the presented graph is that, under static loading the stiffness of the S-P-C wall is much greater compared to the conventionally reinforced wall and that over the range of applied loadings its behaviour can be more or less described as linear.

5.1 Strain:Static Testing

Table 3 outlines the static loading increments utilised in the study. Strain readings for the S-P-C shear wall demonstrated that the top of the wall was in tension and the bottom of the wall in compression under loading. This can be seen in Figures 8 for loading cycles one and three. These figures also illustrate that the action of elastic deformation is taking place, with strain increasing gradually under increased loading and in a linear order. Furthermore, strain in both plates was similar which, infers that the epoxy resin bonding gave an even distribution of strain built up in the steel plates under static loading. These findings are similar to those of Barnes et al [8]. The values were of a small magnitude signifying that the plates were grossly under stressed and very stiff.

Table 3. Static loading increments.

Load cycle	Wall type, Ultimate Load (kg)	
	S-P-C	C-R
1	25	5
2	57	10
3	76	20
4	-	30
5	-	40

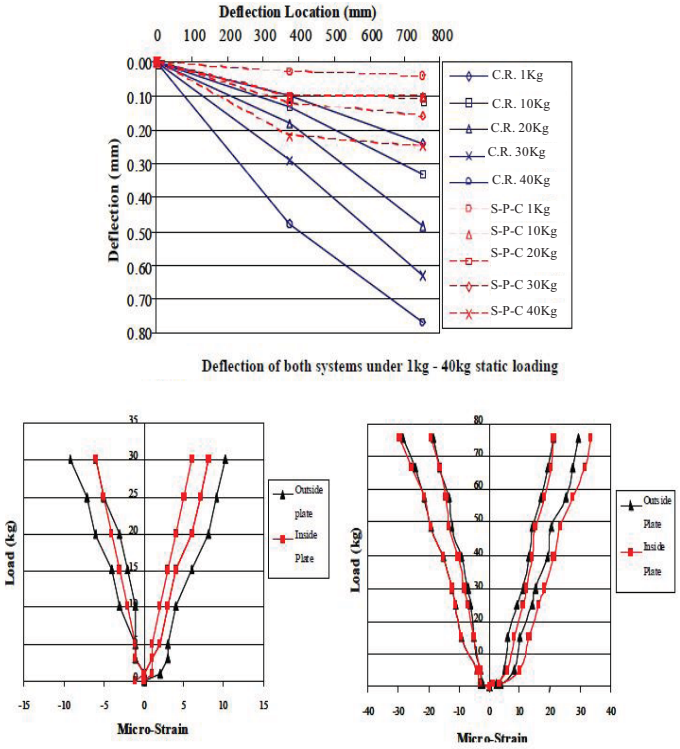


Figure 8. Deflection of both walls and strain in steel plates under static loading cycles 1 and 3 (left - right).

5.2 Crack inspection: Impact testing

All reinforced concrete structures possess cracks in order for reinforcement to function properly, however it is important to limit the developments of these cracks during service in order to achieve serviceability requirements. Table 4 outlines the impact loading increments utilised in the study. Each load was dropped from incremental impact heights which varied from 1.0m - 3.0m.

Throughout the experimental procedure, it was evident that although extensive cracks were developing in the S-P-C wall, it was still structurally sound. The widths of the cracks remained visually small until the ultimate failure mechanism developed. At failure the behaviour was somewhat brittle. This can be attributed to the early peeling and onset of separation of the plates near the base of the concrete wall to the anchor block location as discussed below.

With respect to the conventional wall as the load increased large deflections were observed and accompanied by wider main cracks. Throughout the experiment the S-P-C system possessed a visible resistance to the effects of impact loading with little deflection.

Table 4. Impact loading increments.

Load cycle	Wall type, Ultimate Load (kg)	
	S-P-C	C-R
1	5.0	5.0
2	7.5	7.5
3	10.0	10.0
4	15.0	-
5	17.5	-

Steel plate separation, reduction in shearing, small deflections and increased ultimate strength were the characteristics at failure as observed by Oh et al [9]. All of these mechanisms were observed in this study. In particular, at an early stage the onset of peeling initiated by local buckling of the plates near the base, where high compressive stress occurred, were observed. It was evident from the experiment that extensive cracking of the tensile zone of the wall took place. This can be attributed to a high tensile stress build-up at the top of the wall caused due to a confinement of stresses. The observed defects are presented in Figures 9, 10 and 11 for the conventionally reinforced wall and 12 and 13 for the S-P-C system.

As noted, plate buckling was also visible from an early stage. This would imply that there was an unsatisfactory transfer of shear from the concrete core to the epoxy. The ultimate failure was attributed to the plate peeling accompanied by concrete rip-off as the contact area of concrete with the steel plate was reduced, Figure 13.

In the main, the core observations from the study were: (a) early peeling of plates initiated by the local buckling of the plate on the compression side is a real possibility; (b) as the peeling progresses, the plate-concrete composite action is reduced and appears to be controlled by brittle behaviour of the concrete and; (c) it is clear that preventing early buckling of plates near the base is a very important consideration in the design of S-P-C walls.

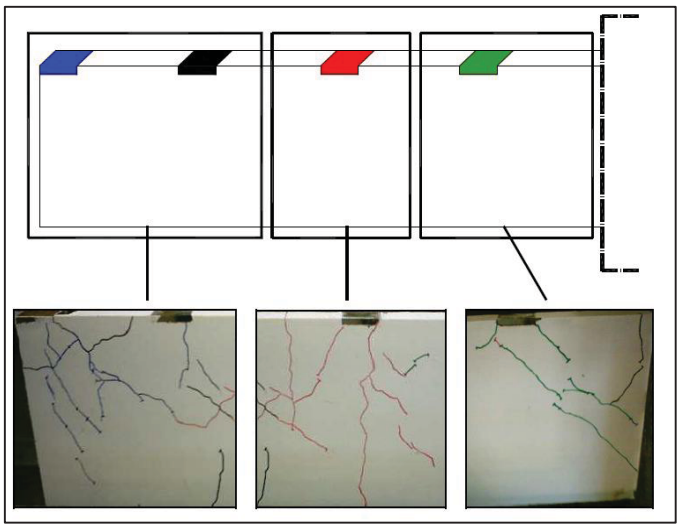


Figure 9. Crack pattern after 2.5kg impact loading cycle.

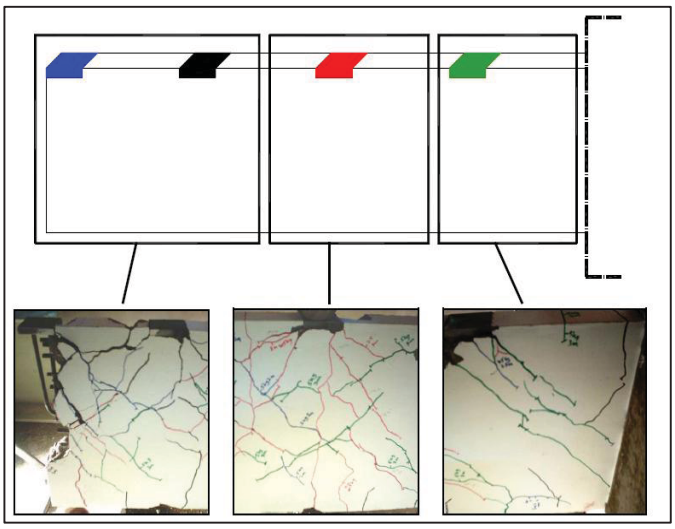


Figure 10. Crack pattern after 5.0kg impact loading cycle.

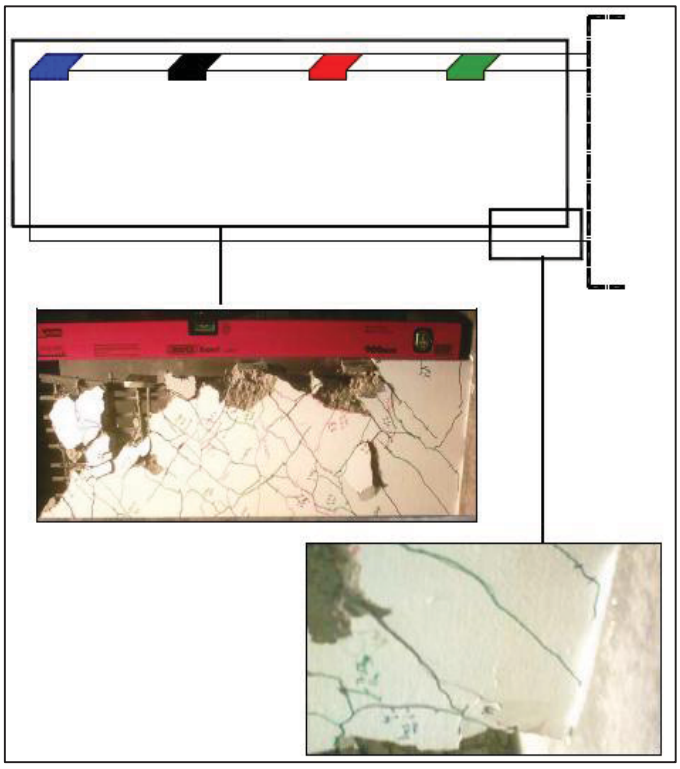


Figure 11. Crack pattern after 10.0kg impact loading cycle.

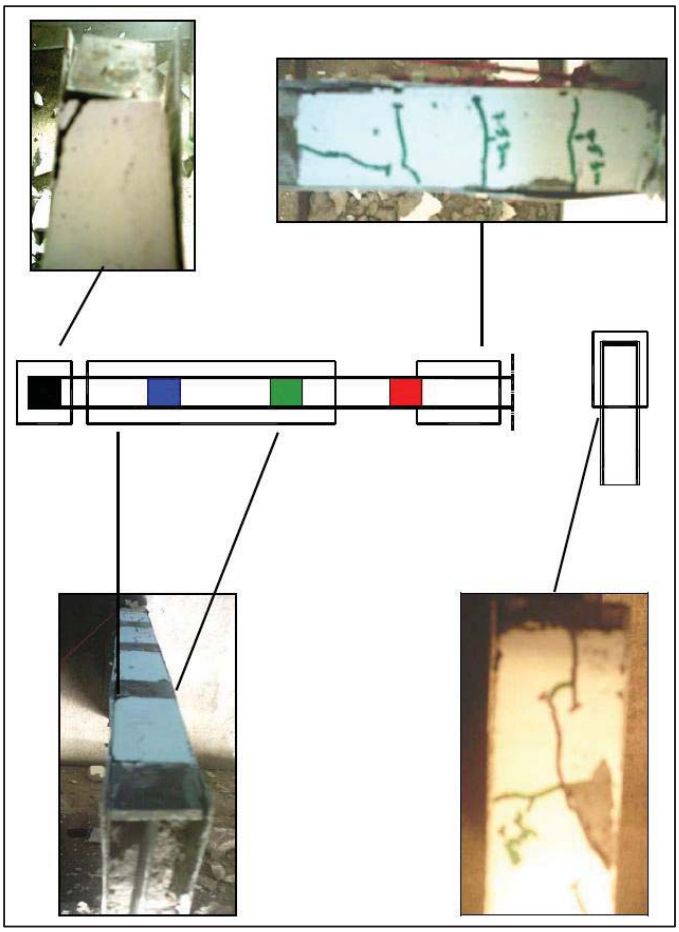


Figure 12. Crack pattern after 5.0kg and 7.5kg impact loading cycle.

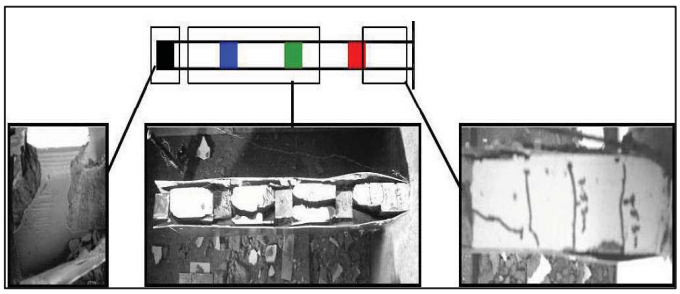


Figure 13. Crack pattern after 17.5kg impact loading cycle.

6 CONCLUSION

Reinforced concrete is designed at ultimate limit state (ULS). Subsequent checks of deflection and minimum crack width control are undertaken at serviceability limit state (SLS). Whilst noting that these checks are less onerous, the use of higher strength materials puts forward the notion of issues whilst in service [10].

Reinforcing steel is critical to the successful attainment of a reinforced concrete (RC) elements in-service capacity. Where two RC elements were investigated, the following conclusions are drawn from the preliminary study.

(i) S-P-C offers an enhanced overall economical structural system with a reduction in construction time, due in the main to a reduced, less complicated cross-section. A direct consequence of the omission of conventional reinforcement.

(ii) S-P-C reinforcement was found to be an inherently stronger and more robust system than the conventional reinforcement.

(iii) Plated elements can resist large degrees of static and impact loading through composite action.

(iv) Failure of the S-P-C system was due to the initiation of local buckling of the plates in the highly compressed area of the wall. The progress of peeling reduced the composite action causing concrete to fail in a brittle manner.

(v) S-P-C is a system highly suitable for tall buildings and other structures where robustness against impact and terrorist activities are the main design considerations.

7 CONCLUSION

The authors would like to acknowledge the University of Dundee, Civil Engineering Department and retired reader of Structural Engineering, Dr. Nutan Subedi for their support in undertaking this research.

8 REFERENCES

[1] Coyle, N.R. (2001), *'Development of fully composite Steel-Concrete-Steel beam elements'*, Ph.D. Thesis, University of Dundee, 2001.

[2] De Nardin, S and El Debs, A. (2013), *'A state of the art of steel-concrete composite structures in Brazil'*, Proceedings of the Institution of Civil Engineers, Civil Engineering Special Issue 166, November, CE6, 20-27.

[3] Prakash Rao, D.S., Sharma, S.P. (1991), *'Steel-concrete composite girder with epoxy bonding'*, Proceedings of the Institute of Civil Engineers, Part 2, 373-375.

[4] Shaw, M. (1997), *'Structural strengthening with external plates'*, Proceedings of the 2nd International Conference on Building Envelope Systems and Technology, Bath University, UK.

[5] Elavenil, S.R.M. and Knight, S. (2012), *'Impact response of plates under drop weight impact testing'*, Daffodil International University Journal of Science and Technology, Vol. 7, Issue No. 1, January.

[6] Dunne, D. (2005), *'Assessment of steel - concrete - steel shear wall'*, BEng (Hons). Dissertation, University of Dundee.

[7] BA 30/94 (1994), *'Strengthening of Concrete Highway Structures Using Externally Bonded Plates'*, Design Manual for Roads and Bridges: Volume 3, Department of Transport, UK.

[8] Barnes, R.A., Baglin, P.S., Mayes, G.C. and Subedi, N.K. (2001), *'External steel plate systems for the shear strengthening of reinforced concrete beams'*, Journal of Engineering Structures, Vol. 23, No. 9, 1162-1176.

[9] Oh, B.Y., Cho, J.Y. and Park, D.G. (2003), *'Failure behaviour and separation criterion for strengthened concrete members with steel plates'*, Journal of Structural Engineering, Vol. 129, No. 9, 2003, 1991-1198.

[10] Soltani, A., Harries, K.A. and Shahrooz, B.M. (2013), *'Crack opening behaviour of concrete reinforced with high strength reinforcing steel'*, International Journal of Concrete Structures and Materials, Vol. 7, No.4, December, 253-264.

Preservation of Titanic's Dry Dock

[1] Mervyn Watley,[2] Gerry Hennity
[1]Director of Corporate Real Estate & Facilities, Northern Ireland Science Park, Queen's Road, Belfast, BT3 9DT
[2] Regional Director, CEI Collins Engineers Ltd, Northern Ireland Science Park, Queen's Road, Belfast, BT3 9DT
email: m.watley@nisp.co.uk, ghennity@collinsengr.com

Titanic's Dry Dock is located on the north eastern shore of Queen's Island, home of Belfast's once prestigious shipbuilding industry, which now forms part of the area now known as 'Titanic Quarter'. Titanic's Dry Dock is a 'scheduled monument' designated by Northern Ireland Environment Agency.

Titanic's Dry Dock remains a highly significant maritime artefact and, together with the Pump-House, is of considerable value which serves as a reminder of the facilities put in place to construct one of the world's most famous icons the 'Titanic'.

CEI Collins Engineers Ltd (Collins) was appointed by the Northern Ireland Science Park (NISP) to undertake an underwater inspection of the Titanic's Dry Dock gate and the outer quay walls. The inspection determined that the Dry Dock gate was in serious condition with substantial steel section loss in some locations and areas of severe corrosion evident.

Collins then reviewed a total of nine different upgrade options to protect both the steel and caisson gate and the dry dock as part of an overall economic appraisal. Each option was chosen on the basis that it would preserve the integrity of the dry dock but not adversely affect the heritage of the overall structure. Each option was discussed with the Built Heritage Department of the Northern Ireland Environment Agency along with other stakeholders and interested groups.

The preferred option involved the installation of a new concrete structure in the outer dock gate position.

Collins was retained by Northern Ireland Science Park to provide assistance with the lodgement of the planning application and to provide both engineering and CDM coordinator services for the implementation phase of the project.

This paper discusses the evaluation of options considered and the construction of the concrete outer defence structure.

KEY WORDS: Caisson; Alexandra Dock; Cofferdam; Concrete; Inspection; Culverts; Dry Dock; Insitu Concrete;

1. INTRODUCTION

The Titanic's Dry Dock is actually called Thompson Dock. It was officially opened on the 1st April 1911. The first ship to enter the Dry Dock was the Olympic – the sister ship of the Titanic and the Britannic. At the time the dock was the largest dry dock in the world. This structure along with the Pump House are of high historic importance as part of the wider story of shipbuilding on Queen's Island and the intertwined story of Titanic's life .



Olympic Liner in the Dry Dock

2. BUILDING OF THE DRY DOCK

The dock was built by Belfast Harbour Commission and then leased to Harland & Wolff. It was purpose built for a commission for three large ships (Olympic, Titanic and Britannic) received from the White Star Line. White Star Line had decided they wanted to compete with the Cunard Line for the North Atlantic route between Britain and America. The need for the dry dock was first realized in 1903 as nowhere in Ireland, Great Britain or in fact the world had the facilities to handle such large ships. The plans for the dock were drawn up by Mr Redfern Kelly who was a Harbour Engineer.

The Works for the Dry Dock were issued in 2No Tenders. The first was for the 'Construction of a Graving Dock and Other Collateral' with tenders having to be lodged on or before 31st August 1903. The second was the tender for 'Caisson, Folding Bridge for New Graving Dock, Co Down'. This was issued on 23rd June 1904 with Tenders having to be lodged on or before Monday the 25th July 1904. Extract from second tender:

All Tenders submitted for this work are be accompanied by fully detailed Drawings and Specifications thoroughly descriptive of the design proposed, and also by a detailed

Schedule showing how the amount of the Tender has been arrived at.

Some people may say that at present there are some very tight schedules to make but how they came up with Drawings and Specifications in such a short turnaround with no CAD or computers is a miracle.

During the build of the Dry Dock the shape of Queen's Island would be changed as the lough had to be dredged and deepened and the reclaimed land was used to expand the island creating new space for two huge slipways over which a massive gantry would stand.

At the same time as the new Dry Dock was being constructed a new Pump House was also being built to replace the existing Pump House. This new Pump House served both the new Dry Dock and also the Alexandra Dock which is adjacent to the Thompson Dock. Up to 500 men were involved in the construction of Thompson Dock.

The Dry Dock was also one of the first major structures which used steel, much stronger then wrought iron which was used to construct other dry docks up to that point and is of considerable technical importance. Given the scale of the project and the difficult ground conditions, the construction of the dock was a considerable feat of engineering on reclaimed land.

Extract from the Original Tender Documentation:

'*The entire structure and workmanship of the Caisson shall be such that no water shall find its way through any part , or under any circumstances, and generally, the workmanship in the Caisson shall come under the highest class of the best shipbuilding work. If mild steel be used, it shall be the best mild steel, of British manufacture, and made according to the Siemens-Martin process, and it shall be of the same quality, and shall be subject to testing under the same conditions, as are required by the Admiralty.'*

The Thompson Dock was named after the Chairman of the Harbour Commission Robert Thompson whilst the Alexandra Dock was named after Princess Alexandra who cut the first sod. Alexandra Dock is currently where the HMS Caroline is docked.

At the time of the building of the Titanic there were over 200 different trades/crafts/professions on Queen's Island.

The process of building each vessel was standard. They first constructed the ship's hull on a slipway by riveting steel plates onto a skeletal ribbed structure, with the keel as the backbone. The engines and propeller shafts were not fitted at this stage as they may have become damaged as the ship was launched from the slipway. Following the launch, the ship would be towed to a fitting out quay. This is where the engine, electrics, plumbing and furnishings were put on board. Thompson Dock was primarily used to fit the propellers, to paint the hull, and remove any launch fittings still attached to the hull while the vessel was mounted onto keel blocks. The dock was also used to repair, to clean and to repaint vessels after time at sea.

When the work was completed the dock would be flooded by opening the sluice gates. The water level would then be the same level inside outside the dock allowing the vessel to sail into the Belfast Lough.

Record drawings indicate that at high tide level the gate retained some 12 metres of seawater and is of massive proportions, displacing some 1900T of water. When operational the water pressures were equalized on each side of the gate and it could then be winched by chains into the caisson chamber to allow passage of vessels into or out from the dock. The gate formed a water tight seal against the dock walls by means of full height timbers fixed to each extreme corner and bearing against the vertical face of Mourne Granite masonry blocks set into the dock wall. The width of bearing at each vertical timber is of the order of 0.2 – 0.25 metres at the upper region.

The Dry Dock can hold up to 21 million gallons of water (95,467,890 litres) which approximately equates to 172 swimming pools or 560,000 baths. This water could be drained in 1 hour 30 minutes.

When completed the dock statistics were:

Description	**Size Feet / Inches**
Nominal length of dock on floor	850ft
Length if caisson be placed against outer quoins	887 ft 6ins
Width of dock on floor	100ft
Width at entrance of dock	96ft
Width of coping level	128ft
Width at lowest altar course	104ft 6ins
Depth of dock floor at centre below level of high water of ordinary spring tides	37ft 3ins
Top of keel blocks below level of high water of ordinary spring tides	32ft 9ins
Height of top of blocks above floor	4ft 6ins
Level of entrance sill above dock floor at centre of dock	2ft
Bottom of dock floor at sides of dock below coping level	43ft 6ins
Thickness of dock floor at centre	17ft



Dry Dock with Vessel on Keel Blocks

3. THE PRESERVATION OF THE DRY DOCK

In November 2004 NISP commissioned a study to close off and protect the existing Thompson Dock and Gate from the influences of the sea. The proposals were then tabled to the Belfast Harbour Commissioners Estates Department.

The options were:

1 Cathodic protection of the existing gate

2 Proposal No1 – propped double sheet piled wall reinforced with concrete

3 Proposal No2 – reinforced concrete retaining structure

4 Proposal No3 – double sheet pile wall infilled with concrete and stone filling

5 Proposal No4 – sheet piling with tie backs to anchors

6 Proposed new gates

7 Flood the dock with tidal water

At that stage Thompson Dock was considered by Environment and Heritage Service (EHS) as a potential World Heritage Site and this was one of the reasons that the study recommended further investigation of Option 6 as this was the only option which would fully preserve the existing dock structure, while maintaining the dock as originally constructed and replicating the original appearance.

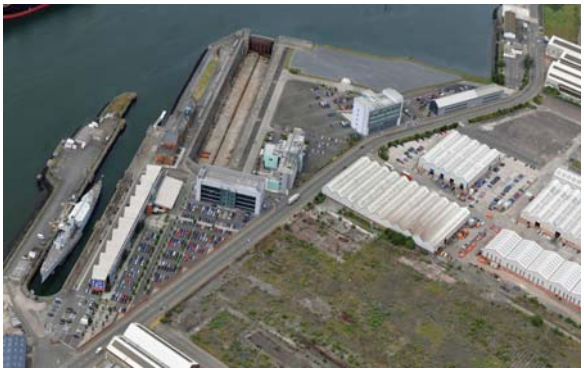
The report commented on the condition of the dock and gate and noted there were several points where significant vertical cracking had been observed in the dock walls and where water was percolating through. The position of the leakage was consistent and was at or near the third step above the near vertical internal dock face. This coincided with the top of the brick wall/permanent shutter outside the concrete walls. The leakage and the resulting growth of moss was more evident on the land face because there was no exposure to the sun, but there was likely to be a greater rate of leakage from the Victoria Channel side because the structure and sea protection there had deteriorated and been repaired.

As a scheduled monument, NISP worked with Northern Ireland Environment Agency (NIEA), formerly EHS, to develop and assess options for securing the structure of the Dry Dock. The key NIEA heritage principles were:

- The intervention should cause no damage to the existing structure
- The intervention should be reversible, should someone either for commercial or tourism reasons want to operate the dock and pump-house again and
- The intervention should match the site outlook, aesthetically.

After due consideration, it was decided that a new outer defence structure in the position of the existing outer gate otherwise known as the Titanic slot was the preferred solution. This solution would effectively retire the 100-year old steel structure from the attacks of the sea. It would enable the metal to be protected in perpetuity, while allowing public access to the Edwardian technology and craftsmanship of what effectively was a similar construction piece of engineering to Titanic itself – made with sheet steel plating, hot-riveted to a steel frame structure. The solution would be aesthetically pleasing, being of a similar scale and finish to what the gate would have looked like in the outer position and so enable this element of heritage intervention to be brought into the interpretation story. Very importantly this new defence structure in the outer position could be reversible, albeit it with difficulty, should it ever be decided to bring the dock into operational use again. Concrete was determined to be the most suitable material for the new defence structure to avoid having to maintain and ultimately replace another steel structure in the future.

Modern staircases were to be included within the scheme to allow the public to go down into the bottom of the dock. All stakeholders were really enthused about the proposals as access to the bottom dock would really compliment the new Titanic Belfast visitor attraction which was planned to open in early April 2012. It was noted that the NISP was acting for the greater good in progressing this plan, as for its own purposes, flooding the dock would have sufficed.



Thompson Dry Dock and Alexandra Dock 2010

CEI Collins Engineers Ltd (Collins) were instructed to undertake an inspection of the Thompson Dry Dock Gate in 2011 by NISP, as the last inspection had been carried out in 2003. The Dry Dock Gate was discovered to be in serious (near critical) condition with 81% steel section loss and severe corrosion evident. It was considered that without immediate intervention measures, the corrosion would reach a critical point where the gate could no longer withstand the water pressure, thus leading to flooding of the Dry Dock. The flooding of the Dry Dock would also inevitably lead to flooding of the Pump House basement, which is a listed building. It was evident that, if the gate was to be retained for posterity with a high degree of authenticity and the threat of flooding of the Dry Dock was to be removed, then a suitable replacement structure would need be installed on the seaward side of the existing gate. This would allow the existing gate to

be cleaned and refurbished in a manner that would allow it to retain its authenticity.



Inspection of Existing Caisson Gate

A recommendation was also made to seal the culverts to the Pump House to protect its subterranean structure, as the water ingress rate around and through the existing caisson gate structure increased, the existing pumping struggling to keep the Dry Dock free of water. Consideration was also to be given to installing submersible pumps in the main sumps of the Dry Dock floor to facilitate direct pumping into Belfast Lough via a discharge pipe laid in a gulley, up the personnel access stair/ramp and trenched across Clarence Wharf in an attempt to retain a Dry Dock free from water.

A load restriction was recommended on the dockside over the caisson gate recess chamber, due to the significant deterioration observed on the longitudinal support beams. It was recommended that NISP should consider making this area a permanent vehicle free zone.

Collins could not state exactly when an irreversible collapse would occur, but informed NISP that if measures were not taken in the short term NISP should consider flooding the Dry Dock to equalize the pressure on either side of the existing gate. Whilst this would prevent a catastrophic failure of the gate it would not prevent its ongoing deterioration, particularly in the intertidal zone. In addition marine growth would form on the base and walls/steps of the Dry Dock and it would then potentially have an adverse effect on the existing settlement cracks which were clearly visible in the walls of the Dry Dock.

Collins were subsequently instructed to undertake a technical report/ feasibility study for Thompson Dock / Gate; a total of nine options were considered and Budget Costs were estimated.

Option appraisal and statutory approval

The appraisal options ranged from

1 Flood the Dry Dock in a controlled way
2 Flood the Dry Dock and aerate the water
3 Repair the existing steel caisson gate
4 Fill the Dry Dock gate and caisson chamber with concrete and allow the gate to corrode away
5 Fabricate and install a new Dry Dock gate
6 Construct a defence structure at the outer gate position
7 Construct a defence structure beyond outer gate position

Collin's commission included an underwater inspection to further assess both the condition of the existing caisson gate and the existing concrete infrastructure around the mouth of the Dry Dock. This survey indicated that the Dry Dock structure was in very good condition for its 100 year old age. Considerable silt deposits were observed on the outer apron which was not surprising as the Dry Dock had not been used for over 10 years.

Accordingly, NISP sought statutory planning and scheduled monument approvals for the proposed outer concrete structure and obtained both. NISP also commenced the application for the Marine Licence, taking it to the stage where the successful Contractor had only to provide their details and construction method statement to NIEA to allow the Marine Licence to be granted for the works.

Meanwhile, a grant for £1.5m to cover all necessary works, against a Central Procurement Directorate (CPD) produced cost-estimate of a similar amount, was sought and obtained from Department of Education (DE) and others. In accordance with the terms of that grant, a full government style procurement process was undertaken by NISP. The Contractor proceeded to seek the Marine Licence.

4. TENDERING OF NEW DEFENCE STRUCTURE TO TITANIC'S DOCK & PUMP HOUSE

The preferred option agreed with NIEA was Option 5 and it was decided to proceed to prepare documentation for a Design and Build tender. The tender was for the provision of a new outer defence structure at the outer Dry Dock or Titanic gate location. This new outer defence structure would allow the original gate to remain insitu without the need for the original to be repaired for functional use. This new defence structure would also support a pedestrian walkway across the top, thus allowing safe access around the dock head and providing significant views up and down the Dry Dock and adjacent Musgrave Channel.

Within the Tender Documentation there was information regarding significant design assumptions and suggested work methods, sequences and/or other control measures. The details included a method of obtaining a waterproof seal between the new and existing structures. The tenderers were also made aware that Collins had prepared a Dive Inspection Report that confirmed that the granite wall only extended downward for a distance of approximately 3. 6 metres between the outer gate position and the seaward extremity. And beneath the masonry was a rough faced concrete wall which had slumped in places, leaving large voids which needed to be infilled. Also from historical drawings the depth on the concrete apron appeared

to be a uniform thickness. Due to a build-up of silt on top of the concrete apron, it was not possible to assess its condition. However, there did not appear to be any evidence of structural problems with the concrete apron within the inward section of the Dry Dock.

The details of how the new structure would be connected to the existing dry dock required to be approved by the Heritage section of the NIEA.

Tenderer's price was to include making good of the existing structure, cutting out from adjoining structures, cutting out wall plugs, preparing existing surfaces, making good and extending existing finishings and decoration, preparing to receive finishes etc.

The section for the insitu concrete asked for construction joints, leveling off the top surfaces with a tamped finish at the junctions or horizontal and vertical members for additional formwork and the casting where required of a continuous upstand section of the vertical member at the same time and integrally with the horizontal member.

The shortlisted tenderer was allowed to undertake some site investigation i) to determine the lengths of sheetpiles required for the cofferdam, ii) to take some samples to determine the waste category of the silt in front of the caisson gate and iii) to take some cores to determine the strength of the existing concrete walls.

A borehole was taken at the mouth of the existing dock and this showed soft to very soft silty clay with traces of timber until a depth of just over 5 metres when a stiff brown clay was encountered. Very strong sandstone was encountered at a depth in excess of 25 metres.

The Waste Acceptance Criteria testing of the silt showed some exceedances for Arsenic, Selenium, Chlorides and Dissolved Solids. It was considered however that overall the silt could be considered as non-hazardous.

5. CONSTRUCTION OF NEW CONCRETE DEFENCE STRUCTURE

The primary aim of the project was to conserve Titanic's dry dock and to safeguard the structural integrity of the Scheduled Monument. It was therefore important to agree protection measures prior to any of the main temporary or permanent works commencing on site. A pre-works photographic survey of the entire site was undertaken to identify any existing structural defects. It was agreed that heavy plant and machinery were not to be used inside restricted zones and the existing Dry Dock structure would be protected against superficial damage. Floating plant was used for the piling works to minimise point loads on the Dry Dock side and to reduce damage caused by heavy piling equipment. No materials or plant were permitted to be stored or work on or in close proximity to the steel caisson gate in order to prevent damage or its unintentional collapse.

Protection measures were also agreed for the caisson gate chamber, mooring bollards,, flushing chambers, cobble setts and kerbs, and other quay furniture.

The contractor obtained approval from Belfast Harbour Commissioners (BHC) to utilise a plough dredger to lower a plough onto the silt and then drag the silt and to deposit it adjacent to the Dry Dock at an agreed location.

The temporary works consisted of a sheetpile cofferdam which was constructed from 3 No steel box trusses spanning 37.5 metres between the ends of the existing Dock walls, installing 3 No. double pile caps and steel H-piles and driving a sheet pile wall against the truss structures.

The trusses were 3.75 metres deep by 3.75 metres in height and were formed from Universal Column sections with fully welded joint connections and were pre-fabricated off site and assembled on Stormont Quay and then transported across the Musgrave Channel by barge.

Once the sheet piling was complete, a non-porous bag was inserted down the last two profiled voids of the sheet pile wall for the entire height of the wall. These bags were then filled with C25/30 with a maximum 10mm aggregate. This effectively inflated the bag to form a seal between the piles and the dock wall, Divers inspected the bags as they were being filled to ensure that a seal was maintained

Dewatering behind the temporary works was then carried out to allow work to commence on the Permanent Structure. The Contractor liaised with NIEA to establish the Discharge Consent requirements. Two high lift 3'' pumps were used and discharged into a suitably sized silt buster to separate all solids from water to minimise turbidity in the water column at the discharge point. All silt was removed and disposed of in line with the Site Waste Management Plan (SWMP). The material was temporarily stored adjacent to the Dry Dock, where it was allowed to drain before being transported offsite. This helped maintain the adjacent road network in a clean condition, which would not have been the case had the material been taken offsite when wet.

In order to ensure that the forces being exerted on the Dry Dock by the cofferdam were not causing damage to the structure a monitoring regime was agreed, which included monitoring various elements of the structure. It was also agreed that bracing consisting of a steelwork frame would be installed across the void in the wall formed by the caisson gate chamber. Strain gauges were fitted to some of the horizontal struts across the opening and were monitored by Queens University Belfast over the initial tide cycles. This monitoring continued until it was demonstrated that there was negligible loading being applied to these struts via loading on the Dry Dock from the cofferdam.

After dewatering was complete, coring was carried out of the existing apron to confirm the strength and overall thickness of the concrete apron.



Dewatering of Cofferdam

A concrete strength of around 35 N/mm^2 was determined by testing which is considerably higher than would have been expected for 100 plus year old concrete.

The new concrete outer defence structure is approximately 32 metres long by 2.5 metres wide and 13 metres in height..The wall reinforcement was designed to "BS 8007: Design of concrete structures for retaining aqueous liquids" in order limit crack widths in service to below 0.2 millimetres and a total of 14 No. concrete pours were used to form the new defence structure.

A Concrete Design Mix was used with a basalt aggregate and a high percentage (50 – 70%) Ground Granulated Blastfurnace Slag to help reduce the heat of hydration and thus minimize early thermal cracking. Cast in thermocouples were used to monitor the temperature gradient across the 2.5 metre wide pours and additional insulation was applied as necessary. An example of some of the thermocouple monitoring is shown in the graph below.



Thermocouple Recording Graph for Pour '8'

The last pour was on 12 December 2012 and the structure was left to cure until late January 2013. Then the outer face was fitted with steel plates to a level between MLWS on the seaward face to replicate the aesthetics of a caisson gate to shipping traffic. Water was then allowed against the new structure in a controlled manner before the cofferdam was removed by the end of March 2013 and taken off site by April 2013 when the works were finally completed.

6. THE DRY DOCK GOING FROM STRENGTH TO STRENGTH

The new concrete outer defence structure allows the visitor a full circulatory path around the Dry Dock and the galvanized access stairs allows access to the floor where the overall size of the Dock can be fully appreciated in safety.

Both the Dry Dock and the caisson gate have been preserved and the Scheduled Monument is protected for the people of Belfast and for all visitors who wish to gain the full Titanic experience.

Since the refurbishment of Thompson Dock it has played host to several Events. Some examples of these events are:

Rock 'N' The Dock. This was a very special floodlit tour of Titanic's Dock and Pump-House rounded off with some of Northern Ireland's top musicians playing in the Pump-House. This event marked the official opening of the new access to the bottom of the Dock. Ticket holders had exclusive floodlit access to Titanic's Dock and Pump-House.

GTI NI Titanic Dubs 2012. The Dock played host to over 200 cars of all shapes and sizes with cars surrounding the Dock. The event also had a DJ, remote control car racing, boat rides and a number of waterski and wakeboard demos.

James Cameron the Director of 'Titanic' the movie visited the Dry Dock in September 2012 and was quoted as saying '

'Without a doubt this was the highlight of my Titanic experience in Belfast'



Director James Cameron on the Floor of Thompson Dock

'Belfast has made a list of Europe's top 10 travel destinations on rise. The dock where the Titanic was built is among must-see attractions listed by influential travellers' website Tripadvisor. The company recognized destinations that have seen the greatest increase in positive feedback and interest from travellers' year on year.'

REFERENCES

[1] Original Tender Documentation, Construction of a Graving Dock and Other Collateral Works, Belfast Harbour 1903.

[2] Original Tender Documentation for Caisson, Folding Bridge, & c, for New Graving Dock, Belfast Harbour, 1904.

[3] Outline Conservation Statement, Consarc Conservation, 2011.

[4] Thompson Dry Dock, Belfast, Protection of Dock from the Sea, Mouchel Parkman, 2005

[5] NEC Option A Open Procedure Ref 2685/11, Works Information – General, New Defence Structure to Titanic's Dock and Pump-House, WH Stephens, 2011

[6] Belfast is top European Travel Destination, Newsletter, 2012

Evaluation and Maintenance of Inland Waterway Weirs

Jim Harvey[1], Kerrie Gillen[2]
[1]Waterways Ireland, 2 Sligo Road, Enniskillen, Co. Fermanagh BT74 7JY
[2]CEI Collins Engineers Ltd., Unit G6 Riverview Business Park, Nangor Road, Dublin 12
email: Jim.Harvey@waterwaysireland.org
kgillen@collinsengr.com

ABSTRACT: Waterways Ireland is responsible for managing and maintaining Ireland's navigable inland waterways, as established under the British-Irish Agreement in December 1999. As part of this cross-border role, Waterways Ireland manage and maintain weirs and an array of other structures on its seven major waterways in order to fulfil their mission of providing a high quality recreational environment on the waterways in their care. Currently, there are approximately 59 weirs over the 1,000 kilometres of waterways and their associated branches. The weirs were originally constructed, in conjunction with locks, to alter the flow of rivers to make the rivers navigable, to prevent flooding and to measure discharge. The primary tasks associated with management of Waterways Ireland's inland waterway structures include the collection of inventory data and the regular determination of structure condition and strength via examination and assessment. This is then followed up with the repair, maintenance, rehabilitation and replacement of structures where necessary, allowing Waterways Ireland to manage its health and safety responsibilities. Dive examinations at river weirs can be high risk. If the Inspector considers there is enough visible evidence of the condition without a dive survey then an above water examination may suffice. The inspector will consider any historical records, evidence from low and high flow conditions, whether the weir is flowing smoothly, any crest subsidence and whether there is excessive turbulence downstream or on the downstream face, which could indicate loss of face material, holes or scour. This paper discusses the techniques involved in the examination of the vast array of historic weirs on Ireland's navigable waterways, the typical defects found, the condition rating and priority rating system adopted and the preservation methods utilised to bring the structures back to their original condition. The paper also discusses the environmental considerations associated with the rehabilitation works. Applicable Topic Areas: structures, materials.

KEY WORDS: Waterways Ireland; Weir; Underwater Examination; Condition; Repair; Birds; Flora; Fauna.

1.0 INTRODUCTION

Waterways Ireland manages and maintains weirs, sluices, locks and other structures on its seven major waterways.

Currently, there are 59 weirs located on the 1,000 kilometres of waterways and their associated branches. Figure 1.1 shows an overview of the Inland Navigable Waterways.

Waterways Ireland initiated an asset management programme for their river assets. This included a detailed examination programme for the weirs. As part of this process, the weirs were assigned a condition rating in accordance with Table 3.1.

To allow Waterways Ireland to prepare long term financial budgets for the maintenance of the weirs, preliminary repair recommendations were included in the examination reports along with associated outline repair costings. This paper also evaluates the environmental impact of the works.

2.0 EXAMINATION

An examination involves visual and tactile techniques in examining a weir, both above and below the waterline. An examination can be undertaken with the use of diving equipment and / or by careful wading. If the inspector considers there is enough visible evidence of the structure's condition without a diving survey, then an above water examination will suffice.



Figure 1.1 Waterways Ireland map

The examination of a weir normally consists of a Level I and Level II examination as defined below:

Level I Examination: A Level I examination includes a visual examination of the entire weir. It is detailed enough to detect obvious damage or deterioration. A Level I examination also includes limited probing of the substructure and adjacent channel bottom.

Level II Examination: A Level II examination is a detailed examination which requires areas of the weir to be cleaned of marine or aquatic growth. Level II examinations are intended to detect and identify damaged and deteriorated areas. The thoroughness of cleaning is governed by what is necessary to determine the condition of the underlying material. After cleaning, damaged areas are measured, and the extent and severity of the damage documented.

Some situations create difficulties for both diving and wading, e.g. fast river flow. In situations such as this, temporary dam measures are normally implemented to allow for examination. Many weir structures do not include adjacent de-watering facilities. In either scenario, sandbags can be utilised for such temporary damming.

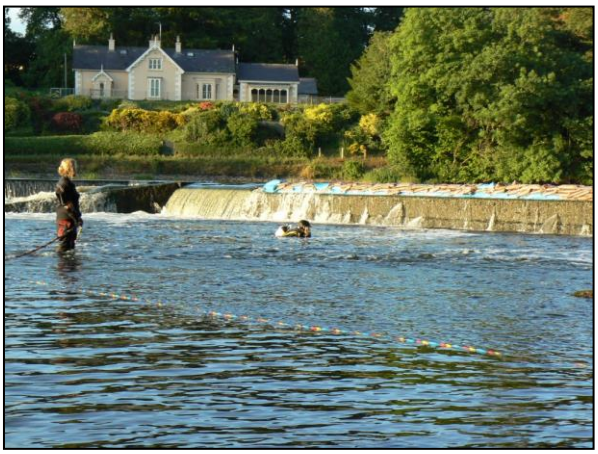


Figure 2.1 Examination of weir with assistance of temporary damming

The examination approach is decided by the team when on site at each location. The approach will depend on the flow conditions, historical records and the 'Toolbox Talk'. A 'Toolbox Talk' is given by the Dive Supervisor / Lead Engineer-Diver at the commencement of each examination, to all members of the team. Points discussed within the team include:

- Objective and plan of proposed works
- Hazards and work environment
- Individual responsibilities of personnel
- Operational equipment and materials
- Access and egress
- Conflicting activities and vessel schedules (if applicable)
- Emergency equipment and procedures

If diving is required, it is performed using full commercial surface supplied diving equipment. A suitable dive boat can also be utilised when required to gain access to each structure. When examining upstream, due to the inherently dangerous environment associated with weirs, a solid platform is preferable when undertaking diving operations.



Figure 2.2 Underwater examination of downstream portion of weir by diving, with evident water penetration through the weir

The current examination programme is a baseline survey. The extent of defects detected and risk analysis will determine the examination interval.

3.0 CONDITION RATINGS

As part of the condition examinations, Waterways Ireland uses a condition rating system ranging from 0 (Excellent Condition) to 5 (Unsafe / Failed Condition). Refer to Table 3.1 below for details:

Condition Assessment Ratings	
Rating	**Description**
0	**Excellent Condition** The structural element is of recent construction and exhibits no signs of deterioration.
1	**Good Condition** The structural element exhibits no significant deterioration or defects. Minor defects / deterioration noted to not more than 5% of any structural element.
2	**Fair Condition** The structural element is intact and its load carrying capacity is considered to be unaffected. Moderate defects / deterioration noted to not more than 30% of the structural element.
3	**Poor Condition** Advanced deterioration or numerous moderate defects noted to the structural element with the load carrying capacity and / or functionality of the element considered to be affected.

4	**Critical Condition** Advanced deterioration and significant defects noted to the structural element with the functionality and / or load carrying capacity of the element considered to be significantly reduced with local failures possible.
5	**Unsafe Condition** Localised failures observed with future and widespread failures of the structural element likely to occur. Structural integrity of the structure is compromised.

Table 3.1 Condition Assessment Ratings

In addition, a critical rating is assigned where a breach is noted in the weir, or where scour is noted in the channel bottom contributing to extensive undermining of the weir.

All the weirs have been examined and evaluated to date for their condition. Table 3.2 below gives a summary of the ratings assigned to those weirs.

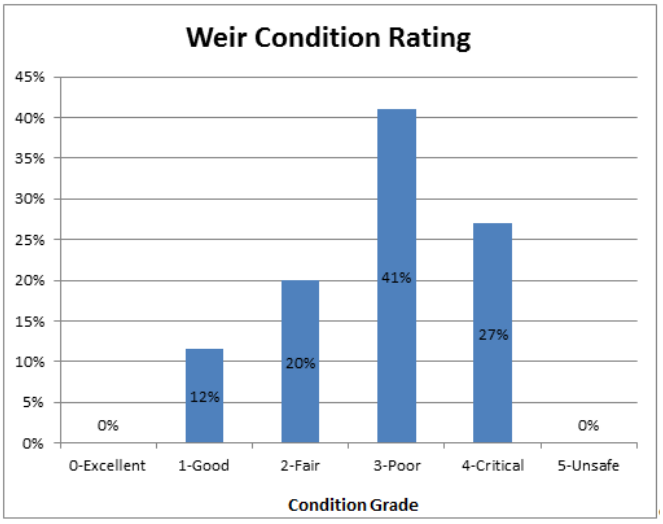


Table 3.2 Weir Condition Rating

4.0 REPAIR WORKS

There are two types of maintenance. Firstly operational maintenance. A relatively small amount of operational maintenance is undertaken. It is generally limited to repairing obvious damage and clearing detritus. The second is major maintenance. Typically defects are scour pockets and undercutting of the downstream apron.

Before any maintenance work is carried out it is important to consult with the various stakeholders, especially when major maintenance is required. The consultation will include:

1. Exploring the opportunities for upgrading benefits, e.g. Waterways Ireland is currently looking at the possibility of small scale hydroelectric generation at weir locations.
2. Avoiding or reducing adverse impacts on any particular stakeholder, e.g. Fisheries are looking to upgrade fish passes when Waterways Ireland are working at the weirs.
3. Establishing rights and responsibilities, e.g. checking with neighbours and landowners for access to the site.
4. Identifying risks and safety issues, e.g. temporary works and plant to be used.
5. Dealing with concerns and expectations before they become issues, e.g. the increasing number of canoeists also increases the demand for consideration of canoe ramps.

Key design issues will include:
1. Fish passes, types and location.
2. Cofferdam details, e.g. stone, puddle clay, piles, rubber dams.
3. Flood protocols – what happens in a high flow event.
4. Hydrological changes.
5. Archaeology, what studies are needed.

There are various repair options available for dealing with wash-out of joint material, voids, undermining and scouring of weirs, which are discussed below.

4.1 Re-pointing of Weirs

Re-pointing of masonry weirs is preferably done in the dry. For pointing in a wet / dry range, 1 part natural cement is normally mixed with 3 parts natural hydraulic lime mortar (NHL) along with well graded sharp sand.

Where pointing underwater cannot be avoided, a neat proprietary product is required which will set quickly. This is normally mixed with a retarder with a working time of 1-2 minutes. The product is mixed to a putty-like consistency before being placed underwater.

4.2 Rip-rap Construction

Rip-rap should, where possible, be laid so that the stones pack into a close interlocking layer with the size of scour minimised. Where laid on geotextile, great care is needed not to damage the geotextile. Ideally, the first layer of stone should be placed to give as much contact with the surface of the geotextile as possible.

A common problem encountered during the construction of rip-rap is quality control of the size and gradation of stone used. Various methods have been developed for quality control of stone for rip-rap. At its most basic, a stockpile should be visually examined to check minimum, maximum and average stone sizes. In addition, it is often useful to weigh stones to obtain an example of each of the three sizes (minimum, maximum and average), which can be set aside for comparison against stockpiles. Where large quantities of stone are used, examination can involve sorting several truckloads of stone into piles of three or four different stone sizes. Each pile is then weighed and compared with the total sample weight, thus giving the proportion of the total stone in each size category. A representative stone in each pile can then be weighed to define the typical weight that each pile represents.

An alternative method is to monitor as-placed rip-rap gradings using surface sampling techniques. This involves measuring the size of stones exposed on a constructed section of rip-rap to give a representation of the plan area occupied by different stone sizes.

Another problem is that the stones can segregate during loading at the quarry, or during handling and placing, giving a different as-laid grading to that at the quarry. Careful quarrying, loading and placing practices are needed to avoid this. The stone may need to be remixed before placing to reduce segregation.

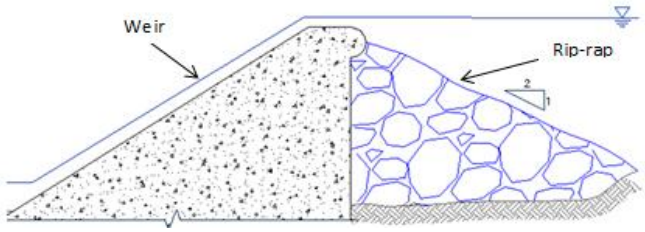


Figure 4.1 Typical Scour Repair Option for Weir

4.3 Grout-filled bags and mattresses

Bags and mattresses filled with cement grout or concrete can be a cost-effective method for infilling voids. The bags may either be filled with a dry mixture that hydrates and hardens on contact with water, or grout can be pumped into the bags. In the past, the fabric used was hessian, but today synthetic fabrics such as polyester and polypropylene are used. The fabric acts as a shutter to retain the grout and form the shape of the voided area. Mattresses (and less commonly bags) can also be laid on stable slopes and beds.

This type of scour protection is used particularly in underwater conditions and for temporary repairs. It is often used to form a concrete apron underwater, with the mattresses being filled from floating or land-based plant using tremie pipes.

The revetment is essentially an impermeable and inflexible revetment. Where a build-up of hydrostatic pressure could occur, the weight should be sufficient to avoid uplift or allowance should be made for pressure relief.

The main mode of failure with this type of protection is undermining, leading to gradual collapse of individual compartments. Vulnerability is greatest where lateral or vertical channel movement can be expected, in which case flexible mattresses or bags may be a better alternative.

4.4 Flexible bags and mattresses

Alternatives to rigid grout-filled systems are flexible filled systems. Flexibility can be introduced to grout-filled mattresses by suitable connectors at joints and, to a certain extent, between pockets, by the use of continuous seams within a mattress. These mattresses can be strengthened with cables.

Bags and mattresses can also be filled with sand or locally won fill to provide a more flexible revetment than grout-filled systems, and where cement or rock is too costly or not readily available.

Whereas concrete grout-filled mattresses remain a robust protection system after the fabric bags deteriorate or are torn, sand-filled mats rely on the retention function of the fabric to be secure and are therefore less robust. Above water, the effects of ultraviolet deterioration and potential vandalism have to be taken into account. Below water, damage by dredging and abrasion has to be considered. Care must be taken to avoid damage during construction.

Sand-filled mats have been found to withstand velocities of typically 2.5 m/s. For protection against higher velocities, large sand-filled bags or cement and concrete grout-filled bags and mattresses should be used.

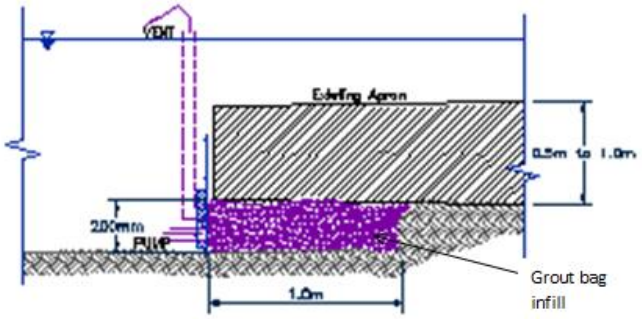


Figure 4.2 Typical Undermining Repair Option

4.5 Access

All repair works require access to the site to allow the movement of plant, labour and materials, and to facilitate the removal of any waste from the site. In the context of river works, sites are often difficult to access and may incur negative environmental impacts. Access requirements should therefore be investigated early in the planning process so that:

- The design can be adapted if necessary to suit any restrictions on access (physical or environmental)
- Negotiations with affected landowners and other interested parties can be started in good time
- Enabling works, such as tree pruning or footpath closure can be organised in advance of the works starting on site. Such works may be season-dependent – this should be considered early on in the planning process.

4.6 Temporary Works

Temporary works are those required as an essential part of the construction works (or demolition works), but which will generally be removed as the construction progresses. Some temporary works may be left in place to form part of the permanent works – for example, sections of steel sheet piling used for a cofferdam can remain to form upstream and downstream cut-offs.

In the context of work on a weir temporary works might include:

- Temporary diversion of the river to allow construction of the weir in dry conditions
- Cofferdams in the river to allow work to progress on the weir in stages
- Access road across a field that will be removed on completion of the work
- Temporary bridge or ford across the stream to facilitate access to both banks
- Temporary fish passage

These works can have significant environmental impacts and therefore should be considered in the development of the design to ensure that adverse impacts are minimised, and that beneficial environmental opportunities are recognised and taken up.

It must also be remembered that temporary works in the river will have to function in varying flow conditions, and may be exposed to large floods. Information on the flow conditions in the river should therefore be made available to those responsible for designing and constructing the weir.

4.7 Sequence and Timing

The best time for carrying out engineering works in a river is normally in the summer (i.e. when flows are at their lowest), but this is often the time when adverse environmental impact is likely to be greatest, and recreational use at its highest. For minimum impact on fish, construction in the autumn and winter is probably the best option. A compromise is often therefore required. With proper planning and consultation it is possible to minimise the impacts without unduly compromising the engineering operation (or greatly increasing costs). Particular seasonal activities to avoid include:

- Angling, especially organised events and competitions
- Navigation and boating (from Easter to Autumn)
- Bird and mammal breeding
- Fish migration, spawning and ova development

4.8 De-watering

Most repair works require de-watering to expose the structure and give reasonably dry conditions. In its simplest form, this might involve sandbagging off part of the weir crest to do a patch repair. For more extensive repairs, the construction of an earth or sheet pile cofferdam to isolate part of the structure is required. There are also proprietary portable dam systems formed from structural frames and an impermeable membrane that can be used to effect a temporary closure of a stream to allow remedial works to go ahead. For major works, the temporary diversion of the river or stream may be considered, allowing unrestricted access to the weir. However, such a diversion would itself require a temporary weir structure as well as a channel diversion, to ensure that the diversion was stable for the duration of the works.

5.0 ENVIRONMENTAL IMPACT

5.1 Desktop review

Historic examination reports are studied / reviewed in advance of field work to identify locations that would be affected by proposed repair works. A desktop review is carried out to identify features of ecological importance within the study area. Potential sites of conservation interest are identified prior to the field survey by an examination of Ordnance Survey (OS) maps.

Special Areas of Conservation (SACs), Special Protection Areas (SPAs), Natural Heritage Areas (NHAs), proposed Natural Heritage Areas (pNHAs), and records of protected species in the vicinity of any proposed works are identified in advance of the field surveys.

During the preparation of an ecological assessment, direct consultation is undertaken with the following statutory bodies and non-governmental organisations:

- Inland Fisheries Ireland;
- National Parks and Wildlife Service;
- Bat Conservation Ireland.

5.2 Field Survey - Habitats and flora

A field survey and ecological site walkover is undertaken at each of the proposed works sites to establish the character of each site and environs and to identify what ecological constraints, if any, are present. A botanical survey of each location is undertaken, during the optimum botanical survey season. Information is recorded in relation to the primary habitats directly affected by and adjacent to the proposed repairs works following the Heritage Council publication '*Best Practice Guidance for Habitat Surveying and Mapping*' (Smith *et al.,* 2011), taking account of the National Roads Authority (NRA) (2009) '*Ecological Surveying Techniques for Protected Flora and Fauna during the Planning of National Road Schemes'*. A list of the dominant and notable plant species is taken for each habitat type, including protected species and non-native species.

Aquatic and riparian habitat assessment is carried out at each of the proposed repair works sites; the identification of Floating River Vegetation habitats is carried out visually at each proposed works site and a species inventory obtained.

The presence and location of non-native invasive flora, is also assessed during the ecological surveys.

5.3 Field Survey - Fauna

Faunal surveys for specific species follows the methodology set out in the NRA (2009) '*Ecological Surveying Techniques for Protected Flora and Fauna during the Planning of National Road Schemes'.*

Otter surveys undertaken at each site follow the methodology set out in the NRA (2009) and also guidance published by English Natura (Chanin, 2003).

With regard to aquatic fauna, a sweep/kick net is used to sample the biota of the substrates, in-stream vegetation, submerged bank-side vegetation and undersides of overhanging clay banks.

An assessment of the usage of each site by lamprey and salmonids include a visual assessment of the river section with regard to suitable spawning habitat.

An inventory of fauna recorded, or likely to occur within each site, is prepared to include mammal species (including bats), breeding bird species (and potential for wintering birds) and invertebrate species recorded during the aquatic and terrestrial site surveys. The presence of non-native invasive fauna, principally aquatic, is assessed during the ecological surveys.

5.4 Appropriate Assessment

A Stage 1 Appropriate Assessment (i.e. a Screening Report to inform Appropriate Assessment) is required for proposed repair works to weirs if located within a Special Protection Area (SPA) or Special Areas of Conservation (SAC).

SPAs and SACs both form part of Natura 2000, a network of protected areas throughout the European Community. Designated Natura 2000 sites within a 15km radius of the proposed repair works are assessed. The context of Appropriate Assessment is with regard to Council Directive 92/43/EEC on the conservation of natural habitats and of wild fauna and flora – 'The Habitats Directive'. The Birds Directive (2009/147/EC) seeks to protect birds of special importance by the designation of Special Protection Areas (SPAs), whereas the Habitats Directive does the same for habitats and other species groups within Special Areas of Conservation (SACs), which are currently designated as candidate Special Areas of Conservation (cSAC) in Ireland.

The Appropriate Assessment Stage 1: Screening exercise can result in one of three conditions:

- An Appropriate Assessment is not required i.e. where the plan / proposal is associated with the management of the site;
- There is no potential for significant effects i.e. Appropriate Assessment is not required;
- Significant effects are certain, likely or uncertain i.e. the project must either proceed to Stage 2: Appropriate Assessment or be rejected.

5.5 Considerations prior to undertaking the works

The timing of the proposed works need to take account of the breeding season of crayfish, as well as spawning seasons at all of the works sites; with sensitive periods avoided.

Any alteration to or construction of new fish passage solutions at proposed works sites require a detailed design and assessment provided by qualified hydraulic engineers and fisheries biologists to ensure that the measures imposed are suitable for all fish.

If proposed works are not completed before the next bird breeding season, a bird survey is normally recommended to be carried out in the vicinity of proposed works areas.

To ensure lampreys and white-clawed crayfish are not killed or displaced by proposed works it is not unusual for them to be translocated from affected areas prior to the works and removed to other parts of the river.

It is normally recommended that an Environmental Management Plan be drawn up prior to any works taking place. This details the extent of proposed repair works at each site including any associated works e.g. access, fish pass proposals, silt / debris removal. This Management Plan provides a framework and parameters for the Method Statement to be prepared by the contractor appointed for the works, limiting / avoiding the potential for ecological impacts.

6.0 CONCLUSION

Weirs, as important assets in controlling river levels and supporting important habitats, require periodic examination and on-going maintenance to ensure the integrity of the structures. Typical defects are scour and undermining.

A limited amount of operational maintenance is undertaken on weirs in good condition. Major maintenance is undertaken as the condition of the weir begins to deteriorate. As over two-thirds of the weirs examined to date are in poor or worse condition, significant funding is needed to return these structures to their original condition. In doing so, it is vital that the surrounding natural environment is not adversely affected and opportunities are taken when major maintenance is occurring to explore benefits such as hydroelectric generation, replacement fish passes or canoe ramps.

REFERENCES

[1] Charles Richard; Rodney Day; Jeremy Purseglove; Mott MacDonald Ltd and University of Hertfordshire on behalf of Environment Agency *River Weirs – Good Practice Guide – Section B2, 2003.*

[2] Ecofact Environmental Consultants, *Ecological Assessment: Proposed Repair Works to Weirs / Sluices on the Barrow Navigation, July 2013.*

[3] Ecofact Environmental Consultants, *River Barrow Navigation – Proposed Repairs to six weirs / sluices on the River Barrow - Screening for Appropriate Assessment July 2013.*

[4] May, R W P; Ackers, J C; Kirby A M, Construction Industry Research and Information Association, *Manual on scour at bridges and other hydraulic structures.*

[5] Smith et al, *Best Practice Guidance for Habitat Surveying and Mapping, 2011.*

[6] NRA, *Ecological Surveying Techniques for Protected Flora and Fauna during the Planning of National Road Schemes.*

Author Index

Al-Sabah, S. A. 131
Allen, B. 439
Amato, G. 51
Archbold, P. 205
Backus, J. 317, 457
Bai, Y. 149, 445
Baily, E. 229
Barrett, R. 167
Barry, J. 433
Basheer, M. 149, 295, 475, 487
Borthwick, A. 7
Boyle, D. 193
Browne, T. 241
Brownjohn, J. 131
Bruton, D. 301
Cahill, F. 21
Cahill, P. 39, 45
Cantero, D. 125
Casey, P. 409
Causer, E. 379
Cleland, D. 173
Colford, B. 1
Coleman, Donogh 445, 469
Coleman, Daniel 81
Collery, D. 333, 505
Collins, T. 241
Connaire, A. 259
Connolly, L. 137
Corbally, R. 21, 179
Daly, A. 21
Deegan, P. 217
Devlin, B. 511
Doherty, C. 173, 185
Doherty, P. 363, 421
Dolan, D. 69
Donnelly, A. 311
Dousti, M. R. 327
Duffy, L. 15
Dunne, D. 333, 505
Dunne, H. 57
Enright, B. 111
Fallah, S. 345
Farrell, E. 339, 397
Farrell, K. A. 351
Farrell, N. 339
Favai, P. 179
Ferrara, L. 227
Finnegan, W. 253
Fleming, M. 409
García-Taengua, E. 217
Gavin, K. 345, 363, 421
Ghosh, B. 481
Gilbert, R. B. 301
Gill, D. 339, 397

Gillen, K. 517

Glennon, C. 75

Goggins, J. 161, 229, 253, 321

González, A. 125

Green, C. 295

Grimes, J. 385

Grimes, M. 311, 385

Hajdukiewicz, M. 161, 321

Hajializadeh, D. 33

Hamill, G. 247

Hanniffah, M. R. M. 7

Hanley, C. 51

Hao, T. Y. 487

Harte, A. 63, 69, 75, 87, 99, 105, 259

Harvey, J. 517

Heanen, A. 173

Hennity, G. 511

Hester, D. 131

Hodge, D. 373

Holmes, N. 451, 457

Hughes, D. 317

Hyde, C. 167

Jackson, N. 39, 45

Jalilvand, S. 421

Kattsardi, V. 7

Keenahan, J. 117

Kenna, F. 205

Kennedy, K. 277

Kieran, P. 229

King, D. 321

Kinnane, O. 155, 385

Kissane, P. 155

Kolakowski, P. 179

Laefer, D. 351, 357

Leahy, C. 111

Leen, S. 167, 259

Long, A. 457

Long, M. 415

Lydon, M. 27, 173, 185

Ma, Q. 149

Magee, B. 487

Malekjafarian, A. 199

Mathewson, A. 39, 45

McCabe, B. 229

McConnell, E. 93

McCracken, C. 27

McCrum, D. 27, 499

McGroarty, C. 357

McIntosh, J. 143

McKenna, T. 367, 445

McKenna, P. 333, 505

McManus, P. 273

McMenamin, P. 493

McNally, C. 469

McNulty, P. 27

McPolin, D. 63, 87, 93, 97, 105, 457

McQuaid, G. 265, 283

McRobert, J. 247, 289

Millar, P. 265, 277, 283

Minehane, M. 235

Mitchell, R. 277

Mohammed, A. K. 311

Mohammed, O. 125

Moore, T. 317

Murphy, J. J. 57, 85, 433, 439, 463

Nanukuttan, S. 149, 289, 295, 475, 487

Newell, S. 311

Noble, D. 427

Nogal, M. 427

Ní Choinne, M. 137

O'Byrne, M. 481

O'Ceallaigh, C. 63, 99

O'Connor, A. 21, 33, 137, 427

O'Donoghue, P. 167

O'Donovan, R. 235, 463

O'Flynn, B. 193

O'Halloran, S. 259

O'Keeffe, B. 235

O'Murchu, O. 357

O'Neill, C. 63, 105

O'Riordan, B. 445

O'Rourke, B. 367, 373, 463, 469

O'Brien, E. 33, 111, 117, 179, 199

Orr, S. 493

Orr, T. 403

Paine, K. 333

Pakrashi, V. 39, 45, 51, 427, 481

Pattarini, A. 217

Pavia, S. 155, 211, 223

Prendergast, L. 363

Quigley, P. 415

Raynor, D. 415

Reape, S. 167

Reilly, C. 403

Richardson, M. 367, 469

Robinson, D. 27, 185

Ruane, K. 57, 235, 379, 391, 433, 463

Ruta, C. 415

Ryan, D. 247

Schoefs, F. 481

Scully, S. 167

Shinnick, D. 391

Sikora, K. 63, 87, 105

Smyth, W. 247

Solan, B. 493

Solera, S. 415

Sonebi, M. 217, 317

Soutsos, M. 143

Staino, A. 499

Swan, C. 7

Strong, A. 273

Taylor, P. H. 7

Taylor, S. 27, 93, 105, 173, 185, 217

Twomey, C. 373

van Loo, H. 179

Walker, R. 211

Walsh, D. 391
Wang, J. 475
Ward, C. 289
Watley, M. 491
West, R. 303, 311, 327, 385, 451
Withworth, J. 493
Woershing, H. 193
Woodward, D. 265, 273, 277, 283
Wu, Z. G. 487
Yang, C. 149
Žnidarič, A. 179